Transactions of the ASME®

Transactions of the ASME, Journal of Heat Transfer (ISSN 0022-1481) is published quarterly (Feb., May, Aug., Nov.) for $150 per year by The American Society of Mechanical Engineers, 345 East 47th Street, New York, NY 10017. Second class postage paid at New York, NY and additional mailing offices. POSTMASTER: Send address changes to The Journal of Heat Transfer, c/o THE AMERICAN SOCIETY OF MECHANICAL ENGINEERS, 22 Law Drive, Box 2300, Fairfield, NJ 07007-2300.
CHANGES OF ADDRESS must be received at Society headquarters seven weeks before they are to be effective. Please send old label and new address.
PRICES: To members, $24.00, annually; to nonmembers, $150.00.
Add $6.00 for postage to countries outside the United States and Canada.
STATEMENT from By-Laws. The Society shall not be responsible for statements or opinions advanced in papers or . . . printed in its publications (B7.1, para. 3).

INDEXED by Engineering Information

Journal of Heat Transfer

Published Quarterly by The American Society of Mechanical Engineers

VOLUME 109 • NUMBER 3 • AUGUST 1987

ANNOUNCEMENTS

TECHNICAL PAPERS

(Contents continued on page 556)

(Contents continued)

(Contents continued on page 568)

(Contents continued)

TECHNICAL NOTES

Integral Solution of Diffusion Equation: Part 1—General Solution

A. Haji-Sheikh
Mem. ASME

M. Mashena[1]

Mechanical Engineering Department,
University of Texas at Arlington,
Arlington, TX 76019

A generalized method is presented that accommodates the linear form of the diffusion equation in regions with irregular boundaries. The region of interest many consist of subregions with spatially variable thermal properties. The solution function for the diffusion equation is decomposed into two solutions: one with homogeneous and the other with nonhomogeneous boundary conditions. The Galerkin functions are used to provide a solution for a diffusion problem with homogeneous boundary condition and linear initial condition. Problems with nonhomogeneous boundary conditions can be dealt with by many other schemes, including the standard Galerkin method. The final solution is a combination of these two solutions.

Introduction

Many partial differential equations do not readily accept exact solutions because of the complicated geometries and/or spatially variable thermal properties. The method presented herein promises to encompass a large class of problems which do not accept simple and closed-form solutions. This method was used by LeCroy and Eraslan (1969) for calculating temperature development in the entrance region of an MHD parallel plate channel. However, because of the complexity associated with the analytical and numerical integration of numerous multiple integrals it has received little attention. The availability of symbolic manipulator software which can carry out analytical differentiation and integrations has greatly enhanced the potential of this method as a powerful tool for heat transfer calculations.

The Galerkin method has been used successfully for obtaining solutions for Poisson and Laplace equations in regions with irregular boundaries (Kantorovich and Krylov, 1960; Ozisik, 1980). The Galerkin functions are arranged in a more generalized form, hence the Galerkin method is extended to accommodate the diffusion equation effectively. The Galerkin method is a useful tool to obtain a variety of closed-form solutions. The method discussed is an approximate closed-form solution and is parallel to the exact solution; hence it requires computation of certain eigenvalues. This paper, Part 1, is devoted to the derivation of the basic solution using the boundary condition of the first kind and matrix algebra for numerical computations. In Part 2, the boundary conditions of the second and third kinds are included, and a Green's function is introduced as a convenient tool to accommodate nonhomogeneous boundary conditions. The procedure described in Parts 1 and 2 is recommended for boundary value problems that do not accept exact solutions despite their simple geometric shape, e.g., electronic cooling, phase-change problems, thermal entry in hydrodynamically fully developed flow in ducts, etc. In many of these applications, the finite difference and finite element methods have a tendency to become computationally time consuming when the number of nodes or elements is large. With the use of a personal computer, this method can provide solutions in minutes whereas a finite difference method that uses body-fitted coordinates would require days of processing. Although it is not an exact solution, it offers the benefits and limitations one expects from an exact solution.

The solution of the diffusion equation in a closed region is divided into two solutions: a quasi-steady solution and a transient solution. All the nonhomogeneous boundary conditions are assigned to the quasi-steady solution in which time is treated as a parameter. The Galerkin functions are well suited to the transient solution with a homogeneous boundary condition.

The accuracy of this method is investigated through a numerical example and yields highly promising results. In many cases, it is possible to obtain an accuracy exceeding four significant figures. The procedure for handling a nonhomogeneous material domain is discussed.

Analysis

One objective of this paper is to demonstrate that the Galerkin functions are useful for handling numerous and various types of diffusion problems. These problems become amenable to the use of Galerkin functions if their boundary conditions are homogeneous. Hence, it is necessary to include the nonhomogeneous boundary conditions in another solution. Accordingly, the solution T is written as

$$T = T^* + T_t \tag{1}$$

where T^* and T_t are quasi-steady and transient solutions. In addition, this scheme promises a faster convergence (Olcer, 1964), at least when this method is considered analogous to the exact solution. It is expected that there will not be a need for a large number of eigenvalues to obtain acceptable accuracy.

The quasi-steady solution T^* accounts for all the nonhomogeneous boundary conditions. The transient solution T_t leads to an eigenvalue problem. For simplicity of presentation, the diffusion problem under consideration will be viewed as the diffusion of heat; hence T may be regarded as temperature. The number of eigenvalues N needed for an accurate solution depends on the rate of change in the surface temperature of the original problem. Therefore, a step change in the surface requires a larger number of eigenvalues, while only a few are sufficient for a slower change in surface temperature.

The governing equation in a relatively general form is written as

$$\nabla \cdot (k \nabla T) + g(\mathbf{r}, t) = \rho C_p \partial T / \partial t \tag{2}$$

where $T = T(\mathbf{r}, t)$ is temperature, $\mathbf{r}$ is position vector, and t is time. It is assumed that the thermal conductivity k, density ρ, and specific heat C_p are independent of temperature; however, no other restriction as to spatial variation of these thermophysical properties is needed. This point will be discussed in further detail following the forthcoming derivations.

The substitution of equation (1) into equation (2) results in the following two equations:

[1]Presently at the University of Al Fateh, Faculty of Engineering, Tripoli, Libya.

Contributed by the Heat Transfer Division and presented at the 23rd National Heat Transfer Conference, Denver, Colorado, August 1985. Manuscript received by the Heat Transfer Division June 10, 1985.

$$\nabla \cdot [k \nabla T^*(\mathbf{r}, t)] = 0 \tag{3a}$$

and

$$\nabla \cdot [k \nabla T_t(\mathbf{r}, t)] + g(\mathbf{r}, t) = \rho C_p \partial T_t(\mathbf{r}, t)/\partial t \tag{3b}$$

Equation (3*a*) is arranged so that the time t, in the time-dependent boundary condition, will be treated as a parameter. Accordingly, equation (3*b*) must satisfy a homogeneous set of boundary conditions, while the initial condition can be nonhomogeneous. A solution of this type is a true solution based on the uniqueness theorem (Churchill, 1941) if T^* and T_t are obtained from the exact solution. However, a solution obtained using a finite number of Galerkin functions is expected only to approximate an exact solution. Theoretical studies on convergence properties of the Galerkin method are presented in Kantorovich and Krylov (1960).

Solution of T_t. The following derivation is aimed toward a generalized solution, but the numerical examples presented are for the Dirichlet-type boundary conditions (first kind). Boundary conditions of the second and third kinds are discussed in Part 2 of this paper. The solution for the complementary form of equation (3*b*), that is, in essence, the diffusion equation in the absence of heat generation

$$\nabla \cdot (k \nabla \theta) = \rho C_p \partial \theta / \partial t \tag{4}$$

with homogeneous boundary conditions can be written as

$$\theta = \sum_{n=1}^{N} c_n F_n(\mathbf{r}) \exp(-\gamma_n t) \tag{5}$$

The function $F_n(\mathbf{r})$ is selected so that (*a*) the homogeneous boundary conditions are satisfied and (*b*) equation (5) is a solution of equation (4). The former condition is exactly satisfied by the use of proper Galerkin functions. The latter is accommodated if equation (5) is substituted into equation (4), resulting in

$$\nabla \cdot [k \nabla F_n(\mathbf{r})] + \rho C_p \gamma_n F_n(\mathbf{r}) = 0 \tag{6}$$

Hence, the diffusion equation has been reduced to an eigenvalue problem. The function $F_n(\mathbf{r})$ becomes the eigenfunction if problem accepts an exact solution. However, for many problems, the function $F_n(\mathbf{r})$ must be constructed from a complete set of functions, each satisfying the homogeneous boundary conditions but not necessarily equation (6). They are selected in accordance with the Galerkin guideline. Therefore, the function $F_n(\mathbf{r})$ can be written as

$$F_n(\mathbf{r}) = \sum_{j=1}^{N} d_{nj} f_j \tag{7}$$

The function f_j is a Galerkin function obtained by multiplying a function $\phi(\mathbf{r})$ by an element of a complete set of functions. The function $\phi(\mathbf{r})$ is selected so that the homogeneous boundary conditions are satisfied. The method of selection of $\phi(\mathbf{r})$ is discussed in a numerical example to appear later.

The Galerkin procedure is utilized by multiplying both sides of equation (6) by $f_i dV$ and integrating over the volume V. The result is then divided by V mainly for convenience of numerical computations

$$\frac{1}{V}\int_V f_i \nabla \cdot (k \nabla F_n) dV + \frac{1}{V}\int_V \rho C_p \gamma_n f_i F_n dV = 0 \tag{8}$$

Substituting for F_n from equation (7) and using the divergence theorem results in the following relation for computation of the eigenvalues

$$(\mathbf{A} + \gamma_n \mathbf{B})\mathbf{d}_n = 0 \tag{9a}$$

in which **A** and **B** are matrices of the size N with elements

$$a_{ij} = \frac{1}{V}\int_V f_i \nabla \cdot (k \nabla f_j) dV = -\frac{1}{V}\int_V k \nabla f_i \cdot \nabla f_j dV \tag{9b}$$

and

$$b_{ij} = \frac{1}{V}\int_V \rho C_p f_i f_j dV \tag{9c}$$

Matrices **A** and **B** are symmetric. The values of a_{ij} and b_{ij} in equations (9*b*) and (9*c*) must be computed analytically or numerically. For complex problems, it is convenient to utilize a symbolic computer system to carry out the analytical integrations which result in more accurate values and often require less computation time. The software with the aforementioned capabilities are available from commercial sources.

From this point on, the computation of T_t can be accomplished following algebraic manipulation of matrices **A** and **B**. The next step is the evaluation of the needed eigenvalues. The eigenvalues $\gamma_1, \gamma_2, \ldots, \gamma_N$ can be obtained analytically if N is small; otherwise numerical steps become necessary. The symmetric nature of **A** and **B** simplifies the numerical computation of the eigenvalues. Once the eigenvalues are in hand, the values of the eigenvector d_{nj} corresponding to the eigenvalue γ_n can be calculated. The coefficient d_{n1} may be selected equal to unity without any loss of generality. Hence, d_{nj} for each n is a row of matrix **D**. However, once the eigenvalues are computed the eigenvectors are readily attainable. As long as the boundary conditions are homogeneous, matrix **A** will be symmetric. Since matrix **B** is positive and symmetric, often the determination of the eigenvalues and eigenvectors can be greatly simplified. An accurate method for computation of the eigenvalues and eigenvectors is to decompose matrix **B** into $\mathbf{LL}^t$, where **L** is a lower triangular

Nomenclature

a_{ij} = element of matrix **A**, equation (9*a*)
A_n = coefficients for initial condition
b = height of the cone
b_{ij} = element of matrix **B**, equation (9*b*)
A, **B** = matrices
c_n = Fourier-type coefficient
C_p = specific heat
d_{nj} = coefficients, equation (7)
$\mathbf{d}_n$ = eigenvector containing d_{nj}
D = matrix with element d_{nj}
e_{in} = element of matrix **E**, equation (12*a*)
E = matrix
f_i = basis functions
F_n = solution function
g = generation per unit time and per unit volume
i, j = indices
k = thermal conductivity
L = lower triangular matrix
l = coordinate index
m, n = indices
N = number of eigenvalues
p_{ni} = element of matrix **P**
P = inverse of matrix **E**
r = radial coordinate
t = time
T = temperature
T_0 = initial temperature distribution
T_s = surface temperature
T_t = transient solution
T^* = quasi-steady solution
u = velocity
V = volume
x = coordinate
z = coordinate
γ_n = eigenvalue
θ = homogeneous solution
λ = element of λ, right-hand side of equation (18)
ρ = density
ϕ = Galerkin function
χ = solution array, equation (13)
ψ_i = element of ψ, right-hand side of equation (11)

matrix and $\mathbf{L}^t$ is its transposed matrix. This decomposition of matrix $\mathbf{B}$ is instrumental in reducing equation (9*a*) to

$$(\mathbf{L}^{-1}\mathbf{A}\mathbf{L}^{-t}+\gamma_n\mathbf{I})\bar{\mathbf{d}}_n=0 \tag{9d}$$

where $\mathbf{L}^{-1}$ and $\mathbf{L}^{-t}$ are the inverses of $\mathbf{L}$ and $\mathbf{L}^t$. The matrix $\mathbf{L}^{-1}\mathbf{A}\mathbf{L}^{-t}$ is a symmetric matrix and d_n is the eigenvector corresponding to the eigenvalue γ_n. The eigenvector $\mathbf{d}_n$ is then equal to $\mathbf{L}^{-t}\bar{\mathbf{d}}_n$.

A solution for the generalized form of equation (3*b*) may be obtained by considering c_n in equation (5) to be time dependent. The remaining algebraic steps are analogous to the method of the variation of coefficients often used to solve nonhomogeneous ordinary differential equations. The general solution will have the following form:

$$T=T^*+\sum_{n=1}^{N}c_n(t)F_n(\mathbf{r})e^{-\gamma_n t} \tag{10}$$

The substitution of equation (10) into equation (2) followed by the use of the standard Galerkin procedure (Kantorovich and Krylov, 1960) results in a system of N equations

$$\sum_{n=1}^{N}c_n'(t)e^{-\gamma_n t}\frac{1}{V}\int_V F_n f_i dV=\psi_i \tag{11a}$$

where

$$\psi_i=\frac{1}{V}\int_V [g(\mathbf{r},\,t)-\rho C_p\partial T^*/\partial t]f_i dV \tag{11b}$$

and $i=1, 2, \ldots, N$. Once the value of $F_n(\mathbf{r})$ from equation (7) is substituted into equation (11*a*) the result will be

$$\sum_{n=1}^{N}e_{in}c_n'(t)e^{-\gamma_n t}=\psi_i \tag{12a}$$

where

$$e_{in}=\sum_{j=1}^{N}d_{nj}b_{ji} \tag{12b}$$

and $i=1, 2, \ldots, N$. Therefore, e_{in} is an element of matrix $\mathbf{E}$. Matrix $\mathbf{E}$ can be defined if $\mathbf{D}$ is multiplied by $\mathbf{B}$ and the resulting matrix is transposed. The values of c_n' are obtainable by inverting matrix $\mathbf{E}$. Now, the following form of equation (12)

$$\mathbf{E}\cdot\chi=\psi \tag{13}$$

is utilized for calculation of c_n' in which the arrays χ and ψ have elements $c_n'(t)\exp(-\gamma_n t)$ and ψ_i. If both sides of equation (13) are multiplied by $\mathbf{E}^{-1}$, the inverse of $\mathbf{E}$, one obtains

$$\chi=E^{-1}\cdot\psi \tag{14}$$

Matrix $\mathbf{E}^{-1}$ may be designated as $\mathbf{P}$ with elements p_{ni} which permits writing the elements of array χ, equation (14), as

$$c_n'(t)e^{-\gamma_n t}=\sum_{n=1}^{N}p_{ni}\psi_i \tag{15}$$

and, following integration, to

$$c_n(t)=A_n+\sum_{i=1}^{N}p_{ni}\int_0^t\psi_i(t')e^{\gamma_n t'}dt' \tag{16}$$

where A_n represents the constant of integration. The substitution of equation (16) into equation (10) yields the final form of the solution

$$T=T^*+\sum_{n=1}^{N}F_n(\mathbf{r})e^{-\gamma_n t}\left[A_n+\sum_{i=1}^{N}p_{ni}\int_0^t\psi_i(t')e^{\gamma_n t'}dt'\right] \tag{17}$$

The second term in equation (17) represents the contribution of basic conduction and the third term contains the influence of an internal heat source. The solution presented by equation (17) is complete once A_n and T^* are evaluated. The initial condition can be utilized for computation of the constant A_n. The use of the Galerkin procedure (Kantorovich and Krylov, 1960) results in a set of linear algebraic equations for the A_n

$$\sum_{n=1}^{N}A_n e_{in}=\lambda_i;\ \text{for}\ i=1, 2, \ldots, N \tag{18a}$$

where

$$\lambda_i=\frac{1}{V}\int_V\rho C_p(T_0-T^*)f_i dV \tag{18b}$$

in which $T_0(\mathbf{r})$ is the initial distribution of T, $T_0^*(\mathbf{r})$ is T^* as $t\to 0$, and e_{in} is the element of matrix $\mathbf{E}$ whose inverse is $\mathbf{P}$ as defined earlier. Then A_n is obtained from

$$A_n=\sum_{n=1}^{N}p_{ni}\lambda_i \tag{18c}$$

The coefficients $A_1, A_2, \ldots, A_N$ are analogous to the Fourier coefficients in the exact solutions.

Solution of T^*. The quasi-steady assumption, described earlier, implies that T^* satisfies equation (3*a*) although it may contain the parameter t. Also, it must satisfy the nonhomogeneous boundary conditions similar to those for function T. A more general method of treating nonhomogeneous boundary conditions is possible by introducing a Green's function, see Part 2. A considerable degree of simplification is realized for a special but widely used boundary condition which is time dependent but independent of position. For boundary conditions of the first kind, the quasi-steady solution becomes

$$T^*=T_s(t) \tag{19}$$

where $T_s(t)$ is the surface temperature. Since the quasi-steady temperature, for this particular case, is independent of position, a section of the contour may be subject to the boundary condition of the second kind without a need for any modification for T^*. However, major changes are necessary if boundary conditions of the third kind are involved. Other cases should be treated individually but in certain circumstances complications may be encountered. An extensive treatment of the solution of the Poisson and Laplace equations by the Galerkin method and numerous detailed theoretical discussions are given in Kantorovich and Krylov (1960).

Numerical Example. The accuracy of this method is examined through a numerical example. Although this example has an exact solution, it has many ingredients of a complicated system for which the manual integration of the elements of matrices $\mathbf{A}$ and $\mathbf{B}$ are cumbersome. A cone is considered to be initially at zero temperature. The surface temperature everywhere on the surface, except at the base, is increased to a unit value. The base of the cone is assumed to be insulated. The equation for this conic surface in the cylindrical coordinates is

$$r^2-(1-z/b)^2=0 \tag{20}$$

where b is the height of the cone. If $\phi(\mathbf{r})$ is selected equal to the left-hand side of equation (20), then $\phi(\mathbf{r})$ will vanish unconditionally on the conic surface. However, it will not satisfy the boundary condition of the second kind at the base where $z=0$. A simple method for accommodating a flat, insulated surface is to treat that surface as a perfect mirror with each point on the conic surface having a mirror image. The mirror image of the conic surface about the $z=0$ plane is

$$r^2-(1+z/b)^2=0 \tag{21}$$

As suggested by the Galerkin method (Kantorovich and Krylov, 1960) $\phi(\mathbf{r})$ is the product of equations (20) and (21)

$$\phi=[r^2-(1-z/b)^2][r^2-(1+z/b)^2] \tag{22}$$

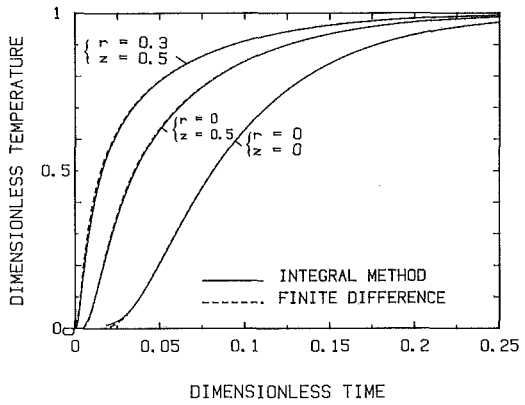

Fig. 1 Temperature distribution in a cone; $b=1$, $T_0=0$, $T_s=1$, $g=0$

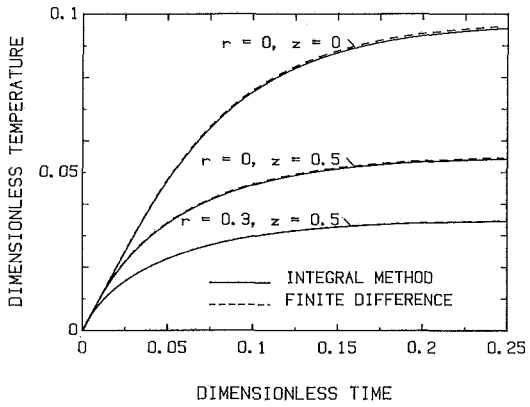

Fig. 2 Temperature distribution in a cone; $b=1$, $T_0=0$, $T_s=0$, $g=1$

Once ϕ is defined, the basis functions $f_1, f_2, \ldots, f_N$ can be determined as

$$f_1=\phi,\quad f_2=\phi r^2,\quad f_3=\phi z^2,\quad f_4=\phi r^4,\quad f_5=\phi r^2 z^2,\quad f_6=\phi z^4,\quad \ldots \tag{23}$$

The elements of matrices **A** and **B** are computed using equations (9*b*) and (9*c*) utilizing the symbolic software "REDUCE"; accordingly, all integrations over the domain of interest were carried out symbolically. Using equation (19), the quasi-steady temperature has a value of unity while the initial temperature is $T_0=0$. In order to conserve space, the matrices **A**, **B**, **D**, **E**, and **P**, for $N=3$, appear in the Appendix. The results when $N=10$ and $b=1$ are computed and presented in Fig. 1. The temperature distribution at three selected points is compared with the results from an explicit finite difference solution. The agreement between this method and the finite difference solution with step size of 0.1 is excellent except when $r=0$, $z=0$, and time is very small. When the step size is reduced to 0.05, the finite difference results coincide with the solid line (Fig. 1). The eigenvalues for different values of N are listed in Table 1. It is of interest to note that the smaller eigenvalues assume highly accurate asymptotic values as the number of terms N increases. This implies that, at higher values of t, an accuracy of better than four significant figures can be realized. This property becomes significant whenever this method is used for computation of the heat transfer coefficient (Haji-Sheikh et al., 1983) in a thermally, fully developed flow in a duct.

The major usefulness of this closed-form solution can be realized by examining the form of the final solution, equation (17). As long as matrices **A**, **B**, **D**, and **P** are available, many other solutions can be obtained quickly with little effort. They include various heat generation cases and many variations of the surface temperature. As an illustration, consider heat being generated at a constant rate in this conical region. The contribution of the quasi-steady solution and conduction due to a change in the surface temperature, equation (17), remains unchanged. The only quantity to be evaluated is the contribution of heat generation which is included in ψ_i. The quantity appearing on the right-hand side of equation (11), when $T_0=0$ and $T_s=1$, is the negative of the quantity on the right-hand side of equation (18*a*). Figure 2 represents the contribution of internal heat generation in equation (17), prepared when $N=10$ for a value of $g=1$. The time, temperature, coordinates, and g in Figs. 1 and/or 2 may be regarded as dimensionless. Other values of g and T can be computed by linear combination of the values in Figs. 1 and 2. Figure 2 represents the solution for temperature distribution in the region under consideration when both the surface temperature and the initial temperature are zero. The results exhibit excellent agreement with the finite difference solution with a step size of 0.1.

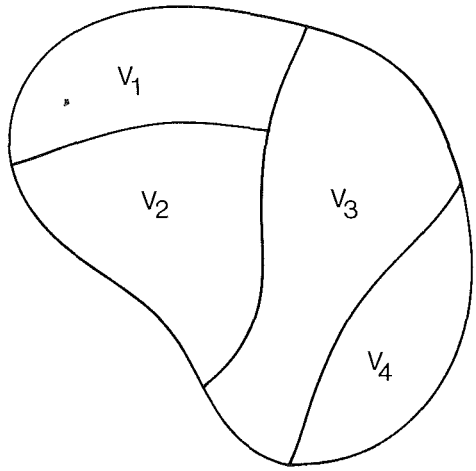

Fig. 3 Schematic of a composite region

Discussion

The strongest and most direct application of this method is to solve conduction problems in arbitrarily shaped bodies with boundary conditions of the first kind. In principle, it is possible to construct basis functions when there are boundary conditions of the first, second, third kinds, or any combinations thereof. To date, the process is simple for some cases and tedious for others; see Part 2. A few classes of important diffusion problems are mentioned in the following portion of this paper.

Composites. A region, as shown in Fig. 3, may include many subregions, each with thermophysical properties designated by subscript m. The mathematical procedure for this class of problems remains the same as in the case for a homogeneous region, except for computation of matrices **A** and **B** whose elements become

$$a_{ij}=-\frac{1}{V}\sum_m \int_{V_m} k_m \nabla f_i \cdot \nabla f_j dV \tag{24a}$$

and

$$b_{ij}=\frac{1}{V}\sum_m \int_{V_m} \rho C_p f_i f_j dV \tag{24b}$$

The basis functions are to be selected for region $V=V_1 \cup V_2 \cup V_3 \cup \ldots$ in the same manner as discussed for a homogeneous region. However, for better accuracy, the basis functions should be modified at the inclusion site to satisfy the continuity of heat flux at the inclusion boundary.

Table 1 Eigenvalues λ_j for the cone when $b = 1$

i	Number of terms				
	M = 1	M = 3	M = 6	M = 10	M = 15
1	17.6	16.97476	16.97141	16.97137	16.97138
2		56.79977	51.83633	51.67740	51.67486
3		80.29486	67.10717	66.57803	66.56943
4			126.4516	107.6688	106.0970
5			160.3773	123.9988	121.2760
6			234.5809	162.3364	155.7838
7				236.0060	187.9589
8				287.3154	206.0081
9				385.3736	247.8598
10				547.9721	318.9747
11					394.5109
12					476.3346
13					603.2707
14					811.1711
15					1108.6164

Thermal Conductivity With Directional Dependence. The modification of the previous case is limited to matrix **A**, where equation (24*a*) becomes

$$a_{ij} = -\frac{1}{V}\sum_m \int_{V_m} \sum_{l=1}^{3} k_{ml}(\partial f_i/\partial x_l)(\partial f_j/\partial x_l)dV \qquad (25)$$

where x_l with $l = 1$, 2, or 3 is the coordinate and k_1, k_2, and k_3 are thermal conductivities in the direction of the respective coordinates. In more complicated cases, the directional dependence of thermal conductivity will influence the quasi-steady solution.

Entrance Heat Transfer in Ducts. Whenever a fluid flow in a duct is considered to be hydrodynamically fully developed, the governing equation is a form of the diffusion equation similar to equation (2), except ρC_p should be replaced by $\rho u C_p$ and t by the axial coordinate in the direction of flow. Of course, the function u is the local velocity in the axial direction and it is position dependent. With the exception of these minor differences, the procedures described for a standard conduction problem should be used. For ducts with constant wall temperature, the first eigenvalue, as shown by Haji-Sheikh et al. (1983), is directly related to the average Nusselt number when the flow becomes thermally fully developed. The excellent accuracy of the first eigenvalue is an interesting feature of this method.

Remarks

The method presented in this paper uses the Galerkin functions and Galerkin procedure and hence it has the same limitations as the Galerkin method. It is an efficient tool for providing closed-form solutions for many problems. This solution provides maximum accuracy in the neighborhood of the boundary, a feature that is not shared by the finite difference solution. This feature is useful whenever an accurate value for heat flux is desirable. Mathematically, it is a general solution; however, its success depends on the availability of the basis functions. In some cases the procedure is simple and in other cases additional effort is necessary.

The strength of this method is its simplicity of utilization and its accuracy. The computer program written for this paper can be used to solve many axisymmetric diffusion problems, within the stated limitations, by specifying the contour of the geometry and the limits of integration. The subroutines for

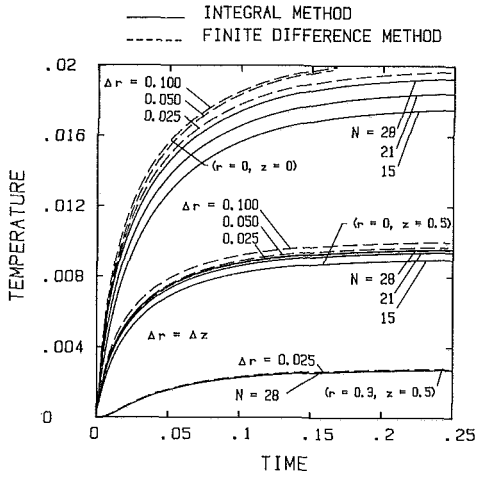

Fig. 4 Temperature distribution in a cone; $b = 1$, $T_0 = 0$, $T_s = 0$, $g = 1$ when $0 < z < 0.5$ and $r < 0.15$ and $g = 0$ elsewhere

computation of **A**, **B**, λ, and ψ are computed and written in a FORTRAN-acceptable code by the computer. Only minor editing need be carried out by the programmer. The simplicity and accuracy of this method can be demonstrated if the same computer program used for a cone is used to calculate temperature as a function of time at the center of a sphere. The boundary condition and the initial condition of the sphere are similar to those stated in Fig. 1. At the center, where the expected error is the largest, a temperature of 0.2924 corresponding to a time of 0.1 is calculated. This compares favorably with the exact value of 0.29290. Moreover, the accuracy improves as the dimensionless time increases. For instance, when the dimensionless time is 0.2, each method yields a value of 0.72292 and a similar or better accuracy is achieved when $t > 0.2$.

More eigenvalues are necessary when dealing with a problem that has a step change in one of the parameters. As an illustration, consider that heat generation in the previous example occurs in a cylindrical subregion between $z = 0$ and $z = 0.5$ with a radius of 0.15, centrally located within the conical geometry discussed earlier. The only quantity to be evaluated is ψ_i, which is integrated analytically and is included in the Appendix for $N = 3$. Similar to the data in Fig. 2, the computations are carried out and results are presented in Fig. 4 for $N = 15$, 21, and 28. Also, the corresponding finite difference solutions for step sizes of 0.1, 0.05, and 0.025 are plotted in the same figure. The agreement between the finite difference and integral methods is excellent except in the neighborhood of $z = 0$ and $r = 0$ point where the true solution appears to be somewhere between the two methods. The deviation of the finite difference or integral method from the true solution is near 1.5 percent, acceptable for many applications, e.g., in electronic cooling. Figure 4 indicates that a larger number of eigenvalues and a finer mesh size for a finite difference solution are needed for better agreement. When $r = 0.3$ and $z = 0.5$, the solutions vary slightly with the value of N or with a refined finite difference step size Δr. Since matrices **A** and **B** are produced and written as a subroutine in a FORTRAN-acceptable code by the computer, this increase in N did not pose any difficulty. There are schemes to improve the speed of the finite difference method and to reduce the number of eigenvalues needed. Further elaboration on this point is beyond the scope of this paper.

The main computer software required is a symbolic mathematical package which can carry out definite integrals and perform differentiation. The availability of a matrix package which includes matrix addition and multiplication, transposing a matrix, matrix inversion, and matrix eigenvalue

computation is also desirable. Many problems can be handled in a much simpler fashion than exact, finite difference, or finite element methods. The proliferation of symbolic software in the scientific community makes solution methods of this type attractive for future research. There are many variations of this method yet to be investigated. For instance, any complete set of basis functions which satisfies the boundary conditions can be used without a major modification of the procedure presented in this paper. Therefore, the use of the Galerkin functions is not a prerequisite for a successful solution.

The similarity of this approach to the so-called exact solution is an interesting feature of this method. Many schemes such as superposition of solutions, Duhamel's theorem, etc., can be used in conjunction with this method. This allows one solution to accommodate many other applications.

Acknowledgments

This work was supported by the National Science Foundation, Grant No. MEA 83-12754, and The Mechanical Engineering Department, University of Texas at Arlington.

References

Churchill, R. V., 1941, *Fourier Series and Boundary Value Problems*, McGraw-Hill, New York.

Haji-Sheikh, A., Mashena, M., and Haji-Sheikh, M. J., 1983, "Heat Transfer Coefficient in Ducts With Constant Wall Temperature," ASME JOURNAL OF HEAT TRANSFER, Vol. 105, pp. 878–883.

Kantorovich, L. V., and Krylov, V. I., 1960, *Approximate Methods of Higher Analysis*, Wiley, New York.

LeCroy, R. C., and Eraslan, A. H., 1969, "The Solution of Temperature Development in the Entrance Region of an MHD Channel by the B. G. Galerkin Method," ASME JOURNAL OF HEAT TRANSFER, Vol. 91, pp. 212–220.

Mashena, M., and Haji-Sheikh, A., 1984, "An Integral-Numerical Solution of Some Diffusion Problems," ASME Paper No. 84-WA/HT-41.

Olcer, N. Y., 1964, "On the Theory of Conductive Heat Transfer in Finite Regions," *Int. J. Heat and Mass Transfer*, Vol. 7, pp. 307–314.

Ozisik, M. N., 1980, *Heat Conduction*, Wiley, New York.

APPENDIX

This appendix is prepared to illustrate the type of output expected from a symbolic mathematical software and a matrix algebra package. Since it is not practical to list all the 10×10 matrices used in the numerical studies, only relevant matrices of the smaller size are given. The following information is for 3×3 matrices to be used with the conic geometry problem discussed in the main portion of this paper.

Matrix A

The elements of matrix **A** are

$$a_{11} = -96(19b^2 + 13)/945b^2)$$
$$a_{12} = -48(9b^2 + 13)/(2079b^2)$$
$$a_{13} = -48(43b^2 + 11)/10395$$
$$a_{22} = -48(53b^2 + 43)/(19305b^2)$$
$$a_{23} = -96(23b^2 + 13)/135135$$
$$a_{33} = -48b^2(45b^2 + 43)/45045$$

Matrix B

The elements of matrix **B** are

$$b_{11} = 384/2079, \qquad b_{12} = 96/3861$$
$$b_{13} = 96b^2/9009, \qquad b_{22} = 192/32175$$
$$b_{23} = 96b^2/96525, \qquad b_{33} = 384b^4/225224$$

Numerical Values of Matrices

The following matrices are computed, for $b = 1$.

$$\mathbf{A} = \begin{matrix} -3.25079 & -0.507937 & -0.249351 \\ -0.507937 & -0.238695 & -0.0255744 \\ -0.249351 & -0.0255744 & -0.0937729 \end{matrix}$$

$$\mathbf{B} = \begin{matrix} 1.84704\text{E}-1 & 2.48640\text{E}-2 & 1.06560\text{E}-2 \\ 2.48640\text{E}-2 & 5.96737\text{E}-3 & 9.94561\text{E}-4 \\ 1.06560\text{E}-2 & 9.94561\text{E}-4 & 1.70496\text{E}-3 \end{matrix}$$

$$\mathbf{D} = \begin{matrix} 1 & -0.56972 & -0.980604 \\ 1 & -12.6942 & 11.9116 \\ 1 & -4.21433 & -8.75332 \end{matrix}$$

$$\mathbf{E} = \begin{matrix} 1.60257\text{E}-1 & -3.99445\text{E}-3 & -1.33566\text{E}-2 \\ 2.05293\text{E}-2 & -3.90401\text{E}-2 & -8.99016\text{E}-3 \\ 8.42421\text{E}-3 & -1.83397\text{-}2 & -8.45948\text{E}-3 \end{matrix}$$

$$\mathbf{P} = \mathbf{E}^{-1} = \begin{matrix} 7.12053 & -4.00866 & -6.98242 \\ 1.40836 & -17.8780 & 16.7759 \\ 10.1441 & -42.7506 & -88.7946 \end{matrix}$$

$$(1/V)\int f_i dV = \{12/35,\ 4/63,\ 8/315\}$$

$$\psi_i = \{3549429/1.28\text{E}8,\ 63264483/2.048\text{E}11,\ 7066881/3.584\text{E}9\}$$

Integral Solution of Diffusion Equation: Part 2—Boundary Conditions of Second and Third Kinds

A. Haji-Sheikh
Mem. ASME

R. Lakshminarayanan
Graduate Student.

Mechanical Engineering Department,
University of Texas at Arlington,
Arlington, TX 76019

An analytical solution of the diffusion equation using the Galerkin method to calculate the eigenvalues is currently available for boundary conditions of the first kind. This paper includes algebraic techniques to accommodate boundary conditions of the second and third kinds. Several case studies are presented to illustrate the utility and accuracy of the procedure. Selected examples either have no exact solutions or their exact solutions have not been cited because of the mathematical or numerical complexity. The illustrations include transient conduction in hemi-elliptical solids with either external convective surfaces or convective bases, and buried pipe in a square enclosure. Whenever possible, symbolic programming is used to carry out the differentiations and integrations. In some cases, however, the integrations must be strictly numerical. It is also demonstrated that a Green's function can be defined to accommodate many geometries with nonorthogonal boundaries subject to more complex boundary conditions for which an exact Green's function does not exist.

Introduction

The solutions of the diffusion equation in various geometries are limited to two types: exact and numerical. Whenever the boundaries are orthogonal, that is, the normal to the boundary at any location points in the direction of a coordinate axis, there is an exact solution when the boundary conditions are linear. If an exact solution is not available, numerical methods are employed. There are other approximate methods, many of them for one-dimensional problems, others with limited capability. The method presented here complements the existing analytical and numerical techniques in two ways. First, it can be used whenever a closed-form solution is needed and an exact solution either does not exist or is too tedious to obtain. Solutions of this type are presented in this paper. Second, it has the potential to solve problems such as transient conduction in heterogeneous materials with numerous inclusions, while a comparable finite difference or finite element solution would require an unreasonably large number of nodes.

The analyses used in this paper are partially developed in the accompanying paper, Part 1, to solve diffusion problems with boundary conditions of the first kind. It is demonstrated herein that this procedure applies equally to boundary conditions of the second and third kinds. Many closed-form solutions of problems that do not accept exact solutions can be solved with personal computers, thus significantly reducing labor and computer costs. For instance, the computation of heat transfer in entrance regions of various triangular ducts using only a standard personal computer has been reported by Lakshminarayanan and Haji-Sheikh (1986). The efficiency and accuracy of this method are superior to the difference methods for many problems and it is an appropriate tool whenever the computation cost is a prime factor. This method is classified as analytical and may be viewed as a spectral-type solution that uses a single element and allows time to remain continuous. The advantages of analytical methods are the compactness of the results, ability to carry out parametric studies, and utilization of many mathematical tools such as superposition of solutions, Duhamel's theorem, Green's function, etc. The Green's function particularly enhances one's ability to deal effectively with nonhomogeneous boundary conditions. Moreover, a parametric study often results in simple relations for limiting or asymptotic solutions. Despite its much broader scope, like other analytical methods, it requires an iterative procedure to deal with nonlinear problems of the Volterra type.

The present work extends the analytical procedure used in Part 1 and by Lakshminarayanan and Haji-Sheikh (1986) and Haji-Sheikh (1986) for boundary conditions of the first kind to solve diffusion problems in the presence of boundary conditions of the second and third kinds. Since the Galerkin procedure is used to calculate the eigenvalues, a complete set of basis functions is needed. The remaining analytical steps to achieve a solution are based on the derivations presented in Part 1. For accurate solutions, a number of multiple integrals must be carried out analytically or numerically. The availability of basis functions that accept analytical integrations is highly desirable whenever the surface temperature suffers a rapid temperature change and a symbolic software that can handle all differentiations and a majority of the integrations is a valuable computational tool, especially for complex geometries. Because the basis functions for any given problem are not unique, the primary goal is to find a set that permits analytical evaluation of the required multiple integrals. A few methods of determining the basis functions that are either available in the literature or developed for this study are discussed. An analytical solution can be used in conjunction with Duhamel's theorem or a Green's function to solve many problems for the same geometry. A Green's function is defined for problems with homogeneous boundary conditions which can be used to accommodate nonhomogeneous boundary conditions (Ozisik, 1980). It will be demonstrated that an alternative form based on the Green's function is mathematically equivalent to a solution prepared using the analytical procedure described in Part 1. The availability of a Green's function based on the Galerkin procedure is a powerful method for solving transient thermal conduction problems.

Contributed by the Heat Transfer Division and presented at the ASME Winter Annual Meeting, Anaheim, California, December 1986. Manuscript received by the Heat Transfer Division June 10, 1985.

Analysis

The integral method under consideration is most effective when used to compute thermal diffusion in a closed region, with or without holes. The region may contain a time or a time- and position-dependent heat source and the thermophysical properties may be position dependent. The governing equation is

$$\nabla \cdot (k \nabla T) + g(\mathbf{r}, t) = \rho C_p \partial T / \partial t \tag{1}$$

where $\mathbf{r}$ is the position vector, $g(\mathbf{r}, t)$ is the volumetric heat source, and $T = T(\mathbf{r}, t)$ is the position- and time-dependent temperature. The general solution requires solution of the homogeneous equation (see Part 1)

$$\nabla \cdot (k \nabla \theta) = \rho C_p \partial \theta / \partial t \tag{2}$$

subject to homogeneous boundary conditions of the first, second, or third kind.

The solution of equation (2) is (see Part 1)

$$\theta = \sum_{n=1}^{N} c_n F_n(\mathbf{r}) \exp(-\gamma_n t) \tag{3}$$

in which

$$F_n(\mathbf{r}) = \sum_{j=1}^{N} d_{nj} f_j(\mathbf{r}) \tag{4}$$

where d_{nj} is the eigenvector corresponding to the eigenvalue γ_n and $f_j(\mathbf{r})$ is the basis function. The numerical values of γ_n and d_{nj} are obtained from the relation

$$(\mathbf{A} + \gamma_n \mathbf{B}) \cdot \mathbf{d}_n = 0 \tag{5}$$

in which $\mathbf{A}$ and $\mathbf{B}$ are matrices of size $N \times N$ with elements

$$a_{ij} = \int_V f_i \nabla \cdot (k \nabla f_j) dV \tag{6a}$$

$$b_{ij} = \int_V \rho C_p f_i f_j dV \tag{6b}$$

and $\mathbf{d}_n$ is the eigenvector corresponding to eigenvalue γ_n with elements $d_{n1}, d_{n2}, \ldots, d_{nN}$. In practice, the volume integrals should be multiplied by the factor $1/V$ to prevent the matrix elements from becoming excessively large or small and to avoid occasional numerical overflow or underflow.

Once the homogeneous solution is available, numerous other problems can be accommodated. Two distinctly different methods are proposed and will be discussed: a direct solution using superposition and the application of Green's function. Also, the equivalence between these two approaches is discussed.

Method 1. The local temperature distribution can be decomposed into two solutions (see Part 1)

$$T = T^*(\mathbf{r}, t) + T_t(\mathbf{r}, t) \tag{7}$$

in which $T^*(\mathbf{r}, t)$ is the solution of equation

$$\nabla \cdot [k \nabla T^*(\mathbf{r}, t)] = 0 \tag{8a}$$

subject to nonhomogeneous boundary conditions. Time in this equation is treated as a parameter. However, $T_t(\mathbf{r}, t)$ must satisfy the equation

$$\nabla \cdot [k \nabla T_t(\mathbf{r}, t)] + g(\mathbf{r}, t) = \rho C_p \partial T_t(\mathbf{r}, t) / \partial t \tag{8b}$$

in conjunction with a set of homogeneous boundary conditions. Therefore, the nonhomogeneous boundary conditions are assigned to equation (8*a*) while equation (8*b*) only satisfies boundary conditions of the homogeneous type. Once the solution of equation (2), that is, equation (3), is in hand, the general solution becomes (see Part 1)

$$T = T^* + \sum_{n=1}^{N} F_n(\mathbf{r}) e^{-\gamma_n t} \left[A_n + \sum_{i=1}^{N} p_{ni} \int_0^t \psi_i(t') e^{\gamma_n t'} dt' \right] \tag{9}$$

where p_{ni} is the element of matrix $\mathbf{P}$ computed from equation

$$\mathbf{P} = [(\mathbf{B} \cdot \mathbf{D})^t]^{-1} \tag{10}$$

in which $\mathbf{D}$ is a matrix whose rows are the eigenvectors. Moreover, the value of $\psi_i(t)$ is obtained from

$$\psi_i(t) = \int_V [g(\mathbf{r}, t) - \rho C_p \partial T^* / \partial t] f_i dV \tag{11a}$$

and the coefficient A_n is computed using the initial condition

$$A_n = \sum_{i=1}^{N} p_{ni} \int_V \rho C_p [T_0(\mathbf{r}) - T^*(\mathbf{r}, 0)] f_i dV \tag{11b}$$

Method 2. The procedure outlined here is that described by Ozisik (1980) for finding a Green's function and the same notations will be used here. However, modifications are made so that the properties ρ, C_p, and k are now position dependent. The description herein highlights the modifications of the derivations presented in Ozisik (1980). The Green's function to be determined must satisfy the equation

$$\nabla \cdot (k \nabla G) + \rho(\mathbf{r}') C_p(\mathbf{r}') \delta(\mathbf{r}' - \mathbf{r}) \delta(\tau - t) = \rho C_p \partial G / \partial t \tag{12}$$

Nomenclature

a = geometric dimension
a_{ij} = element of matrix $\mathbf{A}$, equation (9*a*)
A = constant
A_n = coefficients for initial condition
$\mathbf{A}$ = matrix
b = height of the spheroid
b_{ij} = element of matrix $\mathbf{B}$, equation (9*b*)
$\mathbf{B}$ = matrix
c_n = Fourier-type coefficient
C_p = specific heat
d_{nj} = coefficients, equation (7)
$\mathbf{d}_n$ = eigenvector containing d_{nj}
$\mathbf{D}$ = matrix with element d_{nj}
e_{in} = element of matrix $\mathbf{E}$, equation (12*a*)
$\mathbf{E}$ = matrix
f_i = basis functions
$f_j^{(n)}$ = basis functions with boundary conditions of nth kind
F_n = solution function
g = generation per unit time and per unit volume
G = Green's function
i, j = indices
k = thermal conductivity
m, n = indices
M = number of surfaces
N = number of eigenvalues
p_{ni} = element of matrix $\mathbf{P}$
$\mathbf{P}$ = inverse of matrix $\mathbf{E}$
q_s = surface heat flux
r = radial coordinate
$\mathbf{r}$ = position vector
t = time
T = temperature
T_0 = initial temperature distribution
T_s = surface temperature
T_t = transient solution
T^* = quasi-steady solution
V = volume
x, y, z = coordinates
γ_n = eigenvalues
δ_n = coefficient, equation (24)
Δ = vector with elements δ_n
ϵ = small time
θ = complementary solution
ρ = density
σ = arbitrary function for nonhomogeneous boundary conditions
ϕ = boundary function
ψ_i = see equation (11*a*)
ω_i = elements of array Ω
Ω = vector with elements ω_i, equation (24)

with a generalized boundary condition. The function $G = G(\mathbf{r}, t\,|\mathbf{r}', \tau)$ is the standard Green's function (Ozisik, 1980) which defines the temperature effect at $(\mathbf{r}, t)$ in the solid caused by an impulsive point heat source of strength unity located at $\mathbf{r}'$ and released at time τ. The boundary conditions for equation (12) are homogeneous. Equation (1) can be modified to take the form

$$\nabla \cdot [k \nabla T(\mathbf{r}', \tau)] + g(\mathbf{r}', \tau) = -\rho C_p \partial T(\mathbf{r}', \tau)/\partial \tau \tag{13}$$

The boundary conditions for equation (13) may be nonhomogeneous. Further discussion of boundary conditions is included in a later section. Once equation (12) is multiplied by $T = T(\mathbf{r}', \tau)$ and equation (13) by $G = G(\mathbf{r}', \tau)$, then upon subtracting the former from the latter and following the application of Green's theorem, one obtains

$$\rho(\mathbf{r})C_p(\mathbf{r})T(\mathbf{r}, t) = \int_V \rho(\mathbf{r}')C_p(\mathbf{r}')G\Big|_{\tau=0} T_0(\mathbf{r}')dV'$$

$$+ \int_{\tau=0}^{t} d\tau \int_{V'} g(\mathbf{r}', \tau)GdV' + \int_{\tau=0}^{t} d\tau \int_{S'} k[G\partial T/\partial n - T\partial G/\partial n]_{S'} dS' \tag{14}$$

When T also satisfies homogeneous boundary conditions, the third term on the right-hand side (RHS) of equation (14) will vanish. Then a comparison between equations (14) and (9) reveals (Ozisik, 1980)

$$G(\mathbf{r}, t\,|\mathbf{r}', \tau) = \sum_{n=1}^{N} \rho(\mathbf{r})C_p(\mathbf{r})F_n(\mathbf{r})e^{-\gamma_n(t-\tau)} \sum_{i=1}^{N} p_{ni} f_i(\mathbf{r}') \tag{15}$$

The variable τ serves as a dummy variable in equation (14) which is the same role t' plays in equation (9). Since the Green's function must satisfy homogeneous boundary conditions of the first, second, or third kind, the contribution of different boundary conditions must be included through proper selection of the basis functions. Equation (15) presents a Galerkin-based Green's function for geometries that do not accept exact solutions.

When the quasi-steady temperature $T^* = T_s(t)$ satisfies the nonhomogeneous boundary condition and equation (8*a*), one can explicitly show that equations (9) and (14) are identical. However, when T^* is position dependent, only the first and second terms on the RHS of equation (14) are readily equivalent to the corresponding terms in equation (9) because, for the latter situation, $T^*(\mathbf{r}, t)$ assumes different forms. The equivalence of equations (9) and (14) can be demonstrated if G in equation (15) is substituted in equation (14). The first two terms on the RHS of the resulting relation become identical to the corresponding terms in equation (9). However, to show that the third term on the RHS of equation (14) is also equivalent to the terms containing T^* and $\partial T^*/\partial t$ in equation (9), the following additional algebraic steps are necessary. First, multiply equation (9) by $T^*(\tau)$, integrate the resulting equation over both the V' domain and time τ between 0 and $t + \epsilon$, then use the Green's theorem, and let ϵ go to zero. The resulting equation after integrating over τ by parts is

$$-\int_0^t T^*(\tau)d\tau \int_{S'} k(\partial G/\partial n)dS' = \rho(\mathbf{r})C_p(\mathbf{r})T^*(t)$$

$$+ \int_0^t d\tau \int_{V'} \rho(\mathbf{r}')C_p(\mathbf{r}')(\partial G/\partial \tau)T^*(\tau)dV'$$

$$= \rho(\mathbf{r})C_p(\mathbf{r})T^*(t) - \int_{V'} G\,|_{\tau=0}\rho(\mathbf{r}')C_p(\mathbf{r}')T^*(0)dV'$$

$$- \int_0^t d\tau \int_{V'} \rho(\mathbf{r}')C_p(\mathbf{r}')G[\partial T^*(\tau)/\partial \tau]dV' \tag{16}$$

For the boundary conditions of the first kind, $G = 0$ at the wall and equation (16) replaces the third term on the RHS of equation (14) to complete the proof of this equivalence. A similar but modified analysis applies to boundary conditions of the second and third kinds. For boundary conditions of the second kind, $\partial G/\partial n = 0$ and $k\partial T/\partial n = -q_s$ and for boundary conditions of the third kind, the square bracket in equation (14) will be reduced to hGT_∞/k.

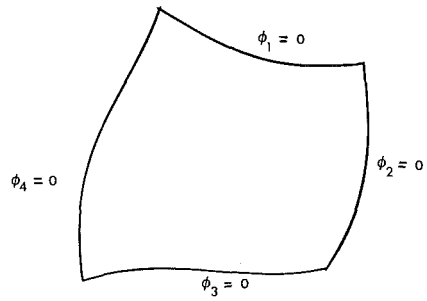

Fig. 1 Schematic of a generalized domain

Basis Functions. An important feature of this method is the determination of a set of linearly independent basis functions which satisfy all homogeneous boundary conditions. Then, one can use method 1 or 2, whichever is more convenient, to handle nonhomogeneous boundary conditions.

First Kind. The method of selection of basis functions, when temperature has a zero value on all surfaces, is available in Part 1 and in Ozisik (1980) and Kantorovich and Krylov (1960). Briefly, if a region is bounded by M surfaces $\phi_1 = 0$, $\phi_2 = 0$, . . . (Fig. 1), the first member of the set of basis functions is

$$f_1(\mathbf{r}) = \phi_1\phi_2\phi_3 \ldots \tag{17}$$

The function $f_1(\mathbf{r})$ selected in this manner vanishes over surfaces $\phi_1 = 0$, $\phi_2 = 0$, etc. Each subsequent member of the basis functions is obtained by multiplying $f_1(\mathbf{r})$ by an element of a complete set, e.g., in a Cartesian coordinate system

$$f_2(\mathbf{r}) = f_1(\mathbf{r})x \tag{18a}$$

$$f_3(\mathbf{r}) = f_1(\mathbf{r})y \tag{18b}$$

$$f_4(\mathbf{r}) = f_1(\mathbf{r})z \tag{18c}$$

$$f_5(\mathbf{r}) = f_1(\mathbf{r})x^2 \tag{18d}$$

This scheme ensures that every basis function assumes a zero value on the contour. It is important to ascertain that $f_1(\mathbf{r})$ does not assume a zero value within the interior of the region. This imposes a limitation on the utility of the Galerkin function but there are ways to circumvent this difficulty. One scheme is to divide the region into different subregions and construct Galerkin functions that are matched at the common boundary of the subregions (Kantorovich and Krylov, 1960). Another scheme is to replace the undesirable portion of the contour by a function or functions that approximate the original boundary but will not vanish within the interior of the region (Mashena and Haji-Sheikh, 1986). Other schemes are also plausible but they are not discussed here because their effectiveness has not yet been studied. Fortunately, this problem appears in a limited number of geometries and construction of the basis functions for boundary conditions of the first kind is usually straightforward.

Second Kind. Attention is now focused on the insulated boundaries. Generalizations that include the prescribed wall heat flux, as discussed earlier, can be facilitated using the Green's function, equation (15). Accordingly, the normal derivatives of all basis functions must vanish on the insulated section of the boundary. The selection of the basis functions

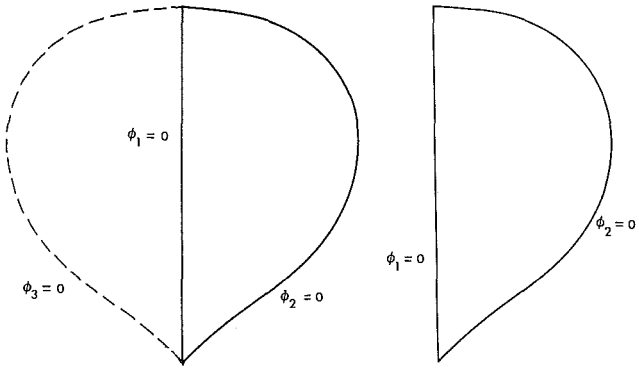

Fig. 2 Region with flat and curved boundary

becomes simple if a flat section of boundary is insulated. As an illustration (Fig. 2*b*), a flat section of the boundary described by $\phi_1 = 0$, is insulated and behaves like a mirror. Now, the original region can be replaced by a new region that includes itself and its mirror image (Fig. 2*a*). If, for instance, x is selected perpendicular to the $\phi_1 = 0$ surface, then the $\phi_3 = 0$ surface is derived from $\phi_2 = 0$ when the variable x is replaced by $-x$. Then, the basis functions using boundary conditions of the first kind, equations (17) and (18), with $f_1 = \phi_2\ \phi_3$, as described earlier, are obtained. This is a desirable situation since it usually permits the use of a symbolic code to carry out the integrations.

Another scheme is to express the basis functions in a series and then compute the coefficients so that the normal derivative of the basis functions vanish on the boundary. This method is applied to rectangular geometries (Kantorovich and Krylov, 1960). The basis functions are the product of $[x^m - ma^2x^{m-2}/(m-2)]$ and $[y^n - nb^2y^{n-2}/(n-2)]$ where m and n take values of 3, 4, 5, . . . , and $2a$, $2b$ designate the length of sides. This scheme is modified to deal with more demanding geometries. Further details on a modified version of this procedure for other geometries are discussed in the following numerical examples. Usually, the basis functions prepared in this manner accept exact integrations, hence computations can be carried out rapidly by symbolic routines.

A general method of selecting the basis functions for boundary conditions of the second kind can be illustrated by a simple example. Consider the geometry depicted in Fig. 2(*b*) to have the following boundary conditions: $f_j^{(2)} = 0$ on the $\phi_1 = 0$ line, while $\partial f_j^{(2)}/\partial n = 0$ on the $\phi_2 = 0$ line. The basis functions that unconditionally satisfy these conditions are

$$f_j^{(2)} = f_j^{(1)}\left\{[(\partial f_j^{(1)}/\partial n)/f_j^{(1)}]\Big|_{\phi_2=0}\left[\phi_2/(\partial\phi_2/\partial n)\Big|_{\phi_2=0}\right] - 1\right\} \tag{19a}$$

where

$$f_j^{(1)} = \phi_1 x^{m_j} y^{n_j} z^{k_j} \tag{19b}$$

and m_j, n_j, and k_j are integer exponents of the ordered terms in the Taylor series. The basis functions prepared in this manner do not always permit the volume integrals to be carried out exactly, hence numerical quadrature is necessary. Also, a removable singularity may appear where two surfaces are in contact.

Third Kind. Generally, the basis functions that satisfy the boundary conditions of the third kind can be constructed from the basis functions that satisfy the boundary conditions of the second kind. For this presentation, $f_j^{(2)}$ will designate the basis functions that satisfy the boundary condition of the second kind, $\phi_1 = 0$ surface. The basis functions that satisfy the boundary conditions of the third kind, when Bi is a constant, are obtained from the simple relation

$$f_j^{(3} = f_j^{(2)}\left[\phi_1/(\partial\phi_1/\partial n)\Big|_{\phi_1=0} - 1/\mathrm{Bi}\right] \tag{20}$$

in which $\phi_1 = 0$ designates the convective surface. It is also possible, for some geometries, to obtain the basis functions using a series expansion technique, as discussed for boundary conditions of the second kind.

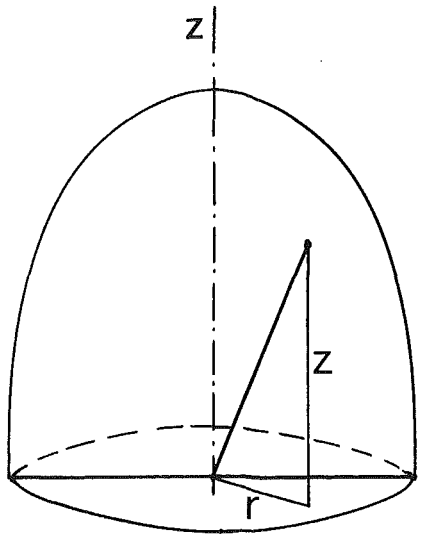

Fig. 3 Hemi-elliptical geometry

Numerical Examples

The numerical examples presented herein are designed to demonstrate the validity of the aforementioned procedure as applied to various types of boundary conditions. All computations were done on standard personal computers with a 4.77 MHz-clock equipped with math processors, except for symbolic differentiations which were carried out on a DEC 20/60 using REDUCE-III. The symbolic integration is also used whenever possible. The solids under consideration are considered to be isotropic and homogeneous. Modifications to accommodate heterogeneous systems are reported in Part 1 of this paper.

The following simple numerical examples introduce the procedures and necessary computational steps to deal with nonhomogeneous boundary conditions and boundary conditions of the second and third kinds.

Example 1. This is designed to demonstrate the method of selecting the basis functions using boundary conditions of the second and third kinds. A hemi-spheroidal solid is selected for this study because the mathematical relations are simple, hence the algebra will not mask the mathematical concept. The following situations are considered. The curved surface convects heat while the base is insulated, and the base convects heat while the curved surface is subject to the boundary conditions of the first kind. The situation when the base convects heat while the curved surface is insulated is studied but not included due to space limitation. When the base is insulated, it serves as a reflective surface. However, a series expansion is used to compute the basis functions when the curved surface is insulated. The generalized equation (20) is then utilized to account for convective conditions.

Consider the hemi-spheroidal solid with insulated base and insulated contour. By locating the x–y plane on the base plane (Fig. 3), and retaining only z's to the power of even numbers, the insulated boundary condition at $z = 0$ is automatically satisfied. The basis functions that satisfy the condition

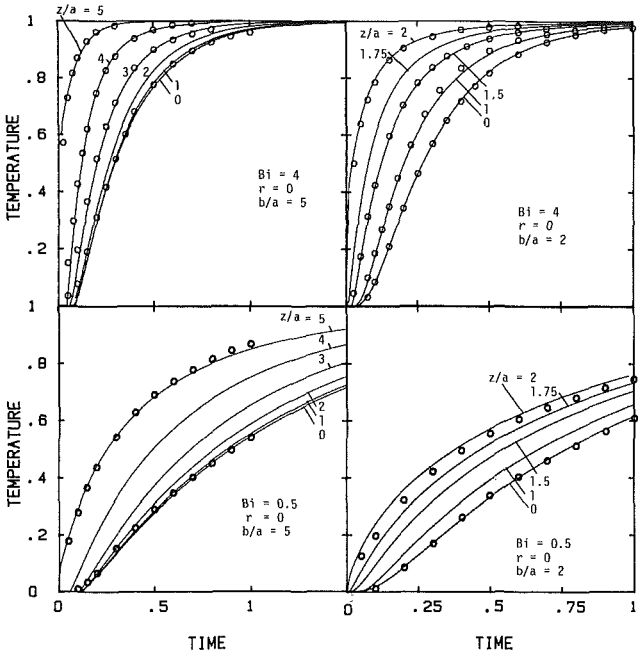

Fig. 4 Temperature distribution in spheroids with convective boundary conditions on curved surfaces

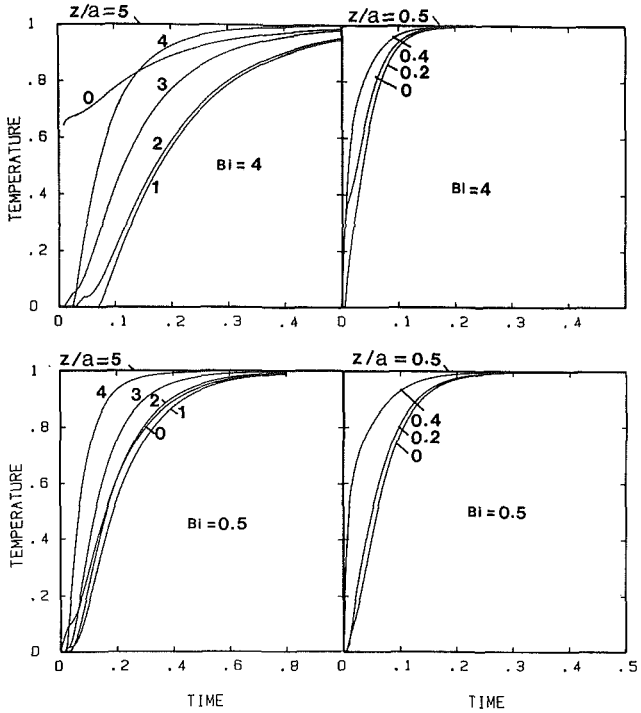

Fig. 5 Temperature distribution in hemispheroids with convective base and a step change in temperature at the curved surface

$\partial f_j(\mathbf{r})/\partial n = 0$ on the external surface can be determined by expressing $f_j(\mathbf{r})$ in a polynomial

$$f_j^{(2)} = r^{m_j} z^{n_j} (B_1 r^2 + B_2 z^2 + B_3) \tag{21}$$

for which $\phi_1 = 1 - r^2 - z^2/b^2 = 0$ describes the external surface (Fig. 3), and b is the aspect ratio. The condition that $\nabla f_1 \cdot \nabla \phi_1 = 0$ when $\phi_1 = 0$ results in the values of $B_1 = -2b^2/[b^2(m_j+2)+n_j]$, $B_2 = -2/[b^2(b^2 m_j + n_j + 2)]$, and $B_3 = 1$. The coefficients m_j and n_j take the values 0, 1, 2, ... The set of basis functions satisfying insulated boundary conditions at $z=0$ and convective boundary conditions on the curved surface are obtained by combining equations (20) and (21). It is possible to show that equation (21) is always positive in the domain of interest.

In this example, the functional relation in the denominator, equation (20), makes analytical integration of the basis function difficult, hence numerical quadrature is used. The results for different positions along the z axis are plotted in Fig. 4. The discrete data points in the figure are from the personal file of the first author and Haji-Sheikh and Sparrow (1967). All computations were straightforward and no unexpected peculiarity was observed. However, as the Biot number Bi was reduced to less than 1, matrices of 10×10 are required, instead of 6×6, for convergence. Also, the larger matrices require selection of a finer step size for integrations. Convergence is assured when the order of basis functions is increased by 1 and a negligible change in temperature is observed. During numerical integration, a removable singularity exists where the curved surface contacts the base.

Another demonstration of the selection of basis functions defines $z=0$ as the convective surface while the elliptical surface is subject to a boundary condition of the first kind. The resulting basis functions are

$$f_j = (1 - r^2 - z^2/b^2)(z + 1/\mathrm{Bi}) \tag{22}$$

Equation (22) admits analytical integrations and computation of matrix elements a_{ij} and b_{ij} can be carried out very rapidly. In this case, the computation accuracy is not controlled by the numerical quadrature, but by the size of the numbers that can be handled by the computing device.

However, since the computer program using equation (21) is available, it is used in lieu of a "symbolic" integration routine. The well-behaved temperature traces in Fig. 4 and 5 indicate the feasibility of this generalized method of selecting the basis functions. In the first situation, only r's and z's with even exponents are retained, but in the latter case all exponents of z must be retained except $n_j = 1$. When z is small (Fig. 5), the temperature of the point is first influenced by convection from the $z=0$ surface. Later, the effect of the step change in temperature at the curved boundary will produce a more rapid temperature change. This effect can be observed in Fig. 5 by small kinks in the temperature traces at early times. The results obtained in this example, method 1, and the use of the Green's functions, method 2, are mathematically equivalent.

Example 2. This example demonstrates the method of calculating the quasi-steady solution for simple problems without the use of the Green's functions. The present scheme is applicable to numerous geometries for which an exact solution does not exist but a solution based on the Ritz-Galerkin variational method is possible. The use of equation (9) is preferable to the use of the Green's function for simple nonhomogeneous boundary conditions. The method of calculating T^* is available in the literature. The computation begins by selecting a function σ that satisfies the boundary conditions but not necessarily the Laplace equation. The solution is constructed as

$$T^* = \sigma + \sum_{n=1}^{N} \delta_n f_n \tag{23}$$

in which σ is an arbitrarily selected function that satisfies the nonhomogeneous boundary conditions. Substituting equation (23) into equation (8*a*) and following the application of the standard Galerkin procedure yields the value of δ_n, the elements of Δ from equation

$$\Delta = \mathbf{A}^{-1}\Omega \tag{24}$$

The vector Ω has elements computed using equation

$$\omega_i = -\int_V \nabla \cdot (k \nabla \sigma) f_i dV \tag{25}$$

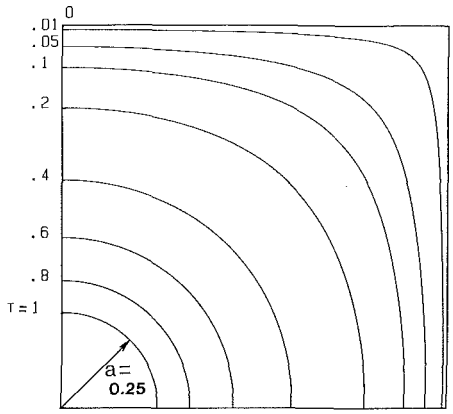

Fig. 6(*a*)

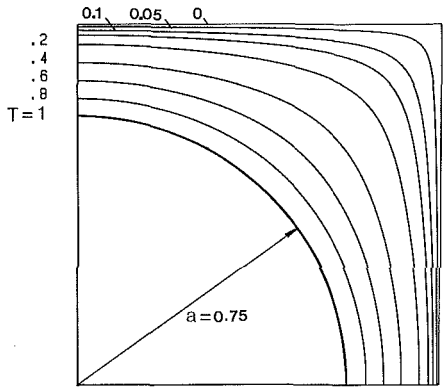

Fig. 6(*b*)

Fig. 6 Quasi-steady temperature in a domain between a circular cylinder and a square box

Consider the classical buried pipe problem, that is, a cylindrical geometry placed in a long box with a square cross section (Fig. 6). The matrix **A** is computed symbolically whereas the numerical quadrature is used for the vector **Ω**. For a fixed number of terms, the accuracy is highly dependent on σ. A simple method of selecting σ is based on the assumption that the conduction, between the pipe and the external surface, is one dimensional. Two relations for σ were selected for this study:

$$\sigma = (x^2y^2 - x^2 - y^2 + 1)/(x^2y^2 - a^2 + 1) \tag{26a}$$

and

$$\sigma = 1 - \ln[(x^2 + y^2)/a^2]/\ln[(1 + x^2y^2)/a^2] \tag{26b}$$

where a is the radius of the pipe. Equations (26*a*) and (26*b*) yield $\sigma = 1$, when $x^2 + y^2 = a^2$ and $\sigma = 0$ when $x = \pm 1$ or $y = \pm 1$. The basis functions for equation (23), using equations (17) and (18), are

$$f_j = (1 - x^2)(1 - y^2)(x^2 + y^2 - a^2)x^{m_j}y^{n_j} \tag{27}$$

Equation (26*b*) needs fewer terms for convergence than equation (26*a*). The isotherms plotted in Fig. 6 are computed to five digits. However, the numerical deviation observed using a 6×6 matrix and a 10×10 matrix varies between 0 and 0.4 percent, which is graphically undetectable. For instance, when $a = 0.75$, the largest deviation is on the 0.05 isotherm along a 45-deg line from the x axis, where the radial coordinate has values of 1.2676 and 1.2616, respectively. It is natural to use this numerical approach to compute T^* with simple boundary conditions since the matrix **A** is already available. Since T^* is calculated using an arbitrarily selected function σ, the nonhomogeneous contributions in equations (26*a*) and (26*b*) are not identical.

For complicated boundary conditions, the Green's function becomes indispensable and deserves a separate study. Extensive studies using the exact values of the Green's function to calculate numerous applications are reported by Beck (1984) and Beck and Keltner (1985). The Green's function presented in this paper is not exact but can be classified as exact in the Ritz–Galerkin sense.

Remarks

Several relations have been introduced to solve many thermal conduction problems involving boundary conditions of the second and third kinds. The flat boundary surfaces are usually easier to accommodate and the corresponding basis functions often produce mathematical formulations that accept analytical integrations. The basis functions for only a few curved surfaces yield exact values for elements of the matrices **A** and **B**. Further research to find the basis functions that will unconditionally accept analytical integration is desirable. This will eliminate the need for numerical integrations, hence increasing the accuracy of the results. When matrices **A** and **B** are obtained analytically, temperatures with accuracies of better than five digits can be computed at moderate computing costs. The accuracy of this integral method is defined as the number of digits that remains unchanged when basis functions of a higher order are used.

Acknowledgments

This work was supported by the National Science Foundation, Grant No. MEA 83-12754, and The Mechanical Engineering Department, University of Texas at Arlington.

References

Beck, J. V., and Keltner, N. R., 1985, "Green's Function Partitioning Procedure Applied to Foil Heat Flux Gages," ASME Paper No. 85-HT-56.

Beck, J. V., 1984, "Green's Function Solution for Transient Heat Conduction Problems," *Int. J. Heat Mass Transfer*, Vol. 27, pp. 1235–1244.

Haji-Sheikh, A., 1986, "On Solution of Parabolic Partial Differential Equations Using Galerkin Functions," *Integral Methods in Science and Engineering*, Hemisphere, New York, pp. 467–479.

Haji-Sheikh, A., and Sparrow, E. M., 1967, "The Solution of Heat Conduction Problems by Probability Methods," ASME JOURNAL OF HEAT TRANSFER, Vol. 89, pp. 121–131.

Kantorovich, L. V., and Krylov, V. I., 1960, *Approximate Methods of Higher Analysis*, Wiley, New York.

Lakshminarayanan, R., and Haji-Sheikh, A., 1986, "A Generalized Closed-Form Solution to Thermal Entrance Problems," *8th Int. Heat Transfer Conference*, San Francisco, CA, Paper No. 86-IHTC-268.

Mashena, M., and Haji-Sheikh, A., 1986, "An Integral Solution of Moving Boundary Problems," *Int. J. of Heat and Mass Transfer*, Vol. 29, No. 2, pp. 317–329.

Ozisik, M. N., 1980, *Heat Conduction*, Wiley, New York.

Effect of the Thermal Capacitance of Contained Fluid on Performance of Symmetric Regenerators

F. E. Romie
Palos Verdes Estates, CA 90274
Mem. ASME

The operation of the symmetric counterflow regenerative heat exchanger is described for conditions under which the thermal capacitance of the contained fluid cannot, as is the usual case, be set equal to zero. The solution of the system equations is found by use of the Laplace transform method. The thermal effectiveness is presented for a range of parameters believed to cover most applications of the symmetric regenerator.

Introduction

The regenerator is distinguished from the usual heat exchanger by the thermal capacitance of its matrix which alternately supplies or accepts heat from two fluids that enter at different but constant temperatures and flow countercurrently but alternately through the same flow passages for time periods t_a and t_b. Steady-state periodic operation is attained after a sufficient number of alternating periods following startup.

Often the regenerator matrix material can be considered to conduct no heat in the direction of fluid flow and to offer no resistance to heat flow in the direction normal to fluid flow. Even with these two simplifying idealizations, six parameters are required to characterize the regenerator. The parameters can be expressed in various forms but the parameters in the form most suited to writing the differential equations are Λ_a, Λ_b, Π_a, Π_b, V_a, and V_b (see nomenclature). In this paper the analysis is restricted to a symmetric regenerator: $\Lambda_a = \Lambda_b = \Lambda$, $\Pi_a = \Pi_b = \Pi$, and $V_a = V_b = V$.

The parameter V is the ratio of the thermal capacitance of the fluid contained, at any instant, in the matrix to the thermal capacitance of the matrix solid. If σ is the porosity of the matrix, then V equals $\sigma/(1-\sigma)$ times the ratio of the volumetric heat capacity of the fluid to the volumetric heat capacity (J/m^{3}K) of the matrix solid. For air (STP) in a matrix with a porosity of 0.5, the order of magnitude of V is 0.0005. This value is so small that the term $V\partial\tau_a/\partial Y$ (see equation (2)) can be set equal to zero with very small consequent error. In this case, the usual descriptions of regenerator performance are applicable (see, for example, Baclic, 1985). For air at room temperature and 10 bar pressure in a matrix with a porosity of 0.8, the magnitude of V is 0.02 and will often be larger under cryogenic conditions. Thus, conditions exist for which the value of V cannot be considered zero.

In the analysis presented in this paper, V can have any assigned value. In particular, the purpose of this paper is to present the thermal performance as a function of Λ, Π, and V for the steady-state periodic operation of a symmetric counterflow regenerator. The solution is found by use of the Laplace transform method.

Previous investigators (Heggs and Carpenter, 1976; Willmott, 1977; Maclaine-cross, 1980) have used finite difference (FD) methods to solve the system equations. The FD method requires considerable computer time. Consequently, the range of parameters for which a solution is available is limited. The advantage of the method used in this paper is primarily the reduced computer time required to find a solution. A simple desk-top computer was used to compute the thermal effectiveness for parameters covering the ranges: Λ = 2 to 32, Π/Λ = 0.025 to 1.0, and $V < \Pi/\Lambda$.

Differential Equations

The following idealizations define the regenerator analyzed: (1) The capacitance rates, $(wc)_a$ and $(wc)_b$, and the thermal conductances for transfer of heat between the matrix and fluids, $(hA)_a$ and $(hA)_b$, are uniform and constant as is the thermal capacitance, WC, of the matrix; (2) no axial conduction of heat occurs in the matrix and the matrix material offers no resistance to heat flow in the direction normal to fluid flow; (3) dead time during flow reversal is zero; (4) the fluids are incompressible; (5) no mixing of the two fluids occurs during the time they are both in the regenerator.

With these idealizations, an energy balance on an elemental length of the regenerator produces two equations applicable during flow period a

$$T_a(x, y) - \tau_a(x, y) = -\frac{\partial T_a}{\partial Y} \tag{1}$$

$$T_a(x, y) - \tau_a(x, y) = \frac{\partial \tau_a}{\partial X} + V\frac{\partial \tau_a}{\partial Y} \tag{2}$$

(Similar equations, of course, apply during period b.)

In these equations, x is the fractional distance into the matrix (always measured from the entrance plane of fluid a) and y is the fractional completion of the duration, t_a or t_b, of the flow periods. The subscript a denotes temperatures in the matrix during period a; $X = x\Lambda$ and $Y = y\Pi$. The equations are linear and no loss of information is introduced by putting the entrance fluid temperature variables equal to 0 and 1 for τ_a and τ_b, respectively. These variables will be referred to as temperatures.

The solution of these two equations must satisfy three conditions: (1) Fluid a enters ($x = 0$) at zero temperature: $\tau_a(0, y) = 0$; (2) the matrix temperature distribution at the beginning ($y = 0$) of period a is expressible as an Nth degree polynomial of X

$$T_a(x, 0) = \sum_0^N A_n \frac{X^n}{n!} \tag{3}$$

(3) the temperature distribution of the fluid in the matrix at the beginning ($y = 0$) of flow period a is also expressible as an Nth degree polynomial of X

$$\tau_a(x, 0) = \sum_0^N B_n \frac{X^n}{n!} \tag{4}$$

Actually, the fluid in the matrix at the beginning of period a is fluid b residing in the matrix at the moment of flow reversal. However, subscript a denotes temperatures in the regenerator

Contributed by the Heat Transfer Division for publication in the JOURNAL OF HEAT TRANSFER. Manuscript received by the Heat Transfer Division April 30, 1986.

during period a. The volumetric heat capacities of the two fluids must be equal because $V_a = V_b$.

For steady-state periodic operation, the coefficients A_n and B_n do not vary from cycle to cycle.

During flow period b, fluid b enters the matrix at $x = 1$ at a temperature of unity. Therefore, for a symmetric regenerator

$$T_b(x, y) = 1 - T_a(1-x, y) \tag{5}$$

and

$$\tau_b(x, y) = 1 - \tau_a(1-x, y) \tag{6}$$

Solution of Equations

The solutions of equations (1) and (2) are found by taking their Laplace transforms with respect to Y and solving the resultant equations for the Laplace transforms $T_a(x, s)$ and $\tau_a(x, s)$ of $T_a(x, y)$ and $\tau_a(x, y)$. (Here the notations $T_a(x, s)$ and $\tau_a(x, s)$ are used for convenience; the Laplace transforms are, as stated, taken with respect to Y.)

$$T_a(x,s) = \sum_{n=0}^{N} \Bigg[A_n \Bigg\{ \frac{X^n}{(s+1)n!} + (-1)^n \Bigg[\sum_{r=0}^{n} (-1)^r \frac{X^r}{r!} \frac{1}{(s+1)^2} \left(\frac{s+1}{Vs(s+a)} \right)^{n+1-r} - \frac{1}{(s+1)^2} \left(\frac{s+1}{Vs(s+a)} \right)^{n+1} e^{-\frac{Xs}{s+1}} e^{-XVs} \Bigg] \Bigg\} + VB_n(-1)^n \Bigg[\sum_{r=0}^{n} (-1)^r \frac{X^r}{r!} \frac{1}{s+1} \left(\frac{s+1}{Vs(s+a)} \right)^{n+1-r} - \frac{1}{s+1} \left(\frac{s+1}{Vs(s+a)} \right)^{n+1} e^{-\frac{Xs}{s+1}} e^{-XVx} \Bigg] \Bigg] \tag{7}$$

$$\tau_a(x,s) = \sum_{n=0}^{N} \Bigg[A_n(-1)^n \Bigg[\sum_{r=0}^{n} (-1)^r \frac{X^r}{r!} \frac{1}{s+1} \left(\frac{s+1}{Vs(s+a)} \right)^{n+1-r} - \frac{1}{s+1} \left(\frac{s+1}{Vs(s+a)} \right)^{n+1} e^{-\frac{Xs}{s+1}} e^{-XVs} \Bigg] + VB_n(-1)^n \Bigg[\sum_{r=0}^{n} (-1)^r \frac{X^r}{r!} \left(\frac{s+1}{Vs(s+a)} \right)^{n+1-r} - \left(\frac{s+1}{Vs(s+a)} \right)^{n+1} e^{-\frac{Xs}{s+1}} e^{-XVs} \Bigg] \Bigg] \tag{8}$$

The constant a is $(1+V)/V$; $1-a = -1/V$.

The inversion of these two equations requires the inverse transforms of $P_{u,v}(X, s)$, $Q_{u,v}(X, s)$, and $R_{u,v}(X,s)$ given below. The inversion uses the convolution integral with the equations and the functions F_n and G_n described by Romie (1987). The appendix gives the equations required to evaluate F_n and G_n.

$$P_{u,v}(X, s) = \frac{e^{\frac{Xs}{s+1}}}{s^u(s+a)^{v+1}} \tag{9}$$

$$Q_{u,v}(X, s) = \frac{P_{u,v}(X,s)}{s+1} \tag{10}$$

$$R_{u,v}(X, s) = \frac{P_{u,v}(X, s)}{(s+1)^2} \tag{11}$$

Numerical evaluation requires the use of a computer and for this reason array coordinates rather than function arguments are indicated on the left sides of following equations. To express the inverse transforms of P, Q, and R, define $p(\ )$, $q(\ )$, and $r(\ )$. (The symbol r is also used as an index.)

$$p(r) = \left(\frac{a}{1-a} \right)^r e^{\frac{aX}{1-a} - aY} F_r\left(\frac{X}{1-a'} \quad Y(1-a) \right) \tag{12}$$

$$q(r) = \left(\frac{a}{1-a} \right)^r \frac{e^{\frac{aX}{1-a} - aY}}{(1-a)} G_r\left(\frac{X}{1-a}, \quad Y(1-a) \right) \tag{13}$$

Nomenclature

a = $(1+V)/V$
A = heat transfer area of matrix, m^2
A_n = coefficient in equation (3)
A_x = free cross-sectioned area for flow, m^2
B_n = coefficient in equation (4)
c = heat capacity per unit mass of fluid, J/kgK
C = heat capacity per unit mass of matrix, J/kgK
$F_n(\ )$ = function described in appendix
$G_n(\ )$ = function described in appendix
h = thermal conductance per unit area, W/m^{2}K
K = $(\bar{\tau}_a - \bar{\tau}^*)/(V\bar{\tau}^*)$
L = flow length of matrix, m
N = degree of polynomial, equations (3) and (4)
Ntu = $\Lambda/2$ for symmetric regenerator
s = Laplace transform parameter
t = time, s
t_a, t_b = duration of period, s
T = matrix temperature
u = velocity of fluid in matrix, m/s
$U(\ )$ = unit step function
V = $A_xL\rho c/WC$
w = mass rate of fluid, kg/s
W = mass of matrix, kg
x = fractional distance from entrance plane of fluid a, z/L
X = $x\Lambda$; also first argument of F_n and G_n)
y = fractional completion of period, t/t_a or t/t_b
Y = $y\Pi$ (also second argument of F_n and G_n)
z = distance from entrance plane of fluid a, m
Λ = $hA/(wc)$
Π = $(hAt)_a/(WC)$
ρ = fluid density, kg/m^3
σ = matrix porosity
τ = fluid temperature
$\bar{\tau}_a$ = thermal effectiveness with $V \neq 0$
$\bar{\tau}^*$ = thermal effectiveness with $V = 0$

Subscripts

a = conditions during period t_a
b = conditions during period t_b

$$r(r)=\left(\frac{-a}{1-a}\right)^r \frac{e^{\frac{aX}{1-a}-aY}}{(1-a)^2}\left[\frac{-Y(1-a)}{X/(1-a)}F_{-1}\left(\frac{X}{1-a},Y(1-a)\right)\right. \tag{14}$$

$$\left.+\sum_{t=0}^{r}(-1)^t G_t\left(\frac{X}{1-a},\ Y(1-a)\right)\right]$$

The inverse transforms can then be written in the following forms:

$$P(u,\ v)=\frac{1}{(-a)^u a^v}\left[\sum_{r_1=0}^{v}\cdots\sum_{r_u=0}^{r_{u-1}}\left(p(r_u)-\sum_{p=0}^{u-1}(-a)^p F_p(X,\ Y)\right)\right] \tag{15}$$

$$Q(u,\ v)=\frac{1}{(-a)^u a^v}\left[\sum_{r_1=0}^{v}\cdots\sum_{r_u=0}^{r_{u-1}}\left(q(r_u)-\sum_{p=0}^{u-1}(-a)^p G_p(X,\ Y)\right)\right] \tag{16}$$

$$R(u,\ v)=\frac{1}{(-a)^u a^v}\left[\sum_{r_1=0}^{v}\cdots\sum_{r_u=0}^{r_{u-1}}\left(r(r_u)+\sum_{p=0}^{u-1}a^p\left[\frac{Y}{X}F_{-1}(X,\ Y)-\sum_{t=0}^{p}(-1)^t G_t(X,\ Y)\right]\right)\right] \tag{17}$$

As indicated, the multiple sums are taken u times.

Equations (9), (10), and (11) show that $Q(u, v) = R(u, v) + R(u-1, v)$ and $P(u, v) = Q(u, v) + Q(u-1, v)$. To write inverse transforms of transforms of the form

$$\frac{1}{(s+1)^i}\left(\frac{s+1}{Vs(s+a)}\right)\int^{n+1} e^{-\frac{Xs}{s+1}},\quad i=0,\ 1,\ 2$$

define $D\ (i,\ n)$

$$D(0,\ n)=\frac{1}{V^{n+1}}\sum_{r=0}^{n+1}\frac{(n+1)!}{(n+1-r)!r!}P(r,\ n) \tag{18}$$

$$D(1,\ n)=\frac{1}{V^{n+1}}\sum_{r=0}^{n+1}\frac{(n+1)!}{(n+1-r)!r!}Q(r,\ n) \tag{19}$$

$$D(2,\ n)=\frac{1}{V^{n+1}}\sum_{r=0}^{n+1}\frac{(n+1)!}{(n+1-r)!r!}R(r,\ n) \tag{20}$$

The inverse transforms of the matrix and fluid transforms (equations (7) and (8)) can now be written

$$T_a(x,\ y)=\sum_{n=0}^{N}\left[A_n\left\{\frac{X^n}{n!}e^{-Y}+(-1)^n\left[\sum_{r=0}^{n}(-1)^r\frac{X^r}{r!}D^*(2,\ n-r)-U(Y-XV)D^{**}(2,\ n)\right]\right\}\right.$$

$$\left.+VB_n(-1)^n\left[\sum_{r=0}^{n}(-1)^r\frac{X^r}{r!}D^*(1,\ n-r)-U(Y-XV)D^{**}(1,\ n)\right]\right] \tag{21}$$

$$\tau_a(x,\ y)=\sum_{n=0}^{N}\left[A_n(-1)^n\left[\sum_{r=0}^{N}(-1)^r\frac{X^r}{r!}D^*(1,\ n-r)-U(Y-XV)D^{**}(1,\ n)\right]\right.$$

$$\left.+VB_n(-1)^n\left[\sum_{r=0}^{n}(-1)^r\frac{X^r}{r!}D^*(0,\ n-r)-U(Y-XV)D^{**}(0,\ n)\right]\right] \tag{22}$$

In these two equations $U(\ )$ is the unit step function, representing zero for a negative argument and unity for a positive argument. The single asterisk indicates variables $X=0$ and $Y=\Pi y$. The double asterisk indicates variables $X=x\Lambda$ and $Y=y\Pi-x\Lambda V$.

Coefficient Evaluation

The matrix temperature distribution at the end of period a is the matrix temperature distribution at the beginning of period b: $T_a(x,\ 1) = T_b(x,\ 0)$. Using equation (5) gives

$$T_a(x,\ 1)+T_a(1-x,\ 0)=1 \tag{23}$$

Similarly, the fluid temperature distribution at the end of period a is the fluid temperature distribution at the beginning of period b: $\tau_a(x,\ 1) = \tau_b(x,\ 0)$. Using equation (6) gives

$$\tau_a(x,\ 1)+\tau_a(1-x,\ 0)=1 \tag{24}$$

The $2(N+1)$ values of A_n and B_n are found by satisfying equations (23) and (24) at $N+1$ points, x_m, along the flow path using equations (3), (4), (21), and (22) for T_a and τ_a. Willmott and Duggan (1980) and later Romie (1979) found the Chebyshev points, $x_m = (1-\cos(\pi m/N))/2$, $m=0,\ 1,\ \ldots,\ N$, advantageous for this purpose.

The parameters Λ, Π, and V have been used in the formulation of the solution for the fluid and matrix temperatures. However, for presentation of the results of calculation, the parameters used will be Ntu, $(wct)_a/WC$, and V. For a symmetric regenerator Ntu $= \Lambda/2$ and $(wct)_a/WC = \Pi/\Lambda$. The parameter $(wct)_a/WC$ is appropriately interpreted as the ratio of the thermal capacitance of the mass of fluid that enters (or leaves) the regenerator during period a to the thermal capacitance of the matrix solid.

Temperature Discontinuity

Let $f(Y)$ be the inverse transform of $F(s)$. If $F(s)$ is multiplied by $\exp(-XVs)$, as in equations (7) and (8), then the function $f(Y)$ becomes $f(Y-XV)$ and in addition is zero if $Y < XV$. The term $\exp(-XVs)$ thus indicates a discontinuity in the fluid temperature distribution and in the time rate of change of the matrix temperature. Both discontinuities occur when $Y=XV$. The physical interpretation is as follows: At the beginning of period a, the matrix is filled with fluid b from the preceding period b. (The temperature distribution of this fluid is denoted as $\tau_a(x,\ 0)$ in equation (4).) At time zero fluid a at temperature zero begins to enter the regenerator. The initial fluid temperature discontinuity at $x = 0$ and $y = 0$ is thus B_0. As fluid a flows into the matrix the two-fluid interface (the

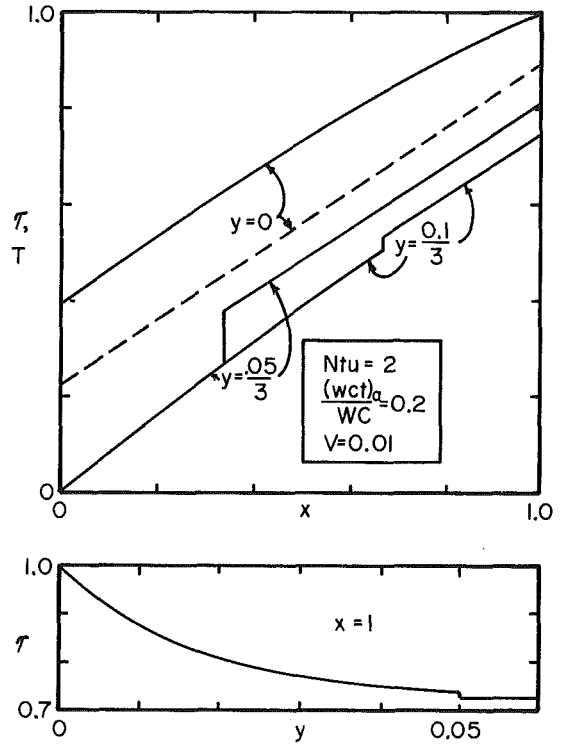

Fig. 1 Temperatures in the matrix during interface transit. The broken line is the matrix temperature. For this example $B_0 = 0.396$.

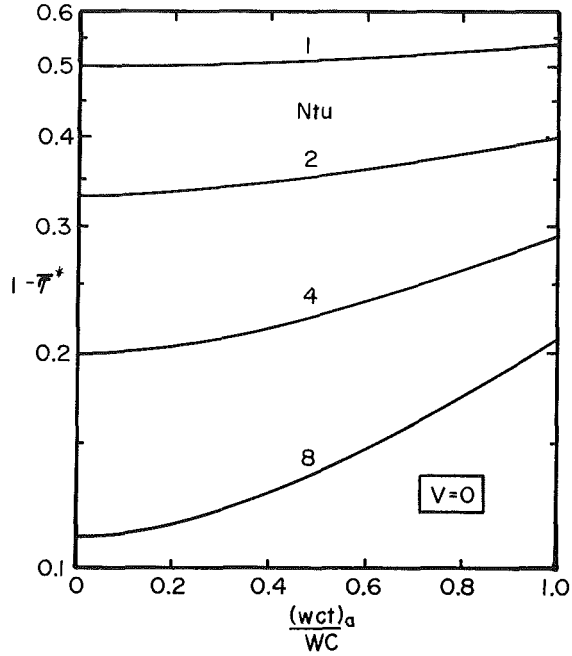

Fig. 2 Complement of the thermal effectiveness with $V = 0$

location of the discontinuity) moves through the matrix with the velocity u_a of fluid flow and leaves the matrix when $t = L/u_a$. The magnitude of the fluid temperature discontinuity can be shown to be $B_0\exp(-2\text{Ntu}\ x)$ and thus diminishes quite rapidly as the interface transverses the matrix.

The upper panel of Fig. 1 shows, for a specific example, temperature distributions in a matrix at three different times during interface transit of the matrix. The matrix temperature and the fluid temperature behind the interface change with time during the traverse but by amounts too small to be shown on the figure. The lower panel of Fig. 1 shows the temperature history of fluid leaving the matrix during and shortly after the traverse. For this example, the discontinuity in exiting fluid temperature occurs when $y = 0.05$ and is only 0.007, about the width of the inked line. The exiting fluid temperature thereafter decreases at nearly a constant rate to its final value of $1 - B_0$ at the end of the period ($y = 1$). The fluid leaving from $y = 0$ to $y = 0.05$ is fluid b; thereafter the exiting fluid is fluid a.

As noted above, the location of the interface is given by $Y - XV = 0$ or, equivalently, $y(wct)_a/WC - xV = 0$. Thus, if $V > (wct)_a/WC$, the interface will still be in the matrix at the end of the period because x will be less than 1 when $y = 1$. For $V > (wct)_a/WC$ only fluid b leaves the regenerator during period a. For $V < (wct)_a/WC$, the fraction of the thermal capacitance of the fluid mass leaving during period a that is that of fluid b is $V/(wct)_a/WC$. The continuity relation, $w = \rho u A_x$, can be used to show that $V/(wct)_a/WC = L/u_a t_a = L/u_b t_b$.

Thermal Effectiveness

The change in internal energy of the regenerator over the duration t_a of a period must equal the enthalpy of the mass of fluid that leaves the regenerator minus the enthalpy of the mass of fluid that enters during the period. The latter enthalpy can be taken to be zero at the constant entrance temperature of zero. The enthalpy of the mass of fluid that leaves the regenerator is the product of $(wct)_a$ and the time-mean temperature $\bar{\tau}_a$ of the leaving fluid. The thermal effectiveness of the regenerator is defined to be $\bar{\tau}_a$.

The change of internal energy, ΔE, of the regenerator during period a is the sum of the internal energy change of the matrix solid plus the difference between the internal energy of the fluid in the matrix at the beginning and at the end of the period

$$\Delta E = WC\left[\int_0^1 T_a(x, 0)dx - \int_0^1 (1 - T_a(1-x, 0))dx\right]$$

$$+ (WC)V\left[\int_0^1 \tau_a(x, 0)dx - \int_0^1 (1 - \tau_a(1-x, 0))dx\right] \tag{25}$$

Carrying out the integrations using equations (3) and (4) gives the thermal effectiveness

$$\bar{\tau}_a \frac{(wct)_a}{WC} = -1 + 2\sum_{n=0}^{N} A_n \frac{\Lambda^n}{(n+1)!}$$

$$+ V\left(-1 + 2\sum_{n=0}^{N} B_n \frac{\Lambda^n}{(n+1)!}\right) \tag{26}$$

It should be observed that this thermal effectiveness characterizes, as is the usual case, the difference in enthalpy of the masses of fluid leaving and entering the regenerator during period a but it is not proportional, unless $V = 0$, to the net heat transferred from the matrix to the fluid during the period. For this reason, the thermal effectiveness of the regenerator can be greater than that of a symmetric counterflow recuperator having the same Ntu.

The thermal effectiveness $\bar{\tau}^*$ of the symmetric regenerator with $V = 0$ is presented by many sources, for example, Baclic (1985). Figure 2 gives the complement of $\bar{\tau}^*$ as a function of $(wct)_a/WC$ for several values of Ntu. Values of $(wct)_a/WC$ greater than unity are of minor interest because the product $\bar{\tau}^*(wct)_a/WC$ cannot exceed unity (Romie, 1979).

The thermal effectiveness $\bar{\tau}_a$ can be computed with good accuracy using the following equation:

$$\bar{\tau}_a = \bar{\tau}^*(1 + KV) \tag{27}$$

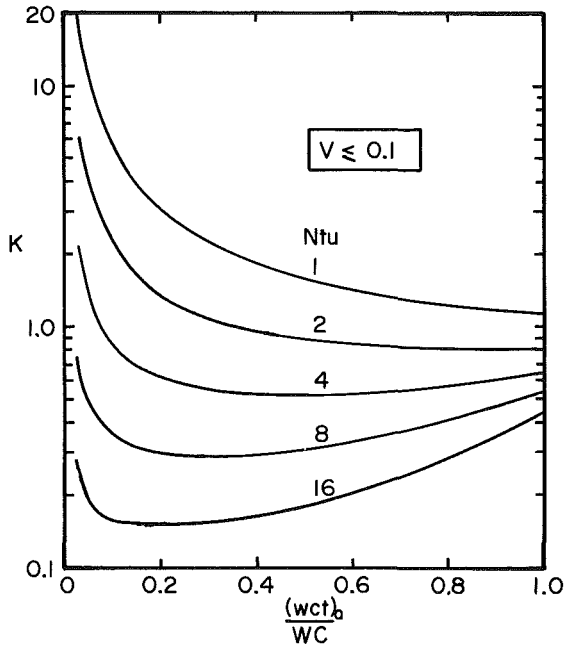

Fig. 3 The variable K defined by equation (27)

The variable K, $K = (\bar{\tau}_a - \bar{\tau}^*)/(\bar{\tau}^* V)$, is found to be a weak function of V and primarily a function of Ntu and $(wct)_a/WC$. This assertion can be verified by inspection of Table 1 which summarizes solutions covering the range Ntu = 1 to 8, $(wct)_a/WC = 0.025$ to 1, and $V \leq (wct)_a/WC$. The effectiveness could also be calculated for $V > (wct)_a/WC$ but this region is outside the normal operating range of a regenerator. In fact, values of V greater than a few hundredths are a contraindication to the selection of a regenerator rather than a recuperator if mixing of the two fluids is undesirable. (Fluid b exiting during period a from $t = 0$ to $t = L/u_a$ and fluid a exiting during period b from $t = 0$ to $t = L/u_b$ can, of course, be "dumped" to avoid mixing but with a decrease in thermal effectiveness as well as loss of fluid.)

Figure 3 shows K as a function of Ntu and $(wct)_a/WC$. Data to construct this figure were calculated using $V = 0.01$ but the figure can be used with good accuracy for $V \leq 0.1$. Figure 3 shows, in conjunction with equation (27), that the effect of V on the value of $\bar{\tau}_a$ becomes smaller as Ntu increases and becomes larger as $(wct)_a/WC$ approaches zero.

To give an example of the use of Fig. 3, suppose a symmetric regenerator has an Ntu of 4, a V of 0.02, and is operating with $(wct)_a/WC = 0.2$. From Fig. 2, $\bar{\tau}^* = 0.795$ and from Fig. 3, $K = 0.61$. Using equation (27) gives $\tau_a = 0.795\ (1 + 0.61 \times 0.02) = 0.805$. This value is greater than 0.800, which is the effectiveness, Ntu/(1 + Ntu), of a symmetric counterflow recuperator having an Ntu of 4. However, the thermal capacitance composition of the fluid leaving the regenerator is 10 percent fluid b.

Only gases will give a small value of V. For this reason, regenerators are effectively restricted to gases.

Comparison With Other Data

Maclaine-cross (1980) uses a finite difference method to solve equations (1) and (2). For three parameter combinations, he gives the thermal effectiveness $\bar{\tau}_a$ to six places and indicates estimated error limits for his values. Table 2 compares his results with the results of this paper. The results of this paper were found by increasing N until the sixth decimal digit ceased to change. The value of N for which the sixth digit ceased to change is shown in the table. The Maclaine-cross values are seen to be more accurate than his error estimates indicate.

Table 1(a) Values of K for Ntu = 1

$(wct)_a/WC$	V										
	.003	.006	.013	.025	.05	.1	.2	.4	.6	.8	1.0
.025	20.7	20.8	21.1	21.7							
.05	10.6	10.6	10.7	10.7	11.0						
.10	5.57	5.57	5.57	5.56	5.56	5.58					
.20	3.07	3.07	3.06	3.05	3.03	2.98	2.89				
.4	1.84	1.83	1.83	1.82	1.80	1.77	1.70	1.57			
.6	1.43	1.43	1.43	1.42	1.41	1.38	1.33	1.23	1.14		
.8	1.24	1.24	1.24	1.23	1.22	1.20	1.16	1.08	1.01	.928	
1.0	1.14	1.14	1.13	1.13	1.12	1.11	1.07	1.01	.941	.876	.812

Table 1(b) Values of K for Ntu = 2

$(wct)_a/WC$	V										
	.003	.006	.013	.025	.05	.1	.2	.4	.6	.8	1.0
.025	7.18	7.19	7.21	7.26							
.05	3.83	3.83	3.82	3.80	3.76						
.10	2.17	2.16	2.15	2.13	2.09	2.01					
.20	1.34	1.34	1.33	1.32	1.29	1.24	1.14				
.4	.948	.946	.941	.933	.916	.882	.817	.701			
.6	.839	.837	.834	.827	.814	.788	.738	.645	.563		
.8	.805	.804	.801	.796	.785	.763	.721	.641	.567	.502	
1.0	.805	.804	.801	.797	.787	.769	.732	.660	.593	.531	.475

Table 1(c) Values of K for Ntu = 4

$(wct)_a/WC$	V										
	.003	.006	.013	.025	.05	.1	.2	.4	.6	.8	1.0
.025	2.34	2.33	2.32	2.28							
.05	1.35	1.34	1.33	1.31	1.26						
.1	.851	.847	.840	.825	.798	.745					
.2	.611	.609	.604	.595	.577	.543	.482				
.4	.518	.516	.513	.506	.493	.468	.422	.348			
.6	.524	.523	.520	.514	.502	.479	.437	.365	.309		
.8	.570	.567	.564	.558	.547	.524	.482	.408	.348	.301	
1.0	.635	.634	.631	.625	.614	.593	.551	.473	.408	.353	.310

Table 1(d) Values of K for Ntu = 8

$(wct)_a/WC$	V										
	.003	.006	.013	.025	.05	.1	.2	.4	.6	.8	1.0
.025	.760	.756	.747	.730							
.05	.486	.483	.477	.466	.446						
.10	.351	.349	.345	.338	.326	.301					
.2	.282	.289	.287	.282	.272	.254	.224				
.4	.291	.289	.286	.282	.273	.256	.228	.184			
.6	.336	.333	.330	.324	.314	.296	.263	.213	.178		
.8	.426	.414	.411	.404	.392	.370	.330	.266	.221	.187	
1.0	.541	.537	.529	.526	.512	.486	.436	.354	.292	.247	.213

Concluding Remarks

The third idealization states that dead time during flow reversal is zero. If the fluid is at rest during a reversal, then the local fluid and matrix temperatures will approach a common value. This change in temperatures does not change the internal energy of the regenerator, and thus the idealization can be relaxed, particularly when V is small. In practice dead time should, of course, be small enough to avoid effects of axial transfer of heat in the regenerator.

Regenerators, other than rotating regenerators, have plenum volumes between the control valves and the entrance planes of the matrix. The fluid in these volumes has been ignored in the analysis given.

Table 2 Comparison of data

			This Paper		Maclaine-cross (1980)	
Ntu	$(wct)_a/WC$	V	$\bar{\eta}_a$	N	$\bar{\eta}_a$	Est. Error
2.5	1	.1	.683236	5	.683237	1.1×10^{-5}
5.0	0.5	.1	.840314	8	.840314	2.3×10^{-5}
10.0	1	.8	.954777	11	.954780	2.4×10^{-5}

References

Baclic, B. S., 1985, "The Application of the Galerkin Method to the Solution of the Symmetric and Balanced Counterflow Regenerator Problem," ASME JOURNAL OF HEAT TRANSFER, Vol. 107, pp. 214–221.

Heggs, P. J., and Carpenter, K. J., 1976, "The Effect of Fluid Hold-up on the Effectiveness of Countraflow Regenerators," *Transactions of the Institution of Chemical Engineers*, Vol. 54, pp. 232–238.

Maclaine-cross, I. L., 1980, "Effect of Interstitial Fluid Heat Capacity on Regenerator Performance," ASME JOURNAL OF HEAT TRANSFER, Vol. 102, pp. 572–574.

Romie, F. E., 1987, "Two Functions Used in the Analysis of Crossflow Exchangers, Regenerators, and Related Equipment," ASME JOURNAL OF HEAT TRANSFER, in press.

Romie, F. E., 1979, "Periodic Thermal Storage: The Regenerator," ASME JOURNAL OF HEAT TRANSFER, Vol. 101, pp. 726–731.

Willmott, A. J., 1977, "A Comment on the Paper 'The Effect of Gas Heat Storage Upon the Performance of the Thermal Regenerator'," *International Journal of Heat and Mass Transfer*, Vol. 20, p. 1267.

Willmott, A. J., and Hinchcliffe, C., 1976, "The Effect of Gas Heat Storage Upon the Performance of the Thermal Regenerator," *International Journal of Heat and Mass Transfer*, Vol. 19, pp. 821–826.

Willmott, A. J., and Duggan, R. C., 1980, "Refined Closed Methods for the Contraflow Regenerator Problem," *International Journal of Heat and Mass Transfer*, Vol. 23, pp. 655–662.

APPENDIX

The functions $F_n(u, v)$ and $G_n(u, v)$ satisfy two first-order partial differential equations

$$\frac{\partial G_n(u, v)}{\partial v} = F_n - G_n = -\frac{\partial F_n(u, v)}{\partial u} \tag{A1}$$

For $n \geq 0$, $F_n(0, v) = v^n/n!$ and $G_n(u, 0) = 0$. Numerical values for F_n, G_n, $n = 0, 1, 2, \ldots$ can be found by evaluating just three functions and then using two recurrence equations. The three functions are

$$F_{-1}(u, v) = e^{-(u+v)} \sum_{r=0}^{\infty} \frac{u^{r+1}}{(r+1)!} \frac{v^r}{r!} \tag{A2}$$

$$G_{-1}(u, v) = e^{-(u+v)} \sum_{r=0}^{\infty} \frac{u^r}{r!} \frac{v^r}{r!} \tag{A3}$$

$$G_0(u, v) = e^{-(u+v)} \sum_{r=0}^{\infty} \frac{v^{r+1}}{(r+1)!} \sum_{p=0}^{r} \frac{u^p}{p!} \tag{A4}$$

The two recurrence equations are

$$F_n(u, v) = G_n(u, v) + G_{n-1}(u, v), \qquad \pm \text{integer } n \tag{A5}$$

$$G_{n+1}(u, v) = \frac{1}{n+1}[(v-u-1-2n)G_n + (2v-n)G_{n-1} + 2vG_{n-2}], \qquad n \geq 0 \tag{A6}$$

Sealing Strips in Tubular Heat Exchangers

C. E. Taylor

I. G. Currie
Mem. ASME

Department of Mechanical Engineering,
University of Toronto,
Toronto, Canada, M5S 1A4

This paper presents design data relating to sealing strips for tubular heat exchangers. Sealing strip shapes, locations, and gap widths (the distance between the sealing strip and the nearest tube) are evaluated as to the pressure drop they create and, more importantly, as to their heat transfer characteristics. Velocity data were collected using a laser-Doppler anemometry system for which the fluid within the test model flow loop was refractive index matched with the pyrex rods that made up the tube bundle. A normalized heat transfer coefficient for each test has been inferred from the local velocity field. Unexpected trends were found in the heat transfer and pressure drop results of the gap width tests. It was concluded that the rectangular sealing strip located at the seventh row with a gap equal to the difference between the tube pitch and the tube diameter was the most effective. The successful application of LDA in the test program introduces a powerful measuring technique for the flow field in and around tube banks. From the measurements, pressure drops and heat transfer coefficients may be deduced. In addition, the technique will prove to be of great value in the field of flow-induced vibrations where detailed velocity data are required.

Introduction

Shell-and-tube heat exchangers contain both baffle plates and sealing strips as shown in Fig. 1. The baffles force the flow to pass normal to the tubes and they serve to support the tubes. In order to facilitate assembly of the heat exchanger, a space exists between the tube bundle and the retaining shell. This space offers a hydraulic short circuit to the fluid, thus reducing the effectiveness of the device to exchange heat. Sealing strips, which are metal strips mounted on the baffles and running parallel to the tubes, are introduced to block this bypass flow partially, thereby increasing the effectiveness of the device.

Until the late 1940s, tubular heat exchanger design was carried out with the aid of previous experience and the ideal tube bank data of such early researchers as Grimison [1]. The addition of baffles, spacers, tie rods, tube-free lanes, and sealing strips led to commercially usable designs for which heat transfer and pressure drop could not be accurately predicted. Experimentation was required to provide a data base from which empirical equations could be developed.

Such a program was initiated in 1947 with Bergelin and Colburn as the principal investigators and was known as the Delaware project. This project adapted a shell-side flow mechanism first presented by Tinker in 1951 [2]. Tinker identified four streams in the shell-side flow of a heat exchanger and a fifth stream was later identified. The main cross-flow stream passed from one baffle window, across the tubes and out through the other window. An ideal baffled heat exchanger would have all of the shell-side fluid following this route. The other four streams were "leakage" or "bypass" streams which reduced the heat exchanger efficiency. One of these streams passed between the baffle and the shell. This bypass area cannot be easily blocked and has therefore become an accepted loss. Another stream passed between the tubes and the shell. Some success has been found in diverting this flow through the use of sealing strips. The importance of this bypass stream has been repeatedly emphasized in papers by Tinker [3], Bergelin et al. [4], Test [5], and Test et al. [6].

The final Delaware report was published in 1963 and has been continually updated since that time. A recent paper by Bell [7] outlined the "Delaware method" that was developed as a quick and easy design tool for rating various heat exchanger geometries. This method dealt with the effectiveness of sealing strips by using a correction coefficient that varied with bypass area and sealing strip location. Even in this current rating method, neither the actual shape of the sealing strip nor the size of the gap between the strip and the tube bundle was considered.

In England, heat transfer research has developed rapidly since the early 1960s. Gay and associates [8, 9] at the University of Aston developed an electrochemical mass transfer technique, using the Chilton–Colburn analogy to predict heat transfer coefficients. The early work was purposely performed in heat exchanger geometries that had previously been tested by conventional methods in the USA. The far greater speed and ease of this new technique made it the choice of H.T.F.S.[1] as they launched an experimental program that has been producing heat-exchanger design data since 1971. No studies on sealing strips have yet been disclosed but Macbeth [10] reported many of the program findings in a 1983 publication.

A review of the problems involved in heat exchanger design, together with a status report on their progress, has been presented by Taborek [11]. This review points out that the current analyses of the problems, such as that presented by Palen and Taborek [12], rely on large data banks for the values of the flow resistances and the heat transfer coefficients. Yet, significant gaps exist in these data banks. For example, Gorman [13] presented data relating to cross-flow vibrations of rods near sealing strips. However, only total flow velocities

H.T.F.S. = Heat Transfer and Fluid-Flow Service, Harwell, England.

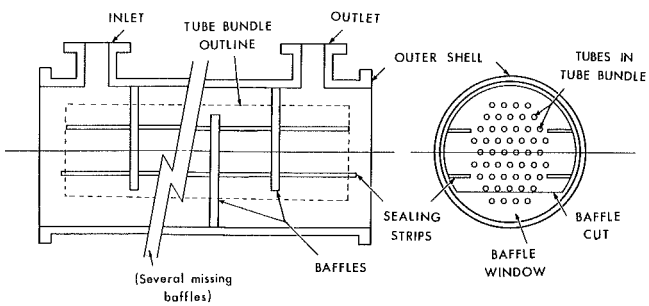

Fig. 1 Shell-and-tube heat exchanger

Contributed by the Heat Transfer Division for publication in the JOURNAL OF HEAT TRANSFER. Manuscript received by the Heat Transfer Division June 3, 1985.

were recorded, not local velocities. That is, the existing data are inadequate with respect to their application to flow-induced vibration analysis or computer code evaluation.

An attempt is made in this paper to illustrate the need for further investigation into the effect of sealing strip geometry and location on the heat transfer characteristics of a tube bundle. This need is especially apparent to those attempting to numerically predict heat exchanger thermal-hydraulics through the use of computer models.

The experimental work outlined in this paper was initiated primarily to supply experimental data which could be used to test the computer code reported by Carlucci et al. [14]. This code has been developed to predict the detailed shell-side flow in a wide range of shell-and-tube heat exchanger geometries. In 1979, Rowe [15] presented a summary of the progress made in the analytical approaches to thermal-hydraulic modeling. He emphasized the need for experimental work dealing with the turbulent mixing in rod bundles and with abnormal flow distributions due to blockage and support structures. An understanding of the effects of sealing strip geometry is indeed important to heat exchanger technology, the development of which grows increasingly as we strive for more efficient devices.

The bypass flow has a significant effect on the temperature profile through a heat exchanger, and on the mean temperature difference across it. This is a consequence of the fact that the bypass flow does not make contact with the same amount of heat transfer area as does the main crossflow. Thus the bypass flow experiences a lower temperature change than the main crossflow, giving rise to a mixing of two flows of differing temperatures at the exit to the tube bank.

2 Test Facilities

The equipment consisted of a transparent heat-exchanger test section, a liquid of matching refractive index, a flow loop, and instrumentation for velocity, pressure, and temperature measurement. Design details can be found in [16].

The test section was constructed of tempered glass with an aluminum frame. The rod bundle geometry, which is shown in Fig. 2, was chosen to represent a section of a nuclear steam generator tube bundle. The heat exchanger tubes were modeled by 12.7 mm o.d. Pyrex rods. The rods were arranged in an equilateral triangular pattern having center-to-center spacing of 19.1 mm. This amounted to a pitch-to-diameter ratio of 1.5. The test section consisted of 12 rows of rods in the streamwise direction, each of these consisting of six rods in the cross-flow direction. In Fig. 2, which shows the test section with 2½ streamwise rows removed, the flow entered at the top and exited at the bottom. The first cross-flow row consisted of six full rods while the second row consisted of five full rods and two half rods. This pattern repeated itself in the streamwise direction.

The Pyrex rods were cantilevered into an end plate of Plexiglass-55 (a particularly corrosion resistant plexiglass). Plexiglass was used because it is difficult to machine Pyrex glass. The full bank of rods was finished on both sides with half rods to simulate the symmetry of a heat-exchanger tube assembly. The half rods rested against thick Pyrex glass slabs that created a 114.3 mm × 114.3 mm cross-sectional area within the test section. After removing three streamwise rows (two of full rods and one of half rods), an aluminum sealing strip could be inserted at any rod row.

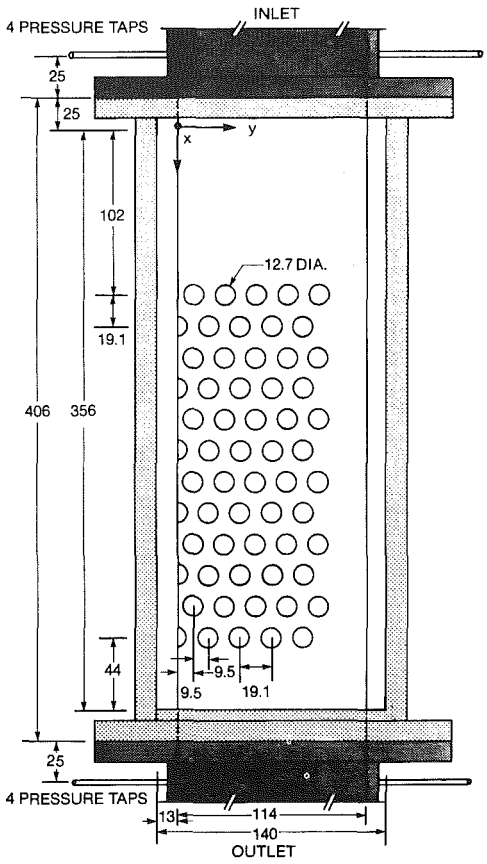

Fig. 2 Test section and tube array

The use of a header (1.1 m above the test section), a settling chamber (0.61 m in length), and an inlet nozzle provided a steady, uniform flow with minimal boundary-layer development. The flow loop could not provide a wide range of flow rates but it was capable of maintaining a Reynolds number of 2.6×10^4 and thus a fully turbulent tube bank flow. The Reynolds number was calculated using the gap velocity u_g for a rod-filled tube bank as the velocity scale and the rod diameter as the length scale.

The velocity measurements were made using a laser-Doppler anemometry (LDA) system because of the need for an unob-

Nomenclature

C = constant in equation (1), W/m²K
D = rod diameter, mm
Eu = Euler number
h = heat transfer coefficient, W/m²K
k = fluid thermal conductivity, W/m K
m = exponent in equation (1)
NHTC = normalized heat transfer coefficient
Nu = Nusselt number
P = tube pitch, mm
Pr = Prandtl number
Δp = pressure drop across the tube bank, N/m²
q = nondimensionalized heat transfer rate
Re = Reynolds number
u = velocity, m/s
ρ = fluid density, kg/m³

Subscripts

A = "all rods" test
g = gap parameter
l = local parameter
∞ = average inlet parameter

Table 1 Test data—summary

Category	*Type	u_∞ ($\frac{m}{s}$)	Euler Number	Normalized Heat Transfer Coefficient
Control Tests	All Rods No Sealing Strip	0.354 0.356	1.84 0.67	1.000 0.666
Shapes	Rectangular Semi-circular Triangular	0.370 0.356 0.366	1.12 0.88 0.83	0.830 0.789 0.798
**Locations	21.6 cm 25.4 cm 29.2 cm	0.370 0.364 0.353	1.12 1.08 0.94	0.830 0.783 0.753
Gap Sizes ***($\frac{Gap}{P-D}$)	No Gap 0.5 0.75 1.0 1.25 1.5	0.364 0.355 0.355 0.370 0.366 0.358	1.47 1.21 1.10 1.12 1.07 0.93	0.842 0.789 0.791 0.830 0.790 0.751

* Unless otherwise noted all tests were run with

Shape = Rectangular
Location = 21.6 cm
Gap/(P-D) = 1.0

** Locations are measured in the x-direction from the origin shown in Figure 2.

*** The gap between the sealing strip and rod has been nondimensionalized by the gap between the tubes (the tube pitch minus the tube diameter).

trusive device to measure the gap velocities. A major obstacle with LDA is the need to make the test section "optically invisible" to the laser beams. This was accomplished by using a fluid mixture of four parts tetrachloroethylene (TCE) and one part Freon-113 which had a refractive index equivalent to that of the Pyrex rods and side plates. A temperature control system provided the fine tuning required to maintain the proper refractive index of the fluid mixture at 1.471. The mixture had a density of 1610 kg/m^3 and a viscosity of 0.844 mPa-s, making it 60 percent more dense than water and 16 percent less viscous than water.

A Spectra Physics HeNe 15 mW laser, OEI transmitting optics, and TSI receiving optics were situated on a traversing mechanism. This mechanism enabled the entire LDA system to move simultaneously from one measuring location to the next without requiring readjustment of the optics.

The LDA system was capable of measuring only one component of velocity at a time. Since both vertical and horizontal components were required, all measurements of a given component were taken and then the test section was traversed again for the second component. Within the tube bank all of the velocity measurements were made midway between the tubes and at the narrowest gap so that the maximum velocity was obtained.

3 Data Analysis

A comparison of the heat transfer coefficients between the various tests was possible because of the high Reynolds number of the flow. It was assumed that the fluid properties were constant throughout the tube bank. This is a reasonable estimate in the fully mixed area of the tube bundle (beyond the first row) and the heat transfer coefficient is then dependent only upon the local velocity. The local velocities are related to the heat transfer rate through the heat transfer coefficient h, which itself is a function of the Nusselt number. A simple form of the Nusselt number for flow across tube bundles of ten or more rows was developed by Grimison [1] and results in the following equation for the heat transfer coefficient:

$$h = C\mathrm{Re}^m \mathrm{Pr}^{\frac{1}{3}} \frac{k}{D} \text{ for } 2000 < \mathrm{Re} < 40{,}000;\ \mathrm{Pr} \geq 0.7 \qquad (1)$$

In order to compensate for the slight variation in inlet velocities over the tests, the heat transfer coefficients were divided by the inlet row equivalent coefficient. The values of C, m, and D all depended only upon the tube bank geometry and therefore did not vary throughout the tube bank. The nondimensionalized value of the heat transfer coefficient h is then simply the ratio of the local velocity u_l to the average inlet velocity u_∞, all raised to the exponent $m = 0.562$. The local velocities within the first row of the tubes were not included in the summation because the flow was not highly turbulent as it entered the tube bank. All summations were performed over the same tube area so that comparisons would be legitimate. A normalized heat transfer coefficient NHTC was inferred from the measured data by dividing by the ideal "all rods" case in which no tube-free lane was present.

$$\mathrm{NHTC} = \frac{h}{h_A} = \frac{\sum \left(\frac{u_l}{u_\infty}\right)^m}{\left[\sum \left(\frac{u_l}{u_\infty}\right)^m\right]_A} \qquad (2)$$

Pressure drop readings taken for each test have been presented in this paper in the nondimensionalized Euler number form. A nondimensionalized form was important due to the dependence of the pressure drop on the average inlet velocity. The equation for the Euler number given below incorporates u_g, the gap velocity, where u_g is equal to the average inlet velocity multiplied by $P/(P-D)$

$$\mathrm{Eu} = \frac{\Delta\rho}{\rho u_g^2} \qquad (3)$$

4 Results

The use of sealing strips to divert flow within heat exchangers was approached by examining the variation of sealing strip shape, location, and gap size. Pressure drop readings as well as complete velocity field measurements were used to determine the Euler number and the normalized heat transfer coefficient for each test. With a greater weighting on the heat transfer results, these two parameters were used to rate the various sealing strip geometries. A summary of the test data is provided in Table 1.

The flow loop could not provide a wide range of flow rates, but it was able to maintain a steady flow. For each test configuration, the flow rate was adjusted to a value between 4.6 and 4.7 liters per second. This resulted in test section approach velocities of between 0.353 and 0.370 m/s, as shown in Table 1. The corresponding Reynolds number, based on the gap velocity for a full array of rods and the diameter of the rods, was 2.6×10^4.

Two full velocity field tests without sealing strips were used as standards. The first test had no tube-free lane while the second test had a tube-free lane but did not have a sealing strip. An ideal heat exchanger has no tube-free lanes for shell-side fluid to pass by the tubes. In accordance with this, the all rods test had a heat transfer coefficient which was 15 percent higher than any other result. In contrast, the second test had a heat transfer result that was almost 10 percent less than any other test, and 33 percent less than the all rods case. Without a sealing strip to divert the flow back into the tube bank, the fluid moved rapidly at first, then more gradually, into the tube-free lane as it passed through the test section.

4.1 Sealing Strip Shape. In practice, the geometry of sealing strip cross sections has been limited to rectangular shapes. In this study semicircular and triangular shapes were also tested, as illustrated in Fig. 3. A large recirculation zone developed behind the rectangular sealing strip while the triangular sealing strip had a narrower zone and the semicircular strip had no noticeable reverse flow area. In selecting the rectangular shape as the most effective, the substantially

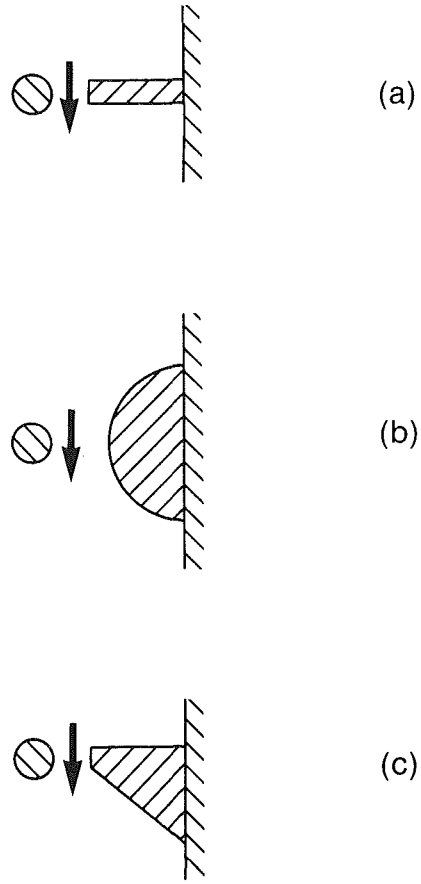

Fig. 3 Sealing strips: (*a*) rectangular, (*b*) semicircular, (*c*) triangular

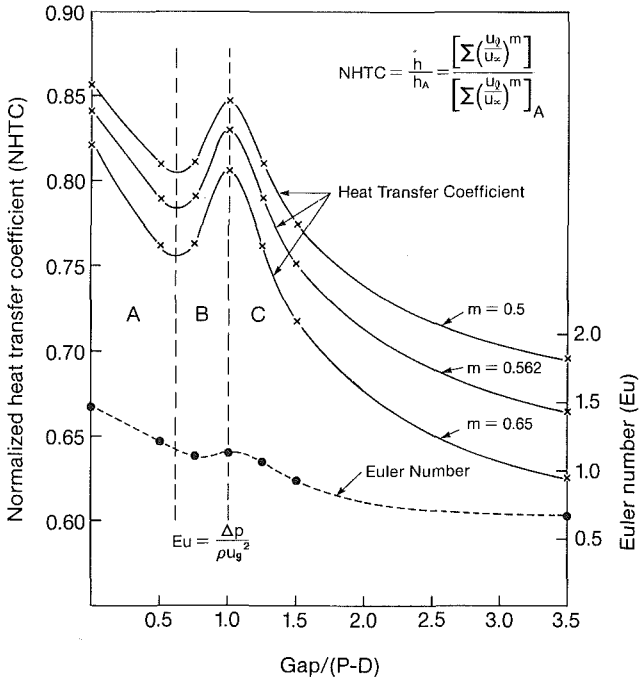

Fig. 4 Variation of heat transfer with sealing strip gap

higher heat transfer coefficient more than compensated for the greater pressure drop which accompanied it. The large recirculation zone created behind the rectangular shape was a desirable phenomenon since it extended the effectiveness of the sealing strip several rows beyond the strip itself.

4.2 Sealing Strip Location. Due to the success of the simple rectangular shape in the pressure test program, the rectangular cross section was used in all of the tests that followed. Moving the sealing strip to different locations within the bypass lane simulated changes in the distance between strips in a full heat exchanger. As the location was lowered, from 21.6 cm to 25.4 cm and finally to 29.2 cm (see Fig. 2 for the x-direction origin), the effective width between the sealing strips increased accordingly. In all cases the effect of the sealing strip was obvious. The heat transfer results shown in Table 1 agree with the Delaware method [7] and suggest that an increase of 15 percent in the heat transfer coefficient would be possible for this particular tube bank geometry if a sealing strip was placed at every fifth row of tubes. Of course, the amount of increase in the heat transfer coefficient will depend on the width of the bypass lane relative to the total flow width of the tube bank.

The rectangular sealing strip was located at $x = 21.6$ cm for all further tests.

4.3 Sealing Strip Gap Size. The most extensive part of this test program was an investigation of the consequences of varying the distance between the end of the sealing strip and the nearest tube. These gap size results did not come out as intuition might suggest. One might expect that as the gap size was decreased more and more, fluid would be diverted into the tube bank and therefore a monotonic increase in heat transfer coefficient would occur. Figure 4 shows a plot of the results obtained in this part of the test program. A peak can be seen at $GAP/(P-D) = 1.0$ in both the heat transfer coefficient and Euler number data. The $m = 0.65$ and $m = 0.5$ heat transfer lines were included to illustrate the fact that the choice of the value for the exponent m was not crucial in determining the existence or even the relative size of the peak.

Some indication as to how the peak happened to occur at $GAP/(P-D) = 1.0$ can be found in Figs. 5 and 6. Figure 5 provides typical streamline diagrams of the flow fields that were measured. These streamline positions were calculated under the premise that an equal volume of fluid should pass between each pair of lines. $GAP/(P-D) = 0.0$ had velocities as high as 1.6 m/s within the tube bank and had a very large recirculation zone behind the sealing strip. The size of this recirculation zone did not simply decrease as the gap widths increased. In fact, $GAP/(P-D) = 0.5$ and 0.75 had slightly smaller areas of reverse flow than did $GAP/(P-D) = 1.0$. As the gaps were increased further the velocities through the bypass lane increased and the recirculation zones decreased in size appropriately.

The heat transfer maps shown in Fig. 6 also illustrate that $GAP/(P-D) = 1.0$ was the most effective gap size. This gap size did not produce the highest heat transfer but the higher values were distributed further into the tube bank. It should be noted that the very low values of heat transfer which occur along the edge of the tube bank were due, first, to the fact that the local velocities were lower in the tube-free lane, and second, to the fact that they were further reduced to compensate for the smaller tube-surface area which the edge flow influences.

Figures 5 and 6 help to explain how a peak happens to appear, but the question still remains as to why it is there. The factors influencing the flow patterns within a tube bank and sealing strip geometry are many. To name a few, the inlet velocity, tube array geometry, bypass lane size, gap size, and fluid properties all affect the local velocities that will be found within the tube bundle. Although only the gap size was altered with each new test, the other factors still remain as part of the balance.

The plot in Fig. 4 has been divided into three regions. Region A represents the "small gap" area. In this area the velocities within the tube bank are very high and a very large

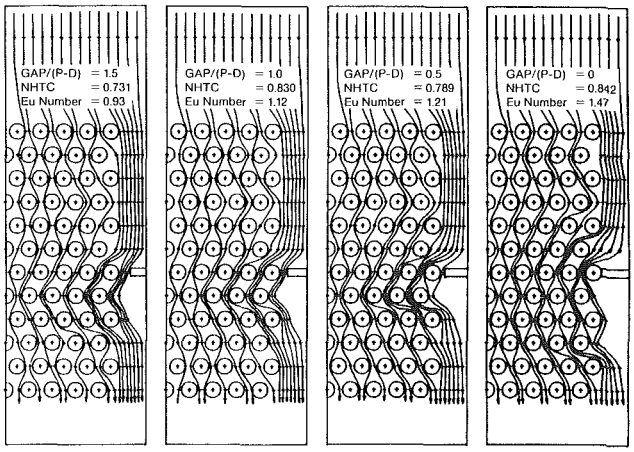

Fig. 5 Typical streamline plots

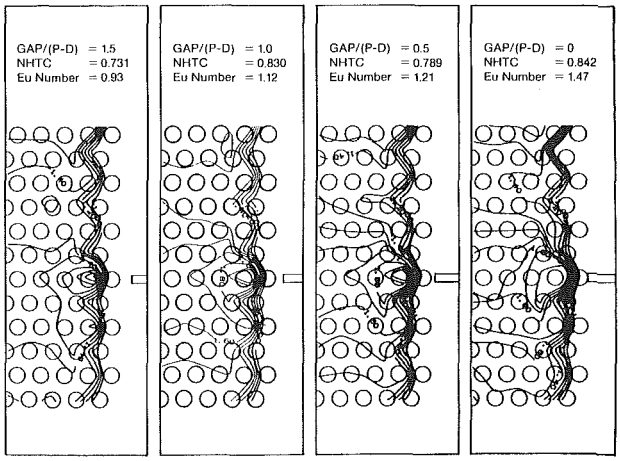

Fig. 6 Typical heat transfer maps

recirculation zone exists. As the gap widens the flow within the tube bank decreases slightly and the momentum no longer carries the flow as far past the sealing strip so that the NHTC decreases. In Region C the same mechanism is at work with the result that the heat transfer decreases as the gap widens. The anomaly occurs in Region B. If one moves from Region C into Region B, one finds that the volume of flow within the tube bank reaches a quantity such that it is forced back into the tube-free lane since its own downward momentum is still not great enough to maintain the tube bank flow. As one continues to narrow the gap the growing momentum of the tube bank flow combined with the increased sealing strip length eventually causes the recirculation zone to grow again and, therefore, the heat transfer coefficient to increase as in Region A. This is one attempt at an explanation as to why GAP/$(P-D) = 1.0$ is the most effective gap size.

The greatest heat transfer coefficient existed when no gap was allowed between the sealing strip and the tube. This was not, however, chosen as the most effective gap width because the Euler number was very high and having the sealing strip touching the tube was not practical.

5 Conclusions

The use of any sealing strip will provide a heat transfer coefficient that will fall between that of the "ideal" rod-filled test section and that of the case with no sealing strip. A test of various sealing strip shapes exposed the fact that a compromise between heat transfer and pressure drop would have to be reached. For the purposes of this study an emphasis was placed on obtaining a high rate of heat transfer. The rectangular cross section then became an obvious first choice.

The placement of the rectangular sealing strip at three different locations within the tube-free lane supported data already given in the literature. Sealing strips placed close together (3.6 rows apart) will provide optimum heat transfer characteristics by diverting a maximum amount of fluid into the tube bundle.

The most significant results were obtained from the tests carried out at various gap widths. It was found that GAP/$(P-D) = 1.0$ was preferable. This corresponds to a gap width equal to the spacing between the rods. The flow mechanisms which produced a peak in the heat transfer results are not easily explained.

The LDA measurement technique has proved to be extremely valuable in the present study. It represents an important contribution to the state of the art in direct velocity measurement and inferred heat transfer coefficients and pressure drops. It is expected to prove to be even more valuable in flow-induced vibration analysis where details of the fluid velocity are required, but are difficult to obtain.

The study on the effect of varying gap widths has indicated that it will be worthwhile performing further tests on actual heat exchanger geometries. In such tests variation of the tube diameter, pitch, layout angle and bundle outer tube diameter could be considered.

Acknowledgments

The authors would like to acknowledge the technical assistance of Dr. R. L. Varty who so capably initiated this research project. Much of the design and construction of the flow loop was carried out by E. Morala. Special thanks are extended to these two individuals for their contributions to this work.

The research which formed the basis of this paper was sponsored by Atomic Energy of Canada Limited, Chalk River Nuclear Laboratories in the form of a research contract held with the University of Toronto. The financial assistance offered through this contract is gratefully acknowledged.

Appreciation is also extended to L. N. Carlucci, of the Engineering Research Branch at the Chalk River Nuclear Laboratories, for contributing his expertise throughout the tenure of the research project.

References

1 Grimison, E. D., *ASME Transactions,* Vol. 59, 1937, pp. 583-594.

2 Tinker, T., "Shell Side Characteristics of Shell and Tube Heat Exchangers," *General Discussion on Heat Transfer,* Institution of Mechanical Engineers, London, England, 1951, pp. 97-116.

3 Tinker, T., "Shell Side Characteristics of Shell and Tube Exchangers – A Simplified Rating System for Commercial Heat Exchangers," *ASME Transactions,* Vol. 80, 1958, pp. 36-52.

4 Bergelin, O. P., Bell, K. J., and Leighton, M. D., "Heat Transfer and Fluid Friction During Flow Across Banks of Tubes – VI, The Effect of Internal Leakages Within Segmentally Baffled Exchangers," *ASME Transactions,* Vol. 80, 1958, pp. 53-60.

5 Test, F. L., "The Influence of Bypass Channels on the Laminar Flow Heat-Transfer and Fluid Friction Characteristics of Shell and Tube Heat Exchangers," ASME JOURNAL OF HEAT TRANSFER, Vol. 83, 1961, pp. 39-47.

6 Test, F. L., and Kingston, R. I., "A Study of Heat Transfer and Pressure Drop Under Conditions of Laminar Flow in the Shell-Side of Cross-Baffled Heat Exchangers," *ASME Transactions,* Vol. 80, 1958, pp. 593-600.

7 Bell, K. J., "Delaware Method for Shell-Side Design," *Heat Exchangers: Thermal Hydraulic Fundamentals and Design,* S. Kakac et al., eds., Hemisphere Publishing Co., New York, 1981, pp. 581-618.

8 Gay, B., and Roberts, P. C. O., "Heat Transfer on the Shell-Side of a Cylindrical Shell-and-Tube Heat Exchanger Fitted With Segmental Baffles. Part II: Flow Patterns and Local Velocities Derived From the Individual Tube Coefficients," *Transactions Institution Chemical Engineers,* Vol. 48, 1970, pp. T3-T6.

9 Gay, B., and Williams, T. A., "Heat Transfer on the Shell-Side of a Cylindrical Shell-and-Tube Heat Exchanger Fitted With Segmental Baffles. Part I: Bundle and Zonal Average Heat Transfer Coefficients," *Transactions Institution Chemical Engineers,* Vol. 46, 1968, pp. T95-T100.

10 Macbeth, R. V., "Heat Exchanger Design and Practices," *Heat Exchangers: Theory and Practice,* J. Taborek et al., Hemisphere Publishing Corporation, New York, 1983, pp. 615-629.

11 Taborek, J., "Heat Exchanger Design," *Proceedings of 6th International Heat Transfer Conference,* Toronto, 1978, pp. 269-283.

12 Palen, J. W., and Taborek, J., "Solution of Shell Side Flow Pressure Drop and Heat Transfer by Steam Analysis Method," *Chemical Engineering Progress Symposium Series,* Vol. 65, 1969.

13 Gorman, D. J., "Experimental Study of Peripheral Problems Related to Liquid Flow Induced Vibrations in Heat Exchangers and Steam Generators," *Proceedings 4th International Conference in Structural Mechanics in Reactor Technology,* San Francisco, 1977.

14 Carlucci, L. N., Galpin, P. F., and Brown, J. D., "Numerical Predictions of Shellside Heat Exchanger Flows," *A Reappraisal of Shellside Flow in Heat Exchangers,* HTD Vol. 36, W. J. Marner and J. M. Chenoweth, eds., ASME, New York, 1984.

15 Rowe, D. S., "Progress in Thermal Hydraulics for Rod and Tube-Bundle Geometries," *Fluid Flow and Heat Transfer Over Rod or Tube Bundles,* ASME Conference, New York, 1979.

16 Taylor, C. E., "Experimental Development of Sealing Strip Design in Tubular Heat Exchangers," Master of Applied Science Thesis, University of Toronto, 1984.

Dehumidification: On the Correlation of Wet and Dry Transport Processes in Plate Finned-Tube Heat Exchangers

P. W. Eckels
Research and Development Center,
Westinghouse Electric Corporation,
Pittsburgh, PA 15235
Mem. ASME

T. J. Rabas
Combustion Turbine Systems Division,
Westinghouse Electric Corporation,
Concordville, PA 19331
Mem. ASME

The transverse velocity of the condensing phase during dehumidification is analogous to the transverse velocity at the wall when exercising boundary layer control by fluid extraction through a permeable wall. Wet and dry pressure drop and heat transfer rates are analyzed for correlation using boundary layer suction theory. Data are presented for flat-plate finned-tube heat exchangers during air heating and dehumidification operations and the data show a significant effect of transverse velocity correlated by the boundary layer suction formulation. The condensate film is considered isothermal in this analysis and the results indicate that an improved modeling of the condensate film is required. We find that the transverse velocity of the condensing phase has an important effect on transport phenomena during dehumidification and that the validity of the Chilton–Colburn heat and mass transfer analogy in describing dehumidification is supported by these results. It should be noted that the dry data form the beginning of a plate fin heat exchanger data base. The present data show the effect of tube diameter and, independently, fin density variation on the Colburn and friction factors with all other geometric parameters held invariant.

Introduction

Many authors, for example, Guillory (1975), report an increase in sensible heat transfer coefficient during dehumidification. Although the increase is frequently attributed to condensate film roughness or droplet formation on the surface, a unique dependence of heat transfer augmentation on film roughness has not been established. This work seeks to provide a better understanding of the dehumidification process through a study of the effects of the transverse velocity of the condensing phase on heat, mass, and momentum transfer. The transverse velocity of the condensing phase in dehumidification causes increases in friction, heat and mass transfer that are analogous to the increases observed in boundary layer control by suction at the wall. Heretofore, this effect has not been considered in attempts to correlate dehumidification and dry transport processes.

Theory and some experimental data, acquired in an effort to comprehend better wet air-side transport processes in flat-plate finned-tube heat exchangers, are presented. In particular, the influence of the transverse velocity of the condensing phase on friction, heat transfer, and the analogy between heat and mass transfer is evaluated. It will become evident to the reader that the effect of the transverse velocity is significant, that progress toward correlation has been made, but that final correlation has not been accomplished. In this study, the condensate film is assumed isothermal and stationary; an assumption which can account for most of the disparities between the correlated wet test data and the dry test data.

The usual approach to the calculation of air-side transport applies the Chilton–Colburn heat and mass transfer analogy (ASHRAE, 1982) to eliminate the mass diffusion coefficient and density difference driving potential from the transport equations. In conventional practice the effects of secondary flows, the transverse velocity of condensing water vapor, and a longitudinal condensate flow velocity, are included only by empirical means. Unfortunately the present work continues to neglect the effects of the condensate layer on the transport processes.

Although the original program intent was to explore only the effect of the transverse velocity of the condensing phase, it was found that an accurate evaluation of the fin surface temperature, which is vital in predicting mass transfer rates, was not possible because the fin–tube contact conductance could not be evaluated. In the course of these experiments, a correlation for dry contact conductance was developed (Eckels, 1977) and the wet conductance of the sample coils was measured. This phase is briefly reviewed.

The effect of the transverse velocity of the condensing phase is described by wall suction theory developed for laminar (Hartnett and Eckert, 1957) and turbulent boundary layers (Kinney and Sparrow, 1970). Theory indicates the transverse velocity tends to increase friction and heat and mass transfer in a similar ratio and data show that analogy exists between the increased heat and mass transfer. However, that part of the pressure drop not associated with shear stress at the wall (form drag, etc.) tends to break down the analogy between pressure drop and heat transfer.

Data presented were acquired testing flat-plate finned-tube heat exchangers (A, B, C, and D in Table 1) in a temperature and humidity-controlled wind tunnel. Figure 1 shows a typical exchanger before any test preparation and Fig. 2, a fin that differs from the flat fins of the present test series only by its corrugations. The testing conditions approximate those used in rating condensers and evaporators of air conditioning units.

Theory

The suction or lateral velocity in the transpiration boundary layer solutions has its analogue in the lateral velocity of the condensing phase during dehumidification. For low condensing rates or high air velocities, the thickness of the condensate film can be neglected in flow area, pressure drop, and film temperature drop computations. Adopting these assumptions,

Contributed by the Heat Transfer Division and presented at the Industrial Heat Exchanger Conference, Pittsburgh, Pennsylvania, November 1985. Manuscript received by the Heat Transfer Division October 23, 1985.

Table 1 Heat exchanger description: a summary of the nominal test coil data

Description	A	B	C	D
Type	Flat-Plate Finned Tube	Flat-Plate Finned Tube	Flat-Plate Finned Tube	Flat-Plate Finned Tube
Face Dimension, mxm	0.91 × 0.3	0.91 × 0.3	0.91 × 0.3	0.91 × 0.3
Depth, mm	66.0	66.0	66.0	66.0
Tubes				
Number of Rows	3	3	3	3
Tubes Per Row	12.0	12.0	12.0	12.0
Pitch	Staggered	Staggered	Staggered	Staggered
Transverse Pitch, mm	25.4	25.4	25.4	25.4
Longitudinal Pitch, mm	22.0	22.0	22.0	22.0
Tube OD, mm	6.731	10.16	13.25	9.804
Tube ID, mm	6.157	9.347	12.38	8.992
Material	Cu	Cu	Cu	Cu
Row Orientation	Horizontal	Horizontal	Horizontal	Horizontal
Number of Circuits	6	6	3 with Crossover	3 with Crossover
Circuitry	Parallel	Parallel	Parallel	Parallel
Fins				
Material	Al	Al	Al	Al
Fins Per mm	0.507	0.472	0.447	0.320
Fin Thickness, mm ± 0.005	0.140	0.140	0.140	0.140
Collar	Full	Full	Full	Full
Area Collar Per Unit Tube Length, mm	20.4	30.48	39.84	30.27
Area Fin Per Unit Tube Length, m	0.5307	0.4465	0.3697	0.3072
Face Area/Minimum Flow Area	1.487	1.82	2.282	1.76
Hydraulic Diameter, D_h, mm	2.74	2.57	2.39	3.76

the condensate film surface becomes the flow boundary and the boundary may be considered permeable to the condensing phase but not to air. It is well known (Eckert and Drake, 1959) that analogy exists between laminar and turbulent heat, mass, and momentum transfer under condensing and evaporating conditions if the partial pressure of the vapor is small and the

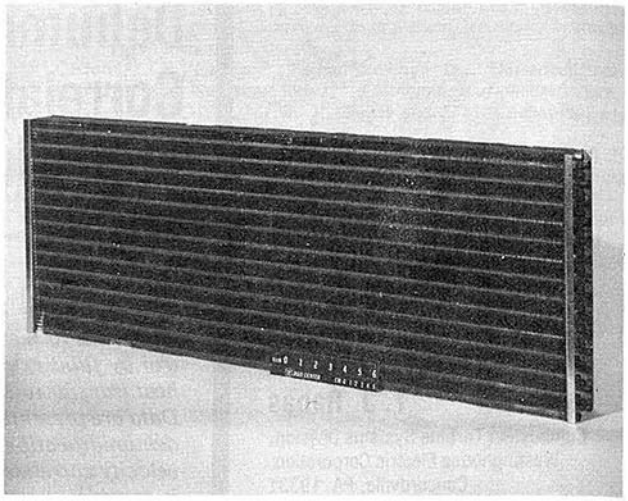

Fig. 1 A typical heat exchanger before test preparation

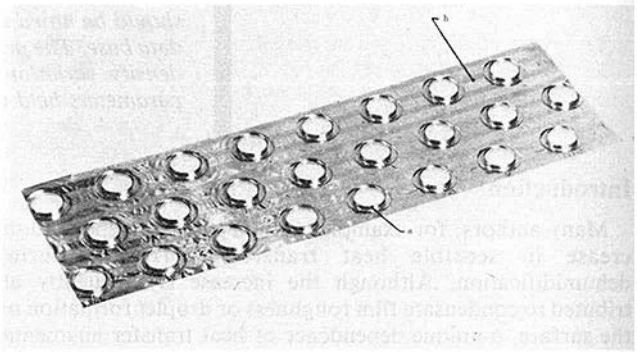

Fig. 2 A corrugated fin typical of flat-plate finned-tube heat exchangers: (*a*) collars, (*b*) corrugations

Nomenclature

A_c = collar area
A_f = fin area
$A_{\min}$ = minimum flow area
A_s = wetted surface area
c_p = specific heat at constant pressure
d_{tb} = tube diameter
d_h = hydraulic diameter = 4•fluid volume/wetted area
D = diffusion coefficient
D_h = hydraulic diameter, equation (9)
f = friction factor, equation (11)
$G_{\max}$ = mass velocity based on $A_{\min}$
Gz = Graetz number = $\mathrm{RePr}d_h/p_1$
h = convection coefficient
h_D = mass diffusion coefficient
j = Colburn j factor, equation (12)
L = heat exchanger streamwise length
Le = Lewis number = $(\mu/\rho D)/\mathrm{Pr}$ = Sc/Pr
m = condensate flow rate
n = number of active tubes
n_f = number of fins/length
Δp = pressure drop, air side
p_1 = streamwise tube pitch
Pr = Prandtl number
q = heat flow rate
R_{ct} = thermal resistance of contact
R_{cl} = thermal resistance of collar
R_f = thermal resistance of refrigerant film or thermal resistance of fin between tube rows
R_t = total thermal resistance
R_{tb} = thermal resistance of tube
R_{tf} = thermal resistance of tube fouling film
R_{wf} = thermal resistance of condensate film
Re_{d_h} = Reynolds number based on hydraulic diameter
Re_{D_h} = Reynolds number based on D_h, equation (10)
Sc = Schmidt number = $\mu/(\rho D)$
t = temperature
t_{cl} = temperature of collar
t_r = temperature of refrigerant
t_w = temperature of wall
U_{ct} = contact conductance
v = air velocity
x = duct center line coordinate
y = exchanger width, horizontal (active tube length)
δ = fin thickness
η = fin efficiency = $\int(t_a - t) \cdot dA/[(t_a - t_a) \cdot \int dA]$
μ = dynamic viscosity
ρ = density
ρ_g = density of water vapor
ρ_{sw} = density of saturated water vapor at wall temperature

Superscripts

$'$ = "per unit tube length"

Subscripts

a = air
e = outlet
eff = effective
i = inlet
t = total
w = at wall
0 = limiting value as condensate flow approaches zero
∞ = free-stream condition

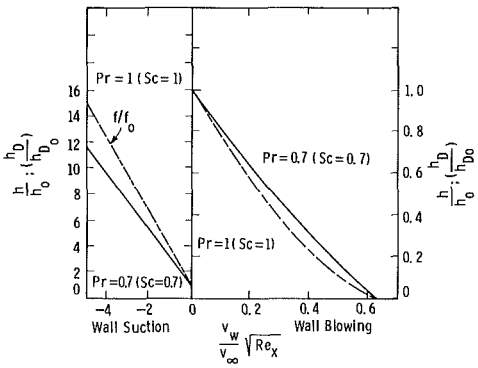

Fig. 3 Heat and mass transfer augmentation for laminar flow on a flat plate with transpiration

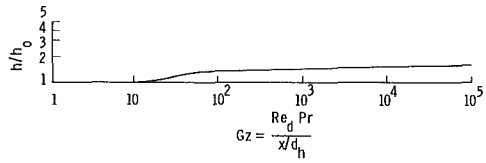

Fig. 4 Maximum heat transfer augmentation due to velocity profile alteration for laminar flow between flat plates as a function of Graetz number. The ratio h/h_0 is uniform velocity profile h divided by the parabolic profile h_0.

Prandtl and Schmidt numbers are near unity. Somewhat less well known is that analogy exists between the constant property boundary layer equations of heat, mass, and momentum transfer with wall injection or suction of the flowing or a different fluid.

Transpiration Theory. Hartnett and Eckert (1957) have solved the constant property boundary layer differential equations for flow along a flat plate with a transverse velocity of a second phase at the wall and have found an analogy similar to that which exists between heat and mass transfer. Figure 3, substantially reproduced from Eckert and Drake (1959), represents their solution in terms of the parameter $(v_w/v_\infty) \cdot \sqrt{\mathrm{Re}}$ where negative values of v_w indicate suction.

Kinney and Sparrow (1970) have numerically solved the problem of boundary suction for turbulent flow in a tube. Considering the velocity profile of turbulent flow, it could be expected that most of the effects of lateral velocity would appear in the laminar sublayer and buffer layers. Thus the form of the laminar solution of Hartnett and Eckert for the effect of the lateral velocity should adequately describe the turbulent case as well. This is found to be the case because a curve fit to the laminar suction solution of Fig. 3

$$h/h_0,\ h_D/h_{D_0} = 1.0 - 2.1(\mathrm{Re}^{0.5})v_w/v_\infty \qquad (1)$$

is found to describe the effect of suction in turbulent tube flow predicted by Kinney and Sparrow up to moderate values of the suction parameter. For friction, f/f_0, the coefficient in equation (1) is 2.8 instead of 2.1. Equation (1), then, can be used to describe condensation in developing laminar flow and turbulent flow.

Since equation (1) is based on a flat plate solution, a question exists as to how it should be applied to well-developed laminar channel flow. Sparrow (1955) has computed the average Nusselt number for parabolic and uniform velocity profile laminar flows between parallel, constant wall temperature flat plates. Taking the ratio of these two gives the maximum effect of the transverse velocity modification of the wall velocity profile on the transport processes if the sensible heat transport by the laterally flowing phase is negligible. Figure 4 shows that the ratio decreases toward 1.0 for $\mathrm{Gz} < 70$. This means, simply stated, that the effect of transverse velocity diminishes as the heat exchanger temperature and vapor density difference approach zero at the outlet. It should be noted that similar behavior is to be expected of condensate roughness because it also acts to modify the velocity profile in a similar way. McQuiston and Parker (1977) identify this behavior in heat exchanger laminar flows which are frequently fully developed and limited in heat transfer by thermal approach at the exchanger outlet.

The approach effect may not be adequately described by the logarithmic temperature and density difference relations if equation (1) is applied to data previously reduced to heat transfer coefficients by using log mean temperature differences. When predicting sensible and latent heat transfer capacity, as in a heat exchanger rating procedure, equation (1) is applied to the heat transfer coefficient before computing exit temperature difference so that the limitation of Fig. 4 is included in the rating computations. In reducing the data for this paper, the approach limitation was not accounted for unless it exceeded the limitation of Fig. 4. Thus, in these data, a tendency to overpredict the effect of the transverse vapor velocity exists at the lowest velocities where the flow is fully developed.

Data Reduction. The mathematical model of the heat exchanger depicted in Fig. 5 and upon which the data reduction computer program is based is the result of several fundamental assumptions which are nearly universally adopted. These are:

1. All heat flow is assumed normal to the tube axis. Thermal resistance due to axial heat conduction in the collar is lumped into the contact impedance. Internal conduction between tubes is neglected.
2. Uniform transport properties are assumed, i.e., constant heat and mass transfer coefficients are assumed.
3. Fin efficiency computation uses the equivalent circular fin method recommended by the ARI (1972) and, in dehumidification, the fin temperature variation is assumed small enough to linearize locally the temperature-saturated vapor density curve. According to Brown (1954), if the total heat equivalent is used, linearization of the vapor density curve implies that the usual constant thickness circular fin efficiency solutions are valid for constant coefficient and property heat and mass transfer.
4. Low vapor pressure approximations are made in the air–water vapor mixture computations. The transformation of Fick's Law which describes simultaneously diffusing species into a moving coordinate system to account for zero counterdiffusion velocity of air at the solid wall is neglected. Negligible counterdiffusion velocity of air implies the molecular transport flux at the condensate surface is very small, hence nearly reversible. Reversible molecular transport occurs only at a saturated interface so a significant departure from the predictions of the analogy can be expected at high mass transfer rates. The reader is referred to the ASHRAE *Fundamentals* (1982) for a full discussion of the implications of the low vapor pressure approximations.
5. Heat exchange surfaces are either fully wetted or dry, i.e., entering air dew point is either above the entering water temperature or below the minimum fin temperature at water outlet. Wet and dry zones within the heat exchanger were not defined although wet and dry partitioning is frequently utilized in the analysis of dehumidification (ARI, 1972).

The equations for raw data reduction to total, sensible plus latent, capacity are detailed in ARI Standard 410 (1972) with additional radiation and mass transfer corrections to the psychrometric data detailed by Threlkeld (1962). From total capacity, air-side transport data are determined by the equation

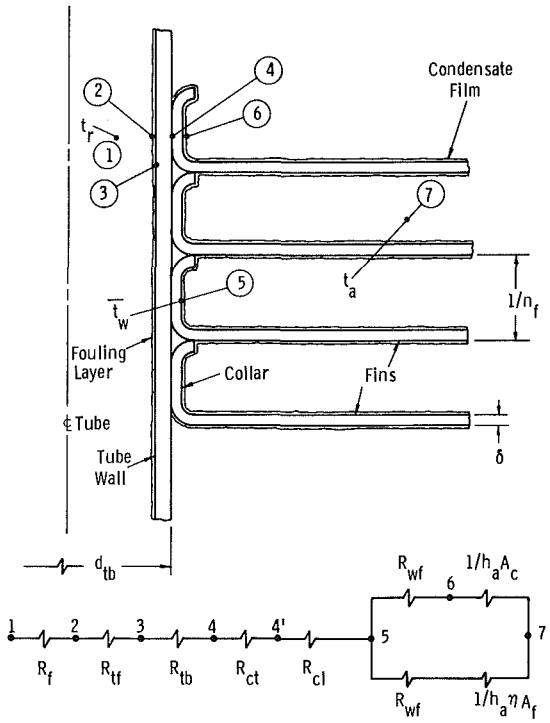

Fig. 5 Physical arrangement of the fin and tube compared to the thermal model

$$h_{\text{eff}} = 1.0/[(A_c' + \eta A_f')(R_t' - R_{tb}' - R_{tf}' - R_f' - R_{ct}' - R_{cl}' - R_{wf}')] \quad (2)$$

which is based on the thermal circuit in Fig. 5. The overall thermal resistance per unit tube length is

$$R_t' = \frac{n \cdot y}{q_t} \cdot \frac{(t_{ri} - t_{ae}) - (t_{re} - t_{ai})}{\ln [(t_{ri} - t_{ae})/(t_{re} - t_{ai})]} \quad (3)$$

For dry surfaces, equation (2) gives the uniform air-side heat transfer coefficient (HTC), but for dehumidification it is only used to determine fin efficiency.

Many methods of representing dehumidification have been developed and are in use. The method developed herein is very fundamental and was selected because its prospects of correlating wet and dry performance through the heat and mass transfer analogy seem best. The sensible heat transfer coefficient is defined by

$$q' = h(A_c' + \eta A_f') \cdot \frac{(t_{ai} - t_{we}) - (t_{ae} - t_{wi})}{\ln [(t_{ai} - t_{we})/(t_{ae} - t_{wi})]} \quad (4)$$

and mass transfer coefficient by

$$m' = h_D (A_c' + \eta A_f') \cdot \frac{(\rho_{gi} - \rho_{swe}) - (\rho_{ge} - \rho_{swi})}{\ln [(\rho_{gi} - \rho_{swe})/(\rho_{ge} - \rho_{swi})]} \quad (5)$$

According to theory t_w should be the temperature at the water film surface on the air side. However, theory for film thickness has not been completed and R_{wf} is assumed 0. Under this assumption t_w and ρ_{sw} refer to the collar surface temperature and saturated water vapor density at t_w. Once fin efficiency has been determined by using equation (2) to determine an effective HTC for sensible plus latent capacity, the experimental values of h and h_D can be found from equations (4) and (5) using the collar temperature at inlet and outlet determined by the thermal resistance ratio expressed as

$$t_w = t_r + (t_a - t_r)(R_{tb}' + R_{tf}' + R_f' + R_{ct}' + R_{cl}' + R_{wf}')/R_t' \quad (6)$$

with h and h_D given as

$$h = q' / \left[(A_c' + \eta A_f') \cdot \frac{(t_{wi} - t_{ae}) - (t_{we} - t_{ai})}{\ln ((t_{wi} - t_{ae})/(t_{we} - t_{ai}))} \right] \quad (7)$$

$$h_D = m' / \left[(A_c' + \eta A_f') \cdot \frac{(\rho_{gi} - \rho_{swe}) - (\rho_{ge} - \rho_{swi})}{\ln ((\rho_{gi} - \rho_{swe})/(\rho_{ge} - \rho_{swi}))} \right] \quad (8)$$

The dry data are reduced to nondimensional form using equations (9)–(12)

$$D_h = 4 A_{\min} L / A_s \quad (9)$$

$$\text{Re}_{D_h} = G_{\max} D_h / \mu \quad (10)$$

$$f = 2(\Delta p) A_{\min} \rho / (G_{\max}^2 A_s) \quad (11)$$

$$j = h \cdot (\text{Pr}^{2/3}) / (G_{\max} c_p) \quad (12)$$

Correlation of Wet and Dry Test Data. A theory has been presented in the previous section that relates the transverse velocity of condensing water vapor to an augmentation factor for momentum, heat, and mass transfer. Equation (1) can be written as equation (13) and applied to Pr = 0.7 and Le = 1.0 fluids with constant properties

$$h/h_0; \quad h_D/h_{D_0} = 1.0 - 2.1 \cdot \frac{m \cdot (\text{Re}_{d_h})^{1/2}}{v \cdot (A_c + A_f) \cdot \rho_{sw}} \quad (13)$$

The assumption of small mass fraction of water is also implicit in equation (13). The augmentation predicted by equation (13) is a strong function of ρ_{sw}, the saturation density of water vapor at the wall temperature. Wall temperature is a mean value approximated by

$$t_w = \frac{t_{cl} A_c + [\eta t_{cl} + 0.5(1 - \eta)(t_{ai} + t_{ae})] A_f}{A_c + A_f} \quad (14)$$

Equation (14) is obtained as an area-weighted average of collar and mean fin temperature which is derived from the usual fin efficiency applied to fin root–air temperature difference.

Correlation of the wet and dry air-side heat and mass transfer coefficients is attempted using the Chilton–Colburn heat and mass transfer analogy as expressed by Kays (1966)

$$h_D = (h/c_p) \cdot (\text{Pr}/(\mu/\rho D))^{2/3} \quad (15)$$

where the diffusion coefficient is given by Eckert and Drake (1959) as

$$D \text{ [sq.ft/hr]} = 0.892 \frac{14.22}{P \text{ [lbf/sq.in.]}} (1 + t \text{ [R]}/460.)^{1.81} \quad (16)$$

The air-side properties are evaluated at the average of collar and fin temperature and mean air temperature.

Test Facility Description

The Heat Exchanger Test facility at the Westinghouse Research and Development Center has been described by Rabas and Eckels (1976) and will only be generally described here. A closed-loop wind tunnel circulates temperature and humidity-controlled air through the test section at preset velocities. The test section volume is 3 cu ft in which R-12, R-22, hot and cold water, and steam working fluids are available. Air-side enthalpy is determined from wet and dry bulb temperature measurements read from mercury-in-glass thermometers located in aspirating-type psychrometers. Heated or cooled water is circulated to the tube side of the heat exchanger and its enthalpy change is determined by thermocouples (TC) with NBS traceable calibration. TC output is read on a L&N type K-3 potentiometer with 0.1 μV minimum subdivision. Air and water mass flow rates are determined by long radius ASME nozzles and a weigh tank, respectively.

Condensate from the air side of the exchanger is collected and compared to the mass flow determined by humidity measurement. This overall mass balance is done in addition to the energy balances required by ARI Standard 410-72 (1972).

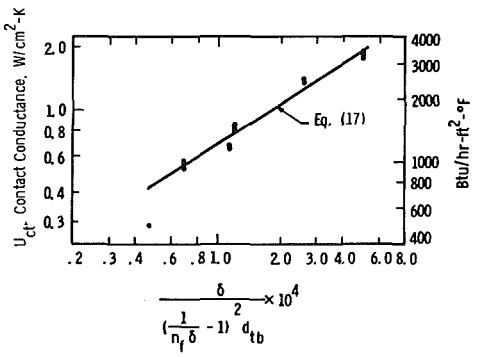

Fig. 6 Dry contact conductance of plate finned-tube heat exchangers versus the parameter of equation (17)

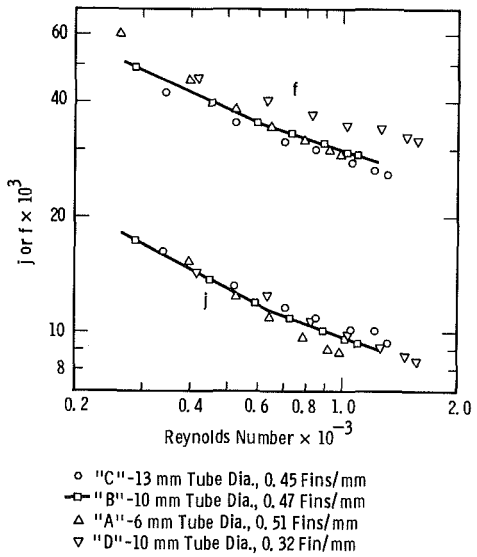

Fig. 7 Flat-plate finned-tube heat exchanger Colburn and friction factors versus maximum Reynolds number

The onset of blow-off of the condensate is determined by visual observation through double glazed windows.

When ready for test each coil has completed preparations which include "Trichlor" decreasing and detergent wash and dry on the air side, mild acid cleaning on the tube side, return bend thermocouple installation, and perimeter thermal insulation. The air side cleaning will typically result in film condensation.

It should be noted that heat exchangers A, C, and D were made in a model shop by mechanically expanding one tube at a time. These coils have visible split collars. Attempts to improve their contact conductance by hydraulic expansion further degraded the conductance. These coils were excluded from the group used to obtain the contact conductance correlation but individual measurements of wet and dry contact conductance were made to enable these coils to be used in the present work.

Contact Conductance

Early in the experimental program it was found that dry air-side data from plate finned exchangers of varying tube diameter, fin number, and fin thickness could not be correlated using a constant contact conductance between fin and tube collar. A correlation for dry contact conductance was developed and reported by Eckels (1977), and is summarized below.

It is well known that the contact conductance between materials is best correlated by interfacial pressure and, therefore, if the state of stress in the collar can be related to interfacial pressure, a reasonable correlation of contact conductance should follow. Two distinct collar zones were considered: The first applies to long collars in exchangers of seven to nine fins per inch where collar hoop stress most strongly influences the interfacial pressure, and the second applies to short collars in exchangers of 15 to 18 fins per inch where the bending moment at the fin root most strongly influences the interfacial pressure.

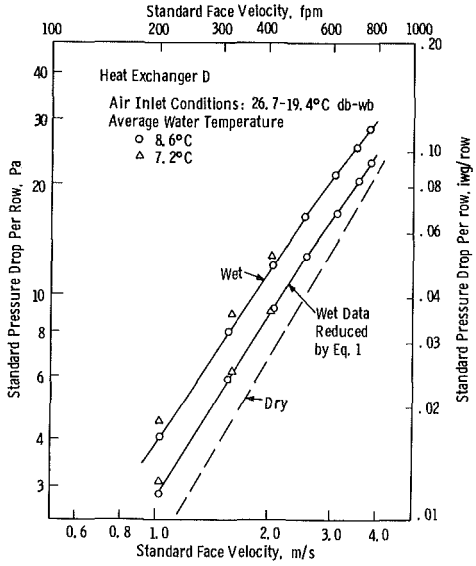

Fig. 8 Wet pressure drop versus face velocity showing the correlating capability of equation (1) on pressure drop

The interface pressure far from the plate fin is related to the collar hoop stress and, near the fin, the collar-to-tube interfacial pressure is related to the moment at the fin root.

These relations are developed by Eckels (1977) and result in equation (17) describing the contact conductance

$$U_{ct} = a[\delta/((1/(n_f\delta) - 1)d_{tb}^2)]^b \tag{17}$$

An experimental program (using a different group of heat exchangers) reported by Eckels (1977) found the values of a and b as

$$a = 256.0 \text{ W/cm}^2\text{-K} \tag{18}$$

$$b = 0.6422 \tag{19}$$

Figure 6 shows the comparison with experimental data. No correlation exists for wet conditions so the wet contact conductance of the test exchanger is experimentally determined. As expected, it is found that the wet conductance to dry conductance ratio is greater for heat exchangers having low values [less than that given by equation (17)] of dry contact conductance. A 30 percent increase is typical for tight collars while 50 percent is not uncommon with split or loose collars. The contact conductance of coil D was estimated using this guide.

Discussion of Results

The pressure drop and heat transfer tests were completed with typical heat and mass balance average errors less than 2 percent and with a standard deviation in the test errors also less than 2 percent. Typical dry test conditions were inlet air at 21°C and inlet water at 48°C. Figure 7 presents the Colburn and friction factors for the air heating or dry test data. The heat exchangers tested were chosen so that their data describe the influence of the variation of tube diameter and fin density with all other parameters held constant.

Wet pressure drop versus face velocity is shown compared

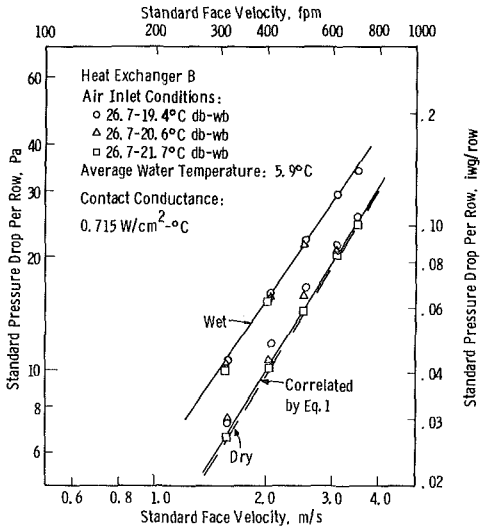

Fig. 9 Dehumidifying pressure drop of a plate finned-tube heat exchanger correlated by equation (1)

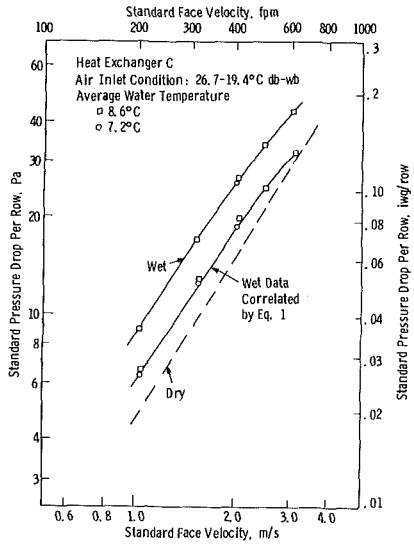

Fig. 11 Wet pressure drop performance of flat-plate finned tubes of 1/2 in. o.d. showing wet, dry, and correlated comparison

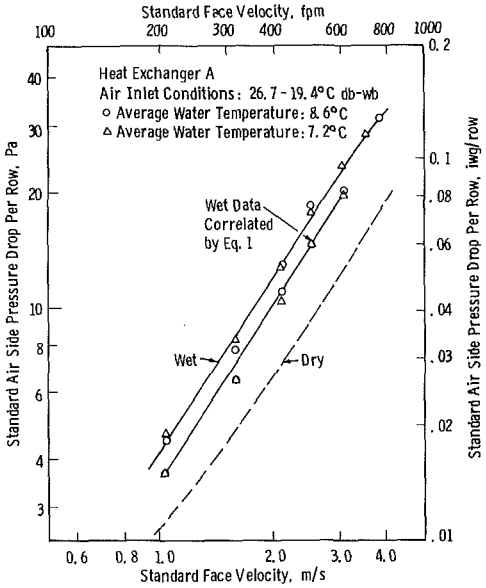

Fig. 10 Wet pressure drop performance of flat-plate finned tubes of 1/4 in. o.d. showing comparison of wet with dry data

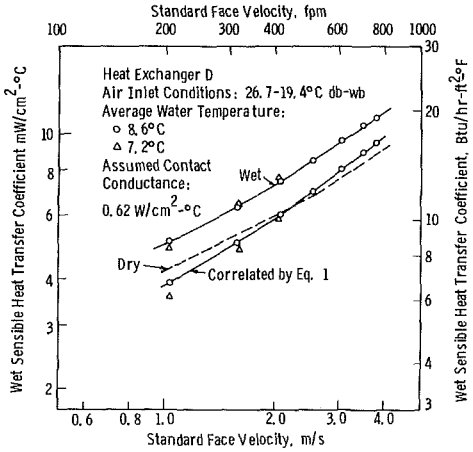

Fig. 12 Wet sensible heat transfer coefficient as a function of face velocity showing the correlation compared to dry data for an 8 fpi coil

to dry data in Figs. 8–11. Also shown on the same figures is the wet pressure drop reduced by the ratio of equation (1) using the 2.8 coefficient. Several features are evident. The characteristic of fin dryout, i.e., closing of the wet and dry pressure drop curves at high velocity, is present. The pressure drop increase due to condensate film effects is most evident in coil A, the coil with the lowest level of turbulence in single phase flow. It is evident from these curves that the transverse velocity can account for a significant fraction of the increased pressure drop during dehumidification. The inability of equation (1) to correlate the wet and dry pressure drop data fully is expected since much of the momentum loss is not frictional in nature.

Figures 12–15 present the measured values of wet, dry, and correlated air-side heat transfer coefficient. In reducing the air-side sensible heat transfer data, the condensate film is assumed to have no resistance to the flow of heat and the exchanger is assumed isothermal. Coil D data, shown in Fig. 12,

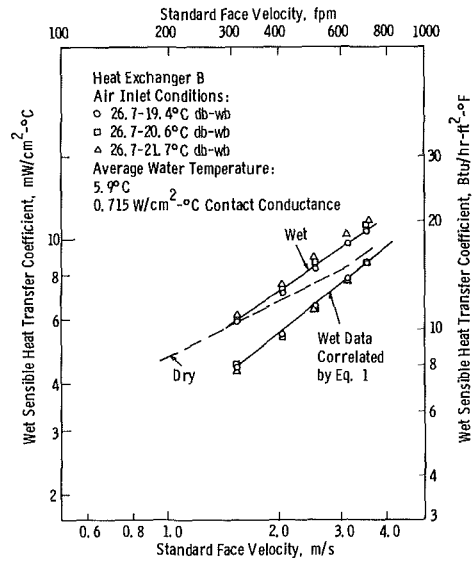

Fig. 13 Dehumidifying sensible heat transfer coefficient correlated by equation (1)

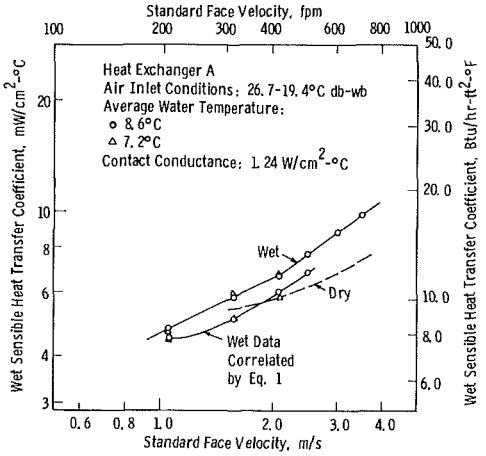

Fig. 14 Wet sensible air-side heat transfer coefficient versus face velocity for 1/4 in. tube exchanger

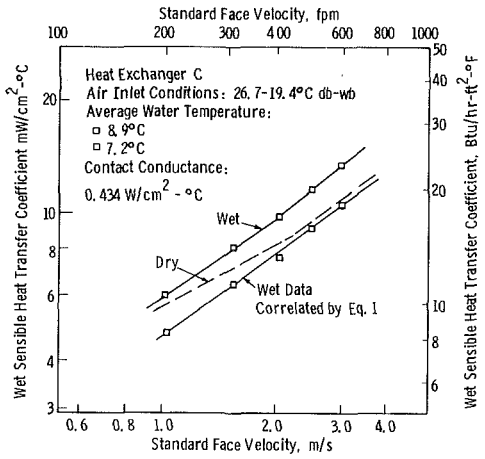

Fig. 15 Wet sensible air-side heat transfer coefficient versus face velocity for 1/2 in. tube exchanger

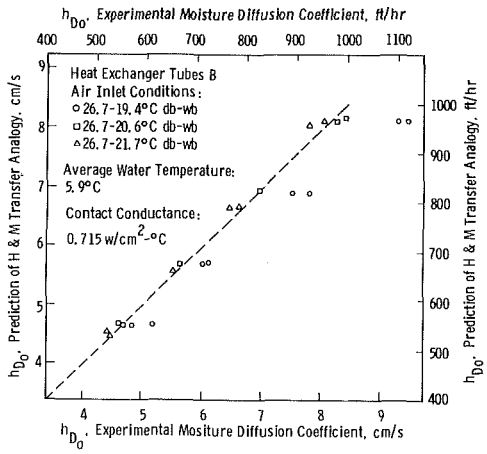

Fig. 16 Prediction of the diffusion coefficient by heat and mass transfer analogy compared to experiment for various values of humidity

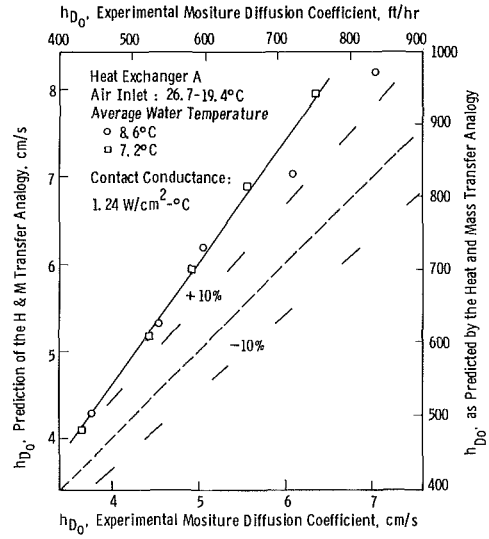

Fig. 17 Sensible-latent heat transfer comparison through the heat and mass transfer analogy

are based on an inferred wet contact conductance which is taken as 33 percent larger than its dry conductance. The sensible heat transfer coefficient is shown for two different average water temperatures as noted on the figure. Several points are noteworthy.

The correlated data cross over and drop slightly below the dry data at low velocities. This can be caused by an actual contact conductance greater than the assumed value or a temperature rise across the condensate film. Crossover at high velocities when the film would be thinned implies that the effect is primarily that of a condensate film and that conclusion is supported by diffusion coefficient data discussed below. Like the data of coil D, the data of coil B show the correlated sensible heat transfer coefficient to be less than that of dry conditions. Again the condensate film temperature rise produces such an effect and the effect is larger for this coil because the cooling water temperature is lower, creating a thicker water film. Noteworthy is the approach of the correlated data to the dry data at high velocity where the assumptions of the data reduction are better satisfied. Coil A test data are shown in Fig. 14. In this solitary case the limitation of Fig. 4 has been applied to the ratio of equation (1) because of severe temperature and density approach problems below 1.0 m/s. Again strong evidence of the effect of the condensate film is present as shown by the shift in the correlated curve to lower velocities; the existence of a wet sensible heat transfer coefficient which is less than the dry heat transfer coefficient; and a definitive change in flow characteristic from a smooth boundary type curve to a rough boundary type curve with a distinctive laminar-turbulent transition. Wet, dry, and correlated heat transfer coefficient data for coil C are displayed in Fig. 15. Again the characteristic better agreement at higher velocities is in evidence as is the effect of the thermal resistance of the water film in reducing the correlated data to less than the dry correlation.

The theoretical development indicates that the condensing phase transverse velocity augmentation applies to diffusion coefficients and so application of the Chilton-Colburn heat and mass transfer analogy is appropriate. Comparison of theory and experiment is accomplished by comparing the lateral phase velocity correlated values of diffusion coefficient given by equation (15) with the diffusion coefficient given by equation (8). Fundamentally this method is a test of the applicability of the heat and mass transfer analogy.

The experimental data of Figs. 16–19 indicate very good agreement between the predictions of the Chilton-Colburn heat and mass transfer analogy and experimental data. Partial dryout of the fin surface is in evidence at high velocities in all of the coil data. Partial dryout of the fin surface occurs as the fin surface temperature approaches the dew point. In finned-tube heat exchangers when the average surface temperature approaches the dew point, a finite condensate flow is provided

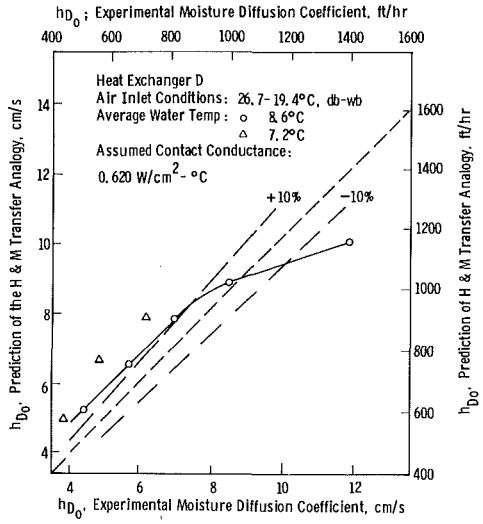

Fig. 18 Prediction of the moisture diffusion coefficient by the Chilton-Colburn heat and mass transfer analogy compared to experimental data

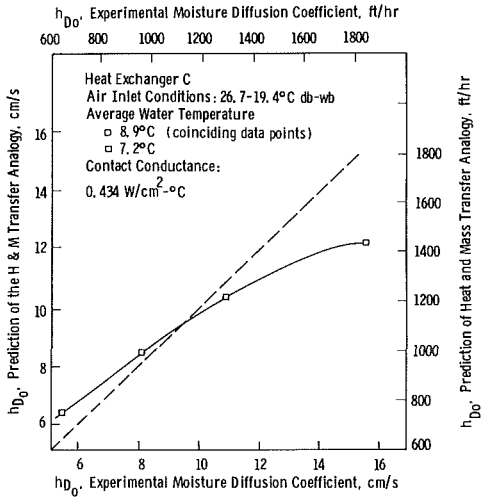

Fig. 19 Comparison of the correlated mass diffusion coefficient predicted by analogy with experimental data

by the colder fin root and collar even though the mass transfer equations based on average density difference predict reduced dehumidification. A decrease in slope of the analogy versus experimental diffusion coefficient curve is the result, as shown by the open circle point markers in Fig. 16. Another effect observed is that data reduction using an erroneous value of contact conductance or neglecting the condensate film thermal resistance produces a noncompensating error in surface temperature and an incorrect slope in the theory–experiment curves. This was reported by Eckels (1977) and is similar to the slope in Fig. 17.

Conclusions

Data are presented for dry heat exchanger sensible heat transfer j and friction factors. The data are unique to the extent that the contact conductance between the fin and tube has been separately determined and extracted from the air-side thermal resistance to yield values more representative of the actual j factor.

The transverse velocity of the condensing moisture vapor during dehumidification is shown to have a significant effect on heat, mass, and momentum transfer augmentation in typical air cooling operations. All of the sensible heat and mass transfer augmentation and a high fraction of the increased pressure drop of dehumidification is shown to be attributable to the transverse velocity of the condensing phase. Condensate film waviness, temperature gradient, and velocity gradient effects have not been included in this analysis, but are seen to have significant influence on the correlation of wet and dry transport processes.

The Chilton-Colburn heat and mass transfer analogy is found to be applicable to the transpiration correlated sensible heat and mass transfer processes of dehumidification.

Acknowledgments

This research program was supported by the ThermoKing Corporation. ThermoKing Corporation, Bohn Manufacturing Company, and McQuay Corporation have provided heat exchangers of consistently high quality for testing in this and other programs. The required experimental work and data reduction were well performed by R. W. Lancaster and A. Montali.

References

ARI Standard 410-72, 1972, "Standard for Forced Circulation Air Cooling and Air Heating Coils," Arlington, VA.

ASHRAE, 1982, *ASHRAE Handbook 1981 Fundamentals*, American Society of Heating, Refrigerating and Air-Conditioning Engineers, Inc., Atlanta, GA, p. 3.10.

Brown, G., 1954, "Theory of Moist Air Heat Exchangers," *Trans. Royal Institute of Technology*, Stockholm, Sweden, Vol. 77, p. 33.

Eckels, P. W., 1977, "Contact Conductance of Mechanically Expanded Plate Finned-Tube Heat Exchangers," ASME Paper No. 77-HT-24.

Eckert, E. R. G., and Drake, R. M., 1959, *Heat and Mass Transfer*, 2nd ed., McGraw-Hill, New York, pp. 460, 512.

Guillory, J. L., 1975, "Sensible Energy Transfer in a Dehumidifying Exchanger," ASME Paper No. 75-HT-34.

Hartnett, J. P., and Eckert, E. R. G., 1957, "Mass-Transfer Cooling in a Laminar Boundary Layer With Constant Fluid Properties," *Trans. ASME*, Vol. 79, pp. 247-254.

Kays, W. M., 1966, *Convective Heat and Mass Transfer*, McGraw-Hill, New York, p. 330.

Kinney, R. B., and Sparrow, E. M., 1970, "Turbulent Flow, Heat Transfer, and Mass Transfer in a Tube With Surface Suction," ASME JOURNAL OF HEAT TRANSFER, Vol. 92, p. 117.

McQuiston, F. C., and Parker, J. D., 1977, *Heating, Ventilating, and Air Conditioning Analysis and Design*, Wiley, New York.

Rabas, T. J., and Eckels, P. W., 1976, "Heat Transfer and Pressure Drop Performance of Segmented Extended Surface Tube Bundles," ASME Paper No. 75-HT-45.

Sparrow, E. M., 1955, "Analysis of Laminar Forced-Convection Heat Transfer in Entrance Region of Flat Rectangular Ducts," NACA TN 3331.

Threlkeld, J. L., 1962, *Thermal Environmental Engineering*, Prentice-Hall, Englewood Cliffs, NJ.

B. D. Crittenden
School of Chemical Engineeering,
University of Bath,
Bath BA2 7AY,
United Kingdom

E. M. H. Khater
National Research Center,
Dokki, Giza, Egypt

Fouling From Vaporizing Kerosine

Fouling rate data have been obtained by passing kerosine at a low flow rate through a small horizontal tubular furnace. Substantial circumferential variations in surface temperature and fouling rate occurred during varporization, the highest rates being at the bottom of the tube where surface temperatures were the lowest. Fouling rates generally increased as pressure increased from 1 to 2.5 bar, but were reduced markedly either by decreasing the feedstock oxygen content or by raising the wall superheat. All the observations are consistent with fouling occurring predominantly via autoxidation and cracking-synthesis mechanisms for the liquid and vapor phases, respectively.

1 Introduction

The annual cost of fouling and corrosion to the U.S. industrial sector has been estimated to be between $3 and $10 billion [1]. For a typical oil refinery, the annual cost of process side fouling is of the order of $10 million [2], and thus there is a clear incentive to study the fundamental relationships between fouling rates and the design and operating parameters of hydrocarbon heat exchangers and furnaces. While much research has been carried out on the stability and degradation of hydrocarbons in storage and in sensible heating, minimal attention has been paid to the vaporization of multicomponent feedstocks, a process which can often give rise to significant rates of fouling in refineries and petrochemical plants [3, 4].

Chemical reaction fouling rates have been found to be strongly dependent upon temperature, pressure, and composition, in particular upon the concentration and type of trace level constituents [5]. Dissolved oxygen plays a key role in the degradation of hydrocarbon feedstocks, although inert gas blanketing of storage tanks is not always effective in eliminating deposit formation [6]. With some exceptions [7] the presence of oxygen or air generally accelerates fouling rates [8–13]; for example, the deposit formation process from jet fuels exhibits a 0.2 order dependence on oxygen partial pressure [14]. The oxygen content of a jet fuel also affects the deposit morphology [15]. The addition of organic peroxides to deoxygenated hydrocarbons is highly detrimental [16] and provides experimental support for the widely held view that the thermal degradation of liquid hydrocarbons occurs via a free-radical autoxidation mechanism [11, 12, 17–19].

Undoubtedly, the physical and chemical mechanisms are complex and therefore a simple dependence of fouling rate on temperature cannot always be expected. Although both the rate of deposition from jet fuels [14] and the initial rate of fouling during the sensible heating of sour gas oils [20] have been found to be well correlated with surface temperature by the Arrhenius expression, later studies [7, 21–23] have shown more complex dependencies, particularly when vaporization is allowed to occur.

Pressure can exert a complex effect on deposit formation rates [10, 23] even though the rate of thermal decomposition of hydrocarbons generally increases with pressure [24]. The presence of oxygen appears to be a critical factor in the rate–pressure relationship [10]. Substantial circumferential variations in the initial fouling rate have been found during the vaporization of air-saturated kerosine at various pressures in a horizontal tubular furnace [22]. The highest rate was at the tube bottom where the temperature was the lowest, but where the liquid phase tended to flow. Release of air bubbles at the heated surface was believed to be responsible for the relatively high fouling rates at locations close to the onset of vaporization. All the experimental results were considered to be consistent with fouling occurring predominantly via a liquid phase autoxidation mechanism [22]. The present research was initiated in order to study experimentally the effects of wall superheat and oxygen concentration on the fouling rate from the same kerosine in the same vaporizing furnace.

2 Apparatus and Experimental Procedure

As described in more detail previously [22], a recycle flow system was used in order to minimize the consumption of kerosine during each experiment which ran continuously for up to 100 hr. For each run in this and the previous study [22], the flow rate of odorless kerosine was maintained by a metering pump at 2.6 kg h^{-1} which corresponded to a Reynolds number of 36 for the liquid entering the furnace. It was necessary to restrict the flow rate to such a low value in order to use moderate but typical heat fluxes in a small-scale furnace. The consequences of this are discussed later. Experimental checks were made to ensure that fouling rates were unaffected by the continual recycling of the kerosine, the principal properties of which have been presented previously [22].

The test tube consisted of a single 0.0103 m i.d. stainless steel tube positioned horizontally along the axis of a furnace in which the temperature of the radiating surface, an alumina tube, was controlled by proportional-integral-derivative action. The section of tube studied was 0.305 m long and its location corresponded with the central isothermal zone of the alumina furnace tube. Ten chromel-alumel thermocouples were silver soldered into grooves cut into the outside surface of the test section at the positions shown in Fig. 1. The feedstock temperatures into and out of the test section were

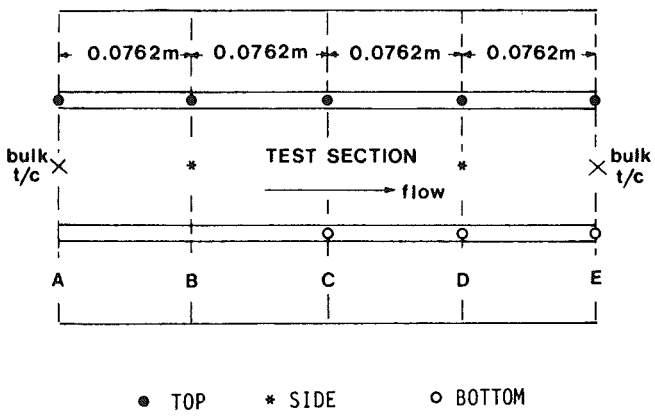

Fig. 1 Location of thermocouples in the test section

Contributed by the Heat Transfer Division for publication in the JOURNAL OF HEAT TRANSFER. Manuscript received by the Heat Transfer Division August 8, 1985.

measured using sheathed chromel-alumel thermocouples. With no fluid flowing through the stainless steel tube, all the thermocouples were calibrated against the 13 percent Rh-Pt/Pt furnace thermocouple, the accuracy of which was quoted by the furnace manufacturer to be ± 1 percent. Variations in the surface thermocouple readings ranged from ± 0.5 percent at a furnace temperature of 904°C to ± 2 percent at a furnace temperature of 103°C. Before each run the test section was cleaned by burning off deposits remaining from a previous run in an air flow maintained at 730°C and then the feed reservoir was filled with fresh kerosine. A check was made to ensure that the tube cleaning procedure gave reproducible fouling rate data. The furnace temperature became steady within the first 4 hr of each run.

Operating data are given in Table 1. Runs 2.1 to 4.5 inclusive were carried out with air-saturated kerosine at five pressures for each of three alumina furnace tube temperatures. Runs 2.1 to 2.5 described in detail earlier [22], were carried out to determine the dependence of fouling rate on the extent of vaporization. Run 5 was a repetition of run 2.2, but with the oxygen concentration in the feedstock reservoir (at ~ 20°C) reduced to 15 percent of the saturation value. Two runs, 1.1 and 1.2 were carried out with the alumina furnace tube temperature sufficiently low that the bubble point of the kerosine was not exceeded and a further run, 6, was carried out with kerosine vapor. For this latter run, it was necessary to use an oil bath and an additional furnace in order to vaporize the feedstock completely before entry to the test section.

The instantaneous fouling resistance $R_{f\theta}$ at time θ and at each location is equal to the difference between the reciprocal values of the overall heat transfer coefficient for the dirty and clean surfaces, U_θ and U_0, respectively. That is

$$R_{f\theta} = \frac{1}{U_\theta} - \frac{1}{U_0} \tag{1}$$

Hence

$$R_{f\theta} = \left(\frac{T_{s\theta} - T_{b\theta}}{\phi_\theta}\right) - \left(\frac{T_{s0} - T_{b0}}{\phi_0}\right) \tag{2}$$

Surface temperatures $T_{s\theta}$ and T_{s0} were measured directly, while the local fluid bulk temperatures $T_{b\theta}$ and T_{b0} and heat fluxes ϕ_θ and ϕ_0 were computed from incremental radiant heat and fluid-side heat balances. The rate of radiant heat transfer to each increment was calculated from the equation for long concentric cylinders, that is, from

$$Q = \frac{\sigma e_f e_s A_f \{T_f^4 - T_{s\theta}^4\}}{e_s + e_f(1 - e_s)(A_f/A_s)} \tag{3}$$

A correlation of the variation of the emissivity of slightly oxidized stainless steel e_s with temperature was prepared using data from a number of sources [25]. The manufacturer of the furnace, Stanton Redcroft Ltd, supplied the emissivity of the pure alumina tube e_f [25]. Despite relatively large circumferential variations in the stainless steel surface temperature at any axial position, the corresponding circumferential variation in heat flux, calculated from equation (3), was always less than ± 5 percent. For example, for location D of run 2.3, the initial values of surface temperature at the top, side, and bottom of the tube were 279, 248, and 221°C, respectively. The corresponding local heat fluxes were calculated to be 27.7, 28.8, and 29.6, kW m^{-2}, respectively. Location of the outlet bulk fluid thermocouple in the center of the tube at the same axial position as three surface thermocouples precluded the use of a mixing section normally essential for good accuracy when flow is in the laminar regime. However, by making the assumption in the heat balances that this thermocouple gave an accurate indication of bulk fluid temperature, it was found that the energy gained by the kerosine was, for all runs, more than 90 percent of the total radiant heat transfer rate calculated from equation (3). This numerical factor, determined individually for each run, was then applied uniformly to the radiant heat flux in all increments in the axial direction in order to calculate the temperature distribution of the bulk fluid. For runs in which vaporization occurred, it was necessary to assume that the liquid and vapor phases were always in equilibrium. The bulk temperature and vapor fraction at any axial position were then found from the local heat balance, fluid enthalpy, and distillation curve. The atmospheric distillation curve was provided by the supplier of the kerosine and checked by the ASTM-D86 method. From the initial boiling point, the lightest component was taken to be *n*-undecane. The variation of boiling point of this alkane with pressure was then used to assist the computation of the kerosine distillation curves at higher pressures [25].

Surface temperatures increased as fouling proceeded, but because the rate of radiant heat transfer is only weakly dependent on the stainless steel surface temperature, the reduction in local heat flux over 100 hr was found to be less than 3 percent. A 1 percent reduction was typical [22]. The temperature of the deposit-fluid interface, at which chemical reaction fouling is usually assumed to occur, remains constant for operation at constant heat flux, provided that the in-tube heat transfer coefficient is unchanged as the deposit forms. Also for operation at constant heat flux, equation (2) reduces to

$$R_{f\theta} = \frac{T_{s\theta} - T_{s0}}{\phi} \tag{4}$$

Hence is is clear that errors in the calculation of bulk temperatures had little effect on the accuracy of $R_{f\theta}$. Once the uncertainties in the estimation of e_s were included, the error in ϕ was estimated to be about ± 7 percent. Thus the error in $R_{f\theta}$ was about ± 10 percent. Experimental tests showed that fouling resistance-time plots were repeatable to within ± 5 percent.

3 Heat Fluxes

Complete vaporization occurred within the test section for all runs at the higher furnace temperatures, i.e., runs 3.1 to 4.5 inclusive. Table 1 shows that the resultant average heat fluxes were relatively high and increased slightly with pressure. Complete vaporization occurred also for runs 2.1 and 2.2. The combination of a low alumina furnace tube temperature and a high kerosine pressure ensured that bulk generation of vapor did not occur for runs 2.4 and 2.5 and Table 1 demonstrates that the corresponding average heat fluxes were low. Nevertheless, surface temperatures exceeding the bubble point of the kerosine were recorded at some locations for these two runs.

Nomenclature

A = surface area
e = emissivity
L = Ostwald coefficient
$p(g)$ = partial pressure of gas
R = universal gas constant
R_f = fouling resistance
T = temperature
U = heat transfer coefficient
$v^0(l)$ = molar volume of solvent at 1 atmosphere
x = mole fraction solubility
σ = Stefan-Boltzmann constant
ϕ = heat flux

Subscripts

b = bulk
f = alumina furnace tube
0 = initial
s = stainless steel surface
θ = at time θ

Table 1 Operating data

Run	Furnace tube temperature, °C	Pressure, bar	Initial boiling point °C	O_2 concentration in reservoir*		Kerosine temperature into test section, °C	Computed vapor fraction		Average heat flux, kW m^{-2}
				Percent saturation	mol fraction × 10^4		Inlet	Outlet	
1.1	300	2.12	236	100	4.21	110	0	0	5.4
1.2	400	2.12	236	100	4.21	140	0	0	10.1
2.1	600	1.08	207	100	4.21	89	0	1	59.2
2.2	600	1.43	219	100	4.21	82.5	0	1	58.8
2.3	600	1.77	226	100	4.21	144	0	0.4	27.5
2.4	600	2.12	236	100	4.21	146	0	0	17.0
2.5	600	2.46	242	100	4.21	181.5	0	0	15.8
3.1	700	1.08	207	100	4.21	96	0	1	60.0
3.2	700	1.43	219	100	4.21	97.5	0	1	61.7
3.3	700	1.77	226	100	4.21	95	0	1	61.3
3.4	700	2.12	236	100	4.21	98	0	1	65.8
3.5	700	2.46	242	100	4.21	91	0	1	63.3
4.1	800	1.08	207	100	4.21	95	0	1	62.1
4.2	800	1.43	219	100	4.21	106	0	1	63.3
4.3	800	1.77	226	100	4.21	103.5	0	1	65.8
4.4	800	2.12	236	100	4.21	110	0	1	67.5
4.5	800	2.46	242	100	4.21	102	0	1	70.0
5	600	1.43	219	15	0.63	83	0	1	57.3
6	700	1.08	207	100	4.21	303	1	1	32.6

*Reservoir temperature = 20°C; reservoir pressure = 1 bar.

4 Nature of Deposits

The deposits from runs 2.1 to 2.5 were generally soft, spongy, and light brown. Examination by scanning electron microscopy revealed a fine porous structure of near-spherical particles, similar to the deposits obtained from an air-saturated, pure compound blend [15] and from an RP-1 kerosine heated at pressures exceeding 135 bar [7]. In contrast, deposits from the runs at the higher furnace temperatures were hard, brittle, and dark black, and examination by SEM revealed a mixture of filament and plate structures with few spherical particles. Varnishlike deposits, with few spherical particles, have been observed when deoxygenated hydrocarbon blends are heated [15]. Filamentary-type coke is more often associated with vapor phase thermal cracking furnaces which are operated at much higher temperatures [26] although dendritic structures have been observed when propane was heated at 138 bar at temperatures in the region of 330°C [7].

5 Fouling Resistances

Fouling was not detected in runs 1.1 and 1.2. For the remaining air-saturated runs, fouling resistances increased with time with some fluctuation. Typical fouling resistances for the comparable air-saturated and deoxygenated feedstock runs, 2.2 and 5, are presented in Fig. 2. There was no evidence in any of the runs of either a tendency toward asymptotic fouling behavior or of induction periods, phenomena which have been observed during the sensible heating of sour gas oils [20]. However, surface temperatures at several locations actually decreased in the early stages of the deoxygenated kerosine experiment giving rise to the apparently negative fouling resistances shown in Fig. 2. This event is believed to have been caused by small amounts of deposits creating a rough surface in the early stages of fouling and thereby increasing the in-tube heat transfer coefficient to an extent sufficient to counteract the additional thermal resistance due to the deposit itself. Such an increase in in-tube coefficient would also lead to a reduction in the fluid–deposit interfacial temperature, leading to reductions in the rates of chemical reactions. The pressure drop across the test section was too small to detect any changes which might have been caused by surface roughening effects.

In some runs, the fouling resistance increased to 0.007 m^{2}K W^{-1}, so exceeding, by more than a factor of 10, the value recommended for design by TEMA [27]. Although it has been noted before [28] that such recommended values can be unrealistic estimates of the extent of fouling in industrial exchangers, it must be pointed out that the use in this study of a low kerosine flow rate through a small-diameter tube is most likely to have promoted rates of fouling [5].

6 Effects of Pressure and Surface Temperature

There was little circumferential variation in surface temperature and fouling rate for runs 1.1, 1.2, and 6 in which only one phase was present in the tube. However, substantial axial and circumferential variations in surface temperature were found for runs 2.1 to 4.5 inclusive. The data for runs 2.1 to 2.5 have been reported previously [22]; further examples are given in Figs. 3 and 6. For each circumferential position, the surface temperature increased along the tube in the direction of flow, as expected. The circumferential variation in surface temperature at each axial position, with the highest temperature being found at the top, is attributed to the tendency for the liquid phase to travel predominantly along the bottom of the tube at the low flow rate used in this study [29]. During vaporization, higher in-tube heat transfer coefficients, which in turn result in lower surface temperatures, are expected at the bottom of the tube where nucleate boiling can occur in the liquid phase. Substantial circumferential varia-

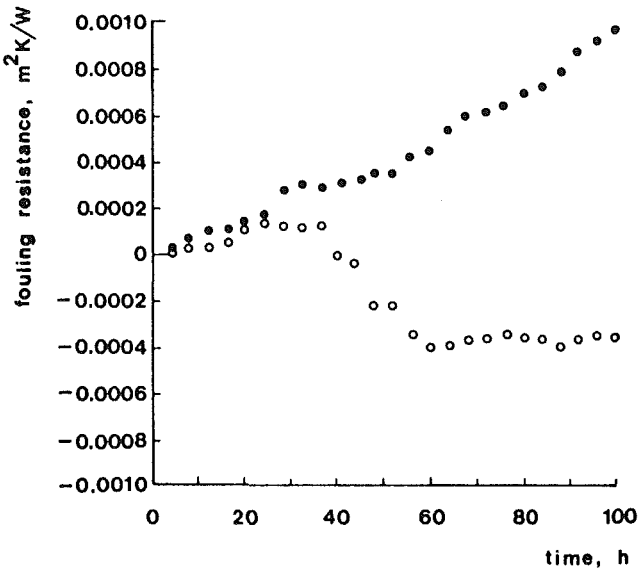

Fig. 2 Typical fouling resistance data (location D, side)

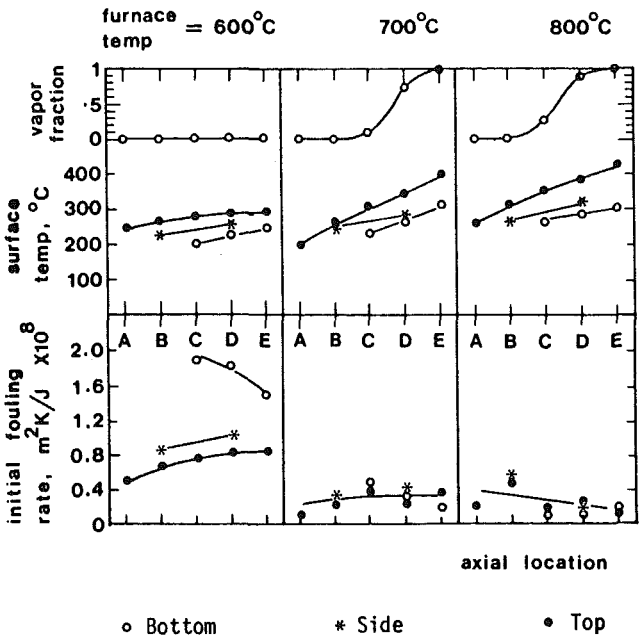

Fig. 3 Effect of alumina furnace tube temperature on fouling rates (2.46 bar)

tions in surface temperature have also been observed with stratified, wavy, and slug flows of binary hydrocarbon mixtures flowing at very much higher Reynolds numbers through a horizontal furnace tube [30]. The circumferential variation which occurs prior to the onset of bulk vaporization is possibly due to pockets of air, which have been released from the liquid phase on contact with the hot metal, traveling along the top of the tube, and thereby reducing the in-tube heat transfer coefficient. Mole fractions of oxygen in the kerosine feed are given in Table 1.

The highest initial fouling rates in the series 2.1 to 4.5 occurred with runs 2.4 and 2.5 in which not only were the heat fluxes low, but also saturated boiling did not occur [22]. These two runs, together with run 2.3, also displayed substantial circumferential variations in the fouling rate. For the remaining runs in the series 2.1 to 4.5, the initial fouling rates were much lower and the axial and circumferential variations were also generally small.

Initial surface temperatures for runs 2.1 to 2.5 did not exceed 380°C, the minimum temperature generally considered to be necessary to achieve significant rates of coking via vapor phase cracking and synthesis reactions [31]. The mole fraction solubility of oxygen in kerosine x is given [32] by equation (5), in which $p(g)$ is the partial pressure of oxygen, L is the Ostwald coefficient, $v^0(l)$ is the molar volume of kerosine at 1 atmosphere, R is the universal gas constant, and T is the local absolute temperature

$$x = \left(\frac{RT}{p(g)Lv^0(l)} + 1\right)^{-1} \tag{5}$$

Hence it is expected that if the rate of the autoxidation mechanism is strongly dependent upon the oxygen concentration in the liquid phase, then fouling rates should increase with increasing pressure. The results reported earlier [22] confirm this although it is important to note that circumferential position and surface temperature are important additional factors. However, at locations where the initial surface temperature was below the initial boiling point of the kerosine, fouling rates increased linearly with pressure [22]. The higher fouling rates at the bottom of the tube are attributed to the tendency for the liquid phase to flow at this location. The presence of a liquid phase is essential for the autoxidation mechanism, and thus fouling rates at the bottom of the tube are high, despite the fact that the surface temperatures are relatively low at this position. Some fouling of the hotter upper surface is believed to be inevitable due to splashing.

For runs 2.1 to 2.5, there was no simple correlation of fouling rate with surface temperature [22]. For each run the rate at the bottom tended to decrease in the axial flow direction as the surface temperature increased, whereas the reverse trend in fouling rate, but not in surface temperature, occurred at the top. Such results are nevertheless consistent with the liquid phase autoxidation mechanism since as the temperature increases in the axial flow direction, equation (5) predicts that there would be a progressive transfer of oxygen from the liquid to the vapor phase. In addition, as the bulk vapor fraction increased along the test section, the circumferential variation in fouling rate became smaller with the rates tending toward relatively low values. This is to be expected as drying out of the tube surface occurs. However, a concomitant circumferential uniformity of surface temperature was not found.

7 Effect of Wall Superheat

Raising the alumina furnace tube temperature from 600 to 700 and 800°C increased the test section surface temperatures and allowed vaporization to occur for all five pressures. Typical results for the three furnace temperatures with the feedstock at 2.46 bar are compared in Fig. 3. For the remaining pressures, the comparisons are broadly similar. It is to be noted that for runs 3.1 to 4.5 inclusive, the fouling rates were all relatively low and there was no clear trend in the variation of fouling rate with pressure, as seen for runs 2.1 to 2.5.

Nevertheless, substantial axial and circumferential variations in surface temperature were still observed for runs 3.1 to 4.5, the lowest temperatures at any axial position again being at the bottom of the tube. Surface temperatures at the top of the test section slightly exceeded 380°C at a few locations only, and therefore the rate of deposit formation via vapor phase cracking-synthesis reactions was unlikely to have been high. Following complete vaporization, the circumferential varia-

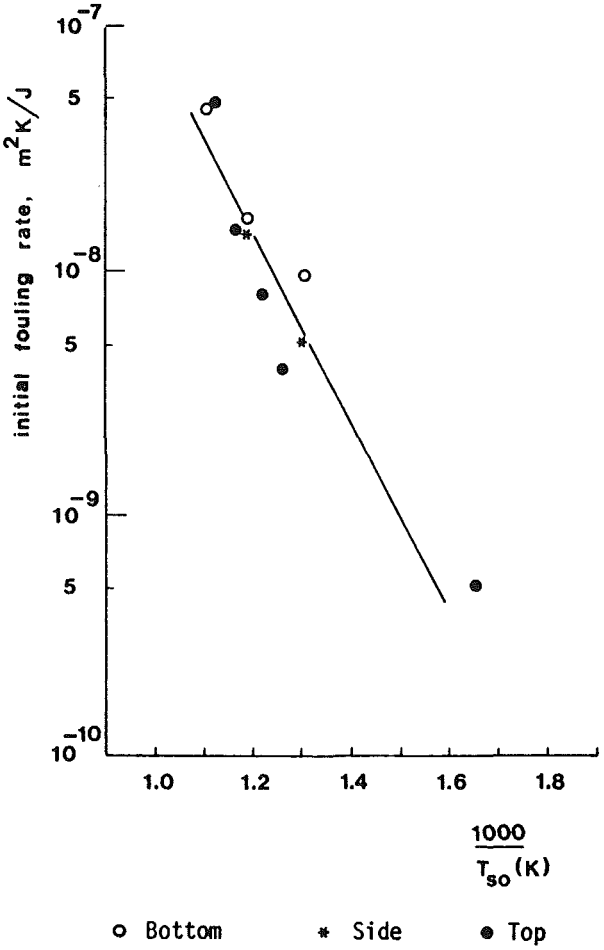

Fig. 4 Arrhenius plot for all vapor phase runs

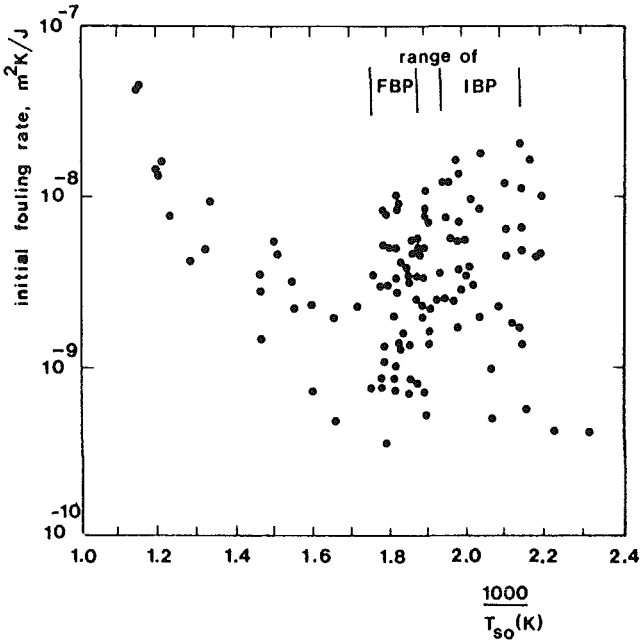

Fig. 5 Arrhenius plot for all air-saturated runs

tion in the fouling rate became small as expected. The persistence of the surface temperature variation, evident in Fig. 3, can only be explained by the continued presence of a liquid phase at the bottom of the tube, despite the fact that sufficient energy had been added completely to vaporize the kerosine. Clearly for this to occur, the liquid and vapor phases near the end of the test section could not be in thermodynamic equilibrium, as was assumed in the heat balance calculations.

Figure 3 clearly illustrates that the outcome of raising the surface temperatures is to allow complete vaporization to occur with a substantial reduction in the fouling rate all round the test section. Two factors may contribute to this reduction. Firstly, and probably the more important, the higher surface temperatures cause a much more rapid and complete degassing from the liquid phase of the oxygen which is necessary to support the autoxidation reactions. Secondly, higher surface temperatures at a given pressure increase the likelihood of a departure from nucleate boiling. This could create a vapor blanket on the tube surface at some locations and thereby hinder deposition by the liquid phase mechanism. Even at these higher surface temperatures the rate of vapor phase cracking–synthesis reactions is still not appreciable. Unfortunately, published data on forced convective vaporization of mixtures are very limited indeed and it is not possible to estimate the critical heat flux.

It has been noted by Vranos [21] that the boiling regime certainly has a marked effect on the thermal decomposition of a puddle of air-saturated *n*-hexadecane. Deposition rates were not reported. A rapid increase in the decomposition rate coincided with the onset of film boiling, which was observed visually, and with the simultaneous, surface-catalyzed decomposition of hexadecyl hydroperoxides originating in the liquid phase. However, the relative unimportance of the decomposition of the hydroperoxides, crucial intermediates in a liquid phase autoxidation mechanism, in the nucleate boiling regime, is unexpected, and apparently at variance with the results from runs 2.1 to 2.5.

8 All Vapor Flow

The vapor phase flow run 6 was terminated after 30 hr because the surface temperatures at axial location E, initially around 625°C, were becoming very high. As would be expected for a single-phase flow, the circumferential variations in both initial surface temperature and initial fouling rate were found to be very small. Figure 4 shows that the logarithm of the initial fouling rate was well correlated with the reciprocal of the absolute surface temperature. Invoking the assumption that the rate constant for the fouling process is proportional to the initial fouling rate, the apparent activation energy of the vapor phase fouling process is about 70 kJ mol^{-1}. Figure 4 also confirms that deposit formation from the vapor phase occurs at relatively low rates at surface temperatures below 400°C.

9 Correlation of Fouling Rates With Surface Temperature

Figure 5 shows the variation of initial fouling rate with initial surface temperature for all the air-saturated runs. No simple correlation of rate with temperature is evident. However, it is apparent that prior to and in the range of the initial boiling point, which varied with pressure in the range 207 to 242°C, there is a general tendency for the initial fouling rate to increase with surface temperature. In the region of the final boiling point, range 260 to 302°C, there is a general tendency for the initial fouling rate to decrease with surface temperature. Beyond 300°C, the initial fouling rate clearly increases again with surface temperature as the rate of deposition via vapor phase reactions becomes significant. Arrhenius-type plots of shape similar in outline to that of Fig. 5 have been found by Taylor and Wallace [14, 23]. They attributed the marked decrease or leveling off of the deposition rate from jet fuels in their kinetic apparatus to a reduction in the autoxidation rate caused by the lowering of the concentration of reactive species

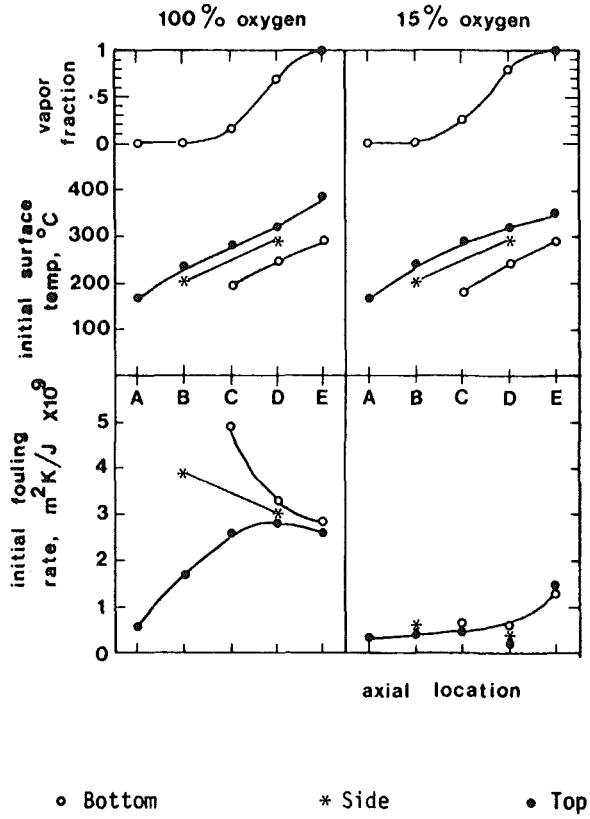

Fig. 6 Effect of oxygen concentration on fouling rates

as the system passed from liquid to the vapor phase. It was further postulated that with increasing temperature the autoxidative rate constant continued to increase so that ultimately the concentration effect was overcome and the overall rate of deposition increased again. The experiments carried out at low pressure with several jet fuels gave a range of cutoff temperatures between 191 and 246°C, but a linear regression of cutoff temperature with ASTM final boiling point was not found to be statistically significant. Up to the cutoff point the apparent activation energy for all jet fuels was 42 kJ mol^{-1}. At the higher pressure of 70 bar the cutoff range was 350 to 425°C with a subsequent increase in deposition rate at higher temperatures. Taylor [23] concluded that the sharp decrease at the higher pressure reflected the transition between the liquid and supercritical vapor phases. The activation energies, omitting the cutoff region, were in the range 20 to 84 kJ mol^{-1}.

10 Effect of Oxygen

The fouling rates for runs 2.2 and 5 are compared in Fig. 6. Agreement of initial surface temperatures and heat balances between the two runs was very good and therefore demonstates the reproducible thermal characteristics of the furnace. Reduction of the oxygen concentration virtually eliminated the circumferential variation in fouling rate. The fouling rates for deoxygenated kerosine were very low and confirm that fouling of both upper and lower surfaces is strongly influenced by oxygen concentration.

11 Design Implications

The rise in surface temperature which accompanies drying out of the liquid phase on the surface is often credited with an increase in fouling rate [4]. For fouling to occur at dryout, rewetting liquid droplets are essential to the liquid phase autoxidation mechanism. In contrast, the results of this study indicate that the commencement of the vaporization process is more likely to be a problem with oxygenated feedstocks.

Deposition patterns during vaporization might be expected to be closely related to the flow and heat transfer regimes, both of which depend upon the flow rate. High chemical reaction fouling rates are normally ascribed to the use of low velocities and high temperatures [5]. A practical application of the use of high velocities to reduce fouling in forced circulation reboilers is described by Chantry and Church [33]. They suggest that at high circulation rates the fractional vaporization per pass can be lowered or even reduced to zero by introducing heat in the sensible form only. The results of this study indicate that doing this by raising the pressure is likely to lead to enhanced rates of fouling of oxygenated feedstocks. Also, fouling rates are not always reduced by operation at high flow rates [34, 35]. Indeed, whether fouling rates increase or decrease with flow rate depends upon the relative balance between mass transfer and kinetic effects [36].

The relatively high fouling rates obtained in this study with a feedstock which is not expected to foul heavily in industrial exchangers is indicative that the use of a low flow rate and a small diameter tube has indeed promoted fouling.

12 Conclusions

The axial and circumferential variations in the initial fouling rate when odorless kerosine was passed at a relatively low flow rate through a horizontal furnace tube are consistent with fouling occurring predominantly via a liquid phase autoxidation mechanism. Deposition via vapor phase reactions was significant only at surface temperatures which well exceeded the final boiling point of the kerosine. The highest fouling rates were found prior to, or at the commencement of, bulk vaporization and at the bottom of the tube where the liquid phase would tend to flow but where surface temperatures were the lowest circumferentially. Low fouling rates were often found at locations where the surface temperature was close to the final boiling point.

Fouling rates generally increased with pressure in the range 1 to 2.5 bar, although the extent of vaporization and surface temperature are additional complicating factors. Decreasing the oxygen content of the kerosine and raising surface temperatures to allow vaporization to occur caused marked reductions in fouling rates.

Further work with higher flow rates and larger tube diameters is required to test whether the results are applicable to industrial size equipment.

13 Acknowledgments

The funding of this study by the Science and Engineering Research Council, United Kingdom, is gratefully acknowledged.

References

1 Garrett-Price, B. A., Smith, S. A., Watts, R. L., Knudsen, J. G., Marner, W. J., and Suitor, J. W., "Fouling of Heat Exchangers: Characteristics, Costs, Prevention, Control and Removal," Noyes Publications, Park Ridge, NJ, 1985, p. 105.

2 Van Nostrand, W. L., Leach, S. H., and Haluska, J. L., "Economic Penalties Associated With the Fouling of Refinery Heat Transfer Equipment," in: *Fouling of Heat Transfer Equipment*, E. F. C. Somerscales and J. G. Knudsen, eds., Hemisphere, Washington, 1981, pp. 619–643.

3 Coggins, J. R., "Blocking of Naphtha Vaporizers," Report of Gas Industy Survey, The Gas Council, Report No. ER117, 1968.

4 Perera, W. J., and Rafique, K., "Coking in a Fired Heater," *The Chemical Engineer*, No. 306, 1976, pp. 107–111.

5 Epstein, N., "Fouling in Heat Exchangers," in: *Fouling of Heat Transfer Equipment*, E. F. C. Somerscales, and J. G. Knudsen, eds., Hemisphere, Washington, 1981, pp. 701–734.

6 Butler, R. C., McCurdy, W. N., and Linden, N. J., "Fouling Rates and Cleaning Methods in Refinery Heat Exchangers," *Transactions ASME*, Vol. 71, 1949, pp. 843–847.

7 Roback, R., Szetela, E. J., and Spadaccini, L. J., "Deposit Formation in Hydrocarbon Fuels," ASME *Journal of Engineering for Power*, Vol. 105, 1983, pp. 59–65.

8 Johnson, D. R., Fink, D. F., and Nixon, A. C., "Stability of Aircraft Turbine Fuels," *Industrial and Engineering Chemistry*, Vol. 46, 1954, pp. 2166–2173.

9 Nixon, A. C., and Henderson, H. T., "Thermal Stability of Endothermic Heat-Sink Fuels," *Industrial and Engineering Chemistry, Product Research and Development*, Vol. 5, 1966, pp. 87–92.

10 Watt, J. J., Evans, A., and Hibbard, R. R., "Fouling Characteristics of ASTM Jet A Fuel When Heated to 700°F in a Simulated Heat Exchanger Tube," NASA TN D-4958, National Aeronautics and Space Administration, Washington, 1968.

11 Braun, R., "The Nature of Petroleum Process Fouling—Results with a Practical Instrument; *Materials Performance*, Vol. 16, No. 11, 1977, pp. 35–41.

12 Hazlett, R. N., and Hall, J. M., "Chemical Aspects of Jet Fuel Thermal Oxidation Stability," in: *Fouling of Heat Transfer Equipment*, E. F. C. Somerscales and J. G. Knudsen, eds., Hemisphere, Washington, 1981, pp. 501–510.

13 Eaton, P., and Lux, R., "Laboratory Fouling Test Apparatus for Hydrocarbon Feedstocks," in: *Fouling in Heat Exchange Equipment*, J. W. Suitor and A. M. Pritchard, eds., HTD-Vol. 35, ASME, New York, 1984, pp. 33–42.

14 Taylor, W. F., and Wallace, T. J., "Kinetics of Deposit Formation From Hydrocarbon Fuels at High Temperatures," *Industrial and Engineering Chemistry, Product Research and Development*, Vol. 6, 1967, pp. 258–262.

15 Frankenfeld, J. W., and Taylor, W. F., "Deposit Formation From Deoxygenated Hydrocarbons, 4, Studies in Pure Compound Systems," *Industrial and Engineering Chemistry, Product Research and Development*, Vol. 19, 1980, pp. 65–70.

16 Taylor, W. F., and Frankenfeld, J. W., "Deposit Formation From Deoxygenated Hydrocarbons, 3, Effects of Trace Nitrogen and Oxygen Compounds," *Industrial and Engineering Chemistry, Product Research and Development*, Vol. 17, 1978, pp. 86–90.

17 Brooks, B. T., "The Chemistry of Gasolines, Particularly With Respect to Gum Formation and Discoloration," *Industrial and Engineering Chemistry*, Vol. 18, 1926, pp. 1198–1203.

18 Canapary, R. C., "How to Control Refinery Fouling," *Oil and Gas Journal*, Vol. 59, No. 41, 1961, pp. 114–118.

19 Vranos, A., "Oxygenate Behavior and Formation From the Vaporization of Air Saturated *n*-Hexadecane," *Industrial and Engineering Chemistry, Product Research and Development*, Vol. 17, 1978, pp. 296–301.

20 Watkinson, A. P., and Epstein, N., "Gas Oil Fouling in a Sensible Heat Exchanger," *Chemical Engineering Progress Symposium Series*, Vol. 65, No. 92, 1969, pp. 84–90.

21 Vranos, A., "Influence of Film Boiling on the Thermal Decomposition of Vaporizing *n*-Hexadecane," *Industrial and Engineering Chemistry, Product Research and Development*, Vol. 20, 1981, pp. 167–169.

22 Crittenden, B. D., and Khater, E. M. H., "Fouling in a Hydrocarbon Vaporizer," *Proceedings of the First UK Conference on Heat Transfer*, I Chem E Symposium Series, No. 86, Institution of Chemical Engineers, Rugby, 1984, pp. 401–414.

23 Taylor, W. F., "Deposit Formation from Deoxygenated Hydrocarbons, 1, General Features," *Industrial and Engineering Chemistry, Product Research and Development*, Vol. 13, 1974, pp. 133–138.

24 Fabuss, B. M., Kafesjian, R., Smith, J. O., and Satterfield, C. N., "Thermal Decomposition Rates of Saturated Cyclic Hydrocarbons," *Industrial and Engineering Chemistry, Process Design and Development*, Vol. 3, 1964, pp. 248–254.

25 Khater, E. M. H., "Fouling in a Hydrocarbon Vaporizer," Ph.D. Thesis, University of Bath, 1983.

26 Kniel, L., Winter, O., and Stork, K., *Ethylene, Keystone to the Petroleum Industry*, Marcel Dekker, New York, 1980, p. 123.

27 Standards of the Tubular Exchanger Manufacturers' Association, 6th ed., Tubular Exchanger Manufacturers' Association, New York, 1968, p. 124.

28 Bott, T. R., and Walker, R. A., "Fouling in Heat Transfer Equipment," *The Chemical Engineer*, No. 255, 1971, pp. 391–395.

29 Mundhane, J. M., Gregory, G. A., and Aziz, K., "A Flow Pattern Map for Gas–Liquid Flow in Horizontal Pipes," *International Journal of Multiphase Flow*, Vol. 1, 1974, pp. 537–553.

30 Crittenden, B. D., and Kolaczkowski, S. T., "Forced Convective Heat Transfer Coefficients to Hydrocarbons Vaporizing in a Horizontal Furnace Tube," in: *Collected Papers on Heat Transfer and Solids Processing and Handling*, Annual Research Meeting, Institution of Chemical Engineers, Rugby, 1978, pp. 25–27.

31 Fitzer, E., Mueller, K., and Schaefer, W., "The Chemistry of the Pyrolytic Conversion of Organic Compounds to Carbon," in: *Chemistry and Physics of Carbon*, P. L. Walker, ed., Vol. 7, Marcel Dekker, New York, 1971, pp. 237–383.

32 *Oxygen and Ozone*, IUPAC Solubility Data Series, Vol. 7, Pergamon Press, Oxford, 1981, p. 445.

33 Chantry, W. A., and Church, D. M., "Design of High Velocity Forced Circulation Reboilers for Fouling Service," *Chemical Engineering Progress*, Vol. 54, No. 10, 1958, pp. 64–67.

34 Smith, J. D., "Fuel for the Supersonic Transport—Effects of Deposits on Heat Transfer to Aviation Kerosine," *Industrial and Engineering Chemistry, Process Design and Development*, Vol. 8, 1969, pp. 299–308.

35 Vranos, A., Marteney, P. J., and Knight, B. A., "Determination of Coking Rate in Jet Fuel," in: *Fouling of Heat Transfer Equipment*, E. F. C. Somerscales and J. G. Knudsen, eds., Hemisphere, Washington, 1981, pp. 489–499.

36 Hout, S. A., "Chemical Reaction Fouling," Ph.D. Thesis, University of Bath, 1983.

On the Calculation of Flow and Heat Transfer Characteristics for CANDU-Type 19-Rod Fuel Bundles

Yuh-Shan Yueh
Graduate Student of
Power Mechanical Engineering.

Ching-Chang Chieng
Professor of Nuclear Engineering.

National Tsing Hua University,
Hsinchu, Taiwan 300,
Republic of China

A numerical study is reported of flow and heat transfer in a CANDU-type 19 rod fuel bundle. The flow domain of interest includes combinations of triangular, square, and peripheral subchannels. The basic equations of momentum and energy are solved with the standard k–ϵ *model of turbulence. Isotropic turbulent viscosity is assumed and no secondary flow is considered for this steady-state, fully developed flow. Detailed velocity and temperature distributions with wall shear stress and Nusselt number distributions are obtained for turbulent flow of* $Re = 4.35 \times 10^4$, 10^5, 2×10^5, *and for laminar flow of* $Re \sim 2400$. *Friction factor and heat transfer coefficients of various subchannels inside the full bundle are compared with those of infinite rod arrays of triangular or square arrangements. The calculated velocity contours of peripheral subchannel agreed reasonably with measured data.*

Introduction

Thermodynamic and fluid dynamic performance of rod bundles is important in the design of fuel elements. Usually, the subchannel method is employed for rod bundle design, which divides the flow domain into lumped subchannels. In this method, the fine structure of both velocity and temperature fields within each subchannel is ignored. The detailed flow and heat transfer characteristics of the fuel bundle can serve as the base to check the accuracy of the subchannel approach. Therefore, predictions of the fine structure are necessary for an optimal bundle design with regard to performance and safety requirements. The detailed velocity and temperature profiles in rod bundles can be obtained by solving the basic differential equations of momentum and energy. Most of previous investigators [2, 4, 11, 15], however, only calculated the structure inside the characteristic flow area of infinite rod arrays of triangular or square arrangement, because the geometry is ideally simple and associated with reactor fuel channels. With the infinite rod array assumption, the interactions of momentum and energy between subchannels are neglected, which may be significant in a finite rod bundle. For finite rod bundles, Benodekar and Date [3] predicted heat transfer characteristics as well as fluid flow for fully developed laminar flow through a circular channel containing 19 to 37 fuel rods. Later, Slagter [17] solved the axial turbulent flow by the finite element method for a 19-rod bundle inside a hexagonal channel; all the rods were in a triangular arrangement, and a one-equation model of turbulence was employed.

The CANDU-type 19-rod fuel bundle shown in Fig. 1 is a doubly connected region and consists of various subchannel shapes. The magnitudes of momentum and energy transport between the subchannels are different in this geometry compared to other reactor geometries. It is believed that the current study is the first attempt to calculate the fine structure of turbulent flow and heat transfer for this type of fuel bundle.

In this study, a 1/12th sector of the pressure tube is considered as the solution domain as shown in Figs. 1 and 2. The detailed velocity, temperature, and wall shear stress distributions, for both laminar and turbulent flows, are solved by the finite difference method. Friction factors and Nusselt numbers of each subchannel as well as the rod bundle obtained from this study are compared with those obtained from an infinite rod array of similar arrangement. In addition, the calculated velocity contours with the measured contours of Chieng and Lin [5] for the peripheral subchannels of the same geometry.

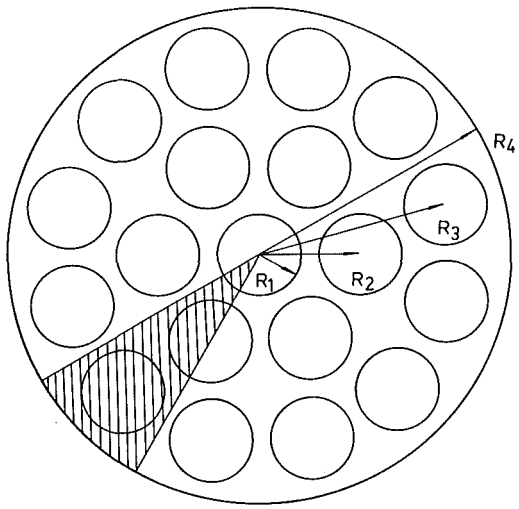

$R_1 = 9.525$mm, $R_2 = 22.0$mm, $R_3 = 42.5$mm, $R_4 = 55.0$mm

Fig. 1 Cross section of the CANDU-type 19-rod fuel bundle

In the investigation of turbulent flow through infinite rod arrays, the effects of anisotropic and secondary flow have been widely recognized and studied. Seale [15] and Bartzis et al. [2] found that the anisotropic effects of eddy viscosity are much more important than the secondary flow effect even if the secondary flow effect can be accurately predicted. The anisotropic factor, which can be adopted to the k–ϵ two-equation model of turbulence, may be defined as the ratio of the eddy viscosities in the tangential and in the normal directions to the wall surface. Anisotropy is essentially a wall effect and it is usually augmented into the diffusivity in the direction parallel to the wall. For infinite rod arrays, the characteristic flow area has only one wall. However, there are four circular surfaces inside the flow domain selected for this study as shown in Fig. 2. The surfaces of Rod A and the pressure tube are parallel to the grid lines of computation but the wall sur-

Contributed by the Heat Transfer Division for publication in the JOURNAL OF HEAT TRANSFER. Manuscript received by the Heat Transfer Division October 24, 1984.

Table 1 Coefficients of the governing equations

equation	ϕ	α_ϕ	S_ϕ
continuity	1	0	0
z-momentum	w	$\mu_t+\mu_\ell$	$F_z^* - \partial p/\partial z$
energy	T	$\frac{\mu_t}{Pr_t}+\frac{\mu_\ell}{Pr_\ell}$	$-\rho w \frac{\partial T}{\partial z}$ **
turbulent kinetic energy Δ	k	$\frac{\mu_t}{Pr_k}$	$G-\rho\epsilon; G=\mu_t\left\{\left(\frac{\partial w}{\partial r}\right)^2+\left(\frac{1}{r}\frac{\partial w}{\partial \theta}\right)^2\right\}$
turbulent energy dissipation rate Δ	ϵ	$\frac{\mu_t}{Pr_\epsilon}$	$\frac{\epsilon}{k}\{C_1 G - \rho C_2 \epsilon\}$

* F_z = external force in z-direction

** $\frac{\partial T}{\partial z} = \frac{dT_m}{dz}\frac{1}{\dot{m}C_p}\int q''_w(r,\theta)\, dL_H$

Δ for turbulent flow only

faces of Rods B and C are not. For the flow regions next to Rods A and B, the ratio of the eddy viscosities in the tangential and the normal directions of the computational grid system cannot describe the anisotropic effect induced by the presence of the circular walls. Besides, the directional component of the diffusivity in the desired orientation cannot be well defined. Moreover, no appropriate and validated anisotropic factor in the published literatures can be employed along the selected grid-line directions of present computation and the interested flow domain, if the eddy viscosity concept is to be applied. Therefore, isotropic viscosity is assumed for the present analyses; the assumption of isotropic viscosity further leads to a null-turbulence-drive secondary flow. The calculated results of isotropic turbulence, however, provide an upper bound for the rod temperature and lower bound to Nusselt numbers. Therefore, the results are conservative predictions of the real situation, but a better estimation than subchannel method, and are valuable for safety requirements.

Mathematical and Physical Model

Governing Equations. For fully developed, steady flow in a constant-property fluid, the governing equations are expressed in cylindrical coordinates (r, θ, z) with the z axis in the longitudinal direction as follows:

$$\frac{1}{r}\frac{\partial}{\partial r}\left(r\alpha_\phi \frac{\partial \phi}{\partial r}\right)+\frac{1}{r}\frac{\partial}{\partial \theta}\left(\frac{\alpha_\phi}{r}\frac{\partial \phi}{\partial \theta}\right)+S_\phi=0 \qquad (1)$$

In equation (1), ϕ represents any of the dependent variables. Diffusion coefficients α_ϕ and source terms S_ϕ for each dependent variable are given in Table 1. The velocity components in the r and θ directions are zero because there is no secondary flow.

The turbulent viscosity μ_t is determined by the terms k and ϵ, and assumed to be isotropic, but it is zero for laminar flow

$$\mu_t = C_\mu \rho \frac{k^2}{\epsilon} \qquad (2)$$

where ρ is the density of the working fluid. The values of all empirical constants in the turbulence model are [9]:

C_μ	C_2	C_1	Pr_k	Pr_ϵ	Pr_t
0.09	1.92	1.44	1.00	1.30	0.9

These constants have been evaluated and the results agree very well with various sets of experimental data for infinite rod arrays [20].

Boundary Conditions. For laminar flow, the boundary conditions are as follows:

- no-slip condition is assumed at the solid surfaces
- constant heat flux is assumed around rod surfaces
- pressure tube wall is adiabatic
- symmetry is assumed at cutting lines of the circular sector

Nomenclature

A_i, A = flow area of ith subchannel and entire bundle, m^2
C_i, C = wetted perimeter of ith subchannel and entire bundle, m
c = clearance gap or spacing between adjacent rods, m
C_p = specific heat of fluid, kJ/kg-K
$D_{h,i}, D_h$ = hydraulic diameter of ith subchannel ($4A_i/C_i$) and entire bundle ($4A/C$), m
f = Darcy friction factor = $8\tau_w/(\rho\bar{w}^2)$
k = turbulent kinetic energy, m^2/s^2
k_c = thermal conductivity of fluid, W/m^2K
h_i = heat transfer coefficient of ith subchannel, W/m^2K
$\dot{m}$ = mass flow rate, kg/s
Nu = Nusselt number
P = pressure, Pa
P/D = pitch-to-diameter ratio
Pr = Prandtl number
q'' = wall heat flux, W/m^2
q''' = heat source, W/m^3
Re = Reynolds number based on D_h and $\bar{w}$
Re_i = Reynolds number based on $D_{h,i}$ and $w_{m,i}$
S_ϕ = source term in equation of ϕ
T = temperature, K
$T_{m,i}$ = average bulk temperature of ith subchannel, K
$\bar{T}_{w,i}$ = average wall temperature of ith subchannel, K
T_{max} = maximum temperature of flow domain, K
T_{min} = minimum temperature of flow domain, K
u = velocity in r direction, m/s
v = velocity in θ direction, m/s
w = velocity in z direction, m/s
$\bar{w}, \bar{w}_m$ = average velocity of entire bundle, m/s
$w_{m,i}$ = mean velocity of ith subchannel, m/s
$w_{max,i}$ = maximum velocity of ith subchannel, m/s
y = distance from wall, m
β = mixing factor [20]
ϵ = turbulent dissipation rate, m^2/s^3
κ = Von Karman constant = 0.4187
μ = viscosity, Pa•s
τ_w = wall shear stress, Pa
Φ = dimensionless temperature = $(T-T_{min})/(T_{max}-T_{min})$

Subscripts

l = laminar
m = mean
p = node next to wall
t = turbulent
w = wall

Superscripts

$\bar{}$ = average

For turbulent flow, the flow properties vary rapidly for the region in the immediate vicinity of the wall; the wall function approach is employed because it requires less computer storage and computing time. The wall functions chosen for this study are as follows [9]:

Axial velocity w

$$w^+ = \frac{w_p}{\left(\frac{\tau_w}{\rho}\right)^{1/2}} = \frac{1}{\kappa} \ln (E y_p^+) \tag{3}$$

$$y_p^+ = y_p (\tau_w/\rho)^{1/2}/\nu, \quad \nu = \mu/\rho$$

Turbulent kinetic energy k

$$k_p = \frac{(\tau_w/\rho)}{C_\mu^{1/2}} \tag{4}$$

Turbulent dissipation rate ϵ

$$\epsilon_p = \frac{C_\mu^{3/4} k_p^{3/2}}{\kappa\, y_p} \tag{5}$$

Temperature T

$$T^+ = \mathrm{Pr}_t (w^+ + \mathrm{Pfun}) \tag{6}$$

$$\mathrm{Pfun} = 9.24\, [(\mathrm{Pr}_l/\mathrm{Pr}_t)^{0.75} - 1.]\, [1 + 0.28 e^{(-0.007 \mathrm{Pr}_l/\mathrm{Pr}_t)}]$$

$$T^+ = C_p \rho (\tau_w/\rho)^{1/2} (T_w - T_p)/q_w''$$

Numerical Scheme. The governing equations are solved by the modified form of TEACH-2E [7] computer program. The modifications include: (1) The pressure calcualtion subroutine is removed, and the fixed value of the pressure gradient is guesesd initially to find the corresponding velocity field and Reynolds number desired. Pressure gradients of desired Reynolds number are obtained after several trials. The staggered grid system of the original computer program is not needed, and all the variables are calculated for the same grid points. (2) The subroutines of velocity calculation are replaced by a new subroutine in which the pressure gradient of the z-momentum equation is included in the source terms of S_w. The convection term of the energy equation is taken care of by the source term S_T.

Grid systems of computation are constructed of orthogonal lines along the radial and tangential directions. Fine grids have been chosen at gap regions. The surfaces of Rod B and Rod C intersect with the grid lines, which results in irregular shapes near these surfaces in computations. Therefore the boundary nodes have to be treated differently. For laminar flow, the boundary nodes are located on the solid surfaces, where zero velocity is assigned. For turbulent flow, the boundary nodes must be shifted, so that the nodes are located a distance $y^+ \geq 35$ away from the solid surfaces and thus the near-wall model can be applied. Although the surfaces of Rod B and Rod C do not coincide with the grid lines, the energy and momentum are balanced on the relevant boundary cells artificially by adopting the concept of control volume approach into the finite difference scheme of the computer program. Besides, the heat flux into the coolant was checked and matched the amount of heat generation.

The numerical accuracy of the laminar solution has been tested by confirming the grid independence of the solutions and calculating the products of f Re. The computations are performed with nonuniform grid systems of 25 × 52, 28 × 56, 30 × 59, and 33 × 66 nodes, for laminar flow of Reynolds number ~2400. According to many investigators, the product of f Re is only a function of geometry for laminar flow. The product can also be calculated exactly from known values of pressure gradient, fluid properties, and average velocity by the definitions of f, Re, and τ_w as follows:

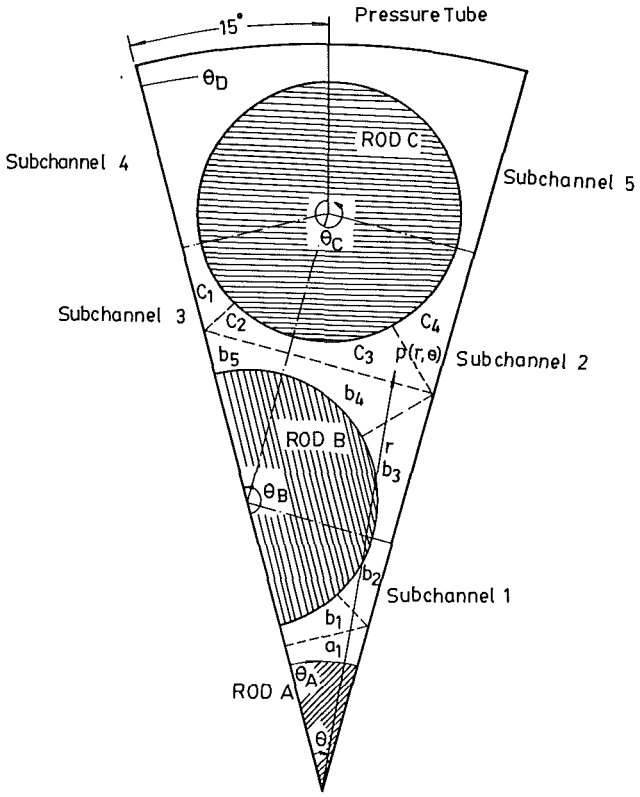

Fig. 2 Labels and numbers of the calculation domain

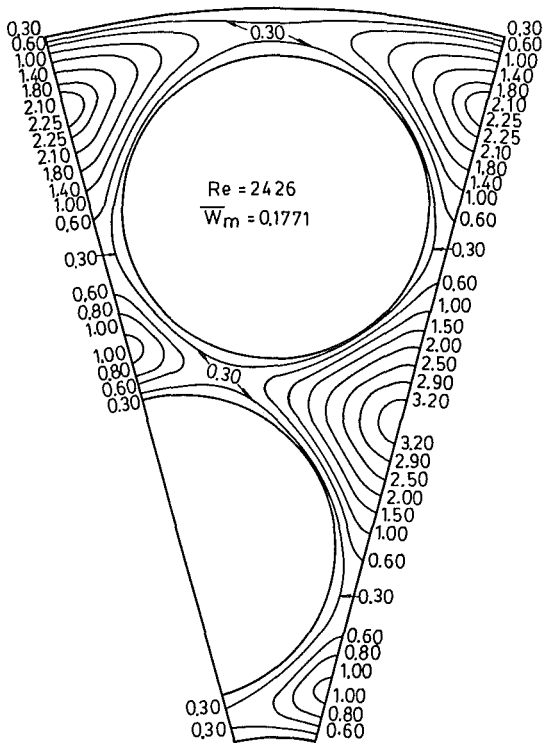

Fig. 3 Velocity contours ($w/\bar{w}_m$) for Re = 2426

$$f\,\mathrm{Re} = \frac{8\tau_w}{\rho \bar{w}^2} \times \frac{\bar{w}_m D_h \rho}{\mu} \qquad \tau_w = -\frac{D_h}{4} \frac{\partial p}{\partial z}$$

which yield

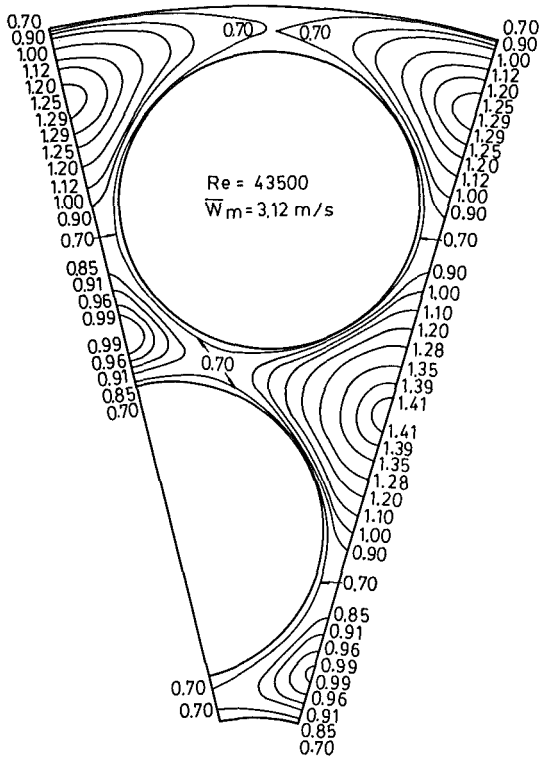

Fig. 4 Velocity contours ($w/\bar{w}_m$) for Re = 43,500

$$f\,\mathrm{Re} = \frac{2D_h^2}{\mu \bar{w}^2}\frac{\partial p}{\partial z} \tag{7}$$

The good agreements on the product f Re between the numerical results and the expected values indicate that the approaches for the four grid systems are all proper. As well known, a fixed pressure gradient leads to a fixed Reynolds number, i.e., the same f Re for the same geometry. The numerical results indicate, however, that different Reynolds numbers are obtained from the four grid systems. These discrepancies are caused by the zigzag boundaries cut by the grid lines on the rod surfaces. The velocity contours obtained are within 0.1 percent difference at >99 percent of the flow domain but ~1 percent difference at the center portion of the subchannels. This paper reports the results of laminar flow obtained from the 33 × 66 grid system. For turbulent flow cases, the grid lines near the rod and wall surfaces must be removed so that the wall functions can be properly implemented; therefore, the 30 × 59 grid system is employed. Nevertheless, smaller grid system can save computational time and space also.

Results and Discussion

For convenience, the flow domain is divided into subchannels which are numbered 1 through 5; the rods are labeled A, B, and C. The tangential positions are represented in the directions as θ_A, θ_B, θ_C (Fig. 2). Subchannels 1 and 3 can be divided into three parts with the same configurations, namely a_1, b_1, b_2 in subchannel 1, b_5, c_1, c_2 in subchannel 3. These two subchannels are the characteristic flow areas between infinite rod arrays of triangular arrangement. Subchannel 2 can be divided into four parts, i.e., b_3, b_4, c_3, c_4, which is the characteristic flow area between infinite rod arrays of square arrangement. Subchannels 4 and 5 are peripheral subchannels adjacent to the pressure tube. The labels of the flow areas are associated with the adjacent fuel rods.

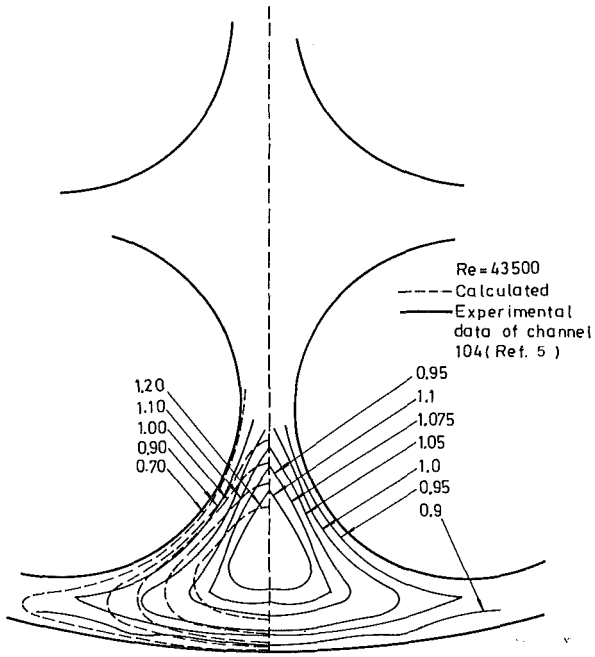

Fig. 5(a) Comparison of measured and predicted isovels ($w/\bar{w}_m$) for peripheral subchannel 5 (channel 104 of [5])

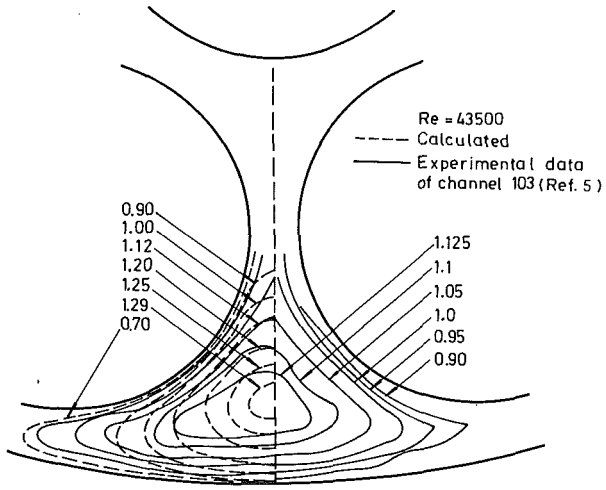

Fig. 5(b) Comparison of measured and predicted isovels ($w/\bar{w}_m$) for peripheral subchannel 4 (channel 103 of [5])

Attention will first be focused on the velocity contours for Re = 2426 (Fig. 3) and their implications. This figure shows that the highest mangitude and gradient of velocity occurred in subchannel 2, which has the largest flow area among all subchannels. The second highest values occurred in subchannels 4 and 5, which have the second largest flow area. This indicates that the magnitude of velocity and its gradients among three types of subchannels is different and is ordered according to the magnitude of the flow areas. This result can be explained by the fact that the pressure drop across each subchannel is the same. Because the pressure drop is generally proportional to the velocity and the inverse of the square of hydraulic diameter for the laminar flow, the same magnitude of the pressure drop for all subchannels implies that the subchannel of larger hydraulic diameter will have a higher velocity.

It is interesting to note that the velocity distribution of sub-

Table 2 Grid system experiments

Grid system	25x52	25x52	28x56	30x59	33x66
$\partial p/\partial z$	20	40	40	40	40
Re	1238	2478	2420	2426	2372
$\bar{w}_m$(m/s)	0.0904	0.181	0.176	0.177	0.173
f	0.0543	0.0271	0.0289	0.0283	0.0289
calculated fRe	67.22	67.15	69.94	68.65	70.21
fRe eqn.(7)	67.24	67.14	69.35	68.75	70.36

Table 3 Peak and mean velocities of each subchannel for Re = 2426, 43,500, 100,000, and 200,000

channel# i / Re		1	2	3	4 (103)*	5 (104)*
43,500	α_i	0.99	1.42	1.01	1.30 (1.31)	1.31 (1.25)
	β_i	0.793	1.13	0.823	0.998 (1.13)	1.00 (1.12)
100,000	α_i	0.98	1.39	1.01	1.28	1.29
	β_i	0.813	1.12	0.853	0.993	0.996
200,000	α_i	0.98	1.39	1.01	1.26	1.27
	β_i	0.823	1.12	0.864	0.990	0.992
2,426	α_i	1.05	3.34	1.05	2.35	2.35
	β_i	0.538	1.395	0.528	0.955	0.955

$\alpha_i = w_{max,i} / \bar{w}_m$

$\beta_i = w_{m,i} / \bar{w}_m$

$w_{max,i}$ = peak velocity of channel i

$w_{m,i}$ = mean velocity of channel i

$\bar{w}_m$ = mean velocity of flow domain

( ) = experimental data of [5]

* channel number in Ref. 5

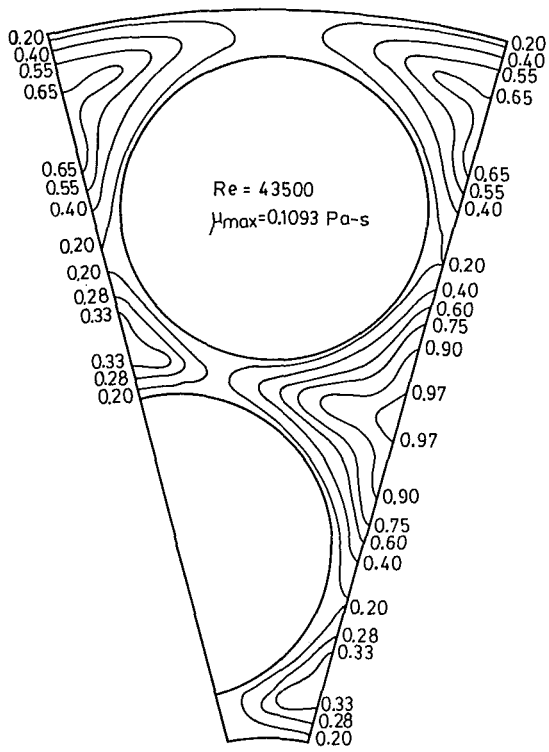

Fig. 6 Turbulent viscosities (μ_t/μ_{max}) for (*a*) Re = 43,500

channel 1 is almost identical to that of subchannel 3; the velocity distribution of subchannel 4 is almost the same as that of subchannel 5. This indicates that the velocity contours are the same if the subchannels have the same shape and size no matter what the adjacent subchannels are. This observation also implies that the velocity gradient is almost zero at the interface of the subchannels and the interchannel mixing is weak for laminar flow. The interchannel mixing is mainly caused by the turbulent interchange, diversion cross flow, and the presence of pin spacers or grids in the flow channel [14]. Therefore, the observation of negligible mixing effect on velocity distributions is reasonable under the conditions of laminar flow through bare rods with no secondary flow.

Figure 4 shows the velocity contours for Reynolds number 43,500. In contrast to Fig. 3, Fig. 4 indicates that the velocity contours of subchannels 1 and 4 are different from those of subchannels 3 and 5, respectively. The degree of difference between the peripheral subchannels 4 and 5 is smaller, however. The difference in velocity distribution between the same type subchannels is believed to be caused by the turbulent mixing between interconnected subchannels. In addition, the velocities at the interfaces of subchannels increase, up to ~70 percent of the average velocity of the flow domain, in contrast to the value of ~30 percent for the laminar flow case. These imply that more flow is distributed at gap regions between adjacent subchannels and the velocity gradient of the individual subchannels decreases for the turbulent flow case. The velocity contours of peripheral subchannels 4 and 5 have also been compared against experimental data which are subchannels 103 and 104 [5] with Re = 43,500. As shown in Figs. 5(*a*) and 5(*b*), the measurements give higher average velocity of the subchannel and higher momentum flux across the subchannel interface, which implies strong interchannel mixing in the test bundle. The underestimation of the interchannel mixing may come from the assumptions of isotropic turbulent viscosity, no secondary flow, and the geometric imperfection of the test section.

To study the effects of Reynolds number, calculations are also made with Re = 10^5 and 2×10^5. Isovels are obtained which are almost identical to those for Re = 43,500. Table 3 compares the peak and mean velocities of each subchannel for various Reynolds numbers. The velocities are normalized to the average velocity of the overall flow domain. The normalized peak velocities α_i are in the range of 0.99–1.42 for turbulent flow and 1.05–3.34 for laminar flow. These values imply that the velocity gradient of the subchannel interior is much lower for turbulent flow than for laminar flow. As the Reynolds number is increasing from 2426 to 2×10^5, the normalized peak velocities α_i are decreasing for all subchannels; the fractions of subchannel flow β_i are decreasing for subchannels 2, 4, and 5, but are increasing for subchannels 1 and 3, which have smaller flow areas. This indicates that, with increasing Reynolds number, more flow is turbulent diffused into subchannels which have smaller flow area and lower velocity from subchannels which have larger flow area and higher velocity. Table 3 also compares the calculated α_i and β_i with experimental data for peripheral subchannels. The table shows that the current calculation gives a good agreement on α_i but lower β_i, 12 percent less flow, in the peripheral subchannels. This may result from the neglect of anisotropy effects in the calculation.

The distribution of normalized turbulent viscosity is shown in Fig. 6 for Reynolds number Re = 43, 500. The patterns of distributions for Re = 10^5 and 2×10^5 are similar to that of Re = 4.35×10^4 except for maximum magnitude. The nor-

Table 4(*a*) Friction factors for the rod bundle and the subchannels

Re	friction factor, f					
	subchannel number					Rod Bundle
	1	2	3	4	5	
43500	0.0264 [0.0280] (0.0305)	.0195 [0.0221] (0.0222)	.0254 [0.0264] (0.0264)	0.0207 [0.0238]	0.0209 [0.0237]	0.0201 [0.0223]
10^5	0.0212 [0.0227] (0.0249)	0.0168 [0.0182] (0.0183)	0.0201 [0.0227] (0.0245)	0.0175 [0.0197]	0.0176 [0.0198]	0.0175 [0.0172]
$2x10^5$	0.0179 [0.0198] (0.0215)	0.0145 [0.0160] (0.0161)	0.0171 [0.0196] (0.0213)	0.0152 [0.0172]	0.0153 [0.0173]	0.0151 [0.0160]
2426	0.0756 - (0.0855)	0.0175 - (0.0170)	0.0792 - (0.0871)	0.030 - -	0.030 - -	0.0292 (0.0292)

unbracket value : present calculation

[ ]: value by G^*-method based on present result of Re=2426.

( ): value by G^*-method based on value of infinite rod array [10]

Table 4(*b*) Friction factor-Reynolds number relationship for individual subchannels

	subchannel number, i			remark
	1	2	3	
Re_i	1060	4075	1040	Reynolds number of ith subchannel
$(f_i Re_i)$	80.14	71.31	82.37	inside CANDU rod bundle
$(fRe)_{inf}$	86	72	86	for infinite rod array [1,19]

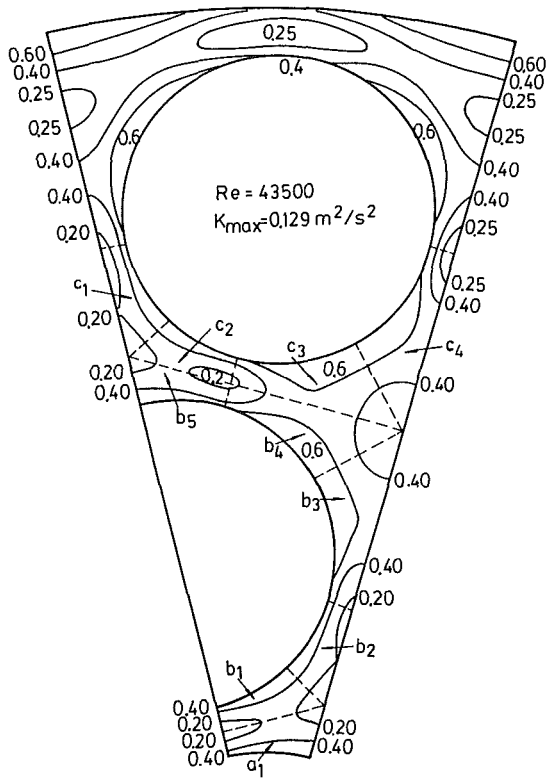

Fig. 7 Contours of turbulent kinetic energy (k/k_{max}) for Re = 43,500

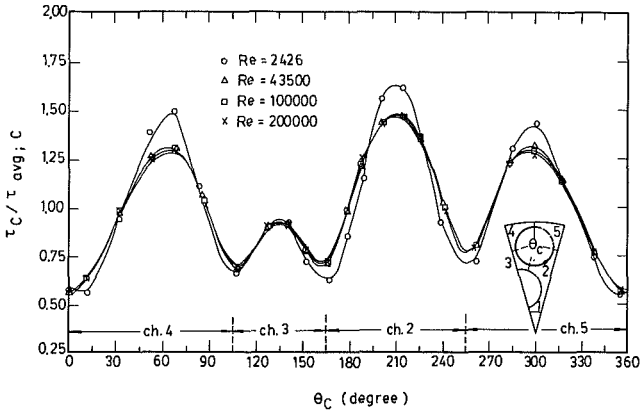

Fig. 8 Circumferential variation of wall shear stress around Rod C

malized turbulent viscosity is higher for subchannels having higher velocity and thus stronger turbulent mixing is expected.

Contours of turbulent kinetic energy are also obtained and are similar for various Reynolds numbers; Fig. 7 is plotted for Reynolds number Re = 43,500 only. It shows that the turbulent kinetic energy is higher at wall regions and is uniform in most of the flow domain. Comparing the measured contours of turbulent kinetic energy for subchannels between infinite triangular rod arrays [4] with those of subchannels 1 and 3, a similar pattern is found at portions of a_1, b_1. Some distortions are observed, however, at the portions of b_2, b_5, c_1, c_2 because these four portions are connected to other subchannels and the interchannel interaction is expected. It is also of interest to see that the contour pattern in peripheral subchannels is similar to that in flat wall subchannels given in [13].

The circumferential variations of wall shear stress around Rod A, Rod B, Rod C, and the pressure tube are calculated. The variations around Rod C are the largest and are shown in Fig. 8. The distributions of normalized wall shear stress are similar for various Reynolds number for turbulent flow. The variations are greater for laminar flow than for turbulent flow. If the effect of anisotropic factor were included, the amplitude of shear stress variations would be decreased for turbulent flow and the difference between laminar and turbulent flows would be even larger in the real situation.

Because no experimental data are available, the friction factors for various Reynolds number are compared with the calculated results of the G^* method suggested by Rehme [12]. As shown in Table 4(*a*), the friction factors obtained by the present work and the G^* method are in agreement with each other for the overall rod bundle. If the pressure drop across each subchannel for turbulent flow is calculated individually using the geometry factor from laminar calculation, the friction factor from the G^* method (in square brackets) is ~10 percent higher than the value of the present computation. For Re = 2426, the friction factors of subchannels 1 and 3 are lower than those of subchannels for infinite rod arrays of triangular arrangement; but the friction factor of subchannel 2 is higher than that of subchannels of infinite rod array of a square arrangement. For turbulent flow, the friction factors from the G^* method based on the results of infinite rod array [10] will give pressure drops even higher for all subchannels. Mottaghian et al. [11] and Benodekar et al. [3] calculated the f Re product for laminar flow through rod bundles of similar arrangement. They reported that the product is geometry dependent and is less than 116 for P/D = 1.155. For a 33 × 66 grid system flow at given $\partial p/\partial z = -40$, which corresponds to Re ≃ 2400, f Re = 70.36 by Table 2 for the full bundle; this value agrees well with 70.21 obtained by detailed calculation. Table 4(*b*) shows that the friction factor–Reynolds number products for the individual subchannels inside the CANDU bundle, $f_i Re_i$, are within 7 percent lower than the values for infinite rod array $(f\,Re)_{inf}$. This indicates that neighboring subchannels influence the product even if the geometry is the same.

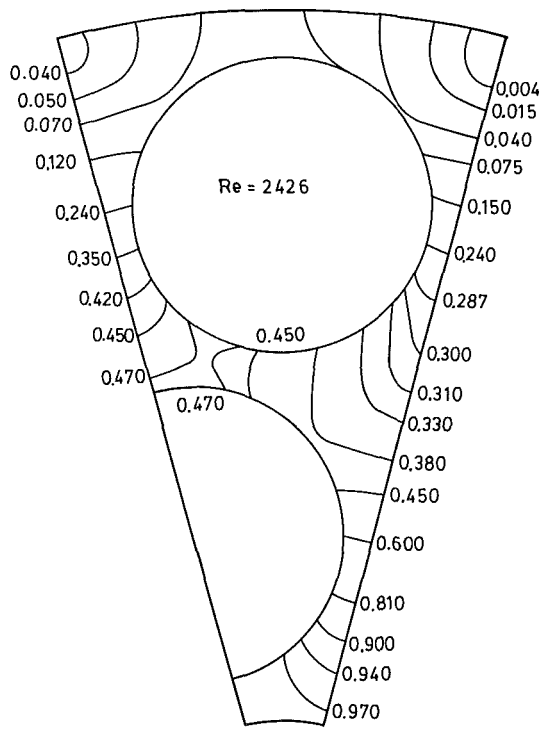

Fig. 9 Temperature contours (constant values of Φ) for Re = 2426

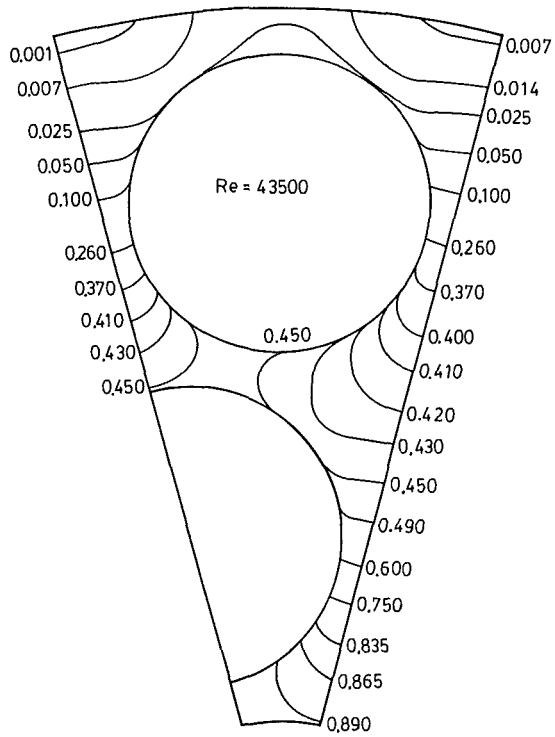

Fig. 10 Temperature contours (constant values of Φ) for Re = 43,500

Heat transfer characteristics are of major interest for fuel rod design; the temperautre distribution may also be of some interest. In this study, constant heat flux from fuel rods and adiabatic pressure tubes is assumed in the heat transfer calculation. Dimensionless temperature Φ defined as

$$\Phi = \frac{T - T_{\min}}{T_{\max} - T_{\min}} \tag{8}$$

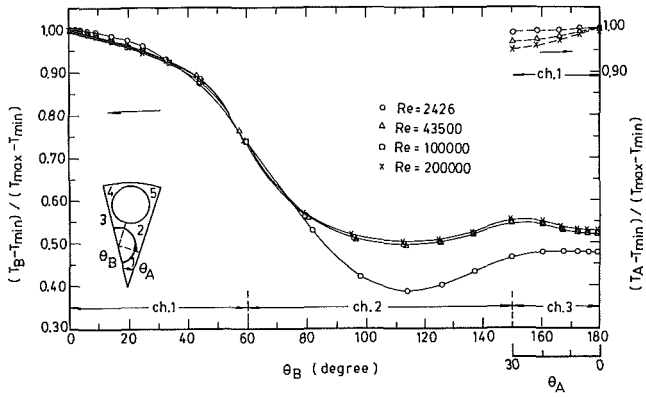

Fig. 11(a) Surface temperature distribution around Rod A and Rod B

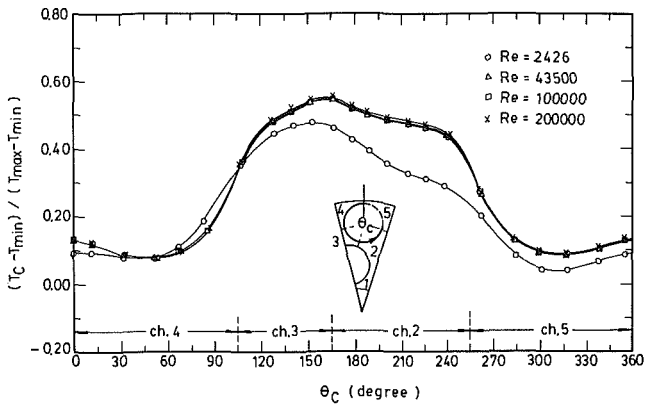

Fig. 11(b) Surface temperature distribution around Rod C

is introduced to describe the temperature distribution of fluid and rod surfaces. The dimensionless temperature contours of the fluids for Re = 2426 are shown in Fig. 9. This figure indicates that the temperature and its gradient in subchannel 1 are the highest among all subchannels because subchannel 1 has the highest ratio of heated area A_H to flow area A_F. Subchannel 3 has the same ratio of A_H/A_F, but it is adjacent to the subchannels of lower temperature. Peripheral subchannels 4 and 5 are adjacent to the adiabatic tube wall; therefore, the temperature is low in these two subchannels. Figure 10 shows the dimensionless temperature contours for Re = 43,500, which are very similar to those of Re = 10^5 and 2×10^5. The average temperature and its gradient in subchannels 1 and 4 are the highest and lowest, respectively, among all subchannels. Comparing Figs. 9 and 10, it is found that the bulk temperatures decrease for subchannels 1, 3, 4, and 5, and the only increase is for subchannel 2. Moreover, the major difference observed is the ranges of ϕ in subchannels 1 and 2: (1.0–0.73) and (1.0–0.66) for subchannel 1, (0.73–0.23) and (0.66–0.26) for subchannel 2, with respect to Figs. 9 and 10. These two findings imply that subchannel 2, which has the largest flow area among subchannels, can remove more energy from fuel rods, so that the surface temperature variation on rods should be decreased (see Figs. 11(*a*) and 11(*b*) and the following discussions).

The surface temperature of fuel rods is important to safe and economic operation of nuclear reactor cores. The following discussions involve the rod surface temperature distributions and the heat transfer coefficients. Figure 11(*a*) shows the surface temperature variation around Rod A and Rod B, and Fig. 11(*b*) shows the variations around Rod C. The slopes of these curves are steep near the intersections of adjacent subchannels 1 and 2, 3 and 4, 2 and 5. The locations of the hottest spots are of interest, which are found at Rod A at $\theta_A = 0$ and

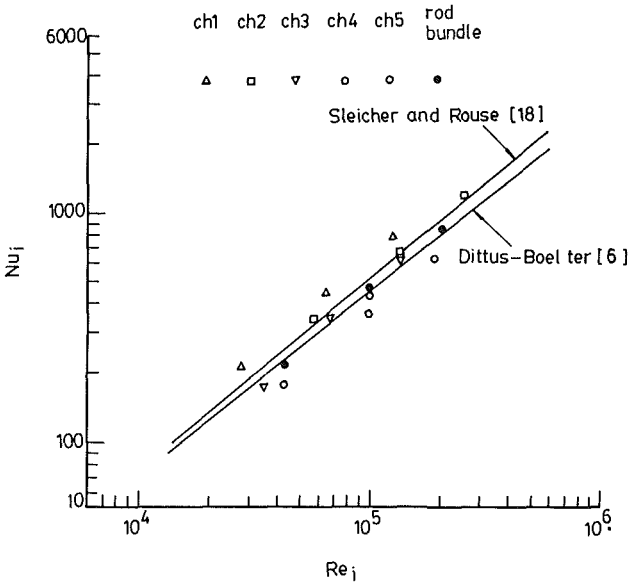

Fig. 12 Nusselt number versus Reynolds number for each subchannel

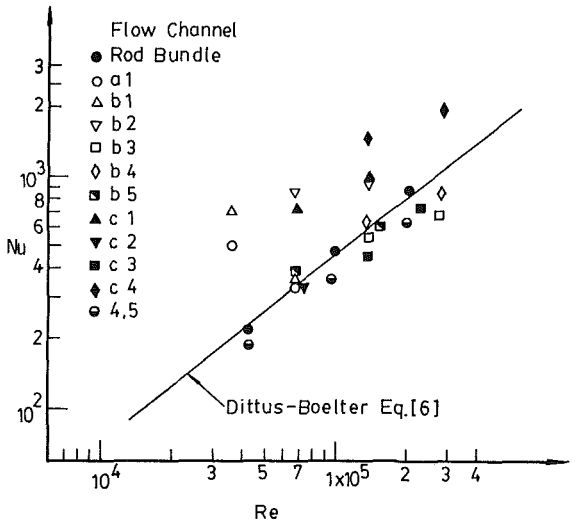

Fig. 13 Nusselt number versus Reynolds numbers for each characteristic flow area

at Rod B at $\theta_B = 0$ (Fig. 11(*a*)). The surface temperature variation around Rod B is the greatest among the three rods, and it decreases as Reynolds number increases. However, the variations increase slightly around Rods A and C as Reynolds number increases.

The average wall-to-bulk temperature difference is a function of pitch-to-diameter ratio P/D, and it can be expressed in terms of the Nusselt number Nu for the fuel bundle where

$$\mathrm{Nu} = q''_w D_h / [k_c (\bar{T}_w - T_m)] \tag{9}$$

Here the hydraulic diameter D_h is the characteristic length. According to Table 3 [3], for laminar flow inside a 19-rod CANDU bundle, the Nusselt numbers are 14.43 and 8.757 for $P/D = 4.0$ and 2.5, respectively. Therefore, the Nusselt number of the present bundle must be much smaller, and is obtained as 1.21 because P/D is 1.155 and the hydraulic diameter of the full bundle D_h is only 1.103 cm. Figure 12 shows that the calculated Nusselt numbers of internal subchannels are higher than the values obtained from the widely used Dittus-Boelter [6] except a single value of subchannel 3, and the calculated Nusselt numbers of peripheral subchannels are all overestimated if the Dittus-Boelter equation is employed. However, the calculated Nusselt numbers for the fuel bundle agree with the equation very well. Furthermore, the Nusselt numbers are different for subchannels 1 and 3, even if they have a flow area of same shape and size.

In order to see whether the performance of the subchannel analysis code can be improved by implementing sub-subchannels as the characteristic flow area, the Nusselt number for sub-subchannels and subchannels are calculated and defined as

$$\mathrm{Nu}_{ch} = \frac{q''_w D_{h,ch}}{k_c (\bar{T}_{w,R} - T_{m,ch})} \tag{9}$$

where ch = index of the characteristic flow area, e.g., a_1, b_1, . . . , or 1, 2, 3, ...

R = index of the fuel rod neighboring the characteristic flow area, e.g., A, B, C.

Figure 13 shows that the calculated Nusselt numbers of sub-subchannels are scattered even more than those of subchannels. This means that implementing correlations of heat transfer coefficient is even more difficult if sub-subchannel analysis is employed. These discrepancies are caused by the definition of q''_w, which is the wall heat flux into the characteristic flow area (either subchannel or sub-subchannel), but the actual heat flux into the characteristic flow area includes the conduction heat flux from adjacent subchannels also and the magnitude is significant. Dividing the subchannel into sub-subchannels yields the influence of conduction heat flux increasing. The only remedy can be introducing the factor which can take account of the mixing between subchannels.

The interchange or mixing of coolant between the subchannels, which is geometry dependent, had been taken care of quantitatively by introducing the correlations of a turbulent mixing parameter[1] in subchannel analysis codes, and the parameter is good for triangular or square subchannels of rod array. In the present study, the calculated average bulk temperatures of all subchannels are used as a check to see whether the turbulent mixing parameter can be extended to combinations of different subchannel shapes. The turbulent mixing parameter correlations of Rogers-Tarasuk [14] and Rowe-Angle [16] have been adapted to the subchannel analysis code COBRA-IIIC/MIT-2 [8]. The results show that these correlations must be raised four times higher to match the bulk temperatures of each subchannel. It is implied that the combinations of different subchannel shapes promote stronger interchannel mixing than subchannels of a single shape.

Conclusions

The flowfield for the CANDU-type 19-rod fuel bundle, obtained by the application of the isotropic "k-ϵ" turbulence model, is reasonably agreed with the available experimental data [5] and the simple predictions by other method [14]. For this doubly connected solution domain, the velocity contours can be approximated by the proper combination of the flowfields obtained individually for infinite rod array of different arrangement; but the patterns of temperature contours can not be approximated.

The surface temperature on fuel rods directly calculated by the present method, which is on the safe side of fuel bundle design by the assumption of isotropic turbulence, is much more realistic than the value obtained by the subchannel

[1] Turbulent mixing parameter is defined as the ratio of turbulent interchange mixing rate between adjacent subchannels and mass flow rate of the entire subchannel.

analysis. However, the detailed calculation indicates that: (1) the heat transfer coefficient by Dittus–Boelter correlation, and (2) the conventional subchannel as the characteristic flow area are sufficiently good in the subchannel analysis if conservatism is the goal of reactor design criteria of the CANDU-reactor.

References

1 Banerjee, S., and Hadaller, G. I., "Longitudinal Laminar Flow Between Cylinders Arranged in Regular Array," *AIChE Journal*, Vol. 5, 1971, pp. 325–330.

2 Bartzis, J. G., and Todreas, N. W., "Turbulence Modelling of Axial Flow in a Bare Rod Bundle," ASME JOURNAL OF HEAT TRANSFER, Vol. 101, 1979, pp. 628–634.

3 Benodekar, R. W., and Date, A. W., "Numerical Prediction of Heat Transfer Characteristics of Fully Developed Laminar Flow Through a Circular Channel Containing Rod Clusters," *International Journal of Heat and Mass Transfer*, Vol. 21, 1978, pp. 935–945.

4 Carajilescov, P., and Todreas, N. E., "Experimental and Analytical Study of Axial Turbulent Flows in an Interior Subchannel of Bare Rod Bundle," ASME JOURNAL OF HEAT TRANSFER, Vol. 98, 1976, pp. 262–368.

5 Chieng, C. C., and Lin, Chaung, "Velocity Measurement in the Peripheral Subchannel of the CANDU-Type 19 Rod Bundle," *Nuclear Engineering and Design*, Vol. 55, 1979, pp. 389–394.

6 Dittus, F. W., and Boelter, L. M. K., Publications in Engineering, California, Vol. 2, 1930, p. 443.

7 Gosman, A. D., and Ideriah, F. J., "TEACH-2E: A General Computer Program for Two-Dimensional, Turbulent, Recirculating Flows," Department of Mechanical Engineering, Imperial College, London, 1976.

8 Jackson, J. W., and Todreas, N. E., "COBRA-IIIC/MIT-2: A Digital Computer Program for Steady State and Transient Thermal Hydraulics Analysis of Rod Bundle Nuclear Fuel Element," Energy Laboratory Report No. MIT-EL 81-018, Massachusetts Institute of Technology, 1981.

9 Jones, W. P., and Launder, B. E., "The Calculation of Low-Reynolds Number Phenomena With 2-equation Model of Turbulence," *International Journal of Heat and Mass Transfer*, Vol. 16, 1973, pp. 1119–1130.

10 Malak, J., Heina, J., and Schmid, J., "Pressure Losses and Heat Transfer in Non-circular Channels with Hydraulically Smooth Walls," *International Journal of Heat and Mass Transfer*, Vol. 18, 1975, pp. 139–149.

11 Mottaghian, R., and Wolf, L., "A Two-Dimensional Analysis of Laminar Fluid Flow in Rod Bundles of Arbitrary Arrangement," *International Journal of Heat and Mass Transfer*, Vol. 17, 1974, pp. 1121–1127.

12 Rehme, K., "Simple Method of Predicting Friction Factors of Turbulent Flow in Non-circular Channels," *International Journal of Heat and Mass Transfer*, Vol. 16, 1973, pp. 933–950.

13 Rehme, K., "The Structure of Turbulent Flow Through a Wall Subchannel of a Rod Bundle," *Nuclear Engineering and Design*, Vol. 45, 1978, pp. 311–323.

14 Rogers, J. T., and Todreas, N. E., "Coolant Interchannel Mixing in Reactor Fuel Rod Bundles Single-Phase Coolants," *ASME Symposium on Heat Transfer in Rod Bundles*, 1978, pp. 1–56.

15 Seale, W. J., "Turbulent Diffusion of Heat Between Connected Flow Passages, Part I: Outline of Problem and Experimental Investigation," *Nuclear Engineering and Design*, Vol. 54, 1979, pp. 183–195.

16 Rowe, D. S., and Angle, C. W., "Experimental Study of Mixing Between Rod-Bundle Fuel-Element Flow Channels During Boiling," *Trans. American Nuclear Society*, Vol. 10, 1967, pp. 655–656.

17 Slagter, W., "Finite Element Solution of Axial Turbulent Flow in a Bare Rod Bundle Using a One-Equation Turbulence Model," *Nuclear Engineering and Design*, Vol. 82, 1982, pp. 243–259.

18 Sleicher, C. A., and Rouse, M. W., "A Convenient Correlation for Heat Transfer to Constant and Variable Property Fluids in Turbulent Pipe Flow," *International Journal of Heat and Mass Transfer*, Vol. 18, 1975, pp. 677–683.

19 Sparrow, E. M., and Loeffler, A. L., Jr., "Longitudinal Laminar Flow Between Cylinders Arranged in Regular Array," *AIChE Journal*, Vol. 5, 1959, pp. 325–330.

20 Yang, A. S., and Chieng, C. C., "Turbulent Heat and Momentum Transports in an Infinite Rod Array," ASME JOURNAL OF HEAT TRANSFER, this issue.

Turbulent Heat and Momentum Transports in an Infinite Rod Array

An-Shik Yang
Graduate Student of Power Mechanical Engineering.

Ching-Chang Chieng
Professor of Nuclear Engineering.

National Tsing Hua University, Hsinchu, Taiwan 300, Republic of China

An anisotropic factor is carefully selected from eleven distributions and adopted to the k–ϵ two-equation model of turbulence to obtain detailed velocity and temperature fields for steady-state, fully developed turbulent flow through infinite triangular/square rod array. The present study covers the ranges of pitch-to-diameter ratio from 1.123 to 1.5, and Reynolds number from 2.4 × 10^4 to 10^6. Velocity and wall shear stress are calculated and compared to experimental data. Normalized fluid temperature, friction factor, and heat transfer coefficient are also computed. The correlations of friction factor and heat transfer coefficients for flow inside circular pipe and flow through finite rod arrays are compared with the results for flow through infinite rod arrays.

Introduction

For a nuclear reactor, the fuel rods are generally arranged in triangular or square arrays. The coolant flows through spaces between rods and the space can be divided into interconnected subchannels. The subchannel method is the most widely used approach among the rod bundle thermal-hydraulic analyses. In this approach, the average mass flow rate and associated Reynolds number must be supplied to give the corresponding heat transfer coefficient from proper correlations for each subchannel. Then the average bulk temperatures of subchannels and the surface temperatures of fuel rods are obtained. Detailed velocity and temperature distributions within rod bundles have recently been predicted by solving the basic differential equations of turbulent flow and energy. The k–ϵ turbulence model and the anisotropic effect of eddy viscosity concept are the most advanced and widely used approaches, for the calculation of turbulent heat and momentum transport in bare rod bundles. While some of the related studies [3, 19] emphasized flow characteristics only, Bartzis et al. [2], Seale [13, 14], and Taylor et al. [18] considered the heat transfer characteristics also. Bartzis et al. estimated the circumferential variations of outside clad temperature via the predicted flowfield. Seale and Taylor et al. solved the Reynolds equations of energy and momentum simultaneously by finite difference and finite element methods respectively, and obtained detailed temperature contours. The above investigators worked on subchannels of triangular rod arrays but Seale worked on subchannels of rectangular rod arrays. They considered the anisotropic effect of turbulence in different ways. In the present paper, both the flow and heat transfer characteristics are obtained for fully developed flows through rod arrays of either triangular or square arrangements. The scope of the study includes the careful selection of anisotropic factor, Nusselt number distribution, temperature of rod surface, fluid temperature contour, kinetic energy of turbulence, and axial velocity distribution. The covered ranges of computation are: pitch-to-diameter ratio P/D = 1.123–1.50, and Reynolds number 2.4 × 10^4–10^6.

Due to geometry symmetry and computer storage, the solution domain of velocity and temperature fields is chosen as the smallest symmetry segment of a subchannel, which is 1/6 or 1/8 of flow domain of a triangular or square subchannel, respectively (Fig. 1(*a*)). Figure 1(*b*) illustrates the coordinate notation such as r, θ, x, y, $\hat{y}$ which will be used for later discussion.

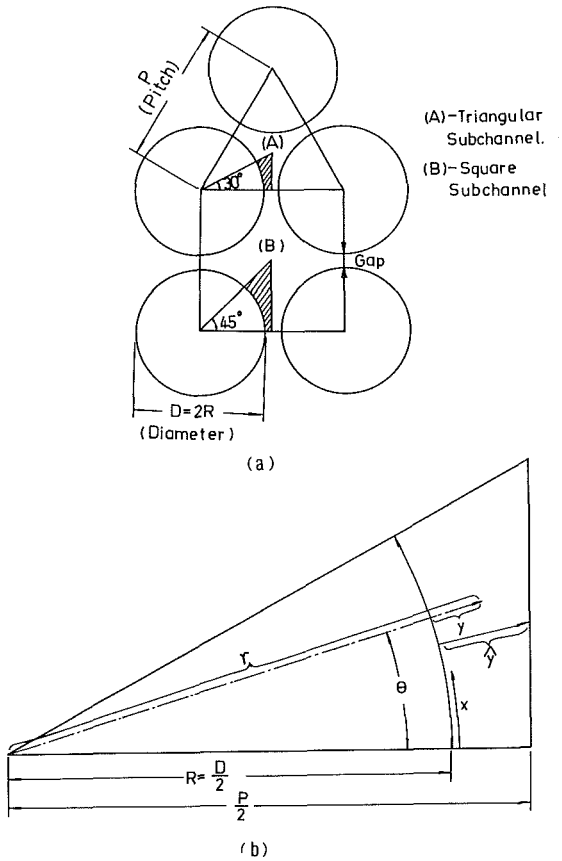

Fig. 1 (*a*) Subchannels of triangular and square rod arrays; (*b*) notations of coordinates

Mathematical and Physical Model

Governing Equations. To predict the flow and heat transfer characteristics, the fundamental physical laws of energy and momentum conservation are employed with transport equations of turbulent kinetic energy k and turbulent dissipation rate ϵ. The mathematical representation of these equations with zero secondary flow of an incompressible, constant fluid property, steady-state, fully developed flow can be written in cylindrical coordinates (r, θ, z) and in a generalized form as

$$\frac{1}{r}\frac{\partial}{\partial r}\left(r\alpha_{r\phi}\frac{\partial \phi}{\partial r}\right)+\frac{1}{r}\frac{\partial}{\partial \theta}\left(\frac{\alpha_{\theta\phi}}{r}\frac{\partial \phi}{\partial \theta}\right)+S_\phi=0 \qquad (1)$$

Contributed by the Heat Transfer Division for publication in the JOURNAL OF HEAT TRANSFER. Manuscript received by the Heat Transfer Division October 24, 1984.

Table 1 Coefficients of the governing equations

equation	ϕ	$\alpha_{i\phi}^{*}$	S_ϕ
continuity	1	0	0
z-momentum	w	$\mu_{t,iz}+\mu_\ell$	$F_z - \partial P/\partial z$
energy	T	$\frac{\mu_{t,iz}}{Pr_t}+\frac{\mu_\ell}{Pr_\ell}$	$-\rho w \frac{\partial T}{\partial z}$ **
turbulent kinetic energy	k	$\frac{\mu_{t,iz}}{Pr_k}$	$G-\rho\epsilon$; $G=\mu_t\left\{\left(\frac{\partial w}{\partial r}\right)^2+\left(\frac{1}{r}\frac{\partial w}{\partial \theta}\right)^2\right\}$
turbulent energy dissipation rate	ϵ	$\frac{\mu_{t,iz}}{Pr_\epsilon}$	$\frac{\epsilon}{k}\{C_1 G-\rho C_2\epsilon\}$

* i = θ or z ; μ_ℓ = laminar viscosity

** $\frac{\partial T}{\partial z}=\frac{dT_m}{dz}=\frac{1}{\dot{m}C_p}\int q_w''(r,\theta)\,dL_H$

In equation (1), ϕ represents any of the dependent variables. Diffusion coefficients ($\alpha_{r\phi}$ and $\alpha_{\theta\phi}$) and source terms (S_ϕ) for each dependent variable are given in Table 1.

The turbulent viscosity $\mu_{t,iz}$ is defined as

$$\mu_{t,rz}=-\rho\overline{v'w'}\Big/\left(\frac{\partial w}{\partial r}\right)$$
$$\mu_{t,\theta z}=-\rho\overline{u'w'}\Big/\left(\frac{\partial w}{r\partial\theta}\right) \tag{2}$$

where u', v', w' represent the velocity fluctuations in the (θ, r, z) directions. If the ratio of $\mu_{t,\theta z}$ and $\mu_{t,rz}$ is defined as the anisotropic factor ψ

$$\psi=\frac{\mu_{t,\theta z}}{\mu_{t,rz}} \tag{3}$$

then $\mu_{t,\theta z}$ can be determined by terms of k, ϵ, and ψ

Table 2 Number of grid points for various subchannels

P /D	number of grid points in (r,θ) directions	subchannel geometry
1.123	21x26	triangular
1.20	20x27	triangular
1.25	21x25	square
4/3	21x27	square
1.35	20x31	triangular
1.50	20x34	triangular

$$\mu_{t,rz}=C_\mu\rho k^2/\epsilon$$
$$\mu_{t,\theta z}=\psi\mu_{t,rz}=\psi C_\mu\rho k^2/\epsilon \tag{4}$$

The values of all empirical constants in the turbulence model are [7]

C_μ	C_2	C_1	Pr_k	Pr_ϵ	Pr_t
0.09	1.92	1.44	1.00	1.30	0.9

which have been adopted by Seale [14] for the rectangular array and extensively examined for both free and confined turbulent flows by Launder and Spalding [8].

Since the hydrodynamic quantities vary rapidly within the wall region, the wall function approach is employed to reduce the number of grid points and obtain sufficiently good results. The wall functions chosen for this study, which are approximate expressions for each variable in the near wall region in turbulent flow, are as follows [5, 7]:

Axial velocity w

$$w^+=\frac{w_p}{\left(\frac{\tau_w}{\rho}\right)^{1/2}}=\frac{1}{\kappa}\ln(Ey_p^+) \tag{5}$$

$$y_p^+=y_p(\tau_w/\rho)^{1/2}/\nu,\quad \nu=\mu/\rho$$

Nomenclature

A = flow area of the subchannel, m²
C = wetted perimeter of the subchannel, m
C_p = specific heat of fluid, kJ/kg-K
D_H = equivalent diameter of the subchannel = $4A/C$, m
E = 9.793 in equation (5), dimensionless number
f = Darcy friction factor = $8\tau_w/(\rho\bar{w}^2)$
h = heat transfer coefficient, W/m²K
k = turbulent kinetic energy, m²/s²
k_c = thermal conductivity of coolant, W/m²k
$\dot{m}$ = mass flow rate, kg/s
Nu = Nusselt number = hD_H/k_c
p = pressure, Pa
P_H = perimeter of heated rod, m
P/D = pitch-to-diameter ratio
Pr = Prandtl number
q_w'' = wall heat flux, W/m²
Re = Reynolds number = $D_H\rho w/\nu$
Re_t = local turbulence Reynolds number = $yk^{1/2}/\nu$
S_ϕ = source term in equation of ϕ
T = temperature, K
T_m = average temperature of the subchannel, K
$\bar{T}_w$ = average wall temperature, K
u, u' = velocity and its fluctuation in r direction, m/s
v, v' = velocity and its fluctuation in θ direction, m/s
w, w' = velocity and its fluctuation in z direction, m/s
$\bar{w}$ = average velocity of subchannel in z direction, m/s
y = distance from wall, m
$\hat{y}$ = normal distance to no-shear surface
y_p = normal distance from node p to the wall, m
α_ϕ = diffusion coefficient of variable ϕ
ϵ = turbulent dissipation rate, m²/s³
κ = Von Kármán constant = 0.4187, dimensionless number
μ = dynamic viscosity, Pa•s
τ_w = wall shear stress, N/m²
Φ = dimensionless temperature = $(\bar{T}_W-T)\ /\ (\bar{T}_w-T_m)$
ψ = anisotropic factor, defined by equation (3)

Subscripts

l = laminar
m = mean
p = node next to wall
t = turbulent
w = wall

Superscripts

$\bar{}$ = average
$+$ = nondimensional variable

Table 3 Anisotropy factor functions

IDIV	ψ	
1	$0.7 + \frac{0.35}{1.0167 - \bar{z}}$	[14]
2	$\frac{1}{1.05 - \bar{z}}$	[14]
3	$\frac{1}{1.025 - \bar{z}}$	[14]
4	$\frac{1}{1.00625 - \bar{z}}$	[14]
5	$30\ e^{-(3y/\hat{y})^2} + 1$	[14]
6	$50\ e^{-(3y/\hat{y})^2} + 2$	[14]
7	$1.5 \times 4.79\ e^{0.99(0.4 - y/\hat{y})}$	[14]
8	$\frac{2.0\{y(1 - e^{-0.018R_{\epsilon}})\}}{0.21\{y[0.25 + 0.066\ \sin(\pi(y/\hat{y} - 0.25)/0.55)]\}}$	[15]
9	$40\ e^{-(3.6y/\hat{y})^2} + 1$	[present work]
10	$60\ e^{-(4.0y/\hat{y})^2} + 1.5$	[present work]
11	$30\ e^{-(4.0y/\hat{y})^2} + 1.5$	[present work]
	$\bar{z} = 1 - y/\hat{y}$	

Table 4 Maximum error induced by various anisotropic factors

IDIV	1	2	3	4	5	6	7	8	9	10	11
Δ_1(%)	-6.5	-4.5	-4.3	-2.0	+5.	+9.	+7.	+11.5	-12.	-3.	-10.
Δ_2(%)	-10.	-9.5	-9.	-8.	-4.	-4.	-5.	-14.	-6.5	-7.	-7.

$\Delta_1 = [(\tau/\bar{\tau}_w)_{exp} - (\tau/\bar{\tau}_w)_{pred}]_{max}$

$\Delta_2 = [(w/\bar{w})_{exp} - (w/\bar{w})_{pred}]_{max}$

IDIV = see Table 3

Turbulent kinetic energy k

$$k_p = \frac{(\tau_w/\rho)}{C_\mu^{1/2}} \tag{6}$$

Turbulent dissipation rate ϵ

$$\epsilon_p = \frac{C_\mu^{3/4} k_p^{3/2}}{\kappa\, y_p} \tag{7}$$

Temperature T

$$T^+ = \sigma_t (w^+ + \text{Pfun}) \tag{8}$$

$$\text{Pfun} = 9.24\ [(\text{Pr}_l/\text{Pr}_t)^{0.75} - 1.]\ [1 + 0.28 e^{(-0.007\text{Pr}_l/\text{Pr}_t)}]$$

$$T^+ = C_p \rho (\tau_w/\rho)^{1/2} (T_w - T_p)/q''_w$$

Numerical Scheme. The well-known TEACH-2E computer program [5], used as the framework for present calculations, employs the SIMPLE [9] solution algorithm of Patankar and Spalding. It solves sets of difference equations for z momentum, energy, and transport. For a fixed geometry of the flow domain, a given value of pressure gradient $\partial P/\partial z$ in the z-momentum equation, which is included in the source term S_w (Table 1), yields only one velocity profile and a single value of Reynolds number based on the average velocity and the hydraulic diameter of the entire subchannel. Therefore, the subroutine of pressure calculation is inactive and a new subroutine of axial velocity w calculation is added to the computer program TEACH-2E. Since the secondary flow is assumed negligible in the present work, the tangential and radial velocity (u, v) calculations are inactive and removed from the program. The simplifications and the fact of fully developed flow imply that no convective term is needed for governing equations, if the term $-w\partial T/\partial z$ in the energy equation is included in the source term of computation (see equation (1) and Table 1).

The number of grid points for each subchannel depends on the pitch-to-diameter ratio and the arrangement of rod arrays, which is summarized in Table 2. For a special case of isotropic turbulent flow, Re = 27,000 and P/D = 1.123, the computation by 11 × 16 grid system is performed to compare it with the results from a 21 × 26 grid system. It is found that the difference for axial velocity and wall shear stress is within 1 percent in most parts of the flow domain and within 4 percent at several spots near θ = 0 deg and $y \to \hat{y}$. Therefore, the 21 × 26 grid system is employed in the present computation to ensure the accuracy of the prediction. It takes approximately 3300 cpu seconds on CDC Cyber 172 to get a converged result for the 21 × 26 grid system, if the initial guess of the flowfield is uniform.

Boundary Conditions. The boundaries of the solution domain consist of three straight lines of geometry symmetry and a sector of circular curve. The boundaries of computational grids are arranged parallel to the boundaries of solution domain except on the no-shear surface. The boundary nodes next to the surfaces at θ = 0 and 30 deg are easy to handle because of the symmetric nature of the geometry. The nodes next to the wall of the fuel rod are located at normalized distances $y^+ \geq 35$, so that the wall function approach is employed (previous section). The computational nodes next to the fourth boundary surface are carefully arranged such that the zigzag surface gets very close to that of the physical problem, and zero gradients of the interested variables along the r direction are assumed at these nodes in the calculation. The calculated results show that negligible flow of momentum or heat is observed in the normal direction to the no-shear surface (0.5 percent error present).

Results and Discussion. The anisotropic character for turbulent flow in rod bundles is suggested by numerous investigators. Two approaches for including anisotropic nature are suggested in the literature: (1) correlate the anisotropic factor with other turbulent quantities, and (2) correlate the anisotropic factor with locations of interest. For the present study, the second approach is employed because of its simplicity and the limitation of the k–ϵ turbulence model. Eleven distributions of anisotropic factor, as listed in Table 3, are employed as the candidates of most proper function to calculate fluid flow and heat transfer characteristics. Since anisotropy is essentially a wall effect, and it falls rapidly from a maximum value [13] (which ranges from 10 to 60 for various P/D) near the wall to a factor of unity at some distance from the wall. The 11 functions can be grouped in several categories; for example, the first to fourth functions are tightly wall bound anisotropy distributions, the others are broader bounded. According to Seale's [14] paper the first and seventh functions seemed to offer the best agreement with the measurements for computed heat flow and gap Stanton number. Moreover, Seale preferred the form of the fifth and sixth functions, because they brought the Stanton numbers of the correct order and enabled him to obtain some of the general features of his experimental results and geometries. The sixth function especially gives the sharply increasing value (~50) at the wall. The eighth function is in a different category, which is a modified form of an empirical relation and related to local turbulence Reynolds number Re_t. The ninth to eleventh functions are of the same form as the fifth and sixth ones but with different constants, where the constants 30–60 are the maximum values of the anisotropy at the

Table 5 Comparison of measured and calculated velocities

P/D	Re	$w_{peak}/\bar{w}$		Δ^{**}
		experiment	prediction	
1.20	23,790	1.18 [19]	1.17	4.50 %
1.20	60,920	1.16 [19]	1.17	1.50 %
1.35	35,860	1.18 [19]	1.16	1.85 %
1.35	77,110	1.16 [19]	1.14	1.85 %
1.50	75,760	1.16 [19]	1.13	2.65 %
1.25	107,500	1.20 [11]	1.19	3.50 %
4/3	1,090,000	1.15 [1]	1.14	5.30 %

Note: triangular channel for P/D=1.20, 1.35, 1.50
square channel for P/D=1.25, 4/3

** $\Delta = \left[\frac{w_{pred} - w_{exp}}{w_{exp}}\right]$ maximum of any point

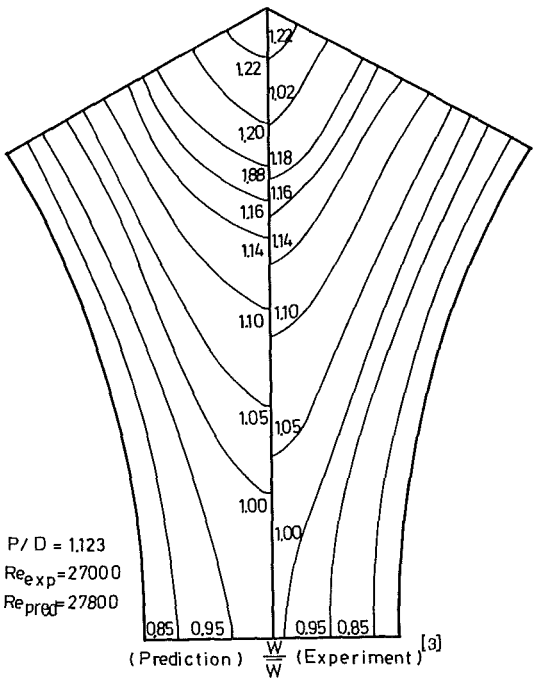

Fig. 2 Predicted and measured velocity contours of triangular subchannel: *P/D* = 1.123, Re = 2.7 × 10^4

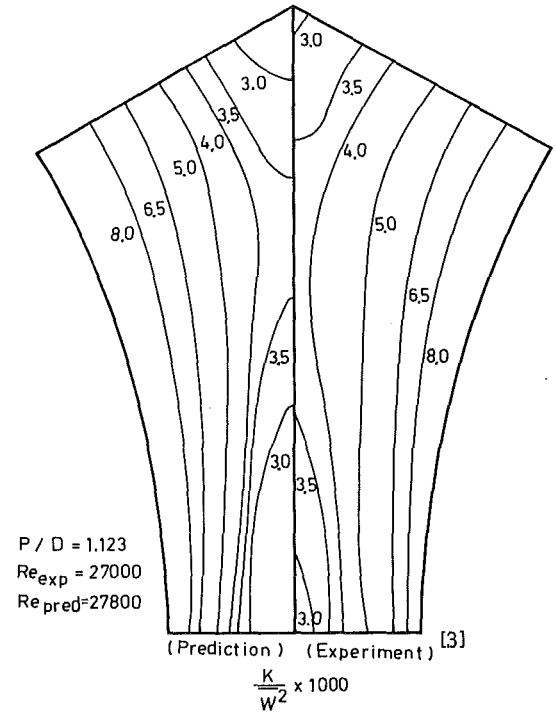

Fig. 3 Predicted and measured turbulent kinetic energy of triangular subchannel: *P/D* = 1.123, Re = 2.7 × 10^4

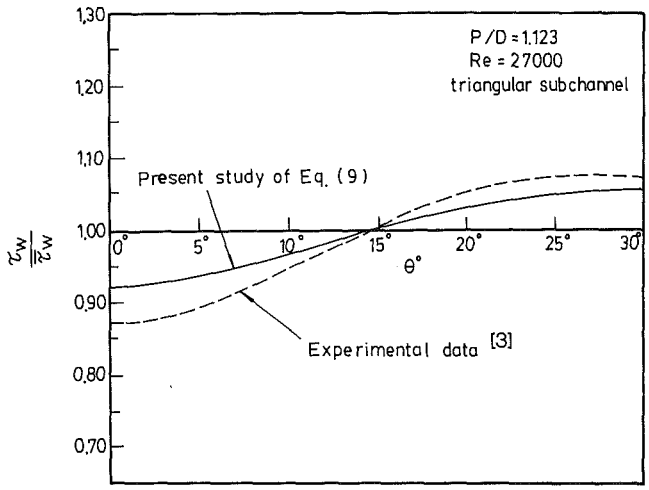

Fig. 4 Wall shear stress, Re = 27,000, *P/D* = 1.123

wall, the constant 3, 3.6, or 4 is the decay constant of the anisotropy away from the wall, and the last constant 1.0, 1.5, or 2.0 represents anisotropy over the bulk. The present study investigates their effects in detail and proposes the most proper function. The bases of adjusting the functions for the anisotropy factor are the distributions of axial velocity w and wall shear stress τ_w from [1]. The maximum differences between measured and predicted values for τ/τ_w and $w/\bar{w}$ are tabulated in Table 4 for all 11 distributions. The table shows that the fifth and sixth functions give the least error in velocity calculations. Besides, the fifth function yields less error than the sixth function in the calculation of wall shear stress. Therefore, the fifth function

$$\Psi = 30\, e^{-(3y/\bar{y})^2} + 1 \qquad (9)$$

is chosen as the basis for the most appropriate correlation for anisotropic factor in present work.

The detailed results of prediction using the anisotropic factor of equation (9) (i.e., the fifth function in Table 3) are compared and discussed against the experimental data of Carajilescov and Todreas [3], for the case of Reynolds number 27,000, P/D = 1.123, and infinite rod array of triangular arrangement. The comparison of the velocity contours between experimental and computational results is plotted in Fig. 2. The comparison shows excellent agreement in the major part of the subchannel, and the maximum disagreement is ≤4 percent, which occurs at the center of the gap line between subchannels (θ = 0 deg, $y = \bar{y}$). The small difference may be caused by the assumption of no secondary flow and no interchannel mixing in the calculation. Figure 3 shows a small difference between the measured kinetic energy of turbulence and present calculation, except at gap regions near the no-shear surface. The calculated kinetic energy of turbulence is slightly lower than experimental data at locations near the intersecting region of adjacent subchannels, which can be explained by a smaller velocity gradient due to the assumption of zero momentum flux across lines of symmetry so that a smaller

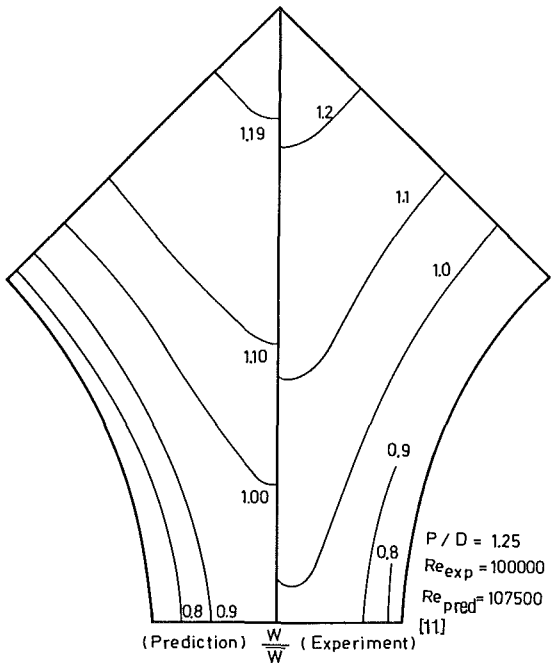

Fig. 5 Predicted and measured velocity contours of square subchannel: *P/D* = 1.25, Re = 10^5

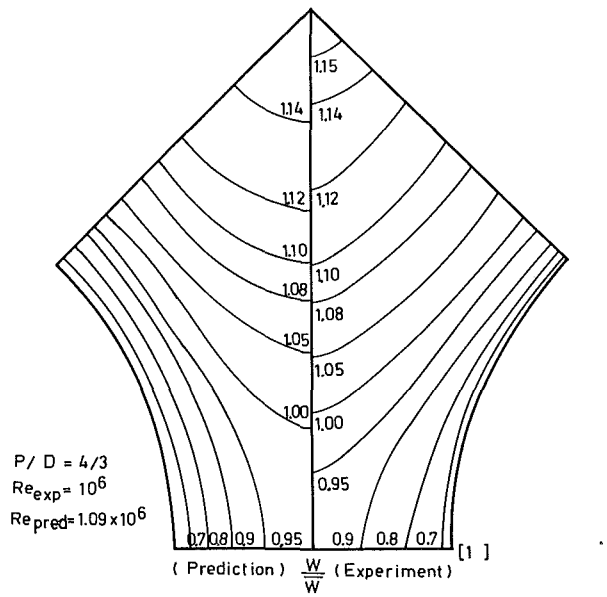

Fig. 6 Predicted and measured velocity contours of square: *P/D* = 1.33, Re = 10^6

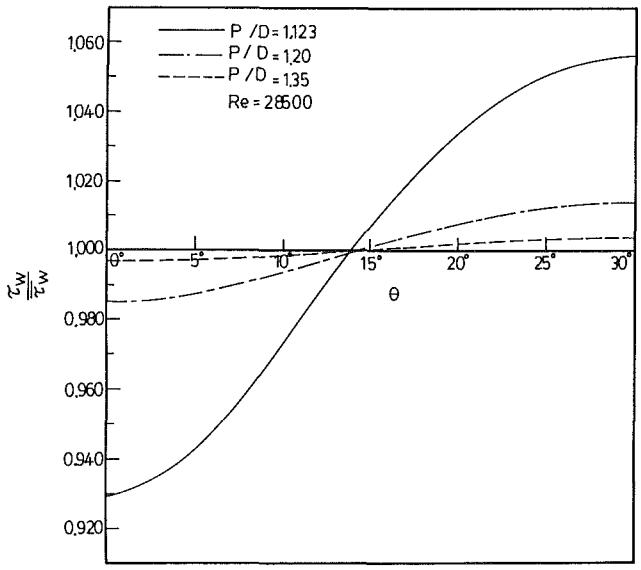

Fig. 7 Wall shear stress, Re = 28,500, *P/D* = 1.123, 1.20, 1.35

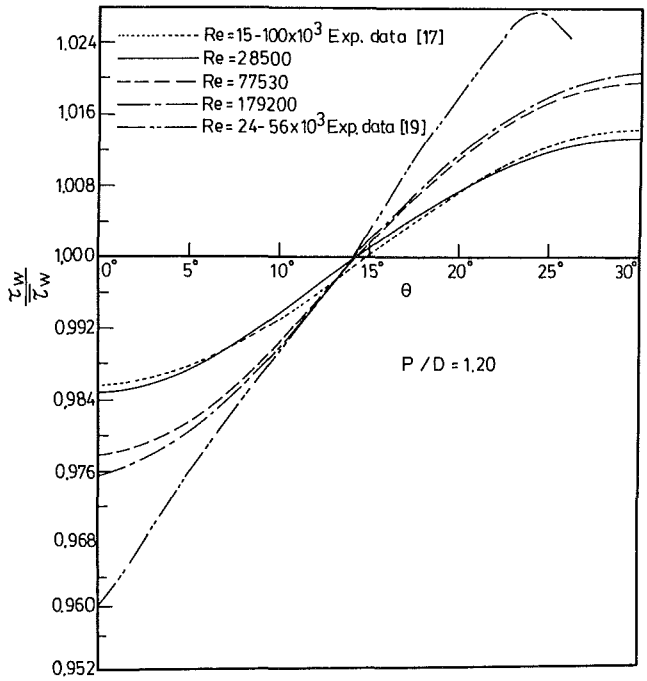

Fig. 8 Wall shear stress, *P/D* = 1.20, Re = 15-1.79 × 10^5

production rate of turbulent kinetic energy is obtained in calculation. Figure 4 shows a small variation of wall shear stress between calculations and measurements. There is within 5 percent underestimation of wall shear stress variation at θ = 0 and 30 deg. To conclude the specific case, the prediction of flow characteristics is excellent using the anisotropic factor of equation (9).

In comparisons with measurements of Trupp [19], for triangular subchannels of finite rod array, the calculations are also performed for cases of P/D = 1.20 (Re = 23,760, 56,020), P/D = 1.35 (Re = 35,700, 72,490), and P/D = 1.50 (Re = 73,370). Table 5 provides the ratios of peak and average velocities ($w_{peak}/\bar{w}$) for the entire subchannel, and the maximum differences of predicted and measured velocities (Δ) at any location in the subchannel. The table confirms the excellent capability in predicting the flow characteristics by anisotropic factor of equation (9) for the subchannels through infinite rod arrays of triangular arrangements.

The anisotropic factor of equation (9) and the same solution algorithm as previous sections are employed to study the flow and heat transfer characteristics for subchannels between infinite square array. Figure 5 compares the predicted velocity contours with experimental data of Rowe [11], Re = 100,000, P/D = 1.25. Figure 6 compares the predicted velocity contours with experimental data of Abdelghany and Roco [1] for Re = 10^6 and P/D = 1.33. Both figures and Table 5 show the excellent agreement with experimental data except for the gap region near the no-shear surface. Therefore, it is concluded that the anisotropic factor of equation (9) is the best choice for both triangular and square subchannels.

Figure 7 shows wall shear stress along the θ direction for various P/D and Re = 28,500. It is found that circumferential variation of wall shear stress decreases from (0.931–1.055) to

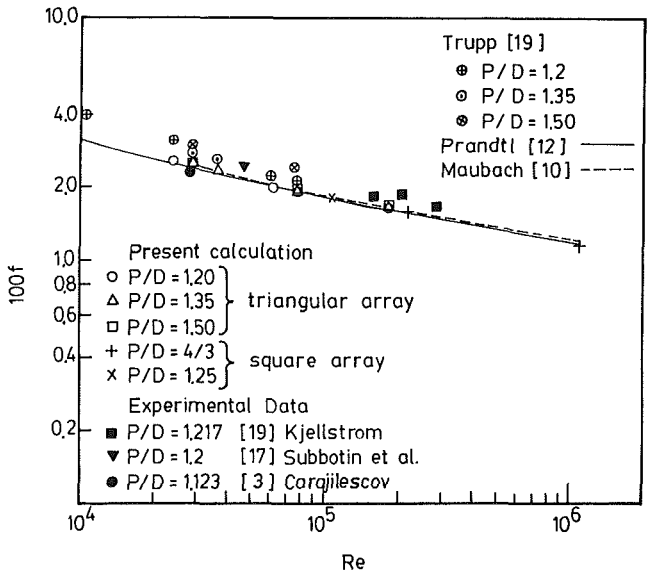

Fig. 9 Friction factor versus Reynolds number and pitch-to-diameter ratio

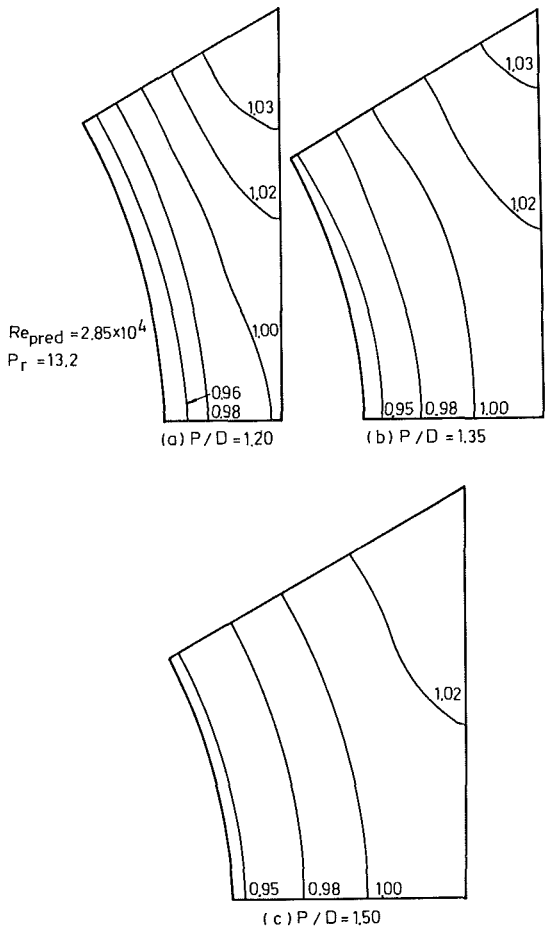

Fig. 10 Isotherm plot of $\Phi = (T - \bar{T}_w)/(T_m - \bar{T}_w)$ for triangular subchannel and Re = 28,500

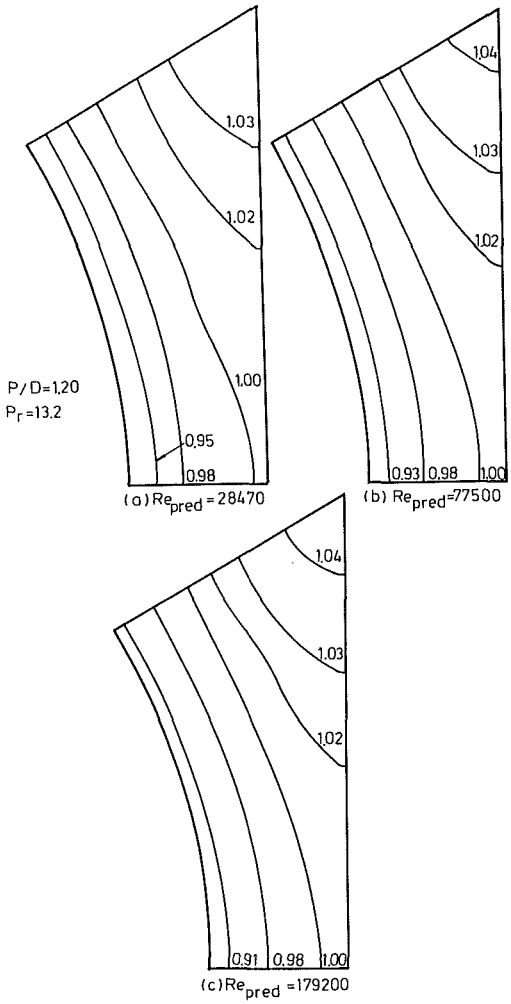

Fig. 11 Isotherm plot of $\Phi = (T - \bar{T}_w)/(T_m - \bar{T}_w)$ for triangular subchannel and $P/D = 1.20$

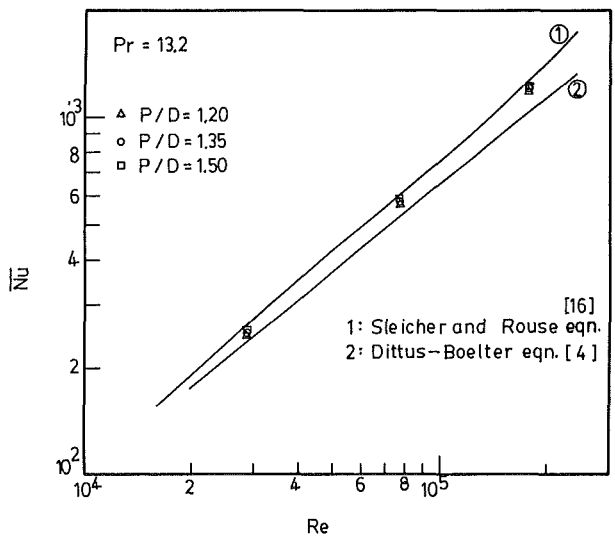

Fig. 12 Nusselt number distribution versus Reynolds number

(0.996–1.003) as P/D increases from 1.123 to 1.35. It is implied that the circumferential variation of wall shear stress is negligible for $P/D > 1.35$. Figure 8 shows wall shear stress along the θ direction for $P/D = 1.2$ and various Reynolds numbers. It is noted that calculated variations of normalized wall shear stress are within 1 percent difference as the Reynolds number increases from 15,000 to 179,200. Trupp's data show the greatest variation along circumferential direction and a different location of the maximum value among these curves: The difference may be induced by the asymmetry of the test section or finite array effects according to Trupp. Figure 9 plots the calculated and well-known correlations [10,

12, 19] between f and Re for various P/D. The calculated friction factors of infinite rod arrays are higher than those from the correlations [10, 12] for the pipe flow, but the discrepancy gets smaller as the Reynolds number gets larger; a similar phenomenon has also been obtained by other investigators [17, 19]. Besides, the values are too low compared to Trupp's correlation, which can be explained by the following facts: The rod arrays are finite, the solid wall has been replaced for the plane of symmetry in the experiments, and no secondary flow is considered in the calculation.

The surface temperature along the circumferential direction in dimensionless form is expressed as $\Phi_w = (T_w - T_m) / (\bar{T}_w - T_m)$. The calculated variations of Φ_w for $P/D = 1.20, 1.35, 1.50$ and fixed Reynolds number 28,500, are in the ranges of (1.028–0.975), (1.002–0.997), (1.001–0.999) as θ varies from 0 to 30 deg, respectively. This confirms that the circumferential variation is decreasing as the pitch-to-diameter ratio is increasing. The location of highest surface temperature occurred at $\theta = 0$ deg which is at the gap. For $P/D = 1.20$ and Re = 28,500, 77,530, and 179,200, the calculated variations are in the ranges of ±2.85 percent, ±1.4 percent, and ±1.5 percent, respectively. It is noted that variation of Φ_w approaches a small value as Reynolds number becomes large, which results from the decrease in $(T_w - T_m)$ with increasing Reynolds number.

The dimensionless fluid temperature is given as $\Phi = (\bar{T}_w - T) / (\bar{T}_w - T_m)$, so that the fluid temperature is high and influenced more by the surface temperature of the fuel rod $(T \rightarrow T_w)$ if Φ is smaller. Figure 10 plots the dimensionless temperature contours of various P/D for Re = 2.85×10^4, and it illustrates an insignificant difference in the peak temperature and the temperature variation versus the y coordinate in dimensionless form for various P/D. The flow area with $\Phi < 0.95$ increases as P/D decreases. Figure 11 plots the dimensionless temperature contours of various Reynolds numbers for $P/D = 1.20$ and it shows insignificant differences of dimensionless peak temperatures for various Reynolds numbers but some variations in the dimensionless temperature gradients in the vicinity of rod surfaces. The magnitude of $(\bar{T}_w - T_m)$ decreases as the Reynolds number increases; a larger fraction of flow area can be obtained for small Φ, i.e., the flow area of <0.91 is larger if the Reynolds number is greater (Fig. 11).

For the same Reynolds number, 28,500, the normalized Nusselt number distributions $(\mathrm{Nu}(\theta)/\overline{\mathrm{Nu}})$ around rod surfaces (θ = 0–30 deg) are varied from 0.990 to 1.009, 0.998 to 1.002, and 0.9995 to 1.0005 for $P/D = 1.20, 1.35$, and 1.50, respectively. For the case of the same pitch-to-diameter ratio $P/D = 1.20$, the normalized Nusselt number distributions around the rod surface are varied from 0.984 to 1.013, 0.986 to 1.012, and 0.990 to 1.009 for Re = 179,200, 77,530, and 28,470, respectively. These values indicate the small variation (≤ 2 percent) of normalized Nusselt number around rod surfaces for the rod arrays tested.

Figure 12 shows that the average Nusselt number $\overline{\mathrm{Nu}}$ around the rod surface increases as the Reynolds number increases; the calculated Nusselt numbers are slightly higher than that of the Dittus–Boelter [4] equation, which is the most popular correlation employed by reactor designers, for example the subchannel analysis computer program COBRA-IIIC/MIT2 [6]. This figure also indicates that Sleicher and Rouse [16] overestimate the heat transfer coefficient for these subchannels. However, the disagreement is small as Fig. 12 shows. Therefore, the heat transfer performance of an infinite rod array can be satisfactorily calculated by the Dittus–Boelter equation with a small degree of underestimation.

Conclusions

The anisotropic character of turbulent flow adapted to the k–ϵ two-equation model of turbulence improves the prediction of flow and heat transfer characteristics inside the subchannels of an infinite rod array. Among various correlations tested, the anisotropic factor $\psi = 30\, e^{-(3y/\bar{y})^2} + 1$ introduced by Seale gives the best agreement with the velocity field and wall shear stress distribution, and reasonable agreement with the kinetic energy of turbulence, if the experimental data from Carajilescov and Todreas of $P/D = 1.123$, Re = 27,000 are chosen as the base case for comparison. Moreover, excellent predictions also for Trupp's experimental data for triangular subchannels over ranges of $P/D = 1.20$–1.50, Re = 2.8×10^4–1.79×10^5, and Rowe's [11] and Abdelghany's [1] of square subchannels over the ranges of $P/D = 1.25$–1.33, Re = 10^5–10^6.

The widely used correlations of Prandtl or Maubach for pipe flow and the present calculation underestimate the friction factor for flows through infinite rod arrays of triangular or square subchannels. The correlation of Dittus–Boelter underestimates the heat transfer coefficients and gives a conservative prediction for the coolant passing through an infinite rod bundle of triangular or square arrangement over the tested cases in this study.

References

1 Abdelghany, M., and Roco, M. C., "Anisotropic Turbulent Flow in Rod Bundles," *CNS/ANS International Conference on Numerical Methods in Nuclear Engineering*, Montreal, Canada, Sept. 1983, Vol. 2, pp. 845–854.

2 Bartzis, J. G., and Todreas, N. E., "Turbulence Modeling of Axial Flow in a Bare Rod Bundle," ASME JOURNAL OF HEAT TRANSFER, Vol. 101, 1979, pp. 628–634.

3 Carajilescov, P., and Todreas, N. E., "Experimental and Analytical Study of Axial Turbulent Flows in an Interior Subchannel of Bare Rod Bundle," ASME JOURNAL OF HEAT TRANSFER, Vol. 98, 1976, pp. 262–268.

4 Dittus, F. W., and Boelter, L. M. K., Publications in Engineering, University of California – Berkeley, Vol. 2, 1930, p. 443.

5 Gosman, A. D., and Ideriah, F. J., "TEACH-2E: A General Computer Program for Two-Dimensional, Turbulent, Recirculating Flows," Department of Mechanical Engineering, Imperial College, London, 1976.

6 Jackson, J. W., and Todreas, N. E., "COBRA-IIIC/MIT-2: A Digital Computer Program for Steady State and Transient Thermal Hydraulics Analysis of Rod Bundle Nuclear Fuel Element," Energy Laboratory Report No. MIT-EL 81-018, Massachusetts Institute of Technology, 1981.

7 Jones, W. P., and Launder, B. E., "The Calculation of Low-Reynolds Phenomena With 2-equation Model of Turbulence," *International Journal of Heat and Mass Transfer*, Vol. 16, 1973, pp. 1119–1130.

8 Launder, B. E., and Spalding, D. B., "The Numerical Computation of Turbulent Flows," *Comput. Methods in Applied Mech. Eng.*, Vol. 3, 1974, pp. 269–289.

9 Patankar, S. V., and Spalding, D. B., "A Calculation Procedure for Heat, Mass and Momentum Transfer in Three-Dimensional Parabolic Flows," *International Journal of Heat and Mass Transfer*, Vol. 15, 1972, pp. 1787–1806.

10 Rehme, K., "The Structure of Turbulent Flow Through a Wall Subchannel of a Rod Bundle," *Nuclear Engineering and Design*, Vol. 45, 1978, pp. 311–323.

11 Rowe, D. S., "Measurement of Turbulent Velocity Intensity, and Scale in Rod Bundle Flow Channels," BNWL-1736, Battelle Pacific Northwest Laboratories, Richland, WA, 1973.

12 Schlichting, H., *Boundary Layer Theory*, 6th ed., McGraw-Hill, New York, p. 597.

13 Seale, W. J., "Turbulent Diffusion of Heat Between Connected Flow Passages, Part I: Outline of Problem and Experimental Investigation," *Nuclear Engineering and Design*, Vol. 54, 1979, pp. 183–195.

14 Seale, W. J., "Turbulent Diffusion of Heat Between Connected Flow Passages, Part II: Predictions Using the 'k–ϵ' Turbulence Model," *Nuclear Engineering and Design*, Vol. 54, 1979, pp. 197–209.

15 Slagter, W., "Finite Element Solution of Axial Turbulent Flow in a Bare Rod Bundle Using a One-Equation Turbulence Model," *Nuclear Science and Engineering*, Vol. 82, 1982, pp. 243–259.

16 Sleicher, C. A., and Rouse, M. W., "A Convenient Correlation for Heat Transfer to Constant and Variable Property Fluids in Turbulent Pipe Flow," *International Journal of Heat and Mass Transfer*, Vol. 18, 1975, pp. 677–683.

17 Subbotin, V. L., et al., "Velocity Field of Turbulence of Turbulent Fluid Flow in a Longitudinal Streamline of Clusters of Rods," AEC-tr-7189, Atomic Energy Commission, USA, 1971.

18 Taylor, C., Thomas, C. E., and Morgan, K., "Turbulent Heat Transfer via the F.E.M.," *International Journal of Numerical Methods in Fluids*, Vol. 3, 1983, pp. 363–375.

19 Trupp, A. C., and Azad, R. S., "The Structure of Turbulent Flow in Triangular Array Rod Bundles," *Nuclear Engineering and Design*, Vol. 32, No. 1, 1975, pp. 47–84.

Numerical Determination of Heat Transfer and Pressure Drop Characteristics for a Converging-Diverging Flow Channel

M. Faghri
Associate Professor,
Department of Mechanical Engineering
and Applied Mechanics,
University of Rhode Island,
Kingston, RI 02881
Mem. ASME

Y. Asako
Associate Professor,
Department of Mechanical Engineering,
Tokyo Metropolitan University,
Tokyo, Japan

A finite difference scheme was utilized to predict periodic fully developed heat transfer and fluid flow characteristics in a converging-diverging flow channel. The basis of the method is an algebraic nonorthogonal coordinate transformation which maps the complex fluid domain onto a rectangle. This transformation avoids the task of numerically generating boundary-fitted coordinates. The transformed equations and the entire discretization procedure were documented in an earlier paper which dealt with a general class of nonperiodic problems. Its adaptation to a periodic sample problem of converging-diverging flow channel will be illustrated in this work. Representative results were carried out for laminar flow, Prandtl number of 0.7, in the Reynolds number range from 90 to 1635, for various taper angles of converging-diverging flow channel, and for three ratios of maximum/minimum height of the flow channel. Moderate enhancement in the Nusselt number results occurred, at higher values of Reynolds number for most cases, when compared with corresponding values for straight ducts.

Introduction

Many investigators have employed general curvilinear coordinate systems in conjunction with finite difference techniques to solve fluid flow problems in and around complex geometries (e.g., [1] and references cited therein). In doing so, both orthogonal and nonorthogonal grids were generated numerically in the physical domain so that the boundaries were grid lines, and then the governing transport equations were solved in the generated coordinate system. In a recent paper [2], an alternate methodology was developed which avoids the task of numerically generating the coordinate system. The basis of the method is an algebraic nonorthogonal coordinate transformation which maps the complex fluid domain onto a rectangle. As a consequence, the derivation of the finite difference representation of the conservation equations involves features that are not found in conventional problems where orthogonal coordinate systems are used. Specifically, the conservation equations were derived for a control volume bounded by coordinate lines in the nonorthogonal transformed coordinate system. Then, these equations are discretized to yield the governing algebraic equations of the problem.

The adaptation of [2] to a periodic sample problem of converging-diverging flow channel will be illustrated in this paper. The concept of the periodic fully developed regime [3] will be utilized for the determination of heat transfer, pressure drops, and fluid flow patterns without dealing with the entrance region. This concept is applicable in this case since the flow pattern repeats itself at corresponding axial stations in successive cycles when the fully developed regime is attained. In practice, the onset of this repetition occurs at an axial coordinate about five hydraulic diameters downstream of the duct inlet [4]. Therefore, in a duct consisting of many facets, the fully developed periodic concept is a reasonable model from which to deduce the performance of converging-diverging flow channels. There are no numerical or experimental results

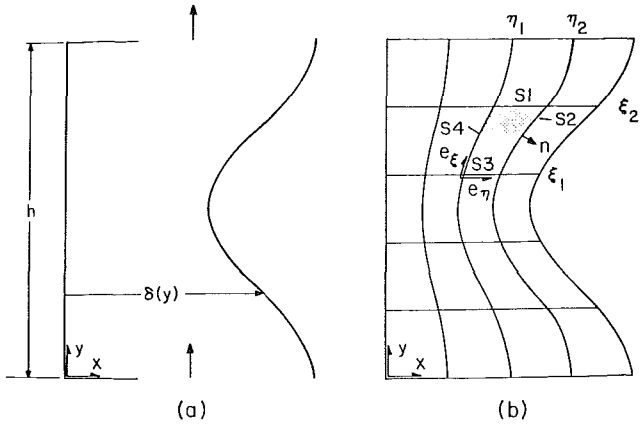

Fig. 1(a) Illustration of a general class of problems; (b) lines of constant η and ξ in the physical domain

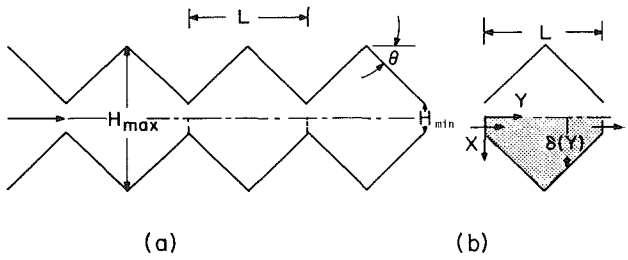

Fig. 2(a) Schematic diagram of a converging-diverging flow channel; (b) solution domain in the physical coordinate

available for comparison of the results for the converging-diverging flow channel with a rectangular cross section. The only related experimental results available are for circular cross sections [5, 6]. The latter problem was solved numerically by an approximation of the sloping walls of the flow passage by a succession of steps [7].

Representative results were carried out for laminar flow and constant surface temperature. Moderate enhancement in the

Contributed by the Heat Transfer Division for publication in the JOURNAL OF HEAT TRANSFER. Manuscript received by the Heat Transfer Division August 27, 1984. Paper No. 84-WA/HT-12.

Nusselt number results occurred, at higher values of Reynolds number for most cases, when compared with the corresponding values for straight duct.

Formulation

Description of a General Problem. Attention will now be focused on a general class of problems. A schematic view of the type of the physical domain being considered is shown in Fig. 1(*a*). As seen there, one wall of the flow channel lies along the y axis, while the other wall of the channel is curved and does not lie along a coordinate line. The cross section of the flow channel varies with y, and it is denoted by $\delta(y)$. The ends of the channel, respectively at $y = 0$ and $y = h$, coincide with coordinate lines.

Coordinate Transformation. The first step in the analysis is to introduce a transformation of coordinates which maps the physical domain onto a rectangle. Specifically, the x, y coordinates are transformed to η, ξ coordinates by the relations

$$\eta = x/\delta(y), \qquad \xi = y \tag{1}$$

such that $\eta = 1$ at all points on the curved boundary. In terms of the new coordinates, the solution domain is defined by $0 < \eta < 1$, $1, 0 < \xi < h$.

Lines of constant η and ξ (i.e., η, ξ coordinate lines) for a given boundary shape are illustrated in Fig. 1(*b*). It is evident that a control volume contained between lines $\eta = \eta_1$, $\eta = \eta_2$ and $\xi = \xi_1$, $\xi = \xi_2$ is a curvilinear element with nonorthogonal sides. The quantities $\mathbf{e}_\eta$ and $\mathbf{e}_\xi$ are unit vectors in the physical coordinate system which respectively lie along the lines of constant ξ and constant η. It is evident from the figure that the direction of $\mathbf{e}_\xi$ changes with position. This is in contrast to the Cartesian unit vectors $\mathbf{e}_x$ and $\mathbf{e}_y$ which, respectively, lie along lines $y = \text{const}$ and $x = \text{const}$. These unit vectors do not change direction throughout the solution domain.

The transformed equations and their complete discretized forms, for the aforementioned general class of problems, are documented in an earlier paper [2]. The discretization procedure and their solutions are tied in with the well-documented practices of the Patankar solution scheme [8, 9]. These equations contain the width of the solution domain δ and its first and higher derivatives, which have to be specified for a particular problem.

The adaptation of the solution methodology to a periodic sample problem of converging–diverging flow channel will now be illustrated. In this regard, the main issue to be dealt with is the description of the periodic fully developed regime, the governing conservation equations, specifications of the boundary conditions, and finally the width of the solution domain $\delta(y)$ and its derivatives.

Description of Sample Problem. The general class of problems described in the previous section includes a large variety of flow configurations of practical interest. Among such configurations are ducts in which the flow cross section varies in a periodic manner along the direction of the flow. One example of these geometries is a converging–diverging flow channel as pictured schematically in Fig. 2(*a*). As seen there, the walls which form the duct are positioned in such a way that the peaks of both the top and bottom walls lie in the same plane. The geometry of the channel may be specified by the cycle length L, the minimum width of the flow domain $H_{\min}$, and the angle θ. The maximum width of the flow domain $H_{\max}$ can be expressed in terms of the other specified parameters.

The solution domain, with the assumption of a periodic fully developed regime, is confined to a typical module shown in Fig. 2(*b*). If δ is defined as shown in this module, then the methodology set forth for the general class of problem is applicable.

Periodic Fully Developed Flow Regime. The fluid flow, in the flow passages with a periodically varying cross section, attains a fully developed regime which differs fundamentally from that for a conventional constant-area flow channel. In the periodically varying cross sections, the fully developed velocity field repeats itself at corresponding axial stations in succesive cycles. Furthermore, in such a regime, the pressures of cyclically corresponding locations decrease linearly in the downstream direction. Similarly, a periodic thermally developed regime exists for commonly encountered boundary conditions such as uniform wall temperature and uniform wall heat flux. Such a regime is characterized by a cycle-averaged heat transfer coefficient which is the same for each cycle of the

Nomenclature

A_w = per-cycle transfer surface area
B = dimensionless per-cycle pressure gradient [equation (3)]
$\mathbf{e}_X$, $\mathbf{e}_Y$ = unit vectors in X, Y directions
$\mathbf{e}_\eta$, $\mathbf{e}_\xi$ = unit vectors in η, ξ directions
$H_{\max}$ = height at maximum cross section
$H_{\min}$ = height at minimum cross section
H^* = equivalent height [equation (20)]
h = heat transfer coefficient, also height of the domain
K = thermal conductivity
L = axial length of a cycle
$\dot{m}$ = total mass flow rate
Nu = Nusselt number = $h(2H^*)/K$
$\mathbf{n}$ = unit vector along the normal to the surface
P = dimensionless periodic pressure [equation (3)]
p = pressure
p' = periodic pressure
ΔP = per-cycle pressure drop
Pr = Prandtl number
Q = per-cycle wall heat transfer rate
Re = Reynolds number = $2\dot{m}/\mu$
T = temperature
T_b = bulk temperature
T_w = wall temperature
U, V = dimensionless velocity components [equation (2)]
u, v = velocity components
X = dimensionless axial coordinate = x/L
x = axial coordinate
Y = dimensionless transverse coordinate = y/L
y = transverse coordinate
β = per-cycle pressure gradient
γ = wall-to-bulk temperature ratio
$\delta(y)$ = width of the solution domain
η = transformed coordinate = x/δ
θ = duct angle
λ = bulk-temperature-gradient parameter [equation (9)]
μ = viscosity
ν = kinematic viscosity
ξ = transformed coordinate = y
ρ = density
σ = right-hand side of equation (8)
ϕ = dimensionless temperature

Subscripts

1 = refers to inlet
2 = refers to exit
$<>$ = refers to converging–diverging flow channel
$\|$ = refers to straight duct

periodic flow channel. It has been demonstrated that solutions for the periodically fully developed regime can be obtained without having to solve the entrance region problem [3]. This scheme will be included in the solution methodology that was developed earlier [2] for nonperiodic problems. Attention will now be directed to the conservation equations to be considered for converging–diverging flow channel with the assumption of a periodic fully developed regime.

Conservation Equations. The governing equations to be considered are the continuity, momentum, and energy equations. Constant thermophysical properties are assumed and natural convection is excluded. The following dimensionless variables are used:

$$X=x/L, \quad Y=y/L, \quad U=u/(\nu/L), \quad V=v/(\nu/L) \tag{2}$$

$$P=p'/\rho(\nu/L)^2, \quad \phi=(T-T_w)/(T_b-T_w),$$

$$B=\beta L/(\nu/L)^2 \tag{3}$$

where L and ν are the periodic cycle length and the kinematic viscosity, respectively. The pressure p is expressed by $p(x, y) = -\beta y + p'(x, y)$, where β is a constant, and $p'(x, y)$ behaves in a periodic manner from module to module. The term βy represents the nonperiodic pressure drop that takes place in the flow direction. Then, upon introduction of the dimensionless variables and parameters, the governing equations have the following forms:

$$\partial U/\partial X+\partial V/\partial Y=0 \tag{4}$$

$$U(\partial U/\partial X)+V(\partial U/\partial Y)=\partial^2 U/\partial X^2+\partial^2 U/\partial Y^2-\partial P/\partial X \tag{5}$$

$$U(\partial V/\partial X)+V(\partial V/\partial Y)=\partial^2 V/\partial X^2+\partial^2 V/\partial Y^2-\partial P/\partial Y+B \tag{6}$$

$$U(\partial\phi/\partial X)+V(\partial\phi/\partial Y)=(1/\mathrm{Pr})(\partial^2\phi/\partial X^2+\partial^2\phi/\partial Y^2)+\sigma/\mathrm{Pr} \tag{7}$$

with

$$\sigma=[2(\partial\phi/\partial Y)-\mathrm{Pr}V\phi]\lambda+\phi(\lambda^2+\partial\lambda/\partial Y) \tag{8}$$

and

$$\lambda=[d(T_b-T_w)/dY]/(T_b-T_w) \tag{9}$$

where σ and λ are periodic parameters arising from the assumptions of the constant wall temperature boundary condition. These values are determined as part of the solution process. Note, equations (5), (6), and (7) retain the streamwise second derivatives $\partial^2 U/\partial Y^2$, $\partial^2 V/\partial Y^2$, and $\partial^2\phi/\partial Y^2$ in recognition of the fact that large local values of these quantities may occur in the periodic fully developed flows. The aforementioned conservation equations have identical form to those for the nonperiodic case, except for the terms σ/Pr and B.

To complete the formulation of the problem in the physical domain, it remains to discuss the boundary conditions. These are $U = V = 0$ and $T = T_w$ on the wall boundaries and $\partial V/\partial X = \partial\phi/\partial X = 0$ and $U = 0$ on the symmetry boundaries. At the inlet and outlet ends of the solution domain, periodic conditions are imposed. These are the equality of U, V, ϕ, and P at the inlet and outlet boundaries.

Numerical Solution. The transformed equations and their complete discretization and solution for U, V, and ϕ (when the terms σ/pr and B are not present) are documented in an earlier paper [2]. The terms σ/pr and B are specified as extra source terms for the periodic example problem.

The main issue to be dealt with in this section is the specification of the width of the domain $\delta(Y)$, and its derivatives. The exact values of these quantities for $0 \le Y \le 1/2$ and $1 \ge Y \ge 1/2$ are, respectively, as follows:

$$\delta/L=H_{\min}/2L+Y\tan\theta \tag{10}$$

$$d\delta/dY=\tan\theta \tag{11}$$

$$d^2\delta/dY^2=d^3\delta/dY^3=0 \tag{12}$$

$$\delta/L=H_{\min}/2L+(1-Y)\tan\theta \tag{13}$$

$$d\delta/dY=-\tan\theta \tag{14}$$

$$d^2\delta/dY^2=d^3\delta/dY^3=0 \tag{15}$$

where $H_{\min}$ and L are the height at the minimum cross section of the converging–diverging channel and the periodic cycle length, respectively.

From an examination of the governing equations (4)–(7), it can be seen that there are two parameters whose values have to be specified prior to the initiation of the numerical solutions. These are the Prandtl number Pr, and dimensionless per-cycle pressure gradient B [equation (3)]. In this example, a value of 0.7 is selected for Pr, and the values chosen for B are selected in such a way that the calculated Reynolds numbers range from 100 to 1650. The involvement of the Reynolds and Prandtl numbers as parameters is a noteworthy difference between conventional fully developed laminar flows and periodic fully developed laminar flows. Aside from Pr and B, there are four geometric parameters which have to be specified. These are the maximum and minimum height of the flow channel $H_{\max}$ and $H_{\min}$, the duct angle θ, and the periodic cycle length L. Of these four quantities, only three are independent. If L, θ, and $H_{\min}$ are chosen and L is used as a reference length, then $H_{\min}/L$ and θ need to be specified as geometric parameters. The quantity $H_{\min}/L$ can also be expressed as a function of $H_{\max}/H_{\min}$ and θ. Therefore, the latter two quantities can also be used instead of the former two as the geometric parameters. The selected values of $H_{\max}/H_{\min}$ are 1.2, 1.5, and 2 and those for θ are 5, 10, and 15.

The computations were performed with (18 × 34) grid points. These grid points were distributed in a uniform manner over the solution domain in η and ξ coordinate directions. Each interior control volume contains one grid point, while the boundary adjacent control volume contains two grid points. Supplementary runs were performed with (26 × 50) grid points to investigate the grid size effect for the case of $H_{\max}/H_{\min} = 2$, $\theta = 15$. Three values of the dimensionless pressure gradient B were selected in such a way that the calculated Reynolds numbers range from 100 to 1000. The maximum change in the Reynolds and the cycle-averaged Nusselt numbers, respectively, between the coarse mesh (18 × 34) and the fine mesh (26 × 50) were within 7 and 4 percent at identical pressure gradients. The maximum change in the local temperature gradient at the wall, $\partial T/\partial\eta$, is within 10 percent. Thus, the coarse mesh (18 × 34) was chosen to maintain relatively moderate computing costs. Comparison of Nusselt number and pressure drop results was also made for the limiting case of $\theta = 0$ with the exact analytical results. They agreed to within 0.03 percent.

The discretized procedure of the transformed equations is based on the power-law scheme of Patankar [8]. The discretized equations are computed by using a line-by-line method. The pressure is computed by adopting the simple algorithm of Patankar [9].

Reynolds Number, Pressure Drop, and Nusselt Number. Attention will now be focused on the calculation of Reynolds number which will be defined as

$$\mathrm{Re}=2\dot{m}/\mu \tag{16}$$

where the mass flow $\dot{m}$ is given by

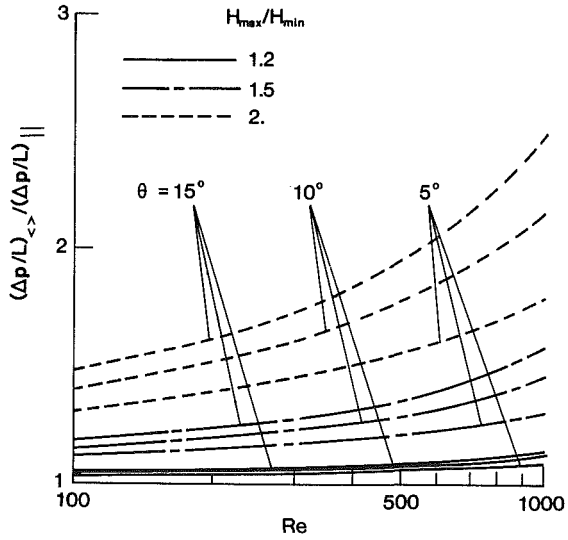

Fig. 3 Comparison of pressure drops for periodic and straight duct

$$Nu(4) = \cos\theta\left(\frac{1-\gamma}{1+\gamma}\right)\left[\frac{Re\ Pr}{2} - 2\int_0^{H_1/L}\left(\lambda\theta + \frac{\partial\theta}{\partial Y}\right) dX\right]\frac{H^*}{L}$$

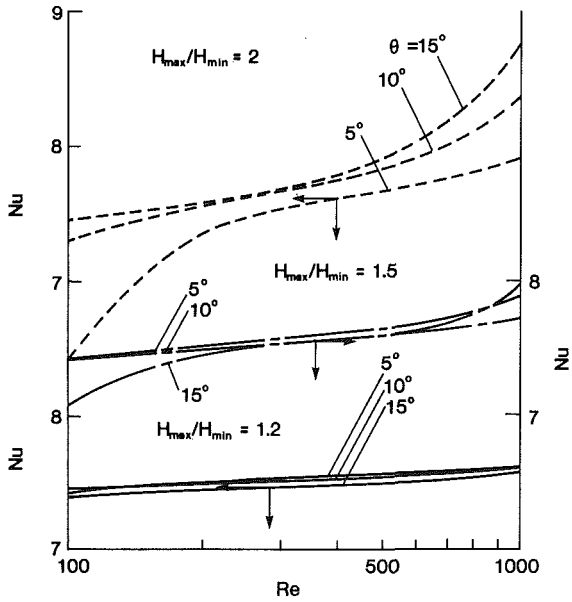

Fig. 4 Comparison of Nusselt number for periodic and straight duct

$$\dot{m} = 2\mu\int_0^{1/2(H_{min}/L)} V dX \tag{17}$$

Since the velocity V depends parametrically on the dimensionless parameter B, equation (16) gives a relationship between B and Re.

Another quantity of interest is the calculation of pressure drop. It is of practical interest to compare this quantity with the corresponding value obtained for the straight duct (plane Poiseuille flow). This ratio can be expressed as follows:

$$(\Delta P/L)_{<>}/(\Delta P/L)_{||} = [B/(48\ \mathrm{Re})][2H^*/L]^3 \tag{18}$$

where $<>$ and $||$ refer to the converging–diverging and straight duct, respectively, and H^* is an equivalent height which is expressed as

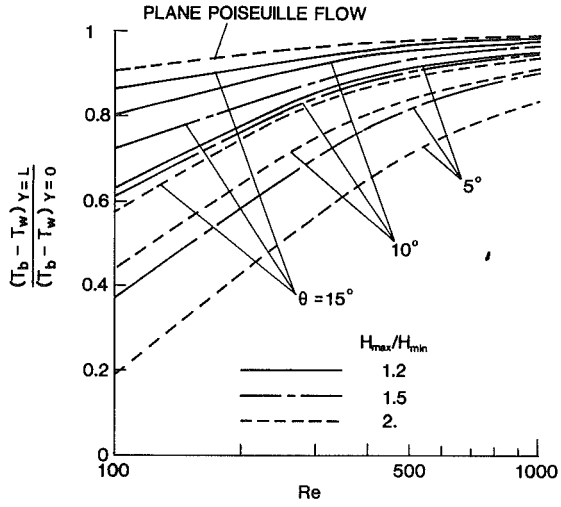

Fig. 5 Wall-to-bulk temperature ratio as a function of Re

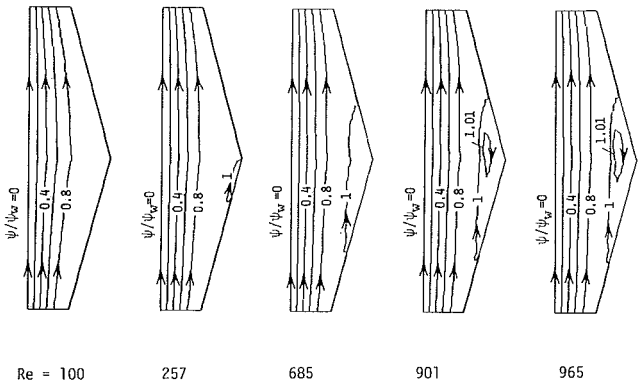

Fig. 6(a) Steamline diagrams for H_{max}/H_{min} = 2 and θ = 15 and Re as parameter

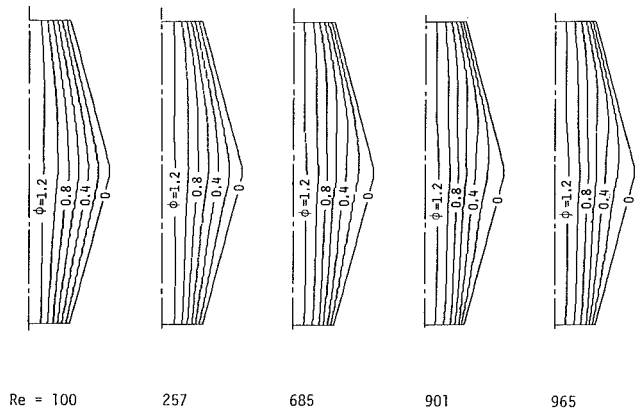

Fig. 6(b) Isotherm maps for H_{max}/H_{min} = 2 and θ = 15 and Re as parameter

$$H^* = 1/2(H_{min} + H_{max}) = \frac{\tan\theta}{2\left(\frac{H_{max}}{H_{min}} - 1\right)}\left(1 + \frac{H_{max}}{H_{min}}\right) \tag{19}$$

Finally, the cycle-averaged Nusselt number is obtained by

$$Nu = h(2H^*)/K \tag{20}$$

and

$$h = Q/A_w\overline{(T_w - T_b)} \tag{21}$$

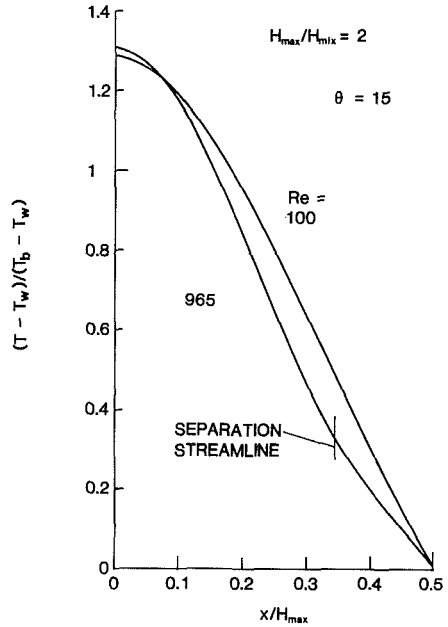

Fig. 7 Temperature profiles at the maximum cross section for Re = 100 and 965 (θ = 15 deg, H_{max}/H_{min} = 2)

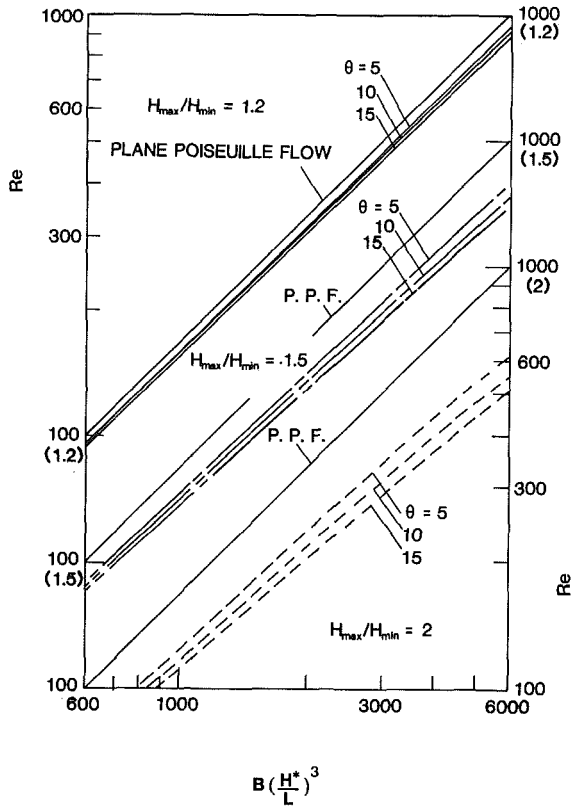

Fig. 8 Reynolds number as a function of dimensionless per-cycle pressure gradient

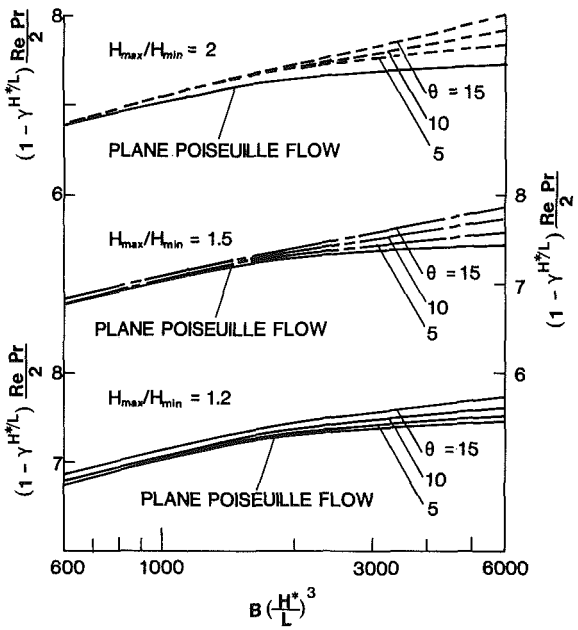

Fig. 9 Average heat transfer rate per cycle as a function of dimensionless per-cycle pressure gradient

where $A_w = 2L/\cos\theta$, Q is the rate of heat transfer from both walls to the fluid per cycle, and $\overline{T_w - T_b}$ is the average wall-to-bulk temperature difference. Both the log-mean and arithmetic-mean temperature differences are used to evaluate $\overline{T_w - T_b}$. Also the effect of the inclusion of axial conduction in per-cycle wall heat transfer Q is investigated. Four different expressions are derived for the calculation of the Nusselt number. Nu(1) and Nu(2) are obtained by assuming log-mean temperature difference, with and without inclusion of axial conduction in the term Q, respectively. Nu(3) and Nu(4) refer to the corresponding expressions by utilizing arithmetic-mean temperature difference. The four expressions used for the calculation of Nusselt number are as follows:

$$\mathrm{Nu}(1) = -\cos\theta\left(\int \lambda dY\right)(H^*/L)\,(\mathrm{RePr}/2) \tag{22}$$

$$\mathrm{Nu}(2) = -\cos\theta\left(\int \lambda dY\right)(H^*/L)\left[(\mathrm{RePr}/2) - 2\int_0^{1/2(H_{\min}/L)} (\lambda\phi + \partial\phi/\partial Y)dX\right] \tag{23}$$

$$\mathrm{Nu}(3) = 2\cos\theta[(1-\gamma)/(1+\gamma)](H^*/L)\,(\mathrm{RePr}/2) \tag{24}$$

$$\mathrm{Nu}(4) = 2\cos\theta[(1-\gamma)/(1+\gamma)](H^*/L)\,(\mathrm{RePr}/2) - 2\int_0^{1/2(H_{\min}/L)} (\lambda\phi + \partial\phi/\partial Y)dX \tag{25}$$

Interested readers may refer to [7] for the derivation of Nu(1) and Nu(2) where arithmetic-mean temperature difference approximation is used. The term γ is wall-to-bulk temperature ratio $(T_w - T_b)_2/(T_w - T_b)_1 = \exp(\int \lambda dY)$.

Results and Discussion

Representative results for the pressure drop ratios are plotted as a function of Reynolds number in Fig. 3 with θ and $H_{\max}/H_{\min}$ as curve parameters. These ratios are determined numerically by dividing Δp for the converging–diverging flow channel to the corresponding values for a straight duct (plane Poiseuille flow), whose equivalent height is H^* [equation (18)]. The mass flow $\dot{m}$ for the converging–diverging channel and straight duct is the same. Therefore, the Reynolds number is the same for the two geometries. The pressure drop ratios are greater than one as is expected and increase with the increase of the duct angle. Furthermore, at larger angles, the effect of $H_{\max}/H_{\min}$ and Re on pressure ratio is accentuated.

Results for the periodic fully developed Nusselt number, as

Table 1 Fully developed per-cycle Nusselt number, pressure drop ratios, and wall-to-bulk temperature ratios as a function of the geometric and flow parameters

$\frac{H_{max}}{H_{min}}$	θ	Re	B	$\frac{(\Delta p/L)_{<>}}{(\Delta p/L)_{\parallel}}$	$\frac{H^*}{L}$	$\int \lambda\, dY$	$Nu_{(1)}$	$Nu_{(2)}$	$Nu_{(3)}$	$Nu_{(4)}$	$\frac{(T_w-T_b)_2}{(T_w-T_b)_1}$
1.2	5.	90.24	5000.	1.029	0.4812	-0.4953	7.499	7.544	7.349	7.393	0.6094
1.2	5.	354.2	20000.	1.049		-0.1269	7.542	7.547	7.532	7.536	0.8808
1.2	5.	999.6	58880.	1.094		-0.04536	7.607	7.609	7.606	7.607	0.9557
1.2	5.	1635.	100000.	1.136		-0.02815	7.720	7.720	7.719	7.720	0.9722
1.2	10.	101.9	700.	1.044	0.9698	-0.2193	7.470	7.488	7.440	7.458	0.8031
1.2	10.	397.7	2800.	1.070		-0.05655	7.517	7.518	7.515	7.516	0.9450
1.2	10.	998.6	7440.	1.133		-0.02279	7.606	7.607	7.606	7.606	0.9775
1.2	10.	1489.	12000.	1.225		-0.01553	7.729	7.729	7.729	7.729	0.9846
1.2	15.	100.8	198.7	1.052	1.474	-0.1476	7.412	7.406	7.398	7.393	0.8628
1.2	15.	491.0	1000.	1.087		-0.03062	7.490	7.487	7.489	7.487	0.9699
1.2	15.	931.1	1987.	1.139		-0.01629	7.557	7.556	7.556	7.556	0.9838
1.5	5.	100.2	64200.	1.117	0.2187	-0.9909	7.571	7.615	7.007	7.047	0.3712
1.5	5.	138.9	90000.	1.130		-0.7157	7.581	7.606	7.273	7.297	0.4888
1.5	5.	197.7	130000.	1.146		-0.5030	7.585	7.599	7.429	7.443	0.6047
1.5	5.	435.1	300000.	1.202		-0.2291	7.602	7.607	7.569	7.573	0.7953
1.5	5.	819.2	600000.	1.277		-0.1228	7.673	7.675	7.663	7.665	0.8844
1.5	5.	998.0	750000.	1.310		-0.1014	7.721	7.722	7.714	7.716	0.9035
1.5	10.	100.3	8090.	1.151	0.4408	-0.4935	7.521	7.560	7.372	7.410	0.6105
1.5	10.	445.2	40000.	1.283		-0.1124	7.604	7.609	7.596	7.601	0.8937
1.5	10.	820.3	80900.	1.408		-0.06242	7.780	7.782	7.777	7.779	0.9395
1.5	10.	976.8	100000.	1.461		-0.05308	7.878	7.880	7.876	7.878	0.9483
1.5	15.	100.2	2360.	1.180	0.6699	-0.3284	7.454	7.480	7.387	7.413	0.7201
1.5	15.	449.0	12000.	1.339		-0.07442	7.567	7.571	7.563	7.567	0.9283
1.5	15.	791.9	23600.	1.493		-0.04334	7.773	7.775	7.772	7.774	0.9576
1.5	15.	957.6	30000.	1.570		-0.03644	7.903	7.904	7.902	7.904	0.9642
2.0	5.	96.09	337500.	1.322	0.1312	-1.762	7.747	7.795	6.216	6.255	0.1717
2.0	5.	164.8	600000.	1.370		-1.027	7.739	7.759	7.124	7.142	0.3582
2.0	5.	419.9	1700000.	1.523		-0.4023	7.730	7.735	7.628	7.633	0.6688
2.0	5.	753.6	3375000.	1.686		-0.2270	7.826	7.828	7.792	7.795	0.7970
2.0	5.	1039.	5000000.	1.811		-0.1674	7.959	7.960	7.940	7.942	0.8459
2.0	10.	100.4	45800.	1.407	0.2645	-0.08378	7.670	7.718	7.250	7.296	0.4327
2.0	10.	266.7	137000.	1.584		-0.03164	7.693	7.704	7.629	7.641	0.7287
2.0	10.	720.7	458000.	1.960		-0.1225	8.049	8.052	8.038	8.042	0.8847
2.0	10.	924.9	635000.	2.117		-0.09835	8.293	8.296	8.286	8.289	0.9063
2.0	10.	994.4	700000.	2.171		-0.09249	8.385	8.384	8.379	8.381	0.9117
2.0	15.	99.91	13660.	1.479	0.4019	-0.5590	7.589	7.634	7.397	7.442	0.5718
2.0	15.	256.9	40000.	1.685		-0.2191	7.649	7.662	7.619	7.632	0.8032
2.0	15.	684.9	136600.	2.158		-0.08775	8.166	8.171	8.161	8.166	0.9160
2.0	15.	901.0	199400.	2.394		-0.06985	8.551	8.555	8.548	8.551	0.9325
2.0	15.	965.2	220000.	2.466		-0.06616	8.677	8.680	8.674	8.677	0.9360
2.0	15.	1523.	440000.	3.126		-0.04806	9.945	9.947	9.943	9.946	0.9531

a function of the Reynolds number, are plotted in Fig. 4 with θ and H_{max}/H_{min} as curve parameters. The Nusselt number is determined using equation (25), where arithmetic-mean temperature difference is used and axial conduction is included in the per-cycle wall heat transfer Q. It is useful to note that the value for Nusselt number for the fully developed straight duct is 7.54 and is independent of both the Reynolds and Prandtl numbers. The periodic fully developed Nusselt number is greater than or less than 7.54, depending on the value of H_{max}/H_{min}, θ, and Reynolds number. The trends are that at higher Reynolds number the periodic fully developed Nusselt number is higher, and at lower Reynolds number, it is lower than the corresponding fully developed values.

In Fig. 5, wall-to-bulk temperature ratio, $(T_b - T_w)_2/(T_b - T_w)_1$, is plotted as a function of Re, with θ and H_{max}/H_{min} as curve parameters. This figure shows that this ratio is smaller than 1 as expected and approaches 1 at higher Reynolds numbers. The magnitude of $(T_b - T_w)_2/(T_b - T_w)_1$ is markedly affected by H_{max}/H_{min} and θ. It is noteworthy that all the curves approach the plane Poiseuille flow at higher values of both H_{max}/H_{min} and θ.

Representative streamline and isotherm maps obtained from the solutions based on the present methodology are presented in Figs. 6(*a*) and 6(*b*). These figures are for $H_{max}/H_{min} = 2.0$ and $\theta = 5$, and in the Reynolds number range from 99 to 965. Each streamline diagram extends over the axial length of one cycle. As seen from Fig. 6(*a*), the separation bubble increases in length with Reynolds number as expected. The core flow is relatively straight and parallel. Figure 6(*b*) shows that the isotherms are relatively independent of Reynolds number.

In Fig. 7, the dimensionless temperature profiles are displayed with θ and H_{max}/H_{min} as curve parameters and for two values of the Reynolds number. These profiles are plotted at the location of maximum cross section where the effect of separation is pronounced. It can be seen from this figure that the effect of separation occurs at higher Reynolds number. The mark on the Re = 965 profile indicates the position of the separation streamline.

Results of the comparison of mass flow rate or Reynolds number as a function of the dimensionless per-cycle pressure gradient are plotted in Fig. 8 with θ and H_{max}/H_{min} as curve parameters. It is seen from this figure that the mass flow rates for the converging–diverging flow channel are lower than those of the plane Poiseuille flow duct under the same average pressure gradient and channel height H^*. Furthermore, at larger values of H_{max}/H_{min}, the effect is accentuated.

The average heat transfer rate per cycle between $y = 0$ and $y = L$ can be expressed as $(1-\gamma^{H^*/L})\mathrm{RePr}/2$. In Fig. 9, this quantity is plotted as a function of the dimensionless per-cycle pressure gradient with θ and H_{max}/H_{min} as curve parameters. This figure shows higher values of average heat transfer rate per cycle for converging–diverging flow channel under the same average pressure gradient and channel height.

The fully developed per-cycle Nusselt number results are calculated by four different expressions and are presented in Table 1. This table also includes the results for the pressure drop ratios $(\Delta p/L)_{<>}/(\Delta p/L)_{\parallel}$ and the wall-to-bulk temperature difference ratios. The parameters Re, θ, H_{max}/H_{min} are varied as shown in Table 1, and Pr is fixed at 0.7. It is seen from this table that the ratio $(\Delta p/L)_{<>}/(\Delta p/L)_{\parallel}$ is always greater than one as expected and increases with θ, H_{max}/H_{min}, and Reynolds number.

The four different values of Nu are tabulated in this table. These values are calculated from equations (22)–(25). It is noteworthy that inclusion of the axial conduction in the term Q, does not affect the results. However, the Nusselt number results are affected by the approximation of wall-to-bulk temperature difference using arithmetic and log-mean temperature difference.

Concluding Remarks

A nonorthogonal coordinate transformation was utilized that mapped the irregular solution domain of a converging–diverging flow channel onto a rectangle. Also, the concept of periodic fully developed regime was used to determine the heat transfer, pressure drop, and fluid flow patterns without having to solve the entrance region problem. Representative results were carried out for laminar flow and for various geometric and flow parameters. Moderate enhancement in the Nusselt number results occurred at high values of Reynolds number with a pressure drop penalty when compared with the corresponding values for a straight duct.

Acknowledgments

The authors would like to acknowledge useful discussions with Professor E. M. Sparrow and Professor A. T. Prata.

References

1 Hsu, C.-F., "A Curvilinear-Coordinate Method for Momentum, Heat and Mass Transfer in Domains of Irregular Geometry," Ph.D. Thesis, Department of Mechanical Engineering, University of Minnesota, 1981.

2 Faghri, M., Sparrow, E. M., and Prata, A. T., "Finite Difference Solutions of Convention-Diffusion Problems in Irregular Domains Using a Nonorthogonal Coordinate Transformation," *Numerical Heat Transfer*, Vol. 7, 1984, pp. 183–209.

3 Patankar, S. V., Liu, C. H., and Sparrow, E. M., "Fully-Developed Flow and Heat Transfer in Ducts Having Streamwise-Periodic Variation of Cross-Sectional Area," ASME JOURNAL OF HEAT TRANSFER, Vol. 99, 1977, pp. 180–186.

4 O'Brien, J. E., and Sparrow, E. M., "Corrugated Duct Heat Transfer, Pressure Drop, and Flow Visualization," ASME JOURNAL OF HEAT TRANSFER, Vol. 104, 1982, pp. 410–416.

5 Souza Mendes, P., "Effects of Periodic, Tapered Enlargement and Contractions on Turbulent Heat Transfer and Fluid Flow in a Circular Duct," Ph.D. Thesis, Department of Mechanical Engineering, University of Minnesota, 1982.

6 Souza Mendes, P., and Sparrow, E. M., "Periodically Converging–Diverging Tubes and Their Turbulent Heat Transfer, Pressure Drop, Fluid Flow, and Enhancement Characteristics," ASME JOURNAL OF HEAT TRANSFER, Vol. 106, 1984, pp. 55–63.

7 Sparrow, E. M., and Prata, A. T., "Numerical Solutions for Laminar Flow and Heat Transfer in a Periodically Converging–Diverging Tube, With Experimental Confirmation," *Numerical Heat Transfer*, Vol. 6, 1983, pp. 441–461.

8 Patankar, S. V., *Numerical Heat Transfer and Fluid Flow*, McGraw-Hill, New York, 1980.

9 Patankar, S. V., "A Calculation Procedure for Two-Dimensional Elliptic Situations," *Numerical Heat Transfer*, Vol. 4, 1981, pp. 409–425.

Heat Transfer to Turbulent Swirling Flow Through a Sudden Axisymmetric Expansion

P. A. Dellenback
D. E. Metzger
G. P. Neitzel

Arizona State University,
Tempe, AZ 85287

Experimental data are presented for local heat transfer rates in the tube downstream of an abrupt 2:1 expansion. Water, with a nominal inlet Prandtl number of 6, was used as the working fluid. In the upstream tube, the Reynolds number was varied from 30,000 to 100,000 and the swirl number was varied from zero to 1.2. A uniform wall heat flux boundary condition was employed, which resulted in wall-to-bulk fluid temperatures ranging from 14°C to 50°C. Plots of local Nusselt numbers show a sharply peaked behavior at the point of maximum heat transfer, with increasing swirl greatly exaggerating the peaking. As swirl incressed from zero to its maximum value, the location of peak Nusselt numbers was observed to shift from 8.0 to 1.5 step heights downstream of the expansion. This upstream movement of the maximum Nusselt number was accompanied by an increase in its magnitude from 3 to 9.5 times larger than fully developed tube flow values. For all cases, the location of maximum heat transfer occurred upstream of the flow reattachment point.

Introduction

Turbulent swirling flow through an abrupt axisymmetric expansion is a complex flow possessing several distinctly different flow regimes, either one or two recirculation regions, extremely high levels of turbulence, and periodic asymmetries under some conditions. An accompanying elevation of heat transfer rates is a principal motivation for application of these flow configurations in dump combustors of gas turbine engines and in solid fuel ramjet combustors. These applications also take advantage of the flow recirculation regions for flameholding, and of the high mixing rates for enhanced combustion efficiency.

Without swirl, flow through a sudden expansion produces mixing rates, and subsequently, heat transfer coefficients which are substantially higher downstream of the expansion than those which would be obtained at the same Reynolds number in the entrance region of a pipe. This enhancement in diffusion rates occurs in spite of a recirculation region extending about nine step heights downstream from the expansion. In this recirculation region, mean velocities are typically only 10 percent as high as those found in the core flow, suggesting that the principle mechanism for heat transfer augmentation is the high turbulence levels which are present. In fact, very high levels of turbulent kinetic energy are generated by shearing as the core flow issues into the larger pipe. Because length scales are large in the shear layer, the turbulent kinetic energy generated there dissipates relatively slowly, maintaining much larger levels than would be found in ordinary pipe flow where no such internal shear layer exists. With high levels of turbulence kinetic energy, diffusion rates are elevated and the thickness of the viscosity-dominated sublayer is reduced, resulting in high rates of heat transfer between the tube wall and mean flow.

Several interesting effects appear in the flow field with the introduction of swirl (Gupta et al., 1984). Among these is an increase in growth rate, entrainment, and decay of the core flow just downstream of the expansion. Consequently, the flow reattachment zone moves upstream as swirl strength is increased. Swirl is also responsible for increased shear rates, greater turbulence production, and longer path lengths for a particular fluid particle so that the effect of swirl, like the effect of the sudden expansion, is also to increase heat transfer rates significantly over those found in purely axial pipe flow (Hay and West, 1975).

A further complex phenomenon which frequently occurs in swirling flow is the development of an unsteady (although usually periodic) asymmetry in the flowfield. These asymmetries are not fully understood, but it is known that they may assume many different forms depending on flow geometry and swirl strength (Dellenback, 1986; Leibovich, 1984; Hallett and Gunther, 1984). At low swirl levels in the present study, the core flow departed from axial symmetry in the neighborhood of the expansion and then proceeded to precess about the tube center line (Dellenback). This flow feature is referred to here as the precessing vortex core (PVC) after Gupta et al. (1984). In most geometries the PVC is only seen for swirl strengths large enough to produce a "bubble" of on-axis recirculating fluid, known as vortex breakdown. However, in the present investigation (and in the work of Hallett and Gunther), oscillatory flow asymmetries were only detected at swirl numbers less than those associated with vortex breakdown. Specifically, the PVC was only present at the lowest nonzero swirl number for each of the three Reynolds numbers examined in this study. Flowfields at higher swirl numbers were symmetric with no apparent PVC (Dellenback).

Present computational capabilities are only able to treat successfully some of the simpler limiting cases of the present problem (Sultanian et al., 1985). Thus the purpose of the present investigation was to measure heat transfer characteristics throughout the separation, reattachment, and redevelopment regions in the downstream tube for a variety of flow conditions.

The present study began with an extensive characterization of the turbulent flowfield throughout the downstream tube and at two locations upstream of the expansion. A laser-Doppler anemometer (LDA) was used to determine axial and tangential mean velocities in conjunction with the two associated normal stresses for nine of the twelve flow conditions reported herein. Upstream profiles for the other three cases were measured so that the present heat transfer data could be correlated with swirl number. Because the swirl

Contributed by the Heat Transfer Division for publication in the JOURNAL OF HEAT TRANSFER. Manuscript received by the Heat Transfer Division February 13, 1986.

number was determined from integration of velocity profiles, it was essentially a dependent variable in these experiments and this accounts for its variability between Reynolds numbers in the following data. Only a summary of the mean velocity field is included in the present paper because of space limitations. Tabular data and additional details, including PVC observations, are described by Dellenback (1986).

Previous Investigations

A number of experiments have been reported which examine heat transfer to purely axial flows through a sudden pipe expansion (Ede et al., 1956; Ede et al., 1962; Krall and Sparrow, 1966; Zemanick and Dougall, 1970; Baughn et al., 1984). However, there have apparently been no heat transfer investigations that incorporated swirl in the sudden expansion geometry. Thus the prior unswirled investigations are important to the present study as a limiting case which can be compared in the present data. Important conclusions from the extensive measurements of Krall and Sparrow (1966) and Zemanick and Dougall (1970) can be summarized as follows:

(*a*) Nu/Nu_{fd} is a weak function of Reynolds number for air, but is a strong function of Reynolds number for water.
(*b*) Maximum Nusselt numbers are well correlated by $Nu_m = C\,Re_d^{2/3}$, where $C = 0.20$ for air and 0.40 for water.
(*c*) Locations of peak Nusselt numbers move slightly upstream with increasing expansion ratio, but show little dependence on Reynolds number.

Recently, Baughn et al. (1984) reported an extension to Zemanick and Dougall's (1970) work. In previous experiments, the region just downstream of the expansion has been subject to relatively high rates of heat conduction in the tube wall with consequently high uncertainty in the heat transfer coefficients. Baughn et al. (1984) devised a test section specifically to minimize the axial conduction problem, thus defeating an effect which they suggest introduced error into Zemanick and Dougall's data. For several expansion ratios, a minimum in the Nusselt number was observed at about one step height downstream and the authors suggest that this is possible evidence for a very small, counterrotating corner eddy.

Habib and McEligot (1982) reported an ambitious calculation of the flowfield and related heat transfer behavior for the present problem, including swirl. Their published results appear to underpredict the peak Nusselt number which is interpolated from the data of Zemanick and Dougall (1970) by about 50 percent for an unswirled flow with Re = 50,000, $D_z/D = 2.0$, and Pr = 0.7. However, they did find the reattachment zone for unswirled flow to be centered at a generally accepted value of 8.2 step heights, while the corresponding location of peak Nusselt number occurred at 6.5 step heights.

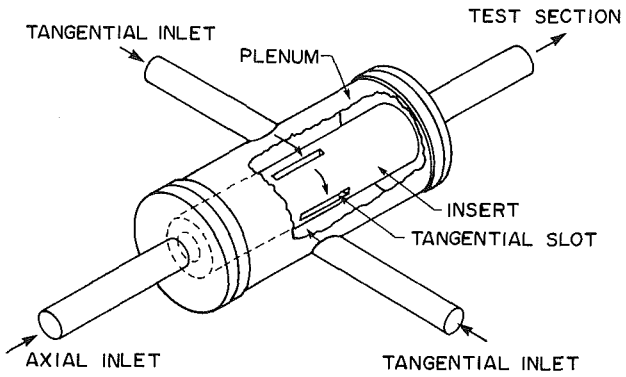

Fig. 1 Detail of the swirl generator

Experimental Apparatus

A stainless steel water flow loop comprised the main element of the test facility. Swirl was generated by tangential slots as shown in Fig. 1. Inside diameters of the axial inlet tube, the swirler insert, and the upstream test section were 5.08 cm. The sudden expansion was 12 diameters downstream of the swirl generator and the axial inlet tube was 31 diameters long to allow axial flow development. Flow rates to the slots and the axial inlet tube could be controlled independently, thus giving capability for a continuously variable swirl strength. Flow rates of the tap water used in the loop were measured with turbine-type flowmeters. The flow loop included an on-line deaerator for removing air which tended to leave solution as a result of elevated water temperatures near the tube wall.

The axial and tangential components of mean and rms velocities were measured, one at a time, with a single-component LDA. The profiles were taken at locations both upstream and downstream of the expansion using plexiglass test sections. Details of the optical system, data analysis, and procedures are described by Dellenback (1986).

Following the flow-field measurements, heat transfer tests were performed in a horizontal stainless steel tube by passing direct current in the tube wall. The steel heat transfer test sec-

Nomenclature

D = diameter of upstream tube
D_2 = diameter of downstream tube
h = local heat transfer coefficient
H = step height = $(D_2 - D)/2$
I = current in tube wall
k = thermal conductivity of water
$\dot{m}$ = mass flow rate
Nu = Nusselt number
Nu_{fd} = fully developed Nusselt number for turbulent pipe flow represented by Dittus-Boelter or Sieder-Tate equations
Nu_m = maximum or peak Nusselt number
q = local heat flux
Q = total heat input
r = radial position relative to tube centerline
R = resistance of tube wall
Re = Reynolds number in upstream tube = $\bar{U}d/\nu$
R_1 = upstream tube inside radius
S = swirl number in upstream tube as defined by

$$S = \frac{1}{R_1}\frac{\int_0^R r^2 UV dr}{\int_0^R rU^2 dr}$$

T_b = bulk fluid temperature
T_o = outside tube wall temperature
T_w = inside tube wall temperature
U = local mean axial velocity
$\bar{U}$ = axial velocity in upstream tube averaged over cross section
U_1 = maximum axial velocity in upstream tube
V = local mean tangential velocity
x = axial distance from expansion face
x_r = reattachment length
$(x/H)_{Nu_m}$ = axial location of peak Nusselt number

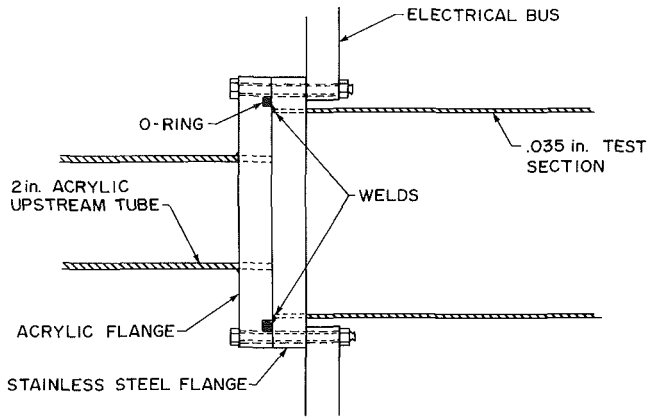

Fig. 2 Detail of the test section near the expansion

tion was of the same dimensions as the acrylic test section used for the velocity measurements. Heating began at, but did not include, the face of the sudden expansion, as shown in Fig. 2. The unheated upstream tube (inside diameter 5.08 cm) and the expansion face were the same plexiglass components used in the flowfield measurements. The tube downstream of the expansion was a commercially available stainless steel tube with an inside diameter of 9.98 cm, a wall thickness of 0.89 mm, and length of 1.04 m. Consequently, the expansion ratio was 1.97:1. Stainless steel flanges were carefully attached to each end of the tube by very shallow welds at the extreme ends of the tube. Although the flange-to-tube fit was snug, it was assumed that all of the electrical current passed through the weld and thus power was dissipated over the full 1.04-m length of the tube. This assumption was important to the computation of heat flux and to determining the location of the point of maximum heat transfer since the flanges were relatively thick at 1.27 cm or 0.5 step heights.

Conduction losses from the heated test section to the upstream tube and expansion face were minimal since the thermal conductivity of plexiglass is relatively low. Heat transfer to the mixing plenum immediately downstream of the test section was minimized by a 1.27-cm-thick spacer made from a machinable dielectric (Melamine) which was placed between the test section's flange and the plenum. Finally, nylon bolts were used to secure the test section to the plenum to further minimize conduction heat losses.

Copper electrical busses consisting of an inner ring and an outer ring connected by six spokes were machined from a single plate 1.27 cm thick. The busses joined current carrying cables to the stainless steel flanges of the test section. Experience showed that a liberally applied film of copper-based antiseize compound between the bus and flange would decrease electrical contact resistance and consequent heat generation. A dedicated 108-kW direct current power supply was coupled via seven 2.5-cm-diameter cables to the outer rims of each bus. Two water-carrying copper tubes were soldered around the periphery of the busses' outer rims for the purpose of guard heating or cooling. Each bus had two pairs of thermocouples imbedded in such a way that temperature gradients across the spokes could be monitored. Due to the large power levels employed in these experiments (22 kW at 8.5 V and 2600 A), ohmic heating in the cables proved to be the dominant heat source in the power connection scheme. Hence, guard cooling was always performed to minimize temperature gradients in the spokes of the bus and heat conduction from the cables to the bus, and in turn, to the heat section.

The tube-wall temperature distributions were measured with commercially available copper-constantan thermocouples mounted on the outside of the tube. The junction of each thermocouple was sandwiched between two 51-μm-thick glass-reinforced polymer-laminate films to provide electrical insulation from the test section. A high-thermal-conductivity paste was applied between the thermocouples and the test section. Flat, well-insulated steel bands encircling the test section held the thermocouples tightly in place. Nineteen thermocouples were employed, spaced at smaller intervals near the upstream end of the test section to provide high resolution in the region of rapidly changing heat transfer coefficients. Four inches of fiberglass insulation surrounded the test section and flanges, and all but the outer rim of the electrical busses.

Power input levels to the working fluid were deduced in two ways. In the first, power was taken as the current–voltage product after measuring the voltage drop across both a shunt and the test section. A thermocouple was affixed to the copper shunt to correct for temperature-dependent resistivity. Input power was also determined from the measured fluid enthalpy rise through the test section. To this end, bulk fluid temperature were measured at the inlet and outlet of the test section with immersion thermocouples. Over the range of test conditions, wall-to-bulk fluid temperatures ranged from 14°C to 50°C.

Procedures and Data Reduction

The 22 kW power levels produced heat fluxes on the order of 6.7 W/cm^2. After applying power to the test section, the time required for the loop to reach steady state was between 30 and 60 min.

For most trials, the wall-temperature measuring thermocouples were located along the top of the tube. However, in order to examine the influence of natural convection on the present problem, for at least one of the multiple trials at each flow condition the entire test section (with thermocouples still attached) was removed, rotated 180 deg about the tube axis, and reinstalled so that the temperature measurements could be made along the bottom of the tube.

Local heat transfer results are presented in terms of Nusselt numbers normalized with those for fully developed nonswirling flow, where

$$\mathrm{Nu} = \frac{hD_2}{k} \tag{1}$$

Here, D_2 is the downstream tube diameter, k is the thermal conductivity of water evaluated at the local film temperature, and h is the local heat transfer coefficient defined as

$$h = \frac{q}{T_w - T_b} \tag{2}$$

The local heat flux is designated by q, the local wall temperature by T_w, and the local bulk temperature by T_b. Because wall-to-bulk fluid temperature differences were moderate to large, and hence property variations appreciable, the Sieder–Tate correlation (Kern, 1950) was used to evaluate reference Nusselt numbers for the corresponding fully developed flow without swirl

$$\mathrm{Nu}_{fd} = 0.027\ \mathrm{Re}^{0.8}\ \mathrm{Pr}^{1/3}(\mu/\mu_w)^{0.14} \tag{3}$$

All fluid properties used in equation (3) were evaluated at the local bulk temperature except μ_w, which was evaluated at the local wall temperature.

Although the present experiments had a nominally uniform heat flux boundary condition, the local heat fluxes were not strictly uniform due to both the temperature dependence of tube material properties and axial heat conduction in the tube wall. The procedure used for finding the local heat fluxes began by dividing the wall into 19 control volumes corresponding to the 19 wall-temperature thermocouples. The magnitude of Joule heating in each volume was determined from I^2R, where a linear curve fit of the temperature-dependent resistivity of the stainless steel (Touloukian, 1967)

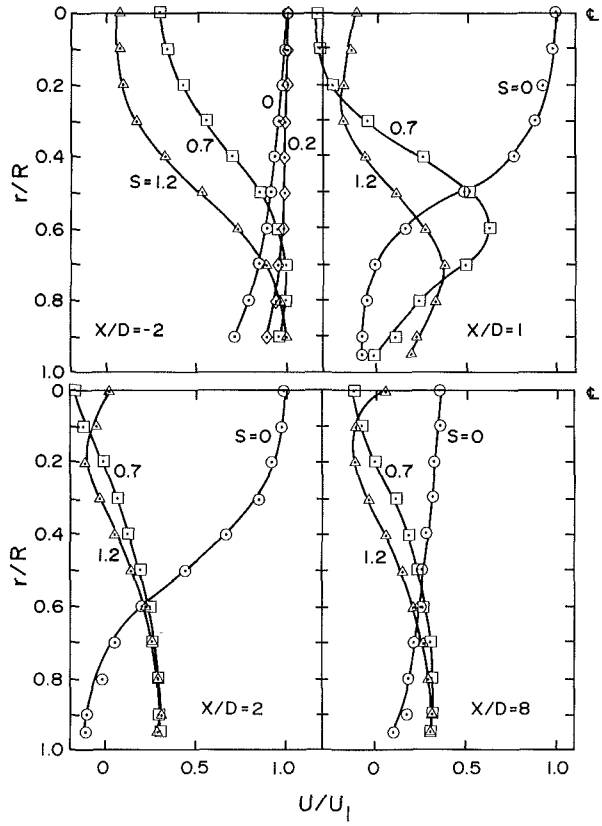

Fig. 3 Axial velocity profiles for Re = 100,000

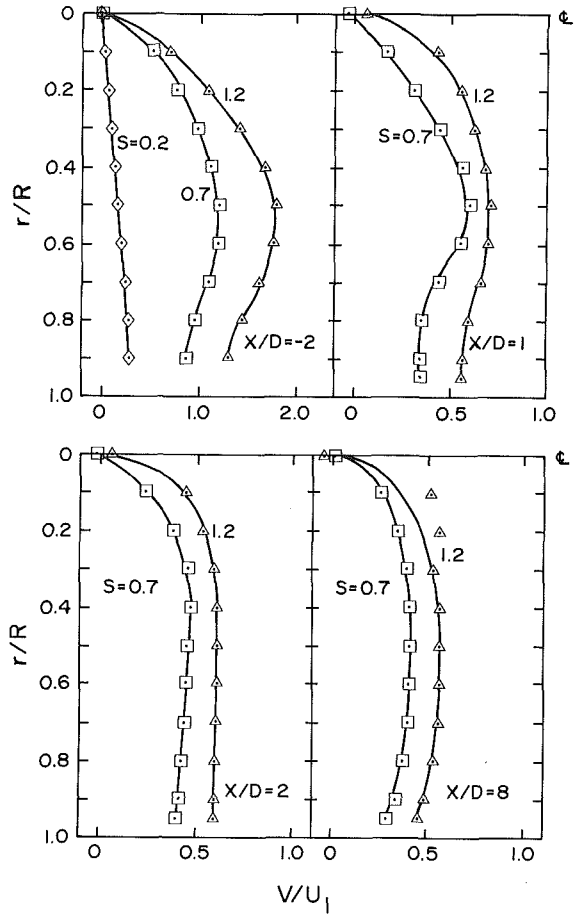

Fig. 4 Tangential velocity profiles for Re = 100,000

test section was used. Heat loss from the outside of the tube wall through the fiberglass insulation which surrounded the test section was assumed negligible. This loss was eventually calculated to be no more than 0.05 percent of the total power input in a worst case analysis of the data. The wall temperature (T_w) in equation (2) is the temperature of the inside surface of the test section wall. Because exterior surface temperatures were actually measured, the interior surface temperatures were determined from the solution of the one-dimensional heat conduction equation for a cylindrical shell. This procedure assumes that only radial conduction is important, an assumption that must be justified since natural convection may cause slight asymmetry in circumferential temperature profiles. Also, the axial variation in heat transfer coefficients gives rise to axial temperature gradients and conduction in the tube wall. However, both circumferential (discussed below) and axial temperature gradients were examined and found to be small compared to those in the radial direction. A worst case computation of axial heat flux for the present results showed that, at most, the net heat conducted out of a tube wall element to an adjacent element was about 1 percent of the Joule heat generated in that element, even near the test section flanges.

Determining the local heat flux and inside wall temperature is inherently an iterative process, but one which converges suitably in one iteration because the temperature differences across the tube wall are small (typically on the order of 2°C). The maximum variation in local heat flux between any two locations on the tube was eventually calculated to be less than 1.5 percent. Finally, to be consistent in methodology, local water enthalpies and bulk temperatures were computed from any energy balance which considered the local, slightly nonuniform, heat input.

The methods of Kline and McClintock (1953) were employed to determine that the largest uncertainties are about 2 percent in upstream Reynolds number and 8 percent in swirl number. The highest uncertainties in Nusselt numbers were computed to be about 9 percent, with these occurring near the location of peak Nusselt number where wall-to-bulk temperature differences were smallest. Details of the analysis and tabular data are given in the dissertation by Dellenback (1986).

Results and Discussion

In the figures which follow, the axial coordinate is nondimensionalized with the upstream tube diameter D. The swirl numbers shown on the plots were evaluated from velocity profiles measured two diameters upstream of the expansion. Similary, Reynolds numbers are based on properties and mean velocities in the upstream tube.

Summary of the Flowfield. Figures 3 and 4 show typical mean velocity profiles for various swirl levels at Re = 100,000. All mean velocities (and the turbulence intensities referred to below) were normalized using the maximum axial velocity in the upstream tube. Data for unswirled flows agreed very well with the recent LDA data of Stevenson et al. (1983), but flow predictions of Habib and McEligot (1982) for strongly swirled flows are in only fair agreement as to locations of peak velocities near the expansion and extents of recirculation regions.

Flow conditions upstream of the expansion varied greatly with swirl number. Upstream velocity profiles for the lowest swirl case at each Reynolds number closely approximated solid body rotation plug flow. Figure 3 shows that with increasing swirl number the highest axial velocities move toward the tube wall. Near the tube center line, large gradients in the mean tangential velocity are responsible for turbulence intensities on the order of 30 percent. Turbulence diffuses away from the tube axis with both the axial and tangential turbulence inten-

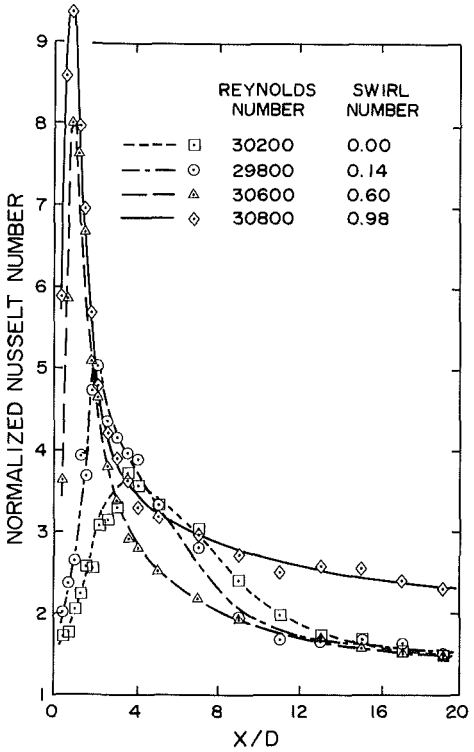

Fig. 5 Local heat transfer results; Re = 30,000

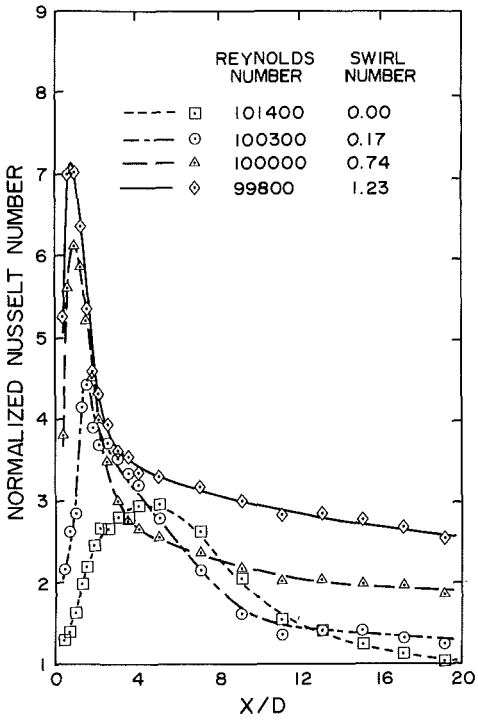

Fig. 6 Local heat transfer results; Re = 60,000

sities decreasing rapidly to about 12 percent between r/R = 0.2 and the wall.

Prandtl numbers of the fluid entering the heated test section were 5.1 at Re = 100,000; 5.8 at Re = 60,000; and from 5.9 to 6.7 for Re = 30,000. This variation in Prandtl number is probably insignificant when examining the present results, as suggested by the near congruence of Krall and Sparrow's (1966) data for Prandtl numbers of 3 and 6.

Axial Heat Transfer Variations. Figures 5–7 show the measured axial variations in normalized Nusselt number as a

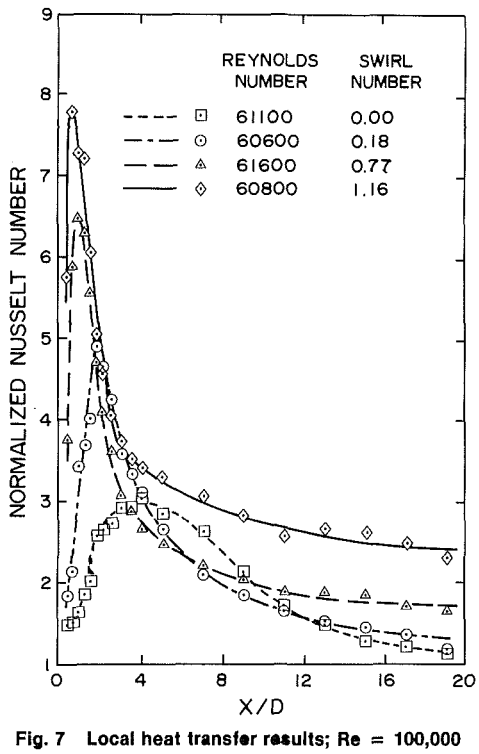

Fig. 7 Local heat transfer results; Re = 100,000

function of swirl for nominal Reynolds numbers of 30,000, 60,000, and 100,000, respectively. The peak Nusselt numbers increase consistently in magnitude and move upstream with increasing swirl strength. This upstream migration of Nu_m is a direct result of the shortening reattachment length discussed previously. The shortening of the recirculation region causes shear rates and hence production of turbulence kinetic energy to increase with consequently higher heat transfer rates. This enhancement is also promoted by higher local mean velocities as the tangential velocity component increases at nominally constant values of mean axial velocity.

Comparison of the unswirled flow results from Figs. 5–7 demonstrates that larger enhancements in heat transfer rates over straight pipe flow occur at lower Reynolds numbers. This feature is simply rationalized by the observation that convection heat transfer behavior in separated flow is commonly found to depend on $Re^{2/3}$ (Krall and Sparrow, 1966; Zemanick and Dougall, 1970), so that when Nusselt numbers are normalized with a fully developed tube-flow value, which depends on $Re^{0.8}$, the ratio depends on $Re^{-0.13}$. For zero swirl, the recovery to fully developed flow Nusselt numbers occurs faster with increasing Reynolds number. Nusselt numbers are strongly influenced by turbulence intensity, which velocity field measurements gave as $\approx$ 8 percent for Re = 30,000 and $\approx$ 3 percent for Re = 100,000 at the end of the test section. The turbulence intensities have relaxed more quickly in the latter case due to higher rates of dissipation at the larger Reynolds numbers (Laufer, 1954).

Table 1 gives a summary of peak Nusselt numbers (Nu_m), locations of Nu_m (x/H_{Num}), and reattachment lengths (x_r/H) for the flows examined in this study. Because there was an inevitable limit to the spatial resolution of the temperatures which could be attained, magnitudes and locations of the maximum Nusselt numbers which are tabulated in Table 1 were determined by interpolation of expanded scale plots of local Nusselt numbers in this region. The tabular results show that the locations of maximum Nusselt number are largely Reynolds number independent, consistent with the unswirled results of investigations discussed previously.

Maximum Nusselt numbers are shown for the present data and five other investigations in Fig. 8. The present unswirled

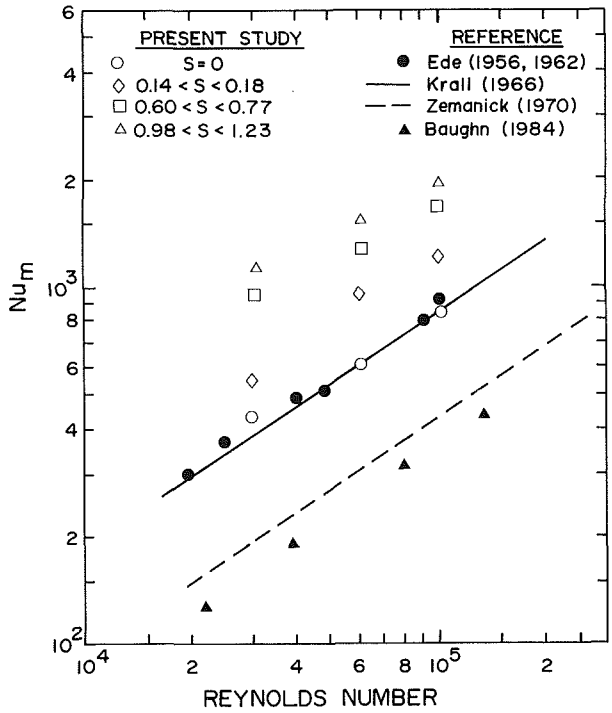

Fig. 8 Comparison of maximum Nusselt numbers between various investigations

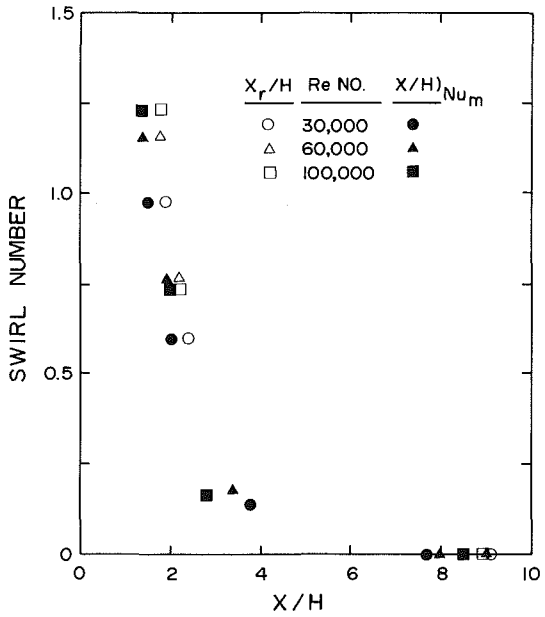

Fig. 9 Comparison of maximum Nusselt number locations with flow reattachment lengths

data for Nu_m fit comfortably among similar water data which show the $Re^{2/3}$ dependence mentioned above. However, at the larger swirl numbers there is a slight, but noticeable, decrease in the slope of the curves. Although the swirl number is not a fixed value at each Reynolds number, we may tentatively infer from Fig. 8 that Nu_m depends approximately on $Re^{0.46}$ for a fixed swirl number in the range $0.60 < S < 1.23$. Thus it appears that heat transfer enhancement due to swirl alone does contain some Reynolds number dependence.

Figure 9 contrasts the locations of maximum Nusselt number with the flow reattachment points determined from LDA measurements. Although it is often assumed that the peak Nusselt number occurs at the reattachment point (Krall and Sparrow, 1966; Zemanick and Dougall, 1970), for this work it fell consistently upstream of the reattachment point for all swirl numbers. The axial distance is nondimensionalized with the step height H of the expansion in Fig. 9 since reattachment lengths have been frequently shown to correlate well with this length scale.

Table 1

Reynolds Number	Swirl Number	T/C loc	% diff in Q[1]	Nu_m	$\frac{Nu_m}{Nu_{fd}}$	$\frac{x^{(2)}}{H_{Nu_m}}$	$\frac{x_r}{H}$
30,200	0	Bot	+1.4	430	3.7	7.7	9.1
29,800	.14	Bot	-1.8	550	4.8	3.8	-
30,600	.60	Top	-1.8	960	8.1	2.0	2.4
30,800	.98	Top	-1.3	1130	9.5	1.5	1.9
61,100	0	Bot	-12.3	610	3.0	8.0	9.0
60,600	.18	Bot	-0.5	960	4.9	3.4	-
61,600	.77	Top	-0.5	1280	6.5	1.9	2.2
60,800	1.16	Top	-1.4	1540	8.0	1.4	1.8
101,400	0	Top	-9.6	850	3.1	8.5	9.0
100,300	.17	Top	-4.9	1230	4.4	2.8	-
100,000	.74	Top	-2.3	1670	6.0	2.0	2.2
99,800	1.23	Top	-4.1	1970	7.1	1.4	1.8

[1] % difference in Q employs $\dot{m}C_p\Delta T$ as the reference value
[2] Locations of Nu_m determined from average of several runs

Maximum Nusselt numbers display a consistent behavior as swirl number is varied at constant Reynolds number, as shown in Fig. 10. These curves lead to speculation that swirl influence on heat transfer may be expressible as a power law, as for example in the work of Hay and West (1975), where $Nu/Nu_{fd} = (S + 1)^{1.75}$ for free swirling flow in a constant diameter pipe. However, an indirect influence of the sudden expansion is that is causes the swirl number to change dramatically just downstream of the expansion (Gupta et al., 1984; Dellenback, 1986), and this feature, along with the difficult-to-specify relationship between Nu_m and Reynolds number, have thus far defeated efforts to separate quantitatively the effects of separation and swirl in the present results.

Computed differences between the two methods which are available for determining energy balances are also shown in Table 1 (as "percent difference in Q"). Incomplete mixing in the downstream plenum is believed to be largely responsible for the discrepancies by giving larger-than-actual downstream bulk temperatures. This hypothesis is consistent with the downstream thermocouple's location which would be within the wall boundary layer if the test section extended approximately 30 cm into the plenum. In almost every case, $\Sigma(I^2R)$ was smaller than $\dot{m}C_p\Delta T_b$, which also supports the present hypothesis but is contrary to normal expectation, where heat losses usually cause the fluid enthalpy rise to be less than the power input.

Rapidly fluctuating wall tempratures were observed at low Reynolds and swirl number combinations, indicating a random unsteadiness at these flow conditions. For example at Re = 30,000 (for both $S = 0$ and 0.14), wall temperatures were repeatedly observed to fluctuate by as much as ±4°C over a short time interval of about 2 s, but these fluctuations were not periodic. Similarly, for Re = 60,000 (both $S = 0$ and 0.18), fluctuations were on the order of ±2°C for the same time frame. When these fluctuations occurred at the lowest swirl strength, there was no apparent correlation with the PVC previously mentioned. Also, because the unsteadiness was apparent for the unswirled flow as well as the weakly swirled flow, it is plausible that the fluctuations are a consequence of slight shifts of the reattachment point within a small, but finite, zone of reattachment. At higher Reynolds and swirl numbers (for which the reattachment zone is narrower), these large fluctuations disappeared.

Impact of Free Convection. The influence of free convection on heat transfer in these experiments was believed to be minimal, especially for the swirled flows, since swirl tends to overpower secondary flow generated by buoyancy forces.

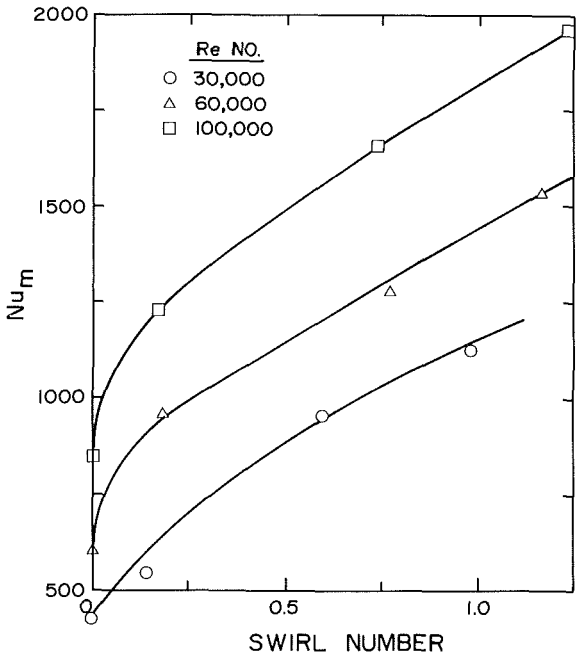

Fig. 10 Relationship between maximum Nusselt number and swirl number

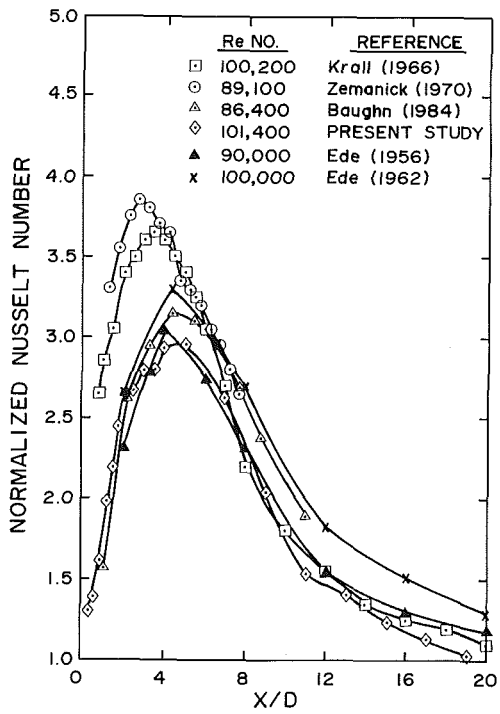

Fig. 11 Comparison of results with other investigations

Hence, temperature asymmetry was not expected, and indeed, none was found in any of the tests where swirl was present.

The measured wall-to-fluid temperature differences were used to compute the largest possible Rayleigh numbers (based on tube diameter) for each flow case. The extreme Rayleigh numbers were found to range from 1.2–3 $\times$ 10^9 and reference to the maps of free, mixed, and forced convection regimes compiled by Metais and Eckert (1964) suggest free convection should have little or no impact on the overall heat transfer for these Rayleigh numbers, even without the presence of swirl. It is only for the Re = 30,000, where temperatures differences were large, that the Rayleigh numbers indicate a proximity to the mixed convection regime where temperature asymmetries might be expected in the absence of swirl.

Further indication that free convection did not make a significant contribution to the overall heat transfer in these experiments may be deduced by comparing Nusselt numbers for runs where the thermocouples were fixed along the top of the tube to those runs where temperatures were measured along the bottom of the tube. Inspection of the results showed that, for all swirled flows, local Nusselt numbers deduced from these two orientations were indistinguishable. For unswirled flows, the only clear contribution by free convection occurred at the last four downstream measurement stations for Re = 30,000. For consistency in comparing low swirl and low Reynolds number cases, only runs where all temperature measurements were made using the bottom-mounted thermocouples have been used in this presentation.

Comparison With Previous Investigations. Comparison of the present results with those of other investigations is limited to the case of unswirled flows for which data are readily available. Figure 11 shows one such comparison for 86,400 < Re < 101,000. The comparison is based on normalized Nusselt numbers, but since fully developed Nusselt numbers used for normalization were obtained in a different manner for each study, this can present problems when comparing results. For example, if the present results had been normalized using the Dittus-Boelter relation rather than the Sieder-Tate correlation, then peak values of Nu/Nu_{fd} would have been 8 percent larger for Re = 100,000 (and about 11 percent larger for Re = 30,000) than the values shown in Figs. 5–7 and 11. However, a study by Malina and Sparrow (1964) concluded that the Sieder-Tate relation overpredicts variable-property enhancement of heat transfer by about 4 percent while the Dittus-Boelter relation underpredicts fully developed tube flow Nusselt numbers by 6–11 percent in the Reynolds and Prandtl number ranges of the present data. Thus the results of Malina and Sparrow suggest that the apparent 10 percent difference in Nu/Nu_{fd}, which is due to the choice of a correlation for normalization, may in fact be much smaller. For the work of Krall and Sparrow (1966), the data of Malina and Sparrow were used to obtain fully developed Nusselt numbers, but the effect of employing the Dittus-Boelter relation would be to increase the peak Nu/Nu_{fd} ratio by 5–10 percent over their values shown in Fig. 11. To complicate the comparison further, Zemanick and Dougall (1970) used their own downstream data for normalization, while the data of Baughn et al. (1984) and Ede et al. (1956, 1962) are normalized with the Dittus-Boelter relation. In any event, the Nusselt numbers of Krall and Sparrow appear somewhat high at several Reynolds numbers. It seems reasonable to conclude that the vena contracta produced by their orifice makes the effective expansion ratio larger than 2:1, and it has been clearly demonstrated (Krall and Sparrow; Zamanick and Dougall; Baughn et al.) that peak Nusselt numbers increase with increasing expansion ratio. The present results exhibit very good agreement with the recent results of Baughn et al., particularly at small x/D. This provides confidence in the present results since the principle motivation for the work of Baughn et al. was to minimize axial heat conduction, especially in the near expansion region where measurement inaccuracies are usually largest.

Closure

The principal contribution of the present results is to specify the quantitative effect of swirl on the heat transfer enhancement for the flow downstream of a sudden axisymmetric expansion. Local heat transfer rates have been shown to increase dramatically in the separated flow region and to peak just upstream of the flow reattachment point. The results also show that the location of peak Nusselt number is a strong

function of swirl number. However, the locations of maximum heat transfer rate are found to be largely Reynolds number independent, particulary at higher swirl numbers.

Acknowledgments

The work reported here was supported by the Office of Naval Research.

References

Baughn, J. W., Hoffman, M. A., Takahashi, R., K., and Launder, B. E., 1984, "Local Heat Transfer Downstream of an Abrupt Expansion in a Circular Channel With Constant Wall Heat Flux," ASME JOURNAL OF HEAT TRANSFER, Vol. 106, pp. 789–796.

Dellenback, P. A., 1986, "Heat Transfer and Velocity Measurements in Turbulent Swirling Flow Downstream of an Abrupt Axisymmetric Expansion," Ph.D. Dissertation, Arizona State University.

Ede, A. J., Morris, R., and Birch, E. S., 1962, "The Effect of Abrupt Changes of Diameter on Heat Transfer in Pipes," Nat. Eng. Lab. Report No. 73, East Kilbride, Glasgow, Scotland.

Ede, A. J., Hilsop, D. J., and Morris, R., 1956, "Effect on the Local Heat Transfer Coefficient in a Pipe of an Abrupt Disturbance of the Fluid Flow: Abrupt Convergence and Divergence of Diameter Ratio 2/1," *Inst. of Mech. Engs. (London)*, Proc. 170 No. 38, pp. 1113–1126.

Gupta, A. K., Lilley, D. G., and Syred, N., 1984, *Swirl Flows*, Abacus Press, Turnbridge Wells, Kent.

Habib, M. A., and McEligot, D. M., 1982, "Turbulent Heat Transfer in a Swirl Flow Downstream of an Abrupt Pipe Expansion," *Proc. of the 7th Int. Heat Transfer Conf.*, Washington, DC, pp. 159–165.

Hallett, W. L. H., and Gunther, R., 1984, "Flow and Mixing in Swirling Flow in a Sudden Expansion," *Canadian J. of Chem. Eng.*, Vol. 62, pp. 149–155.

Hay, N., and West, P. D., 1975, "Heat Transfer in Free Swirling Flow in a Pipe," ASME JOURNAL OF HEAT TRANSFER, Vol. 97, pp. 411–416.

Kern, D. Q., 1950, *Process Heat Transfer*, McGraw-Hill, New York.

Kline, S. J., and McClintock, F. A., 1953, "Describing Uncertainties in Single-Sample Experiments," *Mechanical Engineering*, Vol. 75, No. 1, pp. 3–8.

Krall, K. M., and Sparrow, E. M., 1966, "Turbulent Heat Transfer in the Separated Reattached, and Redevelopment Regions of a Circular Tube," ASME JOURNAL OF HEAT TRANSFER, Vol. 88, pp. 131–136.

Laufer, J., 1954, "The Structure of Turbulence in Fully Developed Pipe Flow," NACA Tech Report 1174.

Leibovich, S., 19843, "Vortex Stability and Breakdown: Survey and Extension," *AIAA J.*, Vol. 22, pp. 1192–1206.

Malina, J. A., and Sparrow, E. M., 1964, "Variable-Property, Constant-Property, and Entrance-Region Heat Transfer Results for Turbulent Flow of Water and Oil in a Circular Tube," *Chem. Eng. Sci.*, Vol. 19, pp. 953–962.

Metais, B., and Eckert, E. R. G., 1964, "Forced, Mixed and Free Convection Regimes," ASME JOURNAL OF HEAT TRANSFER, Vol. 86, pp. 295–296.

Stevenson, W. H., Thompson, H. D., and Gould, R. D., 1983, "Laser Velocimeter Measurements and Analysis in Turbulent Flows With Combustion, Part II," AFWAL-TR-82-2076.

Sultanian, B. K., Neitzel, G. P., and Metzger, D. E., 1985, "Turbulent Flow Predictions in a Sudden Axisymmetric Expansion," *Proc., Int. Symp. on Refined Flow Modeling and Turbulence Measurements*, B22.

Touloukian, Y. S., ed., 1967, *Thermophysical Properties of High Temperature Solid Materials, Vol. 3: Ferrous Alloys,* Thermophysical Properties Research Center, Purdue Univ., McMillan.

Zemanick, P. P., and Dougall, R. S., 1970, "Local Heat Transfer Downstream of Abrupt Circular Channel Expansion," ASME JOURNAL OF HEAT TRANSFER, Vol. 92, pp. 53–60.

Turbulent Heat Transfer Downstream of a Contraction-Related, Forward-Facing Step in a Duct

A. Garcia

E. M. Sparrow

Department of Mechanical Engineering,
University of Minnesota,
Minneapolis, MN 55455

Experiments were performed to investigate the axial distribution of the heat transfer coefficient downstream of an abrupt contraction in a flat rectangular duct. The contraction was created by the presence of a forward-facing step in one of the walls of the duct. The flow arriving at the step was hydrodynamically developed and isothermal. In the contracted duct, the duct wall that constituted the continuation of the step was maintained at a uniform temperature different from that of the entering flow, while the other walls were adiabatic. During the course of the experiments, the Reynolds number of the flow in the contracted duct ranged from 4000 to 24,000, while the ratio of the post-contraction to the precontraction duct heights took on values of 1 (no contraction), 0.8, 0.6, and 0.4. In the presence of the contraction, the axial distribution of the Sherwood number increased at first, attained a maximum, and then decreased monotonically to a fully developed value. In contrast, the no-contraction Sherwood number decreased monotonically and subsequently became fully developed. At a given Reynolds number, the peak Sherwood number for the contraction case was virtually independent of the contraction ratio and exceeded the largest measured Sherwood number for the no-contraction case by about a factor of two.

Introduction

The physical situation to be investigated here is pictured schematically in Fig. 1(*a*). As indicated there, a hydrodynamically developed flow is delivered upstream of an abrupt contraction by a long unheated length of duct of height H (shown truncated in the figure). At a station designated as $x = 0$, there is an abrupt reduction of the duct height, which creates an upstream-facing step. The height of the step and the post-step height of the duct are z and h, respectively, where $z = (H - h)$.

The presence of the step gives rise to an asymmetric contraction of the flow as well as to flow separation at both the foot and apex of the step. The separation bubble which extends downstream from the apex of the step washes the step-adjacent wall of the contracted duct. At the downstream closure of the separation bubble, the flow reattaches to the wall. Thereafter, a redevelopment of the flow takes place, which ultimately leads to the attainment of hydrodynamically developed conditions.

With regard to the heat transfer problem, both the upstream hydrodynamic development section and the upstream face of the step are adiabatic. As a consequence, the fluid passing through the duct cross section at the abrupt contraction (i.e., at $x = 0$) is uniform in temperature. Downstream of the contraction, the step-side wall of the duct (i.e., the upper wall in Fig. 1*a*) is maintained at a uniform temperature which is different from that of the entering fluid, while the other walls are adiabatic.

The objective of the investigation, which was wholly experimental, was to determine the distribution of the heat transfer coefficient along the thermally active wall. Two parameters were varied during the course of the work. One of these was the degree of contraction (i.e., the step height), which will be expressed here by the ratio h/H. This ratio was assigned values of 1, 0.8, 0.6, and 0.4, the first of which, the no-contraction case, serves as a baseline. The other parameter was the Reynolds number based on the hydraulic diameter of the contracted duct, the investigated values of which were 4000, 5700, 8000, 11,500, 16,500, and 24,000. These Reynolds numbers span the transition regime and the low and intermediate ranges of the turbulent regime, which corresponds to operating conditions often encountered in heat exchanger applications. The ducts used in the experiments were all characterized by large cross-sectional aspect ratios W/h (h = duct height, W = duct width), ranging from 5 for the no-contraction case to 12.5 for the $h/H = 0.4$ contraction.

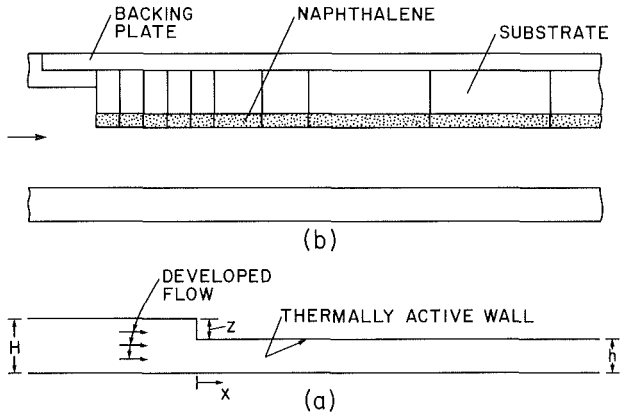

Fig. 1 Schematic diagram of (*a*) the investigated physical situation and (*b*) the experimental apparatus

The work was facilitated by the use of the naphthalene sublimation technique, by means of which mass transfer experiments were performed instead of heat transfer experiments. The boundary condition of the mass transfer experiments, uniform naphthalene vapor density at the mass transfer surface, corresponds to uniform temperature at the analogous heat transfer surface. Whereas localized mass transfer results can be readily obtained from the naphthalene experiments, it is extremely difficult to make localized heat

Contributed by the Heat Transfer Division for publication in the JOURNAL OF HEAT TRANSFER. Manuscript received by the Heat Transfer Division September 10, 1986.

transfer measurements at an isothermal surface. Additionally, adiabatic conditions are particularly difficult to achieve at a surface situated adjacent to a heated wall, as would be the case at the upstream face of the step. On the other hand, for the naphthalene technique, the zero mass transfer condition is perfectly fulfilled at a surface which does not react with naphthalene (e.g., a metal). Other advantages of the naphthalene technique are its accuracy and the simplicity and flexibility of the experimental apparatus with which it is used. The naphthalene sublimation experiments were performed with air as the flowing fluid.

Mass transfer coefficients were obtained at 26 or more axial stations on the mass-transfer-active wall of the duct (slightly fewer stations were used for the no-contraction case). Axial distributions of the mass transfer coefficient will be presented in dimensionless form in terms of the Sherwood number based on the hydraulic diameter of the contracted duct. Separate consideration will be given to the maximum Sherwood number which results from the flow separation and reattachment process and to the fully developed Sherwood number which is attained far downstream. Each of these quantities will be correlated with the Reynolds number. For completeness, representative distributions will be presented for the Sherwood number based on the step height, which is commonly used in presenting results for external flows with separated regions.

A survey of the literature revealed the total absence of prior work on heat transfer associated with an abrupt contraction in a duct (i.e., with a forward-facing step), although there are a number of papers dealing with abrupt expansion (backward-facing steps). A related problem is that of heat transfer in a rectangular duct fed by an infinitely large upstream plenum chamber (the case of an infinite contraction ratio), for which experiments are reported by Sparrow and Cur (1982). The contraction dealt with there was symmetric, in contrast to the asymmetric contraction investigated here.

Experiments

The description of the experimental apparatus will begin by following the path of fluid flow. Air from the naphthalene-free, temperature-controlled laboratory room is drawn into the hydrodynamic development section through a sharp-edged inlet. After traversing the length of the development section, the air encounters the abrupt, asymmetric contraction which marks its entry into the test section. As it passes through the test section, the air receives naphthalene vapor which sublimes from the mass-transfer-active surface. At the test section exit, the flow discharges into a length of duct whose cross section is identical to that of the hydrodynamic development section, and from there it passes successively through a rectangular-to-circular transition piece, a flowmeter, a control valve, and a blower.

The blower is situated in a service corridor adjacent to the laboratory, and its compression-heated, naphthalene-enriched discharge is vented outside the building. The operation of the system in the suction mode, the positioning of the blower outside the laboratory, and the out-of-building venting of the discharge contribute to the thermal stability of the experiment and guarantee that the air entering the apparatus is free of naphthalene vapor.

Aside from the mass transfer surface, all other portions of the rectangular duct were made from aluminum plate stock specially selected for flatness. Prior to the assembly of the duct, all of the aluminum surfaces which bound the air flow were polished to a high degree of smoothness. Positive sealing against leaks was accomplished by the use of O-ring material.

The hydrodynamic development section had internal cross-sectional dimensions of 2.667 × 13.335 cm (height H × width W), with a corresponding hydraulic diameter D_H of 4.445 cm. (Note that the subscript H is used to identify the hydraulic diameter of the development section, where the duct height is H.) The $40D_H$ axial length of the development section was sufficient to provide fully developed flow at its downstream end, as witnessed by the measured linearity of the axial pressure distribution.

Four versions of the test section were used during the course of the experiments, with the duct height h being assigned values equal to H, $0.8H$, $0.6H$, and $0.4H$. The width W of all the test sections was the same, equal to 13.335 cm. Similarly, all test sections were of the same axial length, namely, 57.8 cm. The hydraulic diameter of the cross section of the test section, to be denoted by D_h, has four different values corresponding to the four duct heights. Note that the subscript h is used here to distingish the hydraulic diameter of the test section from that of the duct upstream of the step.

The description of the mass-transfer-active wall is facilitated by reference to Fig. 1(*b*). As seen there, the wall is a composite structure made up of a succession of mass transfer elements mounted on a backing plate. Each element consisted of an aluminum substrate on which a layer of solid naphthalene had been cast. When assembled, the array of mass transfer elements presented a continuous, hydrodynamically smooth surface to the air flow.

Mass transfer coefficients were determined at each of the mass transfer elements of the array. Each such coefficient corresponds to the average value for that element. In order that such average coefficients can serve as quasi-local coefficients, it is necesary that elements having suitably short axial lengths be employed. The most rapid variations of the mass transfer coefficient occur just downstream of the step, with more gradual variations thereafter. Consequently, to accommodate this pattern, mass transfer elements of different axial lengths were used, with the shortest elements near the step and with longer elements farther downstream.

Elements having lengths of 0.635, 1.270, and 3.175 cm were used. The relative lengths of these elements are illustrated in Fig. 1(*b*). In the figure, the deployment of the elements was chosen to enable all three sizes to be pictured within the available space. The actual deployment will be evident from the graphs in which the results are presented, and it will be

Nomenclature

A_i = mass transfer surface area of element i
D = mass diffusion coefficient
D_H = hydraulic diameter of pre-contraction duct
D_h = hydraulic diameter of contracted duct
H = height of precontraction duct
h = height of contracted duct
ΔM_i = net loss of mass of element i during data run
K = quasi-local mass transfer coefficient, equation (2)
$\dot{Q}$ = volumetric flow rate
Re = Reynolds number = $\bar{u}D_h/\nu$
Sc = Schmidt number = ν/D
$\bar{u}$ = mean velocity in contracted duct
W = width of duct
x = axial coordinate (midpoints of mass transfer elements)
z = step height = $(H - h)$
ν = kinematic viscosity
ρ_{nb} = density of naphthalene vapor in bulk flow
ρ_{nw} = density of naphthalene vapor at subliming surface
τ = duration of data run

demonstrated there that the employed array of mass transfer elements provided a quasi-local description of the axial distribution of the mass transfer coefficient.

The first and last mass transfer elements were designed to prevent mass transfer at the forward-facing step at the beginning of the test section and at the rearward-facing step at the end of the test section. This was accomplished by shielding the naphthalene, which would otherwise have been exposed at the step with a 0.0254-cm-thick shroud of aluminum that was integral with the substrate.

The mass transfer elements were held in place by transverse pressure exerted by longitudinal bars positioned along each lateral edge of the backing plate. The pressure was applied by tightening screws on one of the bars, and this feature enabled the elements to be installed or removed very rapidly. The backing plate was also made to be readily removable, so that the entire mass-transfer-active wall of the test section could be removed or installed in a matter of seconds. When installed, the backing plate was fixed in place and pressed against the duct side walls by quick-acting clamps.

The height h of the test section was varied by a combination of two means. One of these was to vary the thicknesses of the aluminum substrate and the layer of solid naphthalene. The second method was to vary the height of the side walls on which the backing plate rested.

The casting of the naphthalene layer of each mass transfer element was accomplished by incorporating the substrate as part of a square-cornered rectangular mold. Molten naphthalene was poured into the mold cavity through an aperture in the substrate. After solidification, the mold was disassembled, exposing the face which was to bound the air flow. This face had been cast against a very highly polished stainless steel plate, and its smoothness was comparable to that of the plate.

During the casting process, a fine-gage, precalibrated, chromel-constantan thermocouple was embedded in each of two mass transfer elements such that the junction was flush with the exposed surface of the naphthalene layer. The thermocouples provided temperature data to be used in the evaluation of the vapor pressure of the naphthalene.

The aforementioned embedded thermocouples were read with a digital voltmeter having a resolution of 1 μV. A 0.1°F ASTM-certified thermometer served to measure the temperature of the air flow. The flowmeter was a calibrated orifice plate. The orifice-related pressure differences were read with a solid-state, capacitance-type pressure meter having a resolution of 10^{-3} Torr. The mass transfer rate at each element was determined from measurements of the mass of the element made just before and just after a data run. An electronic analytical balance able to resolve 0.00001 g was used for the mass measurement. The sublimation-related change in the mass of an element ranged from 0.01 to 0.06 g, depending on the size of the element, its axial location, and the operating conditions.

The attainment of a thermal steady state prior to the initiation of a mass transfer run is a necessary prerequisite for results of high accuracy. This is so because the naphthalene vapor density at the subliming surface, which drives the mass transfer, is a sensitive function of the surface temperature. To ensure that steady conditions were achieved, an equilibration period of suitable duration was allowed prior to each run. During the equilibration period, the mass transfer elements were in place in the duct, but they were shrouded to prevent mass transfer.

The duration of a data run was chosen to limit the recession of the subliming surface to 0.0025 cm. This criterion resulted in run times ranging from 10 to 65 min, depending on the operating conditions. After each run, a calibration procedure was executed to obtain a correction for any extraneous mass transfer which might have occurred during the setup and disassembly of the test section and during the weighing period.

Data Reduction

The successive mass transfer elements will be numbered in sequence, with element 1 being just downstream of the step and with a typical element in the array being denoted by i. Let x_i' and x_i'' respectively denote the upstream and downstream ends of the element i, so that its midpoint x_i is given by

$$x_i = \tfrac{1}{2}(x_i' + x_i'') \tag{1}$$

The average mass transfer coefficient for each element, when presented in the forthcoming section, will be plotted at the element midpoint.

The average mass transfer coefficient K_i for a typical element i was evaluated from its defining equation

$$K_i = \Delta M_i / \tau A_i (\rho_{nw} - \rho_{nb})_i \tag{2}$$

In this equation, ΔM_i is the net loss of mass due to sublimation at element i during time τ, A_i is the surface area of the element, and ρ_{nw} and ρ_{nb} are the naphthalene vapor densities at the subliming surface and in the bulk flow. Under the assumption of solid–vapor equilibrium at the subliming surface, ρ_{nw} is a function of temperature alone. Since the temperature was found to be uniform along the mass-transfer-active wall, so also was ρ_{nw}. The numerical value of ρ_{nw} needed for equation (2) was obtained by first introducing the measured wall temperature into the vapor pressure–temperature equation for naphthalene (Sogin, 1958) and then using the perfect gas law with the vapor pressure and temperature as inputs.

The bulk density ρ_{nb} of the naphthalene vapor varies along the test section. The increase in ρ_{nb} between the upstream and downstream ends of an element j is

$$(\Delta\rho_{nb})_j = (\Delta M_j/\tau)/\dot{Q} \tag{3}$$

where $\dot{Q}$, the volumetric flow rate, was virtually constant along the length of the test section. Since $\rho_{nb} = 0$ at the test section inlet, it follows that the bulk densities of the naphthalene vapor at the upstream and downstream ends of the typical element i are, respectively,

$$\sum_{j=1}^{i-1} (\Delta M_j/\tau)/\dot{Q}, \qquad \sum_{j=1}^{i} (\Delta M_j/\tau)/\dot{Q} \tag{4}$$

The bulk density $\rho_{nb,i}$ was taken as the arithmetic mean of these quantities, so that

$$\rho_{nb,i} = (1/\tau\dot{Q}) \left[\sum_{j=1}^{i-1} \Delta M_j + \tfrac{1}{2}\Delta M_i \right] \tag{5}$$

which provides a means of obtaining $\rho_{nb,i}$ as needed for equation (2). As an alternative to the arithmetic mean, the density difference appearing in equation (2) was evaluated as a log mean, but without discernible differences in the results.

The mass transfer coefficients will be reported in dimensionless terms via the Sherwood number based on the hydraulic diameter D_h of the mass transfer test section

$$K_i D_h / D \tag{6}$$

In addition, since the step height z is commonly used for external flows with separated regions, representative results will also be presented for the Sherwood number $K_i z/D$. The quantity D appearing in the Sherwood number is the naphthalene–air diffusion coefficient. It was eliminated in favor of the kinematic viscosity by making use of the definition of the Schmidt number, $\mathrm{Sc} = \nu/D$ or $D = \nu/\mathrm{Sc}$. The Schmidt number for naphthalene diffusion in air is 2.5 (Sogin, 1958), while ν was taken to be the kinematic viscosity of pure

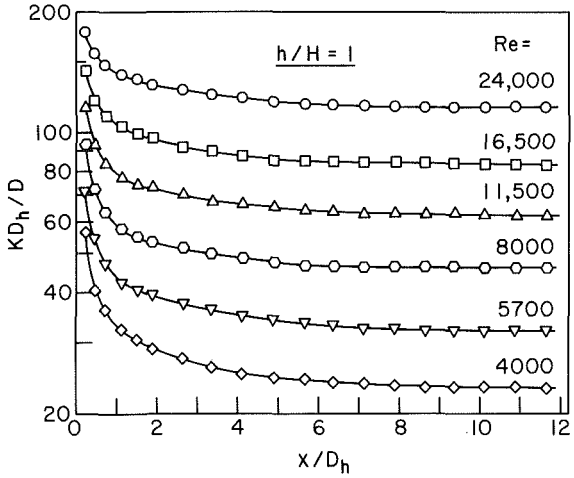

Fig. 2 Axial distributions of the Sherwood number for the no-contraction case

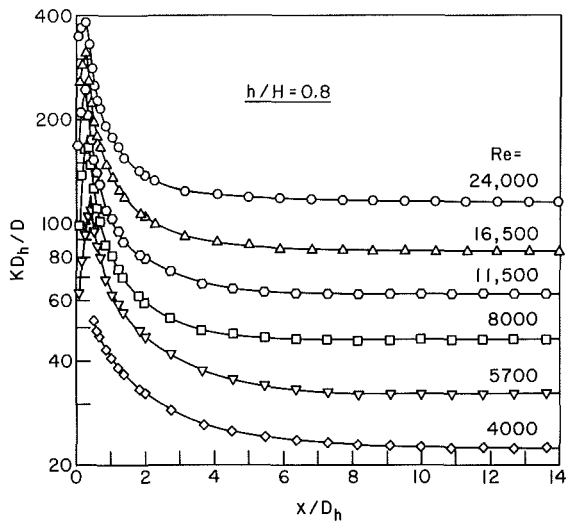

Fig. 3 Axial distributions of the Sherwood number for the h/H = 0.8 contraction

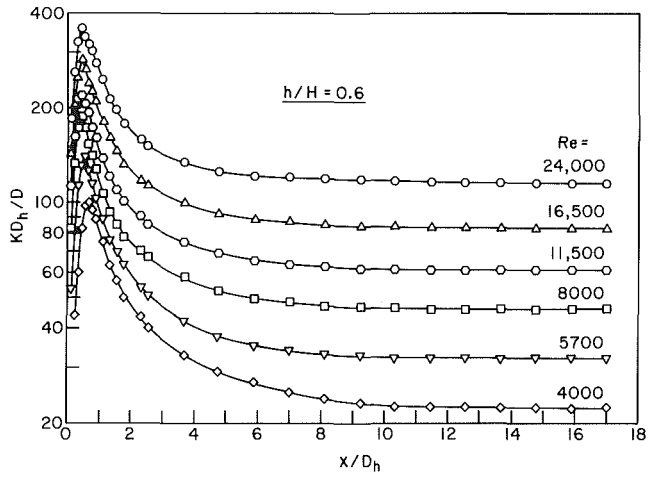

Fig. 4 Axial distributions of the Sherwood number for the h/H = 0.6 contraction

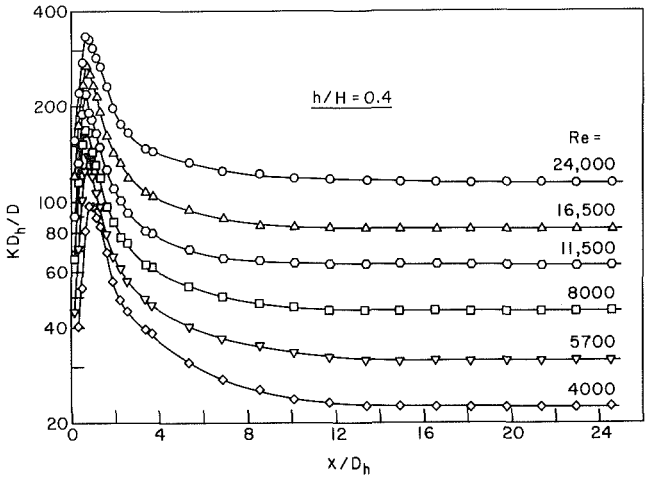

Fig. 5 Axial distributions of the Sherwood number for the h/H = 0.4 contraction

air since the concentrations of the naphthalene vapor were minute.

The fluid flow aspects of the problem will be characterized by the test section Reynolds number

$$\mathrm{Re} = \bar{u}D_h/\nu \tag{7}$$

in which $\bar{u}$ is the mean velocity in the test section.

Results and Discussion

Axial distributions of the Sherwood number for each of the four investigated contraction ratios, h/H = 1, 0.8, 0.6, and 0.4, are respectively presented in Figs. 2–5. In each figure, the Sherwood number KD_h/D is plotted as a function of the dimensionless axial coordinate x/D_h, where x is measured downstream from the step. As noted earlier, the plotted K values represent the average mass transfer coefficients for the respective elements, and the x coordinates of the data points are at the midpoints of the elements. The subscripts i have been omitted for the sake of a neater presentation.

Each figure conveys results for six values of the Reynolds number ranging from 4000 to 24,000, thereby spanning the transition regime and the low and intermediate ranges of the turbulent regime. The data for each Reynolds number have been interconnected by a smooth curve to provide continuity. The observed ascending order of the curves with increasing Reynolds number is as expected.

An overview of Figs. 2–5 reveals the drastic change which occurs in the Sherwood number distributions in the presence of a contraction. For the no-contraction case (Fig. 2), the distributions are those of a conventional thermal entrance region, where the transfer coefficient achieves its highest value at the beginning of the test section and decreases monotonically with increasing downstream distance, ultimately attaining a fully developed value. In contrast, in the presence of a contraction at the beginning of the test section, the transfer coefficient rises rapidly in the region immediately downstream of the contraction, achieves a sharp maximum, and thereafter decreases monotonically toward the fully developed regime. This behavior corresponds to the separation, reattachment, redevelopment sequence experienced by the flow. Although the peak value of the transfer coefficient is often associated with the reattachment of the separated flow to the wall, there is evidence (Vogel and Eaton, 1984; Sparrow et al., 1987) that the axial location of the peak is often situated upstream of the point of reattachment. The factors affecting the relative positions of the reattachment and peak heat transfer points are delineated in the cited references.

The magnitudes of the peak values in the contraction-affected Sherwood number distributions are impressively high compared with the largest measured entrance-region Sherwood numbers for the corresponding (i.e., same Reynolds

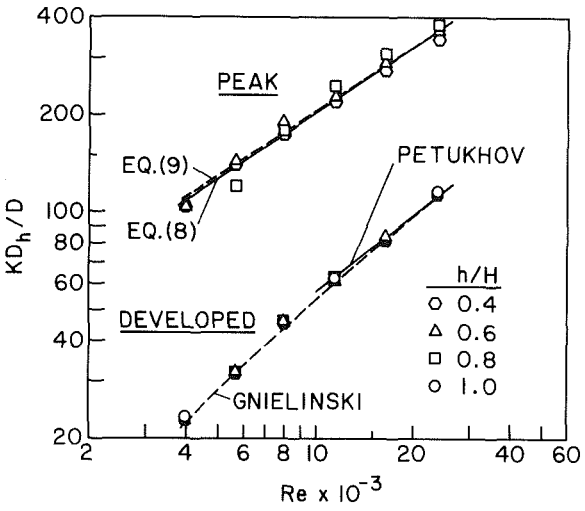

Fig. 6 Peak and fully developed Sherwood numbers

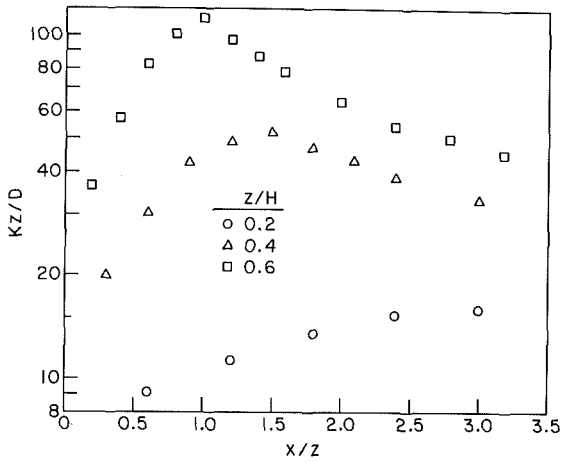

Fig. 7 Axial distributions of the Sherwood number based on the step height z as characteristic dimension, Re = 5700

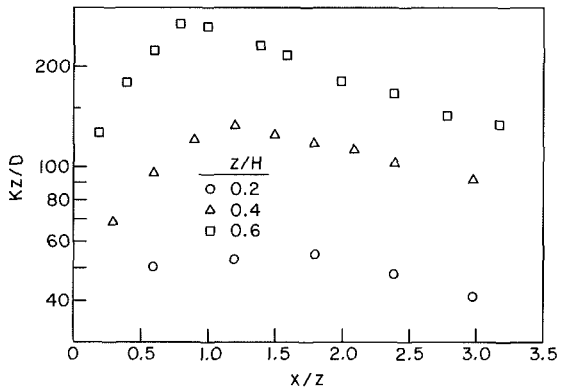

Fig. 8 Axial distributions of the Sherwood number based on the step height z as characteristic dimension, Re = 24,000

number) no-contraction cases. By examining all the cases for which results are conveyed in Figs. 2–5, it was found that the peak Sh values are about twice as large as the largest no-contraction entrance region values. Another perspective may be given to this comparison by ratioing the peak and fully developed Sherwood numbers at a given Reynolds number and by similarly ratioing the largest no-contraction entrance region Sherwood number with the fully developed value. As the Reynolds number decreases from 24,000 to 4000, the ratio of the peak to the fully developed Sherwood number increased from about 3 to 4.4. Over the same Reynolds number range, the corresponding ratio for the no-contraction case increased from about 1.5 to 2.4.

It is particularly noteworthy that the peak Sherwood numbers for a given Reynolds number were little affected by the magnitude of the contraction ratio in the investigated range, i.e., $h/H = 0.4$ to 0.8. Thus, the aforementioned contraction-related enhancements are equally applicable to the smallest contraction as well as for the largest contraction. This finding should not be applied outside the investigated range of h/H without further confirming experiments.

Further inspection of Figs. 3–5 shows that the peak Sherwood numbers occur at a distance from the step that is substantially less than the test section hydraulic diameter. For the $h/H = 0.8$ contraction, the peaks lie in the range of $x/D_h = 0.25$–0.4, while the corresponding ranges are 0.45–0.65 for the $h/H = 0.6$ and 0.4 contractions. For a given contraction ratio, the peaks for Re $\geq$ 11,500 occur at the same x/D_h, but with decreasing Re they tend to shift to larger x/D_h. This shift may be suggestive of an elongation of the separation bubble associated with operation in the transition regime. The aforementioned trend with Reynolds number was also encountered for the case of a symmetric contraction with $h/H = 0$) (Sparrow and Cur, 1982).

It also appears that the thermal development length, measured as a multiple of D_h, increases as the degree of contraction becomes larger (i.e., as h/H decreases). Thus, while the thermal development is completed by $x/D_h = 10$ for $h/H = 0.8$, about $15D_h$ is required to achieve thermal development for $h/H = 0.4$. This trend is not unexpected, since greater disruptions are inflicted on the flow as the degree of contraction increases. Although the least rapid development appears to occur at the lowest Reynolds number, Re = 4000, the Reynolds number effect on the entrance length is slight.

Before concluding the discussion of Figs. 2–5, it may be noted that the initial portion of the distribution for Re = 4000 is absent from Fig. 3. For that case, consistent data could not be obtained despite several repeated runs. It is conjectured that at the conditions in question (relatively small step height and relatively low Reynolds number), the intermittency of the flow caused the reattachment region to shift continuously, thereby giving rise to incoherent data.

Attention is now turned to the correlation of both the peak and fully developed Sherwood numbers, and Fig. 6 has been prepared for this purpose. The fully developed Sherwood number values plotted in Fig. 6 were obtained by averaging the rightmost several points of each of the axial distributions presented in Figs. 2–5. It is seen that the plotted Sherwood numbers are independent of the contraction ratio h/H, as is befitting their fully developed nature. However, the independence of the data from h/H has an added significance here, since the cross-sectional aspect ratio of the contracted ducts ranged from 5 to 12.5 as h/H ranged from 1 to 0.4. It may, therefore, be inferred that all of the employed aspect ratios were sufficiently large so that end effects were of no consequence.

To complement the fully developed data, lines representing the correlations of Petukhov–Popov (Petukhov, 1970, equations (48) and (50)) and of Gnielinski (1976) are shown in Fig. 6. The Petukhov–Popov correlation is specified as being applicable for Re $\geq$ 10,000, while that of Gnielinski is a modification which extends the Petukhov–Popov correlation to the range of low turbulent Reynolds numbers. The excellent agreement of the present data with these well-established correlations lends support to the experimental method.

The peak Sherwood numbers plotted in Fig. 6 are substantially higher than the fully developed values by a factor of 3 to

4.4, as discussed earlier. Although there is some spread of the data, the effect of the contraction ratio h/H on the peak values is unexpectedly small. Aside from a single point, the peak Sh data are well correlated by the least-squares power law

$$\mathrm{Sh} = 0.357\mathrm{Re}^{0.69} \tag{8}$$

which is shown as a solid line in the figure. If the more conventional $\mathrm{Re}^{2/3}$ dependence is used (Krall and Sparrow, 1966; Zemanick and Dougall, 1970), the fit becomes

$$\mathrm{Sh} = 0.442\mathrm{Re}^{2/3} \tag{9}$$

as portrayed by the dashed line. The data are well represented by the 2/3-power dependence, thereby demonstrating its commonality with that for other types of separated flow.

As a final topic in the presentation of the results, representative axial distributions of the Sherwood number will be displayed in which the characteristic dimension is the step height $z = (H - h)$. As noted earlier, the step height is considered here as a characteristic dimension because it is commonly used in presenting results for external flows with separate regions. In Figs. 7 and 8, the Sherwood number Kz/D is plotted against the dimensionless axial coordinate x/z, respectively for Re = 5700 and 24,000. In each figure, data are presented for dimensionless step heights z/H of 0.2, 0.4, and 0.6 (h/H = 0.8, 0.6, and 0.4). In both figures, the range of the abscissa extends from 0 to 3.5, which encompasses the upstream portion of the test section. The reason for confining the axial range is that if the step height z has any special merit as a characteristic dimension, it should be manifested near the step. (Note that far downstream, the hydraulic diameter is the appropriate characteristic dimension.)

Both Figs. 7 and 8 display common trends. As seen there, the axial distributions of the Sherwood number for a given Reynolds number are arranged in ascending order with increasing values of the dimensionless step height and, in particular, the peak Sherwood number varies appreciably with z/H. If it is desired to achieve a peak Sherwood number which is virtually independent of the contraction parameter (h/H or z/H) for a given Reynolds number, then the KD_h/D, x/D_h, h/h presentation parameters of Figs. 2–5 are superior to the Kz/D, x/z, z/H presentation parameters of Figs. 7 and 8.

It is also seen in Figs. 7 and 8 that the peak is attained at fewer step heights (i.e., smaller x/z) downstream of the contraction as the step height z/H increases. In addition, from a study of a succession of figures such as 7 and 8, it was found that for a given step height, the value of x/z at the peak was independent of the Reynolds number for Re = 24,000, 16,500, and 11,500, but as the Reynolds number decreased further, the peak-related x/z values increased.

Concluding Remarks

The experiments performed here have provided a definitive set of results for heat transfer downstream of an unsymmetric contraction in a flat rectangular duct. The contraction is, in effect, a forward-facing step. In the experimental setup, the flow approaching the step was hydrodynamically developed and isothermal. In the contracted duct, the duct wall which constitutes the continuation of the step was maintained at a uniform temperature different from that of the entering fluid, while all of the other walls are adiabatic. Quasi-local heat transfer coefficients were measured along the thermally active wall as a function of the Reynolds number Re of the contracted duct and of the ratio h/H of the heights of the contracted duct and the upstream (uncontracted) duct. As a baseline, the no-contraction case $h/H = 1$ was also investigated. The actual experiments were performed using the naphthalene sublimation technique rather than via direct heat transfer measurements.

In the presence of a contraction, the axial distribution of the Sherwood number (dimensionless mass transfer coefficient) was characterized by an initial rapid rise, the attainment of a sharp maximum, and a subsequent monotonic decrease toward the thermally developed regime. This sequence corresponds to the separation, reattachment, and redevelopment experienced by the flow. The greater the degree of contraction, the greater is the length of duct required to attain thermal development. At a given Reynolds number, the peak Sherwood number was found to be about twice the largest Sherwood number measured for the no-contraction case.

When the Sherwood number was based on the hydraulic diameter of the contracted duct, it was found that the peak values were virtually independent of the contraction ratio for a given Reynolds number in the investigated range of h/H (i.e., between 0.4 and 0.8). The peak Sherwood numbers were well correlated with $\mathrm{Re}^{2/3}$, as was previously encountered in the literature for other types of separated regions. The fully developed Sherwood numbers agreed well with the correlations of Petukhov–Popov and of Gnielinski.

References

Gnielinski, V., 1976, "New Equations for Heat and Mass Transfer in Turbulent Pipe and Channel Flow," *International Chemical Engineering*, Vol. 16, pp. 359–368.

Krall, K. M., and Sparrow, E. M., 1966, "Turbulent Heat Transfer in the Separated, Reattached, and Redevelopment Regions of a Circular Tube," ASME JOURNAL OF HEAT TRANSFER, Vol. 88, pp. 131–136.

Petukhov, B. S., 1970, "Heat Transfer and Friction in Turbulent Pipe Flow With Variable Thermophysical Properties," *Advances in Heat Transfer*, Vol. 6, pp. 503–563.

Sogin, H. H., 1958, "Sublimation From Disks to Air Streams Flowing Normal to Their Surfaces," *Trans. ASME*, Vol. 80, pp. 61–71.

Sparrow, E. M., and Cur, N., 1982, "Turbulent Heat Transfer in a Symmetrically or Asymmetrically Heated Flat Rectangular Duct With Flow Separation at Inlet," ASME JOURNAL OF HEAT TRANSFER, Vol. 104, pp. 82–89.

Sparrow, E. M., Kang, S. S., and Chuck, W., 1987, "Relation Between the Points of Flow Reattachment and Maximum Heat Transfer for Regions of Flow Separation," *International Journal of Heat and Mass Transfer*, Vol. 30 (in press).

Vogel, J. C., and Eaton, J. K., 1984, "Heat Transfer and Fluid Mechanics Measurements in the Turbulent Reattaching Flow Behind a Backward-Facing Step," Report MD-44, Stanford University, Stanford,CA.

Zemanick, P. P., and Dougall, R. S., 1970, "Local Heat Transfer Downstream of Abrupt Circular Channel Expansion," ASME JOURNAL OF HEAT TRANSFER, Vol. 92, pp. 53–60.

Finite-Volume Solutions for Laminar Flow and Heat Transfer in a Corrugated Duct

Y. Asako
Research Associate,
Department of Mechanical Engineering,
Tokyo Metropolitan University,
Tokyo, Japan

M. Faghri
Associate Professor,
Department of Mechanical Engineering,
University of Rhode Island,
Kingston, RI 02881
Mem. ASME

A finite volume methodology was developed to predict fully developed heat transfer coefficients, friction factors, and streamlines for flow in a corrugated duct. The basis of the method is an algebraic coordinate transformation which maps the complex fluid domain onto a rectangle. The method can be adopted for other convection-diffusion problems in which two boundaries of the flow domain do not lie along the coordinate lines. Representative results were found for laminar flow, uniform wall temperature, and for a range of Reynolds number, Prandtl number, corrugation angle, and dimensionless interwall spacing. As seen from the streamlines, the flow patterns are highly complex including large recirculation zones. The pressure drops and friction factor results are higher than the corresponding values for a straight duct. Finally, the performance of the corrugated duct was compared with the straight duct under three different constraints—fixed pumping power, fixed pressure drop, and fixed mass flow rate. There are small differences in the heat transfer rate ratios under these constraints.

Introduction

Faghri et al. (1984a) developed a solution methodology for convection-diffusion problems where one boundary of the solution domain did not lie along the coordinate lines. Its adaptation to periodic and nonperiodic sample problems was illustrated by Faghri (1984b) and Faghri and Asako (1984c). The present investigation constitutes a continuation of those works to a general problem where *both* boundaries of the solution domain do not lie along the coordinate lines. The basis of the method is an algebraic nonorthogonal coordinate transformation which maps the complex fluid domain onto a rectangle. This method is very simple and it is a special case of the general boundary fitted coordinate method. The conservation equations are derived for a control volume bounded by coordinate lines in the nonorthogonal transformed coordinate systems. Then, these equations, in the integrated form, are discretized to yield the governing algebraic equations of the problem.

As an example of the problem where both boundaries of the solution domain do not lie along the coordinate lines, the periodic fully developed heat transfer and fluid flow characteristics for a corrugated duct will be considered. To the authors' knowledge, with the exception of the paper by Amano (1984) for channels with two right-angled bends, the present investigation seems to be the first numerical study for corrugated ducts with an arbitrary corrugation angle. The complexities that would arise from an arbitrary corrugation angle are due to the fact that the boundaries of the solution domain do not lie along the coordinate lines and the usual numerical schemes for orthogonal coordinate systems cannot be employed. A number of experimental results are reported regarding heat transfer in corrugated ducts (Sparrow and Comb, 1983; O'Brien and Sparrow, 1982; Izumi et al., 1982). They will be used for comparison with the numerical results of this paper.

The numerical solutions were performed for laminar flow, and the thermal boundary condition of uniform wall temperature. The calculations were carried out for three values of the corrugation angle θ, including 15, 30, and 45 deg and for a number of dimensionless interwall spacing H'/L. For the duct geometry defined by θ and H'/L, the numerical work encompassed the Reynolds number range between 100 and 1500. The heat transfer solutions were parameterized by Prandtl numbers of 0.7, 4, and 8.

For the purpose of evaluating the performance of the corrugated duct, the pressure drops, friction factors, and Nusselt number results were compared with the corresponding values for a unidirectional duct under three different constraints.

Formulation

Description of a General Problem. Attention will first be focused on a general problem. A schematic view of the type of the physical domain being considered is shown in Fig. 1(*a*). As seen there, both walls of the duct are curved and do not lie along the coordinate lines. The separation distance between the two walls is constant and the distance between the left wall and the y axis varies with y. These distances are denoted by H' and $\epsilon(y)$, respectively. The ends of the duct at $y=0$ and $y=L$ coincide with the coordinate lines.

Coordinate Transformation. The first step in the analysis is to introduce a transformation of coordinates which maps the physical domain onto a rectangle. Specifically, the x, y coordinates are transformed to η, ξ coordinates by the relations

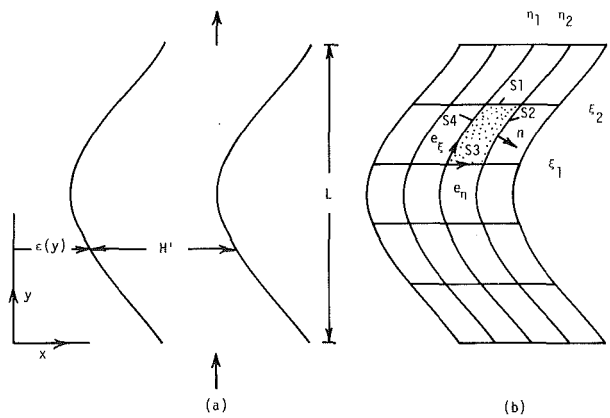

Fig. 1 *(a) Illustration of a general class of problems; (b) lines of constant η and ξ in the physical domain*

Contributed by the Heat Transfer Division for publication in the JOURNAL OF HEAT TRANSFER. Manuscript received by the Heat Transfer Division January 14, 1985.

$$\eta = x/L - \delta(Y), \quad \xi = y/L \text{ where } \delta(Y) = \epsilon/L \qquad (1)$$

such that $\eta = 0$ and H'/L, respectively, at all points on the left and right walls. In terms of the new coordinates, the solution domain is defined by $0 < \eta < H'/L$, $0 < \xi < 1$.

Lines of constant η and ξ (i.e., η, ξ coordinate lines) for a given boundary shape are illustrated in Fig. 1(*b*). It is evident that a control volume contained between lines $\eta = \eta_1$, $\eta = \eta_2$, and $\xi = \xi_1$, $\xi = \xi_2$ is a curvilinear element with nonorthogonal sides. The quantities $\mathbf{e}_\eta$ and $\mathbf{e}_\xi$ are unit vectors in the physical coordinate system which, respectively, lie along the lines of constant ξ and constant η. It is evident from the figure that the direction of $\mathbf{e}_\xi$ changes with position. This is in contrast to the Cartesian unit vectors $\mathbf{e}_x$ and $\mathbf{e}_y$ which, respectively, lie along lines y = const and x = const. These unit vectors do not change direction throughout the solution domain. It should be noted that the proposed transformation is nonconservative. This means that the transformation results in a variety of the source terms which causes fictitious losses (or gains) throughout the computational domain, especially in the regions of large variations of independent variables. The transformation of the conservation equations will be discussed later.

Description of a Sample Problem. The general class of problems described in the previous section includes a large variety of flow configurations of practical interest. One example of these geometries is a periodically corrugated duct as is pictured schematically in Fig. 2(*a*). As seen in this figure, to represent a realistic duct geometry, the sharp-edged corners are approximated with curves whose radius of curvature can be a parameter. These rounded corners are shown by dashed lines. The geometry of the duct may be specified by the axial length of the cycle L, the vertical spacing between corrugated walls H', and the corrugation angle θ. The interwall spacing H can be expressed in terms of H' and θ. The half length of the chord of the corrugation curve is denoted by l and is not varied in the present work and is assumed to be a small number.

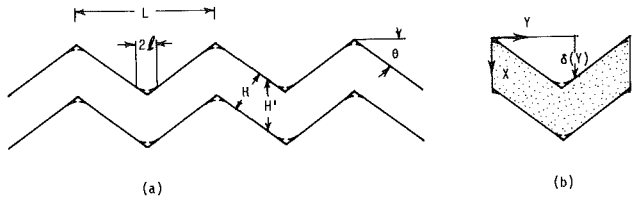

Fig. 2 (*a*) Schematic diagram of a corrugated duct; (*b*) physical domain in physical coordinates

The solution domain, with the assumption of a periodic fully developed regime, is confined to a typical module shown in Fig. 2(*b*). If δ is defined as shown in this module, then the methodology set forth for the general problem is applicable.

Periodic Fully Developed Flow Regime. The fluid flow in a periodically corrugated duct attains a periodic fully developed regime which differs from that of a straight duct. In the periodically corrugated duct, the periodic fully developed velocity field repeats itself at corresponding axial stations in successive cycles. Furthermore, in such a regime, the pressures of cyclically corresponding locations decrease linearly in the downstream direction. Similarly, a periodic thermally developed regime exists for commonly encountered boundary conditions such as uniform wall temperature and uniform wall heat flux. Such a regime is characterized by a cycle average heat transfer coefficient which is the same for each cycle of the

Nomenclature

A_w = per-cycle transfer area per unit depth, m
B = dimensionless per-cycle pressure gradient [equation (3)]
b = source term [equation (31) for U_η, equation (32) for V, equation (33) for T]
$\mathbf{e}_x$, $\mathbf{e}_y$ = unit vectors in x, y directions
$\mathbf{e}_\eta$, $\mathbf{e}_\xi$ = unit vectors in η, ξ directions
f = friction factor [equation (55)]
H = perpendicular spacing between corrugated walls, Fig. 2, m
H' = vertical spacing between corrugated walls, Fig. 2, m
h = fully developed heat transfer coefficient, W/m^{2}K
K = thermal conductivity of the fluid, W/mK
L = axial length of a cycle
l = half length of the chord of the parabolic section, m
$\dot{m}$ = total mass flow rate per unit depth, kg/ms
$\mathbf{n}$ = unit vector normal to surface
P = dimensionless periodic pressure [equation (3)]
p = pressure, Pa
p' = periodic pressure, Pa
Δp = per-cycle pressure drop, Pa
$\dot{p}$ = per-cycle pressure gradient, Pa/m
Pr = Prandtl number
Q = per-cycle wall heat transfer rate per unit depth, W/m
Re = Reynolds number $= 2\dot{m}/\mu$
T = dimensionless temperature
t = temperature, K
t_b = bulk temperature, K
t_w = wall temperature, K
U, V = dimensionless velocity components [equation (2)]
U_η = dimensionless velocity [equation (15)]
u, v = velocity components, m/s
$\forall$ = volume of the control volume
X = dimensionless transverse coordinate $= x/L$
x = transverse coordinate, m
Y = dimensionless axial coordinate $= y/L$
y = axial coordinate, m
α = geometric function $= 1 + \beta^2$
β = geometric function $= \partial\delta/\partial\xi$
Γ = diffusion coefficient
γ = bulk-to-wall temperature ratio
$\delta(Y)$ = dimensionless deviation from y axis $= \epsilon(y)/L$
$\epsilon(y)$ = deviation from y axis
η = transformed coordinate $= (x - \epsilon)/L$
Θ = diffusion term $= -\partial\phi/\partial\xi$
θ = duct angle, deg
Λ = pseudodiffusion term $= \beta(\partial\phi/\partial\xi)$
λ = bulk-temperature-gradient parameter [equation (9)]
μ = viscosity, PaS
ν = kinematic viscosity, m^2/S
ξ = transformed coordinate $= Y$
ρ = density, kg/m^3
σ = right-hand side of equation (8)
ϕ = general dependent variable
ψ = pseudodiffusion term $= \beta(\partial\phi/\partial\eta)$
Ω = diffusion term $= -\alpha/\partial\phi/\partial\eta)$

Subscripts

1 = refers to inlet
2 = refers to exit
$\gg$ = refers to corrugated duct
$\|$ = refers to straight duct

periodic duct. Attention will now be directed to the conservation equations to be considered for a corrugated duct with the assumption of a periodic fully developed regime.

The Conservation Equation. The governing equations to be considered are the continuity, momentum, and energy equations. Constant thermophysical properties are assumed and natural convection is excluded. The following dimensionless variables are used:

$$X=x/L, \quad Y=y/L, \quad U=u/(\nu/L), \quad V=v/(\nu/L) \tag{2}$$

$$P=p'/\rho(\nu/L)^2, \quad T=(t-t_w)/(t_b-t_w),$$
$$B=\dot{p}L/\rho(\nu/L)^2 \tag{3}$$

where L and ν are the periodic cycle length and the kinematic viscosity, respectively. The pressure p is expressed by $p(x, y) = -\dot{p}y + p'(x, y)$, where $\dot{p}$ is a constant, and $p'(x, y)$ behaves in a periodic manner from module to module. The term $\dot{p}y$ represents the nonperiodic pressure drop that takes place in the flow direction. Then, upon introduction of the dimensionless variables, and parameters, the governing equations have the following form:

$$\partial U/\partial X+\partial V/\partial Y=0 \tag{4}$$

$$U(\partial U/\partial X)+V(\partial U/\partial Y)=\partial^2 U/\partial X^2+\partial^2 U/\partial Y^2-\partial P/\partial X \tag{5}$$

$$U(\partial V/\partial X)+V(\partial V/\partial Y)$$
$$=\partial^2 V/\partial X^2+\partial^2 V/\partial Y^2-\partial P/\partial Y+B \tag{6}$$

$$U(\partial T/\partial X)+V(\partial T/\partial Y)$$
$$=(1/\mathrm{Pr})(\partial^2 T/\partial X^2+\partial^2 T/\partial Y^2)+\sigma/\mathrm{Pr} \tag{7}$$

where

$$\sigma=[2(\partial T/\partial Y)-\mathrm{Pr}VT]\lambda+T(\lambda^2+\partial\lambda/\partial Y) \tag{8}$$

and

$$\lambda=[d(t_b-t_w)/dY]/(t_b-t_w) \tag{9}$$

σ and λ are periodic parameters arising from the assumptions of the constant wall temperature boundary condition. These values are determined as part of the solution process. Note that equations (5), (6), and (7) retain the streamwise second derivatives $\partial^2 U/\partial Y^2$, $\partial^2 V/\partial Y^2$, and $\partial^2 T/\partial Y^2$ in recognition of the fact that large local values of these quantities may occur in the periodic fully developed flows.

To complete the formulation of the problem in the physical domain, it remains to discuss the boundary conditions. These are $U = V = 0$ and $t = t_w$ on the wall. At the inlet and outlet ends of the solution domain, periodic conditions are imposed.

Transformation of the Conservation Equations. The methodology for the transformation of the conservation equations is documented by Faghri et al. (1984a). Therefore, only a brief description will be given here. Equations (5) and (6) are the x and y components of the momentum equation. Equation (5) contains the terms that multiply $\mathbf{e}_x$ in the vector momentum equation, while equation (6) contains the terms that multiply $\mathbf{e}_y$. The vector momentum equation is first recast in terms of the unit vectors $\mathbf{e}_\eta$ and $\mathbf{e}_\xi$. These unit vectors are illustrated in Fig. 1(*b*). Since lines of constant ξ coincide with the y coordinate lines, $\mathbf{e}_\eta = \mathbf{e}_x$. To determine $\mathbf{e}_\xi$, consideration is first given to the unit vector $\mathbf{n}$ that is normal to a line of constant η. Since the gradient of η is normal to a line of constant η, it follows that

$$\mathbf{n}=\nabla\eta/|\nabla\eta|=(\mathbf{e}_x-\beta\mathbf{e}_y)/\alpha^{1/2} \tag{10}$$

where

$$\beta=\partial\delta/\partial Y, \quad \alpha=1+\beta^2 \tag{11}$$

The unit vector $\mathbf{e}_\xi$ is perpendicular to $\mathbf{n}$; therefore

$$\mathbf{e}_\xi=(\beta\mathbf{e}_x+\mathbf{e}_y)/\alpha^{1/2} \tag{12}$$

Expressing $\mathbf{e}_x$ and $\mathbf{e}_y$ in terms of $\mathbf{e}_\eta$ and $\mathbf{e}_\xi$ and collecting terms, the momentum equations may be expressed as follows:

$$U(\partial U_\eta/\partial X)+V(\partial U_\eta/\partial Y)=-\partial P/\partial X+\beta(\partial P/\partial Y-B)$$
$$+(\partial^2 U_\eta/\partial X^2+\partial^2 U_\eta/\partial Y^2)-V^2(\partial\beta/\partial Y)+V(\partial^2\beta/\partial Y^2)$$
$$+2(\partial V/\partial Y)(\partial\beta/\partial Y) \tag{13}$$

$$U(\partial V/\partial X)+V(\partial V/\partial Y)$$
$$=-(\partial P/\partial Y-B)+(\partial^2 V/\partial X^2+\partial^2 V/\partial Y^2) \tag{14}$$

where

$$U_\eta=U-\beta V \tag{15}$$

At this point, the momentum, energy, and continuity equations [respectively, equations (13), (14), (7), and (4)] are integrated over a control volume in physical space bounded by lines of constant η and constant ξ. Such a control volume is illustrated in Fig. 1(*b*).

Using the divergence theorem, equation (13) becomes

$$\int_S(\mathbf{U}\cdot\mathbf{n})U_\eta dS-\int_S(\mathbf{n}\cdot\nabla U_\eta)dS$$
$$=\int_\forall[-\partial P/\partial X)+\beta(\partial P/\partial Y-B)]d\forall$$
$$-\int_\forall V^2(\partial\beta/\partial Y)d\forall+2\int_\forall(\partial V/\partial Y)(\partial\beta/\partial Y)d\forall$$
$$+\int_\forall V(\partial^2\beta/\partial Y^2)d\forall \tag{16}$$

Equations (14), (7), and (4) become

$$\int_S(\mathbf{U}\cdot\mathbf{n})VdS-\int_S(\mathbf{n}\cdot\nabla\mathbf{V})dS=-\int_\forall(\partial P/\partial Y-B)d\forall \tag{17}$$

$$\int_S(\mathbf{U}\cdot\mathbf{n})TdS-(1/\mathrm{Pr})\int_S(\mathbf{n}\cdot\nabla\mathbf{T})dS=\sigma/\mathrm{Pr} \tag{18}$$

$$\int_\forall(\nabla\cdot\mathbf{U})d\forall=\int_S(\mathbf{n}\cdot\mathbf{U})dS=0 \tag{19}$$

where $\forall$ and S represent, respectively, the dimensionless volume and surface of the control volume.

For evaluation of the surface integrals, expressions are needed for the element of surface dS, the gradient operator ∇, and the unit vector $\mathbf{n}$. To derive these quantities, it is first necessary to consider a formal coordinate transformation from X, Y to η, ξ, where η and ξ have been defined by equation (1). The transformation is

$$(\partial/\partial X)_Y=(\partial/\partial\eta)\xi \tag{20}$$

$$(\partial/\partial Y)_X=-\beta(\partial/\partial\eta)_\xi+(\partial/\partial\xi)\eta \tag{21}$$

To facilitate evaluation of the surface integrals that appear in equations (16)–(19), reference may be made to the shaded control volume of Fig. 1(*b*). As suggested there, the surface integral may be subdivided into a sum of four surface integrals, respectively, over the segments S_1, S_2, S_3, and S_4.

For surface 1, $\mathbf{n} = \mathbf{e}_Y$, $\mathbf{U}\cdot\mathbf{n} = V$; also ξ = const along S_1. Therefore, an element of surface area can be expressed as

$$dS=dX=d\eta \tag{22}$$

For surface 2,

$$\mathbf{n}=(\mathbf{e}_x-\beta\mathbf{e}_Y)\alpha^{-1/2}, \quad \mathbf{U}\cdot\mathbf{n}=U_\eta\alpha^{-1/2} \tag{23}$$

and

$$dS=(dX^2+dY^2)^{1/2}=(\beta^2+1)^{1/2}d\xi=\alpha^{1/2}d\xi \tag{24}$$

For surfaces S_3 and S_4, dS is identical to those for S_1 and S_2, with the exception that the outward normal $\mathbf{n}$ has the opposite

sign. The volume integrals appearing on the right-hand side of equations (16) and (17) can be evaluated now. The volume element $d\forall$ can be written as

$$d\forall = dX\,dY = d\eta\,d\xi \tag{25}$$

The standard form of the ∇ operator in Cartesian coordinates is

$$\nabla = (\partial/\partial X)\mathbf{e}_X + (\partial/\partial Y)\mathbf{e}_Y \tag{26}$$

which, after substitution for $\partial/\partial X$ and $\partial/\partial Y$ from equations (20) and (21), becomes

$$\nabla = (\partial/\partial\eta)\mathbf{e}_X + [\partial/\partial\xi - \beta(\partial/\partial\eta)]\mathbf{e}_Y \tag{27}$$

The evaluation of the all surface integrals and the volume integrals in equations (16)–(19) can be performed by using equations (20)–(27) in the same manner as in earlier paper by Faghri et al. (1984a). Because of the similarities among equations (16)–(18), it is possible to rewrite them in a common compact form by introducing the abbreviations

$$\Omega = -\alpha(\partial\phi/\partial\eta), \qquad \Theta = -(\partial\phi/\partial\xi) \tag{28}$$

$$\Lambda = \beta(\partial\phi/\partial\xi), \qquad \psi = \beta(\partial\phi/\partial\eta) \tag{29}$$

where ϕ stands for U_η, V, or T. The common form of equations (16)–(18) is

$$\int_1 [(V\phi + \Gamma(\Theta+\psi)]d\eta - \int_3 [V\phi + \Gamma(\Theta+\psi)]d\eta$$

$$\int_2 [(U_\eta\phi + \Gamma(\Omega+\Lambda)]d\xi - \int_4 [U_\eta\phi + \Gamma(\Omega+\Lambda)]d\xi = b \tag{30}$$

where Γ is the diffusion coefficient and is equal to 1 for the momentum equations and 1/Pr for the energy equation. The b term in the η-momentum equation is given by

$$b = -\int_\forall [\alpha(\partial P/\partial\eta) - \beta(\partial P/\partial\xi - B)]d\eta d\xi$$

$$-\int_\forall (V^2(\partial^2\delta/\partial\xi^2) + V(\partial^3\delta/\partial\xi^3) - 2\beta(\partial V/\partial\eta)$$

$$(\partial^2\delta/\partial\xi^2) + 2(\partial V/\partial\xi)(\partial^2\delta/\partial\xi^2)]d\eta d\xi \tag{31}$$

For the ξ-momentum equation, b is given by

$$b = -\int_\forall [(\partial P/\partial\xi) - B - \beta(\partial P/\partial\eta)]d\eta d\xi \tag{32}$$

Finally, b in the energy equation is given by

$$b = \int_\forall (\sigma/\mathrm{Pr})d\eta d\xi \tag{33}$$

Attention will now be focused on the continuity equation (19); the result is

$$\int_1 V\,d\eta + \int_2 U_\eta\,d\xi - \int_3 V\,d\eta - \int_4 U_\eta\,d\xi = 0 \tag{34}$$

The control-volume formulation of the problem is complete. The finite-difference approximation of the integral form of the governing equations is similar to the work documented by Faghri et al. (1984a) and will not be discussed here.

Numerical Solution. The main issue to be dealt with in this section is the specification of the width of the domain $\delta(Y)$, and its derivatives. As seen in Fig. 2(*a*), to represent a realistic duct geometry, the sharp-edged corners are approximated with parabolic curves where l is the half length of the parabolic chord. The exact values of $\delta(Y)$ and its derivatives, are respectively, as follows:

$0 < Y < l/L$ and $1 - l/L < Y < 1$:

$$\delta = \frac{\tan\theta}{2(l/L)}\left[Y^2 + \left(\frac{l}{L}\right)^2\right] \tag{35}$$

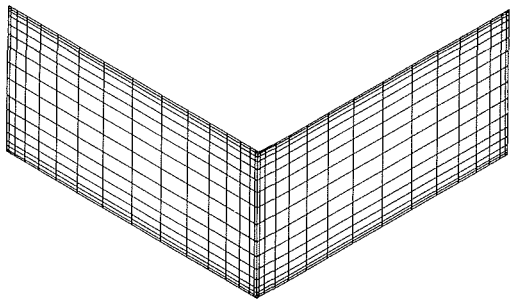

Fig. 3 A typical grid distribution for the main control volume

$$d\delta/dY = \frac{\tan\theta}{(l/L)}\,Y \tag{36}$$

$$d^2\delta/dY^2 = \frac{\tan\theta}{(l/L)} \tag{37}$$

$$d^3\delta/dY^3 = 0 \tag{38}$$

$l/L < Y < 1/2 - (l/L)$:

$$\delta = Y\tan\theta \tag{39}$$

$$d\delta/dY = \tan\theta \tag{40}$$

$$d^2\delta/dY^2 = d^3\delta/dY^3 = 0 \tag{41}$$

$1/2 - (l/L) < Y < 1/2 + (l/L)$:

$$\delta = \frac{-\tan\theta}{2(l/L)}\left[Y^2 - \left(1 - \frac{l}{L}\right)\left(\frac{l}{L}\right)\right] \tag{42}$$

$$d\delta/dY = \frac{-\tan\theta}{(l/L)}\,Y \tag{43}$$

$$d^2\delta/dY^2 = \frac{-\tan\theta}{(l/L)} \tag{44}$$

$$d^3\delta/dY^3 = 0 \tag{45}$$

$1/2 + (l/L) < Y < 1 - (l/L)$:

$$\delta = (1 - Y)\tan\theta \tag{46}$$

$$d\delta/dY = -\tan\theta \tag{47}$$

$$d^2\delta/dY^2 = d^3\delta/dY^3 = 0 \tag{48}$$

where L is the periodic cycle length.

From an examination of the governing equations (4)–(7), it can be seen that there are two parameters whose values have to be specified prior to the initiation of the numerical solutions. These are the Prandtl number Pr, and the dimensionless per-cycle pressure gradient B [equation (3)]. In this paper, values of 0.7, 4, and 8 are selected for Pr, and the values chosen for B are selected in such a way that the calculated Reynolds number range from 100 to 1500. Aside from the Pr and B, there are three geometric parameters which have to be specified. These are the width of the duct H', the duct angle θ, and the periodic cycle length L. If L is used as a reference length, then H'/L and θ need to be specified as geometric parameters. The length of the parabolic section is also a geometric parameter. A very small value is chosen for the length l. The selected values of θ are 15, 30, and 45 deg.

In Fig. 2(*a*), if the lowest points in the top wall and the highest point in the bottom wall lie in the same plane, then $H' = (L/2)\tan\theta$. The selected values of (H'/L) in this work lie in the following range: $\tan\theta/4 \le (H'/L) \le \tan\theta$.

The computations were performed with (18×34) grid points. The grid points in the η and ξ direction were distributed in a nonuniform manner with a higher concentration of grids close to the walls as shown in Fig. 3. This figure represents the main control volumes for $H'/L = 0.2886$ and $\theta = 30$. Each interior control volume contains one grid while

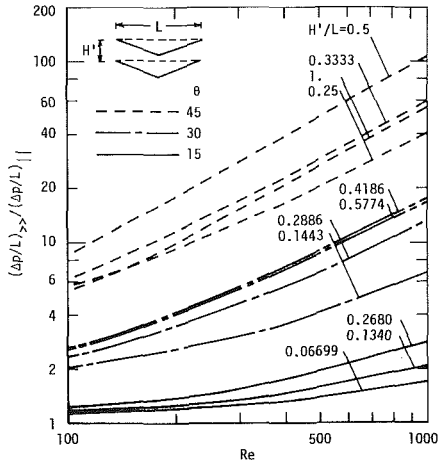

Fig. 4 Comparison of pressure drops for corrugated and straight ducts

the boundary adjacent control volume contains two grid points. Supplementary runs were performed with (26×50) grid points to investigate grid size effects for the case of $\theta = 30$ and $H'/L = 0.1443$. Three values of the nondimensional pressure gradient B were selected in such a way that the calculated Reynolds number range from 100 to 1300. Comparisons of the Nusselt number and pressure drop results were made. The maximum change in the Reynolds and Nusselt numbers, respectively, between the coarse mesh (18×34) and the fine mesh (26×50), were within 3 and 5 percent at an identical pressure gradient. Thus, the coarse mesh (18×34) was chosen to maintain relatively moderate computer costs. The convergence criterion that was used in the computation was that maximum value of mass flux residuals (mass source) in each control volume was less than 10^{-7} percent of the total mass flux. The underrelaxation factor for the velocity and pressure equations was set equal to 0.7 and 0.4, respectively. About 500 iterations were required to obtain a converged solution for the velocity field. The converged velocity field was used as an input to the temperature field calculation which converged within 50 iterations.

The discretized procedure of the transformed equations was based on the power-law scheme (Patankar, 1984). The discretized equations were computed by using a line-by-line method. The pressure was solved by adopting the SIMPLE Algorithm (Patankar, 1984).

Reynolds Number, Pressure Drop Ratio, and Nusselt Number. Attention will now be focused on the calculation of the Reynolds number which will be defined as

$$\mathrm{Re} = 2\dot{m}/\mu \tag{49}$$

where the mass flow $\dot{m}$ is given by

$$\dot{m} = \mu \int_0^{(H'/L)} V dX \tag{50}$$

The definition for the Reynolds number is consistent with the standard definition.

Since the velocity V depends parametrically on the dimensionless parameter B, equation (49) gives a relationship between B and Re.

Another quantity of interest is the calculation of the pressure drop. It is of practical interest to compare this quantity with the corresponding value obtained for the straight duct (plane Poiseuille flow). This ratio can be expressed as follows:

$$(\Delta p/L)_{\gg}/(\Delta p/L)_{\parallel} = [B/(6\,\mathrm{Re})](H'/L)^3 \tag{51}$$

where $\gg$ and $\parallel$ refer to the corrugated duct and straight duct, respectively.

Finally, the cycle average Nusselt number is obtained by

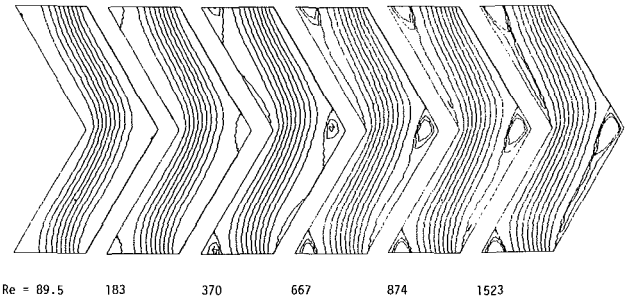

Fig. 5 Streamline diagrams for $H'/L = 0.2886$ and parameters $\theta = 30$ and Re

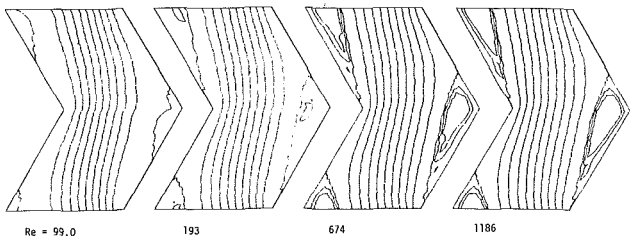

Fig. 6 Streamline diagrams for $H'/L = 0.5774$ and parameters $\theta = 30$ and Re

$$\mathrm{Nu} = h(2H')/k \tag{52}$$

where

$$h = Q/A_w(\overline{t_w - t_b}) \tag{53}$$

and A_w is the per-cycle transfer surface area, approximately equal to $2L/\cos\theta$; Q is the rate of heat transfer from both walls to the fluid per cycle; and $\overline{t_w - t_b}$ is the average bulk-to wall temperature difference. The log-mean temperature difference is used to evaluate $\overline{t_w - t_b}$. The log-mean temperature difference $\overline{t_w - t_b}$ is given by

$$\overline{t_w - t_b} = (t_w - t_b)_{Y=0}(1 - e^{\int_0^1 \lambda dy})/\left(-\int_0^1 \lambda dY\right)$$

The Nusselt number expression that is obtained by assuming a log-mean temperature difference is as follows:

$$\mathrm{Nu} = -(2L/A_w)\left(\int_0^1 \lambda dY\right)(H'/L)\left[(\mathrm{RePr}/2) - \int_0^{(H'/L)} (\lambda T + \partial T/\partial Y)dX\right] \tag{54}$$

Results and Discussion

Representative results for the pressure drop ratios are plotted as a function of the Reynolds number in Fig. 4 with θ and H'/L as curve parameters. These ratios are determined numerically by dividing Δp for the corrugated duct to the corresponding values for straight duct (plane Poiseuille flow), whose equivalent height is H' and length is L. For this case, the mass flow $\dot{m}$ for the corrugated duct and the straight duct is the same. Therefore, the Reynolds numbers are the same for the two geometries. The pressure drop ratios are greater than one as is expected and increase with the corrugation angle θ. When θ is 30 and 45, the pressure ratios take a maximum value somewhere in the middle range of the parameter values of H'/L.

The streamline maps obtained from the solution are presented in Figs. 5 and 6. These figures are for $H'/L = 0.2886$ and 0.5774, respectively, and cover the Reynolds number range from about 90 to 1500. As seen in Fig. 5, at low Reynolds numbers, small separation bubbles can be seen at the corners. A second separation bubble can be seen at the rear-

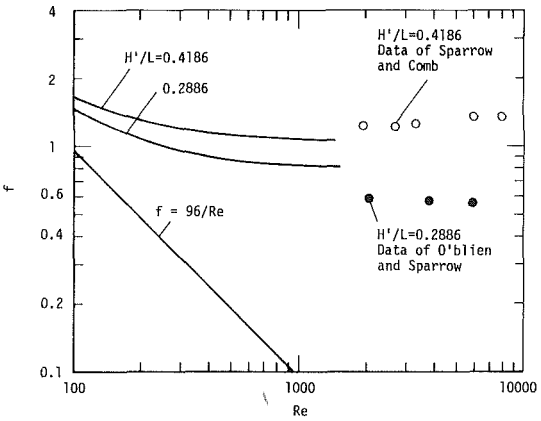

Fig. 7 Comparison of friction factors with experimental data for $\theta = 30$

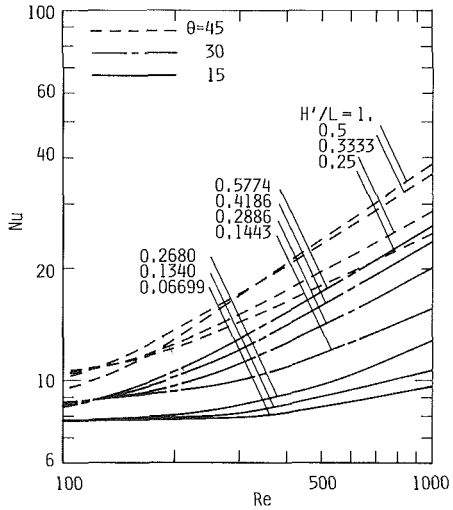

Fig. 8 Comparison of Nusselt numbers for corrugated and straight ducts (Pr = 0.7)

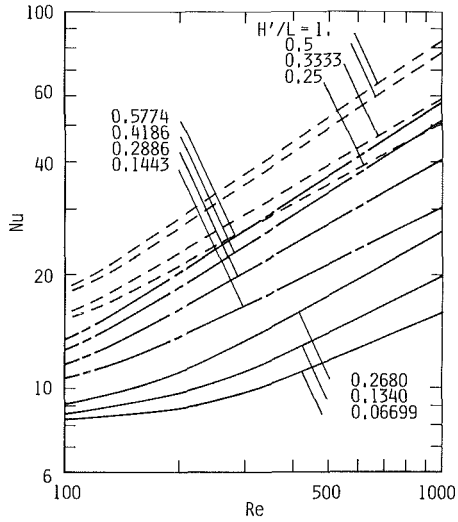

Fig. 9 Comparison of Nusselt numbers for corrugated and straight ducts (Pr = 4)

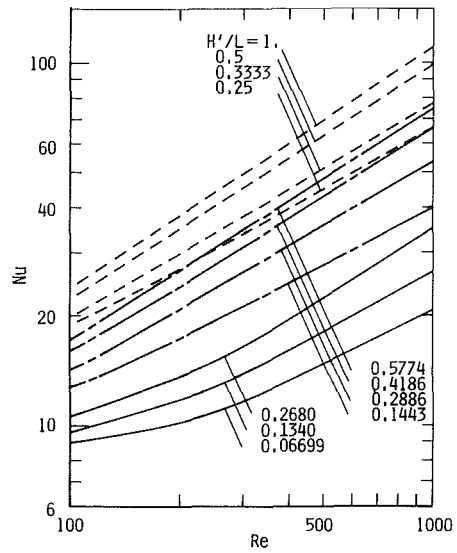

Fig. 10 Comparison of Nusselt numbers for corrugated and straight ducts (Pr = 8)

facing facet for Re = 370. The latter two separation bubbles combine with each other to wash the entire rear-facing facet at Reynolds number greater than 667. This is because the fluid is unable to turn sufficiently sharply to follow the wall at higher Reynolds number. Similar patterns of streamlines are seen in Fig. 6 for the case of $H'/L = 0.5774$, except in this case, small bubbles cannot be seen.

Figure 7 shows the average friction factor f as a function of Reynolds number. The experimental data of Sparrow and Comb (1983), and O'Brien and Sparrow (1982) for turbulent flows and for the same values of H'/L are also depicted in this figure. There are different definitions of the friction factor f. In this paper, the Darcy friction factor definition is used as

$$f = \frac{\overline{(-dp/dy)}(2H)}{(1/2)\rho\bar{v}^2} \tag{55}$$

where $\bar{v} = \dot{m}/\rho H$. The term $\overline{(-dp/dy)}$ represents the average per-cycle pressure gradient. Then $(-dp/dy)$ can be replaced by $\dot{p}$. Therefore, the friction factor f can be expressed as follows:

$$f = \frac{16B}{\mathrm{Re}^2}\left(\frac{H}{L}\right)^3 \tag{56}$$

It is seen from this figure that the range of Reynolds number of the computations does not coincide with that of the experiment. Therefore, no direct comparisons can be made. It is noteworthy to observe that the friction factors for a corrugated duct are higher than that for a straight duct (i.e., 96/Re). Furthermore, they level off at higher Reynolds number values.

Results for the periodic fully developed Nusselt number, as a function of the Reynolds number, are plotted in Figs. 8, 9, and 10 with θ and H'/L as curve parameters. The Nusselt number is determined using equation (54), where log-mean temperature difference is used. It is useful to note that the value for the Nusselt number for the fully developed straight duct is 7.54 and is independent of both the Reynolds and Prandtl numbers. The periodic fully developed Nusselt numbers are greater than 7.54. The trends are that at higher Reynolds numbers the periodic fully developed Nusselt numbers are extremely higher than 7.54. Also, they increase with increasing the duct angle θ, the Prandtl number Pr and H'/L. The only exception is for the case of $\theta = 45$ and Pr = 0.7 where Nu is decreasing with the increase in H'/L at low Reynolds number values.

The periodic fully developed Nusselt number for $\theta = 45$ and Pr = 0.7 is compared with the experimental data obtained by Izumi et al. (1982) and the computed results obtained by Amano (1984) in Fig. 11. It should be noted that Nu* is based on the interwall spacing $2H$ (measured perpendicular to the walls). Therefore, it can be expressed in terms of the Nusselt

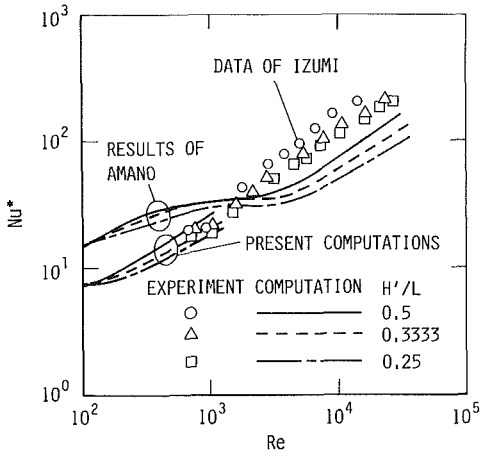

Fig. 11 Comparison of Nusselt numbers with previous data for θ = 45 and Pr = 0.7

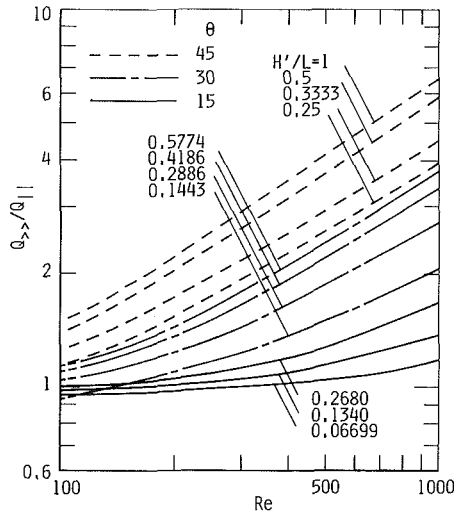

Fig. 12 Heat transfer rate ratios as a function of $Re_{>>}$ for identical pumping power (Pr = 0.7)

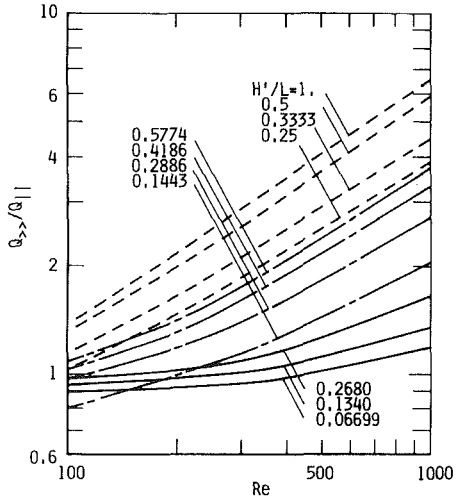

Fig. 13 Heat transfer rate ratios as a function of $Re_{>>}$ for identical pressure drop per cycle (Pr = 0.7)

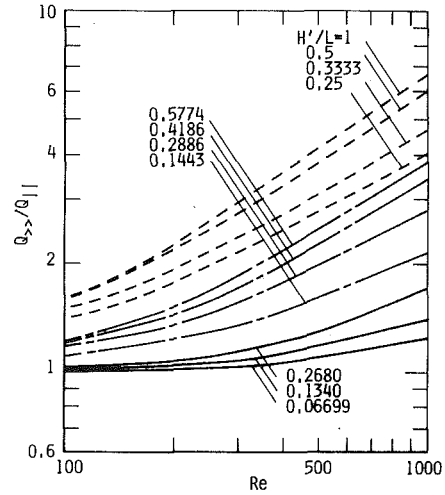

Fig. 14 Heat transfer rate ratios as a function of $Re_{>>}$ for identical mass flow (Pr = 0.7)

number Nu defined in equation (52) as Nu* = Nu cos θ. Data of Izumi et al. (1982) were obtained for air and the log-mean temperature difference is used to determine the Nusselt number.

In appraising the performance of the corrugated duct configuration relative to the corresponding value for a straight duct whose interwall spacing is H' and length is L, comparisons will be made for three different constraints: (I) identical pumping power PP, (II) identical pressure drop per-cycle $\Delta p/L$, and (III) identical mass flow rate $\dot{m}$. The pumping power is equal to the product of the pressure drop and the volume flow, so that $PP \sim \dot{m}(\Delta p/L)$. The heat transfer rate from the walls to the fluid per cycle, Q, is obtained by equations (52), (53), and (54) as follows:

$$Q = K(t_w - t_b)_{Y=0}(1-\gamma)\left[\mathrm{Re\,Pr}/2 - \int_0^{(H'/L)} (\lambda T + \partial T/\partial Y)dX\right] \tag{57}$$

where the bulk-to-wall temperature ratio γ is obtained by integrating equation (9) as

$$\gamma = \frac{(t_w - t_b)_{Y=1}}{(t_w - t_b)_{Y=0}} = e^{\int \lambda dY} \tag{58}$$

The heat transfer rate ratios for three different constraints are plotted as a function of Reynolds number in Figs. 12, 13, and 14 with θ and H'/L as curve parameters for Pr = 0.7. The ratios are determined numerically by dividing Q for the corrugated duct by the corresponding values for the straight duct of length L. In case of the identical pumping power, the dimensionless form of the relation $\dot{m}_{>>}(\Delta p/L)_{>>} = \dot{m}_{\parallel}(\Delta p/L)_{\parallel}$ is expressed by

$$\mathrm{Re}_{>>} B_{>>} = \mathrm{Re}_{\parallel} B_{\parallel} \tag{59}$$

Substituting the relation between $\mathrm{Re}_{\parallel}$ and $B_{\parallel}$ of the straight duct, i.e., $B_{\parallel} = 6\,\mathrm{Re}_{\parallel}/(H'/L)^3$, into equation (59), one can obtain the Reynolds number for the straight duct whose pumping power is equal to that of the corrugated duct as

$$\mathrm{Re}_{\parallel} = \left[\frac{(H'/L)^3 \mathrm{Re}_{>>} B_{>>}}{6}\right]^{1/2} \tag{60}$$

Therefore, the mass flow rate, $\dot{m}_{>>}/\dot{m}_{\parallel}$, and the pressure drop ratio, $(\Delta p/L)_{>>}/(\Delta p/L)_{\parallel}$, are obtained by equations (59) and (60) as follows:

$$\dot{m}_{>>}/\dot{m}_{\parallel} = \mathrm{Re}_{>>}/\mathrm{Re}_{\parallel} = \left[\frac{6\,\mathrm{Re}_{>>}}{(H'/L)^3 B_{>>}}\right]^{1/2} \tag{61}$$

$$(\Delta p/L)_{>>}/(\Delta p/L)_{\parallel} = B_{>>}/B_{\parallel} = \left[\frac{(H'/L)^3 B_{>>}}{6\,\mathrm{Re}_{>>}}\right]^{1/2} \tag{62}$$

In case of identical pressure drop per cycle, the Reynolds number of the straight duct can be expressed as

$$\mathrm{Re}_{\parallel} = (B_{\parallel}/6)(H'/L)^3 = (B_{>>}/6)(H'/L)^3 \quad (63)$$

Therefore, the mass flow ratio and the pumping power ratio are expressed by

$$\dot{m}_{>>}/\dot{m}_{\parallel} = PP_{>>}/PP_{\parallel} = \mathrm{Re}_{>>}/\mathrm{Re}_{\parallel}$$
$$= \mathrm{Re}_{>>}/[(B_{>>}/6)(H'/L)^3] \quad (64)$$

In case of identical mass flow rate, the Reynolds number of the straight duct can be expressed by

$$\mathrm{Re}_{\parallel} = \mathrm{Re}_{>>} \quad (65)$$

The pressure drop per-cycle ratio and the pumping power ratio can then be expressed as

$$(\Delta p/L)_{>>}/(\Delta p/L)_{\parallel} = PP_{>>}/PP_{\parallel} = B_{>>}/B_{\parallel}$$
$$= [B_{>>}/(6\ \mathrm{Re}_{>>})](H'/L)^3 \quad (66)$$

As seen from Figs. 12 and 13, the heat transfer rate ratios under identical pumping power and identical pressure drop per cycle are greater than or less than one, depending on the value of θ and H'/L at low Reynolds number values. However, the heat transfer rate ratio under identical mass flow, as seen in Fig. 14, is always greater than one. There are small differences among these heat transfer rate ratios under the three different constraints. This is because the heat transfer rate of the straight duct is insensible to the mass flow rate.

Concluding Remarks

A finite volume methodology was developed to predict periodic fully developed heat transfer coefficient, friction factors, and streamlines in a corrugated duct. A nonorthogonal coordinate transformation was employed which mapped the irregular solution domain onto a rectangle. The Nusselt number results were compared with the available results in the literature. Finally, from a performance analysis model, it was found that there are small differences in the heat transfer rate ratios under the different constraints – fixed pumping power, fixed pressure drop, and fixed mass flow rate.

References

1 Amano, R. S., 1984, "A Numerical Study of Laminar and Turbulent Heat Transfer in a Corrugated Wall Channel," *Proceedings of the ASME/AIChE National Heat Transfer Conference*, Paper No. 84-HT-73.

2 Faghri, M., Sparrow, E. M., and Prata, A. T., 1984a, "Finite Difference Solutions of Convection-Diffusion Problems in Irregular Domains Using a Non-Orthogonal Coordinate Transformation," *Numerical Heat Transfer*, Vol. 7, pp. 183–209.

3 Faghri, M., 1984b, "Slot Jet Impingement on a Cylinder," *Proceedings of the ASME/AIChE Heat Transfer Conference*, Paper No. 84-HT-7.

4 Faghri, M., and Asako, Y., 1984c, "Numerical Determination of Heat Transfer and Pressure Drop Characteristics for Converging-Diverging Flow Channel," *Proceedings of ASME Winter Annual Meeting*, Paper No. 84-WA/HT-12.

5 Izumi, R., Yamashita, H., Kaga, S., and Miyazima, N., 1982, "Fluid Flow and Heat Transfer in Corrugated Wall Channels – Experimental Study for Many Bends," 19th National Heat Transfer Symposium of Japan, Paper No. A101.

6 O'Brien, J. E., and Sparrow, E. M., 1982, "Corrugated-Duct Heat Transfer, Pressure Drop and Flow Visualization," ASME JOURNAL OF HEAT TRANSFER, Vol. 104, pp. 410–416.

7 Sparrow, E. M., and Comb, J. W., 1983, "Effect of Interwall Spacing and Fluid Flow Inlet Conditions on Corrugated-Wall Heat Exchanger," *International Journal of Heat and Mass Transfer*, Vol. 26, No. 7, pp. 993–1005.

8 Patankar, S. V., 1981, "A Calculation Procedure for Two-Dimensional Elliptic Situations," *Numerical Heat Transfer*, Vol. 4, pp. 409–425.

Fluid Motion and Heat Transfer of a High-Viscosity Fluid in a Rectangular Tank on a Ship With Oscillating Motion

S. Akagi
Professor,
Department of Mechanical Engineering,
Osaka University,
Suita, Osaka, Japan
Mem. ASME

K. Uchida
Engineer,
Matsushita Electric Co. Ltd.,
Kadoma, Osaka, Japan

Fluid motion and heat transfer of a high-viscosity fluid contained in a two-dimensional rectangular ship's tank subjected to oscillating motion are investigated by a finite difference technique. The study is motivated by the thermal design of the heating system of oil tanks on a tanker which is moving in a wavy sea. The bottom of the tank is heated and its side walls are cooled. The motion of the tank is assumed to be a simple harmonic rolling motion. The isotherms and flow velocity vectors are determined by numerical solutions of the basic equations describing the convection flows in a tank with oscillating motion. The heat transfer rates to the tank walls are predicted. The influence of the frequency of the oscillating motion on the heat transfer rate is examined.

1 Introduction

Although natural convection in enclosures has been extensively studied in recent years [1–3], the fluid motion and heat transfer driven by the combined effects of oscillating motion of walls and natural convection in enclosures have received little attention. Yet this particular problem is of practical importance since it appears in heating oil tanks of tankers which are moving in a wavy sea.

High-viscosity fluids such as oil cargoes stored in a ship's tanks are often heated by means of steam heating tubes embedded in the tank so as to maintain their viscosities low enough for easy pumping. Good understanding of the heat transfer process involving the heat transfer rate to the tank walls is important for the thermal design of the heating system to predict the heating load on a ship's boilers, which must supply the steam. Natural convection in such a tank is expected to be strongly affected by the oscillating flows induced by the ship's motion. However, little knowledge has been obtained for this kind of heat transfer problem. The problem is interesting not only from a practical point of view but also from that of the fundamental heat transfer problem.

In this investigation, heat transfer calculations are performed for a two-dimensional ship's tank filled with a high-viscosity fluid when the oscillating motion of the tank is induced by the rolling of a ship in waves. The governing equations for the heat transfer problem are formulated, then numerical solutions are provided using a finite difference technique. The flow and temperature fields in the tank are determined from the numerical solutions. Finally, Nusselt numbers are given for the rate of heat transfer from the fluid to the tank walls during the oscillating motion of the tank.

2 Problem Statement

2.1 Mathematical Formulation. The geometry of the tank and the heating system under investigation is shown in Fig. 1. The ship's tank is assumed to be two dimensional. The boundary conditions are that the bottom of the tank is heated, both side walls are cooled, and the tank top is insulated. The tank is completely filled with a viscous fluid, and is assumed to be initially motionless. The fluid in the tank is also assumed to have an initial uniform temperature T_0.

The natural convection heating is started and continued using a bottom heater at temperature T_w. The temperature of both side walls of the tank is kept at T_0 during the heating. The heating is continued until the mean temperature of the fluid approaches the mean of T_w and T_0. Then, the rolling motion of the ship begins. The motion of the tank is assumed to be a simple harmonic motion around the tank center C as shown in Fig. 1.

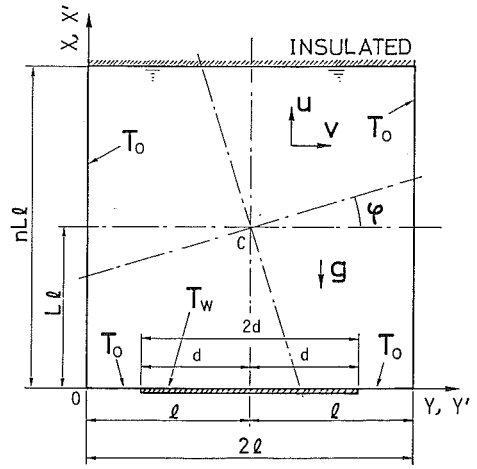

Fig. 1 Coordinate system

The above assumptions are based on the following considerations. Considering the overall thermal resistance of the heat transfer from the heated fluid to the sea water, the thermal resistance inside the tank wall is much higher than that of the outside tank wall or of the tank wall plate. The heat transfer coefficient of the inside tank wall is of the order of 10 W/m^2K or less. On the other hand, that of the water side reaches the order of 5000 ~ 10,000 W/m^2K. This means that the overall thermal resistance is influenced mainly by the heat transfer inside the tank. Thus, the side walls are at a uniform temperature T_0, which is nearly equal to the temperature of the sea water.

The value of the heat transfer coefficient from the tank top to the atmosphere is difficult to estimate because it is strongly influenced by weather conditions, including solar radiation. Therefore, in this calculation, the tank top is assumed to be insulated for simplicity.

The position of the water line of the ship is not specified here. It has been assumed that the side wall is maintained at a

Contributed by the Heat Transfer Division for publication in the JOURNAL OF HEAT TRANSFER. Manuscript received by the Heat Transfer Division September 17, 1984.

uniform temperature T_0, that of the sea water, from the level of the tank top to the bottom because the full-loaded tanker usually has a very small freeboard compared with its draft.

The axis of rotation of a ship is usually taken at the metacenter. In this calculation, however, it is assumed to be at the center of the tank because the tank is assumed to be loaded to the top. The motion amplitude φ of the tank around the center point C due to the ship's motion is given by

$$\varphi = -\bar{\varphi}\cos\omega t \tag{1}$$

where $\bar{\varphi}$ is the maximum amplitude, and ω is the motion frequency.

Two different kinds of coordinate systems are defined as shown in Fig. 1. The space-fixed coordinate system is represented as x–y, and the body-fixed coordinate system is represented as x'–y'. The relationship between the coordinate systems is given by

$$\begin{pmatrix} y-l \\ x-Ll \end{pmatrix} = \begin{pmatrix} \cos\varphi, & -\sin\varphi \\ \sin\varphi, & \cos\varphi \end{pmatrix} \begin{pmatrix} y'-l \\ x'-l \end{pmatrix} \tag{2}$$

If the value of amplitude φ is small, then equation (2) can be approximated as

$$x \simeq x', \qquad y \simeq y' \tag{3}$$

In the usual geometric meaning, this approximation is reasonable for angles less than 10 deg. Actually, calculations show the approximation to be permissible to larger angles of inclination of the tank for the cases of fluid dynamic motion considered here.

Differentiating equation (2) with respect to t and using $\cos\varphi \simeq 1$ and $\sin\varphi \simeq \varphi$, the following equations can be obtained:

$$u \simeq u' + v'\varphi + (y'-l)\dot{\varphi} - (x'-Ll)\dot{\varphi}\varphi \tag{4a}$$

$$v \simeq v' - u'\varphi - (x'-Ll)\dot{\varphi} - (y'-l)\dot{\varphi}\varphi \tag{4b}$$

where u and v are velocity components corresponding to the coordinates x and y, respectively. Velocity components u' and v' correspond to x' and y', respectively. If the terms with the order of φ are neglected in equations (4a) and (4b), they can be approximated as follows. Rewriting the term φ using equation (1) yields

$$u \simeq u' + (y'-l)\omega\bar{\varphi}\sin\omega t \tag{5a}$$

$$v \simeq v' - (x'-Ll)\omega\bar{\varphi}\sin\omega t \tag{5b}$$

The basic equations for convection flow can be introduced using the above assumptions. The continuity equations and Navier–Stokes equations are represented by a space-fixed coordinate system to simplify the equations. If a body(tank)-fixed coordinate system is used, the equations become much more complicated because centrifugal acceleration and angular acceleration terms as well as a Coriolis acceleration term must be included. On the other hand, the energy equation is represented here by the body(tank)-fixed coordinate system to define the fluid temperature distribution in the tank. Considering the above, the governing equations become the following:

The continuity equation with the space-fixed coordinate system

$$\frac{\partial u}{\partial x} + \frac{\partial v}{\partial y} = 0 \tag{6}$$

The Navier–Stokes equations with the space-fixed coordinate system

$$\frac{\partial u}{\partial t} + u\frac{\partial u}{\partial x} + v\frac{\partial u}{\partial y} = -\frac{1}{\rho}\frac{\partial p}{\partial x} - g\{1-\beta(T-T_0)\} + \frac{2}{\rho}\frac{\partial}{\partial x}\left\{\mu\frac{\partial u}{\partial x}\right\} + \frac{1}{\rho}\frac{\partial}{\partial y}\left\{\mu\left(\frac{\partial v}{\partial x}+\frac{\partial u}{\partial y}\right)\right\} \tag{7}$$

$$\frac{\partial v}{\partial t} + u\frac{\partial v}{\partial x} + v\frac{\partial v}{\partial y} = -\frac{1}{\rho}\frac{\partial p}{\partial y} + \frac{2}{\rho}\frac{\partial}{\partial y}\left\{\mu\frac{\partial v}{\partial y}\right\} + \frac{1}{\rho}\frac{\partial}{\partial x}\left\{\mu\left(\frac{\partial v}{\partial x}+\frac{\partial u}{\partial y}\right)\right\} \tag{8}$$

The energy equation with the body-fixed coordinate system

$$\frac{\partial T'}{\partial t} + u'\frac{\partial T'}{\partial x'} + v'\frac{\partial T'}{\partial y'} = \alpha\left(\frac{\partial^2 T'}{\partial x'^2} + \frac{\partial^2 T'}{\partial y'^2}\right) \tag{9}$$

Equations (6)–(9) are coupled with the relations given by equations (3) and (5). Moreover, using the assumption given by equation (3), the coordinates (x, y) and (x', y') become common among equations (6)–(8) and (9). Therefore, the relation between the temperature T and T' in equations (7) and (9) becomes

$$T'(x', y', t) \approx T'(x, y, t) = T(x, y, t) \tag{10}$$

Using equation (10), equation (9) can be rewritten as

$$\frac{\partial T}{\partial t} + u'\frac{\partial T}{\partial x} + v'\frac{\partial T}{\partial y} = \alpha\left(\frac{\partial^2 T}{\partial x^2} + \frac{\partial^2 T}{\partial y^2}\right) \tag{11}$$

Equations (6)–(8) can now be solved using equation (11) together with equation (5). In equations (7)–(9), the thermal diffusivity α and the density ρ of the high-viscosity fluid are assumed to be constant evaluated at the mean temperature $T_m = (T_w + T_0)/2$ except for the buoyancy term, because they are almost invariable with temperature [4]. However, the viscosity μ of the high-viscosity fluid varies steeply with temperature [4]. Therefore, μ is assumed to be a function of temperature T as will be discussed later in detail.

Nomenclature

b = constant in fluid variable viscosity equation
d = half width of the heating element
g = gravitational acceleration
h = mean heat transfer coefficient at the tank side wall
k = thermal conductivity of fluid
K = μ/μ_0 = dimensionless viscosity
l = half height of the tank
N = gl^3/α^2 = dimensionless gravitational acceleration
Nu = $h(2l)/k$ = Nusselt number
p = pressure of fluid
P = $p/(\rho gl)$ = dimensionless pressure of fluid
Pr = ν_0/α = Prandtl number
Q = heat transfer rate to the tank side wall
Ra = $gB(T_w - T_0)(2l)^3/(\nu_0\alpha)$ = Rayleigh number
Ra_l = $gB(T_w - T_0)l^3/(\nu_0\alpha)$ = Rayleigh number defined by l
Re = $\omega l^2\bar{\varphi}/\nu_0$ = Reynolds number
t = time
T = temperature
T^* = similarity parameter defining temperature difference ratio
T_∞ = constant in fluid variable viscosity equation
u, v = velocity components in the x and y directions, respectively
U, V = $u/(\omega l)$, $v/(\omega l)$ = dimensionless velocity components corresponding to u and v, respectively
u', v' = velocity components in the x' and y' directions, respectively
U', V' = $u'/(\omega l)$, $v'/(\omega l)$ =

The above equations (6)–(8) and (11) are transformed into the following dimensionless form:

$$\frac{\partial U}{\partial X}+\frac{\partial V}{\partial Y}=0 \tag{12}$$

$$\frac{\partial U}{\partial \tau}+U\frac{\partial U}{\partial X}+V\frac{\partial U}{\partial Y}=-\frac{N}{\omega^{*2}}\frac{\partial P}{\partial X}-\frac{N}{\omega^{*2}}+\frac{\mathrm{PrRa}_l}{\omega^{*2}}\theta$$
$$+\frac{\mathrm{Pr}}{\omega^*}\left[2\frac{\partial}{\partial X}\left(K\frac{\partial U}{\partial X}\right)+\frac{\partial}{\partial Y}\left\{K\left(\frac{\partial V}{\partial X}+\frac{\partial U}{\partial Y}\right)\right\}\right] \tag{13}$$

$$\frac{\partial V}{\partial \tau}+U\frac{\partial V}{\partial X}+V\frac{\partial V}{\partial Y}=-\frac{N}{\omega^{*2}}\frac{\partial P}{\partial Y}$$
$$+\frac{\mathrm{Pr}}{\omega^*}\left[2\frac{\partial}{\partial Y}\left(K\frac{\partial U}{\partial X}\right)+\frac{\partial}{\partial X}\left\{K\left(\frac{\partial V}{\partial X}+\frac{\partial U}{\partial Y}\right)\right\}\right] \tag{14}$$

The parameter Pr/ω^* included in equations (13) and (14) is proportional to the inverse of the Reynolds number Re

$$\mathrm{Re}\equiv(\omega\bar{\varphi}l)\cdot l/\nu_0=(\omega l^2/\alpha)\bar{\varphi}(\alpha/\nu_0)=\omega^*\bar{\varphi}/\mathrm{Pr} \tag{15}$$

Therefore

$$\mathrm{Pr}/\omega^*=\bar{\varphi}/\mathrm{Re} \tag{16}$$

The equations (12)–(14) can be transformed into the following form using a vorticity Ω and a stream function ψ by eliminating the pressure term P and the gravity term N from equations (13) and (14). Namely,

$$\frac{\partial \Omega}{\partial \tau}+U\frac{\partial \Omega}{\partial X}+V\frac{\partial \Omega}{\partial Y}=-\frac{\mathrm{PrRa}_l}{\omega^*}\frac{\partial \theta}{\partial Y}$$
$$+\frac{\mathrm{Pr}}{\omega^*}\nabla^2(K\Omega)+\frac{\mathrm{Pr}}{\omega^*}A \tag{17}$$

$$-\Omega=\nabla^2\psi \tag{18}$$

where

$$U=\frac{\partial \psi}{\partial Y},\qquad V=-\frac{\partial \Psi}{\partial X} \tag{19}$$

$$A=2\left(\frac{\partial^2 K}{\partial X^2}\frac{\partial U}{\partial X}+2\frac{\partial^2 K}{\partial X\partial Y}\frac{\partial V}{\partial Y}-\frac{\partial^2 K}{\partial Y^2}\frac{\partial V}{\partial X}\right) \tag{20}$$

Equation (11) can also be transformed into dimensionless form

$$\frac{\partial \theta}{\partial \tau}+U'\frac{\partial \theta}{\partial X}+V'\frac{\partial \theta}{\partial Y}=\frac{1}{\omega^*}\nabla^2\theta \tag{21}$$

where U' and V' can be expressed using equation (5) as

$$\begin{aligned}U' &= U-(Y-1)\bar{\varphi}\sin\tau\\ V' &= V+(X-L)\bar{\varphi}\sin\tau\end{aligned} \tag{22}$$

The dimensionless viscosity term K included in equations (17) and (20) can be represented by the viscosity–temperature relation for a high-viscosity fluid given by Vogel [4], namely,

$$\mu=\mu_\infty e^{b/(T-T_\infty)} \tag{23}$$

where μ is the viscosity of a fluid at the temperature T. The constants μ_∞, b, and T_∞ depend on the fluid.

From equation (23), the dimensionless viscosity K can be expressed as

$$K=\frac{\mu}{\mu_0}=\left(\frac{\mu_w}{\mu_0}\right)^{(1+T^*)\theta/(1+T^*\theta)} \tag{24}$$

where μ_w and μ_0 represent viscosities corresponding with temperatures T_w and T_0, respectively. The dimensionless temperature T^* in equation (24) is given by

$$T^*=(T_w-T_0)/(T_0-T_\infty) \tag{25}$$

The parameters μ_w/μ_0 and T^* in equation (24) are similarity parameters which define the effect of viscosity variation with temperature on the heat transfer.

2.2 Initial and Boundary Conditions. The initial conditions for equations (17)–(21) are determined from the pure natural convection condition before oscillation begins. The calculation of pure natural convection is done with the assumption that the fluid contained in the tank is heated by the bottom heater until a steady-state condition has been reached, and then the ship begins to roll. The calculation procedure for pure natural convection is similar to that of Torrance and Rockett [5]. A calculated result will be shown later, but details of the calculation for the pure natural convection [6] are omitted here.

The boundary conditions are determined by the assumptions that the relative velocity components U' and V' are zero at each wall of the tank, in addition to the thermal condition at each wall. Namely,

(*I*) $Y=0$ (*at the left wall shown in Fig. 1*)

$$U=-\bar{\varphi}\sin\tau,\quad V=-(X-L)\bar{\varphi}\sin\tau;\quad \theta=0 \tag{26}$$

(*II*) $Y=2$ (*at the right wall*)

$$U=\bar{\varphi}\sin\tau,\quad V=-(X-L)\bar{\varphi}\sin\tau,\quad \theta=0 \tag{27}$$

(*III*) $X=0$ (*at the tank bottom*)

$$U=(Y-1)\bar{\varphi}\sin\tau,\quad V=L\bar{\varphi}\sin\tau,$$
$$\theta=1\ \text{(heating surface)},\quad \theta=0\ \text{(cooling surface)} \tag{28}$$

Nomenclature (cont.)

dimensionless velocity components corresponding to u' and v', respectively
x, y = space-fixed coordinates
x', y' = body-fixed coordinates
X, Y = x/l, y/l = dimensionless coordinates corresponding to x and y, respectively
X', Y' = x'/l, y'/l = dimensionless coordinates corresponding to x' and y', respectively
α = thermal diffusivity of fluid
β = thermal expansion coefficient of fluid
θ = $(T-T_0)/(T_w-T_0)$ = dimensionless temperature
$\bar{\theta}$ = dimensionless mean temperature in the tank
μ = viscosity of fluid
μ_∞ = constant in fluid variable viscosity equation
μ_w/μ_0 = similarity parameter defining viscosity ratio
ν = kinematic viscosity of fluid
ρ = mass density of fluid
τ = ωt = dimensionless time
φ = amplitude of oscillation of the tank
$\bar{\varphi}$ = maximum amplitude of oscillation of the tank
ψ = dimensionless stream function
ω = frequency of oscillation of the tank
ω^* = $\omega l^2/\alpha$ = dimensionless frequency of oscillation of the tank
Ω = dimensionless vorticity function

Subscripts

0 = cooled surface
w = heated surface
R, L = right and left side of the tank wall, respectively

(*IV*) $X = nL$ (*at the tank top*)

$$U = (Y-1)\bar{\varphi}\sin\tau, \quad V = -(n-1)L\bar{\varphi}\sin\tau, \quad \partial\theta/\partial X = 0. \tag{29}$$

The stream function at the tank wall is determined so as to satisfy the velocity boundary conditions given by equations (26)–(29). A square tank ($n=2$, $L=1$) is assumed here for the calculation. The stream function ψ at the tank wall is given by

$$\psi = \left\{\frac{(X-1)^2}{2} + \frac{(Y-1)^2}{2} - \frac{1}{2}\right\}\bar{\varphi}\sin\tau \tag{30}$$

The velocity components at the walls defined by equations (26)–(29) can be calculated using equation (30). It is ascertained that the velocities given by equation (30) satisfy the values defined by the boundary conditions (26)–(29).

3 Parameter Selection and Solution Procedure

3.1 Parameter Selection. The high-viscosity fluid selected for the calculation was a COM [Coal-Oil Mixture], a fuel alternative consisting of pulverized coal and heavy fuel oil [4]. The viscosity-temperature relation of a COM is similar to many heavy fuel oils.

The values of the constants b, μ_∞, and T_∞ in equation (24) for a COM [4] are

$$\begin{aligned} \mu_\infty &= 5.86 \times 10^{-1}\ [\mathrm{N\cdot s/m^2}] \\ b &= 110.6 \\ T_\infty &= 2.15\ [^\circ\mathrm{C}] \end{aligned} \tag{31}$$

The temperatures of the tank walls were chosen to be $T_w = 150^\circ$C and $T_0 = 30^\circ$C. Using these values, in equation (25) $\mu_w/\mu_0 = 1/25.1$ and $T^* = 4.3$.

The values of the similarity parameters Ra_l, Pr, ω^*, and $\bar{\varphi}$, which appear in equations (18)–(23), are the following:

$$\begin{aligned} &\mathrm{Pr} = 10^3,\ \bar{\varphi} = 25 \text{ deg, and} \\ &\text{①}\ \mathrm{Ra}_l = 10^4;\ \omega^* = 10^4,\ 2\times10^4,\ 10^5,\ 5\times10^5 \\ &\text{②}\ \mathrm{Ra}_l = 10^8;\ \omega^* = 5\times10^6 \end{aligned} \tag{32}$$

3.2 Solution Procedure. Equations (17)–(21), with the initial and boundary conditions given by equations (26)–(29), were solved with a time-marching, finite difference technique. Forward time and central space differences were used, except for the convection terms in equations (17) and (21), for which upwind differencing was employed.

The calculation proceeds by explicitly advancing θ and Ω with difference forms of equations (17) and (21). A difference form of equation (18) is then solved for the new ψ field by a SOR technique. Velocities and vorticities are obtained from the new ψ field using finite difference approximations. Since all fields are then known, the calculations can proceed by further time advancement. The numerical results presented here employed a 21 × 21 mesh or a 41 × 41 mesh for each value of the Rayleigh number.

The result for a Rayleigh number of 10^4 was ascertained to be grid independent, while that for $\mathrm{Ra}_l = 10^8$ might be approximate although it was adequate to examine the temperature distribution in the tank. It is our suspicion that flows at higher Ra_l might require a somewhat finer grid to maintain the finer spatial resolution. Computer time constraint prevented the use of a finer grid.

4 Results

4.1 Flow and Temperature Fields. The computed flow fields and temperature fields in the tank are examined for several Rayleigh numbers Ra_l and dimensionless oscillating frequencies ω^*.

The results for pure natural convection are shown first. Pure natural convection was assumed to begin with an initial

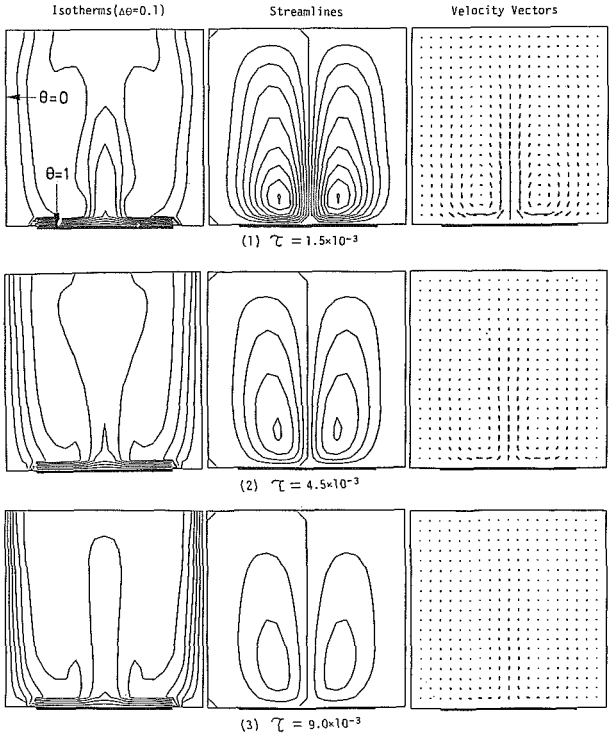

Fig. 2 Time sequence of isotherms, stream lines, and velocity vectors of pure natural convection in the tank ($\mathrm{Ra}_l = 10^4$, $\mathrm{Pr} = 10^3$)

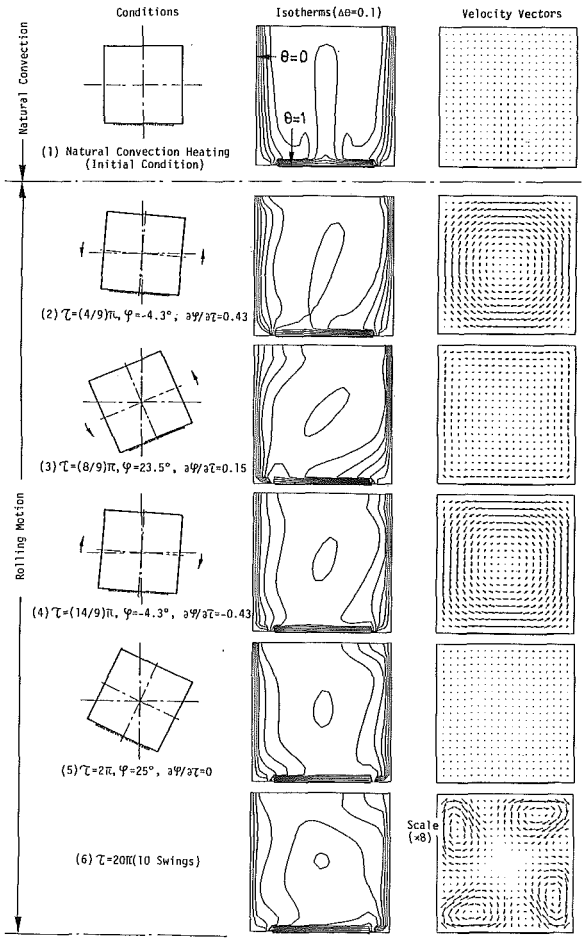

Fig. 3 Time sequence of isotherms and velocity vectors in the tank during natural convection and oscillating motion ($\mathrm{Ra}_l = 10^4$, $\mathrm{Pr} = 10^3$, $\omega^* = 10^5$, $\bar{\varphi} = 25$ deg)

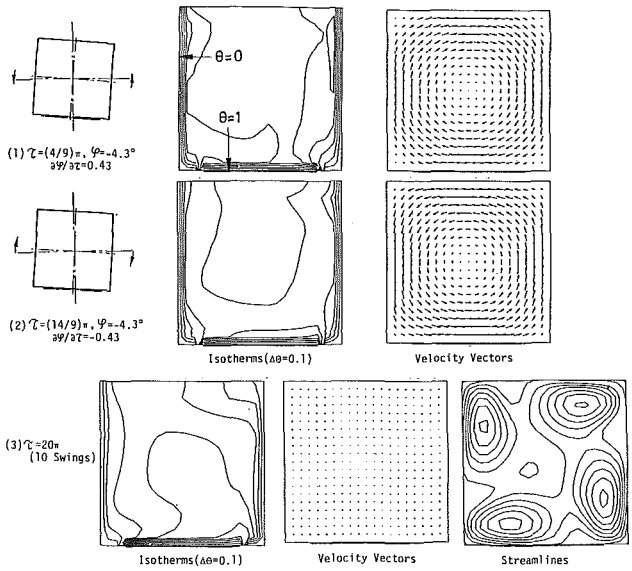

Fig. 4 Isotherms, velocity vectors, and stream lines in the tank ($Ra_l = 10^8$, $Pr = 10^3$, $\omega^* = 5.0 \times 10^6$, $\bar{\varphi} = 25$ deg)

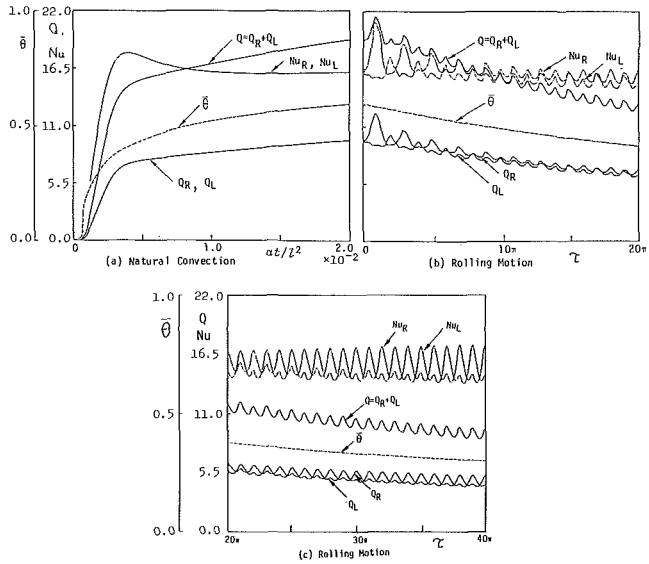

Fig. 6 Heat transfer rate to the side wall Q, mean temperature in the tank $\bar{\theta}$, and Nusselt number at the tank wall Nu during natural convection and oscillating motion ($Ra_l = 10^4$, $Pr = 10^3$, $\omega^* = 10^5$, $\bar{\varphi} = 25$ deg)

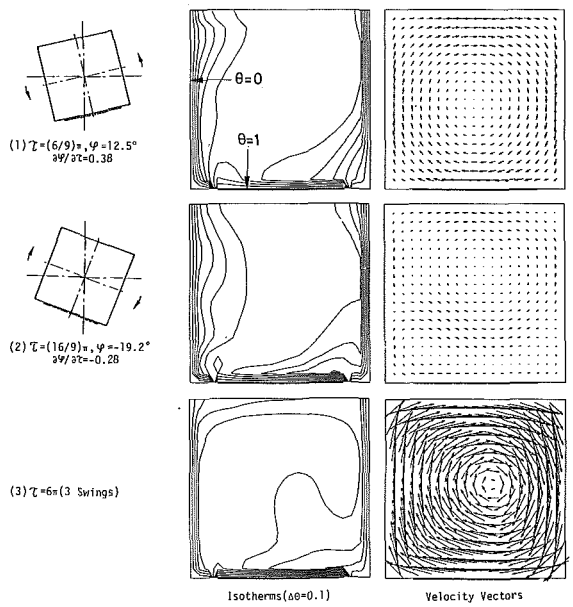

Fig. 5 Isotherms and velocity vectors in the tank ($Ra_l = 10^4$, $Pr = 10^3$, $\omega^* = 10^5$, $\bar{\varphi} = 25$ deg)

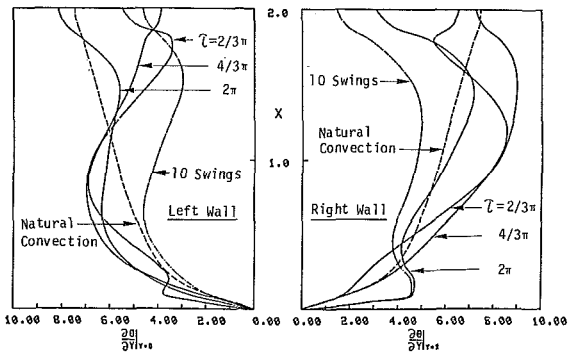

Fig. 7 Heat transfer rate to the side wall for several time steps during oscillating motion ($Ra_l = 10^4$, $Pr = 10^3$, $\omega^* = 10^5$, $\bar{\varphi} = 25$ deg)

uniform temperature in the tank, $\theta = 0$. The temperature of the bottom heater was kept at $\theta = 1$, and the temperature of the side walls of the tank was kept at $\theta = 0$. The convection flow is assumed to be symmetric at the center of the tank.

The calculated isotherms, streamlines, and velocity vectors are illustrated for $Ra_l = 10^4$ and $Pr = 10^3$ in Fig. 2. In Fig. 2, individual graphs from (1) to (3) pertain to a time sequence. It is observed that the heated plume flows up from the bottom toward the tank top, then it flows to each side of the tank. The layer of warm fluid turns the tank corner and flows down along both side tank walls. When the fluid reaches the bottom of the tank, it flows up again due to the bottom heating effect. Thus a circulating flow is formed in the tank. After some time elapses, the circulating flow becomes gradually weaker and the steady-state condition shown in Fig. 2(*c*) is reached. When a steady flow condition has been reached, the oscillating motion of the tank is initiated.

The isotherms and flow velocity vector fields for the oscillating case are illustrated for $Ra_l = 10^4$, $Pr = 10^3$, and $\omega^* = 10^5$ in Fig. 3. The initial value of the temperature and flow velocity distributions in the tank was taken from the condition shown in graph (3) of Fig. 2. Conditions for oscillation are shown to the left of the figure; isotherm fields to the center; and flow velocity vector fields to the right. In Fig. 3, individual graphs from (1) to (6) pertain to a time sequence from $\tau = 0$ (the initial condition) to 20π (10 swings). The maximum oscillating angle was taken to be $\bar{\varphi} = 25$ deg. Oscillating motion was continued to 40π (20 swings) beyond the results shown in graph (6) of Fig. 3. The result of the calculation beyond $\tau = 20\pi$ is shown in Fig. 6(*c*).

As shown in Fig. 3, reciprocal circulating flows relative to the motion of the tank are found. They change their directions of circulation as the motion of the tank reverses. The isotherms fluctuate from side to side of the tank as the flow changes its circulating direction. After 10 swings have passed, isotherms form a small core pattern at the center of the tank as shown in graph (6) of Fig. 3. Vortices are formed at each corner of the tank at the moment when the motion of the tank begins to reverse as shown in graph (6) of Fig. 3.

Figure 4 illustrates similar graphs for the higher Rayleigh number $Ra = 10^8$, $Pr = 10^3$, and $\omega^* = 5.0 \times 10^6$. The isotherms and flow velocity vector fields indicate patterns similar to the case of $Ra = 10^4$ as shown in Fig. 3. The isothermal core at the

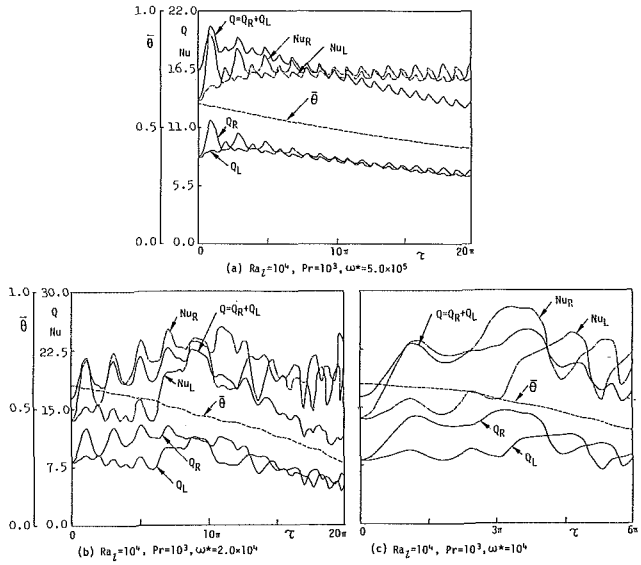

Fig. 8 Heat transfer rate to the side wall Q, mean temperature in the tank $\bar{\theta}$, and Nusselt number at the tank wall Nu for several values of ω^* ($Ra_l = 10^4$, $Pr = 10^3$, $\bar{\varphi} = 25$ deg)

center of the tank shown in Fig. 3 is not observed in Fig. 4, and the temperature in the tank has become uniform.

The influence of the oscillating frequency ω^* on the isotherm field is examined for several values of ω^*. Although the value of the oscillating frequency ω^* has been changed from $\omega^* = 10^5$ in Fig. 3 to $\omega^* = 5.0 \times 10^6$ in Fig. 4, the pattern of isotherms is essentially similar between Figs. 3 and 4. The influence of ω^* is again examined by changing the value of ω^* to $\omega^* = 10^4$.

Figure 5 illustrates the isotherms and flow velocity fields for $Ra = 10^4$, $Pr = 10^3$, and $\omega^* = 10^4$. It is now found that the flow pattern is very different from the previous results shown in Figs. 3 and 4. In Figs. 3 and 4, flows relative to the motion of the tank reverse their directions as the motion of the tank changes its direction. On the contrary, the flow in the case of Fig. 5 tends to be accelerated in the same direction as the initial motion of the tank. As shown in Fig. 5, the flow of the fluid begins at first to circulate in the opposite direction to the motion of the tank. When the motion of the tank reverses its direction, the flow does not completely change direction.

After the motion of the tank reverses again, the flow with the original direction is accelerated. The flow velocity increases chaotically in the time sequence without reversing its original direction as the oscillating motion continues as shown in graph (3) of Fig. 5. This phenomenon begins to appear when the dimensionless oscillating frequency ω^* is reduced to about 2×10^4.

Discussions of the above computed results will be made here based on the similarity parameters which define the physical phenomena. In equations (17), (21), and (22), there exist six similarity parameters. They are basic parameters of heat transfer, i.e., (*i*) Pr, (*ii*) ω^*, (*iii*) $\bar{\varphi}$, and (*iv*) Ra_l/ω^{*2}, and the parameters characterizing viscosity variation with temperature, i.e., (*v*) μ_w/μ_0 and (*vi*) T^*, which appear in equation (24).

First, among these parameters: (*i*) Pr, (*iv*) μ_w/μ_0, and (*v*) T^* are determined from the kind of fluid. In this work, a COM was selected. Second, the parameter (*ii*) ω^* involves Reynolds number Re as defined by $\omega^* = \mathrm{PrRe}/\bar{\varphi}$ in equation (15). Although the value ω^* for an actual ship reaches on the order of $\omega^* = 10^8 \sim 10^9$, the values for the calculation were taken in the range of $\omega^* = 10^4 \sim 5 \times 10^6$; i.e., $\mathrm{Re} = \omega^*\bar{\varphi}/\mathrm{Pr} = 4.4 \times 10^3/10^3 \sim 2.2 \times 10^6/10^3$, because the calculation model was restricted to laminar flow. It was found from the calculations that the value of ω^* strongly affects the flow and heat transfer. When the value of ω^* is reduced to about 2×10^4, the flows lead to the chaotic type mentioned above. This motion is considered to be a kind of self-exciting motion induced by shearing forces in the fluid. This phenomenon, however, would not occur in a full-size ship's tank where the value of ω^* becomes much higher. Third, the parameter (*iii*) Ra_l/ω^{*2} indicates the relative importance of natural convection as indicated in equation (18). When the value of Ra_l/ω^{*2} becomes small, the importance of the body-force term $\partial\theta/\partial Y$ in equation (17) is reduced, and the heat transfer is influenced mainly by the forced flow, i.e., oscillating motion. Although the value of Ra_l for an actual ship is of the order of $Ra_l = 10^{11} \sim 10^{12}$, the values for the calculation were restricted to values of less than 10^8 to insure that the flow was laminar.

The value of Ra_l/ω^{*2} for each case is the following:
For the actual ship, $Ra_l = 10^{11} \sim 10^{12}$, $\omega^* = 10^8 \sim 10^9$, and

$$10^{-7} < Ra_l/\omega^{*2} < 10^{-4} \tag{33}$$

For the calculation, using the values in equation (32),

$$\begin{aligned} &(1)\ Ra_l = 10^4; \quad 4 \times 10^{-8} < Ra_l/\omega^{*2} < 10^{-4} \\ &(2)\ Ra_l = 10^8; \quad Ra_l/\omega^{*2} = 4 \times 10^{-6} \end{aligned} \tag{34}$$

As can be seen, the values of Ra_l/ω^{*2} between equations (33) and (34) are of the same order. Further, the values are of the order of 10^{-4} or smaller, which means that the forced flow (oscillating motion) dominates the natural convection in both cases.

4.2 Heat Transfer Rate and Nusselt Numbers. The heat transfer rate and Nusselt numbers at the tank wall were also examined for the abovementioned cases.

Figure 6 illustrates the mean dimensionless temperature $\bar{\theta}$ in the tank, the heat transfer rate to each tank wall Q_R or Q_L, the respective Nusselt number Nu_R or Nu_L, and the total rate of heat transfer $Q = Q_R + Q_L$ for $Ra_l = 10^4$, $Pr = 10^3$, and $\omega^* = 10^5$. These values are expressed as functions of the dimensionless time variable τ as shown in Fig. 6. The mean temperature $\bar{\theta}$ in the tank was calculated by averaging the temperature θ_{ij} at each mesh point i, j.

The heat transfer rate to the side wall of the tank, Q_R or Q_L, was calculated using numerical values of the temperature gradient at the wall $\partial\theta/\partial Y|_{R,L}$

$$Q_{R,L} = \frac{1}{2}\int_0^2 \frac{\partial\theta}{\partial Y}\bigg|_{R,L} dX = \sum_i \left(\frac{-\theta_{i2} + 4\theta_{i1} - 3\theta_{i0}}{2\Delta Y}\right) \tag{35}$$

where ΔY is the mesh size. The Nusselt numbers are given by

$$Nu_{R,L} = Q_{R,L}/\bar{\theta} \tag{36}$$

The values of $Q_{R,L}$ and $Nu_{R,L}$ for the pure natural convection heating process are shown in graph (*a*) of Fig. 6 and for oscillating motion in graphs (*b*) and (*c*) of Fig. 6. As natural convection heating continues, the mean temperature $\bar{\theta}$ in the tank increases gradually as shown in Fig. 5(*a*). An increase of $\bar{\theta}$ influences the heat transfer rate to each side wall Q_R or Q_L. The corresponding Nusselt number Nu_R or Nu_L increases steeply with time after heating begins, then becomes gradually steady.

After the oscillating motion begins, the heat transfer rates Q_R and Q_L and the mean temperature $\bar{\theta}$ in the tank decrease gradually as shown in Fig. 6(*b*), and then approach the steady-state condition shown in Fig. 6(*c*). The mean values of the Nusselt numbers Nu_R and Nu_L have nearly constant values, although they fluctuate due to the oscillating motion of the tank.

Figure 7 illustrates the vertical profiles of the local heat transfer rate to the tank side walls for $Ra_l = 10^4$, $Pr = 10^3$, and $\omega^* = 10^5$. The profiles of the heat transfer rate are chosen for a sequence of several time steps. The broken lines in Fig. 7 show results for pure natural convection. The solid lines show

results for oscillating motion. It appears that the profiles of the heat transfer rate fluctuate substantially along the wall.

As shown in Fig. 6, the mean fluid temperature is observed to decrease during the oscillation of the tank. The reason is as follows. The fluid selected for the calculation is accompanied with the strong viscosity dependence on temperature. Before oscillation begins, the heat transfer by pure natural convection is promoted near the heated wall due to the lowered viscosity with higher temperature. When oscillation begins, the cooled fluid with higher viscosity near the side wall flows down to the heating surface, which would prevent heat transfer to the fluid. The above effects result in a decrease in heat transfer from the heating surface, which causes a decrease in the mean temperature of the fluid during the oscillation.

On the other hand, although the heat transfer rate to the side wall decreases during oscillation, the mean value of the Nusselt number at the wall is almost constant and nearly the same value as that of pure natural convection. This phenomenon occurs because the cooled fluid with very high viscosity at the side walls of the tank behaves as an insulating film which is less influenced by the oscillating motion of the tank.

The heat transfer rates to the side walls are also examined for several values of ω^* as shown in Fig. 8. Figure 8(*a*) corresponds to the case for $\omega^* = 5.0 \times 10^5$ in Fig. 4, where oscillation of the heat transfer rates appears to be accompanied by oscillating motion of the tank. In this case, although the frequency ω^* has been increased to $\omega^* = 5.0 \times 10^5$ as compared with the case of $\omega^* = 10^5$ in Fig. 6, the profiles of the heat transfer rates and the Nusselt numbers are essentially similar to the case shown in Figs. 6(*b*) and (*c*). Figures 8(*b*) and (*c*) correspond to the cases for $\omega^* = 2.0 \times 10^4$ and 10^4 in Fig. 5, respectively, where the excited chaotic flows have been observed. In these cases, the profiles of heat transfer rates and Nusselt numbers are observed to fluctuate chaotically as the oscillation continues. These profiles are considerably different from the cases shown in Fig. 8(*a*) or Figs. 6(*b*) and (*c*).

5 Summary

Heat transfer within a ship's tank undergoing oscillating motion has been studied numerically. The motivation was to understand the heat transfer process which appears in heating of oils stored in ship's tanks with an oscillating motion. The results obtained are summarized as follows:

1 When the tank oscillates due to the ship's motion, reciprocal circulating flows relative to the tank are observed. The isotherms fluctuate regularly from side to side of the tank as the flow changes its direction. After several swings, the mean fluid temperature in the tank decreases, and then gradually approaches a steady-state value as the oscillation of the tank continues.

2 As the tank oscillates, the heat transfer rate to the side walls of the tank decreases gradually accompanied by oscillation due to the tank motion, and then approaches a steady-state condition.

3 The Nusselt number at the side wall of the tank has nearly the same mean value as that of pure natural convection, although it fluctuates during oscillation of the tank.

4 When the dimensionless oscillating frequency ω^* decreases to about 2×10^4, the circulating flow in the tank tends to be accelerated in the same direction as the initial motion of the tank. The heat transfer rate to the side walls of the tank fluctuates chaotically due to the oscillating motion of the tank.

The above results should be helpful in the thermal design of a heating system for an oil tanker. However, it should be kept in mind that the present result is restricted to laminar flow, and the calculation of turbulent flow is required for further understanding of the phenomena.

References

1 Ostrach, S., "Natural Convection in Enclosures," *Advances in Heat Transfer*, Vol. 8, Academic Press, New York, 1972, pp. 161–227.

2 Catton, I., "Natural Convection in Enclosures," *Proc. 6th Int. Heat Transf. Conf.*, Toronto, Vol. 6, Hemisphere, Washington, D.C., 1978, pp. 13–31.

3 Torrance, K. E., and Catton, I., "Natural Convection in Enclosures," ASME, HTD Vol. 8, 1980.

4 Akagi, S., "A Study on Heat Transfer During Natural Convection Heating of a Coal Oil Mixture (COM)," *Heat Transfer—Japanese Research*, No. 11-4, 1982, pp. 1–26. (Originally appeared in *Trans. JSME*, No. 48-434B, 1982, pp. 2013–2023.)

5 Torrance, K. E., and Rockett, J. A., "Numerical Study of Natural Convection in an Enclosure With Localized Heating From Below—Creeping Flow to the Onset of Laminar Instability," *J. Fluid Mech.*, Vol. 36, 1969, pp. 33–54.

6 Akagi, S., Takemura, M., and Uchida, K., "Simulation for Natural Convection Heating of a Storage Tank Containing High Viscosity Fluids," *Proc. 20th Japan Heat Trans. Symposium*, 1983, pp. 529–531.

M. Choi

H. R. Baum[1]

R. Greif

University of California, Berkeley,
Department of Mechanical Engineering,
Berkeley, CA 94720

The Heat Transfer Problem for the Modified Chemical Vapor Deposition Process

The heat transfer problem related to the modified chemical vapor deposition process has been analyzed in the high Peclet number limit. Variations in the axial, angular, and radial directions are presented. Of particular interest are the effects of tube rotation and variable properties on the temperature profiles.

Introduction

The modified chemical vapor deposition (MCVD) process is used in the manufacture of high-quality glass fiber light guides for lightwave communication systems. In this process, which was first described by MacChesney et al. (1974a, b, 1980), submicron glassy particles are formed by the oxidation of reactant gases. The gases and particles flow through a rotating tube which is heated by a moving torch and some of the particles are deposited on the wall which was heated by the torch. Subsequent heating from the moving torch fuses the deposited material which forms a glassy film.

Most analyses of MCVD and of related processes have assumed fully developed flow conditions and constant properties. One study does present the governing equations and gives numerical results for a developing flow with variable properties (Walker et al. 1979). However, all studies have been two dimensional and, in addition, have neglected the effect of the rotation of the tube on both the flow and the heat and mass transfer. The particulate deposition mechanism in MCVD has been attributed to thermophoresis (Walker et al., 1979, 1980; Simpkins et al., 1979, Weinberg et al., 1982a, b) and the influence of laser radiation on thermophoresis has been studied by Morse et al. (1985) and by Wang et al. (1985). A detailed study of the effects of laser radiation, variable properties, and buoyancy is given by DiGiovanni et al. (1985).

The present work presents a three-dimensional time-dependent formulation of the heat transfer. The effects of variable properties and rotation are investigated for the case of a fast-moving torch. Analytical and numerical results are obtained in the high Peclet number limit and the effects of rotation are displayed in terms of the dimensionless parameter $a\Omega/U_0$.

Analysis

Consider a circular tube of radius a rotating with an angular velocity Ω about its axis. Gas at temperature T_∞ and density ρ_∞ flows through the tube at a prescribed mass flow rate $\dot{M}$. The surface of the tube is heated by a torch moving in the streamwise direction with a velocity $U(t)$. The surface heating pattern is assumed to be steady in a coordinate system at rest with respect to the torch. Thus, the introduction of a coordinate ξ defined by

$$\xi = x - X(t) = x - \int_0^t U(\tau)\,d\tau$$

together with the polar coordinates r, θ as shown in Fig. 1, yields a steady-state reference system. In these coordinates, the energy and mass conservation equations can be written in the form

$$\rho c_p\left\{\frac{\partial T}{\partial t} + [u - U(t)]\frac{\partial T}{\partial \xi} + v\frac{\partial T}{\partial r} + \frac{w}{r}\frac{\partial T}{\partial \theta}\right\} = \frac{1}{r}\frac{\partial}{\partial r}\left(rk\frac{\partial T}{\partial r}\right) + \frac{1}{r^2}\frac{\partial}{\partial \theta}\left(k\frac{\partial T}{\partial \theta}\right) + \frac{\partial}{\partial \xi}\left(k\frac{\partial T}{\partial \xi}\right) \quad (1)$$

$$\frac{\partial(\rho r)}{\partial t} + \frac{\partial}{\partial \xi}\{\rho r[u - U(t)]\} + \frac{\partial}{\partial r}(\rho v r) + \frac{\partial}{\partial \theta}(\rho w) = 0 \quad (2)$$

These equations must be supplemented by an equation of state which can be written in the form

$$\rho T = \rho_\infty T_\infty. \quad (3)$$

Equations (1)–(3) require that the local Mach number in the gas be small compared to unity, but are otherwise general. In particular, they retain three-dimensional, variable property, and transient effects for any Reynolds number.

It is convenient to introduce nondimensional variables as follows:

$$\begin{aligned} \frac{T - T_\infty}{T_\infty} &= H(\tilde{t}, \tilde{\xi}, Y, \theta) \\ \rho/\rho_\infty &= \tilde{\rho}(\tilde{t}, \tilde{\xi}, Y, \theta) \\ k &= k_\infty \tilde{k}(H) \\ U(t) &= U_0 V(\tilde{t}) \\ \xi &= a\tilde{\xi}, \quad t = (a/U_0)\tilde{t}, \quad r = a(1 - \sqrt{\epsilon}Y) \\ \epsilon &= (k_\infty/\rho_\infty c_p U_0 a) = 1/\mathrm{Pe} \end{aligned} \quad (4)$$

Now the imposed fluid velocity u must be of order $(\dot{M}/\rho_\infty a^2)$ in order to supply the required mass flux. Moreover, we also know that the velocity profile in the absence of heating is parabolic, and that u must vanish at $r = a$, $Y = 0$. Thus, in the thermal boundary layer we can expect

$$u \sim 0(\dot{M}/\rho_\infty a^2)\,(1 - r/a)$$

or

$$u \sim \dot{M}\sqrt{\epsilon}/\rho_\infty a^2$$

Similarly, we can anticipate that the departure of the swirl

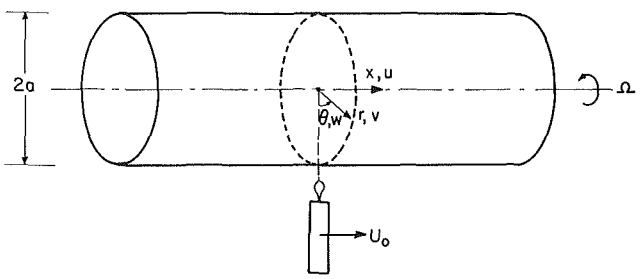

Fig. 1 Sketch of the system

[1]National Bureau of Standards, Gaithersburg, MD 20899.

Contributed by the Heat Transfer Division for publication in the JOURNAL OF HEAT TRANSFER. Manuscript received by the Heat Transfer Division December 13, 1985.

component of the velocity from a rigid body rotation will be $0(\sqrt{\epsilon})$. Finally, in order to preserve conservation of mass, we also require $v \sim \sqrt{\epsilon}\, U_0$. This leads to the following normalization for the velocity components:

$$\begin{aligned} u &= (\dot{M}\sqrt{\epsilon}/\rho_\infty a^2)\,\tilde{u}\,(\tilde{t},\,\tilde{\xi},\,Y,\,\theta) \\ v &= -\sqrt{\epsilon}U_0\tilde{v}(\tilde{t},\,\tilde{\xi},\,Y,\,\theta) \\ w &= a\Omega\{1+\sqrt{\epsilon}\tilde{w}(\tilde{t},\,\tilde{\xi},\,Y,\,\theta)\} \end{aligned} \tag{5}$$

Substitution of equations (4) and (5) into equations (1)–(3) and passage to the high Peclet number limit $\epsilon \to 0$ yields

$$\tilde{\rho}\left\{\frac{\partial H}{\partial \tilde{t}} - V(\tilde{t})\,\frac{\partial H}{\partial \tilde{\xi}} + \tilde{v}\,\frac{\partial H}{\partial Y} + \frac{a\Omega_0}{U_0}\,\frac{\partial H}{\partial \theta}\right\} = \frac{\partial}{\partial Y}\left(\tilde{k}\frac{\partial H}{\partial Y}\right)$$

$$\frac{\partial \tilde{\rho}}{\partial \tilde{t}} - V(\tilde{t})\,\frac{\partial \tilde{\rho}}{\partial \tilde{\xi}} + \frac{\partial}{\partial Y}\,(\tilde{\rho}\tilde{v}) + \frac{a\Omega}{U_0}\,\frac{\partial \tilde{\rho}}{\partial \theta} = 0 \tag{6}$$

$$\tilde{\rho}(1+H) = 1$$

Equations (6) control the evolution of $\tilde{\rho}$, $\tilde{H}$, and $\tilde{v}$ in space and time. They must be supplemented by boundary and initial conditions where appropriate. At the surface $Y = 0$, the temperature excess H is assumed to be known and the radial velocity $\tilde{v}$ must vanish. As $Y \to \infty$, the ambient state in the interior of the tube must be recovered, and no boundary condition can be prescribed for v. The limiting value of $\tilde{v}$ as $Y \to \infty$ will drive perturbations of order $\sqrt{\epsilon}$ to the parabolic velocity profile in the interior of the tube. These perturbations, together with the boundary layer velocity components $\tilde{u}$ and $\tilde{w}$ must ultimately be determined in order to obtain a complete description of the gas and particle velocities in the tube. However, this part of the problem will not be considered here. Rather, attention is confined to the thermal problem described by equations (6) above. For an initial value problem, the boundary conditions must be supplemented by a knowledge of the state everywhere at $\tilde{t} = 0$. Physically, the most interesting initial condition is $H = 0$. For a steady-state problem, the analogous condition is $H \to 0$ as $\tilde{\xi} \to +\infty$. Physically, this means that we require the gas ahead of the advancing torch to be at the ambient temperature. For localized boundary heating, this will also be the state as $\tilde{\xi} \to -\infty$, but this cannot be a prescribed condition at the high Peclet number limit $\epsilon \to 0$.

The equations are greatly simplified if the radial coordinate Y is replaced by the Howarth variable η, defined by

$$\eta = \int_0^Y \tilde{\rho}(\tilde{t},\,\tilde{\xi},\,Y,\,\theta)\,dY \tag{7}$$

In addition, the thermal conductivity is assumed to vary linearly with temperature so that

$$\tilde{\rho}\tilde{k} = 1 \tag{8}$$

Using equations (7) and (8) in the energy and continuity equations, they can be rewritten in the form

$$\begin{aligned} &\frac{\partial H}{\partial \tilde{t}} - V(\tilde{t})\,\frac{\partial H}{\partial \tilde{\xi}} + \Gamma\,\frac{\partial H}{\partial \theta} = \frac{\partial^2 H}{\partial \eta^2} \\ &\frac{\partial Y}{\partial t} - V(\tilde{t})\,\frac{\partial Y}{\partial \tilde{\xi}} + \Gamma\,\frac{\partial Y}{\partial \theta} = -\tilde{v} \\ &Y = \eta + \int_0^\eta H\,d\eta \\ &\Gamma = a\Omega/U_0 \end{aligned} \tag{9}$$

Note that equations (9) are a linear system that can be solved sequentially. The solution for $H(\tilde{t},\,\tilde{\xi},\,\theta,\,\eta)$ is obtained first. Then $Y(\tilde{t},\,\tilde{\xi},\,\theta,\,\eta)$ is obtained by quadrature. Finally, the transformed mass conservative equation (the second of equations (9)) yields the radial velocity component $\tilde{v}$. As mentioned above, the limiting value of $\tilde{v}$ as $\eta \to \infty$ causes inviscid perturbations to the parabolic velocity profile in the interior. These perturbations in turn provide the boundary conditions for the boundary layer velocity components $\tilde{u}(\tilde{t},\,\tilde{\xi},\,\theta,\,\eta)$ and $\tilde{w}(\tilde{t},\,\tilde{\xi},\,\theta,\,\eta)$. Finally, at the steady-state limit, equations (9) can be further simplified. In this case.

$$V(\tilde{t}) = 1 \tag{10}$$

It is convenient to use characteristic coordinates S, ψ, defined by

$$\begin{aligned} S &= -\tilde{\xi} \\ \psi &= (\theta/\Gamma) - S \end{aligned} \tag{11}$$

Substituting equations (10) and (11) into equations (9) the system takes the two-dimensional form

$$\begin{aligned} &\frac{\partial H}{\partial S} = \frac{\partial^2 H}{\partial \eta^2} \\ &Y = \eta + \int_0^\eta H d\eta \\ &\frac{\partial Y}{\partial S} = -\tilde{v} \end{aligned} \tag{12}$$

The surface temperature is defined to have a maximum

Nomenclature

a = tube radius
c_p = specific heat
H = dimensionless temperature = $(T-T_\infty)/T_\infty$
k = conductivity
$\dot{M}$ = mass flow rate
Pe = Peclet number = $U_0 a/\alpha_\infty$
r = radial coordinate
t = time
$\tilde{t}$ = dimensionless time = $U_0 t/a$
T = temperature
u = axial velocity
U, U_0, V = torch velocities
v = radial velocity
w = velocity in the θ direction
x = axial coordinate
$\tilde{x}$ = dimensionless axial coordinate = x/a
$X(t)$ = position of moving torch
Y = stretched dimensionless coordinate in the r direction
$\Gamma = \dfrac{a\Omega}{U_0}$
$\epsilon = \dfrac{1}{\text{Pe}}$
η = Howarth variable
θ = angle
λ = parameter in equation (13)
ξ = moving coordinate = $x - U_0 t$
$\tilde{\xi}$ = dimensionless moving coordinate = ξ/a
ρ = density
ψ = characteristic coordinate
Ω = angular velocity of tube

Subscripts

∞ = ambient
M = maximum
w = wall

Superscript

$\tilde{}$ = dimensionless

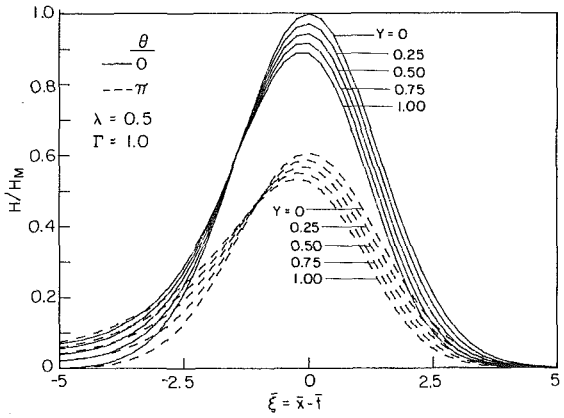

Fig. 2 Dimensionless temperature (H/H_M) variation along the tube at different radial locations: _____ $\theta = 0$, ----- $\theta = \pi$, $\lambda = 0.5$, $\Gamma = 1.0$

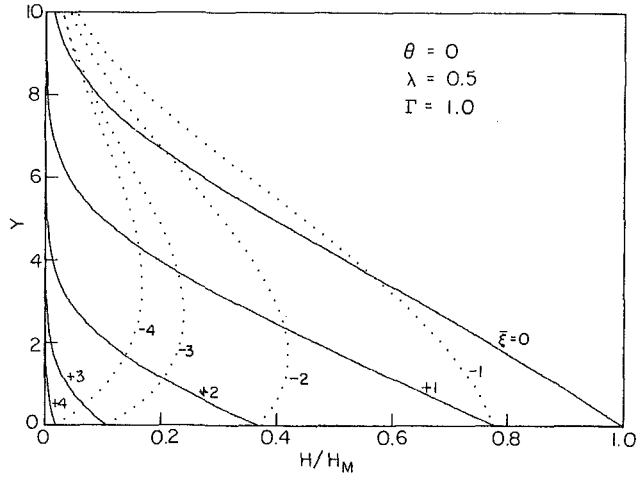

Fig. 3(a) Dimensionless temperature (H/H_M) variation in the radial direction at different axial locations; $\theta = 0$, $\lambda = 0.5$, $\Gamma = 1.0$

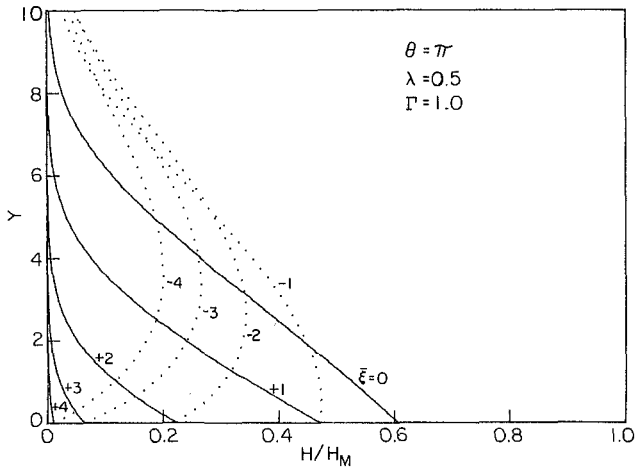

Fig. 3(b) Dimensionless temperature (H/H_M) variation in the radial direction at different axial locations; $\theta = \pi$, $\lambda = 0.5$, $\Gamma = 1.0$

value H_M at the location $\theta = 0$, $S = 0$ ($x = X(t)$) and is assumed to have the form

$$H(S, \theta, \eta = 0) = H_w = H_M \exp(-\lambda^2[S^2 + (1 - \cos\theta)]) \quad (13)$$

The only part of equation (13) that is essential is the requirement that the relation be a periodic function of θ, i.e.,

$$H(S, \theta, 0) = H(S, \theta + 2\pi, 0)$$

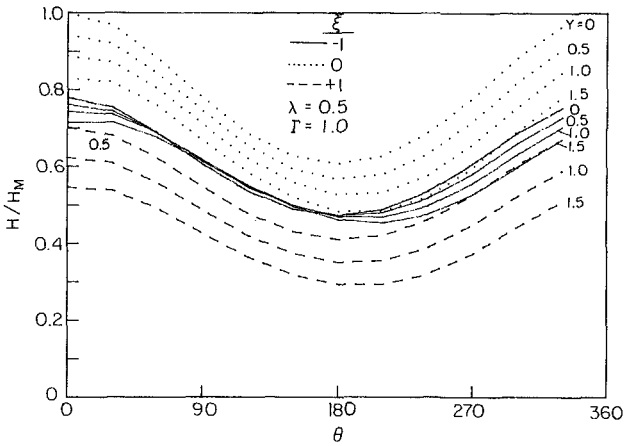

Fig. 4 Dimensionless temperature (H/H_M) variation in the θ direction; $\lambda = 0.5$, $\Gamma = 1.0$

Note that λ is a parameter that characterizes the thickness of the torch. The remaining boundary conditions are

$$H(S, \theta, \infty) = 0 \quad (14a)$$

$$H(-\infty, \theta, \eta) = 0 \quad (14b)$$

The solution for the temperature distribution may be obtained by a Green's function procedure and is given by

$$H(S, \psi, \eta) = H_M \int_{-\infty}^{S} \text{erfc}\,(\eta/2\sqrt{S - S_0}) \cdot \frac{\partial}{\partial S_0} \exp(-\lambda^2\{S_0^2 + 1 - \cos[\Gamma(\psi + S_0)]\})\, dS_0 \quad (15)$$

The wall heat flux, $q_w = k\,\partial T/\partial r\,|_{r=a}$, is obtained from equation (15)

$$\frac{q_w a\sqrt{\epsilon}}{k(T_M - T_\infty)} = -\frac{1}{H_M(1 + H_w)} \frac{\partial H}{\partial \eta}\bigg|_{\eta=0} = \frac{1}{\sqrt{\pi}(1 + H_w)} \int_{-\infty}^{S} \frac{1}{\sqrt{S - S_0}} \frac{\partial}{\partial S_0} \exp(-\lambda^2\{S_0^2 + 1 - \cos[\Gamma(\psi + S_0)]\})\, dS_0 \quad (16)$$

Then, from equations (12) and (15) we obtain

$$Y = \eta(1 + H) + \frac{2H_M}{\sqrt{\pi}} \int_{-\infty}^{S} \sqrt{S - S_0}\,[1 - \exp\{-\eta^2/4(S - S_0)\}] \cdot \frac{\partial}{\partial S_0} \exp(-\lambda^2\{S_0^2 + 1 - \cos[\Gamma(\psi + S_0)]\})\, dS_0 \quad (17)$$

The velocity is then obtained from equations (12) and (16)

$$\tilde{v} = -\frac{H_M}{\sqrt{\pi}} \int_{-\infty}^{S} [1/\sqrt{S - S_0}]\,[1 - \exp\{-\eta^2/4(S - S_0)\}] \cdot \frac{\partial}{\partial S_0} \exp(-\lambda^2\{S_0^2 + 1 - \cos[\Gamma(\psi + S_0)]\})\, dS_0 \quad (18)$$

Results and Discussion

Figure 2 shows the variation of the temperature with respect to axial position $\tilde{\xi}$ for values in the radial direction of Y equal to 0, 0.25, 0.50, 0.75, and 1.0 at two values of θ; namely, θ equal to 0 and to π. The wall temperature distribution (curve 1, $Y = 0$) is given by equation (13) and this general shape extends into the gas. It is important to note that there are regions behind the heat source where the gas temperatures are *greater* than the wall temperatures; for example, for $\tilde{\xi} < -2$ (approximately) at $\theta = 0$ and for $\tilde{\xi} < -1$ (approximately) for $\theta = \pi$. This is related to the specification that the velocity of the gas near the wall is much less than the rate of propagation (axial) of the moving heat source. As the source moves away, the

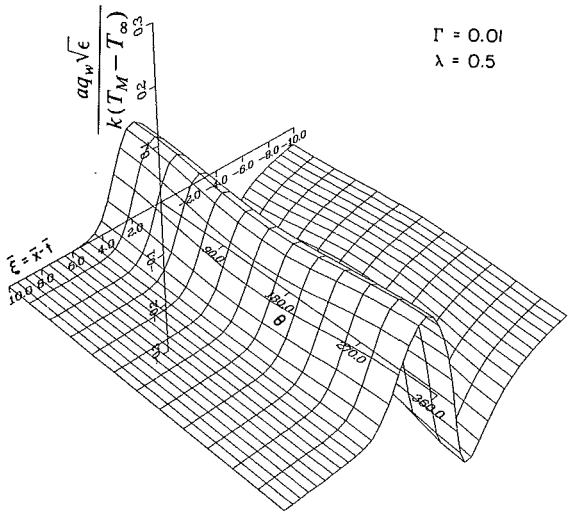

Fig. 5(a) Variation of the dimensionless wall heat flux, $\frac{(aq_w\sqrt{\epsilon})}{k(T_M - T_\infty)}$; $\lambda = 0.5$, $\Gamma = 0.01$

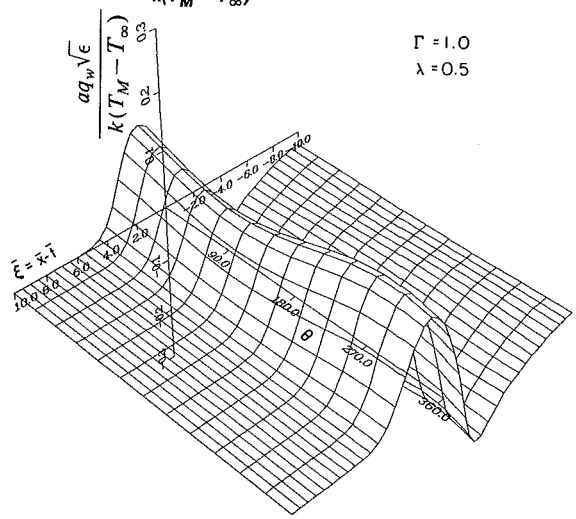

Fig. 5(b) Variation of the dimensionless wall heat flux, $\frac{(aq_w\sqrt{\epsilon})}{k(T_M - T_\infty)}$; $\lambda = 0.5$, $\Gamma = 1.0$

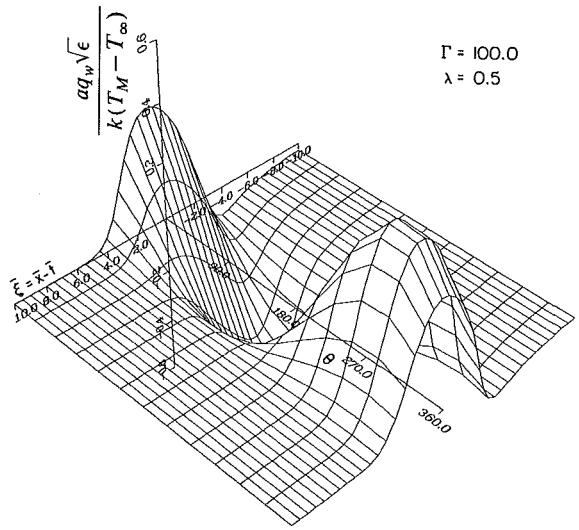

Fig. 5(c) Variation of the dimensionless wall heat flux, $\frac{(aq_w\sqrt{\epsilon})}{k(T_M - T_\infty)}$; $\lambda = 0.5$, $\Gamma = 100.0$

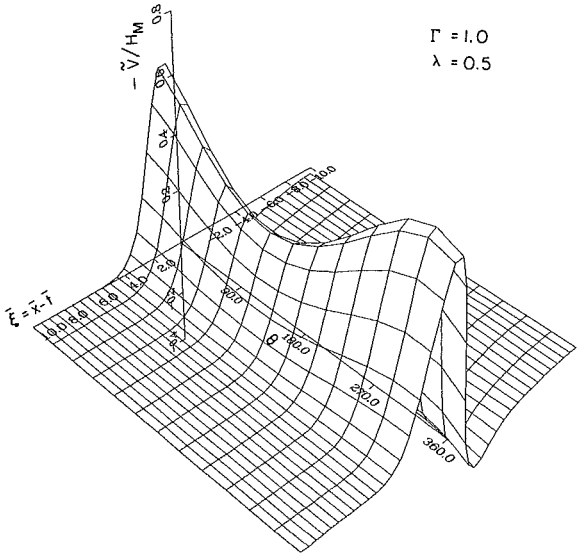

Fig. 6 Dimensionless velocity, $-\tilde{v}/H_M$, as $Y \to \infty$; $\lambda = 0.5$, $\Gamma = 1.0$

temperature of the wall is decreasing according to equation (13). Thus, although the temperature of the gas is also decreasing, it retains enough energy so that its temperature is greater than that of the nearby surface which is cooling more rapidly. Accordingly, the heat flux q_w is negative in this region (cf. Figs. 5*a, b, c*).

The temperature distribution in the radial direction Y is shown in Figs. 3*a* and 3*b* for values of $\theta = 0$ and π, respectively. These results show that the temperature decreases monotonically from the hot wall for positive values of $\tilde{\xi}$; i.e., ahead of the moving torch.[2] Deposition of particles on the wall due to thermophoresis requires a positive temperature gradient, $\partial H/\partial Y$; i.e., a "cold wall." Other studies have obtained a cold wall *in front of the torch* but this is not in agreement with the present hot wall results. This effect, in the present model, is related to the result that the velocity of the torch is greater than the forced flow velocity over a significant portion of the thermal boundary layer. It is also noted that the magnitude of this wall heating on the overall particle deposition process can only be determined when the overall trajectories have been studied. This would include the effects of the induced flow in the interior of the tube, i.e., and nonparabolic velocity profile outside of the thermal boundary layer.

Figure 4 shows the angular (θ) temperature variation for values of $Y = 0$ (wall value), 0.5, 1.0, and 1.5 at values of $\tilde{\xi} = -1$, 0 (torch trajectory), and 1. For most cases the temperatures have a maximum value at $\theta \sim 0$ (2π) and have a minimum value at $\theta \sim \pi$ corresponding to the variation at the wall.

Figures 5(*a, b, c*) show the variation of the dimensionless wall heat flux, cf. equation (16), with respect to $\tilde{\xi}$ and θ for values of Γ equal to 0.01, 1, and 100. For small and moderate values of the rotation parameter Γ ($= a\Omega/U_0$) there is little transport in the θ direction and consequently there is only a small variation of the heat flux in the θ direction (cf. Figs. 5*a, b*). However, for large values of Γ there is significant convection in the θ direction which is accompanied by the large variation in the wall heat flux that is shown in Fig. 5(*c*). The flux is a maximum at a location that is slightly ahead of the moving torch. As discussed above, at some locations behind the torch the flux is negative, i.e., toward the wall.

[2]Note that for some negative values of $\tilde{\xi}$, i.e., behind the torch, the gas temperatures may be greater than the wall temperature (as was previously discussed).

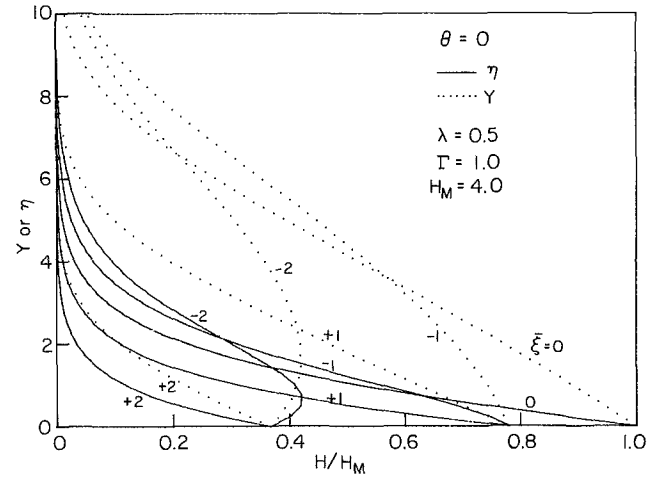

Fig. 7(a) Temperature profiles for constant and variable properties at $\theta = 0$

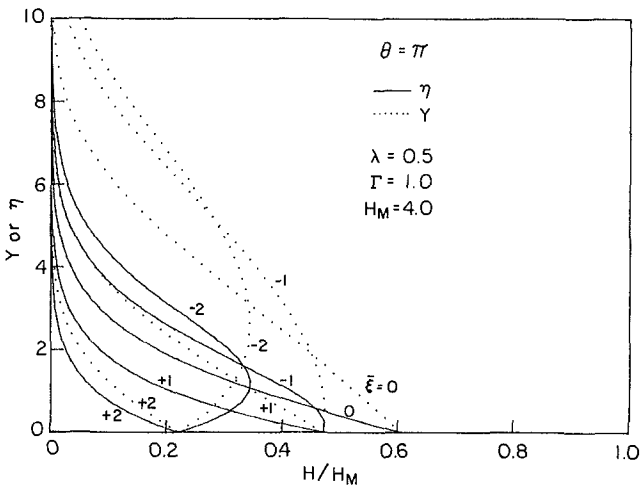

Fig. 7(b) Temperature profiles for constant and variable properties at $\theta = \pi$

In Fig. 6 the velocity at $Y = \infty$ ($\eta = \infty$) is shown. The regions of positive velocity act as sources with respect to the flow in the interior of the tube, while the negative velocity regions represent sinks of fluid. These distributions of sources and sinks around the tube wall cause the flow in the interior to depart from the fully developed parabolic velocity profile.

Figures 7(*a*) and 7(*b*) show a comparison of temperature contours in the physical coordinate Y, and in the Howarth transformed variable η. In the absence of any variable property effects these contours would be identical. The differences between the two sets of curves are thus a measure of the importance of these effects. Since the thermophoretic particle velocity is directly proportional to the local temperature gradient, it is clear that accurate particle trajectories cannot be calculated without accounting for variations in the density and in the thermal conductivity of the gas.

Summary and Conclusions

A study has been made of the heat transfer related to the modified chemical vapor deposition process. The unsteady three-dimensional energy equation and the mass conservation equation were applied to the thermal boundary layer at the large Peclet number limit. Using the Howarth variable, the variations of the density and the thermal conductivity were included. Results were obtained by utilizing characteristic coordinates under the assumption of quasi-steady-state conditions.

The effects of tube rotation and variable properties were examined and both were shown to be important in this limiting case. It was also emphasized that there are regions near the wall (behind the moving torch) where the temperature of the gas is higher than that of the wall.

Acknowledgments

The authors are indebted to Dr. U. C. Paek, AT&T Engineering Research Center for bringing this problem to our attention and providing important background material.

References

DiGiovanni, D., Wang, C. Y., Morse, T. F., and Cipolla, J. W., Jr., 1985, "Laser Induced Buoyancy and Forced Convection in Vertical Tubes," in: *Natural Convection: Fundamentals and Applications*, S. Kakac, W. Aung, and R. Viskanta, eds., Hemisphere, New York, pp. 1118-1139.

MacChesney, J. B., O'Connor, P. B., DiMarcello, F. V., Simpson, J. R., and Lazay, P. D., 1974a, "Preparational Low Loss Optical Fibers Using Simultaneous Vapor Phase Deposition and Fusion," *Proc. 10th Proc. Int. Congr. Glass. 10th*, Kyoto, Japan, pp. 6-40-6-44.

MacChesney, J. B., O'Connor, P. B., and Presby, H. M., 1974b, "A New Technique for Preparation of Low-Loss and Graded Index Optical Fibers," *Proc. IEEE*, Vol. 62, pp. 1278-1279.

Morse, T. F., Wang, C. Y., and Cipolla, J. W., Jr., 1985, "Laser Induced Thermophoresis and Particulate Deposition Efficiency," ASME JOURNAL OF HEAT TRANSFER, Vol. 107, No. 1, pp. 155-160.

Simpkins, P. G., Kosinski, S. G., and MacChesney, J. B., 1979, "Thermophoresis: The Mass Transfer Mechanism in Modified Chemical Vapor Deposition," *J. Appl. Physics*, Vol. 50, pp. 5676-5681.

Walker, K. L., Homsy, G. M., and Geyling, F. T., 1979. "Thermophoretic Deposition of Small Particles in Laminar Tube Flow," *Journal of Colloid and Interface Science*, Vol. 69, pp. 138-147.

Walker, K. L., Geyling, F. T., and Nagel, S. R., 1980, "Thermophoretic Deposition of Small Particles in the Modified Chemical Vapor Deposition (MCVD) Process," *Journal of American Ceramic Society*, Vol. 63, pp. 552-558.

Wang, C. Y., Morse, T. F., and Cipolla, J. W., Jr., 1985, "Laser Induced Natural Convection and Thermophoresis," ASME JOURNAL OF HEAT TRANSFER, Vol. 107, pp. 161-167.

Weinberg, M., and Subramanian, R. S., 1982a, "Thermophoretic Deposition in a Tube With Variable Wall Temperature," *Journal of Colloid and Interface Science*, Vol. 87, No. 2, pp. 579-580.

Weinberg, M., 1982b, Thermophoretic Efficiency in the Modified Chemical Vapor Deposition Process," *Journal of American Ceramic Society*, Vol. 65, pp. 81-87.

Entropy Generation in Convective Heat Transfer and Isothermal Convective Mass Transfer

J. Y. San
W. M. Worek[1]
Z. Lavan

Illinois Institute of Technology,
Department of Mechanical
and Aerospace Engineering,
Chicago, IL 60616

The irreversible generation of entropy for two limiting cases of combined forced-convection heat and mass transfer in a two-dimensional channel are investigated. First, convective heat transfer in a channel with either constant heat flux or constant surface temperature boundary conditions are considered for laminar and turbulent flow. The entropy generation is minimized to yield expressions for optimum plate spacing and optimum Reynolds numbers for both boundary conditions and flow regimes. Second, isothermal convective mass transfer in a channel is considered, assuming the diffusing substance to be an ideal gas with Lewis number equal to unity. The flow is considered to be either laminar or turbulent with boundary conditions at the channel walls of either constant concentration or constant mass flux. The analogy between heat and mass transfer is used to determine the entropy generation and the relations for optimum plate spacing and Reynolds number. The applicable range of the results for both limiting cases are then investigated by non-dimensionalizing the entropy generation equation.

Introduction

Most devices used in conventional energy conversion systems continuously transport mass and/or energy. In such systems, the exchange of momentum, mass and/or energy between the working fluid and the boundaries causes an increase in entropy which results in the destruction of exergy [1]. In order to minimize the exergy destruction, the mechanism of entropy generation in both convective heat transfer and in isothermal convective mass transfer in a two-dimensional channel is studied. The optimum design criteria to minimize the entropy generation are presented.

Recently, entropy generation studies have influenced the design methodology of energy conversion systems [2, 3]. This design methodology is based on minimizing the total entropy generation in the device for a certain fixed working load. In doing so, we can obtain an optimum size of the device with minimum loss of availability.

For the case of convective heat transfer or isothermal convective mass transfer in a channel, the irreversibility is a result of the sum of the lost work to heat or mass transfer and the lost work due to fluid friction. By adjusting the plate spacing or the mass flowrate, the lost work in such systems can be minimized for a certain quantity of heat or mass transfer.

General Formulation of Local Entropy Generation

In a flow field, the nonequilibrium conditions are due to the exchange of momentum, energy, and/or mass within the fluid and at the solid boundaries. This nonequilibrium phenomenon causes a continuous generation of entropy in the flow field. This entropy generation is due to the irreversible nature of heat transfer, mass diffusion, viscosity effects within the fluid and at the solid boundaries, chemical reactions, coupling effects between heat and mass transfer, and body force effects. Every irreversible process can be viewed as the relevant flux driven by the corresponding potential. The flux of heat is driven by the temperature gradient, the flux of mass is driven by the mass concentration gradient, and the flux of momentum is driven by the velocity gradient.

The local entropy generation per unit volume g of an incompressible Newtonian fluid has been derived by Hirschfelder et al. [4] and is given as

$$g=\frac{\mu'}{T}\left(\frac{\partial U_i}{\partial x_j}\right)\left[\frac{\partial U_i}{\partial x_j}+\frac{\partial U_j}{\partial x_i}\right]-\frac{1}{T}\left[\sum_\alpha J_{\alpha i}\left(\frac{\partial \mu_\alpha}{\partial x_i}\right)\right.$$

$$\left.+\frac{\epsilon_i}{T}\left(\frac{\partial T}{\partial x_i}\right)+\sum_\alpha \bar{S}_\alpha J_{\alpha i}\left(\frac{\partial T}{\partial x_i}\right)-\sum_\alpha J_{\alpha i}X_{\alpha i}+\sum_\alpha \bar{K}_\alpha \mu_\alpha\right] \quad (1)$$

where the first term is due to fluid friction, the second is due to mass diffusion, and the third is due to heat conduction. The fourth term represents the coupling between mass diffusion and energy diffusion, the fifth is due to body forces, and the sixth term represents the effect due to chemical reactions. For a two-dimensional fully developed forced convection flow in a channel without chemical reactions, the entropy generation is obtained by considering terms (i) through (iv) in equation (1). The body force effect is small and can be neglected.

Entropy Generation in Convective Heat Transfer

In this section, the entropy generation is determined for heat transfer in a symmetric two-dimensional channel. The analysis considers the flow to be either laminar, or turbulent with both walls maintained at a constant temperature, or with a constant heat flux applied at the surfaces.

Laminar Flow. For a two-dimensional channel flow, the entropy generation is obtained by considering terms (i) and (iv) in equation (1)

$$g=\frac{\mu'}{T}\left\{2\left[\left(\frac{\partial U_x}{\partial x}\right)^2+\left(\frac{\partial U_y}{\partial y}\right)^2\right)+\left[\left(\frac{\partial U_x}{\partial y}+\frac{\partial U_y}{\partial x}\right)\right]^2\right\}$$

$$+\frac{k}{T^2}\left[\left(\frac{\partial T}{\partial x}\right)^2+\left(\frac{\partial T}{\partial y}\right)^2\right] \quad (2)$$

The procedure utilized in this analysis is similar to that used by Bejan [3] for heat transfer in a circular tube. Therefore, many details of the analysis are not presented.

The velocity profile of a fully developed, laminar flow in a two-dimensional channel of width $2D$ is given as

$$U_x(y)=2U_{\max}\left[Y^*-\left(\frac{1}{2}\right)Y^{*2}\right] \quad (3)$$

[1]Present address: University of Illinois at Chicago, Department of Mechanical Engineering, Box 4348, Chicago, IL 60680.

Contributed by the Heat Transfer Division for publication in the JOURNAL OF HEAT TRANSFER. Manuscript received by the Heat Transfer Division November 14, 1985.

where U_{max} is the maximum fluid velocity in the channel and Y^* is a dimensionless position variable, defined as y/D. The well-known similar temperature profiles are solved for both the case of constant wall heat flux and constant wall surface temperature [5]. The results are summarized as follows:

(*a*) *Constant wall heat flux*

$$\frac{T-T_0}{T_m-T_0}=\frac{1}{0.486}\left[Y^*-\tfrac{1}{2}Y^{*3}+1/8\,Y^{*4}\right] \tag{4}$$

(*b*) *Constant wall surface temperature*

$$\frac{T-T_0}{T_m-T_0}=\sum_{i=1}^{12}a_i Y^{*i} \tag{5}$$

where the constants a_i are

$a_1=1.857$, $a_2=a_3=a_6=0$

$a_4=-8.564\times10^{-1}$, $a_5=2.571\times10^{-1}$

$a_7=1.257\times10^{-1}$, $a_8=-7.555\times10^{-2}$

$a_9=-3.682\times10^{-3}$, $a_{10}=1.206\times10^{-2}$

$a_{11}=-3.219\times10^{-3}$, $a_{12}=2.679\times10^{-4}$

Substituting the velocity and temperature profiles into equation (2), assuming small temperature variations between the fluid and the wall and negligible axial conduction in the fluid (high Peclet number), the expressions of entropy generation $\bar{g}$ (per unit length and per unit depth) in a channel of width $2D$ for the case of constant wall heat flux and constant wall surface temperature are as follows:

(*a*) *Constant wall heat flux-entropy generation*

$$\bar{g}=2\int_0^D g\,dy=\frac{3}{2}\left(\frac{\mu'\dot{m}^2}{T_{AV}\rho^2D^3}\right)+\frac{34}{35}\left(\frac{\dot{q}''^2D}{kT_{AV}^2}\right) \tag{6}$$

(*b*) *Constant wall surface temperature-entropy generation*

$$\bar{g}=\frac{3}{2}\left(\frac{\mu'\dot{m}^2}{T_{AV}\rho^2D^3}\right)+1.128\left(\frac{\dot{q}''^2(x)D}{kT_{AV}^2}\right) \tag{7}$$

where T_{AV} is the average fluid temperature in the flow field. In equation (7), the heat transfer rate $\dot{q}''$ is a function of the axial position in the channel. Therefore, in order to determine the total entropy generation in a channel with walls maintained at a constant surface temperature, equation (7) must be integrated over the entire channel length.

Turbulent Flow. A control volume analysis [6] based on average fluid properties over the channel cross-sectional area is developed and solved by using the turbulent convective correlations. Again, small temperature variation between the surface and the core flow temperature is assumed.

The heat transfer rate $\dot{q}''$ is constant in the control volume shown in Fig. 1; however, it can in general be a function of x

Nomenclature

A_0 = parameter 1; for constant heat flux: $\dot{q}''D/kT_{AV}$; for constant mass diffusion rate: $\dot{m}_dD/D_{v,A}C_{AV}M_A$
B_0 = parameter 2; for constant heat flux: $(\mu'/kT_{AV})^{3/2}(\dot{q}''/\rho)$; for constant mass diffusion rate: $(\mu'/D_{v,A}C_{AV})^{3/2}(\dot{m}_d/M_A\rho)(RT)^{-1/2}$
C = molar concentration, mole/m^3
c_P = constant pressure specific heat, kJ/kg K
$2D$ = plate spacing, mm
D_v = mass diffusivity, m^2/s
Ec = Eckert number = U^{*2}/c_pT^*
Eu = Euler number = P^*/ρ^*U^{*2}
f = nondimensional friction coefficient = $(dp/dx)=(f/r_h)(G^2/2\rho)$
g = rate of entropy generation per unit volume, W/m^3-K
$\bar{g}$ = rate of entropy generation per unit length and depth, W/m^2-K
$\bar{\bar{g}}$ = rate of entropy generation per unit depth, W/m-K
G = mass flux, kg/m^{2}s
h = specific enthalpy or convective heat transfer coefficient, kJ/kg or W/m^2-K
H = total enthalpy of mixture, kJ
J = mass diffusion flux, mole/m^{2}s
k = thermal conductivity, W/m-K
k_v = mass transfer coefficient, m/s
$\bar{K}$ = rate of formation per unit volume, mole/m^{3}s
L = length of channel, m
$\dot{m}$ = mass flowrate per unit depth, kg/s m
M = molecular weight, g/mole
$\dot{m}_d$ = mass diffusion rate, kg/m^{2}s
M_D = mass transfer loading per unit depth, kg/m s
n = number of moles
Nu_D = Nusselt number = hD/k
P = local pressure, kPa
Pr = Prandtl number = $\mu'c_p/k$
$\dot{q}''$ = heat transfer rate per unit depth and length, W/m^2
Q = heat transfer loading per unit depth, W/m s
R = gas constant, kJ/kg K
r_h = hydraulic radius, m
Re = Reynolds number = $\rho U(4r_h)/\mu'$
s = specific entropy, kJ/kg K
S = total entropy of mixture, kJ/K
$\bar{S}$ = partial molar entropy of a specie = $-(\partial\mu_\alpha/\partial T)_{P,n_{\beta\neq\alpha}}$, kJ/mole K
Sc = Schmidt number = $\mu'/\rho D_v$
Sh_D = Sherwood number = k_vD/D_v
T = local temperature, K
T_m = mean fluid temperature, K
T_0 = wall surface temperature, K
U = fluid velocity, m/s
v = specific volume, m^3/kg
V = volume, m^3
x, y = coordinate notations
X = body force, kJ/mole m
Y^* = nondimensional coordinate = y/D
ϵ = energy flux, kJ/m^{2}s
η = nondimensional temperature difference = $(T_i-T^*)/T^*$
μ' = friction coefficient, kg/m s
μ = chemical potential, kJ/mole
ξ = nondimensional concentration difference = $(C_{Ai}-C_A^*)/C_A^*$
ρ = fluid density, kg/m^3

Subscripts

1, 2 = inlet and exit conditions
A, α, β = species
AV = average quantity
i = inlet condition or Cartesian tensor notation
j = Cartesian tensor notation
opt = optimum quantity
x, y = Cartesian coordinates

Superscripts

0 = standard quantity
* = characteristic quantity
$\cdot$ = rate

Table 1 Optimum Reynolds numbers and optimum plate spacing in constant heat flux case

	Laminar flow	Turbulent flow
Re	$0<\mathrm{Re}<2300$	$3(10^4)<\mathrm{Re}<10^5$
f	$24/\mathrm{Re}$	$0.046\,\mathrm{Re}^{-0.2}$
Nu_{4D}	8.232	$0.022\,\mathrm{Pr}^{0.5}\,\mathrm{Re}^{0.8}$
$\mathrm{Re}^{*}_{\mathrm{opt}}$	0	$27.13\,\mathrm{A}_0^{1.111}\,\mathrm{Pr}^{-0.139}\,B_0^{-0.556}$
$2D^{\dagger}_{\mathrm{opt}}$	$2.075\left(\frac{T_{Av}k}{\dot{q}''}\right)[\mathrm{Re}\,B_0]^{1/2}$	$0.0986\left(\frac{T_{Av}k}{\dot{q}''}\right)[\mathrm{Pr}^{0.125}\,B_0^{0.5}\,\mathrm{Re}^{0.9}]$

*Spacing $2D$ = constant
†Massflow $\dot{m}$ = constant

in the flow field. Instead of using the local fluid properties, as in the laminar flow case, all fluid properties are based on the average mean values across the channel. The approach developed in this section is not limited to the fully developed flow region, but can also be applied to determine the entropy generation in a channel where the heat transfer coefficient varies in the flow direction. In order to perform the analysis, the distributions of heat flux and heat transfer coefficient in the flow direction must be known.

Considering the first law of thermodynamics as applied to the control volume, we have

$$2\dot{q}''dx = \dot{m}dh \tag{8}$$

The second law of thermodynamics for the control volume gives

$$\bar{g} = \dot{m}\frac{ds}{dx} - \frac{2\dot{q}''}{T+\Delta T} \tag{9}$$

The Gibbs equation for a single component fluid is given as

$$dh = Tds + vdP \tag{10}$$

Combining equations (8), (9), and (10) and using average fluid and heat transfer parameters, the entropy generation $\bar{g}$ can be expressed as

$$\bar{g} = \left[\frac{\dot{m}^3 f}{8\rho^2 D^3 T_{AV}}\right] + \left(\frac{\dot{q}''^2}{T_{\mathrm{AV}}^2}\right)\left[\frac{2D}{(\mathrm{Nu})_D k}\right] \tag{11}$$

By substituting the appropriate nondimensional friction coefficient f and Nusselt number Nu_D (for the case of constant heat flux or constant surface temperature), the entropy generation for turbulent flow in a parallel-plate channel can be expressed in terms of Reynolds number, fluid properties, and channel width.

The laminar flow results, equations (6) and (7), can also be obtained by using the control volume approach. The entropy generation using both methods for the case of laminar flow yield good agreement, except for the second term in equation (7) which has a maximum 6 percent error.

Optimum Design Criterion for Laminar and Turbulent Heat Transfer. To minimize entropy generation for a fixed heat transfer load, either the mass flowrate or the plate spacing is fixed, and the optimum plate spacing or optimum Reynolds number is determined. These results are summarized in Table 1, and the parameters A_0 and B_0 are defined in the nomenclature.

To find the optimum plate spacing $2D_{\mathrm{opt}}$ for the case of constant wall surface temperature, it is necessary to integrate equation (11) in the flow direction in order to obtain the total entropy generation in the channel. For a long channel which satisfies the relation $(L/4r_h) >> 0.05\,\mathrm{Re\,Pr}$, the entire flow field can be approximately considered to be fully developed [5]. Hence, the convective heat transfer coefficient and Nusselt number will be independent of the axial position x. In general, the wall heat flux is very easy to obtain by solving the first-order differential equation governing the mean fluid temperature distribution in the x direction. For a specific total

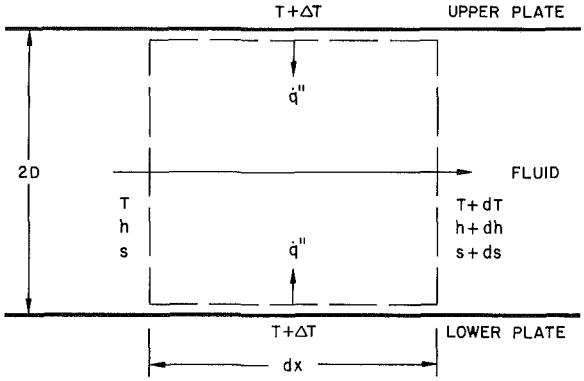

Fig. 1 Differential element illustrating the control volume approach

heat transfer loading Q in a channel with length L and a fixed mass flowrate $\dot{m}$, the optimum plate spacing $2D_{\mathrm{opt}}$ can be obtained by solving the following equation numerically

$$\frac{d}{dD}\left\{\left(\frac{Q}{2c_pT_{AV}\dot{m}}\right)\left[1-\frac{2}{1-\exp\left[\left(\frac{2k}{c_p\dot{m}}\right)\left(\frac{L}{D}\right)\mathrm{Nu}_D\right]}\right] + \frac{\dot{m}^3 f}{8\rho^2 D^3\left(\frac{Q}{L}\right)}\right\} = 0 \tag{12}$$

Also by replacing dD by $d\dot{m}$ in equation (12) and keeping the channel length L and spacing $2D$ fixed, the optimum Reynolds number for the constant surface temperature case can also be determined in a similar manner.

Numerical Example. Consider the flow of air in a channel 0.6 m long having a total air mass flowrate 0.0067 kg/s m passing through the channel with inlet and exit temperatures of

$$T_1 = 39.45°\mathrm{C}, \quad T_2 = 26.44°\mathrm{C}$$

The average fluid temperature is approximately the arithmetic mean between the inlet and exit temperatures, $T_{AV} = 306$ K. For air, we have the following data evaluated at the mean fluid temperature

$$\rho = 1.165\ (\mathrm{kg/m^3}), \quad \mu' = 1.8\times10^{-5}\ (\mathrm{kg/m\,s})$$

$$k = 26.37\times10^{-3}\ (\mathrm{W/m\,K})$$

The Reynolds number based on hydrodynamic diameter for this problem is 732, which is in the laminar flow regime.

Constant Heat Flux Model. The value of the constant heat flux is calculated from the inlet and exit temperatures. Using the appropriate equation given in Table 1, the optimum plate spacing is determined to be

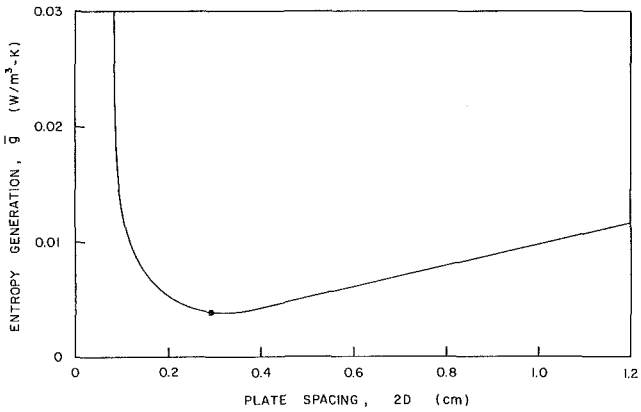

Fig. 2 Entropy generation versus plate spacing for the case of constant surface heat flux

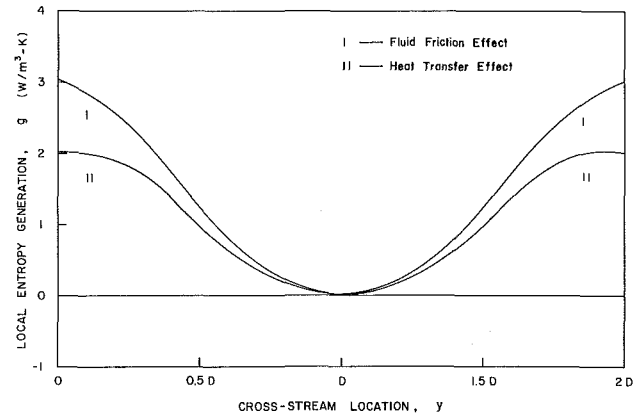

Fig. 3 Local entropy generation across the parallel-plate channel for the case of constant surface heat flux

$$(2D)_{\text{opt}} = 2.88 \text{ mm} \tag{13}$$

For this example, the variation of the entropy generation versus the plate spacing is plotted in Fig 2. The optimum design condition is 2.88 mm. The corresponding distribution of local entropy generation in the channel is shown in Fig. 3. Areas I and II in Fig. 3 represent the entropy generation due to fluid friction and heat transfer, respectively; the sum of these two values is the total entropy generation in the channel.

Constant Surface Temperature Model. Solving equation (12) numerically, the optimum channel spacing for this case is determined to be

$$(2D)_{\text{opt}} = 2.94 \text{ mm} \tag{14}$$

Entropy Generation in Isothermal Convective Mass Transfer

Considering isothermal convective mass transfer, the entropy generation g of an incompressible Newtonian fluid is given by terms (*i*) and (*ii*) in equation (1)

$$g = \frac{\mu'}{T}\left(\frac{\partial U_i}{\partial x_j}\right)\left[\frac{\partial U_i}{\partial x_j} + \frac{\partial U_j}{\partial x_i}\right] - \frac{1}{T}\sum_{\alpha} J_{\alpha i}\left(\frac{\partial \mu_\alpha}{\partial x_i}\right) \tag{15}$$

Assuming the fluid is a perfect gas mixture, the chemical potential of each species can be expressed in the following manner [7]

$$\mu_\alpha(T, P_\alpha) \equiv \mu_\alpha^0(T) + RT \ln P_\alpha \tag{16}$$

The flux of mass due to diffusion $J_{\alpha i}$ in the mixture in the absence of other potential gradients is given by Fick's law

$$J_{\alpha i} = -D_{v,\alpha} \nabla C_\alpha \tag{17}$$

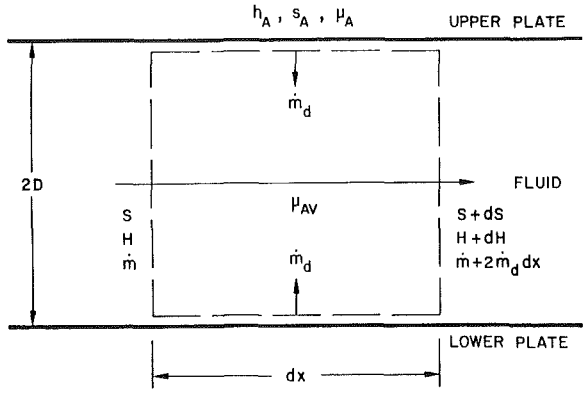

Fig. 4 Differential element illustrating the control volume approach in the case of isothermal mass transfer

Using the definition of $J_{\alpha i}$ and the ideal gas equation of state for each species, $P_A = C_A RT$, together with equations (16) and (17), the entropy generation g in a two-dimensional flow field of single species A diffusing perpendicular to the flow direction can be simplified to

$$g = \frac{\mu'}{T}\left\{2\left[\left(\frac{\partial U_x}{\partial x}\right)^2 + \left(\frac{\partial U_y}{\partial y}\right)^2\right] + \left[\left(\frac{\partial U_x}{\partial y}\right) + \left(\frac{\partial U_y}{\partial x}\right)\right]^2\right\} + R\left(\frac{D_{v,A}}{C_A}\right)\left(\frac{dC_A}{dy}\right)^2 \tag{18}$$

The relative importance of viscous and mass diffusion effects on the entropy generation in isothermal convective mass transfer problems is indicated by the nondimensional group $(\text{Sc}_A/\text{Eu}\ \xi^2)$. This is analogous to the expression $(\text{Ec Pr}/\eta^2)$, which indicates the relative importance between viscous and heat conduction effects in convective heat transfer problems. Equation (18) now can be used to study the generation of entropy in isothermal mass transfer devices.

Control Volume Approach. A control volume approach is developed for the isothermal mass transfer problem. Considering the control volume as shown in Fig. 4, the corresponding first law, second law, and Gibbs equations are as follows

First Law of Thermodynamics:

$$d\dot{H} = 2\dot{m}_d h_A dx \tag{19}$$

Second Law of Thermodynamics:

$$\bar{\dot{g}} = d\dot{S} - 2\,\dot{m}_d s_A dx \tag{20}$$

Gibbs Equation for a Mixture:

$$dH = TdS + VdP + \sum_{\alpha} \mu_{\text{av},\alpha} dn_\alpha \tag{21}$$

Equations (19), (20), and (21) for a single species A diffusing in the flow yield the entropy generation per unit depth $\bar{\dot{g}}$

$$\bar{\dot{g}} = -\left(\frac{\dot{V}}{T}\right)dp + \left(\frac{2\dot{m}_d dx}{TM_A}\right)(\mu_A - \mu_{AV}) \tag{22}$$

Using the definition of chemical potential and assuming small concentration variation in the flow field, the chemical potential difference in equation (22) becomes

$$(\mu_A - \mu_{AV}) = RT[(C_A - C_{AV})/C_{AV}] + \text{higher-order terms} \tag{23}$$

In the case of small mass diffusion rate, the mass flowrate can be assumed to be constant and the volumetric flowrate is equal to the mass flowrate divided by the fluid density, and the

Table 2 Optimum Reynolds numbers and optimum plate spacing in constant mass diffusion rate case

	Laminar flow	Turbulent flow
Re	$0<\mathrm{Re}<2300$	$3(10^4)<\mathrm{Re}\leq 10^5$
f	$24/\mathrm{Re}$	$0.046\ \mathrm{Re}^{-0.2}$
Sh_{4D}	8.232	$0.022\ \mathrm{Sc}_A^{0.5}\ \mathrm{Re}^{0.8}$
$\mathrm{Re}^*_{\mathrm{opt}}$	0	$27.13\ \mathrm{A}_0^{1.111}\ \mathrm{Sc}_A^{-0.139}\ B_0^{-0.556}$
$2D^\dagger_{\mathrm{opt}}$	$2.075\left(\frac{D_{v,A}C_{Av}M_A}{\dot{m}_d}\right)[\mathrm{Re}\ B_0]^{1/2}$	$0.0986\left(\frac{D_{v,A}C_{Av}M_A}{\dot{m}_d}\right)[\mathrm{Sc}_A^{0.125}\ B_0^{0.5}\ \mathrm{Re}^{0.9}]$

*Spacing $2D$ = constant
†Massflow $\dot{m}$ = constant

pressure gradient in the x direction will be the same as that for a flow without mass diffusion. Substituting equation (23) into (22) and neglecting the higher-order terms, the entropy generation per unit depth and length $\bar{g}$ can be expressed as follows

$$\bar{g}=\frac{\dot{m}^3 f}{8\rho^2 D^3 T}+\left(\frac{2}{\mathrm{Sh}_D}\right)\left(\frac{\dot{m}_d^2 RD}{D_{v,A}C_{AV}M_A^2}\right) \tag{24}$$

Entropy Generation and Optimum Design Criterion for Small Diffusion Rates. Two mass transfer problems, of constant surface concentration and constant surface mass flux, are solved by using the analogy between heat and mass transfer. Considering the Lewis number equal to unity and the flow to be fully developed, the results for the case of constant surface mass flux are summarized in Table 2. The analogy between heat and mass transfer assumes that mass diffusion rates are sufficiently small, so that the velocity profile is unaffected by the diffusing species and can be approximately represented by the velocity profile when diffusion is not considered.

Similar to the heat transfer problem, it is impossible to express the optimum plate spacing explicitly for the case of constant surface mass concentration with a specific mass transfer loading M_D in a channel with length L. However, the solution can be obtained numerically by solving the following equation

$$\frac{d}{dD}\left\{\left(\frac{\rho M_D}{2M_A C_{AV}\dot{m}}\right)\left[1-\frac{2}{1-\exp\left[\left(\frac{2\rho D_{v,A}}{\dot{m}}\right)\left(\frac{L}{D}\right)\mathrm{Sh}_D\right]}\right]+\frac{\dot{m}^3 f}{8\rho^2 D^3\left(\frac{M_D RT}{LM_A}\right)}\right\}=0 \tag{25}$$

Limiting Cases of Combined Heat and Mass Transfer

The problems of convective heat transfer and isothermal convective mass transfer considered in this work are two limiting cases of combined heat and mass transfer. In order to determine the relative magnitude of the heat transfer effect as compared to the mass diffuson effect in a combined heat and mass transfer problem, an order-of-magnitude analysis is performed on equation (1). This will provide criteria for when the results presented above can be used.

Assuming the diffusing species is an ideal gas, the entropy generation for combined heat and mass transfer in a two-dimensional flow with single species A diffusing in the y direction can be simplified as

$$g=\frac{\mu'}{T}\left\{2\left[\left(\frac{\partial U_x}{\partial x}\right)^2+\left(\frac{\partial U_y}{\partial y}\right)^2\right]+\left[\left(\frac{\partial U_x}{\partial y}\right)+\left(\frac{\partial U_y}{\partial x}\right)\right]^2\right\}+R\left(\frac{D_{v,A}}{C_A}\right)\left(\frac{dC_A}{dy}\right)^2+\frac{k}{T^2}\left[\left(\frac{\partial T}{\partial x}\right)^2+\left(\frac{\partial T}{\partial y}\right)^2\right]+R\left(\frac{D_{v,A}}{T}\right)\left(\frac{dC_A}{dy}\right)\left(\frac{\partial T}{\partial y}\right) \tag{26}$$

Normalizing equation (26) and then comparing the heat transfer effect with the mass diffusion effect, the result shows that the order of the ratio of heat transfer effect to the mass diffusion effect can be represented as

$$\mathrm{O}\left(\frac{g_{\text{heat transfer effect}}}{g_{\text{mass diffusion effect}}}\right)=\frac{\mathrm{Sc}_A}{\mathrm{Eu\ Pr\ Ec}}\left(\frac{\eta}{\xi}\right)^2 \tag{27}$$

where Sc_A and Eu are the Schmidt and Euler numbers of the diffusing species, and Pr and Ec represent the Prandtl and Eckert numbers of the binary mixture, respectively. The nondimensional characteristic temperature and concentration differences, η and ξ, are defined as

$$\eta\equiv\frac{T_i-T^*}{T^*},\qquad \xi\equiv\frac{C_{Ai}-C_A^*}{C_A^*} \tag{28}$$

where T_i and C_{Ai} are the initial mean fluid temperature and mass concentration at the inlet of the channel and T^* and C_A^* are the characteristic temperature and mass concentration of the diffusing specie A, both of which depend on the boundary conditions.

The nondimensional group $[\mathrm{Sc}_A/\mathrm{Eu\ Pr\ Ec}]$ and the nondimensional ratio $(\eta/\xi)^2$ give the relative importance of the heat transfer effect as compared to the mass diffusion effect. The former term is due to the properties of the substance and the latter term is due to the respective loading between heat transfer and mass transfer.

The cases of purely convective heat transfer and purely convective mass transfer are two limiting cases of the combined heat and mass transfer problem. The present study focuses on these two special cases:

(*a*) The heat transfer effect dominates the entire flow field, i.e.,

$$\mathrm{O}(g_{\text{heat transfer effect}}/g_{\text{mass diffusion effect}})>>1.0$$

Under this condition, $(\xi/\eta)^2\sim\mathrm{O}(1)$ and the coupling effect term as well as the mass diffusion term can be dropped from the entropy generation equation.

(*b*) The mass diffusion effect dominates the entire flow field, i.e.,

$$\mathrm{O}(g_{\text{heat transfer effect}}/g_{\text{mass diffusion effect}})<<1.0$$

Under these circumstances, the coupling effect term can be dropped if $(\eta/\xi)^2<<1.0$, and the remaining terms will be the same as those for the convective mass transfer problem.

Conclusions

Two limiting problems of entropy generation of heat transfer and isothermal mass transfer in a two-dimensional device are considered. The mechanism of entropy generation in isothermal mass diffusion has a similar behavior as that in convective heat transfer. The results show that the entropy generation is minimum for a given plate spacing. The effect of increasing the plate spacing from the optimum point causes gradual increase in the entropy generation. However, as the plate spacing decreases below the optimum plate spacing, the

increase in entropy generation is very steep. These results provide the information and equations necessary to optimize the design of heat or mass exchangers.

Acknowledgments

The work reported in this paper was supported by the U.S. Department of Energy, Office of Solar Applications, Active Solar Heating and Cooling Division, San Francisco Operations Office under Contract DE-AC 03-84SF15257. In addition, the authors wish to acknowledge the helpful discussions and suggestions of R. LeChevalier, DOE-SAN.

References

1 Van Wylen, G. J., and Sonntag, R. E., *Fundamentals of Classical Thermodynamics*, Wiley, New York, 1979, Chap. 8.

2 Bejan, A., "The Concept of Irreversibility in Heat Exchanger Design: Counterflow Heat Exchanger for Gas to Gas Application," ASME JOURNAL OF HEAT TRANSFER, Vol. 99, Aug. 1977.

3 Bejan, A., *Entropy Generation Through Heat and Fluid Flow*, Wiley, New York, 1982, Chap. 7.

4 Hirschfelder, J. O., Curtiss, C. F., and Bird, R. B., *Molecular Theory of Gases and Liquids*, Wiley, New York, 1954.

5 Kays, W. M., and Crawford , M. E., *Convective Heat and Mass Transfer*, McGraw-Hill, New York, 1980, Chap. 8.

6 Bejan, A., "General Criterion for Rating Heat Exchanger Performance," *Int. J. Heat Mass Transfer*, Vol. 21, 1978, pp. 655-658.

7 Denbigh, K., *The Principles of Chemical Equilibrium*, Cambridge University Press, 1981, Chap. 3.

Forced Convection in a Duct Partially Filled With a Porous Material

D. Poulikakos

M. Kazmierczak

Department of Mechanical Engineering,
University of Illinois at Chicago,
Chicago, IL 60680

This paper presents a theoretical study of fully developed forced convection in a channel partially filled with a porous matrix. The matrix is attached at the channel wall and extends inward, toward the centerline. Two channel configurations are investigated, namely, parallel plates and circular pipe. For each channel configuration, both the case of constant wall heat flux and constant wall temperature were studied. The main novel feature of this study is that it takes into account the flow inside the porous region and determines the effect of this flow on the heat exchange between the wall and the fluid in the channel. The Brinkman flow model which has been proven appropriate for flows in sparsely packed porous media and for flows near solid boundaries was used to model the flow inside the porous region. Important results of engineering interest were obtained and are reported in this paper. These results thoroughly document the dependence of the Nusselt number on several parameters of the problem. Of particular importance is the finding that the dependence of Nu on the thickness of the porous layer is not monotonic. A critical thickness exists at which the value of Nu reaches a minimum.

1 Introduction

Convective heat transfer in fluid-saturated porous media has been the topic of several studies published in the literature in recent years. The interest in convection in porous media is motivated by a wide range of thermal engineering applications, such as geothermal systems, oil extraction, solid matrix heat exchangers, ground water pollution, thermal insulation, and the storage of nuclear wastes. A comprehensive review of the majority of the existing studies on the above topics, with a special focus on studies pertinent to geothermal systems, was published by Cheng (1978).

An important class of problems directly related to porous matrix convection is heat and fluid flow in *composite* systems, that is, systems consisting partly of a fluid-saturated porous material and partly of a fluid. The convection phenomenon in these systems is usually affected by the interaction of the temperature and flow fields in the porous spaces and the open spaces. The importance of this class of problem is justified both in a fundamental and in a practical sense. With reference to practical thermal engineering applications which stand to benefit if a better understanding of heat and the fluid flow processes in composite systems is acquired, the following examples are cited: fibrous and granular insulation which occupies only part of the space between a hot and a cold boundary, fault zones in geothermal systems, the cooling of stored grain, and heat removal from nuclear debris beds in nuclear reactor safety. In addition to the above, a less obvious application directly related to composite (porous/fluid) layer heat transfer is that of a solidifying casting. As discussed by Beckerman et al. (1986) and by Fisher (1981) a mushy zone may exist during solidification, consisting of a mesh of dendrites that can be modeled as a porous medium.

Most of the existing studies on convection in composite layers focus on the problem of natural convection in an enclosure (Beckerman et al., 1986) or an infinite horizontal layer partially filled with a porous material (see for example, Somerton and Catton, 1982; Nield, 1977; Nield, 1983). To the best of our knowledge, no studies outside this problem exist in the literature. The present investigation is concerned with the problem of forced convection in a channel with a porous region attached at its walls. Since the porous region near the walls of the channel is permeable, fluid flow will take place *inside* this region. Therefore, the existing results for convection in a channel with solid walls cannot be used to predict the convection phenomenon in the composite (porous/fluid) channel which comprises the main focus of this study. A separate analysis is necessary in order to take into account the fact that the convection phenomenon evolves inside both the porous and the open spaces. Thermal engineering applications related to the problem under investigation are exemplified by fault zones in geothermal systems, solid matrix heat exchangers, and the use of foametals for heat transfer enhancement. In addition, the deposit of materials over long time periods on the inside of channel walls used in heat transfer apparatus often creates porous layers of the type examined in the present study.

Two basic duct geometries will be investigated thoroughly: parallel plates and a circular pipe (Fig. 1). The convection phenomenon for each geometry will be documented for two sets of thermal boundary conditions: isothermal wall and constant heat flux wall.

2 Mathematical Formulation

The configurations of interest are shown schematically in Fig. 1. Specifically, Fig. 1(*a*) is a pictorial view of two parallel porous plates located at a distance $2H$. The gap between the two plates is occupied by a fluid flowing in the x direction. The surfaces of the plate walls facing the outside are impermeable and kept at constant temperature T_w or constant heat flux q''_w condition. However, since the plates are porous, there exists fluid flow *within* the plates. Hence, there is coupling between the temperature and flow fields in the porous and open regions. Both the temperature and the flow fields in the channel are assumed to be fully developed. Figure 1(*b*) shows the second channel configuration of interest, namely, a circular pipe of radius H with porous walls. The previous discussion for the parallel plate channel holds in this case as well.

The governing conservation equations for fully developed heat and flow fields in the channel will be written separately for the fluid and the porous region. For the fluid region the momentum and energy equations, respectively, are

Contributed by the Heat Transfer Division for publication in the JOURNAL OF HEAT TRANSFER. Manuscript received by the Heat Transfer Division April 28, 1986.

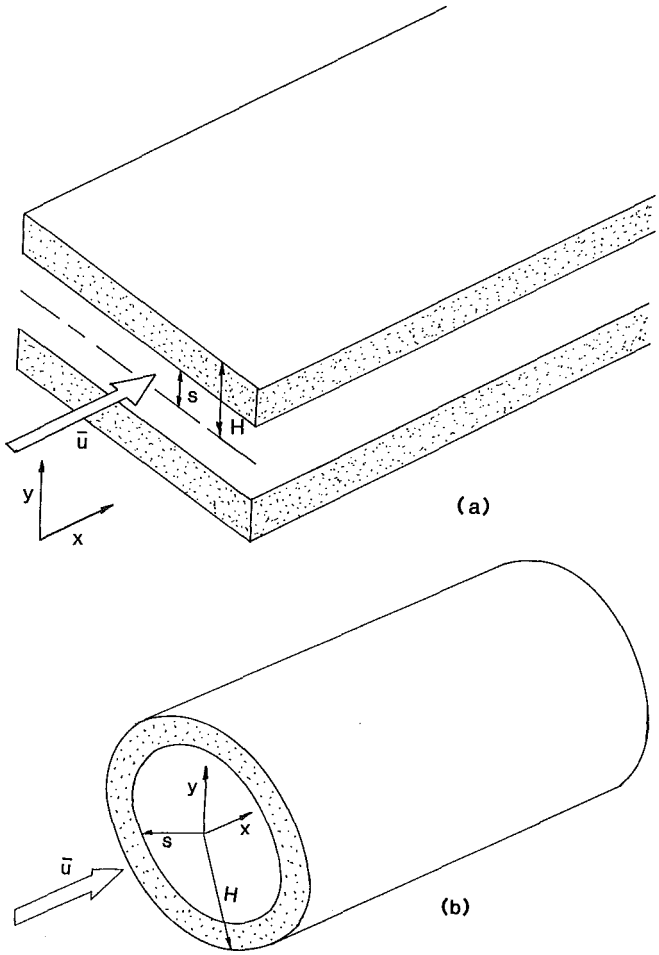

Fig. 1 Pictorial view of the channel configurations of interest: (a) two parallel plates, (b) a circular pipe. Both channel configurations are partially filled with porous medium.

$$0 = -\frac{dP_*}{dx_*} + \mu \frac{1}{y_*^m} \frac{d}{dy_*}\left[y_*^m \frac{du_*}{dy_*}\right] \tag{1}$$

$$\rho c_p u_* \frac{\partial T_*}{\partial x_*} = k \frac{1}{y_*^m} \frac{\partial}{\partial y_*}\left[y_*^m \frac{\partial T_*}{\partial y_*}\right] \tag{2}$$

Note that equations (1) and (2) apply for both the parallel plate channel ($m=0$) and the circular pipe ($m=1$). The temperature is denoted by T_*, the axial velocity by u_*, the pressure by P_*, and the fluid viscosity, density, and thermal conductivity by μ, ρ, and k, respectively.

The conservation equations for the porous region are based on the Brinkman-extended Darcy model. This model features a momentum equation which takes into account friction due to macroscopic shear and reduces to the viscous flow limit for high permeability. In addition, this model satisfies the physically real no-slip condition on a solid boundary. Regarding the energy equation, it is assumed that the fluid and the porous matrix are in local thermal equilibrium. The momentum and energy equations in the porous matrix are

$$0 = -\frac{dP_*}{dx_*} + \mu_{\text{eff}} \frac{1}{y_*^m}\left[y_*^m \frac{du_*}{dy_*}\right] - \frac{\mu}{K} u_* \tag{3}$$

$$\rho c_p u_* \frac{\partial T_*}{\partial x_*} = k_{\text{eff}} \frac{1}{y_*^m} \frac{\partial}{\partial y_*}\left(y_*^m \frac{\partial T_*}{\partial y_*}\right) \tag{4}$$

In the above equations K is the porous medium permeability and μ_{eff}, k_{eff} the effective kinematic viscosity and thermal conductivity of the porous medium. It has been found that taking $\mu_{\text{eff}} = \mu$ in equation (3) provides good agreement with experimental data (Neale and Nader, 1974; Lundgren, 1972). This assumption has been used successfully in several studies exemplified by Beckerman et al. (1986) and Somerton and Catton (1982) and is adopted here as well. Note that the quadratic inertia term (Cheng, 1978) has been neglected in equation (3). Similarly, the thermal dispersion term has been neglected in equations (2) and (4). Therefore, the results of the present model are applicable for relatively low Reynolds numbers.

Nomenclature

A = constant defined by equation (13)
A_c = channel cross-sectional area
B = constant defined by equation (15)
C = constant defined by equation (16)
$\cosh(x)$ = hyperbolic cosine of x
c_p = specific heat of the fluid
Da = Darcy number = K/H^2
D_h = hydraulic diameter of the channel
$f(y)$ = arbitrary function of y
h = heat transfer coefficient
H = pipe radius or half of parallel plate separation distance
$I_0(x)$ = zeroth-order Bessel function of the first kind
$I_1(x)$ = first-order Bessel function of the first kind
k = thermal conductivity of the fluid
k_{eff} = effective thermal conductivity of the porous medium
K = permeability of the porous medium
$K_0(x)$ = zeroth-order Bessel function of the second kind
$K_1(x)$ = first-order Bessel function of the second kind
m = exponent denoting the channel configuration: $m=0$ corresponds to parallel plates and $m=1$ to circular pipe
$M(y)$ = expression defined by equations (21) and (22)
$N(y)$ = expression defined by equations (28) and (29)
Nu = Nusselt number = $D_h h/k$
P = pressure
q'' = heat transfer rate per unit area
q_w'' = heat transfer rate per unit area at the wall
R = thermal conductivity ratio = k_{eff}/k
s = thickness of the open region
$\sinh(x)$ = hyperbolic sine of x
T = temperature
$\tanh(x)$ = hyperbolic tangent of x
T_m = mixed mean fluid temperature = $(1/A_c \bar{u}_*) \int_{A_c} u_* T_* dA_c$
T_w = wall temperature
u = axial velocity
$\bar{u}$ = mean axial velocity
x = axial coordinate
y = coordinate perpendicular to x axis
θ = dimensionless temperature for the isothermal channel case = $(T_* - T_w)/(T_m - T_w)$
λ = binary parameter, equation (18)
μ = dynamic viscosity of the fluid
μ_{eff} = effective dynamic viscosity of fluid-saturated porous medium
ρ = fluid density
ϕ = dimensionless temperature for the constant wall heat flux case = $(T_* - T_w)/(-q_w''/h)$

Superscripts

$*$ = dimensional quantity
w = pertaining to quantities evaluated at the wall

The boundary conditions necessary to complete the problem formulation are

$$T_* = T_w \text{ or } \frac{\partial T_*}{\partial y_*} = \frac{q''_w}{k}, \qquad u_* = 0 \text{ at } y_* = H$$

$$\frac{\partial T_*}{\partial y_*} = 0, \quad \frac{\partial u_*}{\partial y_*} = 0 \quad \text{at } y_* = 0 \tag{5}$$

In addition to boundary conditions (5) the two sets of equations (1), (2) and (3), (4) are coupled by the following matching conditions at the porous/fluid interface:

$$(T_*)_{y_*=s^-} = (T_*)_{y_*=s^+}$$

$$\left(k\frac{\partial T_*}{\partial y_*}\right)_{y_*=s^-} = \left(k_{\text{eff}}\frac{\partial T_*}{\partial y_*}\right)_{y_*=s^+} \tag{6}$$

$$(u_*)_{y_*=s^-} = (u_*)_{y_*=s^+}$$

$$\left(\mu\frac{\partial u_*}{\partial y}\right)_{y_*=s^-} = \left(\mu_{\text{eff}}\frac{\partial u_*}{\partial y_*}\right)_{y_*=s^+}$$

It is worth clarifying that conditions (5) state that the velocity vanishes on the wall, that the temperature or the heat flux is constant on the wall, and that the temperature and velocity gradients vanish at the centerline of the channel. Similarly, conditions (6) stand for temperature, heat flux, velocity, and shear stress continuity at the interface. The physically real shear stress and velocity matching conditions (6) can be satisfied only if Brinkman's extension is used to model the fluid flow. The use of the Darcy model results in unrealistic velocity and shear stress discontinuities at the porous/fluid interface (Beckerman et al., 1986; Neale and Nader, 1974; Beavers and Joseph, 1967).

3 Theoretical Solution

The heat and fluid flow characteristics of the problem modeled mathematically in the previous section will be revealed after the relevant equations and boundary conditions are solved. The flow field in the channel is independent of the temperature field since the present study pertains to forced convection. The momentum equations (1) for the fluid space and (3) for the porous space can be solved theoretically subject to conditions (5) and (6) for both channel configurations of interest, namely the parallel plates and the circular pipe. Omitting the details for brevity we report here only the final results. For the parallel plate channel the velocity distribution is:

(*a*) *Fluid region, $0 \le y \le s$*

$$u = \tfrac{1}{2}(y^2 - s^2) - \mathrm{Da}^{1/2} s \tanh[(1-s)\mathrm{Da}^{1/2}] + \mathrm{Da}\left[\frac{1}{\cosh[(1-s)\mathrm{Da}^{-1/2}]} - 1\right] \tag{7}$$

(*b*) *Porous region, $s \le y \le 1$*

$$u = \frac{\mathrm{Da}\cosh[(s-y)\mathrm{Da}^{-1/2}] - \mathrm{Da}^{1/2} s \sinh[(1-y)\mathrm{Da}^{-1/2}]}{\cosh[(1-s)\mathrm{Da}^{-1/2}]} - \mathrm{Da} \tag{8}$$

Based on equations (7) and (8) the average velocity of the channel is calculated

$$\bar{u} = [\mathrm{Da}^{3/2} - s^2\mathrm{Da}^{1/2}]\tanh[(1-s)\mathrm{Da}^{-1/2}] + s\mathrm{Da}\left[\frac{2}{\cosh[(1-s)\mathrm{Da}^{-1/2}]} - 1\right] - \mathrm{Da} + \tfrac{1}{3}[2 - 3s - (1-s)^2(2+s)] \tag{9}$$

All the variables have been nondimensionalized based on the following definitions:

$$(x, y, s) = (x_*, y_*, s_*)/H,$$

$$(u, \bar{u}) = (u_*, \bar{u}_*)\Big/\frac{H^2}{\mu}\frac{dP_*}{dx_*} \tag{10}$$

A new parameter appeared as a result of the nondimensionalization process, namely, the Darcy number

$$\mathrm{Da} = K/H^2 \tag{11}$$

Note that we chose not to use the average velocity $\bar{u}_*$ as a reference quantity for the nondimensionalization of u_*. The reason behind this choice lies in the fact that the average velocity $\bar{u}_*$ depends on Da and on s, two parameters whose effect on the flow field we plan to investigate thoroughly. In addition, expression (9) is complicated enough not to be inviting as a reference quantity.

The velocity distribution inside the circular pipe geometry was found to be:

(*a*) *Fluid region, $0 \le y \le s$*

$$u = \frac{y^2}{4} + A \tag{12}$$

where

$$A = \frac{\mathrm{Da}K_1(s\mathrm{Da}^{-1/2}) + \dfrac{\mathrm{Da}^{1/2}s}{2}K_0(\mathrm{Da}^{-1/2})}{I_0(\mathrm{Da}^{-1/2})K_1(s\mathrm{Da}^{-1/2}) + I_1(s\mathrm{Da}^{-1/2})K_0(\mathrm{Da}^{-1/2})} \left[I_0(\mathrm{Da}^{-1/2}s) + \frac{I_1(s\mathrm{Da}^{-1/2})K_0(s\mathrm{Da}^{-1/2})}{K_1(s\mathrm{Da}^{-1/2})}\right] - \frac{\dfrac{s\mathrm{Da}^{1/2}}{2}K_0(s\mathrm{Da}^{-1/2})}{K_1(s\mathrm{Da}^{-1/2})} - \left(\mathrm{Da} + \frac{s^2}{4}\right) \tag{13}$$

(*b*) *Porous region, $s \le y \le 1$*

$$u = BI_0(\mathrm{Da}^{-1/2}) + CK_0(\mathrm{Da}^{-1/2}y) - \mathrm{Da} \tag{14}$$

where

$$B = \frac{\mathrm{Da}K_1(s\mathrm{Da}^{-1/2}) + \dfrac{\mathrm{Da}^{1/2}s}{2}K_0(\mathrm{Da}^{-1/2})}{I_0(\mathrm{Da}^{-1/2})K_1(s\mathrm{Da}^{-1/2}) + I_1(s\mathrm{Da}^{-1/2})K_0(\mathrm{Da}^{-1/2})} \tag{15}$$

$$C = \frac{\left[\mathrm{Da}K_1(s\mathrm{Da}^{-1/2}) + \dfrac{\mathrm{Da}^{1/2}s}{2}K_0(\mathrm{Da}^{-1/2})\right]I_1(s\mathrm{Da}^{-1/2})}{[I_0(\mathrm{Da}^{-1/2})K_1(s\mathrm{Da}^{-1/2}) + I_1(s\mathrm{Da}^{-1/2})K_0(\mathrm{Da}^{-1/2})]K_1(s\mathrm{Da}^{-1/2})} - \frac{\mathrm{Da}^{1/2}s/2}{K_1(s\mathrm{Da}^{-1/2})} \tag{16}$$

The expression for the average velocity in this case reads

$$\bar{u} = 2\left[\frac{s^4}{16} + A\frac{s^2}{2} + B\mathrm{Da}^{1/2}\{I_1(\mathrm{Da}^{-1/2}) - sI_1(s\mathrm{Da}^{-1/2})\} - C\mathrm{Da}^{-1/2}\{K_1(\mathrm{Da}^{-1/2}) - sK_1(s\mathrm{Da}^{-1/2})\} - \frac{1-s^2}{2}\mathrm{Da}\right] \tag{17}$$

The features of the velocity field revealed by equations (7)–(9), and (12)–(17) will be discussed in the next section. Here, we will proceed with the solution for the temperature field.

Two types of thermal boundary conditions will be considered: uniform heat flux (q''_w) and uniform temperature (T_w). The analysis is aided somewhat if we observe that equa-

tions (2) and (4) can be combined into a unique energy equation by introducing the following binary parameter:

$$\lambda = \begin{cases} 1 \text{ in the porous region} \\ 0 \text{ in the fluid region} \end{cases} \tag{18}$$

The energy equation then becomes

$$\rho c_p u_* \frac{\partial T_*}{\partial x_*} = [\lambda(k_{\text{eff}} - k) + k] \frac{1}{y_*^m} \frac{d}{dy_*}\left[y_*^m \frac{dT_*}{dy_*}\right] \tag{19}$$

It is understood that the system under investigation is a *single* channel. Neither the porous region nor the fluid region can be solved independently. These regions need to be considered together if a solution is to be obtained. Therefore, the solution of the present problem is based on the usual definition of fully developed heat transfer in a channel, that is, $(T_w - T)/(T_w - T_m) = f(y)$, where T_m is the mean temperature for the whole channel defined in the nomenclature and $f(y)$ an arbitrary function of the coordinate perpendicular to the x axis. The procedure for obtaining the fully developed temperature field in the channel configurations of interest is similar to that used for classical fluids and can be found in the literature in references such as the text by Bejan (1984). Hence, for the sake of brevity, no details are included here. For the constant heat flux case, explicit expressions for the temperature field can be derived. These expressions are:

(*a*) *Parallel plates*

$$\phi = \text{Nu} M(y) \tag{20}$$

where, for the fluid layer ($0 \le y \le s$)

$$M(y) = -\frac{1}{4\bar{u}}\left\{\frac{(1-y)^4}{24} - \frac{(1-y)^3}{6} + \frac{1-y}{3} + \left[-\text{Da}^{1/2} s \tanh[(1-s)\text{Da}^{-1/2}] + \text{Da}\left[\frac{1}{\cosh[(1-s)\text{Da}^{-1/2}]} - 1\right] - \tfrac{1}{2}(1-s)^2 + (1-s)\right]\left(\frac{(1-y)^2}{2} - (1-y)\right) + \frac{1}{R}\left[\frac{\text{Da}^2 - \text{Da}^{3/2} s \sinh[(1-s)\text{Da}^{-1/2}]}{\cosh[(1-s)\text{Da}^{-1/2}]} - \frac{1-s}{3} - \text{Da}\frac{(1-s)^2}{2} - \frac{(1-s)^3}{2} + \frac{(1-s)^4}{6} - \left(-\text{Da}^{1/2} s \tanh[(1-s)\text{Da}^{-1/2}] + \text{Da}\left[\frac{1}{\cosh[(1-s)\text{Da}^{-1/2}]} - 1\right] - \frac{(1-s)^2}{2} + 1 - s\right) s(1-s) + \text{Da}(1-s) - \text{Da}^2\right] - \frac{1-s}{3} + \frac{(1-s)^3}{6} - \frac{(1-s)^4}{24} - \left[-\text{Da}^{1/2} s \tanh[(1-s)\text{Da}^{-1/2}] + \text{Da}\left[\frac{1}{\cosh[(1-s)\text{Da}^{-1/2}]} - 1\right] - \frac{(1-s)^2}{2} + 1 - s\right]\left(\frac{(1-s)^2}{2} - (1-s)\right)\right\} \tag{21}$$

and for the porous layer, ($s \le y \le 1$)

$$M(y) = -\frac{1}{4\bar{u}R}\left\{\frac{\text{Da}^2 \cosh[(s-y)\text{Da}^{-1/2}] - \text{Da}^{3/2} s \sinh[(1-y)\text{Da}^{-1/2}]}{\cosh[(1-s)\text{Da}^{-1/2}]} - \text{Da}\frac{(1-y)^2}{2} + \left[\frac{(1-s)^3}{6} - \frac{(1-s)^2}{2} + \frac{1}{3} - \left(-\text{Da}^{1/2} s \tanh[(1-s)\text{Da}^{-1/2}] + \text{Da}\left[\frac{1}{\cosh[(1-s)\text{Da}^{-1/2}]} - 1\right] - \frac{s^2}{2} + \tfrac{1}{2}\right) s + \text{Da}\right](1-y) - \text{Da}^2\right\} \tag{22}$$

The Nusselt number, the dimensionless temperature, and the ratio of thermal diffusivities, respectively, are defined as

$$\text{Nu} = \frac{D_h h}{k} \tag{23}$$

$$\phi = \frac{T_* - T_w}{-q_w''/h} \tag{24}$$

$$R = \frac{k_{\text{eff}}}{k} \tag{25}$$

where h is the heat transfer coefficient at the channel wall ($y = 1$) and D_h the hydraulic diameter of the channel. The Nusselt number is obtained from the following expression

$$\text{Nu} = \frac{\bar{u}}{\int_0^1 M(y) u dy} \tag{26}$$

(*b*) *Circular pipe*

$$\phi = \text{Nu}\, N(y) \tag{27}$$

where, for the fluid layer ($0 \le y \le s$)

$$N(y) = -\frac{1}{\bar{u}}\left\{\frac{y^4}{64} + A\frac{y^2}{4} + \frac{1}{R}\left[B\text{Da} I_0(\text{Da}^{-1/2}) + C\text{Da} K_0(\text{Da}^{-1/2}) - \text{Da}\frac{s^2}{4} + \ln s\left(\frac{s^3}{16} + B\frac{s}{2} - B\text{Da}^{1/2} I_1(\text{Da}^{-1/2} s) + C\text{Da}^{1/2} K_1(\text{Da}^{-1/2} s) + \text{Da}\frac{s}{2}\right)s + \frac{\text{Da}}{4} - B\text{Da} I_0(\text{Da}^{-1/2}) - C\text{Da} K_0(\text{Da}^{-1/2})\right]\frac{s^4}{64} - A\frac{s^2}{4}\right\} \tag{28}$$

For the porous layer, on the other hand ($s \le y \le 1$)

$$N(y) = \frac{1}{\bar{u}R}\left\{B\text{Da} I_0(\text{Da}^{-1/2} y) + C\text{Da} K_0(\text{Da}^{-1/2} y) - \text{Da}\frac{y^2}{4} + \ln y\left[\frac{s^3}{16} + A\frac{s}{2} - B\text{Da}^{1/2} I_1(\text{Da}^{-1/2} s) + C\text{Da}^{1/2} K_1(\text{Da}^{-1/2} s) + \text{Da}\frac{s}{2}\right]s + \frac{\text{Da}}{4} - B\text{Da} I_0(\text{Da}^{-1/2}) - C\text{Da} K_0(\text{Da}^{-1/2})\right\} \tag{29}$$

The Nusselt number in this case is obtained from the following equation:

$$\text{Nu} = \frac{\bar{u}}{2\int_0^1 N(y) u y dy} \tag{30}$$

It is worth reporting that in deriving equations (20)–(30) the following conditions were satisfied:

$$\frac{d\phi}{dy}=0 \text{ at } y=0, \qquad \phi=0 \text{ at } y=1$$

$$(\phi)_{s^+}=(\phi)_{s^-}, \qquad R\left(\frac{d\phi}{dy}\right)_{s^+}=\left(\frac{d\phi}{dy}\right)_{s^-} \tag{31}$$

The above conditions reflect the symmetry of the temperature field about the centerline, the vanishing of the wall temperature, and the continuity of the temperature and the heat flux at the porous/open interface.

The remaining steps for obtaining the temperature distributions and the Nusselt numbers for both duct geometries are carried out numerically as follows: For prescribed values of Da, R, and s, the Nusselt number is calculated from equation (26) or equation (30). Next, the temperature distribution is obtained directly from equation (20) or equation (27).

The solutions for the isothermal wall boundary condition cases are considerably more complicated and they cannot be obtained analytically. Instead, they are obtained after the following set of equations is solved numerically:

$$-\frac{\mathrm{Nu}/4^{1-m}}{[\lambda(R-1)+1]}\frac{u}{\bar{u}}\theta=\frac{1}{y^m}\frac{d}{dy}\left[y^m\frac{d\theta}{dy}\right] \tag{32}$$

$$y=0, \qquad \frac{d\theta}{dy}=0 \tag{33}$$

$$y=1, \qquad \theta=0 \tag{34}$$

$$\mathrm{Nu}=-(2+2^{1-m})\left(\frac{d\theta}{dy}\right)_{y=1} \tag{35}$$

Note that θ is the dimensionless temperature.

$$\theta=\frac{T_*-T_w}{T_m-T_w} \tag{36}$$

Equations (32)–(35) constitute a differential eigenvalue problem with Nu being the eigenvalue. The solution procedure adopted in this study started with guessing a value for Nu. Next, equations (32)–(35) were solved numerically with the help of the fourth-order Runge-Kutta method. Note that guessing a value for Nu is equivalent to guessing a value for the temperature gradient at the wall. Since the value of the temperature at the wall is also prescribed, two boundary conditions at the wall are known. Consequently, it is possible to begin the Runge-Kutta integration starting from the wall and proceeding toward the centerline. After θ was obtained, the condition of vanishing temperature gradient at the centerline was checked. The above procedure was repeated until the guessed value of Nu yielded a temperature field that satisfied the boundary condition at the centerline. Before closing this section, it is worth clarifying that the Nusselt number definition in this study is based on the fluid thermal conductivity k in order to show directly the effect of the porous region of Nu, relative to the case where no porous region exists (in classical fluid studies, Nu is also customarily based on k). A Nusselt number based on k_{eff} can be easily obtained if the Nusselt number used in this study is divided by the ratio $R = k_{\mathrm{eff}}/k$.

4 Results and Discussion

At first, the effect of the porous region on the flow field in the channel will be described. Figure 2 corresponds to the case where the thickness of porous region near the wall equals 20 percent of the channel half-width. Clearly, the presence of the porous matrix slows down the fluid flow. This effect becomes more dramatic as the Darcy number (permeability) decreases. For all practical purposes, values of Da less than 10^{-5} yield negligible flow in the porous region. However, as the Darcy

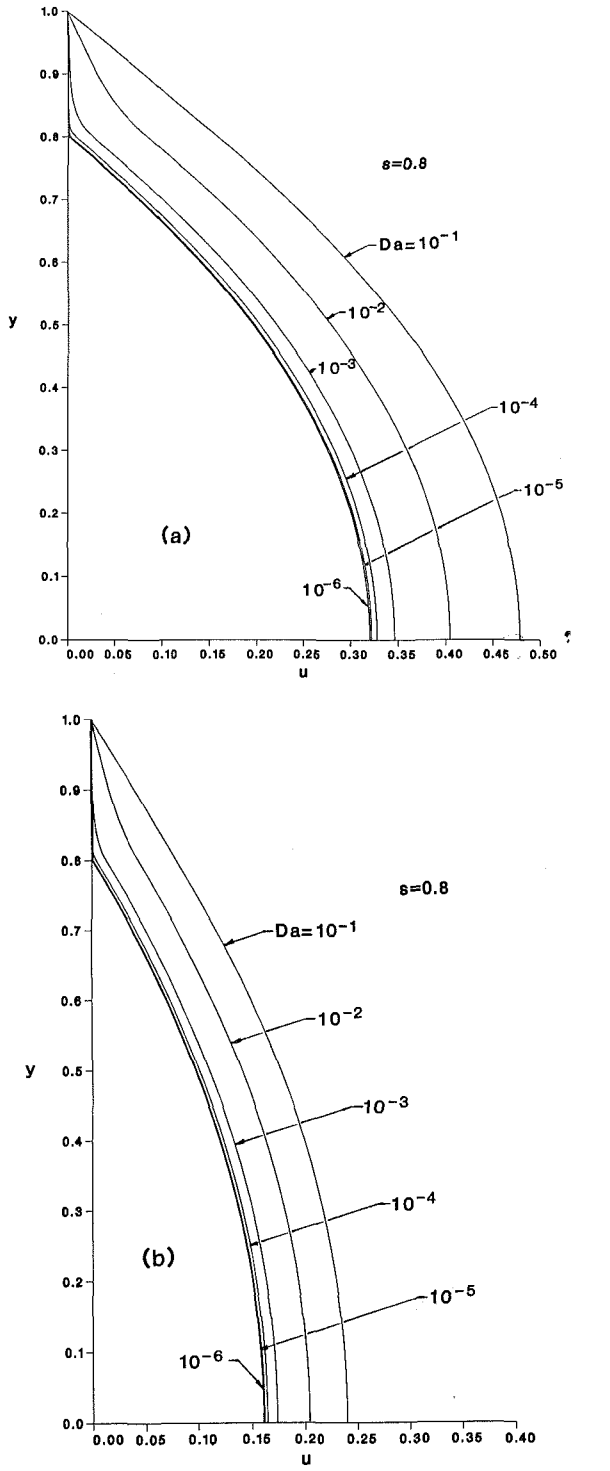

Fig. 2 Velocity profiles for $s = 0.8$ and representative values of Da: (a) parallel plates, (b) circular pipe

number increases the resistance to flow in the porous medium decreases. Both channel configurations, namely, the parallel plates (Fig. 2(a)) and the circular pipe (Fig. 2(b)), behave in a qualitatively similar manner.

The effect of the thickness of the porous region on the velocity profile is illustrated in Fig. 3(a, b) for a fixed value of the Darcy number. Increasing the thickness of the porous region causes a dramatic decrease in the fluid velocity in both the porous and the open spaces. For example, in going from the case of a channel filled with a classical fluid (no porous region, $s = 1$) to the case where 20 percent of the channel

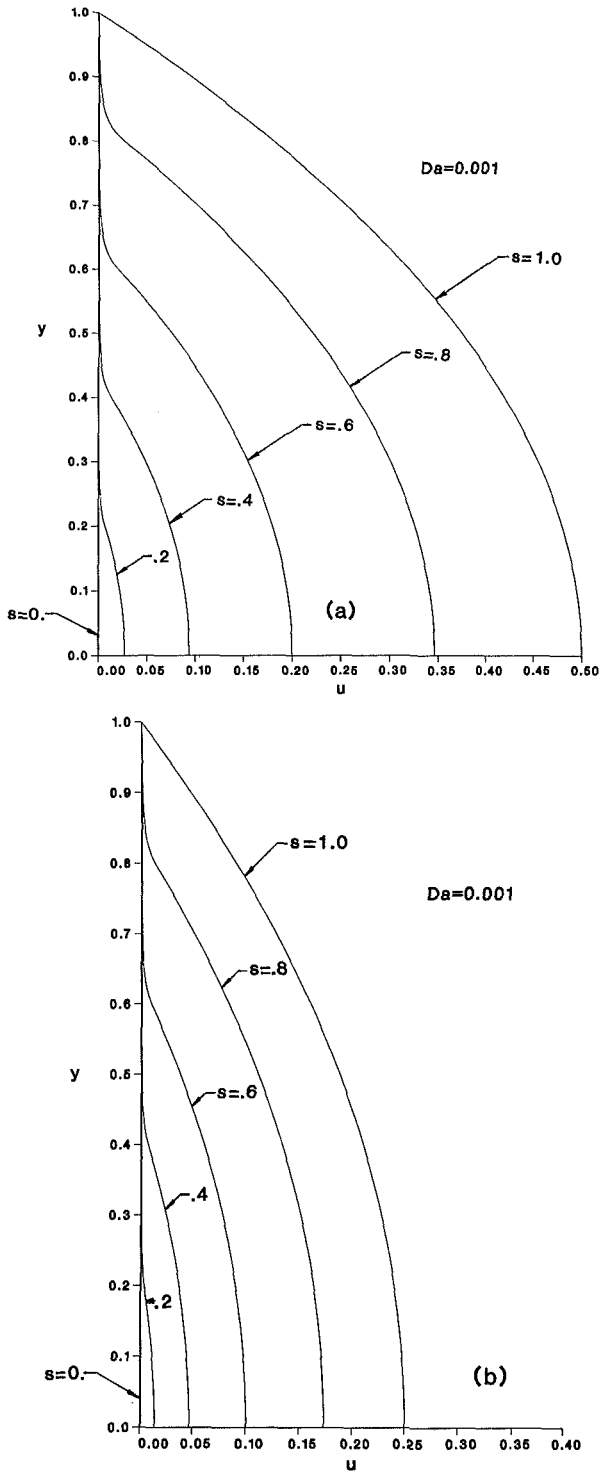

Fig. 3 Velocity profiles for Da = 10^{-3} and representative values of s: (*a*) parallel plates, (*b*) circular pipe

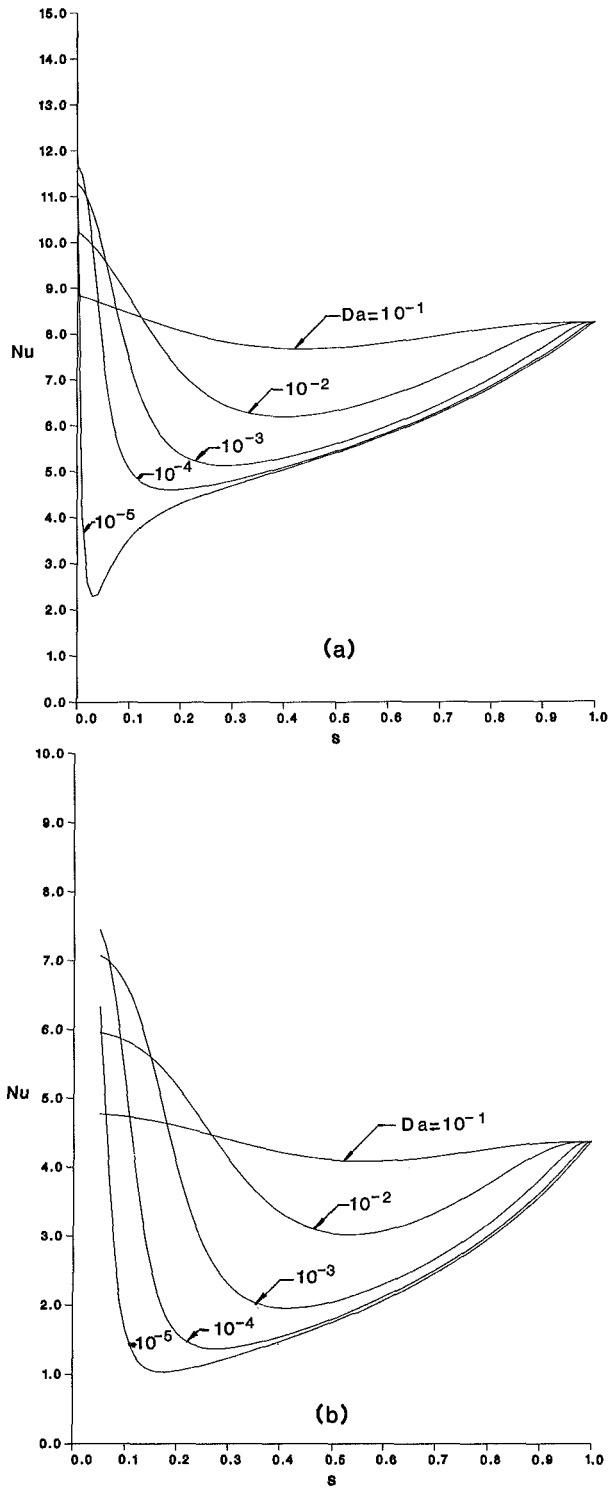

Fig. 4 Nu versus s for constant wall heat flux: (*a*) parallel plates, (*b*) circular pipe; $R = 1$

width is occupied by porous medium, we observe a 30 percent decrease in the maximum velocity (approximately) in both channel configurations (Fig. 3(*a*, *b*)).

An additional question may be raised from studying Figs. 2 and 3. The magnitude of the velocity inside the porous matrix is less than the magnitude of the velocity in the open region. This fact is more noticeable when the Darcy number is small. Therefore, natural convection may appear in the porous region. Since natural convection has been assumed negligible in our model, the results reported in this study will not be accurate in its presence. On the other hand, the following issues, relevant to the presence of free convection, need to be clarified: (*a*) The fact that the velocity magnitude inside the porous region is smaller than the velocity magnitude inside the open region does not necessarily mean that natural convection is of importance in the porous region. The velocity scales for transition from forced to free convection in porous media are different from the respective scales in classical fluids. What appears to be a small velocity from the perspective of classical fluids may actually be a high-enough velocity to sustain forced convection in porous media. (*b*) A "conservative" criterion may be used to decide whether free convection is present in the

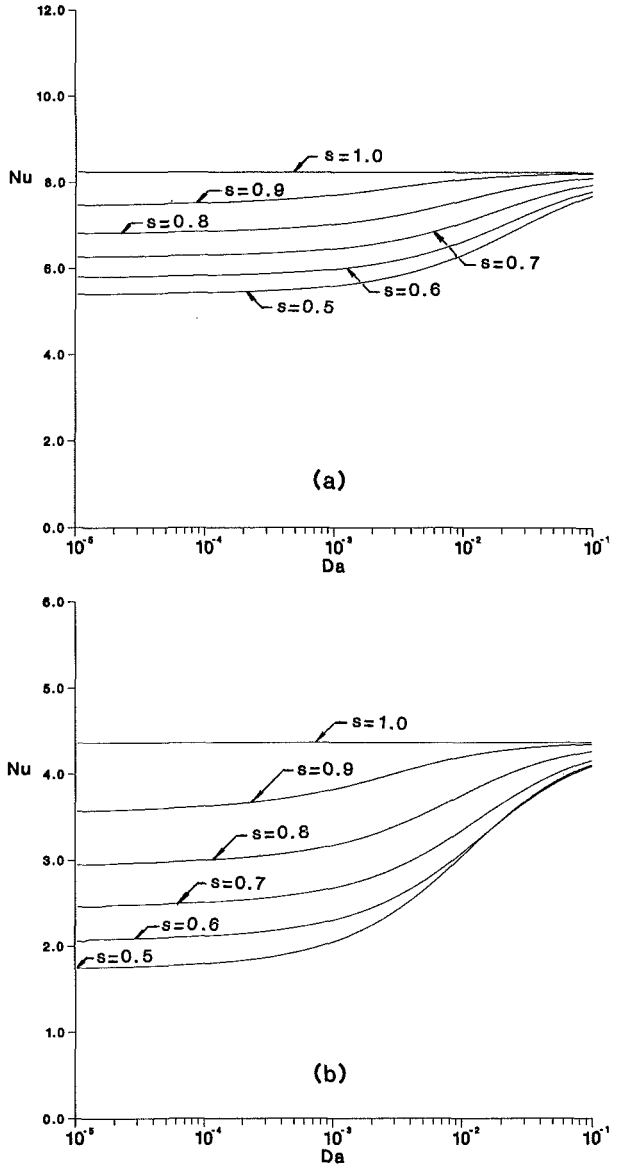

Fig. 5 Nu versus Da for constant wall heat flux: (*a*) parallel plates, (*b*) circular pipe; $R = 1$

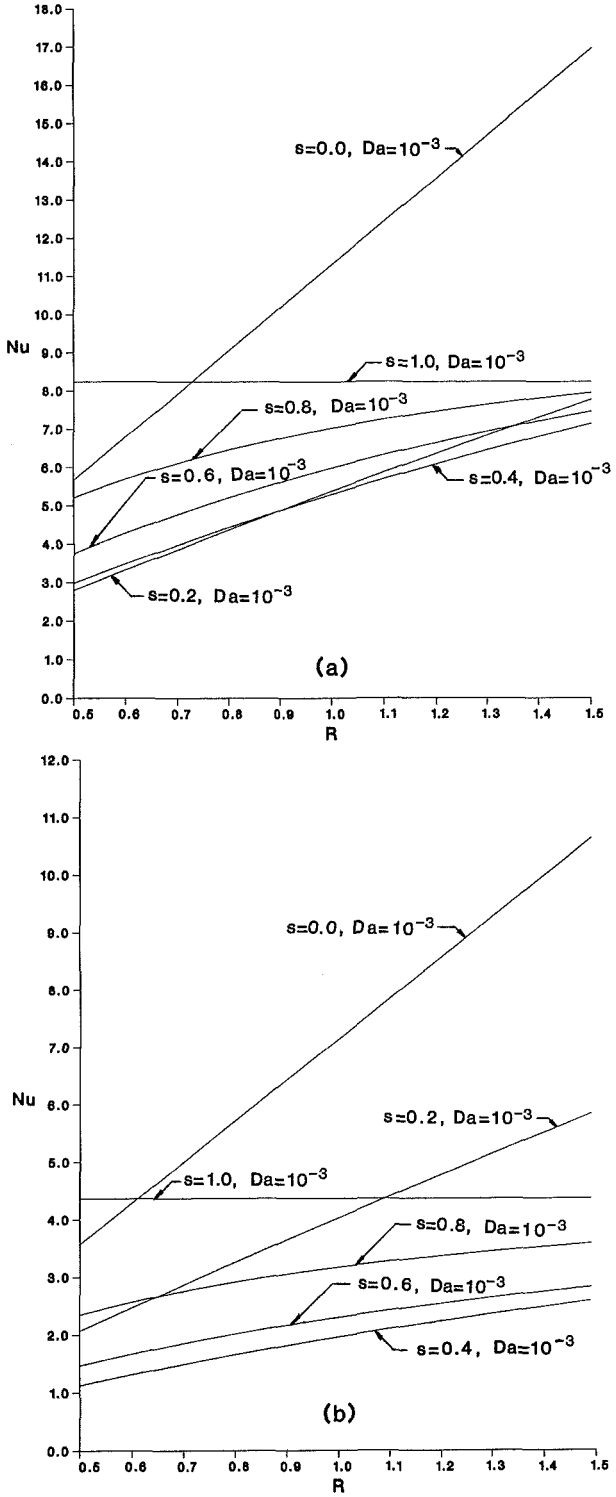

Fig. 6 Nu versus *R* for constant wall heat flux: (*a*) parallel plates, (*b*) circular pipe

system, in the vicinity of the bottom wall, for the parallel plate configuration (the vicinity of the top wall is stably stratified). This criterion consists of calculating the Darcy-modified Rayleigh number based on the porous region thickness and the temperature difference across the porous layer and comparing this Rayleigh number to the critical Rayleigh number for the onset of Benard convection in a horizontal porous layer. If the critical Rayleigh number is smaller (in an order of magnitude sense) than the Rayleigh number for the present system, natural convection will likely exist in the system.

The above discussion makes it clear that the presence of the porous region severely affects the flow field in the channel. Hence, it is expected that the heat transfer process from the channel wall to the fluid inside the channel will be affected as well. To investigate this question we turn our attention to the findings obtained from solving the energy equation. Figures 4–6 pertain to the constant heat flux boundary condition.

Figure 4(*a*, *b*) depicts the dependence of Nu on s for characteristic values of Da. For all values of Da shown in Fig. 4 and for both the parallel plate duct (Fig. 4(*a*)) and the circular duct (Fig. 4(*b*)), the dependence of Nu on s is nonmonotonic. A minimum in Nu exists in all curves. This result is both unexpected and of engineering importance. The physical explanation for this finding is as follows: It can be easily shown via the definition of Nu (equation (23)) that the Nusselt number is inversely proportional to the "effective" temperature difference of the channel, that is, $\mathrm{Nu} \sim 1/(T_w - T_m)$. As the thickness of the porous layer increases, the flowrate through the channel decreases. Since the heat flux through the channel wall is constant, both T_w and T_m at a given distance will increase. For small values of the porous region thickness (s less but close to unity) it is reasonable to ex-

pect that the wall temperature T_w will be affected by the presence of the porous matrix more severely than the average temperature T_m. As a result, the characteristic temperature difference $T_w - T_m$ will increase and the value of Nu will decrease compared to the value of Nu for the case where no porous region exists in the duct. As the thickness of the porous region increases (s decreases) the rise in the mean temperature becomes more pronounced until a "critical" thickness is reached, after which the dependence of T_m on s is stronger than the dependence of T_w on s. After this critical point, decreasing s further decreases the effective temperature difference $T_w - T_m$ and therefore increases the value of Nu. The above line of reasoning explains the U-shape of all the Nu versus s curves. It is worth noting that in the limit $s = 1$ (channel filled with a classical fluid, i.e., no porous region present) the well-known values of Nu for fully developed flow and heat transfer are obtained. As the Darcy number increases, i.e., the permeability increases and the presence of the porous matrix becomes less dominant, the dependence of Nu on s weakens considerably. In addition, the presence of the minimum on the Nu versus s curve shifts to the right. The physical implication of this result is that the value of the critical thickness of the porous layer required for T_m to start increasing faster than T_w is larger for low permeability porous media. A perhaps surprising observation can be made if the case of a channel completely filled with porous medium is examined (Fig. 4(a), $s = 0$). In this case, we see that Nu decreases as Da increases. This is due to the fact that the velocity profile changes between slug flow (very small Darcy number) and parabolic flow (classical fluids very large Darcy number). It is known that the former case yields Da = 12 and the latter case Da = 8.235. The results of the present study in Fig. 4(a) for $s = 0$ verify this trend.

The dependence of Nu on the Darcy number for a channel partially filled with porous medium is shown in Fig. 5(a, b). For the values of s in Fig. 5, increasing Da increases Nu. In the limit $s = 1$ the Nusselt number is independent of Da, as expected. As Da increases the value of Nu approaches the classical fluid limit for all values of s.

The impact of the last parameter of interest, namely the ratio of the effective thermal conductivity of the porous medium to the fluid thermal conductivity, R, on the Nusselt number is shown in Fig. 6(a, b), for a host of values of s. Since the effect of s on Nu was discussed previously in conjunction with Fig. 4, here we will focus on the effect of R on Nu. Clearly, increasing R increases Nu in both channel configurations. The dependence of Nu on R is practically linear. However, the rate of increase of Nu with R (slope of Nu versus R line) decreases as s increases and becomes zero for $s = 1$. In this limit no porous material exists in the channel; hence, the well-known Nusselt number results for fully developed laminar convection in ducts are obtained. The findings that the dependence of Nu on R becomes stronger (steeper slope) as the porous layer becomes thicker (decreasing s) is a natural consequence, since a thicker porous layer means that there exists more porous material to be affected by R and, in turn, to alter the value of Nu.

The last three Figs. 7–9 pertain to the constant wall temperature cases. These results were obtained numerically in the manner explained in the previous section. The dependence of Nu on s (Fig. 7(a, b)) on Da (Fig. 8(a, b)) and on R (Fig. 9(a, b)) for the constant temperature boundary condition is similar qualitatively to the dependence of Nu on the same parameters for the constant heat flux boundary condition (Figs. 4–6). The fact that all the Nu versus s curves possess a minimum (Fig. 7) is justified as follows: Based on the definition of the Nusselt number, equation (26), it is easy to show that $\mathrm{Nu} \sim (dT/dy)_{y=1}/(T_w - T_m)$. As the thickness of the porous layer increases (s decreases) the flowrate is reduced. Hence, it is reasonable to expect that the temperature gradient

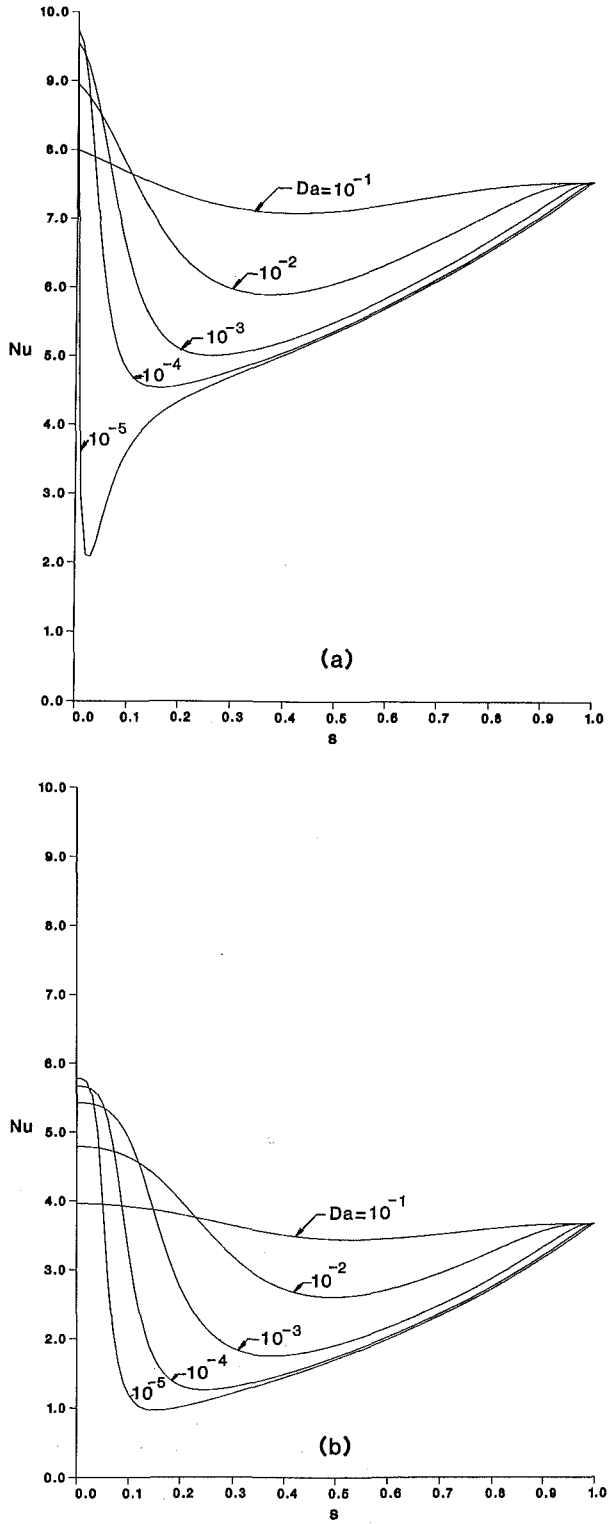

Fig. 7 Nu versus s for constant wall temperature: (*a*) parallel plates, (*b*) circular pipe; $R = 1$

at the wall must decrease to maintain constant T_w. The dependence of T_m on s, on the other hand, is not straightforward to predict, since varying s affects all: the fluid temperature, velocity, and mass flowrate. Based on the results we obtained, it appears that for small values of s (thick porous region) T_m actually increases as s decreases. This increase in T_m is equivalent to a decrease in the effective temperature difference $T_w - T_m$ appearing in the denominator of the expression for Nu (note that T_w = const in this case). The effect of

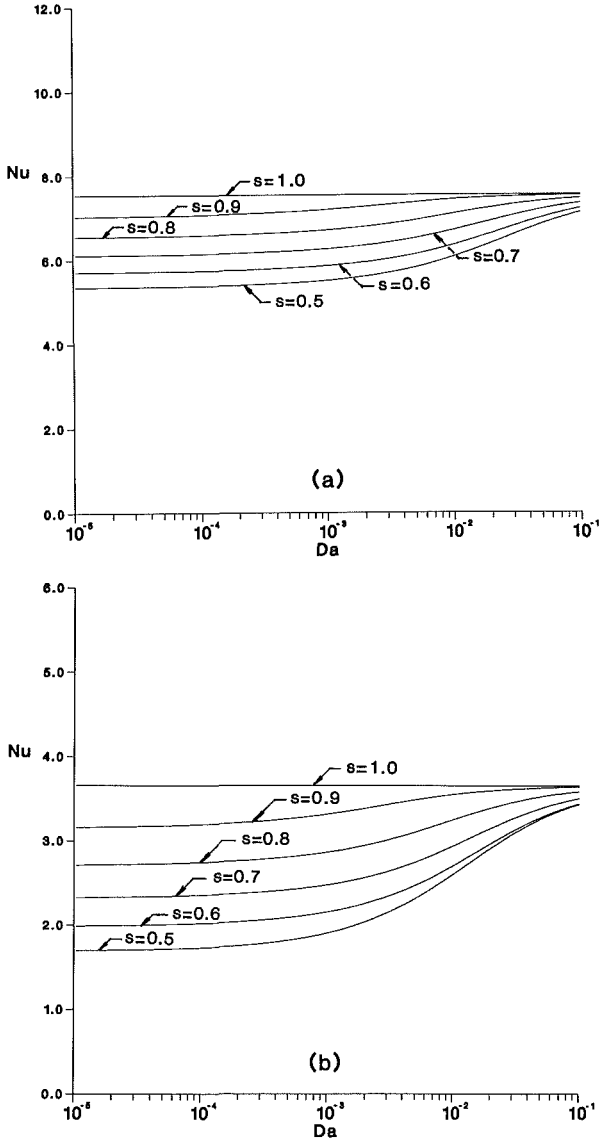

Fig. 8 Nu versus Da for constant wall temperature: (*a*) parallel plates, (*b*) circular pipe; $R = 1$

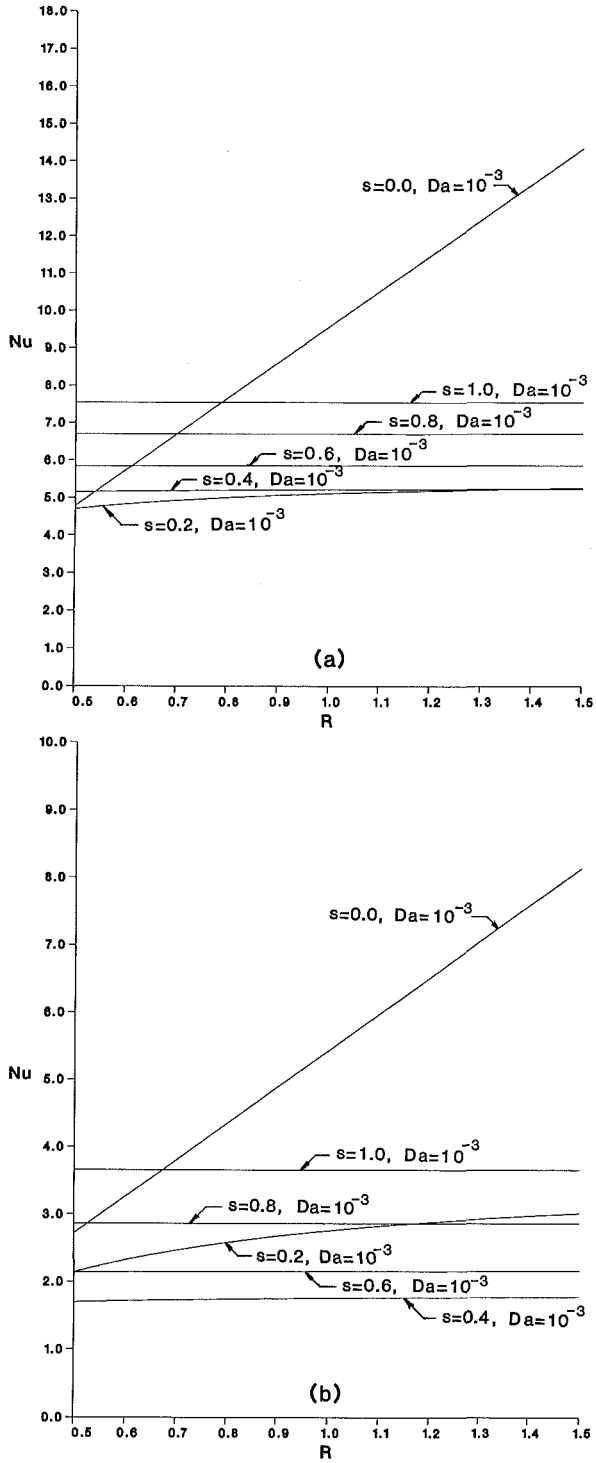

Fig. 9 Nu versus R for constant wall temperature: (*a*) parallel plates, (*b*) circular pipe

decreasing the denominator overrides the influence of decreasing the numerator in the expression $\mathrm{Nu} \sim (dT/dy)_{y=1}/(T_w - T_m)$ thus explaining the increase of Nu as s approaches zero. For higher values of s, however, the influence of the numerator prevails and, subsequently, Nu decreases. This rationale explains the existence of the minimum in all the Nu versus s curves for the constant wall temperature case. The "critical" value of s at which Nu attains a minimum value depends on Da. Increasing Da shifts the location of the minimum to the right.

The dependence of Nu on Da is illustrated in Fig. 8(*a*, *b*). In the limit $s = 1$ (no porous region) the well-known Nu value is obtained. The effect of Nu on Da becomes weaker as s increases. As expected, Nu is independent of Da at $s = 1$. Lastly, the effect of R on Nu is documented in Fig. 9(*a*, *b*). Increasing R increases Nu. The impact of R on Nu weakens as s increases and becomes negligible as the value of s approaches unity. Comparing Figs. 6 and 9 side by side we conclude that the effect of R on Nu is stronger in the case of constant wall heat flux.

5 Conclusions

This paper presented a theoretical study of forced convection in a channel partially filled with a porous medium. The fluid flow within the porous region was taken into account. This fact constitutes the main novel feature of this study. Two channel geometries (parallel plates and circular pipe) and two types of thermal boundary conditions (constant wall heat flux and constant wall temperature) were investigated extensively. The results reported in this paper thoroughly document the effect of a number of parameters on the flow field and on the heat transport in the channel. These parameters are the thickness of the porous region adjacent to the wall, the Darcy number, and the ratio of the effective thermal conductivity of

the porous medium to the fluid thermal conductivity. The impact of the above parameters on the heat and fluid flow characteristics of the channel was similar qualitatively for both channel geometries and boundary conditions. A surprising finding was that the Nusselt number dependence on the thickness of the porous region is not monotonic. A critical value of the porous region thickness exists at which the Nusselt number value reaches a minimum. This result was obtained for both channel configurations and for a host of Darcy number values.

The flow in the porous medium was modeled by using the Brinkman-modified Darcy model. The use of this model is particularly justified in high permeability porous media or in near-wall regions. As the results showed, choosing the Brinkman-modified Darcy model for this problem was appropriate: In the low Da limit ($Da < 10^{-5}$) where the present model is not valid, the flow in the porous medium is very weak and can be neglected altogether without considerable loss of accuracy. The Darcy number used in this study has physical meaning only when the porous region exists in the channel. In the case $s = 1$, the well-known results for classical fluids were recovered. These results were independent of Da, as expected.

Overall, the present study proved that the presence of a porous region near an impermeable wall may significantly alter the convection phenomenon and deserves careful consideration.

Acknowledgment

Financial support for this research provided by the National Science Foundation through grant No. ENG-8451144 is gratefully acknowledged. The authors thank Denise Burt for typing the final version of the manuscript so efficiently.

References

Beavers, G. S., and Joseph, D. D., 1967, "Boundary Conditions at a Naturally Permeable Wall," *Journal of Fluid Mechanics*, Vol. 30, pp. 197–207.

Beckermann, C., Ramadhyani, S., and Viskanta, R., 1986, "Natural Convection Flow and Heat Transfer Between a Fluid Layer and a Porous Layer Inside a Rectangular Enclosure," AIAA/ASME Heat Transfer and Thermophysics Conference, Boston, MA.

Bejan, A., 1984, *Convection Heat Transfer*, Wiley, New York, pp. 86–91.

Brinkman, H. C., 1947, "A Calculation of the Viscous Force Exerted by a Flowing Fluid on a Dense Swarm of Particles," *Applied Scientific Research*, Vol. A1, pp. 27–34.

Cheng, P., 1978, "Heat Transfer in Geothermal Systems," *Advances in Heat Transfer*, Vol. 14, pp. 1–105.

Fisher, K. M., 1981, "The Effects of Fluid Flow on the Solidification of Industrial Castings and Ingots," *PhysicoChemical Hydrodynamics*, Vol. 2, pp. 311–326.

Lundgren, T. S., 1972, "Slow Flow Through Stationary Random Beds and Suspensions of Spheres," *Journal of Fluid Mechanics*, Vol. 51, pp. 1865–1874.

Neale, G., and Nader, W., 1974, "Practical Significance of Brinkman's Extension of Darcy's Law: Coupled Parallel Flows Within a Channel and a Bounding Porous Medium," *Canadian Journal of Chemical Engineering*, Vol. 52, pp. 475–478.

Nield, D. A., 1977, "Onset of Convection in a Fluid Layer Overlaying a Layer of Porous Medium," *Journal of Fluid Mechanics*, Vol. 81, pp. 513–522.

Rohsenow, W. M., Hartnett, J. P., and Ganic, E., eds., 1985, *Heat Transfer Fundamentals*, 2nd ed., McGraw-Hill, New York.

Somerton, C. W., and Catton, I., 1982, "On the Thermal Instability of Superposed Porous and Fluid Layers," ASME JOURNAL OF HEAT TRANSFER, Vol. 104, pp. 160–165.

Turbulence Structure of Vertical Adiabatic Wall Plumes

M.-C. Lai[1]

G. M. Faeth
Fellow ASME

Department of Aerospace Engineering,
The University of Michigan,
Ann Arbor, MI 48109-2140

Weakly buoyant turbulent adiabatic wall plumes along vertical surfaces were studied. Instantaneous velocities and concentrations were measured using laser-Doppler anemometry and laser-induced fluorescence, Earlier work reported mean properties and their comparison with predictions of simplified mixing-length and k–ϵ–g *turbulence models. Velocity and concentration fluctuations and their correlations are reported in the present paper. The results show considerable deficiencies in the simplified models concerning turbulence properties, e.g., anisotropy of turbulence properties, lack of coincidence of maximum velocity and zero Reynolds stress points, and variability of the turbulence Prandtl/Schmidt number. Density/velocity correlations were found which provide a means of estimating differences between Reynolds and Favre averages, effects of turbulence fluxes on conserved quantities, and effects of buoyancy/turbulence interactions on turbulence properties.*

Introduction

Turbulent wall plumes are an important fundamental flow often present during confined natural convection processes and fires within structures. In addition, wall plumes provide an excellent opportunity for studying buoyancy/turbulence interactions since they are relatively thick, reducing problems of spatial resolution, but don't exhibit effects of large-scale disturbances (flapping) encountered in free plumes, due to the stabilizing effect of the wall. An earlier study of turbulent wall plumes reported mean and fluctuating streamwise velocities and concentrations, and used these results to evaluate simplified mixing-length and k–ϵ–g models of the process (Lai et al., 1986). The present study extends this work, providing measurements of various components of mean and fluctuating velocities, the Reynolds stresses, and correlations between velocity and concentration fluctuations. The new findings were used to evaluate predictions of turbulence properties provided by the simplified models and to suggest needed model extensions.

Past measurements of wall plumes turbulence properties are very limited. Grella and Faeth (1975) measured streamwise velocity fluctuations in turbulent adiabatic wall plumes. The flow was generated by a line heat source along the base of a vertical wall. Measurements were made using hot-wire anemometry. Liburdy and Faeth (1978) and Liburdy et al. 1979) studied turbulent thermal plumes along vertical isothermal walls. Hot-wire anemometry was used to measure mean and fluctuating velocities and temperatures and their correlations. These studies have several limitations, however, and no data are available to confirm them. First of all, parasitic heat losses from thermal wall plumes are difficult to control; therefore, adiabatic conditions were only approximated by Grella an Faeth (1975). Furthermore intrusive probes are not very reliable for measuring the properties of wall plumes. Probes have large uncertainties when turbulence intensities are high, and near surfaces; therefore, properties are only measured reliably in a narrow region of the flow. Furthermore, probes also disturb the flow, particularly near the edge of the flow where flow reversals occur.

The objective of the present study was to remove these deficiencies. Adiabatic wall plumes were simulated using carbon dioxide/air mixtures as the buoyancy source, eliminating effects of parasitic heat losses. Nonintrusive optical diagnostics were used to eliminate effects of probe disturbances and to obtain reliable results at high turbulence intensities and near surfaces. Laser-Doppler anemometry (LDA) was used to measure instantaneous velocities while laser-induced fluorescence (LIF) was used to measure the instantaneous concentration of buoyant fluid.

Lai et al. (1986) report the first phase of the study. Measurements of mean and fluctuating streamwise velocities and concentrations were obtained for wall jets and plumes along vertical and inclined plane surfaces. These flows were analyzed using two methods: the mixing-length model of Cebeci and Khattab (1975) along the lines of Liburdy et al. (1979); and a simplified k-ϵ-g turbulence model ignoring buoyancy/turbulence interactions similar to past analysis of round buoyant diffusion flames (Jeng et al., 1982; Jeng and Faeth, 1984). Both methods yielded encouraging predictions of mean quantities in spite of effects of low Reynolds numbers and large-scale coherent structures seen in the flow. Turbulent fluctuations were underestimated, however, which was attributed to effects of buoyancy/turbulence interactions. Tests with inclined surfaces showed that low levels of ambient stratification caused wall plumes to entrain ambient fluid nearly horizontally, rather than normal to the wall, introducing complications of elliptic flow for inclined configurations.

The present study extends this work considering new measurements of turbulence quantities. The study was limited to vertical surfaces, to avoid the problems of ambient stratification mentioned earlier, using the same apparatus as Lai et al. (1986). LDA and LIF techniques were used, both separately and combined, to provide new measurements of mean and fluctuating velocities and concentrations and velocity/concentration correlations. The measurements were used to evaluate deficiencies in predictions of turbulence properties found using the simplified models; to evaluate differences between conventional Reynolds time) and Favre (mass-weighted) averages; to estimate effects of turbulent fluxes on the total fluxes of conserved quantities; and to quantify effects of turbulence production by buoyancy.

The paper begins with a brief description of experimental methods. The new turbulence measurements and their comparison with predictions are then described. The paper concludes with consideration of the implications of these results with respect to types of averaging, conservation checks, and

[1] Present address: Department of Mechanical Engineering, Massachusetts Institute of Technology, Cambridge, MA.

Contributed by the Heat Transfer Division for publication in the JOURNAL OF HEAT TRANSFER. Manuscript received by the Heat Transfer Division January 20, 1986.

buoyancy/turbulence interactions. The present description is brief; Lai (1985) provides more details and a complete tabulation of data.

Experimental Methods

The test apparatus of Lai et al. (1986) was used. Carbon dioxide/air mixtures were introduced from a 20–21 mm wide slot at the top of a vertical plane wall (1000 mm long × 800 mm wide and 305-mm side walls to help preserve two dimensionality). Two wall plumes were considered having initial densities 2 and 4 percent greater than the ambient air. Initial Reynolds numbers, based on the slot width, were relatively low (390 and 474); however, the flow was turbulent at the outset. Initial Froude numbers were equal to five which roughly corresponds to the asymptotic Froude number for vertical wall plumes measured by Grella and Faeth (1975). This reduced distances needed for flow development. Checks of momentum and carbon dioxide fluxes, based on mean properties, were satisfied within 6 percent, which is reasonable in view of effects of wall friction and turbulent fluxes (Lai, 1985; Lai et al., 1986).

The instrumentation was modified somewhat from Lai et al. (1986) to provide combined LDA/LIF measurements; see Lai and Faeth (1987) for a description of the new arrangement. The main differences were that the focused LDA probe volume was also used for LIF measurements and that the LIF signal was separated from light scattered at the laser line using long-pass optical filters rather than a low-resolution monochromator. Both the slot and ambient gases were seeded with aluminum oxide particles (diameter ~ 500 nm) for the LDA measurements. The slot fluid was also seeded with iodine vapor to provide the LIF signal. The LDA and LIF signals were both sampled with an A/D converter (each at 80 Hz using a low-pass anti-aliasing filter with a 40 Hz cutoff frequency) and stored by a microcomputer (100 s sampling time). Measurements of power spectral densities of mixture fraction fluctuations showed that power spectra were on the order of 0.1 percent of maximum values at 40 Hz at the worst (Lai, 1985); therefore, the frequency response of this system was adequate. The signals were processed to yield time averages; however, the distinction between Favre and time-averaged quantities is small for present flows (less than 5 percent).

The measurements are estimated to have the following experimental uncertainties (95 percent confidence): mean and fluctuating velocities less than 4 and 6 percent, mean and fluctuating concentrations less than 5 and 10 percent, Reynolds stress less than 20 percent, and turbulent mass fluxes less than 15 percent. These estimates are based on the maximum value of each quantity and are proportionately higher elsewhere.

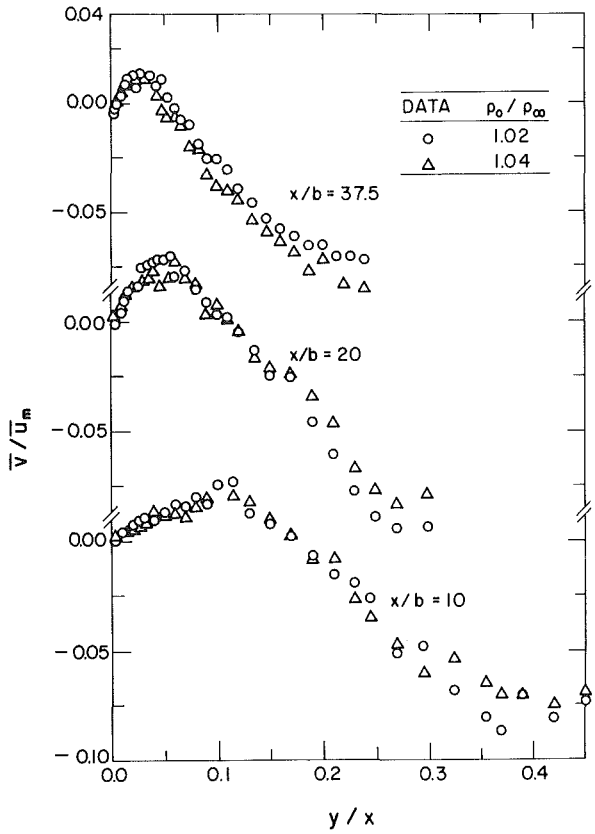

Fig. 1 Profiles of $\bar{v}$

Higher-order correlations have uncertainties which can be evaluated from these estimates using conventional error-propagation analysis.

Results and Discussion—Entrainment

Present work repeated earlier measurements of $\bar{u}$, $\bar{u}'\bar{f}$, and $\bar{f}'$ by Lai et al. (1986). The new results agreed with earlier findings, within the experimental uncertainties stated earlier, and will not be dwelt upon here.

Figure 1 is an illustration of $\bar{v}/\bar{u}_m$ measured for the two wall plumes. The results are plotted as a function of y/x, the approximate similarity variable for wall plumes (Grella and Faeth, 1975), at x/b = 10, 20, and 37.5. The two plumes yield roughly the same results. The general behavior of $\bar{v}$ is similar

Nomenclature

b = slot height at exit
E_0, E_0' = entrainment constants based on $\bar{u}_m$ and $\bar{u}_a$
f = mixture fraction
g = square of mixture fraction fluctuations
k = turbulent kinetic energy
p = pressure
$P(f)$ = Reynolds-averaged probability density function of f
u = velocity parallel to wall
v = velocity normal to wall
x = distance along wall
y = distance normal to wall
δ = boundary-layer thickness
ϵ = rate of dissipation of turbulence kinetic energy
μ_t = turbulent viscosity
ρ = density
σ_f = turbulent Prandtl/Schmidt number

Subscripts

a = average value
m = maximum value
0 = slot exit condition
∞ = ambient condition

Superscripts

$(\bar{\ }), (\tilde{\ })$ = Reynolds or Favre average
$(\ )', (\ )''$ = fluctuations from Reynolds or Favre average
$(\bar{\ })', (\tilde{\ })''$ = root-mean-square Reynolds or Favre-averaged quantity

Table 1 Entrainment coefficients

x/b	$\bar{u}_a$ (m/s)	$\bar{u}_m$(m/s)	E_o' [a]	E_o [a]	E_o [b]
ρ_o/ρ_∞ = 1.02:					
10	0.138	0.370	0.175	0.071	0.076
20	0.131	0.340	0.189	0.080	0.097
37.5	0.134	0.311	0.174	0.080	0.082
ρ_o/ρ_∞ = 1.04:					
10	0.206	0.508	0.209	0.078	0.077
20	0.202	0.479	0.237	0.091	0.089
37.5	0.203	0.442	0.166	0.071	0.071

[a] Based on measured $\bar{v}_\infty$

[b] Based on $\frac{d}{dx}\int_0^\infty \bar{u}\,dy$.

to other wall flows being positive near the wall and then becoming negative near the free stream due to entrainment of ambient fluid.

These measurements provided an opportunity to measure the entrainment coefficient of adiabatic wall plumes directly rather than by integrating the mean velocity profile which is common practice. The entrainment coefficient of integral analyses is defined as follows (Grella and Faeth, 1975):

$$\frac{d}{dx}\int_0^\infty \bar{u}dy = -v_\infty = E_0'\bar{u}_a = E_0\bar{u}_m \tag{1}$$

where $\bar{u}_a$ is the average velocity in the plume

$$\bar{u}_a = \int_0^\delta u\,dy/\delta \tag{2}$$

Values of $\bar{u}_m$, $\bar{u}_a$, E_0', and E_0 are summarized in Table 1 for the present measurements. The average velocity is relatively independent of steamwise position, which is expected for adiabatic wall plumes (Grella and Faeth, 1975). The present flow exhibits effects of development, however, since $\bar{u}_m$ decreases with increasing x. Values of E_0 found from integrating the streamwise velocity profile (the left-hand side of equation (1)) are consistent with values obtained by measuring $\bar{v}_\infty$ directly. Present measurements yield a mean value of E_0 of 0.082 which is greater than the 0.067 value found by Grella and Faeth (1975) for higher Reynolds number plumes. The higher value in the present case is expected due to effects of flow development and lower Reynolds numbers.

Turbulence Properties

Velocities. Measured values of $\bar{u}'$ and $\bar{v}'$ for both wall plumes are plotted in Fig. 2 as a function of y/x for the three streamwise stations considered earlier. Predictions from the k–ϵ–g analysis of Lai et al. (1986) are also shown on the plot. This analysis fundamentally assumes isotropic turbulence; therefore, predictions are based on the same assumption, e.g., $\bar{u}'^2 = \bar{v}'^2 = 2k/3$. When plotted in the manner of Fig. 2, predictions for both flows are the same. Measurements for the two plumes are nearly identical as well.

The measurements illustrated in Fig. 2 exhibit a large degree of anisotropy except near the edge of the flow where ambient disturbances are not particularly directed. This behavior is expected near the wall since motion normal to it is inhibited. Near the maximum velocity position, $y/x \simeq 0.03$–0.05, $\bar{u}'$ exhibits a slight dip due to reduced turbulence production in this

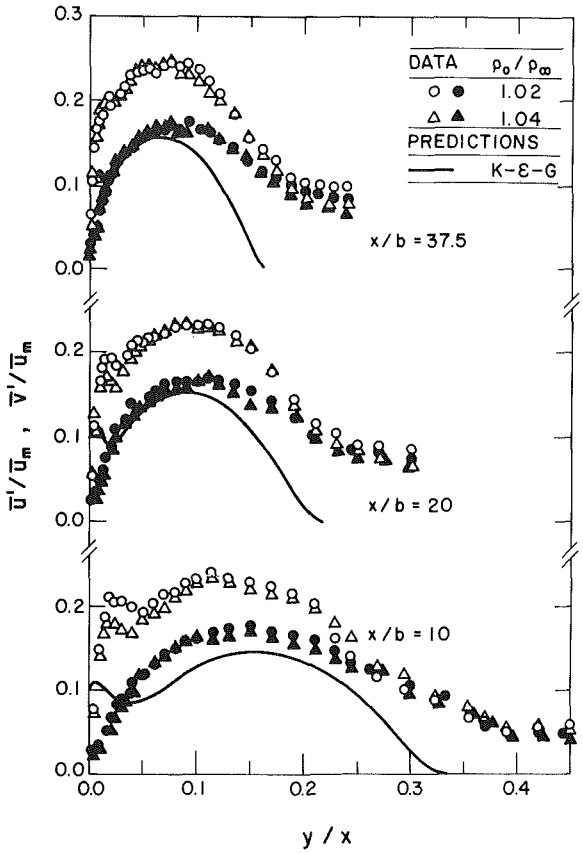

Fig. 2 Profiles of $\bar{u}'/\bar{u}_m$ (open symbols) and $\bar{v}'/\bar{u}_m$ (darkened symbols)

region. The k–ϵ–g model also suggests reduced turbulence intensities in this region, but to a much larger extent than the measurements. Furthermore, the k–ϵ–g model generally underestimates turbulence intensities for the plumes even though it was reasonably successful for the wall jet data obtained from the same apparatus (Lai et al., 1986). Effects of buoyancy/turbulence interactions, which were ignored for present predictions, are probably responsible for both deficiencies. This will be considered more quantitatively later.

Normalized Reynolds stress measurements, plotted in the same manner as Fig. 2, are illustrated in Fig. 3. Predictions of both the mixing-length and k–ϵ–g models of Lai et al. (1986) are also plotted on the figure. As before, both plumes yield nearly identical measurements and predictions are the same when plotted in this manner. The maximum normalized Reynolds stress levels of present measurements are considerably greater then the almost uniform value of 0.008 measured by Liburdy et al. (1979) for isothermal wall plumes. Present results correctly resolve negative values near the wall, rise to maximum values of ~ 0.02, and finally approach zero near the edge of the flow since ambient disturbances are nearly uncorrelated. The predictions exhibit similar trends but maximum predicted values are much lower than the measurements. This is consistent with underestimation of turbulence intensities seen in Fig. 2 and is probably caused by neglecting turbulence/buoyancy interactions.

Another feature of the Reynolds stress profile is that the position of zero shear stress does not coincide with the maximum velocity location. The maximum velocity position coincides roughly with the predicted zero Reynolds stress points illustrated in Fig. 3, while the measured zero stress point is displaced roughly one-third closer to the wall. The gradient-diffusion approximation of the present models is responsible for this deficiency. Full Reynolds stress models have exhibited

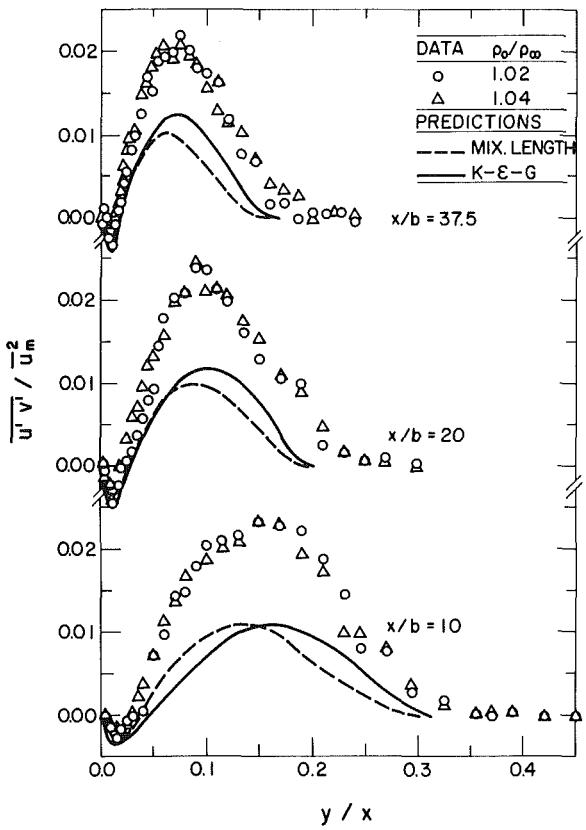

Fig. 3 Profiles of Reynolds stress

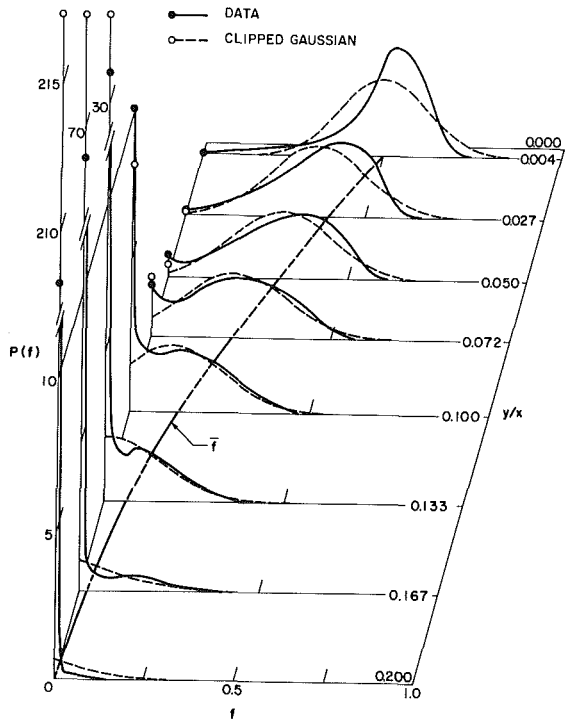

Fig. 4 Predicted and measured $P(f)$ for $\rho_0/\rho_\infty = 1.04$ and $x/b = 37.5$

success in predicting the separation of zero stress and maximum velocity locations, but with additional empiricism (Launder et al., 1975).

Mixture Fraction. Predicted and measured mean and fluctuating mixture fractions have already been discussed (Lai et al., 1986). Similar to the velocity results, the simplified models predicted mean mixture fractions reasonably well; however, mixture fraction fluctuations were underestimated. Present considerations will be limited to the probability density function of mixture fraction, $P(f)$.

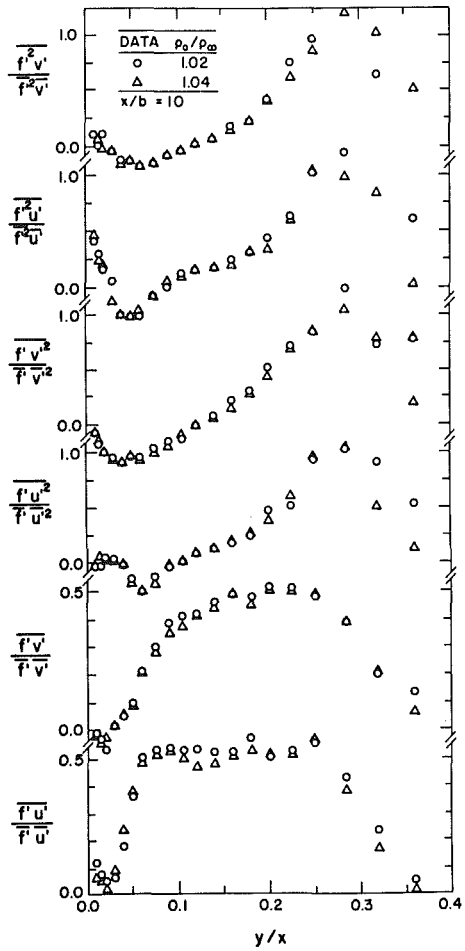

Fig. 5 Velocity/mixture fraction correlations at $x/b = 10$

Measured $P(f)$ at various distances from the wall, for $\rho_0/\rho_\infty = 1.04$ and $x/b = 37.5$, are illustrated in Fig. 4. The measured PDF is plotted as a smooth curve since the spacing between values (typically 0.02) is too small to illustrate the jumps between values on Fig. 4. The measured mean mixture fraction is also plotted on the figure to provide a reference. The high levels of intermittency near the edge of the flow are apparent from the large spike at $f = 0$. Evidence of intermittency, indicated by a measurable value of $P(0)$, extends down to $y/x = 0.027$, which is near the maximum velocity position. This observation agrees with earlier flow visualization and is evidence of the relatively early state of development and low Reynolds numbers of present plumes (Lai et al., 1986).

Also shown in Fig. 3 are clipped Gaussian $P(f)$ constructed using the first and second moments of the measurements. It appears that the clipped Gaussian $P(f)$ provides a reasonable correlation of the measurements. This is helpful since this function is widely used for analysis of turbulent combustion processes (Jeng and Faeth, 1984). In particular, the clipped Gaussian distribution provides a good representation of the magnitude of the intermittency spikes which are sensitive indicators of performance. In the region of the maximum velocity position and the wall, however, the measurements exhibit significant skewness which cannot be properly represented using a two-parameter $P(f)$.

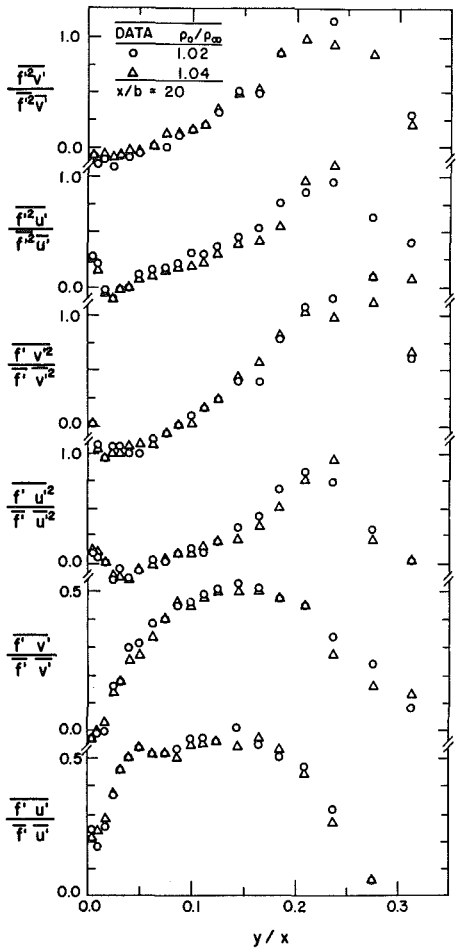

Fig. 6 Velocity/mixture fraction correlations at $x/b = 20$

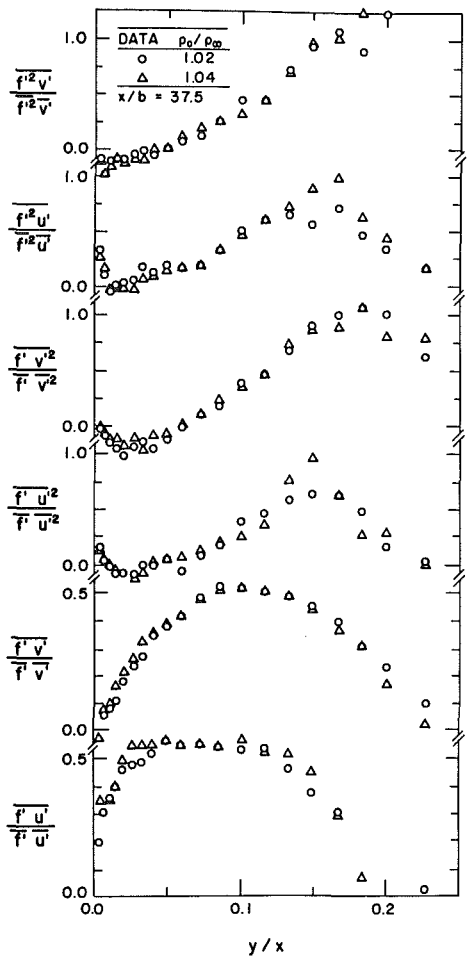

Fig. 7 Velocity/mixture fraction correlations at $x/b = 37.5$

Velocity/Mixture-Fraction Correlations. Figures 5–7 are illlustrations of a variety of velocity/mixture-fraction correlations at $x/b = 10$, 20, and 37.5. When plotted as a function of y/x, all three positions exhibit similar trends. Since noise signals tend to be uncorrelated, all correlations approach zero near the edge of the flow. However, high-order correlations approach zero more slowly due to the small local fluctuation levels appearing in their normalization. Absolute correlation values are generally in the range -1 to 1, consistent with Schwartz inequality (except for a few values of the higher-order correlations where experimental uncertainties are a factor).

The turbulent fluxes of mixture fraction $\overline{f'u'}$ and $\overline{f'v'}$ are nearly all positive. This is consistent with the fact that larger velocities are associated with higher mixture fractions due to effects of buoyancy. $\overline{f'u'}$ has a squarer profile than $\overline{f'v'}$, roughly, corresponding to the shapes of $\overline{u'}$ and $\overline{v'}$. $\overline{f'v'}$ satisfies the gradient-diffusion approximation as to sign (Lai, 1985). This accounts for the success of this approach to estimate mean properties since cross-stream diffusion dominates transport in plumes. Data were not obtained at a sufficient number of stations to determine whether the gradient diffusion approximation was satisfied for the lower levels of turbulent transport in the streamwise direction.

Turbulent Prandtl/Schmidt Number. Figure 8 is an illustration of profiles of the turbulent Prandtl/Schmidt number of mixture fraction deduced from the measurements as follows:

$$\sigma_f = \overline{u'v'}\,\partial\bar{f}/\partial y / (\overline{f'v'}\,\partial\bar{u}/\partial y) \qquad (3)$$

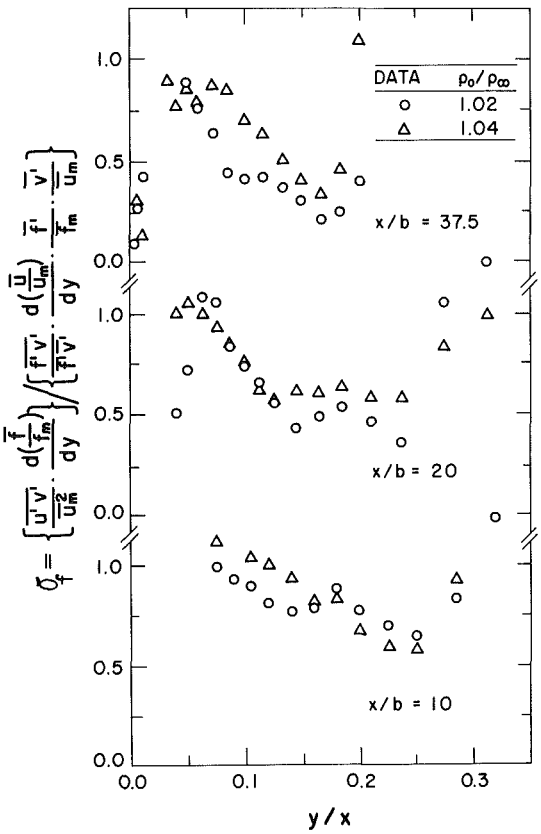

Fig. 8 Profiles of turbulent Prandtl/Schmidt number

Since σ_f involves four measurements, including two gradients, its experimental uncertainties are high, ~ 40 percent (Lai, 1985). Furthermore, σ_f is unbounded at the maximum velocity position where the velocity gradient is zero while all other quantities remain finite in equation (3). In the outer region the behavior of σ_f is similar to measurements of turbulent Prandtl number in a plane jet by Browne and Antonia (1983), decreasing near the edge of the flow to values near 0.5. This tends to confirm the use of $\sigma_f = 0.5$ in order to obtain reasonably good predictions of mean properties with the simplified models (Lai et al., 1986). σ_f increases in the region of the velocity maximum, as noted earlier, and then approaches small values near the wall. Liburdy et al. (1979) observed different behavior for the turbulent Prandtl number in isothermal wall plumes where $\sigma_f = 0.5$ over most of the flow. This behavior follows since positions of maximum temperature and velocity nearly coincide in this flow, minimizing the effect of $\partial\bar{u}/\partial y$ approaching zero. Taken together, the results suggest that $\sigma_f = 0.5$ is an appropriate choice for constant σ_f number modeling of two-dimensional wall flows.

Implications of the Measurements

Types of Averages. When density variations are large, e.g., flames, differences between Reynolds and Favre averages can be significant. Since predictions are often based on Favre averages while measurements are most frequently time averages, estimates of the differences between these quantities can be helpful. Present measurements will be used to evaluate these differences since turbulence correlations tend to vary less than fluctuating quantities themselves when density variations increase.

From the basic definition of a Favre average, the difference between Reynolds and Favre-averaged mean velocities is (Bilger, 1975)

$$(\tilde{u}-\bar{u})/\bar{u}=\overline{\rho' u'}/\bar{\rho}\bar{u} \tag{4}$$

Density is almost linearly proportional to f in the present flows; therefore, all correlation measurements involving $\tilde{f}'$ are identical to those of $\tilde{\rho}'$. The correlation $\overline{\rho' u'}/\bar{\rho}'\bar{u}'$ has also been measured by Starner and Bilger (1981), Schefer and Dibble (1985), and Driscoll et al. (1982) for round jet diffusion flames. Behavior was similar to present findings (except for the sign) with maximum values near -0.5 and values approaching zero near the edge of the flow. This suggests that discussion of differences in averages can be extended to flame environments. For present flows the maximum difference between Favre and Reynolds-averaged mean velocity is in the order of 0.2 percent ($\rho_0/\rho_\infty = 1.04$: $(\bar{\rho}'/\bar{\rho})_m = 0.012$, $(\tilde{u}'/\bar{u})_m = 0.25$). In flame environments, $\tilde{\rho}'/\bar{\rho}$ approaches unity yielding potential differences in mean velocities for these averages of 10 percent, in accord with direct measurements in flames (Starner and Bilger, 1981).

Differences between Reynolds and Favre-averaged velocity fluctuations can be represented by the streamwise component. It can be shown that

$$(\tilde{u}''^2-\tilde{u}'^2)/\tilde{u}'^2=\overline{\rho' u}'^2/\bar{\rho}\tilde{u}'^2-(\overline{\rho' u}')^2/\bar{\rho}^2\tilde{u}'^2 \tag{5}$$

where the correlations can be found from corresponding correlations in terms of $\tilde{f}'$. The general behavior of $\overline{\rho' u}'^2/\bar{\rho}'\tilde{u}'^2$ in flames (Starner and Bilger, 1981) is similar to present measurements. For the present flows, differences between $\tilde{u}'$ and $\tilde{u}''$ are less than 10 percent ($(\rho_0/\rho_\infty) = 1.04$: $(\bar{\rho}'/\bar{\rho}_m) = 0.12$, $(\overline{\rho' u}'^2/\bar{\rho}'\tilde{u}'^2)_m = 1$, and $(\overline{\rho' u'}/\bar{\rho}'\tilde{u}')_m = 0.5$). In flames, however, these averages exhibit differences as large as 70 percent near the flow edge (Starner and Bilger, 1981).

We take mixture fraction to be a representative scalar property since other scalars can be related to it through state relationships (Bilger, 1975). By definition

$$(\tilde{f}-\bar{f})/\bar{f}=\overline{f'\rho'}/\bar{f}\bar{\rho} \tag{6}$$

Table 2 Conservation checks of momentum and mass fluxes

y/x	$(\overline{\rho u^2}-\bar{\rho}\bar{u}^2)/\bar{\rho}\bar{u}^2$	$(\overline{\rho u f}-\bar{\rho}\bar{u}\bar{f})/\bar{\rho}\bar{u}\bar{f}$
x / b = 10 :		
0.05	0.034	0.015
0.12	0.053	0.029
0.25	0.026	0.022
x/b = 20 :		
0.04	0.039	0.031
0.10	0.055	0.042
0.21	0.012	0.007
x/b - 37.5 :		
0.02	0.040	0.030
0.07	0.062	0.042
0.15	0.024	0.012

[a] $\rho_0/\rho_\infty = 1.04$

For the present flows $\overline{f'\rho'}/\bar{f}'\bar{\rho}'$ is nearly unity, but differences between $\bar{f}$ and $\tilde{f}$ are less than 0.03 percent due to the small density variations in the flows. In flames, however, $\bar{f}'/\bar{f} \approx \bar{\rho}'/\bar{\rho} \approx 1$, suggesting differences comparable to the value of the mixture fraction itself. Instances where concentration fluctuations can be resolved normally allow determination of both Reynolds and Favre-averaged quantities; therefore, this parameter will not be discussed.

Conservation Checks. The accuracy of structure measurements is frequently evaluated by examining streamwise conservation of mass, momentum, and mixture fraction. Variable density flows, however, introduce considerable uncertainties in conservation checks due to turbulent fluxes, which are evaluated in the following. From basic definitions

$$\overline{\rho u}^2=\bar{\rho}\bar{u}^2+2\bar{u}\overline{\rho' u'}+\overline{\rho' u}'^2+\bar{\rho}\tilde{u}'^2 \tag{7}$$

$$\overline{\rho u f}=\bar{\rho}\bar{u}\bar{f}+\bar{\rho}\overline{u' f'}+\bar{u}\overline{\rho' f'}+\bar{f}\,\overline{\rho' u'}+\overline{f'\rho' u'} \tag{8}$$

or in terms of $\tilde{f}$

$$\overline{\rho u f}=\bar{\rho}\bar{u}\tilde{f}+\bar{\rho}\overline{u' f''}+\tilde{f}\,\overline{\rho' u'}+\overline{\rho' u' f''} \tag{9}$$

In cases where combined measurements of mixture fraction (density) and velocity are unavailable, momentum and mass fluxes are normally approximated by the first terms on the right-hand side of equations (7)–(9).

Differences between the exact and approximate momentum and mass fluxes for the wall plume having $\rho_0/\rho_\infty = 1.04$ are summarized in Table 2. Results for the lower density-defect plume were similar. For the present study, $(\rho_0 - \rho_\infty)/\rho_0 < 0.04$ and differences between the exact and approximate flux are less than 6 percent; therefore, earlier conservation checks of these flows using the approximate method are justified (Lai et al., 1986). For flame conditions, however, the approximate forms are grossly in error and conservation checks based on them are of little value (Lai, 1985).

Buoyancy/Turbulence Interactions. The effect of buoyancy/turbulence interactions was considered by examining the production term in the Favre-averaged equation for k. Analogous terms appear in the ϵ equation, but order-of-magnitude analysis suggests that the production term is balanced by the destruction term; thus, they are less important to evaluate. Buoyancy affects the production of k through the velocity–pressure gradient correlation which is frequently decomposed as follows (Strahle, 1983):

Table 3 Ratio of buoyancy-to-shear production

y/x	ρ_0/ρ_∞ = 1.02	ρ_0/ρ_∞ = 1.04
x/b = 10 :		
0.05	0.88	1.52
0.12	0.07	0.09
0.25	0.09	0.13
x/b = 20 :		
0.04	0.73	0.34
0.10	0.21	0.17
0.21	0.58	0.44
x/b = 37.5 :		
0.02	1.17	0.98
0.10	0.37	0.48
0.15	0.67	0.47

$$\overline{-u''\frac{\partial p}{\partial x_i}} = -\bar{u}''\frac{\partial \bar{p}}{\partial x_i} - \frac{\partial \overline{p'u''}}{\partial x_i} + \overline{p'\frac{\partial u''}{\partial x_i}} \tag{10}$$

Now, the second term on the right-hand side of equation (11), called the pressure–strain correlation, is generally treated as a term which redistributes turbulent kinetic energy between the various components, e.g., it is neither a source nor sink term. The last term disappears in constant density flows and Starner and Bilger (1981) argue that the term appears acoustic in nature and should be negligible in low Mach number flows. Kollmann and Vandrome (1979) and Bray et al. (1981) also neglect this term. Controversy still surrounds these assessments for variable-density flows; however, for lack of alternative the present evaluation of buoyancy/turbulence interactions approximates equation (10) by the first item, written as follows

$$-\bar{u}''\frac{\partial \bar{p}}{\partial x_i} = \frac{\overline{\rho' u_i'}}{\bar{\rho}}\frac{\partial \bar{p}}{\partial x_i} \tag{11}$$

which is identical to the term $\overline{\rho' u'}\, a_i$ which appears in the conventional Reynolds-averaged equation for k, when the Boussinesq approximation is used (Kennedy and Plumb, 1976).

The production term of equation (11) increases or decreases k, depending on the relative signs of $\overline{\rho' u_i'}$ and $\partial \bar{p}/\partial x_i$. For the present wall plumes, both the vertical hydrostatic pressure gradient and $\overline{\rho' u'}$ are positive and this term increases k. The effect of tranverse pressure gradients can be seen by noting that the mean pressure is smaller than the ambient due to turbulence, e.g.,

$$p_\infty = \bar{p} + \bar{\rho}\bar{v}''^2 \tag{12}$$

from the transverse momentum equation. For free plumes, $\partial \bar{p}/\partial y$ is mostly positive while $\overline{\rho' v'}$ is negative since density is lower in the flow than in the free stream. For the present wall plumes, however, $\bar{v}''$ increases from zero at the wall and decreases again toward the edge of the flow, causing production of k near the wall and suppression near the edge of the flow. However, since $\partial \bar{p}/\partial y$ is proportional to $(\bar{\rho}'/\bar{\rho})^2$, the transverse contribution to production is only comparable to the streamwise production term when $\bar{\rho}'/\bar{\rho} \approx 1$, e.g., flame environments. Its contribution is negligible for present conditions.

Table 3 is a summary of the ratios of buoyancy-to-shear production for the wall plumes, defined as follows:

$$\text{Ratio} = -\bar{u}''\frac{\partial \bar{p}}{\partial x} \Big/ \left(\overline{-u'v'}\frac{\partial \bar{u}}{\partial y}\right) \tag{13}$$

The atmospheric static pressure gradient was taken to be 11.4 Pa/m. It is notable that even for maximum density variations of 2–4 percent, buoyancy still contributes significantly to production of turbulence kinetic energy. The ratio is of course infinite at the maximum velocity position, but is still substantial in the other regions of the flow. It seems quite likely that this effect explains the overestimation of the dip in u' near the maximum velocity position and the general underestimation of turbulence intensities, Reynolds stresses, and concentration fluctuations by the simplified analysis which ignores buoyancy/turbulence interactions.

Conclusions

Major conclusions of the study are as follows:

1 Buoyancy/turbuence interactions are important for wall plumes, even when maximum density variations are small. Omitting buoyancy production is probably responsible for most of the discrepancy between simplified predictions and measurements of turbulence quantities.

2 The simplified models were unable to describe a number of significant features of wall plume turbulence, e.g., anisotropy of turbulence, separation of zero stress and maximum velocity points, and variation of turbulent Prandtl/Schmidt number with position. Clearly, more complete closure methods should be studied for wall plumes.

3 Differences between Favre and Reynolds averages were small for present flows and simplified conservation checks ignoring density fluctuations and fluxes are reasonably accurate. However, these simplifications would lead to substantial errors if density variations were larger, e.g., flame environments.

4 The clipped Gaussian $P(f)$ provided a reasonably good representation of measurements, aside from effects of skewness seen near the maximum velocity position and the surface.

Acknowledgments

This research was supported by the United States Department of Commerce, National Bureau of Standards, under Grant No. 60NANB4D0032. B. J. McCaffrey, of the Center for Fire Research, served as Scientific Officer. The study was initiated while the authors were affiliated with The Pennsylvania State University.

References

Bilger, R. W., 1975, "A Note on Favre Averaging in Variable Density Flows," *Comb. Sci. Tech.*, Vol. 11, pp. 215–217.

Bray, K. N. C., Libby, P. A., Massuya, G., and Moss, J. B., 1981, "Turbulence Production in Premixed Flames," *Comb. Sci. Tech.*, Vol. 25, pp. 127–140.

Browne, L. W. B., and Antonia, R. A., 1983, "Measurements of Turbulent Prandtl Number in a Plane Jet," ASME JOURNAL OF HEAT TRANSFER, Vol. 105, pp. 663–665.

Cebeci, T., and Khattab, A., 1975, "Predictions of Turbulent Free Convection From Vertical Surfaces," ASME JOURNAL OF HEAT TRANSFER, Vol. 97, pp. 469–471.

Driscoll, J. F., Schefer, R. W., and Dibble, R. W., 1982, "Mass Fluxes $\overline{\rho' u'}$ and $\overline{\rho' v'}$ Measured in a Turbulent Nonpremixed Flame," *Nineteenth Symposium (International) on Combustion*, The Combustion Institute, Pittsburgh, pp. 477–485.

Grella, J. J., and Faeth, G. M., 1975, "Measurements in a Two-Dimensional Thermal Plume Along a Vertical Wall," *J. Fluid Mech.*, Vol. 71, pp. 701–710.

Jeng, S.-M., Chen, L.-D., and Faeth, G. M., 1982, "The Structure of Buoyant Methane and Propane Diffusion Flames," *Nineteenth Symposium (International) on Combustion*, The Combustion Institute, Pittsburgh, pp. 349–358.

Jeng, S.-M., and Faeth, G. M., 1984, "Species Concentrations and Turbulence Properties in Buoyant Methane Diffusion Flames," ASME JOURNAL OF HEAT TRANSFER, Vol. 106, pp. 721–727.

Kennedy, L. A., Plumb, O. A., 1976, "Application of a k–ϵ Turbulence

Model to Natural Convection From a Vertical Isothermal Surface," ASME Paper No. 76-HT-17.

Kollmann, W., and Vandromme, D., 1979, "Turbulent Shear Flow With Fluctuating Density," AIAA Paper No. 79-1485.

Lai, M.-C., 1985, "Structure of Turbulent Adiabatic Wall Plumes," Ph.D. Thesis, The Pennsylvania State University, University Park, PA.

Lai, M.-C., Jeng, S.-M., and Faeth, G. M., 1986, "Structure of Turbulent Adiabatic Wall Plumes," ASME JOURNAL OF HEAT TRANSFER, Vol. 108, pp. 827–834.

Lai, M.-C, and Faeth, G. M., 1987, "A Combined Laser-Doppler Anemometer/Laser-Induced Fluorescence System for Turbulent Transport Measurements," ASME JOURNAL OF HEAT TRANSFER, Vol. 109. pp. 254–256.

Launder B. E., Reece, G. J., and Rodi, W., 1975, "Progress in the Development of a Reynolds Stress Turbulence Closure," *J. Fluid Mech.*, Vol. 68, pp. 537–566.

Liburdy, J. A., and Faeth, G. M., 1978, "Heat Transfer and Mean Structure of a Turbulent Thermal Plume Along a Vertical Isothermal Wall," ASME JOURNAL OF HEAT TRANSFER, Vol. 100, pp. 177–183.

Liburdy, J. A., Groff, E. G., and Faeth, G. M., 1979, "Structure of a Turbulent Thermal Plume Rising Along an Isothermal Wall," ASME JOURNAL OF HEAT TRANSFER, Vol. 101, pp. 249–255.

Schefer, R. W., and Dibble, R. W., 1985, "Simultaneous Measurements of Velocity and Density in a Turbulent Nonpremixed Flame," *AIAA J.*, Vol. 23, pp. 1070–1078.

Starner, S. H., and Bilger, R. W., 1981, "Measurements of Scalar Velocity Correlations in a Turbulent Diffusion Flame," *Eighteenth Symposium (International) on Combustion*, The Combustion Institute, Pittsburgh, pp. 921–930.

Strahle, W. C., 1983, "Velocity-Pressure Gradient Correlation in Reactive Turbulent Flows," *Comb. Sci. Tech.*, Vol. 32, pp. 289–305.

Cooling of a Vertical Shrouded Fin Array by Natural Convection: a Numerical Study

K. C. Karki

S. V. Patankar

Mem. ASME

Department of Mechanical Engineering,
University of Minnesota,
Minneapolis, MN 55455

An analysis is made of the laminar natural convection in a vertical shrouded fin array, in which the flow is induced from the surroundings by the chimney effect. This involves the calculation of developing flow in a duct. The results are obtained numerically for representative values of the parameters describing the system geometry and ducts of different lengths. The axial development of various flow quantities, such as the Nusselt number and the bulk temperature, has been presented. In addition, the overall flow and heat transfer characteristics have been discussed.

Introduction

Natural convection is often a convenient and inexpensive mode of heat transfer. It is commonly employed in cooling of electronic equipment, radiators for space heating, heat loss from small engines, and many other applications. A common geometry consists of vertical fins attached to the hot surface as shown in Fig. 1(*a*). Often, a shroud is placed near the fins so that the resulting chimney effect induces increased flow over the fins and leads to higher heat transfer. The purpose of the present paper is to analyze the natural convection flow and heat transfer in such a configuration.

The analysis of the situation in Fig. 1 involves the calculation of the developing flow in a duct. The flow rate, however, is not independently controlled as in forced convection but becomes established as a consequence of the buoyancy of the fluid in the duct.

The buoyancy-induced flow between vertical parallel plates has been analyzed in [1–6]. Similar analysis for vertical circular tubes is given in [7–9]. References [10, 11] deal with natural convection in vertical arrays of interrupted parallel plates. All these analyses involve the calculation of a two-dimensional parabolic flow. For the geometry considered here, a three-dimensional duct flow must be analyzed. The only published analysis for a three-dimensional buoyancy-induced flow in a duct appears to be that for a vertical square duct given in [12].

The configuration of a shrouded fin array considered in this paper has been analyzed in other contexts. Reference [13] deals with the forced convection solution, while mixed convection is studied in [14] for a horizontal orientation and in [15] for a vertical one.

Analysis

Formulation. Because of the geometric symmetry of the configuration shown in Fig 1(*a*), the calculation can be confined to a duct of the cross section shown shaded in Fig. 1(*b*). For the parabolic flow considered here, a marching procedure is employed, which starts at the inlet plane at the bottom of the duct and proceeds downstream until the exit at $z = l$ is reached. The fin thickness t is considered negligible in comparison with the spacing s. The base temperature is taken as uniform, and the same temperature is assumed to prevail over the fins, implying highly conducting fins. The shroud is regarded as adiabatic. The flow is considered to be steady and laminar and the fluid properties as uniform, except for the density in the buoyancy term.

As the flow is confined, the mean cross-sectional pressure $\bar{p}$ within the duct will be less than the ambient pressure p_0 at the same elevation. The difference between the two pressures, $(p_0 - \bar{p})$, is referred to as the pressure defect p_d. Since the variation of the ambient pressure is given by

$$\frac{dp_0}{dz} = -\rho_0 g \tag{1}$$

the gravity and the pressure gradient term in the z-momentum equation can be combined as

$$-\frac{d\bar{p}}{dz} - \rho g = \frac{dp_d}{dz} + (\rho_0 - \rho)g \tag{2}$$

If the density ρ is given by

$$\rho = \rho_0[1 - \beta(T - T_0)] \tag{3}$$

then

$$-\frac{d\bar{p}}{dz} - \rho g = \frac{dp_d}{dz} + \rho_0 g\beta(T - T_0) \tag{4}$$

It may be noted that the gradient of the mean pressure $\bar{p}$ is used in the z-direction momentum equation in conformity with the parabolic-flow practice.

With this background, the differential equations describing conservation of mass, momentum, and energy can be written

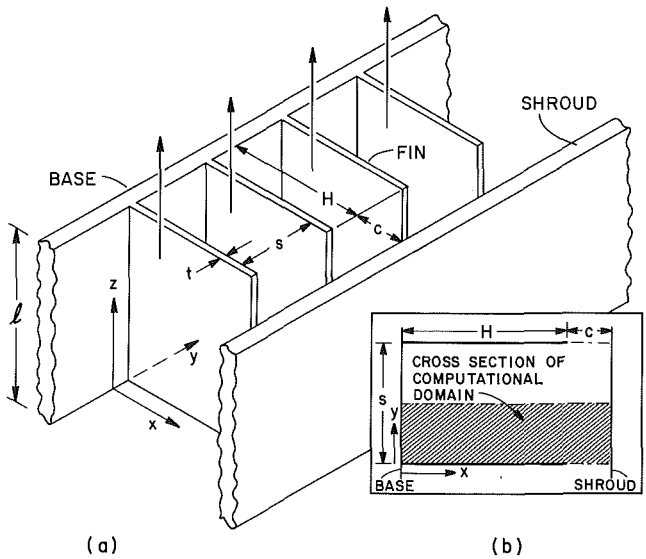

Fig. 1 A shrouded fin array

Contributed by the Heat Transfer Division and presented at the National Heat Transfer Conference, Niagara Falls, NY, August 1984. Manuscript received by the Heat Transfer Division October 22, 1984.

for the three-dimensional parabolic situation under consideration. They can be conveniently expressed in dimensionless form by the use of the following variables:

$$\mathrm{Gr}=\frac{g\beta(T_w-T_0)H^3}{\nu^2} \tag{5a}$$

$$Z=\frac{(z/H)}{\mathrm{Gr}}, \quad X=\frac{x}{H}, \quad Y=\frac{y}{H} \tag{5b}$$

$$U=\frac{uH}{\nu}, \quad V=\frac{vH}{\nu}, \quad W=\frac{wH}{\mathrm{Gr}\nu} \tag{5c}$$

$$\theta=\frac{T-T_0}{T_w-T_0}, \quad P=\frac{p_dH^2}{\rho\mathrm{Gr}^2\nu^2}, \quad P^*=\frac{pH^2}{\rho\nu^2} \tag{5d}$$

$$S=\frac{s}{H}, \quad C=\frac{c}{H} \tag{5e}$$

Here the density ρ_0 has been replaced by ρ in accordance with the Boussinesq approximation. The resulting dimensionless equations are

$$\frac{\partial U}{\partial X}+\frac{\partial V}{\partial Y}+\frac{\partial W}{\partial Z}=0 \tag{6}$$

$$U\frac{\partial U}{\partial X}+V\frac{\partial U}{\partial Y}+W\frac{\partial U}{\partial Z}=-\frac{\partial P^*}{\partial X}+\frac{\partial^2 U}{\partial X^2}+\frac{\partial^2 U}{\partial Y^2} \tag{7}$$

$$U\frac{\partial V}{\partial X}+V\frac{\partial V}{\partial Y}+W\frac{\partial V}{\partial Z}=-\frac{\partial P^*}{\partial Y}+\frac{\partial^2 V}{\partial X^2}+\frac{\partial^2 V}{\partial Y^2} \tag{8}$$

$$U\frac{\partial W}{\partial X}+V\frac{\partial W}{\partial Y}+W\frac{\partial W}{\partial Z}=\frac{dP}{dZ}+\theta+\frac{\partial^2 W}{\partial X^2}+\frac{\partial^2 W}{\partial Y^2} \tag{9}$$

$$U\frac{\partial \theta}{\partial X}+V\frac{\partial \theta}{\partial Y}+W\frac{\partial \theta}{\partial Z}=\frac{1}{\mathrm{Pr}}\left[\frac{\partial^2\theta}{\partial X^2}+\frac{\partial^2\theta}{\partial Y^2}\right] \tag{10}$$

Boundary Conditions. The boundaries of the calculation domain shown in Fig. 1(*b*) consist of solid walls and symmetry lines. All the velocities are zero at the solid walls. At a symmetry line the normal velocity is zero, while the normal gradients of the two other veocity components are zero. For temperature, the boundary condition on the fin and the base surfaces is $\theta = 1$, while a zero-heat-flux condition is used at the symmetry lines and the shroud.

Further, the governing equations require the velocity and temperature conditions at the inlet plane. Here it is assumed that the flow enters in the z direction with a uniform axial velocity W_0 and at a temperature and pressure equal to that of the ambient fluid. In terms of the dimensionless variables, these conditions can be stated as

$$Z=0: \quad U=V=0, \quad W=W_0, \quad P=0, \quad \theta=0 \tag{11}$$

The question of the correct velocity and pressure conditions at the inlet of the duct has been discussed at some length in [4], where more complex inlet conditions are used, which include uniform and parabolic velocity distributions and a pressure drop produced by the acceleration of the fluid from rest. Strictly speaking, the pressure drop at the inlet should be determined from the details of the flow pattern induced in the fluid approaching the bottom of the duct. Anyway, the details of the inlet condition do not have a significant effect on the overall results of the calculation (see, for example, [12]), and therefore, the conditions in equation (11) are considered to be adequate as long as the clearance parameter c/H is not very large. For large clearances, the inlet velocity distribution will become appreciably nonuniform and a much more complex analysis of the approach flow will be necessary. The present analysis with the assumption of a uniform inlet velocity is performed for the clearance values of only up to $c/H = 0.5$. Larger clearances are unlikely to be used in practice.

Governing Parameters. The value of W_0 in the inlet condition now requires further comment. Since this represents the velocity induced by the chimney effect of the heated duct, its

Nomenclature

A = heat transfer area for the whole duct, equation (19)
C = clearance parameter = c/H
c = tip clearance
c_p = specific heat at constant pressure
Gr = Grashof number, equation (5*a*)
g = acceleration due to gravity
H = fin height
k = thermal conductivity
L = dimensionless length of the duct = $(l/H)\ \mathrm{Gr}^{-1}$
l = length of the duct
M = dimensionless mass flow rate, equation (13)
$\dot{m}$ = mass flow rate between two adjacent fins
Nu = local Nusselt number, equation (17)
$\overline{\mathrm{Nu}}$ = mean Nusselt number, equation (18)
P = dimensionless pressure defect, equation (5*d*)
P^* = dimensionless cross-sectional pressure, equation (5*d*)
Pr = Prandtl number
p = cross-sectional pressure
$\bar{p}$ = mean axial pressure
p_d = pressure defect = $(p_0 - \bar{p})$
p_0 = ambient pressure
Q = dimensionless heat absorbed, equation (14)
Q_L = dimensionless heat absorbed from the entrance up to duct exit, i.e., value of Q at $Z=L$
Q' = heat absorbed by the fluid between two adjacent fins from entrance to a certain elevation
Q_l' = value of Q' at $z = l$
$\bar{q}$ = average heat flux at a cross section
S = interfin spacing parameter = s/H
s = interfin spacing
T = temperature
T_b = bulk temperature
T_0 = ambient temperature
T_w = fin and the base surface temperature
t = fin thickness
U, V, W = dimensionless velocities, equation (5*c*)
u, v, w = velocities in x, y, z directions
W_0 = value of W at the inlet, i.e., $Z = 0$
$\bar{W}$ = mean value of W
X, Y = dimensionless coordinates, equation (5*b*)
x, y = cross-stream coordinates
Z = dimensionless axial (parabolic) coordinate, equation (5*b*)
z = axial coordinate
β = thermal expansion coefficient
θ = dimensionless temperature, equation (5*d*)
θ_b = dimensionless bulk temperature, equation (15)
μ = viscosity
ν = kinematic viscosity
ρ = density
ρ_0 = density of ambient fluid

Table 1 Dimensionless lengths and flow rates for the cases presented

	$S=0.5$, $C=0.25$			$S=0.1$, $C=0.25$		
Case No.	$10^3\,(l/H)/\mathrm{Gr}$	$10^3 M$	$10^3 W_0$	$10^5(l/H)/\mathrm{Gr}$	$10^3 M$	$10^3 W_0$
1	7.04	10.0	16.0	45.9	0.250	2.0
2	2.39	8.75	14.0	10.5	0.187	1.5
3	0.88	6.88	11.0	1.87	0.125	1.0
4	0.48	5.63	9.0	0.98	0.106	0.85
—	∞	10.77	17.2	∞	0.265	2.12

value is not known a priori but is determined by the requirement that the nondimensional pressure defect P must become zero at the duct exit. The value of dimensionless axial distance Z at the duct exit thus indirectly controls the value of W_0. Therefore the true parameters of the problem are the ratios S and C describing the cross-sectional geometry, the Prandtl number Pr, and L ($= Z_{\text{exit}}$) which equals $(l/H)\mathrm{Gr}^{-1}$. It may be noted that the parameter is similar to the parameter $(l/D)\mathrm{Re}^{-1}$ encountered in developing forced flow in ducts.

Solution Procedure. The governing differential equations were numerically solved by a modified version of the procedure for three-dimensional parabolic flows described by Patankar and Spalding [16]. The modifications included the use of the SIMPLER procedure [17] for handling the pressure–velocity coupling in the cross section and the incorporation of the method in [18] to calculate the streamwise pressure gradient. Another departure from the practice in [16] was that sufficient iterations were performed at each cross section to account properly for the nonlinearity and interlinkage. The convergence criteria used to terminate these iterations over a cross section were that the local change in W between consecutive iterations became less than $10^{-8}\ W_0$ and that the total heat transfer to the fluid in the forward step changed by less than 10^{-6} percent. It was also checked that the overall momentum balance in the z direction and the overall heat balance were correct to at least six significant figures.

Determination of Inlet Velocity. As already mentioned, the quantity $(l/H)\mathrm{Gr}^{-1}$ is the true parameter of the problem rather than the inlet velocity W_0. However, marching procedure requires the value of W_0 to start the computation. This apparent difficulty is resolved by prescribing a value of W_0 and continuing the marching solution until the dimensionless pressure defect P becomes zero. The value of Z at that location is itself the value of $(l/H)\mathrm{Gr}^{-1}$. By choosing different values of W_0, a range of the values of $(l/H)\mathrm{Gr}^{-1}$ can be covered.

In order to obtain guidance for the choice of W_0, it is useful to consider the limiting case of a very long duct that would produce the largest value of W_0. For such a duct, the fluid temperature would be nearly equal to the wall temperature over a major part of the duct, the flow will be fully developed, and the pressure $\bar{p}$ within the duct would equal the ambient pressure p_0. Under these conditions, equation (9) becomes

$$0 = 1 + \frac{\partial^2 W}{\partial X^2} + \frac{\partial^2 W}{\partial Y^2} \tag{12}$$

The mean velocity $\bar{W}$ obtained from the solution of this equation represents the maximum value of the inlet velocity W_0. The computational runs were made by choosing the values of W_0 in the range 25 to 90 percent of the maximum possible value.

Computational Details. Solutions were obtained for two values of the spacing parameter, $S = 0.1$ and 0.5, for three values of the clearance parameter, $C = 0$, 0.25, and 0.5, and for different flow rates W_0. The Prandtl number was assigned a value 0.7 (for air). Computations were performed on a 29 × 22 grid in the x–y coordinates for $S = 0.5$. For closely spaced fins ($S = 0.1$), a 29 × 12 grid was used. A higher density of grid points was employed close to the solid boundaries and near the fin tip. At each station, the axial step size was selected such that it would cause the bulk temperature to rise by approximately 1 percent of the maximum possible change $(T_w - T_0)$. With this continuously varying step size, about 80–120 forward steps were required to cover the length of the duct. Some runs were repeated by using a 40 × 22 grid and doubling the number of forward steps, and the computed values of the axial pressure gradient and the Nusselt number changed by less than 2 percent.

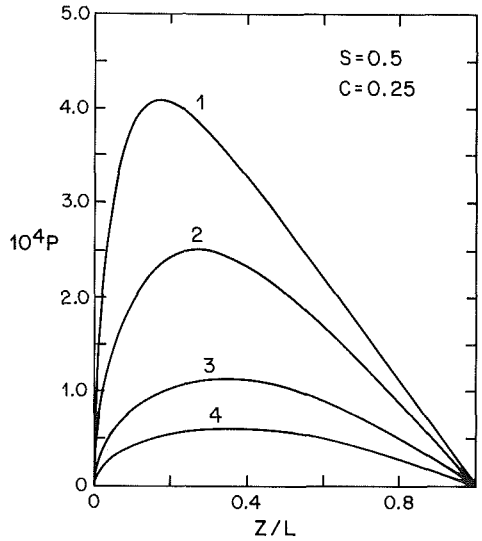

Fig. 2 Axial distribution of mean pressure

Results and Discussion

In this section, the results for various overall quantities will be presented for all the cases studied. The axial variation of certain local quantities will be shown only for a few typical cases. The parameters for these cases are listed in Table 1; the case numbers given in the table will be used to identify the corresponding curves. It should be noted that in most of the figures, logarithmic scale has been used on the abscissa. This permits the resolution of events at small Z which would otherwise have been lost. Also, since the parameter $(l//H)\mathrm{Gr}^{-1}$ is identical to the dimensionless length L of the duct, these terms have been used interchangeably in the following discussion.

Axial Variation of Mean Pressure. Figure 2 shows a typical pressure distribution along the length of the duct for different duct lengths (mass flow rates). In general, P increases with Z in the lower part of the duct, attains a maximum, and then decreases towards zero in the upper part of the duct. It may be remembered that P represents, in dimensionless form, the difference between the ambient pressure and pressure within the duct at a given elevation. For a given combination of S and C, as the duct length is increased, the maximum pressure defect increases. For large duct lengths, as for curves 1 and 2, the pressure gradient can be seen to become constant toward the duct exit, indicating the tendency to approach the fully developed situation.

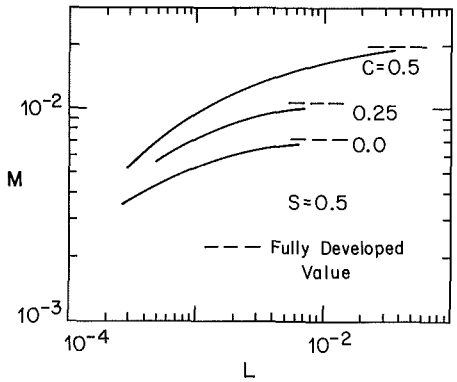

Fig. 3 Variation of mass flow rate with length for $S = 0.5$

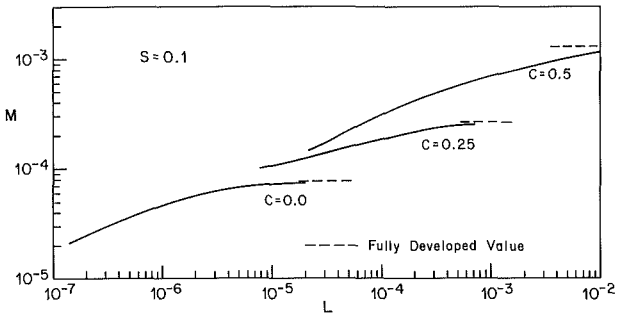

Fig. 4 Variation of mass flow rate with length for $S = 0.1$

Effect of Geometric Parameters on Mass Flow Rate. As stated earlier, for a duct of given length, the condition of zero pressure defect at the exit prescribes the mass flow rate. The flow rate attains a value such that the pressure drop between the inlet and the exit planes of the duct is equal to the externally imposed hydrostatic pressure difference.

The mass flow rate through the duct, in nondimensional form, is given by

$$M = \frac{\dot{m}}{\rho \mathrm{Gr} H \nu} = \iint W dX dY = W_0(1+C)S \qquad (13)$$

for the cross section bounded by two adjacent fins. The variation of mass flow rate with the length of the duct for different geometric parameters has been shown in Figs. 3 and 4. The fin clearance and spacing parameters have considerable influence on the entrained flow rate. Within the range of the clearance parameters considered, the flow rate increases with increasing clearance gap. Other parameters remaining the same, the mass flow rate is greater if the fins are widely spaced.

Figures 3 and 4 can also be used to determine the useful range of the parameter L for ducts with different C and S values. The quantity L equals $(l/H)\mathrm{Gr}^{-1}$ and is thus a measure of the duct length. In general, longer ducts induce more flow and transfer more heat. However, there is an upper limit on these quantities and increasing the duct length beyond a certain value does not result in any significant improvement in performance. This limit of the useful range varies with the geometric parameters depending on when the fluid becomes thermally saturated, i.e., attains the wall temperature. This condition is reached earlier for ducts with closely spaced fins and/or smaller clearance.

Development of Axial Velocity and Temperature Profiles. For the typical case of $S = 0.5$, $C = 0.25$, and $L = 4.8 \times 10^{-4}$, the development of axial velocity and temperature profiles is shown in Fig. 5. At the inlet section, the fluid is at the ambient temperature and has a uniform velocity. For the Prandtl number of 0.7 considered here, the velocity and temperature profiles develop almost simultaneously. At first,

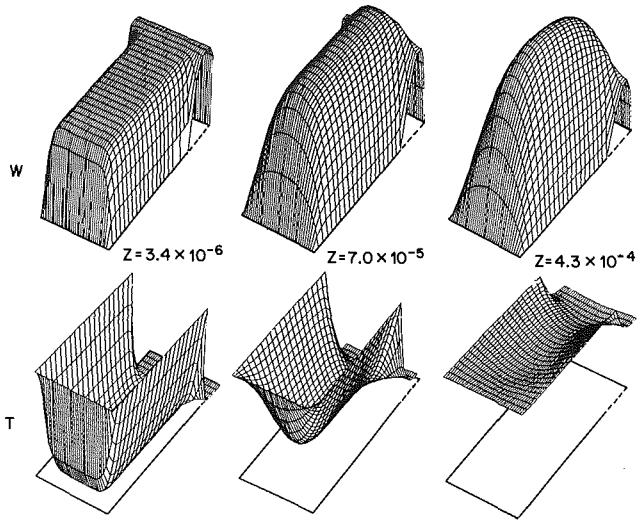

Fig. 5 Axial velocity and temperature distributions for $S = 0.5$, $C = 0.25$, $L = 4.8 \times 10^{-4}$

the fluid near the fins slows down due to wall friction, and the velocities in the clearance region increase as the fluid seeks a path of lesser resistance. Since the shroud is adiabatic, the temperature in the clearance regions remains rather low. Consequently, the fluid is the interfin space experiences a greater buoyancy force than the fluid in the clearance region. The effect of this can be seen at the second axial location shown in Fig. 5, where the velocity maximum has shifted in the direction of the interfin space. As the fluid moves further downstream, toward the exit, the fluid in the interfin region attains a uniform temperature equal to the base temperature, indicating very weak bouyancy force. The temperature of the fluid in the clearance also increases to a nearly constant value. This establishes a temperature differential only in the vicinity of the fin tip, which causes the velocities in this region to increase.

Local Heat Transfer Results. The axial distributions of local Nusselt number, amount of heat absorbed by the fluid, and bulk temperature are presented in Figs. 6 and 7 for $S = 0.5$ and 0.1, respectively. An intermediate value of the clearance parameter, $C = 0.25$, is chosen for these figures. The behavior for other values of C was found to be very similar.

The amount of heat Q' absorbed by the fluid from the inlet to a given elevation can be obtained from

$$Q = \frac{Q'}{\rho c_p \nu \mathrm{Gr} H (T_w - T_0)} = \iint W \theta dX dY \qquad (14)$$

Here Q' refers to the module between two adjacent fins. The nondimensional bulk temperature θ_b at any axial location is given by

$$\theta_b = \frac{T_b - T_0}{T_w - T_0} = \frac{\iint W\theta dX dY}{\iint W dX dY} \qquad (15)$$

It can be seen from equations (13)–(15) that

$$Q = M\theta_b \qquad (16)$$

The axially local Nusselt number is defined as

$$\mathrm{Nu} = \frac{\bar{q} H}{(T_w - T_b)k} \qquad (17)$$

where $\bar{q}$ is average heat flux over the heated area of the cross section consisting of the fin and the base.

The behavior of these quantities is strongly dependent on the fin spacing parameter. For widely spaced fins, the distributions of various quantities shown in Fig. 6 are similar to those

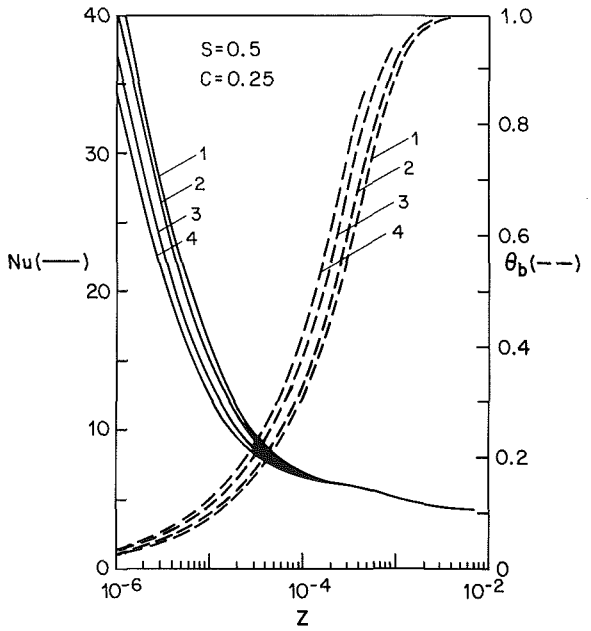

Fig. 6 Axial distributions of local Nusselt number and bulk temperature for $S = 0.5$, $C = 0.25$

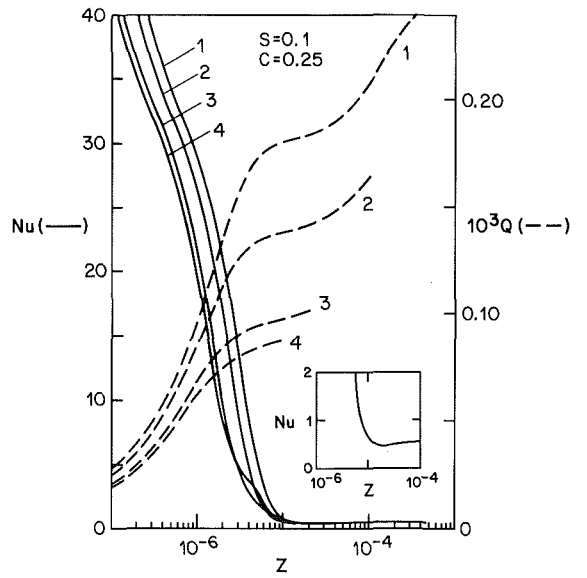

Fig. 7 Axial distributions of local Nusselt number and heat absorbed for $S = 0.1$, $C = 0.25$

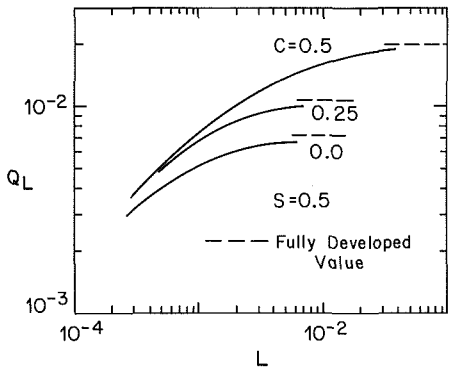

Fig. 8 Variation of total heat absorbed with length for $S = 0.5$

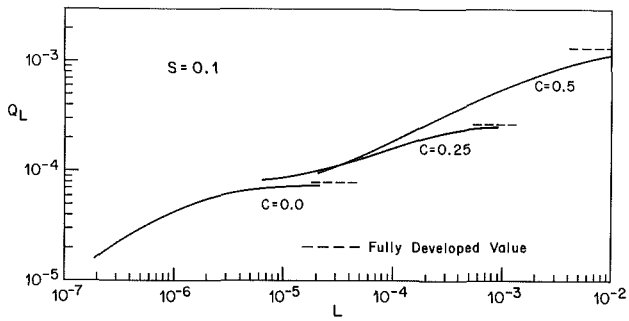

Fig. 9 Variation of total heat absorbed with length for $S = 0.1$

for simple cross-sectional geometries [7–9, 12]. The local Nusslet number decreases monotonically from the inlet to the exit of the duct and approaches the corresponding fully developed forced convection value for long ducts, which is 4.45. Similarly, the bulk temperature (or the amount of heat absorbed) shows a continuous increase along the duct and exhibits an asymptotic behavior for long ducts. For shorter ducts (low mass flow rates), Q and θ_b continue to rise up to the exit plane.

The case of narrow fin spacing ($S = 0.1$) shown in Fig. 7 exhibits rather unusual variation of Q with the axial length. The integrated heat transfer Q rises rapidly with Z in the initial part of the duct, then remains nearly constant for some distance, and begins to rise again toward the duct exit. This behavior can be explained from the development of velocity and temperature fields, which has been discussed already. Initially, the fluid in the interfin region migrates toward the clearance region and its temperature approaches the wall temperature. A stage is reached when the fins are in contact with fluid of nearly the same temperature, and no additional heat transfer can take place. This stage is represented by the flat regions in the variation of Q in Fig. 7. After the stage, under the action of the buoyancy forces, the cold fluid in the clearance region begins to move into the interfin region thus stimulating additional heat transfer.

This phenomenon is noticed for $S = 0.1$ and not for $S = 0.5$ because the interfin space has a tendency to become thermally saturated in the entrance region of the duct only when the fins are closely spaced. Also, the presence of a finite clearance is essential for this phenomenon. For $C = 0$, the flat regions were not observed in the variation of Q.

The behavior of the heat transfer rate Q has its effect on the variation of the local Nusselt number, although this is not very clearly seen in Fig. 7. A closeup of the Nu variation for curve 2 is shown in the inset in Fig. 7, where the local value of Nu can be seen to dip below even the corresponding fully developed value, which is 0.62.

Overall Heat Transfer. The overall heat transfer results are presented in terms of two nondimensional quantities, the total amount of heat absorbed and a mean Nusselt number.

The total heat absorbed Q_L can be obtained from equation (14) by evaluating the integral at the exit of the duct. Figures 8 and 9 show the relationship between the duct length and the total heat absorbed by the fluid. As expected, for longer ducts Q_L shows an asymptotic behavior. The qualitative trend of Q_L for different fin spacing and clearance parameters is similar to that shown by the mass flow rate (Figs. 3 and 4). This is reasonable since both the flow and total heat transfer are caused by the temperature difference $(T_w - T_0)$.

The mean Nusselt number $\overline{\text{Nu}}$ is defined as

$$\overline{\text{Nu}} = \frac{(Q_l'/A)H}{(T_w - T_0)k} \tag{18}$$

where the heat transfer area A for the whole duct is given by

$$A = (2H + s)l \tag{19}$$

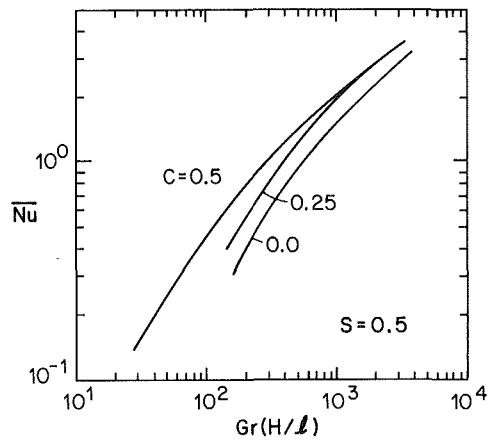

Fig. 10 Variation of mean Nusselt number with Gr(H/l) for S = 0.5

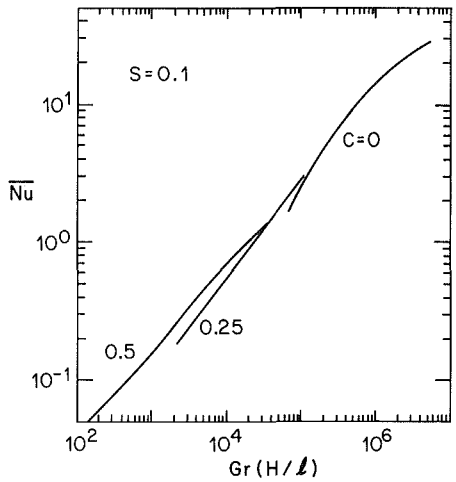

Fig. 11 Variation of mean Nusselt number with Gr(H/l) for S = 0.1

In terms of the nondimensional variables $\overline{\mathrm{Nu}}$ can be expressed as

$$\overline{\mathrm{Nu}} = \frac{Q_L \mathrm{Pr}}{(2+S)\,(l/H)\,\mathrm{Gr}^{-1}} \tag{20}$$

For very long ducts, Q_L attains a constant value; then $\overline{\mathrm{Nu}}$ can be seen to be proportional to Gr(H/l).

The variation of the mean Nusselt number $\overline{\mathrm{Nu}}$ is shown in Figs. 10 and 11 for S = 0.5 and 0.1, respectively. In general, higher values of $\overline{\mathrm{Nu}}$ are encountered for short ducts, i.e., for large values of Gr(H/l). The reason is that the flow is not thermally saturated in short ducts and a large temperature difference exists between the fluid and the heated surface.

Concluding Remarks

Natural convection in a vertical shrouded fin array has been studied. This geometric configuration gives rise to complex flow distribution. The flow characteristics are sensitive to the presence (or absence) of clearance space between the fins and the shroud. For widely spaced fins, the local Nusselt number shows a monotonic decrease from the inlet to the exit of the duct. If the fins are closely spaced, and clearance is provided, the local Nusselt number shows a minimum within the duct. For long ducts, the flow situation at the exit of the duct is very nearly fully developed.

Acknolwedgments

This study was performed under the auspices of a grant from the National Science Foundation. The computational costs were in part covered by a grant from the University of Minnesota Computer Center.

References

1 Bodia, J. R., and Osterle, J. F., "The Development of Free Convection Between Heated Vertical Plates," ASME JOURNAL OF HEAT TRANSFER, Vol. 84, 1962, pp. 40-44.

2 Aung, W., "Fully Developed Laminar Free Convection Between Vertical Plates Heated Asymmetrically," *International Journal of Heat and Mass Transfer*, Vol. 15, 1972, pp. 1577-1580.

3 Aung, W., Fletcher, L. S., and Sernas, V., "Developing Laminar Free Convection Vertical Flat Plates Wtih Asymmetric Heating," *International Journal of Heat and Mass Transfer*, Vol. 15, 1972, pp. 2293-2308.

4 Aihara, T., "Effect of Inlet Boundary-Conditions on Numerical Solution of Free Convection Between Vertical Parallel Plates," Report, Institute of High Speed Mechanics, Tôhoku University, Japan, Vol. 28, 1973, pp. 1-27.

5 Sparrow, E. M., Shah, S., and Prakash, C., "Natural Convection in a Vertical Channel: I. Interacting Convection and Radiation. II. The Vertical Plate With and Without Shrouding," *Numerical Heat Transfer*, Vol. 3, 1980, pp. 297-314.

6 Nakamura, H., Asako, Y., and Naitou, T., "Heat Transfer by Free Convection Between Two Parallel Flat Plates," *Numerical Heat Transfer*, Vol. 5, 1982, pp. 95-106.

7 Davis, L. P., and Perona, J. J., "Development of Free Convection Flow in a Heated Vertical Open Tube," *International Journal of Heat and Mass Transfer*, Vol. 14, 1971, pp. 889-903.

8 Kageyama, M., and Izumi, R., "Natural Heat Convection in a Vertical Circular Tube," *Bulletin JSME*, Vol. 13, 1970, pp. 382-394.

9 Dyer, J. R., "The Development of Natural Convection Flow in a Vertical Uniform Heat Flux Duct," *International Journal of Heat and Mass Transfer*, Vol. 18, 1975, pp. 1455-1465.

10 Sparrow, E. M., and Prakash, C., "Enhancement of Natural Convection Heat Transfer by a Staggered Array of Discrete Vertical Plates," ASME JOURNAL OF HEAT TRANSFER, Vol. 102, 1980, pp. 215-220.

11 Prakash, C., and Sparrow, E. M., "Performance Evaluation for Discrete (in-Line or Staggered) and Continuous-Plate Arrays," *Numerical Heat Transfer*, Vol. 3, 1980, pp. 89-106.

12 Ramakrishna, K., Rubin, S. G., Khosla, P. K., "Laminar Natural Convection Along Vertical Square Ducts," *Numerical Heat Transfer*, Vol. 5, 1982, pp. 59-79.

13 Sparrow, E. M., Baliga, B. R., and Patankar, S. V., "Forced Convection Heat Transfer From a Shrouded Fin Array With and Without Tip Clearance," ASME JOURNAL OF HEAT TRANSFER, Vol. 100, 1978, pp. 572-579.

14 Acharya, S., and Patankar, S. V., "Laminar Mixed Convection in a Shrouded Fin Array," ASME JOURNAL OF HEAT TRANSFER, Vol. 103, 1981, pp. 559-565.

15 Zhang, Z., and Patankar, S. V., "Influence of Buoyancy on the Vertical Flow and Heat Transfer in a Shrouded Fin Array," *International Journal of Heat and Mass Transfer*, Vol. 27, 1984, pp. 137-140.

16 Patankar, S. V., and Spalding, D. B., "A Calculation Procedure for Heat, Mass and Momentum Transfer in Three-Dimensional Parabolic Flows," *Internationl Journal of Heat and Mass Transfer*, Vol. 15, 1972, pp. 1787-1806.

17 Patankar, S. V., *Numerical Heat Transfer and Fluid Flow*, McGraw-Hill, New York, 1980.

18 Raithby, G. D., and Schneider, G. E., "Numerical Solution of Problems in Incompressible Fluid Flow: Treatment of the Velocity-Pressure Coupling," *Numerical Heat Transfer*, Vol. 2, 1979, pp. 417-440.

Thermal Instability of a Fluid-Saturated Porous Medium Bounded by Thin Fluid Layers

G. Pillatsis

M. E. Taslim
Assoc. Mem. ASME

U. Narusawa
Mem. ASME

Department of Mechanical Engineering,
Northeastern University,
Boston, MA 02115

A linear stability analysis is performed for a horizontal Darcy porous layer of depth $2d_m$ *sandwiched between two fluid layers of depth* d *(each) with the top and bottom boundaries being dynamically free and kept at fixed temperatures. The Beavers–Joseph condition is employed as one of the interfacial boundary conditions between the fluid and the porous layer. The critical Rayleigh number and the horizontal wave number for the onset of convective motion depend on the following four nondimensional parameters:* $\hat{d}$ $(=d_m/d$, *the depth ratio),* δ $(=\sqrt{K}/d_m$ *with* K *being the permeability of the porous medium),* α *(the proportionality constant in the Beavers–Joseph condition), and* k/k_m *(the thermal conductivity ratio). In order to analyze the effect of these parameters on the stability condition, a set of numerical solutions is obtained in terms of a convergent series for the respective layers, for the case in which the thickness of the porous layer is much greater than that of the fluid layer. A comparison of this study with the previously obtained exact solution for the case of constant heat flux boundaries is made to illustrate quantitative effects of the interfacial and the top/bottom boundaries on the thermal instability of a combined system of porous and fluid layers.*

1 Introduction

The existence of a fluid layer adjacent to a layer of fluid-saturated porous medium is a common occurrence in both the natural (geophysical) and industrial environments, including such engineering applications as thermal-energy storage systems, a solar collector with a porous absorber, and porous journal bearings. In a system consisting of a fluid and a porous layer, fluid motion in one layer is not independent of that in the other; their interaction is dictated by the conditions at the interface between the two layers. Nield [1, 2] studied the thermal stability of superposed porous and fluid layers, utilizing the Beavers–Joseph condition [3] which is generally accepted as an accurate description of fluid motion at the interface between a fluid layer and a densely packed porous medium. He obtained an exact solution for the stability of a porous layer sandwiched between two fluid layers with rigid top and bottom boundaries when a constant heat flux is applied at the bottom. Although his work was initiated as an approach to incorporate the nonslip condition on rigid boundaries for the Rayleigh–Darcy problem, the geometry also has relevant applications such as stationary air layers separated by a porous material in a building and packed-bed thermal storage units with flow distribution spaces located above and below. Somerton and Catton [4] studied the stability of a fluid-saturated porous medium with internal heat generation overlaid with a fluid layer with a fixed temperature difference between two rigid boundaries. They used the Brinkman equation for the porous layer with continuity of velocity and shear as interfacial conditions: an approach widely used to simulate the fluid motion in a sparsely packed porous medium. Masuoka [5], in his experiments, inserted a wire screen between two horizontal rigid boundaries filled with glycerin. It was shown that the onset of convection could occur either in the lower fluid layer between the (heated) bottom boundary and the wire screen, or over the entire fluid layer, indicating that the form of convective pattern depends on the mesh size (or equivalent permeability) of the screen. Although his study represents a special case in which the porous layer is very thin, the results clearly show the importance of the interaction between fluid and porous layers.

Nield [2] obtained an exact solution for the stability of a porous layer sandwiched between two fluid layers with rigid top and bottom boundaries when constant heat flux is applied at the bottom. The present paper reports the stability analysis of the same configuration as the one studied by Nield for the case of free, fixed-temperature boundaries with the overall objective of understanding the quantitative effects of both hydrodynamic (rigid or free) and thermal (constant-heat or fixed temperature) boundary conditions.

The solution to our problem has to be sought numerically; therefore the present study is focused on a case in which the fluid layer is thin compared with the thickness of the porous layer. In section 2 the formulation of the problem is briefly discussed with an emphasis on the Beavers–Joseph interfacial condition. Section 3 describes solutions in the form of a convergent power series, followed by a discussion in section 4 based on a comparison of the numerical solution for the fixed-temperature case with the exact solutions for the constant-heat-flux cases. Finally, conclusions and a preview of future work in this area are presented in section 5.

2 Formulation

We consider the two-dimensional problem of a porous layer sandwiched between two fluid layers with free and fixed-temperature boundaries at the top and bottom (see Fig. 1). For an incompressible flow with the Boussinesq approximation and a Darcy flow in the porous medium, the governing equations for the study of a steady direct mode of instability may be written as [1, 2]:

For the fluid layer

$$\nabla^4 w + \mathrm{Ra}\partial^2 T_p/\partial x^2 = 0 \tag{1}$$

$$w + \nabla^2 T_p = 0 \tag{2}$$

For the porous layer

$$-\nabla_m^2 w_m + \mathrm{Ra}_m \partial^2 T_{mp}/\partial x_m^2 = 0 \tag{3}$$

$$w_m + \nabla_m^2 T_{mp} = 0 \tag{4}$$

Contributed by the Heat Transfer Division for publication in the JOURNAL OF HEAT TRANSFER. Manuscript received by the Heat Transfer Division June 3, 1985.

where T_p and T_{mp} are nondimensional temperature deviations from the steady conduction state; w and w_m are vertical velocities with Ra = the Rayleigh number for the fluid layer and Ra_m = the Rayleigh number for the porous layer. The nondimensional space coordinates, x, x_m, z, z_m are defined as: $x = x'/d$, $x_m = x'/d_m$, $z = (z' - d_m)/d$, $z_m = z'/d_m$, respectively.

The following are nine out of the required ten boundary conditions:

At z = 1 (the upper boundary)

$$T_p = 0 \tag{5}$$

$$w = 0 \tag{6}$$

$$\partial^2 w/\partial z^2 = 0 \tag{7}$$

At z_m = 1 or z = 0 (the interface between the fluid and the porous layer)

$$T_p = \epsilon_T T_{mp} \tag{8}$$

$$\epsilon_T w = w_m \tag{9}$$

$$\partial T_p/\partial z = \partial T_{mp}/\partial z_m \tag{10}$$

$$\delta^2 \epsilon_T \hat{d}^2 [3(\partial^3 w/\partial x^2 \partial z) + \partial^3 w/\partial z^3] = -\partial w_m/\partial z_m \tag{11}$$

At z_m = 0 (the midplane)

$$\partial T_{mp}/\partial z_m = 0 \tag{12}$$

$$\partial w_m/\partial z_m = 0 \tag{13}$$

where $\epsilon_T = kd_m/k_m d$, $\delta = \sqrt{K}/d_m$, and $\hat{d} = d_m/d$.

Equations (5), (6), and (7) express the fixed-temperature and free boundary conditions, while equations (12) and (13) describe the symmetry of the problem. Equations (8), (9), (10), and (11) are the continuity of temperature, vertical velocity, heat flux, and normal stress across the interface between the fluid and porous layers, respectively.

The last boundary condition is the Beavers–Joseph condition at the interface, which is originally given for a unidirectional flow as shown below [3]

$$\partial u'/\partial z' = \alpha(u' - u'_m)/\sqrt{K} \tag{14a}$$

where α is the constant of proportionality. This condition, which is similar to the boundary conditions used in the field of rarefied gas dynamics, was proposed as an empirical law at first. However, a series of theoretical and experimental studies [6–9] provided further support. Although its full validity requires a thorough description of α and the thickness of the corresponding transition layer near the interface, the Beavers–Joseph condition is currently the most widely accepted interfacial condition. The generalized Beavers–Joseph condition (for multidimensional flow) is also proposed by Jones [10], who suggested that the Beavers–Joseph condition should be regarded as the relationship between the slip velocity and the shear stress. According to this generalization, the proper form of the condition for the present two-dimensional stability problem should be

$$\partial u'/\partial z' + \partial w'/\partial x' = \alpha(u' - u'_m)/\sqrt{K} \tag{15a}$$

As yet, there exists no experimental confirmation as to the selection between the two possible forms of the Beavers–Joseph condition, equation (14*a*) and equation (15*a*); hence, both conditions will be employed alternatingly in this study. Equations (14*a*) and (15*a*), after application of the continuity requirement, can be rewritten in the following form:

$$\epsilon_T \hat{d}[\partial w/\partial z - \Delta \partial^2 w/\partial z^2] = \partial w_m/\partial z_m \tag{14}$$

$$\epsilon_T \hat{d}[\partial w/\partial z - \Delta(\partial^2 w/\partial z^2 + \partial^2 w/\partial x^2)] = \partial w_m/\partial z_m \tag{15}$$

where $\Delta = \delta\hat{d}/\alpha$.

3 Solution

The solution may be sought in the form

$$\begin{Bmatrix} w \\ T_p \end{Bmatrix} = \begin{Bmatrix} W(z) \\ \Theta(z) \end{Bmatrix} \cdot h(x)$$

$$\begin{Bmatrix} w_m \\ T_{mp} \end{Bmatrix} = \begin{Bmatrix} W_m(z_m) \\ \Theta_m(z_m) \end{Bmatrix} \cdot h_m(x_m) \tag{16}$$

where $d^2h/dx^2 + a^2 h = 0$ and $d^2 h_m/dx_m^2 + a_m^2 h_m = 0$, and a and a_m are nondimensional horizontal wave numbers.

3.1 Constant-Heat-Flux Condition. Prior to the study of

Nomenclature

a = nondimensional wave number in the fluid layer
a_m = nondimensional wave number in the porous layer
d = depth of each fluid layer
d_m = half-depth of the porous layer
$\hat{d}$ = d_m/d
D_T, D_{Tm} = thermal diffusivities
g = gravitational acceleration
h, h_m = see equation (16)
k, k_m = thermal conductivities
K = permeability of the porous medium
Ra = Rayleigh number for the fluid layer = $(\alpha_T g \beta d^4)/(\nu D_T)$
Ra_m = Rayleigh number for the porous layer = $(\alpha_T g \beta_m K d_m^2)/(\nu D_{Tm})$
T_l = temperature at the bottom boundary
T_u = temperature at the top boundary
T'_p, T'_{mp} = temperature deviations from the steady conduction state
T_p = $T'_p/(\beta d)$
T_{mp} = $T'_{mp}/(\beta_m d_m)$
u' = horizontal velocity in the fluid layer
u'_m = horizontal velocity in the porous layer
u = $(d/D_T)u'$
u_m = $(d_m/D_{Tm})u'_m$
w' = vertical velocity in the fluid layer
w'_m = vertical velocity in the porous layer
w = $(d/D_T)w'$
w_m = $(d_m/D_{Tm})w'_m$
W, W_m = see equation (16)
x = x'/d
x' = horizontal coordinate (see Fig. 1)
x_m = x'/d_m
z = $(z' - d_m)/d$
z' = vertical coordinate (see Fig. 1)
z_m = z'/d_m
α = constant of proportionality in the Beavers–Joseph condition
α_T = thermal expansion coefficient
β = $\frac{1}{2}k_m(T_l - T_u)/(k_m d + k d_m)$
β_m = $\frac{1}{2}k(T_l - T_u)/(k_m d + k d_m)$
δ = $\sqrt{K}/d_m$
Δ = $\delta\hat{d}/\alpha$
ϵ_T = $kd_m/k_m d$
Θ, Θ_m = see equation (16)
ν = kinematic viscosity
∇^2 = $\partial^2/\partial x^2 + \partial^2/\partial z^2$
∇_m^2 = $\partial^2/\partial x_m^2 + \partial^2/\partial z_m^2$

Subscripts

m = porous layer
p = perturbed quantity

the case of fixed-temperature thermal boundary conditions, which is our main interest here, the stability criterion of a porous layer sandwiched between two fluid layers with free top and bottom boundaries is presented when constant heat flux is applied. Nield [2] gives the exact solution to a similar problem in which the top and bottom boundaries are rigid. A comparison between the solution to the free boundary case and Nield's solution will help understand the difference between the rigid and free boundary problems. The method of solution used by Nield can be applied to the present problem; that is, since the critical wave number is zero in the constant-heat-flux case, we can expand W and Θ in terms of a^2 (and W_m and Θ_m in terms of a_m^2). The solutions to the a^0-order and a^2-order equations, thus generated, yield the following stability criterion for the case of free, constant-heat-flux boundary conditions (see [1, 2] for details of the solution method):

$$\epsilon_T[192+360\Delta\ (1+2\hat{d})+720\hat{d}^3\delta^2+300\hat{d}^2]\ \mathrm{Ra}_c+\hat{d}^2 \cdot\{480+(60/\delta^2\hat{d}^4)\ [5+8\hat{d}+12\Delta\ (1+2\hat{d})+24\hat{d}^3\delta^2]\}\ \mathrm{Ra}_{mc} = 1440\ (\epsilon_T+\hat{d}^2) \tag{17}$$

For comparison, Nield's solution for the case of a rigid, constant-heat-flux boundary is shown below

$$\epsilon_T\ [8+18\Delta+(15+45\Delta)\epsilon_T]\mathrm{Ra}_c+\{120(1+\Delta)\hat{d}^2 +180\hat{d}+60\hat{d}/\epsilon_T+1/\delta^2\ [(30+120\Delta)/\hat{d} +(15+45\Delta)/(\hat{d}\epsilon_T)]\}\ \mathrm{Ra}_{mc}=360(1+\Delta)\ (\epsilon_T+\hat{d}^2) \tag{18}$$

As $d \to 0$ (with $\Delta \to 0$), $\mathrm{Ra}_c = 1440/192 = 7.5\ (= 120/2^4)$ from equation (17), and $\mathrm{Ra}_c = 360/8 = 45\ (= 720/2^4)$ from equation (18), giving the critical Rayleigh number for a fluid layer between two free boundaries, and that for a fluid layer between two rigid boundaries, respectively, when constant heat flux is applied at the bottom. On the other hand, if we let $d \to \infty$, equation (17) yields

$$\mathrm{Ra}_{mc}=1440/480=3.0\ (=12/2^2)$$

and equation (18) becomes

$$\mathrm{Ra}_{mc}=360/120=3.0$$

giving the critical Rayleigh number for a porous layer between two impermeable boundaries for the constant-heat-flux case.

3.2 Case of Fixed-Temperature Condition. Substitution of equation (16) into equations (1)–(15), and elimination of Θ and Θ_m, result in the following set of equations:

$$D^6W-3a^2D^4W+3a^4D^2W+(\mathrm{Ra}a^2-a^6)W=0 \tag{19}$$

$$D_m^4W_m-2a_m^2D_m^2W_m+(a_m^4-\mathrm{Ra}_m a_m^2)W_m=0 \tag{20}$$

$$\left.\begin{aligned}
&(D^2-a^2)^2W(1)=0,\quad W(1)=0,\quad D^2W(1)=0,\\
&\epsilon_T\delta^2\hat{d}^4(D^2-a^2)^2W(0)+(D_m^2-a_m^2)W_m(1)=0,\\
&\epsilon_T^2\delta^2\hat{d}^4D(D^2-a^2)^2W(0)+D_m(D_m^2-a_m^2)W_m(1)=0,\\
&\epsilon_TW(0)=W_m(1),\\
&\epsilon_T\delta^2\hat{d}^3(3a^2D-D^3)W(0)=D_mW_m(1),\\
&D_m(D_m^2-a_m^2)W_m(0)=0,\quad D_mW_m(0)=0,\\
&\epsilon_T\hat{d}[D-\Delta(D^2-K1)]W(0)=D_mW_m(1)
\end{aligned}\right\} \tag{21}$$

where $D = d/dz$, and $D_m = d/dz_m$. The last equation in the set of equations (21) gives the Beavers–Joseph condition with $K1 = 0$ for the original form (corresponding to equation (14)) and with $K1 = a^2$ for the generalized form (corresponding to equation (15)). As can be seen, the sixth-order differential equation (19) for the fluid layer and the fourth-order differential equation (20) for the porous layer are coupled through ten boundary conditions in equation (21). The general solutions to equations (19) and (20) can be represented in two convergent series, similar to the series employed by Sparrow et al. [11].

Let

$$W=\sum_{i=0}^{5}C_i\,f^{(i)}(z), \qquad W_m=\sum_{i=0}^{3}C_{mi}F^{(i)}(z_m) \tag{22}$$

where

$$f^{(i)}(z)=\sum_{n=0}^{\infty}b_n^{(i)}z^n, \qquad F^{(i)}(z_m)=\sum_{n=0}^{\infty}B_n^{(i)}z_m^n \tag{23}$$

$$b_n^{(i)}\quad(0\le n\le 5)\ =\ \begin{cases}1 & \text{for } n=i\\ 0 & \text{for } n\ne i\end{cases}$$

$$B_n^{(i)}\quad(0\le n\le 3)\ =\ \begin{cases}1 & \text{for } n=i\\ 0 & \text{for } n\ne i\end{cases}$$

Then the series coefficients $b_m^{(i)}$ $(n \ge 6)$ and $B_n^{(i)}$ $(n \ge 4)$ obey the following recursion formulae, which are obtained by substituting equation (22) into equations (19) and (20):

$$b_n^{(i)}=(1/n!)[3a^2(n-2)!b_{n-2}^{(i)}-3a^4(n-4)! b_{n-4}^{(i)}-(\mathrm{Ra}a^2-a^6)(n-6)!b_{n-6}^{(i)}] \tag{24}$$

$$B_n^{(i)}=(1/n!)[2a_m^2(n-2)!B_{n-2}^{(i)} -(a_m^4-\mathrm{Ra}_m a_m^2)(n-4)!B_{n-4}^{(i)}] \tag{25}$$

The assumed solutions, equation (22), have to satisfy the boundary conditions, equations (21). The symmetry conditions in equations (21) give $C_{m1} = C_{m3} = 0$ with the remaining eight boundary conditions yielding a set of eight equations for C_i $(i = 0, \ldots, 5)$, C_{m0}, and C_{m2}. The characteristic equation can be obtained by setting the (8×8) determinant, constructed from the coefficients of the C_i $(i = 0, \ldots, 5)$, C_{m0}, and C_{m2} in the above set of equations equal to zero.

4 Results and Discussion

The characteristic equation contains eight nondimensional parameters: Ra, Ra_m, a, a_m, $\hat{d}$, ϵ_T, δ, and Δ. Ra and Ra_m are related by

$$\mathrm{Ra}_m=\delta^2\hat{d}^2\epsilon_T^2\mathrm{Ra} \tag{26}$$

It should also be noted that the dimensional horizontal wave number has to be the same for the fluid and porous layers in order to realize a possible matching of the solutions in two layers (i.e., in order for the assumed solution, equation (16), to satisfy the interfacial boundary conditions, equations (8)–(11)):

$$a_m^2=\hat{d}^2a^2 \tag{27}$$

For the case of free boundaries at constant temperature, the criterion for the onset of convective motion (the critical condition) has to be sought numerically for a given set of values of $\hat{d}$, ϵ_T, δ, and Δ. The critical condition can be determined in the following manner: For a given value of a_m (or a), Ra_m (or Ra), which satisfies the characteristic equation, is found. For each value of a_m, there can be found a value of Ra_m that causes the characteristic equation to be zero. For a particular value of a_m, the corresponding Rayleigh number has a value which is smaller than that for any other a_m, and this is the critical condition (Ra_{mc}, a_{mc}) at which instability sets in. The convergence of the power series solution was tested by varying the number of terms n, retained in the series for typical combinations of nondimensional parameters over the range of this investigation. It was confirmed that for $n \ge 20$, Ra_{mc} thus evaluated did not change up to the third digit after the decimal point. Therefore, throughout this numerical investigation, the results with $n = 30$ were taken as "true" critical conditions.

In this investigation we concentrated on the case in which

Table 1 Comparison between the generalized and the original Beavers – Joseph condition; $\Delta = 5 \times 10^{-2}$, $\hat{d} = \epsilon_T$

$\hat{d}$	δ	critical conditions			
		with generalized condition		with original condition	
		Ra_{mc}	a_{mc}	Ra_{mc}	a_{mc}
10	5×10^{-2}	7.2742	1.341	7.2732	1.341
10	5×10^{-3}	3.1008	0.605	3.1008	0.605
10^2	5×10^{-3}	9.5328	1.544	9.5327	1.544
10^2	5×10^{-4}	5.7771	1.078	5.7770	1.078
5×10^2	1×10^{-3}	9.8004	1.565	9.8004	1.565
5×10^2	1×10^{-5}	3.6630	0.540	3.6630	0.540

Table 2 Numerical results near the fluid layer limit: (a) effect of δ on critical conditions ($\hat{d} = \epsilon_T = 5 \times 10^{-3}$, $\Delta = 10^{-2}$), with the use of the generalized Beavers – Joseph condition; (b) effect of $\hat{d}$ on critical conditions ($\delta = 10^3$, $\Delta = 10^{-2}$)

(a)

δ	Ra_{mc}	a_{mc}
5×10^3	3.658	0.83
3×10^3	8.889	0.85
1.8×10^3	18.180	0.89
10^3	29.964	0.97
10^2	40.394	1.10
70	40.608	1.10

(b)

$\hat{d}$	with original condition		with generalized condition	
	Ra_{mc}	a_{mc}	Ra_{mc}	a_{mc}
10^{-2}	9.587	0.86	9.621	0.86
5×10^{-3}	29.876	0.97	29.964	0.97
10^{-3}	40.695	1.10	40.785	1.10
10^{-4}	40.976	1.10	41.066	1.11

the fluid layer is very thin compared with the layer of porous medium, and three specific values for $\hat{d}$ ($=d_m/d$) equal to 10, 10^2, and 5×10^2 were selected for the generation of numerical results. Although the conductivity ratio, k/k_m, depends on the characteristics of both the fluid and porous layers, it is of the order of unity in many cases of practical interest, particularly for the liquid-saturated porous media; therefore ϵ_T ($=kd_m/k_md$) was assumed to be equal to $\hat{d}$ (i.e., $k/k_m = 1$) in this study.

In order to render a reasonable range of δ ($=\sqrt{K}/d_m$) for this study, the Carman–Kozeny equation [12] is employed

$$K = (1/180)\phi^3/(1-\phi)^2(d_p/d)^2(1/\hat{d}^2) \tag{28}$$

As can be seen, it relates the permeability K to the porosity of the porous medium ϕ, and to an equivalent particle diameter d_p of particles constituting porous matrices. As the magnitude of porosity becomes significantly large, the effect of the viscous shear is believed to be important in the porous medium. The common approach to the inclusion of this effect has been the use of the Brinkman-modified equation [14] which would result in the introduction of another parameter, called "effective" viscosity. However, because of the recent controversy over the use of the Brinkman model [2, 15, 16], it was not used in this investigation. Therefore, it should be noted that the present results should be used with caution for a sparsely packed porous medium ($\phi > \simeq 0.6$).

Table 3 List of selected numerical results, Ra_{mc} [a_{mc}]; $\epsilon_T = \hat{d}$ for all cases

(a) $\hat{d} = 500$

δ	Δ	Ra_{mc} [a_{mc}]
1×10^{-3}	5×10^{-2}	9.8004 [1.565]
1×10^{-4}	5×10^{-2}	7.9620 [1.384]
5×10^{-5}	5×10^{-2}	6.1561 [1.132]
1×10^{-5}	5×10^{-2}	3.6630 [0.540]

(b) $\hat{d} = 100$

δ	Δ	Ra_{mc} [a_{mc}]
5×10^{-3}	5.0	8.2424 [1.418]
5×10^{-3}	5×10^{-1}	9.3763 [1.530]
5×10^{-3}	5×10^{-2}	9.5327 [1.544]
1×10^{-3}	5×10^{-2}	7.5760 [1.342]
5×10^{-4}	5×10^{-2}	5.7770 [1.078]
1×10^{-4}	5×10^{-2}	3.5121 [0.508]

(c) $\hat{d} = 10$

δ	Δ	Ra_{mc} [a_{mc}]
5×10^{-2}	5×10^{-2}	7.2732 [1.341]
1×10^{-2}	5×10^{-2}	3.9445 [0.838]
5×10^{-3}	5×10^{-1}	2.8314 [0.500]
5×10^{-3}	5×10^{-2}	3.1008 [0.605]
5×10^{-3}	5×10^{-3}	3.1545 [0.624]

In the ensuing numerical study the overall range for δ was selected to be $10^{-5} < \delta < 10^{-1}$ (with the higher side of the range for the case of $\hat{d} = 10$ and the lower side for $\hat{d} = 5 \times 10^2$). Experimental studies in the past indicate that α is of the order of 1/10 to 10 [3, 8, 9]. This range of α, combined with the range of δ and $\hat{d}$ discussed above, gives a possible range for Δ ($=\delta\,\hat{d}/\alpha$) of 10^{-4} to 10. Four specific values of Δ ($\Delta = 5$, 5×10^{-1}, 5×10^{-2}, 5×10^{-3}) were selected for the present study.

Prior to the detailed investigation of a combined system of fluid and porous layers, two limits of $\hat{d} \to 0$ (the fluid layer limit: a layer of fluid of depth $2d$ between two free boundaries) and $\hat{d} \to \infty$ (the porous layer limit: a layer of porous medium of depth $2d_m$ between two impermeable boundaries) were examined. These limits yielding correctly that for $\hat{d} \to 0$ [17]

$Ra_c = (27/4)\pi^4/2^4 (= 41.095)$ at

$$a_c = [(\pi^2/2)/2^2]^{1/2} \ (= 1.111),$$

and for $\hat{d} \to \infty$ [18]

$Ra_{mc} = 4\pi^2/2^2 (= 9.870)$ at

$$a_{mc} = (\pi^2/2^2)^{1/2} \ (= 1.571)$$

In the generation of numerical results to be discussed below, both the generalized Beavers–Joseph condition and the original Beavers–Joseph condition were used alternately. Samples of results are listed in Table 1. We found over the range of our study, that there is little difference for Ra_{mc} (and no difference to the third decimal point for a_{mc}) between the

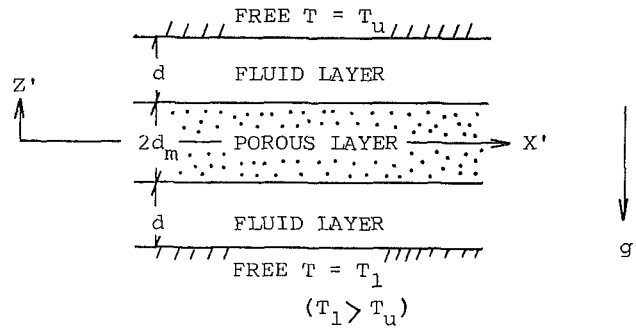

Fig. 1 Schematic diagram of the problem

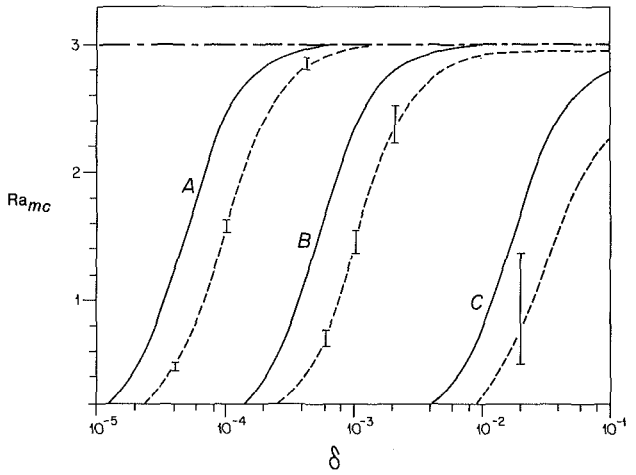

Fig. 2 Ra_{mc} versus δ for the constant-heat-flux case. (A) $\hat{d} = 500$; (B) $\hat{d} = 100$; (C) $\hat{d} = 10$ ($\epsilon_T = \hat{d}$ and $\Delta = 5 \times 10^{-2}$ for all curves); ——: rigid boundary; - - - - -: free boundary; — — —: $Ra_{mc} = 3.0$ for the porous limit; I: range of Ra_{mc} when k/k_m is varied from 10 to 0.1.

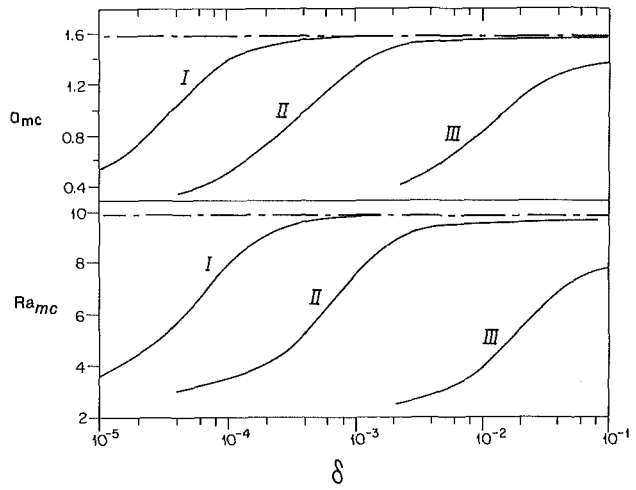

Fig. 3 The effect of δ on Ra_{mc} and a_{mc} for the fixed-temperature case ($\hat{d} = \epsilon_T$ and $\Delta = 5 \times 10^{-2}$); (I) $\hat{d} = 500$; (II) $\hat{d} = 100$; (III) $\hat{d} = 10$; — — —: $Ra_{mc} = 9.870$ and $a_{mc} = 1.571$ for the porous layer limit.

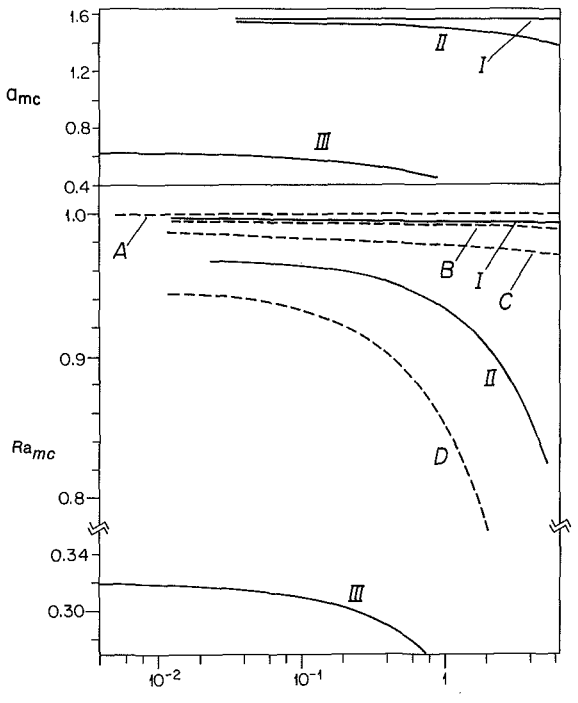

Fig. 4 The effect of Δ (or α) on Ra_{mc} and a_{mc} with $Ra_{mc,PL} = Ra_{mc}$ of the porous layer limit (= 9.870). (I, II, III) numerical results for fixed-temperature free boundary; (I) $\hat{d} = 500$; (II) $\hat{d} = 100$; (III) $\hat{d} = 10$. (A, C) constant-heat-flux, rigid boundary; (B, D) constant-heat-flux, free boundary; (A, B) $\hat{d} = 500$; (C, D) $\hat{d} = 100$; $\delta = 5 \times 10^{-3}$ and $\epsilon_T = \hat{d}$ for all calculated cases.

results obtained through the use of the generalized Beavers–Joseph condition and those obtained through the use of the original condition, indicating that the effect of the interfacial velocity gradient $\partial w/\partial x$ on the critical condition through the use of the generalized Beavers–Joseph condition is very small compared with that of $\partial u/\partial z$. In the Beavers–Joseph condition (i.e., the last equation in equations (21)), $K1$ ($= a^2 = a_m^2/\hat{d}^2$ for the generalized Beavers–Joseph condition) for large values of $\hat{d}$ is less than $1/\hat{d}^2$ as can be deduced from the numerical results reported in Fig. 3, resulting in very small differences between the original and the generalized Beavers–Joseph condition. On the other hand, near the fluid layer limit ($\hat{d} \to 0$), the magnitude of a_c is relatively constant (Table 2(*b*)) and a small difference in results employing different forms of the Beavers–Joseph condition can be attributed to small values of both $\hat{d}$ and Δ (normally a small quantity) in the last equation of equations (21).

The presence of a fluid layer adjacent to the top/bottom boundary influences the critical condition in two different ways. The rigid boundary at the solid–fluid interface tends to suppress the onset of convective motion as opposed to the freeing effect of the free boundary, while the slip effect at the interface between the fluid layer and the porous layer (which is described by the Beavers–Joseph condition) assists in lowering the critical Rayleigh number, compared to the case of impermeable boundaries. Therefore, generally speaking, we can expect the condition of free boundary to work with the Beavers–Joseph condition to lower the critical condition further; whereas, the rigid boundary opposes the freeing effect present at the porous–fluid interface. Figures 2 and 3 summarize the variation of the critical conditions with δ [13]. Figure 2 compares the critical Rayleigh number Ra_{mc} for the case of rigid boundaries (equation (18)), shown as the solid curves, and that for the case of free boundaries (equation (17)), shown as the dotted curves, when constant heat flux is applied at the bottom. Figure 3 shows our numerical results for the fixed-temperature, free boundary case. As has been explained above, the curve for the case of the free boundary is always located below the corresponding curve for the rigid boundary. The decrease in Ra_{mc} with a decrease in δ in both Figs. 2 and 3 suggests that the lower the permeability, the more sensitive the onset of convective motion becomes to the interaction at the interface between the porous and the fluid layers. Or, in terms of the Carman–Kozeny equation (28), the

effect of the fluid layer becomes more pronounced as the thickness d of the fluid layer becomes greater compared with the equivalent particle diameter d_p. For the case of the fixed-temperature boundary, the horizontal wave number is nonzero, and Fig. 3 shows the steady decrease in a_{mc} as the effect of the fluid layer becomes significant, indicating that the horizontal length scale of convection cells near the critical state becomes larger with a decrease in δ.

Figure 4 shows the effect of Δ on the critical conditions. A higher value of Δ indicates more slip at the porous-fluid interface, thereby contributing more to the lowering of Ra_{mc} and a_{mc}, although our results show that the effect of Δ on a_{mc} is small over the range of our interest. The curves for the cases of constant heat flux with $\hat{d} = 10$ are below the scale and not shown in Fig. 4. In Figs. 2 and 3, this means that the Ra_{mc}-δ curve flattens out at a larger value of δ for the fixed-temperature case than the corresponding curve for the constant-heat-flux case. The exact solutions, equations (17) and (18), for the constant-heat-flux boundaries can be used and compared to find the qualitative effects of various parameters on the critical Rayleigh number. As an example, the effect of the thermal conductivity ratio k/k_m is also shown as vertical bars for selected values of δ in Fig. 2 when k/k_m is varied from 10 (the upper bound of each bar) to 0.1 (the lower bound). Because the presence of fluid layers has a destabilizing effect, it can be seen that a larger temperature drop across the porous midlayer ($k/k_m > 1$) stabilizes the system and that the effect of the conductivity ratio is more pronounced as the fluid layers become thicker relative to the porous layer.

Although our interest lies mainly in the case in which $\hat{d}$ is large (i.e., the region near the porous layer limit), the region near the fluid layer limit of small $\hat{d}$ was also investigated to check the convergence of the critical condition to that of the fluid layer limit, and also to find the effect of the Beavers-Joseph condition on Ra_c (the critical Rayleigh number for the fluid layer) and a_c (the critical wave number). The numerical results are summarized in Table 2. The results given in Table 2(a) (the effect of δ on Ra_c and a_c for fixed values of $\hat{d} = \epsilon_T = 5 \times 10^{-3}$ and $\Delta = 0.01$) and in Table 2(b) (the variation of Ra_c and a_c with $\hat{d}$ for fixed values of $\delta = 10^3$ and $\Delta = 0.01$) confirm that as $\hat{d}$ (and/or δ) decreases, Ra_c and a_c approach the critical values of the fluid layer limit. (For a horizontal fluid layer between two free, fixed-temperature boundaries, $\mathrm{Ra}_c = (27/4)\pi^4/2^4 = 41.095$ and $a_c = [(\pi^2/2)/2^2]^{1/2} = 1.11$). In addition, the comparison of Table 2(b) with Table 1 shows that near the fluid layer limit ($\hat{d} \to 0$) the difference between the results obtained with the use of the original Beavers-Joseph condition and those with the use of the generalized Beavers-Joseph condition is slightly larger than the difference near the porous layer limit ($\hat{d} \to \infty$).

Finally, the onset of instability over the whole system is assumed in this paper in accordance with the coupling of thermofluid behavior in the porous and the fluid layers through both hydrodynamic and thermal conditions at the interface. Also the symmetric nature of the problem eliminates any possibility of onset of convection in one (top or bottom) fluid layer only. On the other hand, according to Masuoka's experiment [5], in which two fluid layers were separated by a wire screen, only one of the fluid layers (the bottom layer in his photograph) became unstable, which contradicts our analysis, although his case can be regarded as the one with a thin, highly permeable porous layer separating two fluid layers. Since the study of convective instability in a conjugate system such as the present problem is quite complex, the clarification of this discrepancy as well as its cause can only be accomplished by finite-amplitude (numerical) calculations and/or an experimental study of high accuracy similar to the one reported by Krishnamurti [19] for the Rayleigh-Benard instability problem.

5 Conclusions and Future Work

The major conclusions of this study are:

1 The correct limits as $\hat{d} \to 0$ or $\hat{d} \to \infty$ can be achieved for the problem of superposed porous/fluid layers through the utilization of the Beavers-Joseph condition.

2 As far as the stability criterion is concerned, the selection between the original and the generalized Beavers-Joseph condition does not affect the results significantly over the range of parameters studied in this investigation.

3 The effects of the free boundaries and of the interfacial slipping are additive to lower both Ra_{mc} and a_{mc}.

4 A greater effect of slipping on Ra_{mc} can be felt for the porous layer with lower permeability, while the magnitude of a_{mc} is relatively insensitive to variations of α.

In order to confirm and establish the general formulation and the correct solution procedure for a superposed system of porous and fluid layers, the boundary conditions different from those in Nield's work [2] were purposely selected in the present analysis even though free top and bottom boundaries are difficult to achieve experimentally. Consequently, a study with more realistic boundary conditions for experimental verification is desirable in order to understand the quantitative effects of various parameters including the range of $\hat{d} \simeq 1$. Clarification of these more detailed descriptions of the problem has to await the outcome of our ongoing research which extends into double-diffusive instability with rigid boundaries of specified temperature and solute concentration.

References

1 Nield, D. A., "Onset of Convection in a Fluid Layer Overlaying a Layer of Porous Medium," *J. Fluid Mech.*, Vol. 81, 1977, pp. 513-522.

2 Nield, D. A., "Boundary Correction for the Rayleigh-Darcy Problem: Limitations of the Brinkman Equation," *J. Fluid Mech.*, Vol. 128, 1983, pp. 37-46.

3 Beavers, G. S., and Joseph, D. D., "Boundary Conditions at a Naturally Permeable Wall," *J. Fluid Mech.*, Vol. 30, 1967, pp. 197-207.

4 Somerton, C. W., and Catton, I., "On the Thermal Instability of Superposed Porous and Fluid Layers," ASME JOURNAL OF HEAT TRANSFER, Vol. 104, 1982, pp. 160-165.

5 Masuoka, T., "Convective Currents in a Horizontal Layer Divided by a Permeable Wall," *Bull. Japan Soc. Mech. Engrs.*, Vol. 17, 1974, pp. 232-252.

6 Taylor, G. I., "A Model for the Boundary Condition of a Porous Material, Part 1," *J. Fluid Mech.*, Vol. 49, 1971, pp. 319-326.

7 Richardson, S., "A Model for the Boundary Condition of a Porous Material, Part 2," *J. Fluid Mech.*, Vol. 49, 1971, pp. 327-336.

8 Beavers, G. S., Sparrow, E. M., and Magnuson, R. A., "Experiments on Coupled Parallel Flows in a Channel and a Bounding Porous Medium," ASME *J. Basic Engng.*, Vol. 92, 1970, pp. 843-848.

9 Beavers, G. S., Sparrow, E. M., and Masha, B. A., "Boundary Conditions at a Porous Surface Which Bounds a Fluid Flow," *AIChE J.*, Vol. 20, 1974, pp. 596-597.

10 Jones, I. P., "Low Reynolds Number Flow Past a Porous Spherical Shell," *Proc. Camb. Phil. Soc.*, Vol. 73, 1973, pp. 231-238.

11 Sparrow, E. M., Goldstein, R. J., and Jonsson, V. K., "Thermal Instability in a Horizontal Fluid Layer: Effect of Boundary Conditions and Non-linear Temperature Profile," *J. Fluid Mech.*, Vol. 18, 1964, pp. 513-528.

12 Dullien, F. A., *Porous Media: Fluid Transport and Pore Structure*, Academic Press, New York, 1979.

13 Pillatsis, G., "Convective Instability in a Combined System of a Porous Layer Sandwiched Between Two Layers of Fluid," M.S. Thesis, Northeastern University, Boston, MA, 1985.

14 Brinkman, H. C., "A Calculation of the Viscous Force Exerted by a Flowing Fluid on a Dense Swarm of Particles," *Appl. Sci. Res.*, Vol. A1, 1947, pp. 27-34.

15 Haber, S., and Mauri, R., "Boundary Conditions for Darcy's Flow Through Porous Media," *Int. J. Multiphase Flow*, Vol. 9, 1983, pp. 561-574.

16 Rudraiah, N., "Coupled Parallel Flows in a Channel and a Bounding Porous Medium of Finite Thickness," ASME *J. Fluids Engrg.*, Vol. 107, 1985, pp. 322-329.

17 Nield, D. A., "The Thermohaline Rayleigh-Jeffreys Problem," *J. Fluid Mech.*, Vol. 29, 1967, pp. 545-558.

18 Nield, D. A., "Onset of Thermohaline Convection in a Porous Medium," *Water Resources Res.*, Vol. 3 and 4, 1968, pp. 553-560.

19 Krishnamurti, R., "Finite Amplitude Convection With Changing Mean Temperature. Part 2: An Experimental Test of the Theory," *J. Fluid Mech.*, Vol. 33, 1968, pp. 457-463.

G. El-Khatib

V. Prasad
Mem. ASME

Department of Mechanical Engineering,
Columbia University,
New York, NY 10027

Effects of Stratification on Thermal Convection in Horizontal Porous Layers With Localized Heating From Below

Introduction

Free convection from a heat source located on the bottom surface of a stably stratified horizontal porous layer is a problem of practical importance. This problem is encountered in several geothermal areas which consist of troughs of volcanic debris contained by walls of nonfragmented ignimbrite. Thus, the model region considered is a locally heated trough of isotropic porous medium confined by impermeable surroundings which may also be subjected to an external temperature gradient under certain circumstances. Also, recent motivation to study this problem has come from efforts to identify a geologic repository for the storage of nuclear wastes. Although several attempts have been made to examine the effects of stable thermal stratification in fluid layers heated from below (Torrance, 1979; Fusegi and Farouk, 1985), nothing has been reported thus far for porous media.

The purpose of the present work is to study numerically the natural convection in a horizontal porous layer in the presence of a stable, linear thermal gradient. The geometry considered is a two-dimensional horizontal cavity filled with a fluid-saturated porous medium whose bottom surface is cooled at a constant temperature T_c, except for a central portion of the surface where an isothermal heat source exists (Fig. 1). The temperature on the side walls varies linearly from the bottom surface temperature T_c to the top wall temperature T_t. Detailed flow and temperature field solutions are obtained for various values of thermal stratification ratio S. When $S = 0$, the present problem reduces to natural convection in horizontal porous layers with localized heating from below. This problem has been considered by several investigators in the past (Elder, 1967a,b,; Horne and O'Sullivan, 1974, 1978; Prasad and Kulacki, 1986, 1987).

Formulation and Numerical Method

Consider a rectangular cavity of height L and width $2D$ (Fig. 1) filled with an isotropic, homogeneous, fluid-saturated porous medium which obeys Darcy's law. The temperature of the vertical wall varies linearly from T_c to T_t. On the bottom surface, an isothermal heat source of width $2d$ is centrally located. Characteristic temperature differences for the horizontal and vertical directions are, thus, $\Delta T_H = T_h - T_c$, and $\Delta T_v = T_t - T_c$, respectively.

The horizontal temperature difference ΔT_H serves to induce and sustain a buoyancy-driven flow in the cavity which is then controlled by the vertical temperature difference ΔT_v. The structure of the induced flow thus depends on the stratification ratio

$$S = (T_t - T_c)/(T_h - T_c) = \Delta T_v / \Delta T_H \tag{1}$$

A relevant dimensionless temperature may thus be defined as

$$\theta = [T - T(D, y)]/\Delta T_H \tag{2}$$

Contributed by the Heat Transfer Division and presented at the 4th AIAA/ASME Heat Transfer and Thermophysics Conference, Boston, Massachusetts, 1986. Manuscript received by the Heat Transfer Division January 24, 1986.

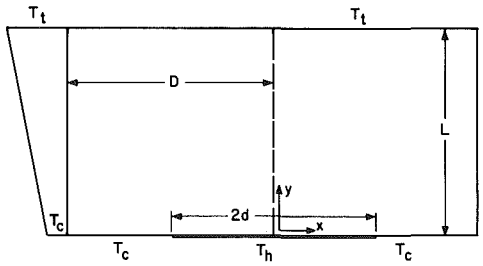

Fig. 1 Geometry, coordinate system, and boundary conditions of the system

With the above assumptions, the governing equations for steady, two-dimensional flow in porous media (Prasad and Kulacki, 1984b) transform into stream function and temperature equations as

$$\frac{1}{A^2}\frac{\partial^2 \psi}{\partial X^2} + \frac{\partial^2 \psi}{\partial Y^2} = \mathrm{Ra}^* \frac{\partial \theta}{\partial X} \tag{3}$$

$$-\frac{\partial \psi}{\partial Y}\frac{\partial \theta}{\partial X} + \frac{\partial \psi}{\partial x}\left(\frac{\partial \theta}{\partial Y} + S\right) = \frac{\partial^2 \theta}{\partial X^2} + A^2 \frac{\partial^2 \theta}{\partial Y^2} \tag{4}$$

with the relevant hydrodynamic and thermal boundary conditions

$$\theta = 1, \; -H \le X \le H \text{ and } Y = 0$$

$$\theta = 0 \text{ on all boundaries except above} \tag{5}$$

$$\psi = 0 \text{ on all boundaries}$$

Owing to the symmetry of the problem, only the right half of the cavity, referred to as the "half-cavity," has been considered for computational purposes. Indeed, the numerical results obtained for the entire cavity indicate that the consideration of symmetry does not produce any significant variation in the temperature and velocity fields.

Finite-difference equations are derived from equations (5) and (6) by integration over finite area elements following a procedure outlined by Gosman et al. (1969). For solving the system of algebraic equations thus obtained, a point iterative method is used which makes use of the new values as soon as they are available. For the present work, uniform mesh sizes have been used for both x and y directions. A nonuniform grid field could not be identified for this problem because the nature of the velocity and temperature fields change substantially with Ra* and S. Based on several trial cases, a suitable grid field of 41×31 mesh was selected for the present calculations. A convergence criterion of 0.01 percent or less change in both ψ and θ at all grid points in the domain was used to test the convergence of the iterative scheme. To obtain faster convergence, θ was generally overrelaxed. However, when the stratification parameter $S = 0$, the stream function ψ needed to be underrelaxed. A detailed description of the numerical procedure has been omitted here for brevity (see Prasad and Kulacki, 1984a).

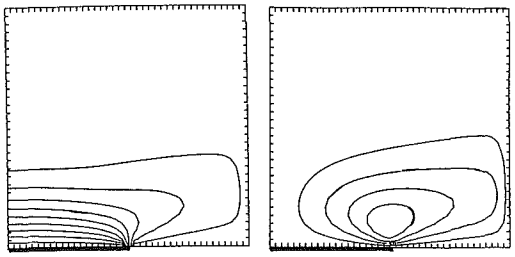

Fig. 2(a)

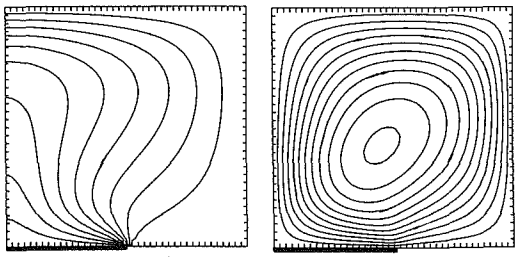

Fig. 2(b)

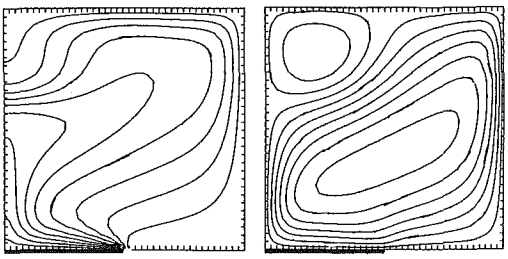

Fig. 2(c)

Fig. 2 Isotherms (left) and streamlines (right) for $S = 0$ (no stratification): (a) Ra* = 20 ($\Delta\theta = 0.1$, $\Delta\psi = 0.2$); (b) Ra* = 100 ($\Delta\theta = 0.1$, $\Delta\psi = 0.5$); (c) Ra* = 1000 ($\Delta\theta = 0.1$, $\Delta\psi = 1.88$)

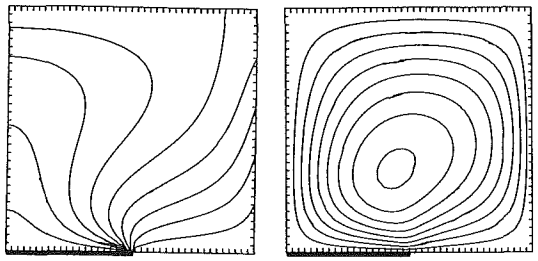

Fig. 3(a)

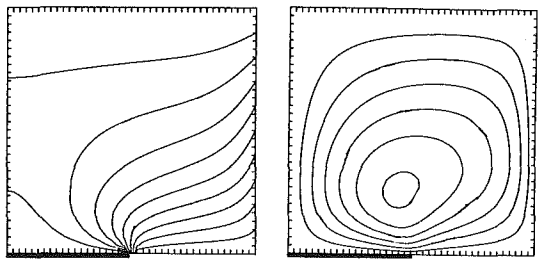

Fig. 3(b)

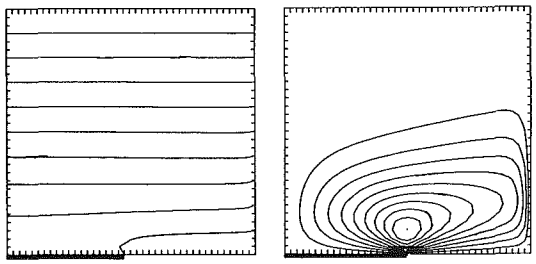

Fig. 3(c)

Fig. 3 Isotherms (left) and streamlines (right) for Ra = 100: (a) $S = 0.5$ ($\Delta\theta = 0.1$, $\Delta\psi = 0.5$); (b) $S = 1$ ($\Delta\theta = 0.1$, $\Delta\psi = 0.5$; (c) $S = 10$ ($\Delta\theta = 1$, $\Delta\psi = 0.1$)

Results and Discussion

Since the primary objective of this study is to examine the effects of wall stratification on free convection from a finite heat source, a wide range of stratification parameter, $0 \le S \le 10$, has been considered for $H = 0.5$ and $A = 1$.

Temperature and Flow Fields. To plot the isotherms, a more realistic dimensionless temperature

$$\theta_R = (T - T_c)/(T_h - T_c) = \theta + YS \tag{6}$$

has been considered which indicates the excess temperature at any location with respect to the temperature of the heat

Nomenclature

A = aspect ratio of half-cavity = D/L
C = specific heat of fluid at constant pressure, J/kg-K
D = width of half-cavity, m
d = length of heat source in half-cavity, m
g = acceleration due to gravity, m/s^2
H = dimensionless length of heat source, = d/D
h = heat transfer coefficient on the bounding surface, W/m^{2}K
K = permeability of saturated porous medium, m^2
k = effective thermal conductivity of porous medium, W/m-K
L = height of porous layer, m
$\overline{\mathrm{Nu}}$ = overall Nusselt number based on layer height = $\bar{h}_d L/k$
Nu_x = local Nusselt number = $h_x L/k$
Ra* = Rayleigh number based on cavity width = $g\beta KL(T_h - T_c)/\nu\alpha$
S = stratification ratio = $(T_t - T_c)/(T_h - T_c)$
T = temperature, K
u = fluid velocity in x direction = $-(\alpha/D)(\partial\psi/\partial Y)$, m/s
v = fluid velocity in y direction = $(\alpha L/D^2)(\partial\psi/\partial X)$, m/s
x, y = Cartesian coordinates, m
X, Y = dimensionless distances on x and y axes = x/D and y/L, respectively
α = thermal diffusivity of porous medium, m^2/s
β = isobaric coefficient of thermal expansion of fluid, K^{-1}
θ = dimensionless temperature = $[T - T(D, y)]/(T_h - T_c)$
θ_R = dimensionless temperature = $(T - T_c)/(T_h - T_c)$
ν = kinematic viscosity, m^2/s
ψ = stream function

Subscripts

c = cooled wall
d = based on the length of heated segment
h = heated segment of bottom surface
max = maximum
t = top surface
x = local value on the horizontal walls

source. The temperature of the upper surface is thus given by $\theta_R = S$, while the temperature of the heat source is $\theta_R = 1$. Hence, the isotherms are plotted for either $0<\theta_R<1$ (no stratification) or $0<\theta_R<S$.

The isotherms and streamlines are, first, presented for $S = 0$ (no stratification) in Figs. 2(*a–c*). The isotherms in Fig. 2(*a*) indicate that the conduction temperature field, particularly near the edge of the heat source, is perturbed at a Rayleigh number as low as 10. This results in a circulatory flow in the lower portion of the cavity. However, these streamline and isotherm patterns (Fig. 2*a*) vary substantially from those reported by Prasad and Kulacki (1987). Since they had considered the vertical walls and the unheated section of the bottom surface as adiabatic, the fluid was required to move all the way up to the top surface to reject the heat gained at the base.

The isotherms and streamlines, however, do shift toward the upper surface if the Rayleigh number is increased: the higher the Rayleigh number, the larger the domain of cavity influenced by the convective flow (Fig. 2*b*). Moreover, owing to the buoyant plume over the heated segment, the upper layers are observed to be stratified and the temperature field exhibits an inverse temperature gradient $\partial\theta_R/\partial Y$ in the core. The isotherms then extend to the right top corner of the cavity. Since the velocities increase in the bottom left and top right corners of the cavity with an increase in Ra*, the axis of the convective cell moves clockwise with Ra*. This produces a region of very low velocities in the left top corner, and tends to reduce the stratification in that region. Finally, a situation comes when a counterrotating secondary cell appears in the left top corner at high Ra* (Fig. 2*c*). Since this cell aids in the heat rejection on the top surface, the temperature in the upper layers directly above the heat source further decreases. Strong inversion in temperature gradient $\partial\theta_R/\partial Y$ is then observed in the core. This complex behavior of the temperature and flow fields at high Ra* is characteristic of the present boundary conditions. No such secondary cells appear in the cavity if the vertical walls and/or the unheated sections of the base are insulated (Prasad and Kulacki, 1987; Horne and O'Sullivan, 1974). Nevertheless, for a fluid-filled cavity, Torrance (1979) and Fusegi and Farouk (1985) have reported multicellular flow behavior for the present type of boundary conditions.

To demonstrate the effect of the wall stratification parameter S, the isotherms and streamlines for Ra* = 100, and S = 0.5, 1, and 10, are presented in Figs. 3(*a–c*). An increase in S beyond zero diminishes the stratification in the upper layers and shifts the isotherms toward the vertical walls (Figs. 2*b* and 3*a*). The velocities thus reduce with S and the axis of the convective cell moves counterclockwise. When S = 0.5, the upper surface temperature θ_R is equal to 0.5. Therefore, the isotherms for $\theta_R < 0.5$ join the vertical walls at corresponding levels. The temperature variation in a large portion of the cavity is then limited to $1 < \theta_R < 0.5$ which significantly affects the heat transfer at various walls. Evidently, the buoyancy effects are greatly reduced with an increase in S.

In Fig. 3(*a*), the isotherm for $\theta_R = 0.5$ joins the upper surface at a location away from the top right edge (1, 1) even though the entire surface is maintained at $\theta_R = 0.5$. This clearly implies that the heat is being gained by the convective medium in the top right corner. When S = 1 the temperature

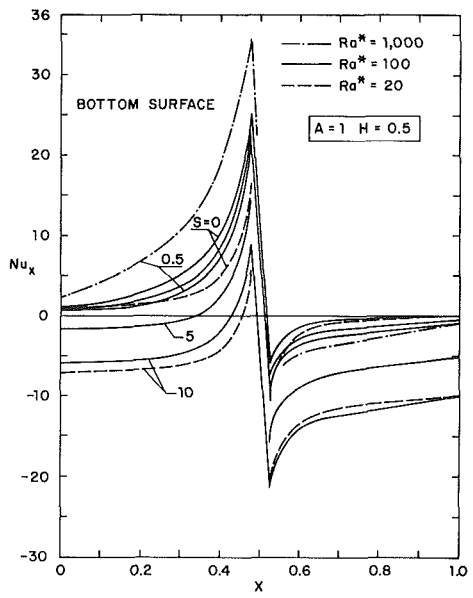

Fig. 4(*a*)

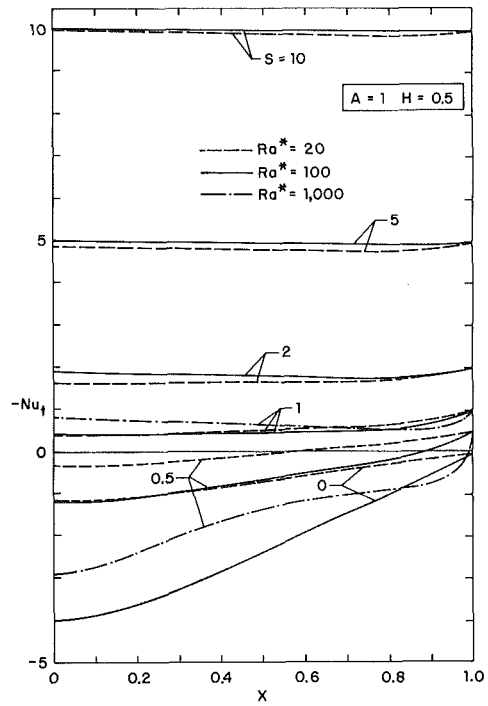

Fig. 4(*b*)

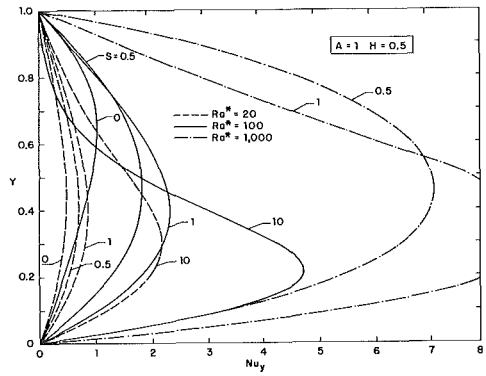

Fig. 4(*c*)

Fig. 4 The local Nusselt number on (*a*) the bottom surface, (*b*) the upper surface, and (*c*) the side wall

of the upper surface is equal to that of the heat source. Though Ra* is still the same, the buoyancy effects are greatly reduced because of the stabilizing effect of the upper boundary. Two isotherms for $\theta_R = 0.9$, one near the heat source and the other near the top surface, are now observed which never meet. Between these two isotherms, the thermal field is very weak. When $S = 10$, the convective cell hardly extends beyond the lower half of the cavity. The temperature distribution in a large portion of the cavity, thus, exhibits the stable stratification unaffected by the buoyant flows (Fig. 3*c*).

Local Heat Transfer Rate. Interesting features of the buoyancy-driven flow are further exhibited by the distributions of local Nusselt number[1] on the vertical and horizontal walls.

Bottom Surface. The local Nusselt number on the bottom surface

$$\mathrm{Nu}_x = h_x L/k = -\partial\theta/\partial Y \text{ at } Y=0 \qquad (7)$$

is presented in Fig. 4(*a*). The cold fluid flowing down on the side wall continues to reject heat through the cold portion of the bottom surface until it reaches the leading edge of the heat source where it picks up energy at a very high rate. When $S = 0$, the energy is gained by the fluid everywhere on the heated segment although Nu_x decreases sharply with x. With an increase in S, the fluid rejects a smaller amount of energy on the top surface and the side wall. This results in a larger fraction of energy being removed in the cold portion of the bottom surface. Since the velocities decrease with an increase in S, Nu_x at any location of the heated segment is substantially reduced. This trend continues until a critical value of S is reached, when T_f is high enough to cause a zero temperature gradient, $\partial\theta/\partial Y$, at $x = 0$, $y = 0$.

Any increase in S beyond S_{critical} then results in heat rejection in a portion of the heated segment while energy is being gained at other locations of the heat source. The larger the wall stratification parameter S, and the smaller the Rayleigh number, the smaller is the portion of the heated segment where energy is gained by the system (Fig. 4*a*). As long as the convective medium gains heat (near the leading edge), the buoyant flow exists, and a convective cell is observed. However, the domain influenced by the convective velocities shrinks significantly with an increase in S (Fig. 3), and finally a situation is achieved when the energy is removed everywhere on the bottom surface. This stable situation characterizes pure conduction from the upper surface to the base.

Upper Surface. The local Nusselt number on the top surface Nu_t is presented in Fig. 4(*b*). When $S = 0$, the energy is removed everywhere on the upper surface; the heat flux is maximum at the center of the top surface owing to the buoyant plume rising from the heat source. However, Nu_t decreases with an increase in x, and is a function of Ra*. This behavior changes drastically with the introduction of wall stratification. In Fig. 4(*b*), $-\mathrm{Nu}_t$ is positive near the right top edge for S as low as 0.5, indicating that energy is gained by the system in some part of the upper surface while the other portion is losing heat. With an increase in S, a situation may be achieved where energy is gained by the system everywhere on the top surface. Another interesting feature of these results is that a large amount of energy may be gained by the convective medium at higher Rayleigh numbers, for a fixed S. For example, the system gains more energy on the top surface for Ra* = 100 compared to that when Ra* = 20 if $S > 2$ (Fig. 4*b*). This is primarily because of the large velocities at high Ra*, and the larger angle that the axis of the convective cell makes with the y axis.

[1]This Nusselt number may have a positive or negative value depending on whether the system gains energy or loses it.

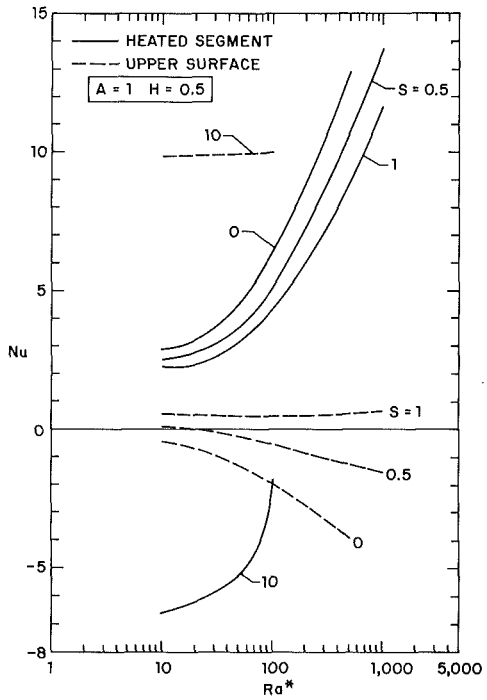

Fig. 5 Overall heat transfer on the heated section of the bottom surface and the top surface

Vertical Wall. Energy is always lost on this surface irrespective of the higher or lower values of Ra* and S. However, the local Nusselt number Nu_y varies significantly with height y and the governing parameters Ra* and S. When $S = 0$ and the Rayleigh number is small (Ra* $\leq$ 20), Nu_y is symmetrically distributed on the vertical wall with its peak at $y \simeq 0.5L$ (Fig. 4*c*). This symmetry is completely destroyed and the peak is moved toward the top edge when Ra* is increased. However, the peak moves downward if S is increased. Aided by conduction from the top surface and natural convection from the heat source, the total heat transfer through this wall always increases with S.

Overall Heat Transfer. The overall Nusselt numbers for both the heated segment and the upper surface are presented in Fig. 5. The Nusselt number for the heat source increases with the Rayleigh number for any value of S. However, it always decreases with an increase in S, and for each Rayleigh number, there exists a critical value of S for which $\overline{\mathrm{Nu}} = 0$ (Fig. 5). Any increase in the wall stratification beyond S_{critical} results in negative heat transfer on the heated section. The heat transfer on the top surface is affected accordingly. When $S = 0$, a larger amount of heat is lost at a higher Ra* (Fig. 5). However, the Nusselt number decreases with an increase in S, and for $S \geq 1$, energy is always gained on the upper surface. In fact, for $S > 1$, the heat gained by the porous layer on the top surface is almost independent of Ra*.

Conclusion

A numerical study has been conducted to analyze the effects of linear thermal stratification on natural convection in horizontal porous layers with localized heating from below, for $A = 1$, $H = 0.5$, $0 \leq S \leq 10$, and Ra* up to 1000. When $S = 0$ (no wall stratification), the effect of an increase in Rayleigh number is to produce a plumelike flow above the heated region. The higher the Rayleigh number, the larger is the domain influenced by the buoyant flows, and the larger is the amount of energy lost by the heat source. Although flow in the half-cavity is unicellular at low Ra*, a secondary cell may

appear at higher Rayleigh numbers. An increase in the wall stratification for a fixed Ra* reduces the convective velocities, and hence, the energy lost by the heat source. Consequently, there exists a critical value of S as a function of Ra*, beyond which the heat source gains energy. Indeed, under certain circumstances, a part of the heated segment may gain energy while the other part of it is losing heat. A similar situation may be encountered on the top surface. For $S>1$, the energy gained on the upper surface is almost independent of Rayleigh number.

References

Elder, J. W., 1967a, "Steady Free Convection in a Porous Medium Heated From Below," *Journal of Fluid Mechanics*, Vol. 27, pp. 29–48.

Elder, J. W., 1967b, "Transient Convection in a Porous Medium," *Journal of Fluid Mechanics*, Vol. 27, pp. 609–623.

Fusegi, T., and Farouk, B., 1985, "Natural Convection in a Thermally Stratified Square Cavity With Localized Heating From Below," *23rd AIChE/ASME National Heat Transfer Conference*, Denver, CO.

Gosman, A. D., Pun, W. M., Runchal, A. K., Spalding, D. B., and Wolfshtein, M., 1969, *Heat and Mass Transfer in Recirculating Flows*, Academic Press, New York.

Horne, R. N., and O'Sullivan, M. J., 1974, "Oscillatory Convection in a Porous Medium Heated From Below," *Journal of Fluid Mechanics*, Vol. 66, pp. 339–352.

Horne, R. N., and O'Sullivan, M. J., 1978, "Convection in a Porous Medium Heated From Below: The Effect of Temperature Dependent Viscosity and Thermal Expansion Coefficient," ASME JOURNAL OF HEAT TRANSFER, Vol. 100, pp. 448–452.

Prasad, V., and Kulacki, F. A., 1984a, "Natural Convection in a Rectangular Porous Cavity With Constant Heat Flux on One Vertical Wall," ASME JOURNAL OF HEAT TRANSFER, Vol. 106, pp. 152–157.

Prasad, V., and Kulacki, F. A., 1984b, "Convective Heat Transfer in a Rectangular Porous Cavity – Effect of Aspect Ratio on Flow Structure and Heat Transfer," ASME JOURNAL OF HEAT TRANSFER, Vol. 106, pp. 158–165.

Prasad, V., and Kulacki, F. A., 1986, "Effects of the Size of Heat Source on Natural Convection in Horizontal Porous Layers Heated From Below," *Proceedings, 8th International Heat Transfer Conference*, San Francisco, CA, *Heat Transfer–1986*, Vol. 5, Hemisphere, New York, pp. 2677–2682.

Prasad, V., and Kulacki, F. A., 1987, "Natural Convection in Horizontal Porous Layers With Localized Heating From Below," ASME JOURNAL OF HEAT TRANSFER, this issue.

Torrance, K. E., 1979, "Natural Convection in Thermally Stratified Enclosures With Localized Heating From Below," *Journal of Fluid Mechanics*, Vol. 95, pp. 477–495.

Natural Convection in a Vertical Porous Cavity: a Numerical Study for Brinkman-Extended Darcy Formulation

G. Lauriat
ISITEM, Université de Nantes,
44092 Nantes, France

V. Prasad
Department of Mechanical Engineering,
Columbia University,
New York, NY 10027
Mem. ASME

A dimensional analysis of the Brinkman-extended Darcy formulation, which includes the transport and viscous terms, leads to four governing parameters for steady-state natural convection in a vertical porous cavity. They are: Rayleigh number, Darcy number, diffusion parameter Ω, and aspect ratio. Numerical results for $0 \le Da \le 10^{-1}$, $10 \le Ra^* \le 5 \times 10^3$, and A = 1 and 5, indicate that the temperature and velocity fields are significantly modified, the flow regimes are delayed, and the heat transfer rate is decreased when the Darcy number is increased beyond 10^{-5} for fixed Ra and A. The slope of the ln $(\overline{Nu})$ versus ln (Ra^*) curve in the boundary layer regime decreases from 0.53 at Da = 0 to 0.264 at $Da = 10^{-1}$ when A = 5. The contribution of the transport term increases with Ω, Da, and Ra*, but the effect on the overall heat transfer is insignificant. However, the problem becomes ill formulated at high values of these parameters and may require the consideration of Forchheimer modifications. A scale analysis is also presented to show that the inertia term is of a low order of magnitude in comparison with the viscous term at high Prandtl numbers.*

Introduction

Natural convection in a rectangular porous cavity, whose vertical walls are maintained at different constant temperatures and the top and bottom walls are adiabatic, is one of the classical problems of free convection in porous media which have been extensively studied. The first study of the problem, an experimental one, was reported by Schneider in 1963. Klarsfeld reported another experimental study in 1970 together with an integral solution. The first extensive theoretical work on this problem also appeared in 1970 from Chan et al. Later on, these studies were followed by a series of investigations, out of which the notable analytical solutions are by Weber (1975), Burns et al. (1977), Walker and Homsy (1978), Bejan and Tien (1978), Bejan (1979), Simpkins and Blythe (1980), Blythe et al. (1983), Tong and Subramanian (1985), and Poulikakos and Bejan (1985). Numerical studies of the problem include the work of Vlasuk (1972), Bankvall (1974), Burns et al. (1977), Hickox and Gartling (1981), Shiralkar et al. (1983), Daniels (1983), and Prasad and Kulacki (1984a, 1984b). However, experimental research on this geometry has been quite limited, and only two significant reports were published after 1970 (Bories and Combarnous, 1973; Seki et al., 1978). In recent years, attempts have also been made to examine the effects of constant flux heating, property variation, etc. However, we will limit our discussion to the isothermally heated and cooled cavity.

With the exception of Chan et al. (1970), Tong and Subramanian (1985), Poulikakos and Bejan (1985), and Prasad and Tuntomo (1987), all other theoretical studies are based on the Darcy's law. However, the experimental results using either various combinations of solids and fluids other than glass–water or high Rayleigh number conditions have never agreed with the theoretical predictions based on the Darcy model (Prasad et al., 1985). It is thus widely realized that the nonlinear boundary layer effects are significant, and must be considered to predict convective heat transfer in porous media accurately.

Contributed by the Heat Transfer Division and presented at the 4th AIAA/ASME Heat Transfer Conference, Boston, Massachusetts, June 2–4, 1986. Manuscript received by the Heat Transfer Division February 20, 1986.

Although as early as 1970, Chan et al. considered the viscous diffusion term, $\mu \nabla^2 \mathbf{V}$ (Brinkman model), in the equation of motion, this term has not been included in later studies. Very recently, Tong and Subramanian (1985) have presented a boundary layer analysis for the Brinkman model, and have reported significant contributions of the diffusion term at high Rayleigh and Darcy numbers. Furthermore, Poulikakos and Bejan (1985) and Prasad and Tuntomo (1987) have considered the Forchheimer-extended Darcy model to study the inertia effects on free convection in a vertical cavity. This clearly indicates that very limited efforts have been made to examine the effects of the diffusion and the inertia (Forchheimer) terms and no efforts have been made to study the significance of the nonlinear transport term in the equation of motion. It should be noted that attempts to consider the effects of inertia and diffusion terms for other types of configurations are also limited.

Based on the results for Ra* up to 100, Chan et al. (1970) concluded that the effect of the viscous term is negligible as long as $Da < 10^{-3}$. The boundary layer solution of Tong and Subramanian (1985) predicts about 8 percent reduction in the Nusselt number when Da is increased from 0 to 10^{-3} at Ra* = 800. The effect of Darcy number (in the range of $0\text{–}10^{-3}$) diminishes as the Rayleigh number is decreased, and the variation is almost negligible at Ra* = 100, which agrees with the observation of Chan et al. (1970). However, their boundary layer solution overpredicts the Nusselt number as is inherent in the Weber-type modified Oseen approach.

The objective of the present work is to consider the Brinkman-extended Darcy equation of motion together with the transport term and examine the significance of each term. A dimensional analysis has shown that only four dimensionless parameters, Ra*, Da, Ω, and A, need to be considered for the steady-state free convection in a rectangular cavity. The finite-difference numerical results are then obtained for Ra* up to 5000 and $0 \le Da \le 10^{-1}$ to characterize the effects of diffusion term. Although the results for very high Darcy number are always questionable from the application point of view, they cover a wide range of Da, and help us in determining the significance of the viscous term, and have lead to

several important conclusions. The importance of the transport term has also been examined.

Governing Equations and Dimensionless Parameters

Consider a two-dimensional, vertical cavity filled with an isotropic, homogeneous, fluid-saturated porous medium whose one vertical wall is isothermally heated and the other is isothermally cooled, and the horizontal walls are adiabatic. The thermophysical properties of the solid and fluid are assumed to be constant except for the density variation in the body force term. Assuming that the solid particles and the fluid are in thermal equilibrium, the governing equations may be written as

Continuity:

$$\nabla \cdot \mathbf{V} = 0, \tag{1}$$

Momentum:

$$\frac{\rho_f}{\epsilon}\frac{\partial \mathbf{V}}{\partial t} + \frac{\rho_f}{\epsilon^2}(\mathbf{V}\cdot\nabla)\mathbf{V} = -\nabla P + \rho_f \mathbf{g} - \frac{\mu_f}{K}\mathbf{V} + \mu'\nabla^2\mathbf{V} \tag{2}$$

energy:

$$(\rho c)_m \frac{\partial T}{\partial t} + (\rho c)_f \mathbf{V}\cdot\nabla T = k_m \nabla^2 T \tag{3}$$

where the Forchheimer inertia term in the momentum equation has been neglected (to be discussed later). The apparent viscosity μ' in equation (2) may have a different value than the fluid viscosity μ_f. A detailed discussion on the values of μ' has been presented by Lundgren (1973). Employing the dimensionless variables and defining the stream function ψ and the vorticity ζ in the usual way, the governing equations are transformed into

$$\nabla^2\psi = -\zeta \tag{4}$$

$$\frac{1}{\epsilon^2 \mathrm{Pr}^*}\left[\epsilon\frac{\partial \zeta}{\partial t} + u\frac{\partial \zeta}{\partial X} + v\frac{\partial \zeta}{\partial Y}\right] = \Lambda\nabla^2\zeta + \frac{1}{\mathrm{Da}}\left(\mathrm{Ra}^*\frac{\partial \theta}{\partial X} - \zeta\right) \tag{5}$$

$$S\frac{\partial \theta}{\partial t} + u\frac{\partial \theta}{\partial X} + v\frac{\partial \theta}{\partial Y} = \nabla^2\theta \tag{6}$$

The relevant thermal boundary conditions for this centrosymmetric problem (Weber, 1975) are

$$X=0,\quad \theta=0.5;\quad X=1,\quad \theta=-0.5;$$
$$\text{and } Y=0 \text{ and } A,\quad \partial\theta/\partial Y = 0 \tag{7}$$

The no-slip boundary conditions for the velocity will be considered later.

The governing parameters for the present problem are, thus,

$$\text{Rayleigh number, } \mathrm{Ra}^* = g\beta KD\nabla T/\nu\alpha \tag{8}$$

$$\text{Prandtl number, } \mathrm{Pr}^* = \nu/\alpha \tag{9}$$

$$\text{Darcy number, } \mathrm{Da}^* = K/D^2 \tag{10}$$

$$\text{viscosity ratio, } \Lambda = \mu'/\mu_f \tag{11}$$

$$\text{specific heat ratio, } S = (\rho c)_m/(\rho c)_f \tag{12}$$

$$\text{aspect ratio, } A = H/D \tag{13}$$

and the porosity ϵ.

Nomenclature

A = aspect ratio = H/D
$\bar{A}$ = coefficient in equation (20)
b = constant in equations (18) and (19)
$\bar{B}$ = coefficient in equation (20)
c = specific heat at constant pressure, J/kg-K
C = constant in equation (28)
D = width of the cavity, m
Da^* = Darcy number = K/D^2
Da = modified Darcy number = $\Lambda\mathrm{Da}^*$
E = dimensionless parameter = $\mathrm{Ra}^*\mathrm{Da}/A$
f = ψ, ζ, or θ, equation (22)
$\mathbf{g}$ = body force vector, m/s^2
g = acceleration due to gravity, m/s^2
$\bar{h}$ = average heat transfer coefficient, W/m^2-K
H = height of cavity, m
k = thermal conductivity, W/m-K
K = permeability of porous medium, m^2
l = length scale = $(A/\mathrm{Ra}^*)^{0.5}D$, m
m = exponent in equation (28)
n = direction normal to wall
Nu = local Nusselt number (equation (24))
$\overline{\mathrm{Nu}}$ = average Nusselt number = hD/k_m
p = stretching parameter in x direction, equations (18) and (19)
P = pressure, Pa
Pr^* = Prandtl number = ν/α
Pr_e^* = modified Prandtl number = $\epsilon^2\mathrm{Pr}^*$
q = stretching parameter in y direction
r = convergence criterion (equation (22))
Ra^* = Rayleigh number for the porous medium = $g\beta KD\Delta T/\nu\alpha$
Re = Reynolds number (equation (25))
S = specific heat ratio = $(\rho c)_m/(\rho c)_f$
$\bar{t}$ = time, s
t = dimensionless time = $\bar{t}/(D^2/\alpha)$
T = temperature, K
T_0 = average temperature = $(T_h+T_c)/2$, K
ΔT = temperature difference = $(T_h - T_c)$, K
$\bar{u}$ = velocity in x direction, m/s
u = dimensionless velocity in x direction = $\bar{u}/(\alpha/D) = \partial\psi/\partial Y$
$\bar{v}$ = velocity in y direction, m/s
v = dimensionless velocity in y direction = $\bar{v}/(\alpha/D) = -\partial\psi/\partial X$
$\mathbf{V}$ = velocity vector, m/s
x, y = Cartesian coordinates, m
X = dimensionless distance in x direction = x/D
Y = dimensionless distance in y direction = y/D
α = thermal diffusivity of porous medium, $k_m/(\rho c)_f$, m^2/s
β = isobaric coefficient of thermal expansion of fluid, K^{-1}
γ = constant in equation (20)
Γ = transport term/(buoyancy + diffusion) terms, equation (29)
ϵ = porosity
ζ = vorticity, $(\partial v/\partial X - \partial u/\partial Y)$
η = constant in equation (20)
θ = dimensionless temperature, $(T-T_o)/(T_h-T_c)$
Λ = viscosity ratio, μ'/μ_f
μ = dynamic viscosity, kg/m − s
μ' = viscosity for Brinkman model (equation 2)
ν = kinematic viscosity, m^2/s
ρ = density, kg/m^2
ψ = stream function
Ω = diffusion parameter, $1/\Lambda\epsilon^2\mathrm{Pr}^*$, equation (17)

Subscripts

c = cold wall
f = fluid; also for ψ, ζ, or θ in equation (22)
h = hot wall
H = based on the cavity height, H
i = number of node in x direction
j = number of node in y direction
m = for fluid-saturated porous medium
w = wall

Table 1 Overall Nusselt numbers for $A = 5$ and Da = 0 (Darcy flow) compared with the published results

Ra*	10	20	30	50	100	200	350	500	750	1000
Present	1.04	1.12	1.24	1.48	2.08	3.03	4.08	4.92	6.07	7.02
Walker and Homsy (1978) and Daniels (1983)							4.18	5.00	6.12	7.07
Shiralkar et al. (1983)		1.13			2.09	3.04		4.91		
Prasad and Kulacki (1984b)	1.04	1.13			2.06	3.01	4.09	4.96		7.25

It is thus apparent that the present formulation leads to six dimensionless parameters, Ra*, Pr*, Da*, Λ, ϵ, and A, which govern the steady-state, buoyancy-driven flow in a cavity. However, the effect of Λ can be included in a modified Darcy number by defining it as

$$\mathrm{Da} = \Lambda \mathrm{Da}^* \tag{14}$$

It should be noted that Chan et al. (1970) and Tong and Subramanian (1985) have considered $\mu' = \mu_f$. However, their results can be conveniently used for $\mu' \neq \mu_f$ by replacing the Darcy number in their formulation by Da.

It is possible to further reduce the number of dimensionless parameters by defining a modified Prandtl number

$$\mathrm{Pr}_e^* = \epsilon^2 \mathrm{Pr}^* \tag{15}$$

Although both ϵ and Pr* have physical importance, their combination provides mathematical convenience. A diffusion parameter may then be obtained as

$$\Omega = 1/\Lambda \epsilon^2 \mathrm{Pr}^* \tag{16}$$

Equation (5) then reduces to

$$\Omega\left[\epsilon\frac{\partial \zeta}{\partial t} + u\frac{\partial \zeta}{\partial X} + v\frac{\partial \zeta}{\partial Y}\right] = \nabla^2 \zeta + \frac{1}{\mathrm{Da}}\left[\mathrm{Ra}^*\frac{\partial \theta}{\partial X} - \zeta\right] \tag{17}$$

The advantage of the above exercise is that now we need to consider only four dimensionless numbers, Ra*, Da, Ω, and A for steady-state problems.

Numerical Solution

As is typical of the present type of problem, a large number of nodes are required near the walls to predict the flow and temperature fields accurately, particularly at high Rayleigh numbers and low Darcy numbers. Hence, the coordinate stretching transformations have been introduced to distribute reasonably large number of grids near the walls. Accordingly, the x and y coordinates are transformed using one-dimensional exponential stretch $x = x(p)$ and $y = y(q)$. For example, the x-grid points are determined as a function of the equally divided coordinate p as follows:

$$X = 0.5(e^{bp} - 1)/(e^{0.5b} - 1), \qquad 0 \le p \le 0.5 \tag{18}$$

$$X = 1 - [0.5(e^{b(1-p)} - 1)/(e^{0.5b} - 1)], \qquad 0.5 \le p \le 1 \tag{19}$$

If the stream-function equation (4) is cast in a parabolic form by inserting a false transient term, the general form of the governing equations may be written in the computational plane as

$$\frac{\partial f}{\partial t} + \gamma\left[\bar{A}_p\frac{\partial (uf)}{\partial p} + \bar{A}_q\frac{\partial (vf)}{\partial q}\right] = \eta\left[\bar{B}_p\frac{\partial f}{\partial p} + \bar{A}_p^2\frac{\partial^2 f}{\partial p^2} + \bar{B}_q\frac{\partial f}{\partial q} + \bar{A}_q^2\frac{\partial^2 f}{\partial q^2}\right] + \bar{\omega} \tag{20}$$

where γ and η are constants, $\bar{A}_p$ and $\bar{B}_p$ are functions of p, and $\bar{A}_q$ and $\bar{B}_q$ are functions of q. The variable f represents ψ, ζ, and θ for equations (4), (17), and (6), respectively, and $\bar{\omega}$ is the source term.

In the present numerical scheme, all spatial derivatives in equation (20) are approximated by the central differences, and an ADI procedure is used to perform the time integration. It is well established that the convective terms cause the main numerical difficulties to achieve a stable solution. In order to achieve both the desirable accuracy and the dominance of the principal diagonal of the tridiagonal systems of the finite difference equations, it is necessary to use very small time steps, especially for the energy equation. Indeed, as will be discussed later, the convective terms in the vorticity equation have a weak contribution of the solution unless Ω is large.

When solving the vorticity equation, an additional difficulty is observed in implementing the boundary conditions. The second-order formulations, Jensen's as well as Wood's forms (Roache, 1982), are found to generate unstable solutions at low Darcy numbers, and hence, the Thom first-order form has to be used. It is believed that this is due to the velocity profiles associated with the Brinkman-extended Darcy model, which displays a peak very close to the wall. Therefore, it is inconsistent to employ a cubic relation for the evaluation of the velocity near the wall as required in order to stabilize the scheme when using the Jensen's form. The hydrodynamic boundary conditions are thus given by

$$\psi = 0, \quad \zeta_w = 2\psi_{w+1}/(\Delta n)^2 \tag{21}$$

where Δn is the grid size normal to the wall.

The computations reported in this paper have been performed on a 41×81 grid for $A = 5$ and 41×41 grid for $A = 1$. The criterion used for the iterative convergence is

$$\left[\sum_{i,j} |f_{i,j\mathrm{new}} - f_{i,j\mathrm{old}}| \Big/ \sum_{i,j} |f_{i,j}|\right] < r_f \tag{22}$$

where r_f has been taken as 10^{-4} for ψ and 5×10^{-6} for both ζ and θ. The solutions are obtained at a sequence of Rayleigh numbers for a given Da.

The stretching parameter b is increased up to 5 for $\mathrm{Da} = 10^{-5}$ so that at least three points along the grid normal to a wall are located between the boundary and the velocity peak. However, the accuracy of the solution deteriorates rapidly by increasing b due to the high values of the derivatives in the transformed equation (20). Moreover, the cell Reynolds numbers increase drastically with b and the method tends to become unstable for $b > 5$. Also, the present scheme fails to converge at high values of Ra*, Da, and Ω.

The average Nusselt number at any location X is obtained as

$$\overline{\mathrm{Nu}}(X) = 1/A\int_0^A \mathrm{Nu}(X, Y)dY \tag{23}$$

where the local Nusselt number

$$\mathrm{Nu}(X, Y) = -\partial\theta/\partial X + u\theta \tag{24}$$

It may be noted that $\overline{\mathrm{Nu}}(X)$ should theoretically be independent of X. For most of the computations reported here, the maximum change in the Nusselt number $\overline{\mathrm{Nu}}(X)$ at various X locations is within 1 percent. Also, an excellent agreement is achieved with the reported values of Nu for the Darcy flow (Table 1).

Results and Discussions

The computations have been, first, carried out for the Brinkman-extended Darcy model, in which the transport term in the momentum equation is neglected. Therefore, the only

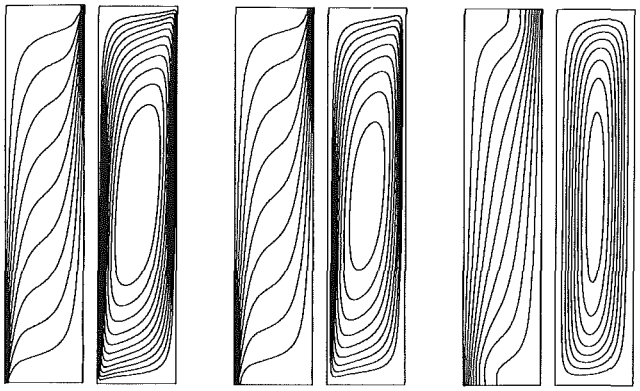

Fig. 1 Isotherms and streamlines for $A = 5$ and $Ra^* = 500$ ($\Delta\theta = 0.1$): (*a*) $Da = 0 - 10^{-5}$ ($\psi_1 = 5$, $\Delta\psi = 2.5$); (*b*) $Da = 10^{-3}$ ($\psi_1 = 5$, $\Delta\psi = 2.5$); (*c*) $Da = 10^{-1}$ ($\Delta\psi = 1$)

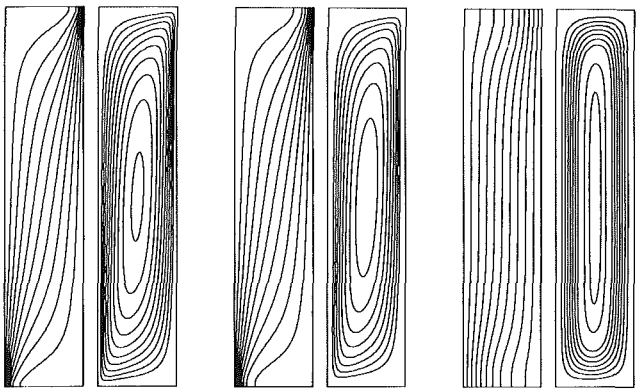

Fig. 2 Isotherms and streamlines for $A = 5$ and $Ra^* = 100$ ($\theta = 0.1$): (*a*) $Da = 0 - 10^{-5}$ ($\psi_1 = 2$, $\Delta\psi = 1$); (*b*) $Da = 10^{-3}$; (*c*) $Da = 10^{-1}$ ($\Delta\psi = 0.2$)

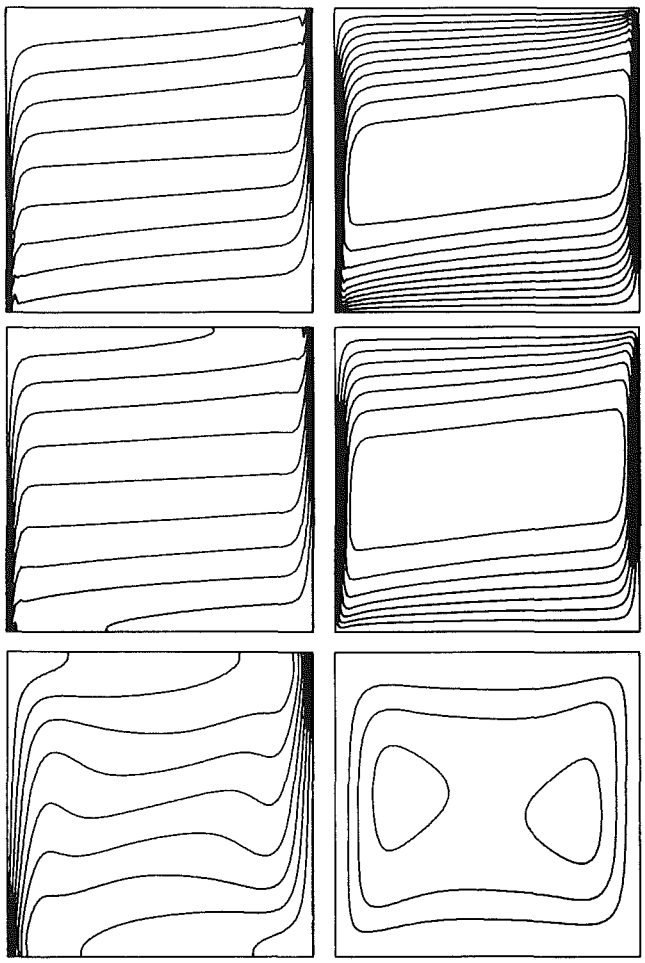

Fig. 3 Isotherms and streamlines for $A = 1$ and $Ra^* = 5000$ ($\Delta\theta = 0.1$, $\Delta\psi = 4.5$): (*a*) $Da = 0 - 0^{-6}$; (*b*) $Da = 10^{-4}$; (*c*) $Da = 10^{-2}$

parameters to consider are the Rayleigh number Ra^*, the modified Darcy number Da, and the aspect ratio A.

Temperature and Velocity Fields. The isotherms and streamlines for $Da = 0 - 10^{-5}$, 10^{-3}, and 10^{-1} are presented in Figs. 1 and 2 for $Ra^* = 500$ and 100, respectively. These values of the Rayleigh number have been selected to represent the boundary layer and asymptotic flow regimes, for the limiting case of a Darcy flow, $Da = 0$ (Prasad and Kulacki, 1984a).

The effect of an increase in Darcy number appears to be very similar at all Ra^*. The flow rate reduces with an increase in Da, and the slope of the axis of the cells changes significantly. For example, at $Ra^* = 500$, and a Darcy flow, the axis is close to the diagonal of the cavity, but with an increase in Da, the axis moves towards the vertical middle plane. This indicates that the viscous forces act in the whole cavity. Therefore, the maximum velocities (horizontal and vertical components) drift from the corners (left bottom and right top corners) to the vertical and horizontal middle planes. Similar effects of Darcy number are also exhibited by the streamlines for $A = 1$ (Fig. 3). It is observed that the flow in a square cavity becomes bicellular when Da is increased beyond 10^{-3} for $Ra^* = 5000$. The flow, however, is unicellular at all Darcy numbers when $Ra^* \leq 2000$. It should be noted that the Darcy flow is always unicellular if $A \geq 1$ (Prasad and Kulacki, 1984a).

A significant change in the velocity field with an increase in Da is demonstrated in Figs. 4(*a–c*) where the vertical velocity is presented for various values of Ra^* and Da together with the Darcy profiles ($Da = 0$). For $Da = 10^{-5}$, the velocity v/Ra^* increases sharply to a maximum and then follows the Darcy profile. The smaller the Rayleigh number, the more closely it follows the Darcy profile. This confirms that the effect of viscous term is more important at high Rayleigh numbers. The peak velocity v_{max} decreases and the peak shifts towards the core when Da increases. Furthermore, the reduction in v/Ra^* with an increase in Da is larger at high Rayleigh numbers except for a region close to $(0.5, 0.5A)$. In fact, the velocities in the core can be greater than the Darcy velocities at high Rayleigh numbers when $Da > 10^{-2}$. A comparison between the magnitudes of the diffusion term ($\nabla^2\zeta$) and the buoyancy term ($Ra\ Da^{-1}\ \partial\theta/\partial X$) clearly shows that the viscous forces have no effects in the core if $Da < 10^{-3}$. Hence, the influence of the diffusion term is largely confined between the walls and the velocity peaks. The highest values of $\nabla^2\zeta$ occur near the top edge of the hot wall and the bottom edge of the cold wall. However, at higher Darcy numbers, the vorticity diffuses in the whole cavity and the viscous and buoyancy terms are of the same order of magnitude.

Figures 5(*a–c*) show similar horizontal viscous layers at the end walls, but the maximum velocities u_{max} are closer to the wall for low Rayleigh numbers. This is contrary to what has been observed on the vertical walls. Also, the reduction in u produced by an increase in Da is relatively smaller at high Ra^*. This behavior is specific of the adiabatic boundary conditions. In fact, the isotherms presented in Figs. 1-3 exhibit quasi-isothermal end regions in the boundary layer regime, the buoyancy term being much lower in relative value than in the conduction regime. The viscous forces, thus, act over a larger region, except near the departure corners.

The above modifications in the velocity field with the Darcy number change the isotherm patterns accordingly. The sharp

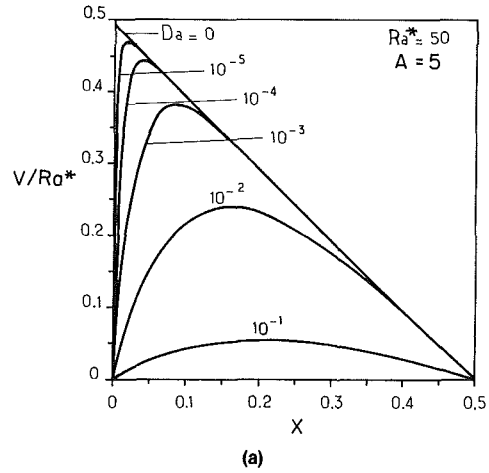

(a)

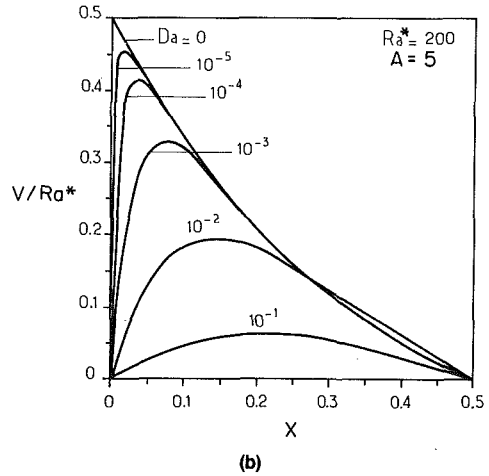

(b)

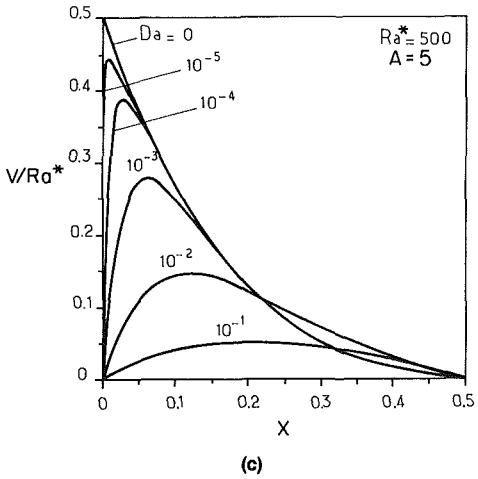

(c)

Fig. 4 Vertical velocity at midheight at Y = 2.5A: (a) Ra* = 50; (b) = Ra* = 200; (c) Ra* = 500, for A = 5

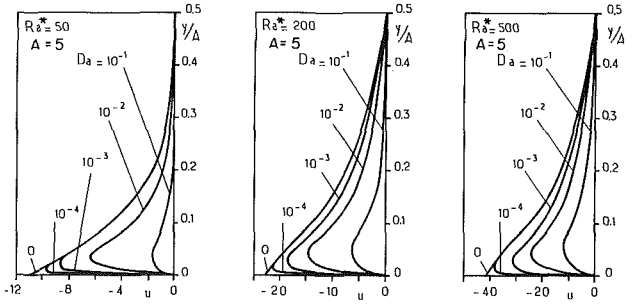

Fig. 5 Horizontal velocity at X = 0.5; (a) Ra* = 50; (b) Ra* = 200; (c) Ra* = 500, for A = 5

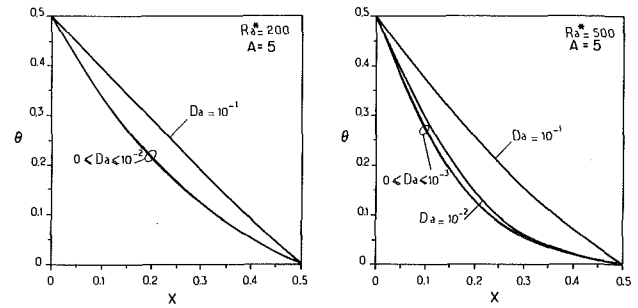

Fig. 6 Dimensionless temperature at midheight at Y = 2.5A: (a) Ra* = 200; (b) Ra* = 200; (b) Ra* = 500, for A = 5

temperature gradients near the bottom left and right top corners are greatly modified by an increase in Da (Figs. 1–3). The transport of energy by convection due to cross flow near the horizontal walls has, thus, decreased and the heat transfer through the core has increased. Although the temperature field has been significantly modified near the horizontal walls, the effect on the temperature distributions in the core is minimal. Hence, the temperature profile at midheight is almost independent of Da for Ra* up to 50. However, the temperature distributions for Ra* = 200 and 500 (Fig. 6) indicate that the higher the Rayleigh number, the larger the effects of increase in Da. In tall cavities, the temperature profiles and the reduced velocity distributions v/Ra* are very close to each other in the horizontal middle plane for a Darcy flow if the vertical temperature stratification is uniform over a large part of the core. When the viscous forces are taken into account, this characteristics of a Darcy flow is still valid in the core region as long as the vorticity does not diffuse far from the walls ($Da < 10^{-3}$ for $Ra^* < 500$). Should it be otherwise, the temperature distributions tend toward a linear profile while the asymptotic velocity profiles are cubic.

From the above discussion, it is clear that the effect of increasing Da is greater at high Rayleigh numbers. However, it should be noted that the Brinkman–Darcy model is valid only at low velocity if the inertial effects are neglected. An inertial resistance term such as Forchheimer's modification must be included in the momentum equation when the pore Reynolds number, based on the square root of permeability as characteristic length, is greater than one. Using the present dimensionless variables, the Reynolds number can be written as

$$\mathrm{Re} = v\mathrm{Da}^{0.5}/\mathrm{Pr}^* \tag{25}$$

For low Darcy numbers, it can be shown that the scale of the Darcy flow still applies. Therefore

$$v_{\max} \sim \mathrm{Ra}^* \tag{26}$$

and the Brinkman–Darcy model is valid if

$$\mathrm{Da} < (\mathrm{Pr}^*/\mathrm{Ra}^*)^2 \qquad \text{for } \mathrm{Da} << 1. \tag{27}$$

However, the reduction in maximum velocity, which occurs when Da is increased, allows the extension of the range of validity of the model far beyond the one prescribed by equation (27), as can be seen in Table 2, where the product RePr* is reported for various Ra*. However, the present calculations appear to be more relevant for porous media having large Prandtl numbers.

Another interesting aspect of these results is that for a fixed

Table 2 Values of RePr* for selected values of Ra* and Da

Ra*/Da	10^{-5}	10^{-4}	10^{-3}	10^{-2}	10^{-1}
50	0.09	0.26	0.64	1.10	0.85
100	0.20	0.55	1.27	2.26	2.02
200	0.42	1.11	2.40	4.05	3.94
500	1.02	2.52	5.01	7.81	8.65
1000	1.92	4.48	8.34	12.13	14.04

Ra*, the flow regime changes with an increase in the Darcy number. For example, the boundary layer regime at Ra* = 500 and Da = 0 changes to an asymptotic regime, and the asymptotic regime at Ra* = 100 and Da = 0 reverts to the conduction flow regime when the Darcy number is increased to 10^{-1}. Hence, the flow regime criteria (Prasad and Kulacki, 1984a) need to be modified to include the effect of Darcy number.

Boundary Layer Flows. For high Rayleigh numbers, the governing equations can be simplified by using the boundary layer approximations. Analytical studies for the boundary layer regime in porous cavities have been presented by many investigators for Darcy flow (see Introduction). More recently, Tong and Subramanian (1985) have solved the boundary layer equations derived from the Brinkman's extended model using the Weber's approach. Introducing the same horizontal length scale as for the Darcy flow (Weber, 1975), they have shown that the field is governed by one parameter only, defined as $E = \text{Ra}^* \text{ Da}/A$. Velocity profiles satisfying the no-slip boundary condition have been presented as a function of E and the heat transfer results given by Weber (1975) are modified in order to include the effect of E. Indeed, Tong and Subramanian have obtained the length scale for boundary layer thickness through a balance between the pressure and buoyancy terms (neglecting the viscous term). From the present numerical results, it can be concluded that this assumption is never satisfied in the vicinity of the walls where the viscous terms always dominate. However, Fig. 4 shows that the length scales corresponding to a Darcy flow are meaningful as long as the vorticity does not diffuse in the core. It is still the case for $\text{Da} = 10^{-3}$ at Ra* = 500 ($E = 0.1$). Therefore, the numerical results lead to a less restrictive criterion for such a boundary layer analysis. It may, thus, be relevant to plot the numerical solutions using the same length scale, namely $l = (A/\text{Ra}^*)^{0.5} D$.

In Fig. 7, the vertical velocity v, presented for $E = 2 \times 10^{-3}$ and $10^2 \le \text{Ra}^* \le 10^3$, shows that the data for Ra* = 500 and 1000 are well correlated while large discrepancies occur both in the locations of the velocity peak and in the velocity profiles in the core if Ra* ≤ 200. Since these data correspond to the low Darcy numbers ($10^{-5} < \text{Da} < 10^{-4}$) for which the Darcy velocity profiles are not modified in the core, it can be concluded that the boundary layer analysis does not accurately predict the Darcy velocities in the core region for Ra* < 200. Similar plots obtained for higher Da indicate that the previous length scale l is relevant only when Ra* ≳ 350 for $A = 5$. When this condition is satisfied, it is possible to correlate the numerical solutions for E as high as 0.2. The locations of velocity peaks at the midheight of the cavity are then in good agreement with the predictions of Tong and Subramanian. Recalling our discussion on the flow regimes, it can now be observed that much larger Rayleigh numbers (relative to Darcy flow) are required at high Darcy numbers for the boundary layer regime to exist.

Heat Transfer Results. The local Nusselt number (equation (24)) on the hot wall $\text{Nu}_w(Y)$ is presented in Fig. 8 for various Darcy numbers when Ra* = 500 and $A = 5$. It is observed that the heat transfer rate is very high at $Y = 0$. However, $\text{Nu}_w(Y)$ decreases at all locations when the Darcy number is increased, with the largest reduction at $Y = 0$. This is consistent with the modifications in the temperature and flow fields with an increase in Da.

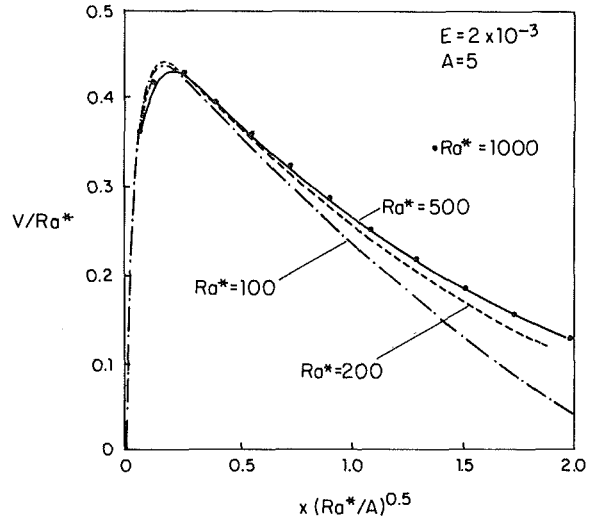

Fig. 7 Variation in vertical velocity with the Rayleigh number for $E = 2 \times 10^{-3}$ and $A = 5$

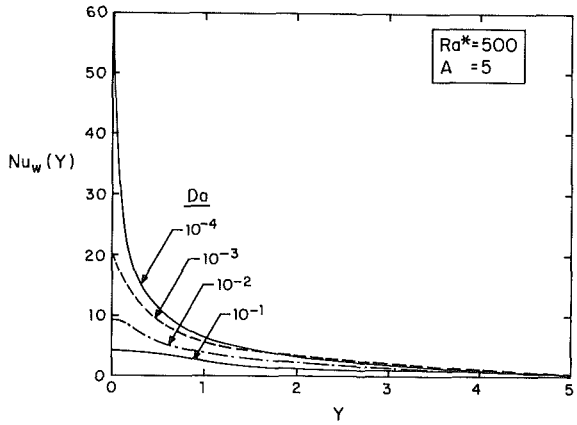

Fig. 8 Effect of Darcy number on the local Nusselt number (heated wall) for $A = 5$

The overall Nusselt number (equation (23)) is presented in Figs. 9 and 10 for $A = 5$ and 1, Rayleigh number up to 10^3, and Darcy number up to 10^{-1}. As expected, the Nusselt number approaches the conduction value, Nu = 1, when Ra* → 0. However, the higher the Darcy number, the larger is the Rayleigh number required for Nu to exceed unity. For example, the heat transfer is by pure conduction even up to Ra* ≃ 70 when Da ≃ 0.1 and $A = 5$. As usual, the Nusselt number always increases with Ra*, but the effect of the Darcy number is just the reverse. From Fig. 9, it is further evident that the Nusselt number decreases at a faster rate with an increase in Da when Ra* is high. Hence, the curves for various values of Da diverge.

In the boundary layer regime, the ln (Nu) versus ln (Ra*) curve, for a fixed Da, is a straight line (Fig. 9). However, the slope of this curve decreases with an increase in Da. For example, the slope decreases from 0.529 at Da = 0 to 0.264 at Da = 0.1 when $A = 5$. This last value of the slope is very close to that reported for the Newtonian fluids, and agrees with the experimental data (Prasad et al., 1985).

Furthermore, in the boundary layer regime, the present values of Nusselt number may be correlated as

$$\overline{\text{Nu}}_H = C\text{Ra}_H^m \qquad \text{for fixed Da and } A \tag{28}$$

where the Nusselt and Rayleigh numbers are based on the height of the cavity. The values of C and m are presented in

Table 3. As noted earlier, the slope m decreases with an increase in Da. However, the constant C increases with Da. Since the ln (Nu) versus ln (Da) curve for a fixed Ra* (Fig. 10) does not show a straight line behavior for a significant range of Darcy number, it is not possible to obtain a simple exponent for Da in equation (28).

A comparison between the present results and those predicted by the boundary layer solutions (Tong and Subramanian, 1985) indicates that the boundary layer analysis overpredicts the Nusselt number by about 20 percent. This difference is of the order of the overprediction by the Weber approach for the Darcy flow. It should be noted that the present disagreement supports the observation of Walker and Homsy (1978), Bejan (1979), and Simpkins and Blythe (1980) that a Weber-type modified Oseen approach overpredicts the heat transfer rates because of the significant errors in the predictions of the core mass flux and the core temperature gradient. It is very likely that this discrepancy in the boundary layer solution may be eliminated if Tong and Subramanian's theory is modified in the sense of Bejan (1979).

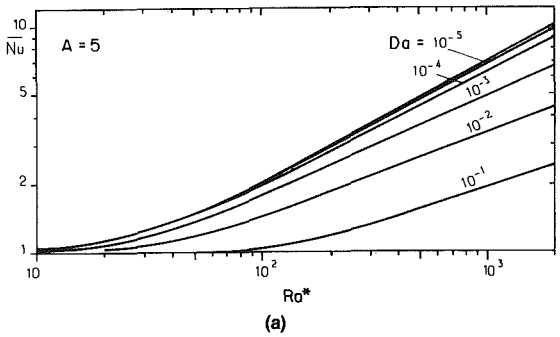

Fig. 9 Overall Nusselt number for $0 \le Da \le 0.1$: (a) $A = 1$; plotted lines are for constant Darcy number

Influence of Transport Term. To investigate the effect of the convective term in vorticity equation (17), computations have been carried out for $A = 5$ and $Ra^* = 100$ and 500 with $Da = 10^{-4}$ and 10^{-2}. A reasonable range of the parameter Ω which governs the relative strength of the transport and diffusion terms, $0.01 \le \Omega \le 10$, has been considered for these calculations. This covers a wide range of porosity ϵ, and Prandtl number Pr*, e.g., $0.04 < Pr^* < 40$ when $\epsilon = 0.5$ and $\Lambda = 1$. To identify importance of the transport term properly, a quantity

$$\Gamma = (\text{transport})/(\text{diffusion} + \text{buoyancy})$$

$$= \Omega\left(u\frac{\partial\zeta}{\partial X} + v\frac{\partial\zeta}{\partial Y}\right)\Big/(\nabla^2\zeta + Ra^*Da^{-1}\partial\theta/\partial X) \qquad (29)$$

has been calculated at each nodal point in the domain. Γ for $Ra^* = 500$, $Da = 10^{-2}$, and $\Omega = 0.1$ is presented in Table 4.

When $\Omega = 0.01$, the ratio of the transport to buoyancy plus diffusion terms, Γ, is almost negligible ($\Gamma < 0.01$) in the entire domain regardless of the values of Ra* and Da. No significant change is observed in the Γ field for an increase in Ω to 0.1 for $Ra^* = 100$ and $Da = 10^{-4}$. However, the value of Γ increases with an increase in Rayleigh number and/or Darcy number. Also, a much larger portion of the cavity, particularly, near the horizontal walls is now being influenced by the convective transport of vorticity. This is clearly exhibited in Table 4. This table further demonstrates that close to the vertical walls, the values of Γ are small. However, the peaks always lie a little away from the side walls.

From the above discussion, it is clear that the contribution of the transport term is, generally, small, but increases with the Darcy number, which is also indicated by equation (29). An increase in Rayleigh number further strengthens the Γ field because the $(\mathbf{V}\cdot\nabla)\zeta$ term becomes more significant at high velocities. It should be noted that the stronger Γ fields near the

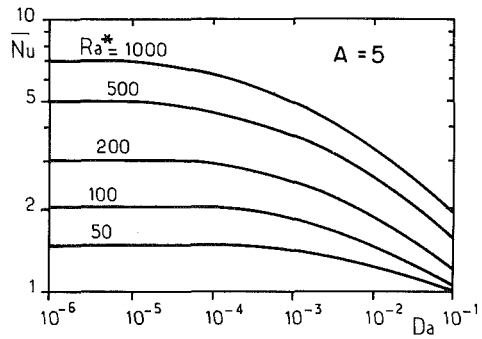

Fig. 10 Effect of Darcy number on the overall Nusselt number for $A = 5$

Table 3 Overall Nusselt number based on the height of the cavity, the leading constant C, and the exponent m, for equation (28)

A	Da/Ra^*_H	500	1000	1750	2500	5000	C	m
	0	10.40	15.15	20.40	24.60	35.10	0.392	0.529
	10^{-5}	10.25	14.90	19.75	23.70	34.00	0.410	0.519
5	20^{-4}	9.95	14.30	18.85	22.35	30.80	0.478	0.491
	10^{-3}	9.15	12.60	16.10	18.50	24.70	0.640	0.430
	10^{-2}	7.25	9.45	11.55	13.20	16.55	0.784	0.360
	10^{-1}		5.95	6.90	7.80	9.85	0.991	0.264

A	Da/Ra*	100	200	500	1000	2000	5000	C	m
	0	3.09	4.92	8.84	13.41	19.60	32.13	0.205	0.599
	10^{-6}	3.06	4.86	8.72	13.22	19.40	31.50	0.205	0.597
1	10^{-5}	3.02	4.76	8.41	12.42	17.90	27.98	0.231	0.570
	10^{-4}	2.84	4.40	7.35	10.34	14.20	20.85	0.293	0.509
	10^{-3}	2.41	3.48	5.42	7.29	9.60	13.10	0.346	0.434
	10^{-2}	1.70	2.28	3.30	4.26	5.37	7.10	0.372	0.351

Table 4 The ratio of transport to buoyancy plus diffusion terms, Γ, in the left half of the cavity; $Ra^* = 500$, $Da = 10^{-2}$, and $\Omega = 0.1$

4.96	-0.02	-0.01	0.01	0.02	0.04	0.04	0.05	0.05	0.05	0.05	0.04	0.04	0.04	0.03	0.03	0.03	0.03	0.02	0.02
4.83	-0.03	-0.06	-0.09	-0.13	-0.18	-0.28	-0.19	-0.09	-0.23	-0.36	-0.53	-0.87	-0.05	0.70	0.77	0.70	0.47	0.35	0.27
4.69	-0.03	-0.06	-0.09	-0.15	-0.27	-1.42	0.33	0.11	0.04	-0.00	-0.03	-0.05	-0.06	-0.07	-0.08	-0.08	-0.08	-0.08	-0.06
4.54	-0.02	-0.05	-0.08	-0.12	-0.22	-0.98	0.31	0.10	0.04	0.01	-0.01	-0.03	-0.04	-0.05	-0.05	-0.06	-0.05	-0.05	-0.04
4.38	-0.02	-0.04	-0.06	-0.10	-0.17	-0.65	0.27	0.08	0.03	0.00	-0.01	-0.02	-0.03	-0.04	-0.04	-0.05	-0.05	-0.04	-0.03
4.22	-0.02	-0.03	-0.05	-0.08	-0.14	-0.48	0.21	0.06	0.02	-0.00	-0.01	-0.02	-0.03	-0.03	-0.04	-0.04	-0.04	-0.03	-0.03
4.04	-0.01	-0.03	-0.04	-0.06	-0.11	-0.39	0.15	0.04	0.01	-0.01	-0.01	-0.02	-0.03	-0.03	-0.03	-0.03	-0.03	-0.03	-0.02
3.86	-0.01	-0.02	-0.04	-0.05	-0.09	-0.35	0.11	0.03	0.00	-0.01	-0.02	-0.02	-0.02	-0.03	-0.03	-0.03	-0.03	-0.02	-0.02
3.66	-0.01	-0.02	-0.03	-0.05	-0.08	-0.35	0.07	0.02	-0.00	-0.01	-0.02	-0.02	-0.02	-0.02	-0.02	-0.02	-0.02	-0.02	-0.01
3.45	-0.01	-0.02	-0.03	-0.04	-0.07	-0.40	0.05	0.01	-0.01	-0.01	-0.02	-0.02	-0.02	-0.02	-0.02	-0.02	-0.02	-0.01	-0.01
3.24	-0.01	-0.02	-0.02	-0.04	-0.06	-0.66	0.03	-0.00	-0.01	-0.01	-0.02	-0.02	-0.02	-0.02	-0.02	-0.02	-0.01	-0.01	-0.01
3.00	-0.01	-0.01	-0.02	-0.03	-0.05	0.98	0.01	-0.01	-0.01	-0.01	-0.02	-0.02	-0.02	-0.02	-0.01	-0.01	-0.01	-0.01	-0.00
2.76	-0.01	-0.01	-0.02	-0.02	-0.04	0.10	-0.01	-0.01	-0.01	-0.01	-0.01	-0.01	-0.01	-0.01	-0.01	-0.01	-0.01	-0.00	-0.00
2.50	-0.01	-0.01	-0.02	-0.02	-0.02	-0.01	-0.02	-0.02	-0.02	-0.01	-0.01	-0.01	-0.01	-0.01	-0.01	-0.00	-0.00	-0.00	-0.00
2.24	-0.01	-0.01	-0.01	-0.01	-0.00	-0.04	-0.02	-0.02	-0.02	-0.01	-0.01	-0.01	-0.01	-0.00	-0.00	0.00	0.00	0.00	0.00
2.00	-0.01	-0.01	-0.01	-0.00	0.04	-0.06	-0.03	-0.02	-0.02	-0.01	-0.01	-0.00	-0.00	0.00	0.00	0.01	0.01	0.00	0.00
1.76	-0.00	-0.01	-0.00	0.01	0.11	-0.07	-0.04	-0.02	-0.02	-0.01	-0.00	0.00	0.00	0.01	0.01	0.01	0.01	0.01	0.00
1.55	-0.00	-0.00	0.00	0.03	0.31	-0.06	-0.04	-0.02	-0.01	-0.01	0.00	0.01	0.01	0.01	0.02	0.02	0.02	0.01	0.01
1.34	-0.00	0.00	0.01	0.05	0.26	-0.08	-0.04	-0.02	-0.01	-0.00	0.01	0.01	0.02	0.02	0.02	0.02	0.02	0.01	0.01
1.14	-0.00	0.01	0.02	0.08	-0.58	-0.09	-0.04	-0.02	-0.01	0.01	0.01	0.02	0.03	0.03	0.03	0.03	0.03	0.02	0.01
0.96	0.00	0.01	0.04	0.15	-0.35	-0.09	-0.04	-0.02	0.00	0.01	0.03	0.03	0.04	0.05	0.05	0.04	0.03	0.02	0.01
0.78	0.01	0.02	0.07	0.28	-0.28	-0.09	-0.04	-0.01	0.01	0.03	0.04	0.05	0.06	0.06	0.06	0.05	0.04	0.03	0.01
0.62	0.01	0.04	0.11	0.69	-0.24	-0.09	-0.03	0.00	0.03	0.05	0.06	0.07	0.08	0.08	0.08	0.07	0.05	0.03	0.01
0.46	0.02	0.07	0.21	-0.42	-0.23	-0.08	-0.02	0.02	0.05	0.08	0.09	0.11	0.11	0.11	0.10	0.09	0.06	0.04	0.01
0.31	0.05	0.14	0.47	-0.91	-0.19	-0.05	0.02	0.07	0.11	0.13	0.15	0.16	0.16	0.16	0.14	0.12	0.08	0.04	0.00
0.17	0.12	0.34	0.73	-0.33	-0.05	0.07	0.14	0.19	0.23	0.26	0.29	0.32	0.36	0.44	0.72	-0.02	-0.03	0.10	0.16
0.04	0.25	0.65	0.44	0.70	0.21	-0.37	-0.40	-0.16	-0.06	-0.01	0.01	0.02	0.03	0.03	0.03	0.03	0.03	0.02	0.02
Y/X	.020	.040	.060	.081	.103	.125	.147	.171	.194	.219	.244	.270	.296	.323	.351	.379	.408	.438	.469

top and bottom walls are primarily because both the velocity u and the vorticity gradient $\partial\zeta/\partial X$ are large in those regions. However, the velocity u, and/or the gradient $\partial\zeta/\partial Y$, is usually small in the domain away from the horizontal walls, which results in a weaker Γ field in that region.

As is evident, the above effects are further magnified when Ω is increased to unity. However, the present numerical scheme fails to converge when $Ra^* = 500$, $Da = 10^{-2}$, and $\Omega = 1$. It is believed that the problem becomes ill-formulated if the transport term exceeds a certain amount such that the flow is similar to the flows observed for the Newtonian fluids. The implication is that if the transport term is of the order of magnitude of the sum (viscous + buoyancy terms), the Darcy term must vanish. Numerically, it appears then impossible to drive the solution to convergence.

It is interesting to note that the above variation in Γ field does not produce any significant change in the overall heat transfer. (Only the third significant figure is modified.)

Scale Analysis. It may be appropriate at this point to carry out a scale analysis to examine the order of magnitude of the transport term. By eliminating the pressure term between the $\bar{u}$ and $\bar{v}$ components of the momentum equation (2), it can be shown that four terms dominate. Hence, for the vertical boundary layer flow, the important terms are:

Inertia	Viscous diffusion	Buoyancy	Darcy
$\frac{1}{\epsilon^2}\frac{\partial}{\partial x}\left(\bar{u}\frac{\partial \bar{v}}{\partial x}\right)$	$\frac{\nu}{\epsilon}\frac{\partial^3 \bar{v}}{\partial x^3}$	$g\beta\frac{\partial T}{\partial x}$	$\frac{\nu}{K}\frac{\partial \bar{v}}{\partial x}$

where μ' has been taken as $\mu_f(\Lambda = 1)$. Dividing these terms by the velocity scale $\nu/K\delta$, and introducing the momentum boundary layer thickness, yields

$\frac{K}{\epsilon^2\nu}\frac{\bar{u}\bar{v}}{\delta}$	$\frac{K}{\epsilon}\frac{\bar{v}}{\delta^2}$	$\frac{g\beta\Delta TK}{\nu}$	$\bar{v}$

Since from continuity equation (1), $(u/\delta) \sim (v/H)$, these quantities in terms of the dimensionless velocity reduce to

$\left(\frac{Da}{\epsilon^2 Pr^*}\right)\frac{v^2}{A}$	$\left(\frac{Da}{\epsilon}\right)\left(\frac{D}{\delta}\right)^2 v$	Ra^*	v

If $Da \to 0$, it can be concluded that $v \sim Ra^*$, which is the Darcy velocity scale (equation (26)). Using the Darcy scale for the horizontal coordinate,

$$\delta^2 = \frac{\nu\alpha H}{g\beta\Delta Tk}$$

we obtain

$$(D/\delta)^2 = Ra^*/A = v/A$$

Hence, the inertia term is negligible when $\epsilon^2 Pr^* >> 1$ (or equivalently $\Omega << 1$). This agrees with the numerical results and our earlier discussions (see Table 4). However, for large Da, this scaling is no longer valid and nothing can be concluded about the relative magnitudes of the four terms (unless $Da >> 1$ so that the Darcy term vanishes).

For the horizontal boundary layer flow, the four important terms are:

Inertia	Viscous diffusion	Buoyancy	Darcy
$\frac{1}{\epsilon^2}\frac{\partial}{\partial y}\left(\bar{u}\frac{\partial \bar{u}}{\partial x}\right)$	$\frac{\nu}{\epsilon}\frac{\partial^3 \bar{u}}{\partial y^3}$	$g\beta\frac{\partial T}{\partial x}$	$\frac{\nu}{K}\frac{\partial \bar{u}}{\partial y}$

By introducing the horizontal boundary layer thickness δ_l, we obtain

$\frac{1}{\epsilon^2}\frac{\bar{u}^2}{D\delta_l}$	$\frac{\nu}{\epsilon}\frac{\bar{u}}{\delta_l^3}$	$g\beta\frac{\Delta T}{D}$	$\frac{\nu}{K}\frac{\bar{u}}{\delta_l}$

From the energy equation, we can write: $\delta_l^2 \sim \alpha D/\bar{u}$. Dividing these terms by the velocity scale, $\nu/K\delta_l$, and writing in terms of dimensionless velocity,

$\left(\frac{Da}{\epsilon^2 Pr^*}\right)u^2$	$\left(\frac{Da}{\epsilon}\right)u^2$	$Ra^{*1/3}$	u

However, it should be noted that the inertia term can be important if $\partial\bar{u}/\partial x$ is not small. The scale for $\partial\bar{u}/\partial x$ is not $(\bar{u}/D)$ in the corner regions. In addition, the isotherm patterns show that the end regions are nearly isothermal, the buoyancy term being less important. Consequently, the highest Γ value should exist near the horizontal boundaries. The numerical results shown in Table 4 support this conclusion.

The above scale analysis thus confirms that the inertia term does not have any appreciable effects on the buoyancy-induced flow and heat transfer for adiabatic horizontal boundaries and low Darcy numbers. Indeed, the heat transfer oc-

curs along the vertical walls only, where the inertia terms have a negligible influence.

The present numerical results together with the above scale analysis have thus shown that the effect of the modified Prandtl number Pr_e^* on free convection in a vertical cavity is insignificant if $\epsilon^2 Pr_e^* >> 1$, and supports the observation of Catton (1985). However, this effect of Prandtl number is only relevant to the inertia term $(\mathbf{V}\cdot\nabla)\zeta$. An examination of Table 2 reveals that Re increases sharply when the Darcy number increases from 10^{-5} to 10^{-2}. For example, when $Pr^* = 1$ ($1 < \Omega < 100$ for $1 < \epsilon < 0.01$ and $\Lambda = 1$), the Brinkman–Darcy model may be valid only if Da is less than 10^{-4} (equation (27)). This critical Darcy number may further decrease with an increase in Ra* or decrease in Pr*. This critical Darcy number may further decrease with an increase in Ra* or decrease in Pr*. This restricts the validity of the present formulation, and requires that the Forchheimer term be included in the equation of motion to account for the inertia effects properly. Indeed, the Brinkman-extended Darcy equation of motion will be valid only when $(Pr^* KC) \to \infty$, i.e., inertia effects are negligible (Georgiadis and Catton, 1986).

Conclusion

A dimensional analysis of the Brinkman-extended Darcy formulation, with the transport term in the equation of motion, leads to four governing parameters for the steady-state natural convection: Rayleigh number Ra*, Darcy number Da, diffusion parameter Ω, and aspect ratio A. The diffusion parameter Ω determines the strength of the transport term. Numerical results have been obtained for a porous cavity whose vertical walls are maintained at different constant temperatures and the horizontal walls are adiabatic, for $0 \le Da \le 10^{-1}$, $10 \le Ra^* \le 5 \times 10^3$, and $A = 1$ and 5. An increase in Darcy number beyond 10^{-5} is observed to influence the temperature and flow fields significantly. However, the viscous effects are largely confined between the velocity peaks and the walls for $Da < 10^{-3}$. The maximum velocity v_{max} reduces with an increase in Da, and the velocity peaks move away from the walls. The temperature gradients close to the vertical walls reduce significantly and the heat transfer through the core is enhanced with Da. For a fixed Ra*, the boundary layer flow regime reverts to the asymptotic and then to the conduction regimes as the Darcy number is increased. Therefore, the higher the Darcy number, the larger is the Rayleigh number required for the boundary layer regime to start.

The local as well as the overall heat transfer rates decrease with an increase in Da, the reduction being larger at higher Rayleigh numbers. The slope of the ln (Nu) verus ln (Ra*) curve for $A = 5$ decreases from 0.53 at $Da = 0$ to 0.264 at $Da = 0.1$. Owing to the approximations associated with the Weber-type approach, the boundary layer analysis of Tong and Subramanian (1985) predicts Nusselt numbers about 20 percent higher than the present values.

The effects of transport term have been examined through a distribution of Γ, the ratio of transport and diffusion plus buoyancy terms, for $0.01 \le \Omega \le 10$. Γ is usually very small (≤ 0.08) for $\Omega < 0.1$. Although the contribution of transport term is enhanced with Ω, Da, and Ra*, the effect on the overall heat transfer is, generally, negligible. The scale analysis for the vertical and horizontal boundary layers support this conclusion to high Prandtl numbers. Also, the present scheme fails to converge at high values of Ra*, Da, and Ω, probably because the problem becomes ill formulated when the transport term exceeds a certain amount. The validity of the present formulation is then questionable and the Forchheimer modifications may need to be considered.

Acknowledgments

The authors gratefully acknowledge the support of this work by the University of Nantes (France) and the National Science Foundation, USA (Grant No. CBT 85-04100). The computational facilities provided by the CIRCE computer center (CNRS, Orsay-France) are highly appreciated.

References

Bankvall, C. G., 1974, "Natural Convection in Vertical Permeable Space," *Warme- und Stoffubertragung*, Vol. 7, pp. 22–30.

Bejan, A., 1979, "On the Boundary Layer Regime in a Vertical Enclosure Filled With a Porous Medium," *Letters in Heat and Mass Transfer*, Vol. 6, pp. 93–102.

Bejan, A., and Tien, C. L., 1978, "Natural Convection in a Horizontal Porous Medium Subjected to an End-to-End Temperature Difference," *ASME* JOURNAL OF HEAT TRANSFER, Vol. 100, pp. 191–198.

Blythe, P. A., Simpkins, P. G., and Daniels, P. G., 1983, "Thermal Cavitation in a Cavity Filled With a Porous Medium: a Classification of Limiting Behavior," *International Journal of Heat and Mass Transfer*, Vol. 26, pp. 701–708.

Bories, S. A., and Combarnous, M. A., 1973, "Natural Convection in a Sloping Porous Layer," *Journal of Fluid Mechanics*, Vol. 57, pp. 63–79.

Burns, P. J., Chow, L. C., and Tien, C. L., 1977, "Convection in a Vertical Slot Filled With Porous Insulation," *International Journal of Heat and Mass Transfer*, Vol. 20, pp. 919–926.

Catton, I., 1985, "Natural Convection Heat Transfer in Porous Media," *Natural Convection: Fundamentals and Applications*, W. Aung, S. Kakac, and R. Viskanta, eds., Hemisphere, New York.

Chan, B. K. C., Ivey, C. M., and Barry, J. M., 1970, "Natural Convection in Enclosed Porous Media With Rectangular Boundaries," ASME JOURNAL OF HEAT TRANSFER, Vol. 2, pp. 21–27.

Daniels, P. G., 1983, "A Numerical Solution of the Vertical Boundary-Layer Equations in a Horizontally Heated Porous Cavity," *Journal of Engineering Mathematics*, Vol. 17, pp. 285–300.

Georgiadis, J. G., and Catton, I., 1986, "Prandtl Number Effect on Benard Convection in Porous Media," ASME JOURNAL OF HEAT TRANSFER, Vol. 108, pp. 284–290.

Hickox, C. E., and Gartling, D. K., 1981, "A Numerical Study of Natural Convection in a Horizontal Porous Layer Subjected to an End-to-End Temperature Difference," ASME JOURNAL OF HEAT TRANSFER, Vol. 103, pp. 797–802.

Klarsfeld, S., 1970, "Champs de Température Associés aux Mouvements de Convection Naturelle Dans un Milieu Poreux Limité," *Revue Gen. Thermique*, Vol. 9, pp. 1403–1424.

Lundgren, T. S., 1972, "Slow Flow Through Stationary Random Beds and Suspension of Spheres," *Journal of Fluid Mechanics*, Vol. 51, pp. 273–299.

Poulikakos, D., and Bejan, A., 1985, "The Departure From Darcy Flow in Natural Convection in a Vertical Porous Layer," *Physics of Fluids*, Vol. 28, pp. 3477–3484.

Prasad, V., and Kulacki, F. A., 1984a, "Convective Heat Transfer in a Rectangular Porous Cavity – Effect of Aspect Ratio on Flow Structure and Heat Transfer," ASME JOURNAL OF HEAT TRANSFER, Vol. 106, pp. 158–165.

Prasad, V., and Kulacki, F. A., 1984b, "Natural Convection in a Vertical Porous Annulus," *International Journal of Heat and Mass Transfer*, Vol. 27, pp. 207–219.

Prasad, V., Kulacki, F. A., and Keyhani, M., 1985, "Natural Convection in Porous Media," *Journal of Fluid Mechanics*, Vol. 150, pp. 89–119.

Prasad, V., and Tuntomo, A., 1987, "Inertia Effects on Natural Convection in a Vertical Porous Cavity," *Numerical Heat Transfer*, in press.

Roache, P. J., 1982, *Computational Fluid Dynamics*, Hermosa Publishers, Albuquerque, NM.

Schneider, K.-J., 1963, "Investigation of the Influence of Free Thermal Convection on Heat Transfer through Granular Material," *Proceedings, International Institute of Refrigeration*, pp. 247–253.

Seki, N., Fukusako, S., and Inaba, H., 1978, "Heat Transfer in a Confined Rectangular Cavity Packed With Porous Media," *International Journal of Heat and Mass Transfer*, Vol. 21, pp. 985–989.

Shiralkar, G. S., Haajizadeh, M., and Tien, C. L., 1983, "Numerical Study of High Rayleigh Number in a Vertical Porous Enclosure," *Numerical Heat Transfer*, Vol. 6, pp. 223–234.

Simpkins, P. G., and Blythe, P. A., 1980, "Convection in a Porous Layer," *International Journal of Heat and Mass Transfer*, Vol. 23, pp. 881–887.

Tong, T. W., and Subramanian, E., 1985, "A Boundary Layer Analysis for Natural Convection in Porous Enclosure – Use of the Brinkman-Extended Darcy Model," *International Journal of Heat and Mass Transfer*, Vol. 28, pp. 563–571.

Vlasuk, M. P., 1972, "Transfert de Chaleur par Convection Dans une Couche Poreuse," *Proceedings, 4th All-Union Heat and Mass Transfer Conference*, Minsk, USSR.

Walker, K. L., and Homsy, G. M., 1978, "Convection in a Porous Cavity," *Journal of Fluid Mechanics*, Vol. 97, pp. 449–474.

Weber, J. E., 1975, "The Boundary Layer Regime for Convection in a Vertical Porous Layer," *International Journal of Heat and Mass Transfer*, Vol. 18, pp. 569–573.

Thermal Convection in a Rectangular Cavity Filled With a Heat-Generating, Darcy Porous Medium

V. Prasad
Mechanical Engineering Department,
Columbia University,
New York, NY 10027
Mem. ASME

Two-dimensional, steady natural convection in a rectangular cavity filled with a heat-generating, saturated porous medium has been studied numerically for the case when the vertical walls of the cavity are isothermal and the horizontal walls are either adiabatic or cold. Results are presented in terms of the streamlines and isotherms, the maximum temperature in the cavity, and the local and overall Nusselt numbers. The buoyant flow together with the uniform heat generation produces a highly stratified medium at high Rayleigh numbers. Although the maximum temperature in the cavity θ_{max} invariably increases with the Rayleigh number Ra and aspect ratio A, the rate of increase diminishes with this enhancement in Ra and A. However, the change in the horizontal wall boundary condition from adiabatic to cold reduces θ_{max}. The local heat flux on the bounding walls is a strong function of the Rayleigh number, the aspect ratio, and the wall boundary conditions. The variation in overall Nusselt number is qualitatively similar to that observed in the case of a differentially heated cavity, and the present heat transfer rates are close to that for the cavity heated by applying a uniform heat flux. Several correlations are presented for maximum temperature and overall Nusselt number.

Introduction

Thermal convection in fluid-saturated, heat-generating porous media has several geophysical and engineering applications, such as postaccident heat removal from particulate nuclear fuel debris that may result from an accident in a nuclear reactor, heat transfer associated with the deep storage of nuclear waste, exothermic reactions in packed-bed reactors, and heat recovery or loss in geothermal systems. Another important area of its application is the heat transfer from stored agricultural products that release energy as a result of metabolism of the products.

Although several studies on free convection heat transfer in heat-generating porous media have been reported [1–9], most of these works are related to the porous layers bounded by cold horizontal walls. Recently, Beukema et al. [10] have studied three-dimensional natural convection in a heat-generating porous medium confined in an isothermally cooled parallelepiped for a range of parameters suitable for the storage of agricultural products. However, there is very little reported on natural convection in rectangular cavities filled with heat-generating porous media and cooled at the side walls. The only study reported thus far for this case is by Haajizadeh et al. [11]. For low Rayleigh numbers, they obtained approximate solutions to the problem using a regular perturbation analysis whereas for high Rayleigh numbers they developed a boundary layer analysis. They also obtained numerical results for $A = 4$ and $\mathrm{Ra} \leq 6250$ to verify their boundary layer solutions.

The purpose of the present work is to study natural convection in a rectangular cavity filled with a heat-generating, saturated porous medium when its vertical walls are isothermally cooled and horizontal walls are either insulated or cold. The problem has been analyzed numerically for two-dimensional, steady-state flow for wide ranges of Rayleigh number and aspect ratio. The present flow patterns and isotherms exhibit distinctly different behavior from that of a differentially heated vertical cavity. Although the effects of Rayleigh number and aspect ratio are qualitatively similar, the correlations for average Nusselt number are quite different. Furthermore, the present heat transfer rates for $A \geq 1$ are very close to that for a cavity heated by applying a uniform heat flux.

Formulation and Solution

A schematic diagram of a two-dimensional rectangular cavity with isothermally cooled vertical walls is shown in Fig. 1. The cavity is filled with a fluid-saturated porous medium which generates heat at a uniform rate. All walls of the cavity are further assumed to be impermeable. In the porous medium, Darcy's law is assumed to hold, and the fluid is assumed to be a normal Boussinesq fluid. The viscous drag (Brinkman model) and inertia terms in the equations of motion are neglected, which are valid assumptions for low Darcy and particle Reynolds numbers, and for high Prandtl and

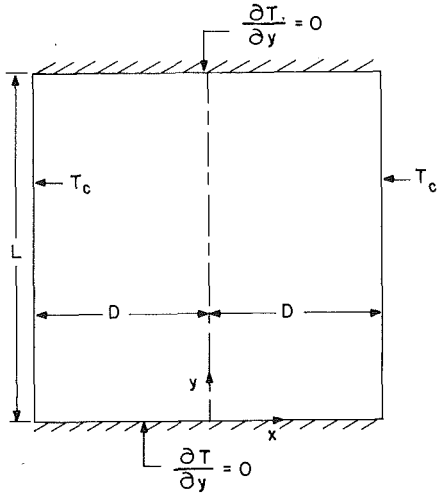

Fig. 1 Vertical cavity filled with a heat-generating porous medium, coordinate system, and thermal boundary conditions

Contributed by the Heat Transfer Division and presented at the National Heat Transfer Conference, Denver, Colorado, August 1985. Manuscript received by the Heat Transfer Division April 9, 1985.

Kozeny–Carman numbers, respectively. Owing to the last assumption, velocity slip at the bounding surface is necessary.

With these assumptions, the conservation equations for mass, momentum, and energy for steady, two-dimensional flow in an isotropic, homogeneous, porous medium are

$$\frac{\partial u}{\partial x}+\frac{\partial v}{\partial y}=0 \tag{1}$$

$$\frac{\partial p}{\partial x}+\frac{\mu}{K}u=0 \tag{2}$$

$$\frac{\partial p}{\partial y}+\rho g+\frac{\mu}{K}v=0 \tag{3}$$

$$u\frac{\partial T}{\partial x}+v\frac{\partial T}{\partial y}=\alpha\left[\frac{\partial^2 T}{\partial x^2}+\frac{\partial^2 T}{\partial y^2}\right]+\frac{S}{\rho C} \tag{4}$$

where S is the rate of volumetric heat generation.

Defining a dimensionless temperature

$$\theta=\frac{(T-T_c)}{SD^2/2k} \tag{5}$$

and a stream function

$$u=-\frac{\alpha}{D}\frac{\partial\psi}{\partial Y},\qquad v=\frac{\alpha L}{D^2}\frac{\partial\psi}{\partial X} \tag{6}$$

the governing equations (1)–(4) together with the Boussinesq approximation for density variation reduce to

$$A^2\frac{\partial^2\psi}{\partial X^2}+\frac{\partial^2\psi}{\partial Y^2}=\mathrm{Ra}\,A\frac{\partial\theta}{\partial X} \tag{7}$$

$$\frac{\partial\psi}{\partial X}\frac{\partial\theta}{\partial Y}-\frac{\partial\psi}{\partial Y}\frac{\partial\theta}{\partial X}=\frac{\partial^2\theta}{\partial X^2}+\frac{1}{A^2}\frac{\partial^2\theta}{\partial Y^2}+2 \tag{8}$$

where the Rayleigh number based on volumetric heat generation is

$$\mathrm{Ra}=\frac{g\beta KSD^3}{2\nu\alpha k} \tag{9}$$

The relevant hydrodynamic and thermal boundary conditions are

$$X=0,\qquad \psi=0,\qquad \frac{\partial\theta}{\partial X}=0 \tag{10}$$

$$X=1,\qquad \psi=0,\qquad \theta=0 \tag{11}$$

$$Y=0 \text{ and } 1,\qquad \psi=0,\qquad \frac{\partial\theta}{\partial Y}=0 \text{ or } \theta=D \tag{12}$$

The zero temperature gradient boundary condition at $X=0$ is based on the symmetry of the problem and it is only necessary to solve the problem for the right half of the cavity. The present results are also applicable to a cavity of width D with one side wall adiabatic and the other cold.

Equations (7) and (8) are transformed into finite difference equations using a scheme developed by Spalding and coworkers. The method is based on the integration of these equations over finite area elements and ensures that the conservation laws are obeyed over arbitrarily large or small portions of the physical domain [12]. The solution technique is well described in the literature [12, 13] and has been widely used for the natural convection problems. The applicability of the method and its accuracy for convective heat transfer in a porous cavity have already been discussed elsewhere [14].

Integration of these equations following Gosman et al. [12] introduces upwind differences for the transport terms in the energy equation and is equivalent to second upwind differencing. All other terms in the energy and momentum equations are discretized by central differencing. The successive substitution formulas derived in this way satisfy the convergence criterion and are quite stable for many circumstances [12]. For solving the simultaneous algebraic equations thus obtained, the Gauss–Seidel point iterative method is used, which makes use of new values as soon as they are available. For low Rayleigh numbers, overrelaxation of temperature helps in obtaining faster convergence whereas for high Rayleigh numbers, underrelaxation of stream function is more helpful. The value of the overrelaxation parameter used is as high as 1.9, and a suitable value of the underrelaxation parameter is between 0.5 and 1. A convergence criterion

$$|(\phi^n-\phi^{n-1})/\phi^n|<10^{-4} \tag{13}$$

is used for both ψ and θ at all grid points in the domain to check the iterative convergence.

For low Rayleigh numbers ($\mathrm{Ra}<500$), a uniform mesh size is used for the numerical calculations whereas a nonuniform mesh is employed at high Rayleigh numbers. In the case of varying mesh size, the finer grid (of the order of $10^{-2}\sim 10^{-3}$) is used near the walls. The number and size of the grids in the x

Nomenclature

A = aspect ratio = L/D
C = specific heat of fluid at constant pressure, J/kg-K
D = width of half cavity, m
g = acceleration due to gravity, m/s^2
$\bar{h}$ = average heat transfer coefficient on the cold wall, W/m^2-K
K = permeability of saturated porous medium, m^2
k = effective thermal conductivity of porous medium, W/m-K
L = height of rectangular cavity, m
Nu = Nusselt number based on cavity width = $\bar{h}D/k$
p = pressure, Pa
$\bar{q}$ = dimensionless local heat flux on vertical wall = $2q_L/SD=-\partial\theta/\partial X$ $(X=1)$
q_L = local heat flux on the cold wall
Ra = Rayleigh number based on cavity width = $g\beta \cdot KSD^3/2k\nu\alpha$
Ra_L = Rayleigh number based on height = $g\beta\, KSD^2L/2k\nu\alpha$
S = volumetric heat generation, W/m^3
T = temperature, K
u = fluid velocity in x direction, m/s
v = fluid velocity in y direction, m/s
x, y = Cartesian coordinates, m/s
X = dimensionless distance on x axis = x/D
Y = dimensionless distance on y axis = y/L
α = thermal diffusivity of porous medium = $k/\rho C$, m^2/s
β = isobaric coefficient of thermal expansion of fluid, K^{-1}
θ = dimensionless temperature = $(T-T_c)/(SD^2/2k)$
ν = kinematic viscosity, m^2/s
ρ = density of fluid, kg/m^3
ϕ = ψ or θ in equation (13)
ψ = stream function (equation (6))

Subscripts

ad = adiabatic horizontal walls
c = cooled wall
cold = cold horizontal walls
cond = conduction
h = heated wall
m = based on mean temperature on the line of symmetry
max = maximum
0 = line of symmetry $(x=0)$
L = based on the cavity height L

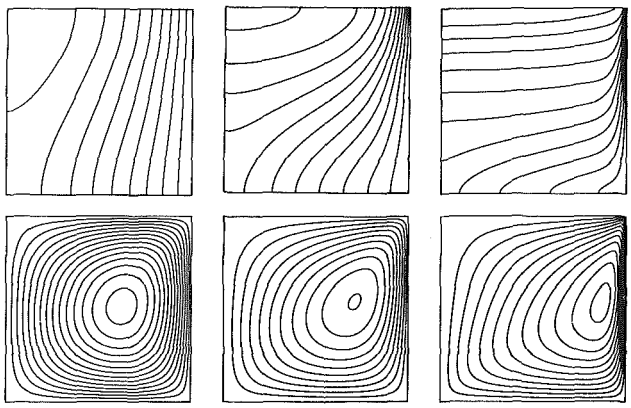

Fig. 2 Isotherms and streamlines for $A = 1$ when horizontal walls are adiabatic: (a) Ra = 10 ($\Delta\theta = 0.1$, $\Delta\psi = 0.05$); (b) Ra = 10^2 ($\Delta\theta = 0.05$, $\Delta\psi = 0.3$); (c) Ra = 10^4 ($\Delta\theta = 0.01$, $\Delta\psi = 2$)

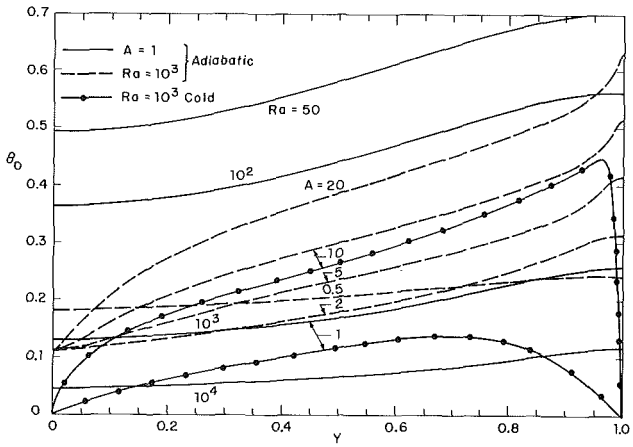

Fig. 3 Temperature distribution on the line of symmetry

and y direction are based on the values of Ra and A. The following are the grid fields used for the present calculations:

	Grid Field
$A<1$	41×31
$A=1$	31×31
$2\le A\le5$	31×41
$A>5$	27×41

These mesh sizes provide Nusselt numbers within 3 percent of their asymptotic values. Indeed, the grid refinement is based on several trial cases for high and low values of Ra and A. The accuracy of the present results has been further checked by employing an energy balance between the heat generated by the porous medium and that removed at the cold wall(s). Generally, energetic closure has been achieved to within 1 percent except for the high Rayleigh numbers and/or the low aspect ratios where it is satisfied within 2 percent. For several trial runs, an energy balance at various x locations of the cavity has indicated that the variation never exceeds the value obtained at the cold wall(s). Moreover, the present results are within 4 percent of the numerical values obtained by Haajizadeh et al. [11]. A detailed discussion of the effect of relaxation parameters, convergence criterion, upwind differencing, and mesh size is presented in [14, 15].

Results and Discussion

Numerical results for a rectangular cavity filled with a heat-generating saturated porous medium have been obtained for cooled, constant-temperature vertical walls and adiabatic or isothermally cooled horizontal walls. The range of parameters considered for the first case is $0.5 \le A \le 20$ and $\text{Ra} \le 10^4$, whereas for the second case, results are obtained for $A = 1$ and 10, and $\text{Ra} \le 2000$. Because of the symmetry, computations have been carried out for only the right half of the cavity (Fig. 1). This region will be referred to as the "half-cavity."

1 Adiabatic Horizontal Walls

Temperature and Flow Fields. Flow patterns and isotherms for $A = 1$ and Ra = 10, 10^2, and 10^4 are presented in Fig. 2 for the adiabatic top and bottom surfaces. For pure conduction (Ra = 0), the isotherms are vertical and the temperature is given by $\theta_{\text{cond}} = 1 - X^2$. As the Rayleigh number increases, a circulatory motion is established because of the buoyancy effects. The flow consists of a single cell filling the entire half-cavity and rotating slowly in the clockwise direction (counterclockwise in the other half). Initially, the convection cell is symmetric about the center of the half-cavity. However, an increase in Ra results in an asymmetric flow pattern producing closer streamlines near the walls (Fig. 2). The velocities are thus higher near the walls and lower near the line of symmetry. As Ra is increased further, the streamlines move closer to the cold wall, producing strong boundary layer effects on the side wall. Although the flow remains unicellular at all Rayleigh numbers, the velocity in the upper left corner decreases substantially. A similar flow behavior has also been reported by Haajizadeh et al. [11].

At Ra = 10, the isotherms (Fig. 2*a*) exhibit minimal distortion from a pure conduction solution indicating that the conduction is still the dominant mechanism of energy transport. However, as the Rayleigh number increases, the temperature field is significantly modified in the region where the convective transport is larger. This distortion of conduction isotherms can be explained by examining the energy equation (8) which can be rewritten as

$$\frac{\partial^2\theta}{\partial X^2}+\frac{1}{A^2}\frac{\partial^2\theta}{\partial Y^2}+\left(2-u\frac{\partial\theta}{\partial X}-v\frac{\partial\theta}{\partial Y}\right)=0 \quad (14)$$

Here, the expression in parentheses can be interpreted as a source term which depends on the location. Since $\partial\theta/\partial X\le 0$ and $\partial\theta/\partial Y\simeq 0$ over the flow field (Fig. 2*a*), the convective flow decreases the strength of the source term in the upper half of the cavity where $u \ge 0$ and increases it in the lower half where $u \le 0$. The modifications in the isotherm shapes are consistent with this interpretation. It may be noted that the maximum cavity temperature $\theta_{\max}$ always occurs at the top edge of the line of symmetry, i.e., at $X = 0$, $Y = 1$.

Any further increase in Ra results in a stably stratified temperature field in the left top corner (Fig. 2*b*). In this region, horizontal conduction is almost negligible. The extent of this stratified region continually increases with Ra and produces a thermal boundary layer on the vertical wall (Fig. 2*c*). As a result, the convective velocities are smaller in the stratified region and are very high in the boundary layer. The higher the aspect ratio, the weaker is the thermal stratification for a given Rayleigh number (also see [11]).

The temperature distributions on the line of symmetry are presented in Fig. 3. As the Rayleigh number increases, the dimensionless temperature θ_0 is observed to decrease from its conduction value of unity except in a small distance near the top edge. This decrease in θ_0 is larger in the lower region owing to higher velocities of the returning cold fluid. However, a decrease in θ_0 does not mean that the actual temperature has dropped. For a given system, Ra can be considered as directly proportional to the volumetric heat generation S, whereas θ_0 is indirectly proportional to S. A tenfold increase in Ra, from 10^2 to 10^3, produces only one-third to one-half reduction in θ_0, for $A = 1$. This clearly implies that for a fixed A, the temperature $(T_0 - T_c)$ increases with Ra (or S). Nevertheless, the rate of enhancement in $(T_0 - T_c)$ diminishes when Ra (or S) is increased.

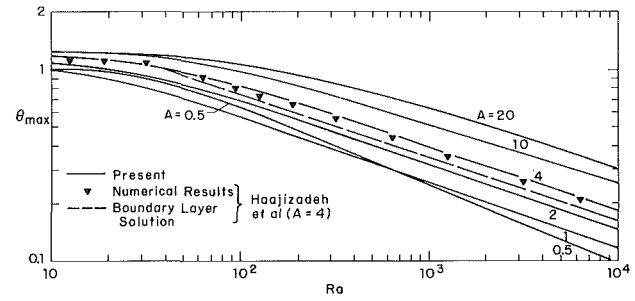

Fig. 4 Variation in maximum cavity temperature for the adiabatic horizontal walls; present values of θ_{max} for $A = 4$ are compared with those reported by Haajizadeh et al. [11]

Furthermore, an increase in aspect ratio beyond two results in a higher temperature at any location Y on the line of symmetry (Fig. 3). The taller the cavity, the larger is the temperature gradient, $\partial\theta_0/\partial Y$. This does not imply that the actual temperature gradient increases with an increase in the aspect ratio. Indeed, for a cavity of given width D, $\partial T/\partial y$ decreases when the cavity is increased for a fixed S. This is evident from the expression

$$\left.\frac{\partial T}{\partial y}\right|_{x=0} = \frac{SD}{2k}\,\frac{1}{A}\,\frac{\partial\theta_0}{\partial Y} \tag{15}$$

and Fig. 3.

However, for $A < 2$, the effect of aspect ratio on θ_0 is not straightforward. Generally, θ_0 on the line of symmetry starts increasing when A is reduced below a certain value between 0.7 and 2, as for example, θ_0 for $A = 0.5$ is higher than that for $A = 1$, at least when $Y < 0.85$ (Fig. 3).

The maximum temperature always occurs at the center of the top wall, and is a function of Ra and A (Fig. 4). At Ra = 0, θ_{max} is unity, but an increase in Rayleigh number results in a higher θ_{max}. This is primarily because the hot fluid reaching the left top corner is unable to reject energy effectively since the velocities are small in that region [11]. However, this increase in θ_{max} with Ra does not continue for long. Indeed, θ_{max} starts decreasing as soon as Ra is high enough to produce sufficiently high convective velocities in the top left corner and enhance the heat rejection.

Although θ_{max} decreases with an increase in Ra, it simply implies that the rate of enhancement in the actual temperature, $T(0, 1)$, diminishes with the convective velocities. For a given A, the reduction in θ_{max} is minimal at low Rayleigh numbers. However, it decreases at a faster rate when the Rayleigh number is large. The curve for ln (θ_{max}) versus ln (Ra) is observed to be a straight line beyond a critical value of Rayleigh number which is a function of aspect ratio. This situation characterizes a strong stratification in the core and the boundary layer flow on the vertical wall.

Moreover, an increase in aspect ratio beyond unity is always associated with an enhancement in θ_{max} (Fig. 4). When $A < 1$, the increase or decrease in θ_{max} depends on the Rayleigh number. If the Rayleigh number is high enough to maintain a strong boundary layer on the cold wall, θ_{max} will decrease with A; otherwise, it will increase.

The maximum cavity temperature can be correlated as

$$\theta_{max} = C\,\mathrm{Ra}^{-m} \qquad \text{for a fixed } A \tag{16}$$

where C and m are given in Table 1 for various values of A. As can be seen, the exponent m increases as the aspect ratio is decreased. However, there exists a critical aspect ratio as a function of Ra beyond which C always increases whether the aspect ratio is increased or decreased. For the present range of Rayleigh number, $A_{critical}$ lies between 0.7 and 1.

Table 1 The constant C and exponent m for the correlation of θ_{max} (equation (16)) for various aspect ratios

A	C_1	m	Rayleigh number range	Percent standard deviation
0.5	4.137	0.408	Ra ≥ 100	1.33
0.7	2.883	0.359	Ra ≥ 100	1.34
1	2.743	0.343	Ra ≥ 50	0.70
2	3.198	0.335	Ra ≥ 100	0.35
5	3.867	0.323	Ra ≥ 100	1.17
10	4.469	0.314	Ra ≥ 200	1.41
20	5.101	0.306	Ra ≥ 500	2.74

Table 2 The constant C_1 and exponent r for the correlation of average Nusselt number (equation (20)) for various aspect ratios

A	C_1	r	Rayleigh number range	Percent standard deviation
0.5	0.395	0.461	Ra ≥ 100	1.09
0.7	0.584	0.421	Ra ≥ 100	1.28
1	0.702	0.399	Ra ≥ 50	0.46
2	0.768	0.377	Ra ≥ 100	0.66
5	0.667	0.365	Ra ≥ 100	0.73
10	0.553	0.361	Ra ≥ 200	0.78
20	0.455	0.306	Ra ≥ 500	0.59

A comparison between the present values of θ_{max} for $A = 4$ and that reported by Haajizadeh et al. [11] (Fig. 4) indicates that the two numerical results agree within 4 percent. However, the boundary layer analysis of Haajizadeh et al. predicts lower values of θ_{max} for Ra > 50. Although the deviation is as large as up to 12 percent, the slope of the θ_{max} versus Ra curve is well-predicted. It may be noted that the boundary layer analysis of Haajizadeh et al. [11] is based on the Oseen linearization of boundary layer equations and employs an integral technique which has been widely used in the literature.

Heat Transfer Results. The overall heat transfer may be expressed in two ways, based on either the maximum temperature in the cavity or the mean temperature on the line of symmetry. When the heat transfer coefficient on the cold wall is defined in terms of the maximum cavity temperature, i.e.,

$$h\,(T_{max} - T_c) = -\frac{k}{L}\int_0^L \left.\frac{\partial T}{\partial X}\right|_{x=D} dy \tag{17}$$

the Nusselt number is obtained as

$$\mathrm{Nu}_{max} = 2/\theta_{max} \tag{18}$$

One can easily obtain this Nusselt number from Fig. 4. The correlations for Nu_{max} in the boundary layer regime are, then, given by equations (16) and (18), and Table 1. Similarly the Nusselt number based on the mean temperature T_m is

$$\mathrm{Nu}_m = 2/\theta_m \tag{19}$$

and is presented in Fig. 5.

In the conduction regime, $\mathrm{Nu}_m \to 2$ for all values of A. An increase in Ra is always associated with an enhancement in the average heat transfer coefficient (Fig. 5). Moreover, the heat transfer behavior in the present case is very similar to what has been reported for a differentially heated vertical cavity [14, 15]. Although the Nusselt number always increases with Ra, the effect of aspect ratio is not straightforward. For a given Ra, there exists an aspect ratio for which the Nusselt number is a maximum. For the present range of Rayleigh number, $A_{critical}$ lies between 0.7 and 2.

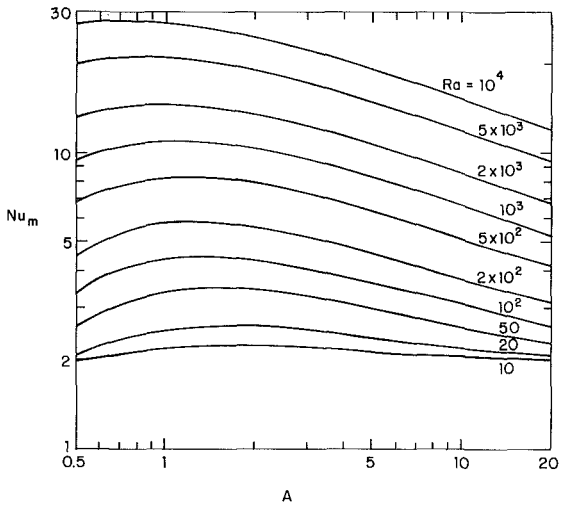

Fig. 5 Variation in average Nusselt number for a cavity with adiabatic horizontal walls

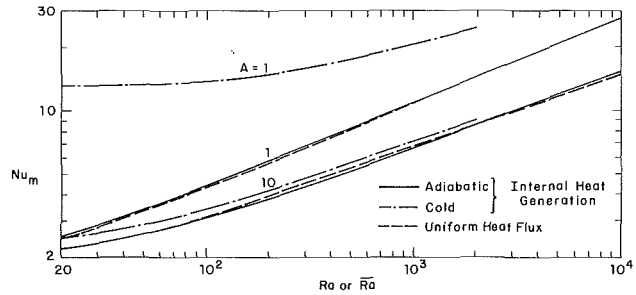

Fig. 6 Present heat transfer results compared with that for a cavity with constant flux heating [14]

In the boundary layer regime, the average Nusselt number may be correlated as

$$\mathrm{Nu}_m = C_1 \mathrm{Ra}^r \qquad \text{for a fixed } A \tag{20}$$

The values of C_1 and r are given in Table 2. These correlations predict Nusselt numbers within 1.5 percent of the numerically obtained values.

A generalized correlation for the tall cavity may be obtained as

$$\mathrm{Nu}_m = 1.163\ \mathrm{Ra}^{0.362} A^{-0.330} \tag{21}$$

which is based on the data for $A \geq 4$. Equation (21) predicts Nusselt number within 2 percent of the correlated data for these aspect ratios. If this correlation is used for $A = 2$, the variation is as large as 7.8 and 5.4 percent at $\mathrm{Ra} = 10^3$ and 10^4, respectively.

Comparison With Other Results. It is worthwhile to compare the present results with those for the differentially heated cavity of width D, whose left vertical wall is heated by applying a constant heat flux and whose right wall is isothermally cooled. If the applied heat flux q is taken as $SD/2$, the Rayleigh number in the present case is identical to that for the constant flux heating [14].

A comparison between the present isotherm and streamline patterns and those reported by Prasad and Kulacki [14] for the constant heat flux case indicates that both are asymmetric. However, the strong boundary layer effects on the heated wall as observed in the case of constant heat flux case are not present here. On the other hand, the boundary layer flow on the cold wall is much stronger in the present case. Nevertheless, the present temperature distributions on the line of symmetry ($x = 0$) are very similar to those obtained for uniformly heated wall [14]. Not only the effects of Ra and A on these temperature profiles are identical, but the values of

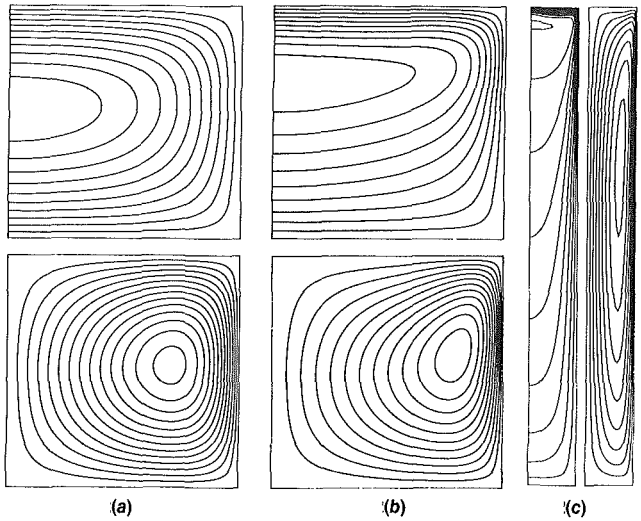

Fig. 7 Isotherms and streamlines when the top and bottom walls are cooled: (a) $\mathrm{Ra} = 10^2$, $A = 1$ ($\Delta\theta = 0.02$, $\Delta\psi = 0.1$); (b) $\mathrm{Ra} = 10^3$, $A = 1$ ($\Delta\theta = 0.015$, $\Delta\psi = 0.6$); (c) $\mathrm{Ra} = 10^3$, $A = 10$ ($\Delta\theta = 0.05$, $\Delta\psi = 0.4$)

$\theta_0(Y)$ are also close. Indeed, the temperatures reported in Fig. 3 are within 20 percent of those obtained for the constant flux heating.

The mean Nusselt numbers for the two cases are compared in Fig. 6 for $A = 1$ and 10. Owing to the present definition of q ($= SD/2$), Nu_m for the constant heat flux case is twice that reported in [14]. In Fig. 6, the two Nusselt numbers are very close to each other. The present agreement is primarily due to the similarity of the boundary layer structure regardless of the heating applied to the cavity. This characterization of a thermally stratified core and thin boundary layers on the cold vertical walls has also been noted by Haajizadeh et al. [11]. However, when the aspect ratio is decreased below unity, the difference between the Nusselt numbers for these two types of heating is observed to increase.

2 Cold Horizontal Walls

Temperature and Flow Fields. A change in the boundary condition at the horizontal wall from $\partial\theta/\partial Y = 0$ to $\theta = 0$ modifies the temperature and velocity fields significantly. For pure conduction, the isotherms are symmetric about the horizontal line at $Y = 0.5$, and the temperature θ is maximum at (0, 0.5). However, the buoyancy-induced flow at $\mathrm{Ra} > 0$ destroys this symmetric property of the temperature field and shifts the location for $\theta_{\max}$ upward (Fig. 7). As a result, when the Rayleigh number is increased, the temperature in the lower portion of the cavity decreases while that in the upper region increases. The stratification in the upper layers is, thus, much stronger than that observed in the case of insulated top and bottom (Figs. 2 and 7). It should be noted that the stratification in the upper region is now reversed because the top wall is cooled and the porous medium generates heat everywhere. However, the inverse stratification in the present case does not produce any flow instability since a positive buoyant effect produced by the uniform heat generation always counteracts a negative buoyancy caused by an unstable stratification. The nature of the convective cell, thus, remains unaltered. These characteristics of the temperature field make the present problem quite different from that of a differentially heated vertical cavity with cold horizontal walls.

The aforementioned unstable stratification is strengthened by an increase in Ra. In Fig. 7, the isotherms in the upper region are almost horizontal for a large portion of the cavity indicating that a substantial amount of energy is rejected on the top wall. The flow field is modified accordingly. The boundary layer effects on the vertical walls are now weaker as

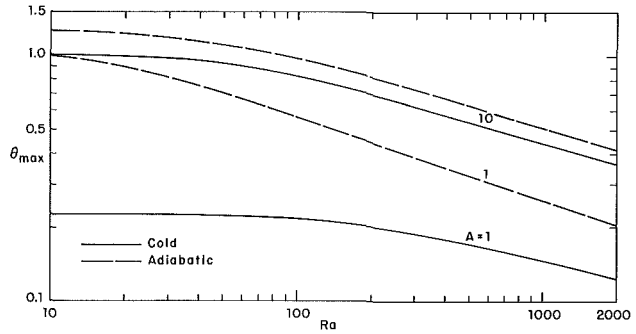

Fig. 8 Variation in maximum cavity temperature for $A = 1$ and 10

compared to that for the adiabatic top and bottom walls (Figs. 2*b* and 7*a*).

Furthermore, the location of θ_{max} and the inverse stratification in the upper layers are significantly affected by an increase in aspect ratio (Fig. 7). When $A = 10$, the temperature is maximum at a location very close to the top edge, e.g., within 8 percent of the height of the cavity for $100 < Ra < 1000$. Also, the temperature gradient $\partial\theta_0/\partial Y$ in a region very close to the upper surface increases substantially with A. Indeed, when the aspect ratio is high, the large-scale modification in the temperature and flow fields due to the change in boundary condition from $\partial\theta/\partial Y = 0$ to $\theta = 0$ is mostly concentrated in the small regions near the top and bottom surfaces. The larger the aspect ratio, the smaller is the region of influence. This is also demonstrated by the temperature distributions on the inner wall shown in Fig. 3 where the variation in θ_0 is observed to be substantial for $A = 1$. However, the two temperatures are quite close to each other for $A = 10$ except for the small distances from the top and bottom edges.

The above influence of the boundary condition at the horizontal wall is directly reflected by the variation in θ_{max}. As expected, θ_{max} decreases with a change in the boundary condition from adiabatic to cold (Fig. 8), the variation being largest in the case of pure conduction. The difference between the two values of θ_{max} continually decreases with an increase in the Rayleigh number and/or the aspect ratio. As an example, for $A = 1$, $(\theta_{max})_{ad}$ is 4.4 times $(\theta_{max})_{cold}$ when $Ra = 10$ whereas at $Ra = 1000$, $(\theta_{max})_{ad} = 1.76\ (\theta_{max})_{cold}$. This difference in θ_{max} further reduces to within 22 percent when the cavity aspect ratio is increased to 10. An interesting aspect of the above variation in θ_{max} is that the slope of the ln (θ_{max}) versus ln (Ra) curve at high Rayleigh numbers is almost independent of the horizontal wall boundary condition. However, the smaller the cavity aspect ratio, the larger is the Rayleigh number required for the two slopes to be close.

Heat Transfer Results. Interesting features of the present heat transfer results are demonstrated in Fig. 9 where the outward local heat flux $\bar{q}$ has been presented for all the impermeable walls. Owing to the buoyant velocity and the uniform heat generation, a large fraction of energy is rejected on the top surface. For a fixed aspect ratio, the amount of energy (as a ratio to the total heat generated) removed on the upper surface is increased with Ra. Even for a large aspect ratio, when the width of the cavity is much smaller than the height, the energy rejected on the top surface is quite significant (Fig. 9*a*).

At low Rayleigh numbers, the local heat flux $\bar{q}$ is largest at the center of the top wall ($X = 0$, $Y = 1$), and decreases with an increase in X. However, at high Ra, the distribution of $\bar{q}$ may be different; it first decreases and then increases until it reaches a peak a little before the right top edge (Fig. 9). It is possible that this peak value of $\bar{q}$ is higher than that at the center of the upper surface (0, 1) for certain combinations of Ra and A.

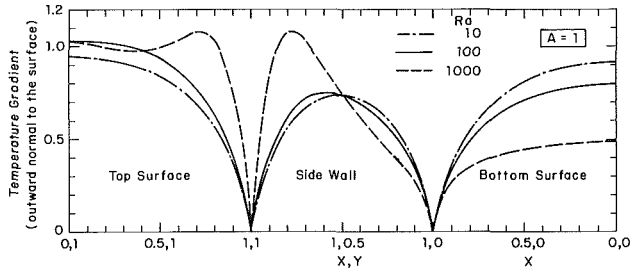

Fig. 9(a)

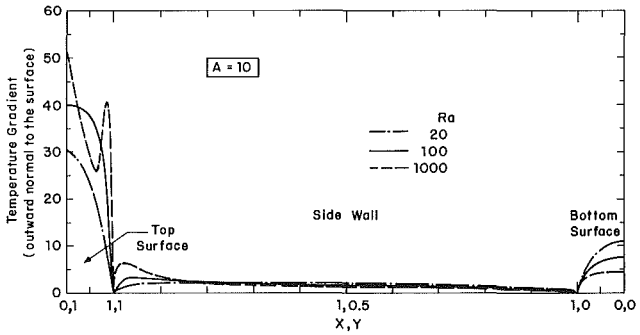

Fig. 9(b)

Fig. 9 Local heat flux on the cold walls: (*a*) $A = 1$ and (*b*) $A = 10$

The local heat transfer rate on the vertical wall increases from zero at $Y = 1$ to a maximum and then back to zero at $Y = 0$. In the conduction regime, the peak occurs at $Y = 0.5$, but with an increase in Ra, the location for the peak value of $\bar{q}$ moves upward (Fig. 9*a*). This is a direct result of the increased convective velocities and the enhanced boundary layer effects on the side wall. However, an increase in aspect ratio reduces the largest value of the local heat flux on vertical wall. In general, the horizontal wall boundary condition has significant influence on the distribution of $\bar{q}$ on the side wall (Fig. 9). It should be noted that the heat transfer rates near the right top edge have reduced substantially because the top wall is now cold.

A significant amount of energy is also rejected at the bottom surface when the Rayleigh number is small. However, the heat transfer on this surface decreases with an increase in Ra which clearly implies that the effect of the bottom wall boundary condition diminishes with higher velocities or higher Rayleigh number.

The overall Nusselt number as defined by equation (19) is presented in Fig. 6 for both the adiabatic and the isothermal horizontal walls. As already indicated by the temperature field, the Nusselt number for the present boundary conditions is much higher than that for the adiabatic case when $A = 1$. However, the difference decreases substantially with an increase in aspect ratio, and at $A = 10$, the two Nusselt numbers are within 12 percent of each other. It is, thus, evident that the effect of the horizontal wall boundary condition is minimal at large aspect ratios, and the results for adiabatic top and bottom can be conveniently used for other types of thermal boundary condition on these walls when $A > 10$.

Conclusion

Natural convection in a rectangular cavity filled with a heat-generating saturated porous medium has been numerically investigated for the case when the vertical walls are cooled at a constant temperature and the horizontal walls are either insulated or isothermally cooled. The results obtained for a wide range of Rayleigh number and $0.5 \leq A \leq 20$ indicate that

unlike the isothermally heated vertical cavity, the temperature and flow fields are asymmetric in the present case. An increase in Rayleigh number results in a stably stratified temperature field for the adiabatic horizontal walls whereas for the cold top and bottom, the stratification in the upper region is inverse. Also, the extent and strength of the stratified region depend strongly on Ra and A. In general, the convective velocities are smaller in the stratified region and are very high in the boundary layers.

The temperature at any location in the cavity increases with Ra, but the rate of increase in temperature invariably diminishes. When the top and bottom walls are adiabatic, the maximum cavity temperature occurs at the center of the top wall. In the boundary layer regime, the maximum temperature can be expressed by a simple correlation (equation (16)). When the boundary condition at the horizontal wall is changed to $\theta = 0$, θ_{max} occurs at a location below $Y = 1$. The higher the aspect ratio and the Rayleigh number, the closer is the θ_{max} location to the top surface.

The local heat flux on the cold wall(s) is a strong function of the boundary condition at the horizontal walls besides Ra and A. However, the effect of the bottom wall boundary condition diminishes with an increase in Ra or A while the influence of the top wall boundary condition is enhanced. The overall Nusselt number increases with the Rayleigh number. For a fixed Ra, the maximum value of Nu_m occurs at $0.7 < A < 2$ beyond which any increase or decrease in A results in a reduction in the heat transfer rate.

Since the boundary layer structure in the present case is very similar to that observed for the differentially heated vertical cavity, the present values of Nu_m are very close to that reported for the constant flux heating. The effect of the geometric parameter A thus seems to be independent of the type of heating for large aspect ratios. Several correlations have also been reported for the maximum cavity temperature and the average Nusselt number.

References

1 Hwang, I.-T., "Finite Amplitude Thermal Convection in Porous Media With Heat Sources and Variable Viscosity," Ph.D. Thesis, University of Minnesota, 1971.

2 Sun, W. J., "Convective Instability in Superposed Porous and Free Layers," Ph.D. Dissertation, University of Minnesota, 1973.

3 Kulacki, F. A., and Ramchandani, R., "Hydrodynamic Instability in a Porous Layer Saturated With a Heat Generating Fluid," *Warme- und Stoffübertragung*, Vol. 8, 1975, pp. 179–185.

4 Gasser, R. D., and Kazimi, M. S., "Onset of Convection in a Porous Medium With Internal Heat Generation," ASME JOURNAL OF HEAT TRANSFER, Vol. 98, 1976, pp. 49–54.

5 Buretta, R. J., and Berman, A. S., "Convective Heat Transfer in a Liquid Saturated Porous Layer," ASME JOURNAL OF APPLIED MECHANICS, Vol. 98, 1976, pp. 249–253.

6 Tveitereid, M., "Thermal Convection in a Horizontal Porous Layer With Internal Heat Sources," *International Journal of Heat and Mass Transfer*, Vol. 20, 1977, pp. 1045-1050.

7 Hardee, H. C., and Nilson, R. H., "Natural Convection in Porous Media With Heat Generation," *Nuclear Science and Engineering*, Vol. 63, 1977, pp. 119-132.

8 Rhee, S. J., Dhir, V. K., and Catton, I., "Natural Convection Heat Transfer in Beds of Inductively Heated Particles," ASME JOURNAL OF HEAT TRANSFER, Vol. 100, 1978, pp. 78-85.

9 Kulacki, F. A., and Freeman, R. G., "A Note on Thermal Convection in a Saturated Heat Generating Porous Layer," ASME JOURNAL OF HEAT TRANSFER, Vol. 101, 1979, pp. 169-171.

10 Beukema, K. J., Bruin, S., and Schenk, J., "Three-Dimensional Natural Convection in a Confined Porous Medium With Internal Heat Generation," *International Journal of Heat and Mass Transfer*, Vol. 26, 1983, pp. 451-458.

11 Haajizadeh, M., Ozguc, A. F., and Tien, C. L., "Natural Convection in a Vertical Porous Enclosure With Internal Heat Generation," *International Journal of Heat and Mass Transfer*, Vol. 27, 1984, pp. 1893-1902.

12 Gosman, A. D., Pun, W. M., Runchal, A. K., Spalding, D. B., and Wolfshtein, M., *Heat and Mass Transfer in Recirculating Flows*, Academic Press, New York, 1969.

13 Roache, R. J., *Computational Fluid Dynamics*, Hermosa Publishers, New York, 1976.

14 Prasad, V., and Kulacki, F. A., "Natural Convection in a Rectangular Porous Cavity With Constant Heat Flux on One Vertical Wall," ASME JOURNAL OF HEAT TRANSFER, Vol. 106, 1984, pp. 152-157.

15 Prasad, V., and Kulacki, F. A., "Convective Heat Transfer in a Rectangular Porous Cavity – Effect of Aspect Ratio on Flow Structure and Heat Transfer," ASME JOURNAL OF HEAT TRANSFER, Vol. 106, 1984, pp. 158-165.

Vorticity-Velocity Method for the Graetz Problem and the Effect of Natural Convection in a Horizontal Rectangular Channel With Uniform Wall Heat Flux

F. C. Chou[1]

G. J. Hwang
Professor.
Mem. ASME

Department of Power Mechanical Engineering,
National Tsing Hua University,
Hsinchu, Taiwan 30043,
Republic of China

Numerical solutions given by a vorticity-velocity method are presented for combined free and forced laminar convection in the thermal entrance region of a horizontal rectangular channel without the assumptions of large Prandtl number and small Grashof number. The channel wall is heated with a uniform wall heat flux. Typical developments of temperature profile, secondary flow, and axial velocity at various axial positions in the entrance region are presented. Local friction factor and Nusselt number variations are shown for Rayleigh numbers Ra = 10^4, 3×10^4, 6×10^4, and 10^5 with the Prandtl number as a parameter. The solution for the limiting case of large Prandtl number and small Grashof number obtained from the present study confirms the data of existing literature. It is observed that the large Prandtl number assumption is valid for Pr = 10 when Ra $\leq 3 \times 10^4$ but for a larger Prandtl number when the Rayleigh number is higher.

Introduction

Previous theoretical analyses for laminar convective heat transfer in the thermal entrance region of rectangular channels have usually neglected the free convection effects [1-3]. This type of problem can be classified as the Graetz problem in honor of Graetz in 1883. However, the buoyancy forces always exist in the thermal entrance region and the natural convection effects on the Graetz problem have been studied by several investigators [4-9]. A large Prandtl number and small Grashof number assumption is frequently used [4-9] to neglect the nonlinear inertia terms in the momentum equations and avoid the complexities in the analysis of the three-dimensional fluid flow.

The effects of natural convection on the Graetz problem were studied, assuming large Prandtl number and small Grashof number, for a horizontal rectangular channel with a uniform wall heat flux for Ra = $0 \sim 10^5$ by Cheng et al. [4], for tube with Ra = $0 \sim 1.56 \times 10^6$ by Cheng and Ou [5], and also for tube with Ra = $0 \sim 10^6$ by Hong et al. [6]. The same problems were also studied for isothermal rectangular channels with Ra = $0 \sim 5 \times 10^5$ by Ou et al. [7] and for an isothermal tube with Ra = $0 \sim 10^6$ by Ou and Cheng [8]. It is noted in [8] that due to the numerical difficulty, the solutions obtained for Ra = 5×10^5 and 10^6 are limited to the region $Z \leq 3 \times 10^{-3}$. Hwang and Lin [9] improved the numerical scheme and obtained results over the whole range of z. Two pairs of counterrotating vortices were observed at $z \geq 2 \times 10^{-3}$ for Ra $\geq 5 \times 10^5$ which reduce the heat transfer rate drastically. Ramakrishna et al. [10] studied the laminar natural convection along vertical square ducts by solving numerically the vorticity-velocity governing equations with a strongly implicit finite-difference procedure.

As for the cases of mixed convection in the entrance region, where the velocity and temperature fields are developing simultaneously, solutions are also available in restricted cases. The assumption of large Prandtl number was also used by Hieber and Sreenivasan [11] for mixed convection in an isothermally heated horizontal pipe with a uniform inlet axial velocity profile. Yao [12, 13] proposed an asymptotic solution of the developing entry flow by perturbing the solution of the developing flow in an unheated pipe. Without the aid of the large Prandtl number assumption Hishida et al. [14] gave numerical solutions for mixed laminar convection in the entrance region of a horizontal isothermal pipe. But the computer time reported, which is about 4 hr on a FACOM M-200 system for one case, is prohibitively large for engineering applications. Thus, only a few data for the cases of Pr = 0.71, Re = 100, and Gr = 5000 and 1000 were presented. Abou-Ellail and Morcos [15] studied buoyancy effects in the entrance region of a horizontal rectangular channel with uniform inlet axial velocity by using a numerical technique described by Patankar and Spalding [16].

The results obtained assuming large Prandtl number [4-9, 11] are obviously unsuitable for ordinary gases and fluids with small Prandtl numbers. The perturbation method [12, 13] is known to be practical only for limited situations. The numerical solutions [14] for the three-dimensional elliptic equations consume a large amount of computer time. To overcome these difficulties, the present investigation uses the vorticity-velocity equations [10] to study the combined free and forced laminar convection in the thermal entrance region of a horizontal rectangular channel without the assumptions of large Prandtl number and small Grashof number. The channel wall is heated with a uniform wall heat flux. The Prandtl numbers studied are 100, 10, 5, 2, 1, and 0.7. The Rayleigh numbers are 10^4, 3×10^4, 6×10^4, and 10^5.

Theoretical Analysis

Consider a steady fully developed laminar flow of a viscous fluid in a horizontal rectangular channel as shown in Fig. 1. A uniform wall heat flux is imposed at $Z \geq 0$. A pair of counterrotating vortices appears near the vertical walls. The axial velocity is reduced and the heat transfer rate is increased due to the formation of the vortices. The Boussinesq approximation is used to characterize the free convection effect. The ax-

[1] Present address: Associate Professor, Department of Mechanical Engineering, National Central University, Chungli, Taiwan.

Contributed by the Heat Transfer Division for publication in the JOURNAL OF HEAT TRANSFER. Manuscript received by the Heat Transfer Division August 16, 1985.

ial diffusion effect is neglected by using the high Peclet number assumption as presented in [4]. Referring to the coordinate system shown in Fig. 1, the following dimensionless variables and parameters are introduced

$$x=X/D_e,\quad y=Y/D_e,\quad z=Z/(\mathrm{Pr}\mathrm{Re}D_e),$$
$$u=U/U_c,\quad v=V/U_c,\quad w_f=W_f/\bar{W}_f,\quad w=W/(\mathrm{Ra}\bar{W}_f),$$
$$p=P/[\rho U_c\nu/D_e],\quad \theta=(T-T_0)/\theta_c,\quad \mathrm{Gr}=g\beta\theta_cD_e^3/\nu^2, \tag{1}$$
$$\mathrm{Pr}=\nu/\alpha,\quad \mathrm{Ra}=\mathrm{PrGr},\quad \mathrm{Re}=\bar{W}_fD_e/\nu,\quad \mathrm{Pe}=\mathrm{PrRe}$$

where $D_e = 4A/S$, $U_c = \mathrm{Gr}\nu/D_e$, and $\theta_c = q_wD_e/k$. The following governing equations can be obtained

$$\frac{\partial u}{\partial x}+\frac{\partial v}{\partial y}+\frac{\partial w}{\partial z}=0 \tag{2}$$

$$\mathrm{Gr}\left(u\frac{\partial u}{\partial x}+v\frac{\partial u}{\partial y}+w\frac{\partial u}{\partial z}\right)+\frac{1}{\mathrm{Pr}}w_f\frac{\partial u}{\partial x}=-\frac{\partial p}{\partial x}+\nabla^2u \tag{3}$$

$$\mathrm{Gr}\left(u\frac{\partial v}{\partial x}+v\frac{\partial v}{\partial y}+w\frac{\partial v}{\partial z}\right)+\frac{1}{\mathrm{Pr}}w_f\frac{\partial v}{\partial z}=-\frac{\partial p}{\partial y}+\nabla^2v+\theta \tag{4}$$

$$\mathrm{Gr}\left(u\frac{\partial w}{\partial x}+v\frac{\partial w}{\partial y}+w\frac{\partial w}{\partial z}\right)+\frac{1}{\mathrm{Pr}}\left(u\frac{\partial w_f}{\partial x}+v\frac{\partial w_f}{\partial y}+w_f\frac{\partial w}{\partial z}\right)=-\frac{1}{\mathrm{Pe}^2}\frac{\partial p}{\partial z}+\nabla^2w \tag{5}$$

$$\nabla^2w_f=-C \tag{6}$$

$$\mathrm{Ra}\left(u\frac{\partial\theta}{\partial x}+v\frac{\partial\theta}{\partial y}+w\frac{\partial\theta}{\partial z}\right)+w_f\frac{\partial\theta}{\partial z}=\nabla^2\theta \tag{7}$$

where $\nabla^2 = \partial^2/\partial x^2 + \partial^2/\partial y^2$, $C = -(D_e^2/\mu\bar{W}_f)\,\partial P_f/\partial Z$ = const. The value C is determined by considering a constraint $\bar{w}_f = 1$. It is noted that if both the large Prandtl number and small Grashof number assumptions are still retained, the left-hand side terms in the momentum equations (3)–(5) can be neglected. Furthermore, equation (5) yields solution $w = 0$ with a large Peclet number, and the continuity equation (2) becomes $\partial u/\partial x + \partial v/\partial y = 0$. Then the two-dimensional stream function is valid and the governing equations will be the same as those in [4]. Ramakrishna et al. [10] employed vorticity-velocity governing equations to study the laminar natural convection along vertical square ducts. Their approach can also be applied to the present problem to overcome the complexities of the three-dimensional fluid flow.

By introducing a vorticity function in the axial direction

$$\xi=\frac{\partial u}{\partial y}-\frac{\partial v}{\partial x} \tag{8}$$

the governing equations (2)–(4) can be reduced as follows:

$$\nabla^2u=\frac{\partial\xi}{\partial y}-\frac{\partial^2w}{\partial x\partial z} \tag{9}$$

$$\nabla^2v=-\frac{\partial\xi}{\partial x}-\frac{\partial^2w}{\partial y\partial z} \tag{10}$$

Nomenclature

A = cross-sectional area of a channel
a, b = width and height of a rectangular channel, respectively
C = $(D_e^2/\mu\bar{W}_f)\partial P_f/\partial Z$
D_e = equivalent hydraulic diameter = $4A/S$
Gr = Grashof number = $g\beta\theta_cD_e^3/\nu^2$
f = friction factor = $2\bar{\tau}_w/(\rho\bar{W}'^2)$
$f_1(z)$ = a function defined in equation (14)
g = gravitational acceleration
$\bar{h}$ = average heat transfer coefficient
k = thermal conductivity
M, N = number of divisions in X and Y directions, respectively
Nu = local Nusselt number = $\bar{h}D_e/k$
n = outward normal direction to the wall
P, P_f = pressure deviation and pressure for fully developed laminar flow before thermal entrance, respectively
p = dimensionless form of P
Pe = Peclet number = Pr•Re
q_w = uniform heat flux at wall
Pr = Prandtl number = ν/α
Ra = Rayleigh number = PrGr
Re = Reynolds number = $\bar{W}'D_e/\nu$
S = circumference of cross section
T = temperature
T_0 = uniform fluid temperature at entrance
U, V, W = velocity components in X, Y, Z directions due to buoyancy effect
u, v, w = dimensionless forms of U, V, and W
W_f = fully developed axial velocity before thermal entrance
w_f = dimensionless form of W_f
W' = axial velocity in the thermal entrance region = $W_f + W$
w' = dimensionless axial velocity = w_f + Ra•w
X, Y, Z = rectangular coordinates
x, y, z = dimensionless rectangular coordinates
α = thermal diffusivity
β = coefficient of thermal expansion
γ = aspect ratio of a rectangular channel = a/b
Δ = finite difference
ϵ = a prescribed error defined by equation (18)
θ = dimensionless temperature difference = $(T-T_0)/\theta_c$
θ_c = characteristic temperature = q_wD_e/k
μ = viscosity
ν = kinematic viscosity
ξ = axial-direction vorticity = $\partial u/\partial y - \partial v/\partial x$
ρ = density
τ = shear stress

Subscripts

c = characteristic quantity
f = fully developed quantity before thermal entrance
i, j = nodal point
w = value at wall
0 = condition for purely forced convection
1, 2 = definitions for Nusselt number

Superscript

$\bar{}$ = average value

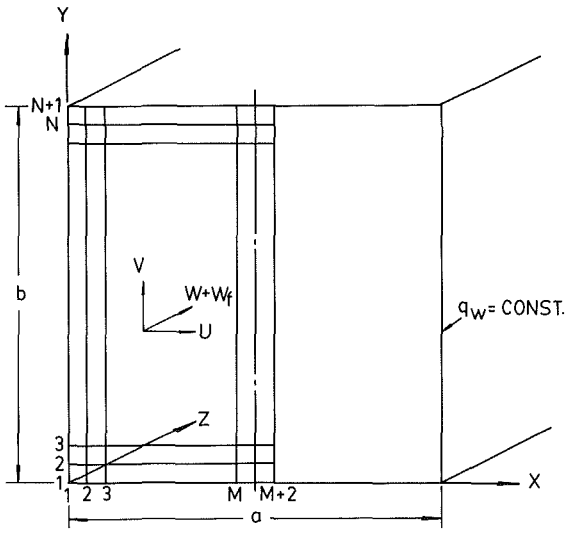

Fig. 1 Physical configuration and coordinates

$$\mathrm{Gr}\left(u\frac{\partial\xi}{\partial x}+v\frac{\partial\xi}{\partial y}+w\frac{\partial\xi}{\partial z}+\frac{\partial u}{\partial x}\xi+\frac{\partial v}{\partial y}\xi+\frac{\partial w}{\partial y}\frac{\partial u}{\partial z}-\frac{\partial w}{\partial x}\frac{\partial v}{\partial z}\right)+\frac{1}{\mathrm{Pr}}\left(\frac{\partial w_f}{\partial y}\frac{\partial u}{\partial z}-\frac{\partial w_f}{\partial x}\frac{\partial v}{\partial z}+w_f\frac{\partial\xi}{\partial z}\right)=\nabla^2\xi-\frac{\partial\theta}{\partial x} \tag{11}$$

The pressure terms in equations (3) and (4) are eliminated by cross differentiation and a single equation (11) is obtained. Equations (9) and (10) can be derived by a combination of the continuity equation (2) and the differentiation of vorticity function (8). Equations (9) and (10) are used for the solutions of u and v in the transverse directions. Because of symmetry, it suffices to solve the problem in half the rectangular region such as that shown in Fig. 1. The boundary conditions are:

$$\begin{aligned} &u=v=w_f=w=0 \quad \text{and} \quad \partial\theta/\partial n=1 \text{ at walls}\\ &u=\partial v/\partial x=\partial w/\partial x=\partial w_f/\partial x=\partial\theta/\partial x=0\\ &\qquad\qquad \text{at symmetry plane } X=a/2\\ &\theta=u=v=w=\xi=0 \text{ at entrance } Z=0 \end{aligned} \tag{12}$$

After the developing velocity and temperature fields along the axial direction are obtained, the computations of the local friction factor and the Nusselt number are of practical interest. Following the usual definitions, the expressions for the product of the friction factor and the Reynolds number $f\cdot\mathrm{Re}$ and the Nusselt number Nu can be written based on the overall force balance for an axial length dZ and the temperature gradient at the wall. The results are:

$$(f\mathrm{Re})_0=2\bar{\tau}_w/(\rho\bar{W}_f^2)\cdot(D_e\bar{W}_f/\nu)=D_e^2(\partial P_f/\partial Z)/(2\rho\nu\bar{W}_f) \tag{13}$$

$$f\mathrm{Re}/(f\mathrm{Re})_0=1+(\partial P/\partial Z)/(\partial P_f/\partial Z)=1+\mathrm{Ra}\cdot f_1(z)/C \tag{14}$$

$$(\mathrm{Nu})_1=\bar{h}D_e/k=1/\overline{w'(\bar{\theta}_w-\theta)} \text{ with } \bar{w}'=1 \tag{15}$$

where the subscript 0 denotes the quantity for purely forced convection, C is determined from equation (6) with the constraint $\bar{w}_f=1$, $f_1(z)=-(\partial p/\partial z)/\mathrm{Pe}^2$ is the pressure term in the axial momentum equation (5), and $w'=w_f+\mathrm{Ra}\cdot w$. If both the large Prandtl number and small Grashof number assumptions remained, the value for the mean axial velocity is kept practically unchanged from that of the purely forced convection [17, 18]. Thus, w will be identically zero and $w'=w_f$ as shown in [4].

The Nusselt number may also be obtained by considering overall energy balance for the axial length dZ as

$$(\mathrm{Nu})_2=\overline{w'(\partial\theta/\partial z)}/4[\overline{w'(\bar{\theta}_w-\theta)}] \tag{16}$$

Simpson's rule is used to compute the average quantities indicated above. It is noted that the arithmetic mean of $(\mathrm{Nu})_1$ and $(\mathrm{Nu})_2$ was taken as the value for the Nusselt number in [4–8], but in [19, 20] the definition $(\mathrm{Nu})_1$ was used. Due to better accuracy only the value of $(\mathrm{Nu})_1$ is used in the present study.

Numerical Method of Solution

The solution for the unknowns u, v, w, w_f, ξ, and θ in equations (5)–(11) satisfying boundary conditions (12) is a matter of considerable mathematical difficulty. A numerical finite-difference scheme is developed in this paper to obtain simultaneously the solution of the set of equations (5)–(11). The procedure is:

1 The Poisson equation (6) with the constraint $\bar{w}_f=1$ for the fully developed velocity w_f is solved independently using a point SOR method. Then the values $\partial w_f/\partial x$ and $\partial w_f/\partial y$ are computed at each grid point.

2 The initial values for velocity components u, v, w, and temperature difference θ are assigned zero at the entrance, $z=0$. Furthermore, $\xi=0$ at $z=0$ results from equation (8).

3 With the results of $\partial w_f/\partial x$ and $\partial w_f/\partial y$ obtained from step 1, the values of $\partial u/\partial z$ and $\partial v/\partial z$ computed by using a two-point backward difference, and the known values of u, v, w, θ, $\partial\theta/\partial x$, ξ, and $-(\partial p/\partial z)/\mathrm{Pe}^2$, the new values of ξ, w, and θ at the interior points of the next axial position are obtained from equations (11), (5), and (7), respectively, by the Du Fort-Frankel method [8].

4 Check if the mean axial velocity $\bar{w}'$ is equal to 1. Otherwise, adjust the value of pressure term $f_1(z)=(\partial p/\partial z)/\mathrm{Pe}^2$ in equation (5) to meet the requirement of constant flow rate. Thus the values of local $f\mathrm{Re}$ in equation (13) along the channel can be determined.

5 By applying the boundary condition $\partial\theta/\partial n=1$ and $\nabla^2\theta=0$ at walls, the wall temperature can be computed by iteration after the temperatures in the interior region are found.

6 The values of $\partial^2 w/\partial z\partial x$, $\partial^2 w/\partial z\partial y$, $\partial\xi/\partial y$, and $\partial\xi/\partial x$ are calculated from the results of step 3 by using the backward difference axially and a central difference in transverse directions. The elliptic-type equations (9) and (10) are solved for u and v by iteration. During the iteration process, the values of vorticity on the boundary are evaluated simultaneously with u and v in the interior region. After trying several schemes, the boundary vorticity on the vertical wall is evaluated as shown in Fig. 2. The result is

$$\xi_{1,j}=-2v_{2,j}/\Delta x+(u_{2,j+1}-u_{2,j-1})/(2\Delta y)-\xi_{2,j} \tag{17}$$

It is noted that the boundary vorticity on the horizontal walls can also be evaluated in a similar expression.

7 Steps 3–6 are repeated until the following convergence criterion is satisfied for the velocity components u and v

$$\epsilon=\Sigma|(u_{i,j}^{(n+1)}-u_{i,j}^{(n)})/u_{i,j}^{(n+1)}|/(M\times N)<5\times10^{-4} \tag{18}$$

where M and N are the number of divisions in the X and Y directions, respectively.

8 The axial step size Δz range is $10^{-4}\sim 4\times10^{-4}$. By numerical experiments, the step size Δz is selected depending on the magnitude of the Prandtl number.

A cross-sectional mesh size ($M\times N$) of 14×28 is used for the square channel. The accuracy by using this mesh size was verified in the previous work [21]. The required computer time for one set of Pr and Ra is approximately 350–600 s on a CYBER-172 system.

Table 1 Numerical experiment for Δz

Δz \ z	0.01	0.03	0.05	0.07	0.1
2×10^{-4}	4.759*	4.191	4.561	4.465	4.408
4×10^{-4}	4.754	4.176	4.57	4.462	4.406

*These are Nusselt numbers for the case of Pr = 0.7 and Ra = 6×10^4.

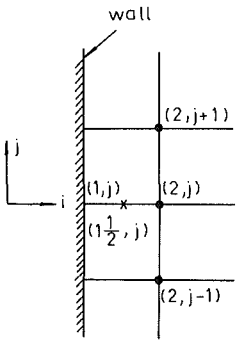

$$\xi_{1\,\frac{1}{2},j} = \frac{1}{2}(\xi_{1,j}+\xi_{2,j}) = \frac{1}{2\Delta y}(u_{1\,\frac{1}{2},j+1} - u_{1\,\frac{1}{2},j-1}) - \frac{v_{2,j}}{\Delta x}$$

$$\text{and } u_{1\,\frac{1}{2},j+1} = \frac{1}{2}u_{2,j+1}$$

$$u_{1\,\frac{1}{2},j-1} = \frac{1}{2}u_{2,j-1}$$

Fig. 2 Evaluation of vorticity at the boundary

Results and Discussion

A numerical experiment was carried out to ensure the independence of the numerical result on the mesh size Δz in the axial direction. Table 1 presents Nu computed by using mesh sizes $\Delta z = 4\times10^{-4}$ and 2×10^{-4} at some selected axial positions for the case of Pr = 0.7 and Ra = 6×10^4. It is seen that the deviations of Nu at each axial position are less than 0.36 percent. This independence of the numerical result on Δz also reveals that the two-point backward difference, employed in the numerical method steps 3 and 6, yields only a small error.

Although the presentation of the local friction factors and the Nusselt numbers in the thermal entrance region is a major goal here, developments of axial velocity and temperature are of engineering interest and useful in clarifying the heat transfer mechanism. The temperature profiles along the vertical and horizontal center plane at various axial positions are shown in Fig. 3 for the case of Pr = 0.7 and 10, and Ra = 10^5. The gradual development of the temperature profile and the constant temperature gradient normal to the wall are clearly observed. The secondary flow carries the fluid heated by the lower horizontal wall, the vertical side wall, and then the upper horizontal wall. The temperature of the fluid rises higher and higher. Therefore the temperature distributions along the vertical center plane $X = a/2$ develop from the case of nearly symmetric with respect to the horizontal center plane $Y = b/2$ at $z = 0.005$ to the cases of gradually increasing temperature difference between the top and bottom walls at $z = 0.01 \sim 0.045$ by the development of secondary flow. Furthermore, the temperature distribution along the horizontal center plane exhibits a reverse temperature gradient $\partial\theta/\partial x$ in the central region after reaching $z \geq 0.03$. This phenomenon will contribute to the decrease of intensity of secondary flow. The effect of Prandtl number on the development of the temperature distribution is of considerable interest. Therefore, the temperature profiles for the case of Pr = 10 and Ra = 10^5 are also shown by dashed lines in Fig. 3 for comparison. It is seen

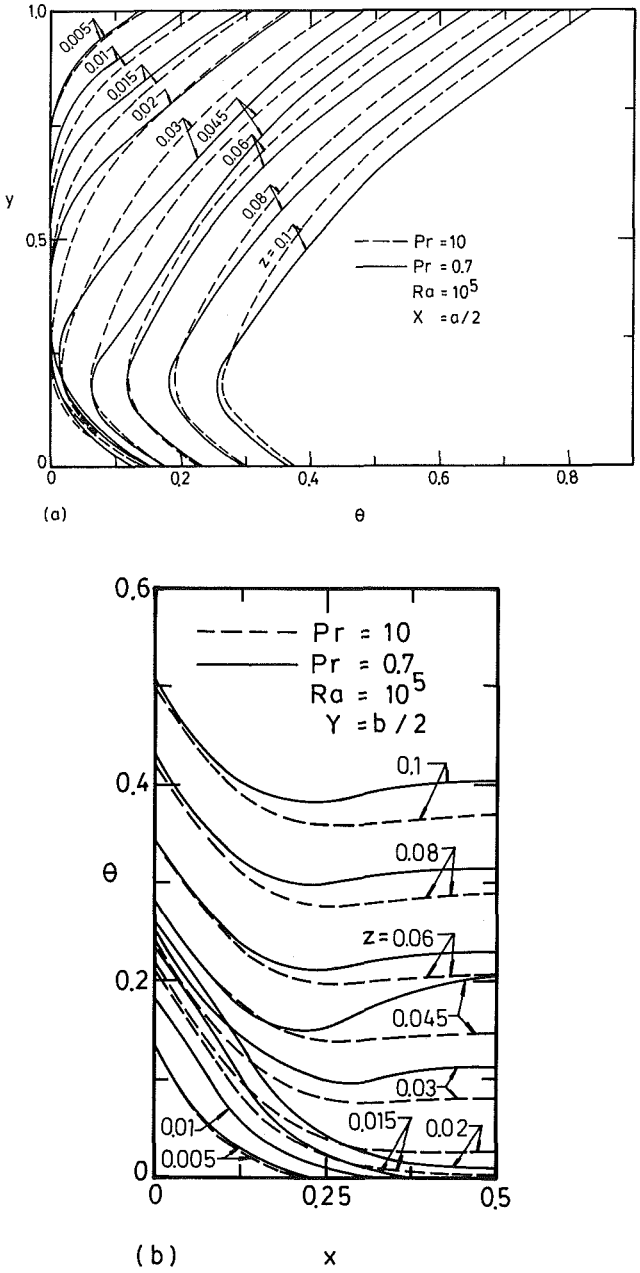

Fig. 3 Development of temperature along: (a) $X = a/2$ and (b) $Y = b/2$ for Ra = 10^5, Pr = 0.7 and 10

that as the Prandtl number increases, the temperature difference between the top and bottom horizontal walls decreases. This phenomenon is due to the weak secondary flow or the small Grashof number Gr = Ra/Pr, which results from the larger Prandtl number. Besides, the reverse temperature gradient $\partial\theta/\partial x$ along the horizontal center plane $Y = b/2$ in the central region also appears at $z \cong 0.03$.

Figure 4 shows the development of axial velocity along the vertical center plane $X = a/2$ for the case of Pr = 0.7 and Ra = 10^5 at various axial positions. The axial velocity profile is symmetric with respect to the horizontal central plane $Y = b/2$ at the entrance $z = 0$. With the natural convection effect, this symmetry is lost and the locations of the maximum axial velocity move toward the bottom horizontal wall as z increases from 0 to 0.045. Then the locations of the maximum w' remained at nearly the same place as z increases to 0.1. As noted in Fig. 3(b), the reverse temperature gradient $\partial\theta/\partial x$, which appeared at $z \geq 0.03$, yields the decrease of intensity of sec-

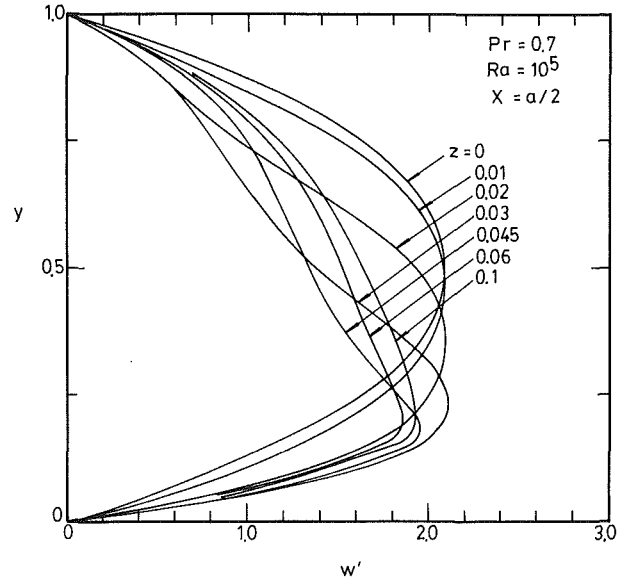

Fig. 4 Development of axial velocity along $X = a/2$ for Pr = 0.7 and Ra = 10^5

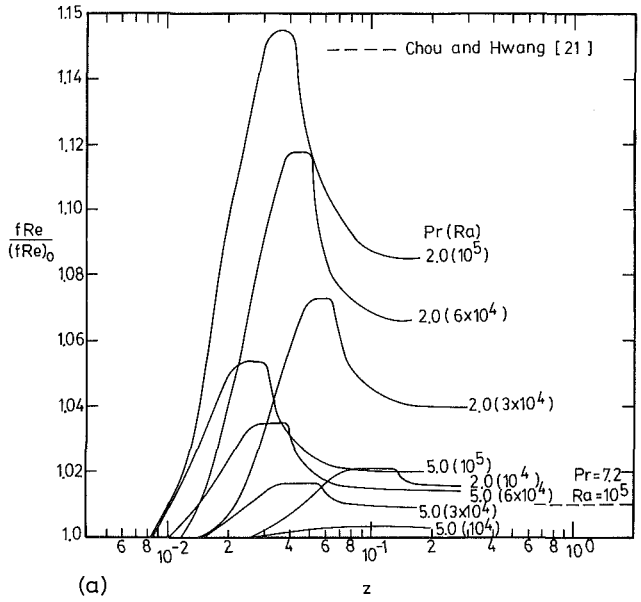

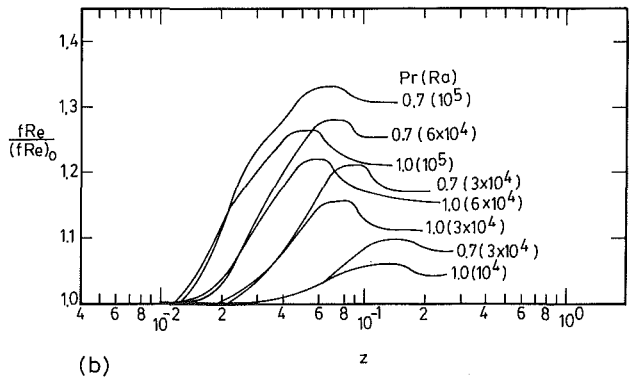

Fig. 5 Local friction factor versus z for various Prandtl numbers in a square channel

ondary flow. The strong secondary flow causes the axial velocity distribution for $z = 0.02$ to depart significantly from that of $z = 0.01$. As $z \geq 0.03$, owing to the decrease of intensity of secondary flow and the effect of gradual velocity and temperature developments along the channel, the axial velocity distributions become more and more uniform.

The flow characteristics of the system are usually presented by the friction factor ratio $f\mathrm{Re}/(f\mathrm{Re})_0$, where the subscript 0 denotes the quantity for purely forced convection. Figures 5(*a*, *b*) show the values of $f\mathrm{Re}/(f\mathrm{Re})_0$ versus dimensionless axial distance z for the cases of Pr = 5 and 2, and Pr = 1 and 0.7 with Ra = 10^5, 6×10^4, 3×10^4, and 10^4, respectively. The curves for Pr = 10 and 100 are not shown here because the increases in the values of $f\mathrm{Re}/(f\mathrm{Re})_0$ are usually less than 1 percent in the present study. The dashed line indicating a value of 1.01 shown in Fig. 5(*a*) is the result presented in Chou and Hwang [23] for the case of Pr = 7.2 and Ra = 10^5 in the fully developed region of a horizontal square channel with uniform wall heat flux. The value 1.01 can be checked exactly with the same set of parameters by the present vorticity-velocity method. It is seen that the curves with higher Pr fall below those of lower Pr for the same value of Ra. The curves of higher Ra lie above those of lower Ra for the same value of Pr. By a further comparison, it is also noted that even for the same value of Gr = Ra/Pr, the curves with higher values of Pr give lower values of $f\mathrm{Re}/(f\mathrm{Re})_0$ when $z > 0.1$ than those with a lower value of Pr. For example, the curve for Pr = 2.0 and Ra = 6×10^4 gives $f\mathrm{Re}/(f\mathrm{Re})_0 = 1.068$ at $z = 0.1$, but the curve of Pr = 1.0 and Ra = 3×10^4 gives $f\mathrm{Re}/(f\mathrm{Re})_0 = 1.108$ at the same axial position. Furthermore, the curve for Pr = 1.0 and Ra = 10^5 gives Gr = 10^5 and $f\mathrm{Re}/(f\mathrm{Re})_0 = 1.214$ at $z = 0.2$, but the curve for Pr = 0.7 and Ra = 6×10^4 gives a lower value of Gr, say 8.571×10^4, and a higher value of $f\mathrm{Re}/(f\mathrm{Re})_0$, say 1.254. The variation of the local friction factor ratio along the channel shows that buoyancy effects are negligible up to a certain entry length z, depending mainly on the magnitude of the Rayleigh number and also the Prandtl number. The curves branch out from the curve for purely forced convection and after reaching a maximum value rapidly approach a limiting value when the velocity profile becomes fully developed.

The local Nusselt number ratio $\mathrm{Nu}/(\mathrm{Nu})_0$ versus z for the cases of Ra = 10^5 and 3×10^4 with Pr = 100, 10, 5, 2, 1, and 0.7 is shown in Fig. 6(*a*). The other two sets of curves of $\mathrm{Nu}/(\mathrm{Nu})_0$ are shown in Fig. 6(*b*) for the cases of Ra = 6×10^4 and 10^4. The present numerical results agree well with the known limiting Nusselt number $(\mathrm{Nu})_0 = 3.091$ [4, 22] for the fully developed case. One can observe that the buoyancy effect is practically negligible when Ra < 10^3 for all values of Pr. For a greater Rayleigh number the natural convection effect appears at a certain distance z from the entrance depending mainly on the magnitude of Rayleigh number. For each curve shown in Fig. 6, a minimum local Nusselt number exists. The occurrence of the minimum Nusselt number is a result of combined entrance and natural convection effects. With further comparison with Fig. 5, one can observe that the locations in axial length z of maximum local $f\mathrm{Re}/(f\mathrm{Re})_0$ lie farther downstream than those of minimum local $\mathrm{Nu}/(\mathrm{Nu})_0$.

The results of Cheng et al. [4] are also shown by dashed lines in Fig. 6 for comparison. It is seen that the results of Cheng et al. lie close to but slightly above the present work for Pr = 100. The difference between them comes from the different computation in the Nusselt number by using $[(\mathrm{Nu})_1 + (\mathrm{Nu})_2]/2$ in [4] and $(\mathrm{Nu})_1$ here. One can observe that the curves with lower values of Pr fall below that with higher values of Pr for a given Rayleigh number. This phenomenon can also be seen in experimental results of Morcos and Bergles [19] and numerical results of Patankar et al. [20]. The question about the range of Prandtl number in which the assumption of large Prandtl number is valid for this problem can be clarified. Cheng et al. [4] proposed a range of Prandtl number from the order of 10 to infinity. In Fig. 6 one can see that the

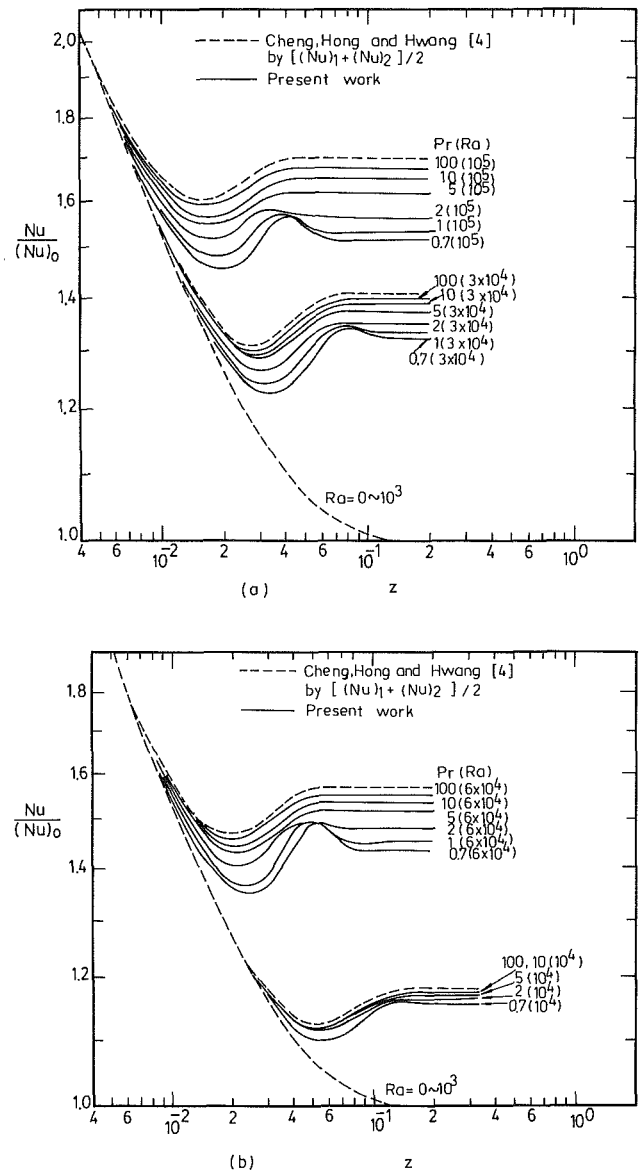

Fig. 6 Local Nusselt number versus z for various Prandtl numbers in a square channel

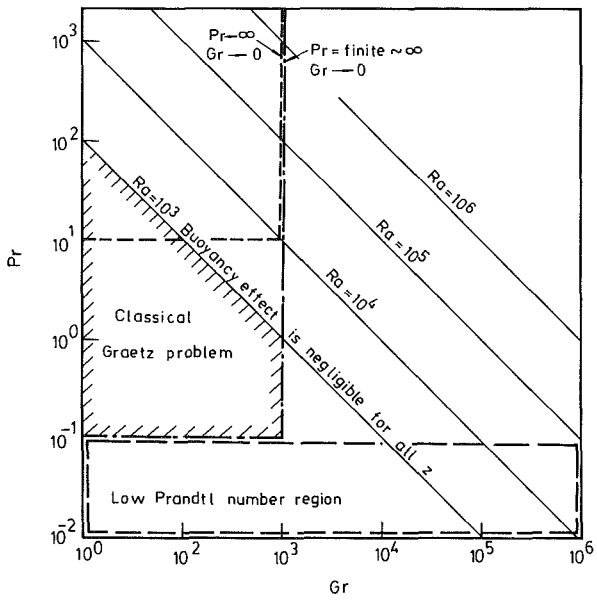

Fig. 7 Regimes with and without the assumptions of Prandtl number and Grashof number for thermal entrance flow in horizontal ducts

curve of Pr = 10 coincides with that of Pr = 100 for the case of Ra = 10^4. The differences of Nusselt number in the fully developed region between the curves of Pr = 10 and 100 are 0.036 for Ra = 3×10^4, 0.057 for Ra = 6×10^4, and 0.076 for Ra = 10^5. It is seen that the difference increases with increase in Ra. Therefore the range over which large Prandtl number assumption is valid for this problem depends on the values of Ra.

To identify the region of validity of previous analytical investigations and the present solutions, Fig. 7 presents the regimes with and without the assumptions of Prandtl number and Grashof number for thermal entrance flow in horizontal ducts. It is well noted that heat conduction in the axial direction cannot be neglected, especially in the thermal entry region for low Prandtl number fluids. Hsu [24] is an example among the many investigations in this region. The slashed area indicates the classical Graetz problem in which the natural convection effect is negligible. There are many investigators who used the assumptions of large Prandtl number and small Grashof number [4–9] and the corresponding regime of Pr→∞ and Gr→0 is marked by a short dashed line within the region of Pr ≥ 10 and Gr ≤ 10^3. The ranges of parameters studied in the present study are Pr = 0.7 ~ 10^2 and Ra = 0 ~ 10^5. Furthermore, the solution for higher Grashof number cases may also be approached by the same numerical method and the aid of a power-law scheme in the formulation of [9, 21, 25].

Concluding Remarks

1 A numerical scheme called the vorticity-velocity method is applied to study the natural convection effect on the Graetz problem without the aid of large Prandtl number and small Grashof number assumptions in a horizontal rectangular channel with uniform wall heat flux. This method is used to solve the parabolic-elliptic type governing equations. The values of vorticity on the wall can be evaluated simultaneously with the velocity components u and v as shown in equation (17).

2 The secondary flow distorts the axial velocity and temperature profiles with the maximum velocity and the minimum fluid temperature displaced toward the bottom horizontal wall.

3 Both the variations of the secondary flow, presented by the friction factor ratio, and the local Nusselt number show that the natural convection effect is negligible up to a certain axial downstream position depending mainly on the magnitude of the Rayleigh number and also the Prandtl number. When the Prandtl number is fixed, the natural convection effect appears earlier with an increase in Rayleigh number. While the Rayleigh number is fixed, the natural convection effect also appears earlier for the curves of local Nusselt number with an increase in Prandtl number, but the trend is reversed for the curves of local friction factor. Each curve of the friction factor ratio increases from zero, and after reaching a maximum value, the curve rapidly approaches a limiting value when the velocity profile becomes fully developed. Each curve of the Nusselt number then branches out from the curve for the purely forced convection and after reaching a minimum value, the curve approaches a limiting asymptotic value when the temperature profile becomes unchanged. It is noted that the variations in the ratio $f\mathrm{Re}/(f\mathrm{Re})_0$ were not realized with the assumptions of large Pr and small Gr made in the existing literature.

4 Cheng et al. [4] proposed that in the range of Prandtl number from the order of 10 to infinity, the assumption of

large Prandtl number is valid. The present numerical solutions of these fairly complete governing equations show clearly that the curve of local Nusselt number for Pr = 10 coincides with that for Pr = 100 for the case of Ra = 10^4 and the deviation between these two curves increases slightly with increase in the Rayleigh number.

Acknowledgments

The authors would like to acknowledge the National Science Council of the ROC for its support of the present work through project NSC 74-0401-E007-005.

References

1 Dennis, S. C. R., Mercer, A. McD., and Poots, G., "Forced Heat Convection in Laminar Flow Through Rectangular Ducts," *Q. Appl. Math.*, Vol. 17, 1959, pp. 285–297.

2 Sparrow, E. M., and Siegel, R., "Application of Variational Methods to the Thermal Entrance Region of Ducts," *International Journal of Heat and Mass Transfer*, Vol. 1, 1960, pp. 161–172.

3 Montgomery, S. R., and Wibulswas, P., "Laminar Flow Heat Transfer in Ducts of Rectangular Cross Section," *Proceedings of the Third International Heat Transfer Conference*, Vol. 1, AIChE, New York, 1966, pp. 104–112.

4 Cheng, K. C., Hong, S. W., and Hwang, G. J., "Buoyancy Effects on Laminar Heat Transfer in the Thermal Entrance Region of Horizontal Rectangular Channels With Uniform Wall Heat Flux for Large Prandtl Number Fluid," *International Journal of Heat and Mass Transfer*, Vol. 15, 1972, pp. 1819–1836.

5 Cheng, K. C., and Ou, J. W., "Free Convection Effects on Graetz Problem for Large Prandtl Number Fluids in Horizontal Tubes With Uniform Wall Heat Flux," *Proceedings of the Fifth International Heat Transfer Conference*, Vol. 3, Tokyo, 1974, pp. 159–163.

6 Hong, S. W., Morcos, S. M., and Bergles, A. E., "Analytical and Experimental Results for Combined Forced and Free Laminar Convection in Horizontal Tubes," *Proceedings of the Fifth International Heat Transfer Conference*, Vol. 3, Tokyo, 1974, pp. 154–158.

7 Ou, J. W., Cheng, K. C., and Lin, R. C., "Natural Convection Effects on Graetz Problem in Horizontal Rectangular Channels With Uniform Wall Temperature for Large Pr," *International Journal of Heat and Mass Transfer*, Vol. 17, 1974, pp. 835–843.

8 Ou, J. W., and Cheng, K. C., "Natural Convection Effects on Graetz Problem in Horizontal Isothermal Tubes," *International Journal of Heat and Mass Transfer*, Vol. 20, 1977, pp. 953–960.

9 Hwang, G. J., and Lin, M. J., "Natural Convection Effects on Laminar Heat Transfer in the Thermal Entrance Region of Horizontal Isothermal Tube," *Journal of the Chinese Institute of Engineers*, Vol. 8, 1985, pp. 343–355.

10 Ramakrishna, K., Rubin, S. G., and Khosla, P. K., "Laminar Natural Convection Along Vertical Square Ducts," *Numer. Heat Transfer*, Vol. 5, 1982, pp. 59–79.

11 Hieber, C. A., and Sreenivasan, S. K., "Natural Convection Effects on Graetz Problem in Horizontal Isothermal Tubes," *International Journal of Heat and Mass Transfer*, Vol. 17, 1974, pp. 1337–1348.

12 Yao, L. S., "Free-Forced Convection in the Entry Region of a Heated Straight Pipe," ASME JOURNAL OF HEAT TRANSFER, Vol. 100, 1978, pp. 212–219.

13 Yao, L. S., "Entry Flow in a Heated Straight Tube," *Journal of Fluid Mechanics*, Vol. 88, 1978, pp. 465–483.

14 Hishida, M., Nagano, Y., and Montesclaros, M. S., "Combined Forced and Free Convection in the Entrance Region of an Isothermally Heated Horizontal Pipe," ASME JOURNAL OF HEAT TRANSFER, Vol. 104, 1982, pp. 152–159.

15 Abou-Ellail, M. M. M., and Morcos, S. M., "Buoyancy Effects in the Entrance Region of Horizontal Rectangular Channels," ASME JOURNAL OF HEAT TRANSFER, Vol. 105, 1983, pp. 924–928.

16 Patankar, S. V., and Spalding, D. B., "A Calculation Procedure for Heat, Mass and Momentum Transfer in Three-Dimensional Parabolic Flows," *International Journal of Heat and Mass Transfer*, Vol. 15, 1972, pp. 1787–1806.

17 Cheng, K. C., Hwang, G. J., and Akiyama, M., "On a Simple Correlation for Prandtl Number Effect on Forced Convective Heat Transfer With Secondary Flow," *International Journal of Heat and Mass Transfer*, Vol. 15, 1972, pp. 172–175.

18 Hwang, G. J., and Cheng, K. C., "Boundary Vorticity Method for Convective Heat Transfer With Secondary Flow – Application to the Combined Free and Forced Laminar Convection in Horizontal Tubes," *Heat Transfer 1970. Proceedings of the Fourth International Heat Transfer Conference*, Vol. 4, NC 3.5, Elsevier Publishing Company, Amsterdam, 1970.

19 Morcos, S. M., and Bergles, A. E., "Experimental Investigation of Combined Forced and Free Laminar Convection in Horizontal Tubes," ASME JOURNAL OF HEAT TRANSFER, Vol. 97, 1975, pp. 212–221.

20 Patankar, S. V., Ramadhyani, S., and Sparrow, E. M., "Effect of Circumferentially Nonuniform Heating on Laminar Combined Convection in a Horizontal Tube," ASME JOURNAL OF HEAT TRANSFER, Vol. 100, 1978, pp. 63–70.

21 Chou, F. C., and Hwang, G. J., "Combined Free and Forced Laminar Convection in Horizontal Rectangular Channels for High ReRa," *Canadian Journal of Chemical Engineering*, Vol. 62, 1984, pp. 830–836.

22 Shah, R. H., and London, A. L., "Thermal Boundary Conditions and Some Solutions for Laminar Duct Flow Forced Convection," ASME JOURNAL OF HEAT TRANSFER, Vol. 96, 1974, pp. 159–165.

23 Chou, F. C., and Hwang, G. J., "Effect of Wall Conduction on Combined Free and Forced Laminar Convection in Horizontal Rectangular Channels," ASME 23rd National Heat Transfer Conference, Denver, CO, 1985.

24 Hsu, C. J., "An Exact Analysis of Low Peclet Number Thermal Entry Region Heat Transfer in Transversely Nonuniform Velocity Fields," *AIChE Journal*, Vol. 17, 1971, pp. 732–740.

25 Patankar, S. V., *Numerical Heat Transfer and Fluid Flow*, McGraw-Hill-Hemisphere, New York, 1980.

S. L. Lee[1]
Department of Power Mechanical Engineering, National Tsing-Hua University, Hsinchu, Taiwan, Republic of China

T. S. Chen
Fellow ASME

B. F. Armaly
Mem. ASME

Department of Mechanical and Aerospace Engineering, University of Missouri—Rolla, Rolla, MO 65401

Mixed Convection Along Vertical Cylinders and Needles With Uniform Surface Heat Flux

Mixed convection along vertical cylinders and needles with uniform surface heat flux is investigated for the entire mixed convection regime. A single modified buoyancy parameter χ and a single curvature parameter Λ are employed in the analysis such that a smooth transition from pure forced convection ($\chi = 1$) to pure free convection ($\chi = 0$) can be accomplished. For large values of the curvature parameter and/or Prandtl number, the governing transformed equations become stiff. Thus, a numerically stable finite-difference method is employed in the numerical solution in conjunction with the cubic spline interpolation scheme to overcome the difficulties that arise from the stiffness of the equations. Local Nusselt numbers are presented for $0.1 \le Pr \le 100$ that cover $0 \le \chi \le 1$ ($\infty \ge \Omega_x \ge 0$) and $0 \le \Lambda \le 50$. For needles ($\Lambda \ge 5$), the local Nusselt numbers $Nu_x/(Re_x^{1/2} + Gr_x^{*1/5})$ are found to be nearly independent of the buoyancy parameter χ. Correlation equations for the local Nusselt numbers are also presented.

Introduction

There are only a few papers in the literature that deal with an analysis of mixed convection along vertical cylinders and needles. Chen and Mucoglu (1975, 1976) were the first to study such a problem for both heating conditions of uniform wall temperature and uniform surface heat flux and obtained their solutions by using the local nonsimilarity method. In the case of uniform surface heat flux, they used the curvature parameter $\Lambda_1 = 4(x/r_0)\mathrm{Re}_x^{-1/2}$ as the nonsimilarity variable for given values of the buoyancy parameter $\Omega_x = \mathrm{Gr}_x^*/\mathrm{Re}_x^{5/2}$. Numerical results were presented in the range of $0 \le \Omega_x \le 1.5$ and $0 \le \Lambda_1 \le 4$ for a Prandtl number of Pr = 0.7. Recently, Bui and Cebeci (1985) worked on the same problem for the case of uniform wall temperature. They employed a finite difference method based on the central difference scheme (Keller and Cebeci, 1972) to solve the system of equations and obtained results for values of curvature parameter $\Lambda_2 = 2(x/r_0)\mathrm{Re}_x^{-1/2}$ between 0 and 15.1 and $0.1 \le \mathrm{Pr} \le 10$. Their results, however, have large errors at large values of Λ_2 (see Lee et al., 1986b).

It is noted that the analyses by Chen and Mucoglu (1975, 1976) and Bui and Cebeci (1985) deal with the effect of buoyancy force on forced convection. No study has been performed to analyze the effect of forced flow on free convection along a vertical cylinder. The purpose of the present paper is to perform a study of the same flow configuration under the uniform surface heat flux condition for the entire regime of mixed convection, from pure forced convection at one end to pure free convection at the other, by employing a single modified buoyancy parameter χ and a single curvature parameter Λ. The modified buoyancy parameter χ spans between 0 and 1, where $\chi = 1$ corresponds to pure forced convection ($\Omega_x = 0$) and $\chi = 0$ to pure free convection ($\Omega_x = \infty$). The range of Prandtl numbers considered is $0.1 \le \mathrm{Pr} \le 100$ and the curvature parameter Λ covered exceeds 50. Thus, the present analysis can be applied particularly well to slender cylinders or needles. To overcome numerical difficulties that arise because of large Λ and Pr values encountered, a finite-difference method based on the weighting function scheme proposed by Lee et al. (1986a) along with the cubic spline interpolation technique (Burden and Faires, 1985) was employed in the numerical solution. A related study of the problem for the case of uniform wall temperature has been reported elsewhere (Lee et al., 1986b).

Analysis

Consider a vertical cylinder of radius r_0 which is aligned parallel to a uniform, laminar free stream with velocity u_∞ and temperature T_∞. A constant heat flux q_w is maintained at the surface of the cylinder. By employing the boundary layer approximations, the conservation equations for a Boussinesq fluid can be written as

$$\frac{\partial}{\partial x}(ru) + \frac{\partial}{\partial r}(rv) = 0 \tag{1}$$

$$u\frac{\partial u}{\partial x} + v\frac{\partial u}{\partial r} = \pm g\beta(T - T_\infty) + \nu\frac{1}{r}\frac{\partial}{\partial r}\left(r\frac{\partial u}{\partial r}\right) \tag{2}$$

$$u\frac{\partial T}{\partial x} + v\frac{\partial T}{\partial r} = \alpha\frac{1}{r}\frac{\partial}{\partial r}\left(r\frac{\partial T}{\partial r}\right) \tag{3}$$

The associated boundary conditions are

$$u(x, r_0) = v(x, r_0) = \partial T(x, r_0)/\partial r + q_w/k = 0$$
$$u(x, \infty) - u_\infty = T(x, \infty) - T_\infty = 0 \tag{4}$$

At the leading edge, the flow and thermal boundary layer thicknesses are assumed to be zero, i.e., $u(0, r) = u_\infty$ and $T(0, r) = T_\infty$. The positive sign in equation (2) applies to upward-forced flow and the negative sign to downward-forced flow.

To transform equations (1)–(4), one introduces the stream function and the dimensionless temperature

$$\psi = \nu r_0(x/\delta)f(\xi, \eta), \qquad \delta = x/(\mathrm{Re}_x^{1/2} + \mathrm{Gr}_x^{*1/5}),$$
$$\theta = (T - T_\infty)/T_c, \qquad T_c = q_w\delta/k \tag{5}$$

along with the dimensionless variables

$$\xi = \xi(x), \qquad \eta = (r^2 - r_0^2)/2r_0\delta,$$
$$\Lambda = 2\delta/r_0, \qquad \chi = (1 + \Omega_x^{1/5})^{-1}, \tag{6}$$
$$\Omega_x = \mathrm{Gr}_x^*/\mathrm{Re}_x^{5/2}, \qquad m = (x/\xi)(d\xi/dx)$$

The end result of the transformation leads to the following system of equations

[1]This work was conducted when S. L. Lee was a Ph.D. candidate at the University of Missouri – Rolla.

Contributed by the Heat Transfer Division for publication in the JOURNAL OF HEAT TRANSFER. Manuscript received by the Heat Transfer Division March 4, 1986.

$$(1+\eta\Lambda)f''' + (\Lambda + af)f'' + bf'^2 + c\theta = d(f''\partial f/\partial\xi - f'\partial f'/\partial\xi) \quad (7)$$

$$(1+\eta\Lambda)\theta'' + (\Lambda + \mathrm{Pr}af)\theta' + \mathrm{Pr}ef'\theta = \mathrm{Pr}d(\theta'\partial f/\partial\xi - f'\partial\theta/\partial\xi) \quad (8)$$

where

$$a=(8-3\chi)/10, \quad b=-3(1-\chi)/5, \quad c=\pm(1-\chi)^5, \quad d=-m\xi, \quad e=-(2+3\chi)/10 \quad (9)$$

The associated boundary conditions are

$$f(\xi,0)=f'(\xi,0)=f'(\xi,\infty)-\chi^2=0$$
$$\theta'(\xi,0)+1=\theta(\xi,\infty)=0 \quad (10)$$

In equations (7) and (8), the primes stand for partial derivatives with respect to η, and the plus and minus signs in the definition of c, equation (9), denote, respectively, buoyancy-assisting and opposing flows. It is noted that the transformed x coordinate ξ is an arbitrary function of x. To maintain the number of parameters at a minimum, one defines the function $\xi(x)$

$$\xi = (x/r_0\mathrm{Re}_0)^{1/4} \quad (11)$$

such that

$$\Lambda = 2\xi^2\chi, \quad \chi=(1+\Omega_0\xi^{6/5})^{-1}, \quad m=1/4,$$
$$\Omega_0=(\mathrm{Gr}_0^*/\mathrm{Re}_0)^{1/5}=(g\beta q_w r_0^3/k\nu u_\infty)^{1/5}=\text{finite} \quad (12)$$

It is noted that the limiting case of $\Omega_0 = \infty$ corresponds to both pure free convection ($u_\infty = 0$) along a vertical cylinder and mixed convection along a vertical flat plate ($r_0 = \infty$). For pure free convection, $\xi(x)$ and its dependent variables are defined by

$$\xi=(x/r_0\mathrm{Gr}_0^*)^{1/10}, \quad m=1/10, \quad \Lambda=2\xi^2, \quad \chi=0 \quad (13)$$

whereas for mixed convection along a vertical flat plate, they are given by

$$\xi=\chi, \quad m=3(\chi-1)/10, \quad \Lambda=0 \quad (14)$$

In the case of $u_\infty \neq 0$ the modified buoyancy parameter χ, which is independent of the radius of the cylinder r_0, starts from unity at the leading edge where $x = 0$ and $\Omega_x = 0$, and keeps decreasing along the flow direction as the buoyancy parameter Ω_x increases (see equation (6)). In the pure free convection case, however, χ is zero for all x values. Also, for a finite value of r_0, the curvature parameter Λ increases from zero at $x = 0$ to infinity at $x = \infty$, as can be seen from equations (12) and (13) for both cases of $u_\infty \neq 0$ and $u_\infty = 0$. Physically speaking, in the case of $u_\infty \neq 0$ the flow field in the region $x << r_0$ approximates the Blasius flow over a flat plate, because near the leading edge the thickness of the boundary layer is much smaller than the radius of the cylinder and the buoyancy effect is negligible in the region $x << r_0$. This can be verified by substituting the value $\xi = 0$ and a finite Ω_0 value (i.e., $\chi = 1$ and $\Lambda = 0$) into equations (7) and (8). With a similar reasoning for the pure free convection case ($u_\infty = 0$), the flow field in the region $x << r_0$ approximates pure free convection flow along a vertical flat plate. This can be seen by substituting $\xi = 0$, $\chi = 0$, and $\Lambda = 0$ into equations (7) and (8). As x increases from zero, Λ keeps increasing along the flow direction. For the limiting case of flat plate ($r_0 = \infty$), the curvature parameter Λ is always zero and the modified buoyancy parameter χ remains as the only nonsimilarity variable.

A computational program is written in terms of the coefficients a, b, c, d, e and the parameters Λ and χ. Thus, one can obtain solutions for all the three cases, vertical cylinders in mixed convection ($u_\infty \neq 0$, Ω_0 = finite), vertical cylinders in pure free convection ($u_\infty = 0$, $\Omega_0 = \infty$), and vertical flat plates in mixed convection, by simply employing the appropriate values of a, b, c, d, e, Λ, and χ for each case in the calculations.

The physical quantities of interest include the local and

Nomenclature

$A(\mathrm{Pr})$ = function defined in equation (21)
$B(\mathrm{Pr})$ = function defined in equation (24)
C_{fx}, $\bar{C}_f$ = local and average friction factors
f = reduced stream function
g = local gravitational acceleration
Gr_0 = Grashof number = $g\beta\ (T_w - T_\infty)\ r_0^3/\nu^2$
Gr_x^*, Gr_0^* = modified Grashof numbers based on x and r_0; $\mathrm{Gr}_x^* = g\beta q_w x^4/k\nu^2$; $\mathrm{Gr}_0^* = g\beta q_w r_0^4/k\nu^2$
h_x = local heat transfer coefficient = $q_w/(T_w - T_\infty)$, $\mathrm{W/m^2-K}$
$\bar{h}$ = average heat transfer coefficient, $\mathrm{W/m^2-K}$
k = thermal conductivity of the fluid, $\mathrm{W/m-K}$
L = an arbitrary length in x, m
Nu_x, $\overline{\mathrm{Nu}_L}$ = local and average Nusselt numbers, $\mathrm{Nu}_x = h_x x/k$; $\overline{\mathrm{Nu}_L} = hL/k$
Pr = Prandtl number = ν/α
q_w = surface heat flux, $\mathrm{W/m^2}$
r, r_0 = radial coordinate and the radius of the cylinder, m
Re_x, Re_0 = Reynolds numbers based on x and r_0; $\mathrm{Re}_x = u_\infty x/\nu$; $\mathrm{Re}_0 = u_\infty r_0/\nu$
T = temperature, K
T_c = characteristic temperature = $q_w\delta/k$
u, v = axial and transverse velocity components, m/s
x = axial coordinate
α = thermal diffusivity, $\mathrm{m^2/s}$
β = volumetric coefficient of thermal expansion, $\mathrm{K^{-1}}$
δ = characteristic boundary layer thickness = $x/(\mathrm{Re}_x^{1/2} + \mathrm{Gr}_x^{*1/5})$
η = pseudosimilarity variable
θ = dimensionless temperature = $(T - T_\infty)/T_c$
Λ = modified curvature parameter = $2\delta/r_0$
ν = kinematic viscosity, $\mathrm{m^2/s}$
ξ = nonsimilarity variable defined by equations (11), (13), or (14)
$\Delta\xi$ = step size in the ξ coordinate
ρ = density, $\mathrm{kg/m^3}$
τ = shear stress, $\mathrm{N/m^2}$
χ = modified buoyancy parameter = $(1+\Omega_x^{1/5})^{-1}$
ψ = stream function, $\mathrm{m^3/s}$
Ω_x, Ω_0 = buoyancy parameters based on x and r_0; $\Omega_x = \mathrm{Gr}_x^*/\mathrm{Re}_x^{5/2}$; $\Omega_0 = (\mathrm{Gr}_0^*/\mathrm{Re}_0)^{1/5}$

Subscripts

w = condition at wall
∞ = condition at free stream

average Nusselt numbers and friction factors. The local Nusselt number Nu_x and the local friction factor C_{fx} are determined from

$$Nu_x/(Re_x^{1/2} + Gr_x^{*1/5}) = 1/\theta(\xi, 0)$$

$$C_{fx} = \tau_w/(\rho u_\infty^2/2) = 2Re_x^{-1/2}\chi^{-3}f''(\xi, 0) \quad (15)$$

For mixed convection the average Nusselt number and the average friction factor over the region $0 \le x \le L$ can be evaluated by the following respective equations:

$$\overline{Nu}_L Re_L^{-1/2} = (4/\xi_L^2)\int_0^{\xi_L} \xi[\theta(\xi, 0)\chi]^{-1}d\xi$$

and (16)

$$\overline{C}_f Re_L^{1/2} = (8/\xi_L^2)\int_0^{\xi_L} \xi[f''(\xi, 0)/\chi^3]d\xi$$

where $\xi(x) = (x/r_0Re_0)^{1/4}$ and $\xi_L = \xi(L)$. For the pure free convection case, the average Nusselt number can be evaluated from the expression

$$\overline{Nu}_L Gr_L^{*-1/5} = (10/\xi_L^8)\int_0^{\xi_L} [\xi^7/\theta(\xi, 0)]d\xi \quad (17)$$

where $\xi(x) = (x/r_0Gr_0^*)^{1/10}$ and $\xi_L = \xi(L)$.

Method of Solution

Equations (7)–(10) constitute a system of coupled, nonlinear partial differential equations in the (ξ, η) coordinates, with parameters Pr and Ω_0 when Λ and χ are properly related to ξ for each case (see equations (12)–(14)). The value of the curvature parameter Λ considered here exceeds 50 and the Prandtl number covers $0.1 \le Pr \le 100$. It should be noted that for large values of Λ (say, $\Lambda \ge 5$, the ratio $|(\Lambda + af)/(1 + \eta\Lambda)|$ becomes very large at $\eta \approx 0$ and becomes very small as $\eta \to \infty$. Equation (7) thus behaves as a second-order equation in the region adjacent to the wall, but retains the third derivative term in the region away from the wall to the edge of the boundary layer. Similarly, equation (8) behaves as a first-order equation in the wall region when Λ is very large. This particular behavior is known as "stiff problem" in numerical analysis. To solve such a stiff problem numerically, an upwind scheme or an equivalent scheme is needed. Some discussions about stiff problems can be found, for example, in Loeb and Schiesser (1973) and Miranker (1981). In solving equations (7)–(10) for large values of Λ ($\Lambda \ge 5$ without a special treatment, the numerical computation may result in large errors if equations (7)–(10) are solved by a central difference scheme such as the box method by Keller and Cebeci (1972) or by the central difference method used by Raju et al. (1984). Similar difficulty arises when the Prandtl number is very large (say, Pr = 100), because the energy equation (8) becomes "stiff." Fortunately, a finite difference method based on a weighting function scheme proposed by Lee et al. (1986a) has been found to solve stiff problems satisfactorily (Lee et al., 1986b). Their solution method thus is employed in the present study. The details are omitted here to conserve space.

Results and Discussion

Numerical results were obtained for the case of buoyancy-assisting flow. They cover Prandtl numbers of 0.1, 0.7, 7, and 100 and Ω_0 values of 0, 0.02, 0.05, 0.1, 0.2, 0.5, 1, 2, 10, and ∞ for each Prandtl number. As mentioned earlier, the case of $\Omega_0 = 0$ corresponds to pure forced convection while the case of $\Omega_0 = \infty$ corresponds to either $u_\infty = 0$ (i.e., pure free convection along a vertical cylinder) or $r_0 = \infty$ (i.e., mixed convection along a flat plate). The step size $\Delta\eta$ was taken as 0.05 which achieved a four-place accuracy for the $f''(\xi, 0)$ and $\theta(\xi, 0)$ results in the region $\Lambda \le 10$. In the region of $\Lambda > 10$, the step size should be reduced to maintain a high accuracy.

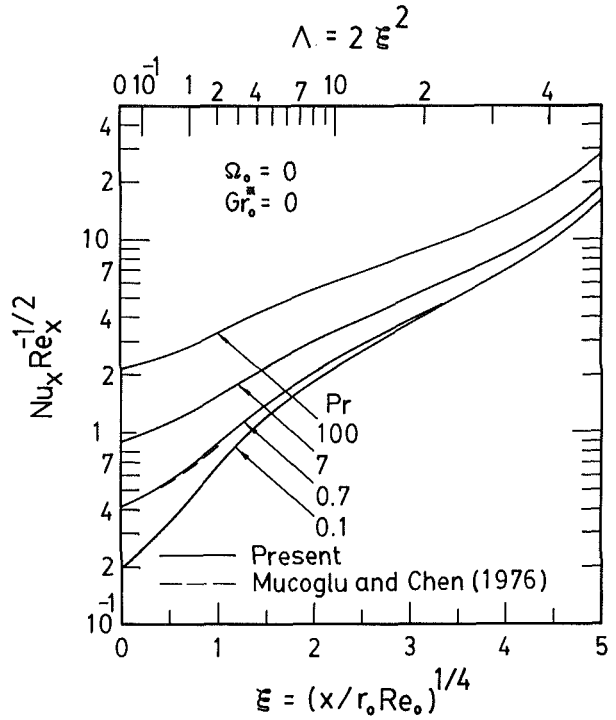

Fig. 1 Local Nusselt number results for pure forced convection (Ω_0 = 0)

To save CPU time, the step size $\Delta\eta = 0.05$ was used for the entire range of $0 \le \Lambda \le 50$. The numerical solution, however, is not sensitive to the step size $\Delta\xi$. The numerical scheme employed in this investigation provided numerically stable solution for all values of Λ and Pr.

Figure 1 shows the local Nusselt number, $Nu_x/Re_x^{1/2}$, as a function of $\xi = (x/r_0Re_0)^{1/4}$ for the case of pure forced convection ($\Omega_0 = 0$) along a vertical cylinder. The curvature parameter $\Lambda = 2\xi^2$ is also provided in the upper abscissa. It can be seen from the figure that fluids with a larger Prandtl number give rise to a higher local Nusselt number. For a given Prandtl number, the local Nusselt number increases from the value for a flat plate ($\Lambda = 0$) as the curvature parameter increases from zero. At large values of Λ, the curves for all Prandlt numbers are seen to merge together. The results of Mucoglu and Chen (1976) for Pr = 0.7 and $0 \le \Lambda \le 1$ are in excellent agreement with the present results. The local Nusselt number, $Nu_x/Gr_x^{*1/5}$, as a function of $\xi = (x/r_0Gr_0^*)^{1/10}$ for the case of pure free convection is illustrated in Fig. 2. The behavior of the curves is similar to the case of pure forced convection shown in Fig. 1.

The local Nusselt number $Nu_x/(Re_x^{1/2} + Gr_x^{*1/5})$ as a function of χ for the entire regime of mixed convection ($0 \le \chi \le 1$) are illustrated in Fig. 3 for Pr = 0.7, with Ω_0 and Λ as parameters. The curve for $\Omega_0 = 0$ is for pure forced convection. The present Nusselt number expression can be converted to the conventional one through the simple relationship

$$Nu_x/(Re_x^{1/2} + Gr_x^{*1/5}) = (Nu_x/Re_x^{1/2})\chi = (Nu_x/Gr_x^{*1/5})(1 - \chi) \quad (18)$$

If the present results are presented in terms of $Nu_x/Re_x^{1/2}$ as in conventional studies for the forced convection dominated case, one will see, as expected, that the local Nusselt number for each Ω_0 increases from 0.4059 at the leading edge of the cylinder to infinity at $x = \infty$ as χ decreases from unity (pure forced convection) to zero (pure free convection).

The case of $\Omega_0 = \infty$ covers both mixed convection along a vertical flat plate ($r_0 = \infty$ and $\Lambda = 0$) and pure free convec-

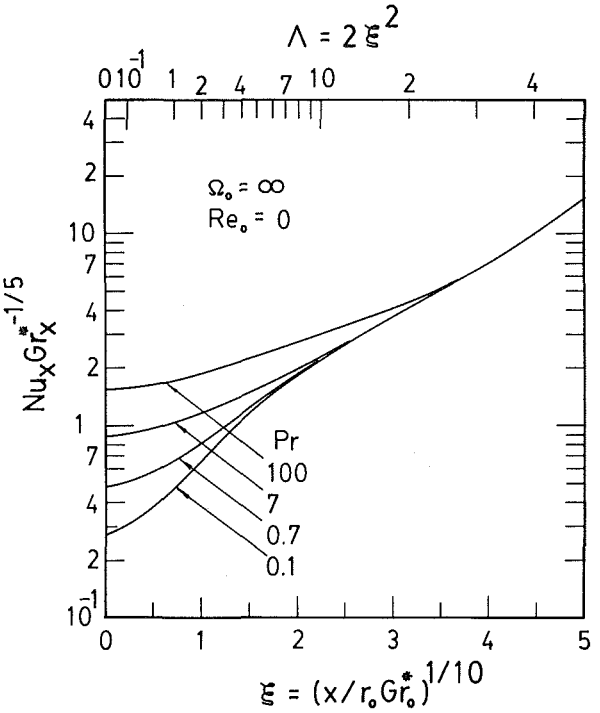

Fig. 2 Local Nusselt number results for pure free convection ($\Omega_0 = \infty$)

Table 1 The $Nu_{x,fp}/(Re_x^{1/2} + Gr_x^{*1/5})$ results for a vertical flat plate ($\Omega_0 = \infty$, $r_0 = \infty$) with uniform surface heat flux

Ω_x	χ	Pr			
		0.1	0.7	7	100
∞	0.00	0.2634	0.4834	0.8697	1.5546
1.303(+5)*	0.05	0.2507	0.4598	0.8270	1.4782
6.561(+3)	0.10	0.2381	0.4365	0.7848	1.4035
1.031(+3)	0.15	0.2256	0.4135	0.7433	1.3314
2.560(+2)	0.20	0.2134	0.3909	0.7028	1.2629
8.100(+1)	0.25	0.2015	0.3688	0.6635	1.1997
2.964(+1)	0.30	0.1899	0.3475	0.6262	1.1442
1.190(+1)	0.35	0.1788	0.3270	0.5916	1.1002
5.063(+0)	0.40	0.1683	0.3080	0.5611	1.0736
2.232(+0)	0.45	0.1586	0.2909	0.5368	1.0721
1.000(+0)	0.50	0.1500	0.2766	0.5220	1.1023
4.481(−1)	0.55	0.1431	0.2667	0.5205	1.1641
1.975(−1)	0.60	0.1386	0.2632	0.5350	1.2485
8.407(−2)	0.65	0.1375	0.2676	0.5639	1.3490
3.374(−2)	0.70	0.1406	0.2799	0.6024	1.4559
1.235(−2)	0.75	0.1476	0.2974	0.6460	1.5669
3.906(−3)	0.80	0.1570	0.3176	0.6921	1.6806
9.698(−4)	0.85	0.1675	0.3391	0.7395	1.7960
1.524(−4)	0.90	0.1784	0.3611	0.7876	1.9131
7.673(−6)	0.95	0.1895	0.3834	0.8364	2.0317
0	1.00	0.2007	0.4059	0.8856	2.1512

* a(b) = a x 10^b

tion ($u_\infty = 0$) along a vertical cylinder. Thus, its Nusselt number starts at $\chi = 1$ with a value of $Nu_x/Re_x^{1/2} = 0.4059$, follows the $\Lambda = 0$ or $r_0 = \infty$ curve for a vertical flat plate to a value of $Nu_x/Gr_x^{*1/5} = 0.4834$ at $\chi = 0$ and then increases along the $\chi = 0$ line for pure free convection ($u_\infty = 0$) along a vertical cylinder. The curves for $\Omega_0 = 1$, 2, and 10 are terminated at a very small χ value of about 0.09, which corresponds to $\Omega_x = 10^5$. If the range of solutions had been extended much further, the curves for $\Omega_0 = 1$, 2, and 10 would go up steeply at small χ values and lie between the two curves for $\Omega_0 = 0.5$ and for $\Omega_0 = \infty$. At a constant Ω_x or χ, an increase in the radius of the cylinder r_0 causes an increase in Ω_0. This results in a decrease in the local Nusselt number, as can be seen from the figure. At $\chi \neq 0$, the limit of r_0 approaching infinity applies to the case of a vertical flat plate ($\Omega_0 = \infty$, $r_0 = \infty$). Thus, the results for $\Omega_0 = 10$ ($Gr_0^*/Re_0 = 10^5$) are very close to those for vertical flat plates. For completeness and for future reference, the local Nusselt number results $Nu_{x,fp}/(Re_x^{1/2} + Gr_x^{*1/5})$ for a vertical flat plate are listed in Table 1.

Curves with constant values of Λ are also given in Fig. 3. It is interesting to note that at large Λ ($\Lambda \geq 5$) the local Nusselt number $Nu_x/(Re_x^{1/2} + Gr_x^{*1/5})$ becomes nearly independent of the buoyancy parameter χ. This is because the two leading terms $(1 + \eta\Lambda)\theta''$ and $\Lambda\theta'$ in equation (8) dominate the energy equation when Λ is sufficiently large. The curves for constant values of Λ are seen to have a minimum point near $\chi = 0.55$. A similar characteristic exists for Prandtl numbers of 0.1, 7, and 100.

Figure 4 reveals the effect of Prandtl number on the local Nusselt number $Nu_x/(Re_x^{1/2} + Gr_x^{*1/5})$ in mixed convection. Only the case of $\Omega_0 = 1$ is shown as an example. For convenience, the curvature parameter is also provided in the upper abscissa as $\Lambda = 2[(1-\chi)/\Omega_0]^{5/3}$. As in Figs. 1 and 2 for the pure forced convection and pure free convection, it is seen from Fig. 4 that a larger Prandtl number gives rise to a larger local Nusselt number. Also, the effect of Prandtl number on the local Nusselt number is seen to decrease as Λ increases or as χ decreases. The result of Mucoglu and Chen (1976) for Pr = 0.7 is also plotted in the figure for comparison. Their results from the local nonsimilarity solution agree well with the present calculations, but give the local Nusselt number that is about 1 percent lower at $\chi = 0.5$. To the best knowledge of the authors, there are no experimental data available for mixed convection along a vertical cylinder that can be used to compare with the present numerical results.

For practical applications, the present local Nusselt number results for pure forced convection along a vertical cylinder in the range of $0.1 \leq Pr \leq 100$ can be correlated by the simple expression

$$\ln[(Nu_x)_F Re_x^{-1/2}] = f(\Lambda_F) + \{\ln[(Nu_{x,fp})_F Re_x^{-1/2}] - f(0)\}\exp(-m_1 \Lambda_F^{0.4}) \quad (19)$$

where

$$m_1 = 0.592\,Pr^{-0.376} + 0.305$$
$$\Lambda_F = 2(x/r_0)Re_x^{-1/2} \quad (20)$$

and for a flat plate

$$(Nu_{x,fp})_F Re_x^{-1/2} = A(Pr)$$
$$A(Pr) = 0.464 Pr^{1/3}[1 + (0.0207/Pr)^{2/3}]^{-1/4} \quad (21)$$

Similarly, the present results for pure free convection for $0.1 \leq Pr \leq 100$ are correlated by

$$\ln[(Nu_x)_N Gr_x^{*-1/5}] = f(\Lambda_N) + \{\ln[(Nu_{x,fp})_N Gr_x^{*-1/5}] - f(0)\}\exp(-m_2 \Lambda_N^{0.6}) \quad (22)$$

where

$$m_2 = 3.06\,Pr^{-0.0485} - 1.86$$
$$\Lambda_N = 2(x/r_0)Gr_X^{*-1/5} \quad (23)$$

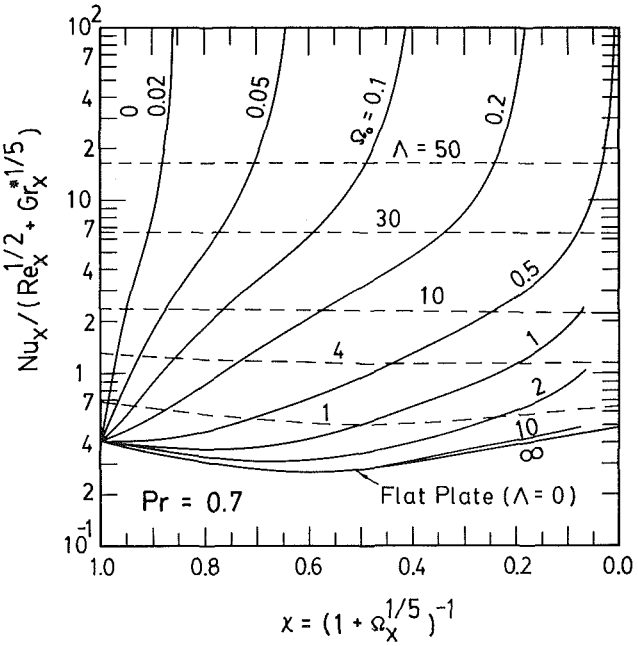

Fig. 3 Local Nusselt number results for mixed convection, Pr = 0.7

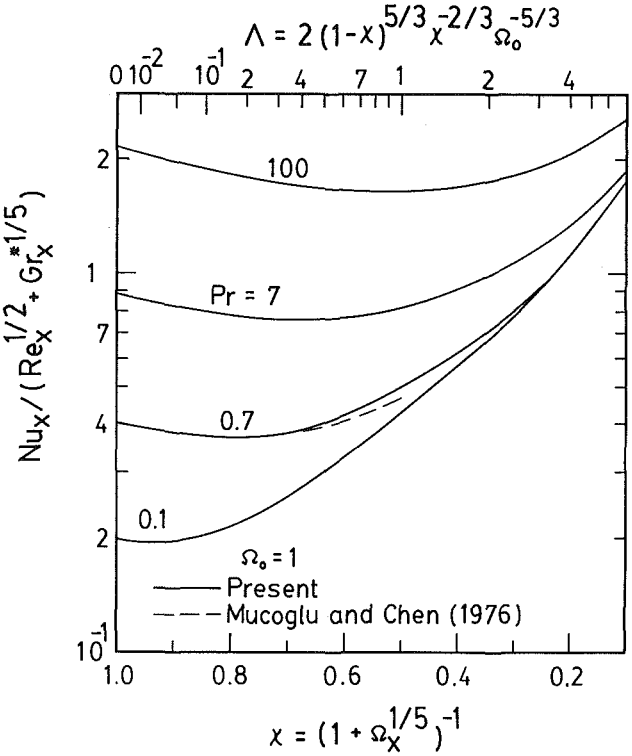

Fig. 4 Local Nusselt number results for mixed convection, $\Omega_0 = 1$

and for a vertical flat plate

$$(\mathrm{Nu}_{x,fp})_N \mathrm{Gr}_x^{*-1/5} = B(\mathrm{Pr})$$

$$B(\mathrm{Pr}) = \mathrm{Pr}^{2/5}(4 + 9\,\mathrm{Pr}^{1/2} + 10\,\mathrm{Pr})^{-1/5} \tag{24}$$

In equations (19) and (22), both the curvature functions $f(\Lambda_F)$ and $f(\Lambda_N)$ are expressed in the same form as

$$f(\Lambda) = -1.993 + 1.395\Lambda^{1/2} - 0.2130\Lambda + 0.01568\Lambda^{3/2} \tag{25}$$

It is noted that when $\Lambda = 0$ the correlation equations (19) and (22) reduce to equations (21) and (24) for flat plates, respectively. The correlation equations (21) and (24) are taken, respectively, from Churchill and Ozoe (1973) and Fujii and Fujii (1976). The maximum error in equations (19) and (22) is about 8 percent.

In the entire mixed convection regime $0 \le \chi \le 1$, the normalized local Nusselt number $N(\chi, \Lambda)$ from the present results for $0.1 \le \mathrm{Pr} \le 100$ can be correlated by

$$N(\chi,\Lambda) = 1 - 0.3726\sin(\pi\chi)\exp(-0.41\Lambda) + 0.02254\sin(2\pi\chi)\exp(-0.71\Lambda) \tag{26}$$

where the normalized local Nusselt number is defined as

$$N(\chi, \Lambda) = \frac{\mathrm{Nu}_x/(\mathrm{Re}_x^{1/2} + \mathrm{Gr}_x^{*1/5})}{[\chi(\mathrm{Nu}_x)_F/\mathrm{Re}_x^{1/2} + (1-\chi)(\mathrm{Nu}_x)_N/\mathrm{Gr}_x^{*1/5}]} \tag{27}$$

in which $(\mathrm{Nu}_x)_F$ and $(\mathrm{Nu}_x)_N$ denoted the local Nusselt numbers for pure forced convection and pure free convection along a vertical cylinder given, respectively, by equations (19) and (22). The maximum error in the correlation equation (26) is 6.9 percent. If the last term in equation (26) is neglected, the maximum error would increase to 7.8 percent. The maximum errors occur at either Pr = 0.1 or Pr = 100. The correlation equation (26), however, is exact at $\Lambda = \infty$, $\chi = 0$, and $\chi = 1$. As a final note, it is mentioned that in terms of the modified buoyancy parameter χ, Churchill's correlation equation (1977) for the entire mixed convection regime, based on pure forced convection and pure free convection, for a vertical flat plate under uniform surface heat flux yields

$$\mathrm{Nu}_{x,fp}/(\mathrm{Re}_x^{1/2} + \mathrm{Gr}_x^{*1/5}) = \{[A(\mathrm{Pr})\chi]^3 + [B(\mathrm{Pr})(1-\chi)]^3\}^{1/3} \tag{28}$$

where $A(\mathrm{Pr})$ and $B(\mathrm{Pr})$ are defined in equations (21) and (24), respectively. The maximum error in the correlation equation (28) is less than 1.5 percent.

Conclusion

The problem of mixed convection along a vertical cylinder with uniform surface heat flux is investigated for the entire mixed convection regime, ranging from pure forced convection ($\chi = 1$) to pure free convection ($\chi = 0$) by employing a single buoyancy parameter χ and a single curvature parameter Λ. Numerical results are obtained by employing a finite-difference method of solution based on a weighting function scheme along with the cubic spline interpolation technique to remove numerical difficulties that arise from large values of the curvature parameter ($\Lambda \ge 5$) and/or large values of the Prandtl number ($\mathrm{Pr} \ge 20$). Local Nusselt numbers for Prandtl numbers of 0.1, 0.7, 7, and 100 are presented for $0 \le \chi \le 1$ and $0 \le \Lambda \le 50$. Correlation equations for the local Nusselt number are also given.

Acknowledgment

The work reported in this paper was supported by grants from the University of Missouri (Weldon Spring: Chen, 1985-86) and the National Science Foundation (NSF MEA 83-00785).

References

Bui, M. N., and Cebeci, T., 1985, "Combined Free and Forced Convection on Vertical Slender Cylinders," ASME Journal of Heat Transfer, Vol. 107, pp. 476-478.

Burden, R. L., and Faires, J. D., 1985, *Numerical Analysis*, 3rd ed., Prindle, Weber and Schmidt Publishers, Boston, MA, pp. 117-129.

Chen, T. S., and Mucoglu, A., 1975, "Buoyancy Effects on Forced Convection Along a Vertical Cylinder," ASME Journal of Heat Transfer, Vol. 97, pp. 198-203.

Churchill, S. W., and Ozoe, H., 1973, "Correlation for Laminar Forced Convection With Uniform Surface Heating in Flow Over a Plate and in Developing and Fully Devloped Flow in a Tube," ASME Journal of Heat Transfer, Vol. 95, pp. 78-84.

Churchill, S. W., 1977, "A Comprehensive Correlating Equation for Laminar, Assisting, Forced and Free Convection," *AIChE Journal*, Vol. 23, pp. 10–16.

Fujii, T., and Fujii, M., 1976, "The Dependence of Local Nusselt Number on Prandtl Number in the Case of Free Convection Along a Vertical Surface With Uniform Heat Flux," *International Journal of Heat and Mass Transfer*, Vol. 19, pp. 121–122.

Keller, H. B., and Cebeci, T., 1972, "Accurate Numerical Methods for Boundary Layer Flows: II: Two-Dimensional Turbulent Flows," *AIAA Journal*, Vol. 10, pp. 1193–1199.

Lee, S. L., Chen, T. S., and Armaly, B. F., 1986a, "New Finite Difference Solution Methods for Wave Instability Problems," *Numerical Heat Transfer*, Vol. 10, pp. 1–18.

Lee, S. L., Chen, T. S., and Armaly, B. F., 1986b, "Mixed Convection Along Isothermal Vertical Cylinders and Needles," *Proceedings of the Eighth International Heat Transfer Conference*, Vol. 3, pp. 1425–1432.

Loeb, A. M., and Schiesser, W. E., 1974, "Stiffness and Accuracy in the Method of Line Integration of Partial Differential Equations," in: *Stiff Differential Systems*, R. A. Willoughby, ed., Plenum Press, New York, pp. 229–243.

Miranker, W. L., 1981, *Numerical Methods for Stiff Equations and Singular Perturbation Problems*, D. Reidel Publishing Company, Dordrecht, Holland.

Mucoglu, A., and Chen, T. S., 1976, "Buoyancy Effects on Forced Convection Along a Vertical Cylinder With Uniform Surface Heat Flux," ASME JOURNAL OF HEAT TRANSFER, Vol. 98, pp. 523–525.

Raju, M. S., Liu, X. Q., and Law, C. K., 1984, "A Formulation of Combined Forced and Free Convection Past Horizontal and Vertical Surfaces," *International Journal of Heat and Mass Transfer*, Vol. 17, pp. 2215–2224.

Marangoni Convection in Radiating Fluids

Y. Bayazitoglu
Associate Professor.
Assoc. Mem. ASME

T. T. Lam
Graduate Student.
Assoc. Mem. ASME

Department of Mechanical Engineering and Materials Science,
Rice University,
Houston, TX 77001

The onset of Marangoni convection driven by surface tension gradients in radiating fluid layers is studied. The system considered consists of a fluid layer of infinite horizontal extent which is confined between a free upper surface and a rigid isothermal lower surface. The radiative boundaries of black-black, mirror-mirror, and black-mirror are considered. The critical conditions leading to the onset of convective fluid motions in a microgravity environment are determined numerically by linear stability theory. The perturbation equations are solved as a Bolza problem in the calculus of variations. The results are presented in terms of the critical Marangoni number and optical thickness for a wide range of some radiative parameters, including the Planck number, nongrayness of the fluid, and the emissivity of the boundaries. It is found that radiation suppresses Marangoni convection during material processing in space.

Introduction

In recent years, processing of new materials in a reduced gravity environment has received a great deal of interest. Reviews of materials processing in space have been given by Naumann (1978) and Witt (1978). It is known that manufacturing of large crystals of uniform properties has been an important part of the space program. It is suggested that surface tension, and not buoyancy, is a mechanism introducing motion in many of the experiments that have been conducted in space (Schwabe et al., 1978, 1982; Scharmann et al., 1978; Wuest and Chun, 1978). Surface-tension-driven flows can influence the material composition and cause crystal defects. Thus, the understanding of controlled convection plays an important role in crystal growth in space.

It is now common knowledge that at the free surface of a liquid, under conditions involving a temperature or concentration gradient, conventional convective flows or unstable cellular flows can be generated. In such cases, the free surface tension becomes an important factor in the convection process. This convective phenomenon, due to nonuniformities in surface tension, is referred to as Marangoni convection. Some earlier experimental and theoretical contributions on Marangoni convection have been made by Block (1956), Pearson (1958), Scriven and Sternling (1964), Nield (1964), Smith (1966), and Birikh (1966). The dimensionless parameter characterizing the surface-tension-driven flows is the Marangoni number, which represents the ratio of the surface tension force to heat diffusion and viscous force. On the other hand, the dimensionless parameter that appears in the buoyancy-driven flows is the Rayleigh number ($\beta g \Delta T d^3/\alpha\nu$), which is a measure of the buoyancy force and the viscous force. By taking the ratio of the Marangoni number and the Rayleigh number, the relative magnitude of the surface-tension and the buoyancy forces can be expressed as $\mathrm{Ma}/\mathrm{Ra} = (-\partial S/\partial T)/(\beta\rho g d^2)$. Since decreasing the gravitational constant g will increase the ratio Ma/Ra, the surface-tension force becomes dominant compared to the buoyancy force in a microgravity (10^{-6}–$10^{-3}g$).

Most of the earlier investigations of Marangoni convection have concentrated upon fluid layers with uniform temperature gradients due to heating from the lower boundary. Debler and Wolf (1970) determined the effects of surface tension and buoyancy on the convection stability of fluid layers with a mean parabolic temperature distribution due to internal heat generation. Nield (1975), Lebon and Cloot (1981), Friedrich and Rudraiah (1984), and Rudraiah et al. (1985) also studied the effect of a nonuniform temperature gradient on the onset of convection in fluid layers with piecewise linear profiles due to transient heating or cooling at the boundaries.

The onset of buoyancy-driven convection in a radiating fluid layer has received considerable attention in the past. In Goody's (1956) original paper he studied the thermal instability of fluid layers having very large and very small absorption coefficients and bounded by free and surfaces. Spiegel (1960), Murgai and Khosla (1962), Khosla and Murgai (1963), and Christophorides and Davis (1970) extended this work to include the effects of magnetic field, rotation, and conduction. Arpaci and Gozum (1973) and Arpaci and Bayazitoglu (1973) studied thermal stability of fluid layers by means of the Eddington approximation. The above studies are restricted to buoyancy-driven convection. The effect of surface tension forces in a radiating fluid layer has not been given much attention. The purpose of the present paper is to determine quantitatively the stabilizing effect of radiation on convection induced by surface tension. It is hoped that the insights gained may lead to better understanding of the mechanism of controlling Marangoni convection in a reduced gravity environment during material processing in space.

The problem will be investigated by means of classical linearized stability theory, formulated in terms of some general boundary conditions. The surface tension effect is included at the deformable free surface. The thermal convective problem is recast as a Bolza problem in the calculus of variations. The sequential gradient-restoration algorithm is used to find the eigenvalues for the stability problem. The results are presented in terms of the critical Marangoni number and optical thickness for a wide range of thermal and radiative properties, including the Planck number, nongrayness of the fluid, and the emissivity of the boundaries.

Governing Equations of the Stability Problem

Consider a radiating nongray incompressible fluid layer of infinite horizontal extent which is subjected to a nonlinear temperature gradient due to internal radiation and heated from below. The viscosity and conductivity are assumed to be constant. We take a Cartesian coordinate system with the origin on the lower boundary of the fluid layer and with the x axis directed vertically upward. The fluid layer is confined to the region $0 \le z \le d + \xi^*$, where d is the mean thickness of the fluid layer and the upper surface has a deflection $\xi^*(x, y)$ from the mean. We wish to study the effect of an infinitesimal

Contributed by the Heat Transfer Division for publication in the JOURNAL OF HEAT TRANSFER. Manuscript received by the Heat Transfer Division April 21, 1986.

disturbance on a static, horizontally radiating fluid layer. The governing equations are the equations of continuity, motion, and energy. The equation which governs the balance of radiative energy can be obtained from the radiative transfer equation using the Eddington (P-1) approximation. The governing equations are as follows:

$$\nabla \cdot \mathbf{V} = 0 \tag{1}$$

$$\frac{\partial \mathbf{V}}{\partial t} + \mathbf{V} \cdot \nabla \mathbf{V} = -\frac{1}{\rho_0} \nabla P + \nu \nabla^2 \mathbf{V} \tag{2}$$

$$\frac{\partial T}{\partial t} + \mathbf{V} \cdot \nabla T = \alpha \nabla^2 T + \left(\frac{\alpha_P}{\rho_0 C_v}\right)(j - 4\sigma T^4) \tag{3}$$

$$\nabla^2 j - 3\alpha_P \alpha_R j = -12\alpha_P \alpha_R \sigma T^4 \tag{4}$$

Since the exchange of stabilities is valid for any optical thickness (see Christopherides and Davis, 1970), the perturbation equations governing the marginal state for stationary instability are

$$(D^2 - a^2)^2 W = 0 \tag{5}$$

$$(D^2 - a^2 - 4\chi\tau^2)\Theta + 3\chi\tau^2 J = -f(Z) W \tag{6}$$

$$(D^2 - a^2 - 3\tau^2) J = -4\tau^2 \Theta \tag{7}$$

with the boundary conditions

at Z = 0:

$$W = 0 \tag{8}$$

$$DW = 0 \tag{9}$$

$$\Theta = 0 \tag{10}$$

$$DJ = 0 \text{ for a mirror surface} \tag{11a}$$

or

$$J - (\eta/3\lambda_0\tau) DJ = 0$$

$$\text{for a gray black-rigid surface with } \lambda_0 = 0.5 \tag{11b}$$

at Z = 1:

$$W = 0 \tag{12}$$

$$D\Theta + \mathrm{Bi}[\Theta - f(1)\xi] = 0 \tag{13}$$

$$(D^2 + a^2) W + a^2 \mathrm{Ma}[\Theta - f(1)\xi] = 0 \tag{14}$$

$$D^3 W - 3a^2 DW - a^4 \mathrm{Cr}\xi = 0 \tag{15}$$

$$DJ = 0 \text{ for a mirror surface} \tag{16a}$$

or

$$J + (\eta/3\lambda_1\tau) DJ = 0$$

$$\text{for a gray black-free surface with } \lambda_1 = 0.5 \tag{16b}$$

It can be seen that the boundary conditions of equations (8)–(10) and (12) are those of the classical Benard problem and boundary conditions of equations (11) and (16) account for the radiative effects. At the free surface, surface tension becomes important. We include some general boundary conditions at the deformable upper surface. These conditions, equations (13)–(15), are essentially those used by Lam and Bayazitoglu (1986a). The boundary condition of equation (13) represents the continuity of constant heat flux at the free surface. The boundary conditions of equations (14) and (15) express the continuity of tangential and normal stress at the free surface.

In equation (6), $f(Z)$ is the temperature gradient of the initial state for the nongray fluid layer, given by Arpaci and Gozum (1973) as

$$f(Z) = C_3 + C_4 \sinh[\varphi\tau(Z - 0.5)] + C_5 \cosh[\varphi\tau(Z - 0.5)] \tag{17}$$

where

$$\mathrm{Po} = \frac{\alpha_M k}{4\sigma T_0^3}, \quad \chi = \frac{\eta}{\mathrm{Po}}, \quad \varphi = \sqrt{3 + 4\chi}$$

$\lambda_0, \lambda_1 = 0$ for mirror surfaces
$= 0.5$ for black-rigid or -free surfaces

$$C_0 = 2\sinh(\varphi\tau/2) + (\varphi/\eta)(\lambda_0 + \lambda_1)\cosh(\varphi\tau/2)$$
$$C_1 = \{[1 + \lambda_0\lambda_1(\varphi/\eta)^2]\sinh\varphi\tau + (\varphi/\eta)(\lambda_0 + \lambda_1)\cosh\varphi\tau\}/C_0$$
$$C_2 = C_1 + (8\chi/3\varphi\tau)\sinh(\varphi\tau/2)$$
$$C_3 = C_1/C_2$$
$$C_4 = (\lambda_0 - \lambda_1)(4\chi\varphi/3\eta)\sinh(\varphi\tau/2)/(C_0 C_2)$$
$$C_5 = (4\chi/3)/C_2$$

We have an eighth-order system of differential equations and, when ξ is eliminated, eigh boundary conditions, forming a standard eigenvalue problem.

Nomenclature

a = horizontal wave number
Bi = Biot number = hd/k
Cr = Crispation number = $Sd/\mu\alpha$
C_v = specific heat at constant volume
d = thickness of the fluid layer
D = operator = d/dZ
$f(Z)$ = initial steady-state temperature distribution
g = gravitational acceleration constant
h = heat transfer coefficient
I = intensity
j = $\int_\Omega I d\Omega$
J = amplitude of disturbance intensity = $j/12\sigma T_0^3$
k = thermal conductivity
Ma = Marangoni number = $(-\partial S/\partial T)(\Delta T d/\mu\alpha)$
P = pressure
Po = Planck number = $\alpha_M k/4\sigma T_0^3$
S = surface tension
t = time
T = temperature
$\mathbf{V}$ = velocity vector
(x, y, z) = Cartesian coordinates
(X, Y, Z) = $(x, y, z)/d$
W = amplitude of disturbance velocity
α = thermal diffusivity
α_M = $\sqrt{\alpha_P \alpha_R}$
α_P = Planck mean absorption coefficient
α_R = Rosseland mean absorption coefficient
β = thermal expansion coefficient
ϵ = emissivity = $1/(0.5 + 1/4\lambda)$
η = $\sqrt{\alpha_P/\alpha_R}$
Θ = amplitude of disturbance temperature
λ = 0 for mirror surface; 0.5 for black-rigid or -free surfaces
μ = dynamic viscosity
ν = kinematic viscosity
ξ = dimensionless interfacial deflection
ρ = density
σ = Stefan–Boltzmann constant
τ = optimal thickness = $\alpha_M d$
χ = η/Po
Ω = solid angle

Subscripts

0 = reference state or lower boundary
1 = upper boundary
c = critical

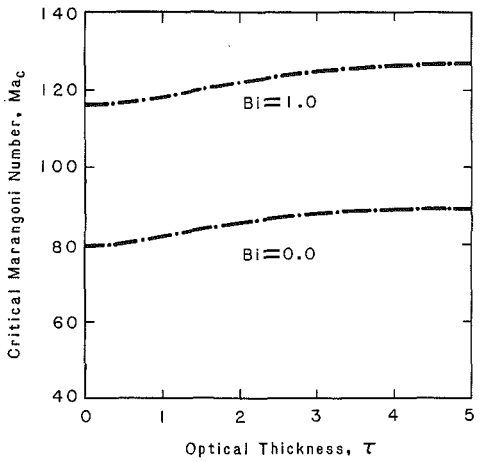

Fig. 1 The effect of thermal boundary conditions on the fluid for Po = 1.0, $\eta = 0.1$, Cr = 10^6, $\epsilon_0 = 1$, and $\epsilon_1 = 0$

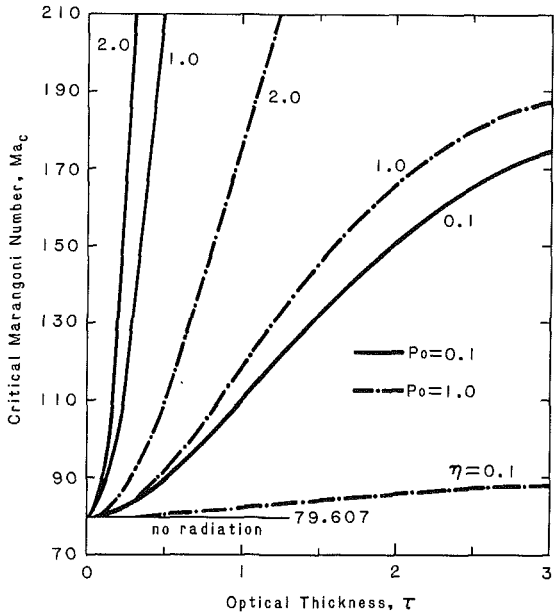

Fig. 2 The effect of nongrayness on the fluid for Bi = 0.0, Cr = 10^6, $\epsilon_0 = 1$, and $\epsilon_1 = 0$

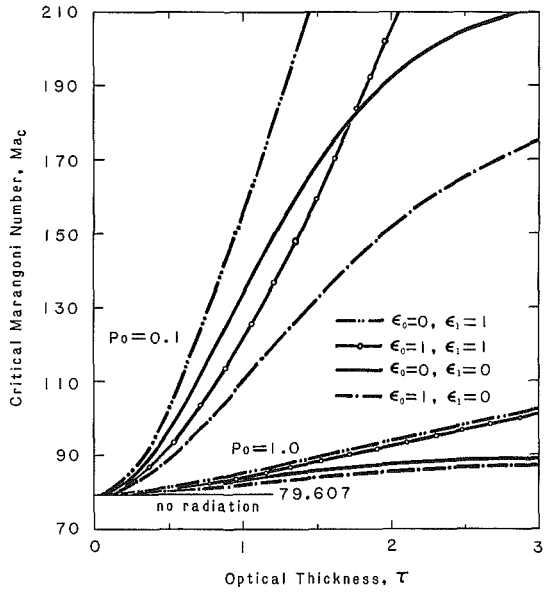

Fig. 3 The effect of radiation on the fluid with various types of boundaries for Bi = 0.0, Cr = 10^6, and $\eta = 0.1$

Method of Solution

The method employed in this study is to solve the governing equations (5)–(7) as a Bolza problem in the calculus of variations. In this section, we demonstrate how the governing equations for the stability problem can be recast into an optimal control problem and we also include a brief discussion on the method of solution.

A Bolza Problem. We consider the problem of minimizing the functional

$$I = \int_0^1 f(x, u, \pi, z)dz + [h(x, \pi)]_0 + [g(x, \pi)]_1 \tag{18}$$

with respect to the state $x(z)$, the control $u(z)$, and the parameter π which satisfy the following constraints:

$$\dot{x} - \phi(x, u, \pi, z) = 0 \qquad 0 \le z \le 1 \tag{19a}$$

$$S(x, u, \pi, z) = 0 \qquad 0 \le z \le 1 \tag{19b}$$

$$[\omega(x, \pi)]_0 = 0 \tag{19c}$$

$$[\psi(x, \pi)]_1 = 0 \tag{19d}$$

The dot sign denotes a derivative with respect to z, that is, $x = dx/dz$. In the above equations, the functions f, h, g are scalar, and the functions ϕ, S, ω, ψ are vectors of appropriate dimensions. The independent variable z is a scalar, and the dependent variables x, u, π, are vectors of appropriate dimensions. The subscript 0 denotes the initial point, and the subscript 1 denotes the final point. In the terminology of the calculus of variations, the above problem is called the Bolza problem and includes as particular cases the Lagrange problem and the Mayer problem. The former occurs when $h = 0$, $g = 0$, and the latter occurs when $f = 0$. We define ten new variables:

$$x_m = W^{(m-1)} \qquad m = 1, 2, 3, 4$$
$$x_m = \Theta^{(m-5)} \qquad m = 5, 6$$
$$x_m = J^{(m-7)} \qquad m = 7, 8$$
$$\Pi_1 = \sqrt{a}$$
$$\Pi_2 = \sqrt{\mathrm{Ma}}$$

With this notation, equations (5)–(7) can be written as a system of first-order differential equations. Thus, we recast the convective instability problem given in the previous section into an optimal control problem which can be stated as follows:

minimize the functional

$$I = \Pi_2^2 \tag{20}$$

subject to the differential constraints

$$\dot{x}_1 = x_2 \tag{21}$$

$$\dot{x}_2 = x_3 \tag{22}$$

$$\dot{x}_3 = x_4 \tag{23}$$

$$\dot{x}_4 = 2\Pi_1^4 x_3 - \Pi_1^8 x_1 \tag{24}$$

$$\dot{x}_5 = x_6 \tag{25}$$

$$\dot{x}_6 = (\Pi_1^4 + 4\chi\tau^2)x_5 - f(Z)x_1 - 3\chi\tau^2 x_7 \tag{26}$$

$$\dot{x}_7 = x_8 \tag{27}$$

$$\dot{x}_8 = (\Pi_1^4 + 3\tau^2)x_7 - 4\tau^2 x_5 \tag{28}$$

and the boundary conditions

at Z = 0:

$$x_1 = 0 \tag{29}$$

$$x_2 = 0 \tag{30}$$

Table 1 Comparison of the critical Marangoni number and corresponding wave number for various values of Bi for $f(Z)=1$ and $Cr-\infty$

	Present analysis		Nield (1966)	
Bi	a_c	Ma_c	a_c	Ma_c
0.0	1.993	79.607	1.993	79.607
0.01	1.997	79.991	1.997	79.991
0.1	2.028	83.427	2.028	83.427
0.2	2.060	87.195	2.060	87.195
0.5	2.142	98.256	2.142	98.256
1.0	2.246	116.127	2.246	116.127
2.0	2.386	150.679	2.386	150.679
5.0	2.598	250.597	2.598	250.598
10.0	2.743	413.439	2.743	413.440

Table 2 The effect of nongrayness on the fluid for $Bi=0.0$, $Cr=10^6$, $Po=0.1$, $\epsilon_0=1$, and $\epsilon_1=0$

	η=0.1		η=1.0		η=2.0	
τ	a_c	Ma_c	a_c	Ma_c	a_c	Ma_c
0.0	1.993	79.607	1.993	79.607	1.993	79.607
0.01	1.993	79.610	1.994	79.667	1.995	79.731
0.1	2.001	80.071	2.071	86.018	2.141	93.315
0.2	2.025	81.435	2.261	105.015	2.465	134.658
0.3	2.059	83.582	2.494	134.514	2.839	198.828
0.4	2.100	86.366	2.733	171.750	3.182	278.243
0.5	2.143	89.650	2.956	214.429		
0.7	2.222	97.294				
0.9	2.282	105.866				
1.0	2.302	110.346				
1.3	2.327	123.938				
1.5	2.320	132.681				
1.7	2.301	140.852				
2.0	2.261	151.698				
2.5	2.193	165.658				
3.0	2.140	175.040				

$$x_5 = 0 \tag{31}$$

$$x_8 = 0 \text{ for a mirror surface} \tag{32a}$$

or

$$x_7 - (\eta/3\lambda_0\tau)x_8 = 0$$

$$\text{for a gray black-rigid surface with } \lambda_0 = 0.5 \tag{32b}$$

at $Z=1$:

$$x_1 = 0 \tag{33}$$

$$x_6 + \mathrm{Bi}x_5 - \mathrm{Bi}\cdot f(1)(x_4 - 3\Pi_1^4 x_2)/(\Pi_1^8 \mathrm{Cr}) = 0 \tag{34}$$

$$x_3 + \Pi_1^4 x_1 + \Pi_1^4\Pi_2^2 x_5 - \Pi_1^4\Pi_2^2 f(1)(x_4 - 3\Pi_1^4 x_2)/(\Pi_1^8 \mathrm{Cr}) = 0 \tag{35}$$

$$x_8 = 0 \text{ for a mirror surface} \tag{36a}$$

or

$$x_7 + (\eta/3\lambda_1\tau)x_8 = 0$$

$$\text{for a gray black-free surface} \tag{36b}$$

The interfacial deflection ξ has been eliminated from the differential systems by the use of equation (15). Since all the differential constraints and boundary conditions, equations (21)–(36), are homogeneous, we are free to impose a suitable normalization condition on the solution. The condition used here is to set $x_4(0)$ equal to a preselected number.

Sequential Gradient-Restoration Algorithm. Over the past several years, a successful family of first-order algorithms for the solution of optimal control problems involving differential constraints, nondifferential constraints, and terminal constraints has been developed at Rice University by Miele and his associates (1970, 1974, 1980). They are called sequential gradient-restoration algorithms (SGRA), and have been designed for the solution of different classes of optimal control problems.

Sequential gradient-restoration algorithms involve a sequence of two-phase cycles, each cycle including the gradient phase and the restoration phase. In the gradient phase, the value of the augmented functional is decreased while avoiding excessive constraint violation; in the restoration phase, the constraint error is decreased while avoiding excessive change in the value of the functional. In a complete gradient-restoration cycle, the value of the functional is decreased while the constraints are satisfied to a predetermined accuracy. Hence, a succession of suboptimal solutions is obtained.

The sequential gradient-restoration algorithm has been successfully applied to the study of convective instability problem by Lam and Bayazitoglu (1986b, c, d). In this paper, we employ the same algorithm to study the critical conditions for Marangoni convection in a radiating fluid layer. Results are presented in the next section.

Results and Conclusion

The purpose of the present paper is to determine quantitatively the stabilizing effect of radiation on convection induced by surface tension. Linear stability theory has been used to determine the condition for the onset of convection motion in a horizontal radiating fluid layer with nonlinear temperature profiles.

The optimal control problem, equations (20)–(36), was solved using the sequential gradient-restoration algorithms (SGRA) as outlined in the previous section. To verify the applicability of the procedure to the present stability problem, a comparison (Table 1) was made with Nield's (1964) Fourier series expansion solution for the case of a rigid isothermal boundary at $Z=0$ with $f(Z)=1$. It is clear that the numerical values of the critical Marangoni number and the corresponding wave number obtained from the present study are in close agreement with the existing work.

Figure 1 illustrates the effect of the thermal boundary condition on the upper surface of the fluid layer for varying optical thicknesses and for $Po=1.0$, $\eta=0.1$, $Cr=10^6$, $\epsilon_0=1$, and $\epsilon_1=0$. Increasing heat transfer at the upper surface and increasing the optical thickness of the fluid layer both delay the onset of Marangoni convection.

The effect of nongrayness on the fluid with upper mirror boundary and lower black-rigid boundary is shown in Fig. 2 for varying the Planck number (that is the ratio of conduction to radiation) and optical thicknesses. As we can see from equation (17), the initial temperature distribution can be flattened as we increase the nongrayness of the fluid for $\eta>1$ and thus delay the onset of instability. The critical Marangoni number increases as the system becomes more stable when the degree of nongrayness of the fluid is increased. Also, it is clear that the critical Marangoni number increases when the Planck

Table 3 The effect of nongrayness on the fluid for Bi = 0.0, Cr = 10^6, Po = 1.0, $\epsilon_0 = 1$, and $\epsilon_1 = 0$

	η=0.1		η=1.0		η=2.0	
τ	a_c	Ma_c	a_c	Ma_c	a_c	Ma_c
0.0	1.993	79.607	1.993	79.607	1.993	79.607
0.01	1.993	79.607	1.993	79.610	1.993	79.616
0.1	1.994	79.636	2.001	80.117	2.009	80.823
0.2	1.996	79.724	2.023	81.732	2.051	84.704
0.3	2.000	79.875	2.055	84.409	2.110	91.129
0.4	2.004	80.087	2.092	87.994	2.176	99.755
0.5	2.009	80.357	2.129	92.303	2.241	110.190
0.7	2.018	81.033	2.196	102.391	2.355	134.959
0.9	2.026	81.827	2.242	113.492	2.430	162.652
1.0	2.029	82.245	2.256	119.147	2.451	176.871
1.3	2.033	83.480	2.267	135.617	2.450	218.289
1.5	2.033	84.245	2.253	145.677		
1.7	2.032	84.942	2.230	154.709		
2.0	2.029	85.849	2.188	166.124		
2.5	2.023	87.029	2.124	179.714		
3.0	2.018	87.890	2.078	187.897		

number Po is decreased, which confirms that radiation does possess a stabilizing effect in Marangoni instability. The numerical values for Fig. 2 are summarized in Tables 2 and 3.

Plots of the critical Marangoni number versus optical thickness τ are shown in Fig. 3 varying the Planck number and the emissivities of the upper and the lower surfaces of the fluid layer. For the upper surface two cases are considered, $\epsilon_1 = 1$ and $\epsilon_1 = 0$. The mirror lower surface, $\epsilon_0 = 0$, stabilizes the fluid layer, and the black lower surface, $\epsilon_0 = 1$, destabilizes the fluid layer for each of the above cases. While the critical Marangoni number increases as we increase the emissivity of the upper surfaces.

The problem of Marangoni convection in a radiating fluid layer has been investigated numerically using the sequential gradient-restoration algorithm. The study examines the effect of radiation (in terms of the Planck number Po), optical thickness τ, nongrayness of the fluid, and the emissivity of the boundaries ϵ_0 and ϵ_1 toward surface-tension-driven flows. The results presented here provide strong evidence that radiation has a stabilizing effect and can be used to suppress Marangoni instability.

References

Arpaci, V. S., and Gozum, D., 1973, "Thermal Stability of Radiating Fluids: The Benard Problem," *The Physics of Fluids,* Vol. 16, pp. 581-588.

Arpaci, V. S., and Bayazitoglu, Y., 1973, "Thermal Stability of Radiating Fluids: Asymmetric Slot Problem," *The Physics of Fluids,* Vol. 16, pp. 589-593.

Birikh, R. V., 1966, "Thermocapillary Convection in a Horizontal Layer of Fluid," *Journal of Applied Mechanics and Technical Physics,* Vol. 6, pp. 43-44.

Block, M. J., 1956, "Surface Tension as the Cause of Benard Cells and Surface Deformation in a Liquid Film," *Nature,* Vol. 178, pp. 650-651.

Christophorides, C., and Davis, S. H., 1970, "Thermal Instability With Radiative Transfer," *The Physics of Fluids,* Vol. 13, pp. 222-226.

Debler, W. R., and Wolf, L. F., 1970, "The Effects of Gravity and Surface Tension Gradients on Cellular Convection in Fluid Layers with Parabolic Temperature Profiles," ASME *Journal of Heat Transfer,* Vol. 92, pp. 351-358.

Friedrich, R., and Rudraiah, N., 1984, "Marangoni Convection in Rotating Fluid Layer with Non-uniform Temperature Gradient," *International Journal of Heat and Mass Transfer,* Vol. 27, pp. 443-449.

Goody, R. M., 1956, "The Influence of Radiative Transfer on Cellular Convection," *Journal of Fluid Mechanics,* Vol. 2, pp. 424-435.

Khosla, R. K., and Murgai, M. P., 1963, "A Study of the Combined Effect of Thermal Radiative Transfer and Rotation on the Gravitational Stability of a Hot Fluid," *Journal of Fluid Mechanics,* Vol. 16, pp. 97-107.

Lam, T. T., and Bayazitoglu, Y. 1986a, "Effects of Internal Heat Generation and Variable Viscosity on Marangoni Convection," *Numerical Heat Transfer,* in press.

Lam, T. T., and Bayazitoglu, Y., 1986b, "Application of the Sequential Gradient-Restoration Algorithm to Thermal Convective Instability Problems," *Journal of Optimization Theory and Applications,* Vol. 49, pp. 47-63.

Lam, T. T., and Bayazitoglu, Y., 1986c, "Solution to the Orr–Sommerfeld Equation for Liquid Film Flowing Down an Inclined Plane: An Optimal Approach," *The International Journal for Numerical Methods in Fluids,* Vol. 6, pp. 883–894.

Lam, T. T., and Bayazitoglu, Y., 1986d, "Marangoni Instability With Non-uniform Volumetric Energy Sources due to Incident Radiation," submitted to *Acta Astronautica*

Lebon, G., and Cloot, A., 1981, "Effects of Non-uniform Temperature Gradients on Benard–Marangoni's Instability," *Journal of Non-equilibrium Thermodynamics,* Vol. 6, 1981, pp. 15-30.

Miele, A., Pritchard, R. E., and Damoulakis, J. N., 1970, "Sequential Gradient Restoration Algorithm for Optimal Control Problems," *Journal of Optimization Theory and Applications,* Vol. 5, pp. 235-282.

Miele, A., Damoulakis, J. N., Cloutier, J. R., and Tietze, J. L., 1974, "Sequential Gradient-Restoration Algorithm for Optimal Control Problems with Nondifferential Constraints," *Journal of Optimization Theory and Applications,* Vol. 13, pp. 218-255.

Miele, A., 1980, "Gradient Algorithms for the Optimization of Dynamic Systems," in: *Control and Dynamic Systems, Advances in Theory and Application,* C. T. Leondes, ed., Academic Press, New York, Vol. 16, pp. 1-52.

Murgai, M. P., and Khosla, P. K., 1962, "A Study of the Combined Effect of Thermal Radiative Transfer and a Magnetic Field on the Gravitational Convection of an Ionized Fluid," *Journal of Fluid Mechanics,* Vol. 14, pp. 433-451.

Naumann, R. J., 1978, "Materials Processing in Space – An Overview of Studies in the U.S.A." *COSPAR: Space Research,* Vol. 19, pp. 489-502.

Nield, D. A., 1964, "Surface Tension and Buoyancy Effects in Cellular Convection," *Journal of Fluid Mechanics,* Vol. 19, pp. 341-352.

Nield, D. A., 1975, "The Onset of Transient Convective Instability," *Journal of Fluid Mechanics,* Vol. 71, pp. 441-454.

Pearson, J. R. A., 1958, "On Convection Cells Induced by Surface Tension," *Journal of Fluid Mechanics,* Vol. 4, pp. 489-500.

Rudraiah, N., Ramachandramurthy, V., and Chandra, O. P., 1985, "Effects of Magnetic Field and Non-uniform Temperature Gradient on Marangoni-Convection," *International Journal of Heat and Mass Transfer,* Vol. 28, pp. 1621-1624.

Scharmann, A., Schwabe, D., Preissner, F., and Oeder, R., 1978, "Experiments on the Relevance of Marangoni Convection for Materials Science in Space," *COSPAR: Space Research,* Vol. 19, pp. 555-558.

Schwabe, D., Scharmann, A., Preisser, F., and Oeder, F., 1978, "Experiments on Surface Tension Driven Flow in Floating Zone Melting," *Journal of Crystal Growth,* Vol. 43, pp. 305-312.

Schwabe, D., Scharmann, A., and Preisser, F., 1982, "Studies of Marangoni Convection in Floating Zones," *Acta Astronautica,* Vol. 9, pp. 183-186.

Scriven, L. E., and Sternling, C. V., 1964, "On Cellular Convection Driven by Surface Tension Gradients: Effects of Mean Surface Tension and Surface Viscosity," *Journal of Fluid Mechanics,* Vol. 19, pp. 320-340.

Smith, K. A., 1966, "On Convective Instability Induced by Surface Tension Gradients," *Journal of Fluid Mechanics,* Vol. 24, pp. 401-414.

Spiegel, E. A., 1960, "The Convective Instability of a Radiating Fluid Layer," *Astrophysical Journal,* Vol. 132, pp. 716-728.

Vidal, A., and Acrivos, A., 1966, "Nature of the Neutral State in Surface-Tension Driven Convection," *The Physics of Fluids,* Vol. 9, pp. 615-616.

Witt, A. F., 1978, "Crystal Growth and Segregation in Space: A Critical Assessment Based on Results Obtained During the ASTP Mission," *COSPAR: Space Research,* Vol. 19, pp. 503-506.

Wuest, W., and Chun, Ch.-H., 1978, "Thermal Marangoni Convection," *COSPAR: Space Research,* Vol. 19, pp. 559-562.

Modeling of the Two-Phase Closed Thermosyphon

J. G. Reed[1]
Research Assistant.
Assoc. Mem. ASME

C. L. Tien
Professor.
Fellow ASME

Department of Mechanical Engineering,
University of California,
Berkeley, CA 94720

A comprehensive model is developed to predict the steady-state and transient performance of the two-phase closed thermosyphon. One-dimensional governing equations for the liquid and vapor phases are developed using available correlations to specify the shear stress and heat transfer coefficients. Steady-state solutions agree well with thermosyphon flooding data from several sources and with film thickness data obtained in the present investigation. While no data are available with which to compare the transient analysis, the results indicate that, for most systems, the governing time scale for system transients is the film residence time, which is typically much longer than the times required for viscous and thermal diffusion through the film. The proposed model offers a versatile and comprehensive analysis tool which is relatively simple.

Introduction

The two-phase closed thermosyphon, which is essentially a gravity-assisted, wickless heat pipe, utilizes the evaporation and condensation of an internal working fluid to transport heat, as shown in Fig. 1. The thermosyphon has been used in a variety of applications taking advantage of its high effective thermal conductivity or its thermal-diode property (the heat input must be in the lower portion of the device to achieve high effective thermal conductivity) [1]. When the thermosyphon is in stable operation, the internal flow is an annular, countercurrent, two-phase flow providing a convenient experimental facility for studying the features of such flows [2]. On the other hand, various fluid flow and heat transfer phenomena which can preclude stable, countercurrent, annular flow may occur. Examples of such flow limiting phenomena are the dryout, burnout (or film-boiling), and flooding limits which have been observed and described by many investigators [2–6].

Reflux condensation and countercurrent, annular, two-phase flows have been studied extensively in the recent past, largely because of their importance in nuclear reactor thermal-hydraulics [6–8]. Because of the many complex physical processes associated with reflux condensation and the nonlinearity of the governing equations, most analytical studies have focused attention on isolated phenomena, such as interfacial waviness. Little attention has been given to incorporating the results into comprehensive system models. This work attempts to overcome this deficiency by using a control-volume formulation which includes many complex physical phenomena, such as the augmentation of interfacial shear stress by film waviness, through empirical relationships, while maintaining the relative simplicity of the mathematical formulation.

The present formulation, similar to but more extensive than that first proposed by Dobran [3], models the thermosyphon directly from first principles and is applicable to either steady-state or transient operation of the device. The approach used here is very powerful because it provides a single system model which can predict most operating parameters and operating limits. Solutions for both steady-state and transient operation of the thermosyphon will be presented in this work. The predictions of the steady-state analysis will be compared with experimental data on film thickness obtained in the present study and with flooding data from the present study and from two other groups of investigators [4, 9]. The flooding predictions will also be compared with the predictions of the existing Tien–Chung correlation [5].

Analytical Model

It will be assumed throughout this analysis that terms of order $(\delta/R)^2$ and ρ_v/ρ_l are negligible relative to unity; that the vapor temperature is constant and the vapor is saturated; and that compressibility effects in the gas phase are negligible. These assumptions are well justified in most systems exhibiting countercurrent, annular flow in tubes [10–12]. This model also neglects entrainment of liquid droplets in the vapor core because this effect is usually insignificant except near the flooding limit.

In the formulation presented below, the thermosyphon is divided into seven control volumes. The liquid film, which is annular in cross section, and the vapor core, which is cylindrical in shape, are each divided into three control volumes,

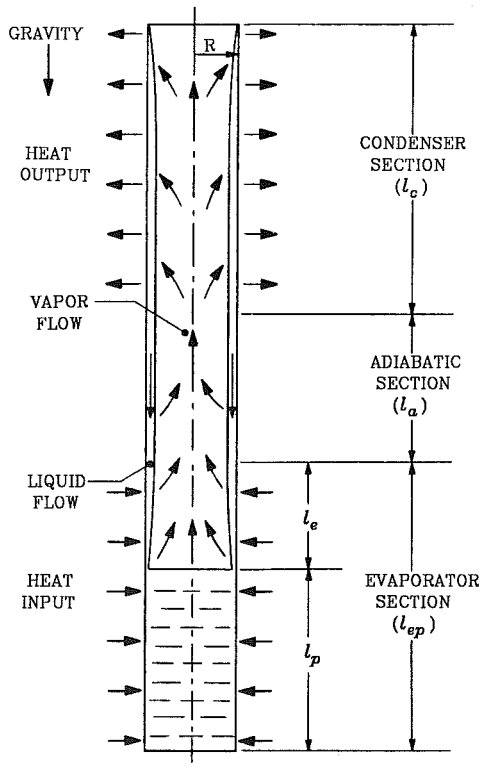

Fig. 1 A two-phase closed thermosyphon

[1]Present address: General Research Corporation, 5383 Hollister Ave., Santa Barbara, CA.

Contributed by the Heat Transfer Division for publication in the JOURNAL OF HEAT TRANSFER. Manuscript received by the Heat Transfer Division November 22, 1985.

one for each section of the device. The final control volume encloses the liquid pool at the bottom of the evaporator. The contribution to the convective flux terms at the top of the liquid pool caused by the motion of the control-volume boundary will be neglected because the assumptions of small δ/R and ρ_v/ρ_l imply that the rate of change of pool depth is small compared to the velocities of both the liquid film and the vapor.

In the following equations, the subscript k will be used to represent an arbitrary section of the thermosyphon and j the next section above it (or the top of the thermosyphon). In the equations using these subscripts, the different versions (a, b, and c) of the equations are obtained by setting $\langle k,j\rangle$ equal to $\langle c,t\rangle$, $\langle a,c\rangle$, and $\langle e,a\rangle$, respectively. If a subscript indicating one of the sections of the thermosyphon appears on a variable which is not an average value for the indicated section, the location to which the subscript refers is the bottom of the section (i.e., the interface with the next lower section).

Equations for the mass, momentum, and energy balances for each section of the liquid film are, respectively:

$$\frac{d}{dt}\left[l_k\rho_l\bar{\delta}_k\left(1-\frac{\bar{\delta}_k}{2R}\right)\right]=\dot{m}_k''l_k\left(1-\frac{\bar{\delta}_k}{R}\right)+\Gamma_j-\Gamma_k \quad (1a,b,c)$$

$$\bar{\delta}_k\left(1-\frac{\bar{\delta}_k}{2R}\right)[\rho_l g l_k-(P_k-P_j)]-l_k\left[\tau_{wk}+\left(1-\frac{\bar{\delta}_k}{R}\right)\tau_{ik}\right]$$
$$=\frac{d}{dt}(l_k\bar{\Gamma}_k)-u_{ik}\dot{m}_k''\left(1-\frac{\bar{\delta}_k}{R}\right)l_k+B_{l_k}\frac{{\Gamma_k}^2}{\delta_k\rho_l}\left(1+\frac{\delta_k}{2R}\right)$$
$$-B_{l_j}\frac{{\Gamma_j}^2}{\delta_j\rho_l}\left(1+\frac{\delta_j}{2R}\right) \quad (2a,b,c)$$

$$\frac{d}{dt}\left[\Delta\bar{T}_kC_p\rho_l\bar{\delta}_k\left(1-\frac{\bar{\delta}_k}{2R}\right)l_k\right]=l_k\left[\left(1-\frac{\bar{\delta}_k}{R}\right)\dot{m}_k''h_g-q_k\right]$$
$$+C_p\Delta T_j\Gamma_j-C_p\Delta T_k\Gamma_k \quad (3a,b,c)$$

Mass and momentum balances for the vapor core are of the form

$$\pi R^2\frac{d}{dt}\left[\rho_v\left(1-\frac{2\bar{\delta}_k}{R}\right)l_k\right]$$
$$=\dot{m}_k-\dot{m}_j-\dot{m}_k''2\pi R\left(1-\frac{\bar{\delta}_k}{R}\right)l_k \quad (4a,b,c)$$

$$\pi R^2\left(1-\frac{2\bar{\delta}_k}{R}\right)[l_kg\rho_v-(P_k-P_j)]+2\pi R\left(1-\frac{\bar{\delta}_k}{R}\right)l_k\tau_{ik}$$
$$=-\frac{d}{dt}(\bar{m}_kl_k)+u_{ik}\dot{m}_a''2\pi R\left(1-\frac{\bar{\delta}_k}{R}\right)l_k$$
$$-B_{vj}\frac{\dot{m}_j^2(1+2\delta_j/R)}{\pi R^2\rho_v}+B_{vk}\frac{\dot{m}_k^2(1+2\delta_k/R)}{\pi R^2\rho_v} \quad (5a,b,c)$$

The system of governing equations is completed by writing equations for the overall conservation of mass in the system and for energy balances on the liquid pool and the vapor core. The respective expressions are

$$M=\pi R^2\rho_l\left[l-\left(1-\frac{2\bar{\delta}_e}{R}\right)l_e-\left(1-\frac{2\bar{\delta}_a}{R}\right)l_a-\left(1-\frac{2\bar{\delta}_c}{R}\right)l_c\right] \quad (6)$$

$$\frac{d}{dt}\{\rho_vh_g[\pi R^2(l_c+l_a+l_e)-2\pi R(l_c\bar{\delta}_c+l_a\bar{\delta}_a+l_e\bar{\delta}_e)\}$$
$$=\rho_vh_g\left\{2\pi R\left[\dot{m}_e''l_e\left(1-\frac{\bar{\delta}_e}{2R}\right)-\dot{m}_a''l_a\left(1-\frac{\bar{\delta}_a}{2R}\right)\right.\right.$$
$$\left.\left.-\dot{m}_c''l_c\left(1-\frac{\bar{\delta}_c}{2R}\right)\right]+\dot{m}_e\right\} \quad (7)$$

$$\pi R^2\frac{d}{dt}[\rho_lC_p\Delta\bar{T}_pl_p]=2\pi R\left[q_el_p-\frac{\dot{m}_e}{2\pi R}h_g+\Gamma_eC_p\Delta T_e\right] \quad (8)$$

In addition to these basic governing equations, auxiliary equations specifying the wall and interfacial shear stresses and the liquid-film heat transfer coefficient are needed. The expressions to be used are listed in Table 1. The turbulent-vapor interfacial friction factor is a recently obtained correlation [13] while the other expressions can be found in textbooks [10–12]. The interfacial friction factor for laminar vapor flow contains a correlation factor as suggested by Blangetti and Naushahi accounting for the influence of interfacial mass flux [14]. For turbulent vapor flow, the effect of interfacial waviness dominates the effect of interfacial mass transfer so the mass transfer effect is not included. Several different values for the film Reynolds number at the transition to turbulent flow, ranging from 1200 to 2400, have been used by various investigators [10–12]. The transition from laminar to turbulent film flow will be assumed here to begin at a

Nomenclature

$B_{\varphi j}$ = ratio of the average squared velocity to the average velocity squared for phase φ at the location specified by subscript j (velocity profile shape factor)
Bo = Bond number $=(4\rho_lgR/\sigma)^{1/2}$
C_f = friction factor defined by $\tau=\frac{1}{2}\rho_lu^2C_f$
C_p = liquid specific heat evaluated at the liquid bulk temperature
g = gravitational acceleration
Gr = two-phase Grashof number $=(8gR^3/\nu_l^2)^{1/2}$
h = liquid film heat transfer coefficient defined by $q=h(T_v-T_w)$
h_g = vapor phase enthalpy $=h_{fg}+C_p(T_v-T_w)$
h_{fg} = latent heat of vaporization evaluated at T_v
Ja = Jakob number $=C_p\Delta T_N/h_{fg}$
k_l = liquid thermal conductivity evaluated at the liquid bulk temperature
l = overall length of the thermosyphon
l_j = length of thermosyphon section indicated by subscript j
$\dot{m}_j''$ = average mass flux due to phase change at the liquid–vapor interface in the thermosyphon section indicated by subscript j
$\dot{m}_j$ = upward mass flow rate of vapor at the location specified by subscript j
P_j = pressure at location j
Pr = liquid Prandtl number $=\mu_lC_p/k_l$
q_j = wall heat flux in section j
Q_e = total heat input in evaporator
R = tube inside radius
Re_φ = Reynolds number of phase φ, $4\Gamma/\mu_l$ for the liquid film, and $2\dot{m}/(\pi R\mu_v)$ or $\mathrm{Re}_l\mu_l/\mu_v$ for the gas core
T_j = bulk temperature of liquid at location j or vapor temperature if $j=v$ (temperature differences are relative to T_w)
t = time
u = streamwise (axial) velocity
x_1, x_2 = parameters used in shear

Table 1 Shear stress and heat transfer coefficient expressions for use in control-volume equations

Quantity	Expression
Wall shear, laminar film	$\tau_w = \mu_l \left(\frac{du}{dy}\right)_w$, from velocity profile
Wall friction factor, turbulent film	$C_f = 0.079\mathrm{Re}^{-1/4}$ (Blasius relation)
Interfacial friction factor, laminar vapor core	$C_f = (16./\mathrm{Re})[\varphi/(e^{\varphi}-1)]$ $\varphi = \dot{m}'' R/(4\mu_v)$
Interfacial friction factor, turbulent vapor core	$C_f = 0.005 + x_1(\delta/R)^{x_2}$ where $x_1 = 0.2574(\mathrm{Bo}/2)^{x_2} 10^{9.07/\mathrm{Bo}}$, $x_2 = 1.63 + 4.74/\mathrm{Bo}$
Film heat transfer coefficient, laminar film	$h = k_l/\delta$
Film heat transfer coefficient, turbulent film	$h = 0.056\mathrm{Re}^{-1/5}\mathrm{Pr}^{1/3} k_l/(\nu_l^2/g)^{1/3}$

Reynolds number of 2040, the point at which the laminar and turbulent wall shear stress expressions match in the absence of interfacial shear. When interfacial shear stress is present, the laminar and turbulent expressions are smoothed together over the Reynolds number range 2040 to 3500.

In addition to predicting the values of various system variables such as film thicknesses in the various sections of the device, mass fluxes, liquid pool depth, and vapor temperature, the present analysis can be used to predict the dryout and flooding operating limits. Dryout phenomena can be predicted by the present model in two ways: (1) The depth of the liquid pool may become equal to zero indicating that the supply of working fluid is insufficient for a complete flow circuit; (2) the value of Γ_e may become equal to zero which means that there is no flow of liquid reaching the liquid pool. In the steady-state case, within the framework of this model, the two types of dryout are essentially the same and the two limits will be reached simultaneously. However, in the transient case, the film may dry out above the liquid pool if the evaporator heat flux is increased rapidly; so, in general, the pool-dryout and film-dryout limits are distinct. When any portion of the evaporator tube wall becomes dry, there is a drastic loss of cooling efficiency and therefore a danger of severe overheating. The flooding, or entrainment, limit is predicted when the calculated rate of change of film thickness with respect to heat input becomes unbounded in some section of the device [8]. Physically, a vertical slope on a film thickness versus heat input curve means that an increase in flow rate will increase the interfacial shear stress too much to be balanced by the corresponding increase in the weight of the liquid film. The result is a net upward force on the liquid film which will retard the downward flow of liquid and a transition to a complicated, nonannular flow regime or an oscillatory flow pattern.

Steady-State Operation

In this section, consideration will be given to situations in which the thermosyphon is in steady-state operation with the evaporator heat flux and condenser wall temperature having constant specified values. In addition to the assumptions made in the general formulation, it will be assumed in the present case that δ/R and Ja/Pr are small relative to unity and that Ja is less than the order of unity. These assumptions are not very restrictive in most cases. Countercurrent annular flow has not been observed for δ/R greater than 0.1 [10], and the restrictions on Ja and Ja/Pr are met by most common working

Nomenclature (cont.)

stress correlation defined in Table 1
α_l = liquid film thermal diffusivity $= k_l/(\rho_l C_p)$
Γ_j = mass flow rate in the liquid film per unit tube perimeter at the location specified by subscript j
δ_j = film thickness at location specified by subscript j
Δ = difference or increment
ϵ_j = dimensionless film thickness in section j
ϑ = dimensionless temperature
μ_φ = dynamic viscosity of phase φ
ν_φ = kinematic viscosity of phase φ
ρ_φ = density of phase φ
σ = liquid surface tension (evaluated at T_v)
τ_{kj} = shear stress on surface k in thermosyphon section j

Subscripts

a = adiabatic section
c = condenser section
e = portion of evaporator above the liquid pool where there is film flow
ep = complete evaporator section including both the liquid pool and film flow regions
i = phase interface
f = final steady state following a transient
l = liquid phase
N = Nusselt solution
p = liquid pool
r = ramp input function for transient analysis
t = top of the thermosyphon
v = vapor phase
w = tube wall
0 = initial state in transient analysis

Superscripts

$\dot{}$ = per unit time
$''$ = per unit area
$\bar{}$ = axially averaged over a given section of the thermosyphon (this designation is omitted if a variable is axially averaged by definition)
$*$ = nondimensional variable

fluids because flooding usually occurs before the heat input is large enough for Ja to exceed unity. It will also be assumed that the dynamic pressure of the vapor, $\rho_v u_v^2$, is small relative to the static pressure head of the liquid film, $\rho_l g l_c$. This is equivalent to the requirement that $(\Gamma^*/\mathrm{Gr})^2 R^*/\rho^*$ be much less than unity. This condition is generally satisfied unless the tube radius is very small or the vapor density is very low. In all cases considered in this study, the above dimensionless group is of the order 0.01 or less. The newly introduced assumptions imply that the temperature profile in the liquid film in the condenser can be well approximated as linear when the film is laminar (i.e., $h = k_l/\delta$) [15] and that, in the liquid-film momentum equations, the pressure drop, interfacial-momentum-flux, and inertia terms are negligible [7, 16].

In thermophysical property calculations and energy convection terms, the bulk temperature of the liquid in the condenser will be taken as the average of the vapor and wall temperatures. In the adiabatic section and the evaporator, it will be assumed that the liquid is at the vapor temperature.

The following variables are introduced for use in nondimensionalizing the steady-state governing equations:

$$q_j^* = \frac{l_j q_j}{\mu_l h_{fg}}, \quad \Gamma_j^* = \frac{\Gamma_j}{\mu_l}, \quad \epsilon_j = \frac{\delta_j}{R},$$

$$\dot{m}_j^* = \frac{\dot{m}_j}{2\pi R \mu_l}, \quad \dot{m}_j''^* = \frac{\dot{m}_j'' l_j}{\mu_l}, \quad M^* = \frac{M}{\pi R^2 l \rho_l},$$

$$\vartheta_j = \frac{\Delta T_j}{\Delta T_N}, \quad \tau_j^* = \frac{\tau_j}{g\rho_l \delta_N}, \quad l_j^* = \frac{l_j}{l},$$

$$R^* = \frac{R}{l}, \quad \rho^* = \frac{\rho_v}{\rho_l}, \quad \mu^* = \frac{\mu_l}{\mu_v} \tag{9a}$$

where

$$\Delta T_N = \left(\frac{q_e l_{ep}}{0.943 l_c}\right)^{4/3} \left[\frac{l_c \nu_l}{g\rho_l h_{fg} k_l^3}\right]^{1/3}$$

and

$$\delta_N = \left[4 \frac{\mathrm{Ja}}{\mathrm{Pr}} \frac{\nu_l^2 l_c}{g}\right]^{1/4} \tag{9b}$$

The definitions in equations (9*b*) are based on the Nusselt solution [11] for laminar condensation on a plate of length l_c with a temperature drop across the film calculated to give the same total heat transfer per unit width as the specified heat input per unit perimeter in the evaporator.

The dimensionless system of steady-state governing equations resulting from introduction of the above variables and the simplifications discussed above is

Mass balances:

$$\dot{m}_k''^* = \Gamma_k^* - \Gamma_j^* \tag{10a, b, c}$$

$$\dot{m}_k''^* - \dot{m}_k^* - \dot{m}_j^* \tag{11a,b,c}$$

$$M^* = 1 - (1 - 2\epsilon_e) l_e^* - (1 - 2\epsilon_a) l_a^* - (1 - 2\epsilon_c) l_c^* \tag{12}$$

Energy balances:

$$\dot{m}_k''^* (1 + \mathrm{Ja}\vartheta_v) = q_k^* l_k + \Gamma_j^* \mathrm{Ja}\vartheta_j - \Gamma_k^* \mathrm{Ja}\vartheta_k \tag{13a,b,c}$$

$$\dot{m}_e^* (1 + \mathrm{Ja}\vartheta_v) = q_e^* l_p^* + \Gamma_e^* Ja\vartheta_e \tag{14}$$

Force balances:

$$\epsilon_k/\epsilon_N = \tau_{wk}^* + \tau_{ik}^* \tag{15a,b,c}$$

Any one of the energy equations, (13*a–c*) or (14), can be replaced by the simpler steady-state system energy balance given by

$$q_c^* l_c^* = q_e^* l_{ep}^* \tag{16}$$

Due to the simplifications in the liquid-film momentum equations, it is not necessary to solve the vapor-core momentum equations simultaneously with the rest of the system. The coupling of the liquid and vapor momentum equations is in the interfacial shear stress, interfacial momentum flux, and pressure drop terms, but in the simplified system, only the vapor flow rate and density are needed, together with the interfacial friction factor, to specify the interfacial shear. The vapor flow rates are obtained in terms of the liquid flow rates by substituting the interfacial mass transfer rates found in equations (10*a, b, c*) into equations (11*a, b, c*). The resulting equations simply state that, under steady-state conditions, the downward mass flow rate of liquid is equal to the upward mass flow rate of vapor at any cross section of the device.

When the film flow is laminar, a differential force balance on the liquid film, of the type used in Nusselt's analysis but including interfacial shear, predicts a parabolic velocity profile in the film. Using this result and the friction factors defined in Table 1, the wall shear stress expressions to be used in equations (15*a, b, c*) for laminar and turbulent films respectively are

$$\tau_{wj}^* = \frac{\tau_{ij}^*}{2} + \frac{24 A_{wj} \bar{\Gamma}_j^*}{\mathrm{Gr}^2 \epsilon_N \epsilon_j^2} \tag{17a}$$

$$\tau_{wj}^* = \frac{0.223 A_{ij} (\bar{\Gamma}_j^*)^{7/4}}{\mathrm{Gr}^2 \epsilon_N \epsilon_j^2} \tag{17b}$$

and the respective interfacial shear stress expressions for laminar and turbulent vapor flow are

$$\tau_{ij}^* = \frac{64 A_{ij} \bar{\Gamma}_j^* [1 + \rho^*/(2\epsilon_j)]}{\mathrm{Gr}^2 \epsilon_N (\rho^*/\mu^*)} \tag{17c}$$

$$\tau_{ij}^* = \frac{16 A_{ij} (\bar{\Gamma}_j^*)^2 [1 + \rho^*/(2\epsilon_j)]^2 (0.005 + x_1 \epsilon_j^{x_2})}{\mathrm{Gr}^2 \epsilon_N \rho^*} \tag{17d}$$

The coefficients A_{wj} and A_{ij} are weight factors accounting for the fact that the average interfacial shear stress in a given section of the device may differ from the product of the average friction factor and the average dynamic pressure. The factors will be approximated by assuming the following: In the condenser, the film thickness and flow rate are given by the Nusselt solution; in the adiabatic section, the film thickness and flow rate are constant; and in the evaporator, the flow rate varies linearly down the tube (because q_e is constant) and the film thickness is constant. Using these assumptions, and the equality of liquid and vapor flow rates, the axial variation of the shear stresses can be estimated and estimates of A_{wj} and A_{ij} obtained.

The interfacial shear stress expressions given above are based on the velocity of the vapor relative to average velocity of the liquid film. The factor $[1 + \rho^*/(2\epsilon_j)]$, seen in equations (17*c*) and (17*d*), represents the ratio of the relative vapor velocity to the absolute vapor velocity. This factor differs considerably from unity under some circumstances.

The system of equations is solved by using the mass and energy equations, (10)–(14), together with the shear stress expressions, equations (17*a–d*), to express all variables in terms of: ϵ_c, ϵ_a, ϵ_e; the specified system geometry and fill quantity; the specified boundary conditions, T_w and q_e; and the thermophysical properties of the working fluid (which are known functions of temperature). The result is a set of three nonlinear, algebraic equations for ϵ_c, ϵ_a, and ϵ_e. The equation for ϵ_c is not coupled to the other two, and the equation for ϵ_a is independent of ϵ_e so the three equations can be solved successively by numerical techniques.

Experimental Study

To assess the accuracy of the analytical model proposed, experimental data have been obtained using a two-phase closed thermosyphon which has been used in previous work [7] but

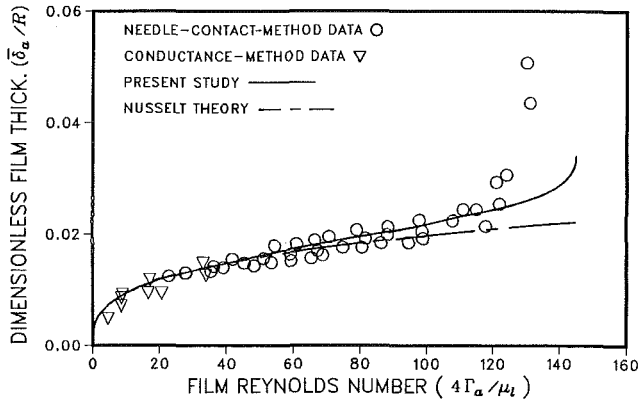

Fig. 2 Experimental data and theoretical predictions from the present study for adiabatic-section film thickness (working fluid is methanol, $R = 0.71$ cm, $l_c = 1.08$ m, $l_a = 0.305$ m, $l_{ep} = 1.03$ m, $T_w = 36°C$)

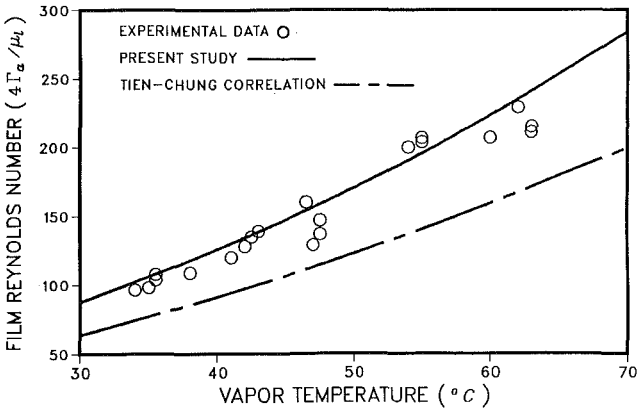

Fig. 3 Experimental data and theoretical flooding predictions from the present study (working fluid is methanol, same device as Fig. 2)

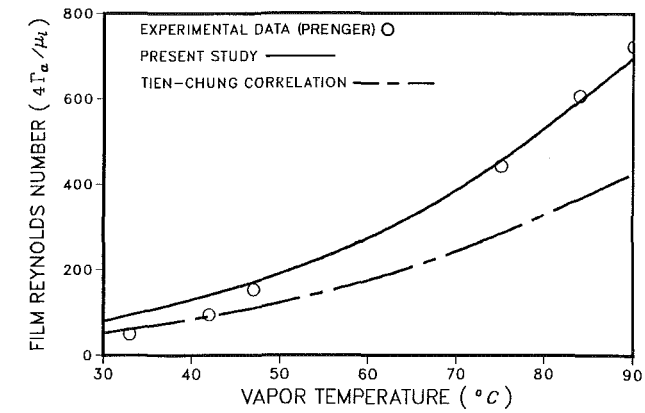

Fig. 4 Experimental data of Prenger [9] and theoretical flooding predictions from the present study (working fluid is water, $R = 1.03$ cm, $l_c = 1.26$ m, $l_a = 1.0$ cm, $l_{ep} = 55.9$ cm)

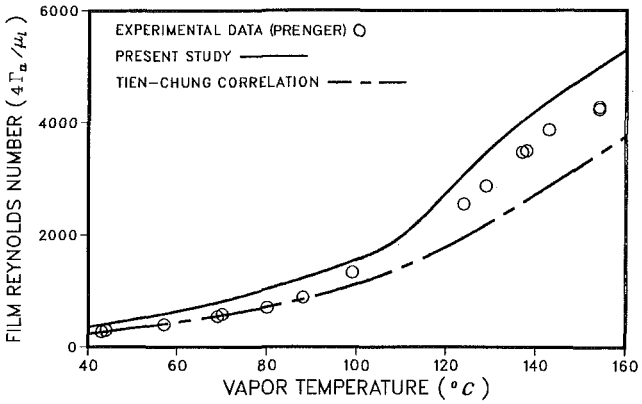

Fig. 5 Experimental data of Prenger [9] and theoretical flooding predictions from the present study (working fluid is methanol, same device as Fig. 4)

which has been modified to include several transparent flow observation sections in the condenser and adiabatic sections. A detailed description of the apparatus and experimental procedures can be found in a supporting document for this paper [16].

Results and Comparison With Experimental Data

The steady-state system of equations has been solved over a range of operating temperatures and heat inputs for several different thermosyphon geometries and two different working fluids chosen to correspond to conditions represented by the experimental data to be presented. Flooding data from the present study and from two other groups of investigators and film thickness data from the present study will be presented [4, 9].

Figure 2 shows the dependence of film thickness in the adiabatic section on the film Reynolds number (essentially evaporator heat input) as predicted by the analysis of the present study and by Nusselt theory, which neglects interfacial shear stress. Corresponding film-thickness data, obtained with the apparatus of the present study using the film-conductance and needle-contact methods, are also presented. The theoretical curves assume a condenser wall temperature of 36°C which is representative of the conditions displayed in the experimental data (the range of condenser inside-wall temperatures represented in the data is approximately 34°C to 38°C, depending on heat input). The agreement between the predictions of the present study and the experimental data is seen to be quite good although the experimental data indicate flooding slightly before the rapid up-turn in the theoretical curve which occurs at $Re_f \approx 145$. For reference, it is noted that

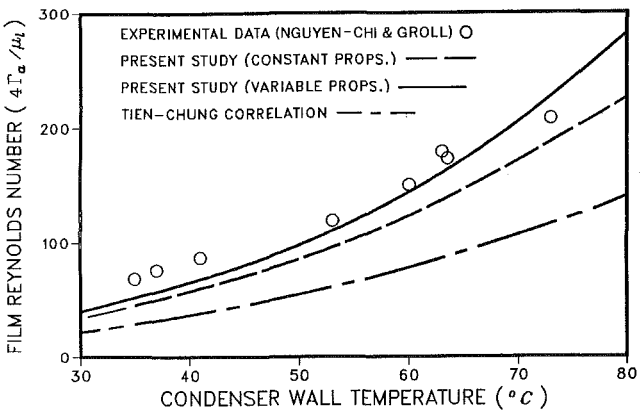

Fig. 6 Experimental data of Nguyen-Chi and Groll [4] and theoretical flooding predictions from the present study (working fluid is water, $R = 0.850$ cm, $l_c = 1.00$ m, $l_a = 50.0$ cm, $l_{ep} = 1.00$ m)

the predicted film Reynolds numbers at flooding corresponding to condenser wall temperatures of 34°C and 38°C are 135 and 156, respectively.

As expected, the film-thickness predictions are very close to those of Nusselt theory for low Reynolds numbers and become progressively greater than those predicted by Nusselt theory as the film Reynolds number, and therefore the interfacial shear stress, increases. The qualitative features of the film thickness versus Reynolds number curves predicted by the present analysis will be similar to the curve shown in Fig. 2 for other working fluids and temperature ranges. However, the

Reynolds number required for flooding and the rapidity of the increase of film thickness with the Reynolds number will depend significantly on the thermophysical properties of the working fluid, particularly through variations in the values of Gr and ρ^*.

Figures 3–6 present experimental flooding data along with the corresponding analytical predictions. Each figure plots the film Reynolds number at flooding versus the working fluid vapor temperature or condenser wall temperature (depending on which temperature was measured in the corresponding experimental investigation). If both the wall temperature and the vapor temperature were measured, the data are presented on the basis of the vapor temperature because the flooding point tends to be more sensitive to the vapor temperature than to the wall temperature. The flooding curve predicted by the commonly used, semi-empirical, Tien–Chung correlation is also presented in each figure for comparison with the current analysis. The Tien–Chung correlation predicts flooding when

$$\left(4\frac{\Gamma_a^*}{\mathrm{Gr}}\right)^{1/2}[1+(\rho^*)^{-1/2}]=\frac{1.79}{\mathrm{Bo}^{1/4}}\tanh(0.5\mathrm{Bo}^{1/2}) \tag{18}$$

From the methanol flooding data of the present study shown in Fig. 3, it can be seen that the present analysis predicts the data very well. On the other hand, while the Tien–Chung correlation correctly predicts the trend of the data, the flooding points tend to be predicted prematurely. The tendency of the Tien–Chung correlation to underpredict thermosyphon flooding data is seen in all of the data sets presented here. This may be a result of the fact that many of the experimental studies from which the constant factor in the correlation was derived used experimental facilities in which test-section entrance effects are significant. In a thermosyphon, the tube is continuous, so entrance effects are eliminated.

Figure 4 shows data collected at Los Alamos National Laboratory (LANL) using water as the working fluid [9]. The device used to obtain the data did not have an adiabatic section but a 1-cm adiabatic section is assumed for calculational purposes. As in the first data set, the present analysis shows good agreement with the data while the Tien–Chung curve lies below the data. The data appear to show a greater increase with temperature of the Reynolds number at flooding than that predicted by either the present analysis or by the Tien–Chung correlation. However, there are not enough data points to judge whether or not this is significant.

Figure 5 presents LANL flooding data for methanol [9]. The agreement between the predictions of the present analysis and the data is quite good. Although the predicted results are slightly above the experimental data, the present analytical model predicts the change in curvature of the flooding curve resulting from the transition to turbulent film flow. This effect is not reflected in the predictions of the Tien–Chung correlation, and the predictions of the correlation fall considerably below the data at the high end of the temperature range. It is interesting to note that, under the conditions represented by the data, the liquid velocity is of the same order of magnitude as the vapor velocity and, near the upper end of the temperature range, the vapor velocity is only about twice as large as that of the liquid. If the absolute vapor velocity, rather than the velocity relative to the liquid film, is used for calculating the interfacial shear stresses, the predictions of the current analysis are as much as 55 percent above the experimental data.

Figure 6 presents thermosyphon flooding data for water reported on the basis of thermosyphon wall temperature [4]. In the constant-property solution, all physical properties are evaluated at the wall temperature while in the variable property solution the properties are evaluated at the local bulk liquid temperature based on the calculated vapor temperature. The data presented are from a thermosyphon operating at an inclination angle of 10 deg from vertical, the closest case to vertical operation for which data were reported. It can be seen that all of the theoretical curves underpredict the heat input at flooding. However, it can be estimated, from data on the effect of thermosyphon inclination on flooding [4], that the heat input at flooding for a vertical thermosyphon, using water as the working fluid, will be below that for a thermosyphon inclined 10 deg from vertical by about 25 percent at a condenser wall temperature of 30°C and by about 5 percent at a wall temperature of 60°C. The agreement between the experimental data and the theoretical predictions of this analysis is very good if the effect of inclination angle is considered.

When all of the flooding and film thickness data are considered, the predictions of the proposed model are seen to be very good. This is significant because it shows that many aspects of the behavior of the thermosyphon can be accurately modeled within a single comprehensive model based on a first-principle analysis. This approach has a sounder basis and is more versatile than analyses relying on simple scaling laws and correlations.

Transient Operation

This section analyzes the transient operation of the two-phase closed thermosyphon. The particular situation considered here is the commonly occurring case of laminar flow of the liquid film accompanied by turbulent flow in the vapor core. In many practical situations, the thermosyphon wall temperature or heat flux will vary with time. This analysis considers the evolution in time of the thermosyphon operating characteristics in response to a time varying heat input in the evaporator with the condenser wall temperature maintained at a constant value. The results are useful in determining the conditions under which the device operation can be treated as a sequence of quasi-steady states and those under which a complete transient calculation is required. The simplicity of the control-volume approach is of great value in the transient analysis because the inclusion of time dependence in the governing equations causes a much less dramatic increase in the complexity of the computations required to obtain numerical solutions than that which would result if a differential formulation were used.

The simplifying assumptions used in the steady-state analysis will also be used here. In addition, the variation of liquid properties with temperature will be neglected. The use of the steady-state shear stress and heat transfer coefficients in the transient analysis implies the assumption that the temperature and velocity profiles respond to transients over time scales much shorter than those characterizing the overall system response. The validity of this assumption is treated in detail elsewhere [16], but it is also justified on the basis of the results of the analysis.

As in the steady-state analysis, the superheat required for boiling or evaporation will be neglected. One consequence of neglecting the details of the boiling phenomena in the evaporator is that the distribution of the heat input to the liquid pool between evaporation of the liquid in the pool and changing its temperature is indeterminate. In the present analysis, it will be assumed that the liquid pool is always at the same temperature as the vapor (i.e., saturated liquid state) unless the vapor temperature is increasing too rapidly for the heat input in the liquid pool to provide the necessary energy to meet this condition. When the condition of equality of liquid pool and vapor temperatures cannot be satisfied, the evaporative mass flux in the pool is set equal to zero and all of the heat input in the liquid pool is assumed to be in the form of sensible heat.

The variables which will be used for nondimensionalizing the governing equations are the same as those used in the steady-state analysis. In the transient analysis the

characteristic temperature difference will be taken as ΔT_0, the initial temperature drop across the liquid film, and the characteristic film thickness is the corresponding film thickness calculated from Nusselt theory [15]. In addition to the previously defined variables, a dimensionless time variable is introduced

$$t^* = t\left(\frac{g\delta_N^2}{3\nu_l l_c}\right) \tag{19}$$

The time scale used here is based on a characteristic film residence time obtained using the film thickness and mass flow rate predicted by the Nusselt theory for a plate of length l_c and a temperature difference of ΔT_0. The film residence time is chosen because the transient evolution of the system is controlled by the film residence time and the condensation rate rather than, for example, the thermal diffusion time of the liquid film.

The system of dimensionless governing equations for transient operation of the thermosyphon, with the introduction of the previously discussed simplifications, is given below. Mass balances for the liquid film, vapor core, and total system, respectively, are

$$\frac{l_j^*}{\epsilon_N}\frac{d\epsilon_j}{dt^*} = \dot{m}_j''^* - \Gamma_j^* + \Gamma_k^* \tag{20a, b, c}$$

$$\frac{l_j}{2\epsilon_N}\frac{d\rho^*}{dt^*} = \dot{m}_j' - \dot{m}_j''^* - \dot{m}_k''^* \tag{21a, b, c}$$

$$M^* = 1 - (1-2\epsilon_e)l_e^* - (1-2\epsilon_a)l_a^* - (1-2\epsilon_c)l_c^* \tag{22}$$

Energy balances for the liquid film and the liquid pool are

$$\mathrm{Ja}\frac{l_j^*}{\epsilon_N}\left(\epsilon_j\frac{d\vartheta_v}{dt^*} + \vartheta_v\frac{d\epsilon_j}{dt^*}\right) = q_j^* l_j^* + \Gamma_k^*\mathrm{Ja}\vartheta_k - \Gamma_j^*\mathrm{Ja}\vartheta_j - \dot{m}_j''^*(1+\mathrm{Ja}\vartheta_v) \tag{23a, b, c}$$

$$\mathrm{Ja}\frac{l_p^*}{\epsilon_N}\frac{d\vartheta_p}{dt^*} = q_e^* l_p^* + \Gamma_e^*\mathrm{Ja}\vartheta_v - \dot{m}_e^*(1+\mathrm{Ja}\vartheta_v) \tag{24}$$

The liquid-film momentum balances are

$$\frac{\epsilon_j}{\epsilon_N} = \tau_{wj}^* + \tau_{ij}^* \tag{25a, b, c}$$

As in the steady-state analysis, the vapor-core momentum equations are omitted because they are decoupled from the rest of the system through the simplifications used in the liquid-film momentum equations. Also note that, because the vapor is assumed saturated, there is no vapor-phase energy equation.

The details of the numerical solution procedure will be omitted for brevity as they are documented elsewhere [16]. In essence, the system can be reduced to a set of four first-order differential equations in time, coupled to ten nonlinear algebraic equations which are used to estimate the values of the time derivatives for stepping the solution out in time. The time integration is performed using a Runge–Kutta technique [17].

Results of Transient Analysis

Solutions of the system of transient governing equations have been carried out for several representative cases to illustrate the type of results obtained from the present model. Figures 7–9 show the response of various system variables to several different transient evaporator heat flux inputs for a thermosyphon using water as the working fluid with the geometry and initial operating state summarized in Table 2.

Figure 7 shows the system response to ramp increases in evaporator heat flux of two different rise times, $\Delta t_r^* = 0.118$ (1.00 s) and $\Delta t_r^* = 2.35$ (20.0 s). The response curve for each variable is plotted in a normalized form as the ratio of the difference between the current and initial values of a variable and

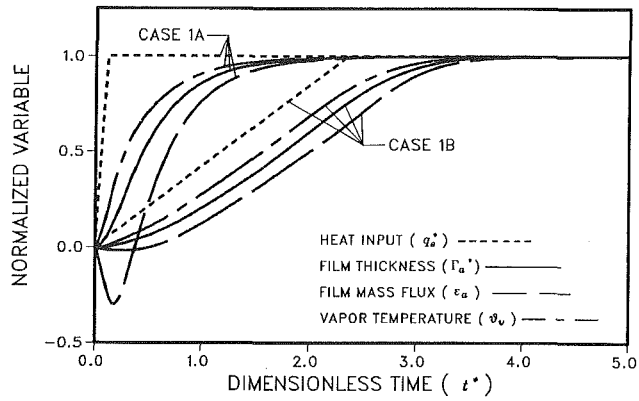

Fig. 7 Transient responses of vapor temperature, film thickness in the adiabatic section, and liquid mass flux in the adiabatic section to ramp increases in evaporator heat flux

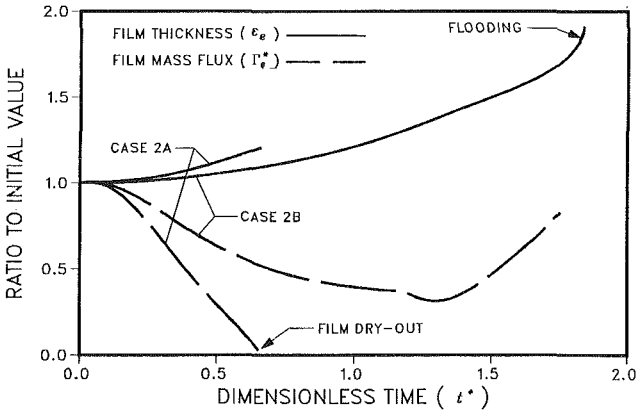

Fig. 8 Flooding and evaporator film dryout under transient conditions

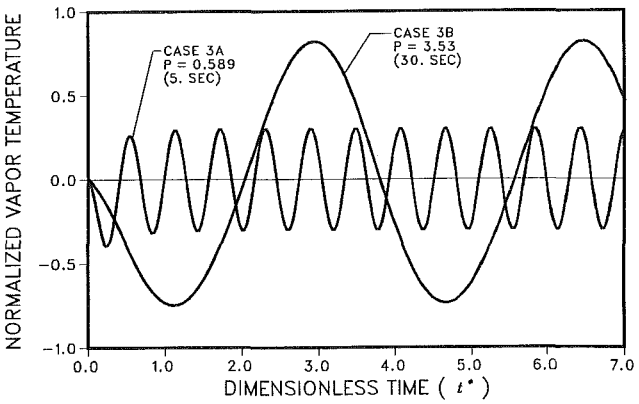

Fig. 9 Response of vapor temperature to sinusoidal variations in evaporator heat input of two different frequencies

the difference between the steady-state values at the beginning and end of the transient. The final values of the variables displayed in Fig. 1 are: $\epsilon_{a_f} = 0.0178$, $\Gamma_{af}^* = 42.8$, and $\vartheta_{v_f} = 1.53$. The dimensionless time variable t^* can be converted to dimensional form (in units of seconds) by multiplying by 8.50. The initial and final values of q_e^* are 32.9 and 42.7 which correspond to approximately 70 percent and 90 percent, respectively, of the value required for flooding. For reference, it is noted that the increases in ϵ_a, Γ_a^*, and ϑ_v displayed in Fig. 7 correspond to 22 percent, 30 percent, and 47 percent of their respective initial values.

The transient response curves in Fig. 7 illustrate several points. First, the vapor temperature response leads the

Table 2 Initial thermosyphon operating state for transient calculations (working fluid is methanol, $T_w = 60.0°C$, $R = 1.0$ cm, $l_c = 1.0$ m, $l_a = 0.25$ m, $l_{ep} = 1.0$ m)

Variable	Value	Variable	Value	Variable	Value
Γ_c^*	32.7	Γ_a^*	32.9	Γ_e^*	13.4
ϵ_c	1.01×10^{-2}	ϵ_a	1.44×10^{-2}	ϵ_e	1.20×10^{-2}
ϑ_v	1.04	M^*	0.100	Bo	24.1
Gr	6.17×10^{4}	Ja	9.02×10^{-3}	ρ^*	1.68×10^{-4}

Table 3 Influence of variation of dimensionless parameters on rise times of selected system variables ($t = 8.5t^*$)

	t_{50}^*			t_{90}^*		
	ϑ_v	ϵ_a	Γ_a^*	φ_v	ϵ_a	Γ_a^*
Case 1A	0.282	0.448	0.681	0.956	1.14	1.35
$M^* \rightarrow 1.5M^*$	0.381	0.558	0.791	1.25	1.45	1.66
$\rho^* \rightarrow 2\rho^*$	0.259	0.433	0.574	0.877	1.04	1.16
Ja→2Ja	0.471	0.645	0.865	1.55	1.74	1.94
Bo→Bo/2	0.264	0.436	0.595	0.879	1.06	1.21
Gr→2Gr	0.139	0.300	0.371	0.596	0.664	0.691

responses of the fluid dynamic variables, ϵ_a and Γ_a^*. This is expected because the temperature difference between the condenser wall and the vapor core provides the driving force for condensation. Second, the dimensionless time required for the system to re-establish steady-state operation, after the transient in heat input, is of the order of unity, verifying that the film residence time is the controlling time scale for the transient evolution of the system. If the dimensionless time scale had been based on film thickness and thermal diffusivity of the liquid, the rise time for the system would be of the order of 10^3 dimensionless time units. Lastly, the convergence of the rise times of the heat input function and the system response between Case 1A with a rapid rise in heat flux and Case 1B, with the heat flux increasing over a period of time comparable to the natural rise time for the system, indicates that for variations of evaporator heat flux with characteristic rise times or periods of oscillation substantially greater than $t^* = 1$, the system response should be well approximated by a sequence of steady-state calculations.

To provide an indication of the influence of the various dimensionless parameters on system response, calculations with the same condenser wall temperature and transient heat-input function as Case 1A of Fig. 7 have been performed with modified values for various parameters as summarized in Table 3. The parameters t_{50}^* and t_{90}^* displayed in Table 3 are the dimensionless rise times required for the indicated system variable to reach 50 percent and 90 percent of its normalized final value. The results displayed in the table indicate that the system response tends to become more rapid if the Grashof number or density ratio is increased or if the Bond number is decreased, and the system response is slowed if the Jakob number or fill quantity is increased. The decreases in system response time caused by increasing Gr, increasing ρ^*, or decreasing Bo can be explained by the fact that each of these changes tends to reduce the film residence time and, thus, speed the response of the system. Reducing Bo or increasing ρ^* will cause a reduction in the interfacial shear stress while an increase in Gr will cause a reduction in wall shear. All of these effects tend to increase the velocity of the film. The slower response times associated with an increased value of M^* or Ja reflect the increase in thermal capacitance of the liquid pool resulting from these changes.

Figure 8 illustrates the progress of the system toward the flooding and film dryout operating limits under transient conditions. The initial operating state is that summarized in Table 2. The variables are normalized by their initial values. In contrast to the cases shown in Fig. 7, the final value of evaporator heat flux is $q_e^* = 51.6$ which is 10 percent above the value required for flooding as predicted by the steady-state analysis. In Case 2A, with a rapid increase in evaporator heat flux, Γ_e, the film mass flux entering the liquid pool becomes equal to zero at $t^* \approx 0.7$ ($t \approx 6$ s) indicating dryout of the liquid film in the evaporator. This case is interesting because dryout would not be predicted by a steady-state calculation. It should be noted that, although in the example case presented the heat flux in the evaporator is above that required for flooding, this is not a necessary condition for dryout of the film. In fact, dryout of the liquid film in the evaporator during a transient increase in evaporator heat flux can be predicted at heat flux values substantially below those required for flooding. The key criterion for this limit is that the time scale for changes in film thickness and mass flux be long compared to the rise time of the change in heat flux. In situations where this criterion is satisfied, dryout of the film would be expected if

$$q_e^* > \frac{\Gamma_e^*}{l_e^*} \tag{26}$$

where the right-hand side is evaluated at the start of the transient. The criterion discussed above also assumes that the mass of the film is small enough that the time required to evaporate the film is small compared to the film residence time.

In Case 2B, the rate of increase of q_e^* is small enough that film dryout is avoided. However, because the heat input exceeds the value required for flooding, the increase in film thickness in the adiabatic section becomes unbounded at $t^* \approx 2.0$. The evaporator mass flux also increases rapidly near the flooding limit but this is believed to be a numerical effect caused by the rapid increase in film thickness. The change in slope of evaporator mass flux at $t^* \approx 1.2$ is caused by the end of the ramp increase in heat flux. The lag in response of ϵ_a indicates that the system can operate in an un-flooded state at values of heat input above the steady-state flooding limit if the duration of the heat flux transient is sufficiently short.

Figure 9 shows the response of system vapor temperature to sinusoidal variations in evaporator heat flux of two different frequencies. The initial operating state is, as before, the one summarized in Table 2. The two heat-flux input functions have the form

$$q_e^* = 32.9 - 9.80\sin(2\pi t^*/p) \quad (27)$$

where p is the period of the input and the amplitude has been chosen so that the peak is the same as the final heat input value of Fig. 7. Figure 9 plots the difference between the current vapor temperature and the initial vapor temperature, normalized by the difference between the steady-state vapor temperature corresponding to the peak of the sinusoidal heat input and the initial vapor temperature. Two points are illustrated in the figure. First, the response curves are slightly asymmetric about the t^* axis. This is to be expected because of the nonlinearity of the governing equations. Second, when the period of the input is small relative to the characteristic rise time of the system, the amplitude of the response is greatly attenuated. On the other hand, if the period of the input is of the same order or greater than the rise time of the system, the response can probably be well approximated as a sequence of steady states.

In order to assess the accuracy of the calculations presented above, it is desirable to compare the results of the analysis with experimental data. Unfortunately, attempts to obtain experimental data on the transient operation of the system used in this study have proven to be unsuccessful because of thermal masses in the system not reflected in the model, and no data are available in the literature. Thus, although the results of the transient analysis are consistent with expected system behavior, quantitative assessment of its accuracy will require a specially designed experiment or an expansion of the model to include the thermal masses of the thermosyphon components.

Conclusions

A first-principle formulation of the governing equations for steady-state and transient operation of the two-phase closed thermosyphon has been solved for several representative cases. The steady-state predictions agree well with available experimental data. The ability of the model to predict the transient response of the system and to predict operating limits under transient conditions has been demonstrated, although experimental data with which to compare the predictions are currently unavailable. The results of the analysis indicate that, in the parameter regime considered, the most important time scale controlling the transient response of the system is the film residence time (or runoff time). On this basis, it can be concluded that steady-state analysis of the thermosyphon will be valid as long as transient inputs to the system have characteristic time constants (or periods of oscillation) which are long compared to the film residence time. The proposed model provides a powerful and versatile analytical model of the two-phase closed thermosyphon while maintaining a relatively simple mathematical formulation.

Acknowledgments

The support of this work by the Electric Power Research Institute under grant EPRI RP 1160-3 is gratefully acknowledged.

References

1 Dunn, P., and Reay, D. A., *Heat Pipes*, 3rd ed., Pergamon Press, New York, 1982.

2 Fukano, T., Chen, S. J., and Tien, C. L., "Operating Limits of the Closed Two-Phase Thermosyphon," *Proc. ASME/JSME Thermal Eng. Conf.*, Vol. 1, 1983, pp. 95–101.

3 Dobran, F., "Steady-State Characteristics and Stability Thresholds of a Closed Two-Phase Thermosyphon," *Int. J. Heat Mass Transfer*, Vol. 28, 1985, pp. 949–957.

4 Nguyen-Chi, H., and Groll, M., "Entrainment or Flooding Limit in a Closed Two-Phase Thermosyphon," *Advances in Heat Pipe Technology*, D. A. Reay, ed., Pergamon Press, New York, 1981, pp. 147–162.

5 Tien, C. L., and Chung, K. S., "Entrainment Limits in Heat Pipes," *AIAA Journal*, Vol. 17, 1981, pp. 643–646.

6 Calia, C., and Griffith, P., "Modes of Circulation in an Inverted U-Tube Array With Condensation," *Thermal-Hydraulics in Nuclear Power Technology*, ASME-HTD, Vol. 15, New York, 1981, pp. 35–43.

7 Chen, S. J., Reed, J. G., and Tien, C. L., "Reflux Condensation in a Two-Phase Closed Thermosyphon," *Int. J. Heat Mass Transfer*, Vol. 27, 1984, pp. 1587–1594.

8 Seban, R. H., and Faghri, A., "Condensation in a Vertical Tube With a Closed Top," *Int. J. Heat Mass Transfer*, Vol. 27, 1984, pp. 944–948.

9 Prenger, F. C., Los Alamos National Laboratory, Los Alamos, New Mexico, private communication, 1984.

10 Wallis, G. B., *One Dimensional Two-Phase Flow*, McGraw-Hill, New York, 1969, Ch. 11.

11 Collier, J. G., *Convective Boiling and Condensation*, 2nd ed., McGraw-Hill, New York, 1981, Ch. 10.

12 Hewitt, G. F., and Hall-Taylor, N. S., *Annular Two-Phase Flow*, Pergamon Press, New York, 1970.

13 Bharathan, D., Wallis, G. B., and Richter, H. J., *Air-Water Counter-Current Annular Flow*, EPRI Report NP-1165, 1979.

14 Blangetti, F., and Naushahi, M., "Influence of Mass Transfer on the Momentum Transfer in Condensation and Evaporation Phenomena," *Int. J. Heat Mass Transfer*, Vol. 23, 1980, pp. 1694–1695.

15 Rohsenow, W. M., "Heat Transfer and Temperature Distribution in Laminar-Film Condensation," *Trans. ASME*, Vol. 83, 1961, pp. 1645–1648.

16 Reed, J. G., *Analytical Modeling of the Two-Phase Closed Thermosyphon*, Ph.D. Thesis, Department of Mechanical Engineering, University of California, Berkeley, CA, 1985.

17 Carnahan, B., Luther, H. A., and Wilkes, J. O., *Applied Numerical Methods*, Wiley, New York, 1969.

Nonequilibrium Modeling of Two-Phase Critical Flows in Tubes

F. Dobran
Applied Science Department,
New York University,
New York, NY 10003
Assoc. Mem. ASME

A nonequilibrium two-phase flow model is described for the analysis of critical flows in variable diameter tubes. Modeling of the two-phase flow mixture in the tube is accomplished by utilizing a one-dimensional form of conservation and balance equations of two-phase flow which account for the relative velocity and temperature differences between the phases. Closure of the governing equations was performed with the constitutive equations which account for different flow regimes, and the solution of the nonlinear set of six differential equations was accomplished by a variable step numerical procedure. Computations were carried out for a steam–water mixture with varying degrees of liquid subcooling and stagnation pressures in the vessel upstream of the tube and for different tube lengths. The numerical results are compared with the experimental data involving critical flows with variable liquid subcoolings, stagnation pressures, and tube lengths, and it is shown that the nonequilibrium model predicts well the critical flow rate, pressure distribution along the tube, and the tube exit pressure.

1 Introduction

1.1 Relevance of the Problem. The rupture of a vessel or pipe containing a subcooled liquid at high pressure may produce a rapid depressurization of the fluid. When this occurs, the liquid flashes soon after its pressure reaches the saturation condition and thereafter flows as a two-phase mixture. With a sufficiently high stagnation pressure upstream of the break, the flow through the break reaches the critical flow condition whereby the flow rate becomes a maximum and independent of the conditions downstream of the break. The critical flow rate through the broken pipe or vessel depends on the state of the fluid upstream of the break and on the characteristics of the break itself.

Knowledge of the critical mass flow rate through the ruptured vessel or pipe is important not only for predicting the depressurization history of the fluid in the vessel and the flow through the broken pipe, but also for calculating the forces produced by the expanding jet on the pipe or vessel and on the surrounding equipment that may be located in the vicinity of the jet. For this purpose, it is important to estimate reliably the two-phase fluid characteristics exiting from a ruptured vessel or piping system.

1.2 Previous Work and Objectives of the Paper. Many models have been proposed in the past for modeling critical two-phase flows; reviews have been written by Wallis [1], Saha [2], Isbin [3], Richter [4], and Dobran [5], among others.

The modeling of two-phase critical flows in ducts can be carried out by the homogeneous (equilibrium) model or by a wide variety of nonequilibrium models. The homogeneous model assumes a thermodynamic equilibrium between the phases and it provides good results for the critical flow rate when there is a sufficient time for the two phases to reach equilibrium as might, for example, occur in long tubes. In short tubes, however, this condition may not be satisfied and the homogeneous model is usually replaced by a nonequilibrium model. The nonequilibrium effects are associated with the relative velocity and temperature differences between the phases and are, thus, functions of the flow regime. The homogeneous model offers no heat transfer resistance and, consequently, the thermal relaxation time is equal to zero. Since the real flow has a finite relaxation time, a departure from the homogeneous flow will occur whenever the two-phase mixture accelerates rapidly or the residence time of a fluid particle in the flow channel is small. For flows in short pipes or nozzles, it may be assumed that the time associated with the phase change is short, and an assumption of a frozen flow (or a constant quality flow) may be reasonable [6].

The early nonequilibrium models were empirical in nature and cannot be used with confidence in the extrapolation of the critical flow parameters. By using separate conservation and balance equations of each phase and solving these equations along the tube, such that the critical flow becomes dependent on the history of flow up to the critical point, the modeling has proved more successful. The advantage of this approach is that the thermal and mechanical nonequilibrium between the phases can be described to a large degree of complexity, but at the expense of a great deal of information which is necessary to complete the model description (such as initial nucleation site density and bubble diameter, interphase friction characteristics and heat transfer, criteria which account for different flow regimes, etc.), and it is possible to reach a point of diminishing returns where the results obtained from such a model are worse than when using a simpler model which requires less input information. Modeling of critical flows utilizing the conservation and balance equations of each phase [4, 5, 7–11] requires the specification of initial conditions which may be in the form of the initial velocities of the two phases, the initial bubble population density and size (or void fraction), and the liquid superheat. Since complete specification of the model also requires specification of tube wall friction, interphase friction, interphase heat transfer coefficient, and flow regime which at the present are incompletely understood, there should be very good reason indeed for modeling critical flows utilizing separate conservation and balance equations of each phase.

The purpose of this paper is to present a nonequilibrium model for the analysis of two-phase critical flows which is based on the separate conservation and balance equations for each phase and to substantiate the analytical predictions with the experimental data. The reasons for developing such a model are twofold: (1) to develop modeling capabilities for two-phase critical flows, and (2) to obtain detailed flow conditions at the tube exit that can be used to study the two-phase flow jet on the outside of the tube. The two-phase critical flow model contains a number of improvements over the models developed in [4, 11]. It uses correct forms of the governing

Contributed by the Heat Transfer Division for publication in the JOURNAL OF HEAT TRANSFER. Manuscript received by the Heat Transfer Division May 1, 1985.

equations and improved correlations for the constitutive equations. With these improvements, the proposed critical flow model is expected to be applicable over a larger range of liquid stagnation conditions and duct geometric conditions.

2 Description of a Two-Phase Critical Flow Model

The two-phase critical flow model will allow for the hydrodynamic and thermal nonequilibrium between the phases, where the former nonequilibrium arises from the velocity and pressure differences between the phases and the latter for the temperature difference between the liquid and gas. To simplify the model it will be assumed that the gas phase is in a thermal equilibrium (at a local saturation pressure) and that both phases are at the same pressure at any cross section of the duct. Furthermore, it will be also assumed that the critical flow through a tube can be modeled by one-dimensional, steady-state forms of the conservation and balance equations for two-phase flow.

2.1 Steady-State, One-Dimensional Forms of Conservation and Balance Equations for Two-Phase Flow. The steady-state, one-dimensional forms of the conservation and balance equations for two-phase flow may be found in Wallis [12], Collier [13] and Dobran [5]. These are:

Conservation of Mass Equations:

From the gas and liquid mass flow rates

$$M_G = \alpha \rho_G A u_G = xM \tag{2.1}$$

$$M_L = (1-\alpha)\rho_L A u_L = (1-x)M \tag{2.2}$$

and equations of state

$$\rho_G = \rho_G(P) \tag{2.3}$$

$$\rho_L = \rho_L(h_L, P) \tag{2.4}$$

we may obtain

$$\rho_G A u_G \frac{d\alpha}{dz} + \alpha A u_G \frac{d\rho_G}{dP}\frac{dP}{dz} + \alpha \rho_G A \frac{du_G}{dz} - M\frac{dx}{dz} = -\alpha \rho_G u_G \frac{dA}{dz} \tag{2.5}$$

$$-\rho_L A u_L \frac{d\alpha}{dz} + (1-\alpha)A u_L \left(\frac{\partial \rho_L}{\partial P}\right)_{h_L}\frac{dP}{dz} + (1-\alpha)\rho_L A \frac{du_L}{dz} + M\frac{dx}{dz} + (1-\alpha)A u_L \left(\frac{\partial \rho_L}{\partial h_L}\right)_P \frac{dh_L}{dz} = -(1-\alpha)\rho_L u_L \frac{dA}{dz} \tag{2.6}$$

where z is the distance along the tube and is defined in Fig. 1.

Momentum Equations:

$$\alpha \rho_G A u_G \frac{du_G}{dz} = -\alpha A \frac{dP}{dz} - F_{LG}A - F_{wG}A - \eta(u_G - u_L)M\frac{dx}{dz} - \rho_G g \alpha A \cos\theta \tag{2.7}$$

$$(1-\alpha)\rho_L A u_L \frac{du_L}{dz} = -(1-\alpha)A\frac{dP}{dz} + F_{LG}A - F_{wL}A - (1-\eta)(u_G - u_L)M\frac{dx}{dz} - \rho_L g(1-\alpha)A\cos\theta \tag{2.8}$$

In the above equations F_{LG} is the drag force per unit volume acting on the liquid phase in the direction of flow, and in the opposite direction on the gas phase; F_{wG} and F_{wL} are the drag forces per unit volume exerted by the tube wall on the gas and liquid, respectively. The terms containing η in equations (2.7) and (2.8) represent the effect of phase change and it appears that this value is close to 1/2 [12]. For horizontal flow $\cos\theta = 0$ and for vertical upflow $\cos\theta = 1$.

Nomenclature

a = interfacial area/unit volume of the mixture
A = tube flow cross-sectional area
C_D = drag coefficient, defined by equations (2.19) and (2.20)
Cf_i = interfacial friction coefficient, defined by equations (2.15)–(2.17)
Cp = specific heat at constant pressure
C_{VM} = coefficient defined by equation (2.28)
d = average bubble diameter, defined by equation (2.23)
D = tube diameter
f = frictional coefficient
F_{LG} = interfacial drag force defined by equation (2.9)
F_{wL} = drag force at the wall defined by equation (2.35)
g = gravitational constant
G = mass flux
h = enthalpy
$\tilde{h}$ = heat transfer coefficient
k = thermal conductivity
K = tube inlet loss coefficient in equation (2.47)
L = tube length
M = mass flow rate
N = bubble density
Nu = Nusselt number
P = pressure
Pr = Prandtl number = $\mu Cp/k$
$\dot{Q}_L$ = heat transfer rate from liquid to gas, defined by equation (2.29)
Re = Reynolds number
S = slip ratio = u_G/u_L
T = temperature
u, u^* = axial velocity in the tube; $u^* = \rho_0' u/G_0$
x = quality
X = vector of dependent variables in equation (2.60)
z = distance along the tube, see Fig. 1
α = gas volumetric fraction or void fraction
Δ = virtual mass coefficient, defined by equation (2.27)
η = energy redistribution coefficient in equations (2.10) and (2.11)
μ = viscosity
ξ = viscous drag coefficient, defined by equation (2.14)
ρ = density
σ = surface tension
τ = shear stress
ϕ = two-phase frictional multiplier, defined by equation (2.38)

Subscripts

a = annular flow
b = bubbly flow
FLO = friction liquid only
G = pertains to the gas phase
GO = gas only
i = pertains to initial point
L = pertains to the liquid phase
LO = liquid only
0 = at the tube inlet
0′ = stagnation state, see Fig. 2
sat = saturation
sub = subcooling
sup = superheating
w = wall

For bubbly and separated flows, where the liquid phase flows adjacent to the tube wall, $F_{wG} = 0$, and it will be assumed in the present model. The interphase drag force F_{LG} may be modeled as follows [5, 14, 15]

$$F_{LG} = \xi_{GG}(u_G - u_L) + \Delta_{GG}\left(u_G \frac{du_G}{dz} - u_L \frac{du_L}{dz}\right) \tag{2.9}$$

where $\xi_{GG} \geq 0$ is the viscous drag coefficient and $\Delta_{GG} \geq 0$ is the virtual mass coefficient which accounts for the relative acceleration between the phases. Substituting equation (2.9) into equations (2.7) and (2.8) results in the following momentum equations for gas and liquid

$$[\rho_G u_G \alpha A + \Delta_{GG} u_G A] \frac{du_G}{dz} + [-A u_L \Delta_{GG}] \frac{du_L}{dz} + [\alpha A] \frac{dP}{dz} + [\eta M(u_G - u_L)] \frac{dx}{dz} = -A\xi_{GG}(u_G - u_L) - \rho_G g \alpha A \cos\theta \tag{2.10}$$

$$[-\Delta_{GG} u_G A] \frac{du_G}{dz} + [\rho_L u_L (1-\alpha) A + \Delta_{GG} u_L A] \frac{du_L}{dz} + [(1-\alpha)A] \frac{dP}{dz} + [(1-\eta)M(u_G - u_L)] \frac{dx}{dz} = A\xi_{GG}(u_G - u_L) - \rho_L g (1-\alpha) A \cos\theta - F_{wL} A \tag{2.11}$$

Energy Equations. A control volume energy balance on the two-phase flow mixture in the tube of length dz with an adiabatic wall and similarly on the liquid phase yields

$$M\left[h_{LG} + \frac{1}{2}(u_G^2 - u_L^2)\right] \frac{dx}{dz} + \left[xM \frac{dh_G}{dP}\right] \frac{dP}{dz} + [xMu_G] \frac{du_G}{dz} + [(1-x)Mu_L] \frac{du_L}{dz} + [(1-x)M] \frac{dh_L}{dz} + Mg\cos\theta = 0 \tag{2.12}$$

$$M\left[h_{LG} + \frac{1}{2}(u_G^2 - u_L^2)\right] \frac{dx}{dz} = \frac{d\dot{Q}_L}{dz} \tag{2.13}$$

where use was made of $h_{LG} = h_G - h_L$ and the equations of state and conservation of mass, equations (2.1)–(2.4). $d\dot{Q}_L/dz$ in the above equation denotes the heat transfer rate per unit tube length from the liquid to the gas.

The two-phase flow nonequilibrium model consists of six equations, (2.5), (2.6), and (2.10)–(2.13), which must be solved for six unknowns: α, x, u_G, u_L, P, and h_L. Before this can be done, however, the constitutive equations for ξ_{GG}, Δ_{GG}, F_{wL}, and $d\dot{Q}_L/dz$ must be specified. The tube geometry is assumed to be known, i.e., $A = A(z)$, and the mass flow rate M is treated as a parameter and is determined as described below. The thermodynamic properties $h_G(P)$, $\rho_G(P)$, $\rho_L(h_L, P)$, $(\partial\rho_L/\partial P)_{h_L}$, and $(\partial\rho_L/\partial h_L)_P$ can be determined for a specific substance from thermodynamic tables.

2.2 Constitutive Equations. As the two-phase flow mixture expands through the tube its flow regime may change from bubbly flow at low void fractions to the annular flow at high void fractions. At intermediate void fractions the flow regime is usually classified as churn-turbulent [12]. The flow regime will be accounted in the model through the specification of constitutive equations for the viscous drag ξ_{GG}, virtual mass Δ_{GG}, for the interfacial heat transfer rate expressed by $d\dot{Q}_L/dz$, and for the viscous drag at the tube wall F_{wL}. These constitutive equations are known reasonably well for bubbly and annular flows only. For the churn-turbulent flow regime, however, it will be assumed that the above constitutive equations can be determined by interpolation.

2.2.1 Viscous Drag Coefficient ξ_{GG}. The viscous drag coefficient ξ_{GG} appearing in equation (2.9) accounts for the interphase friction in the bulk of the flow. Realizing that F_{LG} represents the interfacial shear stress times the interfacial perimeter and divided by the flow area, it follows that

$$\xi_{GG} = \frac{2Cf_i}{D} \sqrt{\alpha}\, \rho_G |u_G - u_L| \tag{2.14}$$

where Cf_i is the interfacial friction coefficient and is given for bubbly, annular, and churn-turbulent flows as [5, 12, 16]

$$Cf_i = \frac{3}{8} C_{D_{1-\alpha}} (1-\alpha)^3 \sqrt{\alpha} \frac{\rho_L}{\rho_G} \frac{D}{d}; \quad 0 < \alpha \leq \alpha_b \tag{2.15}$$

$$Cf_i = 0.079\, \mathrm{Re}_G^{-0.25} \left[1 + 24(1-\sqrt{\alpha}) \left(\frac{\rho_L}{\rho_G}\right)^{1/3}\right]; \quad \alpha_a \leq \alpha < 1 \tag{2.16}$$

$$Cf_i = Cf_{ib} + \left(\frac{Cf_{ib} - Cf_{ia}}{\alpha_b - \alpha_a}\right)(\alpha - \alpha_b); \quad \alpha_b < \alpha < \alpha_a \tag{2.17}$$

where Cf_{ib} is evaluated from equation (2.15) at $\alpha = \alpha_b$ and Cf_{ia} is found from equation (2.16) at $\alpha = \alpha_a$. In equation (2.15) $C_{D_{1-\alpha}}$ is the bubble drag coefficient, which may be determined from the knowledge of a single bubble drag coefficient C_D [12], i.e.,

$$C_{D_{1-\alpha}} = C_D (1-\alpha)^{-4.7} \tag{2.18}$$

$$C_D = \frac{24}{\mathrm{Re}}(1 + 0.15\, \mathrm{Re}^{0.687}); \quad \mathrm{Re} \leq 1000$$
$$C_D = 0.44; \quad \mathrm{Re} > 1000 \tag{2.19}$$

The Reynolds numbers Re in equation (2.19) and Re_G in equation (2.16) are defined as follows

$$\mathrm{Re} = \frac{\rho_L d(1-\alpha)|u_G - u_L|}{\mu_L}$$
$$\mathrm{Re}_G = \frac{\rho_G D |u_G - u_L|}{\mu_G} \tag{2.20}$$

where d is the average bubble diameter, which may be determined from the bubble number density N and interfacial area per unit volume a, i.e.,

$$\alpha \equiv \frac{\pi}{6} N d^3 \tag{2.21}$$

$$a \equiv \pi N d^2 \tag{2.22}$$

$$d \equiv \frac{6\alpha}{a} \tag{2.23}$$

2.2.2 Interfacial Area Per Unit Volume a. For bubbly flow regime, the interfacial area a may be found from equations (2.21) and (2.22), and for annular flow it follows from the definition. Hence

$$a = N\pi \left(\frac{6\alpha}{N\pi}\right)^{2/3}; \quad 0 < \alpha \leq \alpha_b \tag{2.24}$$

$$a = \frac{4}{D}\sqrt{\alpha}; \quad \alpha_a \leq \alpha < 1 \tag{2.25}$$

$$a = a_b + \left(\frac{a_b - a_a}{\alpha_b - \alpha_a}\right)(\alpha - \alpha_b); \quad \alpha_b < \alpha < \alpha_a \tag{2.26}$$

where a_b is evaluated from equation (2.24) at $\alpha = \alpha_b$ and a_a from equation (2.25) at $\alpha = \alpha_a$.

2.2.3 Virtual Mass Coefficient Δ_{GG}. The virtual mass coefficient Δ_{GG} appears in equation (2.9) and it is known reasonably well only for the bubbly flow. It is given by the expression

$$\Delta_{GG} = \alpha \rho_L C_{VM} \tag{2.27}$$

where C_{VM} appears to have the form [17]

$$C_{VM} = 0.3 \tanh(4\alpha) \tag{2.28}$$

2.2.4 Interfacial Heat Transfer $d\dot{Q}_L/dz$. The interfacial

heat transfer rate from the liquid to the gas per unit tube length can be expressed as follows:

$$\frac{d\dot{Q}_L}{dz} \equiv \tilde{h}\, aA\,(T_L - T_G) \tag{2.29}$$

where $\tilde{h}$ is the interfacial heat transfer coefficient and is modeled according to the flow regime [5, 18]. Hence

$$\mathrm{Nu} = \frac{\tilde{h}d}{k_L} = 2 + 0.6\ \mathrm{Re}_b^{1/2}\mathrm{Pr}_L^{1/3}; \qquad 0 < \alpha \le \alpha_b \tag{2.30}$$

$$\mathrm{Nu} = \frac{\tilde{h}D\sqrt{\alpha}}{k_G} = 0.023\ \mathrm{Re}_{Ga}^{0.8}\ \mathrm{Pr}_G^{0.4}; \qquad \alpha_a \le \alpha < 1 \tag{2.31}$$

$$\tilde{h} = \tilde{h}_b + \frac{(\tilde{h}_b - \tilde{h}_a)}{(\alpha_b - \alpha_a)}\ (\alpha - \alpha_b); \qquad \alpha_b < \alpha < \alpha_a \tag{2.32}$$

where $\tilde{h}_b$ is determined from equation (3.30) at $\alpha = \alpha_b$ and $\tilde{h}_a$ from equation (2.31) at $\alpha = \alpha_a$. The Reynolds numbers in the above equations are given as

$$\mathrm{Re}_b = \frac{\mathrm{Re}}{1-\alpha} = \frac{\rho_L d\,|u_G - u_L|}{\mu_L} \tag{2.33}$$

$$\mathrm{Re}_{Ga} = \frac{\rho_G D\sqrt{\alpha}}{\mu_G}\,|u_G - u_L| \tag{2.34}$$

2.2.5 Wall Friction F_{wL}. The drag force per unit volume of the mixture which is exerted by the tube wall on the liquid F_{wL} can be expressed in terms of the wall shear stress τ_w, i.e.,

$$F_{wL} = \frac{4}{D}\,\tau_w = -\left(\frac{dP}{dz}\right)_{\text{wall friction}} \tag{2.35}$$

and it will be modeled by the Chisholm correlation [19] since it fits the advanced empirical correlation curves of Baroczy (cit. [13]) quite well and accounts for the effect of mass flux on the frictional pressure gradient. The correlation is expressed by the following set of equations

$$F_{wL} = -\phi_{LO}^2\left(\frac{dP}{dz}\right)_{\text{FLO}} \tag{2.36}$$

$$\left(\frac{dP}{dz}\right)_{\text{FLO}} = \frac{4}{D} f_{LO}\,\frac{G^2}{2\rho_L} \tag{2.37}$$

$$\phi_{LO}^2 = 1 + (Y^2 - 1)[Bx^{(2-n)/2}(1-x)^{(2-n)/2} + x^{2-n}] \tag{2.38}$$

where f_{LO} is the single-phase frictional coefficient determined from

$$f_{LO} = \frac{16}{\mathrm{Re}_{LO}}; \quad \mathrm{Re}_{LO} = \frac{GD}{\mu_L} \le 2000 \tag{2.39}$$

$$f_{LO} = 0.079\ \mathrm{Re}_{LO}^{-0.25}; \quad \mathrm{Re}_{LO} > 2000 \tag{2.40}$$

n is the power in the friction factor–Reynolds number relationship ($n = 0.25$ for the Blasius equation), and

$$Y^2 = \frac{\left(\frac{dP}{dz}\right)_{GO}}{\left(\frac{dP}{dz}\right)_{LO}} = \frac{f_{GO}}{f_{LO}}\,\frac{\rho_L}{\rho_G} \tag{2.41}$$

Y	G	B
$Y \le 9.5$	≤ 500	4.8
	$500 < G < 1900$	$2400/G$
	≥ 1900	$55/G$
$9.5 < Y < 28$	≤ 600	$520/(YG^{0.5})$
$Y \ge 28$	> 600	$21/Y$
		$\dfrac{15{,}000}{(Y^2G^{0.5})}$

(2.42)

In equation (2.41) f_{GO} is determined from equations similar to equations (2.39) and (2.40), but involving the gas properties.

The utilization of the constitutive equations described above requires the specification of void fractions α_b and α_a where the flow regime changes from bubbly to churn-turbulent and from churn-turbulent to annular, respectively. From experimental data [12, 13] it may be generally assumed that $\alpha_b \simeq 0.3$ and $\alpha_a \simeq 0.8$.

2.3 Initial Conditions. The solution of the ordinary differential equations described in Section 2.1 depends on the initial conditions. As shown in Fig. 1, the fluid in the vessel at $z = 0$ is assumed to be at the stagnation state and it may be a single-phase liquid or a two-phase mixture. Referring to Fig. 2, the *liquid subcooling* is determined from the information on the stagnation state 0′

$$\Delta T_{\text{sub}} = T_{\text{sat}}(P_{0'}) - T_{0'} \tag{2.43}$$

As the subcooled liquid expands it does not in general begin to flash at the saturation pressure corresponding to its stagnation temperature, but at a lower pressure than can be characterized by the liquid superheating which is defined as follows

$$\Delta T_{\text{sup}} = T_{0'} - T_{\text{sat}}(P(z_i)) \tag{2.44}$$

The degree to which the liquid superheats depends on its nucleation characteristics, such as on the amount of dissolved gas present in the liquid and on the rate of depressurization, among other factors. This superheat is usually found to be a few degrees Celsius and will be determined from the following correlation [20]

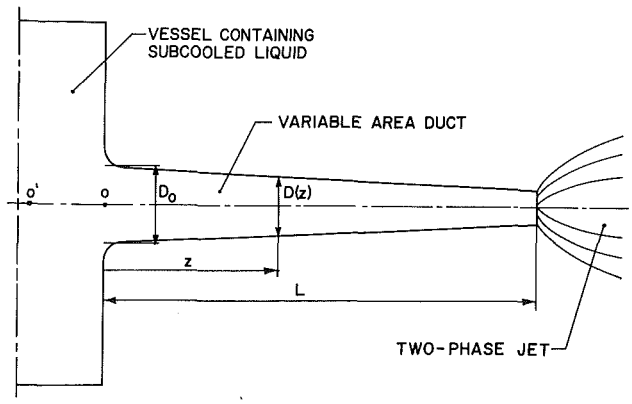

Fig. 1 Two-phase flow discharging through a variable area duct

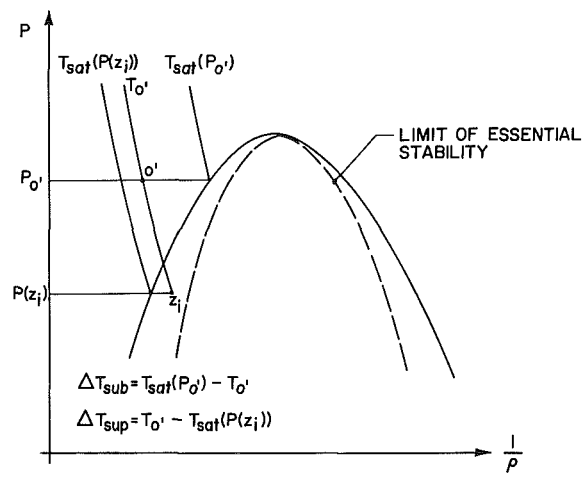

Fig. 2 Representation of subcooled and superheated liquid states on the pressure-volume diagram

$$P(z_i) = P_{sat}(T_0') - C\,\sigma^{1.5}\left(\frac{T_0'}{T_{crit}}\right)^{13.73}/(k_B T_{crit}) \qquad (2.45)$$

where $C = 0.08$.

The initial conditions for the two-phase flow model described above are determined by first locating the position in the tube and the state of fluid at this position where the liquid reaches a specified amount of superheat. This initial position is found by the following procedure:

(*a*) Based on the given stagnation pressure P_0' and liquid subcooling ΔT_{sub}, find from equation (2.43)

$$T_0' = T_{sat}(P_0') - \Delta T_{sub} \qquad (2.46)$$

(*b*) Using T_0' in equation (2.45), determine $P(z_i)$.

(*c*) From the Bernoulli and conservation of mass equations, i.e.,

$$P_0' = P(z_i) + (1+K)\rho_0' \frac{1}{2} u(z_i)^2 + 4\frac{f}{D} z_i \rho_0' \frac{1}{2} u(z_i)^2 \qquad (2.47)$$

$$GA = \rho_0' u(z_i) A(z_i) = G_0 A_0 \qquad (2.48)$$

it can be shown that

$$z_i = \frac{D(z_i)}{4f}\left[\frac{2\rho_0'[P_0' - P(z_i)]}{G_0^2} - (1+K)\right]\left[\frac{A(z_i)}{A_0}\right]^2 \qquad (2.49)$$

where K is the tube entry loss coefficient and is about 0.3 for the radiused entry. The frictional coefficient f is given by

$$\frac{1}{\sqrt{4f}} = -0.86 \ln\left[\frac{\epsilon}{3.7D} + \frac{2.51}{\mathrm{Re}\sqrt{4f}}\right]; \quad \mathrm{Re} = \frac{GD}{\mu_L} \geq 4000$$

$$= \frac{16}{\mathrm{Re}}; \quad \mathrm{Re} < 4000 \qquad (2.50)$$

where ϵ/D is the relative tube roughness.

The initial conditions at $z = z_i$ required to solve the differential equations are, therefore, specified as follows:

1 With the given initial nucleation site density N_i and diameter of nuclei d_i, it follows from equation (2.21) that

$$\alpha_i = \frac{\pi}{6} N_i d_i^3 \qquad (2.51)$$

2 Since the quality $x = M_G/M$, it follows from equations (2.1) and (2.2) that

$$x_i = \frac{1}{1 + \frac{\rho_0'}{\rho_G}\frac{1-\alpha_i}{\alpha_i}\frac{1}{S_i}} \qquad (2.52)$$

where $S_i = u_{Gi}/u_{Li}$ is the initial slip; it may be assumed to be equal to one.

3 From equations (2.1) and (2.52) we have

$$u_{Gi} = \frac{x_i M}{\alpha_i \rho_G A(z_i)} \qquad (2.53)$$

4 The liquid velocity is found from S_i and equation (2.53), i.e.,

$$u_{Li} = u_{Gi}/S_i \qquad (2.54)$$

5 The initial pressure is found from equation (2.45)

$$P_i = P(z_i) \qquad (2.55)$$

6 The liquid enthalpy at $z = z_i$ is determined from the saturated liquid enthalpy at $P(z_i)$ (see Fig. 2) and from the liquid superheating, hence

$$h_{Li} = h_{Lsat}(P(z_i)) = Cp_L[T_0' - T_{sat}(P_i)] \qquad (2.56)$$

where Cp_L may be evaluated at P_i.

Equations (2.51)–(2.56) specify a set of initial conditions for the two-phase flow model described in Sections 2.1 and 2.2. To close this model, however, it is also necessary to specify constitutive equations for the bubble density N and the initial size of nucleation centers. Ardron [21] provided a transport equation for N, while Richter [4] and Dobran [5] assumed a constant value of N and found that the critical flow parameters are not very sensitive to a tenfold variation in this number. In view of this and other studies described in detail in [5], it will be assumed that

$$N = N_i = 10^{11}\ 1/\mathrm{m}^3 \qquad (2.57)$$

$$d_i = 5 \times 10^{-5}\ \mathrm{m} \qquad (2.58)$$

2.4 Solution Procedure. The system of differential equations represented by equations (2.5), (2.6), (2.10), (2.11), (2.12), and (2.13) can be written in the following vector form

$$A^* \frac{dX}{dz} = B^* \qquad (2.59)$$

where X is the vector of dependent variables, i.e.,

$$X = (\alpha, x, u_G, u_L, P, h_L)^T \qquad (2.60)$$

and where the coefficients of matrix A^* and vector B^* depend on the dependent variables. The solution of the above system of equations can be accomplished by utilizing the initial conditions specified by equations (2.51)–(2.56) in terms of the tube geometry (tube length and flow cross-sectional area), fluid stagnation conditions (pressure and subcooling), and the total mass flow rate M. To determine the *critical flow rate* it is necessary and sufficient that [22]

$$\Delta = 0 \quad \text{and} \quad n_i = 0, \quad i = 1, \ldots, 6 \qquad (2.61)$$

where $\Delta = \det(A^*)$ is the determinant of A^*, and n_i is the determinant obtained by replacing the ith column of A^* by the column vector B^*. The critical flow in the tube is, then, obtained by searching for that value of the mass flow rate M which will yield the conditions specified by equation (2.61) at the end of the tube.

The system of differential equations with the initial conditions discussed above was programmed for the numerical solution into a computer program which is fully discussed in [5]. Basically, the numerical integration is accomplished by a variable step Runge–Kutta procedure on the basis of a global error specification. The program automatically determines the critical mass flow rate and it has built-in thermodynamic property data tables.

3 Results and Discussion

In this section the numerical results obtained by the critical two-phase flow model discussed in the previous section are presented and compared with the steam–water experimental data of saturated and subcooled liquid discharging from a vessel through tubes of different lengths.

A comparison of the predicted critical mass fluxes with the experimental data of [23] is illustrated in Fig. 3. This comparison involves stagnation pressures from 1 to 3 MPa and subcoolings up to 40°C, and tube length-to-diameter ratios $L/D = 10 - 287.6$ with $D = 0.0125$ m. As can be seen from Fig. 3, the predicted critical mass fluxes are within ±10 percent of the experimental values, and for the subcooled liquid case with $L/D = 10$ the critical flow rates tend to be underestimated.

The predicted and experimental pressure distribution along the tube are shown in Figs. 4–6. Figures 4 and 5 show a comparison for the situation of a saturated liquid in the vessel, while Fig. 6 shows this comparison for the case of subcooled liquid with $L/D = 97$. As can be seen from these figures, the predicted pressure distributions along the tube are, overall, in a very good agreement with the data. A slight underprediction

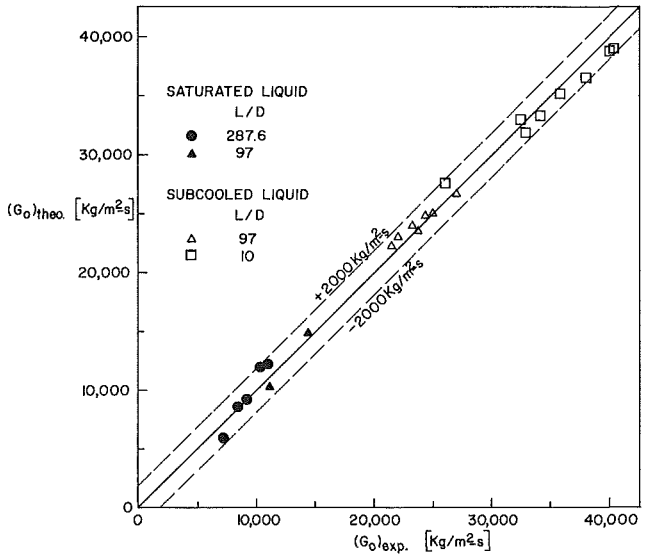

Fig. 3 Comparison of predicted and experimental mass fluxes

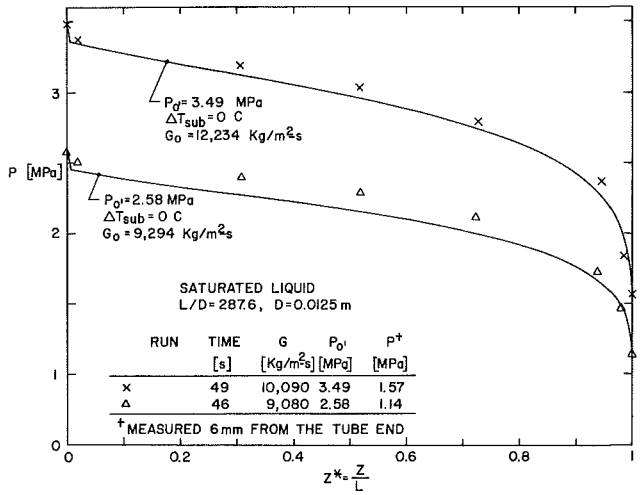

Fig. 4 Comparison of the predicted pressure distribution along the tube with the experimental data of saturated liquid

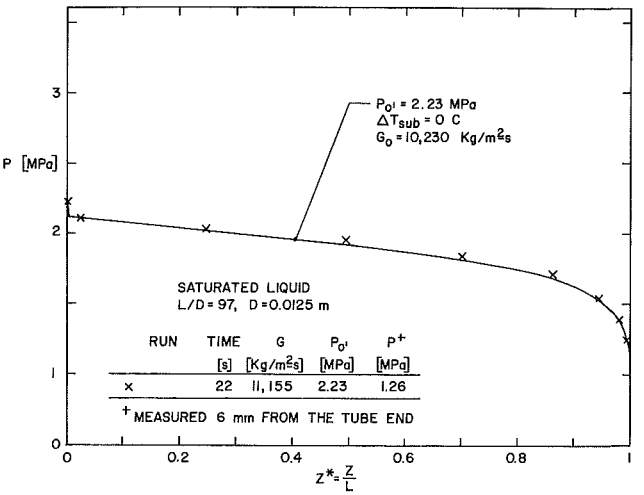

Fig. 5 Comparison of the predicted pressure distribution along the tube with the experimental data of saturated liquid

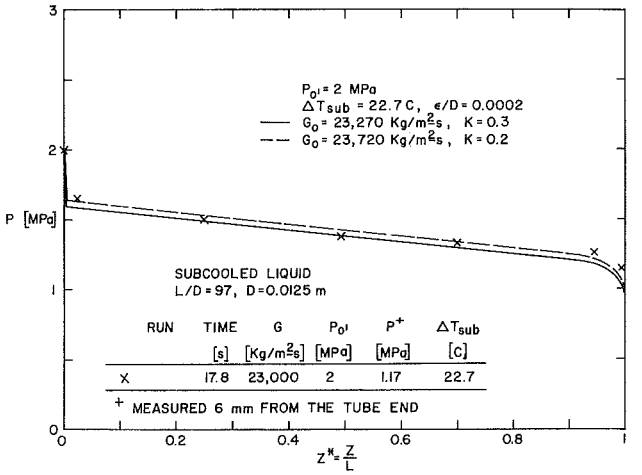

Fig. 6 Comparison of the predicted pressure distribution along the tube with the experimental data of subcooled liquid

of the data for the saturated liquid case with $L/D = 287.6$ in Fig. 4 may be attributed to the error in the specification of initial conditions in the model, since the tube entrance frictional pressure losses and two-dimensional effects may be of importance in inducing the local nucleation characteristics in the liquid which are different from the ones modeled through the simple relations as described in Section 2. In the case of subcooled liquid discharging through tubes the pressure distribution is also sensitive to the relative tube roughness and tube entrance loss coefficient as shown in Fig. 6. Accurate measurements of the tube exit pressure in critical two-phase flow situations do not appear to exit, but as Figs. 4–6 illustrate, the pressure measurements 6 mm from the tube end agree within 10 percent with the experimental data and the model predictions of the steep pressure variations near the tube exit are in accord with the data. However, for the situation [23] corresponding to the saturated liquid case discharging through a pipe with $L/D = 287.6$ the total (static and dynamic) pressure of 2.2 MPa was measured at 0.5 D from the tube exit in the jet expansion region. Using the computed values of pressure and void fraction at the tube exit for this run [5], it may be shown that the total exit pressure is 2.263 MPa which agrees closely with the experimental value of 2.2 MPa. To test further the credibility of the analytical model, a pressure transducer was inserted 0.5 mm from the tube exit [24] for the situation of saturated liquid with $L/D = 100$, $P_0' = 2.13$ MPa, and $P_0' = 2.02$ MPa. The measured pressures at this location were 0.98 and 0.934 MPa, whereas the computed exit pressures turn out to be 1.005 and 0.947 MPa, respectively.

Figures 7 and 8 illustrate the numerical results of the void fraction, quality, velocity, and liquid subcooling distributions along the tube with $L/D = 97$ and for saturated and subcooled conditions of liquid in the vessel. For the saturated liquid case in Fig. 7, the void fraction, quality, and vapor and liquid velocities increase along the tube and show a steep rise close to the tube end where the critical flow point is located. Although an initial slip ratio of 1.2 was assumed, it has no effect on the subsequent evolution of gas and liquid velocities. These velocities are also almost equal to each other, with the gas velocity being larger than the liquid velocity and this difference increasing slightly toward the end of the tube. This, of course, implies a mechanical equilibrium between the phases but not the thermal equilibrium as attested by the distribution of the liquid superheat ΔT_{sup}, which substantially increases toward the tube end where the accelerational effects tend to increase. These nonequilibrium effects also increase in shorter tubes [5].

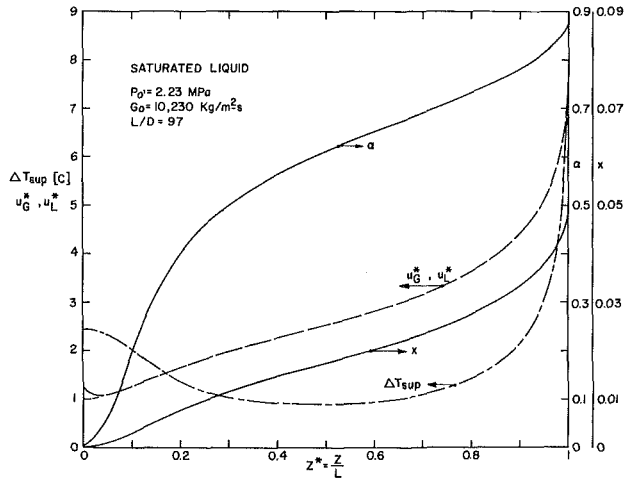

Fig. 7 Numerical results for saturated liquid and *L/D* = 97

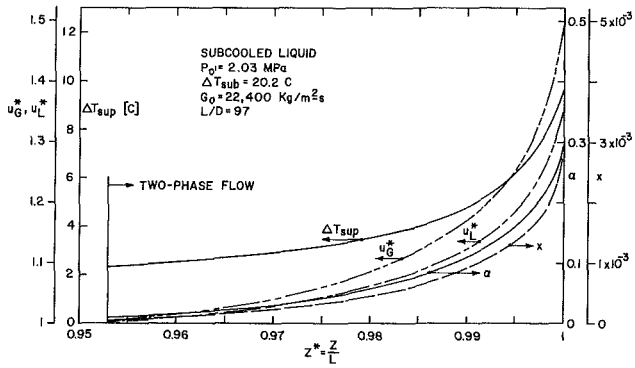

Fig. 8 Numerical results for subcooled liquid and *L/D* = 97

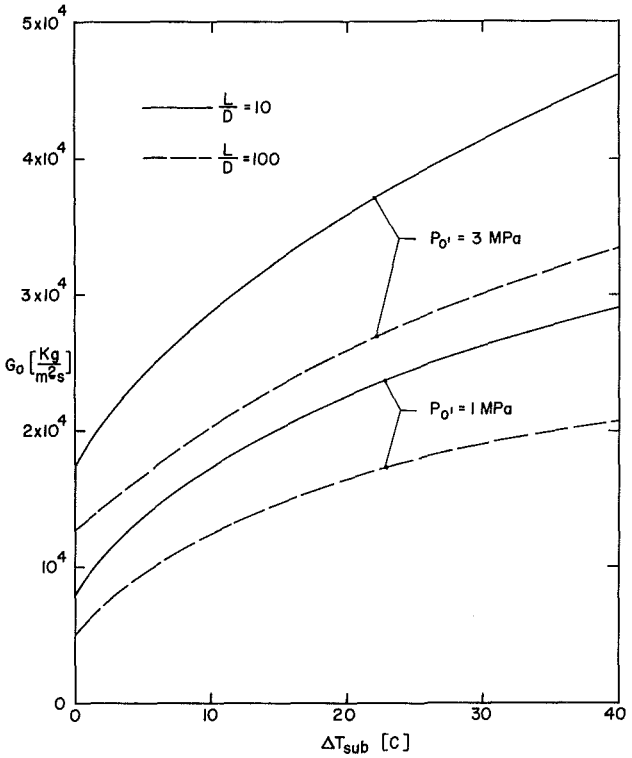

Fig. 9 Relationship between the critical mass flux, subcooling, stagnation pressure, and *L/D*

For the case of subcooled liquid at the tube inlet in Fig. 8, the mechanical and thermal nonequilibrium is significantly increased over that for the saturated liquid situation in Fig. 7, and this increases even further with a decrease in the tube length [5].

The predicted critical two-phase flow results for steam–water are illustrated in Fig. 9 in a plot of critical mass flux versus the liquid subcooling in the vessel for varying stagnation pressures of liquid and tube length to diameter ratios. These results show that higher stagnation pressures, larger liquid subcoolings, and smaller *L/D* ratios produce larger critical mass fluxes.

4 Conclusions

A two-phase flow model was developed for the analysis of critical flows in tubes. The model allows for the thermal and mechanical nonequilibrium between the phases and the resulting nonlinear differential equations were solved by a numerical procedure along the tube until the critical flow is achieved at the tube end. A computer program based on this model was also developed and the predictions of the model were tested with the experimental data of subcooled and saturated water discharging through short and long pipes. It is shown that the model gives very good predictions of the critical flow rates and pressure distributions along the tubes. The numerical results show that increasing the liquid subcooling and decreasing the tube length increases the mechanical and thermal nonequilibrium between the phases and that this nonequilibrium may be considerable close to the tube end. The degree of thermal and mechanical nonequilibrium of the two phases exiting from the tube may have a significant influence on the development of the two-phase flow expansion region on the outside of the tube, and a detailed critical flow modeling as presented in the paper is necessary for reliable prediction of such a flow expansion [25]. The comparison of analytical results of two-phase flow jet expansion with the experimental data in [25] also attests to the credibility of the presented critical flow model.

References

1 Wallis, G. B., "Critical Two-Phase Flow," *International Journal of Multiphase Flow*, Vol. 6, 1980, pp. 97–112.

2 Saha, P., "A Review of Two-Phase Steam–Water Critical Flow Models With Emphasis on Thermal Nonequilibrium," NUREG/CR/0417, BNL-NUREG-50907 Report, 1978.

3 Isbin, H. S., "Some Observations on the Status of Two-Phase Critical Flow Models," *International Journal of Multiphase Flow*, Vol. 6, 1980, pp. 131–138.

4 Richter, H. J., "Separated Two-Phase Flow Model: Application to Critical Two-Phase Flow," *International Journal of Multiphase Flow*, Vol. 9, 1983, pp. 511–530.

5 Dobran, F., "Discharge of Two-Phase Critical Flow Through Tubes," Stevens Institute of Technology Report ME-RT-84016, 1984.

6 Henry, R. E., and Fauske, H. K., "The Two-Phase Critical Flow of One Component Mixtures in Nozzles, Orifices and Tubes," ASME JOURNAL OF HEAT TRANSFER, Vol. 93, 1971, pp. 179–187.

7 Giot, M., and Fritte, A., "Two-Phase Two- and One-Component Critical Flows With the Variable Slip Model," *Prog. Heat Mass Transfer*, Vol. 6, 1972, pp. 651–670.

8 Ardron, K. H., "A Two-Fluid Model for Critical Vapor–Liquid Flow," *International Journal of Multiphase Flow*, Vol. 4, 1978, pp. 323–337.

9 Lyczkowski, R. W., and McFadden, J. H., "Calculations of Nonequilibrium Discharge Flow," *Trans. Can. Society of Mechanical Engineers*, Vol. 4, 1976, pp. 159–166.

10 Rivald, W. C., and Travis, J. R., "A Non-equilibrium Vapor Production Model for Critical Flow," *Nuclear Science Engineering*, Vol. 74, 1980, pp. 40–48.

11 Okazaki, N., "Theoretical Study for Accelerating Two-Phase Flow – I, Constant Area Flow," *Bulletin JSME*, Vol. 23, 1980, pp. 536–544.

12 Wallis, G. B., *One Dimensional Two-Phase Flow*, McGraw-Hill, New York, 1969.

13 Collier, J. G., *Convective Boiling and Condensations*, McGraw-Hill, New York, 1981.

14 Dobran, F., "A Two-Phase Fluid Model Based on the Linearized Constitutive Equations," in: *Advances in Two-Phase Flow and Heat Transfer*, S. Kakac and M. Ishii, eds., Martinus Nijhoff Publishers, Vol. 1, 1983, pp. 41–59.

15 Dobran, F., "Constitutive Equations for Multiphase Mixtures of Fluids," *International Journal of Multiphase Flow*, Vol. 10, 1984, pp. 273–305.

16 Bergles, A. E., Collier, J. G., Delhaye, J. M., Hewitt, G. F., and Mayinger, F., *Two-Phase Flow and Heat Transfer in the Power Process Industries*, Hemisphere, Washington, 1981.

17 Dobran, F., "An Acceleration Wave Model for the Speed of Propagation of Shock Waves in a Bubbly Two-Phase Flow," *ASME/JSME Thermal Engineering Joint Conference*, Y. Mori and W. Yang, eds., Vol. 1, 1983, pp. 1–9.

18 Solbrig, C. W., McFadden, J. H., Lyczkowski, R. W., and Hughes, E. D., "Heat Transfer and Friction Correlations Required to Describe Steam-Water Behavior in Nuclear Safety Studies," *AIChE Symposium Series*, Vol. 174, 1978, pp. 100–128.

19 Chisholm, D., "Pressure Gradients Due to Friction During the Flow of Evaporating Two-Phase Mixtures in Smooth Tubes and Channels," *International Journal of Heat and Mass Transfer*, Vol. 16, 1973, pp. 347–348.

20 Alamgir, M. D., and Lienhard, J. H., "Correlation of Pressure Undershoot During Hot-Water Depressurization," ASME JOURNAL OF HEAT TRANSFER, Vol. 103, 1981, pp. 52–55.

21 Ardron, K. H., "A Two-Fluid Model for Critical Vapor-Liquid Flow," *International Journal of Multiphase Flow*, Vol. 4, 1978, pp. 323–337.

22 Boure, J. A., Fritte, A. A., Giot, M. M., and Reocreux, M. L., "Highlight of Two-Phase Critical Flow," *International Journal of Multiphase Flow*, Vol. 3, 1976, pp. 1–22.

23 Celata, G. P., Cumo, M., Farello, G. E., and Incalcaterra, P. C., "Critical Flow of Subcooled Liquid and Jet Forces," in: *Interfacial Transport Phenomena*, J. C. Chen and S. G. Bankoff, eds., ASME, New York, Vol. 109, 1983.

24 Farello, G. E., "Pressure Measurements in Critical Two-Phase Flows," personal communication, Apr. 1984.

25 Dobran, F., "Distribution of Liquid and Gas in a Jet With Phase Change," *International Symposium on Jets and Cavities*, J. H. Kim, O. Furuya, and B. R. Parkin, eds., ASME, New York, 1985.

A. Bar-Cohen[1]
Corporate Research and Engineering, Control Data Corporation, Minneapolis, MN
Fellow ASME

Z. Ruder
Department of Chemical Engineering, University of Illinois, Urbana, IL

P. Griffith
Department of Mechanical Engineering, Massachusetts Institute of Technology, Cambridge, MA
Fellow ASME

Thermal and Hydrodynamic Phenomena in a Horizontal, Uniformly Heated Steam-Generating Pipe

This study is aimed at elucidating the relationship between the hydrodynamic and thermal phenomena in horizontal boiler tubes. It focuses on the empirical evaluation of the wall temperature distribution in a uniformly heated, 6-m-long, water-carrying pipe, operated at near-atmospheric pressure, over a range of imposed heat fluxes and water flow rates. The results reveal the existence of a complex temperature field on the pipe wall, incorporating circumferentially isothermal and anisothermal regions and a significant axial variation along the top of the pipe. For moderate flow rates these variations were found to give rise to two distinct anisothermal zones: a low-quality zone near the inlet and a moderate-quality zone approximately midway along the pipe. Physical models and semi-analytic relations for the liquid and vapor velocities, constituting the boundaries between isothermal and anisothermal operation, are presented.

Introduction

The structure and magnitude of the temperature field in the wall of a steam-generating pipe is largely determined by the prevailing internal and external heat transfer coefficients, and close coupling thus exists between thermal stress developed in the tube walls and the governing thermal transport processes. Continuous local dryout or repeated dryout and quenching of the internal pipe surface, as may well occur in horizontal two-phase flow, can be expected to produce significant spatial and temporal temperature variations, which could be highly detrimental to the pipe..Carbon-steel pipes, in particular, are unlikely to survive repeated temperature excursions of even 35–50°C for more than several weeks (Bar-Cohen et al., 1983a).

Such performance is clearly incompatible with the extended operating life needed in boiler tubes and it is, therefore, essential that critical temperature fluctuations be avoided by proper design of the steam-generating tubes and selection of the most benign two-phase flow operating regime. Unfortunately, the dearth of analytical relations and/or reliable empirical data for circumferential anisothermality can seriously impair the design of horizontal tube boilers and, thus, hamper the development of fluidized bed combustor and solar-heated boilers using this pipe configuration.

Variations in the mass flow rate, as well as small angular excursions from the horizontal, can markedly affect the primary two-phase flow regime and theoretical considerations suggest that it may be possible to identify specific operating conditions at which temperature variations and their associated thermal stresses will be minimized. Indeed, a recent analysis of data, for the circumferential temperature variation in horizontal boiler tubes, confirmed the validity of interpreting such data in light of the hydrodynamic phenomena accompanying boiling two-phase flow and showed that the parametric and axial variation of the tube top-to-bottom temperature difference reflects the influence of the flow regimes encountered along the appropriate locus in a flow regime map (Bar-Cohen et al., 1983b).

In contrast to the oft-quoted conclusion by Styrikovich and Miropolski (1950), that minimization of the pipe top-to-bottom temperature difference in horizontal pipes is associated with termination of stratified flow, the results of Bar-Cohen et al. (1983b) appear to suggest that it is the transition from the intermittent to the annular flow regime that is generally responsible for circumferential isothermality. Based on the use of flow regime maps appropriate to the specific operating conditions, Bar-Cohen et al. (1983b) further suggest that the peak value of the circumferential temperature difference occurs along the dispersed bubble/intermittent flow regime boundary.

Due to the inherent uncertainty in the prediction and interpretation of two-phase flow phenomena, the above conclusions must be subjected to rigorous empirical verification by direct temperature measurement. The present study seeks to provide such validation by focusing on the presentation and evaluation of the wall temperature distribution in a uniformly heated, 6-m-long, water-carrying pipe, operated at near-atmospheric pressure, over a range of imposed heat fluxes and water flow rates relevant to boiler tubes.

Flow Regimes in Horizontal Two-Phase Flow

Flow Regime Maps. While many investigators have studied the hydrodynamics of two-phase flow and attempted to define the boundaries between the various flow regimes, the mechanistic models and flow regime maps proposed by Taitel and Dukler (1976) have been the most widely accepted. In their analyses, Taitel and Dukler define four primary flow regimes: stratified (wavy and smooth), intermittent, annular-dispersed liquid (henceforth referred to as annular), and dispersed bubble (see Fig. 1). A Taitel and Dukler flow regime map for a water/air mixture flowing in a 2.5-cm smooth horizontal pipe is shown in Fig. 2. As can be seen in this figure, stratified flow is generally associated with low values of both liquid and vapor superficial velocities. Increasing liquid velocity results in transition to intermittent flow and at higher velocities to dispersed bubble flow. Alternately, increasing gas superficial velocities appears to lead to stratified wavy flow and at still higher velocities to the annular regime. The relations used to define the relevant flow regime bound-

[1]On leave from the Department of Mechanical Engineering, Ben Gurion University, Israel.

Contributed by the Heat Transfer Division and presented at the 22nd National Heat Transfer Conference, Niagara Falls, New York, August 5–8, 1984. Manuscript received by the Heat Transfer Division July 20, 1984.

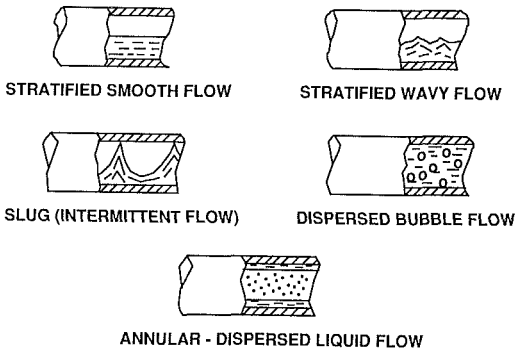

Fig. 1 Two-phase flow patterns inside a horizontal tube

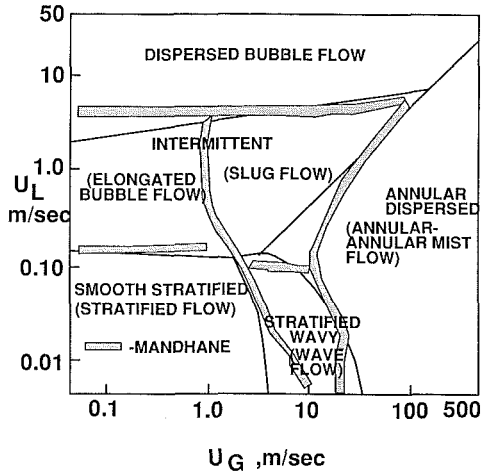

Fig. 2 Flow regimes in a horizontal pipe air/water flow (2.5-cm diameter, 25° C, 1 bar)

aries and the physical mechanisms employed in deriving these relations can be found in the literature (Taitel and Dukler, 1976).

It is of interest to note that a detailed analysis by Weisman et al. (1979) of more recent data confirmed the key role played by the gas and liquid superficial velocities in establishing the flow pattern in horizontal pipes. The specific boundaries suggested by Weisman et al. (1979) agree quite well with the Taitel and Dukler transition for all except the boundary separating the intermittent and annular regimes. While the locus of this boundary in superficial velocity coordinates has been found to have a positive slope (Taitel and Dukler, 1976) the Weisman et al. (1979) relation yields a negative slope. The latter relation was found (Bar-Cohen et al., 1983) to match more nearly the locus of the minimum circumferential wall temperature zone than the Taitel and Dukler expression.

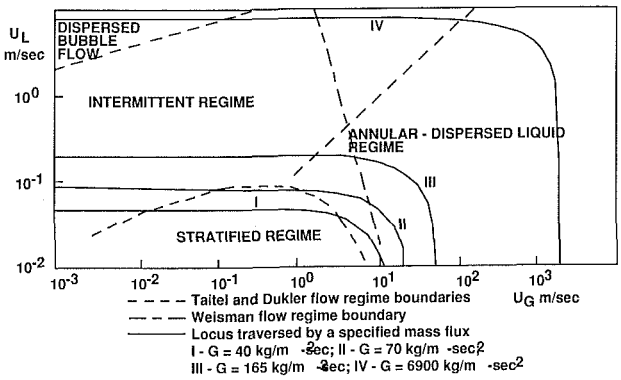

Fig. 3 Flow regime map at 5 bar

Application to Diabatic (Boiling) Flow. Although the adiabatic flow regime boundaries necessarily neglect thermal interactions between the phases, as well as between the pipe and the environment, and are thus not strictly valid for the boiling or condensing flow of water, it has been shown (Bar-Cohen et al., 1983b; Taitel, 1980; Breber et al., 1979) that under saturation conditions and for modest gradients in the vapor fraction or steam quality, the adiabatic flow regime maps offer a guide to the thermal/hydraulic behavior of boiling or condensing flow, with certain variations in the location of the regime boundaries due to the influence of the externally applied heat flux.

The results of Taitel (1980), which incorporate interphase momentum transfer, bubble generation in the liquid, and axial variations in the flow parameters, suggest that for water at boiling heat fluxes as high as 100 kW/m^2, the only significant perturbation in the flow regime map is the shift of the dispersed bubble/intermittent boundary to the right, toward greater U_G values (between 0.1 and 1 m/s).

As opposed to adiabatic flow which can be represented by a single point on the superficial velocity flow-regime map, the flow of boiling water can be expected to trace a locus of points, as the quality (i.e., vapor fraction) increases in the flow direction. This locus may be entirely within a single flow regime or, more generally, pass from one regime to the next, thus crossing the boundaries on the map (Bar-Cohen et al., 1983b). An example of a Taitel and Dukler adiabatic and diabatic map, including the Weisman boundary and the loci traced out by flows in a 25.4-mm i.d. pipe, is shown in Fig. 3.

Thus, for example, at a mass flux of 70 kg/m^2-s close to the pipe inlet, at a quality of 4×10^{-5} the intermittent flow regime prevails. At an x value of 8.3×10^{-3} where the superficial liquid and vapor velocities equal 0.08 and 0.2 m/s, respectively, transition to the stratified region occurs. Further, at x = 0.07 (liquid superficial velocity 0.07 m/s and gas superficial velocity 1.6 m/s) the operating locus proceeds into the annular flow pattern.

Nomenclature

d = tube diameter, m
Fr = Froude number
g = acceleration of gravity, m/s
h_{fg} = latent heat, J/kg
P = pressure, kPa
q'' = heat flux, W/m^2
Re = Reynolds number
t_{ev} = evaporation period, s
t_{sl} = slug passage period, s
T = temperature, °C, °F
ΔT = temperature difference, °C, °F
U_G; U_L = superficial velocities of gas and liquid, respectively, m/s
v_g; v_L = velocities of gas and liquid, respectively, m/s
x = quality
δ = thickness of thin liquid film at the top of the tube, m
δ_0 = initial liquid film thickness, m
ν = slug formation frequency, s^{-1}
ρ_g; ρ_L = densities of gas and liquid, respectively, kg/m^3

Superscripts

$\hat{}$ = upper bound

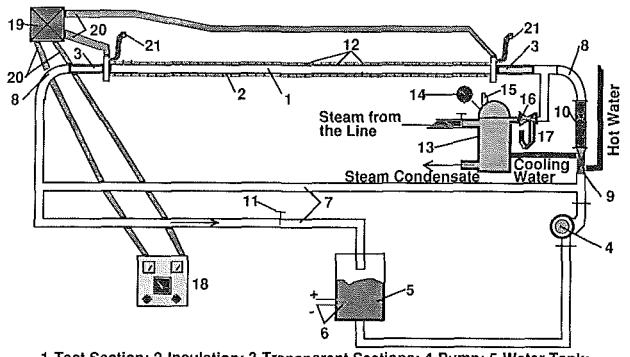

1-Test Section; 2-Insulation; 3-Transparent Sections; 4-Pump; 5-Water Tank; 6-Heating Element; 7-System Pipes; 8-Flexible Pipes; 9-Heat Exchanger; 10-Rotameter; 11-Valves; 12-Thermocouples; 13-Steam Tank; 14-Pressure Gauge; 15-Pressurestat; 16-Venturi Tube; 17-Manometer; 18-Control Board; 19-Electric Generators; 20-Electric Cables; 21-Cooling Tubes

Fig. 4 Experimental apparatus

Experimental Program

The experimental program described herein was aimed at generating detailed temperature distributions along an electrically heated boiler tube and, thereby, providing the necessary data for validating the two-phase flow model of circumferential anisothermality proposed by Bar-Cohen et al. (1983b). To aid in this process, the apparatus was designed to operate over a range of flow rates and heat fluxes which were anticipated to display the flow regimes of interest and to include regimes of both isothermal and anisothermal conditions.

Experimental Apparatus. The experimental apparatus used in the present research is shown schematically in Fig. 4. A stainless steel pipe of 25.4-mm i.d., 3.4-mm wall thickness, and 6.06-m length (1) with a thermal conductivity of 30 W/mK, was heated by a uniform electrical heat flux from a d-c generator (45 kW power supply) (19) available in the lab. Due to the thinness and low thermal conductivity of the pipe wall, stratified flow, in the presence of a uniformly applied heat flux, could be expected to result in a significant top-to-bottom temperature difference, and, thus, allow this flow pattern to be detected by conventional temperature sensors. For a circumferentially uniform heat flux, at even the lowest applied value of 4 kW/m^2, Ruder (1984) has estimated the top-to-bottom temperature difference to be in excess of 30°C for stratified flow with the liquid level at the midplane of the pipe. For relatively large temperature differences, the dependence of electrical resistivity on temperature (approximately 1 percent increase for a 10°C rise) can be expected to reduce the wall heat flux somewhat at the top (i.e., warmer section) of the pipe. However, this variation is likely to be considerably smaller than the present uncertainty in the two-phase flow parameters and not to affect materially the validity of the present results.

This test section was instrumented with 33 copper-constantan thermocouples located along the top and bottom of the pipe (12). Two transparent tubes, at the inlet and outlet (3) were added to the test section for visual observation of the two-phase flow pattern inside the steam-generating tube. After preheating in the storage tank (5) by means of a heating element (power 2 kW) (6), the working fluid (water under saturation conditions) was pumped through the flow meter (rotameter) (10) and entered the test section. The single-phase liquid entering the test section turned into a two-phase mixture, as a result of electrical heating, and, at the outlet, a certain vapor quality was obtained. After leaving the test pipe, the liquid/steam mixture entered the storage tank, thus closing the loop. Two rubber hoses, at the inlet and the outlet of the pipe (8), were needed for changing the angle of inclination of the test section and neutralizing the effect of system vibration.

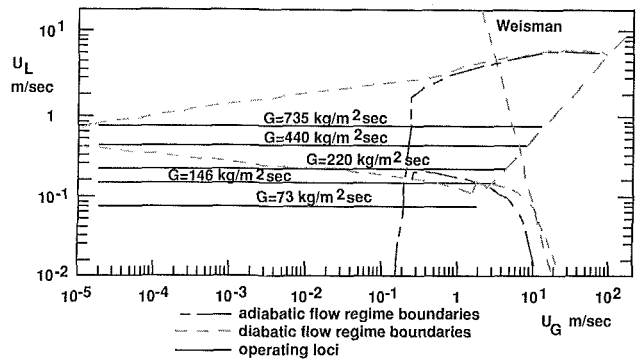

Fig. 5 Flow regime map for near-atmospheric pressure, horizontal tube; 4 kW/m^2, 2.54-cm diameter

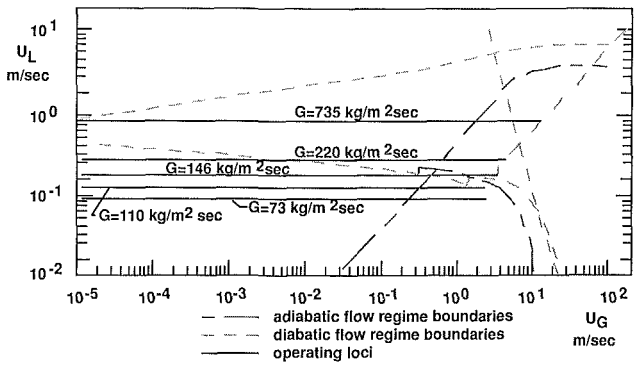

Fig. 6 Flow regime map for near-atmospheric pressure, horizontal tube; 44 kW/m^2, 2.54-cm diameter

A tube-and-shell heat exchanger (9) was located upstream of the rotameter, providing for possible subcooling of feedwater, i.e., decreasing of outlet vapor quality. In order to increase the outlet quality (if needed), the system was assembled with a special device for directing steam into the test section from the lab steam line at the inlet (13–17). By measuring the pressure drop through the Venturi tube (16), the vapor flow rate could be calculated. The flow rate of water could be varied from 73 to 735 kg/m^2-s by means of valves (11) and a bypass loop. The operating range for electrical heat fluxes was 4 to 44.3 kW/m^2, obtained by varying the d-c current flowing through the thin-walled tube. The heat flux could be increased, up to 135 kW/m^2, by moving one of the electrical cables along the tube, thus decreasing the heated length of the test section. A digital thermometer manufactured by Omega, Inc., and a mechanical channel selector were used for temperature measurement.

During the experiment, wall temperatures along the tube were measured for each mass flow rate of water and for each heat flux, and the two-phase flow patterns, observable at the visual section, were recorded for later comparison with the flow regimes shown in the Taitel and Dukler maps.

Taitel and Dukler Maps for the Working Conditions. Two examples of the adiabatic and diabatic two-phase flow maps for imposed heat fluxes of 4 kW/m^2 and 44.3 kW/m^2 are presented in Figs. 5 and 6, respectively. To keep these figures from becoming illegible, the flow regime names have been omitted and only the boundaries are shown. The particular flow regime of interest can be easily determined by comparing these figures to Figs. 2 and 3.

As can be seen, none of the loci superimposed on the maps is located within a single flow pattern region but, rather, they cross the boundaries from one flow regime to another. The loci generated by the lowest mass flow rates of 73 kg/m^2-s and

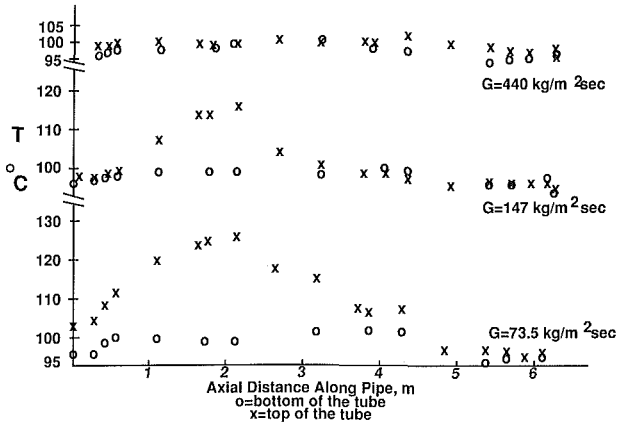

Fig. 7 Empirical temperature distribution for horizontal boiler tube; 4 kW/m^2, 2.54-cm diameter

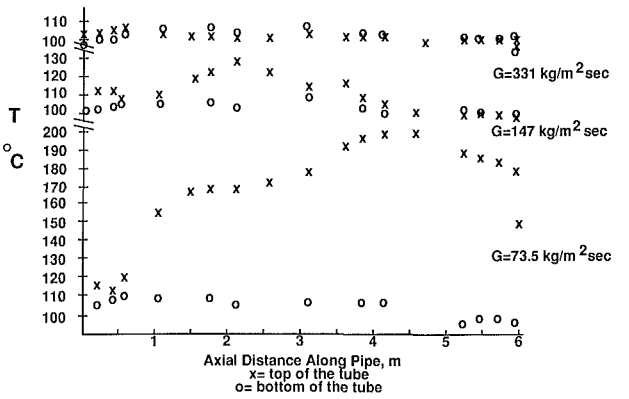

Fig. 8 Empirical temperature distribution for horizontal boiler tube; 14 kW/m^2, 2.54-cm diameter

146 kg/m^2-s are in the regions of dispersed bubble, stratified, and annular regimes. Loci appropriate to higher flow rates are entirely out of the stratified region on the map, proceeding from dispersed bubble through intermittent and on to the annular regime. As noted in the previous section, an imposed heat flux seems to influence mainly the dispersed bubble/intermittent boundary, shifting it essentially to the right. As a result the intersection point between the dispersed bubble/intermittent boundary and the stratified/intermittent boundary is located much more to the right (i.e., at higher values) on the diabatic map than on the adiabatic one, thus reducing the stratified flow area at low values and broadening the dispersed bubble region.

The influence of an applied heat flux on the stratified flow pattern boundaries is seen in Figs. 5 and 6 to be rather modest, resulting in a shift of the stratified/annular boundary somewhat to the left on the map. Similarly, the Taitel and Dukler intermittent/annular boundary appears to be unaffected by the diabatic conditions. The empirical intermittent/annular transition proposed by Weisman was derived for adiabatic conditions and is, thus, unaltered by heat addition.

Results and Discussion

Presentation of Data. The results obtained in the course of the experimental series can be presented in the form of a graph showing the axial variation of wall temperature along the top and bottom of the pipe. Two such examples, of the many presented by Ruder (1984), are shown in Figs. 7 and 8. At the higher heat flux values of Fig. 8, the maximum circumferential temperature difference is seen to reach approximately 90°C at a mass flux of 73.5 kg/m^2-s, to decrease toward 25°C at 147 kg/m^2-s and nearly to vanish at a mass flux of 331 kg/m^2-s. A similar, though less dramatic, variation can be seen in Fig. 7, where the peak circumferential temperature difference is shown to decrease from nearly 30°C at 73.5 kg/m^2-s, to 20°C at 147 kg/m^2-s and to less than 10°C at 440 kg/m^2-s.

These same data can be used to determine the boundary separating the region of high circumferential anisothermality from the region of near isothermality in a gas and liquid superficial velocity coordinate system. The requisite gas and liquid superficial velocities can be determined from the inlet mass flow rate, the applied heat flux, and the physical location of the point of interest along the test section. The paired sets of gas/liquid superficial velocities, calculated in this way, form a "thermal boundary" locus which can be superimposed on the Taitel and Dukler flow regime map for direct comparison between the hydrodynamic and thermal boundaries, as shown in Figs. 9–11.

General Trends. At the lowest mass flow rate of 73 kg/m^2-s all heat fluxes imposed on the test section were found to result in wall overheating. This can be explained by the presence of the locus, appropriate to this flow condition, inside the stratified region (see Figs. 5. and 6). Alternately, at the highest mass flow rate of 735 kg/m^2-s, no tube overheating was found to occur for the entire heat flux operating range. The locus generated by this flow rate is seen in Figs. 5 and 6 to cross from dispersed bubble to intermittent to annular flow and to lie high above the stratified/intermittent boundary.

The results for intermediate flow rates ($146 \leq G \leq 440$ kg/m^2-s), whose loci originate in, cross into, or approach the stratified flow regime, frequently revealed two anisothermal zones along the test section, a dominant zone typically 2-4 m from the inlet and a second erratic zone very close to, or at, the pipe inlet. The "inlet" zone was generally encountered at low, flow quality values, 0-0.25 percent for heat fluxes of 4-10 kW/m^2 and 0-0.5 percent for heat fluxes of 14 to 44 kW/m^2, while the dominant zone was associated with values of 0.5 to 5 percent for the entire heat flux range. The typical moderate heat flux results, displayed in Fig. 10, clearly show these two zones. A closer examination reveals a similar double zone structure for all but the 6 kW/m^2 data plotted in Fig. 9. Under high heat flux conditions (60-100 kW/m^2) only a single anisothermal zone was detected.

At intermediate flow rates it thus appears possible to encounter two anisothermal or "local dryout" regions prior to crossing into annular flow. In annular flow a third anisothermal zone is encountered in the form of complete wall dryout, at x values typically in excess of 25 percent (Biasi et al., 1967).

Visual Confirmation of Flow Regimes. The suitability and general validity of the Taitel and Dukler hydrodynamic boundaries for the conditions of the experimental program were visually checked by means of a "window" located immediately downstream of the test section outlet (3 in Fig. 4). To observe the flow pattern visually at particular values of vapor quality, the points of interest were "moved" to the tube outlet by subcooling the feed water in the tube-and-shell heat exchanger (9 in Fig. 4). The results of such observations were found to agree satisfactorily with the predictions of Taitel and Dukler. It may be noted, however, that due to the characteristics of the experimental apparatus, transition to annular flow was generally encountered in the range of low liquid superficial velocity, where both the Weisman and the Taitel and Dukler criteria predict similar values of gas velocities. It was, thus, not possible to distinguish between these criteria on the basis of the visual observations.

Such visual observations did, nevertheless, confirm that the moderate quality anisothermal zone terminated at or near to the annular flow boundary. Unfortunately, it proved impossible to shift the points of maximum circumferential temperature difference in the moderate quality zone or the

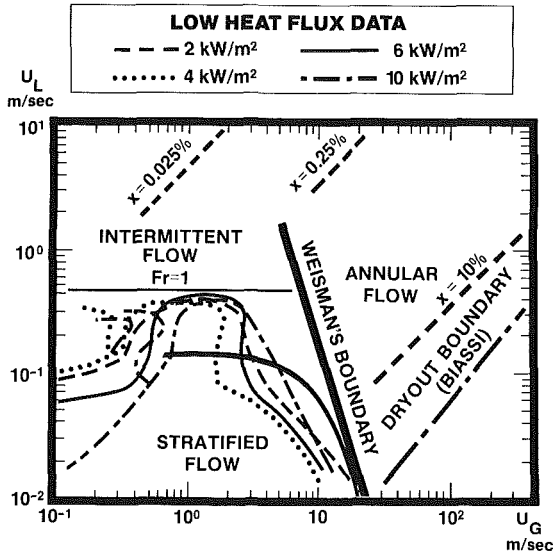

Fig. 9 Experimental and semi-analytical thermal boundaries for low heat fluxes; 4–10 kW/m^2

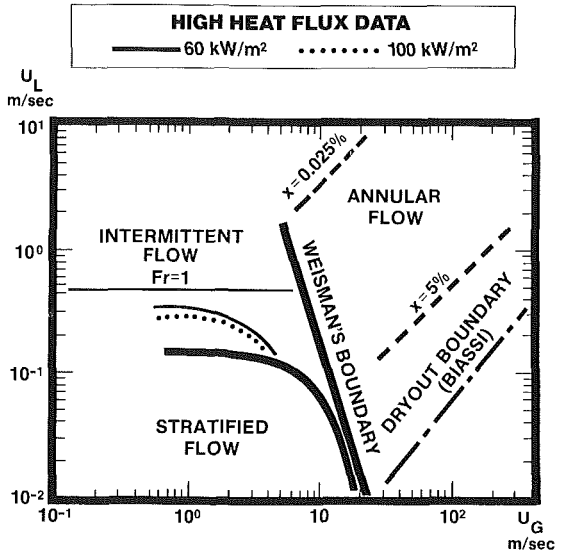

Fig. 11 Experimental and semi-analytical thermal boundaries for high heat fluxes; 60–100 kW/m^2

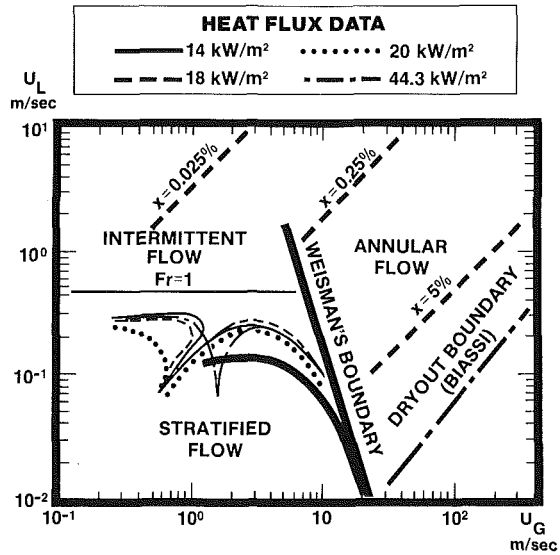

Fig. 10 Experimental and semi-analytical thermal boundaries for moderate heat fluxes; 14–44.3 kW/m^2

boundary of the low-quality anisothermal region to the "window" since such a maneuver required accuracy unavailable at such low values of vapor quality.

Moderate-Quality Anisothermal Zone. The moderate-quality anisothermal zone, apparent in Figs. 9–11, would appear to correspond to the circumferentially anisothermal zone reported in the literature (e.g., Styrikovich and Miropoloski, 1950; Rounthwaite, 1968) and discussed by Bar-Cohen et al. (1983b). This domelike region, in a map based on gas/liquid superficial velocity coordinates, incorporates the stratified flow regime and a segment of the intermittent flow regime. The borders of this anisothermal zone were found to vary in a consistent manner for the range of flow rates and heat fluxes studied.

In Figs. 9–11 the right border of this zone is seen to fall within the error band of both the Weisman intermittent/annular flow transition and the locus of the Taitel and Dukler stratified/annular flow boundary and appears to be only weakly dependent on heat flux. The left border of the domelike region is, on the other hand, highly sensitive to heat flux and appears to lie in proximity to the diabatic dispersed bubble/intermittent flow transition suggested by Taitel and Dukler (1976). Interestingly, both the latter transition and the left border of the moderate-quality anisothermal zone display a shift to the right with increasing heat flux and thus lead to a marked decrease in the area occupied by the anisothermal zone "dome," as the imposed heat flux increases.

Combining the effects noted, it appears that the moderate-quality "local dryout" zone is bounded by the triangular region formed on the gas/liquid superficial velocity map by the Weisman intermittent/annular flow transition and the Taitel and Dukler diabatic dispersed bubble/intermittent flow transition. This conclusion supports the hypothesis proposed by Bar-Cohen et al. (1983b) on the basis of previously published results.

Low-Quality Anisothermal Zone. Due to the appearance of the low-quality anisothermal zone close to the inlet of the heated test section, it was initially difficult to distinguish between possible inlet geometry effects and a true thermohydraulic phenomenon.

In an attempt to separate these two factors, the experimental apparatus was operated with high inlet subcooling, thereby shifting the zero quality point downstream to a flow length as large as 90 pipe diameters. A flow length-to-diameter ratio of 90 was thought to be sufficient to insure fully developed (single-phase) flow at the point of net vapor generation. As a further measure, additional thermocouples (at 10-cm spacing) were added in the low-quality zone to define the axial temperature profile better.

The results of these measurements, already incorporated in Figs. 9–11, indicated that the circumferential temperature difference in the low-quality zone decreased to 10–20°C as this zone was shifted downstream. However, the anisothermality persisted and only moderate changes appeared to occur in the boundaries of this zone, on the superficial gas/liquid velocity map, as a result of this change.

Returning to Figs. 6 and 7, it may be noted that the right border of this low-quality anisothermal zone is relatively close to, but at somewhat lower qualities than, the Taitel and Dukler dispersed bubble/intermittent flow hydrodynamic, diabatic boundary. In traversing the pipe in the streamwise direction, this boundary can be expected to mark the beginning of a new two-phase flow pattern, namely, the intermittent (or slug) regime. Slugs, however, cannot develop directly

from dispersed bubbles and it may be postulated that in the transition zone, where previously dispersed bubbles rise and coalesce near the top of the pipe, a locally stratified flow develops. Such local stratification, at vapor qualities slightly below the dispersed bubble/intermittent flow transition values, could lead to the observed low-quality anisothermal zone. It may be noted that the relatively large area occupied by this zone, in the log–log flow regime map, corresponds to a relatively short length of the test section (50 cm).

In the absence of direct empirical evidence for such a locally stratified transition zone, the above must be viewed as a tentative hypothesis. Nevertheless, it might be anticipated that as the mass flux and/or imposed heat flux increases, the increased frequency of slug formation would result, on average, in a shorter locally stratified section, as was, in fact, observed along the instrumented test section.

Semi-Analytical Bounding Relations

Low-Quality Anisothermal Zone. Regardless of the precise mechanism responsible for the formation of the low-quality isothermal zone, it does appear possible to relate its existence to the presence of a stationary vapor bubble, occupying a relatively short flow length and producing local dryout on the upper part of a steam-generating tube. Furthermore, it might be anticipated that the stability of such a bubble would depend on the balance between buoyancy and inertial forces, expressed, perhaps, in the form of an appropriate Froude number. A sufficiently high liquid velocity would sweep the bubble downstream and eliminate this anisothermal zone.

This velocity can be obtained experimentally, using an air/water simulation of two-phase flow, and can be derived theoretically (to a first approximation) via a potential flow analysis (Bar-Cohen et al., 1983a). The Froude numbers appropriate to each of these approaches (in the range of 0.47–0.52) were found to agree reasonably well with each other. More importantly, however, both the analytical and empirical values for the liquid velocity, needed to wash away the stationary bubble, agreed closely with the maximum superficial liquid velocity in the low-quality anisothermal zone.

The success of this approach suggested that an analogy might exist between the present situation and the conditions required to assure full-pipe flow in a horizontal conduit. This latter condition is generally met when the Froude number, defined as $U_L/\sqrt{gd}$, is equal to unity. For the experimental conditions, $\mathrm{Fr}_L = 1$ yields an upper-bound superficial liquid velocity of 0.3–0.4 m/s. Comparison of these values with the empirical results shows the $\mathrm{Fr}_L = 1$ criteria to overestimate the upper bound by approximately 20 percent, and thus to constitute a most simple, and highly acceptable, upper bound for this zone.

Moderate-Quality Anisothermal Zone. As previously noted, the right border of the moderate quality anisothermal zone falls relatively close to the locus of the Weisman-proposed transition (Weisman et al., 1979) from intermittent to annular flow. This boundary can be expressed in the form of a modified Froude number based on superficial gas velocity which, in addition to the superficial gas velocity, tube diameter, and gravitational acceleration, attempts to address the secondary influence of the superficial liquid velocity, the gas and liquid densities, and the surface tension. Following Weisman et al. (1979)

$$\mathrm{Fr}_G \equiv \hat{U}_G^2/gd = \left\{\frac{1.9(U_G/U_L)^{0.125}[g(\rho_L-\rho_G)\sigma]^{0.05}}{U_G^{0.2}\rho_G^{0.1}}\right\}^{5.56} \quad (1)$$

As previously noted (Bar-Cohen et al., 1983b) and clearly shown in Figs. 9–11, the transition from stratified to intermittent flow is insufficient to assure isothermal operation of horizontal boiler tubes and the moderate-quality anisothermal zone can, in fact, penetrate deeply into the intermittent regime. The extent of this penetration would appear to depend on the balance between the forces working to remove liquid from the surface and the forces working to rewet that same surface. In the heat fluxes of interest in steam generators, evaporation can be shown to constitute the primary drying mechanism, while the periodic passage of liquid plugs, driven through the pipe by vapor slugs, acts to quench and rewet the surface in this moderate-quality region.

The time necessary to evaporate a thin film of initial thickness can be approximated by

$$t_{ev} = \rho_L \delta_0 h_{fg}/q'' \quad (2)$$

Alternately, the slug period can be obtained from an available correlation for slug frequency (Gregory and Scott, 1969) as

$$t_{sl} = \nu_s^{-1} = 44.25\{(U_L/gd)[19.75/(U_L+U_G)+U_L+U_G]\}^{-1.2} \quad (3)$$

While this slug frequency correlation by Gregory and Scott [10] is based on data for 0.03 and 0.038-m i.d. pipes, the results were relatively insensitive to pipe diameter and system geometry effects and equation 3 can, thus, serve as a first approximation for the slug period in the present experimental apparatus.

Equating t_{ev} and t_{sl}, it is possible to determine the paired values of U_L and U_G at which the periodic, slug-driven liquid flow should be sufficient to prevent dryout of the upper surface of the pipe. The locus of these U_L and U_G values constitutes an approximate boundary for the moderate-quality anisothermal region. Numerically computed boundaries, based on equations (2) and (3) and assumed values of δ_0 (in the observed range of 50–90 μm, (Coney, 1973)), can be shown (Bar-Cohen et al., 1986) to offer satisfactory agreement with the data, as well as with boundaries based on the more precise calculations reported by Coney (1973).

Interestingly, however, it is also possible to derive a semi-analytic upper bound on the liquid superficial velocity, i.e., U_L, for this anisothermal region by the use of a relationship between U_L and U_G derived by setting $t_{ev} = t_{sl}$ as shown below

$$gd(U_L+U_G)(q''/0.0226\, h_{f_g}\rho_L\delta_0)^{0.833} = U_L^2(U_L+U_G)+U_LU_G(U_L+U_G)+19.75U_L \quad (4)$$

or

$$U_G^2+[(2U_L^2-B)/U_L]U_G+U_L^2-B+19.75=0 \quad (5)$$

where

$$B = gd(q''/0.0226\, h_{f_g}\rho_L\delta_0)^{0.833}.$$

To find the upper bound liquid superficial velocity, for the moderate-quality anisotherm zone, one can now determine dU_L/du_G from equation (5) and set this derivative to zero. In the present development, however, it appears mathematically less complicated to set dU_G/dU_L equal to infinity. This procedure results in

$$\hat{U}_L = B/8.9 = 2.64gd(q''/h_{f_g}\rho_L\delta_0)^{0.833} \quad (6)$$

Recalling the definition of the modified, liquid superficial velocity Froude number $= \hat{U}_L/\sqrt{gd}$

$$\hat{\mathrm{Fr}}_L = 2.64\sqrt{gd}(q''/h_{f_g}\rho_L\delta_0)^{0.833} \quad (7)$$

Substituting into this relation (equation (7)) the heat fluxes explored in the present investigation, $\hat{\mathrm{Fr}}_L$ is found to lie below unity for all but the highest value of q'' (100 kW/m^2).

Examining Figs. 9–11 once again, it can be seen that the $\hat{\mathrm{Fr}} = 1$ criterion, used to establish an upper bound on the low-quality isothermal region, does indeed constitute an equally effective upper bound for the moderate-quality anisothermal zone.

Conclusions

In the course of the experimental investigation reported herein, circumferential anisothermality in a horizontal, steam-generating tube was found to be intimately related to the various hydrodynamic phenomena occurring along the tube. A high top-to-bottom temperature difference along the entire length of the pipe was encountered at mass fluxes appropriate to the stratified flow regime. Alternately, nearly isothermal pipe operation could be obtained by increasing the mass flux to the high levels required to achieve operation in the dispersed bubble and annular flow regimes. At moderate values of mass flux, associated primarily with intermittent flow, the pipe was found to exhibit complex anisothermal behavior.

The first, low-quality anisothermal zone was found to include a part of the intermittent flow regime closest to the dispersed bubble/intermittent transition and was postulated to result from the presence of a stationary vapor bubble producing a locally stratified flow. A semi-analytic Froude number criterion, based on bubble stability, was found to provide a convenient upper bound on the superficial liquid velocity in this region.

The second, moderate-quality anisothermal zone was found to occur over large sections of the uniformly heated pipe and to include much of the stratified flow regime, as well as a significant segment of the intermittent flow regime. When plotted on coordinates of superficial liquid and vapor velocity, this region was found to be bounded on the right by both the Weisman and Taitel/Dukler criteria for transition from stratified to annular flow. An approximate analysis, based on the evaporation of the liquid film at the top of the pipe and liquid replenishment by slug flow, yielded a modified Froude number upper limit on this zone as well.

Using these formulations, for both the low and moderate-quality zones, it was found possible to bound the operating regions in which the horizontal test section experienced circumferential anisothermality.

Acknowledgments

The subject study was funded by the Israel–USA Binational Science Foundation, grant number 2059-79. The authors are grateful to Prof. Yehuda Taitel, of Tel Aviv University, for his helpful comment and for providing results for his diabatic flow regime analyses. The aid of Mr. T. Calogerro and Mr. F. Johnson of the MIT Heat Transfer Laboratory in constructing the experimental apparatus, and of Mrs. O. Nurenberg of the Ben Gurion University in preparing the illustrations, is similarly acknowledged.

References

Bar-Cohen, A., Griffith, P., Ruder, Z., Klein, Y., and Schweitzer, H., 1983a, "Flow Boiling in Inclined Tubes in Fluidized Bed Combustors," Final Report to U.S.–Israel Binational Science Foundation, Department of Mechanical Engineering, Ben-Gurion University of the Negev.

Bar-Cohen, A., Ruder, Z., and Griffith, P., 1983b, "Circumferential Wall Temperature Variations in Horizontal Boiler Tubes," *Int. J. Multiphase Flow*, Vol. 9, No. 1, pp. 1–12.

Bar-Cohen, A., Ruder, Z., and Griffith, P., 1986, "Development and Validation of Boundaries for Circumferential Isothermality in Horizontal Boiler Tubes," *Int. J. Multiphase Flow*, Vol. 12, No. 1, pp. 63–77.

Biassi, L., et al., 1967, "Studies in Burnout," Part 3, *Energia Nucleare*, Vol. 14, No. 9, pp. 530–536.

Breber, G., Palen, J. W., and Taborek, J., 1979, "Prediction of Horizontal Flow Tubeside Condensation of Pure Components Using Flow Regime Criteria," *NMTC–Condensation Heat Transfer*, ASME Publication No. 100123.

Coney, M. W. E., 1973, "The Analysis of a Mechanism of Liquid Replenishment and Draining in Horizontal Two-Phase Flow," *Int. J. Multiphase Flow*, Vol. 1, pp. 647–669.

Gregory, G. A., and Scott, D. S., 1969, "Correlation of Liquid Slug Velocity and Frequency in Horizontal Cocurrent Gas–Liquid Slug Flow," *AIChE Journal*, Vol. 15, No. 6, pp. 933–935.

Rounthwaite, C., 1968, "Two-Phase Heat Transfer in Horizontal Tubes," *Journal of the Institute of Fufel*, Vol. 41, pp. 66–76.

Ruder, Z., 1984, "The Influence of Two-Phase Flow Regimes on Circumferential Temperature Distribution in Horizontal, Steam Generating Tubes," Ph.D. Thesis, Dept. of Mechanical Engineering, Ben Gurion University, Israel.

Styrikovich, M. A., and Miropoloski, Z. L., 1950, "Rassioyeniye Potoka Paravodynancy Smesi Vysokogo Dovlenia V Obogrevayemoy Gorizontalnoy Trube (Stratification in Vapor-Water Mixture Flow at High Pressure in a Heated Horizontal Tube)" [in Russian], *Dokl. Akad. Nauk SSSR*, Vol. LXXI, No. 2.

Taitel, Y., and Dukler, A. E., 1976, "A Model for Predicting Flow Regime Transitions in Horizontal and Near Horizontal Gas–Liquid Flow," *AIChE Journal*, Vol. 22, No. 1, pp. 47–55.

Taitel, Y., 1980, "Class Notes for Flow with Phase Change," Dept. of Chemical Engineering, University of Houston.

Weisman, J., Duncan, D., Gibson, J., and Crawford, T., 1979, "Effect of Fluid Properties and Pipe Diameter on Two-Phase Flow Patterns in Horizontal Lines," *Int. J. Multiphase Flow*, Vol. 5, pp. 437–462.

Transition Boiling Heat Transfer and the Film Transition Regime

J. M. Ramilison[1]
Research Assistant.

J. H. Lienhard
Professor.
Fellow ASME

Heat Transfer/Phase Change Laboratory,
Mechanical Engineering Department,
University of Houston,
Houston, TX 77004

The "Berenson" flat-plate transition-boiling experiment has been re-created with a reduced thermal resistance in the heater, and an improved access to those portions of the transition boiling regime that have a steep negative slope. Tests have been made in Freon-113, acetone, benzene, and n-pentane boiling on horizontal flat copper heaters that have been mirror-polished, "roughened," or teflon-coated. The resulting data reproduce and clarify certain features observed by Berenson: the modest surface finish dependence of boiling burnout, and the influence of surface chemistry on both the minimum heat flux and the mode of transition boiling, for example. A rational scheme of correlation yields a prediction of the heat flux in what Witte and Lienhard previously identified as the "film-transition boiling" region. It is also shown how to calculate the heat flux at the boundary between the pure-film, and the film-transition, boiling regimes, as a function of the advancing contact angle.

Introduction

Transition boiling has, for 50 years, held its place as the least understood of the several boiling mechanisms. Consequently it has been virtually impossible to design thermal processes to operate in this regime. Indeed, the threat of thermohydraulic nuclear accidents – the possibility of uncovering a nuclear core and then having to rewet it – has done more to demand an understanding of transition boiling than the more positive problems of process design.

The Berenson Experiment. For years, our best knowledge of the regime was that given us by Berenson (1960) in his pioneering study. Berenson used a copper block, heated from below by the condensation of high-pressure steam, and cooled on top by the boiling of a low-boiling-point fluid. He then measured the heat flux q as a function of the almost independently specifiable temperature difference between the top of the copper block and the saturated liquid: $(T_w - T_{sat}) \equiv \Delta T$. He was thus able to obtain nearly complete "boiling curves" (specifications of the $q(\Delta T)$ relationship) for the boiled liquid. The following are among Berenson's more important experimental findings:

- The nucleate boiling heat flux is extremely dependent on surface finish.
- The peak (or "burnout") heat flux q_{max} in pool boiling is only slightly dependent upon the surface condition of the heater. He obtained about a 15 percent total variation of q_{max} over the full range of surface finishes, with the roughest surfaces giving the highest values.
- The film boiling heat flux is independent of the surface condition of the heater.
- The minimum film boiling heat fluxes were fairly consistent with one another if the surface chemistry was such as to give a relatively large contact angle β. If the surfaces were polished with a lapping compound as well, the minimum heat flux q_{min} reached its lowest value which Berenson correlated using a modified Zuber (1959) theory as follows:

$$q_{min} = 0.09 \rho_g h_{fg} \sqrt[4]{\frac{g(\rho_f - \rho_g)}{(\rho_f + \rho_g)^2}} \tag{1}$$

- If the liquid wetted the heater surface significantly, q_{min} was exceedingly high, and the transition heat fluxes were also very high.

Accessibility of Points in the Transition Boiling Regime. Witte and Lienhard (1982) re-examined Berenson's data in light of an observation made by Stefan and Kovalev, Grassman and Ziegler, and others (see, e.g., Hesse (1973)). They noted that not all transition boiling states are accessible in this kind of apparatus. The heat fluxes and ΔT that can be attained for given saturation temperatures of the condensing steam ($T_{cond.stm.}$) and of the boiled liquid (T_{sat}) are

$$q = \frac{(T_{cond.stm.} - T_{sat}) - \Delta T}{R_h + R_c} \tag{2}$$

where R_h is the thermal resistance of the copper plate, (plate thickness)/k_h, and R_c is the resistance of the condensation process, $1/h_{cond}$.

The nearly straight lines specified by equation (2) are displayed in Fig. 1 on q versus ΔT coordinates (for a given system pressure). We call these "accessibility lines" because all q and ΔT data for a given value of $(T_{cond.stm.} - T_{sat})$ must lie along them. Notice that one cannot reach a point lying on the intersection of an accessibility line, and the boiling curve in the transition region, if that point lies between two other points of intersection with the boiling curve. The reason is that, in an approach from either the film or nucleate boiling side, there will be no reason for the system to leave the outer intersections. The role of R_c was ignored by Witte and Lienhard; thus they plotted accessibility lines through Berenson's data that were straight, and which optimistically showed a steeper slope than they should have.

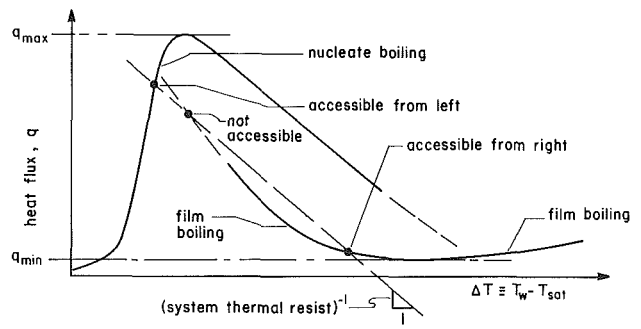

Fig. 1 Accessibility lines on Witte and Lienhard's double boiling curve (coordinates are linear)

[1]Present address: Assistant Professor, Etablissement d'Enseignement Supérieur Polytechnique, Université de Madagascar, C.U.R. d'Antisiranana, Madagascar.

Contributed by the Heat Transfer Division and presented at the ASME Winter Annual Meeting, Anaheim, California, December 1986. Manuscript received by the Heat Transfer Division January 17, 1986.

The important point made by Witte and Lienhard (1982) was that, *for a given combination of liquid and heater condition*, there were two possible transition boiling curves: one that corresponded with a wetted surface and one that corresponded with an unwetted surface. They also noted that in a single process (such as the quenching of a heater) wetting can abruptly set in, causing a dramatic jump in the transitional boiling heat flux.

We shall subsequently argue that these jumps can occur because, once liquid contact becomes sustained, the relevant contact angle becomes the retreating one β_r, instead of the advancing one β_a.

The Minimum Heat Flux. As the wall superheat is decreased, the heat flux and the accompanying vapor volume production also decrease. As the vapor volume rate diminishes, one of two things can happen: One of these is the conventional $q_{\min}$ transition originally proposed by Zuber, and subsequently developed by others (see, e.g., Lienhard and Dhir, 1980). In accordance with Zuber's mechanism, $q_{\min}$ (as described by equation (1)) occurs when vapor is not generated rapidly enough to sustain the natural frequency of the Taylor wave at the liquid–vapor interface.

The other way in which $q_{\min}$ can be set appears to be by the onset of liquid–solid contacts that can occur well above this ultimate minimum value of q. As the vapor volume rate decreases, the vapor film becomes thinner and such contact becomes increasingly likely. Whether or not contact occurs at a given heat (and vapor volume) flux, will undoubtedly depend primarily upon the advancing (or "dry") contact angle since the surface will, in all probability, dry out between contacts.

In any event, while one conventionally identifies the beginning of a transitional boiling where the slope of the boiling curve becomes negative, we must now identify a transition *prior* to that point. This is the transition at which the boiling curve starts to deviate above what has been shown to be the predictable pure-film boiling curve. This kind of transition can occur when the boiling curve *still has a positive slope*. It is at this point that we might say that the liquid has been "informed" on the surface condition, presumably by having made contact.

Whether or not this transition leads into "film-transition," or into a rewetting "nucleate-transition" regime, boiling depends upon the magnitude of the contact angle. We presume that this should be the advancing angle β_a, since the heater surface must be dry before the liquid–vapor interface touches it each time.

Film Boiling. Berenson's original study included a prediction of film boiling heat transfer that involved heat conduction through the laminar vapor film flowing in the space between the heater and the liquid–vapor interface. The prediction was reasonably good at the lower film boiling heat fluxes; however, as ΔT was increased, it yielded values that decreased to about 80 percent of the measurements. While this error was not great, it was extremely systematic in ΔT.

The misbehavior of Berenson's straightforward prediction was studied by Klimenko (1981). Klimenko traced the development of film boiling predictions for horizontal heaters from Chang (1959) through Berenson and beyond, noting that virtually all of them took the form

$$\mathrm{Nu} = A[g\lambda_d^3(\rho_f - \rho_g)h'_{fg}/\alpha_g \nu]^b \tag{3}$$

where the Nusselt number $\mathrm{Nu} \equiv q\lambda_d/k_g\Delta T$, and h'_{fg} is the conventional effective latent heat corrected to account for sensible heat transfer.

Klimenko proposed a new view of the heat transfer process. He suggested that it was the result of a gravity-driven, forced convection flow through the vapor film. This flow, he noted, would be turbulent if

$$M \equiv \frac{g^{1/3}\lambda_d}{\sqrt{3}\nu^{2/3}}\left[\frac{\rho_f - \rho_g}{\rho_f}\right]^{1/3} > 464 \tag{4}$$

Using Reynolds analogy, he then predicted the Nusselt number

$$\frac{\mathrm{Nu}}{M\mathrm{Pr}^{1/3}} = \begin{cases} 0.0086, & \text{for } \mathrm{Ja} > 0.5 \\ 0.00611/\mathrm{Ja}, & \text{for } \mathrm{Ja} < 0.5 \end{cases} \tag{5}$$

where Ja is the Jakob number, $c_p\Delta T/h_{fg}$.

All of the data we deal with subsequently satisfy both the criterion for turbulent flow, $M > 464$, as well as the $\mathrm{Ja} > 0.5$

Nomenclature

A, B, b = unspecified constants
Bi* = modified Biot number, see equation (14)
c_p, c_h = heat capacities of the saturated liquid and the heater, respectively
g = acceleration of gravity
h_c = condensing heat transfer coefficient
h_{fg}, h'_{fg} = latent heat of vaporization; modified latent heat = $h_{fg}(1 + \text{const [Ja]})$
Ja, Ja* = Jakob number = $c_p\Delta T/h_{fg}$; modified Ja, see equation (14)
K = dimensionless function of transport properties defined in equation (6)
k_f, k_g, k_h = thermal conductivities of the saturated liquid, the vapor in the film, and the heater, respectively
M = dimensionless group defined in equation (4)
Nu = Nusselt number for film boiling = $q\lambda_d/k_g\Delta T$
Pr = Prandtl number of the vapor
$q, q_{\max}, q_{\min}$ = heat flux; peak pool boiling heat flux; minimum pool film boiling heat flux
R_c, R_h = thermal resistances of the heater block and the condensing process, respectively
T, T_A, T_c = temperature, limiting temperature for liquid–solid contact, thermodynamic critical temperature
$T_{hn}, T_{\text{sat}}, T_w$ = homogeneous nucleation temperature, saturation temperature, wall temperature
$\alpha_f, \alpha_g, \alpha_h$ = thermal diffusivities of the saturated liquid, the vapor in the film, and the heater, respectively
β, β_a, β_r = contact angle; advancing and retreating contact angles
Δq = difference between the film transition heat flux and the pure film boiling heat flux that would exist without any liquid–solid contact
$\Delta T, \Delta T_A$ = $(T_w - T_{\text{sat}})$; $(T_A - T_w)$
λ_d = most "dangerous" Taylor wavelength, $2\pi\sqrt{3\sigma/g(\rho_f - \rho_g)}$
ν = kinematic viscosity of the vapor
ρ_f, ρ_g = saturated liquid and vapor densities, respectively
σ = surface tension
τ = characteristic period of Taylor wave motion during film boiling

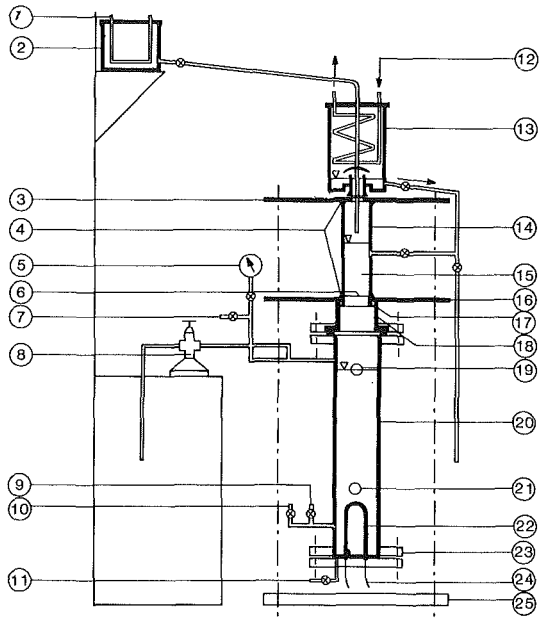

1. immersion heater
2. compensating tank
3. plate A
4. teflon flat gaskets
5. bourdon pressure gauge
6. heat transfer element
7. purge valve
8. back pressure Regulator
9. safety valve
10. loading port
11. drainage tube
12. cooling water
13. condenser
14. boiling vessel
15. test fluid
16. plate B
17. air withdrawal
18. stainless steel mount
19. level sight glass
20. steam chamber
21. level sight glass
22. electrical heater
23. threaded rods
24. 4 electrical leads
25. wooden base

Fig. 2 The present reconstruction of the classical "Berenson experiment"

condition. Notice that this means that if Klimenko is correct, $\mathrm{Nu} \neq fn(\Delta T)$, and q is directly proportional to ΔT, except as the temperature dependence of physical properties influences the relationship. This contradicts the conventional wisdom as expressed in equation (3) and, in fact, we find the physical mechanisms upon which equation (3) is based to be more convincing. Nevertheless, we shall subsequently see that the functional dependence of Klimenko's equation provides more accurate means for extrapolating film boiling data than does equation (3).

Present Aims. The objective of the present study is to measure boiling curves in a Berenson-type apparatus, with an emphasis on the transitional boiling region. We seek to do this with a lowered thermal resistance so as to gain improved access to the transition region, and to do so with a controlled set of surface finishes. We shall then seek to provide a workable description of film transition boiling and to locate its onset.

Experiment

Apparatus. The present experiment is shown schematically in Fig. 2 and described in full detail by Ramilison (1985). It consists of an upper vessel containing a boiled liquid, which is heated through a copper plate by condensing water in a high-pressure chamber below. The plate is 6.35 cm in diameter and made of 99.99 percent copper, 1.524 cm thick. It is flush with the glass sidewalls of the upper chamber, and over 3 λ_d in diameter (for each of the boiled fluids) to guarantee a good approximation to an infinite flat plate geometry. The apparatus was well insulated during the tests.

The plate is supported by a 2.5-mm-thick stainless steel bridge that almost thermally isolates it from the lower chamber. The thermal resistance of the copper plate is 0.000252 m^2-°C/W (exclusive of the condensing film). This is 1/6th of the value in Berenson's experiment. It is equipped with four thermocouples at different locations on the top which verified the unidimensionality of heat flow and gave the basis for specifying the temperature at the bottom of the plate. (The bottom temperature was needed subsequently to predict the condensation resistance.)

Three surfaces were prepared for use in each of the four boiled liquids: reagent grade acetone, Freon-113, *n*-pentane, and benzene. The surfaces were prepared in the following ways:

1 A *rough surface* was obtained by wrapping a #80 emery cloth around a 1-in.-dia shaft and using five strokes in one direction, five strokes at right angles to that direction, etc., until the surface was judged reproducible.

2 A *mirror-polished surface* was prepared by passing through a series of increasingly fine emery papers, and doing the final polish with 0.05μ alumina until the surface served as an optically flawless mirror.

3 A *Teflon-coated surface* was made by commercially coating a previously mirror-polished heater (on the top only) with a 1 mil layer of polytetrafluorethylene. The coating was inspected to verify that it was completely smooth and free of any flaws.

Procedure. The heat flux in the tests was obtained in either or both of two ways. Before each test, the apparatus was operated with no boiled liquid in the upper chamber. This established the heat loss of the insulated container as a function of the temperature of the condensing water. The heat transfer was then determined by subtracting the heat loss from the electrical supply to the water chamber. The heat flow was also computed by condensing the boiled vapor to a temperature as close to saturation as possible, and weighing it. The latter method could only be used accurately at relative higher heat fluxes where it was used to verify the energy-input-minus-loss method discussed above.

The transition-film boiling heat fluxes discussed here were all obtained by the energy-input-minus-loss method. The probable error in the resulting q was found by Ramilison to range downward from a maximum value of 3.8 percent.

The present film and transition-film boiling data were all reached from the film boiling side. First, we established the film boiling heat flux by going to the peak nucleate boiling heat flux, increasing the heat flux slightly, and then stabilizing the system at the highest-heat-flux film-boiling condition. Then we varied the power to pass through decreasing ΔT. This process continued until the system abruptly reverted to nucleate boiling.

The heater surface temperature T_w was measured by a thermocouple less than 1 mm below the surface of the copper block. This gave temperatures within about a tenth of a degree Celsius of the surface temperature at film-transition boiling conditions. The temperature difference ΔT was obtained as the difference between T_w and T_{sat} for the boiled liquid.

The temperature difference, $(T_{cond.stm.} - T_{sat})$ (recall equation (2)), was controlled by regulating the pressure in the lower chamber. This was done by adjusting both the regulating valve and the electric heat supply to the chamber, a process that involved a good deal of technique as described by Ramilison.

Contact Angles. The interpretation of the results of this work required a knowledge of the advancing and retreating contact angles, β_a and β_r, for the various surfaces and liquids used. Measurements of β_r were obtained with the tilting plate method, using the actual heaters as the tilting plates and making the observations at T_{sat}. Since the tilting plate normally involves wetting the surface, we had to modify it to obtain β_a. The heaters had to be set at a given angle, immersed, the shape of the miniscus noted, the heater withdrawn and completely dried out, the angle reset, and the plate re-immersed, until the

Table 1 Complete boiling heat transfer data from the present tests

Point No.	ΔT °C	Heat flux $(W/m^2)10^{-3}$
acetone, teflon-coated		
1	23.6	201.8
2	20.1	137.5
3	21.6	174.4
4	25.8	258.8
5	28.4	306.5
6	32.2	369.5
7	35.7	387.3
8	38.7	396.2
9	142.2	28.6
10	15.4	95.3
acetone, mirror polished		
1	31.5	257.7
2	27.6	172.4
3	29.3	216.6
4	35.3	291.9
5	37.3	310.0
6	22.9	97.4
7	14.8	52.4
8	25.9	127.1
9	98.1	17.8
acetone, rough		
1	13.0	217.4
2	11.7	154.2
3	11.0	72.4
4	10.2	47.7
5	14.0	240.5
6	16.1	327.0
7	17.7	350.7
8	19.4	366.2
9	108.1	19.8
n-pentane, teflon-coated		
1	29.7	224.1
2	27.6	180.8
3	22.9	60.9
4	25.4	130.7
5	36.4	293.6
6	31.9	269.4
7	35.5	287.2
8	119.9	23.7
benzene, teflon-coated		
1	37.9	254.5
2	45.2	334.1
3	52.2	351.3
4	32.9	167.0
5	29.3	107.7
6	40.8	288.2
7	26.4	60.3
8	19.1	34.9
9	113.3	23.7

Point No.	ΔT °C	Heat flux $(W/m^2)10^{-3}$
acetone, teflon-coated		
1	37.3	393.3
2	39.5	399.7
3	136.3	26.9
4	130.1	41.4
5	112.7	141.1
6	71.2	291.0
7	49.9	379.1
8	53.4	370.5
9	69.4	304.5
10	95.1	218.4
acetone, mirror polished		
1	26.9	171.8
2	115.2	22.4
3	98.3	18.5
4	90.4	16.1
5	83.6	15.9
6	74.8	18.0
7	118.6	22.7
8	70.7	18.9
9	67.1	19.9
acetone, rough		
1	14.6	313.0
2	107.2	19.4
3	99.3	17.7
4	86.9	15.8
5	82.1	14.9
6	73.9	15.0
7	68.9	16.3
8	60.8	19.4
9	52.2	23.1
10	116.9	21.4
n-pentane, teflon-coated		
1	24.3	129.7
2	100.3	20.9
3	95.0	21.3
4	89.8	22.6
5	84.2	24.9
6	122.0	24.2
7	80.4	25.6
benzene, teflon-coated		
1	34.5	167.7
2	111.6	23.3
3	101.1	21.1
4	95.2	21.3
5	91.1	22.6
6	83.7	23.9
7	114.3	24.1
8	120.3	24.8
9	107.8	22.0
10	80.6	24.6

Point No.	ΔT °C	Heat flux $(W/m^2)10^{-3}$
n-pentane, mirror polished		
1	34.6	193.9
2	28.4	150.8
3	31.2	166.6
4	24.9	111.3
5	37.9	213.8
6	22.1	84.4
7	36.6	205.1
8	109.8	21.1
n-pentane, rough		
1	12.9	215.0
2	121.0	23.5
3	110.3	21.5
4	101.7	18.9
5	92.1	16.5
6	83.9	15.4
7	75.7	16.3
8	69.4	17.7
9	63.5	19.0
10	57.2	20.0
11	52.1	21.5
12	46.8	24.8
Freon-113, teflon-coated		
1	32.5	216.6
2	29.4	174.9
3	26.9	135.7
4	24.7	99.5
5	22.4	66.2
6	19.7	37.2
7	35.2	237.7
8	34.7	235.2
9	31.6	207.7
10	113.4	20.9
Freon-113, mirror polished		
1	33.5	169.8
2	36.0	195.4
3	26.9	123.6
4	21.7	67.9
5	16.7	48.5
6	31.8	157.7
7	34.7	192.4
8	117.8	21.4
Freon-113, rough		
1	15.3	217.4
2	11.8	101.2
3	12.9	141.7
4	10.6	72.1
5	9.1	38.6
6	13.9	178.9
7	18.0	221.5
8	13.3	169.9
9	121.2	21.9

Point No.	ΔT °C	Heat flux $(W/m^2)10^{-3}$
n-pentane, mirror polished		
1	31.5	166.9
2	120.4	23.7
3	110.4	21.4
4	102.4	19.4
5	94.2	18.9
6	88.9	18.6
7	81.8	19.1
8	77.4	19.8
9	72.0	21.9
10	66.6	25.5
11	61.3	28.7
n-pentane, rough		
1	8.1	105.5
2	12.3	246.5
3	14.8	261.8
4	9.0	135.6
5	10.0	171.4
6	7.5	63.4
7	13.2	251.4
8	10.2	201.3
9	100.4	18.2
Freon-113, teflon-coated		
1	32.0	208.2
2	112.4	20.6
3	99.3	19.2
4	93.2	18.8
5	85.9	19.5
6	80.7	19.9
7	76.4	22.9
8	122.1	21.6
9	119.1	21.0
Freon-113, mirror polished		
1	26.9	123.2
2	107.5	19.3
3	100.1	17.2
4	88.6	15.6
5	84.5	15.1
6	79.7	15.1
7	73.2	16.0
8	66.1	18.4
9	65.4	18.7
10	63.6	19.7
Freon-113, rough		
1	12.6	139.9
2	121.7	21.6
3	114.2	19.6
4	104.4	18.5
5	95.6	16.2
6	85.6	14.6
7	76.7	13.2
8	68.3	12.4
9	61.3	12.1
10	54.9	12.8
11	47.1	14.6
12	41.4	16.3

liquid surface intersected it without being perceptibly bent in either direction. The observations of both contact angles were judged accurate within ±5 percent.

Results and Discussion

Results. The complete heat transfer data and contact angle measurements from the present tests are given in Tables 1 and 2, respectively. Each set of data in Table 1 is ordered in chronological sequence. The heat transfer data were plotted in two ways by Ramilison (1985): as full boiling curves, and as expanded plots in the transition film boiling range. Since the complete data are given in Table 1, we include the complete curves only for acetone and Freon-113 (Figs. 3 and 4) and the expanded curves only for *n*-pentane and benzene (Figs. 4 and 6).

Typical "accessibility lines" are drawn in Figs. 3 and 4. The fact that they are not all the same reflects the fact that each is based on a different condensing heat transfer coefficient, inferred from the measured heat flux.

Nucleate Boiling and Burnout. The nucleate boiling regime exhibits the well-known sensitivity of heat flux on surface finish, although it is interesting to note that the curves for the teflon-finished surfaces are only slightly steeper than those for the mirror-finish data.

The present burnout data and those of Berenson were compared with the hydrodynamic peak heat flux prediction of Lienhard et al. (1973). The present rough surface data were consistently between 93 and 98 percent of the prediction. The highly polished surfaces consistently gave peak heat fluxes that lay between 81 and 87 percent of the prediction. The teflon-coated surfaces gave values that exceeded the prediction by 4 to 10 percent. Berenson found that a rough oxidized surface could give values almost 20 percent above the prediction.

While surface roughness clearly exerts only a second-order influence on burnout, it is an influence that is not yet understood and which merits further study.

Table 2 Contact angle values and temperatures at the onset of the transition-film boiling region

Liquid	Surface Finish	Contact Angle ±5° β_r	Contact Angle ±5° β_a	T_A °C	T_A °C	$\frac{T_A - T_{sat}}{T_{h.n.} - T_{sat}}$
acetone	Teflon	0	5		190.0	0.96
	Mirror	13	40	200.2	142.8	0.59
		15	45		131.4	0.55
Freon-113	Teflon	8	30		161.0	0.82
	Mirror	10	40	177.5	144.9	0.67
	Rough	13	50		132.0	0.58
normal pentane	Teflon	8	25		148.3	0.84
	Mirror	10	35	164.1	138.8	0.80
	Rough	15	45		128.8	0.64
benzene	Teflon	15	40	249.0	189.4	0.56

Stable Film Boiling. The stable film boiling data lie in a range in which radiation heat transfer contributes virtually nothing to the total q. In this range both our data and those of

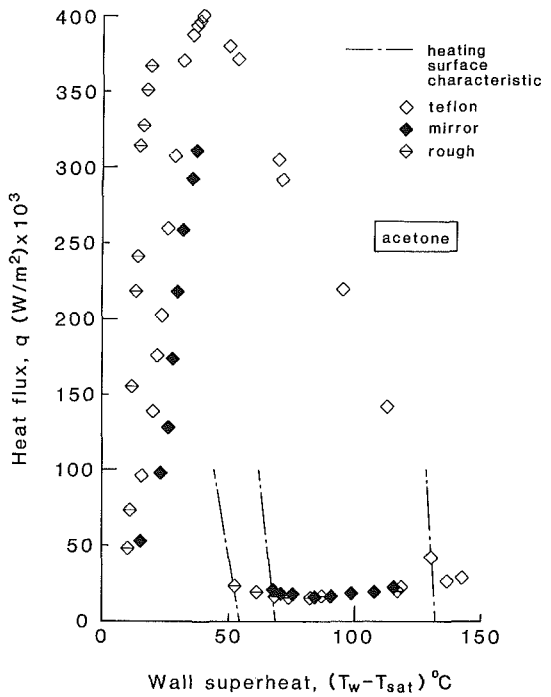

Fig. 3 Boiling curves for acetone boiling on teflon-coated, mirror-finished, and "rough" surfaces

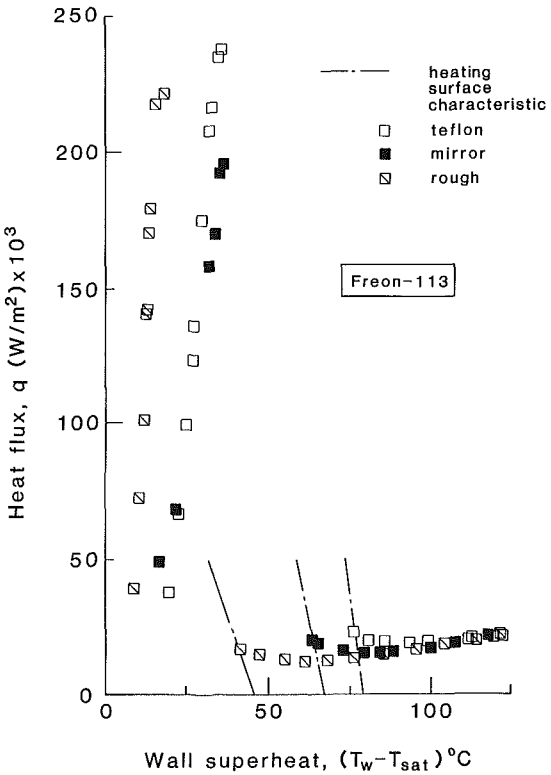

Fig. 4 Boiling curves for Freon-113 boiling on teflon-coated, mirror-finished, and "rough" surfaces

Berenson are almost perfectly represented – within a constant – by Klimenko's turbulent film boiling correlation (equation (15)) for $Ja > 0.5$. This expression tells us that the only temperature dependence of the heat transfer coefficient arises in the temperature dependence of the viscosity and thermal diffusivity of the vapor.

However, we had to replace Klimenko's empirical constant of 0.0086, which had originally been established with a good

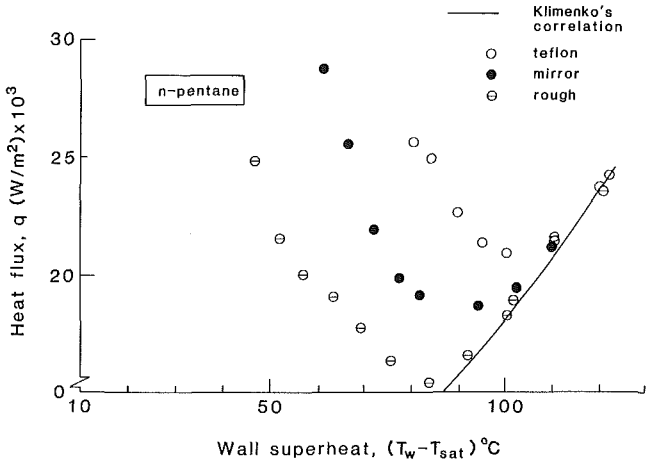

Fig. 5 Film and film-transition regions for *n*-pentane boiling on teflon-coated, mirror-finished, and rough surfaces

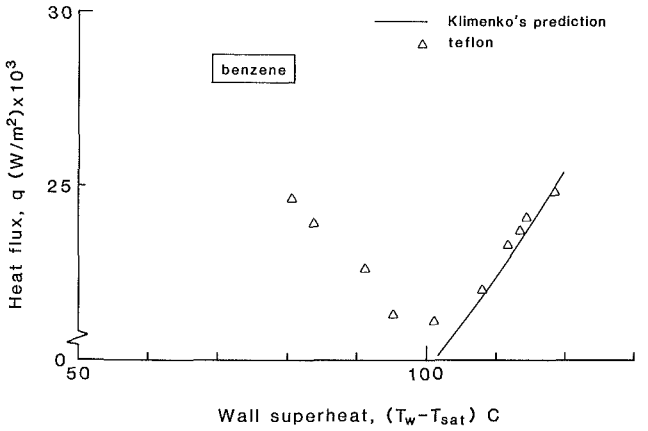

Fig. 6 Film and film-transition regions for benzene boiling on a teflon-coated surface

deal of data scatter based on film boiling in different geometries, with specific values for each liquid. The values used were: 0.0057 for Freon-113 and *n*-pentane; 0.0066 for acetone; and 0.0154 for benzene. The film boiling curve fit is shown graphically in Figs. 5 and 6.

While the details of Klimenko's formulation are probably not perfect, it nevertheless provides us with a very nearly perfect basis for fitting the existing data. We therefore believe that his rationale merits further study.

Film-Transition Region. The data separated fairly abruptly from the film boiling extrapolation as the surface temperature was lowered below a certain point A, which differs in each configuration. This separation doubtless represents the point at which the liquid–vapor interface begins to make contact with the heater. We accordingly define q_A and ΔT_A at that point, where $\Delta T_A \equiv (T_A - T_w)$. The film-transition boiling region then lies to the immediate left of point A. It is worth noting that $q_{\min}$ is less than q_A, and always within 12 percent of it in our experiments.

In the present work, point A was deemed to occur at the point at which the film boiling data first reached a value that was 1.05 times the Klimenko data fit.

The data for acetone on a teflon-coated surface, and only these data, fail to pass into the transition-film boiling region at all. Both contact angles in this case (see Table 1) represent almost perfect wetting. Consequently the q–ΔT data in Fig. 3 do not diverge from the film boiling curve; they leave it very abruptly. This behavior signifies a direct jump to transition-film boiling.

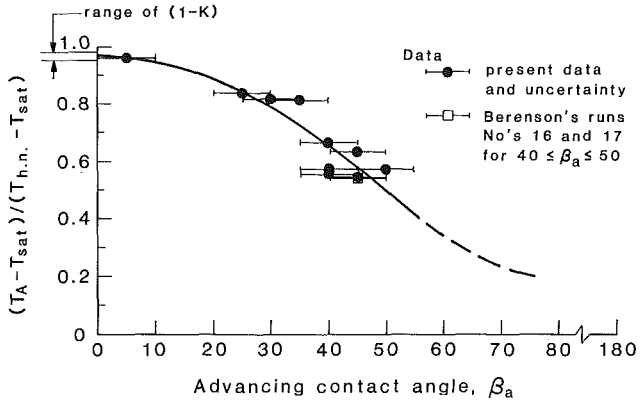

Fig. 7 Variation of the onset of transition boiling with the advancing contact angle

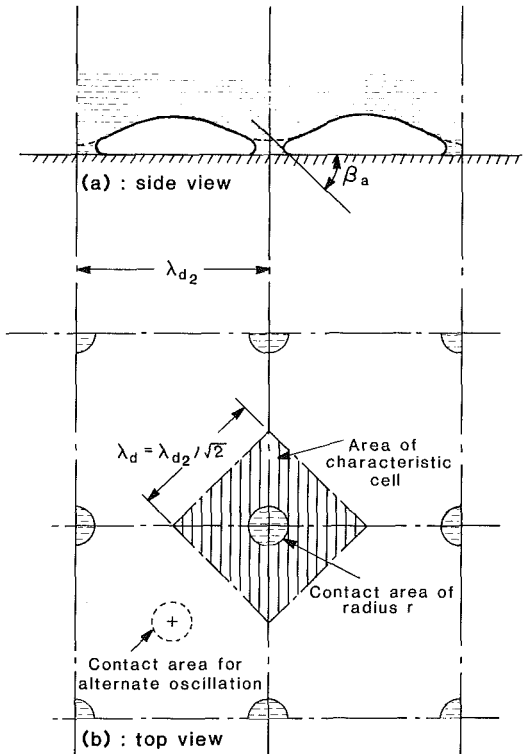

Fig. 8 Model of contact of the liquid-vapor interface with the heater during film-transition boiling

The film-transition boiling curves in each case passed from point A to the left through a minimum and back up to a point at which neighboring points could no longer be reached. It is important to note that, at the last attainable film-transition boiling point, the "accessibility lines" were not tangent to the film-transition boiling curve. If the reason for our inability to measure further in this region had merely been a loss of accessibility, then they *would* have been tangent.

What we therefore witness must be a collapse of the film-transition process. It is our belief that this collapse occurs because, as the extent of surface contact increases, we reach a point at which the surface no longer dries out between contacts with the interface. When this occurs, the contact angle changes from its relatively high advancing value β_r. The system must then leave film-transition boiling and find a new equilibrium in either nucleate transition or nucleate boiling where behavior is dictated by β_r. (When Witte and Lienhard originally discussed the two possible modes of transition boiling, they suggested that the interface might contact the surface tangentially, in the film-transition mode. The recognition of the role of the two contact angles makes it unnecessary to postulate this form of contact.)

A Recent Corroborative Experiment. Chowdhury and Winterton (1985) gave boiling curves obtained by quenching a vertically oriented finite cylinder in water and methanol. They did this for several values of contact angle as given by the sessile drop method. While these experiments cannot be compared quantitatively with ours, they very clearly show that T_A decreases strongly with increasing β.

A Model for the Film-Transition Boiling Heat Flux

Limit of Liquid-Solid Contact. We envision film-transition boiling as involving limited liquid-solid contact. Therefore, we must first consider the temperature at which the first contact can occur. It is well-understood (see, e.g., Yao and Henry, 1978) that, based on the contact of two semi-infinite regions

$$\frac{T_{\text{wall}} - T_{\text{contact}}}{T_w - T_{\text{sat}}} = \frac{k_f/\alpha_f^{1/2}}{k_f/\alpha_f^{1/2} + k_h/\alpha_h^{1/2}} \equiv K \tag{6}$$

The limiting value of the contact temperature should then be the absolute limiting homogeneous nucleation temperature T_{hn}, which has been shown by Lienhard (1982) to be well approximated by

$$T_{hn} = [0.923 + 0.077(T_{\text{sat}}/T_c)^9]T_c \tag{7}$$

In Fig. 7 we indicate the fraction of the limiting liquid superheat at which the first liquid contact occurs. Bearing in mind that $(T_A - T_{\text{sat}})/(T_{\text{hn}} - T_{\text{sat}})$ cannot ever exceed $(1-K)$ for the system, we note that as β_a approaches zero – or perfect wetting – T_A approaches the temperature required by perfect homogeneous nucleation. (Notice that $(1-K)$ is given as a narrow range rather than as a single value, owing to the slight temperature variation of the thermal properties.) At increasing values of β_a, it becomes harder for the liquid to make contact, and easier to carry film boiling down to lower temperatures.

A Model for Correlating the Transition-Film Boiling Heat Flux. The liquid-vapor interface in film boiling takes the form of a cyclically collapsing, two-dimensional, square array of Taylor-unstable waves as shown in Fig. 8. The size of a characteristic cell in this grid is $\lambda_d = 2\pi\sqrt{3\sigma/g(\rho_f - \rho_g)}$ where λ_d is the most rapidly collapsing one-dimensional Taylor wave given by Bellman and Pennington (1955). The two-dimensional wave exceeds λ_d by a factor of $\sqrt{2}$ (see Sernas, 1969).

The liquid-solid contact area can be represented as a fraction of the area of the cell, $(r/\lambda_d)^2$, where r is the radius of the frustrum of the cone of liquid that contacts the surface. The duration of the contact t_c will be a fraction of the characteristic period of the Taylor wave (see, e.g., Zuber)

$$\tau \sim [\sigma/g^3(\rho_f - \rho_g)]^{1/4} \tag{8}$$

Next we wish to relate the heat flux added to the film-boiling heat flux by transient contact Δq to the local transient heat flux to the liquid resulting from liquid-solid contact. Δq is related to $q_{\text{transient}}$ by the simple energy balance

$$\lambda_d^2(\tau)(\Delta q) \sim r^2(t_c) q_{\text{transient}} \tag{9}$$

But $q_{\text{transient}}$ is given by the semi-infinite region expression

$$q_{\text{transient}} = \frac{k_h(T_{\text{sat}} - T_{\text{contact}})}{(\alpha_h \tau)^{1/2}} = \frac{k_h(T_w - T_{\text{sat}})}{(\alpha_h \tau)^{1/2}} K \tag{10}$$

where we use equation (6) to eliminate T_{contact}. If we put this back into equation (9) we obtain an expression for Δq in terms of the unknowns t_c and τ.

To eliminate t_c and τ we make two physical assumptions:

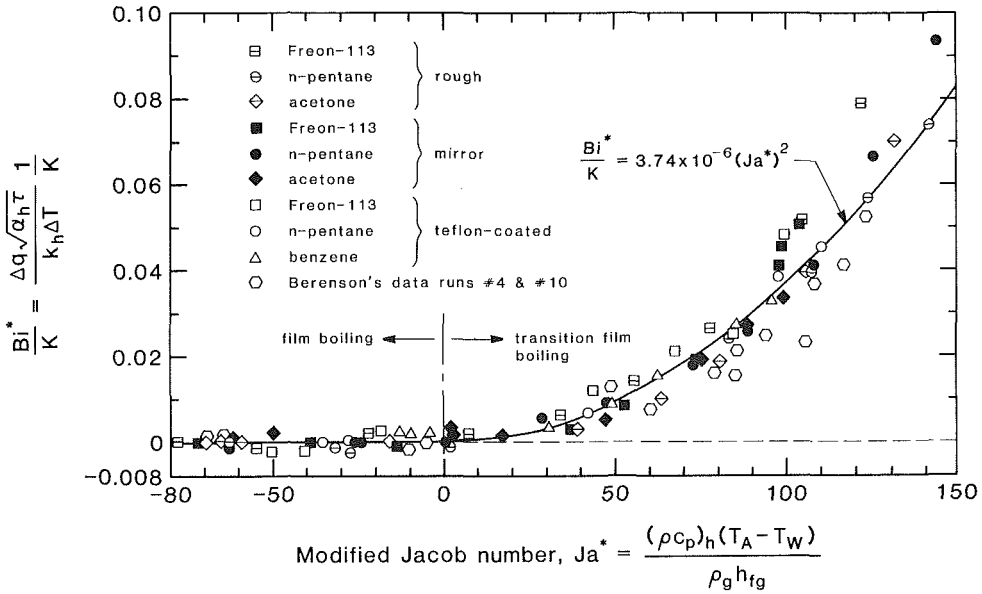

Fig. 9 Correlation for transition film boiling heat transfer on a horizontal flat plate

1 The fractional area of the contact circle increases in direct proportion to the fractional duration of contact

$$t_c/\tau \sim (r/\lambda_d)^2 \tag{11}$$

2 Since the energy storage in the metal as a consequence of contact must be directly proportional to the additional latent heat contributed per unit cell, the fractional contact area $(r/\lambda_d)^2$ can be proportioned as follows:

$$(r/\lambda_d)^2 \sim \frac{(\rho c_p)_h (T_A - T_w)}{\rho_g h_{fg}} = \frac{(\rho c_p)_h \Delta T_A}{\rho_g h_{fg}} \tag{12}$$

When we combine equations (10), (11), and (12) with equation (9) we obtain

$$\mathrm{Bi}^* = \text{const}\ (K)(\mathrm{Ja}^*)^2 \tag{13}$$

where

$$\mathrm{Bi}^* \equiv \frac{\Delta q(\alpha_h \tau)^{1/2}}{\Delta T k_h} \text{ and } \mathrm{Ja}^* \equiv \frac{(\rho c_p)_h \Delta T_A}{\rho_g h_{fg}} \tag{14}$$

We compare equation (13) with the film and film-transition boiling data from Table 1, in Fig. 9. With the constant fixed at 3.74 $(10)^{-6}$, the equation brings all but 7 of our data, and those of Berenson's data that can be used, together within an absolute error of 0.01 in Bi*.

Conclusions

Transition boiling has proven over the years to be a treacherous mine field. Therefore our conclusions should be qualified to some extent. We are very confident that:

1 Part of the region in which $dq/d\Delta T$ is positive, which has appeared in the past to have been pure film boiling with no liquid-solid contact, now seems almost certainly to be "film-transition" boiling with significant contact.

2 The boundary between the pure-film and film-transition regions can be located – at least for a flat plate – using the correlation for T_A given in Fig. 7.

3 The expression

$$\mathrm{Bi}^* = 3.74(10)^{-6}(K)(\mathrm{Ja}^*)^2 \tag{13a}$$

can be used to correlate film-transition and film boiling once T_A is known.

The following item is a strong conjecture rather than a conclusion:

4 We are fairly confident that the jumps that we and so many others observe from film-transition to nucleate-transition boiling occur because the control of the process is shifted from β_a to β_r, or vice versa. (It is certain that these jumps did not occur by virtue of the mere loss of accessibility in our experiments.)

This is a confirmation of prior work rather than a conclusion:

5 The burnout heat flux definitely suffers a secondary dependence on the surface condition.

Acknowledgments

This work has received support under NSF Grant No. MEA-8218708 and NASA Grant NAG 3-537.

References

Bellman, R., and Pennington, R. H., 1955, "Effects of Surface Tension and Viscosity on Taylor Instability," *Q. App. Math.*, Vol. 22, pp. 1605–1610.

Berenson, P. J., 1960, "Transition Boiling Heat Transfer From a Horizontal Surface," M.I.T. Heat Transfer Lab. Tech. Rept. No. 17.

Chang, Y. P., 1959, "Wave Theory of Heat Transfer in Film Boiling," ASME JOURNAL OF HEAT TRANSFER, Vol. 81, p. 112.

Chowdhury, S. K. R., and Winterton, R. H. S., 1985, "Surface Effects in Pool Boiling," *Int. J. Heat Mass Transfer*, Vol. 28, No. 10, pp. 1881–1889.

Hesse, G., 1973, "Heat Transfer in Nucleate Boiling, Maximum Heat Flux and Transition Boiling," *Int. J. Heat Mass Transfer*, Vol. 16, pp. 1611–1627.

Klimenko, V. V., 1981, "Film Boiling on a Horizontal Plate – New Correlation," *Int. J. Heat Mass Transfer*, Vol. 24, pp. 69–79.

Lienhard, J. H., and Dhir, V. K., 1980, "On the Prediction of the Minimum Pool Boiling Heat Flux," ASME JOURNAL OF HEAT TRANSFER, Vol. 102, No. 2, pp. 457–460.

Lienhard, J. H., Dhir, V. K., and Riherd, D. M., 1973, "Peak Pool Boiling Heat-Flux Measurements on Finite Horizontal Flat Plates," ASME JOURNAL OF HEAT TRANSFER, Vol. 95, No. 4, pp. 477–482.

Lienhard, J. H., 1982, "Corresponding States Correlations for the Spinodal and Homogeneous Nucleation Temperatures," ASME JOURNAL OF HEAT TRANSFER, Vol. 104, No. 23, pp. 379–381.

Ramilison, J. R., 1985, "Transition Boiling Heat Transfer and the Film Transition Regime," Ph.D. Dissertation, Mechanical Engineering Department, University of Houston, Oct. 1985.

Sernas, V., 1969, "Minimum Heat Flux in Film Boiling – A Three Dimensional Model," *Proc. 2nd Can. Cong. App. Mech.*, Univ. of Waterloo, 1969, pp. 19–23.

Witte, L. C., and Lienhard, J. H., 1982, "On the Existence of Two 'Transition' Boiling Curves," *Int. J. Heat Mass Transfer*, Vol. 25, No. 6, pp. 771–779.

Yao, S., and Henry, R. E., 1978, "An Investigation of the Minimum Film Boiling Temperature on Horizontal Surfaces," ASME JOURNAL OF HEAT TRANSFER, Vol. 100, No. 2, pp. 260–267.

Zuber, N., 1959, "Hydrodynamic Aspects of Boiling Heat Transfer," AEC Report AECU-4439, Physics and Mathematics.

Boiling Characteristics of Small Multitube Bundles

A. M. C. Chan
Ontario Hydro Research Division,
Toronto, Ontario, Canada

M. Shoukri
Associate Professor,
McMaster University,
Hamilton, Ontario, Canada
Mem. ASME

Boiling characteristics of multitube bundles have been investigated experimentally. Small bundles of up to nine rows were used. Void fraction profiles in the test vessel, tube surface temperatures, power input to individual tubes, and critical heat fluxes were measured for different bundle arrangements and boiling conditions. The data were used to study the system hydrodynamics, bundle heat transfer coefficients, and bundle critical heat flux. The data showed that for lower heat fluxes, the heat transfer characteristics are affected by the system hydrodynamics resulting in higher heat transfer coefficients, whereas at higher heat fluxes nucleate boiling is the dominant mechanism. The data also showed that within a tube bundle, the vapor rising from lower tubes enhances the CHF characteristics of the upper tubes.

1.0 Introduction

The boiling characteristics of multitube bundles are important in a large variety of industrial heat exchange equipment. These include various types of kettle and internal reboilers used in chemical and petroleum process systems. Historically, the design of such equipment was based on single-tube pool boiling data. The departure of the bundle from single tube behavior was accounted for by empirical correction factors. The importance of internal circulation in the reboiler shell was recognized by Fair in 1963 [1]. In recent years, it is increasingly evident that the empirical approach tends to be too conservative, especially for the design of very low temperature difference reboilers and reboilers with very large diameter shells. New design approaches based on mechanistic models are thus needed. Two popular models are:

(*i*) *The Circulation Model* [*1*]. The essence of this model is the recognition of the strong liquid recirculation in the reboiler shell. Reboiler performance is thus dominated by fluid mechanics and convective heat transfer. The bundle boiling heat transfer coefficient is given by

$$h_b = \gamma h_{nb} + \beta h_f \tag{1}$$

where h_{nb} is the single-tube nucleate boiling heat transfer coefficient, h_f is the liquid phase convection heat transfer coefficient, and γ and β are the bundle correction factor and the two-phase convection correction factor, respectively.

(*ii*) *The Thin Film Conduction Model* [*2*]. This model assumes that the bundle boiling heat transfer coefficient is related to conduction through thin liquid films created by bubbles rising through the bundle

$$h_b = R_f h_{nb} + (1 - R_f) h_{tf} \tag{2}$$

where R_f is the liquid volume fraction; h_{tf} is the thin film conduction heat transfer coefficient which can be expressed in terms of the superficial vapor velocity V_{gs}.

$$h_{tf} = 2000 + 1300 \exp\left[- \left(\frac{2000}{V_{gs}} \right)^{1.5} \right] \tag{3}$$

where h_{tf} is in kcal/m^2-hr-°C and V_{gs} is in m/hr.

Both models are capable of explaining, at least qualitatively, the increase in boiling heat transfer coefficients in bundles as compared to single-tube data except near the critical heat flux. Quantitative comparisons, however, proved to be more difficult. This is because many of the variables used in equations (1) and (2) are not readily known.

Contributed by the Heat Transfer Division and presented at the ASME Winter Annual Meeting, New Orleans, Louisiana, December 1984. Manuscript received by the Heat Transfer Division July 20, 1985.

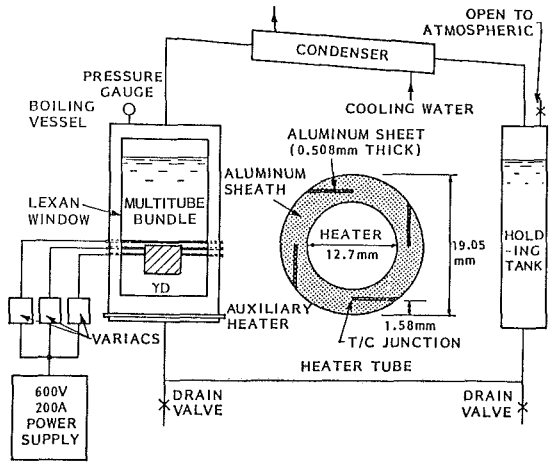

Fig. 1 Schematic of experimental setup

In order to apply the mechanistic models described, it is necessary to know the local flow conditions. This includes liquid and vapor velocities and void fraction. In theory, details of the flow field can be obtained by solving the two-phase field equations in the bundle. This approach will inevitably result in sophisticated multidimensional computer codes which will be difficult and expensive to use. Moreover, the constitutive relationships required to close the set of field equations are not well developed for two-phase flow around horizontal bundles. However, this is probably the most promising approach for future investigations.

A simpler approach which is of interest is to assume one-dimensional upward flow through the bundle. The liquid is assumed to enter the bundle at the bottom and flows vertically upward as it evaporates. For a given heat flux, the circulation rate or total mass flux in the bundle is obtained by a force balance between single- and two-phase friction, acceleration and static losses in the bundle, and the static head of single-phase liquid surrounding the bundle. Other variables are deduced from the flow velocity or external correlations. This approach has been used by different authors with different degrees of sophistication [3–5].

To summarize the state of the art in reboiler design and analysis, mechanistic models exist which include the effect of system hydrodynamics. However, not enough information is available to allow proper quantification of these effects. Most existing data only give the overall kettle performance [6, 7] or local heat transfer rates under very limited conditions [8, 9]. It is, therefore, felt that additional data are needed. Benchmark data with well-controlled operating and boundary conditions

will be useful for the identification of governing mechanisms, development of appropriate constitutive relations, and verification of existing models or those under development.

The work presented herein is part of an overall program to develop and update methods for the thermohydraulic analysis of kettle reboilers. Experimental data on the boiling characteristics of small horizontal bundles are presented. Systematic studies on the interaction of individual tubes in the bundle are described. Detailed data analysis and model development will be discussed in a future paper.

2.0 Experimental Facility

2.1 Experimental Setup. A schematic diagram of the experimental facility is shown in Fig. 1. A rectangular vessel, 546 mm in width, 745 mm in height, and 184 mm in depth, with an electrically heated multitube bundle was used to simulate part of a kettle reboiler. Two large Lexan windows were used for visual observation. Rising vapor from the vessel was condensed in the condenser and drained to the holding tank. Liquid was then circulated to the vessel by gravity. Two auxiliary heaters were located at the bottom of the vessel to preheat the feed and to maintain a more uniform temperature in the vessel. The holding tank was maintained at atmospheric pressure. The level of fluid in the boiling vessel was controlled by adjusting the level of the holding tank.

The electrically heated tubes were specially designed high-heat-flux, aluminum-sheathed tubular heaters 19.05 mm o.d. with a heated length of 520. mm. The tubes in the bundle were arranged in a rectangular array with a pitch of 23.8 mm (vertical) × 31.75 (horizontal) leaving a 50 mm clearance from each of the two side walls. Some of the heaters were instrumented with thermocouples at four circumferential positions in the middle for surface temperature measurements. The thermocouples were attached using a special procedure to ensure good contact. Four slots were machined into the sheath chordally as shown in the inset in Fig. 1. The slots extended from one end to the middle of the heater. Exposed junction stainless steel sheath type-K thermocouples (0.254 mm o.d.) were placed into the slots with the junction positioned at the central plane of the heater. Each slot was then press fitted with an aluminum filler piece, welded, and machined to restore a smooth surface. The power to the heaters was supplied by a 600 V, 200 A, a-c power supply. Power input to the heaters was controlled individually or in groups of three by a set of three variacs.

Average void fractions across and above the bundle at different elevations were obtained using a traversing gamma densitometer. Details of the design and operation of the gamma densitometer can be found in [10]. The system used in the present experiment consisted of a 50 mCi Cobalt-57 line source. The gamma beam was collimated using steel blocks providing a rectangular beam 50.8 mm wide and 12.5 mm high. The transmitted flux was detected by a thallium activated sodium iodide, NaI (Tl), scintillator and then processed using a standard pulse-counting system [10]. The source and the scintillator were mounted on opposite sides of the test vessel on a platform which could be moved in the vertical direction by a variable speed motor. The movement of the densitometer was confined to a vertical plane in the middle of the vessel. When measuring the void fraction between two rows of tubes, the gamma beam (12.5 mm high) covered a small part of the surrounding tubes (heaters). However, since this part of the beam was heavily attenuated by the heaters, the measured value represented the average void fraction in the spacing between the two tube rows. This was confirmed by static calibration of the system [11].

2.2 Experimental Procedures and Test Conditions. Experiments reported in the present paper were performed using Refrigerant R113 as the boiling liquid. R113 has a boiling point of 47.6°C at atmospheric pressure. All tests were performed at pressures close to atmospheric. Data were obtained by increasing the power input to the heaters in steps and taking measurements when steady state was reached. For the critical heat flux measurements, the power input to the heaters was raised very slowly. The criterion used for determining CHF was the visual observation of small amount of smoke in the vessel or a sudden rise in heater surface temperature. Traces of smoke were always observed just preceding the rapid rise in surface temperature.

In order to investigate the bundle effects on the boiling characteristics systematically, experiments were performed on: (*i*) a single tube; (*ii*) three vertical in-line tubes; (*iii*) a nine-tube bundle (3×3 array), and (*iv*) a 27 tube bundle (9×3 array).

The data were collected over a period of about seven months after three months of preliminary testing. The surface aging effect was significant only in the first month of the test period in which the measured surface superheat increased by about 10 percent. The change in surface superheat thereafter was found to be less than 4 percent. The CHF data was also varied by about 1 to 2 percent in general under repeated tests. With the aged surfaces no boiling hysteresis effects were observed.

3.0 Experimental Results and Discussion

A large quantity of data was obtained in the present investigation. The data can be divided into three sets. Each set was obtained to study one aspect of the boiling characteristics around a horizontal multitube bundle, namely: hydrodynamics, heat transfer characteristics, and critical heat flux.

3.1 Hydrodynamics. With the advance in reboiler designs, the importance of system hydrodynamics becomes increasingly apparent. Unfortunately, little is known about two-phase fluid dynamics around multitube bundles. It is thus difficult to separate and quantify the two-phase convection mechanisms from nucleate boiling mechanism in practical designs. In the present investigation, attempts were made to

Nomenclature

A_s = cross-sectional area of test vessel
CHF = critical heat flux
h = heat transfer coefficient
H = pool shallowness
q/A = heat flux
Q = power input
R_f = liquid volume fraction
V = velocity
T = temperature
$\langle\alpha\rangle$ = cross-sectional average void fraction
β = two-phase convection correction factor
γ = bundle correction factor
Δh_{fg} = latent heat of vaporization
ρ = density

Subscripts

b = bundle
e = effective
f = liquid phase
g = vapor phase
sat = saturated
s = superficial
T = total
w = wall

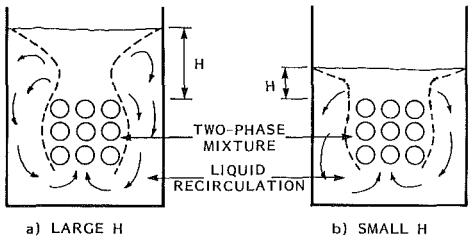

Fig. 2 Observed flow patterns

study the system hydrodynamics using visual observations of flow patterns and the experimentally measured void fraction profiles.

3.1.1 Flow Patterns and Void Distribution. Visual observations revealed strong recirculating liquid flow in the pool. The liquid flowed downward around the tube bundle with the two-phase mixture flowing upward through the bundle and emerging from the bundle toward the free surface. The high-quality mixture emerging from the bundle formed a plume rising to the free surface. The width of the two-phase mixture plume increased significantly near the free surface forming a high-voidage frothy layer. The shape of this plume was found to be dependent on pool shallowness H, defined as the distance between the top of the bundle and the free surface, as well as the total power input. For large values of H, the width of the emerging plume actually decreased just above the bundle followed by a steady increase until reaching the high voidage layer at the free surface. However, for low values of H, the plume width increased steadily towards the free surface. Figure 2 shows a sketch of the observed flow patterns. For the same pool shallowness, however, increasing the power input resulted in the increase of the vapor rise and liquid recirculation velocities as well as the thickness of the high-voidage frothy layer at the free surface.

The aforementioned qualitative description of the flow patterns was supported by measured void fraction profiles obtained from the transmitted gamma flux measurements. The vertical void fraction profiles in the central plane of the boiling vessel were obtained. The results are thus representative of a long bundle. Only void profiles for the 3×3 and 9×3 bundles are presented here. Typical results are shown in Figs. 3 and 4, respectively. Results for the other geometries used can be found in [11]. Plotted in the figures are the distribution of the cross-section averaged void fraction across the vessel from the bottom of the bundle to the liquid free surface at different bundle total power input. The broken lines represent the void profiles within the bundle which were obtained by measurements between tube rows.

For the smaller bundle (Fig. 3), the void fraction decreased slightly at the top of the bundle. Since there is no condensation in the liquid bulk, a drop in local void fraction means an increase in vapor velocity when it emerges from the bundle, i.e., the vapor accelerates as it moves into a more open area. Above the bundle, the void fraction increased as the vapor rose up indicating lateral dispersion of vapor in the pool. This trend is similar to the single-tube case [11]. At higher bundle powers (>10.5 kW), however, the void profile exhibited two local minima: one close to the bundle and the other near the free surface, suggesting a complicated recirculation pattern. For the 27 tube bundle (Fig. 4), however, the void fraction increased fairly uniformly throughout the bundle and increased very rapidly toward the free surface. No decrease in void fraction near the top of the bundle was observed in this case.

These observations can be explained in terms of the free surface and pool shallowness effects. At the free surface, if the total interfacial area of the bubbles reaching the surface, at any time, is greater than the free liquid surface area (corresponding to the vapor flow area), a blockage is created. Accordingly, the rising vapor is forced to disperse laterally to generate additional space for the escaping vapor, and a high void layer is thus formed. This layer of bubbles becomes thicker for higher vapor generation rates, i.e., higher heat flux, corresponding to turbulent-churn flow. The hydrodynamic behavior of the rising vapor bubbles are also affected by the pool shallowness H. For the small bundle (Fig. 3) the vapor velocity through the bundle was generally low (vapor was generated across the entire bundle width). As the vapor emerged from the bundle it accelerated trying to reach

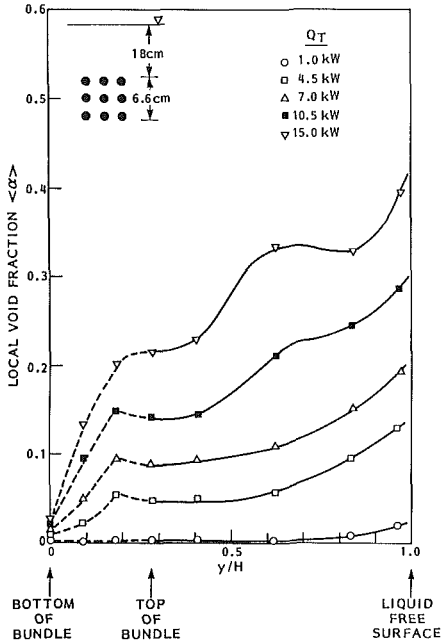

Fig. 3 Void distribution data: 3 × 3 bundle

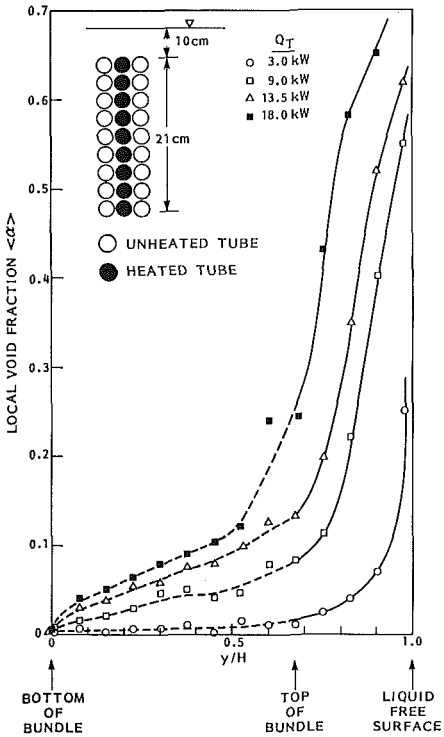

Fig. 4 Void distribution data: 3 × 9 bundle

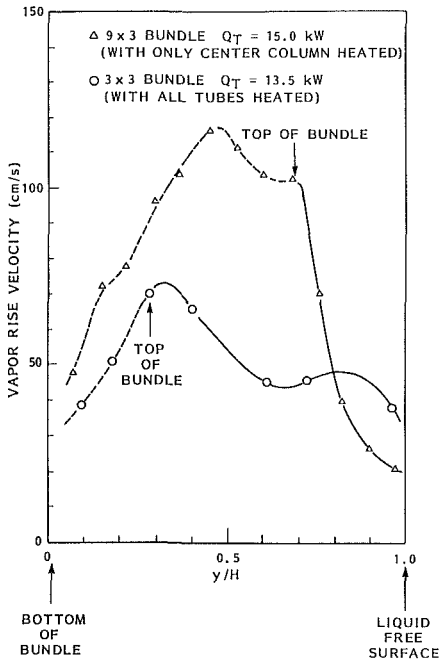

Fig. 5 Vapor rise velocities

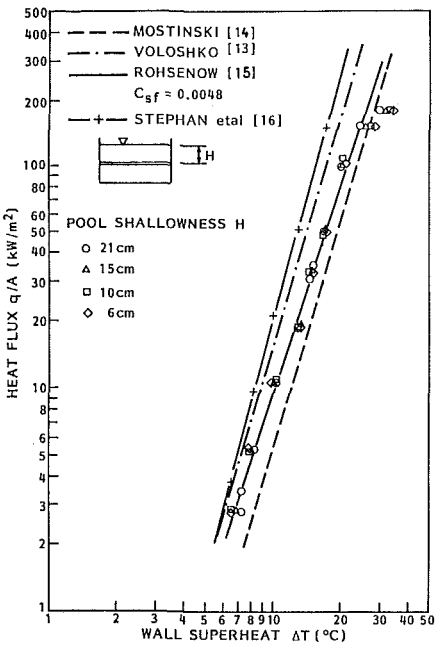

Fig. 6 Pool boiling on a single horizontal tube

its terminal velocity, resulting in a drop in void fraction. However, as it approached the free surface the vapor dispersed into the high void region. For the large bundle (Fig. 4), the vapor rise velocity within the bundle was generally high (because only the central column was heated). Since in this case H was low, the vapor was influenced by the free surface effect as it emerged from the bundle resulting in the rapid increase in void fraction. The effect of pool shallowness was systematically investigated earlier for a 3×1 bundle [12]. It was found that for the same vapor generation rate, the local void fraction increased, i.e., vapor rise velocity decreased, as H decreased.

The average void fraction or vapor holdup in the vessel, obtained by integrating the void distribution curves, was found

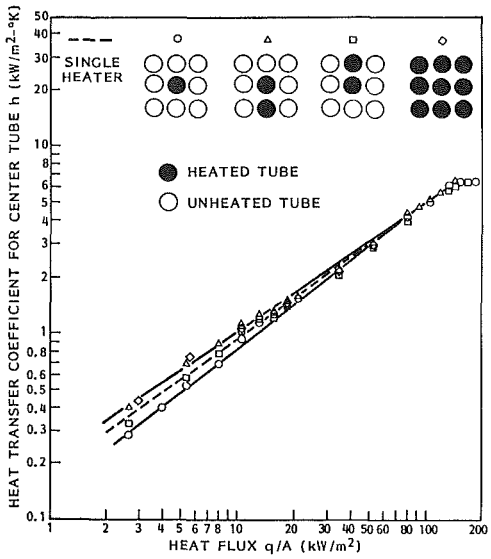

Fig. 7 Bundle effects on the boiling characteristics

to increase linearly with total bundle power and to be insensitive to the power distribution in the bundle [11].

3.1.2 Vapor Rise Velocity. As discussed previously, in order to apply mechanistic models to analyze reboiler performance, it is necessary to know the local mass flux and velocities in the bundle. In the present study, the average vapor velocity was determined experimentally using the void fraction measurements. Assuming the flow in the vessel to be essentially one dimensional with vapor rising in the central region, while single-phase liquid flowing downward along the walls, and since bubble entrainment in the downward liquid flow was negligible, it can be shown by vapor continuity that

$$V_g = \frac{Q_e}{\rho_g \Delta h_{fg} A_s} \frac{1}{<\alpha>} \tag{4}$$

where Q_e is the effective power input, ρ_g is the vapor density, Δh_{fg} is the heat of vaporization, A_s is the cross-sectional area of the vessel, and $<\alpha>$ is the measured cross-sectional average void fraction. Equation (4) thus gives the average vapor rise velocity in the two-phase region.

The variations of V_g in the vertical direction are readily obtainable from the void distribution data (Figs. 3 and 4). Typical results for uniformly heated bundles are shown in Fig. 5. It can be seen that V_g increases as vapor rises in the bundle. For the 3×3 bundle, V_g achieves a maximum just above the top of the bundle, whereas for the 9×3 bundle V_g peaks below the top of the bundle. Above the bundle, V_g tends to decrease rapidly toward the free liquid surface, especially for the larger bundle. It should be noted that vapor rise velocity can be viewed as a summation of two components; one related to the vapor terminal rise velocity (buoyancy) and the other related to flow recirculation in the pool.

3.2 Heat Transfer Characteristics. It is widely recognized that the boiling characteristics of a tube bundle are very different from that of a single tube. The heat transfer coefficient at the bottom of the bundle is similar to that obtained for a single tube [3]. The coefficient at the top of the bundle, however, was found to be significantly higher due to the additional circulation and turbulence caused by bubbles rising from the lower tubes in the bundle [7–9]. The local heat transfer coefficient can be expressed in a form similar to equation (1) if the local convective component can be properly taken into account.

In order to estimate the relative importance of the convective component in the bundle heat transfer coefficient to

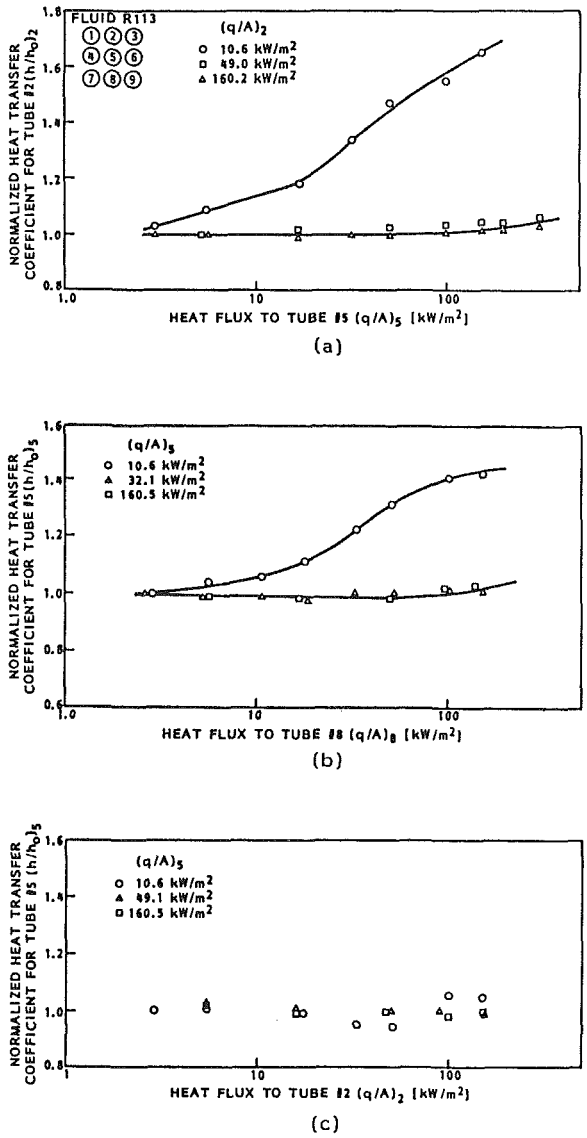

Fig. 8 Effect of boiling on neighboring tubes

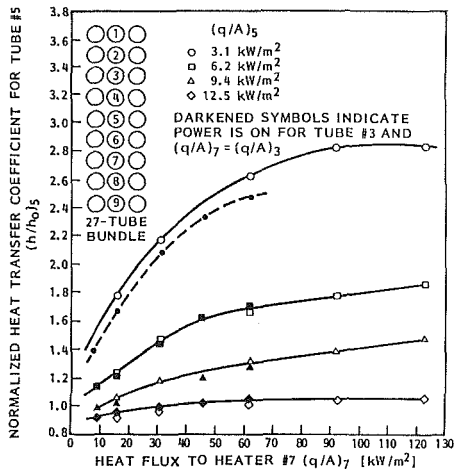

Fig. 9 Effect of boiling on neighboring tubes

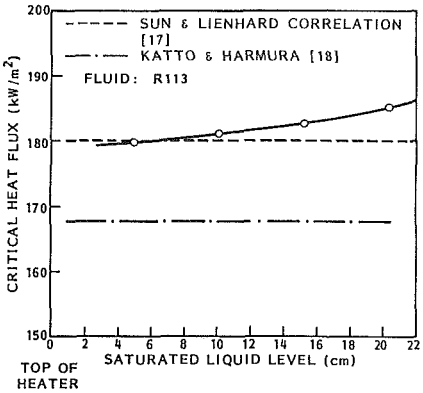

Fig. 10 Critical heat flux for single tube

nucleate boiling, heat transfer data were obtained in the present study for different bundle sizes and under different boiling conditions. This will be described below.

The average heat transfer coefficient for each tube was calculated here from the temperature measurements using

$$\bar{h} = (q/A)/(\bar{T}_w - T_{\text{sat}}) \tag{5}$$

where $\bar{T}_w$ is the average circumferential surface temperature of the tube.

3.2.1 Single Tube. This is the limiting case of a bundle. It was included in the present study for two reasons: (*i*) to compare with the predictions of various known correlations so as to establish the validity of the data obtained, and (*ii*) to provide a reference with which results from other bundle arrangements can be directly compared. Since the mode of heat transfer for a single tube is essentially nucleate pool boiling, the relative importance of the two-phase convective heat transfer for larger bundles can thus be assessed.

Four widely used correlations [13–16] were used for comparison with the R113 data obtained in the present experiment. They are shown in Fig. 6. It can be seen that very good comparisons were obtained. In general, the data lie within the prediction of these correlations and is best fitted by Rohsenow's correlation [15] with $C_{sf} = 0.0048$.

The effect of pool shallowness on single-tube heat transfer is also shown in Fig. 6. Four different values were used. It can be seen that the effect of pool depth is small except at high heat fluxes. In the high-heat-flux region, the wall superheat increases and hence the heat transfer coefficient decreases with increasing pool shallowness for a given heat flux. This is because the magnitude of the recirculation flow in the pool tends to be weaker for shallower pools.

3.2.2 Tube Bundle. The tube bundle effect on the boiling characteristics of individual heater tube(s) is discussed below. The results for the 3×3 bundle are shown in Fig. 7 in which the heat transfer coefficient for the center heater is plotted for different configurations. The single-tube data are also shown for comparison. From the figure, it is obvious that the bundle effects are limited to the lower heat flux region. At higher heat fluxes the data merge together forming almost a single relationship between the heat transfer coefficient and heat flux.

At lower heat flux, the data clearly show a reduction in the heat transfer coefficient of the center tube when surrounded by an unheated tube bundle. However, the heat transfer coefficient of the center tube was enhanced as compared to the single-tube case when either the whole bundle or only the tube below the center one was heated. Heating the tube above the center one resulted in a moderate increase in the heat transfer coefficient of the center tube as compared to the case when it was surrounded by an unheated bundle.

These observations can be explained in terms of the basic mechanisms governing the boiling process. As discussed previously, the tube bundle is actually operating under the combined effect of nucleate and two-phase convective boiling

with the relative importance of each component varying as a function of heat flux and location in the bundle. It is obvious that the convective contribution is highest near the top of the bundle due to increased velocities and flow acceleration caused by the increasing vapor flow. It is accordingly believed that the observed enhancement of the boiling heat transfer of the center tube in the bundle is caused by the increase of convective contribution due to boiling on surrounding tubes. Boiling on the tubes below resulted in the maximum enhancement since it corresponds to the maximum flow velocity at the center tube. It is thus evident that the two-phase convective effects are only significant at lower heat fluxes, while at higher heat fluxes nucleate boiling is the dominant mode of heat transfer. This is in agreement with the findings reported in [2, 7].

The effect of boiling on neighboring tubes was also investigated systematically. In these tests, the heat flux to the tube of interest was maintained at a constant value while the heat flux to another tube in the bundle was varied. The resulting heat transfer coefficient, normalized by that of a single tube, was plotted as a function of the heat flux to the neighboring tube. Figure 8 shows the results obtained for the nine-tube bundle case. It is shown that for low heat flux to the tube of interest, boiling on the tubes below increased its heat transfer coefficient. However, the same figures show that for high heat flux to the tube of interest, the heat transfer coefficient is equal to that of a single tube and independent of the boiling on the tubes below. These observations, again, confirm that at high heat flux nucleate boiling is the dominant heat transfer mechanism while convective effects are only important at low heat fluxes. Physically, it may be said that at high heat fluxes, the vapor produced by the tube tends to shield it from external influences. Figure 8(*c*), on the other hand, shows that the heat transfer coefficient of a tube in a bundle is not affected by boiling around tubes above it.

The effect of boiling on neighboring tubes was further investigated using the 9×3 bundle. The heated tubes are designated as shown in Fig. 9. Again, the heat flux to the tube of interest was fixed and the heat flux to one or more tubes in the bundle was varied. Figure 9 shows the results obtained on the effect of boiling on tube No. 7 (two rows below the tube of interest) on the behavior of the center tube at relatively low heat fluxes. As shown, the enhancement of the heat transfer coefficient above that of a single tube increased with increasing heat flux to tube No. 7. The degree of enhancement also increased with decreasing heat flux to the center tube. The level of enhancement was not generally changed by simultaneous boiling on tube No. 3 (two rows above the tube of interest). This confirmed that it is the rising two-phase mixture (i.e., convective effect) that causes the enhancement. Also, at the higher heat flux used (12.5 kW/m^2) the heat transfer coefficient remained basically constant as the nucleate boiling effect dominated the convective effect.

Similar results were obtained for other tubes in the bundle. In general, the enhancement in heat transfer rate due to boiling on a tube below the tube of interest decreases as we go further down the bundle and the effect of convective boiling decreases at higher heat flux to the tube of interest [11].

3.3 Critical Heat Flux (CHF). The critical heat flux marks the upper limit of nucleate boiling on a heat transfer surface. It is characterized by a sharp reduction in the local heat transfer coefficient due to the change in heat transfer mode from nucleate boiling to transition or film boiling. For a heat flux-controlled heating surface, a rapid rise in surface temperature results when CHF is reached.

Critical heat flux data were obtained in the present study for a single tube and for individual tubes in the 3×3 bundle. Although data and correlations existed for CHF on a single tube, there is a complete lack of both for tube bundles. Only

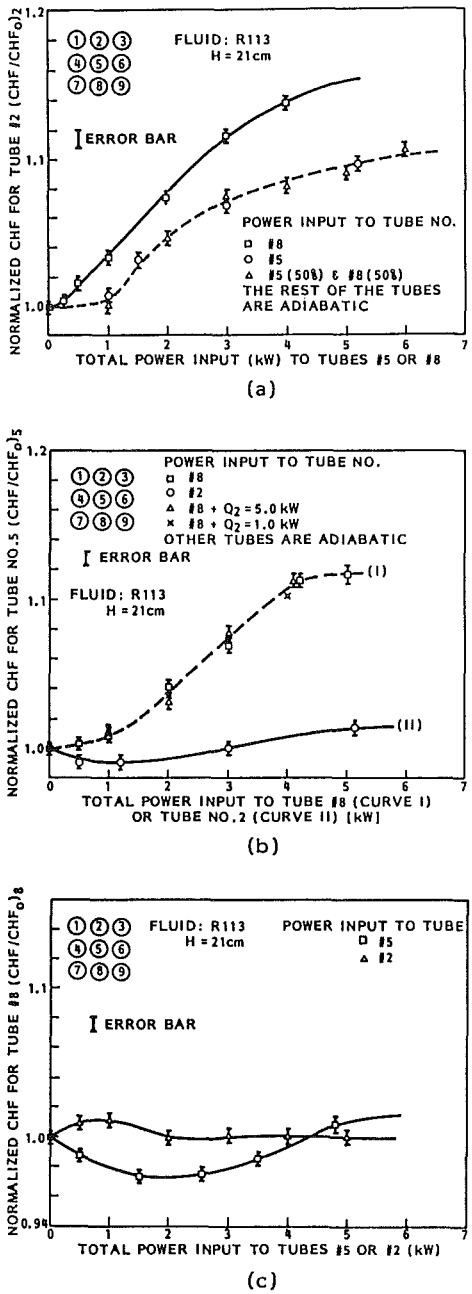

Fig. 11 Effect of neighboring tubes on the CHF of individual tubes

[6] refers to some proprietary data obtained by HTRI for large-scale reboilers. Inaccurate CHF prediction can result in either grossly overdesigned exchangers (i.e., larger than needed surface area) or inoperable heat exchangers.

3.3.1 Single-Tube CHF Results. The single-tube CHF data were obtained here for the same reasons as in the heat transfer characteristics studies. Results are compared with two well-known correlations: the Sun and Leinhard correlation [17] and the Katto and Harmura model [18]. They are shown in Fig. 12. It can be seen that the data agree reasonably well with the correlations and are better predicted by the Sun and Leinhard model. The effect of pool shallowness was also investigated in the present experiment. It was found that the CHF increased slightly as H was increased.

3.3.2 Tube Bundle. Experiments were conducted to obtain the critical heat flux values for the nine-tube (3×3) rec-

tangular bundle. It was found that the CHF for the bundle was reduced to about 168 kW/m^2, as compared to 185 kW/m^2 for a single tube, and it occurred first at the center bottom tube (i.e., tube No. 8).

It is generally believed that in approaching the CHF condition for a tube bundle, two mechanisms are competing and causing its behavior to significantly differ from the single tube case: (*i*) two-phase convection caused by boiling around all tubes and the associated recirculation which may result in CHF enhancement: and (*ii*) increased flow resistance and less space for vapor escape which prevent the liquid from reaching the inner tubes to replenish the boiling process. It is obvious that the lower tubes in the bundle suffer from the second mechanism resulting in premature CHF. On the other hand, strong convective effects are experienced by the upper tubes due to rising vapor which tends to enhance the corresponding CHF, should they be allowed to reach that level of heat flux without the failure of the lower tubes.

Although the lower CHF in the lower part of the bundle represents, in most cases, the limiting factor in heat exchanger design and operation, the enhancement of CHF in the upper part of the bundle is of interest in some practical applications. In very large tube bundle arrangements, large pressure (hydrostatic) and temperature (due to buoyancy effects) gradients may exist with high subcooling and pressure at the bottom of the bundle. Applying existing correlations on different tubes may show that the limiting criterion would be the occurrence of CHF on the upper tubes rather than the bottom ones. Accordingly, quantitative understanding of the basic mechanisms of tube bundle CHF is of great importance in the design of more efficient heat exchangers. Therefore, relevant data were obtained for the 3×3 bundle and are shown in Fig. 11. In these experiments, the critical heat flux was determined for a specific tube in the bundle. CHF enhancement or deterioration to boiling on chosen neighboring tubes was systematically investigated while the other tubes were kept unheated. In Fig. 11, the normalized CHF is the ratio of the measured CHF to that of the same tube with the rest of the bundle unheated and *not* that of a single tube. Figure 11(*a*) shows the CHF enhancement for the upper middle tube (No. 2) due to heat addition to other tubes in the same column. It was interesting to note that boiling on the bottom middle tube (No. 8) was more effective in enhancing CHF for tube No. 2 than that on the tube immediately below (No. 5). This is believed to be due to boiling around the tube immediately below limiting the vapor escape from the tube above and thereby reducing the effect of the convective currents on the CHF. Similar trends are shown in Fig. 11(*b*), where CHF on the center tube (No. 5) is given as a function of power input to the tubes immediately below or above. Heat addition to the tube below resulted in CHF enhancement, while heat addition to the tube above (No. 2) tended to decrease the CHF somewhat. This decrease seemed to be less with increasing heat flux to tube No. 2, probably because of the agitation resulting from stronger boiling in tube No. 2, i.e., convective effect. Figure 11(*c*) shows the deterioration of CHF of the center bottom tube due to boiling around the tube immediately above, i.e., tube No. 5. Again, this deterioration seems to recover with increasing heat flux to the tube above, as shown in Fig. 11(*b*). Boiling around the top center tube (No. 2) had, in general, very little effect on the CHF of the bottom center tube which is two rows below.

The above results show that CHF at the bottom tubes is the limiting design criterion for a uniformly spaced tube bundle. However, the results suggest that in order to utilize the superior CHF characteristics of the upper tubes, tube spacings (pitch) at the lower part of the bundle can be increased in order to provide greater vapor escape passage and hence enhance the CHF of these lower tubes as well. In other words, a bundle with nonuniform tube spacing where large spacings are present at the bottom should have better CHF characteristics than uniformly spaced bundles.

4.0 Conclusions

Boiling characteristics of small multitube bundles of up to nine rows in a rectangular vessel have been investigated experimentally. A large quantity of experimental data has been acquired for the study of system hydrodynamics, bundle heat transfer coefficients, and bundle critical heat flux. From the results obtained, the following important observations and conclusions can be drawn.

4.1 Hydrodynamics. Complicated flow patterns exist around and within a heated tube bundle. Strong liquid recirculation flow occurs around, and high-quality two-phase mixture rises through, the bundle. The local vapor rise velocity varied vertically depending on the vapor dispersion characteristics of the system which is a function of the pool shallowness and vapor generation rate, i.e., bundle power. Lateral vapor dispersion in the pool implies that the local mass flux, i.e., mass flow rate/unit area, will vary vertically. This suggests that current modeling approaches assuming constant mass flux may be oversimplified.

The high void layer which exists just below the liquid free surface tends to reduce the vapor rise velocity or the vertical mass flux in the vessel. Its existence and effects thus have to be properly modeled.

4.2 Heat Transfer Characteristics. The relative importance of the two major heat transfer mechanisms contributing to the boiling process in a multitube bundle has been identified. At low boiling heat flux, the heat transfer process is strongly influenced by the two-phase convection effects, resulting in higher heat transfer coefficients at the upper parts of the bundle as compared with the single-tube case. This is accompanied by a slight reduction in heat transfer coefficients at the bottom of the bundle due to increased resistance for the vapor to escape. On the other hand, at higher heat fluxes, the dominant mode of heat transfer appears to be nucleate boiling. Bundle effects were found to be insignificant and the bundle behavior tends to approach that of a single tube.

The convective effect on a particular tube due to boiling from a tube below appears to decrease when the latter tube is further away from the tube of interest.

4.3 Critical Heat Flux. The bundle critical heat flux was reduced by about 10 percent for the 3×3 bundle as compared to the single-tube case, and it occurred at the bottom center tube.

The presence of, and boiling in, the bundle increase the flow resistance for vapor escape and hence reduce the CHF at the bottom of the bundle. Rising vapor and two-phase mixture from the lower part of the bundle, on the other hand, tend to induce higher turbulence and break up the vapor blanket around upper tubes, resulting in CHF enhancements of up to 15 percent in the upper tubes.

References

1 Fair, J. R., "Vapourizer and Reboiler Design, Part I," *Chemical Engineering*, Vol. 70, 1963, pp. 119–124.

2 Nakajima, K. I., "Boiling Heat Transfer Outside Horizontal Multitube Bundles," *Heat Transfer – Japanese Research*, Vol. 7, 1978, pp. 1–24.

3 Brisbane, T. W. C., Grant, I. D. R., and Whalley, P. B., "A Prediction Method for Kettle Reboiler Performance," ASME/AIChE National Heat Transfer Conference, Orlando, FL, 1980, Paper No. 80-HT-42.

4 Whalley, P. B., and Butterworth, "A Simple Method for Calculating the Recirculating Flow in Vertical Thermosyphon and Kettle Reboilers," in: *Heat Exchanger for Two-Phase Applications*, J. B. Kitto, Jr. and J. M. Robertson, eds., 21st National Heat Transfer Conference, Seattle, WA, 1983, pp. 47–53.

5 Palen, J. W., and Yang, C. C., "Circulation Boiling Model for Analysis

of Kettle and Internal Reboiler Performance," in: *Heat Exchanger for Two-Phase Applications*, J. B. Kitto, Jr. and J. M. Robertson, eds., 21st National Heat Transfer Conference, Seattle, WA, 1983, pp. 55–61.

6 Palen, J. W., Yarden, A., and Taborek, J., "Characteristics of Boiling Outside Large-Scale Horizontal Multitube Bundles," *AIChE Symposium Series*, Vol. 68, 1972, pp. 50–61.

7 Grant, I. D. R., Cotchin, C. D., and Henry, A. R., "Tests on a Small Kettle Reboiler," *Heat Transfer for Two-Phase Applications*, J. B. Kitto, Jr. and J. M. Robertson, eds., 21st National Heat Transfer Conference, Seattle, WA, 1983, pp. 41–45.

8 Leong, L. S., and Cornwell, K., "Heat Transfer Coefficients in a Reboiler Tube Bundle," *Chemical Engineer*, No. 343, 1979, pp. 219–221.

9 Cornwell, K., Duffin, N. W., and Schuller, R. B., "An Experimental Study of the Effects of Fluid Flow on Boiling Within a Kettle Reboiler Tube Bundle," ASME-AIChE National Heat Transfer Conference, Orlando, FL, 1980, Paper No. 80-HT-45.

10 Chan, A. M. C., and Banerjee, S., "Design Aspects of Gamma Densitometer for Void Fraction Measurements in Small Scale Two-Phase Flow," *Nuclear Instruments and Methods*, Vol. 190, 1981, pp. 135–148.

11 Chan, A. M. S., and Shoukri, M., "Boiing Characteristics on the Outside of Small Horizontal Tube Bundles," Ontario Hydro Research Division Report No. 84-373-K, 1985.

12 Revankar, S. T., "Study of Void Fraction and Heat Transfer in Nucleate Pool Boiling," M. Eng. Thesis, McMaster University, 1982.

13 Voloshko, A. A., "Free Convectional Boiling of Freons," *Heat Transfer–Soviet Research*, Vol. 4, No. 4, 1972, pp. 60–66.

14 Mostinski, I. L., "Application of the Rule of Corresponding States for the Calculation of Heat Transfer and Critical Heat Flux," *Teploenergetika*, Vol. 4, 1963, p. 66.

15 Rohsenow, W. M., "A Method of Correlating Heat Transfer Data for Surface Boiling Liquids," *Trans. ASME*, Vol. 74, 1952, pp. 969–975.

16 Stephan, K., and Abdelsalam, M., "Heat Transfer Correlations for Natural Convection Boiling," *Int. J. Heat and Mass Transfer*, Vol. 23, 1980, pp. 73–88.

17 Leinhard, J. H., and Dhir, V. K., "Hydrodynamic Prediction of Peak Pool Boiling Heat Fluxes from Finite Bodies," ASME JOURNAL OF HEAT TRANSFER, Vol. 95, 1973, pp. 152–158.

18 Katto, Y., and Hamura, Y., "Critical Heat Flux on Uniformly Heated Horizontal Cylinder in an Upward Cross Flow of Saturated Liquid," *Int. J. Heat and Mass Transfer*, Vol. 26, 1983, pp. 119–125.

S. Tieszen[1]
Assoc. Mem. ASME

H. Merte, Jr.
Mem. ASME

V. S. Arpaci
Mem. ASME

The University of Michigan,
Ann Arbor, MI

S. Selamoglu
Middle East Technical University,
Ankara, Turkey

Crevice Boiling in Steam Generators

Experimental results are presented on the influence of confinement (normal to heated surface) on nucleate boiling in forced flow. The forced flow conditions and confinement geometry studied are similar to those found for boiling between a primary-fluid tube and a tube-support plate in steam generators of pressurized-water-reactor nuclear power plants. Visual observations of the boiling process within the confined region (crevice) between the tube and its support plate, obtained by high-speed photography, are related to simultaneous two-dimensional temperature maps of the hot primary-fluid-tube surface. The results demonstrate the existence of three confinement-dependent boiling regimes in forced flow conditions that are similar to those found in pool boiling conditions. These regimes are shown to be associated with the Weber number.

Introduction

Confinement normal to a heated surface occurs in two-phase process equipment wherever the heated surface (such as an electrical heater, heat exchange tube, etc.) is mounted so that fluid has access to a gap or crevice formed between the heated surface and any adjacent surface. The study presented here focuses on steam generators in pressurized-water-reactor (PWR) nuclear power plants, where hot pressurized water flows inside a bundle of so-called primary-fluid tubes. Water flowing around these tubes at a lower pressure results in the two-phase secondary-fluid flow. The primary-fluid tubes are supported within the secondary flow by steel tube-support plates, so that the two-phase secondary fluid can flow in small crevices between the tube-support plates and the primary-fluid tubes.

The effect of the confinement on nucleate boiling has been studied in flow boiling conditions [1, 2] and in pool boiling conditions [3–5]. The flow boiling studies, including the present study, were motivated by corrosion problems which occurred in steam generators. The corrosion problems were postulated to be a result of chemical concentration leading to precipitation in the crevices formed between the primary-fluid tubes and their support plates [1]. The purpose of the current study is to examine, with measurements more detailed than heretofore made, the boiling process occurring in the crevices formed by the primary-fluid tubes and drilled-tube-support plates as shown in Fig.1. Various tube-support configurations have been investigated, and it has been concluded that the precipitation leading to significant deposition occurs in crevices of certain tube-support-plate geometries and orientations which give rise to high local wall superheats [1]. A visual study of the boiling process in the crevice for a fixed axial line contact between the tube and support plate has shown several heat flux dependent regimes [2].

Pool boiling studies have shown the existence of three regimes that are dependent on the degree of confinement normal to the heated surface. In relatively unconfined nucleate boiling, the bubbles grow more or less spherically and individually. This is termed the isolated bubble regime, as occurs in "normal" nucleate boiling. As the distance between the heated surface and the confining surface is reduced, a transition occurs and large cylindrical bubbles develop. This regime has been termed the coalesced bubble regime, and is characterized by high rates of heat transfer and high heat transfer coefficients. As the distance between the heated surface and confining surface is reduced even further, liquid is prevented from entering and dryout occurs. This regime is termed the liquid deficient or dryout regime and is characterized by low rates of heat transfer [3, 4]. A more recent study has shown that these pool boiling regimes depend on two dimensionless numbers, a Bond number and a ratio of bubble expansion time to bubble rise time [5].

The existence of these pool boiling reigmes has been observed in the present work in forced flow boiling. The objective of the work here is to relate the visual observations of the boiling process within the crevice, obtained by high-speed photography, to the simultaneous surface temperature maps for prototypical steam generator conditions where the degree of confinement can be varied. The configuration consists of a single primary-fluid tube and a drilled support plate, where the relative position between them is adjustable during operation.

Apparatus and Procedure

The experimental apparatus is designed around a "unit cell" geometry, i.e., a single primary-fluid tube and its associated (tube bundle averaged) secondary-flow area. The primary-fluid tube is a section of Inconel 600 tube 19.05 mm o.d. with 1.092 mm wall thickness. The secondary-flow area has dimensions 27 mm per side and is 42.2 cm long. The primary-tube support plate is 19.05 mm thick axially (Z direction in Fig. 1) by 27 mm per side (X and Y directions in Fig. 1),

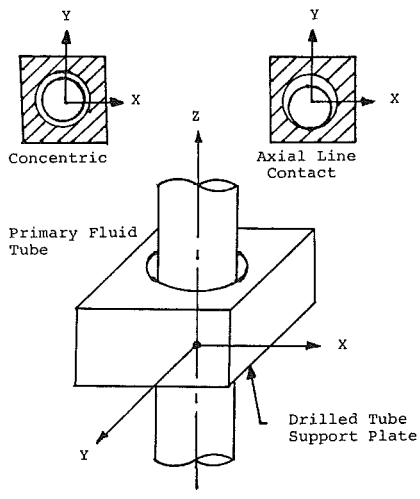

Fig. 1 Tube and unit cell tube support plate

[1]Presently at Sandia National Laboratories, Albuquerque, NM.

Contributed by the Heat Transfer Division and presented at the 22nd National Heat Transfer Conference, Niagara Falls, NY, August 1984. Manuscript received by the Heat Transfer Division December 10, 1984.

made of quartz to allow for high-speed photography. The hole in the support plate through which the primary tube passes is 21.08 mm in diameter, leaving a 2.03 mm diametral gap. The orientation of the support plate relative to the primary fluid tube can be varied under operating conditions by independent translation along the X, Y, and Z axes. Translation along the X or Y axis alters the orientation of the tube relative to the support plate from concentricity to line contact, while translation along the Z axis alters the position of the thermocouples embedded in the tube wall relative to the support plate. Measurements of positions are determined from micrometer devices in conjunction with the construction geometry. The uncertainty in the relative position of the tube and the support plate is $\pm$ 0.051 mm on an absolute basis and better than $\pm$ 0.025 mm on any two consecutive orientations at a given operating condition. The differences between these uncertainties arise because of thermal expansions in the system.

In addition to control of the orientation between the tube and tube support plate, the primary side heat flux, secondary side flow rate, subcooling, and pressure can be varied independently during a test. These variables are controlled by heaters, condensers, and pressurizers in the independent primary and secondary flow loops. A detailed description of the test apparatus is given in [6].

An upper limit of 1379 kPa (200 psi) is placed on the secondary pressure for safety reasons because of the quartz windows used for photography. Although typical steam generators secondary side pressures are on the order of 7000 kPa (1015 psi), the property changes between these levels are relatively small, compared with changes from near atmospheric pressure, and it can be anticipated that results obtained at this lower value will not differ significantly from those at actual operating levels. Other maximum independent variables in the present work are: heat flux $\leq$ 410,000 W/m^2, corresponding to a maximum 44.4°C temperature difference between the primary and secondary flows; secondary flow rate $\leq$ 0.303 kg/s, corresponding to a maximum mass flux of 682 kg/s-m^2; secondary quality $\leq$ 5 percent. The heat flux is controlled by varying the temperature of the primary-side flow, and computed from the measured flow rate and axial primary-fluid temperature changes at nine locations.

The measured dependent variables are: primary-tube wall temperature (24 transverse locations); secondary-fluid temperature (7 axial locations); axial secondary pressure drop (eight locations plus a reference), including the pressure drop across the support plate.

Primary-tube surface temperature "maps" are made from 24 thermocouples in the primary-tube wall that are equally spaced transversely (circumferentially) every 15 deg, with all except two being axially staggered over 19.05 mm. The remaining two thermocouples are mounted axially upstream and downstream of the location of the support plate to provide representative primary-tube surface temperatures uninfluenced by the support plate. By moving the support plate axially (Z direction in Fig. 1) relative to the fixed primary-fluid tube with all other variables held fixed, the primary-tube wall surface temperature map can be obtained for a given orientation. Fifteen axial movements of the support plate of 2.413 mm each produce a dense concentration of 330 temperature measurements in 33 cm^2 with representative up- and downstream surface temperatures.

All primary-tube thermocouples are the chromel-constantan grounded-tip type encased in 0.508 mm o.d. 304SS sheaths and are silver soldered into grooves 0.584 mm wide by 0.686 mm deep cut axially into the 1.092-mm-thick tube wall. Corrections factors to obtain surface temperatures from the measured embedded-thermocouple temperatures were determined for each thermocouple by calibrations under different levels of heat flux with the tube-support plate removed. The readings predicted by different embedded thermocouples fall within $\pm$ 1.7°C, and by the same thermocouple within $\pm$ 0.3°C [6].

Table 1 Test conditions for figures

Figures	Test condition	Value	Range*
High subcooling, near-atmospheric pressure test			
3, 4, 11	Sec. bulk subcool.	20°C	18.2–21.8
	Sec. pressure	152 KPa	149.6–154.4
	Sec. mass flow rate	522 kg/hr	519.8–523.5
	Sec. sat. temp.	111.8°C	111.3–112.3
	Ave. heat flux	203 kW/m^2	201.7–205.2
	Pressure drop	3.35 KPa	3.24–3.45
	Primary temp.	138.2°C	138.1–138.3
Low subcooling, high-pressure test			
5–9, 12–16	Sec. bulk subcool.	3°C	2.4–3.6
	Sec. pressure	1441 KPa	1421–1458
	Sec. mass flow rate	428 kg/hr	425.9–430.5
	Sec. sat. temp.	196.4°C	195.7–196.9
	Ave. heat flux	289 kW/m^2	281.4–294.4
	Pressure drop	3.58 KPa	3.38–3.72
	Primary temp.	226°C	225.6–226.3

*Denotes range of variation of test conditions for the noted figures.

Each test procedure begins by deionizing and deaerating the secondary water. Both primary and secondary flow loops are brought to the desired temperature and pressure and maintained at steady state. The orientation of the primary fluid tube is adjusted to be concentric with the tube-support plate, and the tube-support plate is then moved axially in 15 steps relative to the primary-fluid tube. At each step, the thermocouples, flow rates, and pressure drop across the support plate data are taken with a data acquisition system. During one of the steps, a high-speed 16-mm movie is taken at a rate of 5000 pictures per second. The orientation between the tube and the tube-support plate is then changed while operating conditions are maintained, and the entire process with 15 axial steps is repeated for the new orientation. By conducting a test with concentricity immediately prior to that for other orientations, a reference state is established such that the effects of the various crevice orientations on the surface temperature map can be determined directly, even with minor test-to-test differences and the uncertainties associated with surface temperature extrapolation from thermocouple measurements.

Results

The only orientations investigated to date are those with eccentricities between the tube and tube-support plate that vary from concentric to an axial line contact. The intermediate eccentric cases used were: 0.254 mm from line contact, 0.127 mm from line contact, 0.076 mm from line contact, and 0.025 mm from line contact. Table 1 contains the test conditions for the results presented here.

The two-dimensional tube surface temperature maps are presented in Figs. 3–9. The legend for the interpretation of the results is given in Fig. 2. The temperatures are presented in nondimensional form θ to eliminate the effect of minor differences in operating conditions for comparison purposes. The temperature θ is the difference between the tube surface temperature and the secondary saturation temperature, divided by the difference between the primary fluid temperature and the secondary saturation temperature. The X's shown upstream and downstream of the tube support plate are the locations of those particular thermocouples at the time the associated temperature measurements were made as the support plate was moved axially relative to the tube. With surface temperature distributions available, local heat transfer coefficients can be computed but are of limited value in the present discussion.

Character drawings were made from typical frames of the high speed photographs, and are presented in Figs. 11–15,

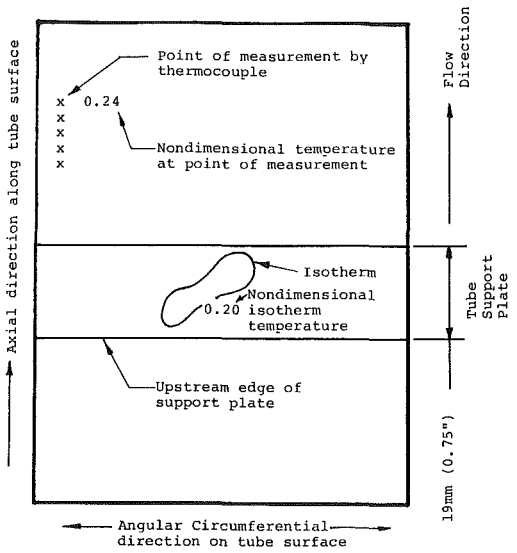

THETA=Nondimensional surface temperature

$$= \frac{\text{Tube Surface Temp.-Secondary Sat. Temp.}}{\text{Primary Temp.-Secondary Sat. Temp.}}$$

Fig. 2 Legend for interpretation of Figs. 3–9

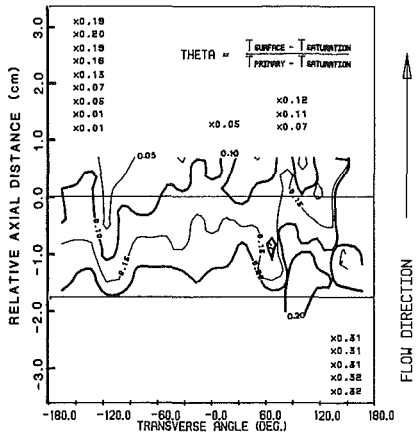

Fig. 3 Surface temperature map; tube centered; large subcooling, near-atmospheric pressure

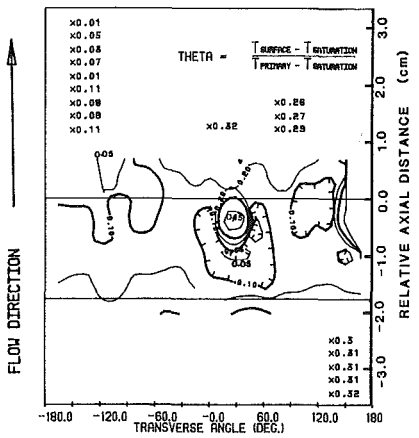

Fig. 4 Surface temperature map for character drawing in Fig. 11; line contact at 30 deg; large subcooling, near-atmospheric pressure

with the appropriate cross references to the temperature maps. The legend for the symbols used for the character drawings is given in Fig. 10.

Figure 3 shows the temperature map for the concentric case

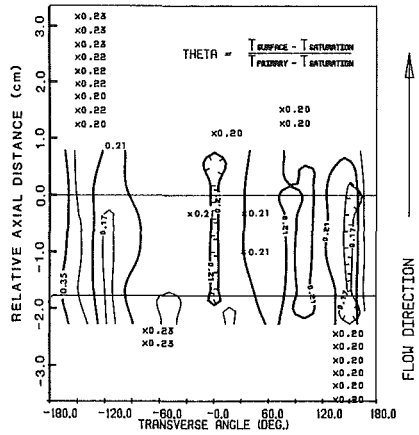

Fig. 5 Surface temperature map for character drawing in Fig. 12; tube centered; low subcooling, high-pressure

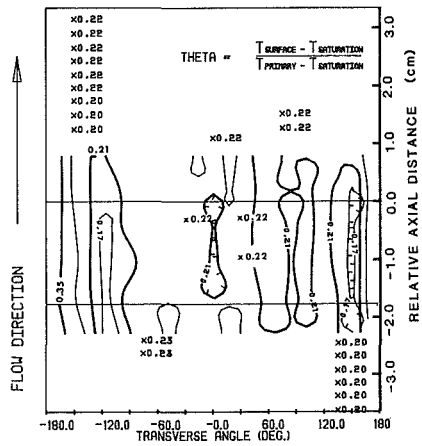

Fig. 6 Surface temperature map; tube and support 0.254 mm from line contact; low subcooling, high-pressure

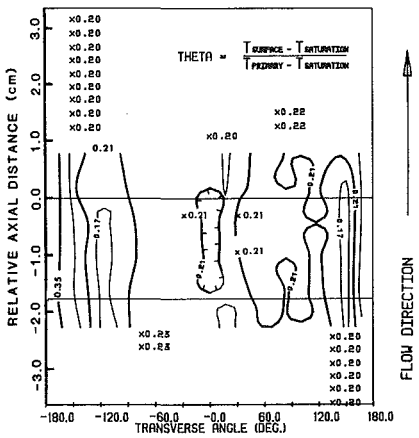

Fig. 7 Surface temperature map for character drawing in Fig. 13; tube and support 0.127 mm from line contact; low subcooling, high pressure

at near-atmospheric secondary pressure with large subcooling. Under ideal circumstances the isotherms should be parallel, perpendicular to the axial flow direction. That they are not is a manifestation of the disturbance of the local heat flux within the tube wall caused by the presence of the thermocouples embedded within the tube wall, or that the calibration procedure adopted to correct the temperature from the interior point where measured to the surface was insufficient. Most likely it is due to a combination of both. Each change of 0.01 in the dimensionless temperature in Figs. 3–9 amounts to an

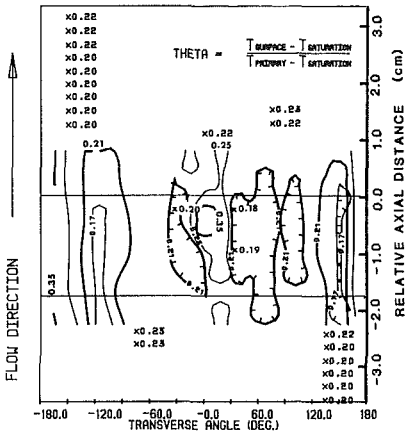

Fig. 8 Surface temperature map; tube and support 0.076 mm from line contact; low subcooling, high pressure

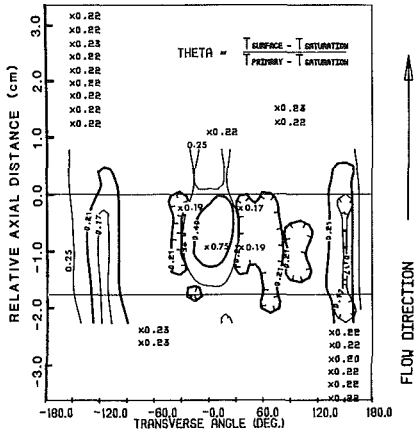

Fig. 9 Surface temperature map for character drawing in Fig. 15; line contact at 0 deg; low subcooling, high pressure

actual temperature change of about 0.28°C. The wall superheat changes from 9°C upstream of the support plate to almost 0°C downstream, with a subsequent recovery indicated. The large velocity within the crevice combines with the large subcooling to completely suppress the boiling process, as was also observed in the photographs for this case [6]. Indeed, using a mean temperature of 0.15 provides agreement within 10 percent of the heat transfer coefficient predicted for laminar flow in such a geometry [7].

Figure 4 shows the temperature map for the same conditions as in Fig. 3 except that line contact exists at a transverse angle of 30 deg. The temperature distribution within the crevice is similar to the concentric case except in the immediate vicinity of the line contact near the downstream edge, where severe temperature gradients are indicated. The maximum surface superheat is considerably above 14°C which, combined with the character drawing in Fig. 11, indicates that a dry spot exists in spite of large bulk subcooling, due to the confinement on the vicinity of the line contact. Another noteworthy difference in Fig. 4 from Fig. 3 is that the low downstream surface temperature, seen on the left side, persists to a greater degree, due to the jet action of the main flow being forced to the opposite side of the line contact.

Figure 5 shows the temperature map for the concentric case at high secondary pressure with low bulk subcooling. The fact that the isotherms are parallel to the tube axis, both within and outside the crevice, indicates that for the concentric case the confinement due to a gap of 1.01 mm has no effect on the boiling process, i.e., the surface superheats are not influenced by the presence of the support plate. Except for the isotherm on the left side of Fig. 5, the transverse variation of the surface temperatures is less than 1.7°C. The high isotherm on the left side is associated with a single thermocouple and is high (θ = 0 .35) for all cases witth low subcooling (Figs. 5–9). This behavior is assumed to be associated with some anomalous local nucleation behavior, and will be considered as a singularity. The corresponding character drawing made from the high-speed photographs is shown in Fig. 12, and indicates several vapor masses being ingested through the crevice from upstream. This periodic vapor ingestion appears to have no measurable effect on the boiling occurring in the crevice.

Beginning in Fig. 6, the support plate is moved to provide successively increasing eccentricity in Figs. 7 and 8 until a line contact at a transverse angle of 0 deg occurs, shown in Fig. 9. The operating conditions are the same for all of these orientations.

With a minimum gap of 0.127 mm, the only change noted in Fig. 7 over those in Figs. 5 and 6 is a widening on the isotherm labeled 0.21 that is centered around the 0 deg transverse angle. This isotherm surrounds an enclosed depression on surface temperature, indicating a local higher rate of heat transfer at 0 deg. The character drawing made from high-speed photographs which corresponds to Fig. 7 is shown in Fig. 13. This drawing shows rapid interfacial motion near the smallest gap at 0 deg, indicating that a transition in boiling regime has occurred. The interfacial motion indicates that drying and rewetting is occurring. The displacement of the liquid within the gap by the vapor results in the formation of a thin liquid film or microlayer. It is the evaporation of this thin film that produces the high local rate of heat transfer, and the temperature depression noted in Fig. 7.

As the minimum gap is decreased further to 0.076 mm in Fig. 8, a temperature peak occurs in the tube surface at 0 deg, indicating low rates of heat transfer, bounded transversely by temperature troughs, indicating high rates of heat transfer. The surface temperature peak indicates that another change in boiling regime has occurred at the minimum gap region. The temperature peak corresponds to a dry region. While a dry region was not noted in the high-speed photography for this gap, it was noted as the gap was reduced further to 0.025 mm at 0 deg as shown in Fig. 14.

Finally, as the gap was reduced to a line contact at 0 deg in Fig. 9, the temperature peak increases both in size and in level, indicating a further decrease in heat flux in this region. The character drawing in Fig. 15 from the high-speed photographs also shows a distinct dry spot, but not significantly different in size or character from the previous one, Fig. 14. Three boiling regimes are apparent in Figs. 9 and 15. In the smallest gap, dry areas with high surface temperatures of the dryout regime are surrounded by areas of rapid interfacial motion with large, almost continuous, vapor bubbles of the coalesced bubble regime. The coalesced bubble regime corresponds to the region of low surface temperature in Fig. 9, indicating high levels of heat flux. Surrounding the coalesced bubble regime is a region of bulk liquid in which nucleate boiling is occurring and where isolated bubble masses pass through from upstream.

The same three boiling regimes are also seen in the high subcooling, near-atmospheric pressure case with line contact between the tube and support plate, shown in Figs. 4 and 11. A high-surface-temperature region in Fig. 4 corresponds to a dry spot in Fig. 11, which is surrounded by a region of interfacial activity. In the high subcooling case the interface appears to be continuous and formed from a single nucleation site. This region is surrounded by liquid flow which is not boiling due to the high subcooling.

For the low subcooling case, Figs. 5–9, it is noted that in the isolated bubble regime in the wider gap region, the tube surface temperature changes very little as the orientation is changed successively from concentric to line contact, in-

dicating no change in behavior of the boiling process from gap heights ranging from 0.254 mm to 1 mm. Comparison of the up- and downstream surface temperatures to those in the gap shows that the boiling in the gap is little different than that outside the gap. This result indicates that normal nucleate boiling in an unconfined region changes very little with confinement until a distinct change in the boiling process takes place.

Reviewing Figs. 5–9 and 12–15, the transition from the isolated bubble regime to the coalesced bubble regime occurs somewhere between 0.127 mm and 0.254 mm for this low-subcooling, high-pressure condition. The transition to the dryout regime occurs between 0.025 mm and 0.076 mm.

Discussion

The visual observations of the boiling process within the crevice and the corresponding two-dimensional surface temperature maps show the existence of three boiling regimes, dependent primarily upon the degree of local confinement, perpendicular to the hot surface, of the vapor bubbles. These three regimes are similar to those found in pool boiling studies and shows that these boiling regimes exist for a broad range of boiling conditions.

In the pool boiling, where buoyancy drives the fluid motion in the gap, the gap height at which transition occurs from regular nucleate boiling to the coalesced bubble regime is related to the bubble departure diameter. The ratio between the gap height and bubble departure diameter has been expressed as a Bond number [5]. Similary, for the forced convective case, a ratio of the gap height and bubble departure diameter can be calculated. The bubble departure diameter can be estimated for the low subcooling conditions in Figs. 5–9 using a departure diameter correlation for forced convection [8]

$$D_d = 0.05\,(4\sigma dz/dP)^{1/2} \quad (1)$$

where dz/dP is the inverse of the frictional pressure drop and σ is the surface tension.

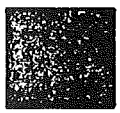

Bulk Liquid Region. This is a liquid region composed of the bulk flow. For subcooling less than nominally 5°C, the bulk liquid region adjacent to the primary fluid tube has small bubbles on the order of 0.1 mm dispersed throughout.

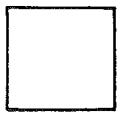

Vapor Region. The vapor region grows and collapses as bubbles are entrained in the axial flow. It cannot be determined from the films if there is a thin liquid film beneath the vapor.

Interfacial Region. This region is also a vapor region but contains vigorous interfacial activity from growing bubbles.

Non-Interfacial Region. This region is a vapor region where no interfacial activity is occurring. It cannot be determined from the high speed photographs whether or not this region is completely liquid deficient.

Liquid Segment Region. The region is a liquid region that has been separated from the bulk flow.

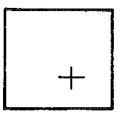

Nucleation Site. The cross marks a site where nucleation is clearly occurring in the high speed photographs.

Fig. 10 Legend for character drawings for Figs. 11–16 obtained from high-speed photographs

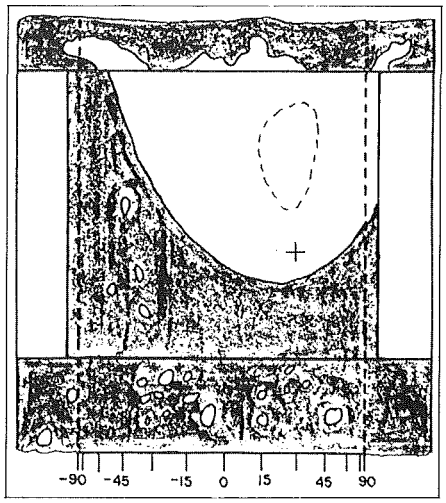

Fig. 11 Character drawing for temperature map in Fig. 4; line contact at 30 deg; large subcooling, near-atmospheric pressure

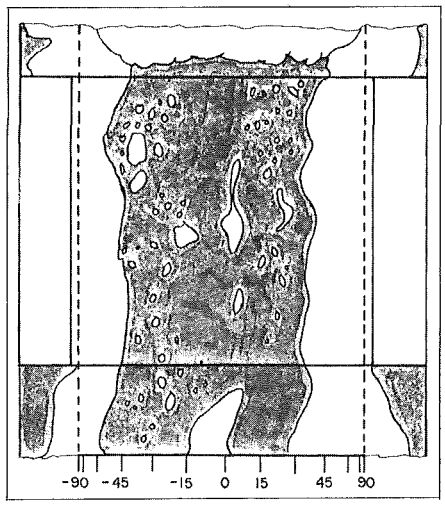

Fig. 12 Character drawing for temperature map in Fig. 5; tube centered; low subcooling, high pressure

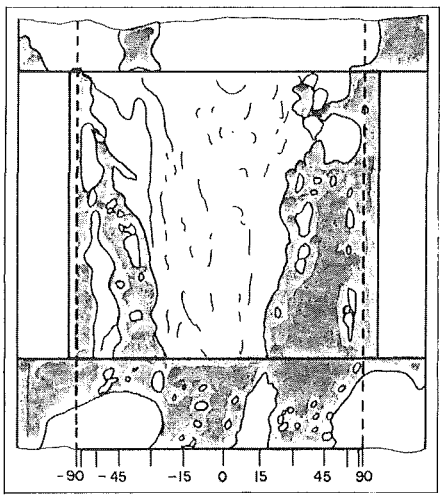

Fig. 13 Character drawing for temperature map in Fig. 7; tube and support 0.127 mm from line contact; low subcooling, high pressure

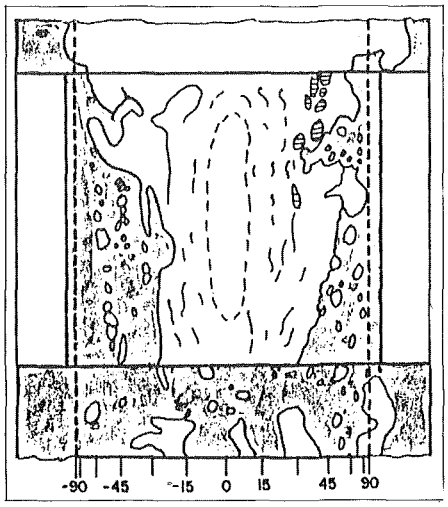

Fig. 14 Character drawing; tube and support 0.025 mm from line contact; low subcooling, high pressure

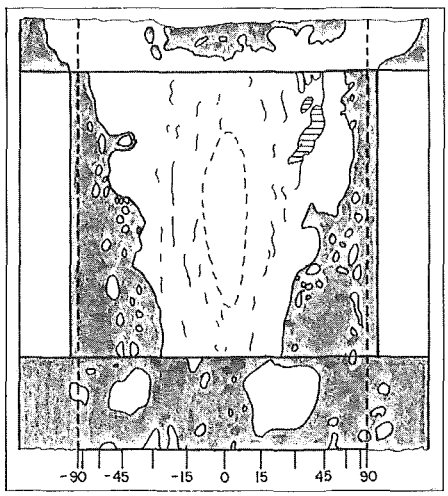

Fig. 15 Character drawing; for temperature map in Fig. 9; line contact at 0 deg; low subcooling, high pressure

Using an average measured pressure drop across the support plate of 1.5 kPa/cm gives a departure diameter of 0.015 mm. The ratio of the gap height at which transition occurs to the computed departure diameter is in the range of 9–18. This ratio would be expected to be on the order of 1, rather than 10, if the transition were related to the bubble departure diameter.

The discrepancy in the present case may be explained in terms of the approximations made in estimating the bubble departure diameter. The frictional pressure drop correlation, equation (1), used to calculate the departure diameter applies to an unconfined boiling case. Further, in the experiments shown in Figs. 5–9, the locations of the pressure measurements are 180 deg from the minimum gap where the transition to coalesced boiling is occurring. Two-dimensional effects associated with jetting action at the wide part of the asymmetric gap will produce significant local differences in the static pressure drop, with smaller values expected in the more confined portion of the gap. Smaller values of pressure drop give larger departure diameters, and hence a smaller ratio than computed above.

An alternative to describing the transition to the coalesced bubble regime as a ratio of characteristic length scales is to describe the transition as a ratio of characteristic forces. For pool boiling this ratio is the Bond number, i.e., the ratio between the buoyant force and the surface tension force. For

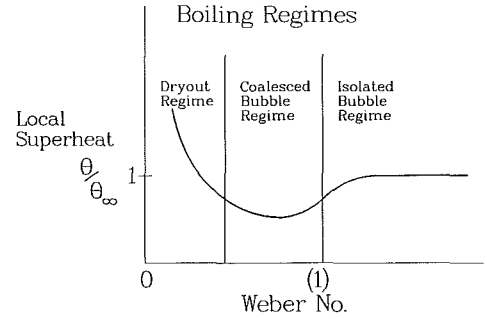

Fig. 16 Boiling regime dependence on the Weber number ($\rho V^2 H/\sigma$); note: θ/θ_∞ is the difference between the tube surface temperature and the secondary saturation temperature at a given gap height H divided by the same difference for an infinite gap height

flow boiling this ratio is the Weber number, i.e., the ratio of the inertial force to the surface tension force

$$\mathrm{We} = \frac{\rho V^2 H}{\sigma} \tag{2}$$

where ρ is the liquid density, σ is the surface tension, H is the gap height, and V is the liquid velocity.

As a first approximation the Weber number will be defined in terms of single-phase liquid values. The velocity is the local velocity corresponding to a given gap height. Local velocity measurements were not made in the present experiments, but a single-phase estimate of the average velocity is on the order of 2 m/s in the concentric gap corresponding to a single phase Reynolds number on the order of 13,000. The Weber number for these conditions is on the order of 100. Assuming that the velocity is roughly proportional to the gap height, the Weber number scales as the cube of the gap height. The transition from regular nucleate boiling to the coalesced bubble regime has been observed to occur with local gaps in the range between 1/4 and 1/8 the concentric gap height, giving a value of the Weber number for transition on the order of 1.

Because of the approximations required, it has not been demonstrated quantitatively that the transition to the coalesced bubble regime occurs at, or near, the bubble departure diameter. However, the data appear to support this postulate qualitatively. For the line contact case, the gap diameter varies continuously from 0 to 2 mm. The Weber number then extends from 0 to over 100 and is plotted in Fig. 16 as a function of the dimensionless local surface superheat, i.e., the difference between the tube surface temperature and the secondary saturation temperature at the local gap height, divided by the same difference at an infinite gap height.

The coalesced bubble regime has been observed to be associated with high rates of heat transfer and low wall superheats in both the present study and previous pool boiling studies. It was speculated in these latter works that thin film evaporation is the cause of the high heat transfer rates [4, 9]. The confined bubbles grow in a direction parallel to the heated surface due to perpendicular confinement, leading to large areas of thin film formation under the growing bubbles. Thin film formation and evaporation were not observed visually from the high-speed photographs in this study because the high contrast and resolution required were beyond the capabilities of the film with the restricted access available for lighting.

It appears that it is the repetitive wetting and complete evaporation of the thin films associated with the coalesced bubble regime that is responsible for the corrosion problems experienced in steam generators. A study conducted under prototypical steam generator conditions showed that the presence of dissolved solids in the secondary fluid resulted in large amounts of precipitation in the confined regions between

the primary-fluid tubes and support plates, compared to any deposition taking place outside the confined region [1]. Deposition occurs as a result of the formation and evaporation of these thin films, particularly near the dryout regime.

While the deposition study [1] did not include the ability to determine the characteristics of the boiling occurring in the confined area, the conditions of the present study were similar to those in the deposition study, except for the lower pressure (1.4 MPa versus 7 MPa) and did show the existence of the coalesced boiling regime. The possibility of enhanced deposition of dissolved solids which may lead to corrosion by the coalesced bubble regime is of concern because of the broad range of flow conditions in which the coalesced bubble regime has now been seen to exist.

Conclusions

Three confinement-dependent flow-boiling regimes exist in conditions similar to those found in PWR steam generators. These regimes have also been found in pool boiling studies and are termed the dryout regime, the coalesced bubble regime, and the isolated bubble regime. The isolated bubble regime is associated with a low degree of confinement perpendicular to the heated surface, and in the limit of no confinement becomes normal nucleate boiling. At higher degrees of confinement the coalesced boiling regime forms. The characteristics of the coalesced bubble regime are large coalesced or cylindrical-type bubbles with a relatively high local heat flux. At a still higher degree of confinement, a liquid deficiency or dyout occurs and results in a relatively low local heat flux. The degree of perpendicular confinement at which transition from the isolated bubble regime to the coalesced bubble regime occurs is related to the Bond number for pool boiling and is expressed in terms of the Weber number for flow boiling.

It is postulated that the corrosion problems experienced in PWR steam generators in the confined area between the primary-fluid tube and support plate may be a result of deposition of dissolved solids associated with the evaporation of large areas of thin liquid film in the coalesced bubble regime. It is believed that the coalesced bubble regime will exit over a broad range of flow boiling (and pool boiling) conditions as the perpendicular confinement approaches the bubble departure diameter in the fluid. It is important that the creation of confined regions be avoided in the design of two-phase equipment, where the confining dimensions are of the order of the bubble departure diameter for the expected conditions of use.

Acknowledgments

This work was supported by the Electric Power Research Institute.

References

1 Curlee, N. J., Jr., and Baum, A. J., "Single-Tube Thermal and Hydraulic Tube Support Test," Final Report, EPRI Research Project S118-1, NP-2046, Sept. 1981.

2 Bankoff, S. G., et al., "Boiling Heat Transfer in a Narrow Eccentric Annulus," Final Report, EPRI Research Project S133-1, NP-2610, Sept. 1982.

3 Ishibashi, E., and Nishikawa, K., "Saturated Boiling Heat Transfer in Narrow Spaces," *International Journal of Heat and Mass Transfer*, Vol. 12, 1969, pp. 863–894.

4 Katto, Y., and Yokoya, S., "Experimental Study of Nucleate Pool Boiling in Case of Making Interference-Plate Approach to the Heated Surface," *Proceedings of the Third International Heat Transfer Conference*, Vol. 3, 1966, pp. 219–227.

5 Yao, S., Chang, Y., "Pool Boiling Heat Transfer in a Confined Space," *International Journal of Heat and Mass Tranfer*, Vol. 26, 1983, pp. 841–848.

6 Merte, H., et al., "Boiling in Narrow Crevices in Steam Generators," Final Report EPRI Research Project S134-1, NP-2638, Nov. 1982.

7 Shah, R. K., and London, A. L., "Thermal Boundary Conditions and Some Solutions for Laminar Duct Flow Forced Convection," ASME JOURNAL OF HEAT TRANSFER, Vol. 96, 1974, pp. 159–165.

8 Levy, S., "Forced Convection Subcooled Boiling—Prediction of Vapor Volumetric Fraction," *International Journal of Heat and Mass Transfer*, Vol. 10, 1967, pp. 951–965.

9 Jensen, M. K., Cooper, P. E., and Bergles, A. E., "Boiling Heat Transfer and Dryout in Restrticted Annular Geometries," *AIChE Symposium Series*, No. 164, Vol. 73, 1974, pp. 205–514.

K. M. Holden

A. S. Wanniarachchi
Assoc. Mem. ASME

P. J. Marto
Fellow ASME

D. H. Boone

Department of Mechanical Engineering,
Naval Postgraduate School,
Monterey, CA 93943

J. W. Rose
Department of Mechanical Engineering,
Queen Mary College,
University of London,
London, United Kingdom

The Use of Organic Coatings to Promote Dropwise Condensation of Steam

Fourteen polymer coatings were evaluated for their ability to promote and sustain dropwise condensation of steam. Nine of the coatings employed a fluoropolymer as a major constituent; four employed hydrocarbons and one a silicone. Each coating was applied to 25-mm-square by approximately 1-mm-thick metal substrates of brass, copper, copper–nickel, and titanium. While exposed to steam at atmospheric pressure, each coating was visually evaluated for its ability to promote dropwise condensation. Observations were also conducted over a period of 22,000 hr. Hardness and adhesion tests were performed on selected specimens. On the basis of sustained performance, six coatings were selected for application to the outside of 19-mm-dia copper tubes in order to perform a heat transfer evaluation. These tubes were mounted horizontally in a separate apparatus through which steam flowed vertically downward. Steam-side heat transfer coefficients were inferred from overall measurements. Test results indicate that the steam-side heat transfer coefficient can be increased by a factor of five to eight through the use of polymer coatings to promote dropwise condensation.

Introduction

For almost 50 years, it has been known that dropwise condensation can produce heat transfer coefficients up to 20 times those of filmwise condensation. This marked increase is attributed to the process of drop formation and removal from the condenser surface. Unfortunately, filmwise condensation is the normal, stable mode of condensation on virtually all condenser materials. Therefore, in order to take advantage of dropwise condensation, steps must be taken to promote the dropwise mode.

Dropwise condensation can be promoted by: (1) applying a suitable chemical, such as oleic acid or montan wax, to the condenser surface, (2) injecting nonwetting chemicals into the vapor which are deposited on the condenser surface, and (3) using a low-surface-energy polymer or a noble-metal coating.

Both the first and second methods are limited in that neither produces a permanent hydrophobic coating. Results vary widely but usually the effectiveness of these promoters is measured in the hundreds of hours. The third method, the use of permanent coatings, has been the subject of considerable interest. Of the noble metals, only gold and silver have been shown consistently to produce excellent dropwise condensation [1, 2]. This would appear to contradict theory since the surface energy of noble metals is relatively high. Recent experiments have shown that a "clean" gold surface applied under carefully controlled conditions will spontaneously wet as predicted [3]. However, gold has the ability to attract and retain organics which render the surface hydrophobic. For this reason, gold is referred to as a "self-promoter." An extensive investigation by Woodruff and Westwater [1] concluded that the promotion of dropwise condensation of a gold-plated surface was directly related to the surface gold and carbon concentrations and inversely related to the copper, aluminum, and oxygen concentrations. O'Neill and Westwater [2] showed very similar results with silver-electroplated copper surfaces.

The second method of producing permanent dropwise condensation is to apply an organic polymer with a low surface energy to the condensing surface. Although many experiments have been conducted with this type of coating, virtually all of the research has been done using a fluorocarbon or silicone polymer. Fluorocarbon polymers exhibit the desirable characteristics of high thermal stability and very low surface energy and they are highly resistant to chemical attack. However, they also have a relatively low thermal conductivity, so that the maximum coating thickness which could be employed to produce an increase in the condensing heat-transfer coefficient would be about 20 μm. Coatings of greater thickness would impose a large thermal barrier to negate any benefit derived from altering the mode of condensation. The most common polymer which has been employed is PTFE (polytetrafluoroethylene), commonly referred to as Teflon.

In 1956, Smith [4] concluded that, when applied by utilizing the existing application techniques, thin PTFE coatings were not satisfactory for increasing overall heat transfer rates for Naval applications. In 1964, Fox [5] reported on tests conducted with a small condenser in which the tubes had been coated by PTFE to a thickness of 12.5 μm. Performance was not significantly improved. Shortly thereafter, the Navy suspended further studies into dropwise condensation. In 1966, Brown and Thomas [6] conducted experiments with tubes of Admiralty brass coated with 2.5 μm of PTFE. The outside heat transfer coefficient for dropwise condensation averaged approximately three times that of filmwise condensation. In 1969, Graham [7] also achieved a threefold increase using flat copper plates coated with a PTFE film estimated to be 1.5 μm thick. This represented the practical limit for the application of PTFE films using standard techniques. In 1979, both Manvel [8] and Perkins [9] used vacuum-deposition sputtering to apply ultrathin layers of PTFE. Although their thicknesses ranged from a minimum of 0.04 μm to a maximum of only 0.13 μm, their results were disappointing and unexpected. The dropwise appearance was good, but the steam-side heat transfer coefficient was increased by a maximum of only 1.6. This result was attributed to the presence of noncondensing gases. In addition, all of the coatings showed signs of physical deterioration after very short operating periods.

The use of silicones to promote dropwise condensation began in the 1950s and continued into the early 1960s. In 1959, Kullberg and Kendall [10] experimented with a commercially available, semipermanent silicone release agent, R-671. With a film thickness estimated to be 10 μm, an increase of 1.5 in the overall heat transfer coefficient was obtained. Preliminary en-

Contributed by the Heat Transfer Division and presented at the ASME Winter Annual Meeting, New Orleans, Louisiana, December 1984. Manuscript received by the Heat Transfer Division September 10, 1985.

durance tests indicated that the coating was capable of producing dropwise condensation for periods in excess of 1500 hr. A subsequent study conducted by the Westinghouse Corporation for the U.S. Navy investigated several organic compounds, including PTFE [5]. These tests produced only moderate increases in the overall heat transfer coefficient. Most importantly, all of the silicone coatings exhibited limited endurance. The best silicone compound had become 20 percent filmwise within 135 hours of operation. From these tests, it was concluded that PTFE was the only coating of the group that exhibited a life expectancy sufficient to warrant investigation.

In 1966, Erb and Thalen [11] conducted an extensive investigation of permanent hydrophobic coatings. Although they were primarily concerned with sulfide films and noble metals, they also investigated organic polymers. One of the polymers investigated was PTFE and another was a relatively new compound parylene-N developed by the Union Carbide Corporation. Parylene-N is a polymer of para-xylylene which can be vapor-deposited in very thin films. Unlike PTFE, parylene-N contains no fluorine and therefore would not be expected to be as hydrophobic as the fluoropolymers. However, a 1-μm thick film produced good dropwise condensation in excess of 2400 hr of continuous operation. The overall heat transfer coefficient was increased by a factor of approximately 1.5.

In the last 10-15 years, recent developments in techniques for the application of ultrathin coatings, in addition to the development of new organic compounds, have generated renewed interest in the use of organic polymers as dropwise promoters. Therefore, the overall purpose of this study was to evaluate the long-term endurance and thermal performance of various hydrophobic organic coatings and application techniques when exposed to steam.

Experimental Apparatus

Endurance Test Apparatus. Endurance tests were made by exposing prepared samples, which were mounted on a heat sink, to steam at atmospheric pressure. The heat sink was necessary to provide a thermal gradient of sufficient magnitude to induce vigorous condensation. Because the endurance tests were to run continuously for an indefinite period, a principal concern was to design and construct a facility which was simple, reliable, and could be left unattended for extended periods. The endurance apparatus, depicted in Fig. 1, consisted of three major components: (1) steam chamber, (2) heat sink, and (3) de-superheater. Complete details of this apparatus and its operation are given in [12].

The test specimens were mounted on a water-cooled, copper heat sink which was centered within the chamber. The heat sink was designed to hold 84, 25-mm-square specimens. The thickness of the specimens was nominally 0.76 mm or 1.5 mm depending upon the substrate material and coating system. A primary concern was the ability to hold the specimens tightly against the heat sink in order to minimize contact resistance. In order to accomplish this, four equi-spaced stainless-steel tracks, 3.2 mm by 4.7 mm, were fastened to each face of the heat sink with countersunk machine screws. The tracks were predrilled and tapped to receive stainless-steel clips which were held in place by set screws. The clips were designed to securely clamp each specimen against the heat transfer surface by the upper and lower edges.

Operation commenced by injecting steam into the bottom of the de-superheater (see Fig. 1) through a sparger tube. The amount of steam was controlled by a throttling valve. The steam passed through the de-superheater to the chamber, condensed on the heat sink and the condensate returned to the de-superheater. After approximately one hour, steady-state conditions prevailed in which the de-superheater was approximately one-third full of water and the return condensate was balanced by overflow from the de-superheater.

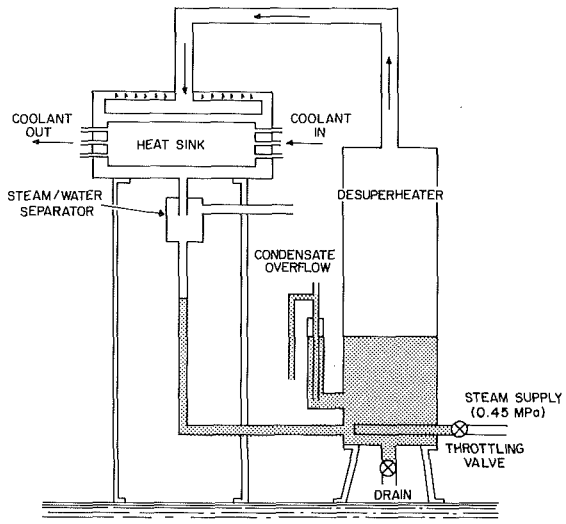

Fig. 1 Schematic of endurance test apparatus

Test Specimens. Four metals used in the construction of condensers were selected for use as test substrates: copper, brass (70 percent copper, 30 percent zinc), copper–nickel (90 percent copper, 10 percent nickel), and titanium. The copper, brass, and titanium specimens were 0.76 mm thick, while the copper–nickel was 1.52 mm. The sheets were sheared into 25-mm squares. Care was exercised to ensure that the shearing operation did not bend the specimens. Prior to surface preparation, the edges were lightly dressed with a file to remove slight burrs left by the shearing process.

Two surface finishes were used during this stage of testing. A "smooth" surface finish was produced by lapping the front face on a belt sander using 180-grit silicon carbide abrasive paper. This was followed by hand stroking the specimens on 400-grit followed by 600-grit abrasive paper mounted on a glass table. When changing grit, the specimen was rotated 90 deg and stroked in only one direction until the markings from the previous abrasive were removed. The specimen was then placed in an ultrasonic bath containing methanol for 15 min and then blown dry. For adhesion purposes, a mirrorlike finish was deemed undesirable. The procedure described was designed only to provide a uniform surface, free of gross irregularities.

A "rough" surface was prepared by grit blasting with size 40 glass beads with the air pressure set at 0.138 MPa. The surface roughness produced by this procedure was determined by means of a surface profilometer. Representative samples were found to have a surface roughness ranging from 0.76 to 1.3 μm rms. These specimens were also cleansed in the ultrasonic bath as previously described.

The surface preparation for the commercial coatings that were tested was dictated by the coating manufacturer. In most cases, the preparation was considered to be proprietary information. Therefore, if the actual surface preparation was not known, this fact was so noted. Otherwise, the terms "smooth" and "rough" refer to the procedures described in this section. Table 1 provides a listing of the 14 different polymer coatings which underwent endurance testing.

Heat Transfer Apparatus. In order to determine the quantitative effect of a coating on the heat transfer coefficient, a separate apparatus was used to study dropwise condensation on a horizontal tube. This apparatus is described in detail by Poole [13] and Wanniarachchi et al. [14], and a schematic is shown in Fig. 2.

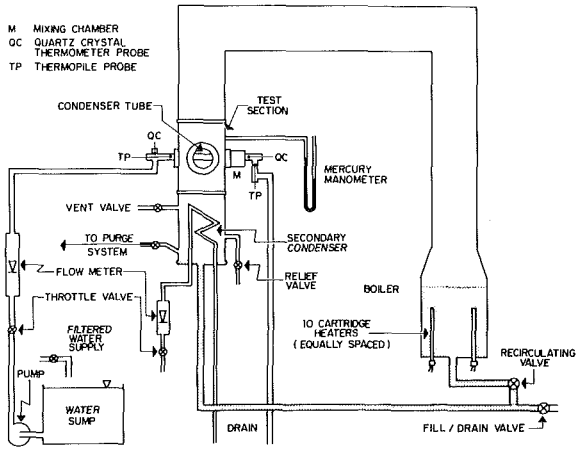

Fig. 2 Schematic of heat transfer test apparatus

Steam was generated from distilled water in a 0.305-m-diameter glass boiler using ten 4000-W immersion heaters. The steam then passed through a 0.305-m to 0.152-m reducer into a 2.44-m-long vertical section, through a 180-deg bend, and then down a 1.52-m-long vertical section before entering the stainless-steel test section. The test tube was mounted horizontally behind a viewing port in the center of the test section. Each tube was machined from thick wall, low-oxygen copper pipe, and was 0.133 m long with an inside diameter of 12.7 mm and an outside diameter of 19.0 mm. Steam that did not condense on the tube passed to an auxiliary condenser. All condensate was returned to the boiler by gravity through stainless-steel tubing. Operating under vacuum conditions, at an absolute pressure of about 11 kPa, the test apparatus produced vapor velocities of approximately 2 m/s past the test tube.

Cooling water for the tubes was provided by a centrifugal pump. A throttling valve was employed to control the cooling water flow from zero to a maximum velocity of 4.3 m/s through the tube. A continuous supply of tap water was used for cooling the auxiliary condenser. By throttling the flow of tap water to the auxiliary condenser, the pressure within the system could be regulated.

Instrumentation of Heat Transfer Apparatus. The power to the heaters was regulated through a silicon-controlled rectifier. This provided precise control and an accurate measure of the power being consumed. A mercury-in-glass manometer, calibrated in millimeters, was used to measure the internal pressure of the system. The temperature rise through the test tube was measured by a dual-channel Hewlett-Packard 2804A quartz thermometer as well as by a copper-constantan thermopile with ten junctions on either end. Proper shielding of the thermopile wires eliminated the considerable radio-frequency interference generated by the boiler rectifier at low voltages. Throughout all of the runs, the measured temperature rise of the quartz thermometer and the thermopile agreed to within ± 0.03 K. A calibrated rotameter was used to measure the coolant flow rate through the tube. All raw data were recorded on disk by a Hewlett-Packard 9826A computer. With the exception of the manometer and rotameter readings, which were entered manually, all data were interfaced through a Hewlett-Packard 3497A Data Acquisition/Control Unit.

Experimental Procedures

Endurance Tests. Forceps were used to hold the specimens against the heat sink while they were clamped in place. Glass side panels were then placed in position and the nuts secured finger-tight. After allowing a sufficient flow of cooling water through the heat sink, steam was gradually introduced into the test chamber. As the steam condensed, the condensate would return and commence filling the de-superheater. A steady-state condition was reached in approximately 1 hr when the de-superheater was roughly one-third full. At this point, the returned condensate was balanced by overflow from the de-superheater discharge. The steam supply valve was adjusted to ensure that the chamber pressure remained slightly above atmospheric and a small amount of excess steam was vented to the atmosphere.

Table 1 Endurance specimens and test results

Coating	Substrate/ Surface	Thickness μm	Dropwise Initial	Appearance Long-Term	Hours of Operation
No-Stik	CuNi, Ti/U	60	Excellent	Excellent	>22,000
No-Stik	Cu, Br/U	60	Excellent	Excellent	>20,000
Nedox	Cu/U	5	Excellent	Excellent	4000
Nedox	Ti/U	5	Excellent	Poor	<1000
Nedox	Br/U	5	Excellent	Poor	<400
Nedox	CuNi/U	5	Excellent	Poor	<300
Emralon 333	Cu/U	20	Poor	Poor	<500
Emralon 333	Ti/U	20	Poor	Excellent	>22,000
Emralon 333	Br/U	20	Poor	Fair/Good	>22,000
Emralon 333	CuNi/U	20	Poor	Fair/Good	6500
C-6 Fluoroepoxy	Cu, Ti, CuNi/S	1-10	Good	Fair/Good	2000
C-6 Fluoroepoxy	Cu/R	1-10	Good	Fair/Good	6500
C-6 Fluoroepoxy	Ti/R	1-10	Good	Fair/Good	>22,000
C-6 Fluoroepoxy	CuNi/R	1-10	Good	Fair/Good	6500
C-6' Fluoroepoxy	Cu, Ti, CuNi/S	1-10	Good	Fair/Good	1000
C-6' Fluoroepoxy	Cu, Ti, CuNi/R	1-10	Good	Fair/Good	>2000
BCE-7 Fluoroepoxy	Cu/S	1-10	Fair	Failed	<20
Fluoroacrylate	Cu/S	1-10	Fair	Failed	<20
Fluoroacrylic	Cu, Ti, CuNi/S	1-10	Good	Failed	<20
Fluoroacrylic	Cu, Ti, CuNi/R	1-10	Good	Good/Fair	>20,000
Pepco 6122	All/U	5-10	Good	Poor	>2000
Isonel 472	All	5-10	Fair	Failed	<24
Isonel 31-398	All	5-10	Good	Failed	<24
Sputtered PTFE	Cu/S & R	0.4	Excellent	Poor	2000
Sputtered PTFE	Ti/S & R	0.4	Excellent	Failed	<48
Sputtered PTFE	Br/S & R	0.4	Excellent	Failed	<48
Sputtered PTFE	CuNi/S & R	0.4	Excellent	Failed	<48
Parylene-N	All	0.5	Good	Failed	<20
Parylene-N	Cu/AD	1.0	Good	Failed	<100
Parylene-N	Ti/AD	1.0	Good	Failed	<100
Parylene-N	Br/AD	1.0	Good	Failed	<100
Parylene-N	CuNi/AD	1.0	Good	Good	4000
Silicone	All	U	Fair	Poor	<50

Where AD = As delivered R = rough S = smooth U = unknown

Visual observations were conducted daily. In order to provide a permanent, visual record, photographs were taken at least once every two or three months. Periodically, the system was shut down in order to remove specimens which were performing unsatisfactorily. These were set aside for examination under a scanning electron microscope (SEM), and new samples were installed in their places. In addition to the endurance test, two standard testing procedures to measure hardness and adhesion were employed [15, 16]. Since both of these tests are destructive, it was not possible to subject actual endurance specimens to these tests. Instead, at least one specimen from each group of coatings was held back for destructive testing.

Heat Transfer Tests. Since the presence of noncondensing gases can have a relatively large effect on the heat transfer coefficient, extreme care was taken to ensure that the heat transfer test apparatus was virtually leak free. As documented by Poole [13], the experimental apparatus was successively improved until it could be repeatedly demonstrated that the rise in pressure due to the ingress of noncondensing gases under vacuum was less than 2 mmHg in a 24-hr period. When the system was operational, an air ejector was used to reduce the system pressure to roughly 100 mmHg. At this point, the air ejector was secured and the boiler was energized. After boiling had commenced, the air ejector was again activated for ap-

Table 2 Steam-side* heat transfer coefficients

Coating Type	$h_o/(kW/m^2.K)$
Uncoated	10 ± 0.5
No-Stik	4 ± 0.5
Nedox	86 ± 13
NRL C-6 Fluoroepoxy	20 ± 1
NRL Fluoroacrylic	53 ± 7
Parylene-N, 0.5 μm	67 ± 10
Parylene-N, 1.0 μm	52 ± 8

Steam Velocity ≈ 2.2 m/s
Steam pressure ≈ 11 kPa (85 mmHg)
Tube O.D. = 19 mm

* includes coating and condensate.

proximately 10 min to degas the operating fluid. Over many data runs, this purging procedure was validated by the absence of any improvement in the heat transfer by additional purging. All heat transfer tests were conducted at a steam absolute pressure of about 11 kPa (85 mmHg).

Based upon the results of the previously described endurance tests, several coatings were selected for heat transfer evaluations. A spiral insert was placed within the tube being tested in order to enhance the inside heat transfer coefficient. This was done to improve the accuracy in the steam-side coefficient which was obtained by subtracting water-side and wall resistances from the measured overall resistance. The water-side coefficient had been predetermined (as a function of coolant conditions) using a tube fitted with wall thermocouples and having the same inside diameter and spiral insert as the tubes tested (see [14]). Additional details of the process used to determine the steam-side coefficient are provided in [14].

Since the insides of the tubes were thoroughly cleaned before testing and were found to remain clean and bright throughout the investigation, no allowance was made for fouling. A typical test run took around 2 hr and two or three runs were made for each tube to ensure repeatability. The total exposure time for a newly coated tube was therefore less than 6 hr.

Results and Discussion

Fourteen organic polymer coatings were considered for endurance testing, and six of these were selected for heat transfer measurements. Although ideal dropwise condensation was the most desirable characteristic, durability and ease of application were also important considerations. Therefore, a number of coatings which exhibited somewhat less-than-ideal dropwise-condensation characteristics were still considered for heat transfer measurements. A summary of all the coatings and the results of the endurance tests are provided in Table 1.

A complete description of the performance of the coatings is given in [12, 17]. The following discussion pertains to only the six coatings which were selected for heat transfer measurements. Table 2 lists the measured heat transfer coefficients for these coatings.

No-Stik

Endurance. No-Stik is a thermally conducting coating, impregnated with PTFE, as developed by Plasma Coatings, Inc. It is applied by a thermal or plasma spray technique and is used as a hard-wearing, corrosion-resistant mold release. Two identical sets, each consisting of four samples representing the four different substrates, were tested. Application and surface preparation were performed by the manufacturer. In order to verify previous observations, the second set was installed in the steam chamber approximately 2000 hr after the first set. Micrometers were used to determine a mean coating thickness of approximately 60 μm. Owing to the uneven texture, an exact measurement of the coating thickness was not possible. Excellent quality dropwise condensation with this coating is readily apparent in Fig. 3. The drops are nearly spherical, exhibit a relatively large contact angle, and grow to only approximately 2.5 mm in diameter before departure. However, the rate at which the drops departed the surface was noticeably less than that of other specimens with thinner coatings. This indicated a lower heat flux caused by the thermal barrier imposed by the coating itself.

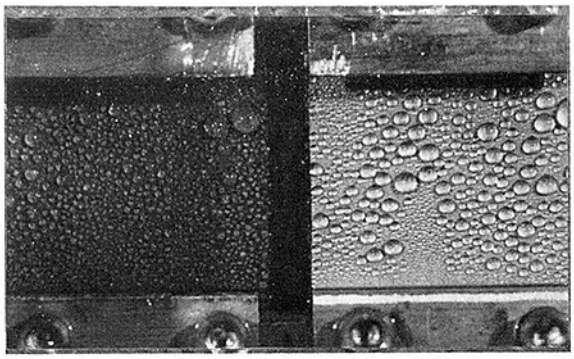

Fig. 3 Initial dropwise condensation on copper-nickel coated with No-Stik (left) and Nedox

After more than 22,000 hr of continuous exposure, this coating showed virtually no signs of physical degradation. The brass and copper samples were lightly speckled with green which was attributed to oxidation of the copper. An examination of an "as-delivered" sample with the SEM revealed small holes in the coating which exposed the substrate. Examination of an exposed specimen revealed that, although the coating was not affected, the substrate was being attacked at these void sites. However, this did not appear to affect the quality of the dropwise condensation, nor did the oxidation appear to undermine the coating in the immediate vicinity of the voids.

Heat Transfer Performance. Even though this coating produced excellent dropwise condensation, the steam-side heat transfer coefficient was only around 40 percent of that for an uncoated tube undergoing filmwise condensation (see Table 2). This result is explained by the thickness of the coating. Although the coating was heavily doped with copper to improve conductivity, the thermal resistance imposed by the coating was far too great to be offset by the beneficial effects of dropwise condensation.

Nedox

Endurance. Nedox is a commercially available coating developed by the General Magnaplate Corporation for use as a corrosion-resistant mold release. The coating process is a proprietary process in which a very porous, hard surface of chrome-nickel alloy is electrodeposited on the substrate surface. The pores are enlarged through a series of processes to accept an infusion of PTFE which forms a clear, ultrathin coating over the entire surface. A total of eight Nedox samples were tested, two sets of the four different substrates. Surface preparation and application were performed by the manufacturer. The coating thickness, supplied by the manufacturer, was approximately 5 μm. This was confirmed by viewing a sectioned sample under the SEM.

As can be seen in Fig. 3, the initial dropwise condensation with this coating was excellent. However, after 24 hr, all of the

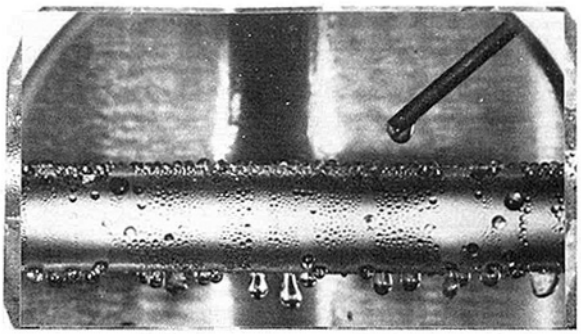

Fig. 4 Dropwise condensation on Nedox-coated copper tube

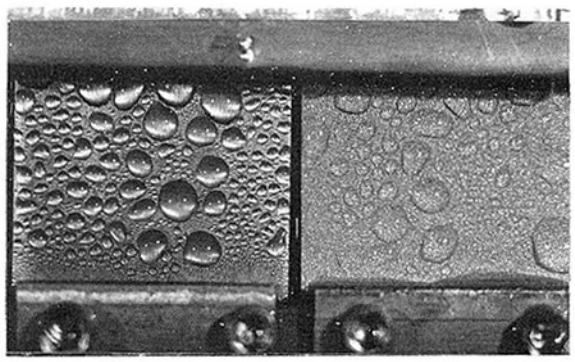

Fig. 5 Dropwise condensation on smooth (left) and rough titanium specimens coated with NRL C-6 fluoroepoxy (790 hr)

samples were noticeably darker in color, indicating a reaction of the substrate with the environment. At this point, the quality of the dropwise condensation was not noticeably affected. After 240 hr, the condensation mode on the upper-half of the copper–nickel specimen was filmwise while the lower half exhibited mixed-mode condensation. This specimen was then removed for examination. After 1200 hr, only the copper specimen exhibited any degree of dropwise condensation. After 3000 hr, the remaining specimens were removed and the second set was installed. Although the exposure time varied, the pattern of performance was virtually the same; very good to excellent dropwise condensation occurred initially, with a gradual darkening of the substrate followed by a gradual degradation in dropwise performance.

Examination of an unexposed specimen under the SEM revealed a mottled surface covered by a thin, smooth, transparent film. The transparent film was presumed to be the PTFE coating while the mottled appearance was due to the chrome–nickel plating. Examination of an exposed specimen revealed that, although the chrome–nickel plating was intact, the PTFE film had been peeled back or completely removed. Pieces of the film still partially attached were visible with the naked eye. The loss of the PTFE film accounted for the loss of the hydrophobic characteristics of the coating. However, the exact cause of this could not be determined.

Heat Transfer Performance. Despite reservations about the durability of this coating, it is clearly seen in Table 2 that it produced the best thermal performance, improving the steam-side heat transfer coefficient by a factor of 7 to 10. Because of the relatively short duration of exposure, no degradation was evident during the heat transfer tests. Figure 4 shows the quality of dropwise condensation of the Nedox-coated copper tube.

NRL C-6 Fluoroepoxy

Endurance. The NRL C-6 fluoroepoxy is an experimental fluoropolymer developed by Griffith at the Naval Research Laboratory [18]. It was developed in an effort to produce a tough, protective coating which would also provide extremely low fluid absorption. Six C-6 samples were tested; substrates of copper, copper–nickel, and titanium were used with the two surface finishes previously described. The Cu–Ni samples were reserved for destructive testing. Because this compound is only available in limited quantities, application of the coating was by brushing rather than by spraying or spinning. This resulted in an uneven surface texture estimated to be 5.0 to 10.0 μm thick. The estimate of the coating thickness was determined with micrometers and confirmed by viewing a sectioned portion of a specimen with the SEM.

All of the test specimens produced fair to good dropwise condensation. As can be seen in Fig. 5, the drops are somewhat flat, irregular in shape, and grow to about 4 mm in diameter before slowly departing the surface. After 100 hr of exposure, the surfaces of the copper and copper–nickel specimens showed signs of oxidation. The oxidation grew progressively worse until, after 1000 hr, the surfaces were completely black. The oxidation of the surfaces of the reactive substrates indicated that the coating was incapable of completely insulating the substrate from the environment. However, this did not seem to affect the performance of the coating adversely; it remained virtually unchanged during the first 2000 hr of operation. After 2400 hr, all of the smooth samples exhibited some degree of separation of the coating from the substrate. After 3000 hr, the coating became unbonded from the smooth samples causing blisters and bare spots over 20 to 30 percent of the surface. This condition existed after an operating time in excess of 4000 hr.

Although the oxidation of the copper and copper–nickel surfaces could be blamed for the deterioration of the adhesive qualities of the epoxy, oxidation is not realistic with titanium. As a result, this condition seems to indicate an inadequate bond with the smooth surfaces. However, fair to good dropwise performance has been observed on a rough titanium specimen after operation in excess of 22,000 hr, while rough copper and copper–nickel samples produced similar performance only for 6500 hr.

Heat Transfer Performance. The NRL C-6 fluoroepoxy produced an improvement in the steam-side heat transfer coefficient by a factor of about 2 (see in Table 2). Although considerably greater than an uncoated tube undergoing filmwise condensation, these results are substantially less than those achieved by the Nedox coating. This poorer performance was probably a result of the coating thickness. Application by brush produces a coating which is nonuniform and too thick. The thickness on the test tube was estimated to be 10 to 20 μm. Although very durable, an application technique which will consistently produce an ultrathin, uniform coating must be utilized if this coating is to be exploited for enhancing heat transfer.

NRL Fluoroacrylic

Endurance. The NRL fluoroacrylic, also an experimental coating, was characteristic of a linear thermoplastic. As with the fluoroepoxies, six samples were tested. The three smooth samples failed almost immediately. Small patches of the coating could be seen floating away with the condensate. However, all of the rough specimens produced fair to good condensation in excess of 20,000 hr, with no signs of physical or hydrophobic degradation, as seen in Fig. 6. Although the drops are somewhat large, about 4 mm in diameter before departure, they exhibit a larger contact angle and a more circular shape than those formed on the C-6 fluoroepoxy surfaces. In addition, the oxidation rate of the reactive substrate surfaces was noticeably less than any of the epoxy-coated surfaces. This indicates that the acrylic was better able to protect the substrate from the environment.

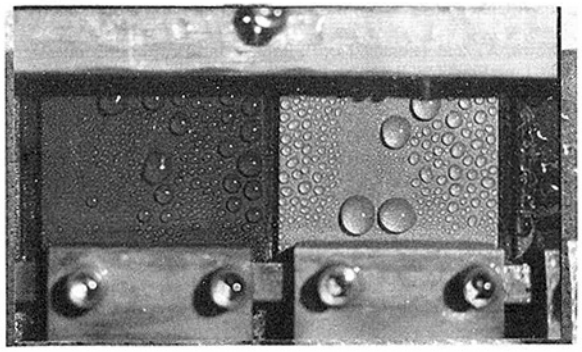

Fig. 6 Dropwise condensation on rough copper (left) and titanium specimens coated with NRL fluoroacrylic (2500 hr)

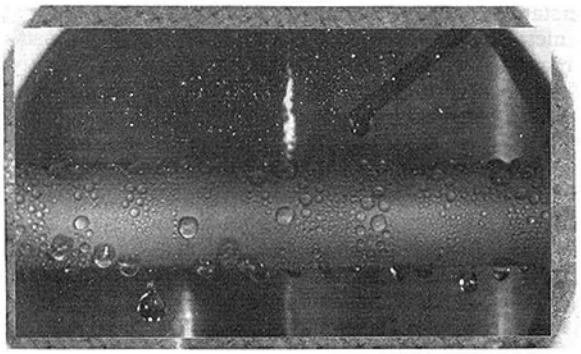

Fig. 7 Dropwise condensation on fluoroacrylic-coated copper tube

Heat Transfer Performance. Since the NRL fluoroacrylic is a thermoplastic polymer, it can be thinned easily prior to application. This makes a thin, uniform coating more easily obtainable when compared to the epoxies. In this case, the coating thickness was estimated to be 5 to 10 μm. As a result, the fluoroacrylic coating which was tested produced enhancements in the outside heat transfer coefficient of 5 to 6 (see Table 2). Figure 7 shows the quality of dropwise condensation on the fluoroacrylic-coated copper tube.

Parylene-N

Endurance. Parylene is a generic name for a family of thermoplastic polymers developed by the Union Carbide Company for use as conformal, insulating coatings for the electronics industry. A total of eight samples, four different substrates with two coating thicknesses of 0.5 μm and 1.0 μm, were tested. These coatings were applied by the Lawrence Livermore National Laboratory, and due to scheduling difficulties, it was not possible to prepare the substrate surfaces prior to coating. Therefore, unlike the other specimens, none of the specimens to be coated with parylene-N underwent any surface preparation. All of the specimens were plated in the "as-delivered" condition. For the copper, brass and titanium substrates, the as-delivered condition was similar to the "smooth" surface previously described. However, the copper–nickel specimen was received with a surface similar to the "rough" surface of the prepared specimens.

Upon exposure to steam, seven of the specimens failed within 24 hr. Large, water-filled blisters covered as much as 90 percent of the substrate surfaces. The only specimen to perform satisfactorily was the 1-μm-thick coating on the copper–nickel substrate. As can be seen in Fig. 8, this coating produced dropwise condensation which could be characterized as good. The drops are somewhat irregular but grow to only 3 to 4 mm in diameter before quickly departing the surface. While no degradation was seen for about 1500 hr, further operation showed gradual degradation and, after a total of 4000 hr, the sample was removed. Based upon the limited number of parylene samples involved and observations of other coatings under similar conditions, failure can be attributed to two causes: surface finish and coating thickness. The fact that only the naval brass specimen with the 1-μm coating endured indicates that a rough surface is necessary to ensure proper bonding. This finding is consistent with observations of other coatings. In addition, thicknesses of less than 1 μm appear to be incapable of withstanding the test environment. It is surmised that water can penetrate the ultrathin coatings sufficiently to eventually undermine the bond between the coating and substrate surface. This observation is supported by the failure of the 0.5-μm coating on the rough, copper–nickel substrate and the appearance of water-filled blisters on all of the failed specimens. The blisters indicated that, although the coating was continuous and firmly attached at the edges, condensate had somehow collected between the film and the substrate.

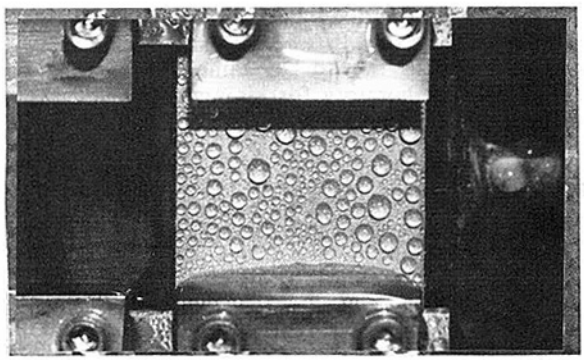

Fig. 8 Dropwise condensation on copper–nickel specimen coated with parylene-N (1500 hr)

Heat Transfer Performance. As shown in Table 2, two thicknesses of parylene-N were tested: 0.5 and 1.0 μm. The 0.5-μm coating enhanced the outside coefficient from 6 to 7.5 times, and, due to the increased thickness, the 1.0-μm coating produced a lower enhancement of 4.5 to 6. However, close inspection of the 0.5-μm coating after the heat transfer tests revealed small areas in which the coating was beginning to peel or crack. The 1.0-μm coating showed no signs of deterioration. This result was consistent with the endurance test which indicated that a 0.5-μm-thick coating was too thin to produce reliable durability.

Conclusions

During condensation of steam on horizontal tubes, the steam-side heat transfer coefficient can be enhanced five to ten times through the use of organic polymer coatings. A five- to sixfold increase can be achieved with coatings of demonstrated durability (i.e., coatings which showed no degradation over a long period; for example, 4000 hr for parylene-N on copper–nickel and fluoroacrylic on rough copper, titanium, and copper–nickel specimens), whereas larger increases can be achieved at present only by coatings of questionable durability. Because of their hydrophobic characteristics and ease of application, and their ability to be applied in ultrathin layers (less than 1 μm), the fluoroepoxies and fluoroacrylics represent the best alternative for the long-term application of a low-energy, fluorocarbon surface. The highly durable No-Stik coating resulted in poor heat transfer performance due to the large coating thickness. It appears worthwhile, however, to attempt to obtain thinner No-Stik coatings that may result in good heat transfer performance.

Regardless of the heat transfer characteristics, none of the ultrathin coatings was capable of completely protecting the reactive substrates from the environment, and a better

understanding of the mechanisms which occur at the interface of a metallic substrate and an organic coating is needed. In this regard, considerable insight has been gained recently in the field of corrosion control [19]. Apparently, local chemical and electrochemical reactions occur at the metal/organic coating interface and these reactions depend upon the rate at which reactive species, such as oxygen, can reach the interface. Therefore, the diffusion of oxygen through a coating and the presence of nonhomogeneities within a coating can have a substantial influence on the substrate, such as by grit blasting, can improve upon the adhesion of a coating and reduce corrosive action. Also, nonreactive substrates or substrates plated with a nonreactive sublayer should be utilized where feasible.

Acknowledgment

This work was supported by the National Science Foundation through Grant No. MEA 82-03567. The authors wish to express their appreciation to Dr. James R. Griffith of the Naval Research Laboratory for his assistance and support throughout this investigation.

References

1 Woodruff, D. M., and Westwater, J. W., "Steam Condensation on Various Gold Surfaces," ASME *Journal of Heat Transfer*, Vol. 103, 1981, pp. 685-692.

2 O'Neill, G. A., and Westwater, J. W., "Dropwise Condensation of Steam on Electroplated Silver Surfaces," *International Journal of Heat and Mass Transfer*, Vol. 27, No. 9, 1984, pp. 1539-1549.

3 Wilkins, D. G., Bromley, L. A., and Read, S. M., "Dropwise and Filmwise Condensation of Water Vapor on Gold," *AIChE Journal*, Vol. 19, No. 1, 1973, pp. 119-123.

4 Smith, G. F., "Promotion of Dropwise Condensation by Teflon Coated Tubes," Evaluation Report 030038B, NS-643-078, U.S. Naval Engineering Experimentation Station, Annapolis, MD, Oct. 12, 1956.

5 Fox, R. M., "A Review of Literature on the Promotion of Dropwise Condensation," United States Navy Marine Engineering Laboratory Report 71 106, July 7, 1964.

6 Brown, A., and Thomas, M., "Filmwise and Dropwise Condensation of Steam at Low Pressures," *Proceedings 3rd International Heat Transfer Conference*, Vol. 2, 1966, pp. 300-305.

7 Graham, C., "The Limiting Heat Transfer Mechanisms of Dropwise Condensation," Ph.D. Thesis, M.I.T., Cambridge, MA, 1969.

8 Manvel, J. T., "An Experimental Study of Dropwise Condensation on Horizontal Condenser Tubes," M.S. Thesis, Naval Postgraduate School, Monterey, CA, June 1979.

9 Perkins, P. K., "An Experimental Study of Dropwise Condensation on Vertical Discs," M.S. Thesis, Naval Postgraduate School, Monterey, CA, Dec. 1979.

10 Kullberg, G., and Kendall, H., "Improved Heat Transfer Coefficients With Silicone Resin Coatings," *Chemical Engineering Progress*, Vol. 56, No. 1, 1960.

11 Erb, R. A., and Thalen, E., "Dropwise Condensation Characteristics of Permanent Hydrophobic Systems," Office of Saline Water R&D Report 184, Apr. 1966, pp. 54-57.

12 Holden, K. M., Wanniarachchi, A. S., Marto, P. J., Boone, D. H., and Rose, J. W., "Evaluation of Organic Coatings for the Promotion of Dropwise Condensation of Steam," *Fundamentals of Phase Change: Boiling and Condensation*, HTD-Vol. 38, C. T. Avedisian and T. M. Rudy, eds., Dec. 1984, pp. 89-97.

13 Poole, W. M., "Filmwise Condensation of Steam on Externally Finned Horizontal Tubes," M.S. Thesis, Naval Postgraduate School, Monterey, CA, Dec. 1983.

14 Wanniarachchi, A. S., Marto, P. J., and Rose, J. W., "Film Condensation of Steam on Horizontal Finned Tubes: Effect of Fin Spacing," ASME JOURNAL OF HEAT TRANSFER, Vol. 108, 1986, pp. 960-966.

15 "Standard Methods for Measuring Adhesion by Tape Test, Designation: D 3359-78," *Annual Book of American Society for Testing and Materials (ASTM) Standards*, Vol. 06.01, 1983, pp. 666-669.

16 Standard Test Method for Film Hardness by Pencil Test, Designation: D 3363-74, ibid., pp. 674-675.

17 Holden, K. M., II, "An Evaluation of Polymer Coatings for the Promotion of Dropwise Condensation of Steam," M.S. and Mechanical Engineer Thesis, Naval Postgraduate School, Monterey, CA, Mar. 1984.

18 Griffith, J. R., and Quick, J. G., 155th Meeting, Am. Chemical Soc. Div. of Org. Coatings and Plastics Chemistry, Preprint No. 28, No. 1, 1968, p. 342.

19 Leidheiser, H., "Corrosion of Painted Metals – A Review," *Corrosion Source Book*, S. K. Coburn, ed., American Society of Metals and National Association of Corrosion Engineers, 1984, pp. 215-224.

Thermal Conductivity of Metal Cloth Heat Pipe Wicks

J. R. Phillips

L. C. Chow[1]

W. L. Grosshandler

Department of Mechanical Engineering,
Washington State University,
Pullman, WA 99164-2920

Heat conduction through a metal cloth wick saturated with a fluid has been investigated. An apparatus used to measure thermal conductivity, in which the condition of wick packing geometry is carefully controlled, and the basic experimental procedure are described. Experimental results are presented and compared to a new mean-gap-conductance model based upon the wick geometry, and to the simple series model. The mean-gap-conductance model evaluates the effects of the mesh geometry, and with the addition of a correction term to account for three-dimensional effects and layer-to-layer contact, the effective conductivity can be accurately predicted. In addition, a correlation of the mean gap which directly includes three-dimensional and contact conductance effects is presented. The correlation predicts the data within 10 percent whereas the series model may be more than 40 percent in error. From a parametric study using the new model, theoretical limits on the maximum and minimum conductivity enhancement have been determined as a function of geometric parameters. The implications of the research on heat pipe wick design are discussed.

Introduction

The prediction of the effective thermal conductivity of layered cloth wicks saturated with a fluid is an important consideration in the development of heat pipe technology. A knowledge of the wick's thermal conductivity is essential when calculating the overall performance of a heat pipe design. The necessity of predicting the wick thermal conductivity, coupled with the scarcity of experimental data and the lack of satisfactory design information, makes the present research of particular interest to current heat pipe research and development.

A considerable amount of work has been done on the experimental measurement of effective thermal conductivities for packed beds, but these results are not directly applicable for heat pipe wicks made of layered screens. Theories predicting thermal conductivity, such as those developed and presented by Chi (1976) and Gorring and Churchill (1961) are commonly used for layered cloth wicks even though considerable error may occur. These theories are based on simplified models which fail to describe satisfactorily the behavior of the layered cloth wick subjected to various design conditions.

One of the few references found which contained measured conductivity values for layered cloth heat pipe wicks is that of VanSant and Malet (1975). Although this work is quite extensive, it does not contain the necessary experimental parameters to make the work useful for most heat pipe designs. The particular design of interest in this study is that of the double-wall artery heat pipe. In the design in question, the wick is constrained in an annular region between an inner and outer wall without the aid of adhesives or sintering. A description of the design is given by Ponnappan and Mahefkey (1983).

Theoretical models have been developed for the thermal contact conductances which occur in packed beds (Yovanovich, 1982). In general, the dimensionless conductances are expressed as functions of the relative contact pressure, surface parameters, conductivity ratio, and some fluid parameters. Correlations have been obtained for the thermal contact conductances of nominally flat surfaces (Tien, 1968), sphere–sphere contacts (Ogniewicz, 1975), and sphere–flat contacts (Kitscha, 1975). These models are primarily concerned with higher contact pressures than would generally be found in heat pipe wicks (VanSant and Malet, 1975). In addition, many of the experiments were conducted in a vacuum, which is not the case in operating heat pipes.

The mean thermal gap conductance between curved cylindrical surfaces is of importance when low pressures are exerted on the wick (Yovanovich et al., 1982). At very high contact pressures, a contact model (Cividino et al., 1974) may be added to form a more comprehensive model, but such a model for multiple cloth layers has not been found in the literature and is beyond the scope of the present work.

Theoretical Analysis

Heat Conduction in a Mesh Layer. Within the continuum limit, the equation describing steady-state conduction in a three-dimensional stationary medium can be written as

$$\bar{\nabla}\,(k\,\bar{\nabla}\,T)=0 \tag{1}$$

Although this expression appears to be simple, the thermal conductivity k is a scalar function of position, leading to substantial geometric complexities.

An obvious way to obtain a solution to equation (1) for a heat pipe wick would be to solve it by dividing the region into a liquid and solid phase, with a heat flux and temperature balance at the interface between the mesh and the saturating fluid. A finite element or finite difference scheme could then be applied to obtain a solution. Two significant drawbacks to such an approach are the complicated geometry and the fine grid necessary to describe the boundary conditions at the interface.

Another possibility is a Monte-Carlo approach. In the event that a statistical function describing the conductivity could be found, such an equation might yield to a numerical solution. Finding such a function and solving the multidimensional equation would require a very fine grid structure to provide consistent results. This would indicate considerable computation for either solution method.

In light of the above, a one-dimensional approximation based on the fundamental parameters of the wick and saturating fluid is an appropriate alternative. As was mentioned earlier, there have been several attempts to model the physics using a one-dimensional assumption, but only moderate success has been achieved. In most cases the lack of

[1]Present address: Department of Mechanical Engineering, University of Kentucky, Lexington, KY 40506-0046.

Contributed by the Heat Transfer Division for publication in the JOURNAL OF HEAT TRANSFER. Manuscript received by the Heat Transfer Division June 9, 1986.

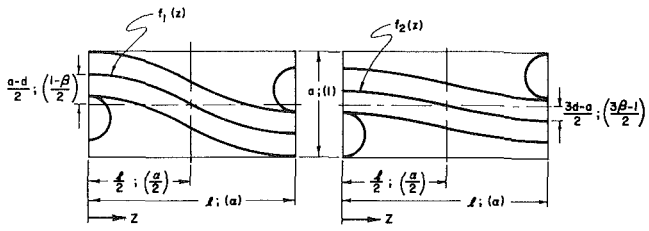

Fig. 1 Geometry of a unit cell in a woven cloth

success is attributable to oversimplification. Therefore, a more comprehensive model is needed.

The conduction of heat through a layer of self-supporting cloth is more readily understood if one examines the geometry of the unit cell shown in Fig. 1. If the flux is assumed to be primarily normal to the cloth layer and if the conductivity of the cloth is much greater than that of the fluid, the flux will travel primarily through the solid mesh. Conversely, when the fluid conductivity is much higher than that of the mesh, the heat flux will avoid the mesh and flow primarily through the open area of the cloth layer. In the case where the fluid and mesh conductivities are approximately the same, the effective conductivity can be accurately calculated using the simplest one-dimensional models. For the most part, high mesh and low fluid conductivity will be considered, but the model will also describe the other two cases.

The parameters involved in the calculation of the effective conductivity k_e are both material and geometric. The thermal conductivities of the mesh k_m and of the fluid k_f must be known; four length measurements are required to describe the geometry: inverse mesh number l, thickness of a single mesh layer a, the wire diameter d, and the total thickness of the multilayered wick D. In addition, the apparent contact area fraction A_c^* (the apparent area of metallic contact in the wick divided by the total wick cross-sectional area) must be known to add the effect of layer-layer contacts.

Despite previous misconceptions, the mesh thickness is not equivalent to twice the wire diameter, but is somewhat larger in most cases. This results in three independent geometric parameters, and a fourth to describe the packing density of n layers of cloth. By nondimensionalizing, the following equation for the dimensionless effective thermal conductivity k_e^* results:

$$k_e^* = k_e^*(k^*, \alpha, \beta, A_c^*, \omega) \tag{2}$$

where $k_e^* = k_e/k_f$, $k^* = k_m/k_f$, $\alpha = l/a$, $\beta = d/a$, and $\omega = D/na$ (3)

Electrical Analog Circuit Model. Conduction of heat through the various regions in the cloth layers may be approximated using an electrical analog of series and parallel conductances. In Fig. 2, such a model is illustrated, in which a fluid conductance representing open pore heat conduction is in a parallel arrangement with a solid-fluid series and a solid

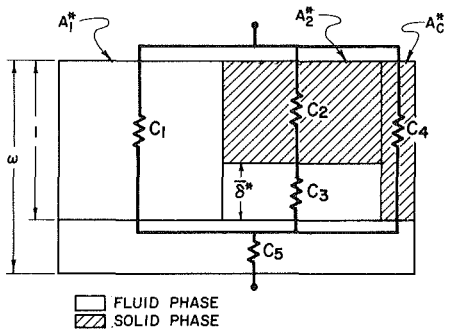

Fig. 2 Series/parallel model of layered cloth wick

representing conduction through two phase paths and solid-solid contacts, respectively. In addition, this effective circuit is in series with a fluid layer representing the contribution of packing density on effective conductivity.

In general, the conductance of an element may be written as

$$C \equiv \frac{kA}{\delta} \tag{4}$$

where k, A, and δ are the conductivity, cross-sectional area, and the length of the element, respectively. From this definition and Fig. 2, an expression for the dimensionless effective conductivity for the case of packing number ω equal to unity can be given as

$$k_e^*\Big|_{\omega=1} = A_1^* + \frac{k^*}{1+\delta^*(k^*-1)} A_2^* + k^* A_c^* \tag{5}$$

In addition, the normalization equation for the area fractions is

$$A_1^* + A_2^* + A_c^* = 1 \tag{6}$$

where each area is nondimensionalized by the total cross-sectional area. Similarly, the relationship between void fraction ϕ and the model geometry is

$$(1-\delta^*)A_2^* + A_c^* = (1-\phi) \tag{7}$$

In the case of a metal cloth wick, the contact area is normally very small unless excessive pressure is applied to the wick. This condition corresponds to $A_c^* \ll 1$, and simplifies equations (5), (6), and (7) into a single equation:

$$k_e^*\Big|_{\omega=1} = 1 + \frac{(1-\phi)}{(1-\delta^*)}\left[\frac{k^*}{1+\delta^*(k^*-1)} - 1\right] + A_c^* k^* \tag{8}$$

From Fig. 2, the equation for effective conductivity for packing numbers greater than unity can then be given as

$$k_e^* = 1 + \frac{k_e^*\Big|_{\omega=1} - 1}{1 + (\omega-1)k_e^*\Big|_{\omega=1}} \tag{9}$$

Nomenclature

a = thickness of single mesh layer
A = cross-sectional area
$A(z)$ = area distribution function
C = conductance
C_1 = alignment fraction
C_2 = effective wire diameter fraction
d = wire diameter
D = distance across wick
f = wire shape function
k = conductivity
l = unit cell length (inverse mesh number)
n = number of layers
T = temperature
z = dimensionless position along length of unit cell
α = dimensionless unit cell length
β = dimensionless wire diameter
δ = gap thickness
ϕ = void fraction
ω = packing number

Subscripts

e = effective
f = fluid
m = mesh material

Superscripts

$\bar{}$ = mean value
$*$ = dimensionless

At this point it is convenient to discuss the weave geometry so that the parameters $(1 - \phi)$ and $\bar{\delta}^*$ (mean thermal gap length) can be defined as functions of the purely geometric variables α and β. In order to accomplish this, dimensionless shape functions for the individual wires in the mesh $f(z)$ must be obtained. From Fig. 1, the position of the wire centerlines as a function of nondimensional distance across the unit cell z are known at the points $z = 0$ and $z = \alpha/2$. In addition, the slope of the centerline is known at $z = 0$. If the weave is eccentric ($d \neq a/2$), a shape function describing each of the two wire directions is necessary to describe the mesh. Given the above six conditions, it has been shown (Phillips, 1986) that the following second-order polynomials adequately describe the shape:

$$f_1(z) = \left(\frac{1-\beta}{2}\right) - 2(1-\beta)\left(\frac{z}{\alpha}\right)^2; \qquad 0 \le z \le \alpha/2 \qquad (10a)$$

$$f_2(z) = \left(\frac{3\beta-1}{2}\right) - 2(3\beta-1)\left(\frac{z}{\alpha}\right)^2; \qquad 0 \le z \le \alpha/2 \qquad (10b)$$

Given these shape functions, it can be shown further (Phillips, 1986) that the solid volume fraction $(1 - \phi)$ can be written as

$$(1-\phi) = \frac{\pi\beta^2}{8\alpha}\left\{\frac{1}{u_1}[u_1\sqrt{u_1^2+1} + \ln|u_1 + \sqrt{u_1^2+1}|] + \frac{1}{u_2}[u_2\sqrt{u_2^2+1} + \ln|u_2 + \sqrt{u_2^2+1}|]\right\} \qquad (11)$$

where $u_1 = -(2/\alpha)(1-\beta)$ and $u_2 = -(2/\alpha)(3\beta - 1)$.

Although the void fraction can be measured, it is much more convenient to use equation (11).

Mean Gap Conductance Model. The mean thermal gap length $\bar{\delta}^*$ is an important parameter to determine the relative importance of gross wire geometry on the overall effective conductivity. Since heat follows the path of greatest conductance, the fluid gap between adjacent wire surfaces can be modeled as parallel conductances of small cross sections such that a mean length can be determined.

Given that the projected area of the wire surface is properly normalized, an area distribution function $A(z)$ can be written such that

$$\int_0^{\alpha/2} A(z)dz = 1 \qquad (12)$$

The differential dimensionless gap conductance can be expressed as

$$dC^* = \frac{A(z)dz}{\delta^*(z)} \qquad (13)$$

where $\delta^*(z)$ is the dimensionless gap length as a function of z. Integrating both sides

$$C^* = \int_0^{\alpha/2} A(z)\left(\frac{1}{\delta^*(z)}\right)dz = \frac{1}{\bar{\delta}^*} \qquad (14)$$

Therefore, the dimensionless mean thermal gap length is defined as

$$\bar{\delta}^* = \left[\int_0^{\alpha/2} A(z)\left(\frac{1}{\delta^*(z)}\right)dz\right]^{-1} \qquad (15)$$

for one wire direction and one side of the wire layer. The final mean gap will consider both sides of the wire layer and both wire directions.

From equations (10*a*) and (10*b*) it can be shown (Phillips, 1986), assuming circular wire cross sections as a first approximation, that

$$\delta_i^*(z) = \sqrt{(1-2f_i(z))^2 + (C_1\alpha)^2} - C_2\beta; \qquad i = 1, 2 \qquad (16)$$

where C_1 is the alignment fraction and C_2 is the effective wire diameter fraction. The value of C_1 may vary between zero and 1/2 representing perfect alignment and perfect misalignment of adjacent cloth layers, respectively. As the number of layers goes to infinity the average alignment is $C_1 = 1/4$ given that each possibility is weighted equally; therefore, this value for C_1 is used to compute C_2 and $\bar{\delta}^*$.

The effective wire diameter fraction C_2 is calculated by determining the mean gap that occurs in the direction across the wire cross section at each position of z. In order to reduce the computation time, it is expedient not to calculate unnecessary second-order effects; therefore, the value of C_2 is calculated only at $z = 0$. This is a reasonable simplification since C_2 is not a strong function of z.

$$C_2 = \frac{\sqrt{\beta^2 + (C_1\alpha)^2}}{\beta} - \left[\int_0^{\beta/2} \frac{2\,dz^*}{\sqrt{\beta^2 + (C_1\alpha)^2 - 2\sqrt{(\beta/2)^2 - z^{*2}}}}\right]^{-1} \qquad (17)$$

Once C_2 has been calculated the mean gap for the unit cell can be determined by averaging the conductances for the two wire directions. Since the area under consideration is the projected area, the area distribution function is simply a constant, or $A(z) = 2/\alpha$ for each direction. This gives the expression for the mean gap

$$\bar{\delta}^* = 2\alpha\left[\int_0^{\alpha/2}\left(\frac{1}{\delta_1^*} + \frac{1}{\delta_2^*}\right)dz\right]^{-1} \qquad (18)$$

Effects of Contact and Three-Dimensional Conduction. The contact conductance occurring when a single layer of metal cloth is compressed between two flat surfaces has been successfully measured by Cividino et al. (1974) and by O'Callaghan et al. (1975). Due to large deviations from theory and its empirical nature, this information is not directly transferrable to the case of multiple layers saturated with a conducting liquid. However, for the low-pressure case (no deformation), it is expected that contact area is very small and dependent only on geometry.

Since the physics suggests that the contact area depends on geometry, the parameter A_c^* in the electrical analog model should depend solely on geometry if the quasi-one-dimensional assumption for the mean gap model is valid. This is indeed the case for the trivial situation of $k^* = 1$. However, if $k^* \gg 1$ the one-dimensional gap becomes a function not only of geometry but also of conductivity ratio and must be correlated to take three-dimensional effects into account.

Parametric Study

A parametric study of the mean-gap-conductance model (setting $A_c^* = 0$) was performed to establish the effects of the key parameters. A listing of the documentation and code used to generate the computer plots is included in the report by Phillips (1986).

Figure 3 shows the effect of the material conductivity ratio k^*, on the effective conductivity as a function of packing number ω. The curves show an upper and lower limit on the effective conductivity. The upper limit is the most interesting since it clearly shows the dominance of the fluid region when values of k^* exceed 100.

In Figs. 4 and 5, the effect of nondimensional unit cell length α and wire diameter β on effective conductivity are shown, respectively. It is apparent that conductivity increases as the ratio of β over α increases. The parameter β varies between 1/3 and 1/2, whereas α generally varies between 2β and 3 but can hypothetically be much larger. Therefore the ratio β/α has an upper bound of 1/2 and a lower bound of zero.

The most interesting result of the parametric study is obtained by letting β/α equal 1/2 and setting k^* to the limits of

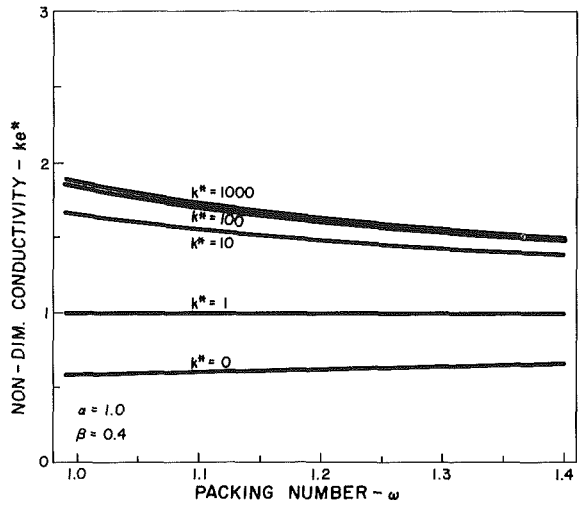

Fig. 3 Effect of cloth-to-fluid conductivity ratio on effective conductivity

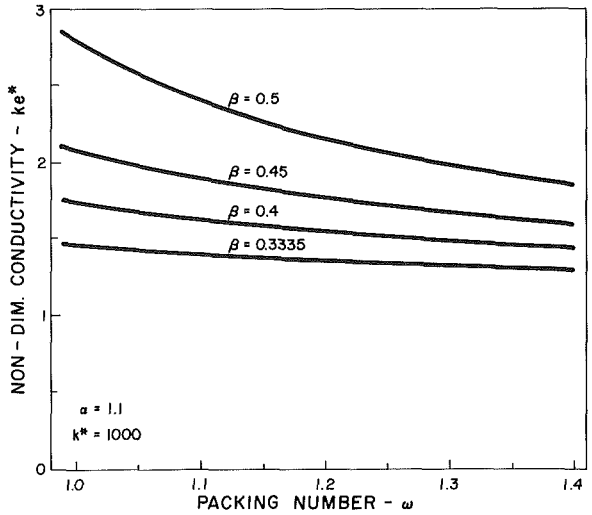

Fig. 5 Effect of wire diameter-to-layer thickness ratio on effective conductivity

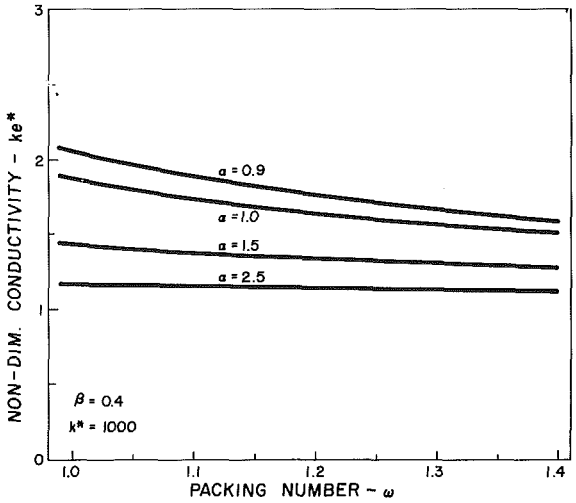

Fig. 4 Effect of unit cell length-to-layer thickness ratio on effective conductivity

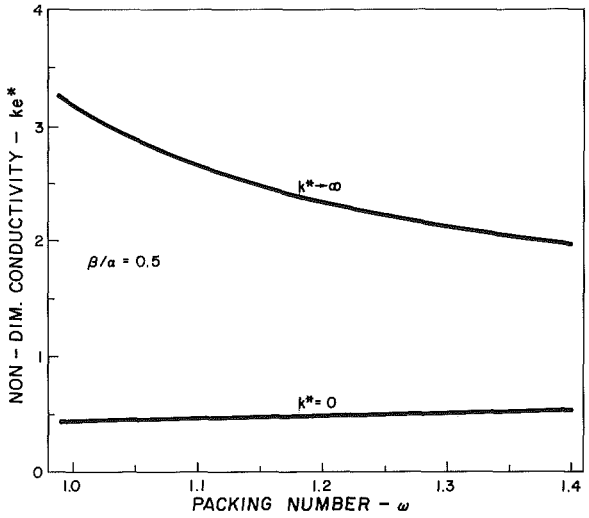

Fig. 6 Maximum and minimum effective conductivity enhancement

infinity and zero, respectively. The two resulting curves, shown in Fig. 6, represent a theoretical maximum and minimum effective conductivity enhancement possible for any layered cloth wick saturated with a fluid.

Measurements of Layered Cloth Thermal Conductivity

Description of Apparatus. An experimental facility has been built to measure the thermal conductivity of wick specimens. In Fig. 7 a cross-sectional view of the apparatus is shown. This assembly is enclosed in an insulated housing to reduce heat loss. A unique feature of the apparatus is that the thickness of the sample can be controlled and measured to ± 6 μm. This is in contrast to the common practice of measuring the pressure exerted on the sample. It is felt that, in heat pipe applications, the pressure exerted on the wick is not usually known. However, the total thickness of the wick may be a known design parameter.

Conductivity values were determined using Fourier's heat conduction law. The temperature gradient across the wick specimen was measured by six type-T thermocouples placed near the specimen surface in both the heat source and heat sink. During the course of the experiments, the source and sink were isothermal across the specimen surface within ±0.1°C. Heat flux was measured by a power meter monitoring the electrical heating.

The packing condition of the wick specimen was determined by measuring both the thickness of one cloth layer and the thickness of the entire wick specimen. A micrometer was used to measure the single layer thickness while the dial indicator on the apparatus was used to determine overall specimen thickness.

The data were acquired and the system controlled with a microcomputer. This provided for consistency of data collection and a greater amount of data to be taken since constant supervision of the experiment was not necessary.

Experimental Method. All cloth samples were cleaned prior to testing to remove any grease or oxide films. The samples were then saturated with a degassed fluid and placed in the apparatus. Once the insulation was placed in position around the test assembly, a d-c power supply was set to a selected power level.

Before taking data, the coolant flow rate and power supply were given time to become steady. Once this condition had occurred, all necessary information was entered into the microcomputer and the data acquisition and reduction pro-

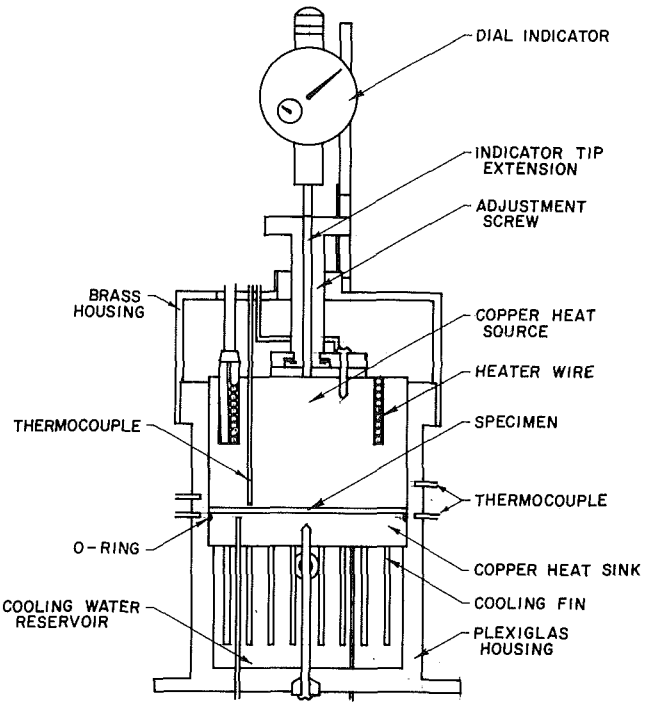

Fig. 7 Experimental apparatus for measuring wick thermal conductivity

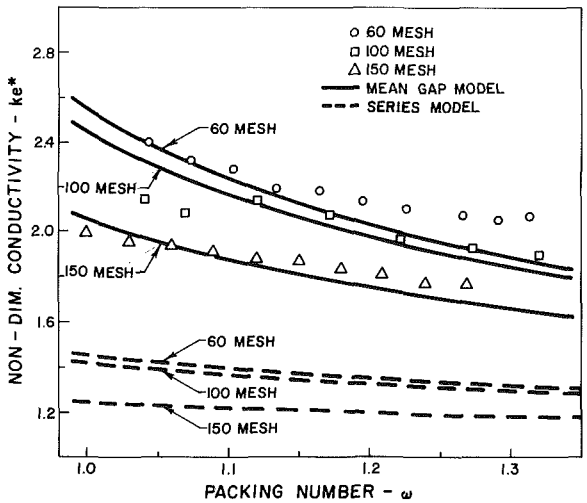

Fig. 8 Effective conductivity versus packing number for copper/water experiments

gram was initiated. The program read the apparatus temperatures until no temperature readings fluctuated by more than $\pm 0.3°C$ over a half-hour period. When steady state occurred, a final data reading was taken and both the raw data and the reduced data were printed. The time required for steady state to occur varied from a half hour to four hours, depending on environmental conditions and the specimen being tested.

Data were generally taken in sets starting with a low packing density and proceeding to a higher packing density. In this manner cloth samples were changed only between data sets rather than for every test. For details concerning experimental procedure see the report by Phillips (1986).

Prior to taking wick conductivity measurements, the apparatus was calibrated by taking several measurements of the thermal conductivity of distilled water. These measurements deviated from published values by less than ± 2 percent. The

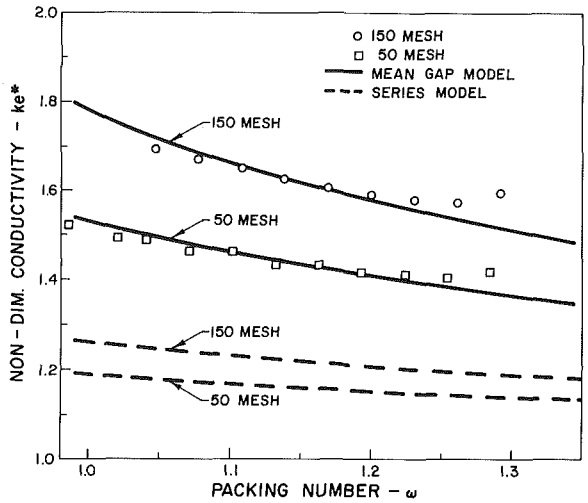

Fig. 9 Effective conductivity versus packing number for stainless/water experiments

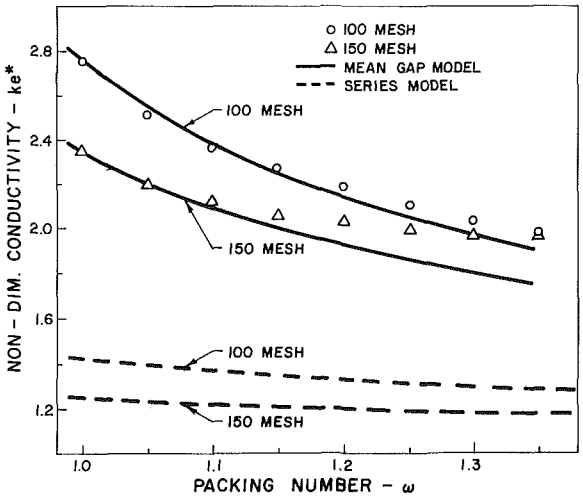

Fig. 10 Effective conductivity versus packing number for copper/glycerol experiments

Table 1 Properties and dimensions of cloth samples

Material	Threads/in.	α (l/a)	β (d/a)	k_m @ 30°C, W/m°C
Copper	150	1.22	0.378	397
Copper	100	0.939	0.395	397
Copper	60	1.08	0.440	397
Stainless steel (AISI 301)	150	1.14	0.379	14.7
Stainless steel (AISI 301)	50	2.18	0.471	14.7

estimated heat loss varied from about 3 to 7 percent, with the higher values occurring at measurements at the higher packing numbers.

Results and Discussion

Some properties and dimensions of the cloth samples tested and information concerning the experiments are listed in Tables 1 and 2. Figures 8–10 show experimental results, and comparisons to theory. The predictions of the mean-gap-conductance model (solid line in the figures) show good agreement with the measured data. The series model as given by

Table 2 Experimental conditions

Exp. No.	Mat'l	Fluid	th/in.	n	ϕ	k^*	Average specimen temperature, °C
1	Cu	water	150	18	0.801	646.0	31.9
2	Cu	water	100	10	0.706	646.0	31.7
3	Cu	water	60	8	0.687	646.0	31.7
4	SS	water	150	16	0.785	23.9	32.0
5	SS	water	50	12	0.835	23.9	34.2
6	Cu	glycerol	150	11	0.801	1395	31.6
7	Cu	glycerol	100	6	0.706	1395	31.4

Table 3 Apparent contact area values

Exp. No.	Material	Fluid	l/d	k^*	$A_c^*(\times 10^{-3})$
1	Cu	water	3.23	646.0	0.734
2	Cu	water	2.38	646.0	0.758
3	Cu	water	2.45	646.0	0.876
4	SS	water	3.01	23.9	8.860
5	SS	water	4.63	23.9	8.390
6	Cu	glycerol	3.23	1395	0.590
7	Cu	glycerol	2.38	1395	0.578

Gorring and Churchill (1961) (dashed line), however, deviates on the average by 40 percent and does not adequately show the effect of mesh geometry on effective conductivity.

The values of the apparent contact area fraction A_c^* were determined from the data using equations (5), (6), and (7). The results are shown in Table 3. An interesting result is evident at this point; namely, that the values of A_c^* appear to depend mostly on conductivity ratio as opposed to geometry. This is apparent since A_c^* changes very little (on the order of experimental uncertainty) within the metal/fluid categories even though mesh geometry changes considerably. Since an obvious conductivity ratio dependence was determined, the values of A_c^* were averaged in each metal/fluid category and the average values were used in equations (8) and (9) as shown in Figs. 8–10.

Correlation of the Mean Thermal Gap. The observed behavior of the apparent contact area fraction A_c^* demonstrates that three-dimensional conduction cannot be neglected if $k^* \gg 1$. By including the relatively small effects of contact and the larger effects of the three-dimensional geometry into the evaluation of the mean gap, a linear correlation was found to predict the gap within 12 percent.

$$\delta^* = 0.200 + 0.0162(\alpha/\beta) - 6.85 \times 10^{-5}(k^*) \qquad (19)$$

This correlation is valid over the range of experiments in this study.

The ratio of α to β by its definition is a significant geometric parameter, namely the unit cell length to wire diameter ratio l/d. The physical interpretation of equation (19) is straightforward. As k^* increases (ratio of mesh to fluid conductivity), three-dimensional and contact effects increase, which then decreases the mean thermal distance between the wires. As l/d increases, the mean thermal distance between wires also increases; hence its competition with k^* in the correlation.

The correlation of the mean gap should be used with a form of equation (8) in which the contact area fraction is set to zero

$$k_e^*\Big|_{\omega \approx 1} = 1 + \frac{(1-\phi)}{(1-\bar{\delta}^*)}\left[\frac{k^*}{1+\bar{\delta}^*(k^*-1)} - 1\right] \qquad (20)$$

Because of its functional form, equation (20) is not very sensitive to the values of the mean gap calculated by equation (19). As a result, the effective conductivity is predicted within 9 percent when the packing number is unity. For the case of $\omega > 1$, equation (9) can be used with the result above.

The effects of possible heat loss should be considered when making comparisons of data and theory. The estimated heat loss increases by approximately 5 percent as the packing number varies from $\omega = 1.0$ to $\omega = 1.3$. This suggests that the slope of the data would agree more closely with theory if measured values for heat loss were available to correct the data.

Conclusions

Some suggestions for the design of heat pipe wicks now may be given. Since the conductivity enhancement is dependent upon α, β, and k^*, these are the parameters under greatest consideration.

First, the greatest enhancement occurs when α/β (or l/d) approaches 2. This also corresponds to the lowest ϕ value. Based on this observation, mesh number and wire diameter must both be considered to optimize enhancement.

The greatest enhancement occurs when $k^* > 100$. This may be an important consideration when selecting materials. For example, if water is the working fluid of a particular heat pipe, copper, aluminum alloy, and brass cloths will all produce about the same conductivity enhancement assuming their geometries are the same. Therefore the most convenient and inexpensive material may be chosen. However, combinations which have higher values of k^* will generally have somewhat greater enhancement.

It must be kept in mind that the geometric parameters which effect conductivity also influence fluid flow in the cloth. An appropriate balance of flow properties and conductivity enhancement must be considered.

Finally, if it is possible to exert mechanical pressure on the wick such that the porosity and permeability are not substantially reduced, the conductivity enhancement may increase by as much as 400 percent or more due to metallic contact (Van-Sant and Malet, 1961).

The following conclusions can be drawn from the theoretical and experimental analyses performed on metal cloth heat pipe wicks:

1 The mean-gap-conductance model satisfactorily predicts layered cloth wick effective conductivity for packing numbers greater than unity.

2 The mean-gap-conductance model predicts a theoretical maximum and minimum possible effective conductivity enhancement. The maximum value is approached as the ratio of the wire thickness to mesh cell size approaches 1/2 and $k^* > 100$. This shows that the dimensional effective conductivity is limited primarily by the fluid conductivity.

3 For packing numbers less than unity, contact conductances and correlations for contact parameters become dominant factors in predicting effective conductivity.

Acknowledgments

This work was cosponsored by the Air Force Office of Scientific Research and the Nuclear/Thermal Technology Group of the Air Force Aero Propulsion Laboratory.

References

Chi, S. W., 1976, *Heat Pipe Theory and Practice*, McGraw-Hill, p. 47.

Cividino, S., Yovanovich, M. M., and Fletcher, L. S., 1974, "A Model for Predicting the Joint Conductance of a Woven Wire Screen Contacting Two Solids," *Progress in Astronautics and Aeronautics*, Vol. 39, pp. 111–128.

Gorring, R. L., and Churchill, S. W., 1961, "Thermal Conductivity of Heterogeneous Materials," *Chemical Engineering Progress*, Vol. 57, pp. 53–59.

Kitscha, W. W., 1982, "Thermal Resistance of Sphere-Flat Contacts," MaSc Thesis, Department of Mechanical Engineering, University of Waterloo, Waterloo, Ontario, Canada.

O'Callaghan, P. W., Jones, A. M., and Probert, S. D., 1975, "The Thermal Behavior of Gauzes as Interfacial Inserts Between Solids," *Journal Mechanical Engineering Science*, Vol. 17, No. 4, pp. 233–236.

Ogniewicz, Y., 1975, "Conduction in Basic Cells of Packed Beds," MaSc Thesis, Department of Mechanical Engineering, University of Waterloo, Waterloo, Ontario, Canada.

Phillips, J. R., 1986, "Thermal Conductivity of Layered Cloth Heat Pipe Wicks," MS Project Report, Washington State University, Department of Mechanical Engineering, Pullman, WA.

Ponnappan, R., and Mahefkey, E. T., 1983, "Development of a Double-Wall Artery High-Capacity Heat Pipe," *Progress in Astronautics and Aeronautics*, Vol. 86, pp. 202–221.

Tien, C. L., 1968, "A Correlation for Thermal Contact Conductance of Nominally Flat Surfaces in a Vacuum," *Proceedings of 7th Thermal Conductivity Conference*, U.S. Bureau of Standards, pp. 755–759.

VanSant, J. H., and Malet, J. R., 1975, "Thermal Conductivity of Some Heat Pipe Wicks," *Letters in Heat and Mass Transfer*, Vol. 2, pp. 199–206.

Yovanovich, M. M., 1982, "Thermal Contact Correlations," *Progress in Astronautics and Aeronautics*, Vol. 83, pp. 83–95.

Yovonovich, M. M., DeVaal, J., and Hegazy, A. H., 1982, "A Statistical Model to Predict Thermal Gap Conductance Between Conforming Rough Surfaces," AIAA/ASME Third Joint Thermophysics, Fluids, Plasma and Heat Transfer Conference, St. Louis, MO, June 7–11, AIAA Paper No. 82-0888.

Journal of Heat Transfer

Technical Notes

This section contains shorter technical papers. These shorter papers will be subjected to the same review process as that for full papers.

Material and Load Optimization by the Adjoint Variable Method

R. A. Meric[1]

Introduction

The adjoint variable method (AVM) was originally borrowed from the optimal control theory (Lions, 1971; Bryson and Ho, 1975) and extensively applied in various "inverse" problems (e.g., identification, estimation, optimization, etc.) of such diverse fields as structural systems (Haug et al., 1986) water resources (Carrera and Neuman, 1986), thermal systems (Haftka, 1981), history matching of petroleum reservoirs (Dogru and Seinfeld, 1981), nuclear reactor assessments (Oblow, 1978), and others.

The present study is concerned with the static optimization of material parameters and loading functions of heat conducting solids. The sensitivity analysis (SA), i.e., evaluation of the variations of system's response functionals with respect to changes in decision variables, is performed by the AVM. The present problem is similar to certain structural optimization problems in which the decision variables appear explicitly in the governing equations (i.e., as coefficients of the state variables), and where the variations are taken on a fixed domain. Shape optimization problems, on the other hand, involve variations on varying domains and need further techniques of design optimization (compare the material derivative concept of Haug et al., 1986).

After performing the SA for a general performance criterion (GPC), i.e., basically an integral functional, by the AVM, a two-dimensional sample problem is solved numerically by the boundary element method (BEM) and nonlinear programming methods.

Primary Problem

Under steady-state conditions, the thermal conduction in a nonhomogeneous, anisotropic solid body of arbitrary geometry in three-dimensions is governed by the following equilibrium equation:

$$\text{in } D\text{: } -q_{i,i} + a(T, u) = 0 \tag{1}$$

where D is the fixed domain of interest; q_i is the heat flux vector; $a(T, u)$ is the distributed heat source function, the functional form of which is given in the problem. It is noted that the heat source may be a nonlinear function of temperature T and a space-dependent controllable function u, in general.

Temperature and heat flux conditions are taken on the portions S_T and S_q of the boundary S

$$\text{on } S_T\text{: } T = \theta \tag{2}$$

$$\text{on } S_q\text{: } q_n \equiv q_i n_i = b(T, v) \tag{3}$$

where θ is the controllable temperature on S_T; q_n represents the outer boundary heat flux; n_i is the unit vector normal to the boundary; the functional form of $b(T, v)$ is prescribed; v may represent a space-dependent controllable function on S_q.

The second and third kind of boundary conditions are encompassed in condition (3). The radiation type of boundary condition is also allowed as b may be taken as a nonlinear function of T. The controllable functions v may be visualized as the boundary heat flux, heat transfer coefficient, ambient temperature, or emissivity coefficient according to the needs of a specific problem at hand.

Fourier's law of heat conduction is given in the form

$$q_i = -k_{ij}(T, k_0)T_{,j} \tag{4}$$

where k_{ij} is the (symmetric) thermal conductivity tensor which is a function of T and a space dependent (controllable) function k_0.

General Performance Criterion

In the present material and load optimization problem, T represents the primary (system state) variable, while the functions k_0, u, θ, and v are taken as the decision variables. A general performance criterion (GPC) is now chosen as follows:

$$I = \int_D f(x_i, T, q_i, k_0, u)dD + \int_{S_T} g(x_i, \theta, q_n)dS + \int_{S_q} h(x_i, T, q_n, v)dS \tag{5}$$

where I is the GPC, representing either the objective function of optimization to be minimized, or an equality/inequality behavioral constraint to be satisfied; x_i are the Cartesian coordinates; f, g, and h are continuous and differentiable functions with respect to their arguments. It is assumed that local constraints may be converted into equivalent integral functions (Chun and Haug, 1978). Side constraints (explicit in character) may also be present in the problem, involving lower and upper bounds on the decision variables.

Sensitivity Analysis

The AVM is basically a variational technique using Lagrange multiplier (adjoint) functions. Incorporating the first variational forms of equations (1)–(4) into (5), and using integration by parts, it may be shown that (Meric, 1984–1986b) the first variation of I is explicitly given in terms of the variations of the decision variables as follows:

[1]Department of Applied Mathematics, Research Institute for Basic Sciences, TUBITAK, Gebze, Kocaeli, Turkey.

Contributed by the Heat Transfer Division for publication in the JOURNAL OF HEAT TRANSFER. Manuscript received by the Heat Transfer Division February 10, 1986.

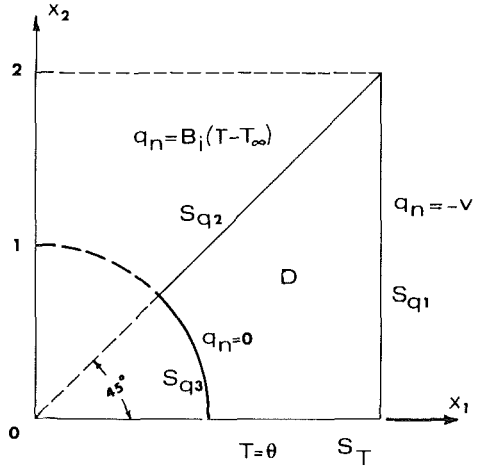

Fig. 1 Sample problem geometry and boundary conditions

$$\delta I = \int_D \left\{ \left[\frac{\partial f}{\partial k_0} - \frac{\partial k_{ij}}{\partial k_0} T_{,i} \left(T^*_{,j} + \frac{\partial f}{\partial q_j} \right) \right] \delta k_0 + \left(\frac{\partial f}{\partial u} + \frac{\partial a}{\partial u} T^* \right) \delta u \right\} dD + \int_{S_T} \left(\frac{\partial g}{\partial \theta} + q_n^* \right) \delta\theta \, dS + \int_{S_q} \left[\frac{\partial h}{\partial v} + \frac{\partial b}{\partial v} \left(\frac{\partial h}{\partial q_n} - T^* \right) \right] \delta v \, dS \tag{6}$$

The adjoint problem corresponding to I is defined by the following:

$$\text{in } D: \quad -q^*_{i,i} - \frac{\partial k_{ij}}{\partial T} T_{,i} \left(T^*_{,j} + \frac{\partial f}{\partial q_j} \right) + \frac{\partial f}{\partial T} + \frac{\partial a}{\partial T} T^* = 0 \tag{7}$$

$$\text{on } S_T: \quad T^* = \frac{\partial g}{\partial q_n} \tag{8}$$

$$\text{on } S_q: \quad q_n^* = q_i^* n_i = \frac{\partial b}{\partial T} \left(T^* - \frac{\partial h}{\partial q_n} \right) - \frac{\partial h}{\partial T} \tag{9}$$

and

$$q_i^* = -k_{ij} \left(T^*_{,j} + \frac{\partial f}{\partial q_j} \right) \tag{10}$$

where T^* and q_i^* are the adjoint temperature and heat flow vectors, respectively.

Evaluation of δI requires the solution of both the primary and adjoint problems. It is also noted that the SA must be performed for the objective function and for each of the integral constraints present in a specific optimization problem.

Sample Problem

A two-dimensional load optimization problem for a homogeneous, isotropic solid body with no heat sources is analyzed numerically. The primary problem is given in terms of nondimensional quantities as follows:

$$\text{in } D: \quad T_{,ii} = 0 \tag{11}$$

$$\text{on } S_T: \quad T = \Theta \tag{12}$$

$$\text{on } S_{q1}: \quad q_n = -v \tag{13}$$

$$\text{on } S_{q2}: \quad q_n = \text{Bi}(T - T_\infty) \tag{14}$$

$$\text{on } S_{q3}: \quad q_n = 0 \tag{15}$$

where the problem domain and boundary conditions are shown in Fig. 1; Θ, Bi, and T_∞ are given problem parameters. The space-dependent function v constitutes the decision variable, which represents the applied boundary heat flux on S_{q1}.

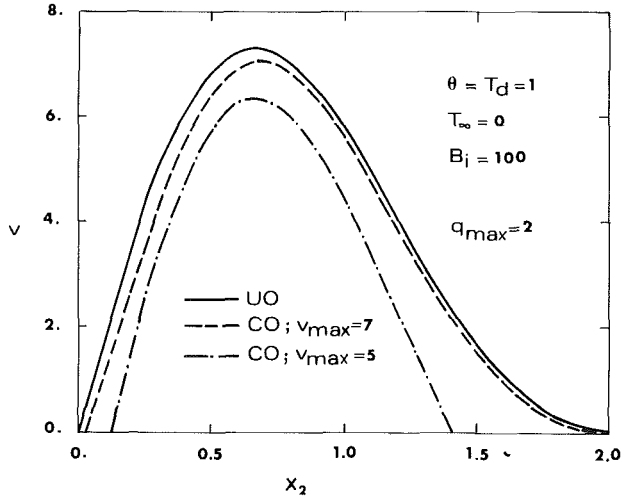

Fig. 2 Optimal boundary heat flux on S_{q1}, v, as a function of x_2 for $q_{max} = 2$ (legend: UO = unconstrained optimization, CO = constrained optimization)

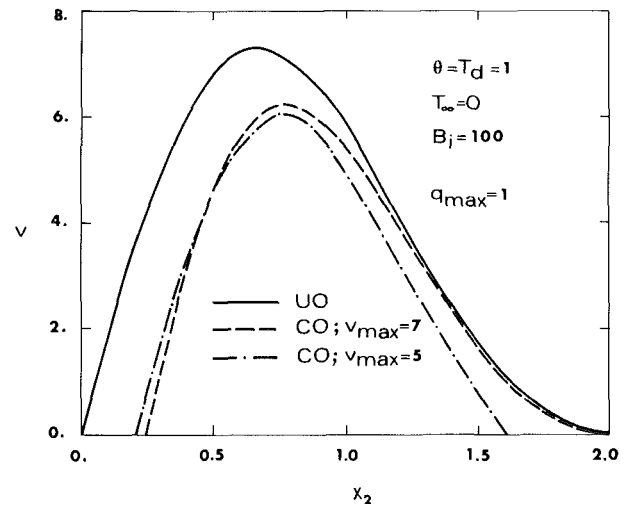

Fig. 3 Optimal boundary heat flux on S_{q1}, v, as a function of x_2 for $q_{max} = 1$ (legend: UO = unconstrained optimization, CO = constrained optimization)

The optimization problem is defined as:

$$\text{minimize } J = \frac{1}{2} \int_{S_{q3}} (T - T_d)^2 dS \tag{16}$$

$$\text{Subject to } \psi_1 = v_{\max} - \int_{S_{q1}} v \, dS \geq 0 \tag{17}$$

$$\psi_2 = q_{\max} - \int_{S_T} q_n \, dS \geq 0 \tag{18}$$

$$v \geq 0 \tag{19}$$

where T_d, $v_{\max}$, and $q_{\max}$ are problem parameters.

The variation of ψ_1 is directly given in terms of δv from equation (17), while the SA is performed for J and ψ_2.

Numerical Method of Solution and Results

The primary and adjoint problems and discretized in space by the BEM (Banerjee and Butterfield, 1981) using constant elements. Starting from an initial guess for the discretized decision variable v, the minimization of J subject to the constraints is then achieved by means of nonlinear programming methods (NAG Library, 1984). The problem parameters were fixed as $\Theta = T_d = 1$; $T_\infty = 0$, and Bi = 100.

An unconstrained optimization (UO), with no constraints

present, was first done by the conjugate gradient method of optimization, providing an initial estimate of v for constrained optimization (CO). The CO was then performed by a sequential augmented Lagrangian method.

Figures 2 and 3 depict the optimal decision variable v as a function of x_2 coordinate for various values of v_{max} and q_{max}. Both UO and CO results are plotted in the figures in order to show the effects of the constraints (17)–(19).

Conclusions

The following concluding remarks can be made:

1 The adjoint problem is linear in terms of T^*, although the primary problem may be nonlinear in T.

2 A continuous variable approach is adopted for the SA, i.e., optimization is performed after discretization, but not vice versa (Haftka, 1981).

3 The AVM of SA can be applied to systems described by time-dependent, integro-differential equations, as well.

4 Varying domain problems (i.e., shape optimization or identification problems) need further techniques for the SA besides the AVM (Haug et al., 1986; Meric, 1986b). However, if the decision variables are simply shape functions appearing explicitly in the equations, then the AVM is sufficient for the SA.

References

Banerjee, P. K., and Butterfield, R., 1981, *Boundary Element Methods in Engineering Science*, McGraw-Hill, New York.

Bryson, A. E., and Ho, Y. C., 1975, *Applied Optimal Control*, Wiley, New York.

Carrera, J., and Neuman, S. P., 1986, "Estimation of Aquifer Parameters Under Transient and Steady State Conditions: 2. Uniqueness, Stability, and Solution Algorithms," *Water Resources Research*, Vol. 22, pp. 211–227.

Chun, Y. W., and Haug, E. J., 1978, "Two-Dimensional Shape Optimal Design," *Int. J. Numer. Meths. Eng.*, Vol. 13, pp. 311–336.

Dogru, A., and Seinfeld, J., 1981, "Comparison of Sensitivity Coefficient Calculation Methods in Automatic History Matching," *Soc. Pet. Eng. J.*, Vol. 21, pp. 551–557.

Haftka, R. T., 1981, "Techniques for Thermal Sensitivity Analysis," *Int. J. Numer. Meths. Eng.*, Vol. 17, pp. 71–80.

Haug, E. J., Choi, K. K., and Komkov, V., 1986, *Design Sensitivity Analysis of Structural Systems*, Academic Press, New York.

Lions, J. L., 1971, *Optimal Control of Systems Governed by Partial Differential Equations*, Springer-Verlag, Berlin.

Meric, R. A., 1984, "Boundary Elements for Static Optimal Heating of Solids," ASME JOURNAL OF HEAT TRANSFER, Vol. 106, pp. 876–880.

Meric, R. A., 1985, "Optimization of Thermal Conductivities of Iostropic and Orthotropic Solids," ASME JOURNAL OF HEAT TRANSFER, Vol. 107, pp. 508–512.

Meric, R. A., 1986a, "Optimal Thermal Insulation by the Boundary Element Method," *Numer. Heat Transfer*, Vol. 9, pp. 163–182.

Meric, R. A., 1986b, "Boundary Elements in Shape Optimization of Thermoelastic Solids," *Proc. NATO Advanced Study Institute on Computer Aided Optimal Design: Structural and Mechanical Systems*, Troia, Portugal, Vol. 2, pp. 215–227.

Oblow, E., 1978, "Sensitivity Theory for Reactor Thermal Hydraulic Problems," *Nucl. Sci. Eng.*, Vol. 68, pp. 322–337.

Design Methodology for a Counter-current Falling Film Evaporative Condenser

A. T. Wassel[1] and A. F. Mills[2]

Nomenclature

b = mean half-channel width, m
C_{fG} = gas phase skin friction coefficient
C_p = specific heat, J/kg K
g = gravitational acceleration, m/s^2
h = heat transfer coefficient, W/m^2 K
$\hat{h}$ = specific enthalpy, J/kg
$\hat{h}_{fg}$ = latent heat of vaporization, J/kg
k = thermal conductivity, W/(m K)
K = mass transfer coefficient, kg/(m^2 s)
m = mass fraction
$\dot{m}$ = mass flow rate, kg/s
n_1 = mass flux, kg/(m^2 s)
N = number of channels
P = static pressure, N/m^2 = Pa
Pr = Prandtl number
q = heat flux, W/m^2
Re = Reynolds number
Sc = Schmidt number
T = temperature, K
u = velocity, m/s
W = channel depth, m
z = exchanger running length measured from the top, m
β_m = mass transfer driving force
Γ = liquid film mass flow rate per unit depth, kg/(s m)
δ = film thickness, m
μ = dynamic viscosity, N s/m^2 = Pa s
ν = kinematic viscosity, m^2/s
ρ = fluid density, kg/m^3
σ = surface tension, N/m

Subscripts

atm = atmospheric
e = evaporation
G = gas phase
L = liquid phase
L, N = liquid flow rate per channel
m = mass transfer
s = s-surface
sat = saturation
w = wall
1, 2 = water vapor, noncondensable air

Superscripts

$\hat{}$ = specific property
$\cdot$ = corrected for high mass transfer rate effects
c = condenser

Introduction

Direct contact simultaneous heat and mass transfer processes involve at least two phases and two chemical species. Thus, analysis is inherently complex owing to the number of conservation equations to be solved, the nonlinear coupling of heat and mass transfer through the saturation vapor pressure relationship, and the dependence of properties on both temperature and composition. Given the present stage of development in the use of computers by engineers, it is suggested that the *minimum* level of approach should involve simultaneous solution of one-dimensional forms of the governing conservation equations using appropriate numerical methods. In this note we give, as an example, the analysis of a counter-current falling film evaporative condenser. In addition, some results of parametric design calculations are presented, and the essential features explained.

Figure 1 shows a schematic of a flow channel in the unit. Counter-current film condensation on the condenser side is coupled, through stainless steel plates, to counter-current film evaporation into air on the evaporator side. The water film on the evaporator side is in turbulent flow ($Re_L > 1800$), while the condensate film has laminar, wavy-laminar, and turbulent

[1]Science Applications International Corporation, Hermosa Beach, CA; Mem. ASME.

[2]University of California at Los Angeles, Los Angeles, CA; Assoc. Mem. ASME.

Contributed by the Heat Transfer Division for publication in the JOURNAL OF HEAT TRANSFER. Manuscript received by the Heat Transfer Division July 12, 1984.

present, was first done by the conjugate gradient method of optimization, providing an initial estimate of v for constrained optimization (CO). The CO was then performed by a sequential augmented Lagrangian method.

Figures 2 and 3 depict the optimal decision variable v as a function of x_2 coordinate for various values of v_{max} and q_{max}. Both UO and CO results are plotted in the figures in order to show the effects of the constraints (17)–(19).

Conclusions

The following concluding remarks can be made:

1 The adjoint problem is linear in terms of T^*, although the primary problem may be nonlinear in T.

2 A continuous variable approach is adopted for the SA, i.e., optimization is performed after discretization, but not vice versa (Haftka, 1981).

3 The AVM of SA can be applied to systems described by time-dependent, integro-differential equations, as well.

4 Varying domain problems (i.e., shape optimization or identification problems) need further techniques for the SA besides the AVM (Haug et al., 1986; Meric, 1986b). However, if the decision variables are simply shape functions appearing explicitly in the equations, then the AVM is sufficient for the SA.

References

Banerjee, P. K., and Butterfield, R., 1981, *Boundary Element Methods in Engineering Science*, McGraw-Hill, New York.

Bryson, A. E., and Ho, Y. C., 1975, *Applied Optimal Control*, Wiley, New York.

Carrera, J., and Neuman, S. P., 1986, "Estimation of Aquifer Parameters Under Transient and Steady State Conditions: 2. Uniqueness, Stability, and Solution Algorithms," *Water Resources Research*, Vol. 22, pp. 211–227.

Chun, Y. W., and Haug, E. J., 1978, "Two-Dimensional Shape Optimal Design," *Int. J. Numer. Meths. Eng.*, Vol. 13, pp. 311–336.

Dogru, A., and Seinfeld, J., 1981, "Comparison of Sensitivity Coefficient Calculation Methods in Automatic History Matching," *Soc. Pet. Eng. J.*, Vol. 21, pp. 551–557.

Haftka, R. T., 1981, "Techniques for Thermal Sensitivity Analysis," *Int. J. Numer. Meths. Eng.*, Vol. 17, pp. 71–80.

Haug, E. J., Choi, K. K., and Komkov, V., 1986, *Design Sensitivity Analysis of Structural Systems*, Academic Press, New York.

Lions, J. L., 1971, *Optimal Control of Systems Governed by Partial Differential Equations*, Springer-Verlag, Berlin.

Meric, R. A., 1984, "Boundary Elements for Static Optimal Heating of Solids," ASME JOURNAL OF HEAT TRANSFER, Vol. 106, pp. 876–880.

Meric, R. A., 1985, "Optimization of Thermal Conductivities of Iostropic and Orthotropic Solids," ASME JOURNAL OF HEAT TRANSFER, Vol. 107, pp. 508–512.

Meric, R. A., 1986a, "Optimal Thermal Insulation by the Boundary Element Method," *Numer. Heat Transfer*, Vol. 9, pp. 163–182.

Meric, R. A., 1986b, "Boundary Elements in Shape Optimization of Thermoelastic Solids," *Proc. NATO Advanced Study Institute on Computer Aided Optimal Design: Structural and Mechanical Systems*, Troia, Portugal, Vol. 2, pp. 215–227.

Oblow, E., 1978, "Sensitivity Theory for Reactor Thermal Hydraulic Problems," *Nucl. Sci. Eng.*, Vol. 68, pp. 322–337.

Design Methodology for a Counter-current Falling Film Evaporative Condenser

A. T. Wassel[1] and A. F. Mills[2]

Nomenclature

b = mean half-channel width, m
C_{fG} = gas phase skin friction coefficient
C_p = specific heat, J/kg K
g = gravitational acceleration, m/s^2
h = heat transfer coefficient, W/m^2 K
$\hat{h}$ = specific enthalpy, J/kg
$\hat{h}_{fg}$ = latent heat of vaporization, J/kg
k = thermal conductivity, W/(m K)
K = mass transfer coefficient, kg/(m^2 s)
m = mass fraction
$\dot{m}$ = mass flow rate, kg/s
n_1 = mass flux, kg/(m^2 s)
N = number of channels
P = static pressure, N/m^2 = Pa
Pr = Prandtl number
q = heat flux, W/m^2
Re = Reynolds number
Sc = Schmidt number
T = temperature, K
u = velocity, m/s
W = channel depth, m
z = exchanger running length measured from the top, m
β_m = mass transfer driving force
Γ = liquid film mass flow rate per unit depth, kg/(s m)
δ = film thickness, m
μ = dynamic viscosity, N s/m^2 = Pa s
ν = kinematic viscosity, m^2/s
ρ = fluid density, kg/m^3
σ = surface tension, N/m

Subscripts

atm = atmospheric
e = evaporation
G = gas phase
L = liquid phase
L, N = liquid flow rate per channel
m = mass transfer
s = s-surface
sat = saturation
w = wall
1, 2 = water vapor, noncondensable air

Superscripts

$\hat{}$ = specific property
$\cdot$ = corrected for high mass transfer rate effects
c = condenser

Introduction

Direct contact simultaneous heat and mass transfer processes involve at least two phases and two chemical species. Thus, analysis is inherently complex owing to the number of conservation equations to be solved, the nonlinear coupling of heat and mass transfer through the saturation vapor pressure relationship, and the dependence of properties on both temperature and composition. Given the present stage of development in the use of computers by engineers, it is suggested that the *minimum* level of approach should involve simultaneous solution of one-dimensional forms of the governing conservation equations using appropriate numerical methods. In this note we give, as an example, the analysis of a counter-current falling film evaporative condenser. In addition, some results of parametric design calculations are presented, and the essential features explained.

Figure 1 shows a schematic of a flow channel in the unit. Counter-current film condensation on the condenser side is coupled, through stainless steel plates, to counter-current film evaporation into air on the evaporator side. The water film on the evaporator side is in turbulent flow ($Re_L > 1800$), while the condensate film has laminar, wavy-laminar, and turbulent

[1]Science Applications International Corporation, Hermosa Beach, CA; Mem. ASME.

[2]University of California at Los Angeles, Los Angeles, CA; Assoc. Mem. ASME.

Contributed by the Heat Transfer Division for publication in the JOURNAL OF HEAT TRANSFER. Manuscript received by the Heat Transfer Division July 12, 1984.

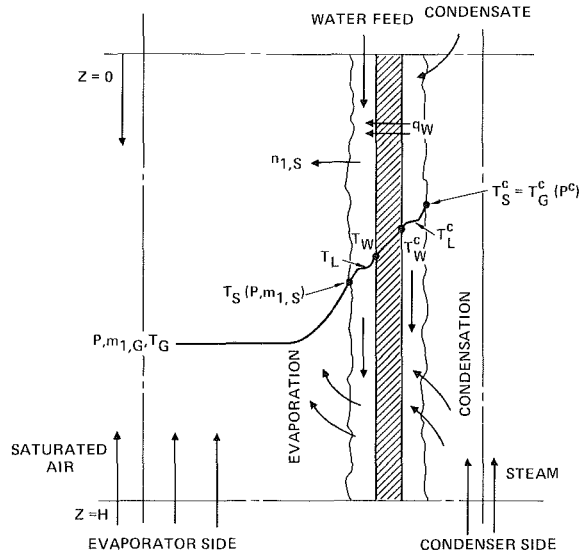

Fig. 1 Schematic of temperature profile between evaporator and condenser sides

flow regimes. The air flow is turbulent. Attractive features of the evaporative condenser are that it combines the functions of the condenser and a cooling tower in one unit, and it is able to provide required condensation rates over a wide range of ambient air conditions by varying the evaporator feed conditions. At all times, it is desirable to maximize the fraction of the latent heat of condensation transferred to the air stream and rejected to the atmosphere; the amount of mixing water required to maintain the evaporator feed at the desired temperature is then minimized. Of course, makeup water is required to replace the amount evaporated and to control scale formation. As in all exchanger designs, the objective is to minimize the plate area subject to constraints, the most important being as follows: (1) The air pressure drop and, hence, fan power must be minimized; and (2) the air velocity between the plates must not exceed entrainment or flooding limits.

Analysis

The steady-state one-dimensional equations governing conservation of mass, mass species, momentum, and energy for the gas phase are [1]

$$\frac{d}{dz}(\rho_G u_G) = n_{1,s}/(b-\delta) \tag{1}$$

$$\frac{d}{dz}(m_{1,G}\rho_G u_G) = n_{1,s}/(b-\delta) \tag{2}$$

$$\frac{d}{dz}(\rho_G u_G^2) = -\frac{dP}{dz} + \rho_G g - 0.5\ C_{fG}^{\cdot}\rho_G u_G |u_G|/(b-\delta) \tag{3}$$

$$\frac{d}{dz}(\rho_G u_G \hat{h}_G) = [h_G^{\cdot}(T_s - T_G) + n_{1,s}\hat{h}_{1,s}]/(b-\delta) \tag{4}$$

where a low-speed flow has been assumed. Equation (3) is rearranged to give the pressure gradient explicitly as

$$\frac{dP}{dz} = -\rho_G u_G \frac{du_G}{dz} - [u_G n_{1,s} + 0.5\ C_{fG}^{\cdot}\rho_G u_G |u_G|]/(b-\delta) + \rho_G g \tag{5}$$

The mass and energy conservation equations for the evaporator liquid phase are

$$\frac{d\Gamma}{dz} = -n_{1,s} \tag{6}$$

$$\Gamma C_{PL}\frac{dT_L}{dz} = -h_L^{\cdot}(T_L - T_s) + q_w \tag{7}$$

Energy conservation for the condensate film requires that

$$\frac{d\Gamma^c}{dz} = \frac{q_w}{\hat{h}_{fg}} = \frac{T_G^c - T_L}{(1/h_L^c + \delta_w/k_w + 1/h_w)h_{fg}} \tag{8}$$

where it has been assumed that the steam is saturated, and subcooling of the condensate is negligible. In addition, the pressure is assumed constant along the condenser.

The water vapor mass flux at the liquid-gas interface in the evaporator is given by

$$n_{1,s} = K_G^{\cdot}\beta_m; \qquad \beta_m = (m_{1,G}^* - m_{1,s})/(m_{1,s} - 1) \tag{9}$$

where $m_{1,G}^* = m_{1,G}$ if $m_{1,G} \le m_{1,G,\text{sat}}$ and $m_{1,G}^* = m_{1,G,\text{sat}}$ if $m_{1,G} > m_{1,G,\text{sat}}$. The interface energy balance indicates a coupled heat and mass transfer process

$$h_L^{\cdot}(T_L - T_s) = n_{1,s}\hat{h}_{fg} + h_G^{\cdot}(T_s - T_G) \tag{10}$$

where T_s is related to $m_{1,s}$ by the saturation vapor pressure relation and ideal gas laws. The gas phase temperature is obtained from the gas enthalpy using ideal mixture rules.

Correlations are required for the transfer coefficients $h_G^{\cdot}$, $K_G^{\cdot}$, $C_{fG}^{\cdot}$, h_L, h_w, and h_L^c. The gas side coefficients were obtained from zero mass transfer limit correlations and corrected for finite mass transfer rates using stagnant film theory [2, 3]

$$\phi^{\cdot}/\phi = (n_{1,s}/\phi)/[\exp(n_{1,s}/\phi) - 1] \tag{11}$$

where $\phi = K_G$, h_G/C_{P1}, and $\rho_G u_G\ C_{fG}/2$, respectively. The coefficient K_G was obtained from the correlation of Kafesgian et al. [4]

$$K_G/\rho_G u_G = 0.00814\ \mathrm{Re}_G^{-0.17}\ \mathrm{Re}_L^{0.15}\ \mathrm{Sc}^{-0.56} \tag{12}$$

and h_G by analogy replacing K_G with h_G/C_{PG} and Sc with Pr. Equation (12) is based on experimental data for $\mathrm{Re}_L < 1500$; no information is available for higher values of Re_L so that extrapolation is required. For the parameter range under consideration here, K_G and h_G given by equation (12) are about 75 percent higher than values given by the Dittus-Boelter correlation for smooth walls.

The coefficient C_{fG} was obtained from the correlation of Chien and Ibele [5]

$$C_{fG} = 0.92\times 10^{-7}\ \mathrm{Re}_G^{0.582}\ \mathrm{Re}_L^{0.705} \tag{13}$$

and is valid for $28{,}000 < \mathrm{Re}_G < 350{,}000$ and $250 < \mathrm{Re}_L < 22{,}000$. The coefficient h_L describes heat transfer from the bulk evaporator film to the liquid-gas interface, and was obtained from the mass transfer correlation of Won and Mills [6] by analogy. The coefficient h_w describes heat transfer from the wall to the bulk evaporator film and was based on the correlations given by Fujita and Ueda [7]. The coefficient h_L^c describes heat transfer across the condensate film and was obtained from correlations given by Edwards et al. [2] for the laminar, wavy-laminar, and turbulent regimes. The film thickness δ in the evaporator was calculated from the Brötz formula [8] for a turbulent film. All these liquid phase correlations ignore any effects of interfacial shear. Details of the correlations can be found in Wassel et al. [9], as can the data and methods used to evaluate thermophysical properties.

The evaporator is a countercurrent exchanger; the water inlet conditions are specified at the top, and the air flow inlet conditions are specified at the bottom. The air velocity, temperature, pressure, and water vapor mass fraction at the inlet ($z = H$) are given by $\rho_G u_G = \dot{m}_G/[2NW(b-\delta)]$, $T_{G,in} = T_{G,\text{atm}}$, $P_{in} = 1$ atm, and $m_{1,G,in} = m_{1,G,\text{sat}}\ (T_{G,in})$. The water inlet conditions (at $z = 0$) are given by specifying $\dot{m}_{L,in} = 2NW\Gamma_{in}$, and $T_{L,in}$. The ordinary differential equations (1), (2), and (4-8), were solved numerically using a fourth-order Adams-Moulton predictor-corrector method, and because of the split boundary conditions, iteration is required. The following cycle was adopted:

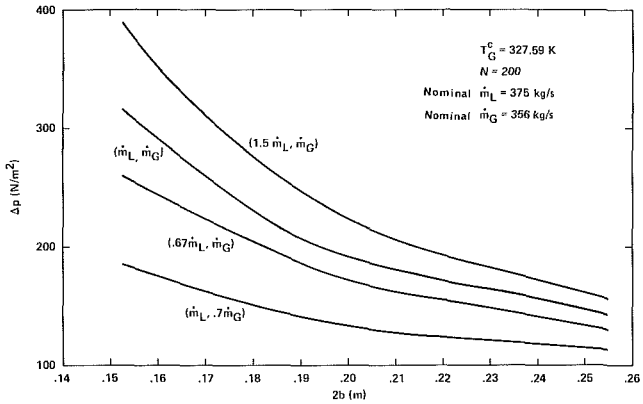

Fig. 2 Pressure drop across evaporator versus plate spacing: effect of $\dot{m}_{G,in}$ and $\dot{m}_{L,in}$

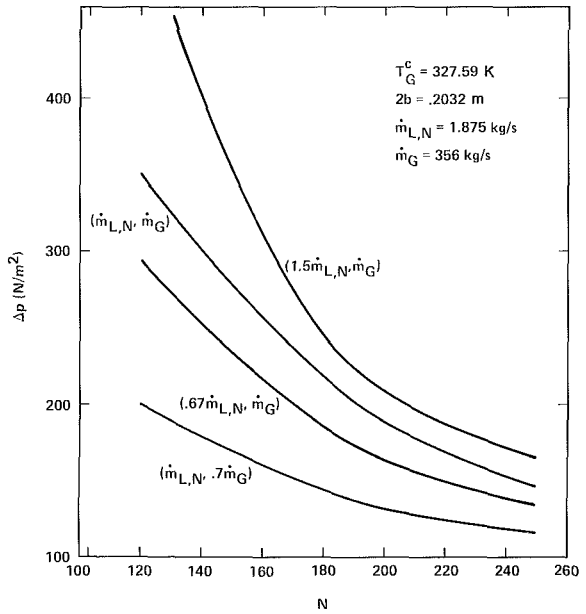

Fig. 3 Pressure drop across evaporator versus number of channels: effect of $\dot{m}_{G,in}$ and $\dot{m}_{L,in}$

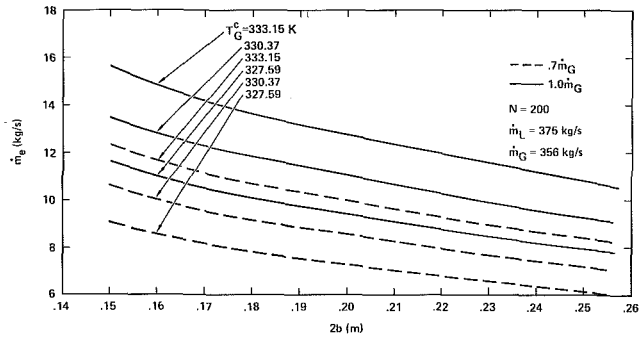

Fig. 4 Water evaporation rate versus spacing: effect of $\dot{m}_G$ and T_G^c

(*i*) An initial profile of gas phase conditions is assumed.
(*ii*) The evaporative flux is calculated along the exchanger.
(*iii*) The liquid and gas phase conservation equations are all integrated.
(*iv*) The profile of gas phase conditions is updated.
(*v*) The process is repeated until a converged solution is obtained. Typically, five to ten sweeps were required to obtain a converged solution [9].

Results and Discussion

Solutions were obtained for the following constant parameter values: W = 1.2192 m (4 ft), H = 7.3152 m (24 ft), $T_{G,in}$ = 299.82 K (80°F), P_{atm} = 1.01325 × 10^5 N/m² (1 atm), $m_{1,G,in}$ = 0.0217. Other parameters were varied as follows:

$2b$ = 0.1524–0.2540 m (6–10 in.)

N = 120–240

T_G^c = 327.59–335.93 K (130–145°F)

$T_{L,in}$ = 319.26–324.82 K (115–125°F)

$\dot{m}_{L,N} = \dot{m}_L/N$ = 1.25–2.813 kg/s (20–45 gpm)

$\dot{m}_{G,in}$ = 249.4–356 kg/s (455,000–650,000 CFM)

The corresponding ranges of inlet Reynolds numbers are Re_L = 3700–8300, Re_G = 110,000–200,000. The values of plate height and width correspond to commercially available units. In specifying the water inlet temperature, there is no attempt made to satisfy an overall system energy balance. In current applications of this exchanger, there is mixing water available at temperatures which allow the energy balance to be satisfied; the objective is to minimize the cooling demands on this water supply.

The pressure drop across the exchanger is shown in Fig. 2 as a function of plate spacing $2b$, with $\dot{m}_L$ and $\dot{m}_G$ as parameters. The pressure drop increases markedly as the plate spacing is reduced, and also increases with both air and water flow rates. These trends can be readily explained if one substitutes equation (13) in the viscous drag form of equation (5) and expresses the results in terms of geometric and flow parameters as

$$\Delta P \propto H\, \dot{m}_G^{2.582} \dot{m}_L^{0.705} (NW)^{-3.287} (2b)^{-3.0} \tag{15}$$

Equation (15) shows the strong dependence of ΔP on $2b$, $\dot{m}_G$ and, to a lesser extent, on $\dot{m}_L$. Figure 3 shows the pressure drop as a function of the number of channels N, with the flow rate per channel $\dot{m}_{L,N} = \dot{m}_L/N$ held constant. Equation (15) is accordingly rearranged as

$$\Delta P \propto H\, \dot{m}_G^{2.582} \dot{m}_{L,N}^{0.705}\, W^{-3.287} (2b)^{-3.0} N^{-2.582} \tag{16}$$

which is in line with the trends displayed.

Figure 4 shows the water evaporation rate which increases with decreasing plate spacing, and increasing air flow rate. These trends can be explained if it is recognized that the evaporation process is nearly gas-side controlled. Substituting equation (12) in equation (9) and writing the result in terms of the flow and geometric parameters

$$\dot{m}_e \propto \beta_{m,\text{avg}} H\, \dot{m}_G^{0.83} \dot{m}_L^{0.15} (2b)^{-1.0} (NW)^{0.02} \tag{17}$$

Equation (17) also shows that the evaporation rate increases with water flow rate. The increase in evaporation rate with increasing condensation saturation temperature is simply due to the higher values of T_s, $m_{1,s}$, and hence the mass transfer driving force β_m.

Figures 5 and 6 show the steam condensation rate which is seen to increase with decreasing plate spacing and water film inlet temperature, and with increasing water and air flow rates. A lower inlet water temperature or higher gas flow rate results in lower water film temperatures and hence higher heat fluxes and condensation rates. A higher water flow rate increases the film heat transfer coefficient and the capacity flow rate of the film to give an increased condensation rate.

Figure 7 shows the effects of flow and geometric parameters on the exit air velocity. The exit velocity increases as the plate spacing decreases for a fixed number of channels: There is but a small change in velocity along the exchanger so that $u_{G,out} \simeq u_{G,in} = \dot{m}_G/\rho_G(2b)NW$. Superimposed on Fig. 7 are the air velocities for the onset of flooding, as predicted by various flooding and entrainment correlations. It is clear that

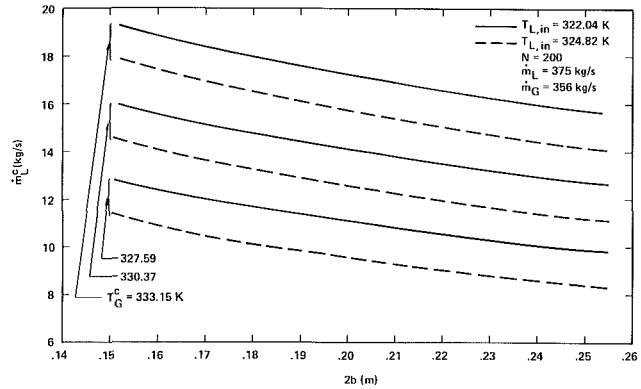

Fig. 5 Steam condensation rate versus plate spacing: effect of $T_{L,in}$ and T_G^c

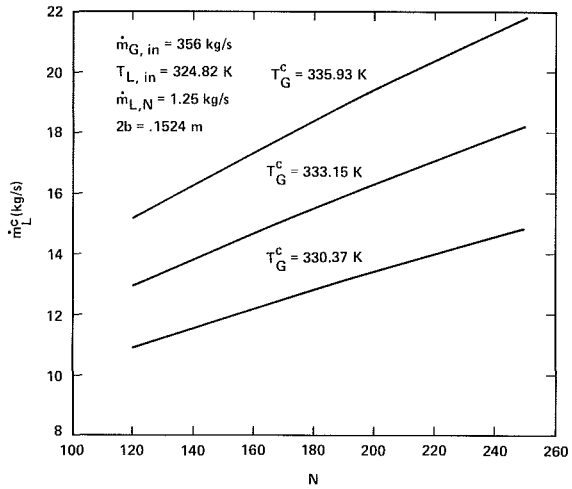

Fig. 6 Steam condensation rate versus number of channels: effect of T_G^c

avoidance of flooding does constrain the minimum plate spacing which can be used. However, it must be noted that the flooding correlations are based on experimental data for lower water flow rates than considered here, and extrapolation might be unwarranted.

Concluding Remarks

A design methodology for falling film simultaneous heat and mass exchangers has been demonstrated for an evaporative condenser, and some sample results displayed and discussed. The results show that it is advantageous to reduce the plate spacing to a minimum, subject to pressure drop and flooding limitations. Two of the most important factors influencing the results are the gas-side heat and mass transfer coefficients and the flooding criteria, both of which are obtained by extrapolation of correlations based on data at lower water flow rates than considered here. Thus, an experimental program to generate appropriate data is indicated.

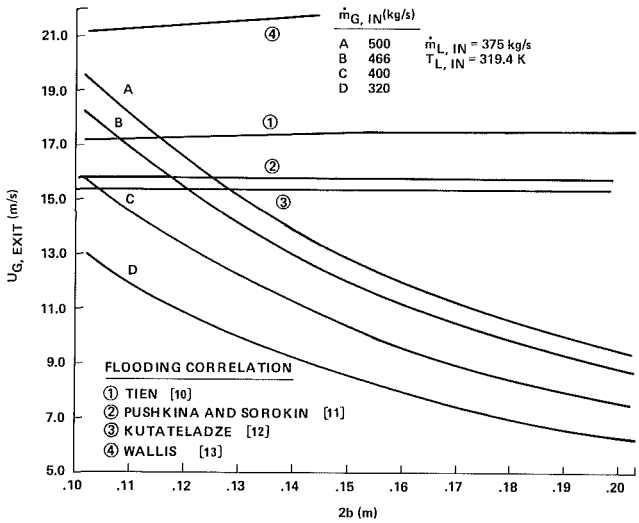

Fig. 7 Exit gas velocity versus plate spacing for four inlet gas mass flow rates

References

1 Wassel, A. T., and Mills, A. F., "Turbulent Falling Film Evaporators and Condensers for Open Cycle Ocean Thermal Energy Conversion," *Proceedings of the International Center for Heat and Mass Transfer 1981 and Advancement in Heat Exchangers*, Hemisphere, New York, 1983.

2 Bird, R. B., Stewart, W. E., and Lightfoot, E. N., *Transport Phenomena*, Wiley, New York, 1960.

3 Edwards, D. K., Denny, V. E., and Mills, A. F., *Transfer Processes*, 2nd ed., Hemisphere McGraw-Hill, New York, 1979.

4 Kafesgian, R., Plank, C. A., and Gerhard, E. R., "Liquid Flow and Gas Phase Mass Transfer in Wetted-Wall Towers," *AIChE Journal*, Vol. 7, 1961, pp. 463–466.

5 Chien, S. F., and Ibele, W., "Pressure Drop and Liquid Film Thickness of Two Phase Annular and Annular-Mist Flows," ASME JOURNAL OF HEAT TRANSFER, Vol. 86, 1964, pp. 29–36.

6 Won, Y. S., and Mills, A. F., "Correlation of the Effects of Viscosity and Surface Tension on Gas Absorption Rates Into Freely Falling Turbulent Liquid Films," *Int. J. Heat and Mass Transfer*, Vol. 25, 1982, pp. 222–229.

7 Fujita, T., and Ueda, T., "Heat Transfer to Falling Liquid Films and Film Breakdown—I. Subcooled Liquid Films," *Int. J. Heat Mass Transfer*, Vol. 21, 1978, pp. 97–108.

8 Brötz, W., "Uber die Vorausberschnung der Absorptions geschwindigwert von Gasen in Stramen der Flussigkeitschichten," *Chem. Eng. Tech.*, Vol. 26, 1954, pp. 470–478.

9 Wassel, A. T., Bugby, D. C., and Farr, J. L., Jr., "Design Analysis of Evaporative Condensers, Vol. 2," Science Applications Inc., report number SAI-083-83R-008LA, Los Angeles, CA, July 1982.

10 Chung, K. S., Liu, C. P., and Tien, C. L., "Flooding in Two Phase Counter-Current Flows—II. Experimental Investigations," *Physicochemical Hydrodynamics*, Vol. 1, 1980, pp. 209–220.

11 Pushkina, O. L., and Sorokin, Y. L., "Breakdown of Liquid Film Motion in Vertical Tubes," *Heat Transfer—Soviet Research*, Vol. 1, 1964, pp. 56–64.

12 McCarthy, G., and Lee, H. M., "Review of Entrainment Phenomena and Application to Vertical Two-Phase Counter Current Flooding," EPRI NP-1284, Electric Power Research Institute, Palo Alto, CA, Dec. 1979.

13 Wallis, G. B., *One-Dimensional Two-Phase Flow*, McGraw-Hill, New York, 1969.

Axial Heat Conduction Effects in Unsteady Forced Convection Along a Cylinder

C. D. Surma Devi,[1] M. Nagaraj,[2] and G. Nath[3]

Nomenclature

C_f = skin-friction coefficient
f = dimensionless stream function
f', g = dimensionless velocity and temperature, respectively

[1]Lecturer, Department of Mathematics, Bangalore Institute of Technology, Bangalore University, Bangalore 560004, India.

[2]Professor, Department of Mathematics, Central College, Bangalore University, Bangalore 560001, India.

[3]Professor, Department of Applied Mathematics, Indian Institute of Science, Bangalore 560012, India (to whom correspondence should be addressed).

Contributed by the Heat Transfer Division for publication in the JOURNAL OF HEAT TRANSFER. Manuscript received by the Heat Transfer Division April 23, 1985.

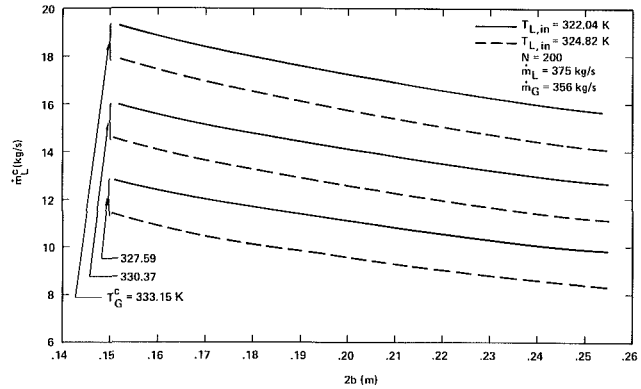

Fig. 5 Steam condensation rate versus plate spacing: effect of $T_{L,in}$ and T_G^c

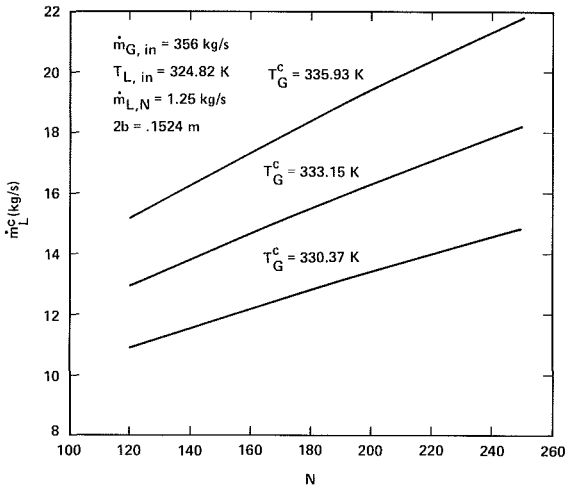

Fig. 6 Steam condensation rate versus number of channels: effect of T_G^c

avoidance of flooding does constrain the minimum plate spacing which can be used. However, it must be noted that the flooding correlations are based on experimental data for lower water flow rates than considered here, and extrapolation might be unwarranted.

Concluding Remarks

A design methodology for falling film simultaneous heat and mass exchangers has been demonstrated for an evaporative condenser, and some sample results displayed and discussed. The results show that it is advantageous to reduce the plate spacing to a minimum, subject to pressure drop and flooding limitations. Two of the most important factors influencing the results are the gas-side heat and mass transfer coefficients and the flooding criteria, both of which are obtained by extrapolation of correlations based on data at lower water flow rates than considered here. Thus, an experimental program to generate appropriate data is indicated.

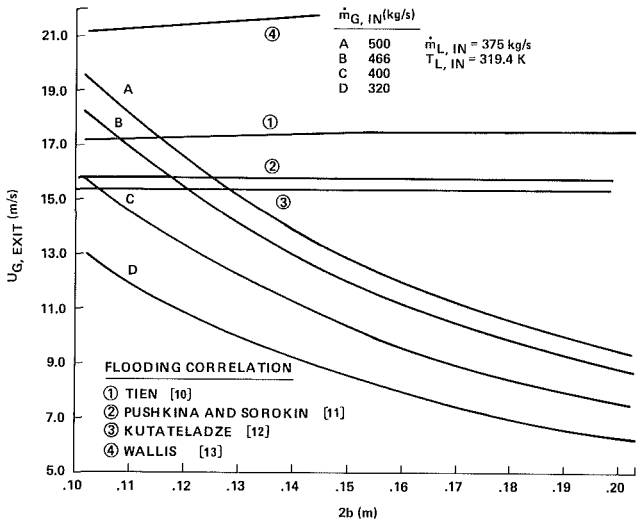

Fig. 7 Exit gas velocity versus plate spacing for four inlet gas mass flow rates

References

1 Wassel, A. T., and Mills, A. F., "Turbulent Falling Film Evaporators and Condensers for Open Cycle Ocean Thermal Energy Conversion," *Proceedings of the International Center for Heat and Mass Transfer 1981 and Advancement in Heat Exchangers*, Hemisphere, New York, 1983.

2 Bird, R. B., Stewart, W. E., and Lightfoot, E. N., *Transport Phenomena*, Wiley, New York, 1960.

3 Edwards, D. K., Denny, V. E., and Mills, A. F., *Transfer Processes*, 2nd ed., Hemisphere McGraw-Hill, New York, 1979.

4 Kafesgian, R., Plank, C. A., and Gerhard, E. R., "Liquid Flow and Gas Phase Mass Transfer in Wetted-Wall Towers," *AIChE Journal*, Vol. 7, 1961, pp. 463–466.

5 Chien, S. F., and Ibele, W., "Pressure Drop and Liquid Film Thickness of Two Phase Annular and Annular-Mist Flows," ASME JOURNAL OF HEAT TRANSFER, Vol. 86, 1964, pp. 29–36.

6 Won, Y. S., and Mills, A. F., "Correlation of the Effects of Viscosity and Surface Tension on Gas Absorption Rates Into Freely Falling Turbulent Liquid Films," *Int. J. Heat and Mass Transfer*, Vol. 25, 1982, pp. 222–229.

7 Fujita, T., and Ueda, T., "Heat Transfer to Falling Liquid Films and Film Breakdown—I. Subcooled Liquid Films," *Int. J. Heat Mass Transfer*, Vol. 21, 1978, pp. 97–108.

8 Brötz, W., "Uber die Vorausberschnung der Absorptions geschwindigwert von Gasen in Stramen der Flussigkeitschichten," *Chem. Eng. Tech.*, Vol. 26, 1954, pp. 470–478.

9 Wassel, A. T., Bugby, D. C., and Farr, J. L., Jr., "Design Analysis of Evaporative Condensers, Vol. 2," Science Applications Inc., report number SAI-083-83R-008LA, Los Angeles, CA, July 1982.

10 Chung, K. S., Liu, C. P., and Tien, C. L., "Flooding in Two Phase Counter-Current Flows—II. Experimental Investigations," *Physicochemical Hydrodynamics*, Vol. 1, 1980, pp. 209–220.

11 Pushkina, O. L., and Sorokin, Y. L., "Breakdown of Liquid Film Motion in Vertical Tubes," *Heat Transfer—Soviet Research*, Vol. 1, 1964, pp. 56–64.

12 McCarthy, G., and Lee, H. M., "Review of Entrainment Phenomena and Application to Vertical Two-Phase Counter Current Flooding," EPRI NP-1284, Electric Power Research Institute, Palo Alto, CA, Dec. 1979.

13 Wallis, G. B., *One-Dimensional Two-Phase Flow*, McGraw-Hill, New York, 1969.

Axial Heat Conduction Effects in Unsteady Forced Convection Along a Cylinder

C. D. Surma Devi,[1] M. Nagaraj,[2] and G. Nath[3]

Nomenclature

C_f = skin-friction coefficient
f = dimensionless stream function
f', g = dimensionless velocity and temperature, respectively

[1]Lecturer, Department of Mathematics, Bangalore Institute of Technology, Bangalore University, Bangalore 560004, India.

[2]Professor, Department of Mathematics, Central College, Bangalore University, Bangalore 560001, India.

[3]Professor, Department of Applied Mathematics, Indian Institute of Science, Bangalore 560012, India (to whom correspondence should be addressed).

Contributed by the Heat Transfer Division for publication in the JOURNAL OF HEAT TRANSFER. Manuscript received by the Heat Transfer Division April 23, 1985.

f''_w, g'_w = skin-friction and heat transfer parameters, respectively
k = thermal conductivity
Nu, Pr = Nusselt number and Prandtl number, respectively
q = heat transfer rate
r, x = radial and axial coordinates, respectively
R, Re_x = radius of cylinder and local Reynolds number, respectively
t, t^* = dimensional and dimensionless times, respectively
T = temperature
u, v = velocity components in x and r directions, respectively
U_∞, u_∞ = free-stream velocity at $t^* > 0$ and at $t^* = 0$, respectively
α = thermal diffusivity of the fluid
η, ξ = transformed coordinates
λ, μ, ν = axial heat conduction parameter, viscosity and kinematic viscosity, respectively
ρ, φ, ψ = density, function of t^*, and dimensional stream function, respectively
ω^* = frequency parameter

Subscripts

r, t, t^*, x, ξ = derivatives with respect to r, t, t^*, x, ξ, respectively
w, ∞ = conditions at the wall and in the free stream, respectively

Superscript

$'$ = derivatives with respect to η

Introduction

In convective heat transfer problems over surfaces involving moderate or high Prandtl numbers, the effect of axial heat conduction is small as compared to heat conduction normal to the surface. However, for fluids with very low Prandtl number, such as liquid metals, the axial heat conduction becomes significant and cannot be neglected. Heat transfer problems involving liquid metals are important in the heat exchanger of a liquid metal fast breeder reactor. The heat transfer for low Prandtl number fluids on flat plates and circular cylinders has been studied by several investigators [1-4]. However, these studies pertain to steady flows, but in most problems of practical interest, the flow may be unsteady.

The aim of the present analysis is to study the effect of the axial heat conduction on the unsteady incompressible laminar forced convective heat transfer of liquid metals along an isothermal circular cylinder in longitudinal flow when the free-stream velocity varies arbitrarily with time. The partial differential equations involving three independent variables have been solved numerically using an implicit finite-difference scheme. The particular cases of our results have been compared with the results available in the literature [4, 11-14].

Governing Equations

We consider a semi-infinite circular cylinder which is aligned longitudinally parallel to a time-dependent free-stream velocity. The surface and free-stream temperatures are constant. It is assumed that the Reynolds number is sufficiently high that the boundary-layer equations are valid, but the Prandtl number of the fluid is low enough that the axial heat conduction effect becomes significant. The viscous dissipation term is neglected as its effect is assumed to be small. All properties of the fluid are considered to be constant. Under the abovementioned assumptions, the boundary layer equations governing the unsteady incompressible laminar flow can be expressed as

$$u_x + r^{-1}(rv)_r = 0 \tag{1}$$

$$u_t + uu_x + vu_r = \nu r^{-1}(ru_r)_r \tag{2}$$

$$T_t + uT_x + vT_r = \alpha[T_{xx} + r^{-1}(rT_r)_r] \tag{3}$$

The initial and boundary conditions can be expressed as

$$u(x, r, 0) = u_i(x, r), \quad v(x, r, 0) = v_i(x, r), \quad T(x, r, 0) = T_i(x, r) \tag{4}$$

$$u(x, R, t) = v(x, R, t) = 0, \quad T(x, R, t) = T_w$$
$$u(x, \infty, t) = u_\infty \varphi(t^*), \quad T(x, \infty, t) = T_\infty \tag{5a}$$

$$u(0, r, t) = u_\infty \varphi(t^*), \quad T(0, r, t) = T_\infty, \quad r \geq R, \quad t \geq 0 \tag{5b}$$

$$T_x(x, r, t) = 0 \text{ for } x \to \infty, \quad r \geq R, \quad t \geq 0 \tag{5c}$$

Here the function φ is an arbitrary function of t^* having a continuous first derivative.

The condition (5b) implies that the velocity and thermal boundary layers begin with zero thickness at the leading edge of the cylinder ($x = 0$) and that the axial heat conduction upstream of the leading edge ($x < 0$) is neglected [4]. However, it has been shown by Seban and Bond [5] that for forced convection flow along a cylinder without axial heat conduction effect, the applicability of the solution is not restricted by the assumption of the boundary layer thickness at $x = 0$. Equation (5c) assumes the axial energy diffusion flux to be negligible far downstream. The present analysis, although based on somewhat unrealistic assumptions, is expected to provide satisfactory results except very near $x = 0$ when the Prandtl number is small [4].

Applying the following transformations

$$\xi = (4/R)(\nu x/u_\infty)^{1/2}, \quad \eta = (u_\infty/\nu x)^{1/2}(r^2 - R^2)/4R$$
$$t^* = (\nu/R^2)t, \quad u = r^{-1}\psi_r, \quad v = -r^{-1}\psi_x, \quad U_\infty = u_\infty \varphi(t^*) \tag{6a}$$
$$\psi(x, r, t) = R(\nu u_\infty x)^{1/2} \varphi(t^*) f(\xi, \eta, t^*)$$
$$g(\xi, \eta, t^*) = (T - T_\infty)/(T_w - T_\infty), \quad \lambda = \alpha/(u_\infty x) \tag{6b}$$

to equations (1) to (3), we find that equation (1) is satisfied identically and equations (2) and (3) reduce to

$$(1 + \xi\eta)f''' + (\xi + \varphi f)f'' - (\xi^2/4)[f'_{t^*} + \varphi^{-1}\varphi_{t^*}(f' - 2)] = \xi\varphi(f'f'_\xi - f''f_\xi) \tag{7}$$

$$\mathrm{Pr}^{-1}(1 + \xi\eta)g'' + (\mathrm{Pr}^{-1}\xi + \varphi f)g' - (\xi^2/4)g_{t^*} + \lambda(\eta^2 g'' + 3\eta g' - 2\xi\eta g'_\xi - \xi g_\xi + \xi^2 g_{\xi\xi}) = \xi(f'g_\xi - g'f_\xi) \tag{8}$$

The boundary conditions (5) can be expressed as

$$\left.\begin{aligned} &f = f' = 0, \quad g = 1 \quad \text{at} \quad \eta = 0, \quad \xi \geq 0 \\ &f' = 2, \quad g = 0 \quad \text{as} \quad \eta \to \infty, \quad \xi \geq 0 \\ &g_\xi = 0 \quad \text{as} \quad \xi \to \infty, \quad \eta \geq 0 \end{aligned}\right\} \quad \text{for } t^* \geq 0 \tag{9}$$

The initial conditions (i.e., the conditions at $t^* = 0$) can be obtained from equations (7) and (8) by setting

$$\varphi = 1, \quad \varphi_{t^*} = f'_{t^*} = g_{t^*} = 0 \quad \text{at } t^* = 0 \tag{10}$$

Table 1 Comparison of heat transfer parameter $-g'_w$ for $t^* = 0$

ξ	Pr	Present calculation			Chen and Lohman		
		$\lambda=0$	$\lambda=0.1$	$\lambda=0.2$	$\lambda=0$	$\lambda=0.1$	$\lambda=0.2$
0	0.03	0.1688	0.1814	0.1987	0.1689	0.1816	0.1989
1.0	0.03	0.3772	0.3906	0.4020	0.3736	0.3869	0.3983
2.0	0.03	0.5385	0.5531	0.5669	0.5350	0.5496	0.5633
3.0	0.03	0.6842	0.7004	0.7155	0.6790	0.6952	0.7102
4.0	0.03	0.8179	0.8352	0.8514	0.8136	0.8309	0.8470
0	0.003	0.0585	0.0623	0.0679	0.0587	0.0625	0.0680
1.0	0.003	0.2276	0.2327	0.2375	0.2257	0.2307	0.2355
2.0	0.003	0.3549	0.3610	0.3669	0.3528	0.3589	0.3647
3.0	0.003	0.4703	0.4776	0.4844	0.4673	0.4745	0.4812
4.0	0.003	0.5774	0.5856	0.5933	0.5747	0.5828	0.5904

The steady-state equations are now given by

$$(1+\xi\eta)f''' + (\xi+f)f'' = \xi(f'f'_\xi - f''f_\xi) \tag{11}$$

$$\mathrm{Pr}^{-1}(1+\xi\eta)g'' + (\mathrm{Pr}^{-1}\xi+f)g' + \lambda(\eta^2 g'' + 3\eta g' - 2\xi\eta g'_\xi - \xi g_\xi + \xi^2 g_{\xi\xi}) = \xi(f'g_\xi - g'f_\xi) \tag{12}$$

It may be remarked that the steady-state equations (11) and (12) are the same as those of Chen and Lohman [4] who solved them using the local nonsimilarity method [6, 7]. Furthermore, equations (11) and (12) for $\lambda = 0$ (i.e., without axial heat conduction effect) reduce to those of steady forced convection flow which has been studied by several investigators [6-11] who have used various approximate and exact methods. The comparison of the results obtained by these methods has been shown in [11]. Also our unsteady-state equations (7) and (8) for $\lambda = 0$ are identical to those studied by Reddy [12] using an implicit finite-difference scheme. It is also noted that $\xi = 0$ corresponds to the flat plate case and ξ represents the transverse curvature effect. Also, it provides a measure of the distance along the cylinder.

The skin friction and heat transfer coefficients can be expressed as

$$C_f = 2\tau_w/\rho u_\infty^2 = 2^{-1}\varphi(t^*)(\mathrm{Re}_x)^{-1/2} f''_w \tag{13a}$$

$$\mathrm{Nu} = x q_w/[k(T_w - T_\infty)] = 2^{-1}(\mathrm{Re}_x)^{1/2} g'_w$$

where

$$\tau_w = \mu(\partial u/\partial r)_{r=R},\ q_w = -k(\partial T/\partial r)_{r=R},\quad \mathrm{Re}_x = u_\infty x/\nu \tag{13b}$$

We have taken two types of time-dependent free-stream velocity distributions: (1) acceleration flow given by $\varphi(t^*) = 1+\epsilon t^{*2}$, $\epsilon > 0$ and (2) oscillating flow represented by $\varphi(t^*) = (1 + \epsilon_1 \cos \omega^* t^*)/(1+\epsilon_1)$, $\epsilon_1 > 0$.

Results and Discussion

It may be noted that we have solved the partial differential equations (7) and (8) with three independent variables, without making any approximation, by using an implicit finite-difference scheme described in [13]. Accordingly, the derivatives with respect to ξ and η in equations (7) and (8) have been replaced by a central difference formula and the derivatives with respect to time t^* by a backward difference formula [13]. Consequently, the partial differential equations (7) and (8) are reduced to a system of algebraic equations. Knowing the solution at the nth time step, we can obtain the solution at the $(n+1)$th time step. The above system of equations has been solved by an iterative technique (Gauss-Seidel method) which reduces considerably the computer storage requirement.

We have considered the effect of step sizes $\Delta\eta$, $\Delta\xi$, Δt^*, the edge of the boundary layer η_∞, and the maximum value of the axial distance ξ_∞ on the solution in order to optimize them. Consequently, we have taken $\Delta\eta = 0.125$, $\Delta\xi = 0.05$, $\Delta t^* = 0.1$, $12 \le \eta_\infty \le 25$, $\xi_\infty = 5$. The results presented here are independent of the step sizes η_∞ and ξ_∞, at least up to the fourth decimal place.

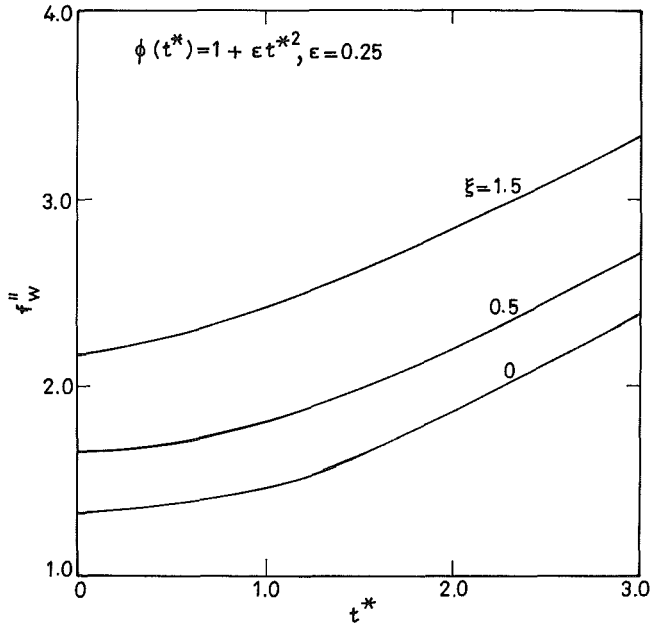

Fig. 1 Skin-friction parameter f''_w ($f''_w = (4/U_\infty)(\nu x/u_\infty)^{1/2}(\partial u/\partial r)_{r=R}$) for $\varphi(t^*) = 1+\epsilon t^{*2}$, $\epsilon = 0.25$

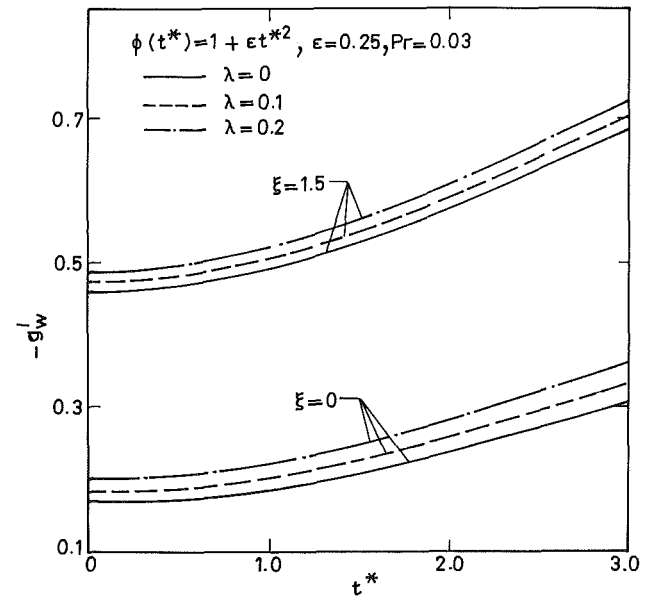

Fig. 2 Heat transfer parameter $-g'_w$ ($g'_w = 2(T_w - T_\infty)^{-1}(\nu x/u_\infty)^{1/2}(\partial T/\partial r)_{r=R}$) for $\varphi(t^*) = 1+\epsilon t^{*2}$, $\epsilon = 0.25$, Pr = 0.03; ——, $\lambda = 0$; - - - - -, $\lambda = 0.1$; ——·——, $\lambda = 0.2$

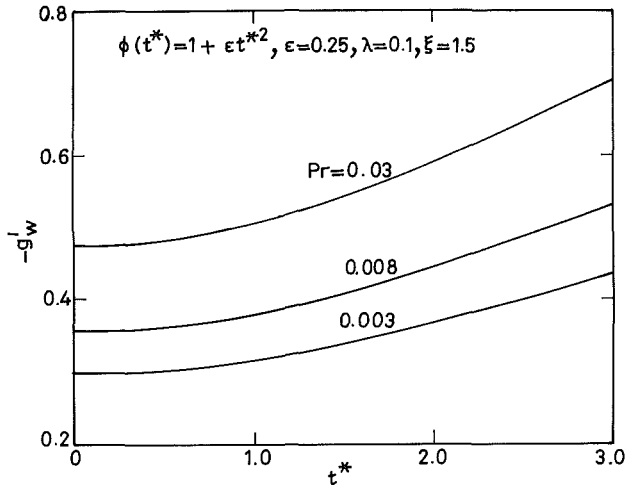

Fig. 3 Heat transfer parameter $-g'_w$ ($g'_w = 2(T_w - T_\infty)^{-1}(\nu x/u_\infty)^{1/2}(\partial T/\partial r)_{r=R}$) for $\varphi(t^*) = 1+\epsilon t^{*2}$, $\epsilon = 0.25$, $\lambda = 0.1$, $\xi = 1.5$

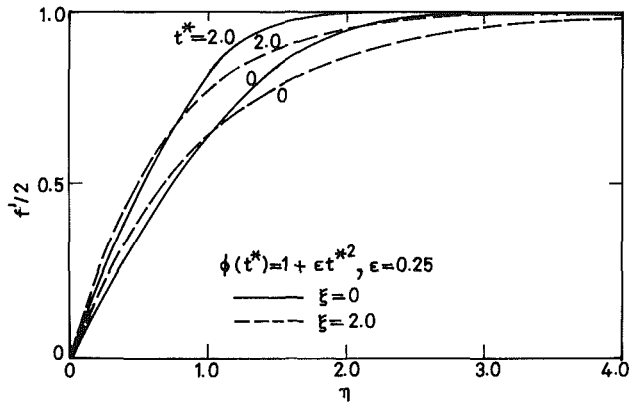

Fig. 4 Velocity profile $f'/2$ ($f'/2 = (u/U_\infty)$) for $\varphi(t^*) = 1+\epsilon t^{*2}$, $\epsilon = 0.25$; ——, $\xi = 0$; -----, $\xi = 2.0$

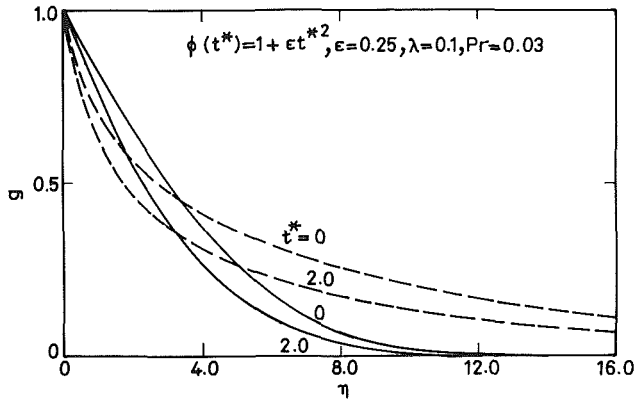

Fig. 5 Temperature profile g ($g = (T-T_\infty)/(T_w-T_\infty)$) for $\varphi(t^*) = 1+\epsilon t^{*2}$, $\epsilon = 0.25$, $\lambda = 0.1$, Pr = 0.03; ——, $\xi = 0$; -----, $\xi = 2.0$

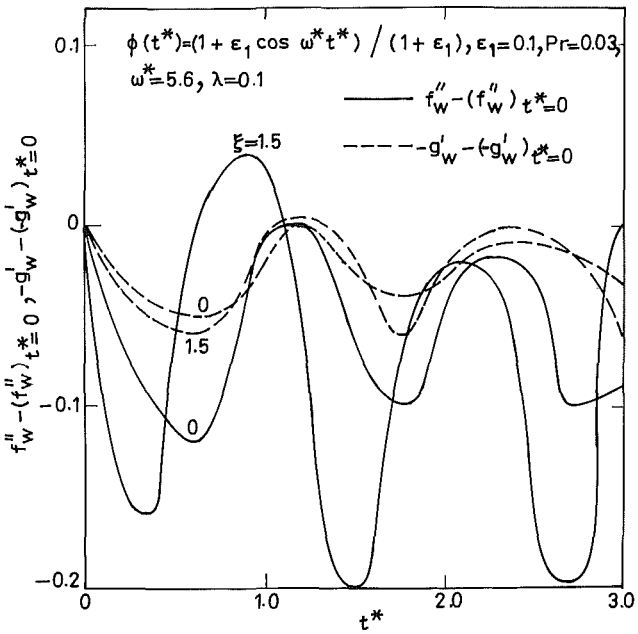

Fig. 6 Skin-friction and heat transfer parameters ($f''_w - (f''_w)_{t^*=0}$, $-g'_w - (-g'_w)_{t^*=0}$) for $\varphi(t^*) = [1+\epsilon_1 \cos(\omega^* t^*)]/(1+\epsilon_1)$, $\epsilon_1 = 0.1$, $\omega^* = 5.6$, $\lambda = 0.1$, Pr = 0.03; ——, $f''_w-(f''_w)_{t^*=0}$; -----, $-g'_w-(-g'_w)_{t^*=0}$

In order to assess the accuracy of our method, we have compared our steady-state heat transfer results with those of Chen and Lohman [4] and found them in very good agreement. The comparison is shown in Table 1. Also, we have compared our heat transfer result (Nu $Re_x^{-1/2}$) for $\xi = \lambda = 0$, Pr = 0.7 (i.e., flat-plate case without axial heat conduction effect) with the forced convection result ($\Omega = 0$) of Oosthuizen and Hart [14], who used a finite-difference scheme, and with the experimental data of Kliegel [15]. The present result is 0.2927 which is identical to that of [14], whereas the experimental data gave 0.281. Furthermore, we have compared our steady-state results for $\lambda = 0$ with the finite-difference results obtained in [11] for $M = 0$ (without magnetic field). Also, the unsteady-state results for $\lambda = 0$ were also compared with the finite-difference results both for accelerating ($\varphi(t^*) = 1+\epsilon t^{*2}$) and oscillating ($\varphi(t^*) = (1+\epsilon_1 \cos \omega^* t^*)/(1+\epsilon_1)$) free-stream velocities [12]. In all the cases the results were found to be in very good agreement. However, the comparison is not shown here for the sake of brevity.

Figures 1 and 2 show the variation of skin-friction and heat transfer parameters (f''_w, $-g'_w$) with time t^* for free-stream velocity distribution $\varphi(t^*) = 1+\epsilon t^{*2}$ for several values of the heat conduction parameter λ and transverse curvature parameter ξ. It is observed that both skin friction and heat transfer (f''_w, $-g'_w$) increase with time t^* and transverse curvature ξ. The effect is more pronounced for large t^* ($t^* > 1$). The heat transfer parameter ($-g'_w$) increases with the heat conduction parameter λ and this is true for all values of t^* and ξ. The heat conduction parameter λ does not affect f''_w. It may be remarked that here the free-stream velocity distribution has been taken to be increasing with time t^*(i.e., $\varphi(t^*) = 1+\epsilon t^{*2}$, $\epsilon > 0$). If it is taken as decreasing with time (i.e., $\varphi(t^*) = 1-\epsilon t^{*2}$, $\epsilon > 0$), then the skin friction and heat transfer (f''_w, $-g'_w$) will decrease with time t^*. However, the results are not presented here for the sake of brevity.

The effect of the Prandtl number Pr on the heat transfer parameter ($-g'_w$) for $\varphi(t^*) = 1+\epsilon t^{*2}$ is shown in Fig. 3. The heat transfer parameter ($-g'_w$) is found to decrease as Pr decreases, because a lower Prandtl number fluid has a relatively high thermal conductivity which promotes conduction and thereby reduces the variations. This results in increase in the thermal boundary layer thickness and reduction in the convective heat transfer. The Prandtl number does not affect the skin friction.

The velocity and temperature profiles (f', g) for $\varphi(t^*) = 1+\epsilon t^{*2}$ are presented in Figs. 4 and 5. The velocity and temperature profiles (f', g) depend strongly on the transverse curvature parameter ξ and the momentum and thermal boundary layer thicknesses increase with ξ. The effect of time t^* is just opposite. For small Prandtl number fluid, the thermal boundary layer is found to be thicker than the momentum boundary layer. The thermal boundary layer thickness does

not change significantly with the heat conduction parameter λ (not shown here to reduce the number of curves for the sake of clarity).

The effect of oscillatory free-stream velocity $\varphi(t^*) = 1 + \epsilon_1 \cos \omega^* t^*/(1+\epsilon_1)$ on the velocity and temperature fields has been shown in Fig. 6. Both skin friction and heat transfer respond significantly to the oscillatory free-stream velocity. However, the effect is more pronounced on the skin friction, because skin friction depends explicitly on the velocity gradient which is directly affected by the free-stream velocity distribution. The heat transfer depends on the temperature gradient which is comparatively less affected by the free-stream velocity distribution.

Conclusions

The effect of the axial heat conduction on the unsteady incompressible laminar forced convection flow of a liquid metal along a vertical cylinder has been studied when the free-stream velocity varies with time. The results indicate that both skin friction and heat transfer change significantly with the time-dependent free-stream velocity distribution. The affect of axial heat conduction on the heat transfer is more pronounced for the small values of the transverse curvature. The skin friction is unaffected by the Prandtl number and axial heat conduction parameter, whereas the heat transfer increases with them. Also, the skin friction and heat transfer increase with the transverse curvature. The thermal boundary layer has been found to be thicker than the velocity boundary layer. Also, the thermal boundary layer depends strongly on the Prandtl number.

References

1 Grosh, R. J., and Cess, R. D., "Heat Transfer to Fluids With Large Prandtl Numbers for Flow Across Plates and Cylinders of Various Cross Section," *Trans. ASME,* Vol. 80, 1958, pp. 667-676.

2 Pozzi, A., and Contursi, F., "Energy Equation for Large Reynolds Numbers and Small Prandtl Numbers," *American Rocket Society Journal,* Vol. 32, 1962, pp. 1278-1280.

3 Sparrow, E. M., Heinisch, R. P., and Yu, H. S., "Streamwise Heat Conduction Effects in Forced-Convection Boundary Layers Without and With Superposed Free Convection," *Nuclear Science and Engineering,* Vol. 39, 1970, pp. 387-393.

4 Chen, T. S., and Lohman, M. E., "Axial Heat Conduction Effects in Forced Convection Along a Cylinder," ASME JOURNAL OF HEAT TRANSFER, Vol. 97, 1975, pp. 185-190.

5 Seban, R. A., and Bond, R., "Skin Friction and Heat Transfer Characteristics of a Laminar Boundary Layer on a Cylinder in Axial Incompressible Flow," *Journal of the Aeronautical Sciences,* Vol. 18, 1951, pp. 671-675.

6 Sparrow, E. M., Quack, H., and Boerner, C. J., "Local Nonsimilar Boundary Layer Solutions," *AIAA Journal,* Vol. 8, 1970, pp. 1936-1942.

7 Sparrow, E. M., and Yu, H. S., "Local Nonsimilarity Thermal Boundary Layer Solutions," ASME JOURNAL OF HEAT TRANSFER, Vol. 93, 1971, pp. 328-334.

8 Wanous, D. J., and Sparrow, E. M., "Heat Transfer for Flow Longitudinal to a Cylinder With Surface Mass Transfer," ASME JOURNAL OF HEAT TRANSFER, Vol. 87, 1965, pp. 317-319.

9 Glauert, M. B., and Lighthill, M. J., "The Axisymmetric Boundary Layer on a Long Cylinder," *Proceedings of the Royal Society,* Vol. 230A, 1966, pp. 188-203.

10 Jaffe, N. A., and Okamura, T. T., "The Transverse Curvature Effect on the Incompressible Laminar Boundary Layer for Longitudinal Flow Over a Cylinder," *Journal of Applied Mathematics and Physics (ZAMP),* Vol. 19, 1968, pp. 564-574.

11 Venkatachala, B. J., and Nath, G., "Incompressible Boundary Layer for Longitudinal Flow Over a Cylinder With an Applied Magnetic Field," *Archive of Mechanics,* Vol. 32, 1980, pp. 270-283.

12 Reddy, A. V., "Numerical Studies of Some Laminar Boundary Layer Flows Using Finite-Difference Methods," Ph.D. Thesis, Indian Institute of Science, Bangalore, 1984.

13 Telionis, D. P., *Unsteady Viscous Flows,* Springer-Verlag, New York, 1981, pp. 46-49.

14 Oosthuizen, P. H., and Hart, R., "A Numerical Study of Laminar Combined Convective Flow Over Flat Plates," ASME JOURNAL OF HEAT TRANSFER, Vol. 95, 1973, pp. 60-63.

15 Kliegel, J. R., "Laminar Free and Forced Convection Heat Transfer From a Vertical Flat Plate," Ph.D. Thesis, University of California, 1959.

Conjugated Laminar Forced Convective Heat Transfer From Internally Finned Tubes

Wen-Quan Tao[1]

Nomenclature

c_p = specific heat
f = cross-sectional area
F_c = specific heat ratio = c_p/c_{p1}
F_k = conductivity ratio = k/k_1
F_ρ = density ratio = ρ/ρ_1
h = heat transfer coefficient
H = heat capacity ratio = $(f\rho w_m c_p)_2/(f\rho w_m c_p)_1$
k = thermal conductivity
K_f = conductivity ratio = k_2/k_1
K_w = conductivity ratio = k_w/k_1
l = fin height
L = relative fin height = l/r_i
N = number of fin
p = pressure
Pe = Peclet number = $r_i w_{m1}\rho_1 c_{p1}/k_1$
Q = heat transfer rate per unit axial length
r = radius
r_i, r_j = inner and outer radius of finned tube
r_0 = inner radius of envelope
S = source term
T = temperature
w = axial velocity
W = dimensionless axial velocity
z = axial coordinate
α = half the angle between the flanks of two adjacent fins
β = half the angle subtended by one fin
Γ = nominal diffusion coefficient
ζ = dimensionless axial coordinate = z/r_0
η = dimensionless radius = r/r_0
Θ = dimensionless temperature
λ = eigenvalue constant
μ = dynamic viscosity
ρ = density
φ = angular coordinate
Φ = scaled temperature variable

Subscripts

1 = tube side
2 = annular side
b = bulk
m = mean
w = wall

Introduction

The use of internal fins is a very effective means of augmenting heat transfer in a tubular heat exchanger, especially for the laminar flow case. Several theoretical investigations have been undertaken to determine heat transfer performance under fully developed conditions (Soliman and Feingold, 1978; Soliman et al., 1980). Results reported in the literature are derived for prescribed thermal boundary conditions, either with axially uniform heat flux with peripherally uniform

[1]Department of Power Machinery Engineering, Xi'an Jiaotong University, Shaanxi, Xi'an, The People's Republic of China.

Contributed by the Heat Transfer Division for publication in the JOURNAL OF HEAT TRANSFER. Manuscript received by the Heat Transfer Division March 10, 1986.

not change significantly with the heat conduction parameter λ (not shown here to reduce the number of curves for the sake of clarity).

The effect of oscillatory free-stream velocity $\varphi(t^*) = 1 + \epsilon_1 \cos \omega^* t^*/(1+\epsilon_1)$ on the velocity and temperature fields has been shown in Fig. 6. Both skin friction and heat transfer respond significantly to the oscillatory free-stream velocity. However, the effect is more pronounced on the skin friction, because skin friction depends explicitly on the velocity gradient which is directly affected by the free-stream velocity distribution. The heat transfer depends on the temperature gradient which is comparatively less affected by the free-stream velocity distribution.

Conclusions

The effect of the axial heat conduction on the unsteady incompressible laminar forced convection flow of a liquid metal along a vertical cylinder has been studied when the free-stream velocity varies with time. The results indicate that both skin friction and heat transfer change significantly with the time-dependent free-stream velocity distribution. The affect of axial heat conduction on the heat transfer is more pronounced for the small values of the transverse curvature. The skin friction is unaffected by the Prandtl number and axial heat conduction parameter, whereas the heat transfer increases with them. Also, the skin friction and heat transfer increase with the transverse curvature. The thermal boundary layer has been found to be thicker than the velocity boundary layer. Also, the thermal boundary layer depends strongly on the Prandtl number.

References

1 Grosh, R. J., and Cess, R. D., "Heat Transfer to Fluids With Large Prandtl Numbers for Flow Across Plates and Cylinders of Various Cross Section," *Trans. ASME,* Vol. 80, 1958, pp. 667-676.

2 Pozzi, A., and Contursi, F., "Energy Equation for Large Reynolds Numbers and Small Prandtl Numbers," *American Rocket Society Journal,* Vol. 32, 1962, pp. 1278-1280.

3 Sparrow, E. M., Heinisch, R. P., and Yu, H. S., "Streamwise Heat Conduction Effects in Forced-Convection Boundary Layers Without and With Superposed Free Convection," *Nuclear Science and Engineering,* Vol. 39, 1970, pp. 387-393.

4 Chen, T. S., and Lohman, M. E., "Axial Heat Conduction Effects in Forced Convection Along a Cylinder," ASME JOURNAL OF HEAT TRANSFER, Vol. 97, 1975, pp. 185-190.

5 Seban, R. A., and Bond, R., "Skin Friction and Heat Transfer Characteristics of a Laminar Boundary Layer on a Cylinder in Axial Incompressible Flow," *Journal of the Aeronautical Sciences,* Vol. 18, 1951, pp. 671-675.

6 Sparrow, E. M., Quack, H., and Boerner, C. J., "Local Nonsimilar Boundary Layer Solutions," *AIAA Journal,* Vol. 8, 1970, pp. 1936-1942.

7 Sparrow, E. M., and Yu, H. S., "Local Nonsimilarity Thermal Boundary Layer Solutions," ASME JOURNAL OF HEAT TRANSFER, Vol. 93, 1971, pp. 328-334.

8 Wanous, D. J., and Sparrow, E. M., "Heat Transfer for Flow Longitudinal to a Cylinder With Surface Mass Transfer," ASME JOURNAL OF HEAT TRANSFER, Vol. 87, 1965, pp. 317-319.

9 Glauert, M. B., and Lighthill, M. J., "The Axisymmetric Boundary Layer on a Long Cylinder," *Proceedings of the Royal Society,* Vol. 230A, 1966, pp. 188-203.

10 Jaffe, N. A., and Okamura, T. T., "The Transverse Curvature Effect on the Incompressible Laminar Boundary Layer for Longitudinal Flow Over a Cylinder," *Journal of Applied Mathematics and Physics (ZAMP),* Vol. 19, 1968, pp. 564-574.

11 Venkatachala, B. J., and Nath, G., "Incompressible Boundary Layer for Longitudinal Flow Over a Cylinder With an Applied Magnetic Field," *Archive of Mechanics,* Vol. 32, 1980, pp. 270-283.

12 Reddy, A. V., "Numerical Studies of Some Laminar Boundary Layer Flows Using Finite-Difference Methods," Ph.D. Thesis, Indian Institute of Science, Bangalore, 1984.

13 Telionis, D. P., *Unsteady Viscous Flows,* Springer-Verlag, New York, 1981, pp. 46-49.

14 Oosthuizen, P. H., and Hart, R., "A Numerical Study of Laminar Combined Convective Flow Over Flat Plates," ASME JOURNAL OF HEAT TRANSFER, Vol. 95, 1973, pp. 60-63.

15 Kliegel, J. R., "Laminar Free and Forced Convection Heat Transfer From a Vertical Flat Plate," Ph.D. Thesis, University of California, 1959.

Conjugated Laminar Forced Convective Heat Transfer From Internally Finned Tubes

Wen-Quan Tao[1]

Nomenclature

c_p = specific heat
f = cross-sectional area
F_c = specific heat ratio = c_p/c_{p1}
F_k = conductivity ratio = k/k_1
F_ρ = density ratio = ρ/ρ_1
h = heat transfer coefficient
H = heat capacity ratio = $(f\rho w_m c_p)_2/(f\rho w_m c_p)_1$
k = thermal conductivity
K_f = conductivity ratio = k_2/k_1
K_w = conductivity ratio = k_w/k_1
l = fin height
L = relative fin height = l/r_i
N = number of fin
p = pressure
Pe = Peclet number = $r_i w_{m1}\rho_1 c_{p1}/k_1$
Q = heat transfer rate per unit axial length
r = radius
r_i, r_j = inner and outer radius of finned tube
r_0 = inner radius of envelope
S = source term
T = temperature
w = axial velocity
W = dimensionless axial velocity
z = axial coordinate
α = half the angle between the flanks of two adjacent fins
β = half the angle subtended by one fin
Γ = nominal diffusion coefficient
ζ = dimensionless axial coordinate = z/r_0
η = dimensionless radius = r/r_0
Θ = dimensionless temperature
λ = eigenvalue constant
μ = dynamic viscosity
ρ = density
φ = angular coordinate
Φ = scaled temperature variable

Subscripts

1 = tube side
2 = annular side
b = bulk
m = mean
w = wall

Introduction

The use of internal fins is a very effective means of augmenting heat transfer in a tubular heat exchanger, especially for the laminar flow case. Several theoretical investigations have been undertaken to determine heat transfer performance under fully developed conditions (Soliman and Feingold, 1978; Soliman et al., 1980). Results reported in the literature are derived for prescribed thermal boundary conditions, either with axially uniform heat flux with peripherally uniform

[1]Department of Power Machinery Engineering, Xi'an Jiaotong University, Shaanxi, Xi'an, The People's Republic of China.

Contributed by the Heat Transfer Division for publication in the JOURNAL OF HEAT TRANSFER. Manuscript received by the Heat Transfer Division March 10, 1986.

temperature, or with constant temperature axially as well as circumferentially. However, for double pipe heat exchangers, the thermal boundary condition of the separating wall can not be prescribed a priori; it is determined by the thermal interaction between the fluid inside the tube and that in the annular space. Mikhailov and Shishedjiev (1981), and Tao (1986) have shown that Nusselt number of the tube and that of the annular are strongly dependent upon the heat capacity ratio of the two fluids. In this investigation, a performance analysis is conducted numerically for an internally finned tube which serves as the inner tube of a double pipe heat exchanger.

Analysis and Solution

The analysis is based on the following assumptions: (1) The flows and heat transfer of both fluids are laminar and assumed fully developed; (2) the fluid physical properties are assumed constant; (3) the outside surface of the heat exchanger is insulated; (4) the axial conduction, in both fluids and wall, are neglected; (5) the fin is defined by two radial flanks and its tip is a circular arc concentric with the tube (Fig. 1); (6) the heat exchanger is of counterflow type.

The heat transfer problem investigated is a conjugated one, for which the temperature distribution of both fluids and separating wall are determined simultaneously. The problem is characterized by a large number of geometric and physical parameters which may be reduced to the following groups: (1) number of fins N; (2) relative fin height L; (3) half fin angle β; (4) heat capacity ratio H; (5) conductivity ratio of the separating wall to the inner tube fluid K_w; (6) conductivity ratio of the two fluids K_f; (7) relative radius based on the outside surface of the inner tube η_j; (8) relative thickness of the separating wall, $\eta_j - \eta_i$.

It is neither practical nor economical to investigate the effects of variations of all these parameters. To simplify the mathematical model, this analysis has concentrated on variations of only the three most important parameters, N, L, and H. All other parameters were kept constant. Specifically, the following range of parameters was considered:

$$N=4\text{–}32,\quad L=0.2\text{–}0.8,\quad H=0.5\text{–}4,\quad \beta=3\ \text{deg},$$
$$\eta_j=0.75,\quad \eta_i=\eta_j/(1+2\beta),\quad K_f=1,\quad K_w=100$$

The axial momentum equation of the tube side fluid reduces to

$$\frac{1}{r}\frac{\partial}{\partial r}\left(r\mu\frac{\partial w}{\partial r}\right)+\frac{1}{r^2}\frac{\partial}{\partial \varphi}\left(\mu\frac{\partial w}{\partial \varphi}\right)=\frac{dp}{dz} \tag{1}$$

Defining a dimensionless velocity and radius

$$W=\frac{\mu w}{-r_i^2\dfrac{dp}{dz}},\qquad \eta=r/r_0 \tag{2}$$

equation (1) can be transformed to

$$\frac{1}{\eta}\frac{\partial}{\partial \eta}\left(\eta\frac{\partial W}{\partial \eta}\right)+\frac{1}{\eta^2}\frac{\partial}{\partial \varphi}\left(\frac{\partial W}{\partial \varphi}\right)+\frac{1}{\eta_i^2}=0 \tag{3}$$

with boundary conditions $W = 0$ on all solid surfaces and $\partial W/\partial\varphi = 0$ on all symmetry lines. The following analytical result (Bird et al., 1960) may be used for the velocity distribution in the annular space

$$\frac{W}{W_{m2}}=2\frac{1-\eta^2+\dfrac{1-\eta_j^2}{\ln(1/\eta_j)}\ln\eta}{\dfrac{1-\eta_j^4}{1-\eta_j^2}-\dfrac{1-\eta_j^2}{\ln(1/\eta_j)}},\qquad \eta_j<\eta<1 \tag{4}$$

The flow direction of the inner fluid is taken as positive, thus making that of the outer fluid negative.

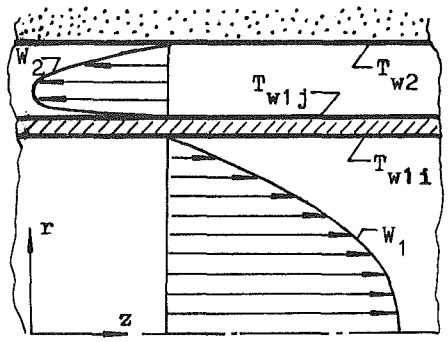

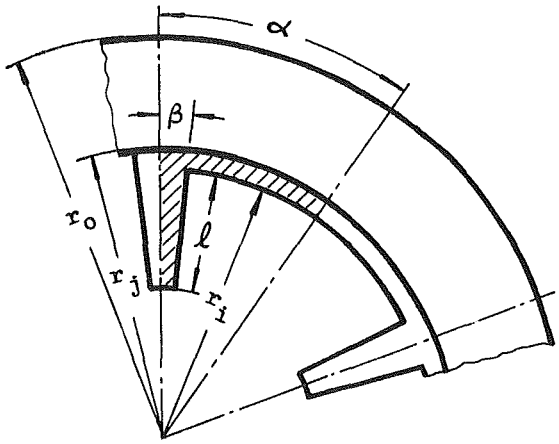

Fig. 1 Tube geometry

The temperature distribution of the whole solution domain is governed by the energy equation

$$\rho c_p w\frac{\partial T}{\partial z}=\frac{1}{r}\frac{\partial}{\partial r}\left(rk\frac{\partial T}{\partial r}\right)+\frac{1}{r^2}\frac{\partial}{\partial \varphi}\left(k\frac{\partial T}{\partial \varphi}\right) \tag{5}$$

with boundary conditions

$$\varphi=0,\quad \frac{\partial T}{\partial \varphi}=0;\quad \varphi=\alpha,\quad \frac{\partial T}{\partial \varphi}=0;$$
$$r=0,\quad \frac{\partial T}{\partial r}=0;\quad r=r_0,\quad \frac{\partial T}{\partial r}=0$$

The physical properties ρ, c_p, and k and the velocity w are defined as follows:

$$k=k_1,\quad \rho=\rho_1,\quad c_p=c_{p1},\quad w=w_1,$$
$$\text{for } r<r_i,\quad \varphi>\beta \text{ and } r<(r_i-l),\quad \varphi<\beta$$
$$k=k_w,\quad w=0,\quad \text{for } (r_i-l)<r<r_j,\quad \varphi<\beta$$
$$\text{or } r_i<r<r_j,\quad \beta<\varphi<\alpha$$
$$k=k_2,\quad \rho=\rho_2,\quad c_p=c_{p2},\quad w=w_2$$
$$\text{for } r>r_j,\quad 0<\varphi<\alpha$$

Define a reference temperature

$$T^*=-\frac{(f\rho w_m c_p T_b)_1-(f\rho w_m c_p T_b)_2}{(f\rho w_m c_p)_1+(f\rho w_m c_p)_2} \tag{6}$$

which can be shown to be independent of the z coordinate. Referring to Fig. 2, an energy balance on the indicated control volume yields

$$(f\rho w_m c_p T_b)_1'+(f\rho w_m c_p T_b)_2'=(f\rho w_m c_p T_b)_1''+(f\rho w_m c_p T_b)_2''$$

or, after rearrangement,

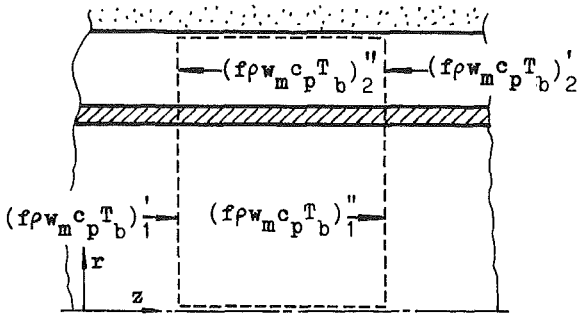

Fig. 2 Energy balance on an arbitrary control volume

$$(f\rho w_m c_p T_b)'_1 - (f\rho w_m c_p T_b)''_2 = (f\rho w_m c_p T_b)''_1 - (f\rho w_m c_p T_b)'_2$$

Since the control volume faces are arbitrarily positioned, it follows that

$$(f\rho w_m c_p T_b)_1 - (f\rho w_m c_p T_b)_2 = \text{const} \tag{7}$$

at any cross section. Furthermore, the quantity $(f\rho w_m c_p)_1 + (f\rho w_m c_p)_2$ is independent of z. These two facts indicate that T^* defined by equation (6) is a constant throughout the heat exchanger.

A dimensionless temperature is defined by

$$\Theta = \frac{T - T_{w2}}{T^* - T_{w2}} \tag{8}$$

Introducing Θ into equation (5) and making use of the fully developed thermal condition, $\partial\Theta/\partial z = 0$, and the fact $\partial T^*/\partial z = 0$, the energy equation can be recast in the following dimensionless form:

$$\frac{dT_{w2}/d\zeta}{T^* - T_{w2}} \mathrm{Pe} = \left[(1-\Theta)\frac{W}{W_{m1}}\frac{1}{\eta_i}F_p F_c\right]^{-1} \left[\frac{1}{\eta}\frac{\partial}{\partial\eta}\left(\eta F_k \frac{\partial\Theta}{\partial\eta}\right) + \frac{1}{\eta^2}\frac{\partial}{\partial\varphi}\left(F_k\frac{\partial\Theta}{\partial\varphi}\right)\right] \tag{9}$$

Examination of equation (9) reveals that the left-hand side is a function of ζ only, while the right-hand side is a function of η and φ. Therefore, the two sides are each equal to a constant λ. By setting the right-hand side equal to λ, we obtain

$$\frac{1}{\eta}\frac{\partial}{\partial\eta}\left(\eta F_k\frac{\partial\Theta}{\partial\eta}\right) + \frac{1}{\eta^2}\frac{\partial}{\partial\varphi}\left(F_k\frac{\partial\Theta}{\partial\varphi}\right) - \frac{\lambda}{\eta_i}F_p F_c\frac{W}{W_{m1}}(1-\Theta) = 0 \tag{10}$$

The boundary conditions of equation (10) are

$$\eta = 0, \quad \frac{\partial\Theta}{\partial\eta} = 0; \quad \eta = 1, \quad \Theta = 0; \quad \varphi = 0, \quad \frac{\partial\Theta}{\partial\varphi} = 0; \quad \varphi = \alpha, \quad \frac{\partial\Theta}{\partial\varphi} = 0 \tag{11}$$

It should be noted that there is one more boundary condition at $\eta = 1$, i.e., $\partial\Theta/\partial\eta = 0$. On the other hand, λ is an unknown constant. It is an eigenvalue (Sparrow et al., 1978), because only a particular value of λ will enable equation (10) to be solved. The seemingly extra boundary condition will be used in determining the eigenvalue λ.

To solve the velocity field of the tube side fluid, the momentum equation (3) is generalized into the following form:

$$\frac{1}{\eta}\frac{\partial}{\partial\eta}\left(\eta\Gamma\frac{\partial W}{\partial\eta}\right) + \frac{1}{\eta^2}\frac{\partial}{\partial\varphi}\left(\Gamma\frac{\partial W}{\partial\varphi}\right) + S = 0$$

$$\eta = 0, \quad \frac{\partial W}{\partial\eta} = 0; \quad \eta = 1, \quad W = 0; \quad \varphi = 0, \quad \frac{\partial W}{\partial\varphi} = 0;$$

$$\varphi = \alpha, \quad \frac{\partial W}{\partial\varphi} = 0; \quad \eta < \eta_i, \quad \beta < \varphi < \alpha \text{ and } \eta < (\eta_i - L), \tag{12}$$

$$\varphi < \beta, \quad \Gamma = 1, \quad S = 1/\eta_i^2; \quad (\eta_i - L) < \eta < 1, \quad \varphi < \beta$$

$$\text{and } \eta_i < \eta < 1, \quad \beta < \varphi < \alpha, \quad \Gamma = 10^{20}, \quad S = 0$$

The very large number of Γ in the second region of the solution domain will ensure that the zero velocity specified at $\eta = 1$ will prevail throughout this region, and thus the tube side fluid will experience the correct velocity boundary condition. Equation (12) can be identified as a Poisson equation with a known source term. Its finite difference solution can be obtained by a standard method and will not be elaborated here. For the velocity field in the annular side, equation (4) is used.

To obtain the temperature field of the whole domain, the method described by Sparrow et al. (1978) is modified and used here. By introducing a scaled temperature $\Phi = \Theta/\lambda$, equation (10) can be rewritten in the form

$$\frac{1}{\eta}\frac{\partial}{\partial\varphi}\left(\eta F_k\frac{\partial\Phi}{\partial\eta}\right) + \frac{1}{\eta^2}\frac{\partial}{\partial\varphi}\left(F_k\frac{\partial\Phi}{\partial\varphi}\right) + S_\Phi = 0 \tag{13}$$

where the source term S_Φ and the conductivity ratio F_k are defined as follows:

$$\eta < \eta_i, \quad \beta < \varphi < \alpha \text{ and } \eta < (\eta_i - L), \quad 0 < \varphi < \beta,$$

$$S_\Phi = -\frac{1}{\eta_i}\frac{W}{W_{m1}}(1 - \lambda\Phi), \quad F_k = 1; \quad \eta > \eta_j, \quad 0 < \varphi < \alpha,$$

$$S_\Phi = \frac{1}{\eta_i} H \frac{f_1}{f_2}\left|\frac{W}{W_{m2}}\right|(1 - \lambda\Phi), \quad F_k = K_f$$

For the other region, $S_\Phi = 0$, $F_k = K_w$. The associated boundary conditions, equation (11), remain as they are, but with Θ replaced by Φ.

To establish a formulation for iterative computation of λ, equation (13) is integrated over the solution domain. After substituting the boundary conditions the following result is obtained:

$$\lambda = \frac{\int_0^{\eta_i}\int_0^{\alpha}\eta\left(\frac{W}{W_{m1}}\right)d\varphi d\eta - \int_{\eta_j}^{1}\int_0^{\alpha}\eta H\left(\frac{f_1}{f_2}\right)\left|\frac{W}{W_{m2}}\right|d\varphi d\eta}{\int_0^{\eta_i}\int_0^{\alpha}\eta\left(\frac{W}{W_{m1}}\right)\Phi d\varphi d\eta - \int_{\eta_j}^{1}\int_0^{\alpha}\eta H\left(\frac{f_1}{f_2}\right)\left|\frac{W}{W_{m2}}\right|\Phi d\varphi d\eta} \tag{14}$$

The solution procedure is as follows: Guess an initial distribution of Φ, evaluate λ from equation (14), and compute S_Φ. Then solve equation (13) numerically with its boundary conditions to yield a new distribution of Φ. The above procedure is repeated until convergence is reached. Within the range of parameters considered, the aforementioned iterative procedure converged quite rapidly. This is because Φ appears in both the numerator and denominator of the term $\lambda\Phi$, making the source term of equation (13) not dependent on the absolute magnitude of Φ but only on the variation of Φ over the cross section.

Table 1 Values of Nu_1 and Nu_2 for $H = 1$ and $L = 0.01$

η_j	N	Nu_1	Nu_2
0.25	8	4.369 (4.364)	7.731 (7.753)
0.50	16	4.371 (4.364)	6.175 (6.181)
0.75	16	4.363 (4.364)	5.615
0.90	28	4.343 (4.364)	5.355 (5.470)

Table 2 Nu_1 results ($\beta = 3$ deg, $k_2/k_1 = 1$, $k_w/k_1 = 100$)

L	H	$N=4$	$N=8$	$N=12$	$N=16$	$N=20$	$N=24$	$N=28$	$N=32$
0.2	0.5	5.316	5.561	5.553	5.419	5.278	5.191	5.146	5.104
	1.0	4.643	4.789	4.773	4.675	4.550	4.517	4.477	4.459
	2.0	4.304	4.409	4.392	4.310	4.185	4.179	4.146	4.129
	4.0	4.131	4.234	4.203	4.128	4.061	4.012	3.981	3.964
0.6	0.5	12.61	23.07	21.40	15.24	10.56	8.047	6.725	6.020
	1.0	11.06	17.92	14.58	10.15	7.594	6.217	5.460	5.038
	2.0	10.16	14.86	11.35	8.175	6.411	5.439	4.887	4.567
	4.0	9.706	13.28	9.942	7.333	5.891	5.084	4.615	4.337
0.8	0.5	19.81	46.78	84.66	122.2	125.4	88.49	52.49	28.03
	1.0	18.50	44.74	81.94	113.0	97.07	56.43	29.97	16.96
	2.0	17.80	43.60	80.42	106.2	76.80	39.45	21.30	12.99
	4.0	17.38	42.86	79.41	100.2	64.02	31.64	17.82	11.38

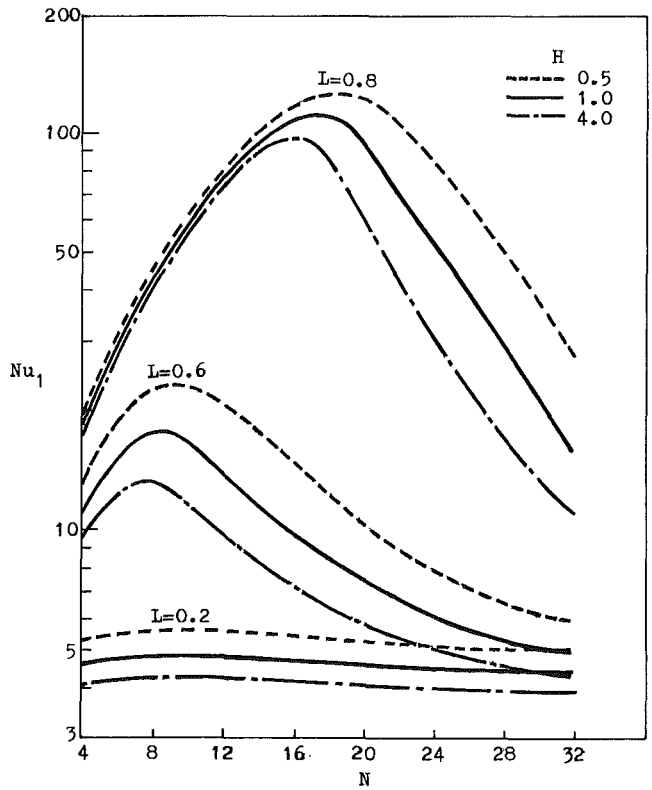

Fig. 3 Nusselt number variation with number of fins for different fin heights

Results and Discussion

The heat transfer coefficient and its corresponding Nusselt number for the tube flow are defined as

$$h_1 = \frac{Q/(2\pi r_i)}{T_{w1i} - T_{b1}}, \quad \mathrm{Nu}_1 = \frac{2h_1 r_i}{k_1} \tag{15}$$

and those for the annular flow are

$$h_2 = \frac{Q/(2\pi r_j)}{T_{b2} - T_{w1j}}, \quad \mathrm{Nu}_2 = \frac{2h_2(r_0 - r_j)}{k_2} \tag{16}$$

where T_{w1i} and T_{w1j} are the averaged wall temperature of the tube inner surface (including fins) and that of the tube outer surface, respectively. The Nusselt numbers thus defined can be used for comparing with those obtained in literature.

The computations were performed on a 50 × 18 grid in the r–φ plane. It was found that the Nusselt numbers from finer grids agreed within about 0.5 percent with the present results. To check the validity of the model and the computer code, a comparison has been made. It is well known that for a counterflow double pipe heat exchanger of smooth tubes, a uniform heat flux thermal boundary condition will occur when the heat capacity ratio of the two fluids equals one. The computational results for $H = 1$ and $L = 0.01$ (thus the inner tube is nearly smooth) are listed in Table 1. Numbers in parentheses are for smooth tube cases (Shah and London, 1978). It can be seen that the agreement is excellent, with a maximum deviation of 2.1 percent.

In the range of parameters considered, the calculated values of Nu_1 are listed in Table 2 and illustrated in Fig. 3. It is useful to compare the present results with those reported by Masliyah and Nandakumar (1976). For the cases of $L = 0.2$–0.8, $N = 4$–24, and $H = 1$, the agreement is, in general, fairly good, with a maximum difference of 5.3 percent. The disparities may be caused by two facts: (1) The fin shapes are different; the fins investigated by Masliyah and Nandakumar are of triangular shape; (2) the boundary conditions are slightly different. In their investigation, the axial heat flux is assumed constant with peripherally uniform temperature (including fins), which would be realized only for metals of very high thermal conductivity. The present computation shows that from the fin base to its tip the dimensionless temperature increases. For the case of $H = 1$ the maximum variation is about 40 percent. Soliman and Feingold (1978) conducted a similar investigation with fin shapes identical to the present study. Their results are all presented by figures; therefore, an accurate comparison can not be performed. Qualitatively, the variations of Nu_1 with N and L shown in Fig. 3 are similar to those provided by them. However, there is one important difference. The results given here show that the ratio of the fluid heat capacity H has a significant effect on the finned tube heat transfer performance. At the same values of N and L, the values of Nu_1 can be doubled as H decreases from 4 to 0.5. By comparing the results reported by Soliman and Feingold (1978), it can be seen that when H is less than 1, the values of Nu_1 can be much larger than those for the uniform heat flux condition. Such strong dependence of heat transfer performance of finned tubes on the heat capacity ratio should be taken into account in heat exchanger design and operation.

References

Bird, R. B., Stewart, W. E., and Lightfoot, E. N., 1960, *Transport Phenomena*, Wiley, New York, p. 53.

Masliyah, J. H., and Nandakumar, K., 1976, "Heat Transfer in Internally Finned Tubes," ASME JOURNAL OF HEAT TRANSFER, Vol. 98, pp. 257–261.

Mikhailov, M. D., and Shishedjiev, B. K., 1981, "Heat Transfer in Counter Flow Double Pipe Heat Exchanger," in: *Heat Exchangers: Thermal-Hydraulic Fundamentals and Design*, S. Kakac et al., eds., Hemisphere, Washington, DC, pp. 153–163.

Shah, R. K., and London, A. L., 1978, "Laminar Flow Forced Convection in Ducts," *Advances in Heat Transfer*, Supplement 1, Academic Press, New York, pp. 83, 291.

Soliman, H. M., and Feingold, A., 1978, "Analysis of Heat Transfer in Internally Finned Tubes Under Laminar Flow Conditions," *Proceedings, 6th International Heat Transfer Conference*, Vol. 2, pp. 571–576.

Soliman, H. M., Chau, T. S., and Trupp, A. C., 1980, "Analysis of Laminar Heat Transfer in Internally Finned Tubes With Uniform Outside Wall Temperature," ASME JOURNAL OF HEAT TRANSFER, Vol. 102, pp. 598–604.

Sparrow, E. M., Patakar, S. V., and Shahrestani, H., 1978, "Laminar Heat Transfer in a Pipe Subjected to a Circumferentially Varying External Heat Transfer Coefficient," *Numerical Heat Transfer*, Vol. 1, pp. 117-127.

Tao, W. Q., 1986, "A Numerical Solution Scheme to the Conjugated Problem of Double Pipe Heat Exchangers," *Proceedings, 1984 Heat and Mass Transfer Conference of the Chinese Society of Engineering Thermal Physics*, Science Press, Beijing, pp. 377-382.

Natural Convection in Horizontal Porous Layers With Localized Heating From Below

V. Prasad[1] and F. A. Kulacki[2]

Nomenclature

A = aspect ratio = D/L
D = width of half cavity, m
d = length of heat source in half cavity, m
g = acceleration due to gravity, m/s^2
H = dimensionless length of heat source = d/L
H_1 = dimensionless length of heat source = $d/D = H/A$
h = average heat transfer coefficient, W/m^2-K
K = permeability of saturated porous medium, m^2
k = effective thermal conductivity of porous medium, W/m-K
L = height of porous layer, m
Nu = Nusselt number based on layer height = hL/k
Ra* = Rayleigh number based on cavity height = $g\,\beta\,KL\,(T_h - T_c)/\nu\alpha$
T = temperature, K
u = fluid velocity in x direction = $-(\alpha/D)\,(\partial\Psi/\partial Y)$, m/s
v = fluid velocity in y direction = $(\alpha L/D^2)\,(\partial\Psi/\partial X)$, m/s
x, y = Cartesian coordinates, m/s
X, Y = dimensionless distance on x and y axes = x/D and y/L, respectively
α = thermal diffusivity of porous medium, m^2/s
β = isobaric coefficient of thermal expansion of fluid, K^{-1}
θ = dimensionless temperature = $(T - T_c)/(T_h - T_c)$
ν = kinematic viscosity, m^2/s
Ψ = stream function

Subscripts

c = cooled wall
d = based on length of heated segment
h = heated wall
max = maximum
0 = line of symmetry ($x = 0$)

[1]Department of Mechanical Engineering, Columbia University, New York, NY 10027; Mem. ASME.

[2]Department of Mechanical and Aerospace Engineering, University of Delaware, Newark, DE 19716; present address: Office of the Dean, Colorado State University, Fort Collins, CO 80523; Mem. ASME.

Contributed by the Heat Transfer Division for publication in the JOURNAL OF HEAT TRANSFER. Manuscript received by the Heat Transfer Division April 9, 1985.

Introduction

Convective flow of fluid through saturated porous media heated from below is of considerable interest, and has been extensively studied. Most of these studies are concerned with either infinite horizontal porous layers or rectangular (or cylindrical) porous cavities with adiabatic vertical walls [1, 2]. A related problem of practical importance occurs when only a portion of the bottom surface is heated and the rest of it is either adiabatic or isothermally cooled. This situation is encountered in several geothermal areas which consist of troughs of volcanic debris contained by walls of nonfragmented ignimbrite. Thus, the model region considered is a locally heated long trough of isotropic porous medium confined by impermeable and insulating surroundings. Also, the recent motivation to study this problem has come from the efforts to identify a geologic repository for nuclear waste disposal.

Elder [3] was the first to study free convection in a horizontal cavity with localized heating from below (Fig. 1, $\partial T/\partial x = 0$ replaced by $T = T_c$). He observed that more than one cell exists in the "half cavity" for $H \geq 1.5$, and the Nusselt number is a function of H and the number of cells. Later, he conducted a numerical and experimental study for the transient problem, and reported several interesting features of the growth of eddies, and an alternation between the periods of slow gradual adjustment and the periods of rapid change for cellular flow behavior [4].

Horne and O'Sullivan [5] considered the problem for the case when the vertical walls of the cavity are adiabatic (Fig. 1; $y = 0, x > d, T = T_c$). Their results indicate that if the lower boundary is partially heated, the system is self-restricting, and either stabilizes into steady multicellular flow or regularizes into periodic oscillatory flow, depending on how much of the boundary is heated. However, oscillatory flow generally exists at high Rayleigh numbers. Later, they [6] also studied the effects of temperature-dependent viscosity and thermal expansion coefficient on temperature and flow fields.

Although the preceding studies [3-6] report interesting features of free convection in porous media for localized heating from below, they are generally concerned with the flow structure and provide little information on heat transfer rates. To characterize the effects of heat source size and strength fully, as well as the vertical and horizontal extent of the porous layer and its boundary conditions, a series of studies is required for a wide range of parameters, namely dimensionless heated length H, aspect ratio A, and Rayleigh number Ra*. The purpose of the present work is to consider the effects of aspect ratio and Rayleigh number on free convection heat transfer from an isothermal heat source centrally located on the bottom surface of a horizontal porous cavity (Fig. 1).

Formulation and Numerical Method

Consider a fluid-saturated horizontal porous layer enclosed by adiabatic vertical walls. An isothermal heat source of length $2d$ is centrally located on the bottom surface which is otherwise adiabatic (Fig. 1). The upper surface is considered

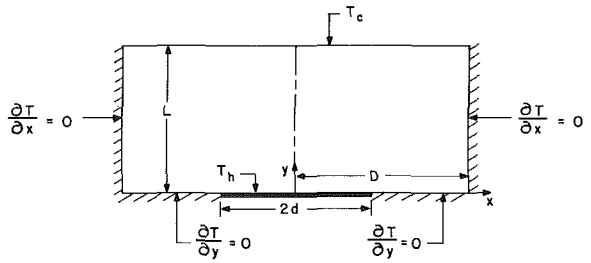

Fig. 1 Two-dimensional horizontal porous layer with localized heating from below

Sparrow, E. M., Patakar, S. V., and Shahrestani, H., 1978, "Laminar Heat Transfer in a Pipe Subjected to a Circumferentially Varying External Heat Transfer Coefficient," *Numerical Heat Transfer*, Vol. 1, pp. 117-127.

Tao, W. Q., 1986, "A Numerical Solution Scheme to the Conjugated Problem of Double Pipe Heat Exchangers," *Proceedings, 1984 Heat and Mass Transfer Conference of the Chinese Society of Engineering Thermal Physics*, Science Press, Beijing, pp. 377-382.

Natural Convection in Horizontal Porous Layers With Localized Heating From Below

V. Prasad[1] and F. A. Kulacki[2]

Nomenclature

A = aspect ratio = D/L
D = width of half cavity, m
d = length of heat source in half cavity, m
g = acceleration due to gravity, m/s^2
H = dimensionless length of heat source = d/L
H_1 = dimensionless length of heat source = $d/D = H/A$
h = average heat transfer coefficient, W/m^2-K
K = permeability of saturated porous medium, m^2
k = effective thermal conductivity of porous medium, W/m-K
L = height of porous layer, m
Nu = Nusselt number based on layer height = hL/k
Ra* = Rayleigh number based on cavity height = $g\,\beta\,KL\,(T_h - T_c)/\nu\alpha$
T = temperature, K
u = fluid velocity in x direction = $-(\alpha/D)\,(\partial\Psi/\partial Y)$, m/s
v = fluid velocity in y direction = $(\alpha L/D^2)\,(\partial\Psi/\partial X)$, m/s
x, y = Cartesian coordinates, m/s
X, Y = dimensionless distance on x and y axes = x/D and y/L, respectively
α = thermal diffusivity of porous medium, m^2/s
β = isobaric coefficient of thermal expansion of fluid, K^{-1}
θ = dimensionless temperature = $(T - T_c)/(T_h - T_c)$
ν = kinematic viscosity, m^2/s
Ψ = stream function

Subscripts

c = cooled wall
d = based on length of heated segment
h = heated wall
max = maximum
0 = line of symmetry ($x = 0$)

[1]Department of Mechanical Engineering, Columbia University, New York, NY 10027; Mem. ASME.

[2]Department of Mechanical and Aerospace Engineering, University of Delaware, Newark, DE 19716; present address: Office of the Dean, Colorado State University, Fort Collins, CO 80523; Mem. ASME.

Contributed by the Heat Transfer Division for publication in the JOURNAL OF HEAT TRANSFER. Manuscript received by the Heat Transfer Division April 9, 1985.

Introduction

Convective flow of fluid through saturated porous media heated from below is of considerable interest, and has been extensively studied. Most of these studies are concerned with either infinite horizontal porous layers or rectangular (or cylindrical) porous cavities with adiabatic vertical walls [1, 2]. A related problem of practical importance occurs when only a portion of the bottom surface is heated and the rest of it is either adiabatic or isothermally cooled. This situation is encountered in several geothermal areas which consist of troughs of volcanic debris contained by walls of nonfragmented ignimbrite. Thus, the model region considered is a locally heated long trough of isotropic porous medium confined by impermeable and insulating surroundings. Also, the recent motivation to study this problem has come from the efforts to identify a geologic repository for nuclear waste disposal.

Elder [3] was the first to study free convection in a horizontal cavity with localized heating from below (Fig. 1, $\partial T/\partial x = 0$ replaced by $T = T_c$). He observed that more than one cell exists in the "half cavity" for $H \geq 1.5$, and the Nusselt number is a function of H and the number of cells. Later, he conducted a numerical and experimental study for the transient problem, and reported several interesting features of the growth of eddies, and an alternation between the periods of slow gradual adjustment and the periods of rapid change for cellular flow behavior [4].

Horne and O'Sullivan [5] considered the problem for the case when the vertical walls of the cavity are adiabatic (Fig. 1; $y = 0, x > d, T = T_c$). Their results indicate that if the lower boundary is partially heated, the system is self-restricting, and either stabilizes into steady multicellular flow or regularizes into periodic oscillatory flow, depending on how much of the boundary is heated. However, oscillatory flow generally exists at high Rayleigh numbers. Later, they [6] also studied the effects of temperature-dependent viscosity and thermal expansion coefficient on temperature and flow fields.

Although the preceding studies [3-6] report interesting features of free convection in porous media for localized heating from below, they are generally concerned with the flow structure and provide little information on heat transfer rates. To characterize the effects of heat source size and strength fully, as well as the vertical and horizontal extent of the porous layer and its boundary conditions, a series of studies is required for a wide range of parameters, namely dimensionless heated length H, aspect ratio A, and Rayleigh number Ra*. The purpose of the present work is to consider the effects of aspect ratio and Rayleigh number on free convection heat transfer from an isothermal heat source centrally located on the bottom surface of a horizontal porous cavity (Fig. 1).

Formulation and Numerical Method

Consider a fluid-saturated horizontal porous layer enclosed by adiabatic vertical walls. An isothermal heat source of length $2d$ is centrally located on the bottom surface which is otherwise adiabatic (Fig. 1). The upper surface is considered

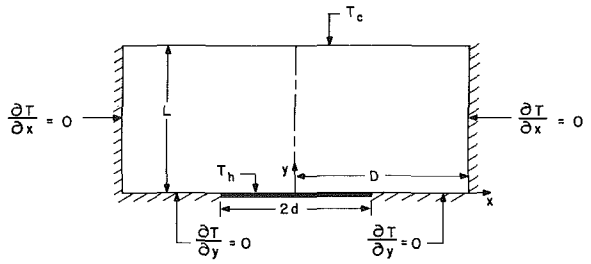

Fig. 1 Two-dimensional horizontal porous layer with localized heating from below

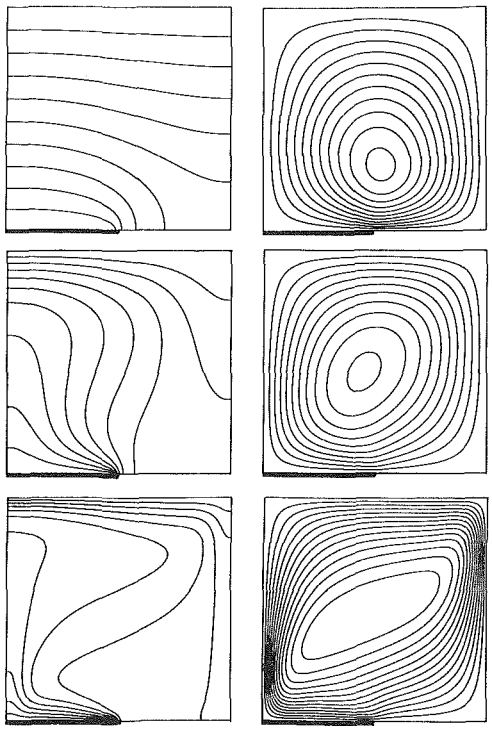

Fig. 2 Isotherms ($\Delta\theta = 0.1$) and streamlines for the half cavity, $A = 1$, $H = 0.5$: (*a*) $Ra^* = 10$ ($\Delta\Psi = 0.015$), (*b*) $Ra^* = 100$ ($\Delta\Psi = 0.5$), and (*c*) $Ra^* = 1000$ ($\Delta\Psi = 1.5$)

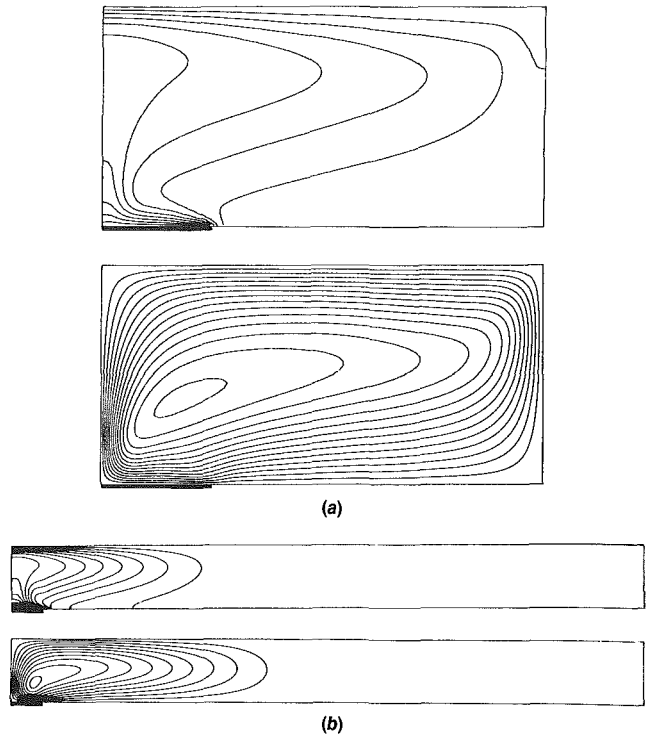

Fig. 3 Isotherms and streamlines for the half cavity, $H = 0.5$, $Ra^* = 1000$: (*a*) $A = 2$ ($\Delta\theta = 0.1$, $\Delta\Psi = 3.0$), and (*b*) $A = 10$ ($\Delta\theta = 0.05$, $\Delta\Psi = 20$)

to be maintained at a temperature T_c. In the porous medium, Darcy's law is assumed to hold, the fluid is assumed to be a normal Boussinesq fluid, and the viscous drag and inertia terms of the momentum equations are neglected because their magnitudes are of small order compared to other terms for low Darcy numbers and low particle Reynolds numbers. With these assumptions, the conservation equations for steady, two-dimensional flow in an isotropic, homogeneous porous medium reduce to [7]

$$\frac{1}{A^2}\frac{\partial^2\Psi}{\partial X^2} + \frac{\partial^2\Psi}{\partial Y^2} = Ra^*\frac{\partial\theta}{\partial X} \tag{1}$$

$$\frac{\partial\Psi}{\partial X}\frac{\partial\theta}{\partial Y} - \frac{\partial\Psi}{\partial Y}\frac{\partial\theta}{\partial X} = \frac{\partial^2\theta}{\partial X^2} + A^2\frac{\partial^2\theta}{\partial Y^2} \tag{2}$$

The relevant hydrodynamic and thermal boundary conditions are (Fig. 1)

$$\theta(X, 0) = 1, \quad 0 \le X \le H_1 \tag{3a}$$

$$\frac{\partial\theta}{\partial Y}(X, 0) = 0, \quad H_1 < X \le 1 \tag{3b}$$

$$\theta(X, 1) = 0 \tag{3c}$$

$$\frac{\partial\theta}{\partial X}(0, Y) = \frac{\partial\theta}{\partial X}(1, Y) = 0 \tag{3d}$$

$$\Psi = 0 \text{ on all boundaries} \tag{3e}$$

Owing to the symmetry of the problem (Fig. 1), only the right half of the cavity has been considered for computational purposes. This will be referred to as the "half cavity" in the discussions later.

Finite-difference equations are derived from equations (1) and (2) by integration over finite area elements following a procedure developed by Spalding and co-workers [8]. This introduces upwind differences for the convective terms in the energy equation. The successive-substitution formulas derived in this way satisfy the convergence criterion and are quite stable for many circumstances [8, 9]. For solving the system of algebraic equations thus obtained, a point iterative method is used. The solution technique is well described in the literature [8] and has been widely used for natural convection problems [7, 10].

In the present work, uniform mesh sizes are used in both x and y directions. The number of grids in the y direction is always taken as 31 whereas that in the x direction is varied between 31 and 61 depending on the aspect ratio. In general, the stream function Ψ is underrelaxed and the temperature θ is overrelaxed to obtain faster convergence. A convergence criterion of maximum 0.01 percent change in both Ψ and θ at all grid points in the domain is used to test the convergence of the iterative scheme. A detailed discussion on the numerical scheme is presented in [7, 10].

Results and Discussion

To study the effects of the size of the heat source and the extent of the horizontal layer on temperature and flow fields and heat transfer rates, two situations are examined in this study. First, the width of the horizontal layer D is varied from a low to high value for a fixed length of heated segment and a fixed height, i.e., $H = 0.5$. In the second part, the results are obtained for $H = 0.2$, 0.5, and 0.8, and $A = 1$.

Temperature and Flow Fields. Flow patterns and temperature fields for some typical values of Ra^*, A, and H are presented in Figs. 2 and 3. Figure 2(*a*) shows that the conduction temperature field is modified and a recirculatory motion is set at a Rayleigh number as low as 10. This is primarily due to the strong influence of the size of the heat source. It is well established that if the entire bottom surface is heated, the onset of convection takes place at $Ra^* \simeq 40$ [1, 2]. Hence, for a given Ra^*, the heat transfer rate per unit area of the heat source has increased by a decrease in the length of the heated segment.

At $Ra^* = 10$, the velocity field is symmetric about the vertical axis at $X = 0.5$ (Fig. 2*a*), and the disturbance in the temperature field is mostly near the heat source. As Ra^* increases, the isotherms move toward the upper surface produc-

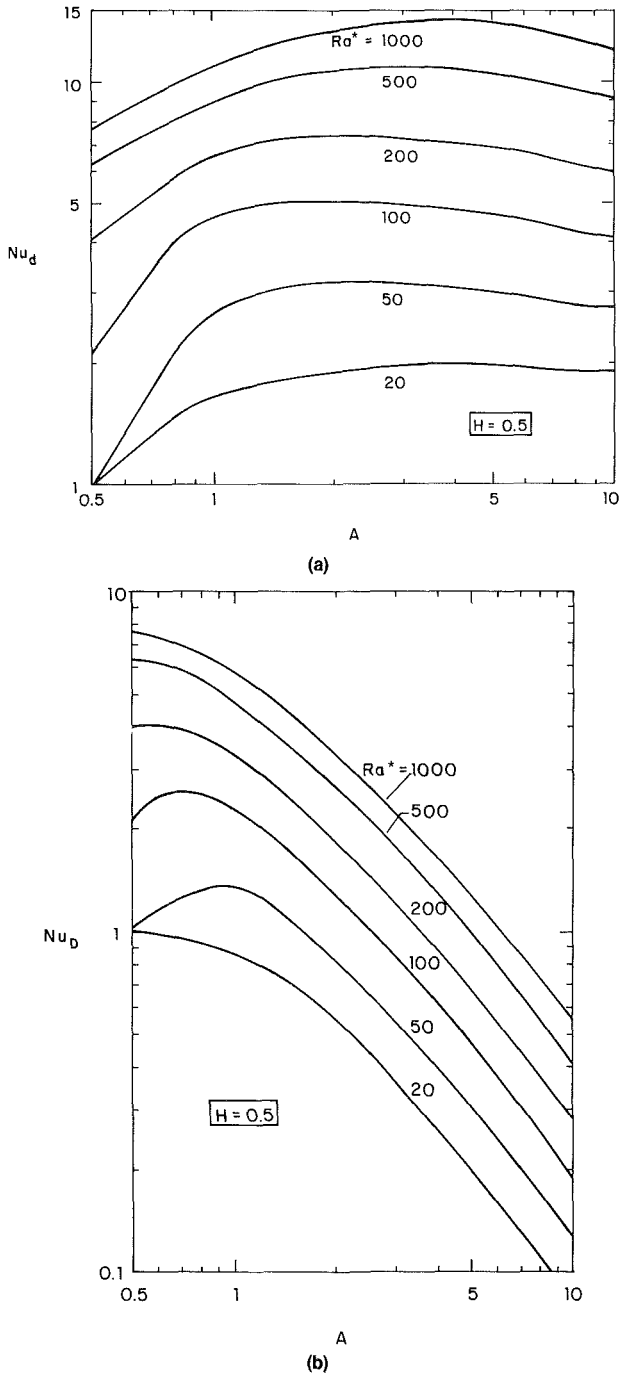

Fig. 4 Average Nusselt number for $H = 0.5$: (*a*) heat source, and (*b*) upper surface (values for $A = 0.5$ have been obtained from Caltagirone [11])

ing a highly stratified region near $Y = 1$, particularly for $0 < X < 0.5$ (Fig. 2*b*). The velocities are then higher in the bottom left corner indicating strong buoyancy effects near the heated portion and the temperature gradient is large close to the leading edge of the heated segment ($X = 0.5$, $Y = 0$).

If Ra* is further increased, the stratification in the upper layers is strengthened and the temperature decreases very fast near the hot surface (Fig. 2*c*). An inversion in temperature takes place in the middle region (the so-called core), particularly when $0 < X < 0.5$. This inversion in temperature starts at a Rayleigh number as low as 100 and becomes more distinct at higher Ra* (Fig. 2*c*), and is a direct consequence of the strong convective flows near the walls. The returning cold fluid is observed to move at a higher velocity toward the hot surface particularly in a region close to the bottom surface. This results in a sharp temperature gradient in that region. However, the heated fluid fills the upper half of the cavity which produces an inverse temperature gradient in the core, and smaller velocities around the center of the half cavity (Fig. 2*c*). Moreover, the inverse stratification in the core tends to diminish the heat transfer rates, and as a result the rate of increase in Nusselt number decreases with an increase in Ra*.

In Figs. 3(*a*, *b*), the temperature and flow fields are presented for $A = 2$ and 10, and $H = 0.5$. As expected, the fluid velocities in the region away from the heat source decrease with an increase in the layer width (Figs. 2*c*, 3*a*, *b*). Conversely, the velocities in the left corner of the half cavity are higher for larger aspect ratios. When A is increased from 1 to 2, the inversely stratified fluid fills the entire core (Figs. 2*c* and 3*a*). In fact, this behavior is consistently followed for an increase in aspect ratio beyond 0.5 (fully heated bottom surface). However, the extent of the porous layer significantly affected by the convective transport of energy decreases with an increase in aspect ratio beyond 2, for fixed Ra* and H (Fig. 3).

The above decrease in the domain of strong thermal activity results in complex heat transfer behavior. The heat transfer rate does not continually increase with an increase in the surface area for heat rejection. In the present case ($H = 0.5$, Ra* = 1000), the heat transfer rate is observed to be maximum for $A \simeq 4$, beyond which it starts decreasing. However, the aspect ratio for which it is largest is a strong function of H and Ra* (to be discussed later).

Heat Transfer Results. The two most appropriate ways of considering the overall heat transfer are to obtain either (*i*) a Nusselt number for the heat source as

$$\mathrm{Nu}_d = \bar{h}_d L/k = -\frac{A}{H}\int_0^{H_1} \frac{\partial\theta}{\partial Y}\Big|_{Y=0} dx \qquad (4)$$

or (*ii*) the Nusselt number based on the area of the upper surface

$$\mathrm{Nu}_D = \bar{h}_D L/k = \frac{H}{A}\,\mathrm{Nu}_d = -\int_0^{H_1} \frac{\partial\theta}{\partial Y}\Big|_{Y=0} dx \qquad (5)$$

The Nusselt number based on the area of the heated region Nu_d is presented in Fig. 4(*a*) for $H = 0.5$. For a fixed Ra*, the Nusselt number increases with the aspect ratio ($A > 0.5$) indicating that the heat source loses more and more energy as the end walls are moved away from the leading edge of the heated segment. However, the rate of increase in Nu_d with A is a strong function of Ra* and A: the smaller the Rayleigh number, the higher the rate of increase in Nu_d. Also, for a fixed Ra*, the slope of the $\ln(\mathrm{Nu}_d)$-versus-$\ln(A)$ curve decreases with an increase in A. Finally, the slope approaches zero, beyond which a negative gradient is established (Fig. 4*a*). This clearly indicates that there exists an aspect ratio as a function of Ra* and H, for which the heat transfer rate is maximum: the higher the Rayleigh number, the larger the aspect ratio required for $(\mathrm{Nu}_d)_{\max}$ to occur (Fig. 4*a*). Furthermore, there is a wide range of aspect ratio for any fixed values of H and Ra*, for which the variation in Nusselt number is minimal. For example, the heat transfer rate varies by only 7 percent when the aspect ratio is changed from 2 to 7 for Ra* = 1000.

The negative slope of $\ln(\mathrm{Nu}_d)$-versus-$\ln(A)$ curve (Fig. 4*a*) is also a function of Rayleigh number: the higher the Rayleigh number, the larger this slope. However, for a fixed Ra*, the Nusselt number finally approaches an asymptotic value (Fig. 4*a*) indicating that the location of the end walls no longer affects the overall heat transfer. Present computational results support this for at least Ra* $\leq$ 100. For higher Rayleigh numbers, Ra* $>$ 100, this occurs at $A > 10$, which is beyond the present computational range.

Numerical results of Caltagirone [11] for a fully heated bot-

Table 1 Nusselt number on the upper surface Nu_D for aspect ratio $A = 1$ (values for $H_1 = 1$ are obtained from Caltagirone [11])†

Ra* \ H_1	0.2	0.5	0.8	1.0
20	0.620	0.855	0.970	1.0
50	0.823	1.360	1.368	1.450
100	1.345	2.290	2.631	2.676
200	1.970	3.296	3.810	3.813
500	3.132	4.640	5.556	5.618, 5.332
1000	5.374	5.875		

†For $A = 1$, $H = H_1$.

tom surface ($H_1 = 1$) support the present observation that for fixed values of Ra* and H, the Nusselt number goes through a maximum as a function of aspect ratio. However, there exists a basic difference, that is, in the case of fully heated bottom surface, the larger the Rayleigh number, the smaller is the aspect ratio required for Nu_{max}. It will be interesting to know when and why the behavior is reversed when the heater size, H_1 is reduced below unity.

Figure 4(b) shows that the Nusselt number for the upper surface, Nu_D, decreases with an increase in aspect ratio except for a small range of Ra* and A. The increase in Nu_D for Ra* $\leq$ 100 is because of an extremely high rate of increase in Nu_d for $0.5 \leq A \leq 1$ (Fig. 4a). The rate of decrease in Nu_D is smaller at low values of A and is observed to increase with A. Finally, the $\ln(Nu_D)$-versus-$\ln(A)$ curve approaches a fixed slope for any given Ra*. This situation is achieved when Nu_d has reached an asymptotic value and the end effects are not significant.

The Nusselt numbers for various sizes of heat source are presented in Table 1, for $A = 1$. These values of Nu_D indicate that the overall heat transfer rate always increases with an increase in the size of heat source H_1. However, the rate of increase in Nu_D, which is very high at low values of H_1, decreases with an increase in H_1, and finally, approaches zero as $H_1 \to 1$. Indeed, the heat transfer rates for $H_1 = 0.8$ are very close to that for $H_1 = 1$ (Table 1).

It should be noted that owing to the present formulation of the steady problem (equations (1) and (2)), no oscillatory flow behavior could be observed in the present case. For a fully heated bottom surface, $H_1 = 1$, Caltagirone [11] has reported that fluctuating convection may be observed at Ra* > 380. Similar oscillatory flow behavior has also been reported by Horne and O'Sullivan [5]. The critical Rayleigh numbers for such a behavior are approximately 480 and 450 for $H_1 = 0.5$ and 0.25, respectively. Interestingly, the flow is steady for Rayleigh numbers up to 1250 when $H_1 = 0.75$ [5]. However, in a later work on property variation, Horne and O'Sullivan [6] have observed that oscillatory fluid flow instabilities may not be as prominent as might be expected using a constant viscosity analysis [6]. This may restrict the validity of present computational results at high Rayleigh numbers. It should, however, be noted that Horne and O'Sullivan [5, 6] have considered $\theta = 0$ for $X > H_1$ whereas the present study is for $\partial\theta/\partial Y = 0$ for $X > H_1$.

Conclusion

A numerical study has been reported for natural convection in a horizontal porous layer with localized heating from below. The isotherms and streamlines indicate that the conduction temperature field is modified and a recirculatory motion is set at very low Ra*. An increasing Rayleigh number produces a plumelike flow above the heated region and an inversely stratified temperature field in the core. The temperature gradients and velocities are high near the heat source and are observed to decrease continually with an increase in the horizontal distance away from the heat source.

The overall heat transfer rate always increases with the Rayleigh number. However, the rate of increase in Nu_D decreases with an increase in Ra* owing to the enhanced inverse stratification in the core. For fixed A, the overall heat transfer rate increases asymptotically with H. As the aspect ratio is increased for a fixed length of the heated segment, the portion of the cavity which is significantly affected by the convective transport of energy tends to be a smaller percentage of the total domain. For fixed values of Ra* and H, the Nusselt number first increases with aspect ratio and then decreases to an asymptotic value. Consequently, there exists an aspect ratio as a function of Ra* and H, for which the heat transfer rate is maximum.

Acknowledgments

The support of this work by the Department of Mechanical Engineering, Columbia University, and the U.S. Nuclear Regulatory Commission under Contract No. NRC-04-84-126 to the University of Delaware is appreciated.

References

1 Combarnous, M. A., and Bories, S. A., "Hydrothermal Convection in Saturated Porous Media," *Advances in Hydroscience*, Vol. 10, 1975, pp. 231-307.

2 Cheng, P., "Heat Transfer in Geothermal Systems," *Advances in Heat Transfer*, Vol. 14, 1978, pp. 1-105.

3 Elder, J. W., "Steady Free Convection in a Porous Medium Heated From Below," *Journal of Fluid Mechanics*, Vol. 27, 1967, pp. 29-48.

4 Elder, J. W., "Transient Convection in a Porous Medium," *Journal of Fluid Mechanics*, Vol. 27, 1967, pp. 609-623.

5 Horne, R. N., and O'Sullivan, M. J., "Oscillatory Convection in a Porous Medium Heated From Below," *Journal of Fluid Mechanics*, Vol. 66, 1974, pp. 339-352.

6 Horne, R. N., and O'Sullivan, M. J., "Convection in a Porous Medium Heated From Below: The Effect of Temperature Dependent Viscosity and Thermal Expansion Coefficient," ASME JOURNAL OF HEAT TRANSFER, Vol. 100, 1978, pp. 448-452.

7 Prasad, V., and Kulacki, F. A., "Convective Heat Transfer in a Rectangular Porous Cavity—Effect of Aspect Ratio on Flow Structure and Heat Transfer," ASME JOURNAL OF HEAT TRANSFER, Vol. 106, 1984, pp. 158-165.

8 Gosman, A. D., Pun, W. M., Runchal, A. K., Spalding, D. B., and Wolfshtein, M., *Heat and Mass Transfer in Recirculating Flows*, Academic Press, New York, 1969.

9 Roache, P. J., *Computational Fluid Dynamics*, Hermosa Publishers, Hermosa, CA, 1976.

10 Prasad, V., and Kulacki, F. A., "Natural Convection in a Rectangular Porous Cavity With Constant Heat Flux on One Vertical Wall," ASME JOURNAL OF HEAT TRANSFER, Vol. 106, 1984, pp. 152-157.

11 Caltagirone, J. P., "Thermoconvective Instabilities in a Horizontal Porous Layer," *Journal of Fluid Mechanics*, Vol. 72, 1975, pp. 269-287.

Unsteady Natural Convection in a Partially Heated Rectangular Cavity

D. Kuhn[1] and P. H. Oosthuizen[1]

1 Introduction

The present numerical study is concerned with two-dimensional unsteady natural convective flow in a rectangular enclosure with a partially heated vertical wall; the flow situation considered is shown in Fig. 1. It has been assumed that the fluid is initially at a uniform temperature and motionless. Then, at time zero, the heated element is heated to a higher uniform temperature, while the opposite wall is held at the initial fluid temperature with the remaining wall surfaces being assumed adiabatic. The development of the flow following this temperature change has been studied numerically. Results have been obtained for a number of heated surface element

[1]Department of Mechanical Engineering, Queen's University, Kingston, Ontario, Canada.

Contributed by the Heat Transfer Division for publication in the JOURNAL OF HEAT TRANSFER. Manuscript received by the Heat Transfer Division April 7, 1986.

Table 1 Nusselt number on the upper surface Nu_D for aspect ratio $A = 1$ (values for $H_1 = 1$ are obtained from Caltagirone [11])†

Ra* \ H_1	0.2	0.5	0.8	1.0
20	0.620	0.855	0.970	1.0
50	0.823	1.360	1.368	1.450
100	1.345	2.290	2.631	2.676
200	1.970	3.296	3.810	3.813
500	3.132	4.640	5.556	5.618, 5.332
1000	5.374	5.875		

†For $A = 1$, $H = H_1$.

tom surface ($H_1 = 1$) support the present observation that for fixed values of Ra* and H, the Nusselt number goes through a maximum as a function of aspect ratio. However, there exists a basic difference, that is, in the case of fully heated bottom surface, the larger the Rayleigh number, the smaller is the aspect ratio required for Nu_{max}. It will be interesting to know when and why the behavior is reversed when the heater size, H_1 is reduced below unity.

Figure 4(b) shows that the Nusselt number for the upper surface, Nu_D, decreases with an increase in aspect ratio except for a small range of Ra* and A. The increase in Nu_D for Ra* $\leq$ 100 is because of an extremely high rate of increase in Nu_d for $0.5 \leq A \leq 1$ (Fig. 4a). The rate of decrease in Nu_D is smaller at low values of A and is observed to increase with A. Finally, the $\ln(Nu_D)$-versus-$\ln(A)$ curve approaches a fixed slope for any given Ra*. This situation is achieved when Nu_d has reached an asymptotic value and the end effects are not significant.

The Nusselt numbers for various sizes of heat source are presented in Table 1, for $A = 1$. These values of Nu_D indicate that the overall heat transfer rate always increases with an increase in the size of heat source H_1. However, the rate of increase in Nu_D, which is very high at low values of H_1, decreases with an increase in H_1, and finally, approaches zero as $H_1 \to 1$. Indeed, the heat transfer rates for $H_1 = 0.8$ are very close to that for $H_1 = 1$ (Table 1).

It should be noted that owing to the present formulation of the steady problem (equations (1) and (2)), no oscillatory flow behavior could be observed in the present case. For a fully heated bottom surface, $H_1 = 1$, Caltagirone [11] has reported that fluctuating convection may be observed at Ra* > 380. Similar oscillatory flow behavior has also been reported by Horne and O'Sullivan [5]. The critical Rayleigh numbers for such a behavior are approximately 480 and 450 for $H_1 = 0.5$ and 0.25, respectively. Interestingly, the flow is steady for Rayleigh numbers up to 1250 when $H_1 = 0.75$ [5]. However, in a later work on property variation, Horne and O'Sullivan [6] have observed that oscillatory fluid flow instabilities may not be as prominent as might be expected using a constant viscosity analysis [6]. This may restrict the validity of present computational results at high Rayleigh numbers. It should, however, be noted that Horne and O'Sullivan [5, 6] have considered $\theta = 0$ for $X > H_1$ whereas the present study is for $\partial\theta/\partial Y = 0$ for $X > H_1$.

Conclusion

A numerical study has been reported for natural convection in a horizontal porous layer with localized heating from below. The isotherms and streamlines indicate that the conduction temperature field is modified and a recirculatory motion is set at very low Ra*. An increasing Rayleigh number produces a plumelike flow above the heated region and an inversely stratified temperature field in the core. The temperature gradients and velocities are high near the heat source and are observed to decrease continually with an increase in the horizontal distance away from the heat source.

The overall heat transfer rate always increases with the Rayleigh number. However, the rate of increase in Nu_D decreases with an increase in Ra* owing to the enhanced inverse stratification in the core. For fixed A, the overall heat transfer rate increases asymptotically with H. As the aspect ratio is increased for a fixed length of the heated segment, the portion of the cavity which is significantly affected by the convective transport of energy tends to be a smaller percentage of the total domain. For fixed values of Ra* and H, the Nusselt number first increases with aspect ratio and then decreases to an asymptotic value. Consequently, there exists an aspect ratio as a function of Ra* and H, for which the heat transfer rate is maximum.

Acknowledgments

The support of this work by the Department of Mechanical Engineering, Columbia University, and the U.S. Nuclear Regulatory Commission under Contract No. NRC-04-84-126 to the University of Delaware is appreciated.

References

1 Combarnous, M. A., and Bories, S. A., "Hydrothermal Convection in Saturated Porous Media," *Advances in Hydroscience*, Vol. 10, 1975, pp. 231-307.

2 Cheng, P., "Heat Transfer in Geothermal Systems," *Advances in Heat Transfer*, Vol. 14, 1978, pp. 1-105.

3 Elder, J. W., "Steady Free Convection in a Porous Medium Heated From Below," *Journal of Fluid Mechanics*, Vol. 27, 1967, pp. 29-48.

4 Elder, J. W., "Transient Convection in a Porous Medium," *Journal of Fluid Mechanics*, Vol. 27, 1967, pp. 609-623.

5 Horne, R. N., and O'Sullivan, M. J., "Oscillatory Convection in a Porous Medium Heated From Below," *Journal of Fluid Mechanics*, Vol. 66, 1974, pp. 339-352.

6 Horne, R. N., and O'Sullivan, M. J., "Convection in a Porous Medium Heated From Below: The Effect of Temperature Dependent Viscosity and Thermal Expansion Coefficient," ASME JOURNAL OF HEAT TRANSFER, Vol. 100, 1978, pp. 448-452.

7 Prasad, V., and Kulacki, F. A., "Convective Heat Transfer in a Rectangular Porous Cavity—Effect of Aspect Ratio on Flow Structure and Heat Transfer," ASME JOURNAL OF HEAT TRANSFER, Vol. 106, 1984, pp. 158-165.

8 Gosman, A. D., Pun, W. M., Runchal, A. K., Spalding, D. B., and Wolfshtein, M., *Heat and Mass Transfer in Recirculating Flows*, Academic Press, New York, 1969.

9 Roache, P. J., *Computational Fluid Dynamics*, Hermosa Publishers, Hermosa, CA, 1976.

10 Prasad, V., and Kulacki, F. A., "Natural Convection in a Rectangular Porous Cavity With Constant Heat Flux on One Vertical Wall," ASME JOURNAL OF HEAT TRANSFER, Vol. 106, 1984, pp. 152-157.

11 Caltagirone, J. P., "Thermoconvective Instabilities in a Horizontal Porous Layer," *Journal of Fluid Mechanics*, Vol. 72, 1975, pp. 269-287.

Unsteady Natural Convection in a Partially Heated Rectangular Cavity

D. Kuhn[1] and P. H. Oosthuizen[1]

1 Introduction

The present numerical study is concerned with two-dimensional unsteady natural convective flow in a rectangular enclosure with a partially heated vertical wall; the flow situation considered is shown in Fig. 1. It has been assumed that the fluid is initially at a uniform temperature and motionless. Then, at time zero, the heated element is heated to a higher uniform temperature, while the opposite wall is held at the initial fluid temperature with the remaining wall surfaces being assumed adiabatic. The development of the flow following this temperature change has been studied numerically. Results have been obtained for a number of heated surface element

[1]Department of Mechanical Engineering, Queen's University, Kingston, Ontario, Canada.

Contributed by the Heat Transfer Division for publication in the JOURNAL OF HEAT TRANSFER. Manuscript received by the Heat Transfer Division April 7, 1986.

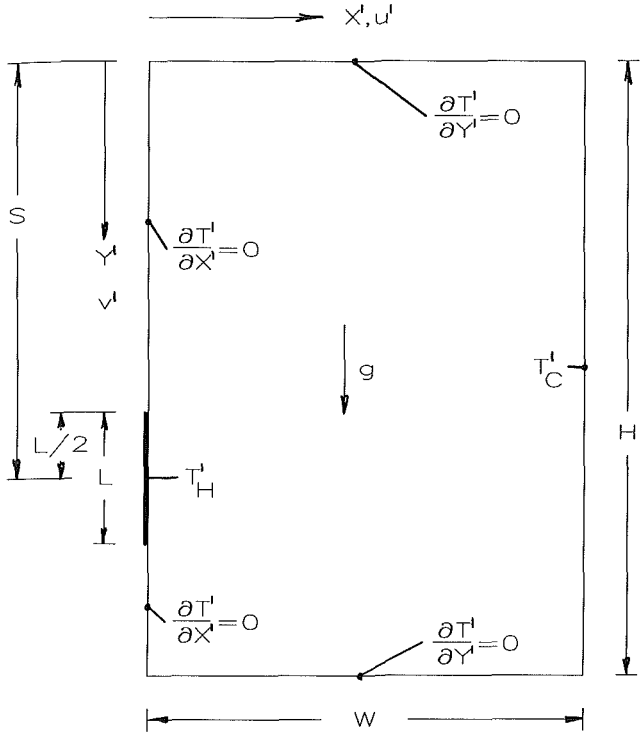

Fig. 1 Thermal boundary conditions

sizes and locations, cavity aspect ratios, and Rayleigh numbers.

Natural convection in enclosures has recently attracted considerable attention. Part of this attention is due to the fact that cavity flow is a reasonably good model of some situations that arise in the cooling of electronic equipment. The performance and life of microelectronic components are strongly temperature dependent and for proper operation they must be maintained within a specific temperature range (Mayer, 1983). Now, following startup, the natural convective heat transfer from a heated vertical surface may be expected to pass through a minimum before a higher steady-state heat transfer rate is achieved. Hence, the transient development of the heat transfer rate may be of importance in the natural convective cooling of electronic devices. A partially heated wall has been considered in the present study in order to model a discrete component on a circuit board approximately.

Previous studies of natural convection in enclosures have concentrated mainly on steady-state natural convective flow in rectangular cavities with both vertical walls at uniform but different temperatures. Comprehensive reviews of existing studies have been presented by Ostrach (1982, 1972) and Catton (1979). Steady-state natural convection in a rectangular enclosure with partially heated vertical wall has attracted less attention but has been extensively studied by Chu et al. (1976). Recent studies of the unsteady fully heated vertical side wall problem have been presented by Patterson et al. (1980) and Küblbeck et al. (1980). The situation considered here, i.e., the transient flow development in an enclosure following the sudden increase in temperature of a portion of a vertical wall, has attracted little attention.

In the present study, solutions have been obtained for a Prandtl number of 0.71 for Rayleigh numbers, based on the overall temperature difference and distance between the vertical walls, of between 0 and 100,000. The results have been used to examine the effect of heated element locations, cavity aspect ratio, and Rayleigh number on the variation of the mean heat transfer from the heated surface element with time.

2 Formulation

The study is based on the use of the two-dimensional time-dependent Navier–Stokes and energy equations. Fluid properties have been assumed constant except for the density change with temperature which has been treated using the Boussinesq approximation. The nondimensional stream function–vorticity formulation of these governing equations in Cartesian coordinates has been used with the dimensionless variables being defined as follows:

$$\phi=\frac{\phi' W^2}{\alpha} \qquad X=\frac{X'}{W} \qquad Y=\frac{Y'}{W}$$

$$\psi=\frac{\psi'}{\alpha} \qquad t=\frac{t'\nu}{W^2} \qquad \theta=\frac{(T'-T'_C)}{(T'_H-T'_C)}$$

The prime denotes a dimensional variable.

The finite difference model and solution procedure of Oosthuizen and Kuhn (1984) have been modified to apply to the present situation. The solution procedure is an underrelaxation Gauss–Seidel method using central differencing with iteration at each time step. The convergence criterion at each time step was $|(\theta^n-\theta^{n-1})/\theta^n| < 0.005$, where superscript n denotes the iteration number. $21 \times (15A+1)$ uniformly spaced grid points were used, where $A = (H/W)$ is the cavity aspect ratio. It has been shown (Kuhn, 1984) that this solution is grid independent to within 3 percent for a mesh size less than (1/16).

The average heat transfer rate from the heated element was determined by numerically integrating the local heat transfer rates. At the edge of the heated elements a singularity exists due to the mixed thermal boundary conditions. However, previous numerical studies, for example Torrance et al. (1969), have found that despite this type of singularity there is good agreement between results computed using the procedure adopted here and experimental results. A recent study by Bassani et al. (1986) presents a method for more accurately dealing with this type of singularity. A further confirmation of the adequacy of the adopted procedure is that the total amounts of heat transfer from the hot and cold surfaces in the steady state were always found to be in close agreement (better than about 2 percent).

3 Results and Discussion

Before considering the partially heated wall case, results for the fully heated wall case were first obtained and compared with those given in previous studies in order to validate the numerical procedure used in the present study. The average heated element Nusselt number Nu, based on the heated element length, and the maximum stream function ψ_{max} have been compared where possible with values given in these previous studies. Three previous transient studies have been considered for comparison. All of these studies considered the fully heated vertical side problem with the temperature of the enclosed fluid initially set at the mean of the wall temperatures. Results obtained by Küblbeck et al. (1980) are presented as stream function, temperature, and vorticity profiles at discrete times making comparison with present results difficult. However, their predicted flow development appears to agree with the present results and an estimate of the steady-state maximum stream function value from their steady-state stream function profile is in good agreement with the present results. Excellent agreement was found with the results of Patterson et al. (1980). The present results and those of Wilkes and Churchill (1966) show the same general variation of Nu with time, the times at which the initial temporal minimum and maximum Nusselt number occur agreeing to within $t = 0.018$. However the Nu values differ by as much as 10 percent. This difference is to be expected since the steady-state Nu

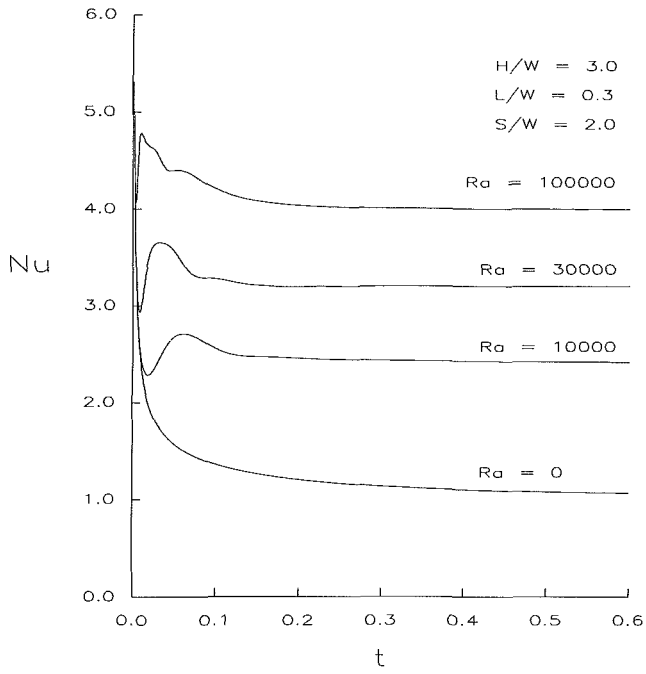

Fig. 2 Effect of Rayleigh number on the variation of Nu with time

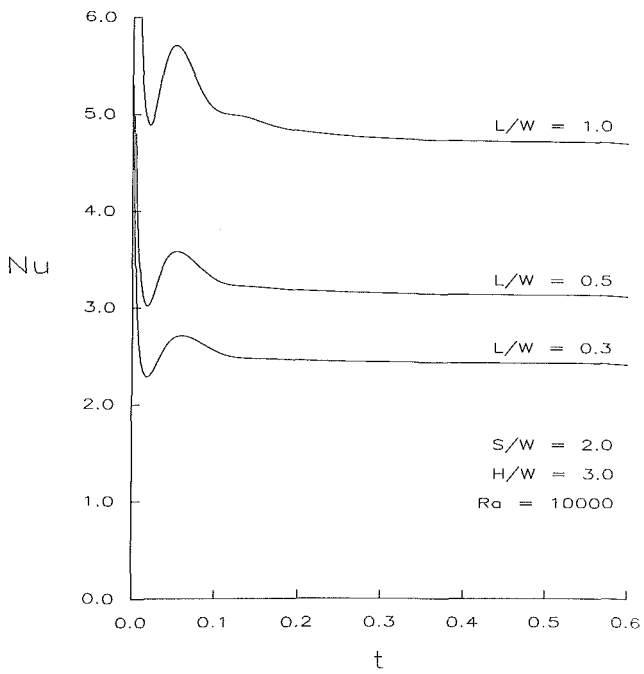

Fig. 4 Effect of heated element size on the variation of Nu with time

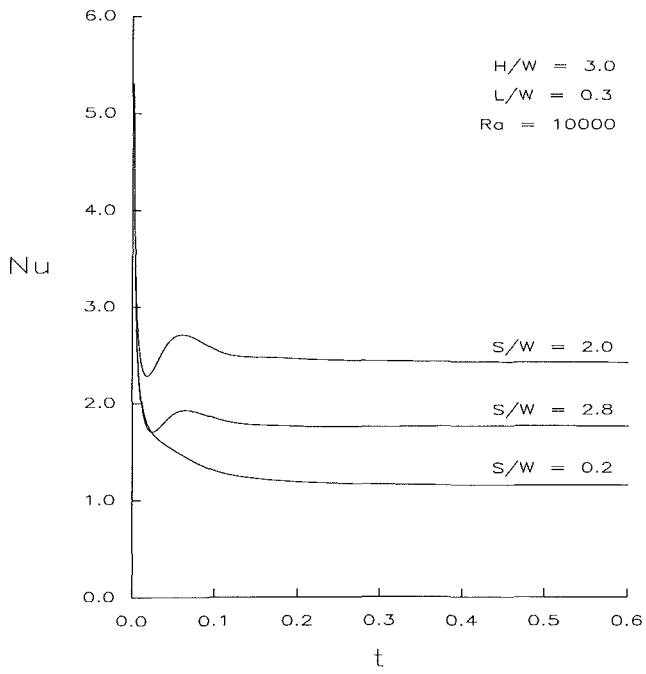

Fig. 3 Effect of heated element position on the variation of Nu with time

value obtained by Wilkes and Churchill (1966) using the same grid system as used in the transient analysis is significantly higher than the steady value they obtained using a more refined grid and values interpolated from the de Vahl Davis benchmark solution (1983). It was found in the present study that in all cases considered steady state was achieved by a dimensionless time of 0.6. The flow conditions at this time were compared with those given by the corresponding steady state results of de Vahl Davis (1983). Good agreement was found with these benchmark results.

The case where only part of the vertical wall is heated will now be considered. The effect of the heated element size, heated element location, and Rayleigh number on the variation of Nu with dimensionless time is shown in Figs. 2–4. From these figures it is clear that transition to steady state, for heated elements not located near the horizontal walls, consists of three distinct phases; namely:

(*i*) an initial phase where Nu decreases rapidly from an initially infinite value to a local temporal minimum. Heat transfer in the early stage of this phase is by conduction and is later added to by induced fluid motion;

(*ii*) a short phase where Nu increases to a local temporal maximum as the fluid motion intensifies; and

(*iii*) a phase where initially Nu decreases rapidly then slowly approaches the final steady-state value.

As mentioned, the first of these transient heat transfer phases where Nu is decreasing consists of two stages. In this first stage, the heat transfer is essentially by pure conduction. However the results differ from those for the case of a suddenly heated semi-infinite vertical plate in an infinite fluid (Ede, 1967) due to the finite height of the heated element and the finite volume of cooling fluid. Most recent work on the semi-infinite plate situation has been concerned with the effects of the plate thermal capacity, e.g., see Carey (1984). This thermal capacity effect has not, of course, been considered here.

The effect of Rayleigh number on the above transient phases for a given aspect ratio, heated element length, and position is shown in Fig. 2. As is to be expected, the temporal minimum, maximum, and steady-state Nu values are reached earlier for higher Rayleigh numbers. The relative value of the temporal minimum to the steady state Nu is of particular interest since the minimum heat transfer rate may be of significant importance. The temporal minimum Nu is lower than the steady-state Nu at the lower Rayleigh numbers, but for higher Rayleigh numbers this temporal minimum Nu becomes larger tending to be above the final steady-state value at the higher Rayleigh numbers considered. The conduction phase shortens for higher Rayleigh number and as a consequence the temporal minimum Nu occurs earlier. Hence, as the Rayleigh

number increases an increase in the temporal minimum Nu relative to the steady-state value is to be expected. The influence of Rayleigh number on the transient phases outlined above has been studied for other enclosure geometries and boundary conditions. The results indicate that Fig. 2 is representative of the effect of Rayleigh number on the variation of Nu with time for aspect ratios of 2:1, 3:1, and 4:1, for $L < W$ and for heated element locations $2L < S < (H-2L)$, i.e., for a heated element not located near the horizontal walls.

The effect of the heated element location, i.e., the influence of the horizontal wall, on the variation on Nu with time is illustrated by Fig. 3. All results for heated element locations in the range $2L < S < (H-2L)$ closely coincide with the curve of $S/W = 2$ shown in this figure. The variation of the heat transfer rate with time for elements located outside of this range is however strongly influenced by the heated element position. Heated elements located near the top, e.g., $S/W = 0.2$, experience no temporal maximum Nu. Here there is little fluid motion since the fluid heated by the element is unable to rise and hence heat transfer progresses mainly by conduction. The transient heat transfer development is not as strongly effected by the bottom wall. However, it will be noted from the curve of $S/W = 2.8$ that the heat transfer rate is still significantly reduced by the presence of the wall and that the local minimum and maximum are reached later, this being due to the restriction of fluid entrainment by the bottom wall. Hence, the variation of Nu with time is largely unaffected by the location of the heated element except when the heated element is close to a horizontal wall. The aspect ratio was found to have little effect on this result as long as S was within the "middle" region as defined above.

The variation of the heat transfer rate with time for various heated element sizes is shown in Fig. 4. With an increase in the heated element size the temporal minimum Nu occurs later, while the temporal maximum Nu occurs earlier. Also with increasing element size the temporal minimum Nu becomes larger than the steady-state Nu. The temporal minimum occurs later for larger elements since heated element edge effects take longer to extend past the longer elements, while the local maximum Nu occurs earlier for larger heated elements since the fluid is heated more rapidly by the larger heated elements.

Chu et al. (1976) studied the corresponding steady-state problem of localized heating in rectangular enclosures. The steady-state results of the present study agree with general trends outlined by Chu et al. (1976), namely:

(*i*) As the heater location moves from the top to the bottom Nu increases to a maximum then decreases;

(*ii*) as Ra increases the position of the heated element for the maximum Nu moves closer to the bottom;

(*iii*) as the aspect ratio increases for a given heater location, Nu approaches a constant value.

A comparison of the steady-state results obtained in the present study and results given by boundary layer theory for a vertical heated plate in an infinite environment suggests that boundary layer theory provides a good approximation of the computed values under constraints outlined below. The following relation can be developed from boundary layer theory (Schmidt, 1930):

$$\mathrm{Nu} = 0.52\,\mathrm{Ra}_L^{0.25} \tag{1}$$

This relationship may be related to the present enclosure problem by redefining the Rayleigh number on the width of the enclosure and equation (1) becomes

$$\mathrm{Nu} = 0.52(L/W)^{0.75}\mathrm{Ra}_W^{0.25} \tag{2}$$

Results from the present study agree to within 10 percent of those predicted by equation (2) under the following constraints:

$$10^4 \le \mathrm{Ra}_W \le 10^5, \qquad \frac{L}{W} \le 1, \qquad (2L) < S < (H-2L)$$

It may be noted that Chu et al. (1976) concluded that boundary layer theory was not useful for the prediction of computed values. However most of their results under the constraints and thermal boundary conditions outlined above agree to within 10 percent of Nu values predicted by equation (2). It is of interest to note that the fully heated wall case gives substantially lower steady-state Nu values than predicted by boundary layer theory; e.g., at $\mathrm{Ra} = 10^4$ the Nu value is 2.243 for a square enclosure (de Vahl Davis, 1983) compared to a value of 5.2 predicted by boundary layer theory.

4 Conclusions

The results indicate that it is possible for the temporal minimum heat transfer rate to be less than the steady-state value at lower Rayleigh numbers. The results also show that the temporal changes in the heat transfer rate are little affected by the position of the heated element unless this element is very close to a horizontal wall.

Acknowledgments

This work was supported by the Natural Sciences and Engineering Research Council of Canada.

References

Bassani, J. L., Nansteel, M. W., and November, M., 1986, "Adiabatic-Isothermal Mixed Boundary Conditions in Heat Transfer," *International Journal of Heat and Mass Transfer*, in press.

Carey, V. P., 1984, "Surface Thermal Capacity Effects in Transient Natural Convection Flows at High Prandtl Number," *International Journal of Heat and Mass Transfer*, Vol. 27, pp. 419–431.

Catton, I., 1978, "Natural Convection in Enclosures," *Proceedings of the 6th International Heat Transfer Conference*, J. T. Rodgers et al., eds., Hemisphere, Washington, DC, Vol. 6, pp. 13–31.

Chu, H. H.-S., Churchill, S. W., and Patterson, C. V. S., 1976, "The Effect of Heater Size, Location, Aspect Ratio, and Boundary Condition on Two-Dimensional, Laminar, Natural Convection in Rectangular Channels," ASME JOURNAL OF HEAT TRANSFER, Vol. 98, pp. 194–201.

de Vahl Davis, G., 1983, "Natural Convection of Air in a Square Cavity: A Bench Mark Solution," *International Journal for Numerical Methods in Fluids*, Vol. 3, pp. 249–264.

Ede, A. J., 1967, "Advances in Free Convection," *Advances in Heat Transfer*, J. P. Hartnett and T. E. Irvine, eds., Vol. 4, pp. 1–64.

Küblbeck, K., Merker, G. P., and Straub, J., 1980, "Advanced Numerical Computation of Two-Dimensional Time-Dependent Free Convection in Cavities," *International Journal of Heat and Mass Transfer*, Vol. 23, pp. 203–217.

Kuhn, D., 1984, "A Numerical Solution of Unsteady Free Convective Flow in a Square and a Circular Container Filled With a Liquid and a Gas," M.Sc. Thesis, Queen's University, Kingston, Canada.

Mayer, A. H., 1983, "Heat Transfer Technology in the Service of the Microelectronic Revolution," *Heat Transfer in Electronic Equipment – 1983*, S. Oktay and A. Bar-Cohen, eds., ASME HTD Vol. 28, pp. 1–3.

Oosthuizen, P. H., and Kuhn, D., 1984, "Unsteady Free Convective Heat Transfer Through a Closed Square Container Filled With a Liquid and a Gas," ASME Paper No. 84-HT-66.

Ostrach, S., 1982, "Natural Convection Heat Transfer in Cavities and Cells," *Proceedings, 7th International Heat Transfer Conference*, U. Grigul et al., eds., Hemisphere, Washington, DC, Vol. 1, pp. 365–379.

Ostrach, S., 1972, "Natural Convection in Enclosures," *Advances in Heat Transfer*, J. P. Hartnett and T. E. Irvine, eds., Vol. 8, pp. 161–227.

Patterson, J., and Imberger, J., 1980, "Unsteady Natural Convection in a Rectangular Cavity," *Journal Fluid Mechanics*, Vol. 100, Part 1, pp. 65–86.

Torrance, K. E., 1969, "Numerical Study of Natural Convection in an Enclosure With Localized Heating From Below – Creeping Flow to the Onset of Laminar Instability," *Journal of Fluid Mechanics*, Vol. 36, Part 1, pp. 33–54.

Schmidt, E., and Beckmann, W., 1930, *Tech. Mech. Thermodyn.*, Vol. 1, p. 341.

Wilkes, J. O., and Churchill, S. W., 1966, "The Finite Difference Computation of Natural Convection in a Rectangular Enclosure," *AIChE Journal*, Vol. 12, pp. 161–166.

Mixed Layer Development in a Salt-Stratified Solution Destabilized by a Discrete Heat Source

T. L. Bergman,[1] A. Ungan,[2] F. P. Incropera,[2,3] and R. Viskanta[2,3]

Nomenclature

c = specific heat
g = gravitational acceleration
m_s = salt mass fraction
q_b = bottom heat flux
Ri = Richardson number = $g\Delta\rho\delta_b/\rho_0 u_*^2$
t = time
T = temperature
u_e = entrainment velocity = $d\delta_b/dt$
u_* = convective velocity = $(g\ \beta_T\ q_b\ \delta_b/\rho_b\ c_b)^{1/3}$
z = vertical coordinate positive upward
β_T = thermal expansion coefficient
δ_b = bottom mixed layer height
$\Delta\rho$ = mass density difference across the interfacial boundary layer
ρ = mass density

Subscripts

b = bottom
i = initial

Introduction

Progress has recently been made in correlating mixed layer growth rates in linearly salt-stratified solutions which are destabilized by uniform bottom heating (Bergman et al., 1986). The correlation for the mixed layer growth rate, normalized with a convective velocity, is expressed in terms of a Richardson number Ri associated with convective conditions within the mixed layer.

The present study was conducted to investigate further the extent to which mixed layer growth depends on flow conditions within the mixed layer. In particular, a linearly salt-stratified solution was destabilized by a heated strip embedded in an otherwise adiabatic bottom surface. In contrast to the three-dimensional flow resulting from uniform bottom heating, flow conditions in the present study are, in general, two-dimensional. Variations in the mixed layer growth rate would reinforce the notion that entrainment rates vary with flow conditions within the mixed layer.

Experimental Apparatus

The test cell described by Bergman et al. (1986) was modified to provide localized bottom heating (Fig. 1). Its bottom was equipped with a heated strip (102 mm wide) extending along the center of the test cell base (305 mm × 305 mm). The strip was constructed in a sandwich configuration and was flush-mounted into an acrylic sheet (25 mm thick), which was the bottom of the test cell. The heated strip consisted of (top to bottom): (*i*) a 3.2 mm copper plate, (*ii*) an electric patch heater (main heater), (*iii*) a 98 × 305 × 19 mm styrofoam sheet, and (*iv*) a second patch (guard) heater. The 2 mm gaps

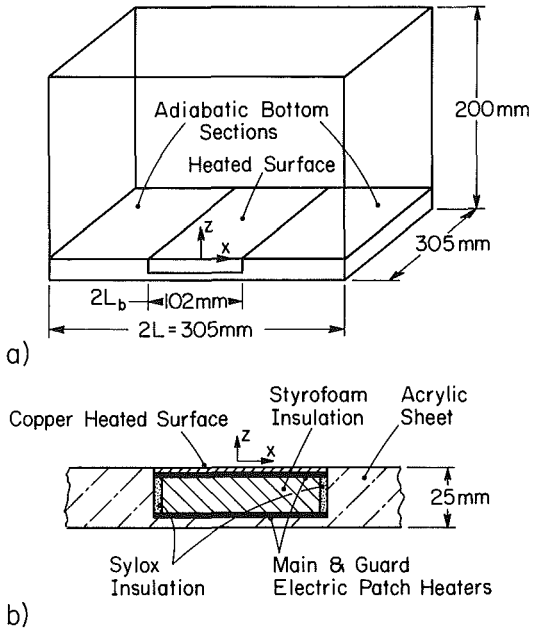

Fig. 1 Schematic of the test cell (*a*) and the heater assembly (*b*)

Table 1 Experimental conditions

Experiment	q_b, W/m^2	$\partial m_s/\partial z\|_i$, percent/m
1	100	15
2	100	5
3	500	25

on either side of the styrofoam were filled with Sylox to minimize lateral heat transfer. The test cell walls were insulated with removable styroform sheets which allowed flow visualization (laser illumination of injected fluorescein dye) to be performed. Vertical temperature distributions were measured with a thermocouple rake positioned at the center of the test cell. Guard heater operation is described by Bergman et al. (1986).

Three experiments were performed with various applied heat fluxes q_b and initial salinity gradients (Table 1). To facilitate a meaningful comparison with the results of Bergman et al. (1986), q_b is based on the bottom area of the test cell, rather than the area of the heated strip.

Results and Discussion

Figure 2 shows typical flow visualization during the initial stages of experiment 3. Convective motion begins above the heated strip and propagates laterally to the test cell walls. The fluid motion is nearly two-dimensional, and remained so throughout each experiment which was allowed to continue for approximately 12 h. The bottom mixed layer becomes warmer with time and serves as a heat source for the overlying stratified fluid. Thermocouples placed to the side of the center rake indicated that horizontal temperature gradients were small.

Mixed layer temperatures and heights were recorded for experiments 1 and 2, permitting evaluation of growth rates, thermophysical properties (U.S. Office of Saline Water, 1964), convective velocities, and Richardson numbers. Experiment 3 was characterized by multiple mixed layer development and, as such, could not be used to verify the Ri correlation shown in Fig. 3. A least-squares fit of the data yields $u_e/u_* = 1.35\ \mathrm{Ri}^{-1.4}$, which is contrasted with the upper and lower bounds of results obtained for uniformly heated solutions (indicated by the solid lines of Fig. 3, Bergman et al., 1986).

[1]Department of Mechanical Engineering, University of Texas at Austin, Austin, TX 78712; Assoc. Mem. ASME.
[2]Department of Mechanical Engineering, Purdue University, West Lafayette, IN 47907.
[3]Fellow ASME.

Contributed by the Heat Transfer Division for publication in the JOURNAL OF HEAT TRANSFER. Manuscript received by the Heat Transfer Division January 30, 1986.

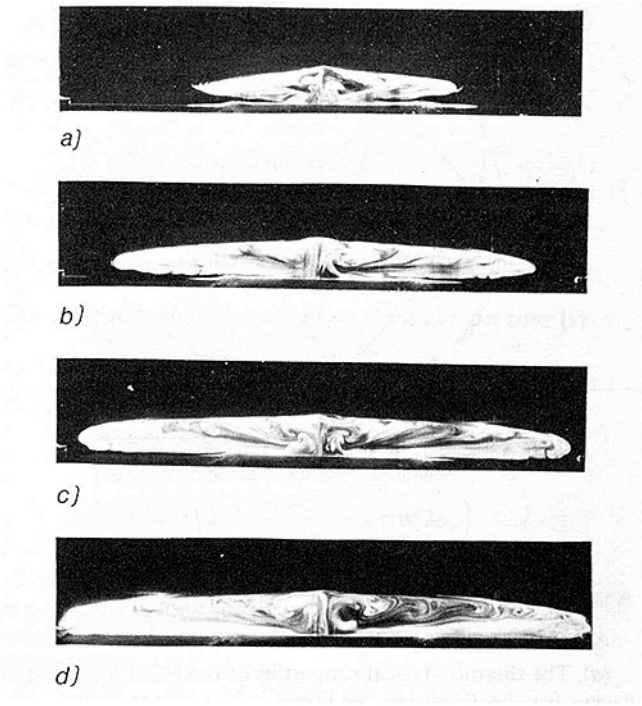

Fig. 2 Fluorescein dye visualization of the two-dimensional convective flow of experiment 3: (*a*) $t = 90$ s, (*b*) $t = 150$ s, (*c*) $t = 210$ s, (*d*) $t = 330$ s

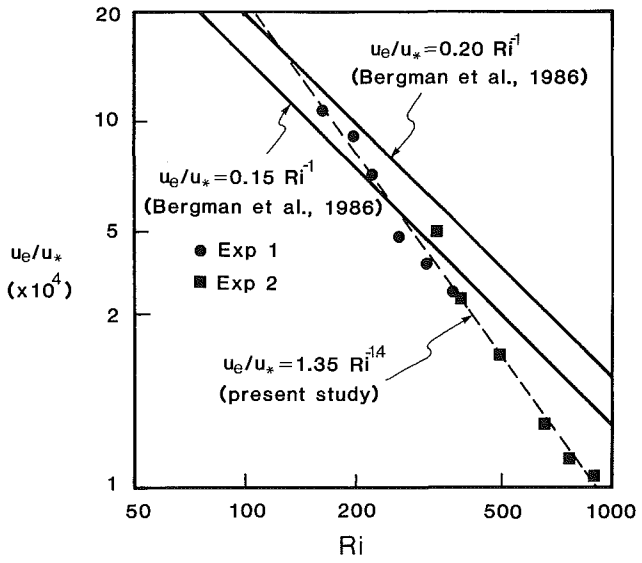

Fig. 3 Mixed layer growth correlations

Although the magnitudes of the entrainment rate are similar, slopes of the correlations are different. This confirms the influence of the structure of the convective motion on entrainment. Since Ri increases with increasing mixed layer height, Fig. 3 indicates that, relative to uniform bottom heating, entrainment due to the heated strip becomes less effective at large ($\simeq 100$ mm) δ_b. This trend is attributed to a three-dimensional oscillation in the central plume which developed as δ_b increased. The oscillation increased dissipative effects in the mixed layer, leaving less convective energy available for entrainment. Since the experiments of the present and previous studies were performed in the same test cell, variations in the correlation can not be atrributed to test-cell-dependent effects other than those associated with modification of the bottom thermal boundary condition.

Further consideration of two-dimensional effects could be accomplished by varying the width of the heated strip. These considerations may be addressed in future studies.

Acknowledgments

Support of this work by the National Science Foundation under Grants CBT-8316580 and CBT-8552806 is gratefully acknowledged.

References

Bergman, T. L., Incropera, F. P., and Viskanta, R., 1986, "Correlation of Mixed Layer Growth in a Double-Diffusive, Salt-Stratifed System Heated From Below," ASME JOURNAL OF HEAT TRANSFER, Vol. 108, pp. 206–211.

U.S. Office of Saline Water, 1964, Technical Data Book.

Numerical Investigation of Melting Inside a Horizontal Cylinder Including the Effects of Natural Convection

A. Prasad[1] and S. Sengupta[2]

Nomenclature

- Ar = Archimedes number
- Cp = specific heat
- D = cylinder diameter
- F1(ϕ) = circumference of cylinder
- F2(ϕ, t) = interface position
- g = acceleration due to gravity
- Gr = Grashof number
- h = latent heat of fusion
- k = thermal conductivity
- Nu = Nusselt number
- P = pressure
- Pr = Prandtl number
- r = radial coordinate in physical plane
- Ra = Rayleigh number
- s = drop of original center of solid core
- Ste = Stefan number
- t = time in the physical plane
- T = temperature
- u = velocity in the radial direction
- v = velocity in the tangential direction
- V = velocity vector
- α = thermal diffusivity
- β = coefficient of thermal expansion of liquid
- η = radial coordinate in transformed plane
- θ = angular coordinate in the transformed plane
- ν = kinematic viscosity
- ρ = density
- τ = time in the transformed plane
- ϕ = angular coordinate in physical plane

[1]Research Assistant, Department of Mechanical Engineering, Stanford University, Stanford, CA 94305.

[2]Professor, Department of Mechanical Engineering, University of Miami, Coral Gables, FL 33124.

Contributed by the Heat Transfer Division and presented at the ASME Winter Annual Meeting, Miami Beach Florida, November 17–21, 1985. Manuscript received by the Heat Transfer Division October 2, 1985.

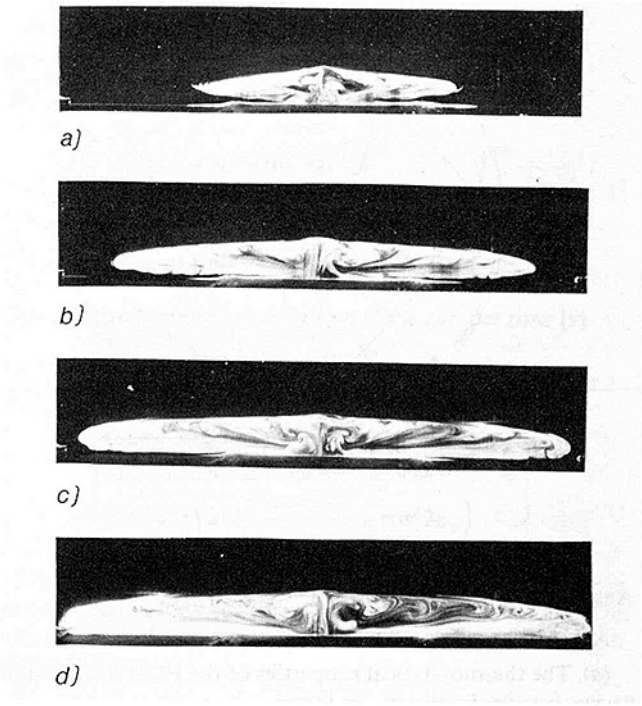

Fig. 2 Fluorescein dye visualization of the two-dimensional convective flow of experiment 3: (*a*) $t = 90$ s, (*b*) $t = 150$ s, (*c*) $t = 210$ s, (*d*) $t = 330$ s

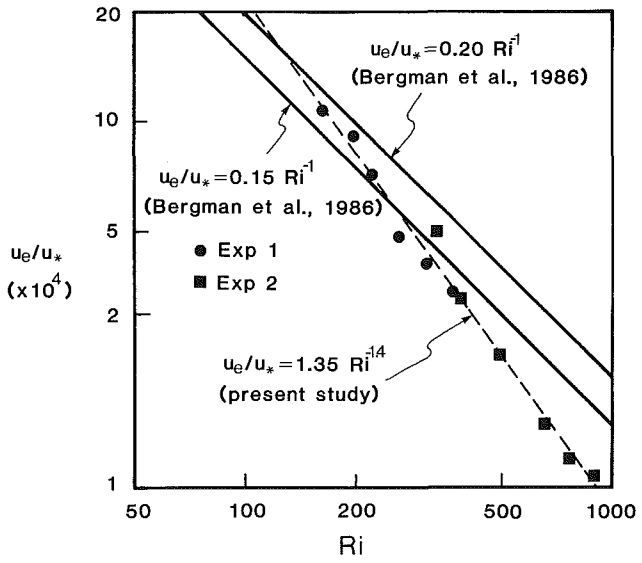

Fig. 3 Mixed layer growth correlations

Although the magnitudes of the entrainment rate are similar, slopes of the correlations are different. This confirms the influence of the structure of the convective motion on entrainment. Since Ri increases with increasing mixed layer height, Fig. 3 indicates that, relative to uniform bottom heating, entrainment due to the heated strip becomes less effective at large ($\simeq 100$ mm) δ_b. This trend is attributed to a three-dimensional oscillation in the central plume which developed as δ_b increased. The oscillation increased dissipative effects in the mixed layer, leaving less convective energy available for entrainment. Since the experiments of the present and previous studies were performed in the same test cell, variations in the correlation can not be atrributed to test-cell-dependent effects other than those associated with modification of the bottom thermal boundary condition.

Further consideration of two-dimensional effects could be accomplished by varying the width of the heated strip. These considerations may be addressed in future studies.

Acknowledgments

Support of this work by the National Science Foundation under Grants CBT-8316580 and CBT-8552806 is gratefully acknowledged.

References

Bergman, T. L., Incropera, F. P., and Viskanta, R., 1986, "Correlation of Mixed Layer Growth in a Double-Diffusive, Salt-Stratifed System Heated From Below," ASME JOURNAL OF HEAT TRANSFER, Vol. 108, pp. 206–211.

U.S. Office of Saline Water, 1964, Technical Data Book.

Numerical Investigation of Melting Inside a Horizontal Cylinder Including the Effects of Natural Convection

A. Prasad[1] and S. Sengupta[2]

Nomenclature

- Ar = Archimedes number
- Cp = specific heat
- D = cylinder diameter
- F1(ϕ) = circumference of cylinder
- F2(ϕ, t) = interface position
- g = acceleration due to gravity
- Gr = Grashof number
- h = latent heat of fusion
- k = thermal conductivity
- Nu = Nusselt number
- P = pressure
- Pr = Prandtl number
- r = radial coordinate in physical plane
- Ra = Rayleigh number
- s = drop of original center of solid core
- Ste = Stefan number
- t = time in the physical plane
- T = temperature
- u = velocity in the radial direction
- v = velocity in the tangential direction
- V = velocity vector
- α = thermal diffusivity
- β = coefficient of thermal expansion of liquid
- η = radial coordinate in transformed plane
- θ = angular coordinate in the transformed plane
- ν = kinematic viscosity
- ρ = density
- τ = time in the transformed plane
- ϕ = angular coordinate in physical plane

[1]Research Assistant, Department of Mechanical Engineering, Stanford University, Stanford, CA 94305.

[2]Professor, Department of Mechanical Engineering, University of Miami, Coral Gables, FL 33124.

Contributed by the Heat Transfer Division and presented at the ASME Winter Annual Meeting, Miami Beach Florida, November 17–21, 1985. Manuscript received by the Heat Transfer Division October 2, 1985.

Subscripts

a = point of contact between upper solid–liquid interface and outer wall
l = liquid
o = reference, fusion
w = cylinder wall

Introduction

Heat transfer problems involving phase change occur in a large number of practical situations: solidification in casting processes, purification of silicon wafers using laser-induced melting, and in latent-heat storage devices. Latent heat storage devices posses the advantages of a high density of energy storage and the ability to supply heat at a constant temperature. This allows the design of compact storage systems. For such a design we must know the duration of a complete melting cycle and the variation of the Nusselt number over time, given the storage configuration, the phase change material (PCM) used, and the heat transfer conditions at the boundary.

We chose a configuration consisting of a horizontal circular cylinder, initially filled with solid PCM at the saturation temperature and then subjected to a constant wall temperature. This configuration finds application in solar energy systems, wherein the working fluid is heated directly by the concentrator; the hot working fluid in turn flows over the storage cylinders and transfers heat to the PCM within by melting the PCM. During the period of heat extraction, the PCM releases the heat back to the environment by solidifying.

The problem of melting inside a horizontal cylinder has been studied by several investigators. The earlier studies [1, 2] assumed that conduction was the only mode of heat transfer, while others [3–6] assumed that the solid core was supported at the center, which prevented the unmelted solid from sinking to the bottom. Nicholas and Bayazitoglu [7] performed experiments which confirmed that the solid core does move downward; they also solved the problem numerically, but without the presence of natural convection. Elmasry and Sengupta [8] solved the problem numerically, taking all its features into account; however, their solution was handicapped by the presence of a singularity at the origin. Finally, Beer and Bareiss [9] performed an analytical solution which was confirmed by experiments. In this study, we have considered all the features of the problem; we have also made use of Beer's results to model the melting in the contact zone.

Problem Definition

At the outset the solid PCM completely fills the horizontal cylinder, and the temperature is at the melting point throughout. The wall temperature is then suddenly raised, and melting begins. Initially, the melt rate is uniform around the circumference. However, due to density differences, the solid core begins to sink, and the gap between the top of the core and the wall increases, while at the bottom the two are separated by a thin film of liquid where a high temperature gradient exists. This results in a large heat flux and consequently, a quick rate of melting in the contact zone. The rate of this bottom melting is modeled after Beer's findings.

This study strives to go beyond previous investigations by considering the effect of not only conduction, but also natural convection as the mechanisms of heat transfer from the outer wall to the solid core. The solution also models the gravity-induced downward motion of the core and determines the temperature and flow fields in the liquid region ($DF2 \le r \le DF1$ and $\phi_a \le \phi \le \pi/2$).

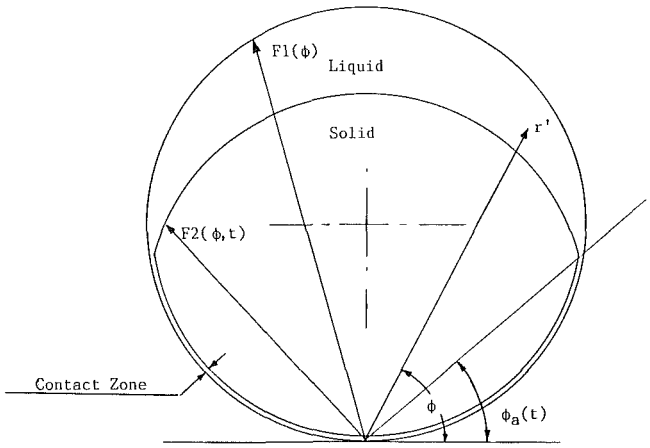

Fig. 1 Schematic diagram of coordinate system

Analysis

Assumptions

(*a*) The thermophysical properties of the PCM are constant except for the density of the liquid, which varies linearly with temperature.
(*b*) The Boussinesq approximation is valid.
(*c*) There exists a sharp interface between the solid and the liquid (no "mushy" region).
(*d*) End effects are neglected, which reduces the problem to two dimensions.
(*e*) The assumptions used by Beer to model the contact zone also apply to this study.
(*f*) The existence of the narrow jet that issues from the contact zone into the bulk of the melt pool is assumed to play an insignificant role.

Governing Equations. The governing equations were written using the bottommost point of the cylinder as the origin (Fig. 1).

The equations which refer to the melt region only are:

(*a*) *Continuity*

$$\nabla \cdot V = 0 \tag{1}$$

(*b*) *Momentum*

$$\frac{DV}{Dt} = -\frac{1}{\rho_0}\nabla P + G\left(\frac{\rho}{\rho_0} - 1\right) + \nu \nabla^2 V \tag{2}$$

where

$$\rho = \rho_0(1 - \beta(T - T_0)) \tag{3}$$

and

$$G = (-g \sin \phi, -g \cos \phi) \tag{4}$$

(*c*) *Energy*

$$\frac{DT}{Dt} = \alpha \nabla^2 T \tag{5}$$

(*d*) *Interface heat balance*

$$\rho h \frac{\partial r^*}{\partial t} \cdot \hat{n} = -k \nabla T(r, \phi, t) \cdot \hat{n} \tag{6}$$

at $r = r^*(\phi, t) = 0$, $t > 0$.

(e) *Solid core drop rate equation* [9]

$$\frac{ds'}{d\tau} = 1.608\left\{\frac{\text{Pr Ar } \rho'^3}{\text{Ste}}\right\}^{1/4} \cdot \text{Ste} \cdot \left\{\frac{2\phi_a - (\sin 4\phi_a)/2}{\sin 2\phi_a\left(2/3 + \frac{\cos^2 2\phi_a}{3} - \cos^4 2\phi_a\right)}\right\}^{1/4} \tag{7}$$

(f) *Nusselt number distribution in the contact zone* [9]

$$\text{Nu} = 1.608\rho'\left\{\frac{\text{Pr Ar}\rho'^3}{\text{Ste}}\right\}^{1/4} \cdot \frac{\sin 2\phi_a}{2\phi_a} \cdot \left\{\frac{2\phi_a - (\sin 4\phi_a)/2}{\sin 2\phi_a \cdot \left(2/3 + \frac{\cos^2 2\phi_a}{3} - \cos^4 2\phi_a\right)}\right\}^{1/4}$$

Since the problem is symmetric about the vertical diameter, we only need to look for a solution over half the domain. This property of half symmetry is reflected in the boundary and initial conditions.

Boundary Conditions:

(a) *Velocity*

$u = v = 0$ at $r' = D \cdot \sin\phi$, $\quad \phi_a \le \phi \le \pi/2, t > 0$

$u = v = 0$ at $r' = D \cdot \text{F2}(\phi, t)$ $\quad \phi_a \le \phi \le \pi/2, t > 0$

$\frac{\partial u}{\partial \phi} = v = 0$ at $\phi = \pi/2$, $\quad D \cdot \text{F2}(\phi, t) \le r \le D, t > 0$

(b) *Temperature*

$T = T_w$ at $r' = D \cdot \sin\phi$, $\quad \phi_a \le \phi \le \pi/2, t > 0$

$T = T_0$ at $r' = D \cdot \text{F2}(\phi, t)$, $\quad \phi_a \le \phi \le \pi/2, t > 0$

$\frac{\partial T}{\partial \phi} = 0$ at $\phi = \pi/2$, $\quad D \cdot \text{F2}(\phi, t) \le r \le D, t > 0$

Initial Conditions:

(a) *Velocity*

$u = v = 0$ in $D \cdot \text{F2}(\phi, t) \le r \le D \cdot \sin\phi$, $\phi_a \le \phi \le \pi/2, t = 0$

(b) *Temperature*

$T = T_0$ in $D \cdot \text{F2}(\phi, t) \le r \le D \cdot \sin\phi$, $\phi_a \le \phi \le \pi/2, t = 0$

The governing equations are then nondimensionalized. Next, they are subjected to two transformations, the first of which immobilizes the interface and converts the irregularly shaped melt region into a sector of a circle. The second transformation eliminates the angular spread of this sector with time, and fixes it at one radian. Prasad and Sengupta [10] list a detailed account of this procedure.

Method of Solution

We used the projection method [11] to solve the momentum equations. The temperature field was first calculated using the temperatures and velocities from the previous time step. Next, the momentum equations were solved using the old velocities and the updated temperatures while setting the pressure term to zero. This resulted in an "intermediate" velocity field. The new pressures were then solved for using the Poisson equation with Neumann boundary conditions, using an SOR scheme with a high relaxation factor. We then obtained the corrected velocities using the pressure solution and the conservation of mass. Thus, it was an explicit fractional step method. The interface was calculated from the temperature gradient in the liquid which determined the local melt rate, and more importantly, by the drop rate of the solid core as given by equation (7). At each time step, the new interface is computed, and the coefficients for the numerous terms resulting from the transformations are calculated. In order to start the solution, we require a small amount of initial melt volume. We used an initial melt volume fraction of less than 5 percent, which we confirmed was small enough to cause no effect on the solution at a later stage of melting.

The transformed plane was covered by a grid of 10 × 11 points, and we employed the FTCS scheme for the derivatives in the finite differenced form of the transformed governing equations. The computations were carried out on the UNIVAC 1100 mainframe at the Computer Center, and the Harris 800 super-mini at the College of Engineering, University of Miami.

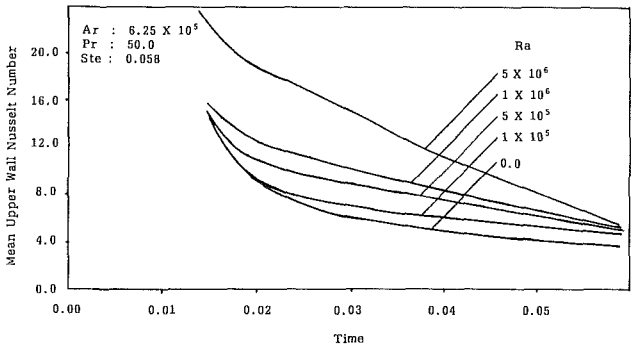

Fig. 2 Variation of mean upper wall Nusselt number with time

Results and Discussion

We solved this problem for a range of Rayleigh numbers from 0 to 5×10^6. We observed that the Nusselt numbers along the upper wall as well as along the upper interface ("upper" implies $\phi_a \le \phi \le \pi/2$) are strongly dependent on the Rayleigh number. Figure 2 shows the variation of the mean Nu along the upper wall as a function of time for different Ra. These numbers represent the mean heat flux entering the melt region through the upper wall. Increasing the Rayleigh number causes a significant increase in Nu. This is to be expected since at higher Ra, we have a more mobile melt pool for the same temperature differential, resulting in higher heat transfer coefficients. Figure 3 is a plot of the local Nu over the upper interface at a time of 0.06. The maximum occurs at $\phi = 180$ deg. Beer used the empirical relationship $\text{Nu} = 0.2(\text{Ra})^{1/4}$ for this very point on the upper interface. Our results agree closely with this prediction up to $\text{Ra} = 5 \times 10^5$. At higher Ra, Beer's predicted value seems to underestimate the heat flux.

We also observe that the heat flux resulting from the natural convection in the melt region is an order of magnitude smaller than the heat flux in the contact region.

Conclusions

The problem of melting inside a horizontal tube subjected to an isothermal wall condition has been solved numerically. The effect of Ra varying from 0 to 5×10^6 has been studied.

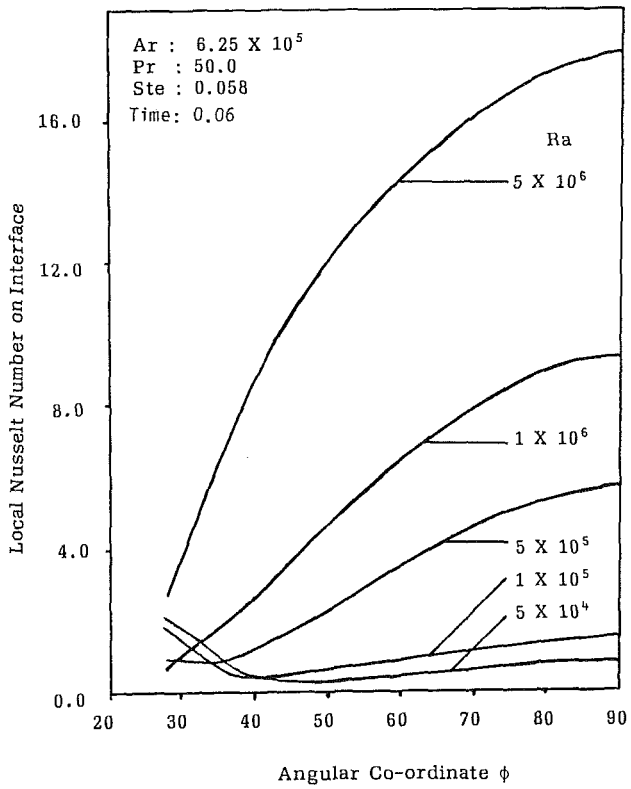

Fig. 3 Variation of local Nusselt number on upper interface with angular coordinate

The model includes conduction as well as natural convection in the melt region, while melting in the contact zone was modeled after Beer's results. The movement of the solid core due to gravity has also been considered. This study yielded the following conclusions:

1 The Nusselt numbers along the upper wall and the upper interface are dependent on the Rayleigh number.

2 The heat flux and hence, the melt rate at the upper interface, is an order of magnitude smaller than that in the contact region. Therefore the solid core still retains its circular profile at the upper interface.

References

1 Shamsundar, N., and Sparrow, E. M., "Storage of Thermal Energy by Solid-Liquid Phase Change – Temperature Drop and Heat Flux," ASME Journal of Heat Transfer, Vol. 96, 1974, pp. 541-543.

2 Katayama, K., Saito, A., Utaka, Y., Saito, A., Matsui, H., Maekawa, H., and Saifullah, A. Z. A., "Heat Transfer Characteristics of the Latent Heat Thermal Energy Storage Capsule," *Solar Energy*, Vol. 27, No. 2, 1981, pp. 91-97.

3 Pannu, J., Joglekar, G., and Rice, "Natural Convection to Cylinders of Phase Change Material Used for Thermal Storage," *AIChE Symposium Series*, 1980, pp. 47-55.

4 Saitoh, T., Hirose, K., "High Rayleigh Number Solutions to Problems of Latent Heat Thermal Energy Storage in a Horizontal Cylinder Capsule," ASME Journal of Heat Transfer, Vol. 104, 1982, pp. 545-553.

5 Rieger, H., Projahn, U., Bareiss, M., and Beer, H., "Heat Transfer During Melting Inside a Horizontal Tube," ASME Journal of Heat Transfer, Vol. 105, 1983, pp. 226-234.

6 Ho, C.-J., and Viskanta, R., "Heat Transfer During Inward Melting in a Horizontal Tube," *International Journal of Heat and Mass Transfer*, Vol. 27, No. 5, pp. 705-716, 1984.

7 Nicholas D., and Bayazitoglu, Y., "Heat Transfer and Melting Front Within a Horizontal Cylinder," ASME *Journal of Solar Energy Engineering*, Vol. 102, 1980, pp. 229-232.

8 Elmasry, S., and Sengupta, S., "Phase Change Heat Transfer Inside a Horizontal Tube: Effects of Rayleigh Number," ASME Paper No. 84-HT-4.

9 Bareiss, M., and Beer, H., "An Analytical Solution of the Heat Transfer Process During Melting of an Unfixed Solid Phase Change Material Inside a Horizontal Tube," *International Journal of Heat and Mass Transfer*, Vol. 27, No. 5, 1984, pp. 739-746.

10 Prasad, A., and Sengupta, S., "Numerical Investigation of Melting Inside a Horizontal Cylinder Including the Effects of Natural Convection," ASME Paper No. 85-F-79.

11 Peyret, R., and Taylor, T. D., *Computational Methods for Fluid Flow*, Springer-Verlag, New York, 1984.

Analysis of Gravity and Conduction-Driven Melting in a Sphere

P. A. Bahrami[1] and T. G. Wang[1]

Nomenclature

Ar = Archimedes number, equation (18)
c = specific heat of liquid
Fo = Fourier number, equation (19)
F_p = upward force on solid
F = polynomial, equation (23)
g = acceleration of gravity
k = thermal conductivity of liquid
p = pressure
Pr = Prandtl number, equation (17)
Q = volumetric flow rate
r = radius coordinate
R = radius of sphere
R^* = radius of lower solid surface
s = solid travel distance
$\dot{s}$ = downward speed of solid
Ste = Stefan number, equation (7)
t = time
T_w = sphere wall temperature
T^* = melting point
V = volume of solid, equation (15)
V_r = radial velocity
V_θ = polar velocity
δ = thickness of molten layer
θ = polar angle
λ = heat of melting (energy per unit mass)
μ = dynamic viscosity
ξ = $s/2R$
ρ = density of liquid
ρ_s = density of solid
τ = Ste•Fo
ϕ = volume flow rate

Introduction

Melting processes within spherical containments have been of fundamental interest; for example, the well-known Stefan and Neumann problems (Carslaw and Jeager, 1959; Tao, 1967). The voluminous analytical literature on this subject, however, widely presumes that the yet unmolten part of the phase-change material remains at the center of the sphere. This is an unlikely occurrence in nature. The differing densities of the liquid and the solid may readily cause a force imbalance on the solid in gravitational and perhaps microgravitational environments, thereby moving the solid away from the center. Numerical results for the initial stages

[1]Jet Propulsion Laboratory, California Institute of Technology, Pasadena, CA 91109.

Contributed by the Heat Transfer Division for publication in the Journal of Heat Transfer. Manuscript received by the Heat Transfer Division April 11, 1986.

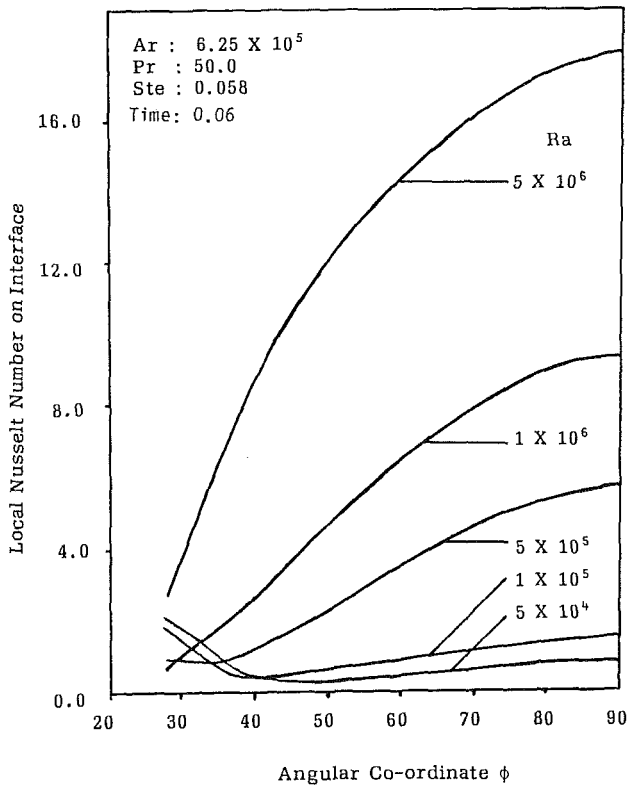

Fig. 3 Variation of local Nusselt number on upper interface with angular coordinate

The model includes conduction as well as natural convection in the melt region, while melting in the contact zone was modeled after Beer's results. The movement of the solid core due to gravity has also been considered. This study yielded the following conclusions:

1 The Nusselt numbers along the upper wall and the upper interface are dependent on the Rayleigh number.

2 The heat flux and hence, the melt rate at the upper interface, is an order of magnitude smaller than that in the contact region. Therefore the solid core still retains its circular profile at the upper interface.

References

1 Shamsundar, N., and Sparrow, E. M., "Storage of Thermal Energy by Solid-Liquid Phase Change – Temperature Drop and Heat Flux," ASME JOURNAL OF HEAT TRANSFER, Vol. 96, 1974, pp. 541-543.

2 Katayama, K., Saito, A., Utaka, Y., Saito, A., Matsui, H., Maekawa, H., and Saifullah, A. Z. A., "Heat Transfer Characteristics of the Latent Heat Thermal Energy Storage Capsule," *Solar Energy*, Vol. 27, No. 2, 1981, pp. 91-97.

3 Pannu, J., Joglekar, G., and Rice, "Natural Convection to Cylinders of Phase Change Material Used for Thermal Storage," *AIChE Symposium Series*, 1980, pp. 47-55.

4 Saitoh, T., Hirose, K., "High Rayleigh Number Solutions to Problems of Latent Heat Thermal Energy Storage in a Horizontal Cylinder Capsule," ASME JOURNAL OF HEAT TRANSFER, Vol. 104, 1982, pp. 545-553.

5 Rieger, H., Projahn, U., Bareiss, M., and Beer, H., "Heat Transfer During Melting Inside a Horizontal Tube," ASME JOURNAL OF HEAT TRANSFER, Vol. 105, 1983, pp. 226-234.

6 Ho, C.-J., and Viskanta, R., "Heat Transfer During Inward Melting in a Horizontal Tube," *International Journal of Heat and Mass Transfer*, Vol. 27, No. 5, pp. 705-716, 1984.

7 Nicholas D., and Bayazitoglu, Y., "Heat Transfer and Melting Front Within a Horizontal Cylinder," ASME *Journal of Solar Energy Engineering*, Vol. 102, 1980, pp. 229-232.

8 Elmasry, S., and Sengupta, S., "Phase Change Heat Transfer Inside a Horizontal Tube: Effects of Rayleigh Number," ASME Paper No. 84-HT-4.

9 Bareiss, M., and Beer, H., "An Analytical Solution of the Heat Transfer Process During Melting of an Unfixed Solid Phase Change Material Inside a Horizontal Tube," *International Journal of Heat and Mass Transfer*, Vol. 27, No. 5, 1984, pp. 739-746.

10 Prasad, A., and Sengupta, S., "Numerical Investigation of Melting Inside a Horizontal Cylinder Including the Effects of Natural Convection," ASME Paper No. 85-F-79.

11 Peyret, R., and Taylor, T. D., *Computational Methods for Fluid Flow*, Springer-Verlag, New York, 1984.

Analysis of Gravity and Conduction-Driven Melting in a Sphere

P. A. Bahrami[1] and T. G. Wang[1]

Nomenclature

Ar = Archimedes number, equation (18)
c = specific heat of liquid
Fo = Fourier number, equation (19)
F_p = upward force on solid
F = polynomial, equation (23)
g = acceleration of gravity
k = thermal conductivity of liquid
p = pressure
Pr = Prandtl number, equation (17)
Q = volumetric flow rate
r = radius coordinate
R = radius of sphere
R^* = radius of lower solid surface
s = solid travel distance
$\dot{s}$ = downward speed of solid
Ste = Stefan number, equation (7)
t = time
T_w = sphere wall temperature
T^* = melting point
V = volume of solid, equation (15)
V_r = radial velocity
V_θ = polar velocity
δ = thickness of molten layer
θ = polar angle
λ = heat of melting (energy per unit mass)
μ = dynamic viscosity
ξ = $s/2R$
ρ = density of liquid
ρ_s = density of solid
τ = Ste•Fo
ϕ = volume flow rate

Introduction

Melting processes within spherical containments have been of fundamental interest; for example, the well-known Stefan and Neumann problems (Carslaw and Jeager, 1959; Tao, 1967). The voluminous analytical literature on this subject, however, widely presumes that the yet unmolten part of the phase-change material remains at the center of the sphere. This is an unlikely occurrence in nature. The differing densities of the liquid and the solid may readily cause a force imbalance on the solid in gravitational and perhaps microgravitational environments, thereby moving the solid away from the center. Numerical results for the initial stages

[1]Jet Propulsion Laboratory, California Institute of Technology, Pasadena, CA 91109.

Contributed by the Heat Transfer Division for publication in the JOURNAL OF HEAT TRANSFER. Manuscript received by the Heat Transfer Division April 11, 1986.

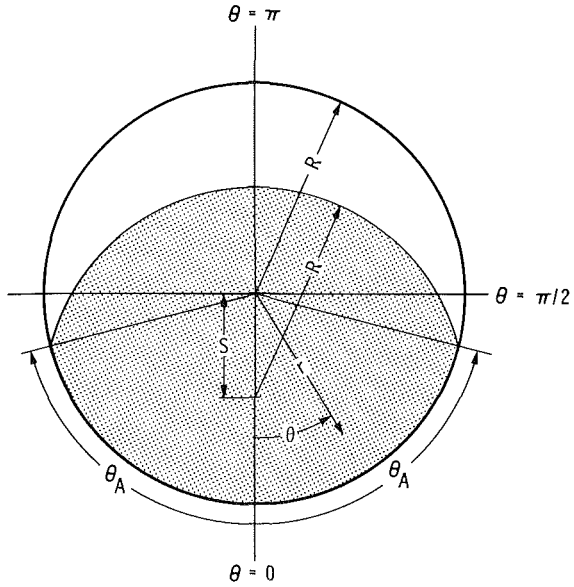

Fig. 1 Spherical polar coordinate system

of melting and tests of a qualitative nature, while movement of the solid was not restricted, have been reported recently (Moore and Bayazitoglu, 1982). Melting of a cold medium by a hot rigid sphere in a related problem concerned with magma migration and geophysics was analyzed by Emerman and Turcotte (1983).

The analysis and experiments on melting within cylinders have also overwhelmingly ignored or artificially restricted the movement of the solid due to gravity. There are, however, a few exceptions. Nicholas and Bayazitoglu (1980) assumed that the solid phase settled to the base of horizontal cylinder, and conduction was the heat transfer mechanism in the liquid phase. Limited experimental studies were also reported. Katayama and Utaka (1981) presented results of experiments concerned with contact heat transfer while melting took place. Moallemi and Viskanta (1985) analyzed the problem of melting around a moving cylindrical heat source and also performed experiments with paraffin. Of particular relevance to the present work are the analysis and experiments of Bareiss and Beer (1984). Using assumptions similar to the lubrication theory, they investigated melting in a horizontal cylinder and obtained a closed-form solution of the melting process. Their experimental results are in agreement with the theory. The thrust of the analysis in the present work is the application of a similar technique to melting within a sphere. This analysis, to the best of our knowledge, has not been reported in the literature before.

Analysis

The procedure we shall use for the development of the fluid mechanics equations and the energy fluxes is related to the approaches employed in the theories of lubrication (Schlichting, 1979) and film condensation (Nusselt, 1916). As noted earlier Bareiss and Beer (1984) considered melting in a horizontal cylinder. They concluded that melting at the upper solid surface was approximately 10-15 percent of the total melt in their experiments. We shall apply a similar technique to melting in a sphere and assume that melting at the upper solid surface can be neglected.

Consider a sphere of radius R containing a phase-change material initially in the solid phase and entirely at the melting point temperature T^*. The wall temperature is suddenly raised to T_w, a constant greater than T^*. Inward melting of the solid starts and simultaneously the solid acquires a vertically downward speed $\dot{s}$ (Fig. 1). The motion of the solid is accompanied by generation of liquid at the melting interface and the liquid is pushed up through a narrow layer to the space above the solid. The motion can be categorized as quasi-steady and one in which the viscous forces are dominant. The flow is axisymmetric around the vertical axis of the sphere and a two-dimensional spherical polar coordinate system (Fig. 1) can be employed. In this coordinate system, r is the radius measured from the center of sphere and θ is the polar angle. We denote the surface of the solid by $R^*(\theta)$ and the thickness of the molten layer by $\delta(\theta)$.

$$\delta(\theta) = R - R^*(\theta) \tag{1}$$

It was observed by the aforementioned experimenters that $\delta(\theta) \ll R$. Thus the polar velocity V_θ is similar to pressure-driven flow through parallel plates.

$$V_\theta = \frac{1}{2\mu R}\frac{dp}{d\theta}[(r-R^*)^2 - (R-R^*)(r-R^*)] \tag{2}$$

The volumetric flow rate $Q(\theta)$ across a surface described by a constant θ is

$$Q(\theta) = \frac{-\pi \sin\theta}{6\mu}\frac{dp}{d\theta}\delta^3(\theta) \tag{3}$$

Now suppose $\phi(\theta)$ is the liquid volume flux across R^* (Fig. 2). Then,

$$Q(\theta) = 2\pi\int_{\theta=0}^{\theta} \Phi(\theta) R^{*2} \sin\theta \, d\theta \tag{4}$$

Using equations (3) and (4)

$$\frac{dp(\theta)}{d\theta} = \frac{-12\mu R^2}{\sin\theta\,\delta^3(\theta)}\int_0^\theta \Phi(\theta)\sin\theta\, d\theta, \qquad \delta(\theta) > 0 \tag{5}$$

Using the equations of conservation of energy and conservation of mass in the liquid and the familiar integral technique (Finlayson, 1972), Emerman and Turcotte (1983) obtained the following relationship for the thickness of the molten layer

$$\delta(\theta) = \frac{k}{c\rho_s \dot{s}\cos\theta}\left[\frac{-3}{4}\,\mathrm{Ste} - 5 + \left(\frac{9}{16}\,\mathrm{Ste}^2 + \frac{70}{4}\,\mathrm{Ste} + 25\right)^{1/2}\right] \tag{6}$$

where Ste is the Stefan number

$$\mathrm{Ste} = \frac{c(T_w - T^*)}{\lambda} \tag{7}$$

The quantity in the square bracket approaches Ste as Ste$\to$0. In many problems of practical interest Ste is in fact very small. The heat transfer to the melting front is then essentially by conduction through the thin molten layer.

$$\delta(\theta) = \frac{k(T_w - T^*)}{\rho_s \lambda \dot{s}\cos\theta} \tag{8}$$

Noting that

$$\Phi(\theta) = \left(\frac{\rho_s}{\rho}\right)\dot{s}\cos\theta \tag{9}$$

equation (5) is integrated using equations (8) and (9)

$$\frac{dp(\theta)}{d\theta} = \frac{-6\mu R^2 \rho^3 \lambda^3 \dot{s}^4 \cos^3\theta \sin\theta}{k^3(T_w - T^*)^3}\left(\frac{\rho_s}{\rho}\right)^4 \tag{10}$$

Denoting the polar angle at which the upper solid surface meets the sphere wall by θ_A, and noting that the pressure $p(\theta) = p(\theta_A)$ for $\theta_A \le \theta \le \pi$, equation (10) can be integrated.

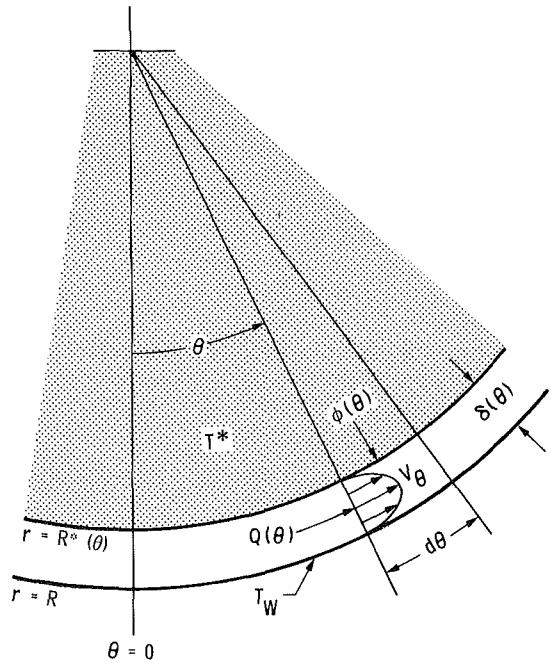

Fig. 2 Schematic of flow in the gap

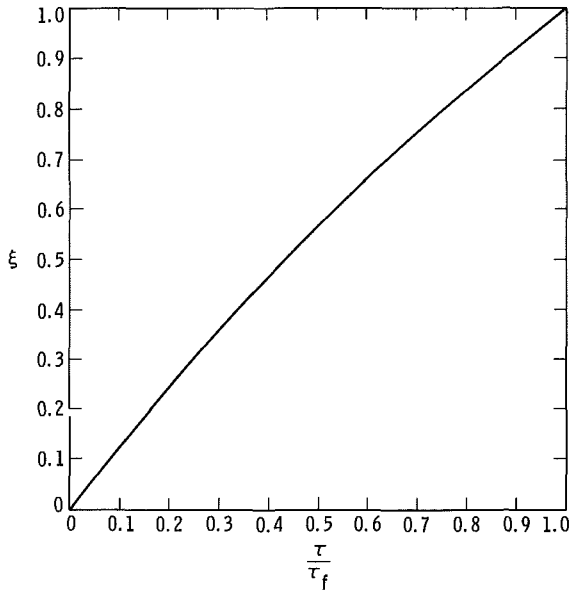

Fig. 3 Ratio of solid travel distance to sphere diameter as a function of time elapsed relative to the time required for complete melting

$$p(\theta)=\frac{3}{2}\mu R^2\dot{s}^4\left(\frac{\rho_s}{\rho}\right)^4\left[\frac{\rho\lambda}{k(T_w-T^*)}\right]^3(\cos^4\theta-\cos^4\theta_A) \quad (11)$$

The upward pressure force F_p acting on solid from the molten layer is

$$F_p=2\pi R^2\int_0^{\theta_A}p(\theta)\sin\theta\cos\theta\,d\theta \quad (12)$$

$$F_p=\pi\mu R^4\dot{s}^4\left(\frac{\rho_s}{\rho}\right)^4\left[\frac{\rho\lambda}{k(T_w-T^*)}\right]^3\left[-\frac{1}{2}(\cos^6\theta_A-1)-\frac{3}{2}\sin^2\theta_A\cos^4\theta_A\right] \quad (13)$$

But from the static equilibrium of the solid

$$F_p=gV(\rho_s-\rho) \quad (14)$$

where g is the acceleration of gravity, and V is the volume of the solid bounded by spherical surfaces

$$V=\frac{2}{3}\pi R^3[2(1-\cos\theta_A)-\sin^2\theta_A\cos\theta_A] \quad (15)$$

By equating equations (13) and (14) and using the kinematic relationship

$$\cos\theta_A=s/2R \quad (16)$$

and introducing the following dimensionless parameters:

$$\mathrm{Pr}=\frac{c\mu}{k} \quad (17)$$

$$\mathrm{Ar}=\frac{\rho g(\rho_s-\rho)R^3}{\mu^2} \quad (18)$$

$$\mathrm{Fo}=\frac{kt}{\rho cR^2} \quad (19)$$

$$\tau=\mathrm{Ste}\cdot\mathrm{Fo} \quad (20)$$

$$\xi=\frac{s}{2R} \quad (21)$$

where s is the downward distance the solid has traveled in time t, the following differential equation is finally arrived at:

$$\frac{d\xi}{d\tau}=\left(\frac{\mathrm{PrAr}}{12\,\mathrm{Ste}}\right)^{1/4}\cdot\left(\frac{\rho}{\rho_s}\right)\left[\left(\frac{2-3\xi+\xi^3}{1-3\xi^4+2\xi^6}\right)^{1/4}\right] \quad (22)$$

The inverse of the quantity in the square brackets was approximated by a third-order polynomial $F(\xi)$

$$F(\xi)=0.841+0.300\xi+0.420\xi^2-0.147\xi^3 \quad (23)$$

Integration of equation (22) using (23) resulted in τ as a function of the dimensionless travel distance of the solid ξ

$$\tau=\left(\frac{\mathrm{Ste}}{\mathrm{PrAr}}\right)^{1/4}\left(\frac{\rho_s}{\rho}\right)(1.56\xi+0.279\xi^2+0.261\xi^3-0.0686\xi^4) \quad (24)$$

The entire mass is molten when $\xi=1$ or $\tau=\tau_f$

$$\tau_f=2.03\left(\frac{\rho_s}{\rho}\right)\left(\frac{\mathrm{Ste}}{\mathrm{PrAr}}\right)^{1/4} \quad (25)$$

A useful relationship may be obtained by dividing equation (24) by equation (25). More specifically, τ/τ_f, the fraction of time elapsed relative to the time required for complete melting, can be expressed in terms of ξ, the ratio of the distance the solid has traveled to the sphere diameter. Furthermore, τ/τ_f has been plotted in Fig. 3. Interestingly, only a modest departure from linearity is apparent. This implies that the solid descends with a relatively constant speed. Further inspection of equation (25) reveals that the required time for complete melting of the solid remains finite even for very small values of Ar owing to the $-1/4$ power dependence of τ_f on Ar. For extremely small values of Ar, however, such as may be encountered in extremely low gravitational environments and for substances exhibiting inappreciable changes in density, equation (25) is no longer valid since the solid may not move to the sphere wall and the assumption $\delta \ll R$ may be violated.

As pointed out earlier only limited experimental data are available for comparison with the present analysis. In Fig. 4, data of Moore and Bayazitoglu (1982) (circle and square symbols) have been recast in terms of the parameters of the present study. The solid curves in Fig. 4 are our analytical predictions for the values of Ste, Pr, and Ar pertaining to the above experiments. In recasting these data we have evaluated the fluid viscosity using the arithmetic mean of the wall and melting temperatures. Inspection of Fig. 4 reveals that use of the product Fo•Ste instead of Fo alone resulted in an im-

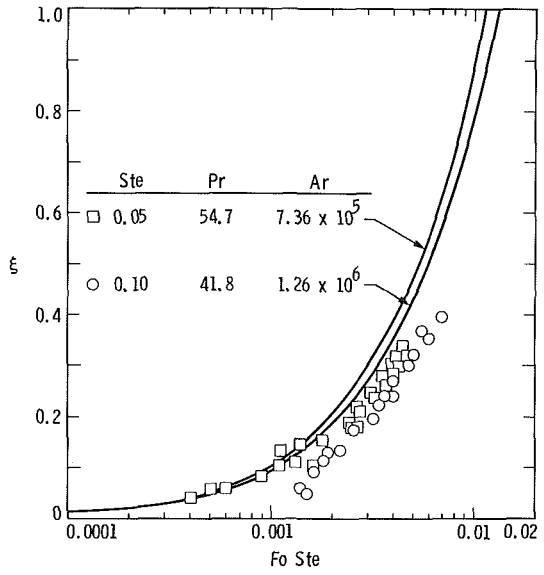

Fig. 4 Comparison of the ratio of solid travel distance to sphere diameter predicted by the present analysis (solid curves) to the experiments of Moore and Bayazitoglu (square and circle symbols) as a function of the product Fo•Ste

proved correlation of the data by bringing the data together. The agreement between the theory and the experiments appears to be reasonable for small values of Fo•Ste. The agreement is lessened for larger Fo•Ste values with the experimental data laying approximately 20 percent below the theory.

While the present theory is supported by the experimental data of Moore and Bayazitoglu (1982), a more precise comparison cannot be made. Their numerical analysis takes cognizance of the solid–liquid density difference only so far as repositioning of the solid toward the base of the shell is concerned. As a result the Archimedes number Ar does not appear in their presentation. Furthermore, the resistance to heat flow in the glass shell was assumed to be negligible and reasonable agreement between the experiments and the numerical results was reported. Unfortunately, this assumption is not entirely valid. The temperature drop in the shell may amount to a fraction of the overall wall to melting temperature difference. This would cause an overestimation of Ste which should be based on spatially uniform and constant inner wall temperature rather than the water bath temperature. The experimental data in Fig. 4 are, therefore, somewhat systematically shifted to the right. Another factor that may have contributed to the slower rates of melting than predicted in the present study is the absence of forced circulation and the limited heat capacity of the water bath used in the experiments. It may, therefore, be concluded that closer agreement between theory and experiments may be expected if more stringent boundary conditions are imposed.

Conclusion

An approximate closed-form solution of melting within spheres was obtained by the use of assumptions similar to the theories of lubrication and film condensation. By simple algebraic manipulation of equations (22) and (24), relationships between the solid speed, position, and time can be easily obtained. The dimensionless group $(\mathrm{PrAr/Ste})^{1/4}$ and its inverse is common to the present analysis as well as the results of Bareiss and Beer (1984) for cylinders. As may be expected, however, the functional dependence of τ on ξ is different for spheres than cylinders. Equations (20) and (25) reveal that the dimensionless time required for the complete melting of the solid Fo_f is remarkably close to twice (ρ_s/ρ) $(\mathrm{Ste}^3\ \mathrm{Pr}\ \mathrm{Ar})^{-1/4}$.

Acknowledgments

This work represents one phase of research carried out at the Jet Propulsion Laboratory, California Institute of Technology, under contract with the National Aeronautics and Space Administration.

References

1 Bareiss, M., and Beer, H., 1984, "An Analytical Solution of the Heat Transfer Process During Melting of an Unfixed Solid Phase Change Material Inside a Horizontal Tube," *Int. Journal Heat Mass Transfer*, Vol. 27, pp. 739–746.

2 Carslaw, H. S., and Jaeger, J. C., 1959, *Conduction of Heat in Solids*, Oxford University Press, Cambridge, U.K., pp. 284–287.

3 Emerman, S. H., and Turcotte, D. L., 1983, "Stokes's Problem With Melting," *Int. Journal Heat Mass Transfer*, Vol. 26, pp. 1625–1630.

4 Finlayson, B. A., 1972, *The Method of Weighted Residuals and Variational Principles*, Academic Press, New York, pp. 61–62.

5 Katayama, K., and Utaka, Y., 1981, "A Study on Contact Heat Transfer With Melting," *Proceedings of the 19th National Heat Transfer Symposium*, Japan, pp. 70–72.

6 Moallemi, M. K., and Viskanta, R., 1985, "Melting Around a Migrating Heat Source," ASME JOURNAL OF HEAT TRANSFER, Vol. 107, pp. 451–458.

7 Moore, F. E., and Bayazitoglu, Y., 1982, "Melting Within A Spherical Enclosure," ASME JOURNAL OF HEAT TRANSFER, Vol. 104, pp. 19–23.

8 Nicholas, D., and Bayazitoglu, Y., 1980, "Heat Transfer and Melting Front Within a Horizontal Cylinder," ASME *Journal of Solar Energy Engineering*, Vol. 102, pp. 229–232.

9 Nusselt, W. Z., 1916, "Die Oberflachenkondensation des Wasserdampfes," *Ver. Deut. Ing.*, Vol. 60, pp. 541–569.

10 Schlichting, H., 1979, *Boundary-Layer Theory*, McGraw-Hill, New York, pp. 112–126.

11 Tao, L. C., 1967, "Generalized Numerical Solutions of Freezing of a Saturated Liquid in Cylinders and Spheres," *AIChE Journal*, Vol. 13, pp. 165–169.

Discrete Ordinate Methods for Radiative Heat Transfer in Isotropically and Anisotropically Scattering Media

W. A. Fiveland[1]

Introduction

The objective of this note is to focus on the discrete ordinate method [1–5] as a method for analyzing radiative heat transfer in isotropically and anisotropically scattering media. In particular, one dimension is chosen only for simplicity, since exact solutions are available for benchmarking the discrete ordinate method.

One-dimensional radiative heat transfer has been analyzed in many previous investigations and has been extensively reviewed by Viskanta [6]. The development of the discrete ordinate method has been described in detail by Chandrasekhar [7] and Lathrop [8]. The discrete ordinate method using Gauss quadrature has been compared with approximate solutions in [5]. In the cases previously analyzed in [5], with Gauss quadrature points and weights, accurate solutions were obtained using ordinate sets that were larger than necessary. This note demonstrates that if ordinate sets are chosen to satisfy key moments of the radiative intensity, the resulting Nth order solution with the proposed quadrature is superior to the Nth order solution using Gauss quadrature.

Analysis

The equation of transfer for azimuthally symmetric radia-

[1]Babcock & Wilcox Research and Development Division, Alliance, OH 44601.

Contributed by the Heat Transfer Division and presented at the 1985 National Heat Transfer Conference, Denver, Colorado, August 5–7, 1985. Manuscript received by the Heat Transfer Division September 19, 1985.

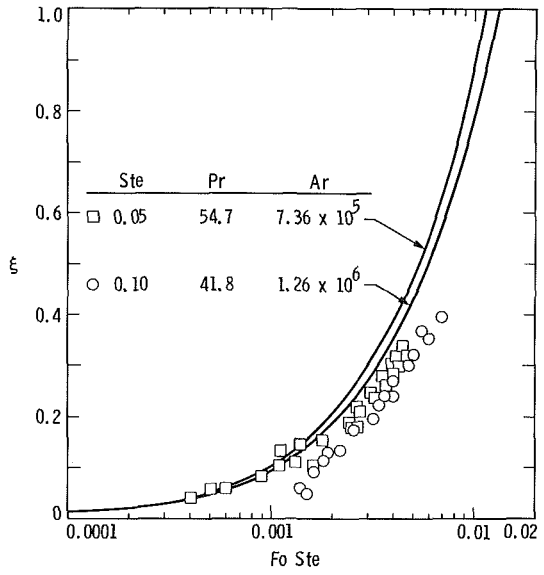

Fig. 4 Comparison of the ratio of solid travel distance to sphere diameter predicted by the present analysis (solid curves) to the experiments of Moore and Bayazitoglu (square and circle symbols) as a function of the product Fo•Ste

proved correlation of the data by bringing the data together. The agreement between the theory and the experiments appears to be reasonable for small values of Fo•Ste. The agreement is lessened for larger Fo•Ste values with the experimental data laying approximately 20 percent below the theory.

While the present theory is supported by the experimental data of Moore and Bayazitoglu (1982), a more precise comparison cannot be made. Their numerical analysis takes cognizance of the solid–liquid density difference only so far as repositioning of the solid toward the base of the shell is concerned. As a result the Archimedes number Ar does not appear in their presentation. Furthermore, the resistance to heat flow in the glass shell was assumed to be negligible and reasonable agreement between the experiments and the numerical results was reported. Unfortunately, this assumption is not entirely valid. The temperature drop in the shell may amount to a fraction of the overall wall to melting temperature difference. This would cause an overestimation of Ste which should be based on spatially uniform and constant inner wall temperature rather than the water bath temperature. The experimental data in Fig. 4 are, therefore, somewhat systematically shifted to the right. Another factor that may have contributed to the slower rates of melting than predicted in the present study is the absence of forced circulation and the limited heat capacity of the water bath used in the experiments. It may, therefore, be concluded that closer agreement between theory and experiments may be expected if more stringent boundary conditions are imposed.

Conclusion

An approximate closed-form solution of melting within spheres was obtained by the use of assumptions similar to the theories of lubrication and film condensation. By simple algebraic manipulation of equations (22) and (24), relationships between the solid speed, position, and time can be easily obtained. The dimensionless group $(\mathrm{PrAr/Ste})^{1/4}$ and its inverse is common to the present analysis as well as the results of Bareiss and Beer (1984) for cylinders. As may be expected, however, the functional dependence of τ on ξ is different for spheres than cylinders. Equations (20) and (25) reveal that the dimensionless time required for the complete melting of the solid Fo_f is remarkably close to twice $(\rho_s/\rho)\ (\mathrm{Ste}^3\ \mathrm{Pr}\ \mathrm{Ar})^{-1/4}$.

Acknowledgments

This work represents one phase of research carried out at the Jet Propulsion Laboratory, California Institute of Technology, under contract with the National Aeronautics and Space Administration.

References

1 Bareiss, M., and Beer, H., 1984, "An Analytical Solution of the Heat Transfer Process During Melting of an Unfixed Solid Phase Change Material Inside a Horizontal Tube," *Int. Journal Heat Mass Transfer*, Vol. 27, pp. 739–746.

2 Carslaw, H. S., and Jaeger, J. C., 1959, *Conduction of Heat in Solids*, Oxford University Press, Cambridge, U.K., pp. 284–287.

3 Emerman, S. H., and Turcotte, D. L., 1983, "Stokes's Problem With Melting," *Int. Journal Heat Mass Transfer*, Vol. 26, pp. 1625–1630.

4 Finlayson, B. A., 1972, *The Method of Weighted Residuals and Variational Principles*, Academic Press, New York, pp. 61–62.

5 Katayama, K., and Utaka, Y., 1981, "A Study on Contact Heat Transfer With Melting," *Proceedings of the 19th National Heat Transfer Symposium*, Japan, pp. 70–72.

6 Moallemi, M. K., and Viskanta, R., 1985, "Melting Around a Migrating Heat Source," ASME JOURNAL OF HEAT TRANSFER, Vol. 107, pp. 451–458.

7 Moore, F. E., and Bayazitoglu, Y., 1982, "Melting Within A Spherical Enclosure," ASME JOURNAL OF HEAT TRANSFER, Vol. 104, pp. 19–23.

8 Nicholas, D., and Bayazitoglu, Y., 1980, "Heat Transfer and Melting Front Within a Horizontal Cylinder," ASME *Journal of Solar Energy Engineering*, Vol. 102, pp. 229–232.

9 Nusselt, W. Z., 1916, "Die Oberflachenkondensation des Wasserdampfes," *Ver. Deut. Ing.*, Vol. 60, pp. 541–569.

10 Schlichting, H., 1979, *Boundary-Layer Theory*, McGraw-Hill, New York, pp. 112–126.

11 Tao, L. C., 1967, "Generalized Numerical Solutions of Freezing of a Saturated Liquid in Cylinders and Spheres," *AIChE Journal*, Vol. 13, pp. 165–169.

Discrete Ordinate Methods for Radiative Heat Transfer in Isotropically and Anisotropically Scattering Media

W. A. Fiveland[1]

Introduction

The objective of this note is to focus on the discrete ordinate method [1–5] as a method for analyzing radiative heat transfer in isotropically and anisotropically scattering media. In particular, one dimension is chosen only for simplicity, since exact solutions are available for benchmarking the discrete ordinate method.

One-dimensional radiative heat transfer has been analyzed in many previous investigations and has been extensively reviewed by Viskanta [6]. The development of the discrete ordinate method has been described in detail by Chandrasekhar [7] and Lathrop [8]. The discrete ordinate method using Gauss quadrature has been compared with approximate solutions in [5]. In the cases previously analyzed in [5], with Gauss quadrature points and weights, accurate solutions were obtained using ordinate sets that were larger than necessary. This note demonstrates that if ordinate sets are chosen to satisfy key moments of the radiative intensity, the resulting Nth order solution with the proposed quadrature is superior to the Nth order solution using Gauss quadrature.

Analysis

The equation of transfer for azimuthally symmetric radia-

[1]Babcock & Wilcox Research and Development Division, Alliance, OH 44601.

Contributed by the Heat Transfer Division and presented at the 1985 National Heat Transfer Conference, Denver, Colorado, August 5–7, 1985. Manuscript received by the Heat Transfer Division September 19, 1985.

tion in a scattering gray medium between a one-dimensional, plane parallel slab can be written [7] as

$$\mu \frac{\partial I(\tau, \mu)}{\partial \tau} = -I(\tau, \mu) + \frac{1}{2}\int_{-1}^{1} p(\mu, \mu')I(\tau, \mu')d\mu' \quad (1)$$

where $I(\tau, \mu)$ is the total intensity at an optical distance τ in the direction μ. The value τ is defined as $d\tau = \sigma dx$ where σ is the scattering coefficient and x is the distance. The parameter $p(\mu, \mu')$ is the scattering phase function for azimuthally symmetric radiation.

Chandrasekhar [7] has discussed the development of the discrete ordinate equations. Simply, the governing equations are evaluated for a discrete number of ordinate directions m, and the integrals are replaced by a numerical quadrature as follows:

$$\mu_m \frac{\partial I_m}{\partial \tau} = -I_m + \frac{1}{2}\sum_{m'=1}^{N} \Phi_{mm'} w_{m'} I_{m'} \quad (2)$$

where $\Phi_{mm'} = a_0 + a_1 \mu_m \mu_{m'}$ for linear anisotropic scattering. The $\Phi_{mm'}$ function can be computed one time, once the values a_0 and a_1 are known and the ordinate values are chosen. At the boundaries the incoming and outgoing intensities are balanced. The outgoing intensity for $\tau = \tau_1 = 0$ can be written

$$I_m = \epsilon_1 I_{b,1} + 2(1-\epsilon_1)\sum_{m'=1}^{N} \mu_{m'} w_{m'} I_{m'} \quad (3)$$

where the summation extends only over the incoming directions, $\mu_m' < 0$. The outgoing intensity at $\tau = \tau_2$ can be written

$$I_m = \epsilon_2 I_{b,2} + 2(1-\epsilon_2)\sum_{m'=1}^{N} \mu_{m'} w_{m'} I_{m'} \quad (4)$$

where the summation is over the directions $\mu_m' > 0$.

Solution of the Discrete Ordinate Equations

Evaluating equation (2) at the midpoint between two nodes gives rise to the difference form of the equation

$$I_{j+1}^m = \frac{\left(\frac{\mu_m}{\Delta\tau} - \frac{1}{2}\right) I_j^m + \frac{1}{2}\sum_{k=1}^{N} w_k \Phi_{mk} I_{j+1/2}^k}{\left(\frac{\mu_m}{\Delta\tau} + \frac{1}{2}\right)} \quad (5)$$

for ordinate directions that are positive. Iteration takes place for the nodes $j = 1, \ldots, n$. The initial value I_1^m is computed from the relation

$$I_1^m = \epsilon_1 I_{b,1} + 2(1-\epsilon_1)\sum_{m'=1}^{N} w_{m'}, \mu_{m'} I_1^{m'} \quad (6)$$

The $I_1^{m'}$ represents incoming intensities at $\tau = \tau_1$ for the directions $\mu_{m'} < 0$. Similar expressions can be written for directions with negative ordinates in which the iteration proceeds from $j = n, \ldots, 1$. Net heat flux at the wall ($\tau = \tau_1$) can be found from the relation

$$q_1 = \pi\epsilon_1 \left(I_{b,1} - 2\sum_{k=1}^{N} w_k \mu_k I_k\right) \quad (7)$$

and at the wall ($\tau = \tau_2$) using a similar expression.

Selection of Ordinate Directions

Equations (5) and (6) represent the discrete ordinate equations for the directions μ_m. The radiative transport equation and its associated boundary conditions contain several key moments of radiant intensity: full-range moments over the range $[-1, 1]$ in the source term of equation (1), and first moments over the half ranges $[-1, 0]$ and $[0, 1]$ in the boundary conditions. An integral over the interval is approximated as follows:

$$\int_{-1}^{1} \mu^i f(\mu) d\mu = \sum_{k=1}^{N} a_k \mu_k^i f(\mu_k)$$

where the superscript i represents the power for the ith moment of intensity. To obtain reasonable solutions, these moments must be satisfied. Gauss quadrature points [9] and the associated weights are constructed to satisfy every power of i less than $2N$, but only for the full-range moments $[-1, 1]$. In heat transfer problems, the surface radiative heat flux (first moment) is quite important especially in combined mode problems when a balance of convection, radiation, and wall heat losses is necessary to determine the surface temperature. Inaccurate calculation of radiative heat flux will lead to poorly predicted surface temperatures and erroneous results. Low orders of Gauss quadrature do not accurately predict the half-range heat fluxes

$$\int_0^1 I(\mu)\mu d\mu \text{ or } \int_{-1}^0 I(\mu)\mu d\mu$$

To obtain accurate discrete ordinate solutions with Gauss quadrature, unnecessary high order solutions are required, which are computationally inefficient. An ordinate set is constructed with the following characteristics: (1) The weight values are nonnegative and (2) the point values are symmetric.

Thus, it is sufficient to consider only the relationship

$$2\int_0^1 \mu^i d\mu = \sum_{k=1}^{N} w_k \mu_k^i \quad (8)$$

where $i = 0, 1, 2, \ldots, N$. The equation satisfies all powers of μ less than N for an arbitrary polynomial of radiant intensity expressed in terms of μ and for the related moments of the intensity, in addition to the first moment over the half range, either $[-1, 0]$ or $[0, 1]$. Choosing the special case of equal weights, $w_1 = w_2 = w_k = \ldots w_N$ and knowing $\Sigma w_k = 2$, equation (8) is solved by the Newton–Raphson method. The associated points and weights are tabulated in Table 1 for the first six approximations. Solutions are found using these ordinate sets S-2 to S-6 and the Gauss sets G-2 to G-6, and are compared to exact solutions.

Stability of Numerical Solutions

The discrete ordinate solutions are iterative and at any numerical step negative intensities can occur. A condition for positive intensities can be written

$$\left(\frac{\mu_m}{\Delta\tau} - \frac{1}{2}\right) I_j^m + S > 0$$

Table 1 Weight and point values for *S-N* method

S-N	w	±μ	S-N	w	±μ
S-2	1.	.500000	S-10	1/5	.083752
				1/5	.312729
S-4	1/2	.211325		1/5	.500000
	1/2	.788675		1/5	.687270
				1/5	.916248
S-6	1/3	.146446			
	1/3	.500000	S-12	1/6	.066877
	1/3	.853554		1/6	.366693
				1/6	.288732
S-8	1/4	.102672		1/6	.711267
	1/4	.406205		1/6	.633307
	1/4	.593795		1/6	.933123
	1/4	.897327			

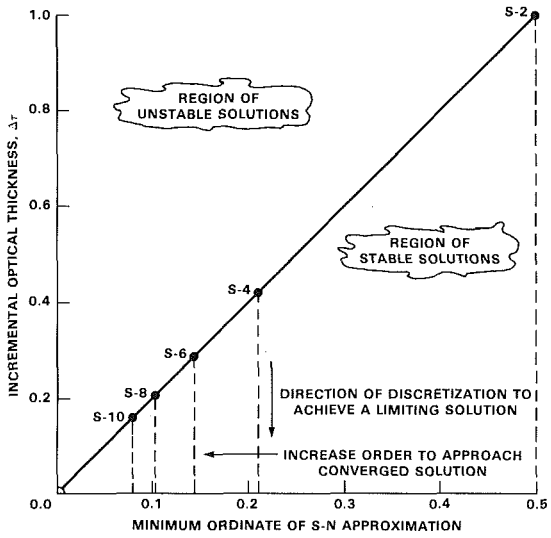

Fig. 1 Map of region for stable discrete ordinate solution

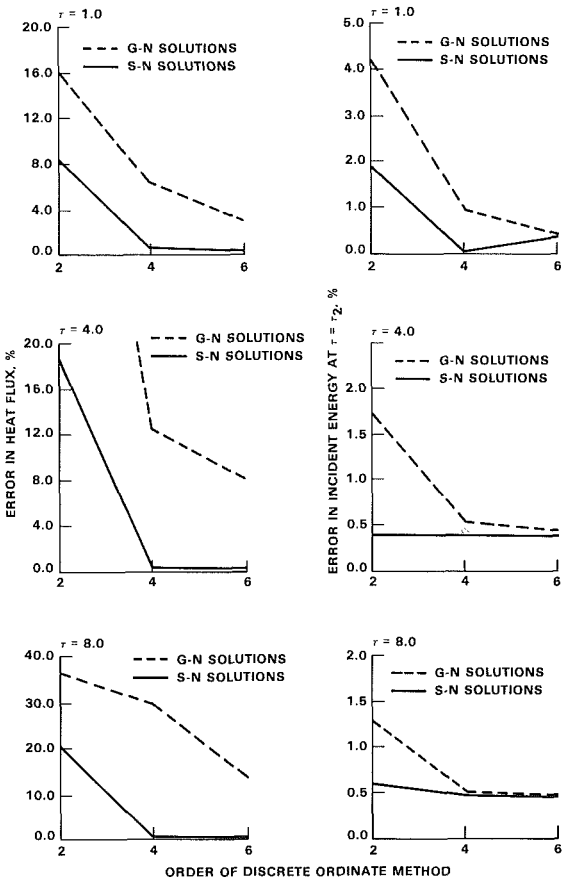

Fig. 2 Comparing solution errors for *S-N* and *G-N* discrete ordinate methods

where the parameter S represents the source term due to in-scattering from other directions. Source terms are positive, and tend to stabilize the solution keeping the calculated intensity positive. A simple relationship to maintain stable solutions can be written

$$\text{Min}\left(\frac{|\mu_m|}{\Delta\tau}\right) > \frac{1}{2} \tag{9}$$

It is clear, however, that as higher ordinate sets are chosen to improve solution accuracy, the minimum ordinate in any set tends to zero, which requires finer discretization in equation (5) to maintain stable solutions. The region of stable solutions is shown in Fig. 1. Increasing the level of discretization (along a vertical line toward $\Delta\tau = 0$), a given *S-N* solution will approach a limiting solution; however, a converged solution will also require improving the number of ordinate directions, *S*-4, *S*-6, etc.

Results

Solutions for the discrete ordinate method were found using the Gauss points and weights, tabulated in [9], and the oridinates listed in Table 1. Numerically converged solutions were obtained if an incremental optical thickness one-fifth the condition for stability was used:

$$\Delta\tau \leq 0.4\text{MIN}|\mu_m| \text{ for } m = 1, \ldots, N$$

***(a)* Isotropic Scattering in One-Dimensional, Conservative Slabs With Black Walls.** Consider the radiative heat transfer between two black walls (ϵ_1, $\epsilon_2 = 1.0$): one maintained at a constant temperature T_1, the other maintained at zero temperature $T_2 = 0$. The medium between the walls is assumed to scatter energy isotropically and does not absorb energy. Solutions were found for *S*-2, *S*-4, *S*-6, and *G*-2, *G*-4, *G*-6 ordinate sets. The exact results have been taken from Heaslet and Warming [10]. The error in the radiative heat flux is shown in Fig. 2. As shown in Fig. 2, *S*-4 solutions are within 0.5 percent for the range of optical thicknesses studied. Solutions with the Gauss points and weights are not as accurate. This is because the Gauss sets do not integrate the half-range first moment exactly. As higher order sets are used the half-range first moment is approximated better, but unnecessary computational work is required.

Errors in incident energy are also presented in Fig. 2. Errors between the exact results [10] and the *S*-6 or *G*-6 solutions are nearly equivalent. This is not surprising since *G-N* methods integrate $2N-1$ even powers of the ordinate (μ) exactly. The errors in the discrete ordinate solution do not diminish monotonically as noted by Clark [11], and the results for $\tau = 1.0$ indicate an oscillation of *G*-2 as *S-N* solutions are examined.

***(b)* Isotropic Scattering in a One-Dimensional Conservative Slab With Gray Walls.** Consider the radiative exchange between parallel gray walls, $\epsilon_1 = 0.8$ and $\epsilon_2 = 1.0$, 0.5, and 0.1. One wall is maintained at a constant temperature T_1 to maintain an emissive power of unity, while the other wall is maintained at a temperature $T_2 = 0$. Solutions were found using *S*-6 and *G*-6 ordinate sets. The *S*-6 ordinate set exactly integrates the half-range first moment, while the *G*-6 ordinate set has an error of 2 percent. Discrete ordinate and exact [10] solutions are summarized in Table 2. Radiative heat flux at $\tau = 0$ and the incident energy at $\tau = \tau_2$ are tabulated.

The radiative heat flux is accurately computed (error < 0.5 percent) by the *S*-6 discrete ordinate method for all optical thicknesses presented. The *G*-6 discrete ordinate method does not accurately predict radiative heat flux for the range of optical thicknesses. Errors increase as the optical thickness increases for fixed surface emissivities and errors increase as the walls become grayer for fixed optical thickness. An error of 36 percent was found in the *G*-6 heat flux solution with $\epsilon_2 = 0.1$ and $\tau = 3.0$, despite only a 2 percent error in the *G*-6 half-range first moment integral using equation (18) and the values tabulated in [9]. Since half-range moment errors are larger at lower orders (*G*-2, *G*-4), radiative flux will be even more inaccurate. To achieve reasonable solution accuracy for the radiative surface, heat flux higher order solutions (*G*-8, *G*-10, *G*-12) would be required, unless the *S-N* ordinate sets are used.

Incident energy G is listed in Table 2 as well. The *S*-6 solu-

Table 2 Radiative heat flux and incident energy for a one-dimensional conservative slab with gray boundaries

			Radiant Heat Flux, q_1			Incident Energy, G_1		
ϵ_1	ϵ_2	τ_2	G-6	S-6	Exact (10)	G-6	S-6	Exact (10)
0.8	1.0	0.1	0.74240	0.74372	0.74512	1.4440	1.4140	1.3965
		1.0	0.47293	0.48545	0.48599	0.8660	0.8558	0.8499
		3.0	0.26374	0.28008	0.28045	0.5031	0.4912	0.4861
0.8	0.5	0.1	0.41072	0.42653	0.42697	2.5640	2.5172	2.5080
		1.0	0.30917	0.32693	0.32705	1.9140	1.8832	1.8801
		3.0	0.20015	0.21844	0.21903	1.2880	1.2668	1.2558
0.8	0.1	0.1	0.06231	0.09675	0.09669	3.7420	3.6628	3.6622
		1.0	0.05796	0.09075	0.09044	3.5212	3.4120	3.4138
		3.0	0.05028	0.07940	0.07958	3.1520	3.0000	3.0029

Table 3 Diffuse hemispherical reflectance of a conservative slab for scattering with a phase function $p(\mu) = 1 + B\mu$

Optical Thickness	Hemispherical Reflectivity			
τ_2	Eddington	S-4	S-6	Exact (12)
		b = 0.0		
1.0	0.4286	0.4492	0.4475	0.4466
2.0	0.6000	0.6108	0.6105	0.6099
3.0	0.6923	0.6995	0.6993	0.6984
4.0	0.7500	0.7548	0.7548	0.7540
5.0	0.7895	0.7931	0.7931	0.7923
6.0	0.8182	0.8209	0.8209	0.8203
7.0	0.8400	0.8425	0.8425	0.8417
8.0	0.8571	0.8594	0.8594	0.8585
9.0	0.8710	0.8728	0.8728	0.8721
10.0	0.8824	0.8842	0.8842	0.8833
		b = 0.5		
1.0	0.3846	0.4081	0.4062	0.4055
2.0	0.5556	0.5699	0.5688	0.5678
3.0	0.6522	0.6609	0.6608	0.6599
4.0	0.7143	0.7204	0.7204	0.7195
5.0	0.7576	0.7622	0.7622	0.7614
6.0	0.7895	0.7931	0.7931	0.7923
7.0	0.8140	0.8170	0.8170	0.8162
8.0	0.8333	0.8358	0.8358	0.8351
9.0	0.8491	0.8511	0.8511	0.8505
10.0	0.8621	0.8629	0.8629	0.8633
		b = 1.0		
1.0	0.3333	0.3606	0.3583	0.3577
2.0	0.5000	0.5172	0.5162	0.5154
3.0	0.6000	0.6093	0.6092	0.6102
4.0	0.6667	0.6750	0.6750	0.6738
5.0	0.7143	0.7180	0.7180	0.7195
6.0	0.7500	0.7557	0.7557	0.7540
7.0	0.7778	0.7791	0.7791	0.7810
8.0	0.8000	0.8046	0.8046	0.8026
9.0	0.8182	0.8223	0.8223	0.8203
10.0	0.8333	0.8330	0.8330	0.8351

tion results compare better with the exact solution [10] than the *G*-6 solution. For incident energy, the *S*-6 errors increase as the emissivity increases. The largest error in the *S*-6 solutions is about 1 percent. The *G*-6 solution errors increase slightly (~1 percent) with increasing optical thickness ($1.0 \le \tau \le 3.0$). The *G*-6 solution errors are about 3 percent at $\epsilon_2 = 1.0$ and are about 5 percent at $\epsilon_2 = 0.1$. The increase in error with decreasing surface emissivity is likely due to the inaccurate surface heat flux at $\epsilon_2 = 0.1$, which affects the radiant intensity and therefore the incident energy.

(c) Anisotropic Scattering. The assumption of isotropic scattering is often inappropriate, and it is necessary to consider anisotropic scattering. Discrete ordinate solutions were found for a conservative plane parallel slab (refer to Table 3). The slab has an optical thickness τ_2 and transparent boundaries, and scatters energy according to the phase function $p(\mu) = 1 + b\mu$. The *S*-4 and *S*-6 discrete ordinate solutions for hemispherical reflectivity are compared to the Eddington approximation and exact results from [12]. The predicted reflectivity of the *S*-4 and *S*-6 discrete ordinate method compares well with exact results [12]. The largest error between the exact and *S*-4 solutions is about 1 percent and occurs at small optical thickness. The *S*-6 and exact results are within 0.25 percent for all optical thicknesses. The discrete ordinate solutions are clearly more accurate over the range of optical thickness and the factor *b* than the Eddington approximation.

Conclusion

Radiative heat transfer in a planar medium has been predicted using the discrete ordinate method. A new set of ordinate values was proposed that satisfy key lower moments of intensity including the half-range first moment, which is important for heat transfer calculations. Discrete ordinate solutions, using these ordinate values and associated weights, are more accurate for heat transfer analysis than solutions found with Gauss quadrature applied on the interval $[-1 \le \mu \le 1]$.

References

1 Love, T. J., and Grosh, R. J., "Radiative Heat Transfer in Absorbing, Emitting and Scattering Media," ASME JOURNAL OF HEAT TRANSFER, Vol. 87, 1965, pp. 161–166.

2 Khalil, E., and Truelove, J., "Calculation of Radiative Heat Transfer in a Large Gas Fired Furnace," *Letters in Heat and Mass Transfer*, Vol. 4, Pergamon Press, 1977.

3 Fiveland, W. A., "A Discrete Ordinates Method for Predicting Radiative Heat Transfer in Axisymmetric Enclosures," ASME Paper No. 82-HT-20, 1982.

4 Fiveland, W. A., "Discrete Ordinates Solutions of the Radiative Transport Equation for Rectangular Enclosures," ASME JOURNAL OF HEAT TRANSFER, Vol. 106, 1984, pp. 699–706.

5 Khalil, E., Schultis, J. K., and Lester, T. W., "Comparison of Three Numerical Methods for Evaluation of Radiant Energy Transfer in Scattering and Heat Generating Media," *Numerical Heat Transfer*, Vol. 5, 1982, pp. 235–252.

6 Viskanta, R., "Radiation Heat Transfer: Interaction With Conduction and Convection and Approximate Methods in Radiation," *Proceedings of the Seventh International Heat Transfer Conference*, Munich, Germany, 1982, pp. 103–121.

7 Chandrasekhar, S., *Radiative Transfer*, Clarendon Press, Oxford, 1950.

8 Lathrop, K. D., "Use of Discrete-Ordinate Methods for Solution of Photon Transport Problems," *Nuclear Science and Engineering*, Vol. 24, 1966.

9 *Handbook of Mathematical Functions*, M. Abramowitz and I. Stegun, eds., U.S. Department of Commerce and National Bureau of Standards, Series 55, 1964, p. 916.

10 Heaslet, M., and Warming, R., "Radiative Transfer and Wall Temperature Slip in an Absorbing Planar Medium," *Int. J. of Heat and Mass Transfer*, Vol. 8, 1965, pp. 979–994.

11 Clark, B. A., "The Development and Application of the Discrete Ordinates–Transfer Matrix Hybrid Method for Deterministic Streaming Calculations," Los Alamos Report No. LA9357-T, Los Alamos National Laboratory, NM, 1982.

12 Busbridge, I. W., and Orchard, S. E., "Reflection and Transmission of Light by a Thick Atmosphere According to the Phase Function: $1 + x \cos\theta$," *Journal of Astrophysics*, Vol. 149, 1967, pp. 655–664.

Measurement of the Reflectance of Tooth Enamel

R. F. Boehm[1] and G. R. Cunnington, Jr.[2]

Introduction

There has been some interest over the past several years in the modeling of thermal processes in teeth. See, for example, Boehm (1985) and Spierings et al. (1984). Included in the motivation are the desires to investigate temperatures in restoration processes in dentistry and to probe new dental disease preventive treatment methods, some using lasers (Boehm, 1985). In many cases a reasonably accurate representation of the thermal radiation effects would be of value.

Measurement of radiative properties of teeth is a very complicated situation. This is true for a variety of reasons. First, the enamel portion of the tooth is translucent in the visible

[1]Professor of Mechanical Engineering, Mechanical and Industrial Engineering Department, University of Utah, Salt Lake City, UT 84112; Fellow ASME.

[2]Senior Member Research Laboratory, Lockheed Palo Alto Research Laboratory, Palo Alto, CA 94304.

Contributed by the Heat Transfer Division for publication in the JOURNAL OF HEAT TRANSFER. Manuscript received by the Heat Transfer Division February 18, 1986.

Table 2 Radiative heat flux and incident energy for a one-dimensional conservative slab with gray boundaries

			Radiant Heat Flux, q_1			Incident Energy, G_1		
ϵ_1	ϵ_2	τ_2	G-6	S-6	Exact (10)	G-6	S-6	Exact (10)
0.8	1.0	0.1	0.74240	0.74372	0.74512	1.4440	1.4140	1.3965
		1.0	0.47293	0.48545	0.48599	0.8660	0.8558	0.8499
		3.0	0.26374	0.28008	0.28045	0.5031	0.4912	0.4861
0.8	0.5	0.1	0.41072	0.42653	0.42697	2.5640	2.5172	2.5080
		1.0	0.30917	0.32693	0.32705	1.9140	1.8832	1.8801
		3.0	0.20015	0.21844	0.21903	1.2880	1.2668	1.2558
0.8	0.1	0.1	0.06231	0.09675	0.09669	3.7420	3.6628	3.6622
		1.0	0.05796	0.09075	0.09044	3.5212	3.4120	3.4138
		3.0	0.05028	0.07940	0.07958	3.1520	3.0000	3.0029

Table 3 Diffuse hemispherical reflectance of a conservative slab for scattering with a phase function $p(\mu) = 1 + B\mu$

Optical Thickness	Hemispherical Reflectivity			
τ_2	Eddington	S-4	S-6	Exact (12)
		b = 0.0		
1.0	0.4286	0.4492	0.4475	0.4466
2.0	0.6000	0.6108	0.6105	0.6099
3.0	0.6923	0.6995	0.6993	0.6984
4.0	0.7500	0.7548	0.7548	0.7540
5.0	0.7895	0.7931	0.7931	0.7923
6.0	0.8182	0.8209	0.8209	0.8203
7.0	0.8400	0.8425	0.8425	0.8417
8.0	0.8571	0.8594	0.8594	0.8585
9.0	0.8710	0.8728	0.8728	0.8721
10.0	0.8824	0.8842	0.8842	0.8833
		b = 0.5		
1.0	0.3846	0.4081	0.4062	0.4055
2.0	0.5556	0.5699	0.5688	0.5678
3.0	0.6522	0.6609	0.6608	0.6599
4.0	0.7143	0.7204	0.7204	0.7195
5.0	0.7576	0.7622	0.7622	0.7614
6.0	0.7895	0.7931	0.7931	0.7923
7.0	0.8140	0.8170	0.8170	0.8162
8.0	0.8333	0.8358	0.8358	0.8351
9.0	0.8491	0.8511	0.8511	0.8505
10.0	0.8621	0.8629	0.8629	0.8633
		b = 1.0		
1.0	0.3333	0.3606	0.3583	0.3577
2.0	0.5000	0.5172	0.5162	0.5154
3.0	0.6000	0.6093	0.6092	0.6102
4.0	0.6667	0.6750	0.6750	0.6738
5.0	0.7143	0.7180	0.7180	0.7195
6.0	0.7500	0.7557	0.7557	0.7540
7.0	0.7778	0.7791	0.7791	0.7810
8.0	0.8000	0.8046	0.8046	0.8026
9.0	0.8182	0.8223	0.8223	0.8203
10.0	0.8333	0.8330	0.8330	0.8351

tion results compare better with the exact solution [10] than the *G*-6 solution. For incident energy, the *S*-6 errors increase as the emissivity increases. The largest error in the *S*-6 solutions is about 1 percent. The *G*-6 solution errors increase slightly (~ 1 percent) with increasing optical thickness ($1.0 \le \tau \le 3.0$). The *G*-6 solution errors are about 3 percent at $\epsilon_2 = 1.0$ and are about 5 percent at $\epsilon_2 = 0.1$. The increase in error with decreasing surface emissivity is likely due to the inaccurate surface heat flux at $\epsilon_2 = 0.1$, which affects the radiant intensity and therefore the incident energy.

(c) Anisotropic Scattering. The assumption of isotropic scattering is often inappropriate, and it is necessary to consider anisotropic scattering. Discrete ordinate solutions were found for a conservative plane parallel slab (refer to Table 3). The slab has an optical thickness τ_2 and transparent boundaries, and scatters energy according to the phase function $p(\mu) = 1 + b\mu$. The *S*-4 and *S*-6 discrete ordinate solutions for hemispherical reflectivity are compared to the Eddington approximation and exact results from [12]. The predicted reflectivity of the *S*-4 and *S*-6 discrete ordinate method compares well with exact results [12]. The largest error between the exact and *S*-4 solutions is about 1 percent and occurs at small optical thickness. The *S*-6 and exact results are within 0.25 percent for all optical thicknesses. The discrete ordinate solutions are clearly more accurate over the range of optical thickness and the factor *b* than the Eddington approximation.

Conclusion

Radiative heat transfer in a planar medium has been predicted using the discrete ordinate method. A new set of ordinate values was proposed that satisfy key lower moments of intensity including the half-range first moment, which is important for heat transfer calculations. Discrete ordinate solutions, using these ordinate values and associated weights, are more accurate for heat transfer analysis than solutions found with Gauss quadrature applied on the interval $[-1 \le \mu \le 1]$.

References

1 Love, T. J., and Grosh, R. J., "Radiative Heat Transfer in Absorbing, Emitting and Scattering Media," ASME JOURNAL OF HEAT TRANSFER, Vol. 87, 1965, pp. 161–166.

2 Khalil, E., and Truelove, J., "Calculation of Radiative Heat Transfer in a Large Gas Fired Furnace," *Letters in Heat and Mass Transfer*, Vol. 4, Pergamon Press, 1977.

3 Fiveland, W. A., "A Discrete Ordinates Method for Predicting Radiative Heat Transfer in Axisymmetric Enclosures," ASME Paper No. 82-HT-20, 1982.

4 Fiveland, W. A., "Discrete Ordinates Solutions of the Radiative Transport Equation for Rectangular Enclosures," ASME JOURNAL OF HEAT TRANSFER, Vol. 106, 1984, pp. 699–706.

5 Khalil, E., Schultis, J. K., and Lester, T. W., "Comparison of Three Numerical Methods for Evaluation of Radiant Energy Transfer in Scattering and Heat Generating Media," *Numerical Heat Transfer*, Vol. 5, 1982, pp. 235–252.

6 Viskanta, R., "Radiation Heat Transfer: Interaction With Conduction and Convection and Approximate Methods in Radiation," *Proceedings of the Seventh International Heat Transfer Conference*, Munich, Germany, 1982, pp. 103–121.

7 Chandrasekhar, S., *Radiative Transfer*, Clarendon Press, Oxford, 1950.

8 Lathrop, K. D., "Use of Discrete-Ordinate Methods for Solution of Photon Transport Problems," *Nuclear Science and Engineering*, Vol. 24, 1966.

9 *Handbook of Mathematical Functions*, M. Abramowitz and I. Stegun, eds., U.S. Department of Commerce and National Bureau of Standards, Series 55, 1964, p. 916.

10 Heaslet, M., and Warming, R., "Radiative Transfer and Wall Temperature Slip in an Absorbing Planar Medium," *Int. J. of Heat and Mass Transfer*, Vol. 8, 1965, pp. 979–994.

11 Clark, B. A., "The Development and Application of the Discrete Ordinates–Transfer Matrix Hybrid Method for Deterministic Streaming Calculations," Los Alamos Report No. LA9357-T, Los Alamos National Laboratory, NM, 1982.

12 Busbridge, I. W., and Orchard, S. E., "Reflection and Transmission of Light by a Thick Atmosphere According to the Phase Function: $1 + x \cos \theta$," *Journal of Astrophysics*, Vol. 149, 1967, pp. 655–664.

Measurement of the Reflectance of Tooth Enamel

R. F. Boehm[1] and G. R. Cunnington, Jr.[2]

Introduction

There has been some interest over the past several years in the modeling of thermal processes in teeth. See, for example, Boehm (1985) and Spierings et al. (1984). Included in the motivation are the desires to investigate temperatures in restoration processes in dentistry and to probe new dental disease preventive treatment methods, some using lasers (Boehm, 1985). In many cases a reasonably accurate representation of the thermal radiation effects would be of value.

Measurement of radiative properties of teeth is a very complicated situation. This is true for a variety of reasons. First, the enamel portion of the tooth is translucent in the visible

[1]Professor of Mechanical Engineering, Mechanical and Industrial Engineering Department, University of Utah, Salt Lake City, UT 84112; Fellow ASME.

[2]Senior Member Research Laboratory, Lockheed Palo Alto Research Laboratory, Palo Alto, CA 94304.

Contributed by the Heat Transfer Division for publication in the JOURNAL OF HEAT TRANSFER. Manuscript received by the Heat Transfer Division February 18, 1986.

region of the spectrum, is a scatterer to incident radiation, and is underlain by dentine, which is generally opaque. The translucent nature of enamel and its minor differences in composition result in optical property variations between teeth, even from the same person. Secondly, the tooth is a composite structure, and the enamel layer is found to be of varying thickness around the tooth. The thickness of the enamel also varies from tooth to tooth in the same individual, and from individual to individual.

Reports of the measurements of the reflectance of tooth enamel, either alone or with the complete tooth structure, are very limited. Much interest has existed in the measurement of the relative transmission properties (usually in terms of linear absorptance) of ground tooth enamel powder in the infrared for the purpose of developing a basic understanding of enamel's chemical makeup. Very few attempts to measure the radiation properties of tooth surfaces have been made.

Boehm and Gregory (1975) reported measurements of transmission through carefully prepared human tooth enamel slabs of discrete thicknesses (less than 1 mm) with essentially parallel surfaces. These measurements were made over the visible wavelength region, approximately 0.46 μm to 0.65 μm. They then used the measurements to infer values of reflectivity, index of refraction, and extinction coefficient. Scattering effects were neglected in the calculation, and this was recognized as being a shortcoming of the approach used.

A detailed study of the scattering aspects of both human and bovine enamel was reported by Spitzer and Ten Bosch (1975). They measured the reflectance and transmission of thin slabs of dental enamel in the wavelength range between 0.22 μm and 0.70 μm using an integrating sphere. While their particular interest was an analysis of the true scattering and absorption coefficients, they did present a single curve of the spectral reflectance of a polished and etched bovine enamel slab of 0.17 mm thickness. Because of their detailed analysis of the scattering phenomena, they were able to make a more realistic estimate of the index of refraction for enamel than did Boehm and Gregory (1975). Spitzer and Ten Bosch found values of index of refraction of approximately 1.62 over most of the wavelength range they investigated, increasing to about 1.72 at the lower wavelength values. The values they tabulated are in good agreement with comparable values for hydroxiapatite material, a major constituent of tooth enamel.

It was our desire to estimate the spectral properties of typical tooth enamel. Clearly, many approaches could be used because the physical nature of tooth enamel and its irregular formation on teeth yield a very complicated geometry and enamel composition. Obviously no single approach would satisfy all of the needs regarding optical properties of tooth enamel and the even more complex complete tooth structure. Depending upon the situation, any experiment may not be applicable to a given application. Use of a complete tooth structure could yield results that might be unique to that particular tooth. On the other hand, any measurement of enamel alone has certain shortcomings also. A particular set of measurements is described below.

Experimental Technique

Enamel slabs were cut from "flat" portions of both bovine and human incisors. The cut surfaces were then smoothed to various degrees by using successively finer grades of emery cloth, over which the slabs were reciprocated with the cloth resting upon a plane surface. The resulting enamel samples had one irregular surface (that of the naturally occurring outer enamel) and one plane surface. A measurement of the maximum thickness characterized the slabs sufficiently for the present measurement program, but this clearly does not completely describe the actual geometry. The slabs were kept moist except for the brief periods of preparation from the time of tooth extraction until the measurements were performed. The exteriors of the samples were blotted dry just prior to the mounting in the reflectance-measuring device.

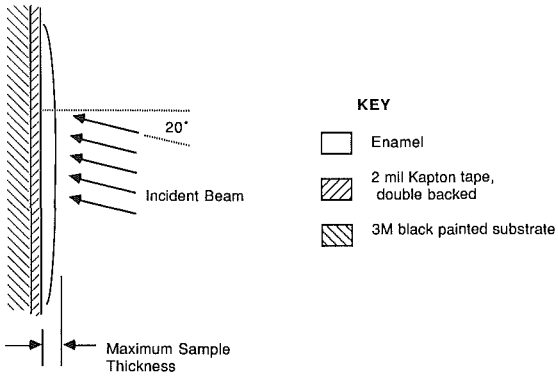

Fig. 1 A sketch of the experimental test arrangement of the enamel sample and backing assembly. Also shown is the typical angle of beam incidence used during the measurements reported here.

To obtain data, the smoothed surfaces were applied with a dual-surface adhesive tape to the sample holder of an integrating sphere reflectance accessory (Gier-Dunkle Model SP210) used in conjunction with a monochromator (Perkin-Elmer Model 98 prism monochromator with fused SiO_2 prism). This device determines the directional-hemispherical spectral reflectance as defined by Siegel and Howell (1981). For measuring the reflectance, the specimen was mounted centrally in the 24-cm-dia sphere and illuminated monochromatically with energy in an f/60 beam coming from the monochromator. Accuracy of the reflectance measurements is 0.005 in absolute reflectance units.

The backing system that held the samples in place consisted of a layer of Kapton film (2 mil) coated on both surfaces with an adhesive layer. This adhesive tape held the rear surface of the specimen to a 3M black-painted holder in the integrating sphere. A sketch of the sample and holding arrangement is shown in Fig. 1. Since it will be noted later that the samples transmitted some energy, the reflectance of the attaching arrangement can be important. The reflectance of the base assembly, including the attaching tape, was taken from the measured reflected energy from an f/60 monochromatic beam incident at 20 deg with the normal to the surface (see more discussion on this point below). The substrate assembly had a reflectance of 0.05 to 0.07 over the wavelength region of 0.35 to 2.4 μm.

In the case of the device used, the angle of incidence was 20 deg from the normal. Generally the value so obtained closely approximates the reflectance for normal incidence, that is, where the incident beam is perpendicular to the surface being investigated. Some measurements were also made of the effect of orientation at three discrete wavelengths. In all cases a sample irradiation area of about 5 mm high by 0.1 mm to 1.5 mm wide was used, the latter range of dimensions being the monochromator slit width.

Since there can be significant transmission of energy through the samples prepared in the manner described, transmittance measurements were made to complete the experimental characterization. These measurements were made with the samples mounted in front of a 2.5 mm by 5 mm aperture at the entrance port of the integrating sphere, after checking to make sure that 100 percent of the incident beam passed through the aperture opening. The angle of incidence for all of the transmission data was normal to the tooth surface. Note that transmitted energy during the reflectance-measurement mode must be reflected from the backing and then be transmitted back out through the sample to contribute to what was considered to be the reflected energy.

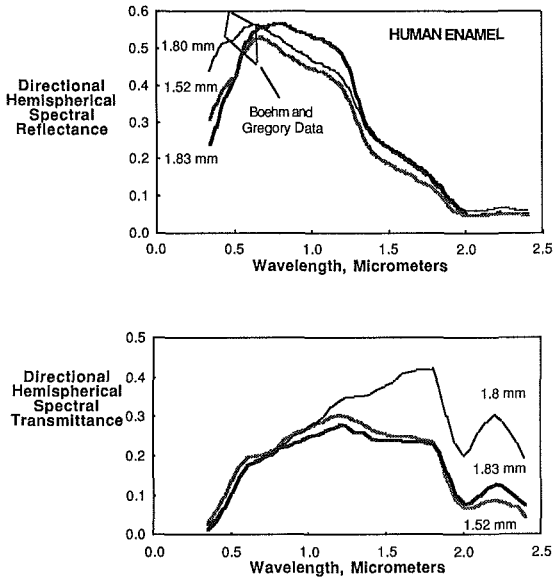

Fig. 2 The spectral hemispherical reflectance (upper graph) and transmittance (lower graph) for three slabs of human dental enamel shown for the wavelength range of 0.35 μm to 2.4 μm. The slab maximum thicknesses are shown as parameters. In all cases a 20 deg beam angle of incidence (relative to the normal direction) was used. Also shown on the upper graph is the approximate location of the data of Boehm and Gregory (1975).

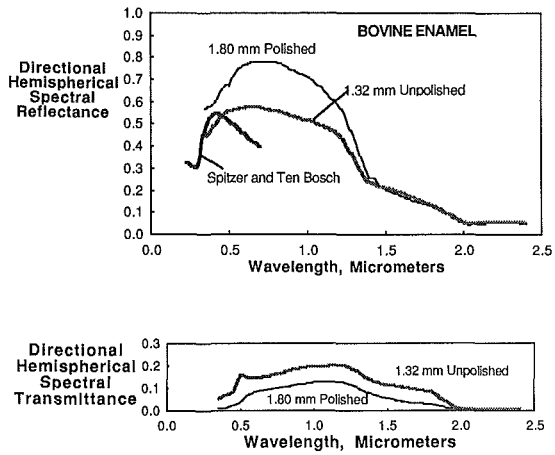

Fig. 3 The spectral hemispherical reflectance (upper graph) and transmittance (lower graph) for two slabs of bovine dental enamel shown for the wavelength range of 0.35 μm to 2.4 μm. The slab maximum thicknesses are shown as parameters. In all cases a 20 deg beam angle of incidence (relative to the normal direction) was used. Also shown on the upper graph are the data of Spitzer and Ten Bosch (1975) for related measurements.

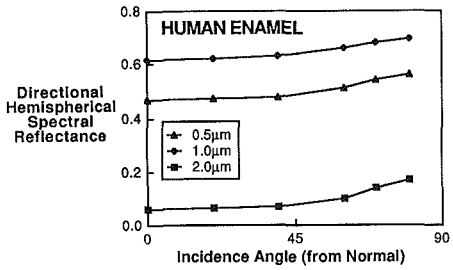

Fig. 4 A plot of the variation of spectral hemispherical reflectance for human tooth enamel is given as a function of beam incidence angle and wavelength

In all, three samples of human tooth enamel were evaluated. Two samples of bovine enamel, one with an irradiated surface as taken from the animal and one with that surface highly polished, were also measured. One set of measurements for the angular effect of beam incidence was made for a human sample at three wavelengths.

Results and Discussion

The results of the measurements of spectral hemispherical reflectance and transmittance of the human and bovine tooth samples are shown in Figs. 2 and 3, respectively. In all cases the reflectance increases with increasing wavelength to a peak value in the 0.6–0.8 μm range, and then it decreases as the wavelength is increased further. All samples showed a significant drop-off of reflectance readings in the 1.2 to 1.4 μm range, reaching a low value of about 5 percent near 2 μm. The reflectance remained fairly constant at this value over the remainder of the range investigated (out to 2.4 μm). While there is a variation in the reflectance readings between samples, particularly in the visible region of the spectrum, this variation did not seem to correlate strongly with the thickness of the sample. Instead, this difference between samples is probably due to apparent color difference effects (possibly due to trace element composition) in the various teeth used in the study.

Variations in the spectral transmittance effects are more pronounced than are the reflectance effects. This is particularly true in the infrared end of the measurements. Transmission is seen to be low in the short wavelength portion of the visible, to reach a peak about 1.2 μm, and then to decrease to very low values above 2.0 μm. It might be anticipated that water in tooth enamel might affect the absorption characteristics. Water absorption is not seen in the 1.3 to 1.5 μm region, but it may be present in the 1.8 to 2 μm band.

A plot of how the reflectance values vary with sample irradiation angle is shown in Fig. 4. Results given there are typical of dielectric materials that reflect diffusely.

The nature of the enamel can have a large effect on the radiation properties. This can be clearly seen from the two samples for bovine enamel. Polishing greatly increases the reflectivity in the visible region (see Fig. 3).

Comparisons between the reflectance results reported here and the previously reported work are given in Figs. 2 and 3. Figure 2 shows the results of our work with human dental enamel compared to the results of Boehm and Gregory (1975). A comparison of the bovine readings is shown in Fig. 3 and compared to the somewhat differently prepared sample readings given by Spitzer and Ten Bosch (1975). Considering the differences in sample preparation, measurement techniques, and normal variation among enamel samples, similar results are shown.

From the measurements made here, there is clear evidence that dental enamel is highly absorbing for wavelengths greater than (about) 1.5 μm. Both the reflectance and the transmittance show low values near 2.0 μm. This same general conclusion can also be reached by examining the transmission measurements of ground enamel powders (Boehm, 1985). The infrared radiation properties could be very critical in the evaluation of laser processes on teeth (Boehm, 1985), and more measurements should be made farther into the infrared region.

It must be kept in mind that each application may have different values of reflectance compared to those reported here, for the various reasons already discussed. The transmission effects and the backing will have some effect upon the result (Hsieh and Coldewey, 1975). Using the backing reflectance data and transmittance results shown here in Fig. 2, it appears that the maximum possible contribution to the overall reflectance from energy being transmitted through the sample, reflecting from the backing and being transmitted back

through the sample is on the order of 1 percent. Based upon our experience, the major variations between samples demonstrated here could very easily be due to differences in the makeup of dental enamel.

Conclusions and Recommendations

1 Measurements have been made on the spectral hemispherical reflectance and transmittance of human and bovine dental enamel samples in the wavelength region 0.35 μm to 2.4 μm. The samples were cut from outer portions of teeth, had maximum thicknesses ranging between 1.32 and 1.88 mm, and were irradiated from the normal exterior surface.

2 All reflectance variations were similar, starting at low values near 0.35 μm, rising to a peak value of between 50 and 60 percent in the wavelength range of 0.6 to 0.8 μm, and then falling to a low value (about 5 percent) near 2.0 μm. The largest variation between samples occurred near the largest value of reflectance, and this may have been due largely to the composition differences between teeth. Effects of the tooth thickness and irradiation interaction with the sample mounting arrangement could have had an effect on this also. Polishing of tooth enamel apparently greatly increases the reflectance in the visible region.

3 Values for transmittance of dental enamel show a variation similar to that shown by the reflectance, except that the peak of the transmittance curve often occurs at approximately 1.2 μm. The transmittance is low in the ultraviolet and the infrared.

4 Results of reflectance measurements of the effect of angle of incidence on human dental enamel show behavior characteristic of a diffusely reflecting dielectric material.

5 Comparison to the limited previous data shows good agreement considering the differences in the experimental approaches used and the normal variation among teeth.

6 Measurements similar to those made here should be made in the longer wavelength portion of the spectrum, perhaps out to 20 μm. This would enable the full evaluation of laser interaction processes on teeth, as well as a full representation of radiation effects during thermal modeling.

Acknowledgment

The use of the experimental apparatus located at the Lockheed Palo Alto Research Laboratory is gratefully acknowledged.

References

Boehm, R. F., and Gregory, R. W., 1975, "An Estimation of the Optical Properties of Human Tooth Enamel in the Visible Wavelength Region," AIAA Paper No. 75-714.

Boehm, R. F., 1985, "Heat Transfer in Teeth," in: *Heat Transfer in Medicine and Biology*, Vol. II, A Shitzer and R. Eberhart, eds., Plenum Press, New York, Chap. 24, pp. 307–327.

Hsieh, C. K., and Coldewey, R. W., 1975, "Errors in Reflectance Measurement of Transparent Substances Due to Nonblackness of Backing Materials," *Solar Energy*, Vol. 17, pp. 201–202.

Siegel, R., and Howell, J., 1981, *Thermal Radiation Heat Transfer*, 2nd ed., McGraw-Hill, New York, Chap. 3.

Spierings, T., de Vree, J., Peters, M., and Plasschaert, A., 1984, "The Influence of Restorative Dental Materials on Heat Transmission in Human Teeth," *Journal of Dental Research*, Vol. 63, pp. 1096–1100.

Spitzer, D., and Ten Bosch, J. J., 1975, "The Absorption and Scattering of Light in Bovine and Human Dental Enamel," *Calcified Tissue Research*, Vol. 17, pp. 129–137.